Matthew J. Budoff
Stephan S. Achenbach
Harvey S. Hecht
Jagat Narula
Editors

Atlas of Cardiovascular Computed Tomography

Second Edition

Springer

Atlas of Cardiovascular Computed Tomography

Matthew J. Budoff • Stephan S. Achenbach
Harvey S. Hecht • Jagat Narula
Editors

Atlas of Cardiovascular Computed Tomography

Second Edition

Springer

Editors
Matthew J. Budoff
Los Angeles Biomedical Research Institute
UCLA
Torrance, California, USA

Stephan S. Achenbach
Department of Cardiology
Universitätsklinikum Erlangen
Erlangen, Germany

Harvey S. Hecht
Mount Sinai Hospital
New York City, New York, USA

Jagat Narula
Department of Cardiology
Mount Sinai Hospital
New York City, New York, USA

Previously published by Springer, New York (2007) 978-1-57340-267-5
ISBN 978-1-4471-7356-4 ISBN 978-1-4471-7357-1 (eBook)
https://doi.org/10.1007/978-1-4471-7357-1

Library of Congress Control Number: 2017964096

Printed on acid-free paper

This Springer imprint is published by the registered company Springer-Verlag London Ltd. part of Springer Nature.
The registered company address is: The Campus, 4 Crinan Street, London, N1 9XW, United Kingdom

Preface

Over the past decade, the technology of cardiovascular CT and its clinical utility have grown enormously. Appropriateness use criteria and credentialing standards are being developed at a record pace.

Physicians currently training in cardiology and radiology undergo mandatory training in cardiac CT, and the American College of Cardiology, American Heart Association, Society of Cardiovascular Computed Tomography and American College of Radiology have published scientific statements and guidelines to support the use of this diagnostic modality in clinical practice. Although this rapid evolution of knowledge and experience has been accompanied by a large number of scientific publications, there has been a relative lack of high-quality, practical, and comprehensive training material. In an area based on imaging, a comprehensive atlas should form a central piece of information and reference. We have assembled the foremost authorities in the field to author chapters for this Atlas of Cardiovascular Computed Tomography. The images within will provide the cardiac CT enthusiast with a didactically useful introduction to the field yet sufficiently comprehensive to provide the advanced user with excellent examples of common and uncommon CT findings.

The evolution of cardiovascular CT imaging has been accompanied by significant controversy regarding its clinical applicability. However, the breathtakingly rapid improvement in CT imaging technology, especially since the introduction of advanced multidetector CT systems, has vaulted CT imaging into mainstream cardiology practice, and there is uniform consensus that its utility will continue to expand in the coming years. Imaging with multidetector CT allows assessment of coronary artery stenoses with stunning spatial and temporal resolution. Beyond the mere detection of flow-limiting stenoses in coronary artery disease, great strides have been made in the identification of plaque characteristics that confer higher risk. The diagnosis of coronary artery disease has evolved from the assessment of disease sequelae to the early detection of the pathologic process itself, before the consequences become clinically manifest through ischemic symptoms, myocardial infarction, or sudden death. As presented in the following chapters, cardiac CT has matured significantly and become a valid risk-stratifying tool for the early detection of atherosclerosis through coronary artery calcium scanning, a possible replacement for noninvasive exercise testing as the test of choice for the evaluation of chest pain in stable patients, and a powerful tool to image for congenital heart disease, venoatrial anatomy before electrophysiologic testing, and peripheral artery disease. The atlas focuses on the pearls and pitfalls of cardiovascular CT and not only offers excellent images but also discusses problems encountered during CT imaging and suboptimal results.

We are confident that this atlas offers an exceptional compilation of information and comprehensively reflects the current state of the art in cardiovascular CT. We believe that you will find this atlas as enjoyable as it is educational.

Torrance, CA, USA — Matthew J. Budoff
Erlangen, Germany — Stephan S. Achenbach
New York, NY, USA — Harvey S. Hecht
New York, NY, USA — Jagat Narula

Contents

Contributors

Suhny Abbara Department of Radiology, Division of Cardiothoracic Imaging, UT Southwestern Medical Center, Dallas, TX, USA

Jamil A. Aboulhosn Ronald Reagan/UCLA Medical Center, Ahmanson Adult Congenital Heart Disease Center, Los Angeles, CA, USA

Stephan S. Achenbach Department of Cardiology, University of Erlangen, Erlangen, Germany

Amir Ahmadi Department of Cardiology, Icahn School of Medicine at Mount Sinai, New York, NY, USA

Philipp Blanke Department of Radiology, Centre for Heart Valve Innovation, St Paul's Hospital, Vancouver, BC, Canada

Matthew J. Budoff UCLA Los Angeles Biomedical Research Institute, Torrance, CA, USA

Peter S. Fail Department of Interventional Cardiology, Cardiovascular Institute of the South/ Terrebonne General Medical Center, Houma, LA, USA

Maros Ferencik Knight Cardiovascular Institute, Oregon Health and Science University, Portland, OR, USA

Khristine Ghemigian Department of Radiology, Massachusetts General Hospital and Harvard Medical School, Boston, MA, USA

Harvey S. Hecht Department of Cardiology, Icahn School of Medicine at Mount Sinai, New York, NY, USA

Udo Hoffmann Department of Radiology, Massachusetts General Hospital, Boston, MA, USA

Annapoorna Kini Department of Cardiology, Icahn School of Medicine at Mount Sinai, New York, NY, USA

Jonathon Leipsic Department of Radiology, St. Paul's Hospital, Vancouver, BC, Canada

Andreas H. Mahnken Department of Diagnostic and Interventional Radiology, Marburg University Hospital, Marburg, Germany

James K. Min Dalio Institute of Cardiovascular Imaging, New York-Presbyterian Hospital and Weill Cornell Medicine, New York, NY, USA

Jamaluddin Moloo Cardiac Vascular Center, University of Colorado, Denver, CO, USA

Vinod Nair Cardiovascular Institute of the South, Houma, LA, USA

Sanjiv M. Narayan Department of Medicine/Division of Cardiology, Stanford University, Stanford, CA, USA

Jagat Narula Mount Sinai Heart, Icahn School of Medicine at Mount Sinai, New York, NY, USA

Edward D. Nicol Department of Cardiac CT, Royal Brompton Hospital, London, UK

Koen Nieman Stanford University School of Medicine, Stanford, CA, USA

Simon P.G. Padley Department of Cardiac CT, Royal Brompton Hospital, London, UK

Priya Pillutla Division of Cardiology, Department of Medicine, Los Angeles Medical Center, Harbor-University of California, Torrance, CA, USA

Kenichi Sakakura CVPath Institute Inc., Gaithersburg, MD, USA

Farhood Saremi Department of Radiology, University of Southern California, USC University Hospital, Los Angeles, CA, USA

Joshua Schulman-Marcus Department of Cardiology, Albany Medical Center, Albany, NY, USA

Samin Sharma Cardiovascular Institute, Icahn School of Medicine at Mount Sinai, New York, NY, USA

Angus Thompson Department of Radiology, St Paul's Hospital, University of British Columbia, Vancouver, BC, Canada

Quynh A. Truong Department of Radiology, Weill Cornell Medical Center, New York, NY, USA

Renu Virmani CVPath Institute Inc., Gaithersburg, MD, USA

Christopher M. Walker Department of Radiology, Saint Luke's Hospital of Kansas City, Kansas City, MO, USA

Joel Wilson Division of Cardiovascular Medicine, UCSD Medical Center, La Jolla, CA, USA

Kazuyuki Yahagi CVPath Institute Inc., Gaithersburg, MD, USA

Historical Perspective

1

Stephan S. Achenbach

On November 8, 1895, Wilhelm Conrad Röntgen (1845–1923) discovered X-rays in his laboratory at the University of Würzburg, Germany. In 1901, he was awarded the first Nobel Prize in Physics "*in recognition of the extraordinary services he has rendered by the discovery of the remarkable rays subsequently named after him.*" Röntgen declined to patent his discovery, so that it could be more widely used. Consequently, imaging with X-rays was rapidly introduced into medical diagnostics.

The diagnostic capabilities of X-ray imaging were dramatically increased when computed tomography (CT) was developed in the late 1960s. X-ray CT became possible because of the advent of digital data processing through computers and the availability of mathematical methods to generate cross-sectional images based on numerous X-ray projections obtained from various orientations. The required mathematical methods had been pioneered by scientists such as the Norwegian Niels Henrik Abel (1802–1829), the Austrian Johann Radon (1887–1956), and the South African physicist Allen McLeod Cormack (1924–1988), who, in fact, built a prototype tomographic device in 1963 but was not interested in any practical applications [1]. Independently, the British engineer Sir Godfrey Newbold Hounsfield (1919–2004) conceived the concept of computed tomography X-ray imaging in the late 1960s while he was working as an inventor for a company called "Electrical and Musical Industries" (EMI) and was generously funded by income EMI generated through the tremendous commercial success that the Beatles enjoyed under their cover [2]. Allegedly, Hounsfield developed the basic idea during an outing in the country. Unaware of previous work, he solved the underlying mathematical problem and constructed a prototype CT scanner in 1967, originally using a source of gamma radiation, then to be replaced by an X-ray tube. Initial acquisitions on preserved human brains took 9 days for a single cross-sectional image. The invention was patented in 1968. On October 1, 1971, X-ray CT was introduced into medical practice when a first patient with a cerebral cyst underwent a brain scan at Atkinson Morley Hospital in Wimbledon, London, United Kingdom. The scan time was 4.5 min to generate an image 13 mm thick with a resolution of 80 × 80 pixels. Technical progress rapidly improved both acquisition protocols and image quality. CT scanners, initially with scan times of about 20 s per image, became commercially available through numerous companies from 1973 on. In 1979, Cormack and Hounsfield jointly received the Nobel Prize in Physiology or Medicine.

This chapter is dedicated to the memory of David G. King (1947–2004), an assistant to Sir Godfrey Hounsfield in his early career and a tireless supporter of research in cardiac CT, often referred to as the "father of coronary calcium scanning."

S.S. Achenbach
Department of Cardiology, University of Erlangen,
Erlangen, Germany
e-mail: stephan.achenbach@uk-erlangen.de

M.J. Budoff et al. (eds.), *Atlas of Cardiovascular Computed Tomography*, https://doi.org/10.1007/978-1-4471-7357-1_1

Approaches to Cardiac Computed Tomography

The principle of computed tomography (CT) is to obtain a cross-sectional image based on X-ray acquisitions obtained from various orientations in a single slice of the body. Roughly speaking, at least 180° of projections are required (as acquisitions from exactly opposite directions would yield identical attenuation data). CT systems that required mechanical motion of an X-ray source around the body had scan times of approximately 3 s per slice into the 1980s. Even after the introduction of slip-ring technology, which allowed continuous rotation of the gantry, and "helical" or "spiral" acquisition, which combined continuous gantry rotation with continuous table motion in 1989 by Willi Kalender [3], image acquisition times remained in the 1-s range, which was too slow for imaging of the rapidly moving heart. All the same, interest in extending the advantages of tomographic imaging to the heart led to specific developments that were designed to maximize the temporal resolution of CT and allow synchronization to the heartbeat through the patient's ECG, so that cardiac imaging would become possible.

One approach developed in the early 1980s was the Dynamic Spatial Reconstructor, which consisted of 28 X-ray tubes that rotated around the patient at 50 rotations per minute; the images were amplified by 28 TV cameras mounted behind a curved fluorescent screen (58-cm radius) opposite the tubes. Temporal resolution was 16 ms per cross-sectional image and cardiac imaging was possible, but because of its immense size and weight (15 tons), the system was not practical for clinical use and only one such device was ever installed (at the Mayo Clinic in Rochester, MN) [4].

A second approach was the "electron beam computed tomography" (EBCT) system introduced in the late 1980s [5]. Instead of an X-ray tube, which must rotate mechanically around the patient, it used an electron beam, which was deflected by electromagnetic coils to sweep across semicircular targets arranged around the patient. Where the electron beam hit the targets, X-rays were created. The radiation passed through the patient and attenuation was recorded by stationary detectors arranged on the opposite side. Temporal resolution was high at 100 ms, but slice thickness was limited to 1.5 or 3.0 mm, image noise was relatively high, and the cost was substantially more than conventional, mechanical CT systems. The EBCT system was initially designed to study myocardial perfusion and cardiac function, but it was not extensively used for this purpose. Instead, pioneers of cardiac CT such as Arthur Agatston and Warren Janowitz demonstrated the utility of CT imaging for coronary calcium assessment in 1989 and subsequent years [6]. Following were the first contrast-enhanced acquisitions to visualize the coronary artery lumen in 1994 and the first reports that coronary artery stenoses could be detected [7–9]. Ultimately, the image quality that could be obtained by EBCT was not sufficient for clinical applications, but its success in visualizing the coronary arteries and the early demonstration of clinical applications for risk stratification and stenosis detection sparked tremendous interest in further developing mechanical CT, with the aim of providing high-resolution imaging of the heart and coronary arteries [10]. This third approach to cardiac CT imaging, which became available around the year 2000, required several developments: First, CT systems with gantry rotation times of 0.5 s or less were combined with ECG-synchronized image reconstruction methods that used only parts of the rotation, so that high temporal resolution could be achieved. Second, strong X-ray tubes provided sufficient output to keep image noise low despite thin-slice acquisition and short acquisition times. Finally, the acquisition of several slices simultaneously allowed the creation of thin images while keeping overall acquisition time short enough to complete an examination with one breathhold. The first systems acquired four slices simultaneously, so that approximately 35–40 s were required to obtain one data set of the heart with a slice thickness of 1.0 mm [10]. Manufacturers rapidly introduced systems with faster rotation and the ability to acquire more and thinner slices. For example, 16-slice CT with 375 ms rotation time was introduced in 2004, and 64-slice CT systems with rotation times of 330 ms became available around 2005. Currently, high-end systems provide rotation times of about 300 ms, and the widest detectors have 320 rows. At a collimated slice thickness of 0.5 mm, a scan volume of 16 cm can be covered, which is sufficient to cover the heart in one single partial rotation.

A further significant direction of development was dual-source CT, first introduced in 2006 [11]. It combines two X-ray tubes and two detectors arranged at an angle of approximately 90°. Hence, dual-source CT permits the collection of the required data in 180° of projections during a quarter rotation of the X-ray gantry, whereas single-source CT requires a half rotation. Dual-source CT therefore improves temporal resolution by a factor of two. With a gantry rotation time of 0.28 s for the latest dual-source CT system, the temporal resolution of each acquired slice is 75 ms. (It does not exactly correspond to a one-quarter rotation time because the two tubes and detectors are not aligned exactly at a 90° angle.)

Overall, numerous hardware advancements have had substantial influence on image quality in cardiac CT, far beyond the rotation time and number of acquired slices. Over the years, CT imaging—which was initially almost entirely focused on visualization of the coronary arteries—has been able to substantially increase robustness, image quality, and clinical applicability for coronary artery visualization (Figs. 1.1, 1.2, 1.3, 1.4, 1.5, 1.6, 1.7, 1.8, and 1.9).

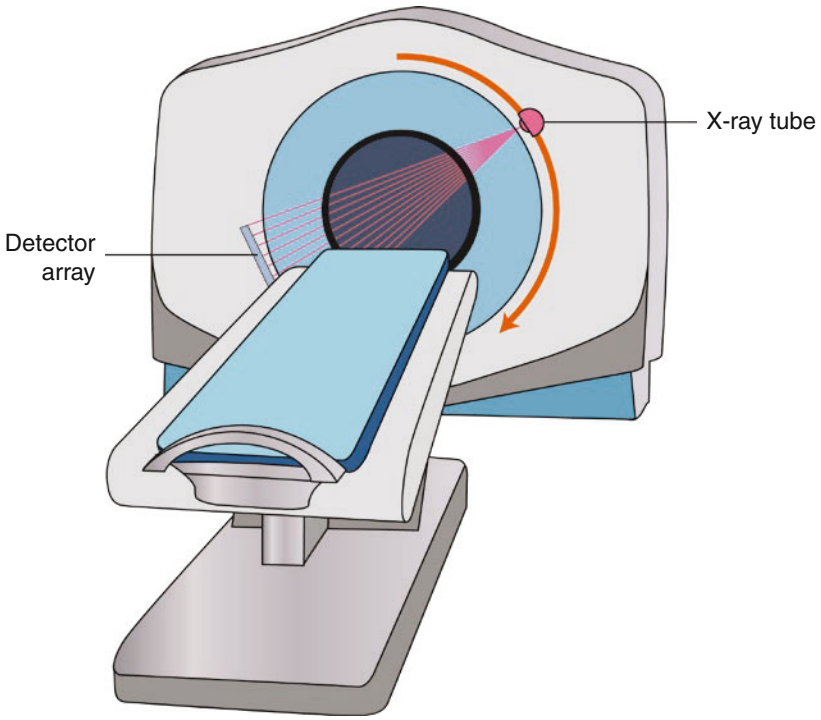

Fig. 1.1 Principle of computed tomography (CT) for imaging. X-ray attenuation data must be acquired from a multitude of projections (at least 180° plus the width of the fan angle of the X-ray beam). This aim is typically achieved by rotating around the patient a gantry that contains an X-ray tube on one side and a detector array on the opposite side. The rotation speed determines the temporal resolution of the acquired image. Systems with multiple detector rows permit the acquisition of more than one cross-sectional image during one rotation

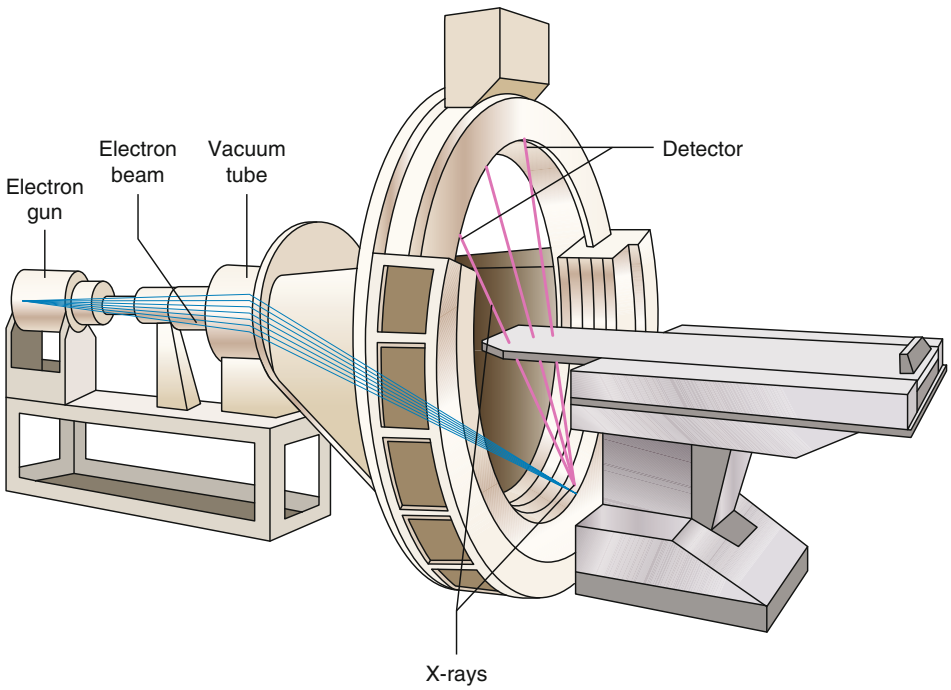

Fig. 1.2 Electron beam CT. The electron beam CT (EBCT) scanner was designed to provide sufficient temporal resolution for cardiac imaging. To avoid rotation of an X-ray tube, an electron beam was created by an electron gun inside a very large vacuum tube. The electron beam was focused and deflected by electronic coils to rapidly sweep across stationary, semicircular targets that were arranged below and around the patient. Where the electron beam hit the targets, X-rays were created. The collimated X-rays penetrated the patient, and attenuation was recorded by stationary detectors. Temporal resolution was 100 ms, with the ability to trigger image acquisition by the patient's ECG. Stepwise motion of the patient table would allow acquisition of a set of approximately 40 slices of 3.0 mm slice thickness to cover the volume of the heart

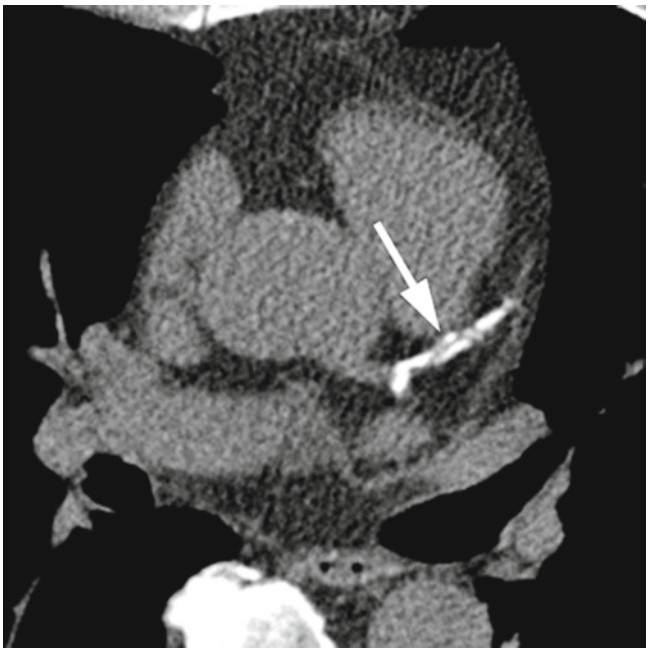

Fig. 1.3 Detection of coronary calcium by EBCT. The first clinical application of cardiac CT was the detection and quantification of coronary calcium for the purpose of risk stratification. Here, a cross-sectional EBCT image (3.0 mm slice thickness, 100 ms acquisition time) shows calcification of the left main bifurcation, proximal left circumflex, and proximal left anterior descending coronary artery (*arrow*)

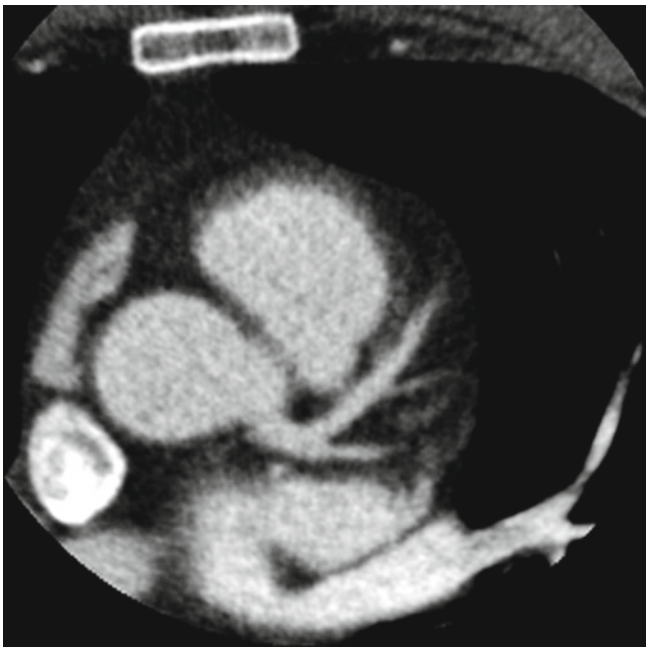

Fig. 1.4 Coronary CT angiography by EBCT. This contrast-enhanced transaxial image shows the proximal left main, left anterior descending, and left circumflex coronary arteries (3.0 mm slice thickness, 100 ms acquisition time)

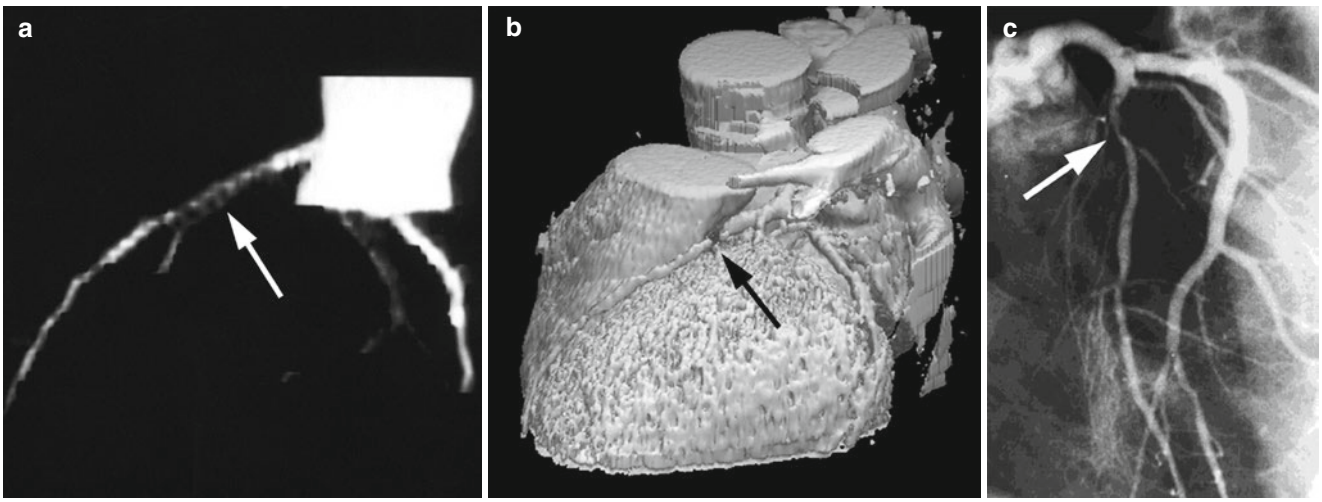

Fig. 1.5 Detection of coronary artery stenoses by EBCT. Multiplanar reconstruction (**a**) and three-dimensional reconstruction (**b**) of the left anterior descending coronary artery show a high-grade stenosis (*arrow*). The invasive coronary angiogram (**c**) confirms the presence of a high-grade stenosis. Though the 3D reconstruction conveys a smooth image impression, the multiplanar reconstruction reveals the relatively crude image quality of EBCT. With 3.0 mm slice thickness per acquired axial image and the need for a breathhold of approximately 40 s, EBCT was not clinically robust enough to reliably detect and rule out coronary artery stenoses

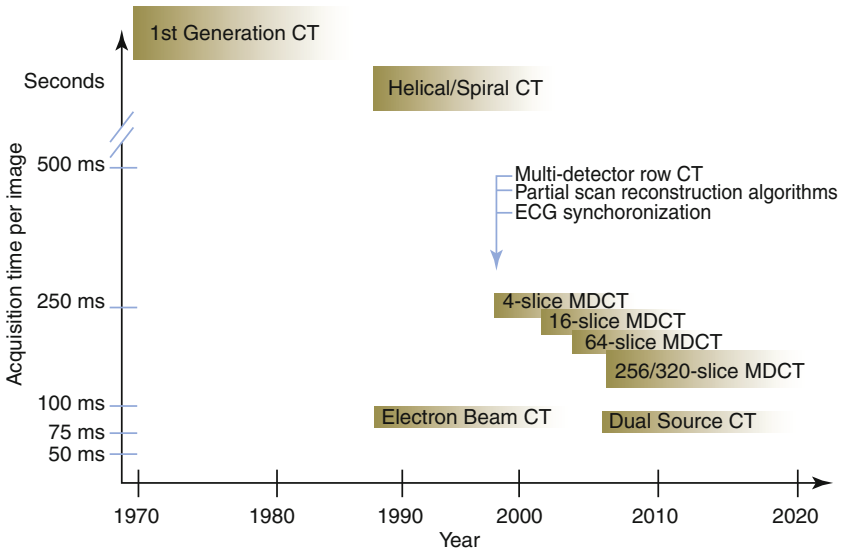

Fig. 1.6 Evolution of technology for cardiac CT. This schematic representation (approximate and not to scale) illustrates the various generations of CT technology in relation to the time of first availability and approximate temporal resolution (time to acquire one cross-sectional image). Note that beyond the acquisition time and number of acquired slices, numerous other factors influence image quality. For multi–detector row CT systems, a higher number of slices does not per se increase temporal resolution, but subsequent generations of CT, while increasing the number of detector rows, typically also provided faster rotation and hence higher temporal resolution. This schematic representation does not consider that by combining data from consecutive heartbeats, some multi–detector row CT systems allow reconstruction of images with shorter data acquisition windows than required for a 180° rotation

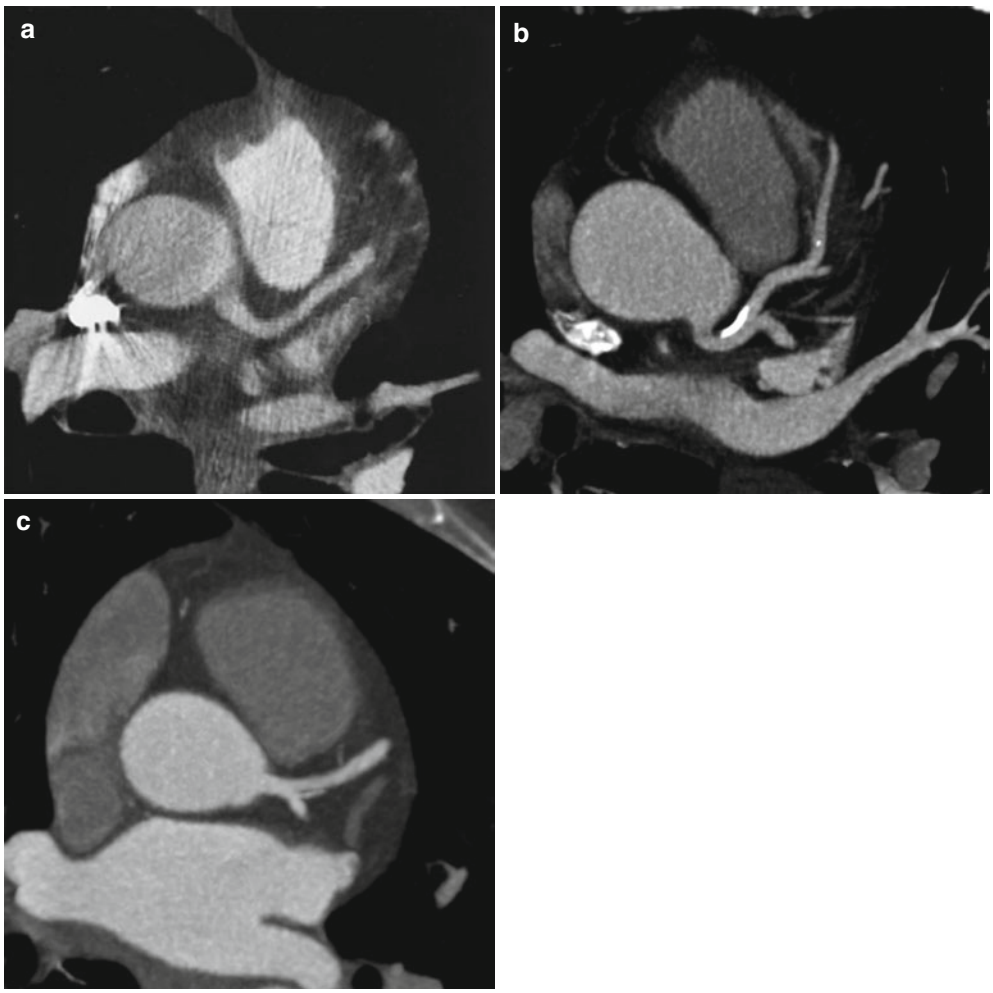

Fig. 1.7 Transaxial contrast-enhanced images obtained with various generations of multi–detector row CT (MDCT): (**a**) Four-slice CT with 4 × 1.0 mm collimation, 500 ms rotation time, and a temporal resolution of 250 ms. (**b**) 16-slice CT with 16 × 0.75 mm collimation, 375 ms rotation time, and a temporal resolution of 185 ms. (**c**) 64-slice CT with 64 × 0.6 mm collimation, 330 ms rotation time, and a temporal resolution of 165 ms

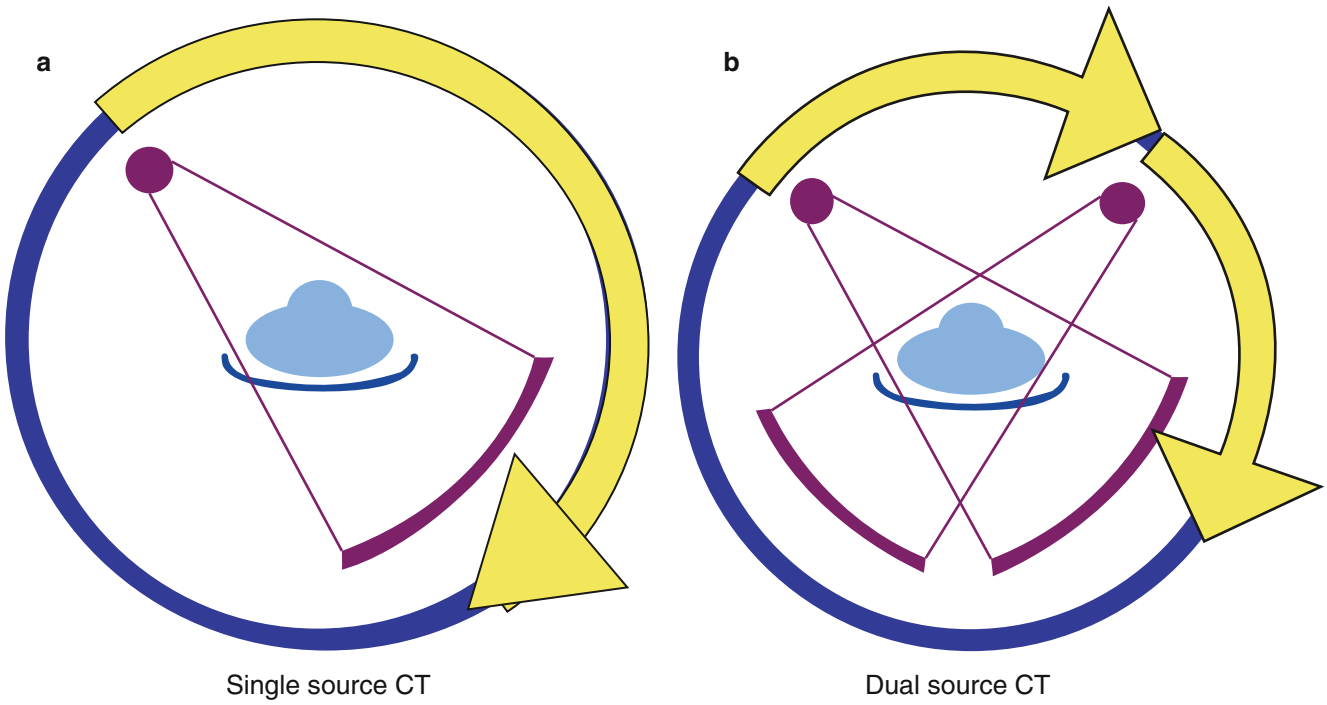

Fig. 1.8 Comparison of single-source and dual-source CT. Acquisition of X-ray data in projections over approximately 180° is required to reconstruct cross-sectional images. (**a**) In single-source CT, this requirement is achieved during approximately a half rotation of the X-ray tube and detector. (**b**) In dual-source CT, two sets of X-ray tube and detector are arranged at an angle of 90° and acquire data simultaneously. Hence, approximately a quarter rotation is sufficient to complete data acquisition, and temporal resolution is twice as high

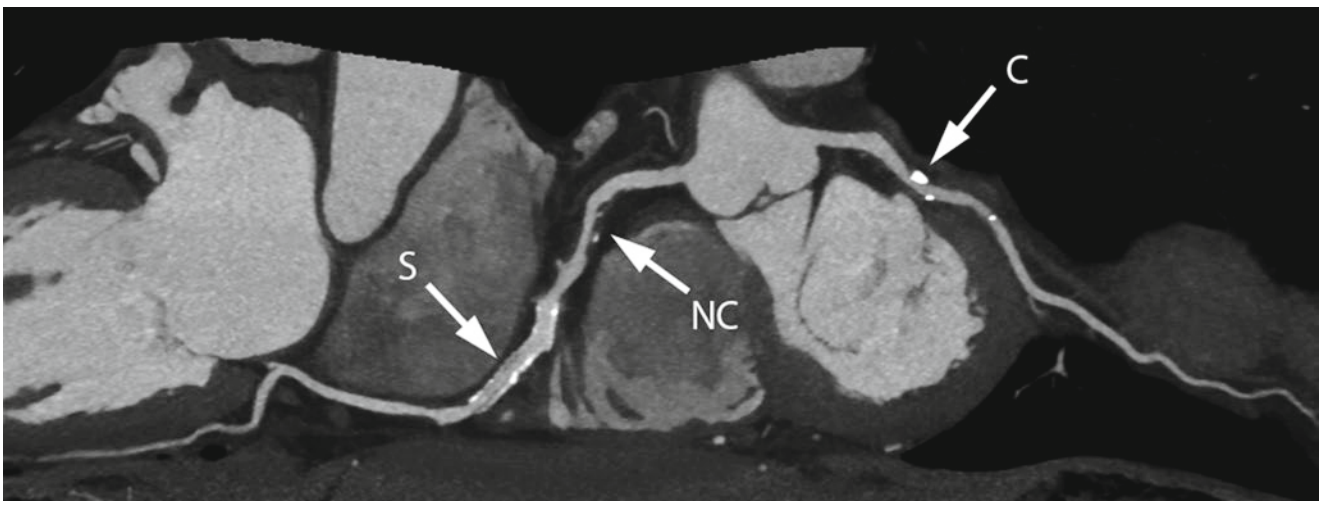

Fig. 1.9 Contemporary contrast-enhanced coronary CT angiography data set, in this case acquired with dual-source CT, 2 × 192 slice acquisition, 250 ms rotation time, and a temporal resolution of 66 ms. The image depicts a curved multiplanar reconstruction of the right and left circumflex coronary arteries, and shows examples of calcified plaque (C), noncalcified plaque (NC), and an implanted stent (S)

Fig. 1.10 Data acquisition modes in coronary CT angiography. (**a**) Retrospectively ECG-gated helical/spiral acquisition: During continuous table movement, the tube and detectors perform a helical/spiral path relative to the patient. X-ray data are continuously acquired with substantial oversampling (all levels of the heart are covered during several rotations); during the image reconstruction process, only data acquired at specific time instants of the cardiac cycle (e.g., mid diastole) are used. (**b**) Prospectively ECG-triggered axial acquisition: Data are acquired without table motion at a given level, and after completion of data acquisition, the table is moved to the next position. The X-ray tube is activated in synchronization with the patient's ECG ("ECG trigger"). The data acquisition window at each position can be kept very short so that radiation exposure is low. If the detector is wide enough (e.g., 320-slice CT), acquisition at only one table position can be sufficient. A complete data set can therefore be acquired within one single cardiac cycle. (**c**) Prospectively ECG-triggered high-pitch helical/spiral acquisition. This image acquisition uses very fast table speed so that a "pulled-open" spiral data set is acquired. At each level, just enough data are collected to reconstruct one image by combining detectors from the various detector rows. Subsequent images are reconstructed at slightly later time instants in the cardiac cycle

Modes of Data Acquisition and Radiation Exposure

Data acquisition in cardiac CT can follow various principles that have been developed over time as technology grew more sophisticated. Importantly, the mode of data acquisition has profound implications regarding radiation exposure. *Retrospectively ECG-gated acquisition* in "helical" mode (also called "spiral" mode) was the acquisition algorithm that was initially used for cardiac CT. Data are acquired during constant slow table motion with a relatively high amount of oversampling. It provides robust image quality and maximum flexibility to choose the cardiac phase during which images are reconstructed, including the ability to reconstruct dynamic data sets throughout the entire cardiac cycle, to assess ventricular function or valve motion. *Prospectively ECG-triggered axial acquisition* requires fast temporal resolution and relatively wide detectors because the images are acquired without table motion during the acquisition and with stepwise advancement of the patient table between consecutive heart beats. It is associated with substantially lower radiation exposure and image quality is high, especially in patients with stable and low heart rates. Less flexibility to reconstruct data at different time instants in the cardiac cycle, as well as greater susceptibility to artefacts caused by arrhythmia, can be downsides of this acquisition mode. In recent years, prospectively ECG-triggered axial acquisition has replaced retrospectively gated helical/spiral acquisition as the preferred acquisition mode in many experienced centers. Finally, *prospectively ECG-triggered high-pitch "helical" or "spiral" acquisition*, also referred to as "*Flash*" acquisition, is an imaging mode that combines aspects of the former two techniques, but it can be used only on selected dual-source CT systems and single-source CT systems with very wide detectors, and only in patients with low and truly regular heart rates. It can cover the volume of the heart within a very short time and maximizes the efficiency of radiation use, so that it is associated with very low radiation exposure (Fig. 1.10).

Next to the selected image acquisition mode, numerous other factors influence image quality and radiation exposure in cardiac CT. As coronary CT angiography (CTA) became a clinically useable imaging modality but hardware was not yet fully

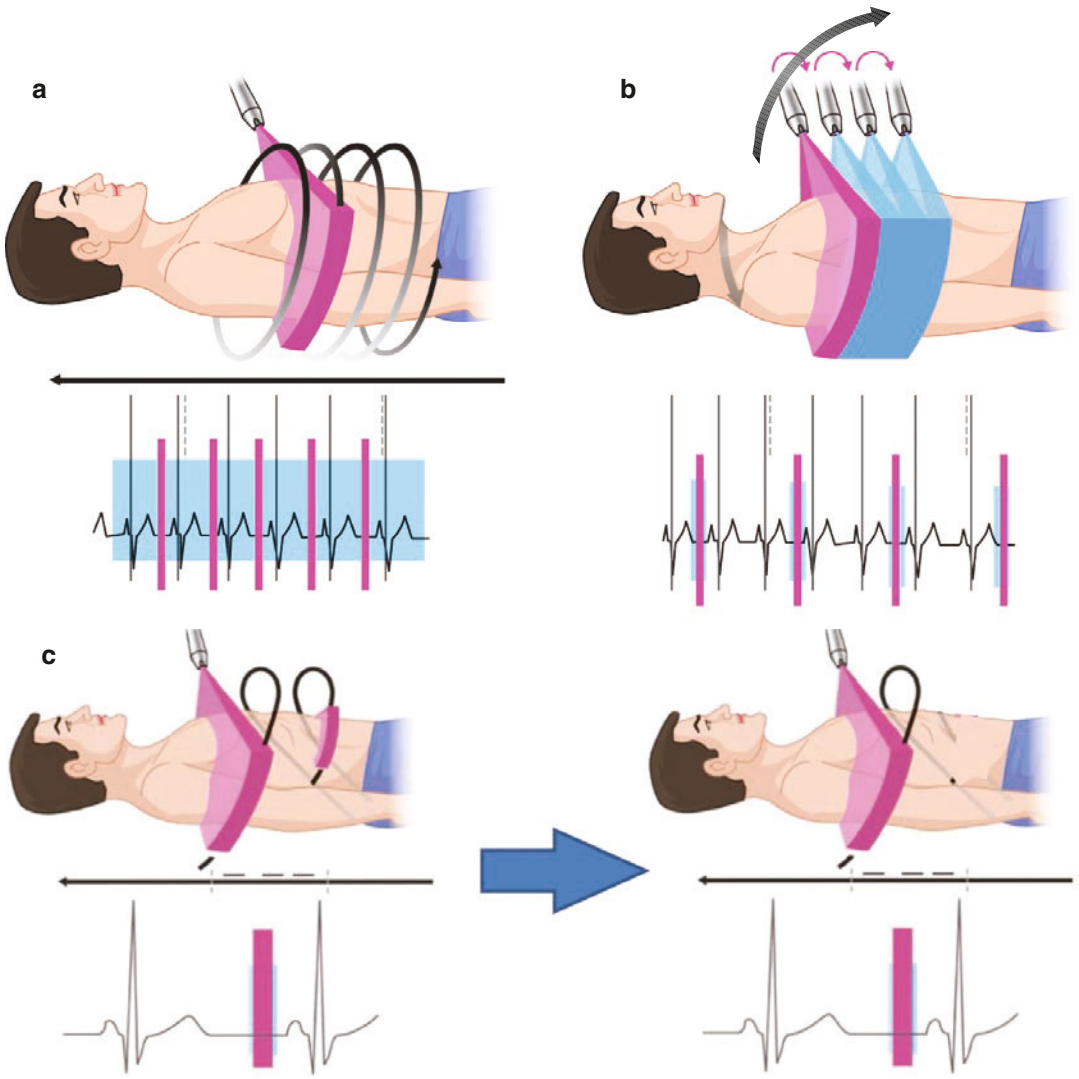

developed, radiation exposures were high. Subsequent improvements in scanner hardware, the development of the aforementioned image acquisition modes, further technical improvements, and physician education have led to a continued decrease in reported radiation exposures for coronary CTA. Currently, typical average effective doses range between 2 and 6 mSv [12, 13]. Effective doses below 1.0 mSv are well possible [14]. In very strictly selected patient cohorts, it has even been reported that doses of less than 0.5 mSv and even below 0.1 mSv can be achieved [15, 16]. Image quality at this extreme end of the spectrum is not robust enough for clinical application across a wide variety of patients, however (Fig. 1.11).

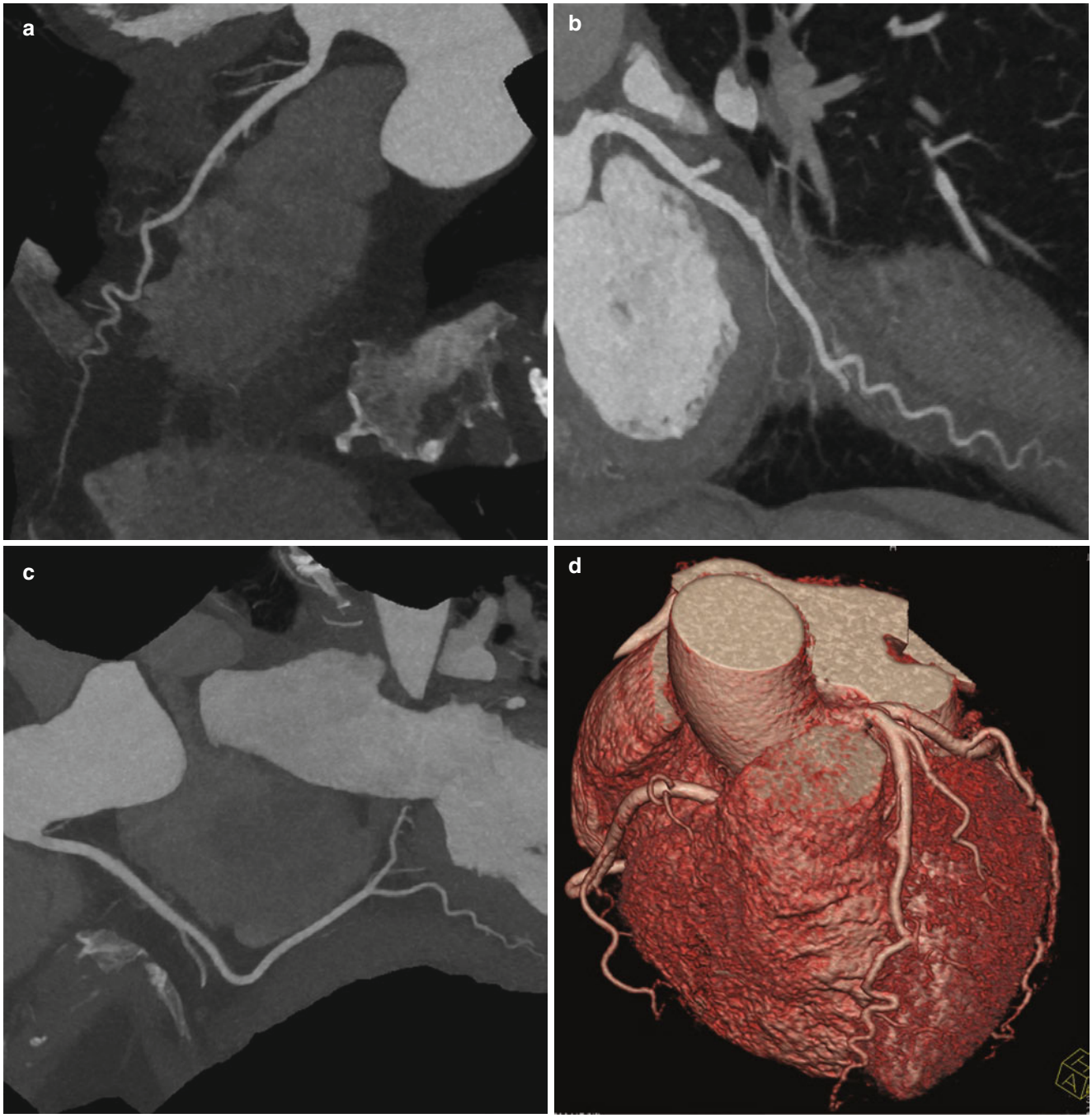

Fig. 1.11 Low-dose coronary CT angiography. By combining various methods to reduce radiation exposure, low-dose imaging is possible in coronary CT angiography. Here, the coronary arteries of a 56 years-old woman are depicted, based on a data set acquired with dual-source CT, using prospectively ECG-triggered high-pitch spiral acquisition at 70 kV tube voltage, with a dose-length product of 19.4 mGy/cm and an estimated effective dose of approximately 0.3 mSv. Image quality is high. Imaging at such dose levels is currently possible in only very selected patients with low body weight and low heart rates. (**a**) Curved multiplanar reconstruction of the left anterior descending coronary artery. (**b**) Curved multiplanar reconstruction of the left circumflex coronary artery. (**c**) Curved multiplanar reconstruction of the right coronary artery. (**d**) Three-dimensional reconstruction

Image Reconstruction and Post-processing

The technical development of cardiac CT has included not only hardware for data acquisition, but also the reconstruction algorithms that are used to generate images based on the acquired X-ray attenuation data. The conventional method to reconstruct images based on the acquired X-ray attenuation data is called "filtered back projection." Although this method does not make full use of the information in the X-ray data, it is computationally efficient and has therefore traditionally been used in order to keep image reconstruction time acceptable in clinical practice. "Iterative reconstruction" makes better use of the information in the X-ray attenuation data, but it requires substantially longer times for reconstruction than filtered back projection. Because modern computers provide increased processing power, iterative reconstruction methods can now be applied clinically and have been implemented on most CT systems that are used for cardiac imaging. Iterative reconstruction alters the visual impression of the reconstructed image data, but the substantial advantage is lower image noise. Hence, iterative reconstruction can be used either to improve image quality or, in combination with low-dose tube settings, to maintain an acceptable noise level in the images while substantially reducing radiation exposure [17] (Fig. 1.12).

Increasing computing power has affected not only image reconstruction based on X-ray attenuation data, but also the analysis of CT data sets. For example, fully automated algorithms can be used to evaluate coronary CTA data sets regarding the presence, volume, and type of atherosclerotic plaque [18]. Fluid dynamic modeling has been applied to simulate blood flow in the coronary arteries and permit

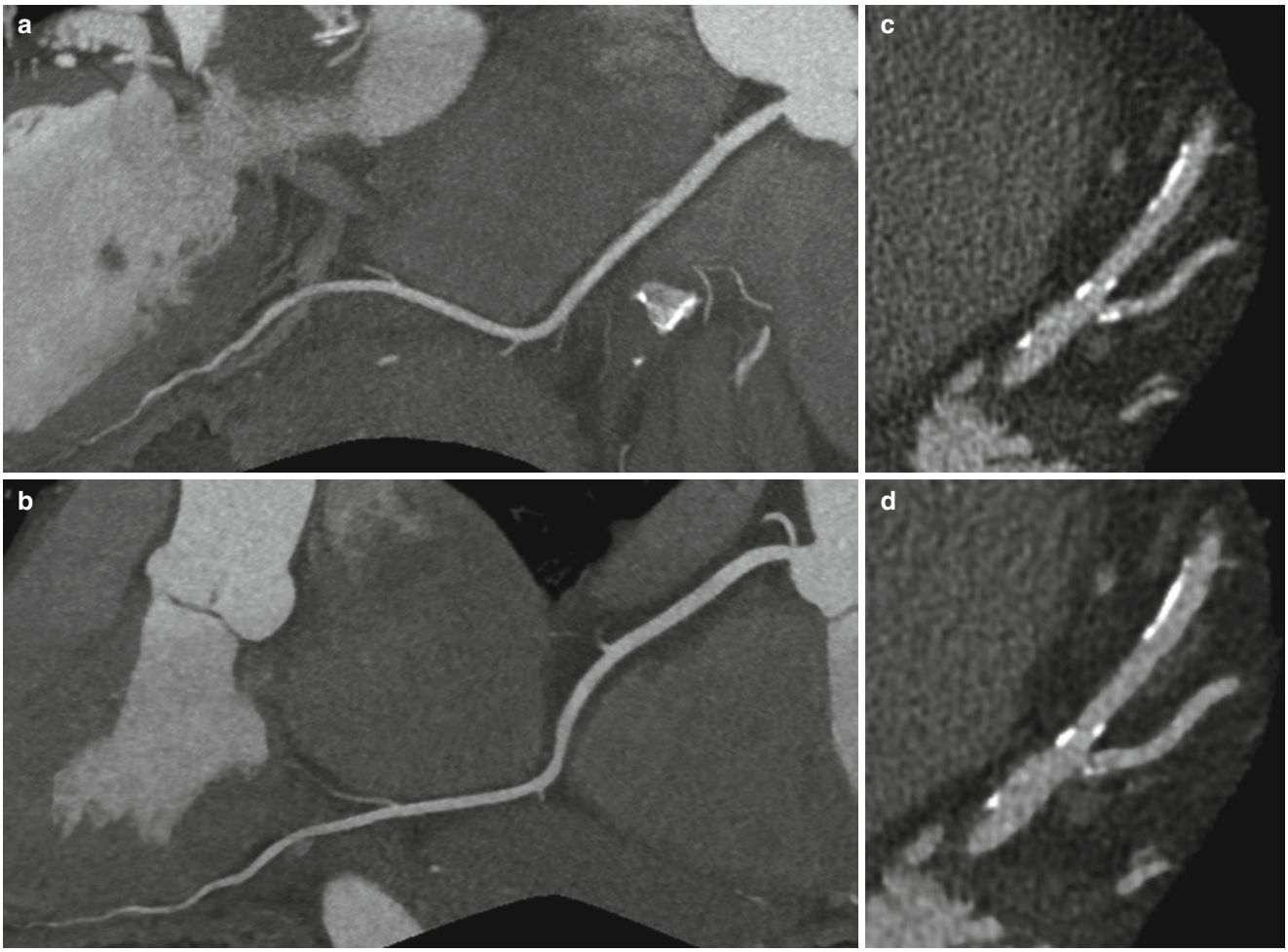

Fig. 1.12 Influence of iterative reconstruction on image quality. Identical raw data sets are reconstructed with traditional filtered back projection (**a**, **c**) and using more computationally elaborate iterative reconstruction (**b**, **d**), which has recently become available as a result of more sophisticated computing power. Noise in the image obtained with iterative reconstruction is considerably lower. Iterative reconstruction changes the image impression when compared with filtered back projection, but numerous authors have been able to show that the lower image noise allows the use of lower-radiation acquisition protocols while preserving diagnostic capability

virtual assessment of the fractional flow reserve (FFR-CT) [19]. It can be expected that software applications to evaluate cardiac CT data sets and to provide information beyond that visually assessable by a skilled interpreter will become even more widely available and clinically used in the future (Figs. 1.13 and 1.14).

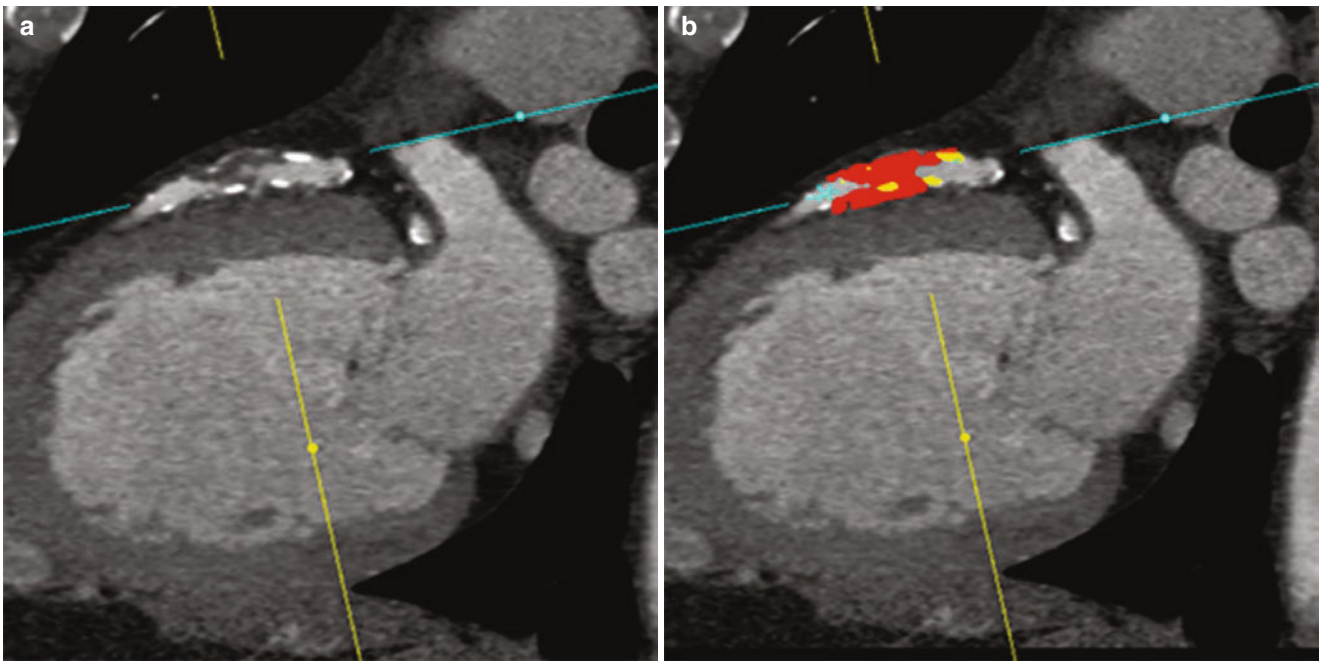

Fig. 1.13 Automated detection and characterization of coronary atherosclerotic plaque using specific software [18]. (**a**) Contrast-enhanced image of a proximal left anterior descending coronary artery showing complex plaque with positive remodeling. (**b**) The same image after automated identification of coronary atherosclerotic plaque (*red* = non-calcified plaque; *yellow* = calcified plaque). (*Images courtesy of* Dr. Damini Dey.)

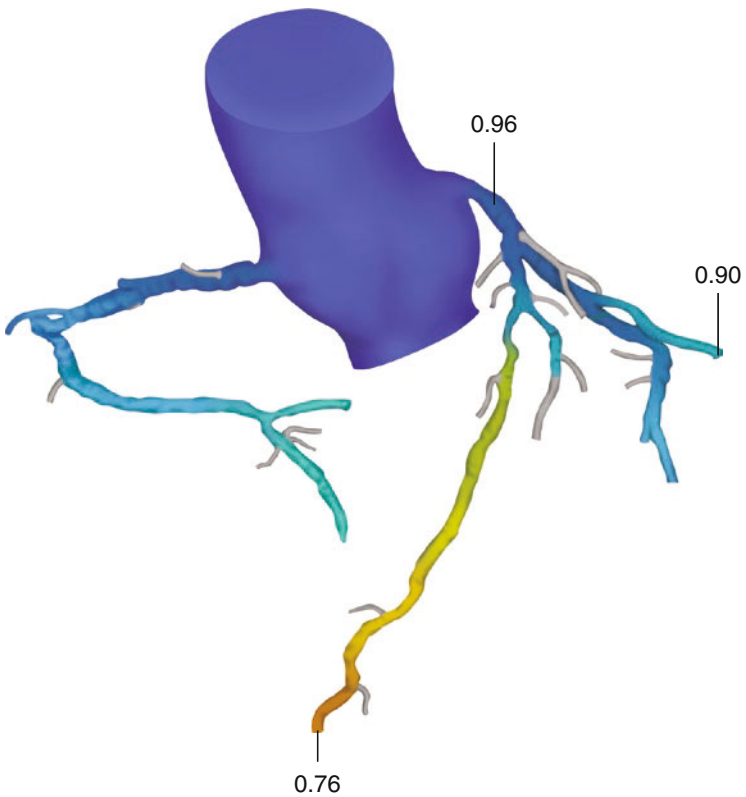

Fig. 1.14 Determination of virtual, CT-derived fractional flow reserve (FFR-CT). Based on the high-resolution anatomic data set obtained by coronary CT angiography, fluid dynamics modeling is used to simulate FFR (under the assumption of full microvascular dilatation) throughout the entire coronary tree [19]. According to published data, such simulated FFR-CT results correlate quite closely with invasively measured FFR values. In the "NXT Trial" [20], the sensitivity of FFR-CT to identify coronary lesions with an invasively measured FFR ≤ 0.80 was 86%, specificity was 79%, and overall accuracy was 81%

Noncoronary Applications of Cardiac CT

Since its development, the application of cardiac CT has focused on visualization of the coronary arteries—initially, on coronary calcium, and then almost entirely on contrast-enhanced coronary CT angiography. With the increasing robustness of cardiac CT, however, including its ease of applicability, coverage of large volumes, and low radiation exposure, and because of the growing need for high-resolution anatomic imaging in the context of complex interventions, noncoronary applications of cardiac CT play an increasingly important role in clinical practice. CT is used as an anatomic reference method for electrophysiologic interventions, to thoroughly assess patient characteristics before noncoronary interventions such as transcatheter aortic valve replacement (TAVR), and for the analysis of myocardial perfusion (Fig. 1.15).

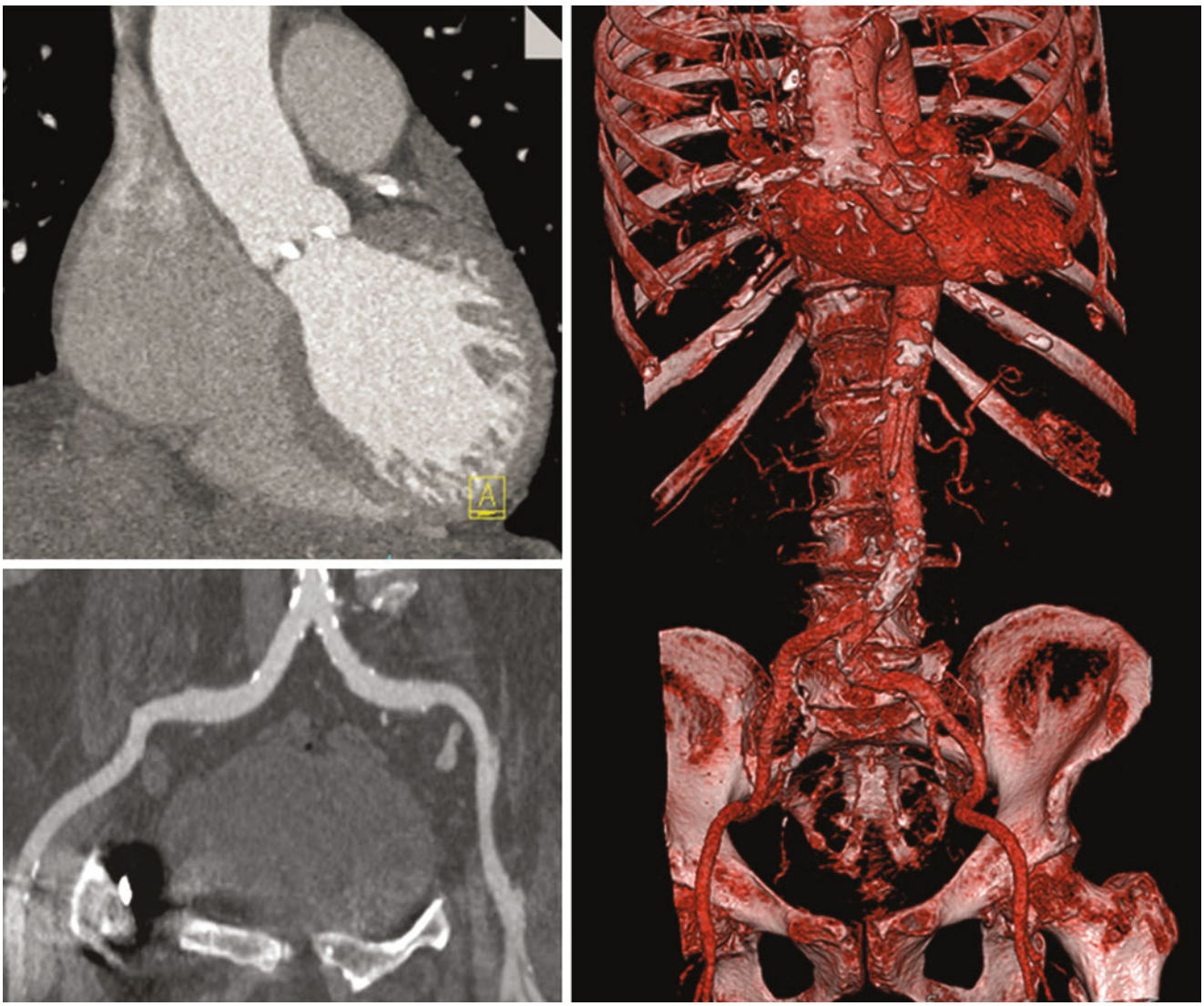

Fig. 1.15 Use of cardiac CT to assess a patient prior to transcatheter aortic valve replacement (TAVR). CT imaging is routinely used in candidates who undergo workup for potential TAVR. With high and isotropic spatial resolution and the ability to generate a large-volume data set within a short time, CT is well suited to support cardiac interventions by providing specific anatomic information. The 3D reconstructions show the scan range acquired with a single contrast bolus, in high-pitch acquisition mode within less than 1 s scan time. Out of this data set, information can be obtained regarding both aortic root anatomy (*top left*) and the anatomy of the pelvic and femoral access vessels (*bottom left*)

Future Developments

Future developments in cardiac CT will undoubtedly include a further evolution of technology with stronger X-ray tubes, faster gantry rotation, and more sophisticated detectors, such as photon count detectors that will provide increased resolution at lower noise. Along with the resulting increase in image quality, software applications for data reconstruction and analysis will expand the range of applications of cardiovascular CT, making coronary artery imaging even more robust and clinically applicable, and permitting new applications outside the coronary vessels.

References

1. Cormack AM. Reconstruction of densities from their projections, with applications in radiological physics. Phys Med Biol. 1973;18:195–207.
2. Hounsfield GN. Computerized transverse axial scanning (tomography) – part I. Description of the system. Br J Radiol. 1973;46:1016–22.
3. Kalender WA, Seissler W, Klotz E, Vock P. Spiral volumetric CT with single-breathhold technique, continuous transport, and continuous scanner rotation. Radiology. 1990;176:181–3.
4. Robb RA. The dynamic spatial reconstructor: An X-ray videofluoroscopic CT scanner for dynamic volume imaging of moving organs. IEEE Trans Med Imaging. 1982;1:22–33.
5. Lipton MJ, Higgins CB, Farmer D, Boyd DP. Cardiac imaging with a high-speed Cine-CT scanner: preliminary results. Radiology. 1984;152:579–82.
6. Agatston AS, Janowitz WR, Hildner FJ, Zusmer NR, Viamonte M Jr, Detrano R. Quantification of coronary artery calcium using ultrafast computed tomography. J Am Coll Cardiol. 1990;15:827–33.
7. Moshage WE, Achenbach S, Seese B, Bachmann K, Kirchgeorg M. Coronary artery stenoses: three-dimensional imaging with electrocardiographically triggered, contrast agent-enhanced, electron-beam CT. Radiology. 1995;196:707–14.
8. Schmermund A, Rensing BJ, Sheedy PF, Bell MR, Rumberger JA. Intravenous electron-beam computed tomographic coronary angiography for segmental analysis of coronary artery stenoses. J Am Coll Cardiol. 1998;31:1547–54.
9. Achenbach S, Moshage W, Ropers D, Nossen J, Daniel WG. Value of electron-beam computed tomography for the noninvasive detection of high-grade coronary-artery stenoses and occlusions. N Engl J Med. 1998;339:1964–71.
10. Achenbach S, Ulzheimer S, Baum U, Kachelriess M, Ropers D, Giesler T, et al. Noninvasive coronary angiography by retrospectively ECG-gated multislice spiral CT. Circulation. 2000;102:2823–8.
11. Flohr TG, McCollough CH, Bruder H, Petersilka M, Gruber K, Süss C, et al. First performance evaluation of a dual-source CT (DSCT) system. Eur Radiol. 2006;16:256–68. Erratum in Eur Radiol. 2006;16:1405.
12. Chinnaiyan KM, Boura JA, DePetris A, Gentry R, Abidov A, Share DA, Raff GL. Advanced Cardiovascular Imaging Consortium Coinvestigators. Progressive radiation dose reduction from coronary computed tomography angiography in a statewide collaborative quality improvement program: results from the advanced cardiovascular imaging consortium. Circ Cardiovasc Imaging. 2013;6:646–54.
13. Rochitte CE, George RT, Chen MY, Arbab-Zadeh A, Dewey M, Miller JM, et al. Computed tomography angiography and perfusion to assess coronary artery stenosis causing perfusion defects by single photon emission computed tomography: the CORE320 study. Eur Heart J. 2014;35:1120–30.
14. Achenbach S, Marwan M, Ropers D, Schepis T, Pflederer T, Anders K, et al. Coronary computed tomography angiography with a consistent dose below 1 mSv using prospectively electrocardiogram-triggered high-pitch spiral acquisition. Eur Heart J. 2010;31:340–6.
15. Schuhbaeck A, Achenbach S, Layritz C, Eisentopf J, Hecker F, Pflederer T, et al. Image quality of ultra-low radiation exposure coronary CT angiography with an effective dose <0.1 mSv using high-pitch spiral acquisition and raw data-based iterative reconstruction. Eur Radiol. 2013;23:597–606.
16. Hell MM, Bittner D, Schuhbaeck A, Muschiol G, Brand M, Lell M, et al. Prospectively ECG-triggered high-pitch coronary angiography with third-generation dual-source CT at 70 kVp tube voltage: Feasibility, image quality, radiation dose, and effect of iterative reconstruction. J Cardiovasc Comput Tomogr. 2014;8:418–25.
17. Naoum C, Blanke P, Leipsic J. Iterative reconstruction in cardiac CT. J Cardiovasc Comput Tomogr. 2015;9:255–63.
18. Dey D, Diaz Zamudio M, Schuhbaeck A, Juarez Orozco LE, Otaki Y, Gransar H, et al. Relationship between quantitative adverse plaque features from coronary computed tomography angiography and downstream impaired myocardial flow reserve by 13N-ammonia positron emission tomography: a pilot study. Circ Cardiovasc Imaging. 2015;8:e003255.
19. Min JK, Taylor CA, Achenbach S, Koo BK, Leipsic J, Nørgaard BL, et al. Noninvasive fractional flow reserve derived from coronary CT angiography: clinical data and scientific principles. JACC Cardiovasc Imaging. 2015;8:1209–22.
20. Nørgaard BL, Leipsic J, Gaur S, Seneviratne S, Ko BS, Ito H, NXT Trial Study Group, et al. Diagnostic performance of noninvasive fractional flow reserve derived from coronary computed tomography angiography in suspected coronary artery disease: the NXT trial (Analysis of Coronary Blood Flow Using CT Angiography: Next Steps). J Am Coll Cardiol. 2014;63:1145–55.

2 Preparation, Image Acquisition and Reconstruction, and Post-processing

Jamaluddin Moloo, Udo Hoffmann, and Harvey S. Hecht

Patient Selection and Preparation

There are no absolute contraindications to CT imaging. Table 2.1 lists the relative contraindications for the use of CT scans in cardiac imaging, and Table 2.2 outlines the steps in preparing a patient for the examination. The use of contrast agents contributes to the contraindications and preparatory steps. Traditionally, solid foods are discontinued 4 h before obtaining a contrast scan, to lower the risk of aspiration if a severe contrast reaction were to occur, but significant nausea and emesis occur infrequently with the use of modern contrast agents. Unless clinically contraindicated, liquids should be encouraged before the scan to ensure a patient is adequately hydrated to reduce the risk of contrast-induced nephropathy. Finally, patients with a contrast allergy require premedication to reduce the risk of a severe reaction.

Table 2.1 Patient selection: relative contraindications to cardiac CT

Relative contraindications
Pregnancy
Renal insufficiency (creatinine clearance <30 mL/min/1.73 m^2)
Radioactive iodine therapy (competitive binding with iodinated contrast)
Patient in an acute thyroid storm (can potentiate thyrotoxicosis)
Inability to perform breathhold ≥5 s

Table 2.2 Patient preparation

Prior to arrival
Consider holding caffeine 12 h before the scan if heart rate should be lower for the study
Consider beta-blocker administration to lower the heart rate (*e. g.*, metoprolol 50 mg PO 2 h prior to the study)
Discontinue phosphodiesterase inhibitors (if nitroglycerin will be utilized)
Consider holding nonsteroidal anti-inflammatory drugs (to limit the risk of contrast-induced nephropathy)
Hold glucophage the morning of the scan and for 48 h after
May continue other medications
No solid foods 4 h before the scan
May continue usual intake of liquids
Immediately before the scan (in holding area)
Obtain a brief history
Review indications
Screen for relative contraindications
Obtain IV access (ideally an 18 gauge in the R AC to allow injection of contrast at high flow rates of 5–7 mL/s)
Optimize heart rate with additional metoprolol IV if needed
Within the gantry
Heart should be centered within the gantry, to maximize spatial resolution
Appropriate placement of ECG leads
Provide nitroglycerin for coronary cases (0.4 mg SL or spray, to dilate coronaries and optimize coronary lumen visualization)
Practice breathhold and assess impact on heart rate
Optimize heart rate with additional metoprolol IV if needed

J. Moloo
Cardiac Vascular Center, University of Colorado, Denver, CO, USA
e-mail: jamaluddin.moloo@ucdenver.edu

U. Hoffmann (✉)
Department of Radiology, Massachusetts General Hospital, 165 Cambridge Street, Boston, MA 02114, USA
e-mail: uhoffmann@partners.org

H.S. Hecht
Department of Cardiology, Icahn School of Medicine at Mount Sinai, New York, NY, USA
e-mail: Harvey.Hecht@mountsinai.org

M.J. Budoff et al. (eds.), *Atlas of Cardiovascular Computed Tomography*, https://doi.org/10.1007/978-1-4471-7357-1_2

The Impact of Heart Rate

In photography, a moving object can be captured as a still image only if the shutter speed is sufficiently fast. The CT equivalent of shutter speed is gantry rotation time—that is, the time required for the radiograph tube and detector to rotate around the patient, thereby gathering the information needed to construct a single image. If the heart rate is higher than the temporal resolution of the CT scanner, motion artifact will obscure the CT image (Fig. 2.1). Newer generation CT scanners are able to obtain motion free images at significantly higher heart rates (70 bpm and higher). However, radiation dose generally increases as the heart rate increases given that the lowest dose imaging protocols are insufficient in such situations. The optimal heart rate for a given study is dependent on the indication for the study; for example, pulmonary vein imaging may be scanned at any heart rate while the ideal heart rate for coronary imaging is generally ≤60 bpm.

If the heart rate needs lowering, consider prescribing metoprolol 50 mg PO to be taken 2 h prior to the study (the peak serum concentration occurs approximately 1.5–2 h after oral administration). If additional B-blocker is needed after the patient arrives (ideally within a holding area), consider prescribing intravenous metoprolol, given in 5-mg increments up to 30 mg while monitoring clinical parameters (peak response of IV metoprolol occurs in approximately 20 min).

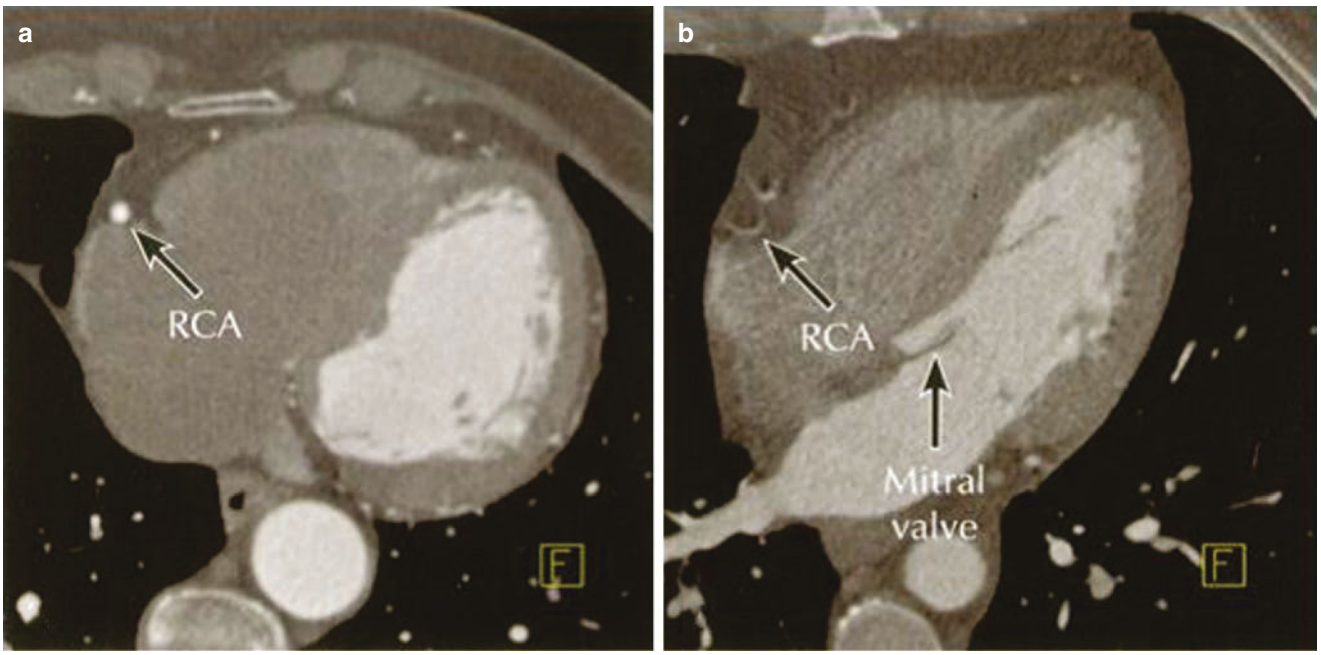

Fig. 2.1 Patient preparation: impact of heart rate. (**a**), Image obtained in a 74-year-old woman with a history of chest pain. The patient's mean heart rate at the time of image acquisition was 54 beats per minute and images were reconstructed in diastole at 65% of the R-R interval. The mid right coronary artery (RCA, *arrow*) shows sharp, distinct borders, and the lumen shows complete filling with contrast, without evidence of calcified or noncalcified plaque. (**b**), Image obtained in a 50-year-old man with a history of diabetes, dyslipidemia, and an equivocal nuclear stress test. The patient's mean heart rate at the time of image acquisition was 82 beats per minute and images were reconstructed in diastole at 65% of the R-R interval (mitral valve remains open; *arrow*). Motion artifact is substantial and obscures visualization of the mid RCA and the adjacent acute marginal branch (*arrow*). The streak pattern and central "hole" form a classic pattern of motion artifact

ECG Lead Placement

All cardiac studies are gated and hence require appropriate ECG lead placement. Artifact from external metallic devices, including ECG leads, may create streak artifact on CT images. To avoid artifact from ECG leads, the leads should be placed outside of the central field of view (Fig. 2.2). Once leads are in position, ensure that the scanner is appropriately sensing each R-wave. Occasionally, tall T-waves may be confused for the R-wave.

Breathhold Instructions

Motion artifact frequently limits one's ability to obtain CT images of diagnostic quality [1] (Fig. 2.3). Respiratory motion is an important source of motion artifact, and its impact is eliminated by acquiring all images during a breathhold, so that inability to perform an adequate breathhold is considered a relative contraindication to performing a cardiac CT. The duration of the breathhold varies depending on the scanning time. As the number of detectors has

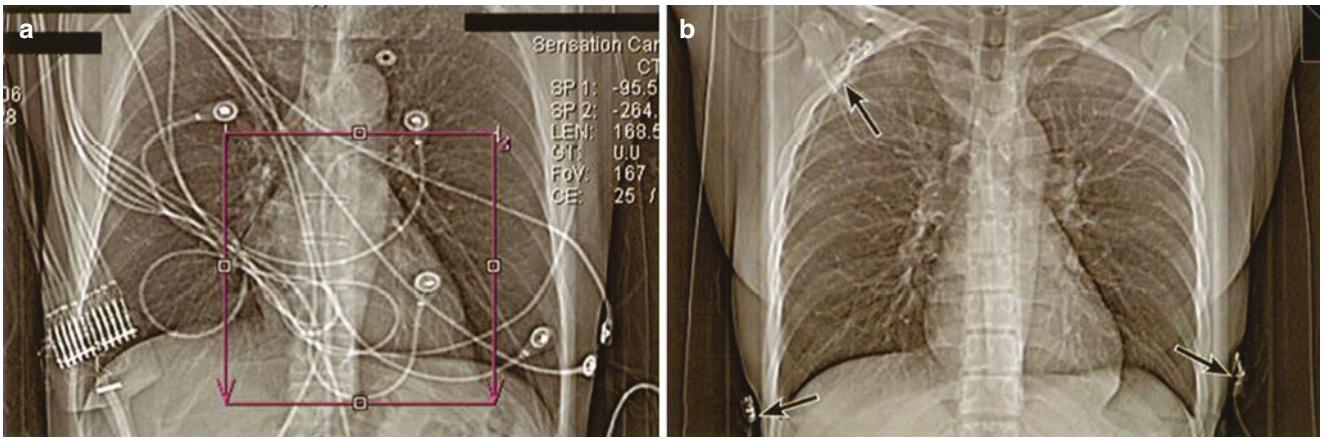

Fig. 2.2 Patient preparation: ECG lead placement. (**a**), A topogram of a patient whose ECG leads are incorrectly placed. The leads course over the chest wall and may create streak artifact. (**b**), Appropriate ECG lead placement (*arrows*) with the leads outside of the field of view. The "RA" ECG lead is placed over the right superior-lateral chest, and the "LL" ECG lead is placed in the left inferior-lateral chest; this pair generally provides an excellent rhythm strip, given its alignment along the cardiac electrical axis. A third "LA" ECG lead is then placed over the right inferior-lateral chest. The resultant rhythm strip should be reviewed to ensure that the R-wave is clearly visible and its amplitude is sufficient for ECG gating

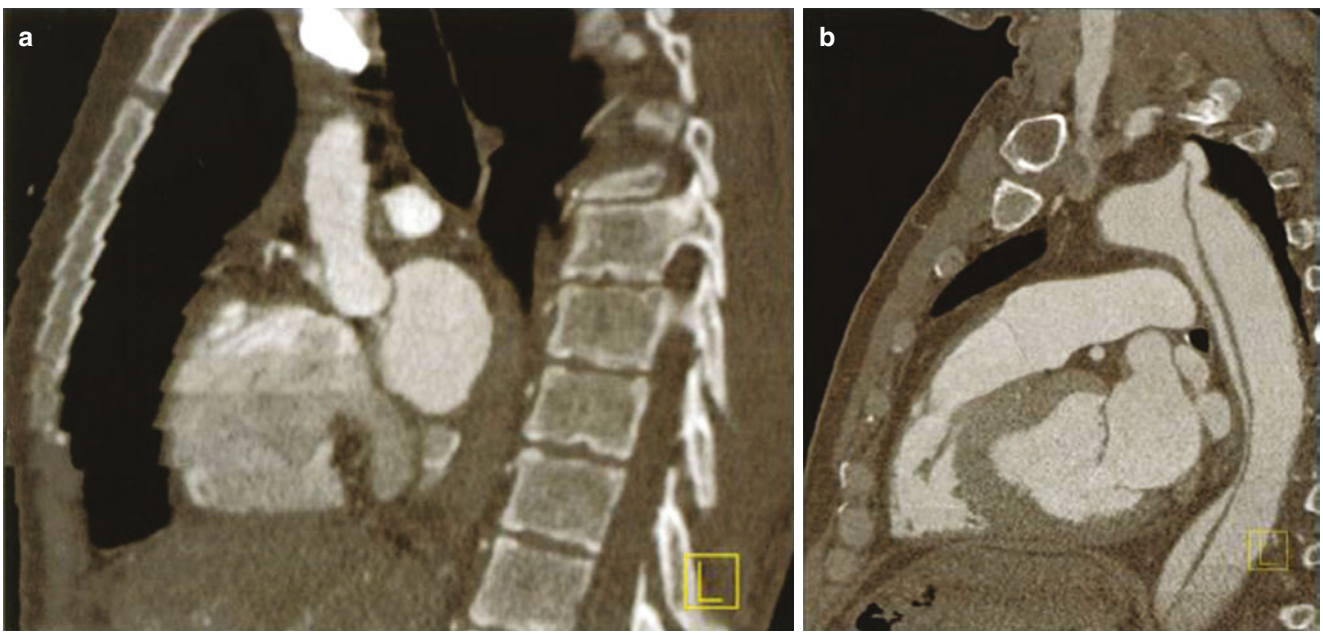

Fig. 2.3 Patient preparation: breathhold instructions. (**a**), A sagittal view of a patient who failed to appropriately hold her breath during image acquisition. The images were obtained in a cranio-caudal direction. Stair-step artifacts are visible over the sternum and the anterior myocardium, a consequence of exhaling during image acquisition. Respiratory artifact can be delineated from other forms of motion artifact most easily on such a sagittal view. (**b**), A sagittal view of a patient who was able to hold his breath appropriately; no evidence of motion is visible. This patient does have an aortic dissection extending from the left subclavian artery to the distal descending aorta

increased from 64 to 128 to 320, the area in the z-axis (cranio-caudal) covered by a single rotation of the gantry has increased, shortening the time required for image acquisition and for holding one's breath. With current scanners, a cardiac CT generally requires a 3–10-s breathhold. When obtaining a CT scan to assess coronaries, we tell the patient, "Take a breath in, breathe out, take a second breath in, and hold your breath." Thus, images are acquired at end inspiration. If the images are to be coregistered with a differing dataset, such as for pulmonary vein mapping and electrophysiologic studies, the CT images should be obtained at mid-expiration, allowing for improved coregistration. For pulmonary vein mapping, we tell the patient, "Take a breath in, breathe out, take a second breath in, breathe out, stop breathing." Of utmost importance is the need to practice the breathhold multiple times and ensure that the patient is able to comply.

Contrast Administration

Injection of an iodinated contrast agent allows one to enhance cardiac cavities and the coronary lumen so that they appear bright, in contrast to the surrounding tissues, myocardium, and epicardial fat. Appropriate delivery of the contrast agent is paramount to achieving diagnostic image quality (Table 2.3). To ensure adequate opacification of the coronary lumen (>300 HU), injection rates of 5–7 mL/s are used. Because the final concentration of contrast within the vessel lumen is dependent on the rate of injection and the patient's blood volume (which generally increases as patient size increases), we inject higher flow rates (6–7 mL/s) in larger or obese patients and in patients who have undergone coronary artery bypass grafting, to ensure maximal opacification of native vessels and the larger-gauge graft vessels. The total volume of contrast required is determined by the time required to complete image acquisition and rate of contrast injection. This ensures the presence of sufficient contrast within the distal coronary beds when the scanner reaches its most caudal location. Following contrast, saline is injected to ensure that the contrast bolus remains compact. Dual-head injectors should be used, typically with biphasic injection protocols. In a typical coronary study, 80 mL of contrast is injected at 5 mL/s and followed by 40 mL of saline at 5 mL/s. When right-sided visualization is required, such as for combined coronary and pulmonary embolus studies, a 50:50 mixture of contrast and saline replaces the saline flush.

Table 2.3 Use of contrast agents for cardiac CT

Contrast delivery rate
Coronary evaluation: 5–7 mL/s
CABG: May consider 6–7 mL/s
Contrast volume: Dependent on scanning time
Saline "chaser"
After test bolus: 20 mL NS
After full contrast: 40 mL NS

CABG Coronary artery bypass grafts, *NS* Normal saline

Image Acquisition and Reconstruction

Once a patient is adequately prepared and the contrast administration protocol has been established, the process of image acquisition can begin. The process of acquiring CT images can be broken down into three sequential steps. The first consists of obtaining a scout image of the chest, which is used to designate the anatomic region of interest. By narrowing the scanning field (cranialcaudal) to the region of interest, radiation exposure is minimized. To visualize the coronary lumen, image acquisition must be timed to coincide with the delivery of contrast to the coronary circulation. As such, the second step, contrast injection, is configured to ensure appropriate timing of scanning relative to the delivery of contrast. The final step involves selecting the appropriate parameters for cardiac CT image acquisition.

Figure 2.4 shows two topograms (similar to conventional chest radiographs) used to delineate the anatomic volume to be scanned as the first of the three image acquisition steps. Although protocols may differ by vendor, the topogram is always acquired as a low-energy scan. The tube voltage is set at 120 Kv and the amperage at 35 mAs.

A critical aspect of cardiac imaging is determining the contrast transit time. This allows one to ensure maximal contrast opacification of the coronary vessels during image acquisition, while minimizing radiation exposure. For coronaries, image acquisition should be initiated only after contrast reaches the coronaries from the patient's intravenous site (Figs. 2.5 and 2.6). Two methods, the test bolus method and the bolus trigger method, can be used to determine the time required for contrast to reach the coronaries. Both methods monitor contrast enhancement (in Hounsfield units) in the ascending aorta at the level of the carina, as a means of monitoring delivery of contrast to the coronaries. This information is utilized to calculate the total contrast transit time. The test bolus injection and breathing instructions are initiated at the same time (Fig. 2.5g). This approach requires that the rate of injection of the test bolus equals the rate utilized for the coronary evaluation sequence. The second approach to determining contrast transit time, the bolus tracking method, uses a series of low-dose axial scans (every 2 s) to track entry of contrast into the ascending aorta at the level of the carina. The coronary CT angiography imaging sequence is initiated when contrast enhancement reaches a predefined threshold, usually 100–110 HU. Both methods provide similar results in studies. An advantage of the test bolus method is it allows for a "trial run" in patients who may have difficulty following the instructions or those who have never had a contrast injection, as well as allowing one to gauge whether the heart rate is adequate for scanning. Disadvantages include the additional time required to perform the sequence and the additional 10 mL of contrast (Fig. 2.6).

As noted above, the final step in cardiac CT image acquisition involves selecting the appropriate imaging parameters. Among these is gantry rotation relative to movement of the scanner bed (Fig. 2.7). The CT gantry consists of a radiograph tube and a row of detectors opposite the tube. Photons traverse through the body from the tube to the detectors and are absorbed at differing rates by differing tissues; these differences are the basis on which CT images are developed. Given

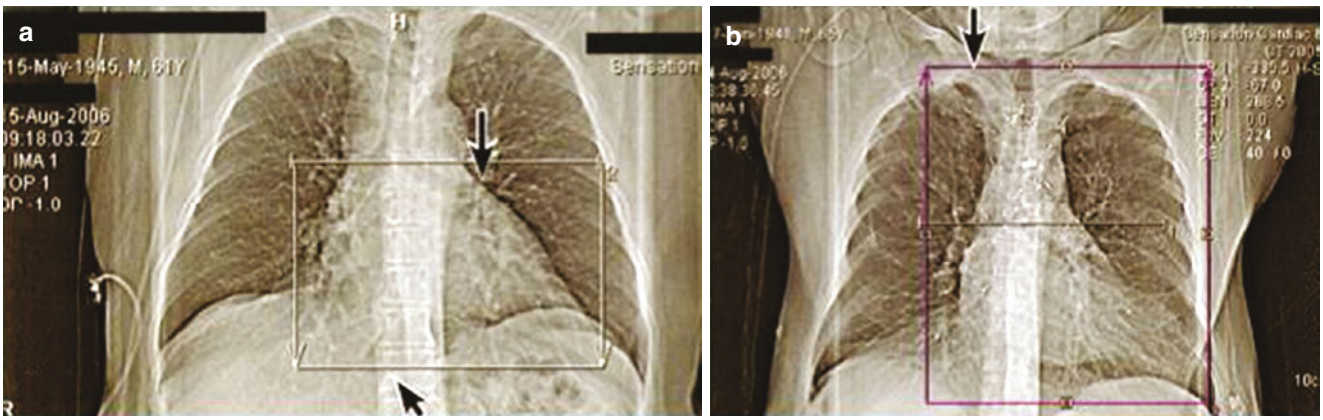

Fig. 2.4 (**a**), Topogram of a 61-year-old man with a history of chest pain and dyspnea on exertion. Evaluation of this patient requires imaging of the coronaries from their origin to the inferior aspect of the heart. As such, markers were set (*arrows*) to initiate scanning at the carina and end where the inferior aspect of the heart is projected to lie. Frequently the inferior aspect of the myocardium must be estimated, because the heart silhouette is incompletely visualized below the dome of the diaphragm. The scanning range should be extended an extra 1–2 cm in case the patient's inspiratory breathhold increases, secondarily shifting the heart caudally during coronary image acquisition. (**b**), Topogram of a 65-year-old man with prior coronary artery bypass grafting (CABG), with a recent nondiagnostic nuclear stress test. The exercise stress test was considered nondiagnostic because of a failure to achieve an adequate heart rate. Markers were set to initiate imaging at the clavicles to include the origins of internal mammary grafts (*arrow*). The breathhold duration is determined by and equal to the time required to acquire images. Heart coverage is possible within a single breathhold of 13 s with 32-slice CT, and 5–10 s with 64-slice CT. Imaging of patients who have undergone CABG requires breathholds approximately 30% longer in duration (if the internal mammary artery is imaged at its origin)

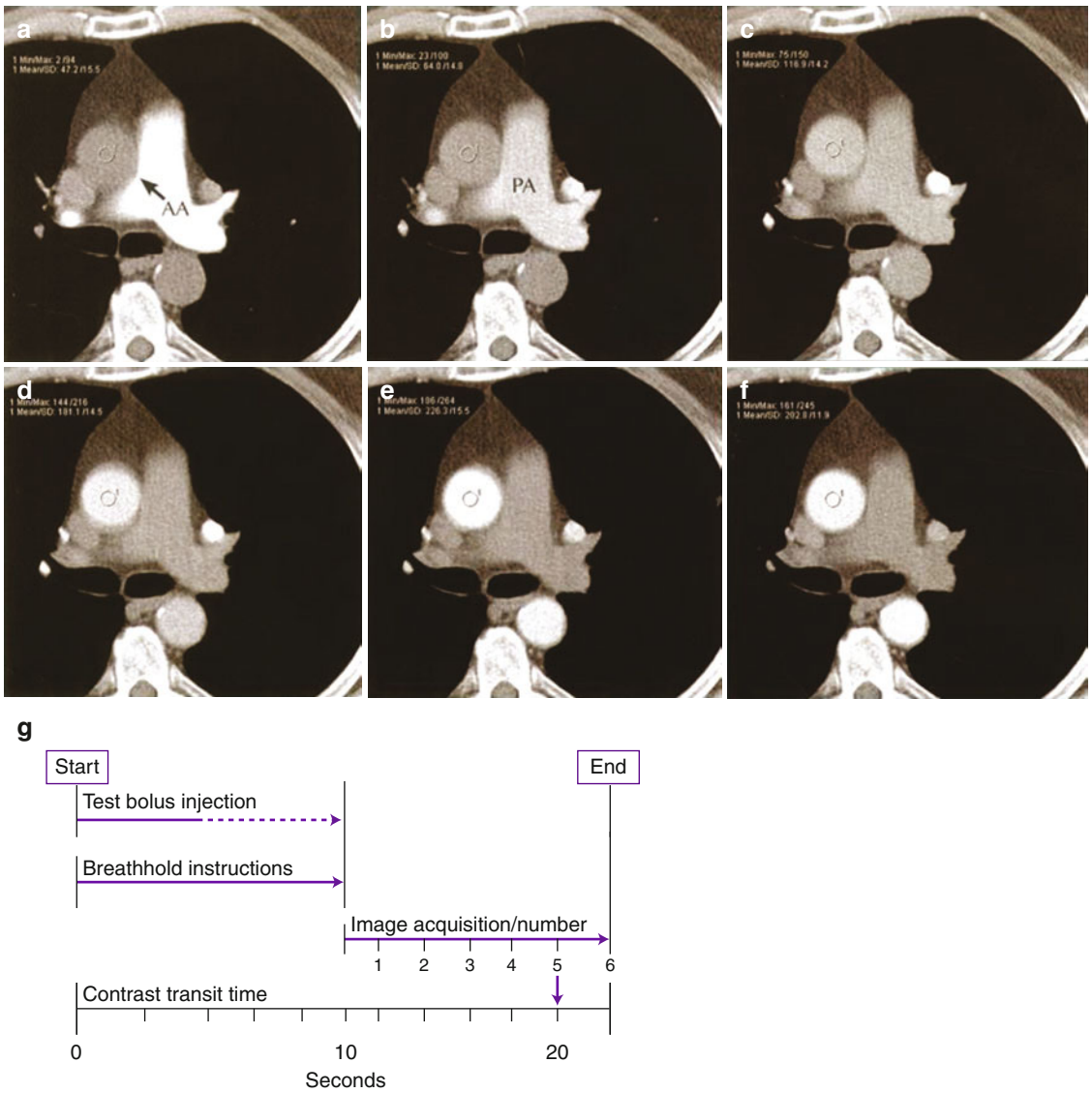

Fig. 2.5 Image acquisition: determining contrast transit time. (**a**–**f**), The test bolus method monitors contrast enhancement in the ascending aorta (AA; *arrow*) at the level of the carina, as a means of monitoring delivery of contrast to the coronaries. In the test bolus, 10 mL of iodinated contrast is injected at 5–7 mL/s, followed by a saline chaser. These six sequential, ungated axial images were obtained at 2-s intervals after injection; the flow of contrast is monitored as it enters the pulmonary outflow tract (**a**) and subsequently returns to the left side with maximal opacification in the aorta (Ao) occurring in image (**e**). This information is utilized to calculate the total contrast transit time. (**g**), Diagram showing that the test bolus injection and the breathing instructions are initiated at the same time point. Breathing instructions are constructed to extend for a total of 10 s; at completion of the breathing instructions, the patient will have initiated the breathhold, allowing one to initiate imaging. Knowing that peak enhancement was achieved on image (**e**) and given that each image was obtained at 2-s intervals results in a contrast transit time of 20 s (10 s for the breathhold plus 10 s, given that peak enhancement was achieved on image #5). Thus, for coronary CTA image acquisition, scanning should be delayed for 20 s after initiating injection of contrast in this patient. *PA* pulmonary artery

that the photons traverse through the patient, images can be reconstructed using data from half a rotation of the gantry around the patient. Hence, the standard mode by which CT images are reconstructed is a "half-scan" reconstruction algorithm. As the gantry rotates around the patient, the scanner bed moves forward, producing a spiral path relative to the patient, hence the term *spiral* or *helical* CT. More recently, axial or "step and shoot" acquisitions are employed in prospectively gated studies. In axial mode, the scanner bed remains in place while the gantry rotates around the patient then moves in a step wise fashion as each additional set of axial images is acquired.

Another important parameter is pitch. As the gantry rotates around the patient, the scanner bed advances. If the bed advances more quickly relative to the time it takes for the gantry to revolve around the patient and acquire a set of axial

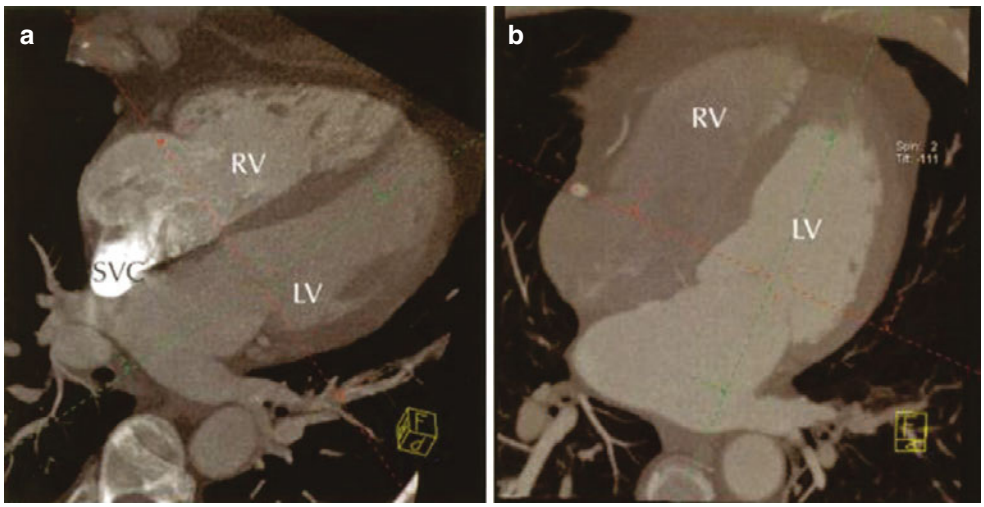

Fig. 2.6 Image acquisition: contrast timing. (**a**), In this example of image acquisition occurring too early, contrast is still visible entering the superior vena cava (SVC), and enhancement is greater within the right ventricle (RV) than in the left ventricle (LV). Coronary vessel assessment is usually severely limited in such cases. (**b**), In this example of optimal timing of contrast injection, contrast within the right ventricle is minimal, and the greatest contrast is seen within the left ventricle and the coronaries

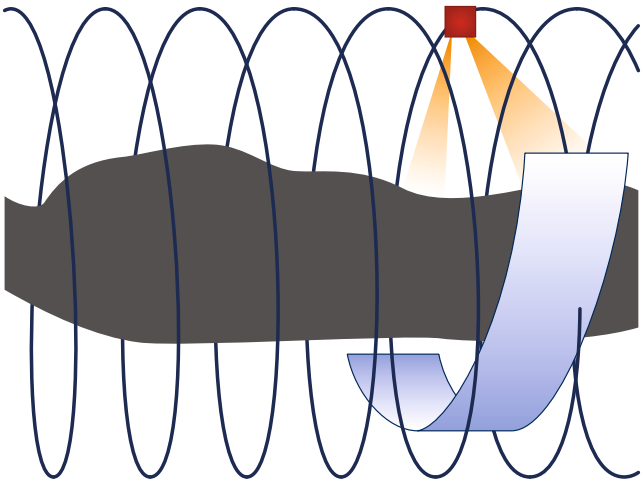

Fig. 2.7 Image acquisition: gantry rotation. The standard mode by which CT images are reconstructed is a "half-scan" reconstruction algorithm. As the gantry rotates around the patient, the scanner bed moves forward, producing a spiral path relative to the patient

slices, gaps are created in the data/image set, whereas if the bed advances slowly, data overlap (Fig. 2.8). Although the pitch used during acquisition differs across differing vendors, most utilize a pitch of approximately 0.2–0.3. The advantage of using a pitch less than one and acquiring overlapping data is that it allows greater flexibility when reconstructing images. For example, if a premature ventricular contraction occurs during scanning one is able to "ignore" data from the PVC and reconstruct the image using data from the next heart-beat. Overlap also decreases the amount of artifact created as the gantry rotates around the patient, and it improves the signal-to-noise ratio of the images. The drawback to utilizing a lower pitch is its higher radiation dose. Thus, protocols aim for a compromise between image quality and radiation exposure. Fast-pitch scanners have been introduced to dramatically shorten the acquisition times and radiation exposure, but these are most suitable for low heart rates.

Scanners with 64 or 128 detectors are unable to obtain cardiac images in a single rotation, which can be done routinely using 320-detector scanners. Because the heart is constantly oscillating between systole and diastole, images must be constructed at a given phase of the R-R interval to minimize motion artifact. *Retrospective acquisition* allows one to obtain images throughout the entire cardiac cycle and construct cine images, which are used to evaluate wall motion, ejection fraction, and valvular function. All cardiac CT images are ECG-gated, and retrospective studies are typically reconstructed at 10% intervals. Figure 2.9 illustrates several ECG rhythm strips with the associated CT tube current, the final parameter to be selected along with KVp. To lower radiation exposure [2], one can turn on tube modulation and lower the tube current during phases not being used for image reconstruction. Images produced when the tube current is lowered are of lower quality, but they are of sufficient quality to evaluate noncoronary structures. The radiation dose reduction depends on the heart rate; it varies between 30 and 50%, but the dose is lowered more in patients with lower heart rates. Dose modulation should be utilized in all retrospective acquisitions unless optimal images are needed throughout the entire cardiac cycle (i.e.: when evaluating an atrial septal defect or a paravalvular leak).

Although specifications differ by vendor, typical image acquisition parameters include a kilovoltage peak (kVp) of 120 kVp for larger patients, 100 kVp for intermediate sizes, and 80 kVp for small patients; exposure time in milliamp seconds (mAs), ranging from 600 to 900 mAs; slice thickness of

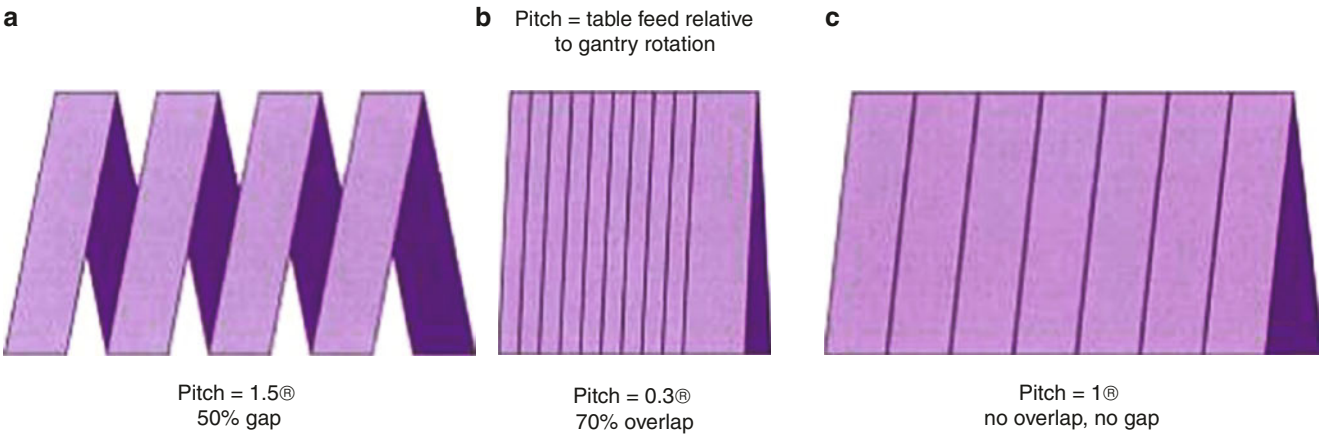

Fig. 2.8 Image acquisition: pitch. (**a**), A pitch of 1.5 is set, providing a gap of 50%. (**b**), A pitch of 0.3 produces 70% overlap. (**c**), A pitch of 1, with no overlap. (*Courtesy of* Dr. S. Abbara.)

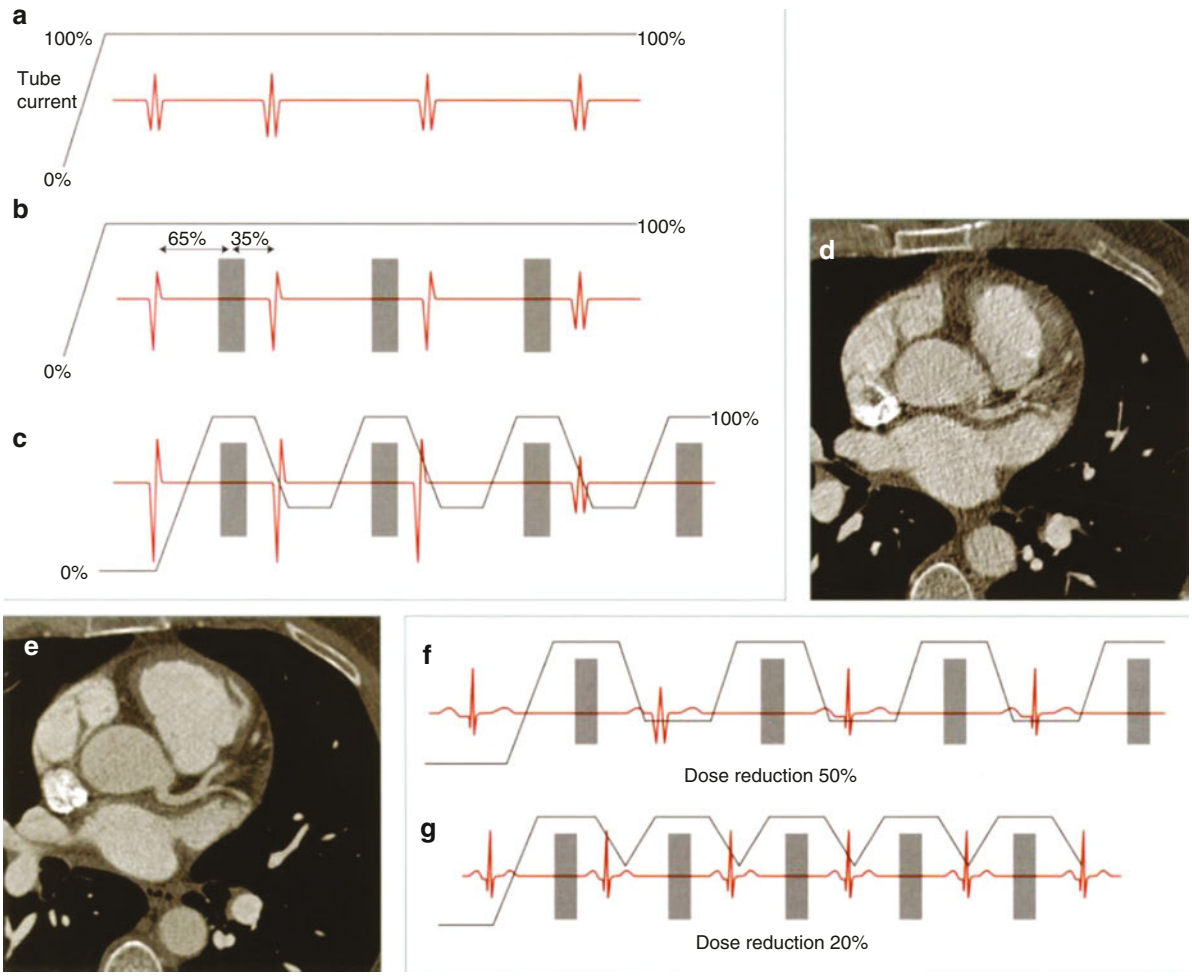

Fig. 2.9 Image acquisition and reconstruction. (**a**), An ECG rhythm strip and the associated CT tube current (a). In this case of retrospective acquisition, the tube current is turned to 100% at the start of image acquisition and remains so till completion of the study. For this patient in normal sinus rhythm, image reconstruction is at 65% of the R-R interval, and the tube current is at 100% (**b**). Tube modulation (**c**) is used to lower the tube current during phases not being used for image reconstruction. Image produced when the tube current is lowered; the image quality is reduced (**d**). Image produced when the tube current is 100% (**e**). Comparison of these strips shows that the radiation dose is lowered to a greater extent in patients with lower heart rates (**f** and **g**). (Parts A–C, F, and G *adapted from* Dr. S. Abbara.)

0.5–0.625 mm; and a pitch of 0.2–0.3. The scanning direction is generally craniocaudal. In obese individuals (>200 pounds), the mAs may be increased to reduce image noise. Alternatively, slice thickness may be increased to 1 mm, which improves the signal-to-noise ratio at the expense of lower spatial resolution.

With *prospective* (axial or step and shoot) *acquisition*, current is applied only during a specified phase, usually 75% of the R-R interval, or slightly longer (padding), resulting in a dramatic reduction in radiation exposure, proportional to the number of acquired phases. The 40% phase may be used at higher heart rates. Prospective acquisition is preferred to retrospective imaging given lower radiation doses. Retrospective imaging should be reserved for specific cases such as irregular or rapid heart rates, or for the evaluation of valvular function.

Standard reconstruction algorithms employ filtered back projection, but more recently, *iterative reconstruction* (IR) has become available on all scanners and yields a significant improvement in signal-to-noise ratio with smoother images. This improvement facilitates radiation dose reduction proportional to the iterative reconstruction level, sometimes exceeding 50%. Iterative model-based reconstruction (IMBR) provides even greater improvement in signal-to-noise ratio and radiation dose reduction. Such iterative reconstruction algorithms are becoming the standard of care.

Post-processing

Once the axial dataset has been obtained, the post-processing phase begins. The primary objective of the post-processing phase is to reconstruct the axial data and construct a specific set of images allowing one to evaluate the coronaries, cardiac function (data is not available in prospective studies), and extracardiac anatomy. A systematic approach simplifies this process (Fig. 2.10). For coronary evaluation, the steps include (1) Review of the ECG for ectopy or arrhythmias, which may impact the quality of images constructed. (2) Selection of the optimal phase for image reconstruction, to avoid motion artifact. (3) Selection of the kernel and reconstruction parameters; this choice will be influenced by the presence of stents and other patient factors. (4) Review of the source (axial) dataset. (5) Evaluation of potential stenoses in the true short axis using maximum intensity projection (MIP) images and multiplanar reformats (MPR). (6) Confirmation of stenoses in a second phase. To evaluate cardiac function, one should construct a dataset that captures images across the entire cardiac cycle and evaluate cine images. A dataset including the full field of view is constructed to evaluate extracardiac anatomy.

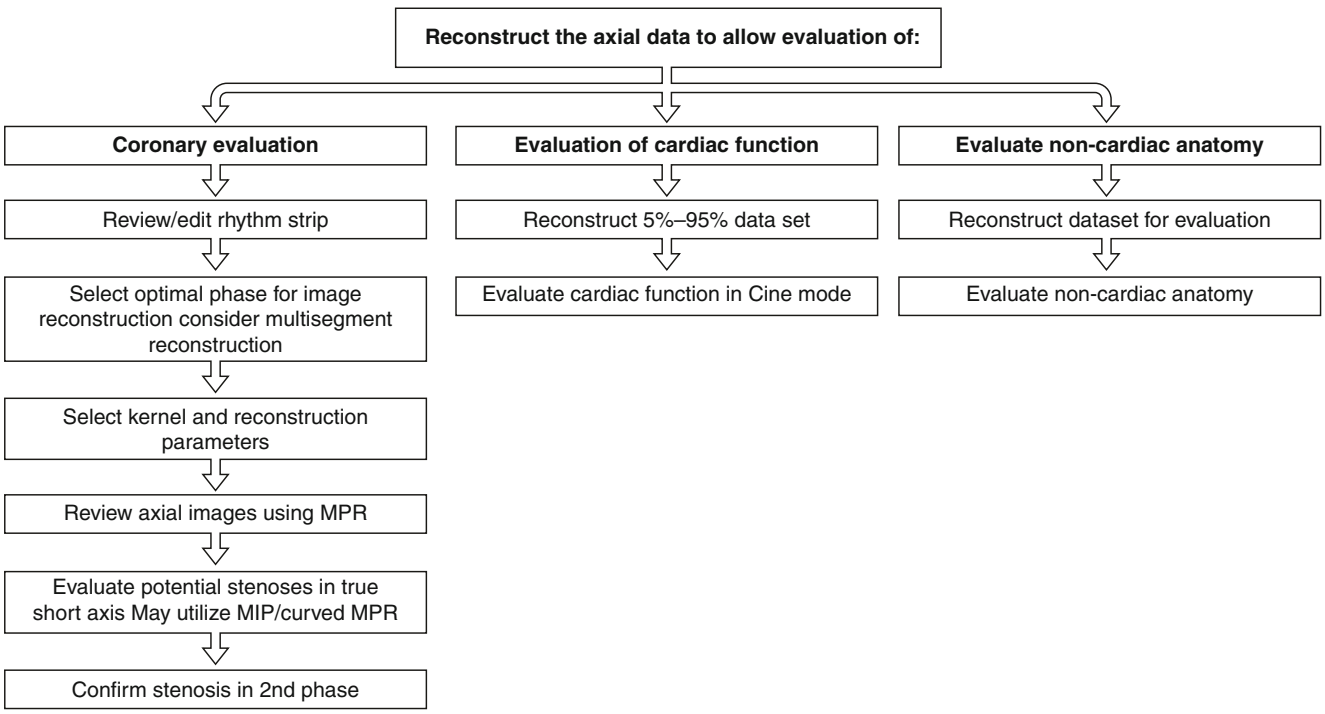

Fig. 2.10 Post-processing: objectives. A systematic approach to the evaluation of the coronaries, cardiac function, and noncardiac anatomy. *MIP* maximum intensity projection, *MPR* multiplanar reformats

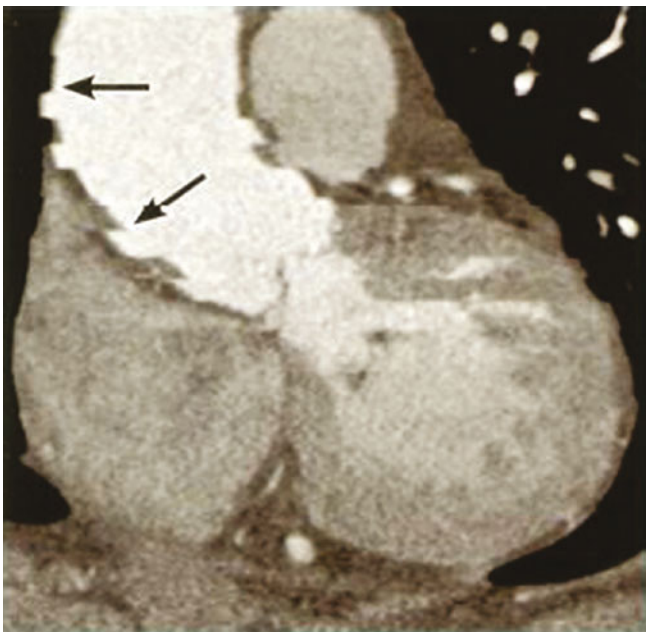

Fig. 2.11 Coronary evaluation: gating artifact. An example of an artifact resulting from beat-to-beat differences in the cardiac cycle (*arrows*). This form of artifact is frequently referred to as a *misalignment* or *banding* artifact

Review of the Electrocardiogram and Phase Selection

Once the axial dataset has been obtained and before constructing an image set, the ECG rhythm strip should be reviewed for potential sources of artifact. Cardiac images are created by sequentially adding data from several heartbeats (320 detector scanners and high-pitch protocols obtain images within a single heartbeat). If the phase of the cardiac cycle from which data are utilized differs from beat to beat, artifact will be introduced (Fig. 2.11). Editing of the ECG to increase the likelihood of capturing the same point in diastole, as illustrated in Fig. 2.12, frequently produces images of better diagnostic quality in patients with variable heart rates [3] (Fig. 2.13).

Vendors differ in their approach to presenting ECG data. Some allow simultaneous correlation of a single image slice with its corresponding ECG, as seen in Fig. 2.14, so that gating errors can be identified and corrected.

Because the heart is in constant flux as it cycles between systole and diastole, another approach to improving cardiac CT images is selecting the optimal phase for reconstruction. Though motion is least in late diastole, occasionally use of a systolic phase will alleviate motion artifact (Figs. 2.15 and 2.16).

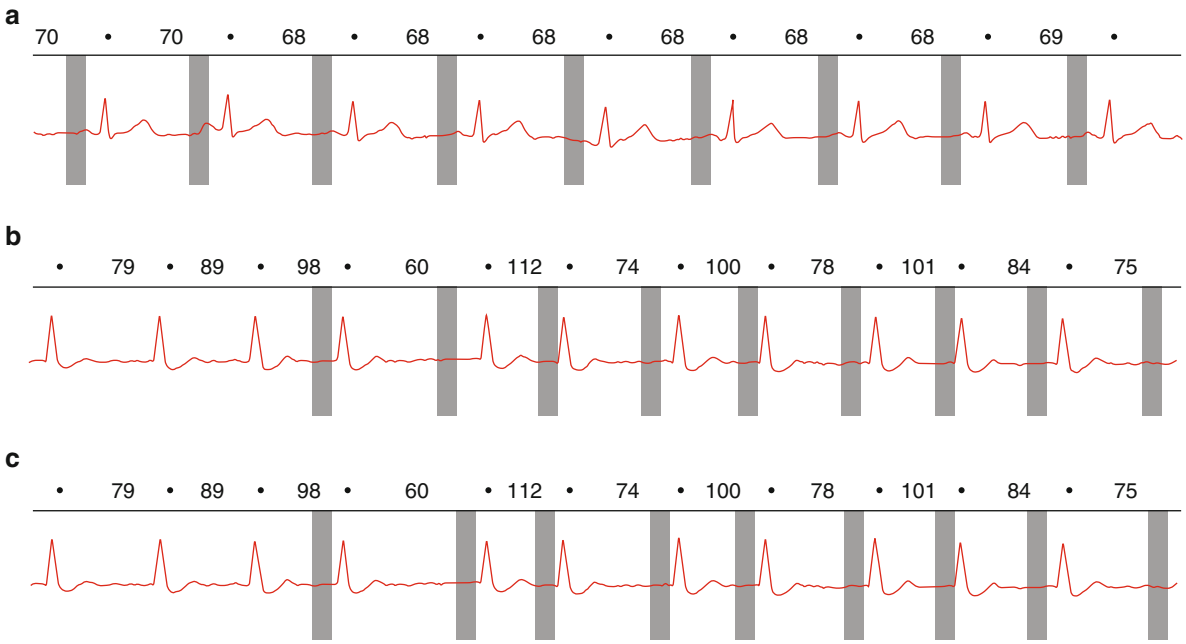

Fig. 2.12 Coronary evaluation: editing the ECG. (**a**), ECG rhythm strip of a patient in normal sinus rhythm, without ectopy and with tube modulation turned on. Images are set to be reconstructed (*gray bars*) at 65% of the R-R interval. Given that each gray bar falls at the appropriate R-R interval, no ECG editing is needed. (**b**), ECG strip from a patient in atrial fibrillation with an R-R interval that varies with each beat. If images were reconstructed at 65% of the R-R interval, the image would be constructed using data from slightly differing points in diastole. (**c**), The same study from (**b**) is reconstructed at −225 ms relative to each R-wave

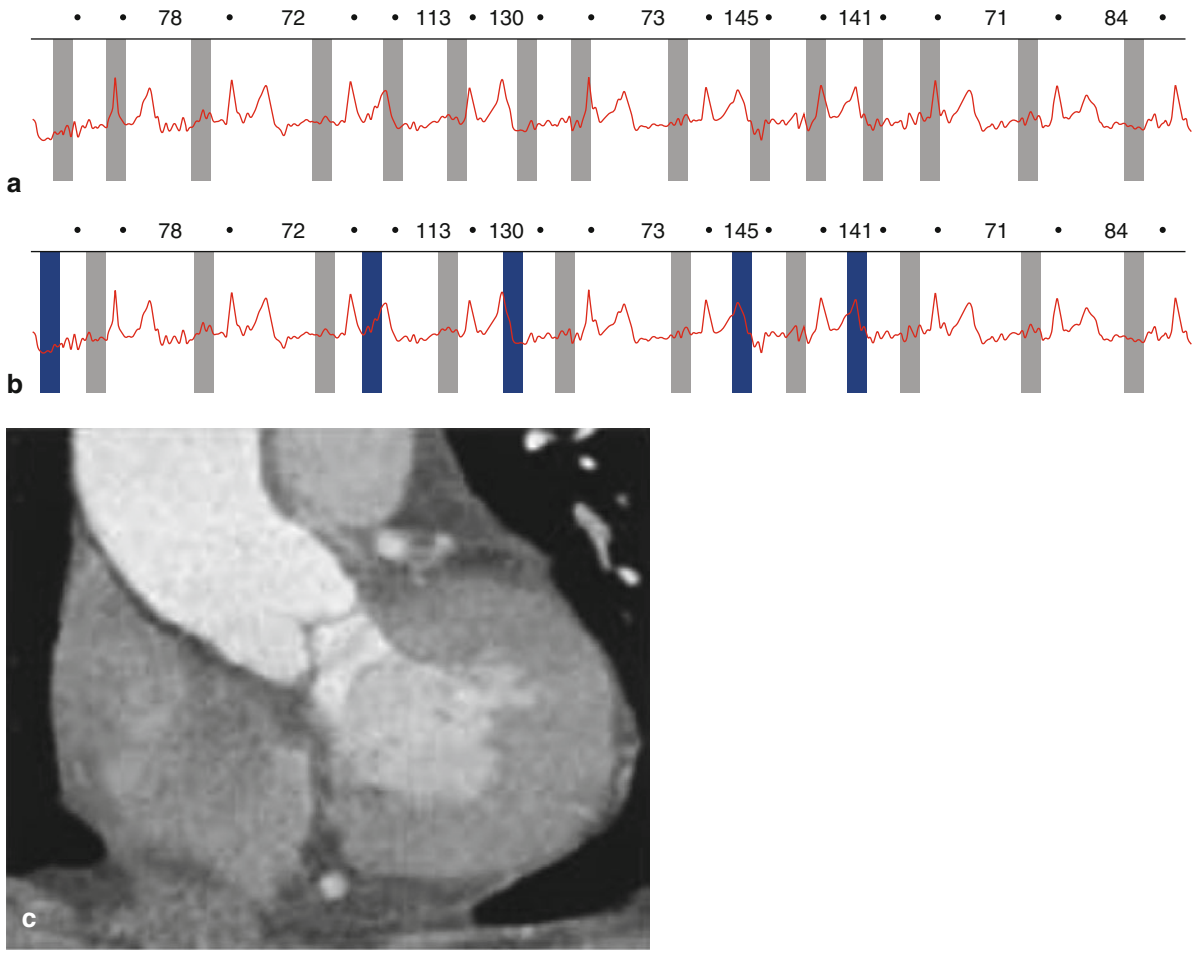

Fig. 2.13 Coronary evaluation: cardiac gating. (**a**), ECG associated with the image shown in Fig. 2.11. The image was reconstructed at 65% of the R-R interval. A review of the ECG tracing shows that T-waves were incorrectly identified as R-waves, and this leads to incorrect gating. Although reconstruction was set at 65% (late diastole), the *gray bars* fall inappropriately at differing points of the cardiac cycle, including over the QRS complex. (**b**), The edited ECG used to create the final image. Reconstruction was set at −250 ms relative to the R-wave. T-waves incorrectly identified as R-waves were "disabled" (*blue bars*) and were ignored by the computer. (**c**), The final image shows nearly complete resolution of the misalignment artifact

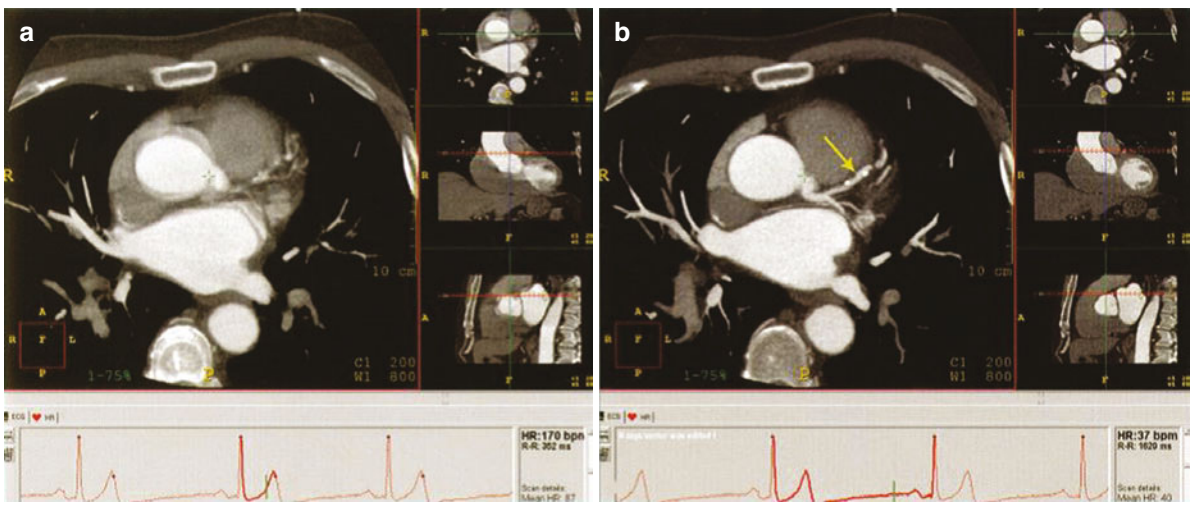

Fig. 2.14 Coronary evaluation: cardiac gating. (**a**), An axial image constructed at 75% of the R-R interval. Motion artifact makes analysis of the left anterior descending artery (LAD) impossible. The accompanying ECG depicts the R-R interval (*green bar*) from which the image was reconstructed. The *red dots* indicate the computer's assessment of R-wave peaks. As can be seen in the ECG tracing, the computer incorrectly identifies T-waves as R-waves. Thus, although the images were to be constructed at 75% of the R-R interval, the incorrect ECG gating created an image from late systole. (**b**), An edited ECG tracing for the same patient; the red dots correctly represent R-wave peaks. The resulting image shows a distinct proximal LAD with calcified plaque (*arrow*). (*Courtesy of* NY Heart Center.)

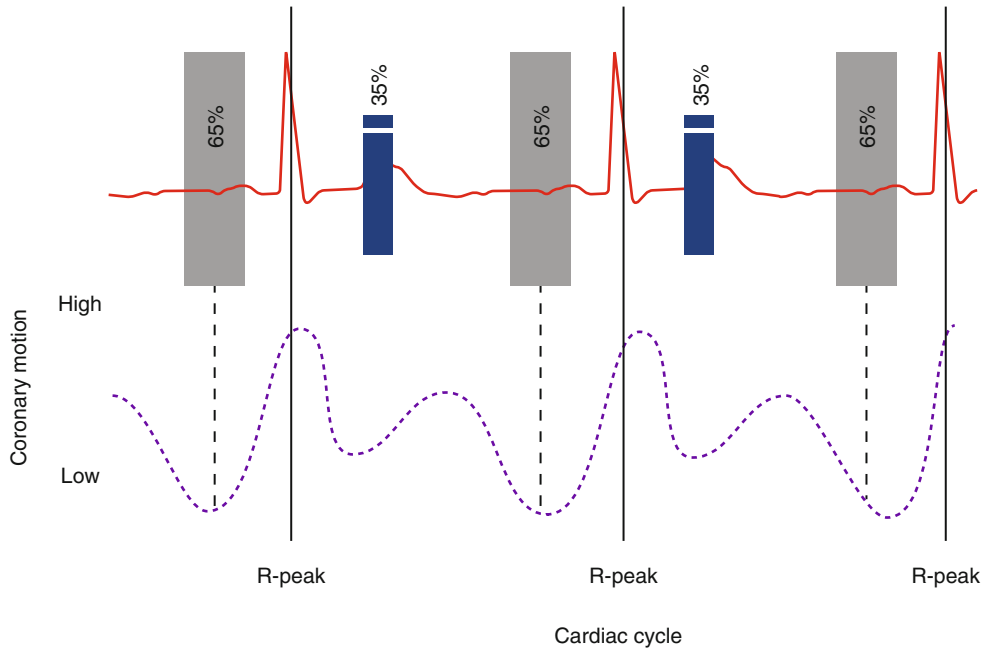

Fig. 2.15 Coronary evaluation: selecting the optimal phase for reconstruction. This image illustrates motion of the right coronary artery in the X, Y, and Z axes during the cardiac cycle. Motion is least in late diastole, at approximately 60–80% of the R-R interval. On occasion, a systolic phase is required to alleviate motion artifact. In such instances, reconstruction at 35% is frequently helpful, given the relatively slower motion in this phase [4]. (*Courtesy of* NY Heart Center.)

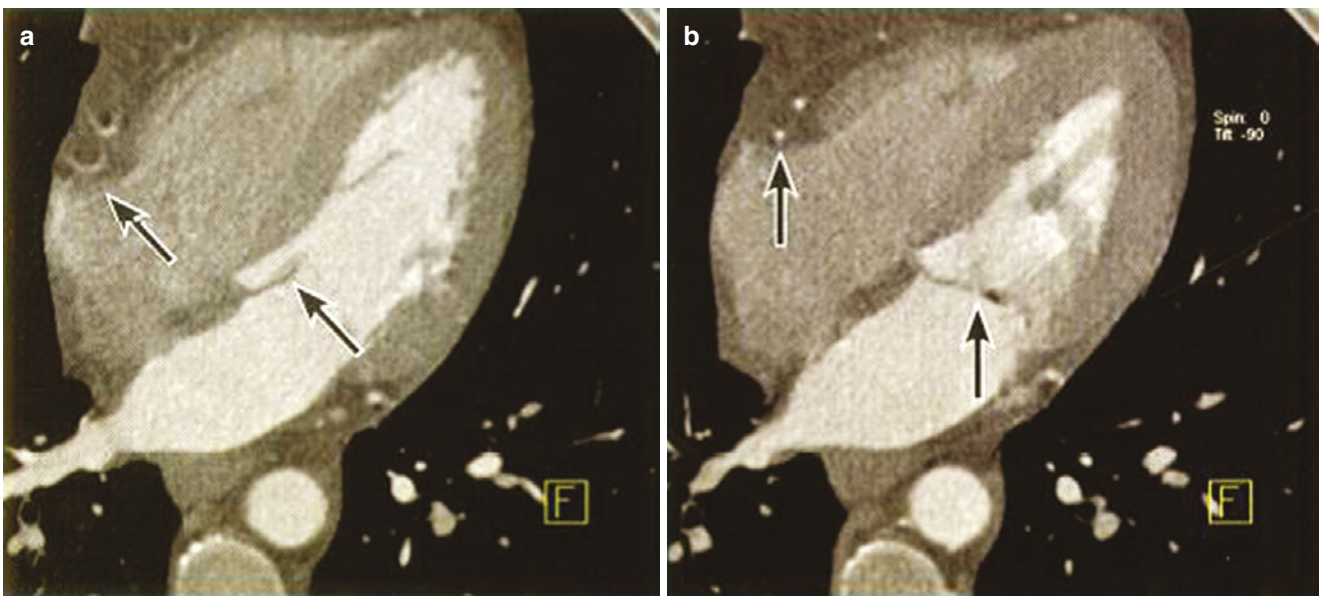

Fig. 2.16 Coronary evaluation: diastolic and systolic reconstructions. (**a**), An image reconstructed at 65% of the R-R interval. The mitral valve remains open, and substantial motion artifact is visible at the mid right coronary artery and acute marginal branch (*arrows*). (**b**), The image was subsequently reconstructed at 35%. The mitral valve is now closed and the left ventricle shows appropriate systolic thickening. A distinct mid right coronary artery and acute marginal branch are now visible

Reconstruction Algorithm Selection

As the gantry rotates around the patient, the scanner obtains axial data. These data are ECG-gated, and a stack of images is constructed from a specified phase in the cardiac cycle (Fig. 2.17). Because photons travel through the entire patient, only one half rotation of the gantry is required to produce each set of axial slices, hence the term *half-scan reconstruction*.

Half-scan reconstructions are the default mode of reconstruction for most scanners, but to improve temporal resolution (and decrease motion artifact in patients with higher heart rates), a narrower window from each heartbeat can be used and summed with subsequent heartbeats to produce the final 180-degree projection. This process is termed *multisegment reconstruction* (Fig. 2.17b). Motion artifact frequently occurs with heart rates greater than 65 beats per minute, and use of the multisegment reconstruction approach is valuable to improve image quality in selected patients [5]. The algorithms used assume that the heart returns to exactly the same location in every heartbeat, however, so mixed results have been reported.

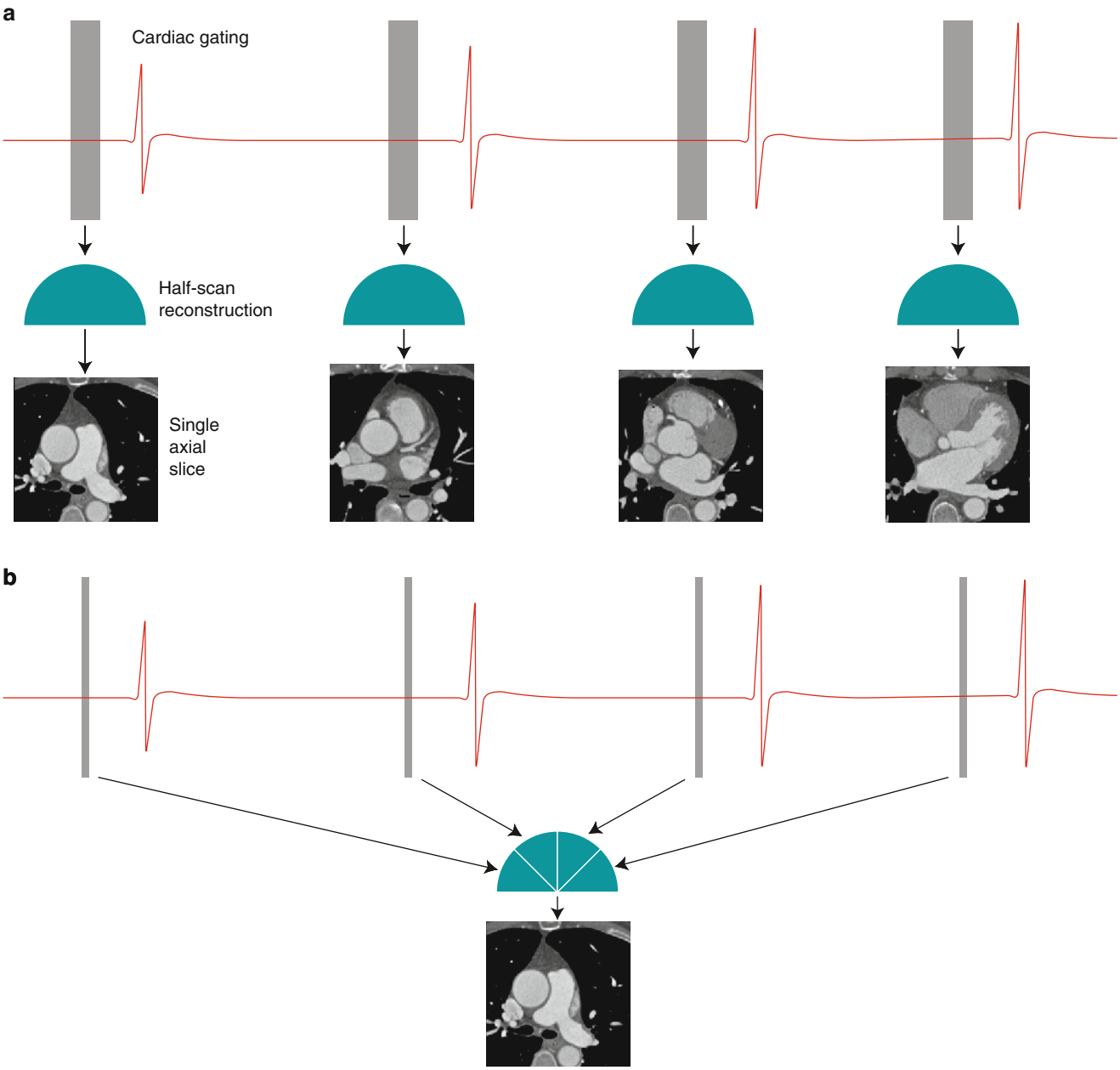

Fig. 2.17 Partial and multisegment reconstruction. (**a**), The scanner obtains axial data, which are ECG-gated and a stack of images is constructed from a specified phase in the cardiac cycle (in this example, 65% of the R-R interval). Only a half rotation of the gantry is required to produce each set of axial slices—hence *half-scan reconstruction*. (**b**), A narrower window from each heartbeat can be used and summed with subsequent heartbeats to produce the final 180-degree projection—hence *multisegment reconstruction*

Kernel Selection

In addition to selecting the phase and reconstruction algorithm, a kernel must be selected before constructing an image. *Kernels* refer to the computer algorithms and processing that allow one to take data on photon attenuation and convert it into a recognizable image. Each vendor develops its own unique set of kernels, but some generalizations can be made. "Softer" kernels have lower image noise but lesser degrees of edge detection. "Harder" kernels improve spatial resolution and edge detection, but they also have more image noise, producing grainier images. Softer kernels are generally used when evaluating coronaries; harder kernels improve the evaluability of stents and, frequently, calcified plaque (Fig. 2.18).

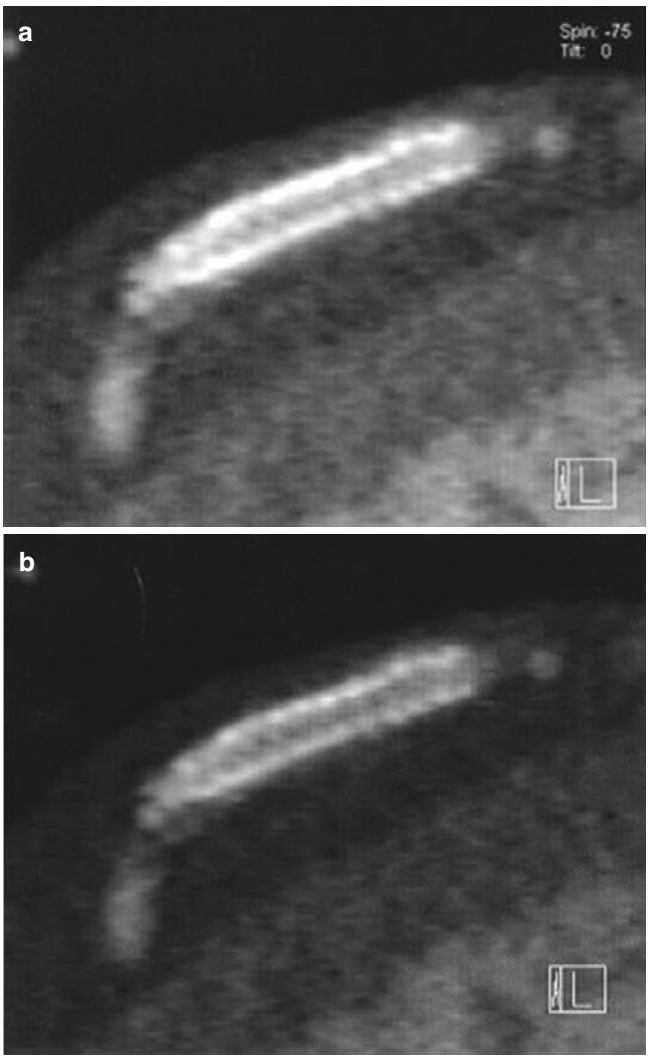

Fig. 2.18 Kernel selection. Both images show a stent in the mid LAD artery. (**a**), A softer kernel. (**b**), A hard kernel. The harder kernel has more image noise but better edge detection and spatial resolution

Coronary Evaluation

Once images have been constructed, the initial step should be to review the axial dataset in thin slice (0.6–0.75 mm) (Fig. 2.19). As previously discussed, in certain cases (such as obese patients), slice thickness may be increased to 1 mm to improve the signal-to-noise ratio. It is important to recognize that all data are contained within the axial images. Maximum intensity projections, multiplanar reformats, curved multiplanar reformats, and three-dimensional volume-rendered images (*see below*) are developed from this axial image set. These additional image types are helpful when assessing tortuous coronary vessels.

A multiplanar reformat (MPR))uses the source dataset and creates a new slice with a different orientation (Fig. 2.20). The slice thickness can also be altered. A curved MPR goes one step further, creating a two-dimensional image of a three-dimensional object, allowing one to follow the course of a vessel as it crosses multiple planes (Fig. 2.21). Creating a two-dimensional image of a three-dimensional structure results in the distortion of adjacent anatomic structures. Therefore, in a curved) MPR only the target vessel can be assessed. Although the specific steps for creating a curved MPR differ by vendor, they are created in two ways. One can manually tag the vessel of interest by scrolling through a stack of axial images, or one can use the automated approach available on most workstations, in which the computer detects the vessel lumen by tracking Hounsfield units (iodinated contrast). Given that a certain threshold of Hounsfield units is required to track a vessel, smaller vessels and vessels with incomplete opacification frequently go undetected and require manual editing. The advantage of the manual approach is increased accuracy, but the automated approach has a speed advantage.

An additional image type frequently used to assess coronaries is the maximum intensity projection (MIP). MIP differs from the prior image formats in one specific manner—in a thick MIP, the highest Hounsfield unit within the stack of pixels (making up the slice) is projected to the new image; lower Hounsfield units are masked (Fig. 2.22). The thickness of an MIP can be adjusted, and it has the advantage of improving the image-to-noise ratio and increasing the depth of field, thereby making it easier to follow the path of tortuous vessels (Fig. 2.23). A risk of relying on MIP images is that non-calcified plaque (of relatively lower Hounsfield units) can

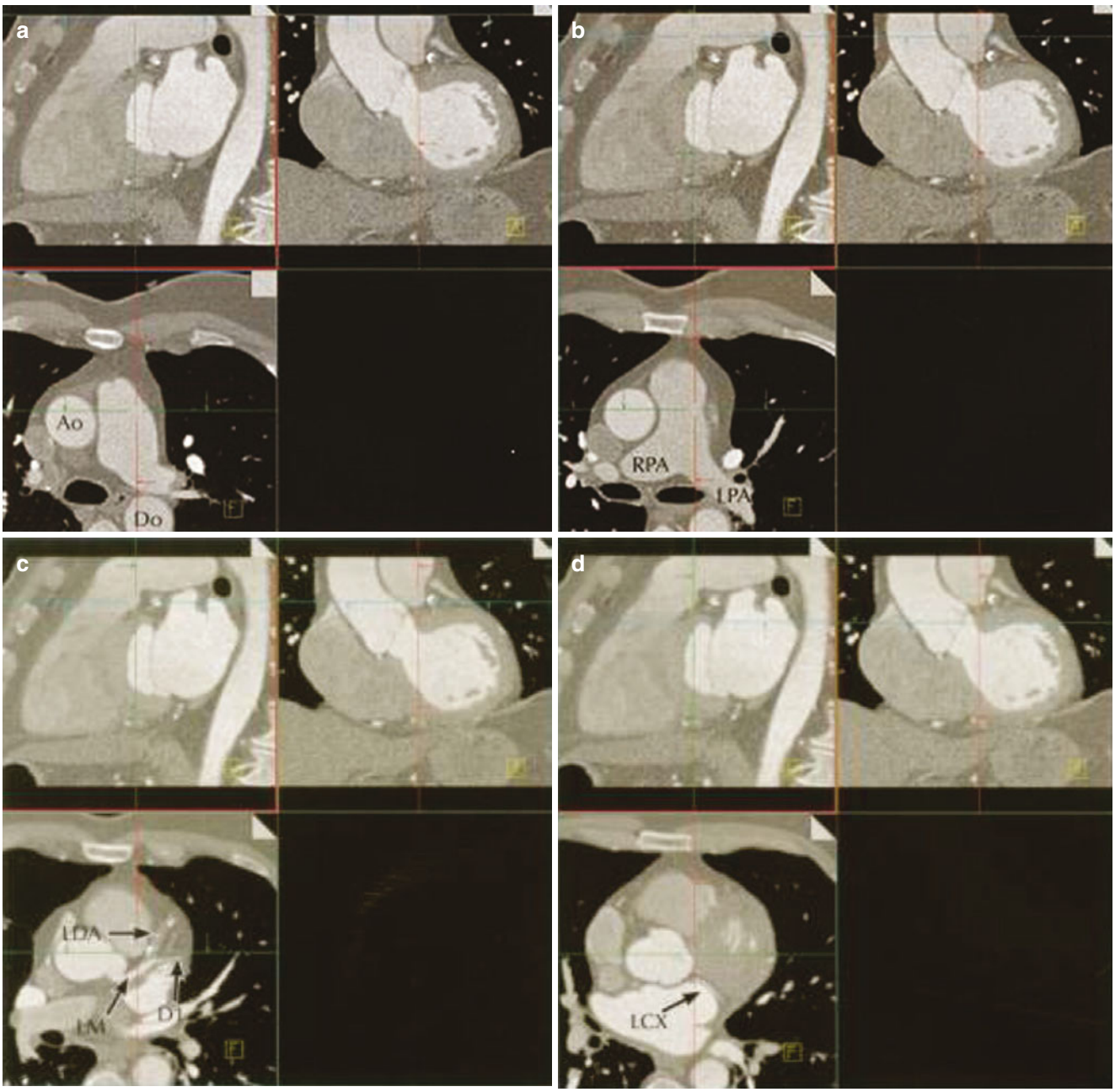

Fig. 2.19 Coronary evaluation: reviewing axial data. Scrolling in a caudal direction with a focus on the axial dataset reveals much about a patient's coronary arteries: (**a**), Pulmonary outflow tract and the ascending aorta (Ao) and descending aorta (Do). (**b**), Right pulmonary artery (RPA) and left pulmonary artery (LPA). (**c**), Left main (LM), an occluded proximal left anterior descending (LAD), and first diagonal (D1). Note that the origin of the circumflex is not visible. (**d**), Anterior to the left atrium, a segment of the left circumflex (LCX) is visualized. Additional views showed that the LCX originates from the right coronary artery (RCA). (**e**), The proximal RCA is visualized, showing extensive plaque. (**f**), The mid RCA is free of plaque. (**g**), The distal RCA, posterior descending artery (PDA), and posterolateral branch (PL) are visible and patent

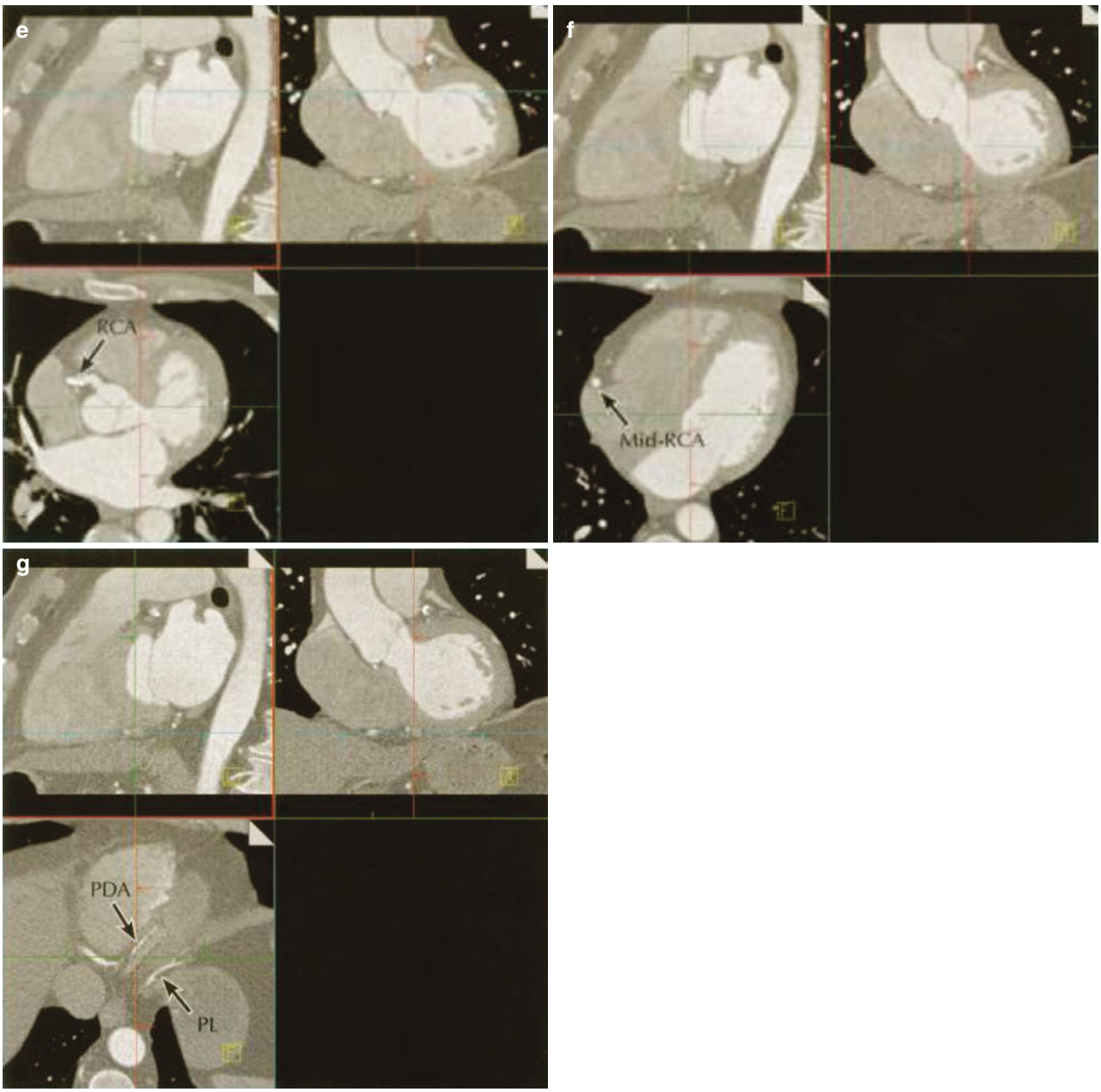

Fig 2.19 (cintinued)

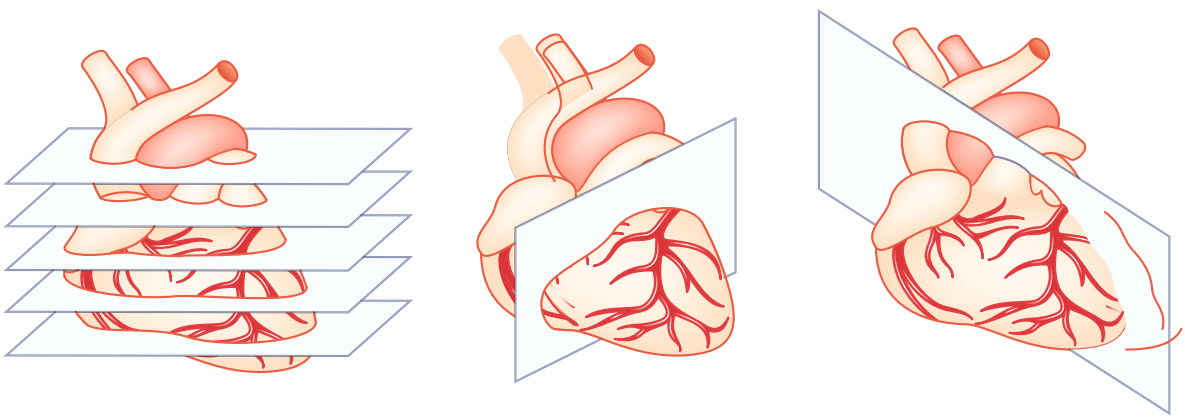

Fig. 2.20 Multiplanar reformats. The "source" (primary) dataset consists of a stack of axial images (*left*). This dataset can be manipulated to create a multiplanar reformat with a differing orientation (*middle* and *right*)

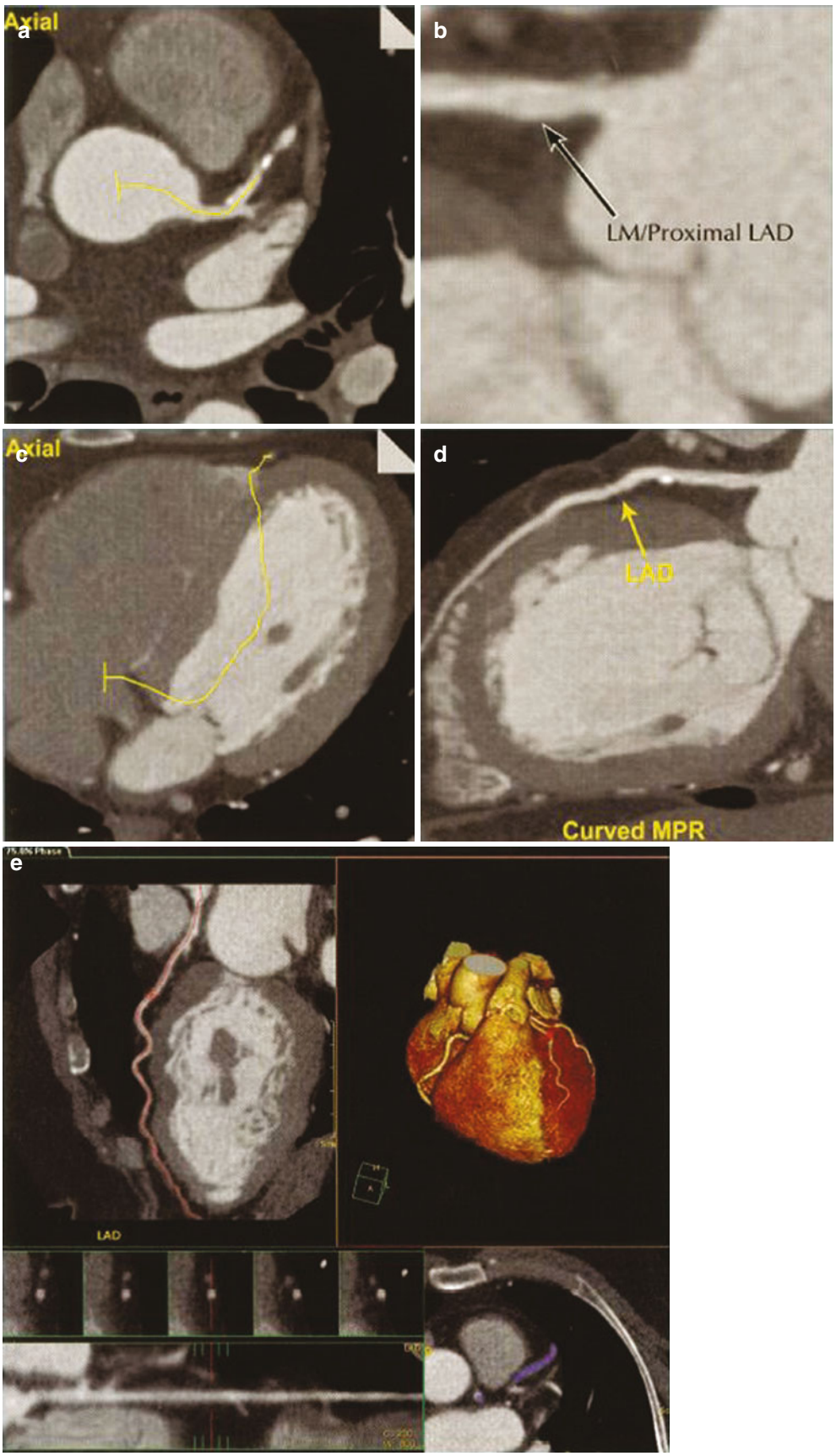

Fig. 2.21 Curved multiplanar reformats (MPRs). A curved MPR can be created manually or using an automated approach. (**a**), The left anterior descending artery (LAD) is tagged manually starting at the aorta and continuing to the proximal LAD. (**b**), The accompanying curved MPR. (**c**, **d**), This process is extended to the distal LAD. (**e**), Using an automated approach, the computer detects vessel lumen by tracking Hounsfield units (iodinated contrast). *LM* left main. (*Panel E courtesy of* NY Heart Center.)

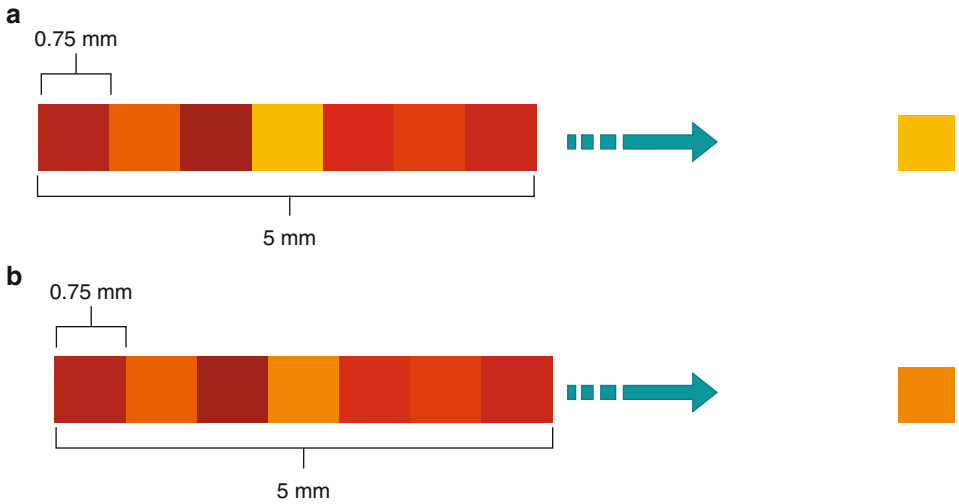

Fig. 2.22 Maximum intensity projections (MIP). (**a**, **b**), Two sets of 5-mm-thick MIPs. Although the individual pixels making up the thick slices include varying intensities of contrast (Hounsfield units), the MIP image projects only the highest value

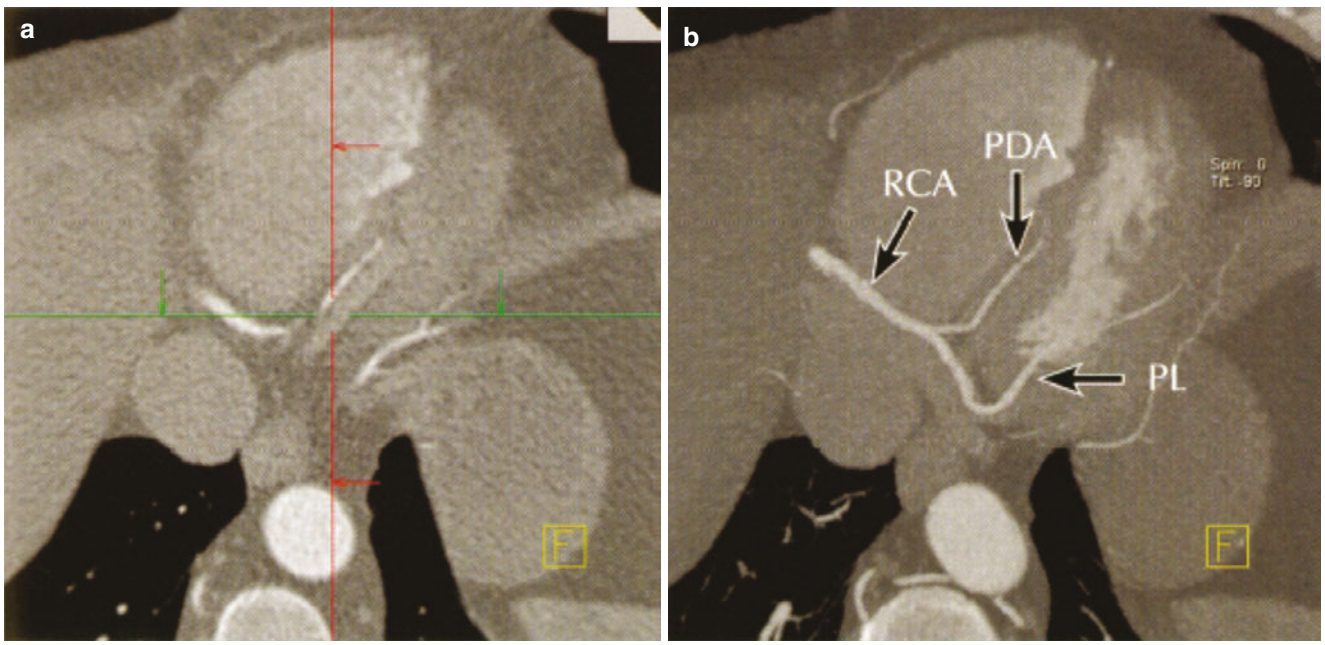

Fig. 2.23 Maximum intensity projection (MIP) images. (**a**), A 0.75-mm axial image (previously shown as Fig. 2.20g). (**b**), A 5-mm MIP image at the same anatomic level. This 5-mm MIP allows one to follow the distal right coronary artery (RCA) as it gives off the posterior descending artery (PDA) and right posterolateral branch (PL)

be masked within a thick MIP, if adjacent pixels have higher Hounsfield units.

When assessing coronaries, the first step should always be to review the axial images. If a potential stenosis requires further assessment, one can use MIPs and MPRs to obtain a true cross-section of the region of interest to determine if a significant stenosis is present (Fig. 2.24). Such an approach minimizes error as compared to utilizing curved MPRs when evaluating the degree of a coronary stenosis.

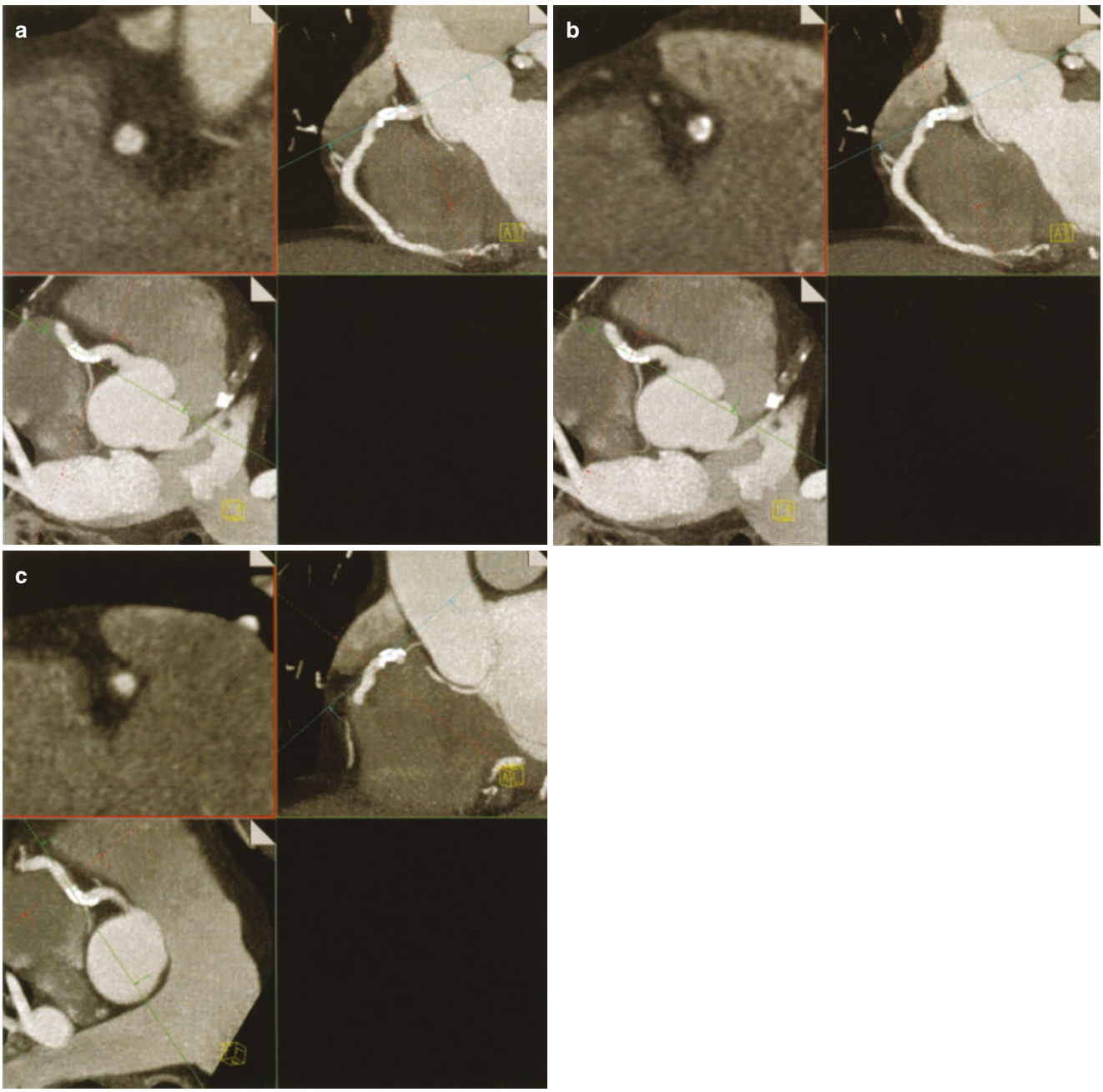

Fig. 2.24 Using MPR and MIP to evaluate a stenosis. An initial review of the axial images in Fig. 2.20e showed plaque in the proximal right coronary artery (RCA). Two 5-mm MIPs and a thin MPR were created to evaluate the lumen proximal to the stenosis (**a**), at the site of plaque (**b**), and distal to the lesion (**c**). The 5-mm MIPs allow one to follow a longer segment of the proximal RCA. Each of the MIPs is orthogonal to the other MIP, allowing one to create a true cross-section of the RCA (*red box*). The *red dashed line* shows the anatomic location of each cross-sectional image shown in the upper left panel. As can be seen, in true cross-section (as a thin MPR), extensive calcified plaque is present within the proximal RCA, but a significant stenosis is not present

Evaluating Cardiac Function

In addition to evaluating coronary vessels, cardiac CT angiography also allows one to evaluate cardiac function. For functional analysis, data from multiple phases of the cardiac cycle are included so that the myocardium can be viewed in motion as it oscillates through the cardiac cycle (Fig. 2.25). The authors construct a dataset at 10% intervals from 5 to 95% of the R-R interval. Including fewer than ten phases decreases the size of the dataset and minimizes the time required to process the images, but it may fail to accurately capture end-diastole and end-systole. Constructing thicker slices without overlap also helps to reduce the size of the dataset. Limiting the volume of the dataset used for reconstruction to the myocardium (the region of interest for functional analysis) limits the size of this dataset.

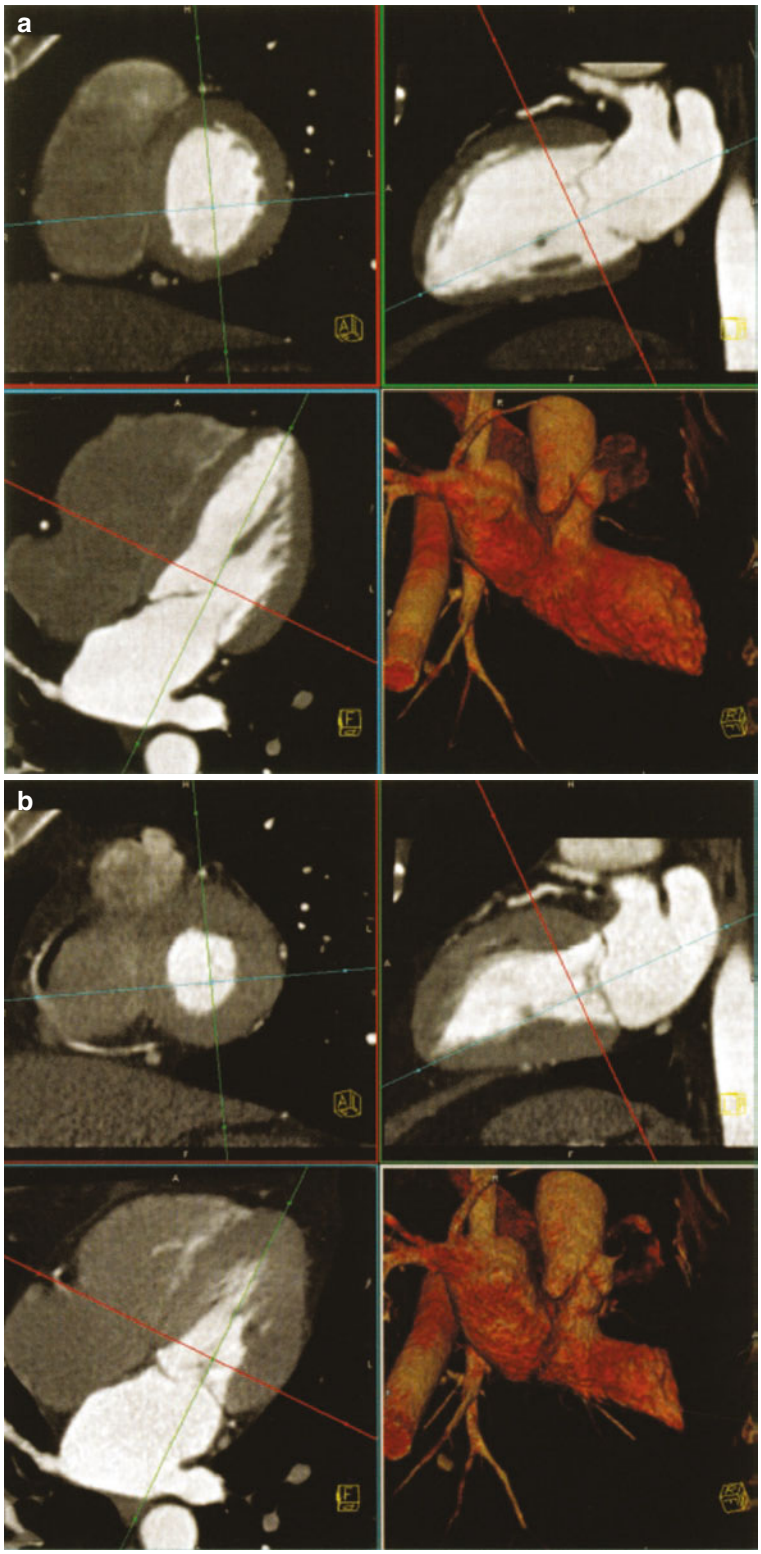

Fig. 2.25 Evaluation of cardiac function. The primary views utilized to assess left ventricle function. The *upper left box* in each group shows a true short axis of the left ventricle. This was formed by creating two longitudinal views (*upper right and lower left boxes*), each orthogonal to the other, with the axis coursing through the mitral valve and the apical thin point of the left ventricle. Once the views are created, one can evaluate function by playing a cine loop of the views, monitoring wall thickening and motion as the heart oscillates from diastole to systole. (**a**), A still frame at 65% (late diastole) of the R-R interval. (**b**), A still frame at 25% (systole) of the R-R interval. Normal thickening and wall motion is seen at this level. By scrolling from the base to the apex, all myocardial regions can be assessed. The sagittal view in the *upper right box* also provides excellent visualization of the anterior and inferior aspects of the left ventricle. The *bottom right box* shows a volume-rendered image of the heart and great vessels. These images are constructed at a slice thickness of 1.5 mm and a reconstruction increment of 1.5 mm

Evaluating Noncardiac Anatomy

A final step in the post-processing phase is the creation of a dataset to evaluate extracardiac anatomy. The topogram is used to set the anatomic boundaries for the reconstruction. The cranial and caudal boundaries are set during the data acquisition step. The entire thorax may appear on the topogram, though CT data were previously confined to more limited cranial and caudal boundaries. The lateral boundaries should include all soft tissues. In such a manner, lung and bone windows are used to assess extracardiac anatomy (Fig. 2.26).

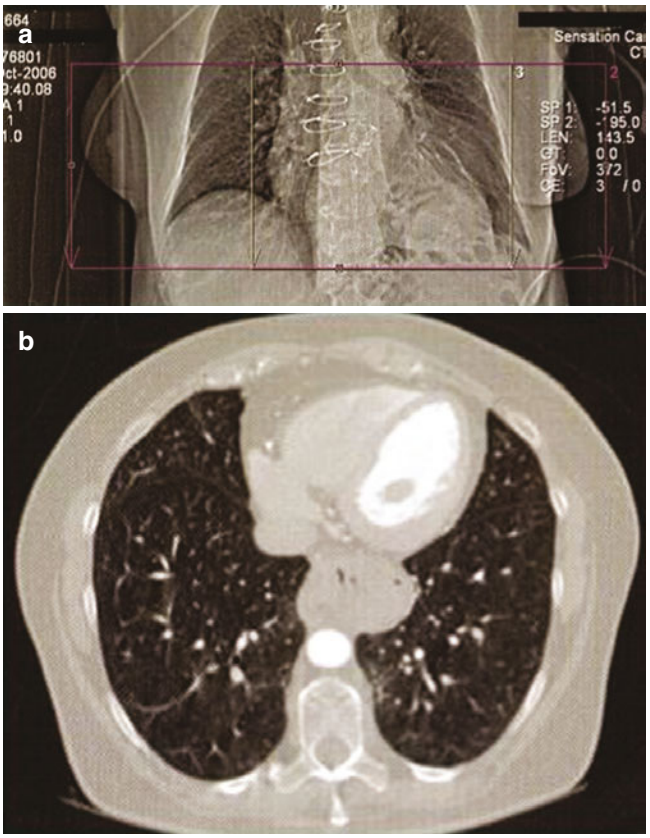

Fig. 2.26 Evaluating noncardiac anatomy. (**a**), The topogram, which is used to set the anatomic boundaries (*purple rectangle*) for the reconstruction. Although the entire thorax appears on the topogram, CT data was previously limited to the boundaries within the purple rectangle. The lateral boundaries require adjustment and should include all soft tissues. (Note that all breast tissue has been included.) The reconstruction parameters for constructing this data set include a medium-sharp kernel, slice thickness of 1.5 mm, and a reconstruction increment of 0.8 mm, which provides overlap and improves the signal-to-noise ratio. (**b**), An example of a lung window obtained to evaluate extracardiac anatomy. The mass anterior to the descending aorta is not an uncommon finding. Scrolling through the dataset shows it to be a large hiatal hernia

References

1. Ferencik M, Nomura CH, Maurovich-Horvat P, Hoffmann U, Pena AJ, Cury RC, et al. Quantitative parameters of image quality in 64-slice computed tomography angiography of the coronary arteries. Eur J Radiol. 2006;57:373–9.
2. Hundt W, Rust F, Stäbler A, Wolff H, Suess C, Reiser M. Dose reduction in multislice computed tomography. J Comput Assist Tomogr. 2005;29:140–7.
3. Cademartiri F, Mollet NR, Runza G, Baks T, Midiri M, McFadden EP, et al. Improving diagnostic accuracy of MDCT coronary angiography in patients with mild heart rhythm irregularities using ECG editing. AJR Am J Roentgenol. 2006;186:634–8.
4. Sanz J, Rius T, Kuschnir P, Fuster V, Goldberg J, Ye XY, et al. The importance of end-systole for optimal reconstruction protocol of coronary angiography with 16-slice multidetector computed tomography. Investig Radiol. 2005;40:155–63.
5. Dewey M, Laule M, Krug L, Schnapauff D, Rogalla P, Rutsch W, et al. Multisegment and halfscan reconstruction of 16-slice computed tomography for detection of coronary artery stenoses. Investig Radiol. 2004;39:223–9.

Normal Coronary Anatomy

3

Farhood Saremi, Stephan S. Achenbach, and Jagat Narula

Since its introduction by Mason Sones in 1959, the standard clinical tool to visualize the coronary artery has been invasive cardiac catheterization and coronary angiography. With high spatial resolution (approximately 0.2 mm), invasive coronary angiography can reliably demonstrate the anatomy of the epicardial coronary arteries down to their third-generation branches. Invasive coronary angiography provides projectional images of the coronary arteries that can make orientation difficult and, because of overlap and foreshortening, can prevent adequate visualization of certain coronary segments. On the other hand, accurate image interpretation requires visualization of the coronary arteries from different imaging planes. CT imaging, as opposed to invasive coronary angiography, generates a data set volume consisting of many 0.5-mm cross-sectional images in transaxial (transverse) orientation, which can be reconstructed in any planes desired. Although the spatial and temporal resolutions are lower than in invasive coronary angiography, the noninvasive nature of the test has led to a rapidly increasing use in clinical practice.

By increasing the post-processing power of modern workstations, CT analysis of coronary vessels is substantially improved. The use of curved multiplanar reformation (MPR), often created by an automated or semi-automated algorithm, allows for display of the entire coronary vessel in a single two-dimensional (2D) image, with the ability to rotate the artery around a focal point. Maximum intensity projections (MIP) are created using thicker sections and can be helpful to reduce image noise and/or visualize a longer vessel segment. Volume rendered three-dimensional (3D) images allow for rapid interpretation of structural relationships such as vessel course in relation to other cardiac or vascular structures. Over years, vessels tracking and segmentation methods are improved, and with color-coding the quality of 3D images is further enhanced. Although many post-processing tools and techniques are available to generate 2D and 3D reconstructions of the heart and coronary arteries, review of the original transaxial slices is the key step in evaluation of cardiac CT examinations.

This chapter will place special emphasis on typical coronary anatomy as seen in coronary CT angiography (Figs. 3.1, 3.2, 3.3, 3.4, 3.5, 3.6, 3.7, 3.8, 3.9, 3.10, 3.11, 3.12, 3.13, 3.14, 3.15, 3.16, 3.17, 3.18, and 3.19).

F. Saremi
Department of Radiology, University of Southern California,
USC University Hospital, Los Angeles, CA, USA

S.S. Achenbach (✉)
Department of Cardiology, University of Erlangen,
Ulmenweg 18, 91054 Erlangen, Germany
e-mail: stephan.achenbach@uk-erlangen.de

J. Narula
Mount Sinai Heart, Icahn School of Medicine at Mount Sinai,
New York, NY, USA
e-mail: narula@mountsinai.org

M.J. Budoff et al. (eds.), *Atlas of Cardiovascular Computed Tomography*, https://doi.org/10.1007/978-1-4471-7357-1_3

a **Simplified Coronary Artery Segment Model**

Right coronary artery	
1	Proximal RCA (to one half the distance to the acute margin of the heart)
2	Mid RCA (from end of segment 1 to acute margin of the heart)
3	Distal RCA (to origin of posterior descending branch)
4	Right posterior descending branch, when present
Left main coronary artery	
5	Left main coronary artery
Left anterior descending artery	
6	Proximal LAD (to the first major septal perforator)
7	Mid LAD
8	Apical LAD
9	First diagonal
10	Second diagonal
Left circumflex	
11	Proximal LCX (up to the origin of the obtuse marginal branch)
12	Obtuse marginal
13	Distal LCX (from obtuse marginal origin, in AV groove)
14	Left posterolateral (may be absent or may be a division of the obtuse marginal branch)
15	Left posterior descending, when present as a branch from the LCX

b

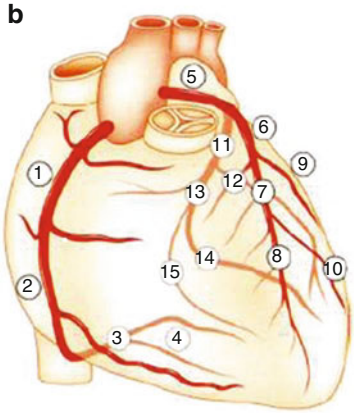

Fig. 3.1 Society of Cardiovascular Computed Tomography (SCCT) coronary segmentation diagram. *Dashed lines* represent division between RCA, LAD, and LCx and the end of the LM. *PLB* posterior-lateral branch, *PLV* posterior left ventricular branch. Definitions derived and adjusted from the report by Austen et al. [10]. The abbreviation and description for each segment can be found in Appendix 1 2009. Society of Cardiovascular Computed Tomography. (**a**) Location of segment, (**b**) Schematic of segments. (Adapted from Leipsic et al. [3])

a **Classification System for Coronary Artery Segments [3]**

Right coronary artery		Left main coronary artery		Left circumflex	
1	Proximal RCA	11	Left main coronary artery	18	Proximal LCX
2	Mid RCA	12	Proximal LAD	19	Distal LCX
3	Distal RCA	13	Mid LAD	20	First obtuse marginal
4	Right posterior descending branch (if from RCA)	14	Distal LAD	21	Second obtuse marginal
5	Right posterior atrioventricular branch	15	First diagonal	22	Third obtuse marginal
6	First right posterolateral (if from RCA)	16	Second diagonal	23	LCX atrioventricular groove
7	Second right posterolateral (if from RCA)	17	LAD septal perforators	24	First left posterolateral branch (if from LCX)
8	Third right posterolateral (if from RCA)	28	Ramus intermedius	25	Second left posterolateral branch (if from LCX)
9	Posterior descending septals (if from RCA)	29	Third diagonal	26	Third left posterolateral branch (if from LCX)
10	Acute marginal segment			27	Left posterior descending branch (if from LCX)

b

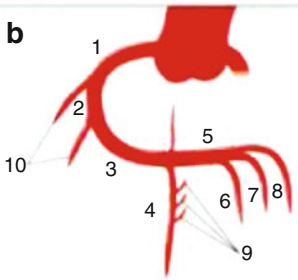

c

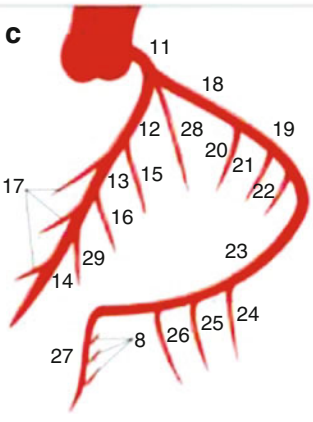

Fig. 3.2 (**a**) Classification system for coronary artery segments according to the American College of Cardiology/American Heart Association Guidelines for Invasive Coronary Angiography [4]. (**b**, **c**), Schematic drawing of the lesion classification system. Each coronary segment will only be considered if it is actually present. For example, the posterior descending coronary artery will be segment four in the case of right dominance; it will be segment 27 in the case of left dominance. *LAD* left anterior descending, *LCX* left circumflex, *RCA* right coronary artery. ((**b**, **c**) adapted from The American College of Cardiology/American Heart Association [4])

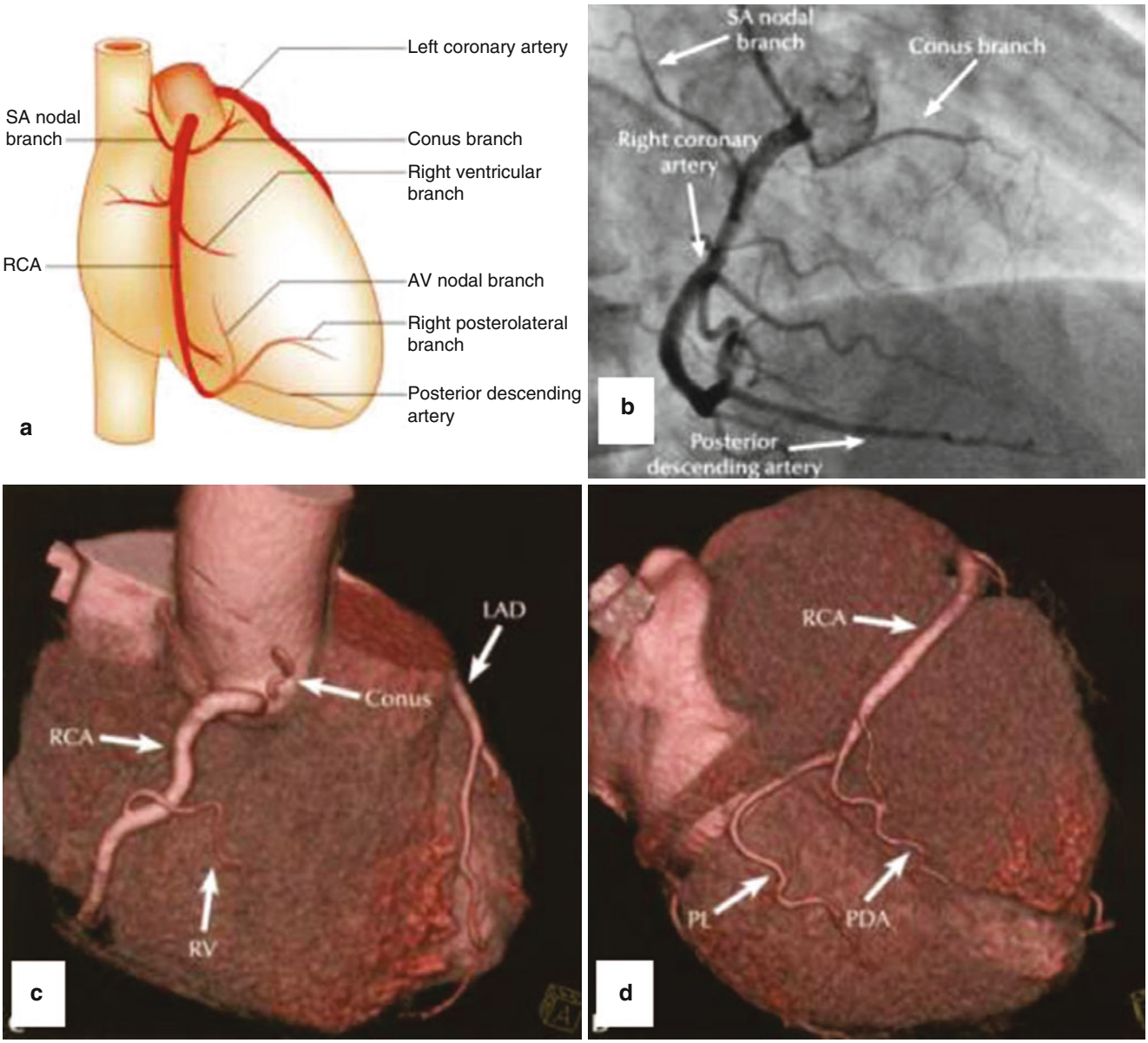

Fig. 3.3 Right coronary artery (RCA) anatomy. (**a**) Schematic right anterior oblique view. (**b**) Invasive angiography, right anterior oblique projection. (**c**) Volume rendered CT angiography, anterior view. (**d**) CT posteroinferior view. The RCA ostium has a more anterior position in the right sinus of Valsalva. The RCA descends into the right atrioventricular groove. Very proximally, the small conus branch arises from the RCA (or from a separate ostium) and is directed toward the right ventricular outflow tract. The sinoatrial (SA) nodal artery usually also arises from the proximal RCA. Several right ventricular branches can arise from the descending section of the RCA. In most individuals, the artery continues to the diaphragmatic surface of the heart. At the crux, the RCA then gives rise to a very small atrioventricular (AV) nodal branch. The RCA usually then descends into the inferior (posterior) interventricular groove to provide the posterior descending branch. The posterior descending artery can reach the apex and provides some septal branches. If the right coronary artery extends beyond the crux, the branches are called right posterolateral branches

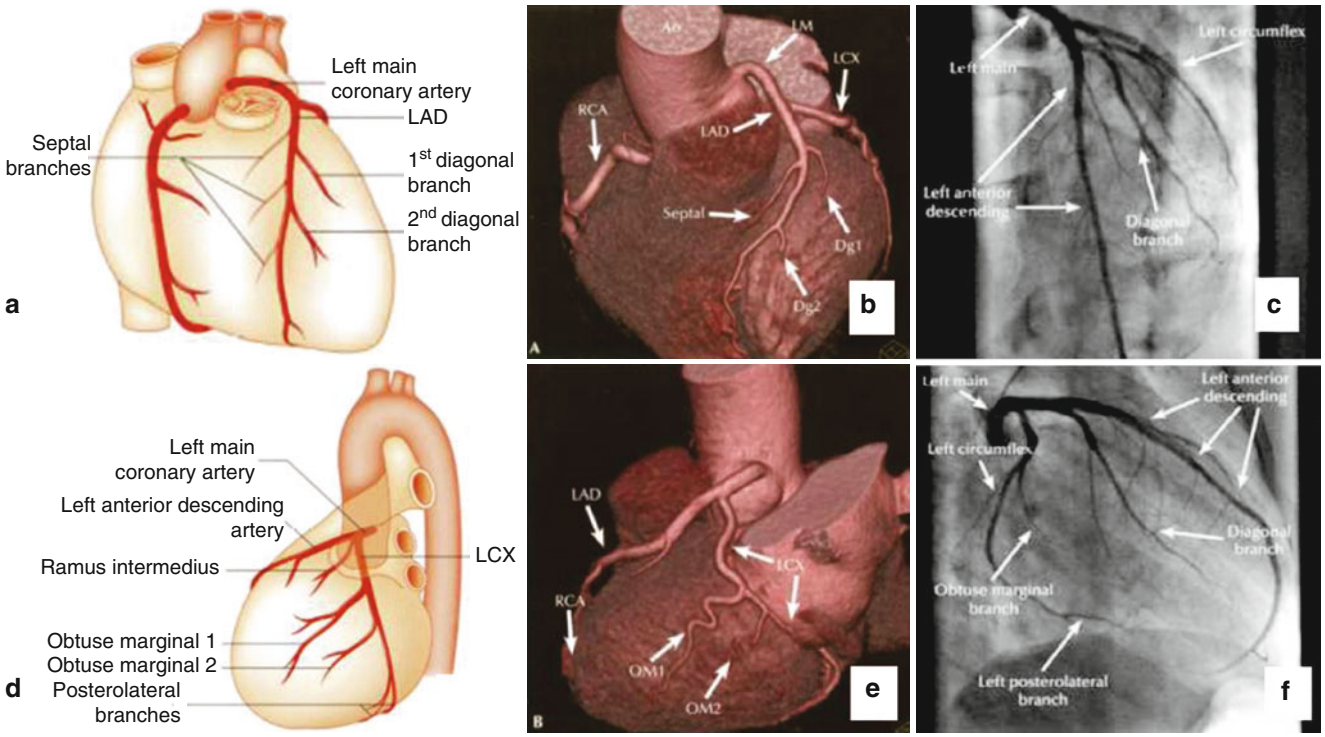

Fig. 3.4 Left coronary system. (**a**) Schematic frontal view. (**b**) Volume rendered CT angiography, left anterior oblique projection. (**c**) Invasive angiography, left anterior oblique and cranial projection. (**d**) schematic left lateral view. (**e**) Volume rendered CT angiography, left lateral view. (**f**) Invasive angiography, right anterior oblique and caudal projection. The left main (LM) coronary artery arises several millimeters higher in the superior part of the left coronary sinus. The left main coronary artery then divides into the left anterior descending (LAD) artery and the left circumflex (LCx) artery. The LAD descends in to the anterior interventricular groove. It will usually reach the apex, and in some cases, extends beyond the apex to the inferior wall. A short intramyocardial segment is often present. During its entire course, the LAD gives rise to septal branches that penetrate the interventricular septum; the first septal branch is often large. The diagonal (Dg) branches arising from the LAD toward the left lateral wall are variable in size and number. Usually, one or two larger diagonal branches are present. On rare occasions, a diagonal branch can be larger than the LAD. The LCX enters the left atrioventricular groove and usually gives rise to one or several obtuse marginal (OM) branches and will then continue to end in several left posterolateral branches. Very commonly, the OM branch or branches are larger than the segment of the LCX that continues beyond their origin

Coronary Arteries

The epicardial coronary arteries supply the heart with oxygen and nutrients. At rest, approximately 5–8% of cardiac output is directed toward coronary circulation. Because the myocardium extracts approximately 70% of oxygen out of the blood, increases in myocardial oxygen demand—for example, during exercise—can only be compensated for by increasing coronary blood flow. The necessity to provide blood flow to all segments of the myocardium with the ability to regulate blood flow over a very wide range thus constitutes the background for coronary artery anatomy and physiology. Recent histological analysis in mouse and cardiac organ culture has shown that coronary vessels arise from angiogenic sprouts of the sinus venosus, the major vein that returns circulating blood to the embryonic heart [1]. Some sprouting venous endothelial cells dedifferentiate into arteries and capillaries as they invade the myocardium, and some remain on the surface and differentiate into veins [1].

There is substantial variability of the distribution pattern and coronary anatomy from one individual to the next, constitutional as well as in response to cardiac disease [2].

In general, coronary vessels are named for the structures that they supply rather than for their origin. This nomenclature is based on the embryologic development pattern created when the coronary vessels sprouts arise on the surface of the heart, and only later connect to the aorta. Thus, various perturbations in the connections of the coronary vessels to each other and to the aorta occur after the formation of the coronary vessels. Despite variability in coronary artery origin, course, and branching, the vast majority of individuals have two coronary arteries; the right coronary artery and the left coronary

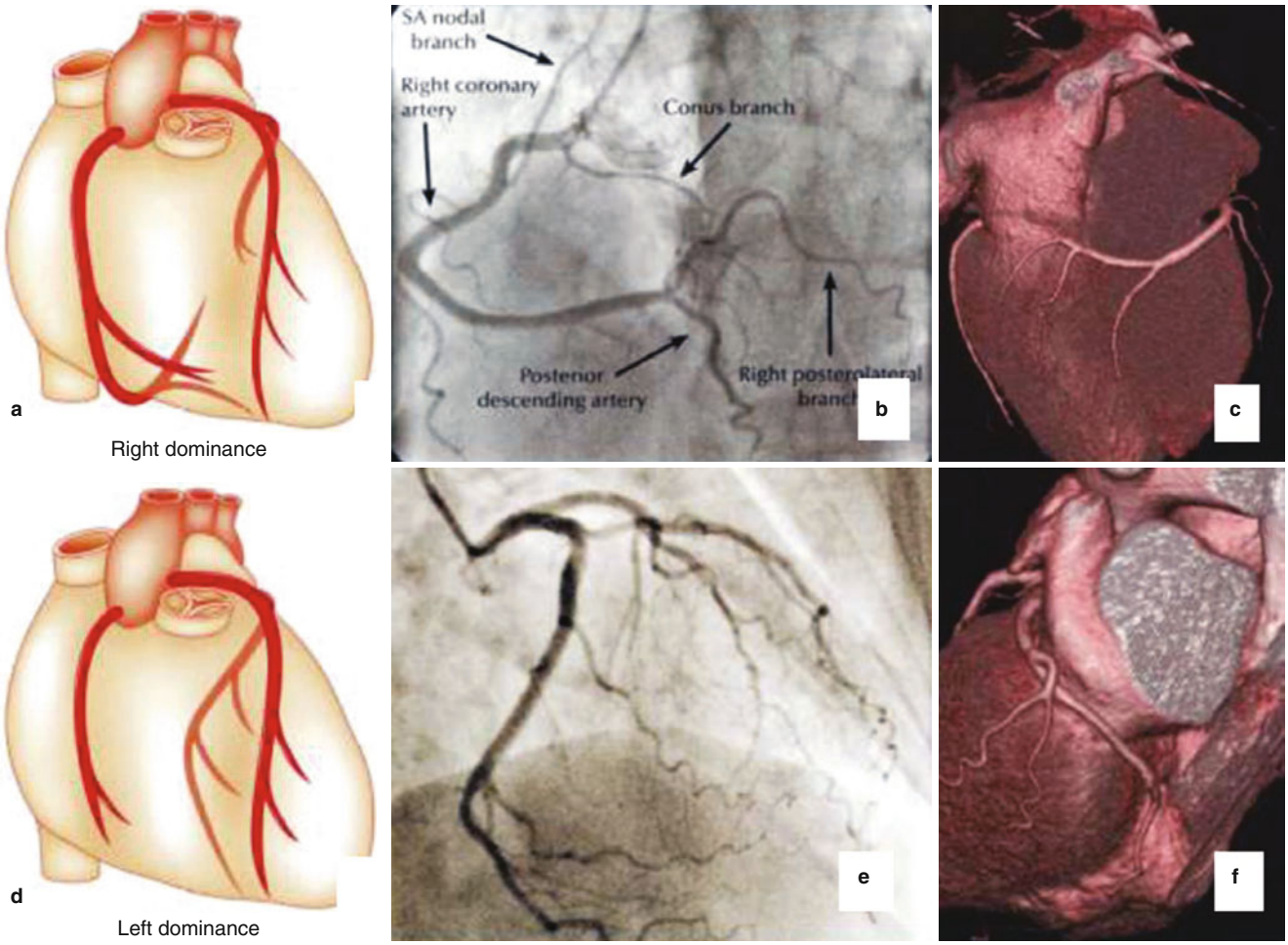

Fig. 3.5 Coronary dominance. (**a**–**c**) = right dominant, (**d**–**f**) = left dominant. (**a**) Schematic frontal view. (**b**) Invasive angiography, left anterior oblique projection. (**c**) Volume rendered CT angiography, posterior view. (**d**) schematic frontal view. (**e**) Invasive angiography, right anterior oblique and caudal projection. (**f**) Volume rendered CT angiography, left posterolateral view. In right dominant system, the right coronary artery (RCA) gives rise to the posterior descending artery (PDA) and at least one right posterolateral branch. In left dominant, the left circumflex coronary artery is large and provides a PDA. The RCA is small and does not extend beyond the acute margin of the heart. In approximately 85% of all patients, a right dominant pattern of coronary circulation is present, whereas in 15%, the right coronary artery is non-dominant, with "codominance" and left dominance found each in approximately one half of (2). *SA* sinoatrial

artery, which branches into the left anterior descending and left circumflex coronary artery. These three main coronary vessels are considered arteries and the smaller, more distal vessels are generally termed coronary branches. However, it is not uncommon for some branches to be called arteries, i.e., sinoatrial node artery or posterior descending artery [3–5].

There are several commonly recognized variations in normal coronary artery anatomy. Instead of bifurcating into the left anterior descending and left circumflex arteries, in some patients the left main trifurcates into a left anterior descending, left circumflex and ramus intermedius arteries. The origin of the posterior descending artery and posterolateral branches that supply the inferior wall can originate from the right coronary artery only (right dominant), the left circumflex artery (left dominant), or from both arteries (co-dominant). Another definition of coronary dominance involves the artery that gives rise to the atrioventricular node artery. The sinoatrial node)is supplied by a single branch from the proximal right coronary artery in two-thirds of people [6]. Other variants include from the proximal left circumflex and distal right coronary artery. An)S-shaped variant is relatively common [7]. Some patients have smaller branches that arise directly from the aorta as opposed to from the coronary arteries, including direct origin of the conus or sinuatrial node branch from the aorta. Myocardial bridging of the proximal left anterior descending artery is common and refers to the intramyocardial course of a portion of a normally positioned epicardial coronary artery. The degree in which the coronary artery "dives" into the myocardium is variable in depth and length.

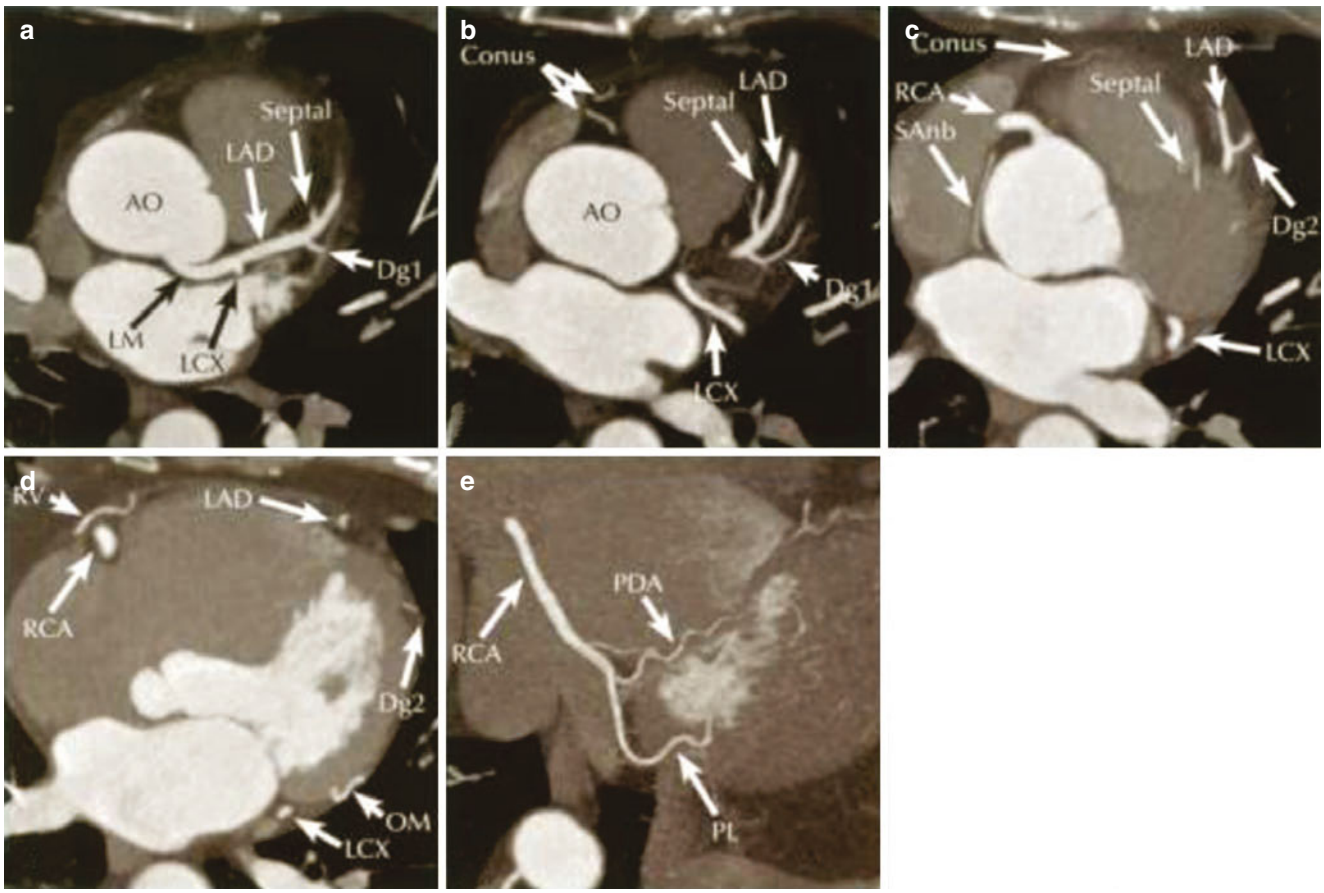

Fig. 3.6 Anatomy of the coronary arteries in transaxial slices of coronary CT angiography. (**a**) The left main (LM) and the proximal left anterior descending (LAD) arteries follow a horizontal and slightly anterior course in the transaxial plane. The origin of the left circumflex artery (LCx), first diagonal (Dg) branch, and septal perforator branch are usually seen in the same plane. (**b**) The LAD enters the anterior interventricular groove and takes a course toward the apex. The left circumflex artery enters the left atrioventricular groove. Portions of a tortuous right conus branch are visualized anterior to the right ventricle outflow tract. (**c**) The right coronary artery (RCA) ostium is several millimeters below the LM ostium. The RCA often gives rise to the sinoatrial nodal branch (SAnb). The LAD continues and gives rise to additional diagonal branches. (**d**) The RCA follows a course in the right atrioventricular groove. In its proximal and mid-segment, it is usually oriented orthogonally to the axial imaging plane so that a cross-section of the artery is seen. The LCx remains in the atrioventricular groove, but an obtuse marginal (OM) branch crosses the lateral wall of the left ventricle. (**e**) The distal RCA takes a horizontal course; therefore, it can be visualized over a long segment using transaxial images. At the cardiac crux, the RCA gives rise to a posterior descending artery (PDA) and, in cases of right dominance, to one or several right posterolateral (PL) branches. *AO* aorta, *RV* right ventricular branch, *Septal* septal perforator branch

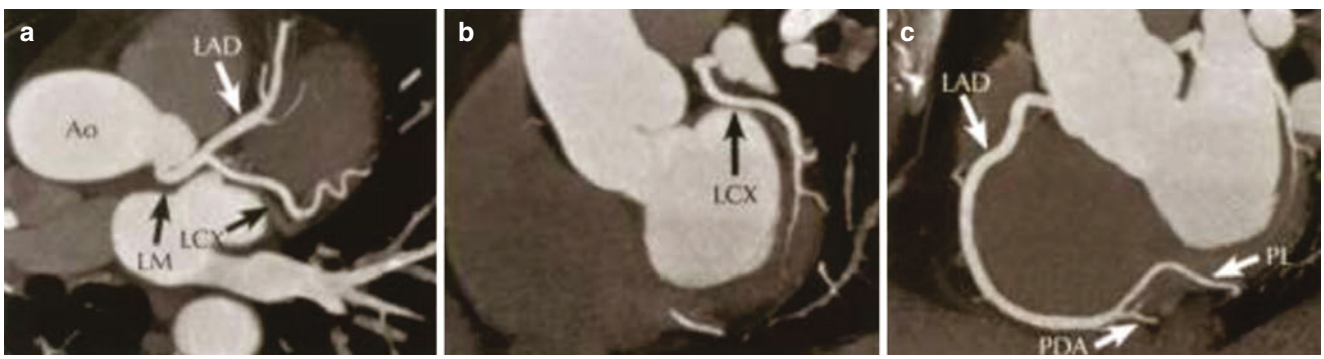

Fig. 3.7 In oblique MIP orientations, longer segments of the coronary arteries can be recorded in one view. (**a**) Axial oblique reconstruction of the proximal left coronary artery showing the left main (LM), left anterior descending (LAD), and left circumflex (LCx) arteries. (**b**) Short axis oblique reconstruction of the proximal LCx. (**c**) Short axis oblique reconstruction of the RCA. The imaging plane is aligned with the atrioventricular groove. *Ao* aorta, *PDA* posterior descending artery, *PL* right posterolateral branch

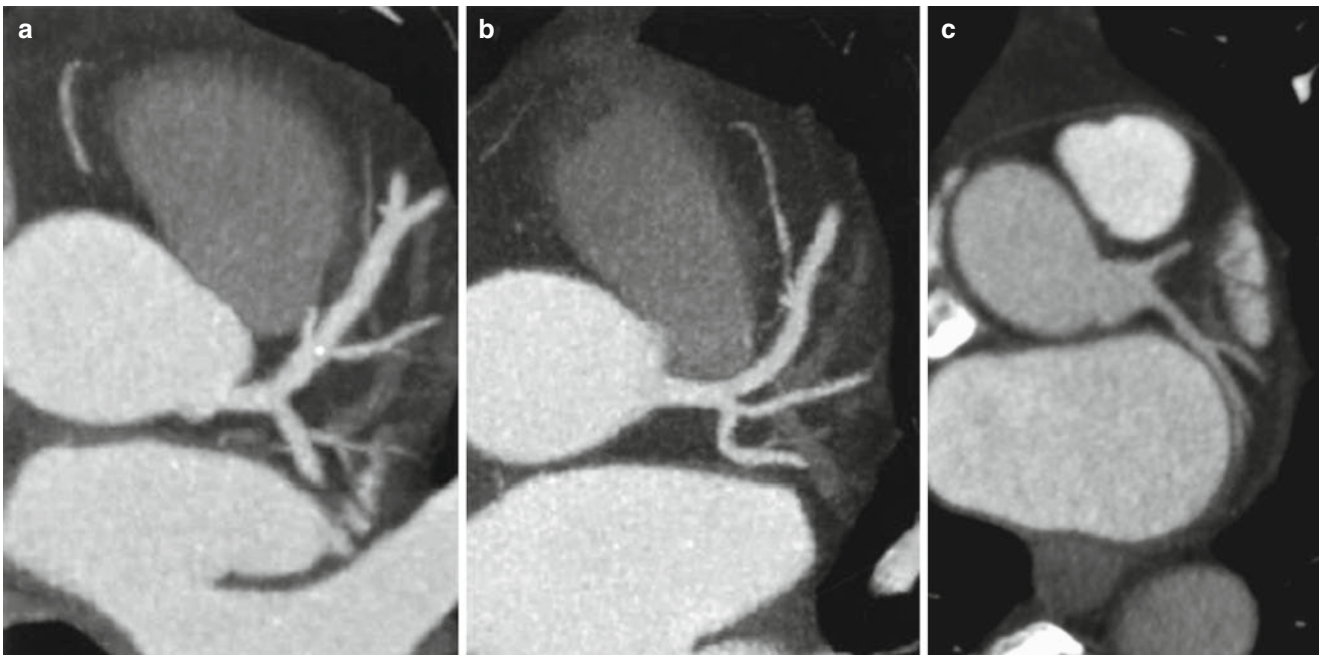

Fig. 3.8 Patterns of left main bifurcation. (**a**) The left main coronary artery bifurcates into a left anterior descending (LAD) artery and left circumflex (LCx) artery. The angle is usually obtuse (average angle: 80° [5]). Soon after the bifurcation, the LAD gives rise to a first diagonal branch and the LCx gives rise to a first obtuse marginal branch. (**b**) Trifurcation of the left main coronary artery into a LAD, ramus intermedius, and LCx coronary artery. The ramus intermedius, also known as the intermediate branch, or ramus, varies in length and size. It typically supplies the lateral wall of the left ventricle in a territory similar to that supplied by the diagonal or obtuse marginal branches. As a result, the branches that would normally supply these regions may be diminutive. (**c**) absence of the left main and separate origins of the LAD and LCx from the left coronary sinus

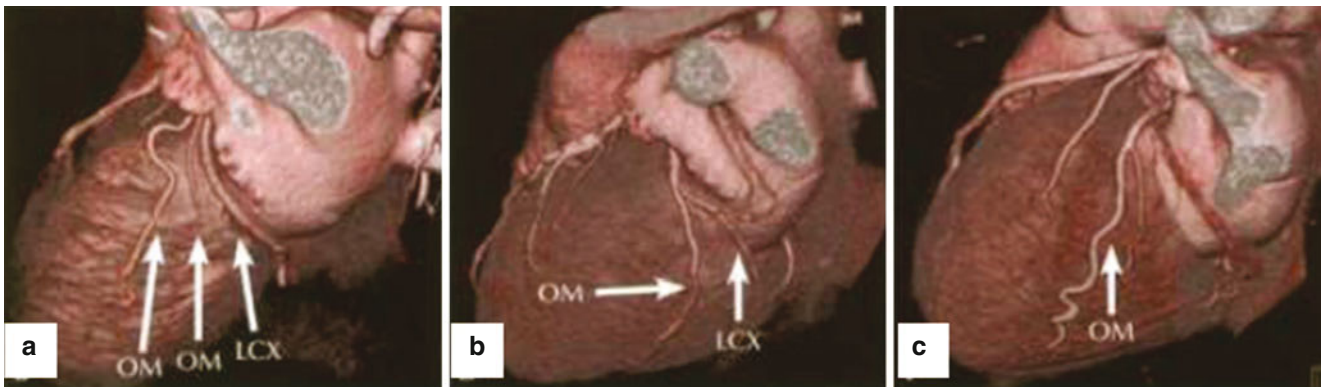

Fig. 3.9 (**a**–**c**) The anatomy of the left circumflex (LCx) artery is variable. As long as the vessel runs in the atrioventricular groove, it is called left circumflex coronary artery. Branches toward the left lateral wall are called obtuse marginal (OM), and branches toward the posterolateral wall are called left posterolateral branches. Frequently, the obtuse marginal or posterolateral branches have a larger caliber than the LCx itself. The LCx artery often ends as an obtuse marginal or posterolateral branch. (**a**, **b**) Pattern with a large LCx artery in the atrioventricular groove and two smaller OM branches. (**c**, **d**) Pattern with a large OM branch and a smaller left circumflex coronary artery in the atrioventricular groove

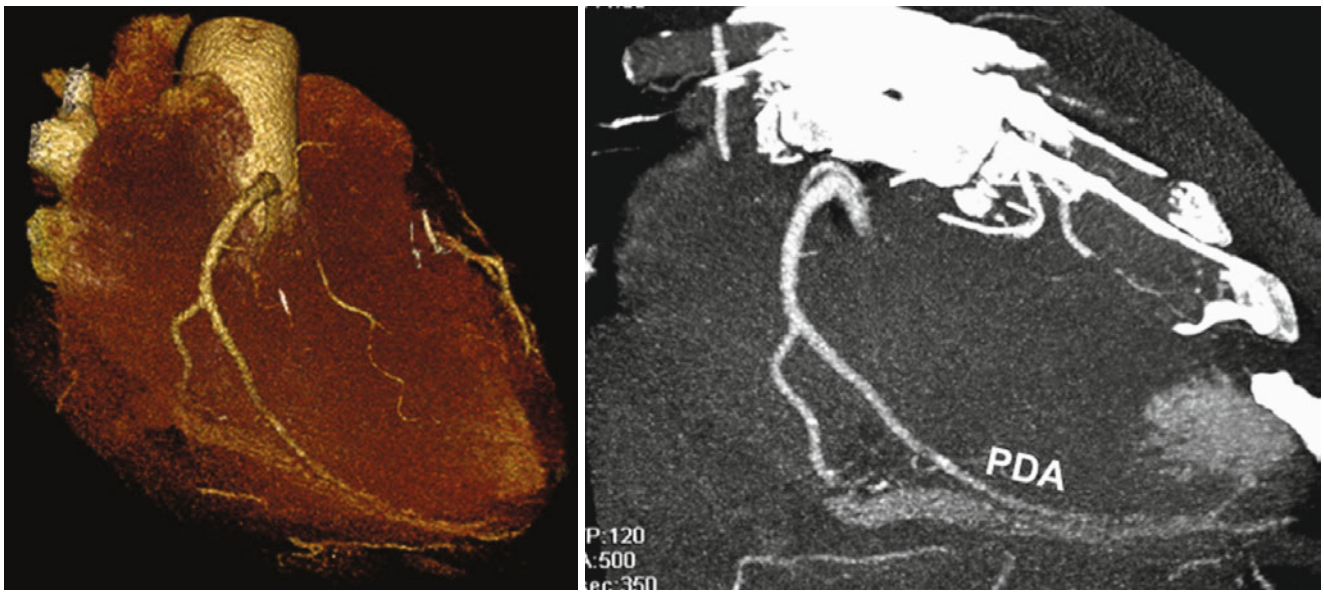

Fig. 3.10 Split right coronary artery (RCA). In most patients, the posterior descending artery (PDA) arises from the distal portion of the coronary artery, but some patients (approximately 1%) have early take-off of the PDA (long PDA) from the RCA (split RCA), which then courses toward the apex along the inferior interventricular groove. The proximal part of the inferior interventricular groove may be supplied by a short PDA

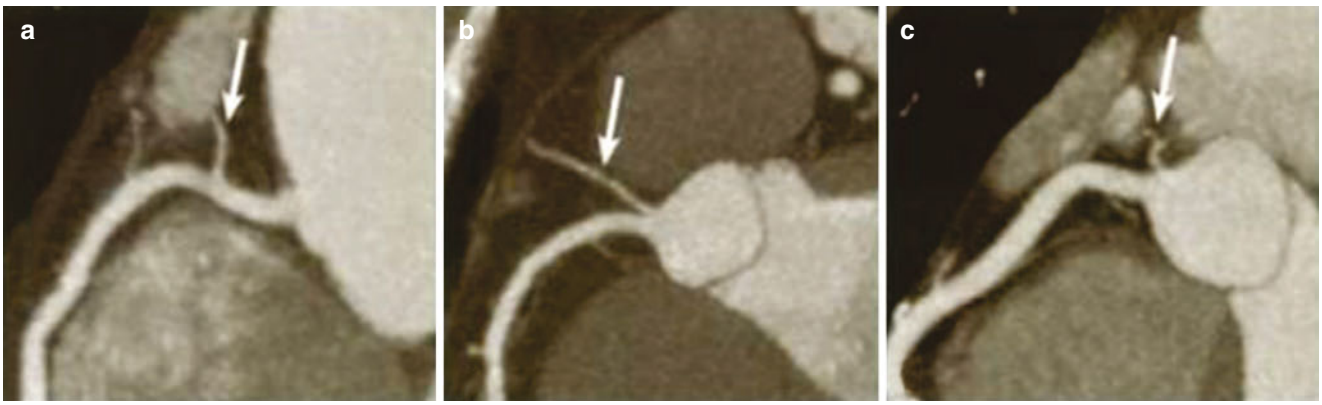

Fig. 3.11 Variants of the right conus branch (*arrows*) from the proximal right coronary artery (**a**), from a joint ostium with the right coronary artery (**b**), or directly from the aorta (**c**)

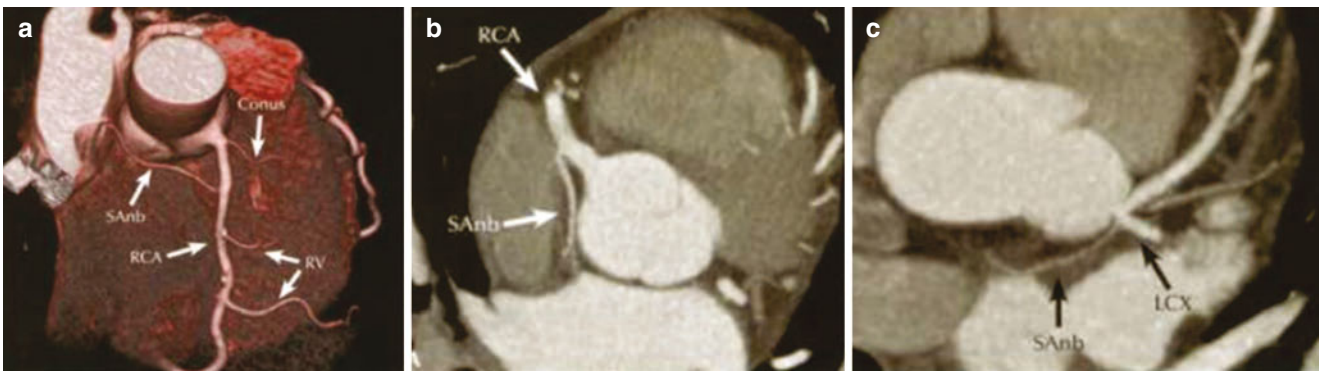

Fig. 3.12 Sinoatrial nodal branch (SAnb). The sinuatrial node is an electrically active tissue bundle that sits laterally at the junction of the right atrium and superior vena cava and serves as the primary pacemaker of the heart. The SAnb can arise from the right coronary artery (RCA) (**a**, **b**) or from the left circumflex coronary (LCx) artery (**c**). Usually, the origin of the SAnb will be in the very proximal segment of these arteries, but, occasionally, the vessel can arise further distal and take an atypical course toward the sinus node region. The SA node is supplied by a single branch from the proximal RCA in 60% of people. Other variants include SAnb from the proximal LCx or distal RCA or LCx artery [6]

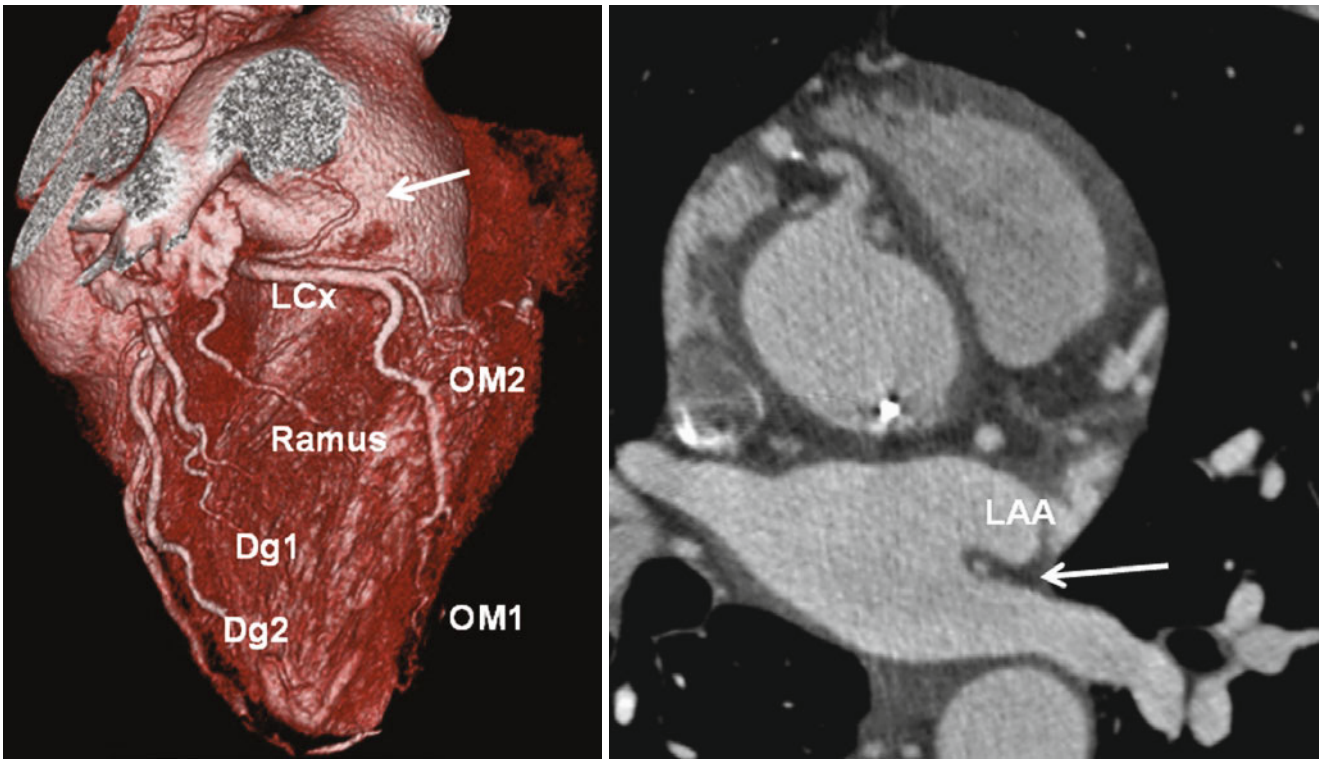

Fig. 3.13 S-shaped sinoatrial node artery (SAna) (*arrow*) is an anatomic variant of SA node artery originating from the proximal left circumflex (LCx) artery. It can be found in 14% of coronary CT angiographies [7]. The S-shaped SAna has a predictable proximal course, in the groove between the orifices of the left superior pulmonary vein and the left atrial appendage (LAA) close to the left atrial wall (*arrow*). This artery can be at risk in Maze surgery or catheter-based left atrial interventions. *Dg* diagonal branch, *OM* obtuse marginal

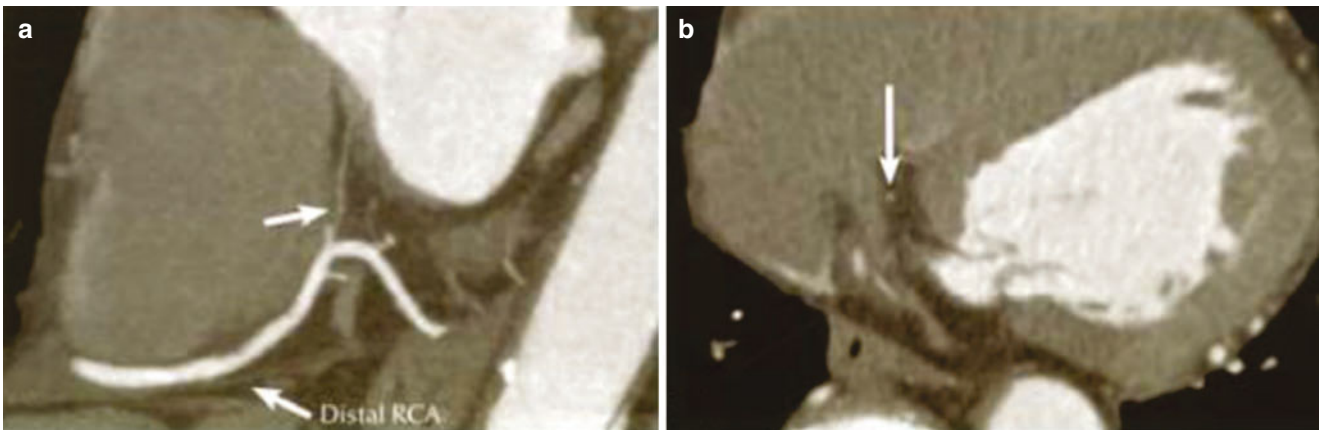

Fig. 3.14 (**a**, **b**) The atrioventricular (AV) nodal branch (*arrow*) is a small vessel that typically arises from the distal right coronary artery (RCA) in the area of the crux (atrioventricular septal junction). The AV node branch travels toward the AV node (apex of the Koch triangle) in the inferior pyramidal space filled with epicardial fat. The AV node is an electrically active bundle of tissue that delays conduction of impulses from the atria to the ventricles. Typically, the dominant artery that supplies the PDA and inferior wall also gives rise to small branches at the base of the heart that supply the AV node

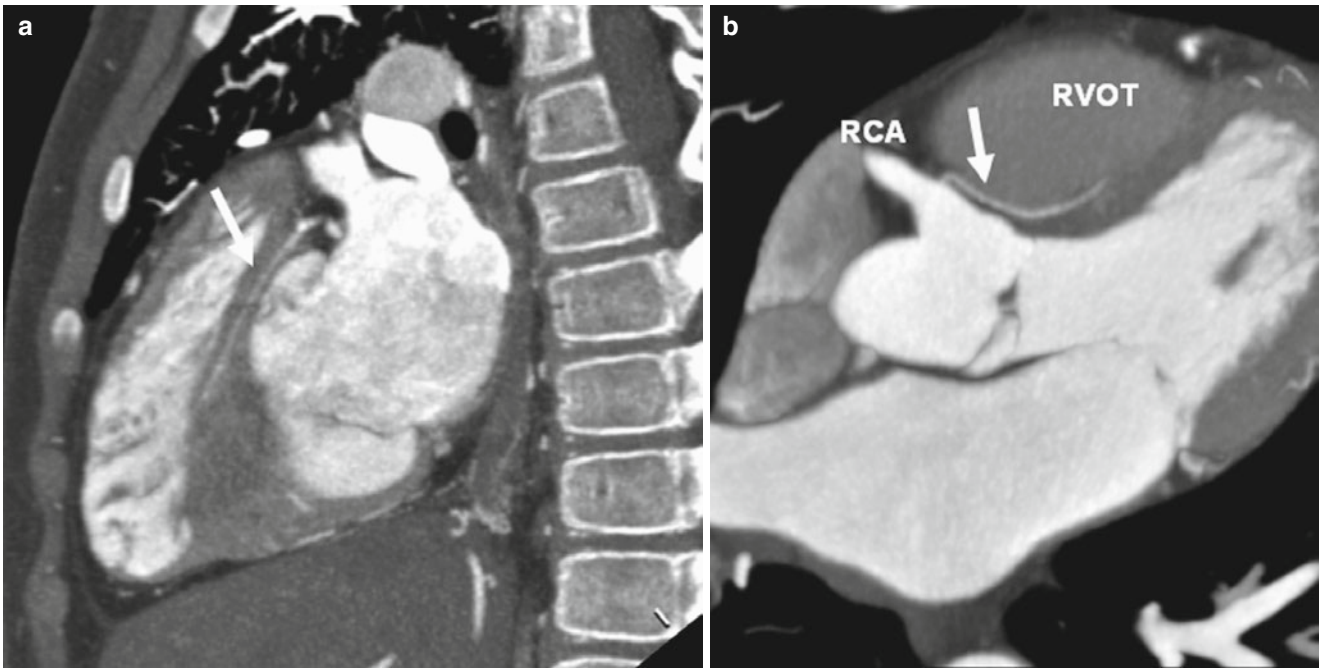

Fig. 3.15 (**a**) First septal perforating artery of the left anterior descending artery (LAD). Septal perforating arteries originate at a right angle from the LAD and travel on the right side of the interventricular septum. The first septal artery (*arrow*) is usually the largest and varies in length from 2 to 5 cm. The inferior branches of the first septal perforator are directed toward the moderator band and supply the anterior papillary muscle of the tricuspid valve. Its superior branches supply the right bundle branch and the bundle of His. (**b**) Right superior septal artery (*arrow*). This artery supplies the infundibular septum and can participate in retroconal and retroaortic circulation. It is seen in 3% of angiographic studies and 27% of pathologic heart dissections. It is not uncommon in CT angiographies. *RCA* right coronary artery, *RVOT* right ventricle outflow tract

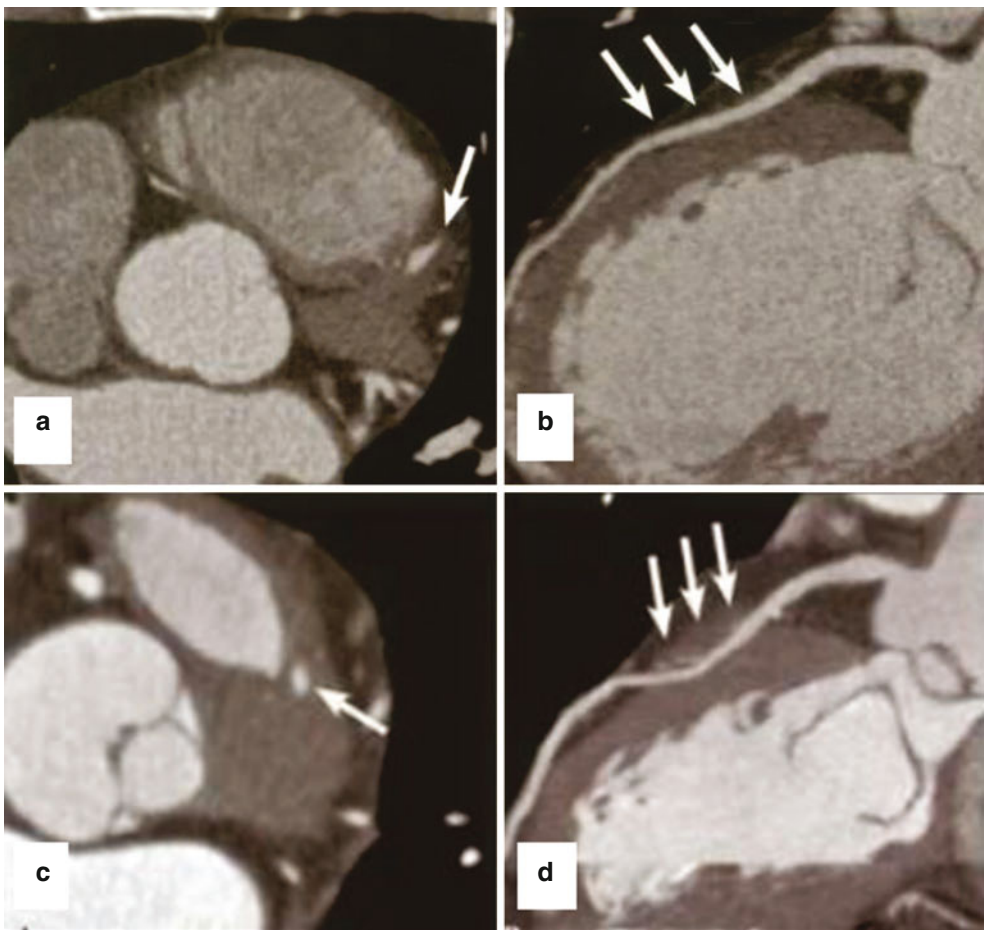

Fig. 3.16 Pseudo versus true myocardial bridging. A small segment of the proximal left anterior descending coronary (LAD) artery is often embedded into the surrounding myocardium. In cross-sectional slice of the embedded segment (*arrow*; **a**) and in a longitudinal reconstruction of the LAD, the artery is not entirely surrounded by myocardium (*arrows*; **b**). This represents an anatomic variant. (**c**, **d**) show similar views in a true LAD myocardial bridging. The vessel is deeply embedded in the left ventricular myocardium (*arrows*). Although typically seen in the mid-LAD segment, myocardial bridges can occur in any coronary artery segment. Although systolic narrowing may be visualized on coronary artery imaging, these findings are rarely clinically significant since most coronary blood flow occurs in diastole

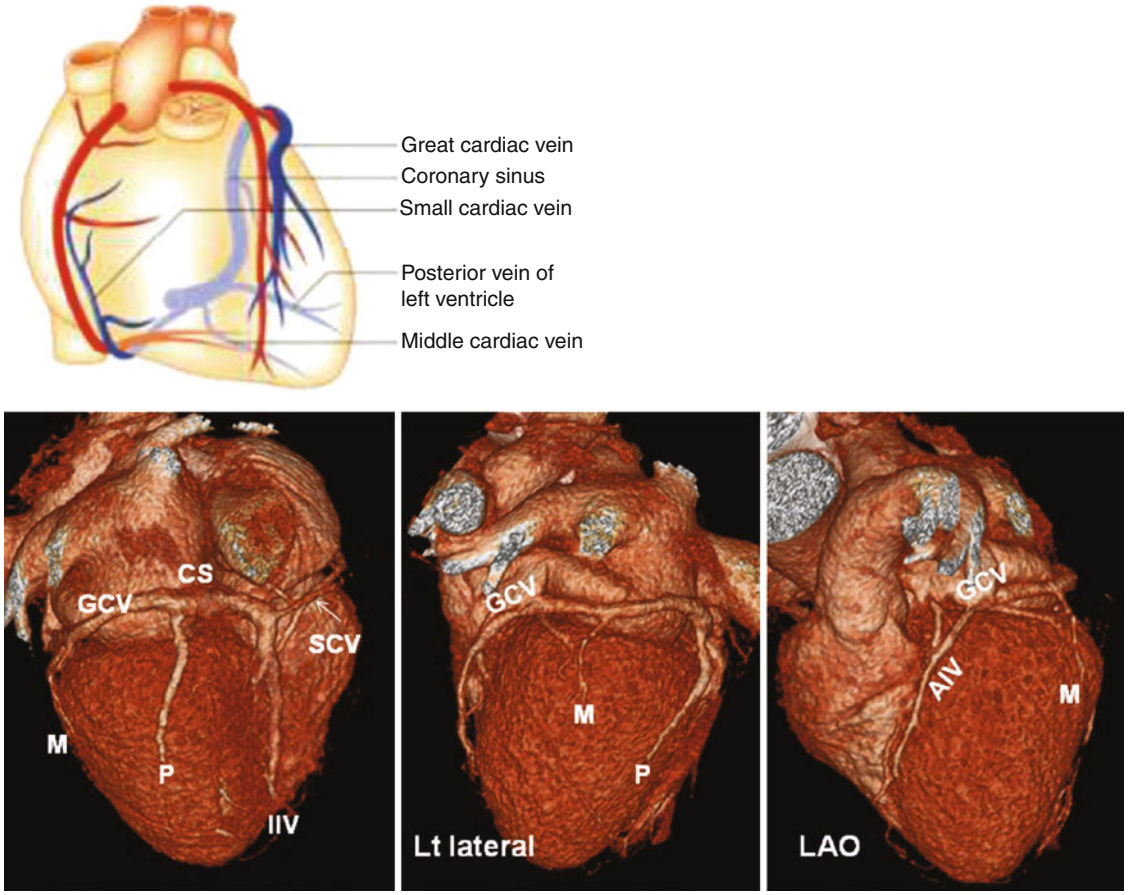

Fig. 3.17 Normal coronary veins. The veins of the heart are even more variable than the arteries. Approximately 80% of venous blood return is achieved via coronary veins on the surface of the heart. The remaining 20% of drainage is into the Thebesian veins (venae cordis minimae), which drain directly into the cardiac chambers. Several small "anterior" cardiac veins may drain directly into the right atrium (not shown here). The remaining blood drainage is achieved via the anterior interventricular vein/great cardiac vein (AIV/GCV) that runs parallel to the left anterior descending coronary artery. Close to the left main bifurcation, it enters the atrioventricular groove and runs parallel to the left circumflex coronary artery. The left marginal (M) vein and posterior (P) vein of the left ventricle enter the great cardiac vein, which is then referred to as the coronary sinus (CS). The coronary sinus enters the right atrium. Immediately before the ostium, the inferior interventicular (middle cardiac) vein (IIV) (which has a course alongside the posterior descending artery) and the small cardiac vein (SCV) (parallel to the right coronary artery) also drain into the coronary sinus

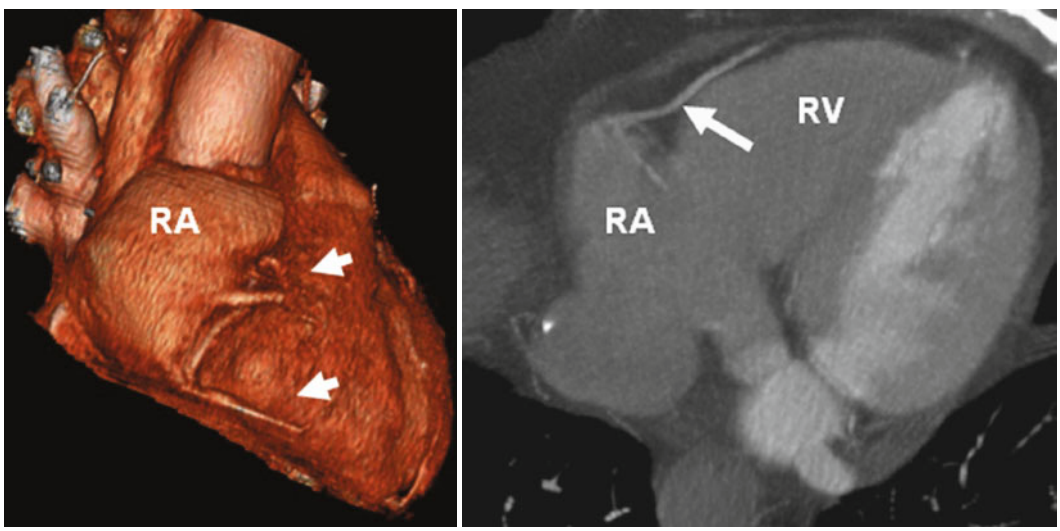

Fig. 3.18 Right ventricle venous system. The anterior cardiac veins (*arrows*) drain two-thirds of the right ventricle (RV), including the anterior and anterolateral walls of the RV. These veins are frequently seen in coronary CT angiographies. They are variable in size and number and usually drain into the right atrium (RA) above the atrioventricular groove

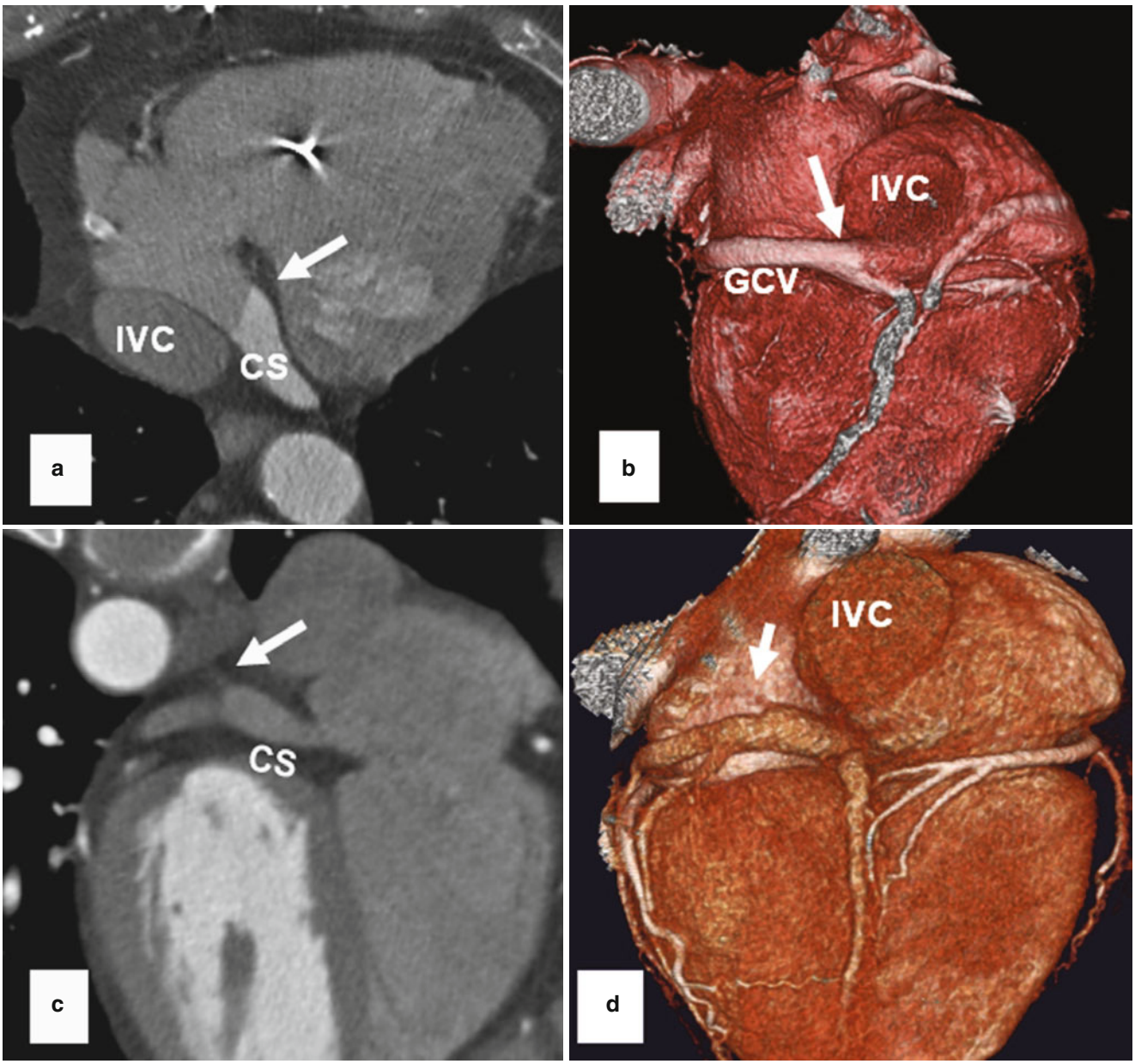

Fig. 3.19 Coronary sinus (CS) boundaries. (**a**, **b**) The Thebesian valve (*arrow*) demarcates the distal end of CS. It can be seen in 70–80% of CT scans and is highly variable in size and morphology. The CS length is between 30 and 50 mm in 75% of the anatomic sections. (**c**, **d**) In order to identify the proximal end of the CS, it is important to localize its origin. Demonstration and localization of the oblique vein of Marshall (*arrows* in **c**, **d**) and the valve of great cardiac vein (Vieussens) is important for ablation approaches and cannulation of the coronary venous system. *GCV* great cardiac vein, *IVC* inferior vena cava

Coronary Veins

Modern anatomical classification divides the cardiac veins into two main groups: tributaries of the Greater Cardiac Vascular System (CVS) and tributaries of the Smaller CVS, consisting of the Thebesian vessels [8, 9]. The Greater CVS is subdivided into two groups including coronary sinus and non-coronary sinus tributaries. In ventricular myocardium, the external two-thirds are drained by the Greater CVS and the internal third is mainly drained by tributaries of the Smaller CVS. The left ventricle, part of the right ventricle, and the left atrium are drained by the coronary sinus tributaries. The majority of the right ventricle and both atria are drained by the non-coronary sinus tributaries. Almost all veins of the Greater CVS are finally drained into the right atrium. The coronary sinus tributaries include: the coronary sinus, the great cardiac vein, the left marginal vein, the posterolatral vein of the left ventricle, and the inferior interventricular vein (middle cardiac vein). In 30% it receives the right marginal vein blood through the small cardiac vein.

References

1. Vrancken Peeters MP, Gittenberger-de Groot AC, Mentink MM, Hungerford JE, Little CD, Poelmann RE. Differences in development of coronary arteries and veins. Cardiovasc Res. 1997;36:101–10.
2. MacAlpin RN, Abbasi AS, Grollman JH, Eber L. Human coronary artery size during life: a cinearteriography study. Radiology. 1973;108:567–76.
3. Leipsic J, Abbara S, Achenbach S, Cury R, Earls JP, Mancini GJ, et al. SCCT guidelines for the interpretation and reporting of coronary CT angiography: a report of the Society of Cardiovascular Computed Tomography Guidelines Committee. J Cardiovasc Comput Tomogr. 2014;8(5):342–58.
4. Scanlon PJ, Faxon DP, Audet AM, Carabello B, Dehmer GJ, Eagle KA, et al. ACC/AHA guidelines for coronary angiography: a report of the American College of Cardiology/American Heart Association Task Force on Practice Guidelines (Committee on Coronary Angiography). Developed in collaboration with the society for cardiac angiography and interventions. J Am Coll Cardiol. 1999;33:1756–824.
5. Pflederer T, Ludwig J, Ropers D, Daniel WG, Achenbach S. Measurement of coronary artery bifurcation angles by multidetector computed tomography. Investig Radiol. 2006;41:793–8.
6. Saremi F, Abolhoda A, Ashikyan O, Milliken JC, Narula J, Gurudevan SV, et al. Arterial supply to sinuatrial and atrioventricular nodes: imaging with multidetector CT. Radiology. 2008;246(1):99–107. discussion 108–9.
7. Saremi F, Channual S, Abolhoda A, Gurudevan SV, Narula J, Milliken JC. MDCT of the S-shaped sinoatrial node artery. Am J Roentgenol. 2008;190(6):1569–75.
8. von Lüdinghausen M. Clinical anatomy of cardiac veins, Vv. cardiacae. Surg Radiol Anat. 1987;9:159–68.
9. Saremi F, Muresian H, Sánchez-Quintana D. Coronary veins: comprehensive CT-anatomic classification and review of variants and clinical implications. Radiographics. 2012;32(1):E1–32.
10. Austen WG, Edwards JE, Frye RL, Gensini GG, Gott VL, Griffith LS, et al. A reporting system on patients evaluated for coronary artery disease. Report of the ad hoc Committee for Grading of Coronary Artery Disease, Council on Cardiovascular Surgery, American Heart Association. Circulation. 1975;51(4 Suppl):5–40.

Coronary Artery Calcium in Primary Prevention

4

Harvey S. Hecht and Matthew J. Budoff

Background

Calcific deposits in coronary arteries are pathognomonic of atherosclerosis (Fig. 4.1) [1].

Histopathology [2] and intravascular ultrasound studies [3–5] confirm the close correlation between atherosclerotic plaque burden and the extent of coronary artery calcification (CAC). Calcification of the atherosclerotic plaque is a highly regulated and active process of mineralization. A strong relationship ($r = 0.8$–0.9) between CAC and histologic plaque areas has been demonstrated at autopsy, in whole arteries and whole hearts [6]. Although the total atherosclerotic plaque burden is proportional to the total calcium burden, not all plaques are calcified.

Other noninvasive modalities to diagnose coronary artery disease focus on physiologic consequences of coronary obstruction, whereas the detection of CAC by noncontrast CT scans represents an anatomic measure of plaque burden. CAC may be present with areas of minimal or severe disease, so it is suboptimal for site-specific detection of luminal stenosis. The value of detecting the extent of CAC lies in its ability to closely approximate the total atherosclerotic plaque area; using the commonly derived Agatston score, this extent is directly proportional to coronary heart disease death, nonfatal myocardial infarction, and revascularization, as well as to all-cause mortality.

Without question, CAC scanning is one of the most important diagnostic achievements in the primary prevention of coronary heart disease in the past generation. Through the accumulation of data on many tens of thousands of primary prevention patients and the efforts of numerous dedicated investigators has CAC achieved the status it currently enjoys.

H.S. Hecht, MD
Department of Cardiology, Icahn School of Medicine at Mount Sinai, New York, NY, USA
e-mail: harvey.hecht@mountsinai.org

M.J. Budoff, MD (✉)
UCLA, Los Angeles Biomedical Research Institute, 1124 W Carson Street, Torrance, CA 90502, USA
e-mail: mbudoff@labiomed.org

M.J. Budoff et al. (eds.), *Atlas of Cardiovascular Computed Tomography*, https://doi.org/10.1007/978-1-4471-7357-1_4

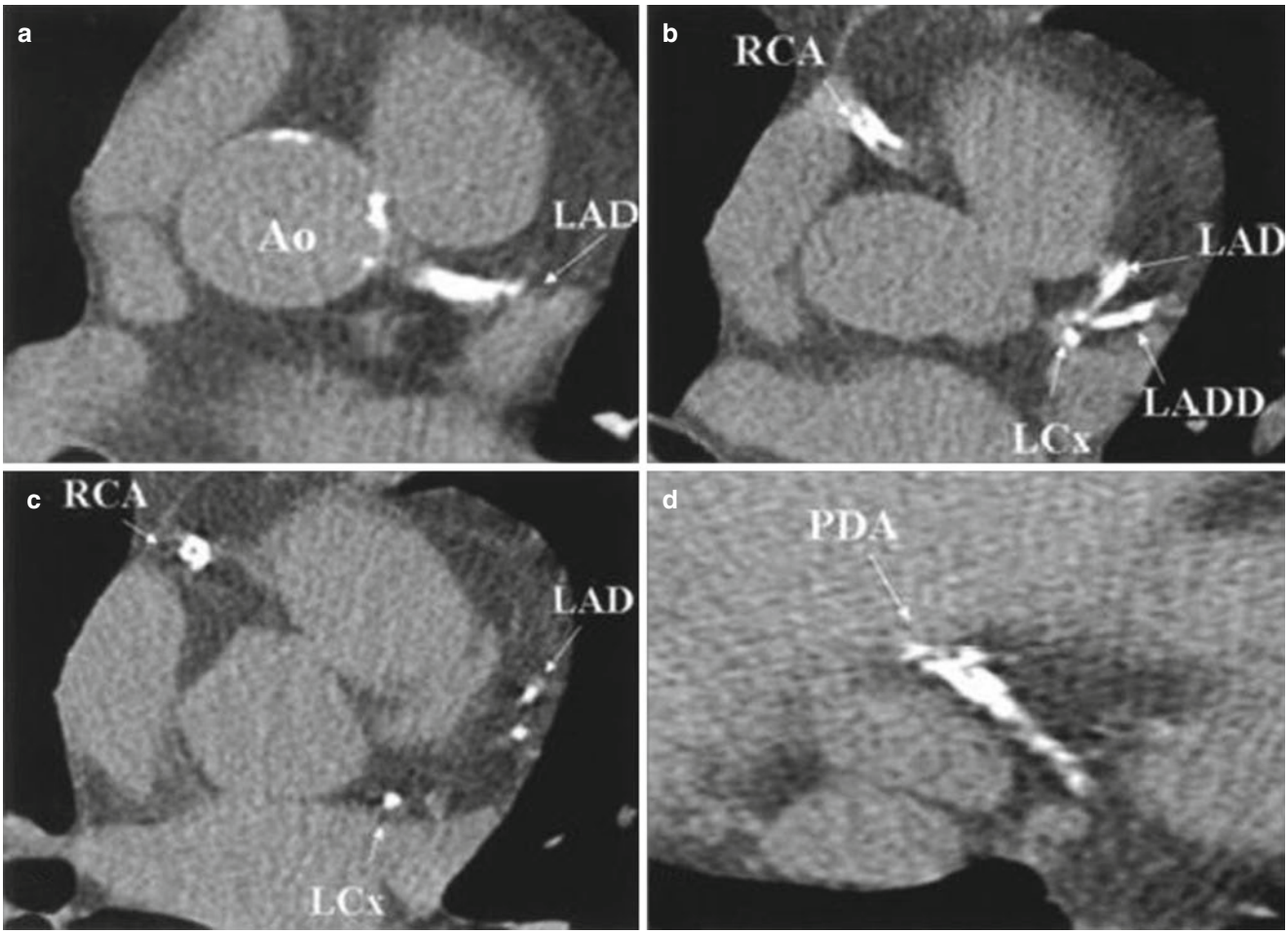

Fig. 4.1 (**a**–**d**), Examples of coronary artery calcium scans. *Ao*—aorta, *LAD*—left anterior descending, *LADD*—left anterior descending diagonal branch, *LCx*—left circumflex, *PDA*—posterior descending artery, *RCA*—right coronary artery

Risk Assessment in Asymptomatic Patients

With the advent of coronary computed tomographic angiography for the evaluation of symptomatic patients and patients with cardiomyopathies, the use of CAC has been restricted to the asymptomatic patient. However, a recent study from the PROMISE Trial demonstrated that CAC has the same prognostic power as functional testing, with a markedly higher sensitivity for future cardiovascular events in a symptomatic population of almost 10,000 persons.

Prognostic Value

As shown in Table 4.1, every study, whether retrospective, self-referred, or based on a prospective population, has consistently and conclusively shown CAC to be the most powerful predictor of risk in asymptomatic patients [7–22].

CAC is the only parameter that offers sufficiently high hazard ratios (~10) to significantly increase the area below the receiver operator characteristic (ROC) curve above that of other risk factors, whether combined, as in the Framingham Risk Score (FRS), or singly (Fig. 4.2). Head-to-head comparisons show CAC to be the best method for risk stratification, with the greatest area under the ROC curve. The Rotterdam Heart Study [16], the Multi-Ethnic Study of Atherosclerosis [20], and Heinz Nixdorf Recall Study [21] all demonstrate that CAC outperforms the FRS, carotid intima media thickness, brachial artery reactivity, ankle brachial index, and serum biomarkers, including C-reactive protein.

Pooled 10-year event rates [14, 19–21, 24] for the conventional CAC cutpoints and their FRS equivalents are shown in Table 4.2. These data provide the basis for quantitating the level of risk and appropriate aggressiveness of treatment. These CAC risk determinations take precedence over the risk factor–based FRS. Though all agree that CAC should upgrade risk in the low and intermediate FRS groups, there is still reluctance to downgrade high-risk FRS patients who have lower-risk CAC, even those with 0 scores, despite the absence of data demonstrating that treating patients with 0 CAC improves outcomes.

The prognosis of patients with 0 CAC has been extensively evaluated, with consistently low event rates. These findings provide a rationale for downgrading such patients with higher-risk FRS (Table 4.3) [24, 25].

The 0 CAC score maintains its overriding importance regardless of the number of traditional risk factors, including smoking, dyslipidemia, diabetes, and hypertension (Fig. 4.3) [26]. In 44,052 asymptomatic individuals with a 0 CAC score, the 5-years all-cause mortality was 0.3% for those with none of these risk factors, 0.7% for those with one or two of the risk factors, and 1% for those with three or more, over 5.6 ± 2.6 years of follow-up. Those with three or more risk factors and a 0 CAC experienced 2.72 events per 1000 person-years, whereas those with no risk factors but a CAC score of 400 experienced 16.89 events [26]. These figures suggest that it is more appropriate to view traditional risk factors as potentially treatable targets in patients who have already had risk determined by CAC, rather than to use them to determine risk.

Table 4.1 Prognostic power of Coronary Artery Calcium (CAC) for coronary events in asymptomatic patients

Study	Patients, *N*	Mean age, *y*	Follow-up, *y*	Calcium score cutoff	Comparator group for relative risk calculation	Relative risk (*RR*) ratio
Arad et al. [7]	1173	53	3.6	CAC > 160	CAC < 160	20.2
Park et al. [8]	967	67	6.4	CAC > 142.1	CAC < 3.7	4.9
Raggi et al. [9]	632	52	2.7	Top quartile	Lowest quartile	13
Wong et al. [10]	926	54	3.3	Top quartile (>270)	First quartile	8.8
Kondos et al. [11]	5635	51	3.1	CAC	No CAC	10.5
Greenland et al. [12]	1312	66	7.0	CAC > 300	No CAC	3.9
Shaw et al. [13]	10,377	53	5	CAC ≥ 400	CAC ≤ 10	8.4
Arad et al. [14]	5585	59	4.3	CAC ≥ 100	CAC < 100	10.7
Taylor et al. [15]	2000	40–50	3.0	CAC > 44	CAC = 0	11.8
Vliegenthart et al. [16]	1795	71	3.3	CAC > 1000 CAC 400–1000	CAC < 100 CAC < 100	8.3 4.6
Budoff et al. [17]	25,503	56	6.8	CAC > 400	CAC = 0	9.2
Lagoski et al. [18]	3601	45–84	3.75	CAC > 0	CAC = 0	6.5
Becker et al. [19]	1726	57.7	3.4	CAC > 400	CAC = 0	6.8 men 7.9 women
Detrano et al. [20]	6814	6.2	3.8	CAC > 300	CAC = 0	14.1
Erbel et al. [21]	4487	45–75	5	>75th percentile	<25th percentile	11.1 men 3.2 women
Taylor et al. [22]	1634	42	5.6	CAC > 0	CAC = 0	9.3

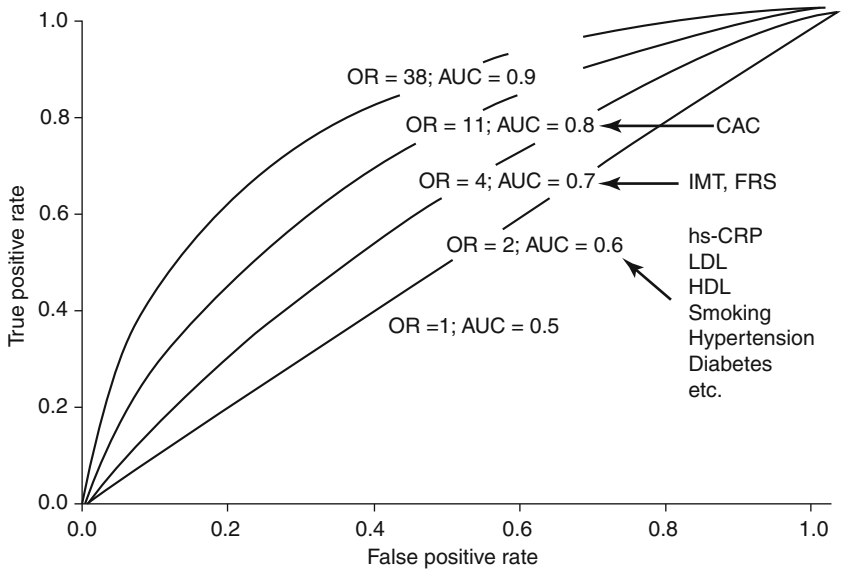

Fig. 4.2 Receiver operator characteristic (*ROC*) curves plotting the sensitivity and specificity for cardiac events of various risk factors, carotid intima media thickening (*IMT*), the Framingham Risk Score (*FRS*) , and coronary artery calcium (*CAC*). The risk factors, singly or in combination, have odds ratios of about two, which are significant but are not sufficiently high to increase the area under the curve (AUC) in a meaningful way. The IMT and FRS have higher odds ratios (~4), but they are not nearly as powerful as CAC (odds ratio ~10), which has been shown to be additive to and greater than both in predicting cardiac events. *HDL*—high-density lipoprotein, *hs-CRP*—high-sensitivity C-reactive protein, *LDL*—low-density lipoprotein. Based on the paper by Pepe et al. [23]

Table 4.2 Event rates of Coronary Artery Calcium (CAC) scores in asymptomatic patients and their Framingham Risk Score (FRS) equivalents

CAC	10-years event rate	FRS risk
0	1.1–1.7%	Very low
1–100	2.3–5.9%	Low
100–400	12.8–16.4%	Intermediate
>400	22.5–28.6%	High
>1000	37%	Very high

Table 4.3 Prognostic studies of a zero coronary artery calcium score

Study	Patients, *N*	Zero-CAC patients, *N* (%)	Follow-up, *y*	All events, % per year (*N*)
Pooled prospective	14,303	5282 (36.9)	3.9	0.17% (35)
Meta-analysis: prospective and retrospective				
Sarwar et al. [25]	71,595	29,132 (41.0)	4.2	0.1% (154)
Retrospective all-cause mortality				
Blaha et al. [24]	44,052	19,898 (45.5)	5.6	0.1% (104)

44, 052 asymptomatic pts; 5.6±2.6y follow up
RF: smoking, dyslipidemia, diabetes, hypertension

0 CAC patients

RF	0	1	2	≥3
5 yr all cause mortality	99.7%	99.3%	99.3%	99.0%

	Events/1000 person yrs
0 RF, CAC 400	16.89
≥ 3 RFs, CAC 0	2.72

	0 RF	1 RF	2 RF	≥3 RF	Total
CAC = 0	9,805	4,558	3,322	2,123	19,898
CAC 1–100	5,994	3,250	2,913	2,204	14,181
CAC 101–400	1,883	1,301	1,371	1,184	5,739
CAC >400	1,047	984	1,148	1,055	4,234
Total	18,819	10,093	8,754	6,386	44,052

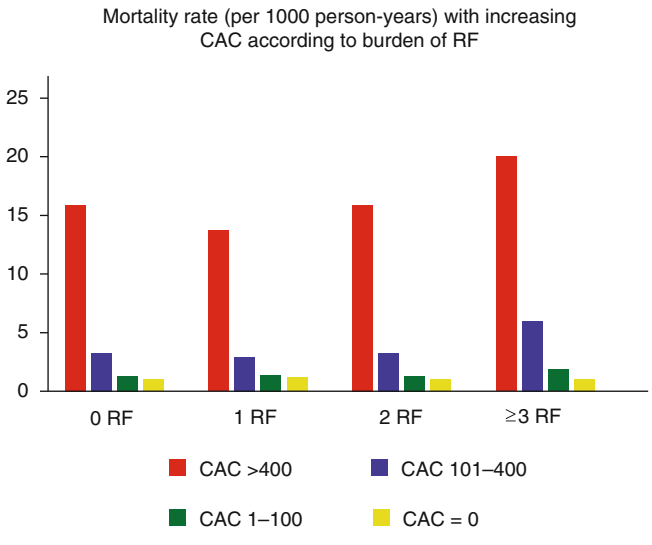

Fig. 4.3 The relationship between traditional risk factors (*RF*) and CAC scores. The relative lack of importance of risk factors, which may predispose to atherosclerosis, compared with CAC, which *is* atherosclerosis, is clearly demonstrated by the trivial increases in events associated with increasing numbers of risk factors in the setting of a 0 CAC and the high event rate with a high CAC and no risk factors

Reclassification

Reclassification of FRS risk based on CAC has received increasing attention (Table 4.4) [20, 21, 27]. The percentage of asymptomatic patients whose FRS prediction of events is correctly reclassified by CAC (Net Reclassification Improvement, NRI) ranges from 19 to 25% in the three major prospective studies. The reclassification is greatest in the intermediate FRS group (52–65.6%), but reclassification in the high-risk group is also high (34.2–35.8%). The studies are remarkably consistent, similar to the uniformity of positive results as shown in Table 4.1. These data emphasize the inability of physicians to accurately predict risk and correctly treat their patients without employing CAC (unfortunately, the standard of care).

The number of patients needed to scan to correctly identify a high-risk patient across the spectrum of FRS [29] is shown in Table 4.5. Only 30% of the FRS high-risk group were high risk by CAC, however, and the number needed to scan to correctly identify a high-risk patient was 3.3, compared with 4.2–6.4 in the intermediate-risk FRS group and 7.6–59.7 in the low-risk FRS group. The number of patients needed to scan to identify a high-risk patient (CAC > 300) dramatically decreases as the FRS increases. These data suggest that the best candidates for CAC are the FRS high-risk and intermediate-risk groups.

In MESA, 10.1% of 5660 asymptomatic patients had CAC greater than 300; 20.6% had CAC greater than 100, and 46.4% had CAC greater than 0. The percentage with 0 CAC was 53.6% [29]. The prevalence and severity of CAC increases significantly with increases in FRS, as shown in Fig. 4.4.

Table 4.4 Reclassification of FRS risk by Coronary Artery Calcium (CAC): primary prevention outcome studies

Study	FRS risk	Reclassified	Patients, *N*	Age, *y*	Follow-up, *y*
MESA [20]	0–6%	11.6%	5878	62.2	5.8
	6–20%	54.4%			
	>20%	35.8%			
		NRI 25%			
Heinz Nixdorf [21]	<10%	15.0%	4487	45–75	5.0
	10–20%	65.6%			
	>20%	34.2%			
		NRI 22.4%			
Rotterdam [27]	<10%	12%	2028	69.6	9.2
	10–20%	52%			
	>20%	34%			
		NRI 19%			

FRS Framingham Risk Score, *MESA* Multi-Ethnic Study of Atherosclerosis, *NRI* Net Reclassification Improvement
Adapted from Hecht and Narula [28]

Table 4.5 Number of patients needed to scan to correctly identify a high-risk patient across the spectrum of Framingham risk score[a]

FRS	CAC >300	NNS
0–2.5%	1.7%	59.7
2.6–5%	4.4%	22.7
5.1–7.5%	7.5%	13.4
7.6–10%	13.1%	7.6
10.1–15%	15.6%	6.4
15.1–20%	24%	4.2
>20%	30%	3.3

CAC coronary artery calcium, *FRS* Framingham risk score, *NNS* number needed to scan
[a]Based on 5660 asymptomatic patients in Multi-Ethnic Study of Atherosclerosis [29]

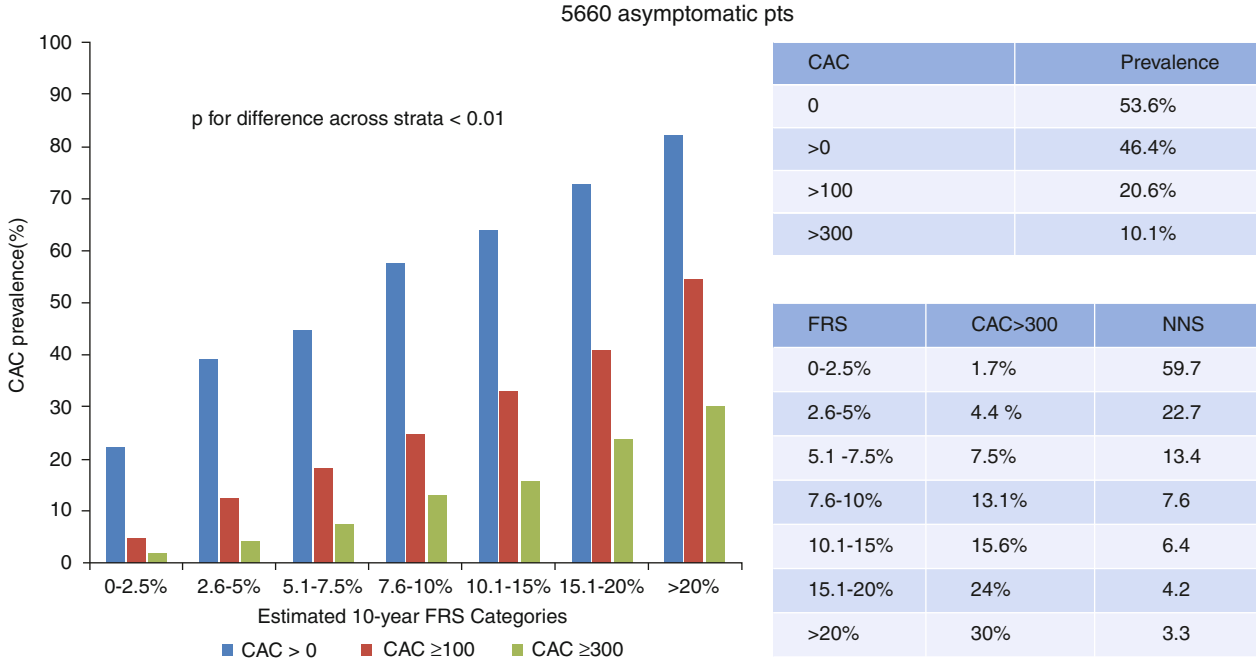

CAC	Prevalence
0	53.6%
>0	46.4%
>100	20.6%
>300	10.1%

FRS	CAC>300	NNS
0-2.5%	1.7%	59.7
2.6-5%	4.4 %	22.7
5.1 -7.5%	7.5%	13.4
7.6-10%	13.1%	7.6
10.1-15%	15.6%	6.4
15.1-20%	24%	4.2
>20%	30%	3.3

Fig. 4.4 Distribution of coronary artery calcium (CAC) by Framingham Risk Score (FRS) in the Multiethnic Study of Atherosclerosis (MESA). (*From* Okwuosa et al. [29])

Societal Guidelines

In 2006, the SHAPE (Screening for Heart Attack Prevention and Education) guidelines (Fig. 4.5) were the first to recognize the validity of an approach based on subclinical atherosclerosis [30], recommending that all but the very lowest-risk patients be evaluated for either CAC or carotid intima-media thickening, with the intensity of therapy depending on the test results. Supported by the available outcome data and based upon the simple concept that the amount of atherosclerosis determines both the risk and the aggressiveness of therapeutic interventions, these guidelines were greeted with widespread criticism, but their recommendations (with minor differences) have been incorporated into the most recent societal guidelines and appropriateness criteria.

In the 2010 ACC/AHA Guideline for Assessment of Cardiovascular Risk in Asymptomatic Adults [31] CAC indications (Table 4.6) were class IIa for cardiovascular risk assessment in asymptomatic adults at intermediate risk (10–20% 10-year risk) and for diabetics >40 years of age. Class IIb criteria include patients at low to intermediate risk (6–10% 10-year risk); there was no benefit (class III) for low-risk (patients with 0–6% 10-year risk). These guidelines represented a dramatic breakthrough for CAC, with class IIa recommendations for all intermediate-risk asymptomatic patients as well as for all diabetics over the age of 40.

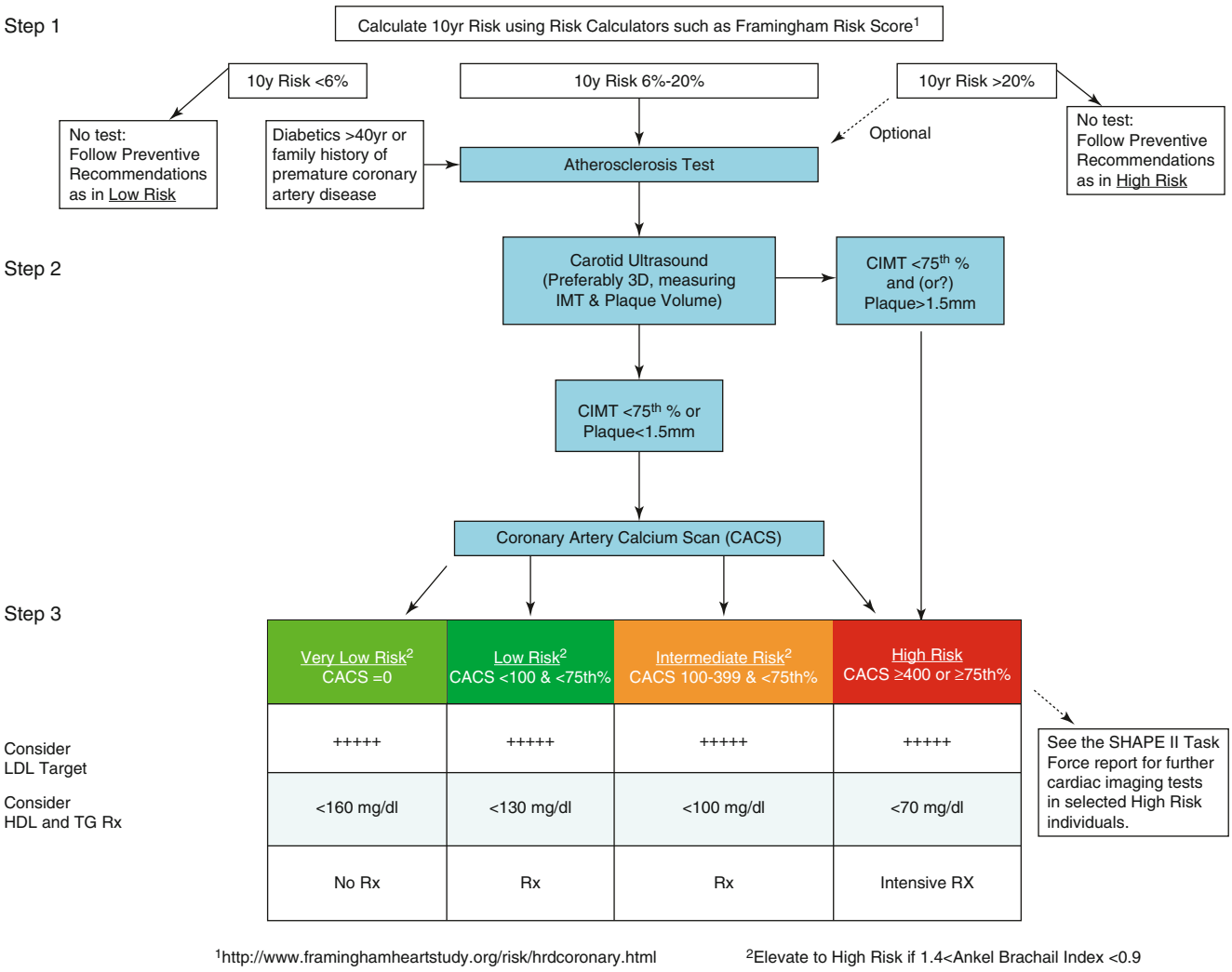

Fig. 4.5 The SHAPE Guideline. In 2006, a group of leading cardiologists broke with tradition and issued the first risk analysis recommendations based upon subclinical atherosclerosis determined by CAC or carotid intima-media thickening (CIMT) rather than risk factors. Since then, CIMT has fallen into disfavor but CAC has become even more robust. (*From* Naghavi et al. [30]) In 2015, the SHAPE Guidelines were revised to reflect more emphasis on CAC to risk stratify and determine LDL targets

The 2010 CAC Appropriate Use Criteria [32] considered CAC "appropriate" for asymptomatic patients with an intermediate global coronary artery disease (CAD) risk estimate, as well as those with a family history of premature CAD and a low global risk estimate. The indication for high-risk asymptomatic patients was given as "uncertain" (not enough data to render a decision). Subsequently, the 2013 ACC/AHA Guideline on the Treatment of Blood Cholesterol to Reduce Atherosclerotic Cardiovascular Risk in Adults assigned a class IIb (may be considered) recommendation to CAC, and recommended its use in patients in whom the Pooled Cohort Equation risk decision was unclear [33]. The 2013 ACC/AHA Guideline on the Assessment of Cardiovascular Risk stated that CAC was "likely to be the most useful of the current approaches to improving risk assessment among individuals found to be at intermediate risk after formal risk assessment" [34]. The 2016 European Society of Cardiology Guidelines on Cardiovascular Disease Prevention in Clinical Practice also issued a class IIb recommendation for CAC to risk stratify asymptomatic individuals [35–37]. The 2016 Society of Cardiovascular Computed Tomography and Society of Thoracic Radiology guidelines for coronary artery calcium scoring of noncontrast noncardiac chest CT scans stated that CAC should be evaluated and reported on all noncontrast chest CT examinations by Agatston, ordinal or visual scoring [36]. Subsequent to the 2013 ACC/AHA guideline [31], CAC was revisited in the 2017 Clinical indications for coronary artery calcium scoring in asymptomatic patients: Expert consensus statement from the Society of Cardiovascular Computed Tomography. The major recommendations were as follows: 1. It is appropriate to perform CAC testing in the context of shared decision making for asymptomatic individuals without clinical ASCVD who are 40-75 years of age in the 5–20% 10-year ASCVD risk group and selectively in the <5% ASCVD group, such as those with a family history of premature coronary artery disease.

Table 4.6 CAC recommendations for assessment of cardiovascular risk in asymptomatic patients

Study	Risk	Recommendation
2010 ACC/AHA risk guidelines [31]	10–20% intermediate risk	IIa
	Patients with diabetes >40 yo	IIa
	6–10% low-to-intermediate risk	IIb
2010 appropriate use criteria [32]	10–20% intermediate risk	Appropriate
	Low risk with family history of premature coronary disease	Appropriate
	High risk	Uncertain
	Low risk	Inappropriate
2013 ACC/AHA cholesterol and risk guidelines [33, 34]	Uncertain risk after pooled Cohort equations	IIb
2016 ESC cardiovascular [35] Disease prevention guideline	Around the 5% or 10% SCORE threshold	IIb
2017 SCCT CAC expert	5–20% 10 year ASCVD risk	Appropriate
Consensus statement [37]	<5% 10 year ASCVD risk	Selectively appropriate

Special Groups

Family History of Premature CAD

Patients with a family history of premature CAD, regardless of their age, are an overlooked higher-risk group who would not qualify for treatment based on the FRS. Because CAC is also likely to yield a 0 score, the best approach would be to perform CAC alone if any calcified plaque is detected. If the CAC is 0, prospectively gated coronary CT angiography with a low radiation dose may be appropriate to evaluate for noncalcified plaque.

Diabetes

Diabetes is considered to be a CAD risk equivalent, to be treated by secondary prevention standards. In MESA, however, there was no significant difference in distribution of calcium scores and outcomes between nondiabetics, patients with metabolic syndrome, and diabetics [38]. In an earlier study, diabetics had a worse prognosis than nondiabetics in the same CAC range, but there was no difference in survival between diabetics and nondiabetics with a 0 CAC [39]. The class IIa recommendation given in the 2010 ACC/AHA Risk Guideline [31] for diabetics over 40 years of age (Table 4.6) is designed to identify those who are at highest risk and would, therefore, be candidates for ischemia imaging. The CAC literature related to diabetes (Table 4.7) [40–44] confirms the prognostic power of CAC in this group and its superiority to predictions based on risk factors. The hazard ratios for high versus low CAC in diabetic patients are similar to those in patients without diabetes, as is the superiority of CAC to conventional risk factor–based paradigms.

Table 4.7 Relationship between Coronary Artery Calcium (CAC) and events in asymptomatic diabetic patients

Study	Patients, *n*	Prevalence	Hazard Ratio	AUC	Event Rate/*y*
Wong et al. [40]	1823	Any CAC			0 CAC: 0.2%
		No DM: 53%			CAC >400: 5.6%
		DM: 73.5%			
Becker et al. [41]	716 DM	0 CAC: 15%		CAC: 0.77	
				FRS: 0.68	
				UKPDS: 0.71	
		CAC >400: 42%		$P < 0.01$	
Elkeles et al. [42]	589 DM		Compared with CAC 0–10:	CAC: 0.73	CAC < 10.0%
				UKPDS: 0.63	
			CAC >1000: 13.8	$p < 0.03$	
			CAC 401–1000: 8.4		
			CAC 101–400: 7.1		
			CAC 11–100: 4.0		
Anand et al. [43]	510 DM	CAC <10: 53.7%	Compared with CAC <100:	CAC: 0.92	
			CAC >1000: 58	UKPDS: 0.74	
			CAC 401–1000: 41	FRS: 0.60	
			CAC 101–400: 10	$p < 0.001$	
Malik et al. [44]	881 DM1		Increasing CAC: 2.9–6.5	CAC + RF: 0.78–0.80	1.5%
	4036 no DM		Increasing CAC: 2.6–9.5	RF: 0.72–0.73	0.5%
				$p < 0.001$	

AUC area under curve, *DM* diabetes mellitus, *FRS* Framingham risk score, *RF* risk factors, *UKPDS* UK Prospective Diabetes Study

CAC Progression

A significant increase in CAC plaque burden is associated with adverse outcomes. Without tracking subclinical atherosclerosis, the only method for assessing treatment failure is the occurrence of an event or the development of symptoms. The ability to identify treatment nonresponders by progressive excessive increases in CAC offers the opportunity to intervene with more aggressive treatment and possibly affect outcomes. Clinical scenarios are illustrated in Figs. 4.6 and 4.7, with Tables 4.8 and 4.9. These scenarios illustrate that favorable risk factor changes may not be accompanied by

		Baseline	1 year later
Lipids:	TC	244	163
	LDL	149	92
	HDL	39	52
	TG	280	94
Plaque:	Calcium Score	12	56
	Calcium Percentile	75	89
Treatment:	Statin	none	10 mg
	Niacin	none	2000 mg

Baseline: CAC 12

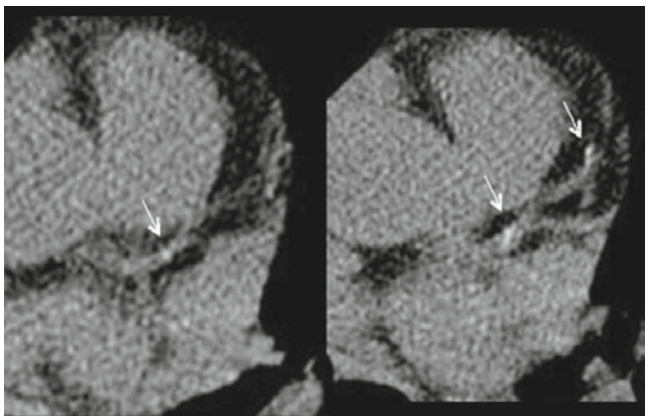

1 year later: CAC 56

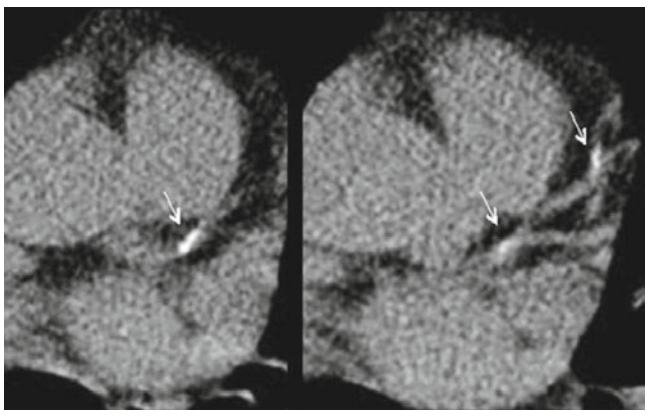

Fig. 4.6 CAC progression clinical scenario. A 43-years-old man whose father experienced a myocardial infarction at age 41 underwent CAC scanning for risk prediction. The CAC of 12 placed him in the high-risk 75th percentile for age, sex, and ethnicity, so combination therapy with a statin and niacin was implemented. After 1 year of treatment, his lipid values were dramatically improved, but repeat CAC scanning revealed an almost fivefold CAC increase, consistent with failure to halt progression of atherosclerosis and an increased risk of a cardiac event, and mandates more aggressive lipid lowering. The disconnect between changes in plasma lipids and changes in plaque, as well as in risk factors and baseline plaque, highlights the missing link that determines an individual's susceptibility to a given risk factor and response to changes in these potentially damaging metabolic states

Baseline: CAC 436 1 year later: CAC 445

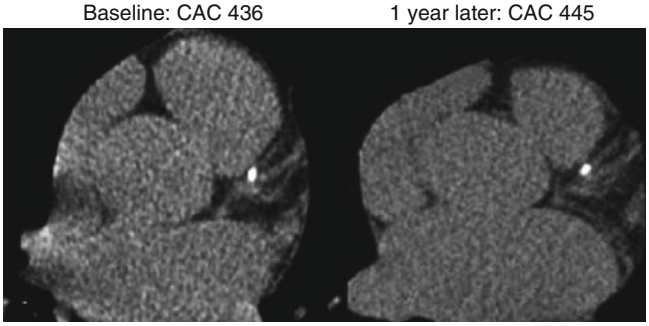

		Baseline	1 year later
Lipids:	TC	234	156
	LDL	154	96
	HDL	39	53
	Trig	206	35
Plaque:	Calcium Score	436	445
	Calcium Percentile	97	97

Fig. 4.7 CAC progression clinical scenario. A 52-years-old man whose father experienced a myocardial infarction at age 46 underwent CAC scanning for risk prediction. A CAC of 436 (97th percentile) categorized him as high-risk. His abnormal lipid profile was very similar to the patient in Fig. 4.6, and with similar therapy he showed a very similar risk-factor improvement after 1 year. Unlike that patient, however, his CAC was essentially unchanged, indicating successful treatment of the disease process

Table 4.8 Clinical scenario: 43-years-old man (Fig. 4.6)

		Baseline	1 year
Lipids	TC	244	163
	LDL	149	92
	HDL	39	52
	TG	280	94
Plaque	Calcium score	12	56
	Calcium percentile	75	89
Treatment	Statin	None	10 mg
	Niacin	None	2000 mg

HDL high-density lipoprotein, *LDL* low-density lipoprotein, *TC* total cholesterol, *TG* triglycerides

Table 4.9 Clinical scenario: 52-years-old man (Fig. 4.7)

		Baseline	1 year
Lipids	TC	234	156
	LDL	154	96
	HDL	39	53
	TG	206	35
Plaque	Calcium score	436	445
	Calcium percentile	97	97
Treatment	Statin	None	20 mg
	Niacin	None	4000 mg

HDL high-density lipoprotein, *LDL* low-density lipoprotein, *TC* total cholesterol, *TG* triglycerides

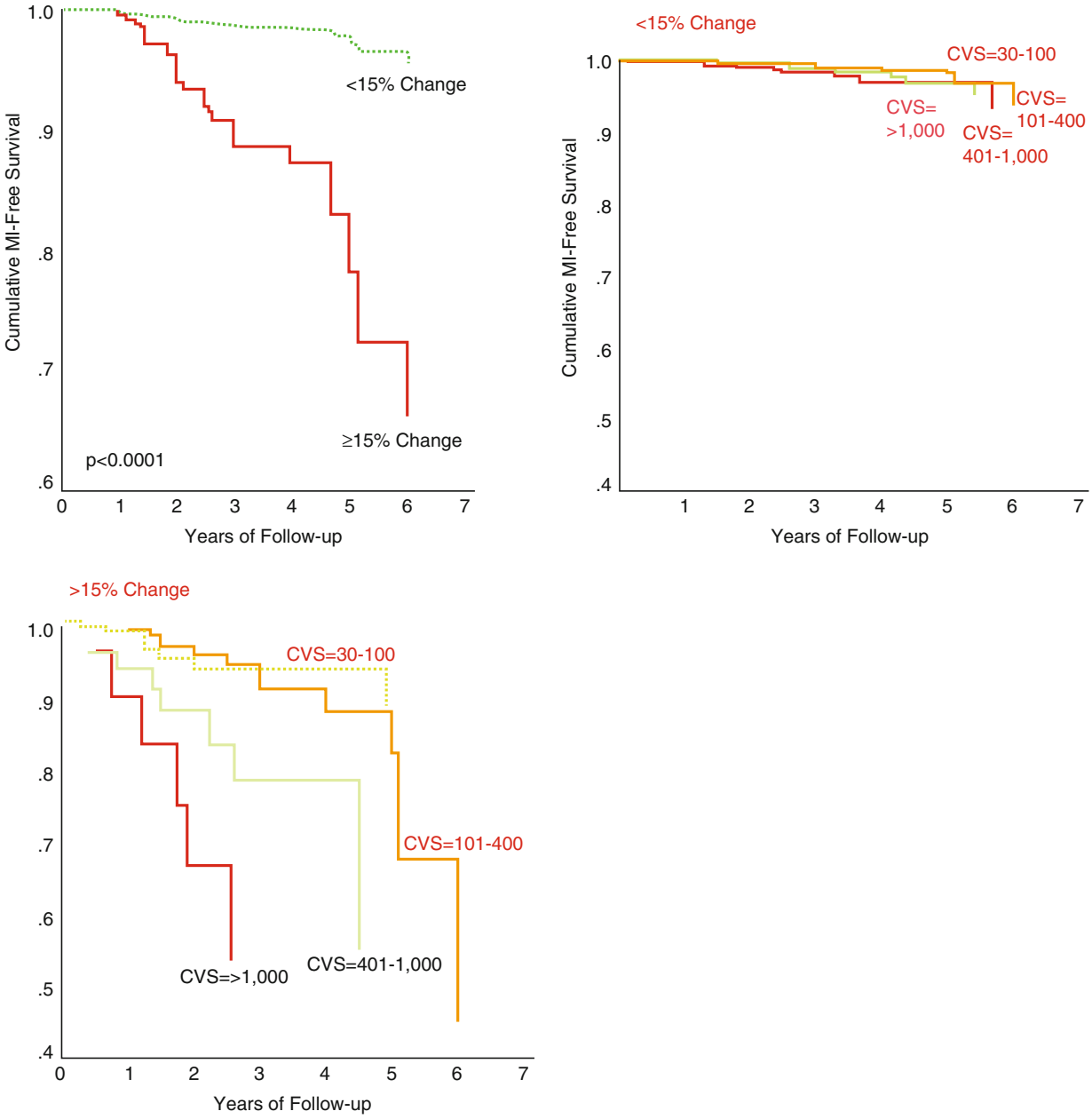

Fig. 4.8 Progression of CAC and risk of first myocardial infarction in asymptomatic patients receiving lipid-lowering therapy. *Top left panel*, In 800 asymptomatic patients, the risk of a myocardial infarction was virtually nil in those with less than 15% annual CAC increase, but it increased sharply with >15% annual increase. The achieved LDL cholesterol was similar in both groups. *Top right panel*, In the setting of less than 15% CAC increase, the event rate was uniformly low, even in those with baseline CAC greater than 1000. *Bottom left panel*, Conversely, with an annual increase greater than 15, event-free survival dropped off sharply and was directly related to the baseline CAC. (*From* Raggi P et al. [45])

successful treatment of the atherosclerotic process; such an assumption is simply not predictable without documentation by CAC. The alternative to repeat CAC scanning is to wait for a clinical event to determine the success or failure of treatment—an unacceptable choice.

Based on convincing data linking increasing CAC progression to increasing cardiac risk [45–47] (Figs. 4.8, 4.9 and 4.10, Tables 4.10, 4.11 and 4.12), serial CAC scanning to evaluate progression has been addressed in the 2017 SCCT Consensus Statement as follows: In patients for whom the development or progression of CAC would support intensification or alteration in preventive management, it may be appropriate to consider repeat CAC scanning at an interval of 5 years for patients with 0 CAC and a 3 to 5-year interval for patients with >0 CAC [37].

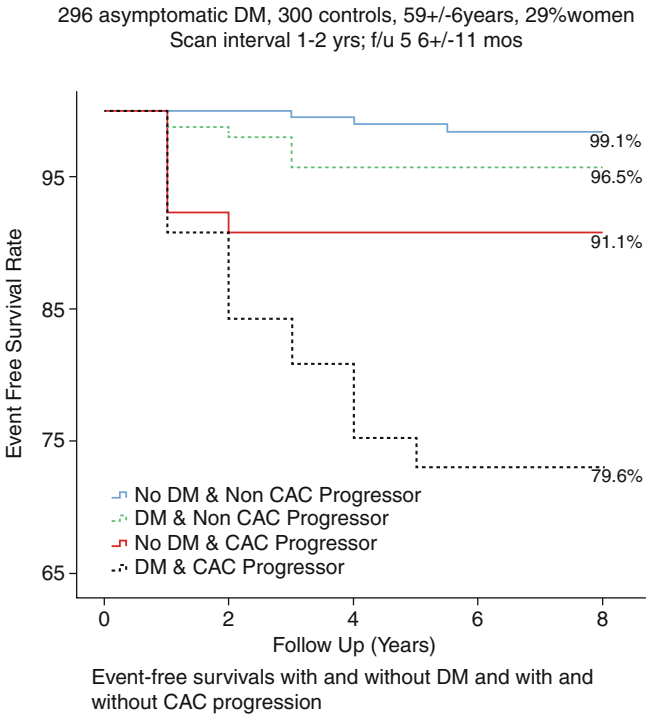

Fig. 4.9 Impact of CAC progression on outcome in subjects with and without diabetes. There was a progressive decline in survival of asymptomatic patients with and without diabetes (DM) associated with increasing CAC progression on scans performed at an interval of 1–2 years. The decline in survival was more pronounced in those with DM, with a 79.6% versus 90.6% event-free survival in those with an annual increase greater than 30%, compared with nondiabetics. (*From* Kiramijyan et al. [46])

Table 4.10 Impact of CAC progression on outcome in patients with and without diabetes[a] (Fig. 4.9)

	Event-free survival	
Change in CAC	DM	No DM
<10%	97.9%	100%
10–20%	95.9%	97.2%
21–30%	92.7%	94%
>30%	79.6%	90.6%

[a]296 asymptomatic patients with DM and 300 controls, age 59 ± 6 years (29% women). Follow-up was 5.6 years ± 11 months

Table 4.11 Hazard ratio for death for patients with DM versus controls[a] (Fig. 4.9)

Change in CAC	Matched controls	DM	*p* value
10–20% *vs* < 10%	1.0	1.88	0.0001
21–30% *vs* < 10%	1.0	2.29	0.0001
>30% *vs* < 10%	1.0	6.95	0.0001

[a]Same group as Table 4.10. Adjusted for risk factors and baseline CAC

6,778 pts, 45-84 yo
2 scans: baseline and 2.5yrs later
7.6y follow up: 343 total, 206 hard events

	Hazard Ration 0 Baseline CAC	
N	3,396	3,382
Events	Total	Hard
Per 5AU/y	1.4	1.5
	>0 Baseline CAC	
Per 100AU/y	1.2	1.3
>300 AU/y	3.8	6.3
<5 %/y	1.0	1.0
5-14%/y	1.1	1.0
15-29%/y	1.6	1.4
>30%/y	1.5	1.4

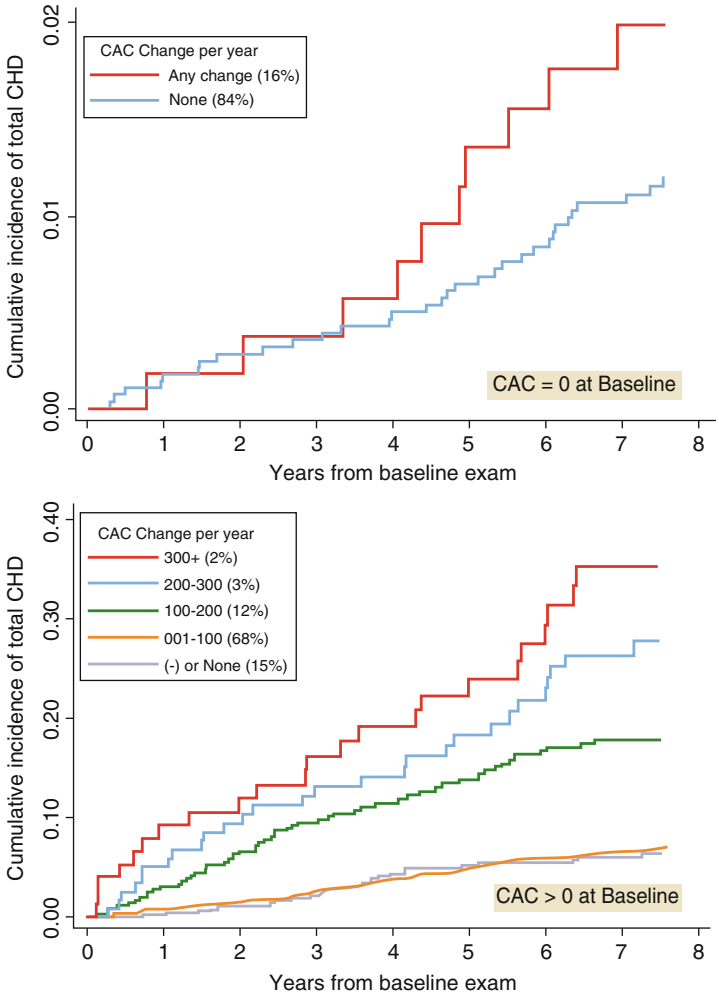

Fig. 4.10 Coronary calcium progression and incident cardiac events. Kaplan Meier plots of cumulative incidence of total coronary heart disease (CHD) among persons with CAC of 0 at baseline (*top*) and with CAC greater than 0 at baseline (*bottom*). (*From* Budoff et al. [47])

Table 4.12 Coronary Artery Calcium (CAC) progression and incident coronary heart disease events[a] (Fig. 4.10)

	Hazard ratio: total events	Hazard ratio: hard events
0 baseline CAC (N = 3396)		
Per 5 AU/*y* CAC progression	1.4	1.5
>0 baseline CAC (N = 3382)		
Per 100 AU/*y* CAC progression	1.2	1.3
Per >300 AU/*y* CAC progression	3.8	6.3
Annual CAC progression		
<5%/*y*	1.0	1.0
5–14%/*y*	1.1	1.0
15–29%/*y*	1.6	1.4
>30%/*y*	1.5	1.4

AU Agatston unit
(*Adapted from* Budoff et al. [47])
[a]6778 patients, age 45–84 years. Two scans were performed, at baseline and 2.5 years later. Over 7.6 years of follow-up, 304 total events occurred (206 hard events)

Patient Adherence

When patients are shown their CAC scans, a positive effect on patient adherence to statin medications, aspirin, diet, and exercise programs has been consistently demonstrated, with greater adherence reflecting higher CAC scores [48–51] (Table 4.13).

Table 4.13 Effect of coronary calcium on patient adherence

Study	*N*	Follow-up, *y*	CAC	Adherence				
				Statin	ASA	Diet	Exercise	Statin + ASA
Kalia et al. [48]	505	3.6	>400	90%				
			100–400	75%				
			1–99	63%				
			0	44%				
Orakzai et al. [49]	980	3	>400		61%	67%	56%	
			0		29%	33%	44%	
Taylor et al. [50]	1640	6	>0 *vs* 0	OR 3.5	OR 3.1			OR 7.0

ASA aspirin, *CAC* coronary artery calcium, *OR* odds ratio

CAC Prevalence in First Cardiac Events

CAC has been noted in 95% of both older and younger patients who present with an acute myocardial infarction or unstable angina as their first event [3, 51] (Fig. 4.11).

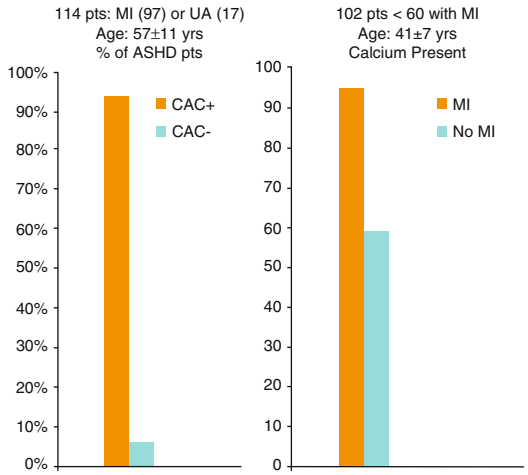

Fig. 4.11 Coronary calcium in patients with first myocardial infarction or unstable angina. CAC was noted in 95% of patients in both older (57 + 11 years) and younger (41 + 7 years) age groups who presented with either a myocardial infarction or unstable angina as their first event. Thus, CAC can identify the group of high-risk patients out of which 95% of events will emerge. ASHD—arteriosclerotic heart disease

CAC and Myocardial Perfusion

The relationship of CAC to abnormal myocardial perfusion in predominantly asymptomatic populations has been well described [43, 52–55] (Fig. 4.12). CAC less than 400 does not warrant perfusion imaging in asymptomatic patients, but the yield of abnormal perfusion in patients with CAC greater than 400 justifies functional evaluation to determine the amount of ischemic myocardium. Exceptions may occur (Fig. 4.13) but do not justify more widespread testing in lower CAC groups.

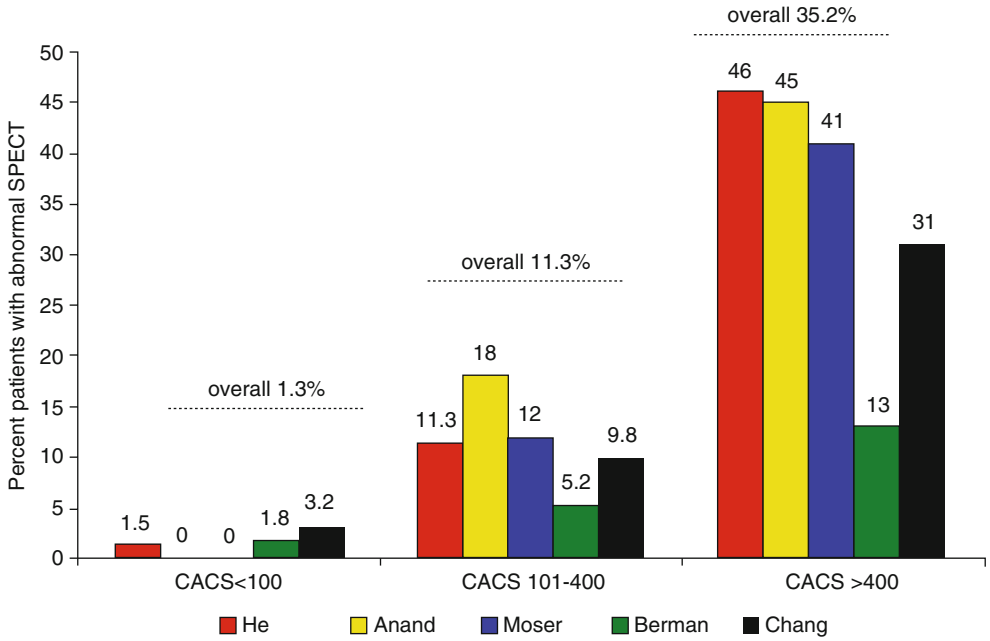

Fig. 4.12 Relationship between CAC score results and an abnormal SPECT study. The average percentage of patients from four studies with abnormal SPECT imaging is sufficiently high (35.2%) in those with CAC greater than 400 to warrant stress testing in this group regardless of symptoms. CAC less than 400 does not have sufficient pretest probability of stress myocardial defects to warrant further testing in the asymptomatic population. The studies shown are He et al. [52], Anand et al. [43], Moser et al. [53], Berman et al. [54], and Chang et al. [55]

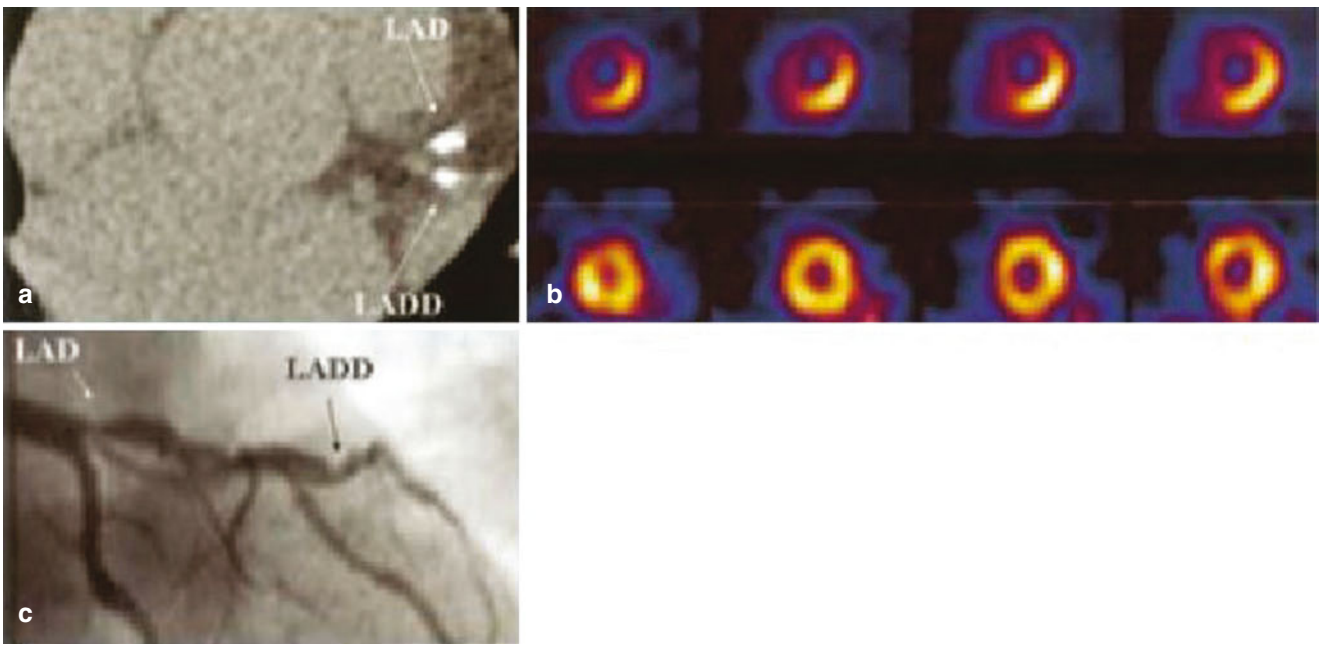

Fig. 4.13 A 41-years-old asymptomatic woman with a family history of premature coronary disease and normal lipid values underwent CAC (**a**) with a score of 110, in the 99th percentile for her age. Myocardial perfusion imaging revealed severe anteroseptal ischemia (**b**), and coronary angiography demonstrated critical ostial left anterior descending (*LAD*) and moderate diagonal (*LADD*) stenosis (**c**)

Noncoronary Vascular Calcification

Aortic, aortic valve, and mitral annular calcification (Fig. 4.14) are common findings that have been extensively evaluated and should be reported in a semiquantitative manner (absent, mild, moderate, severe) rather than assigned an Agatston score.

The literature uniformly agrees that aortic calcified plaque correlates well with CAC but has no additive prognostic value [56–60] (Table 4.14).

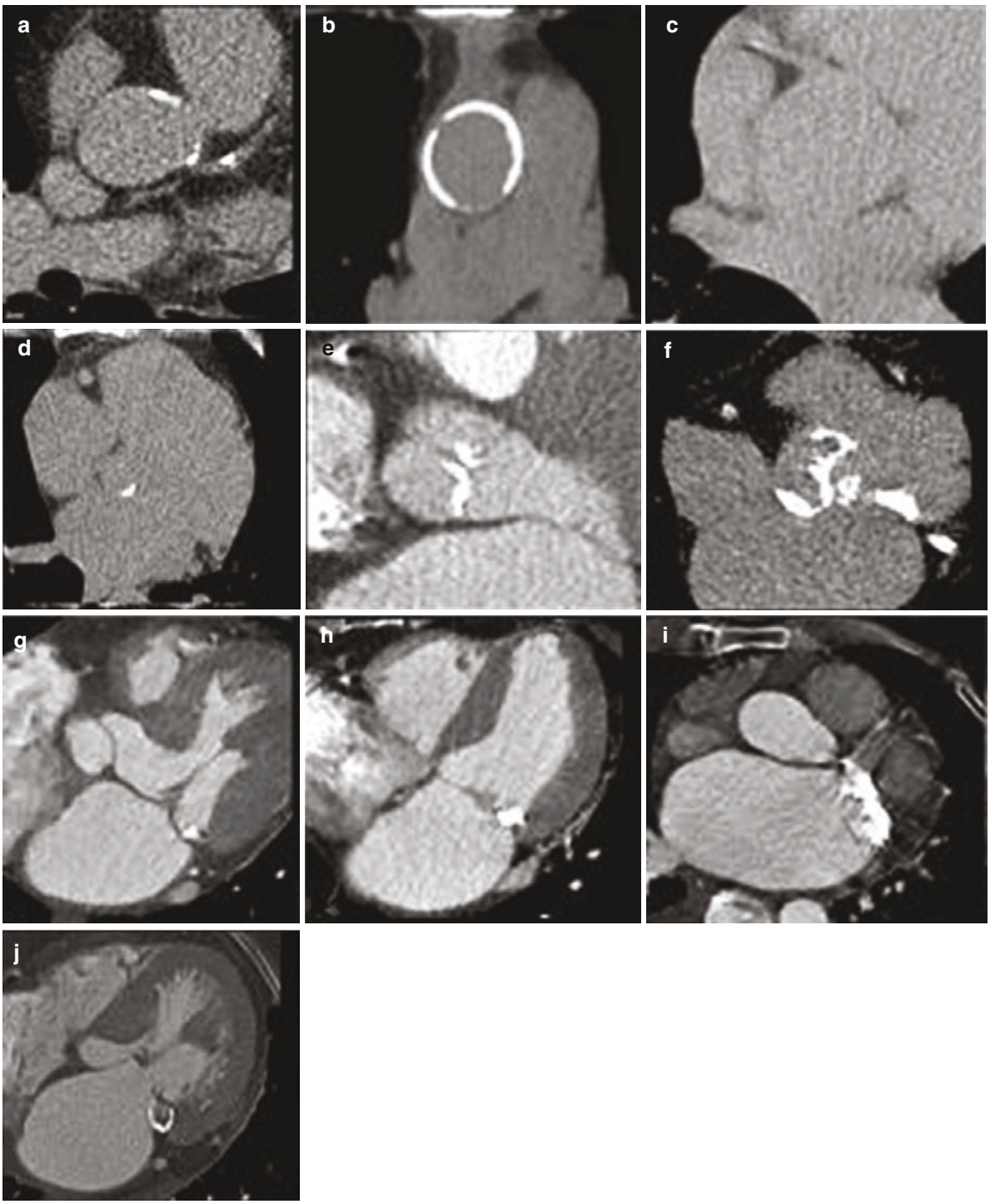

Fig. 4.14 Examples of aortic, aortic valvular and mitral annular calcification: (**a**), Mild ascending aortic calcified plaque. (**b**), Very extensive aortic calcified plaque, potentially posing problems for surgical cannulation. (**c**), Normal aortic valve; calcification not present. (**d**), Mild aortic valve calcification. (**e**), Moderate aortic valve calcification. (**f**), Severe aortic valve calcification. (**g**), Mild mitral annular calcification. (**h**), Moderate mitral annular calcification. (**i**), Severe mitral annular calcification. (**j**), Mitral annular calcification with caseation necrosis

Aortic and mitral annular calcification correlate well in some studies [58–61] but not in others [62, 63] (Table 4.15).

Noncoronary vascular calcification provides an estimate of the diffuseness of the atherosclerotic disease. Specific instances can provide critical information, such as the presence of "porcelain" aorta for surgeons planning aortic cannulation, or very extensive mitral annular calcification if mitral valve replacement or repair is indicated [66].

Table 4.14 Literature summarizing the relationship between Coronary Artery Calcium (CAC) and aortic calcified plaque

Study	Methods	Results	Remarks
Adler et al. [56]	405 patients with at least two risk factors had chest CT for CC and aortic calcification	Demonstrated a strong association of CAC and calcification of the thoracic aorta	The study also sees the association between CAC and aortic calcification as a possible basis between CAD and cerebrovascular disease
Takasu et al. [57]	Studied the MESA cohort of 6814 women and men 45–84 years of age	Descending thoracic aortic calcification was found to be a strong predictor of CAC independent of CV risk factors	This is the largest such study
Eisen et al. [58]	361 patients with stable angina pectoris	Significant correlation of aortic calcification with CAC	Study also noted significant correlation between aortic calcification and aortic valve and mitral annular calcification
Wong et al. [59]	2740 persons without known CHD, 20–79 years of age	Significant correlation of thoracic aortic calcification (TAC), aortic valvular calcification (AVC), and CAC	TAC and AVC provide incremental value for predicting estimated 10-years risk of CHD over CAC
Raggi et al. [60]	245 self-referred patients	Signification correlation between CAC and AVC	Only age, male sex, and Lp(a) were associated with CAC

CAD coronary artery disease, *CC* coronary calcium, *CHD* coronary heart disease, *CV* cardiovascular *MESA* Multi-Ethnic Study of Atherosclerosis

Table 4.15 Literature summarizing the relationship between aortic and mitral annular calcification

Study	Method	Results	Remarks
Takasu et al. [61]	620 asymptomatic referred patients studied twice, 12 months apart	Significant correlation between presence of AVC and CAC on initial studies and parallel increase in progression	Most participants with AVC and CC scores of 0 on initial scan did not have a significant calcium deposit on repeated scan
Adler et al. [64]	376 patients with hypertension	Significant differences in CAC score and number of vessels calcified between the groups with and without AVC	Strengthens the significant association between the presence of AVC and advanced CAC
Tenenbaum et al. [65]	522 patients with hypertension	Advanced MAC was correlated with very high CAC score and proven CAD	This study raises a role for echocardiogram in the indirect diagnosis of CAD
Cury et al. [66]	420 subjects without known CAD underwent MDCT	Presence of AVC and mitral valvular (annular and leaflet) and descending aortic calcification increased the likelihood of CAC	Used a scoring system analogous to the Agatston scoring system due to poor applicability of the latter to noncoronary calcium scoring
Pohle et al. [62]	104 subjects with presence of AVC on EBCT done for CAC score. Performed two studies on a particular subject, separated by a mean of 15.3 months	There was no significant correlation between AVC and CAC on initial assessment	CAC and AVC progression had a significant correlation; the rate of CAC progression predicted the rate of AVC progression. High LDL levels predicted higher rates of progression of both CAC and AVC. Treatment with statins decreased the progression of both
Walsh et al. [63]	327 subjects drawn from the Framingham offspring study who had undergone EBCT between 1997 and 1999	Thoracic aortic calcification and CAC did not correlate with AVC with any statistical significance	Another aspect of the study revealed poor sensitivity of EBCT (with fair specificity) in detecting aortic valve degenerative disease

AVC aortic valvular calcification, *CAD* coronary artery disease, *CC* coronary calcium, *CHD* coronary heart disease, *CV* cardiovascular, *EBCT* electron beam computed tomography, *LDL* low-density lipoprotein, *MAC* mitral annular calcification, *MDCT* multidetector computed tomography

Conclusion

A large body of literature supports the role of the CAC score as the pivotal tool in the prevention of coronary artery disease. Its unparalleled power to predict events has resulted in its incorporation into the most important guidelines.

References

1. McCarthy JH, Palmer FJ. Incidence and significance of coronary artery calcification. Br Heart J. 1974;36:499–506.
2. Eggen DA, Strong JP, Mcgill HC. Coronary calcification: relationship to clinically significant coronary lesions and race, sex and topographic distribution. Circulation. 1965;32:948–55.
3. Schmermund A, Baumgart D, Görge G, Seibel R, Grönemeyer D, Ge J, et al. Coronary artery calcium in acute coronary syndromes: a comparative study of electron-beam computed tomography, coronary angiography, and intracoronary ultrasound in survivors of acute myocardial infarction and unstable angina. Circulation. 1997;96:1461–9.
4. Mintz GS, Pichard AD, Popma JJ, Kent KM, Satler LF, Bucher TA, Leon MB. Determinants and correlates of target lesion calcium in coronary artery disease: a clinical, angiographic and intravascular ultrasound study. J Am Coll Cardiol. 1997;29:268–74.
5. Baumgart D, Schmermund A, Goerge G, Haude M, Ge J, Adamzik M, et al. Comparison of electron beam computed tomography with intracoronary ultrasound and coronary angiography for detection of coronary atherosclerosis. J Am Coll Cardiol. 1997;30:57–64.
6. Sangiorgi G, Rumberger JA, Severson A, Edwards WD, Gregoire J, Fitzpatrick LA, Schwartz RS. Arterial calcification and not lumen stenosis is highly correlated with atherosclerotic plaque burden in humans: a histologic study of 723 coronary artery segments using nondecalcifying methodology. J Am Coll Cardiol. 1998;31:126–33.
7. Arad Y, Spadaro LA, Goodman K, Newstein D, Guerci AD. Prediction of coronary events with electron beam computed tomography. J Am Coll Cardiol. 2000;36:1253–60.
8. Park R, Detrano R, Xiang M, Fu P, Ibrahim Y, LaBree L, Azen S. Combined use of computed tomography coronary calcium scores and C-reactive protein levels in predicting cardiovascular events in nondiabetic individuals. Circulation. 2002;106:2073–7.
9. Raggi P, Callister TQ, Cooil B, He ZX, Lippolis NJ, Russo DJ, et al. Identification of patients at increased risk of first unheralded acute myocardial infarction by electron beam computed tomography. Circulation. 2000;101:850–5.
10. Wong ND, Hsu JC, Detrano RC, Diamond G, Eisenberg H, Gardin JM. Coronary artery calcium evaluation by electron beam computed tomography and its relation to new cardiovascular events. Am J Cardiol. 2000;86:495–8.
11. Kondos GT, Hoff JA, Sevrukov A, Daviglus ML, Garside DB, Devries SS, et al. Electron-beam tomography coronary artery calcium and cardiac events: a 37-month follow-up of 5,635 initially asymptomatic low to intermediate risk adults. Circulation. 2003;107:2571–6.
12. Greenland P, LaBree L, Azen SP, Doherty TM, Detrano RC. Coronary artery calcium score combined with Framingham score for risk prediction in asymptomatic individuals. JAMA. 2004;291:210–5.
13. Shaw LJ, Raggi P, Schisterman E, Berman DS, Callister TQ. Prognostic value of cardiac risk factors and coronary artery calcium screening for all-cause mortality. Radiology. 2003;228:826–33.
14. Arad Y, Goodman KJ, Roth M, Newstein D, Guerci AD. Coronary calcification, coronary disease risk factors, C-reactive protein, and atherosclerotic cardiovascular disease events: the St. Francis heart study. J Am Coll Cardiol. 2005;46:158–65.
15. Taylor AJ, Bindeman J, Feuerstein I, Cao F, Brazaitis M, O'Malley PG. Coronary calcium independently predicts incident premature coronary heart disease over measured cardiovascular risk factors: mean three-year outcomes in the prospective Army coronary calcium (PACC) project. J Am Coll Cardiol. 2005;46:807–14.
16. Vliegenthart R, Oudkerk M, Song B, van der Kuip DA, Hofman A, Witteman JC. Coronary calcification detected by electron-beam computed tomography and myocardial infarction. The Rotterdam coronary calcification study. Eur Heart J. 2002;23:1596–603.
17. Budoff MJ, Shaw LJ, Liu ST, et al. Long-term prognosis associated with coronary calcification. Observations from a registry of 25,253 patients. J Am Coll Cardiol. 2007;49:1860–70.
18. Lakoski SG, Greenland P, Wong ND, Schreiner PJ, Herrington DM, Kronmal RA, et al. Coronary artery calcium scores and risk for cardiovascular events in women classified as "low risk" based on Framingham risk score: the multi-ethnic study of atherosclerosis (MESA). Arch Intern Med. 2007;167:2437–42.
19. Becker A, Leber A, Becker C, Knez A. Predictive value of coronary calcifications for future cardiac events in asymptomatic individuals. Am Heart J. 2008;155:154–60.
20. Detrano R, Guerci AD, Carr JJ, Bild DE, Burke G, Folsom AR, et al. Coronary calcium as a predictor of coronary events in four racial or ethnic groups. N Engl J Med. 2008;358:1336–45.
21. Erbel R, Möhlenkamp S, Moebus S, Schmermund A, Lehmann N, Stang A, et al. Coronary risk stratification, discrimination, and reclassification improvement based on quantification of subclinical coronary atherosclerosis. The Heinz Nixdorf recall study. J Am Coll Cardiol. 2010;56:1397–406.
22. Taylor AJ, Fiorilli PN, Wu H, Bauer K, Bindeman J, Byrd C, et al. Relation between the Framingham risk score, coronary calcium, and incident coronary heart disease among low-risk men. Am J Cardiol. 2010;106:47–50.
23. Pepe MS, et al. Limitations of the odds ratio in gauging the performance of a diagnostic, prognostic or screening marker. Am J Epidemol. 2004;159:882–90.
24. Blaha M, Budoff MJ, Shaw LJ, Khosa F, Rumberger JA, Berman D, et al. Absence of coronary artery calcification and all-cause mortality. JACC Cardiovasc Imaging. 2009;2:692–700.
25. Sarwar A, Shaw LJ, Shapiro MD, Blankstein R, Hoffmann U, Cury RC, et al. Diagnostic and prognostic value of absence of coronary artery calcification. JACC Cardiovasc Imaging. 2009;2:675–88.
26. Nasir K, Rubin J, Blaha MJ, Shaw LJ, Blankstein R, Rivera JJ, et al. Interplay of coronary artery calcification and traditional risk factors for the prediction of all-cause mortality in asymptomatic individuals. Circ Cardiovasc Imaging. 2012;5:467–73.
27. Elias-Smale SE, Proença RV, Koller MT, Kavousi M, Van Rooij FJ, Hunink MG, et al. Coronary calcium score improves classification of coronary heart disease risk in the elderly: the Rotterdam study. J Am Coll Cardiol. 2010;56:1407–14.
28. Hecht HS, Narula J. Coronary artery calcium scanning in asymptomatic patients with diabetes mellitus: a paradigm shift. J Diabetes. 2012;4:342–50.
29. Okwuosa TM, Greenland P, Ning H, Liu K, Bild DE, Burke GL, et al. Distribution of coronary artery calcium scores by Framingham 10-year risk strata in the MESA (multi-ethnic study of atherosclerosis): potential implications for coronary risk assessment. J Am Coll Cardiol. 2011;57:1838–45.
30. Naghavi M, Falk E, Hecht HS, Jamieson MJ, Kaul S, Berman D, et al. From vulnerable plaque to vulnerable patient—part III: executive summary of the screening for heart attack prevention and education (SHAPE) task force report. Am J Cardiol. 2006;98:2H–15H.
31. Greenland P, Alpert JS, Beller GA, Benjamin EJ, Budoff MJ, Fayad ZA, et al. 2010 ACCF/AHA guideline for assessment of cardiovascular risk in asymptomatic adults: a report of the American College of Cardiology Foundation/American Heart Association Task Force on Practice Guidelines. J Am Coll Cardiol. 2010;56:e50–103.

32. Taylor AJ, Cerqueira M, Hodgson JM, Mark D, Min J, O'Gara P, et al. ACCF/SCCT/ACR/AHA/ASE/ASNC/NASCI/SCAI/SCMR 2010 appropriate use criteria for cardiac computed tomography. A report of the American College of Cardiology Foundation appropriate use criteria task force, the Society of Cardiovascular Computed Tomography, the American College of Radiology, the American Heart Association, the American Society of Echocardiography, the American Society of Nuclear Cardiology, the north American Society for Cardiovascular Imaging, the Society for Cardiovascular Angiography and Interventions, and the Society for Cardiovascular Magnetic Resonance. J Am Coll Cardiol. 2010;56:1864–94.
33. Stone NJ, Robinson J, Lichtenstein AH, Bairey Merz CN, Blum CB, Eckel RH, American College of Cardiology/American Heart Association Task Force on Practice Guidelines, et al. 2013 ACC/AHA guideline on the treatment of blood cholesterol to reduce atherosclerotic cardiovascular risk in adults: a report of the American College of Cardiology/American Heart Association Task Force on Practice Guidelines. J Am Coll Cardiol. 2014;63:2889–34.
34. Goff DC Jr, Lloyd-Jones DM, Bennett G. 2013 ACC/AHA guideline on the assessment of cardiovascular risk. J Am Coll Cardiol. 2014;63:2935–59.
35. Piepoli MF, Hoes AW, Agewall S, Albus C, Brotons C, Catapano AL, et al. 2016 European guidelines on cardiovascular disease prevention in clinical practice: the sixth joint task force of the European Society of Cardiology and Other Societies on cardiovascular disease prevention in clinical practice (constituted by representatives of 10 societies and by invited experts). Developed with the special contribution of the European Association for Cardiovascular Prevention and Rehabilitation (EACPR). Eur Heart J. 2016;37(29):2315–81.
36. Hecht HS, Cronin P, Blaha MJ, Budoff MJ, Kazerooni EA, Narula J, et al. 2016 SCCT/STR guidelines for coronary artery calcium scoring of noncontrast noncardiac chest CT scans: a report of the Society of Cardiovascular Computed Tomography and Society of Thoracic Radiology. J Cardiovasc Comput Tomogr. 2017;11:74–84.
37. Hecht H, Blaha MJ, Berman DS, Nasir K, Budoff M, Leipsic J, et al. Clinical indications for coronary artery calcium scoring in asymptomatic patients: expert consensus statement from the Society of Cardiovascular Computed Tomography. J Cardiovasc Comput Tomogr. 2017;11:157–68.
38. Malik S, Budoff M, Katz R, Blumenthal RS, Bertoni A, Nasir K, et al. Utility of coronary artery calcium in identifying whether metabolic syndrome and diabetes are coronary heart disease risk equivalents [abstract 1704]. Circulation. 2009;120:S547.
39. Raggi P, Shaw LJ, Berman DS, Callister TQ. Prognostic value of coronary artery calcium screening in subjects with and without diabetes. J Am Coll Cardiol. 2004;43:1663–9.
40. Wong ND, Sciammarella MG, Polk D, Gallagher A, Miranda-Peats L, Whitcomb B, et al. The metabolic syndrome, diabetes, and subclinical atherosclerosis assessed by coronary calcium. J Am Coll Cardiol. 2003;41:1547–53.
41. Becker A, Leber AW, Becker C, von Ziegler F, Tittus J, Schroeder I, et al. Predictive value of coronary calcifications for future cardiac events in asymptomatic patients with diabetes mellitus: a prospective study in 716 patients over 8 years. BMC Cardiovasc Disord. 2008;8:27.
42. Elkeles RS, Godsland IF, Feher MD, Rubens MB, Roughton M, Nugara F, et al. Coronary calcium measurement improves prediction of cardiovascular events in asymptomatic patients with type 2 diabetes: the PREDICT study. Eur Heart J. 2008;29:2244–51.
43. Anand DV, Lim E, Hopkins D, Corder R, Shaw LJ, Sharp P, et al. Risk stratification in uncomplicated type 2 diabetes: prospective evaluation of the combined use of coronary artery calcium imaging and selective myocardial perfusion scintigraphy. Eur Heart J. 2006;27:713–21.
44. Malik S, Budoff M, Katz R. Impact of subclinical atherosclerosis on cardiovascular disease events in individuals with metabolic syndrome and diabetes: the multi-ethnic study of atherosclerosis. Diabetes Care. 2011;34:2285–90.
45. Raggi P, Callister TQ, Shaw LJ. Progression of coronary artery calcium and risk of first myocardial infarc tion in patients receiving cholesterol-lowering therapy. Arterioscler Thromb Vasc Biol. 2004;24:1–7.
46. Kiramijyan S, Ahmadi N, Isma'eel H, Flores F, Shaw LJ, Raggi P, Budoff MJ. Impact of coronary artery calcium progression and statin therapy on clinical outcome in subjects with and without diabetes mellitus. Am J Cardiol. 2013;111:356–61.
47. Budoff MJ, Young R, Lopez VA, Kronmal RA, Nasir K, Blumenthal RS, et al. Progression of coronary calcium and incident coronary heart disease events: MESA (Multi-Ethnic Study of Atherosclerosis). J Am Coll Cardiol. 2013;61:1231–9.
48. Kalia NK, Miller LG, Nasir K, Blumenthal RS, Agrawal N, Budoff MJ. Visualizing coronary calcium is associated with improvements in adherence to statin therapy. Atherosclerosis. 2006;185:394–9.
49. Orakzai RH, Nasir K, Orakzai SH, Kalia N, Gopal A, Musunuru K, et al. Effect of patient visualization of coronary calcium by electron beam computed tomography on changes in beneficial lifestyle behaviors. Am J Cardiol. 2008;101:999–1002.
50. Taylor AJ, Bindeman J, Feuerstein I, Le T, Bauer K, Byrd C, et al. Community-based provision of statin and aspirin after the detection of coronary artery calcium within a community-based screening cohort. J Am Coll Cardiol. 2008;51:1337–41.
51. Pohle K, Ropers D, Mäffert R, Geitner P, Moshage W, Regenfus M, et al. Coronary calcifications in young patients with first, unheralded myocardial infarction: a risk factor matched analysis by electron beam tomography. Heart. 2003;89:625–8.
52. He ZX, Hedrick TD, Pratt CM, Verani MS, Aquino V, Roberts R, Mahmarian JJ. Severity of coronary artery calcification by electron beam computed tomography predicts silent myocardial ischemia. Circulation. 2000;101:244–51.
53. Moser KW, O'Keefe JH Jr, Bateman TM, McGhie IA. Coronary calcium screening in asymptomatic patients as a guide to risk factor modification and stress myocardial perfusion imaging. J Nucl Cardiol. 2003;10:590–8.
54. Berman DS, Wong ND, Gransar H, Miranda-Peats R, Dahlbeck J, Hayes SW, et al. Relationship between stress-induced myocardial ischemia and atherosclerosis measured by coronary calcium tomography. J Am Coll Cardiol. 2004;44:923–30.
55. Chang SM, Nabi F, Xu J, Peterson LE, Achari A, Pratt CM, et al. The coronary artery calcium score and stress myocardial perfusion imaging provide independent and complementary prediction of cardiac risk. J Am Coll Cardiol. 2009;54:1872–82.
56. Adler Y, Fisman EZ, Shemesh J, Schwammenthal E, Tanne D, Batavraham IR, et al. Spiral computed tomography evidence of close correlation between coronary and thoracic aorta calcifications. Atherosclerosis. 2004;176:133–8.
57. Takasu J, Budoff MJ, O'Brien KD, Shavelle DM, Probstfield JL, Carr JJ, Katz R. Relationship between coronary artery and descending thoracic aortic calcification as detected by computed tomography: the Multi-Ethnic Study of Atherosclerosis. Atherosclerosis. 2009;204:440–6.
58. Eisen A, Tenenbaum A, Koren-Morag N, Tanne D, Shemesh J, Imazio M, et al. Calcification of the thoracic aorta as detected by spiral computed tomography among stable angina pectoris patients: association with cardiovascular events and death. Circulation. 2008;118:1328–34.
59. Wong ND, Sciammarella M, Arad Y, Miranda-Peats R, Polk D, Hachamovich R, et al. Relation of thoracic aortic and aortic valve calcium to coronary artery calcium and risk assessment. Am J Cardiol. 2003;92:951–5.
60. Raggi P, Cooil B, Hadi A, Friede G. Predictors of aortic and coronary artery calcium on a screening electron beam tomographic scan. Am J Cardiol. 2003;91:744–6.

61. Takasu J, Shavelle DM, O'Brien KD, Babaei A, Rosales J, Mao S, et al. Association between progression of aortic valve calcification and coronary calcification: assessment by electron beam tomography. Acad Radiol. 2005;12:298–304.
62. Pohle K, Mäffert R, Ropers D, Moshage W, Stilianakis N, Daniel WG, Achenbach S. Progression of aortic valve calcification: association with coronary atherosclerosis and cardiovascular risk factors. Circulation. 2001;104:1927–32.
63. Walsh CR, Larson MG, Kupka MJ, Levy D, Vasan RS, Benjamin EJ, et al. Association of aortic valve calcium detected by electron beam computed tomography with echocardiographic aortic valve disease and with calcium deposits in the coronary arteries and thoracic aorta. Am J Cardiol. 2004;93:421–5.
64. Adler Y, Shemesh J, Tenenbaum A, Hovav B, Fisman EZ, Motro M. Aortic valve calcium on spiral computed tomography (dual slice mode) is associated with advanced coronary calcium in hypertensive patients. Coron Artery Dis. 2002;13:209–13.
65. Tenenbaum A, Shemesh J, Fisman EZ, Motro M. Advanced mitral annular calcification is associated with severe coronary calcification on fast dual spiral computed tomography. Investig Radiol. 2000;35:193–8.
66. Cury RC, Ferencik M, Hoffmann U, Ferullo A, Moselewski F, Abbara S, et al. Epidemiology and association of vascular and valvular calcium quantified by multidetector computed tomography in elderly asymptomatic subjects. Am J Cardiol. 2004;94:348–51.

Assessment of Native Coronary Artery Disease

5

Stephan S. Achenbach

The assessment of native coronary artery disease is one of the major applications of cardiac CT. Coronary CT angiography (coronary CTA) has high accuracy to identify coronary artery stenoses. Of importance, sensitivity approaches 100%, so that the presence of relevant coronary artery stenoses can be ruled out with a high degree of confidence, making further work-up unnecessary. In a meta-analysis of 30 studies with a total of 3722 patients, Menke et al. [1] demonstrated a sensitivity of 95.6% and specificity of 81.5% for coronary CTA performed with systems of at least 64 slices, in comparison with invasive coronary angiography. Accuracy was significantly lower for systems with fewer than 64 slices. Heart rate also influenced accuracy, with significantly higher accuracy for heart rates less than 62 beats per minute, compared with higher heart rates. Importantly, the high sensitivity of coronary CT angiography translates to an excellent ability to rule out coronary artery stenoses: the negative likelihood ratio for systems with at least 64 slices in the above-named study was 0.022. As a consequence of its high accuracy in ruling out coronary artery stenoses, coronary CTA has been incorporated into several guidelines published by US and European professional societies. Its use is generally endorsed as an alternative to other forms of noninvasive testing when the pretest likelihood is relatively low and patient characteristics make a fully diagnostic study very likely. It is also recommended that coronary CTA be considered when other noninvasive forms of testing are inconclusive [2–6].

S.S. Achenbach, MD
Department of Cardiology, University of Erlangen,
Ulmenweg 18, 91054 Erlangen, Germany
e-mail: stephan.achenbach@uk-erlangen.de

M.J. Budoff et al. (eds.), *Atlas of Cardiovascular Computed Tomography*, https://doi.org/10.1007/978-1-4471-7357-1_5

Stenosis Visualization in Coronary CTA

For the evaluation of coronary CTA data sets concerning the presence of coronary artery stenoses, several forms of image display are used:

- The review of original transaxial cross-sections
- Multiplanar reformations in arbitrary planes that make use of the isotropic spatial resolution of coronary CTA data sets
- "Maximum intensity projections," which delineate the coronary vessel segments in a thickened slab of the data set

Visual assessment of stenosis severity is preferred over attempts to perform percentage-based grading (Figs. 5.1, 5.2 and 5.3) [7].

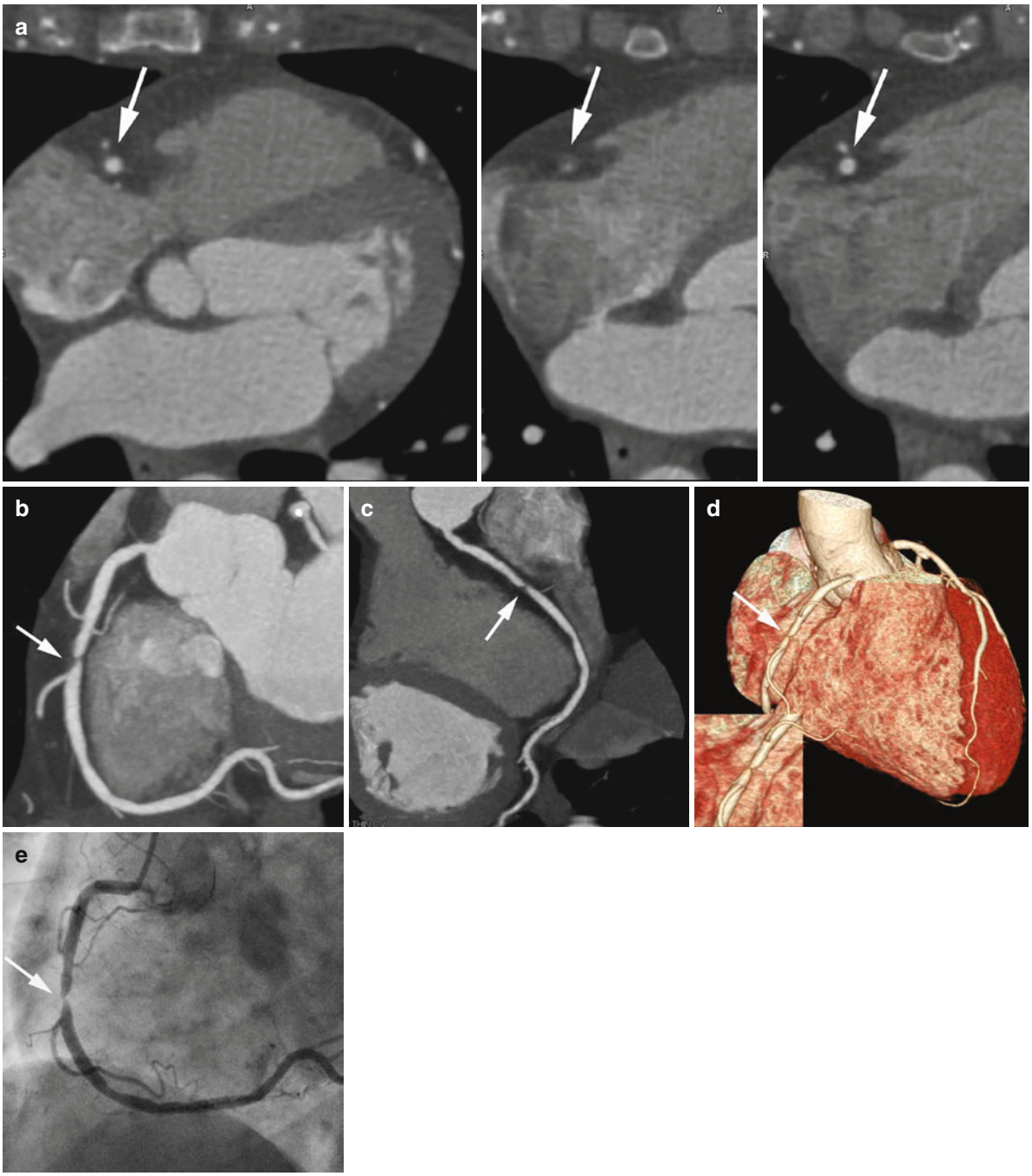

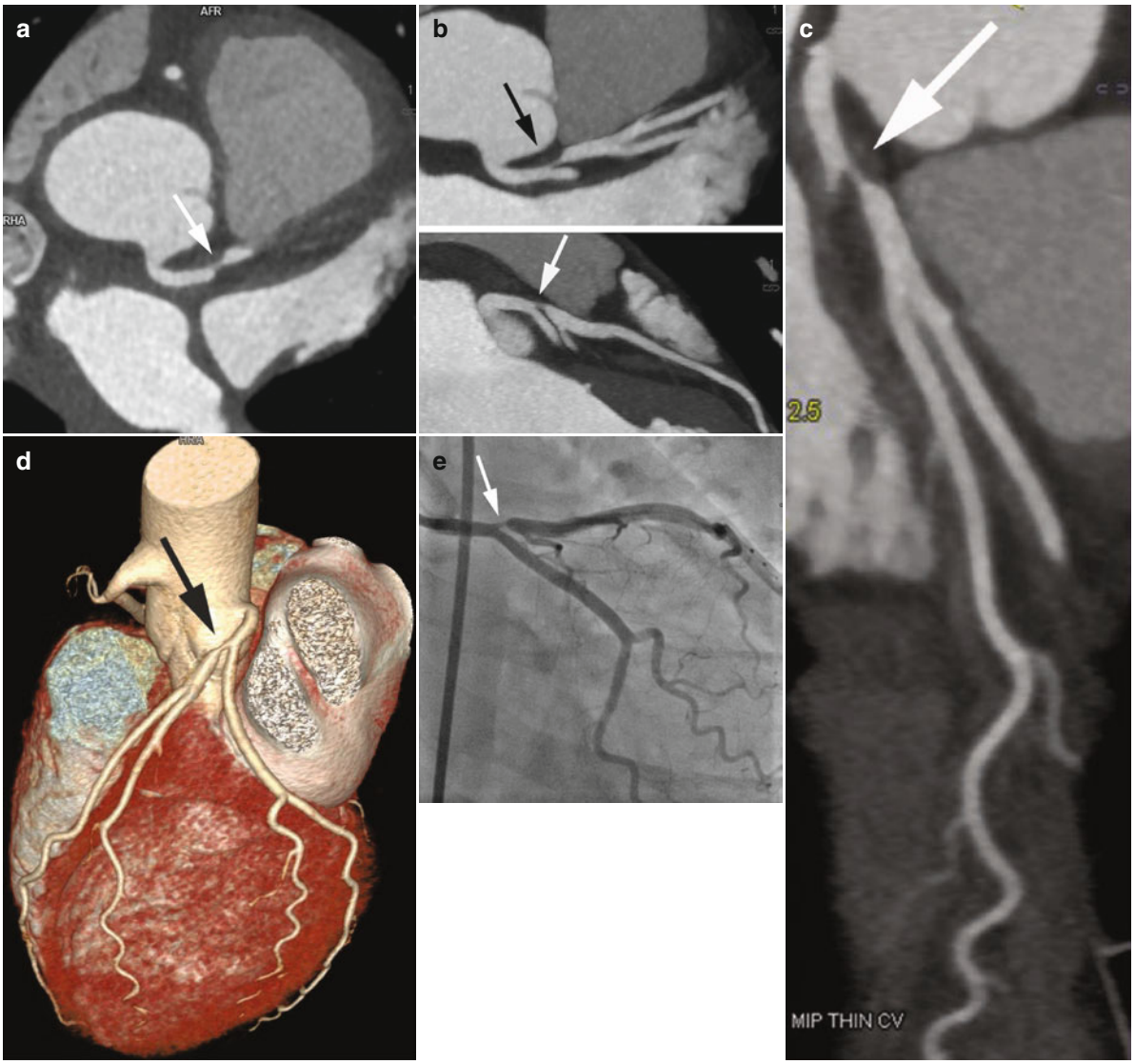

Fig. 5.2 Severe ostial stenosis of the left anterior descending coronary artery (segment 6 [7]). (**a**) Transaxial image (0.6 mm slice thickness) that shows the lumen narrowing—caused by entirely noncalcified plaque—in the ostium of the left anterior descending coronary artery (*arrow*). (**b**) Multiplanar reconstructions show longer segments of the left main and left anterior coronary artery in two different double-oblique planes (5 mm–thick maximum intensity projection). The *arrows* indicate the ostial stenosis of the left anterior descending coronary artery. (**c**) Curved multiplanar reconstruction of the left main and left anterior descending coronary artery, showing the stenosis (*arrow*). (**d**) Three-dimensional reconstruction showing the stenosis stenosis of the left anterior descending coronary artery (*arrow*). (**e**) Invasive angiography of the left coronary artery, with an ostial stenosis of the left anterior descending coronary artery (*arrow*)

Fig. 5.1 Severe coronary artery stenosis in the mid segment of the right coronary artery (segment 2 [7]). (**a**) Three consecutive transaxial sections in cranio-caudal sequence show the normal cross-sectional lumen of the right coronary artery (RCA), followed by severe narrowing of the lumen, which reconstitutes a few millimeters further distally (*arrows*). (**b**) Multiplanar reconstruction in a double-oblique plane, which shows the entire course of the RCA. The rendering has a thickness of 5 mm ("maximum intensity projection") and clearly shows a short, severe, noncalcified stenosis in the mid RCA (*arrow*). (**c**) Curved multiplanar reconstruction of the RCA, which also shows the severe stenosis (*arrow*). Such reconstructions can be rendered automatically by modern workstations. (**d**) Three-dimensional reconstruction showing the stenosis (*arrow*). (**e**) Invasive coronary angiogram, which confirms the short, severe stenosis (*arrow*)

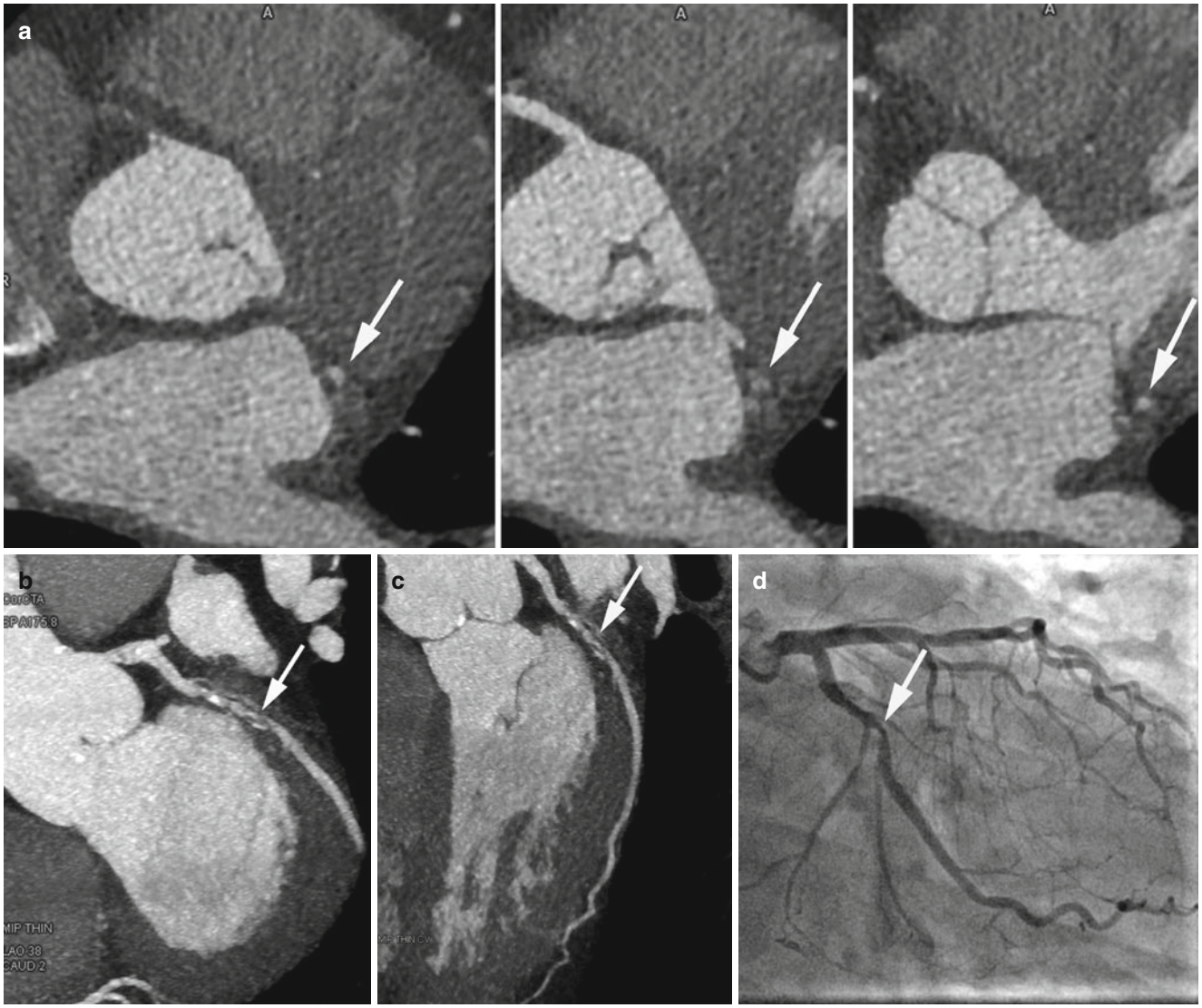

Fig. 5.3 Severe stenosis of the first obtuse marginal branch (segment 12 [7]). The data set has relatively high image noise due to patient obesity. (**a**) Three consecutive transaxial sections in cranio-caudal sequence show cross-sections of the first obtuse marginal branch (*arrows*), which is considerably larger than the left circumflex coronary artery distal to the bifurcation. Severe luminal narrowing in one level can be appreciated. (**b**) Multiplanar reconstruction in a double-oblique plane, which shows the proximal left circumflex and first posterolateral branch. The rendering has a thickness of 5 mm ("maximum intensity projection"). A long lesion with calcified and noncalcified plaque and severe narrowing of the lumen can be identified (*arrow*). (**c**) Curved multiplanar reconstruction of the left main and proximal left circumflex artery and the first obtuse marginal branch shows stenosis (*arrow*). (**d**) Invasive coronary angiography demonstrating a high-grade stenosis of the first obtuse marginal branch (*arrow*)

Classification of Stenosis Severity

Because of insufficient spatial resolution, exact quantification of stenosis severity by coronary CT angiography is not possible (Figs. 5.4, 5.5, 5.6 and 5.7). To quantify single lesions, it is recommended to use levels of stenosis severity as listed in Table 5.1 [7]. For classification of an entire patient, the Coronary Artery Disease Reporting and Data System (CAD-RADS™) classification system has been developed (Table 5.2) [8]. However, it has currently not been clinically validated regarding its relevance for patient management and prognosis. It is based

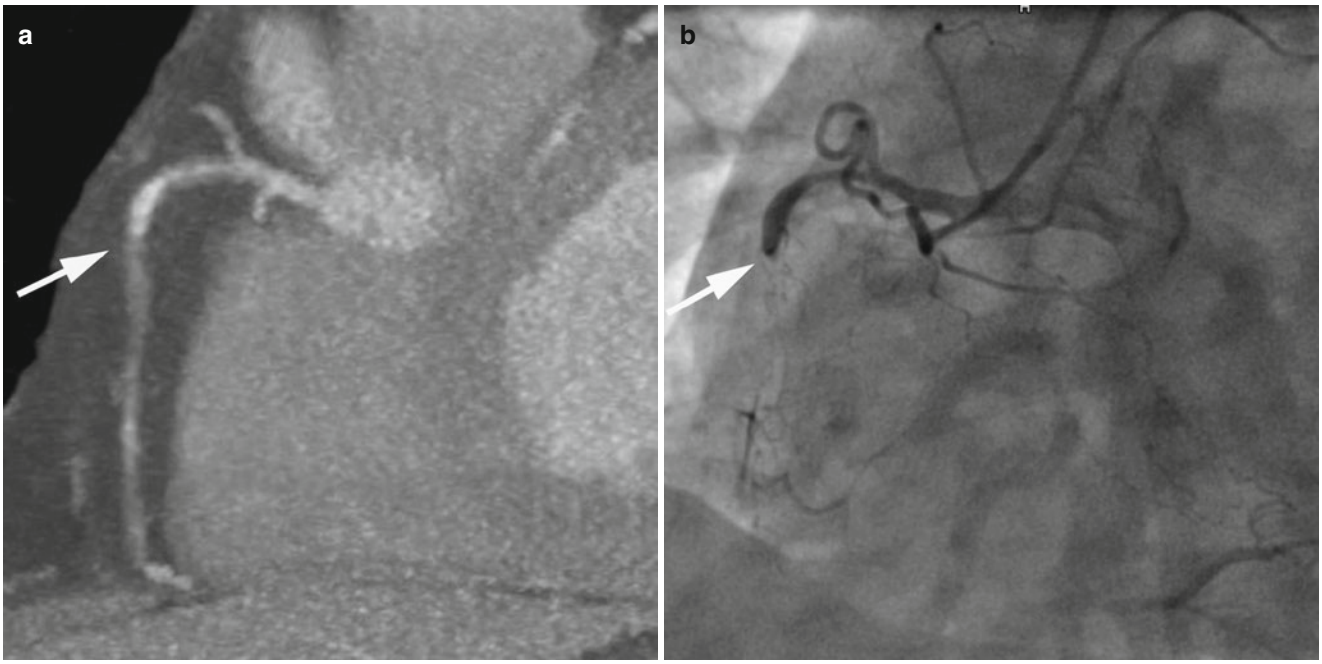

Fig. 5.4 Complete occlusion of the proximal right coronary artery. (**a**) Multiplanar reconstruction (maximum intensity projection) in coronary CTA. A proximal severe stenosis is followed by a complete interruption of the contrast-enhanced lumen (*arrow*) which corresponds to an occlusion of the artery. Image quality is not very high due to obesity and some motion blurring. (**b**) Invasive coronary angiography demonstrates a proximal severe stenosis followed by a complete occlusion of the artery (*arrow*)

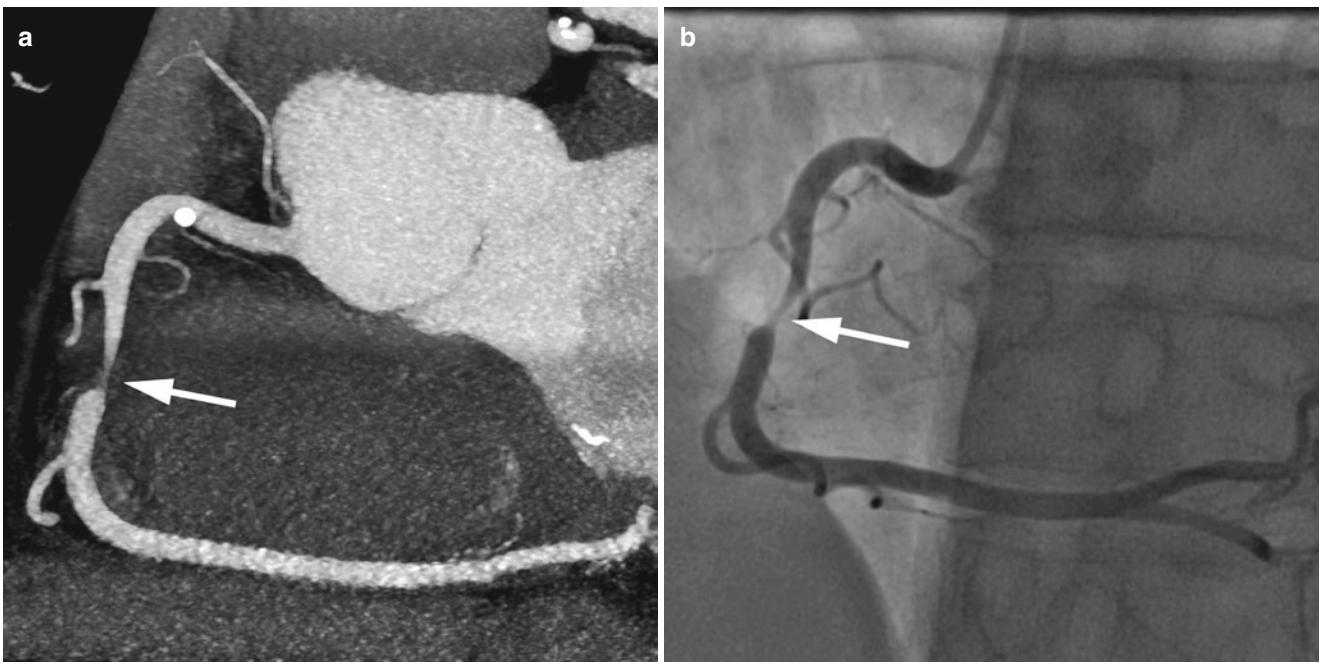

Fig. 5.5 Severe stenosis of the mid right coronary artery. (**a**) Multiplanar reconstruction (maximum intensity projection) of the right coronary artery. Severe luminal narrowing is present in the mid segment of the right coronary artery (*arrow*). (**b**) Invasive coronary angiography demonstrates a severe stenosis in the mid segment of the right coronary artery (*arrow*)

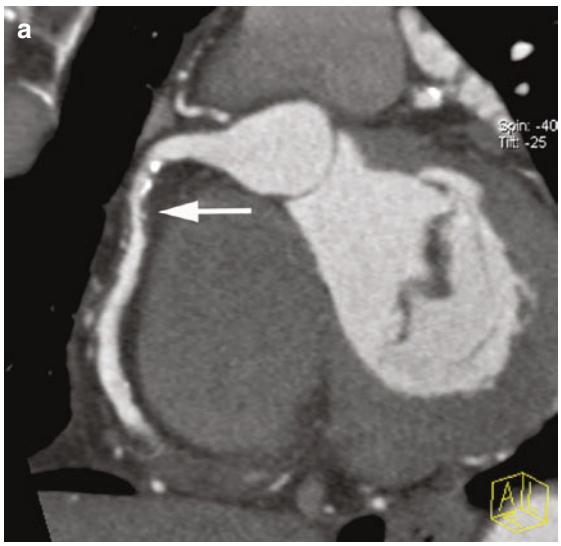

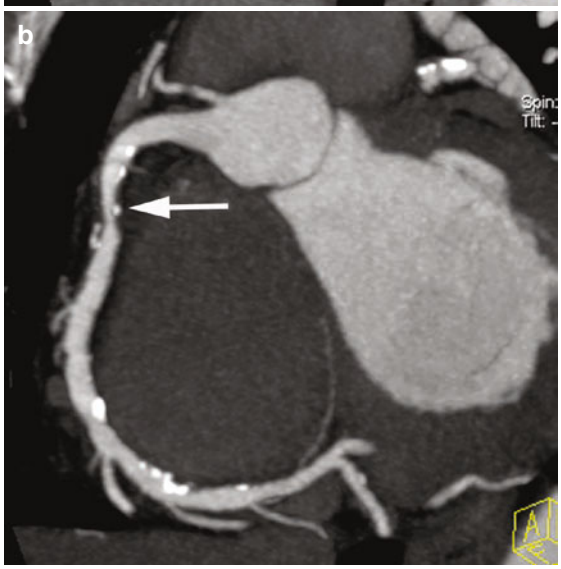

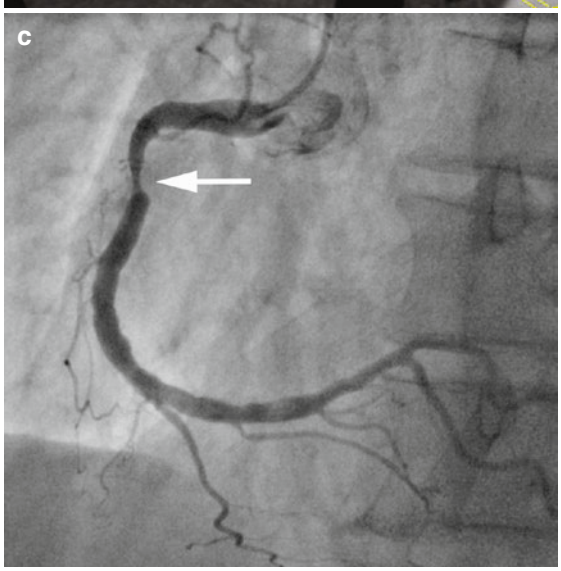

Fig. 5.6 Moderate stenosis of the proximal right coronary artery. Multiplanar reconstruction (**a**) 0.75 mm slice thickness; (**b**) maximum intensity projection, 8 mm thickness) of the right coronary artery. A moderate (50–69%) luminal stenosis is present in the proximal segment of the right coronary artery (*arrows*). (**c**) Invasive coronary angiography demonstrates a moderate stenosis in the proximal segment of the right coronary artery (*arrow*)

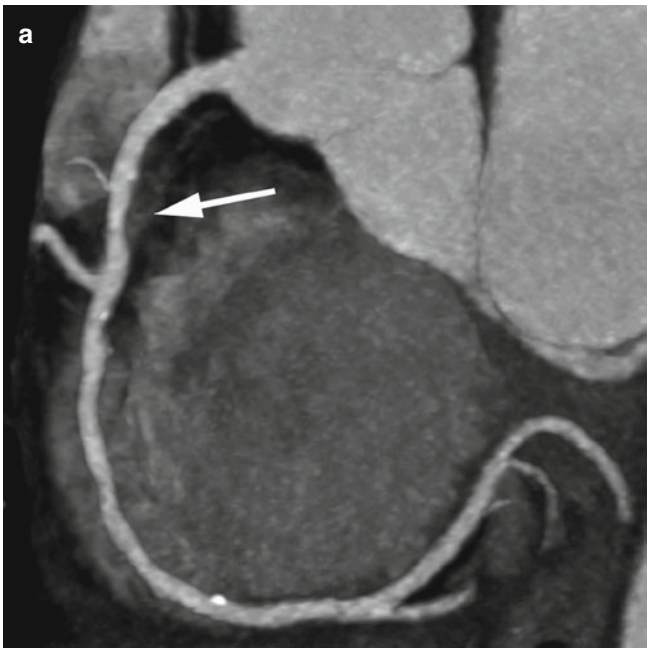

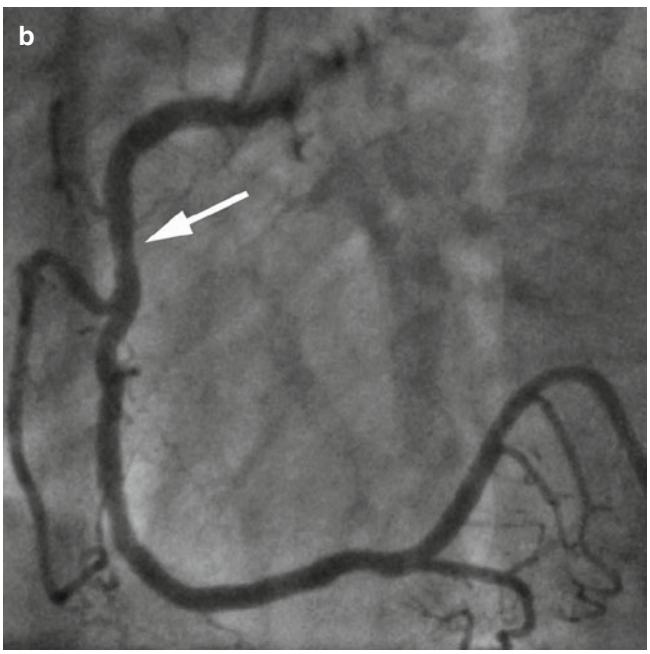

Fig. 5.7 Minimal stenosis of the proximal right coronary artery. In spite of a large plaque with positive remodeling, the degree of luminal stenosis is only very slight. This is a situation in which stenosis severity can easily be overestimated by CT. (**a**) Multiplanar reconstruction (maximum intensity projection) of the right coronary artery. A large, noncalcified atherosclerotic plaque with positive remodeling and only minimal luminal narrowing is present in the proximal right coronary artery (*arrow*). (**b**) Invasive coronary angiography demonstrates minimal luminal narrowing (often referred to as "wall irregularities") in the proximal segment of the right coronary artery (*arrow*). The extent of coronary atherosclerotic plaque is not visualized by invasive angiography

Table 5.1 Recommended stenosis grading

0 normal	Absence of plaque and no luminal stenosis
1 minimal	Plaque with <25% stenosis
2 mild	25–49% stenosis
3 moderate	50–69% stenosis
4 severe	70–99% stenosis
5 occluded	

on the quantification of the most severe luminal narrowing found per patient, with specific consideration of left main stenoses and three-vessel disease. Additional modifiers take into consideration the presence of stents and bypass grafts, and highlight the presence of atherosclerotic coronary plaque, showing characteristics of plaque vulnerability (Fig. 5.8) [8].

Table 5.2 Coronary Artery Disease Reporting and Data System (CAD-RADS™) to classify the severity of coronary artery disease per patient

	Maximal coronary artery stenosis severity (per patient)	Interpretation	Recommended further cardiac investigation
CAD-RADS 0	0%	"No plaque or stenosis"	None
CAD-RADS 1	1–24%[a]	"Plaque without stenosis"	None
CAD-RADS 2	25–49%	"Mild stenosis"	None
CAD-RADS 3	50–69%	"Moderate stenosis"	Consider functional testing
CAD-RADS 4A	70–99%	"Severe stenosis"	Consider functional assessment or invasive coronary angiography
CAD-RADS 4B	Left main >50% or 3-vessel disease ≥70%		Invasive coronary angiography is recommended
CAD-RADS 5	100%	"Total coronary occlusion"	Consider invasive angiography and/or testing for viability
CAD-RADS N	Non-diagnostic	"Coronary artery disease cannot be excluded"	Additional or alternative testing

[a]To include plaque without stenosis due to positive remodeling

G graft, *N* non-diagnostic, *S* stent, *V* plaque vulnerability

The classification emphasizes the lesion with the most severe luminal stenosis per patient, independent of its location in a small *versus* a larger vessel. Left main stenoses and three-vessel severe stenoses are classified separately because of their high prognostic relevance

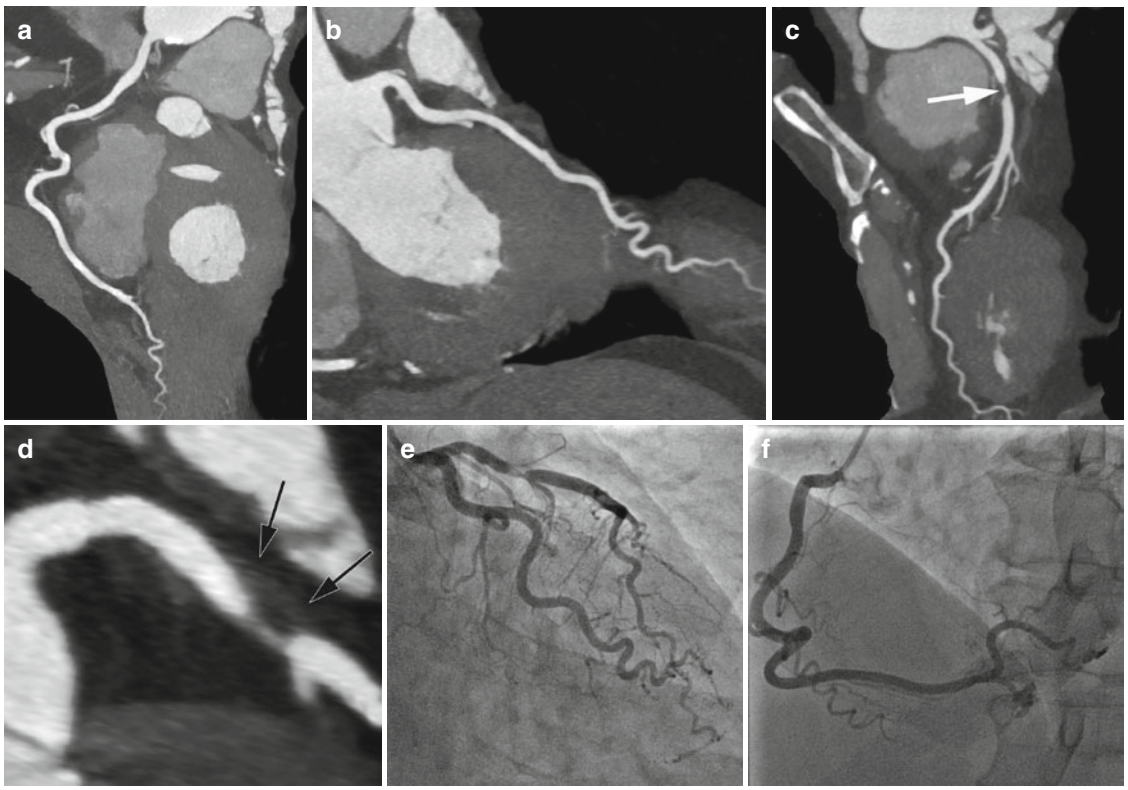

Fig. 5.8 Classification of a patient data set in the CAD-RADS™ system. The patient has no plaque or stenosis in the right coronary artery (**a**) and no plaque or stenosis in the left main and left circumflex coronary artery (**b**). However, there is a coronary artery stenosis with severe luminal narrowing (70–99%) in the proximal *left* anterior descending coronary artery (**c**), which corresponds to the category "CAD-RADS 4A". Because the lesion demonstrates signs of plaque vulnerability (a core of low CT attenuation and pronounced positive remodeling, *arrows* in (**d**) the classifier "/V" is added, for a final classification "CAD-RADS 4A/V" [8]. (**e**) and (**f**) show the corresponding invasive coronary angiograms of the *right* and *left* coronary arteries

Plaque Type

In coronary CT angiography, plaque can be classified as "non-calcified," "partly calcified," or "(entirely) calcified." Coronary artery stenoses can be caused by all types of coronary atherosclerotic plaque. Noncalcified and partly calcified lesions that cause severe luminal stenosis are substantially more frequent than entirely calcified plaque causing a severe stenosis. The latter is possible, however, and can be a cause of misinterpretation in coronary CT angiography (Figs. 5.9, 5.10 and 5.11).

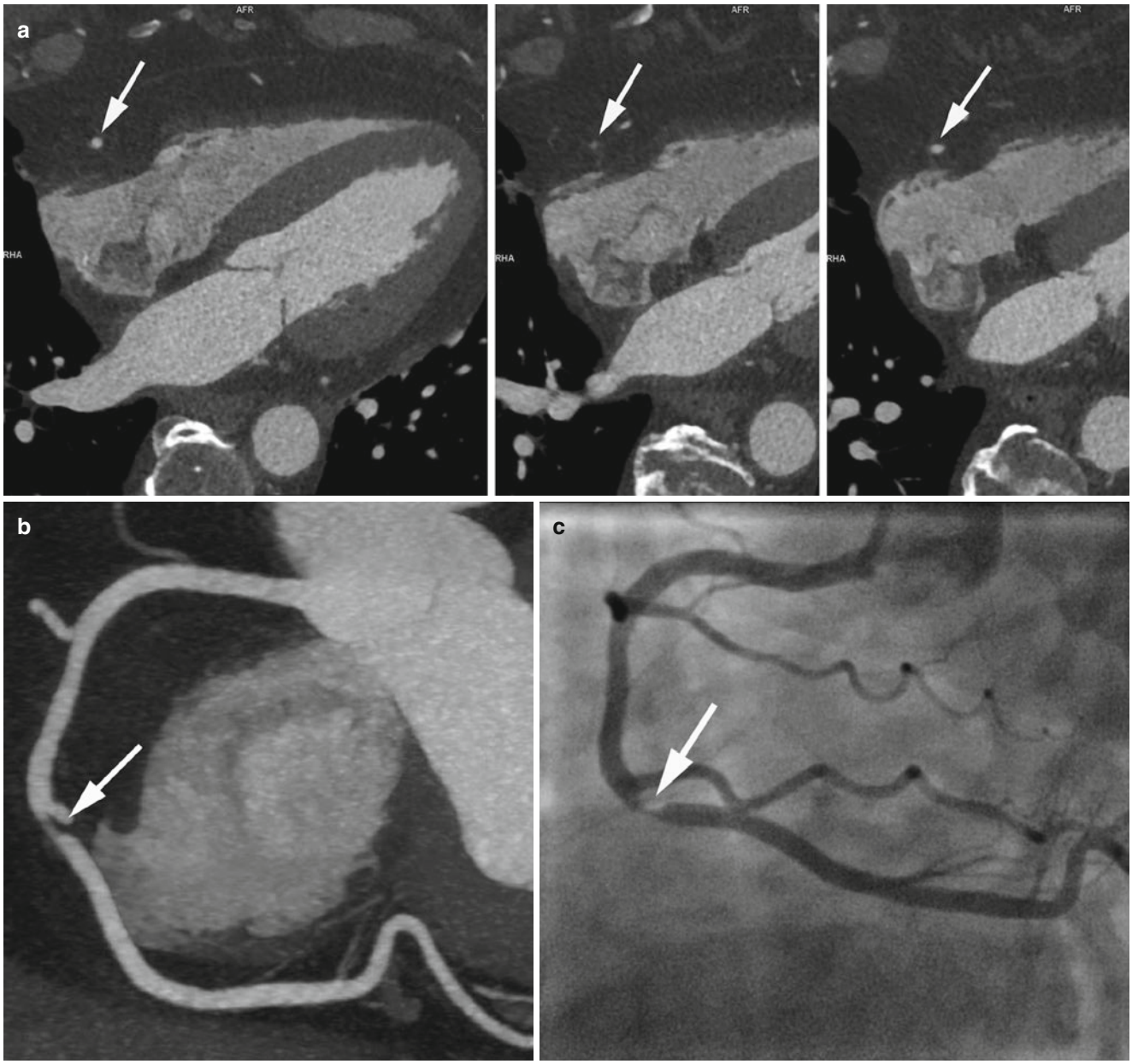

Fig. 5.9 Noncalcified stenosis of the mid right coronary artery. (**a**) Three consecutive transaxial images in cranio-caudal sequence showing cross-sections of the right coronary artery (*arrows*). An interruption of luminal continuity (*middle*) can be appreciated. No calcification is present. (**b**) Multiplanar reconstruction in a double-oblique plane, which shows the proximal and mid right coronary artery. The rendering has a thickness of 5 mm ("maximum intensity projection") and demonstrates a short, severe, noncalcified stenosis (*arrow*). (**c**) Invasive coronary angiography demonstrates a severe stenosis in the mid right coronary artery (*arrow*)

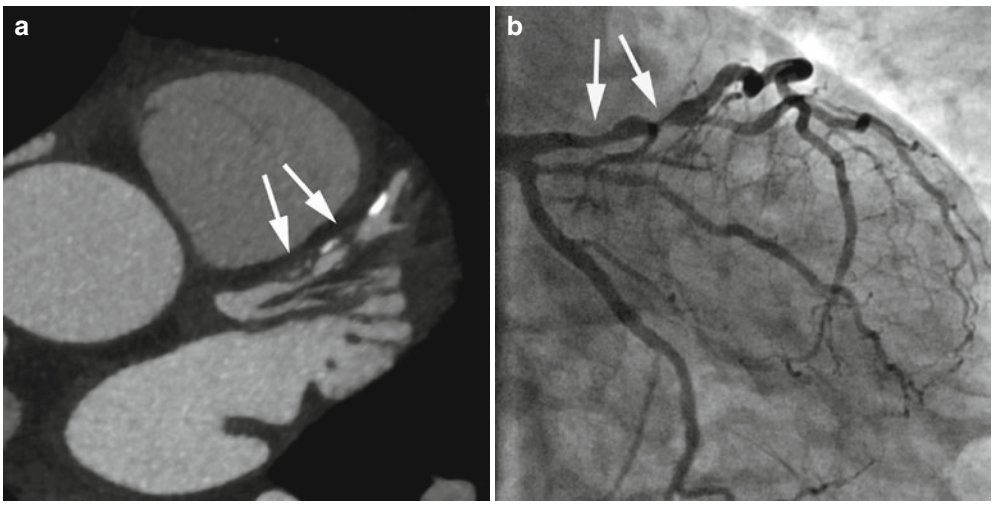

Fig. 5.10 Partly calcified tandem stenosis of the proximal left anterior descending coronary artery. (**a**) Transaxial image, 0.75 mm slice thickness, demonstrating two consecutive severe stenoses of the proximal left anterior descending coronary artery (*arrows*) caused by partly calcified atherosclerotic plaque with substantial plaque burden. (**b**) Invasive coronary angiography demonstrates two sequential stenoses of the proximal left anterior descending coronary artery (*arrows*)

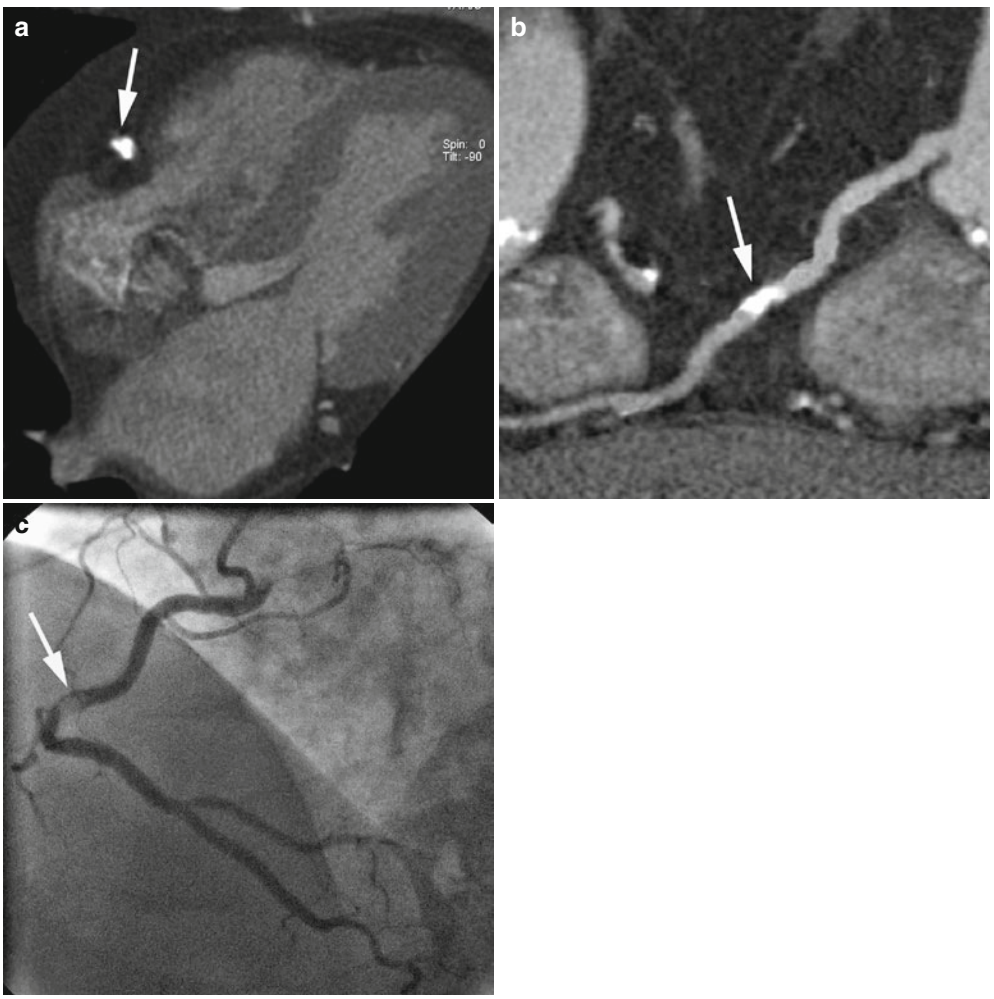

Fig. 5.11 Short, severe stenosis of the mid right coronary artery caused by a severely calcified atherosclerotic plaque (16-slice CT data set). (**a**) Transaxial image, 0.75 mm slice thickness, demonstrating obstruction of the right coronary artery lumen by a calcified lesion (*arrow*); no noncalcified plaque is detectable. (**b**) Curved multiplanar reconstruction, 3 mm thickness, demonstrating obstruction of the right coronary artery lumen by an entirely calcified lesion (*arrow*). (**c**) Invasive coronary angiography demonstrates a severely calcified, severe stenosis of the mid right coronary artery (*arrow*)

Extent of Coronary Atherosclerotic Plaque and Severity of Luminal Stenosis

There is no relationship between the type and volume of coronary atherosclerotic plaque and the severity of associated luminal stenosis in coronary CT angiography. Severe luminal stenosis can be associated with very small amounts of plaque. Especially in the setting of slightly elevated image noise, small amounts of atherosclerotic plaque may be virtually indiscernible by coronary CTA. On the

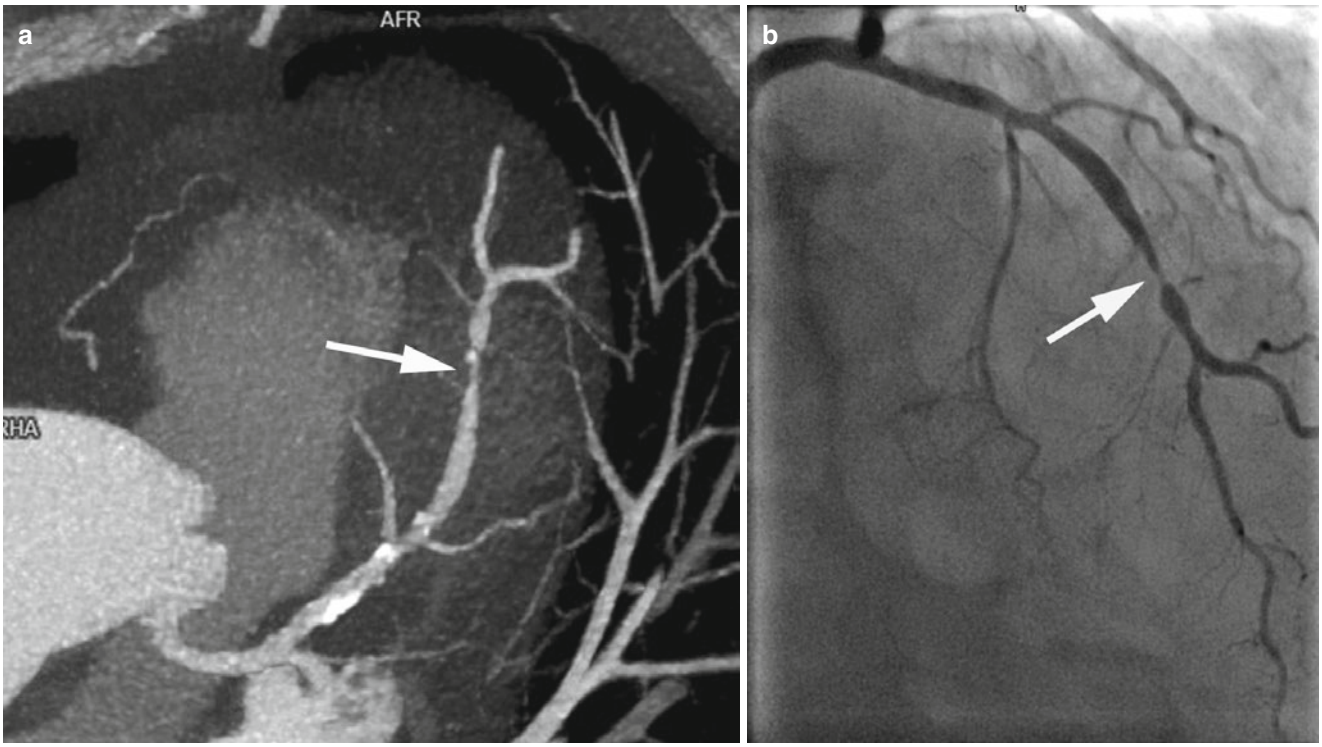

Fig. 5.12 Severe coronary artery stenosis (70–99%) in the mid left anterior descending coronary artery without detectable plaque in coronary CTA. (**a**) Maximum intensity projection in coronary CTA. A luminal stenosis of severe degree is present (*arrow*), but—next to a very small calcification—no plaque is detectable. This lack may be partly due to image noise. (**b**) Invasive coronary angiography in the same patient

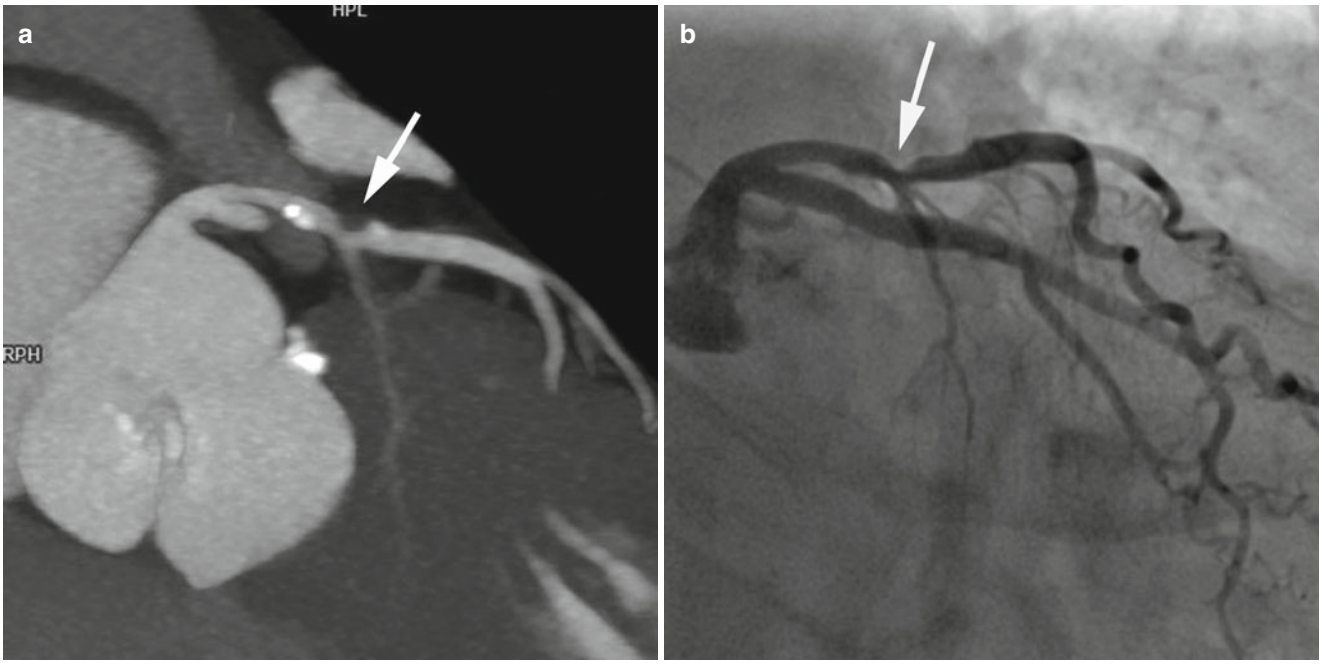

Fig. 5.13 A moderate amount of plaque causing a moderate luminal stenosis (50–69%). (**a**) Double-oblique maximum intensity projection showing a moderate stenosis of the proximal left anterior descending coronary artery in the presence of a moderate amount of positively remodeled, partly calcified atherosclerotic plaque (*arrow*). (**b**) Invasive coronary angiogram in a similar projection

other hand, even very voluminous coronary atherosclerotic plaque can be found with only minimal luminal reduction—or the entire absence of it. Separation of "plaque type and volume" and "luminal stenosis" is an important concept in the interpretation of coronary CTA data sets (Figs. 5.12, 5.13, 5.14 and 5.15).

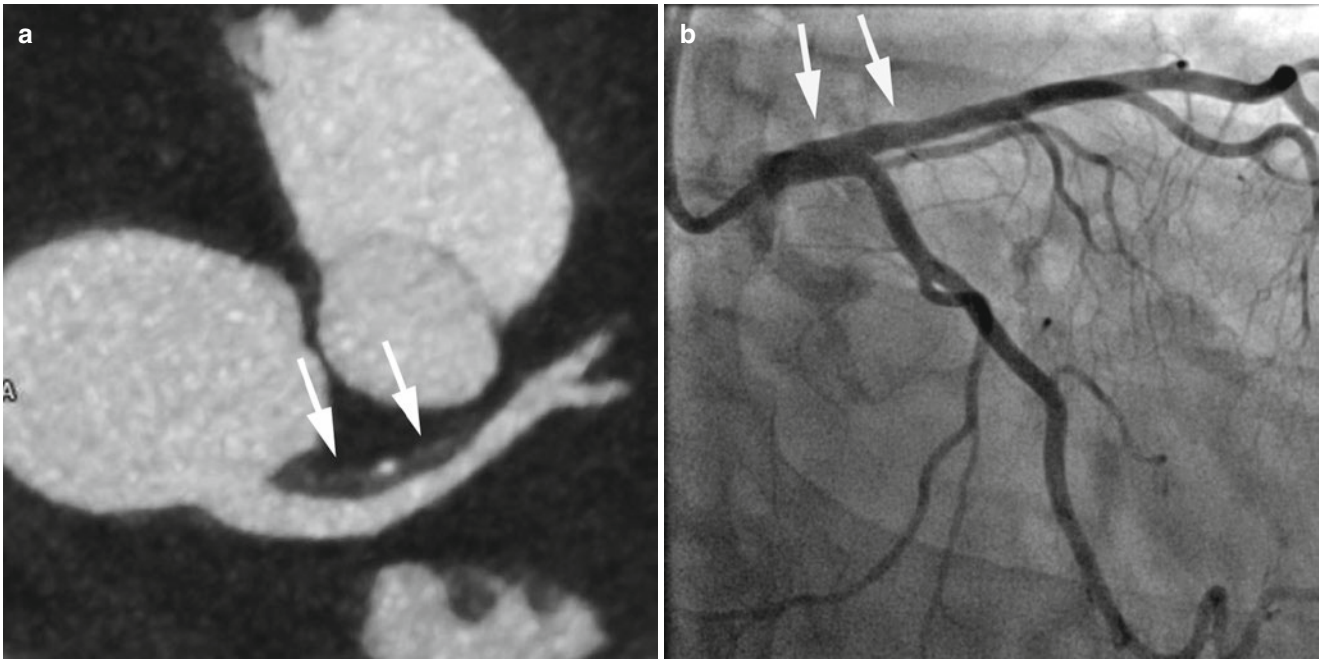

Fig. 5.14 Large coronary atherosclerotic plaque with minimal luminal stenosis (1–24%). (**a**) Transaxial maximum intensity projection showing a large atherosclerotic plaque with minimal calcification (*arrows*) in the left main and proximal left anterior descending coronary artery. The degree of luminal narrowing in CTA appears minimal. (**b**) Invasive coronary angiogram shows minimal luminal narrowing and wall irregularities (*arrows*) in the left main and proximal left anterior descending coronary artery

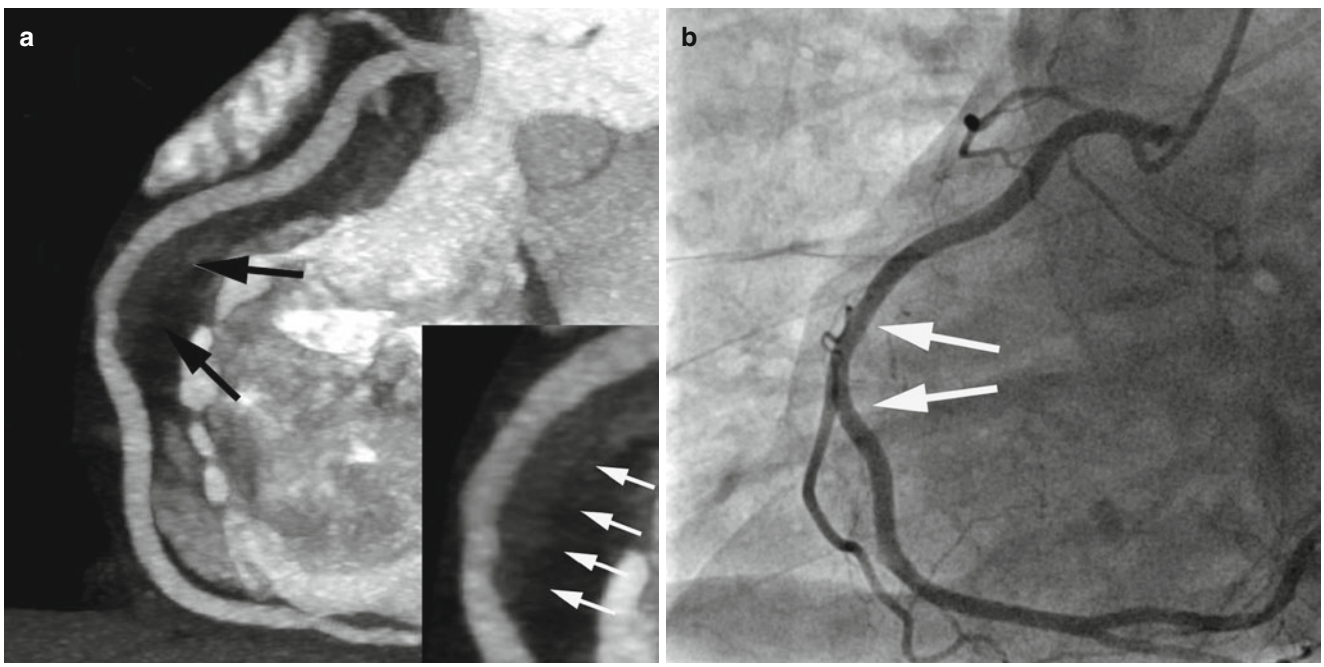

Fig. 5.15 Large coronary atherosclerotic plaque without luminal stenosis. (**a**) Maximum intensity projection of the right coronary artery showing a large, noncalcified and severely positively remodeled atherosclerotic plaque in the proximal-to-mid segment of the vessel (*arrows*). (**b**) No appreciable luminal stenosis in invasive angiography (*arrows*)

Left Main Coronary Artery Stenosis

Left main coronary artery stenoses carry particularly high prognostic relevance. A threshold of 50% luminal narrowing is typically used to classify "relevant" left main coronary artery stenoses. In coronary CT angiography, left main stenoses may at times be difficult to identify. Stenoses of the distal bifurcation of the left main coronary artery are more frequent than stenoses at the ostium. Shaft stenoses are very infrequent (Figs. 5.16, 5.17 and 5.18).

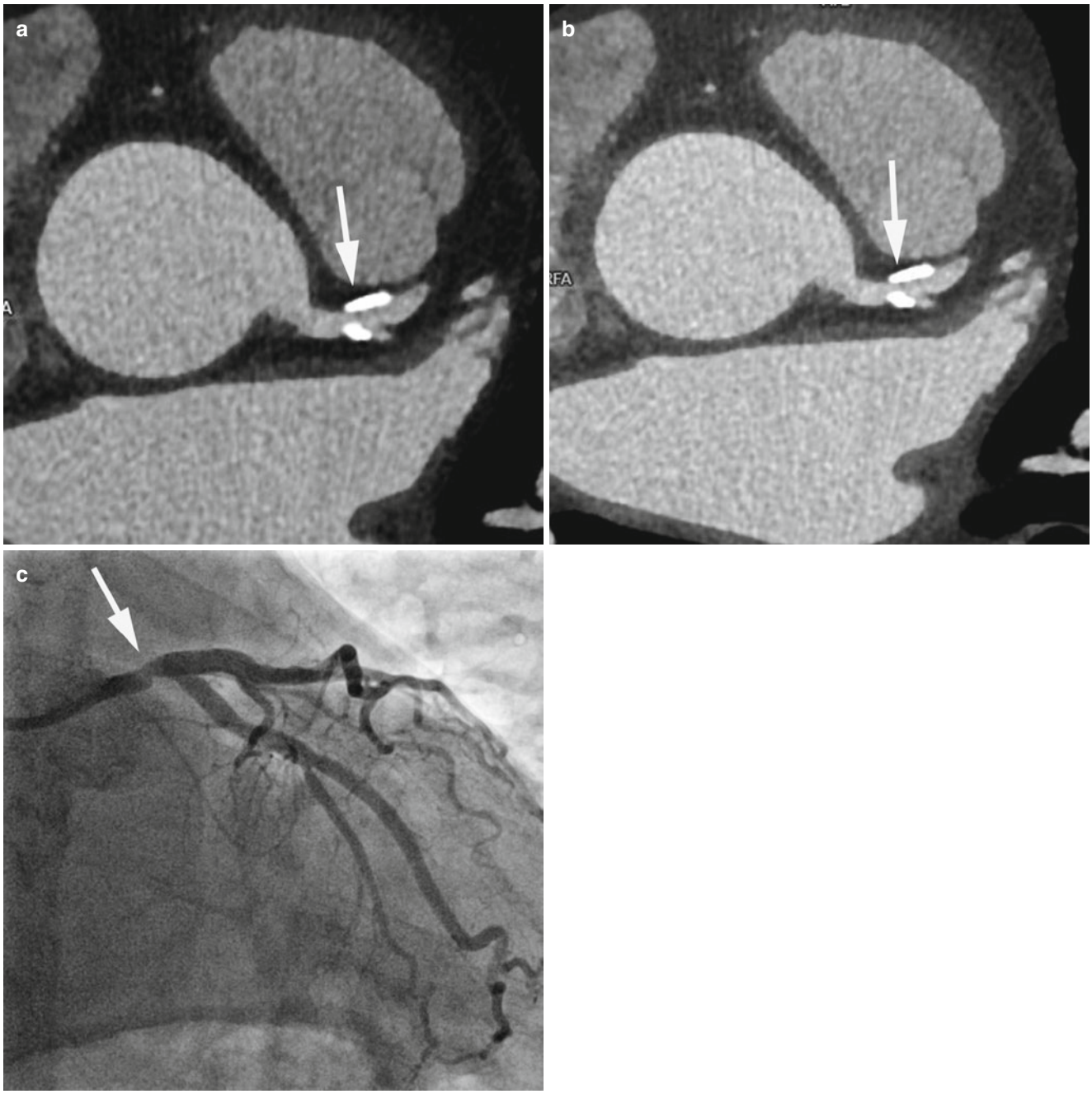

Fig. 5.16 Calcified, moderate stenosis of the distal left main bifurcation in coronary CTA and invasive angiography. (**a**) Thin transaxial slice (0.6 mm thickness). (**b**) 2-mm thick maximum intensity projection in the same orientation. Completely calcified plaque causes a moderate stenosis of the distal left main coronary artery immediately proximal to the bifurcation. (**c**) Invasive coronary angiography. The *arrow* indicates a moderate stenosis of the distal left main coronary artery

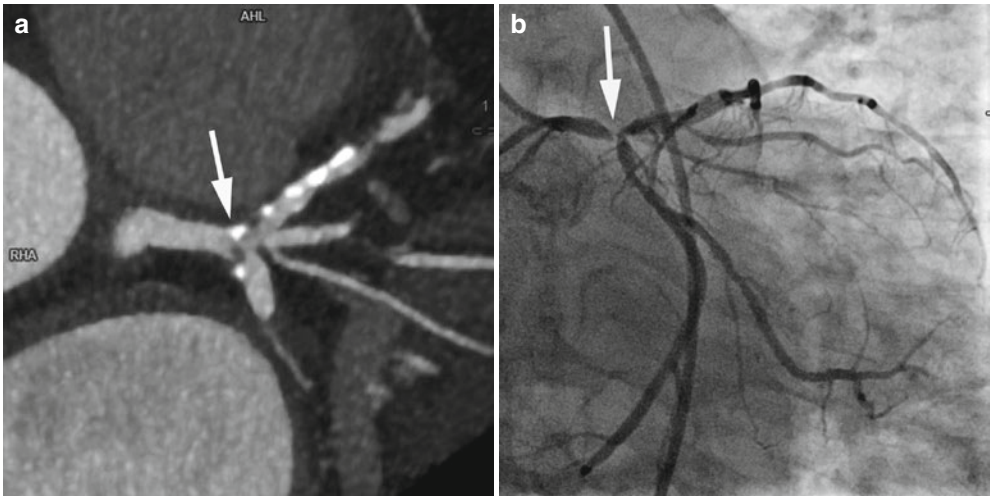

Fig. 5.17 Severe stenosis of the distal left main coronary artery. (**a**) Transaxial slice of a left main trifurcation with a severe luminal stenosis caused by partly calcified plaque (*arrow*). The calcified component of the plaque obstructs part of the lumen, leading to a visual underestimation of stenosis severity when compared with the invasive coronary angiogram in (**b**). Clinical experience confirms a tendency towards underestimating left main stenosis severity by coronary CTA, especially in the presence of calcified plaque

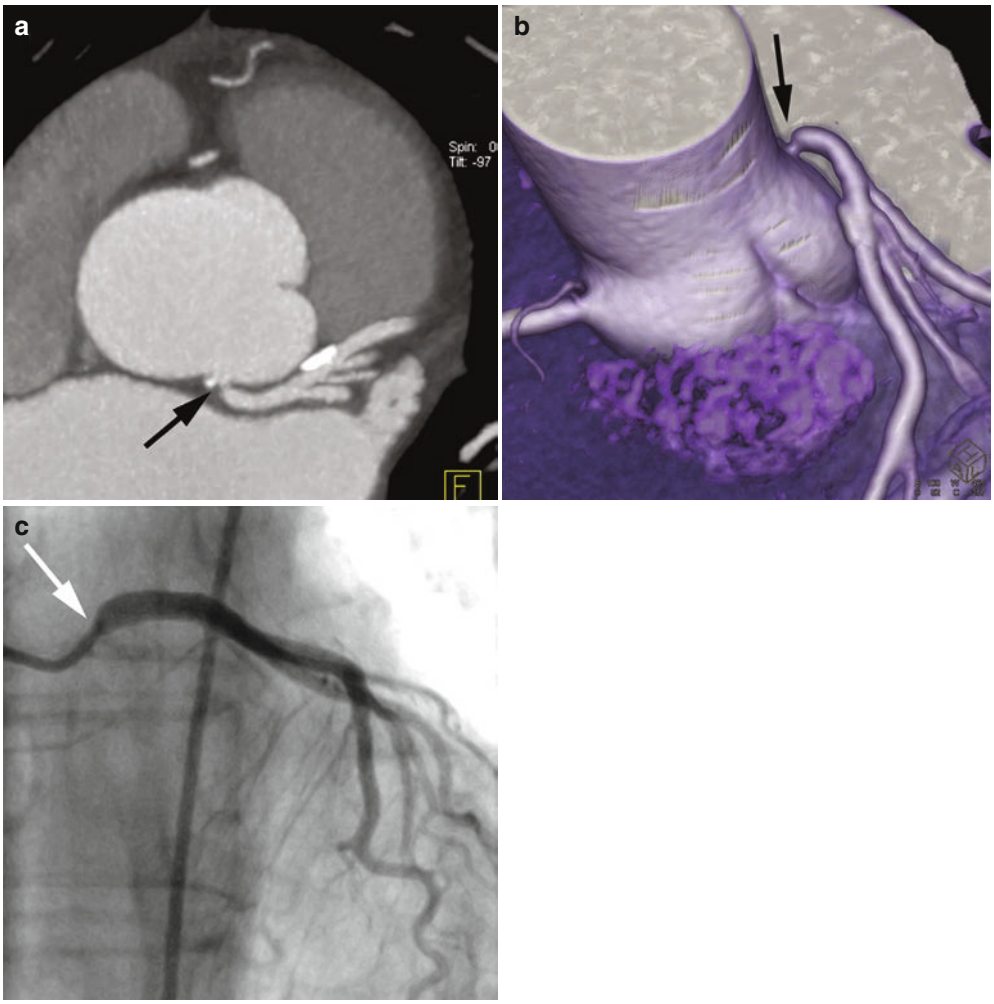

Fig. 5.18 Ostial stenosis of the left main coronary artery. A maximum intensity projection (**a**) and a three-dimensional reconstruction (**b**) show a severe narrowing of the ostium of the left main coronary artery (*arrows*). Ostial stenoses can be very short, even when severe. Invasive coronary angiography (**c**) shows a short left main ostial stenosis (*arrow*)

Stenosis Degree and Ischemia

There is no close relationship between the anatomic degree of stenosis severity and the hemodynamic relevance of a coronary atherosclerotic lesion. Even severe luminal stenoses, especially when short, do not necessarily cause stress-induced ischemia, whereas stenoses of a lesser degree, especially when long, can be associated with relevant ischemia. Comparisons to invasively measured fractional flow reserve (FFR) suggest that plaque volume and plaque characteristics associated with "plaque vulnerability" influence the hemodynamic relevance of coronary artery stenoses, potentially more than the anatomic degree of luminal narrowing [9–11] (Fig. 5.19). Hence, the interpretation of

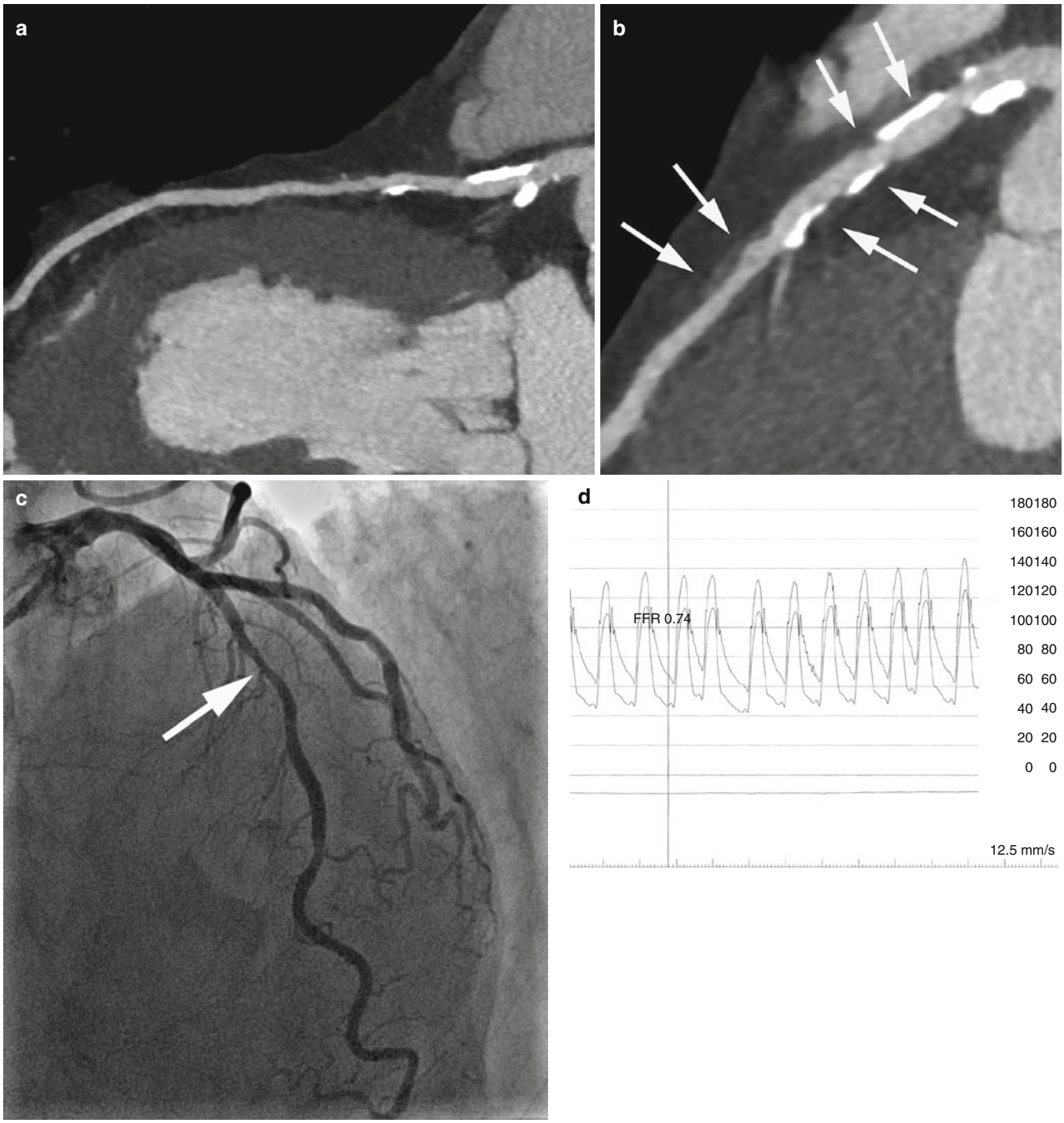

Fig. 5.19 Hemodynamically relevant left anterior descending coronary artery lesion in the absence of severe stenosis. (**a**) Coronary CTA of a left main and left anterior descending coronary artery with presence of calcified and noncalcified plaque, but absence of severe luminal narrowing. (**b**) A magnified view shows a relatively large plaque volume and "positive remodeling" (*arrows*), two signs of plaque vulnerability. (**c**) Invasive coronary angiogram shows a stenosis of moderate degree in the mid left anterior descending coronary artery. (**d**) Invasive fractional flow reserve (FFR) measurement was performed with adenosine-induced vasodilation and demonstrated a value of 0.74, thus indicating the hemodynamic relevance of the lesion, even though the degree of luminal narrowing is not severe

coronary CTA must consider that the relationship between stenosis degree and ischemia is not a close one, and testing for ischemia may be necessary as a basis for revascularization decisions. A method to derive information on hemodynamic relevance from anatomic coronary CTA data sets is "virtual FFR"—also called "FFR-CT"—which is derived from CT data sets using fluid dynamic modeling [12] (Fig. 5.20). Clinical trials have shown an accuracy of 86% of FFR-CT in comparison with invasively measured FFR [13]. (*See also* Chap. 9.)

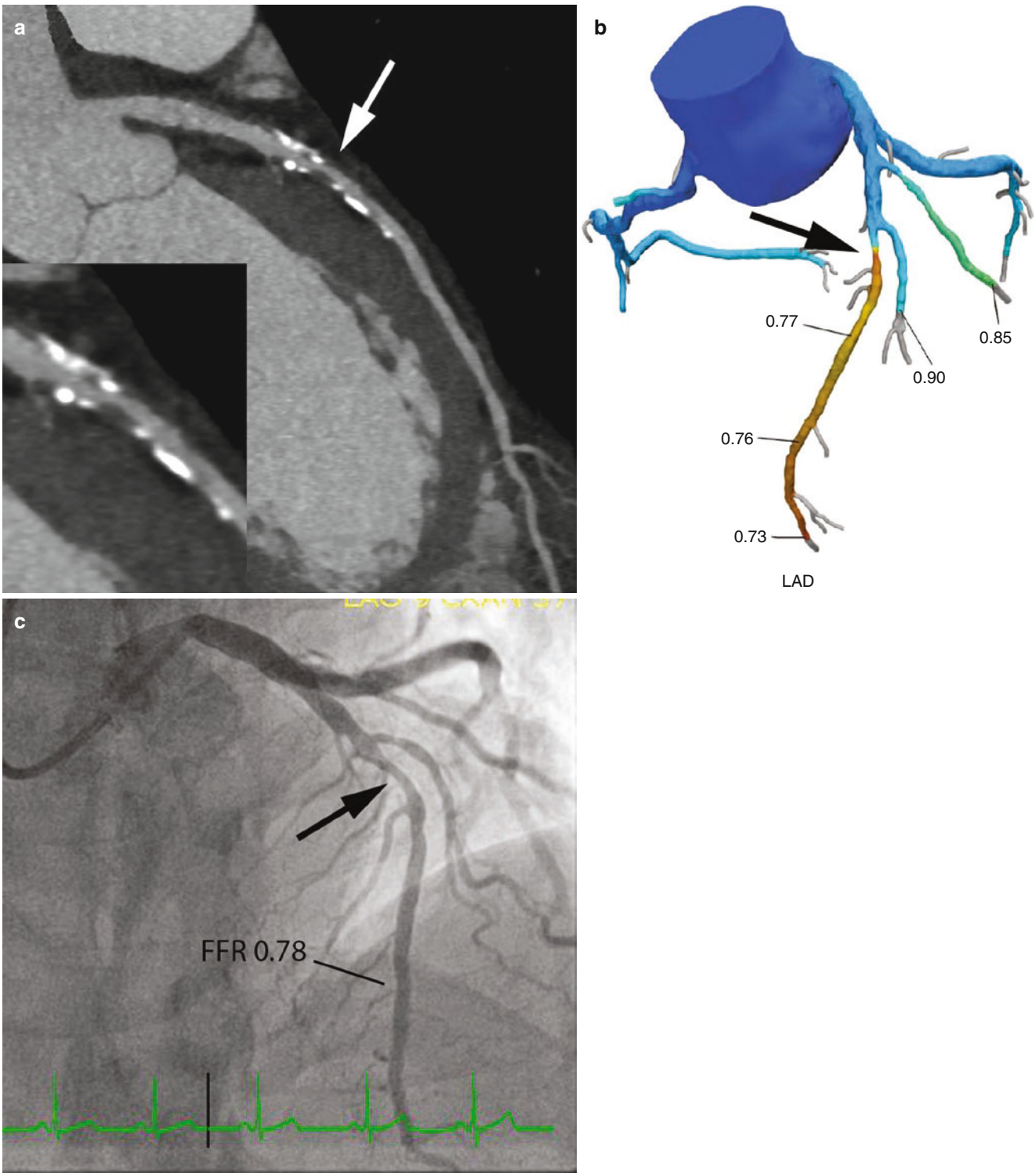

Fig. 5.20 Calculation of FFR-CT. (**a**) Coronary CT angiography shows a moderate (50–69%) stenosis of the mid left anterior descending coronary artery. Similar to Fig. 5.19, this lesion demonstrates a large volume of plaque and positive remodeling. (**b**) FFR-CT suggests hemodynamic relevance of the stenosis in the mid segment of the left anterior descending (LAD) coronary artery. (**c**) Invasive coronary angiography confirms a moderate stenosis in the mid segment of the LAD coronary artery (*arrow*). Invasive FFR reveals a value of 0.78 distal to the lesion, indicating hemodynamic relevance

Bifurcation Lesions

About 20% of all coronary artery stenoses that undergo revascularization are bifurcation lesions [14]. The type of involvement of the main branch and bifurcation branches has substantial influence on the interventional strategy if percutaneous revascularization is considered [15]. Frequently, the "Medina Classification" is used to describe the localization of stenoses in a coronary bifurcation [16]. This classification uses the numbers 0 and 1 for the absence or presence of a significant stenosis, following the sequence "main branch proximal/main branch distal/side branch" to indicate locations. Hence, a Medina Classification 1/0/1 would be used to describe a significant stenosis of the main branch proximal to the bifurcation and a significant stenosis of the side branch ostium, with the absence of stenosis in the main branch immediately distal to the bifurcation (Figs. 5.21, 5.22, 5.23, 5.24 and 5.25).

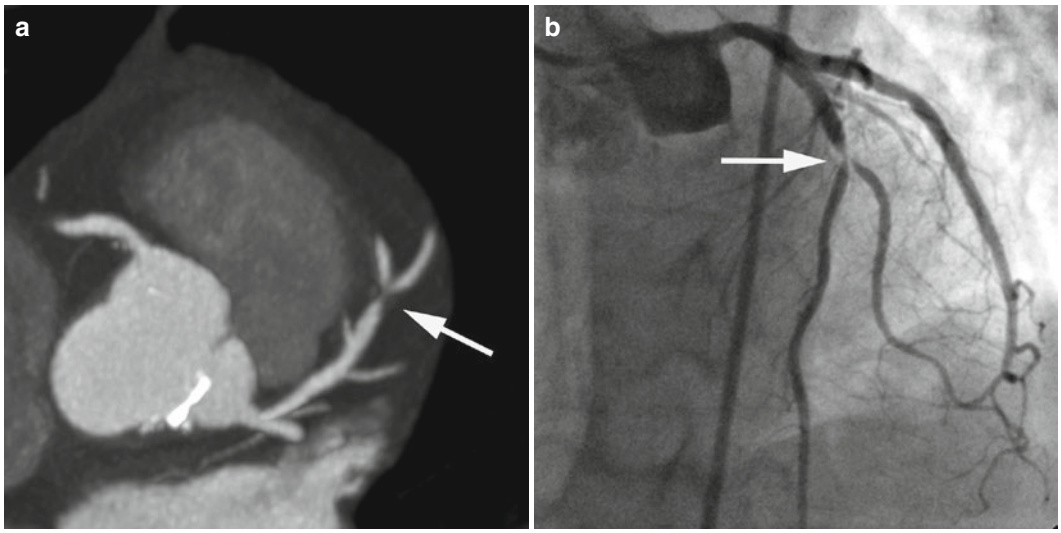

Fig. 5.21 High-grade stenosis of the bifurcation of the left anterior descending coronary artery and first diagonal branch, with involvement of the main branch immediately proximal to the bifurcation, the main branch immediately distal to the bifurcation, and the side branch (*arrows*), corresponding to Medina Classification 1/1/1. The stenosis is not calcified. (**a**) Coronary CT angiography. (**b**) Invasive coronary angiography

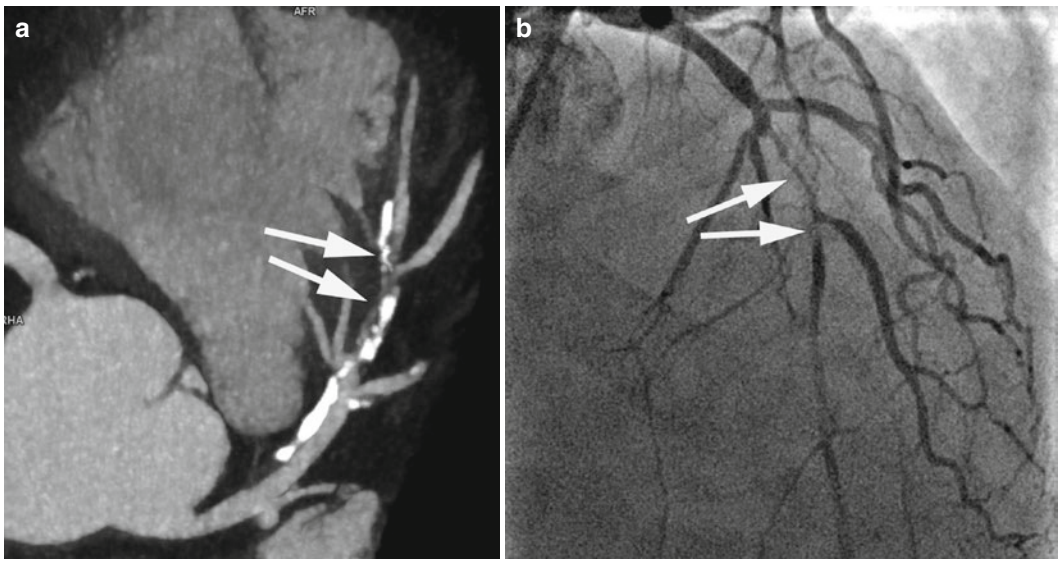

Fig. 5.22 High-grade, severely calcified stenosis of the left anterior descending coronary artery proximal and distal to the origin of the second diagonal branch (*arrows*), but no severe stenosis of the diagonal branch ostium, corresponding to Medina Classification 1/1/0. (**a**) Coronary CT angiography. (**b**) Invasive coronary angiography

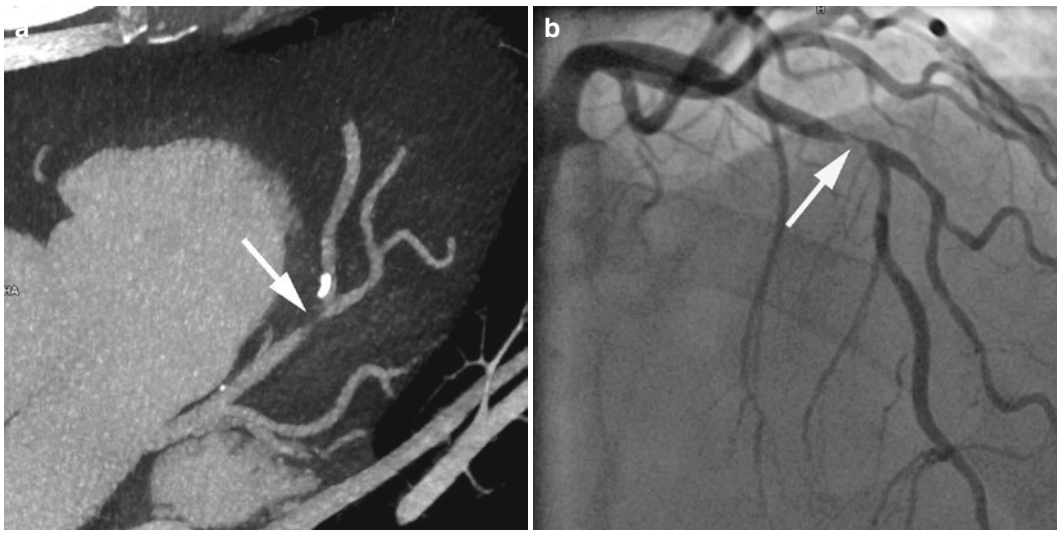

Fig. 5.23 Severe stenosis of the left anterior descending coronary artery proximal to the bifurcation to the first diagonal branch (*arrow*), Medina Classification 1/0/0. (**a**) Coronary CT angiography. (**b**) Invasive coronary angiography

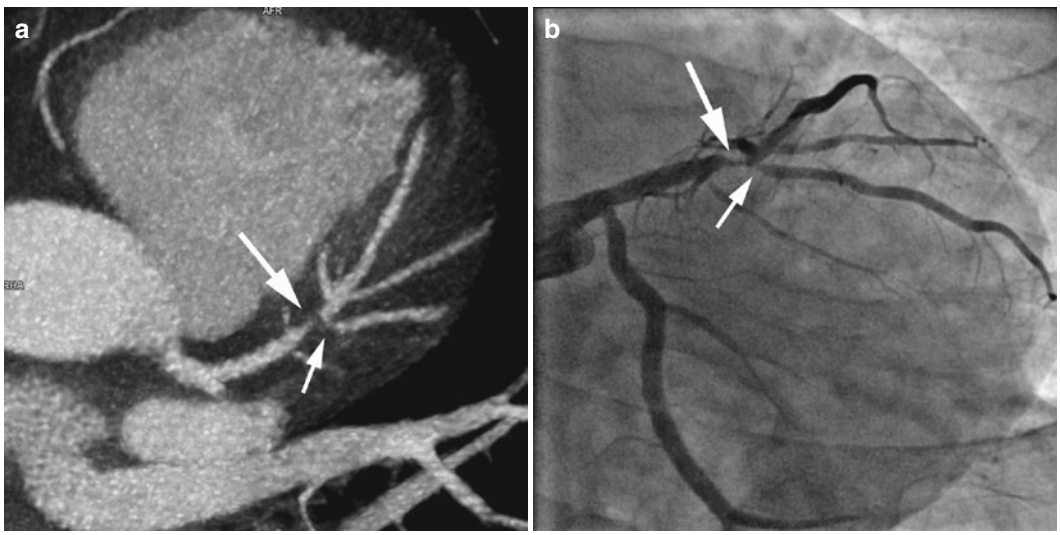

Fig. 5.24 Severe stenosis of the left anterior descending coronary artery proximal to the bifurcation to the first diagonal branch (*large arrow*) and of the diagonal branch ostium (*small arrow*), corresponding to Medina Classification 1/0/1. (**a**) Coronary CT angiography. (**b**) Invasive coronary angiography

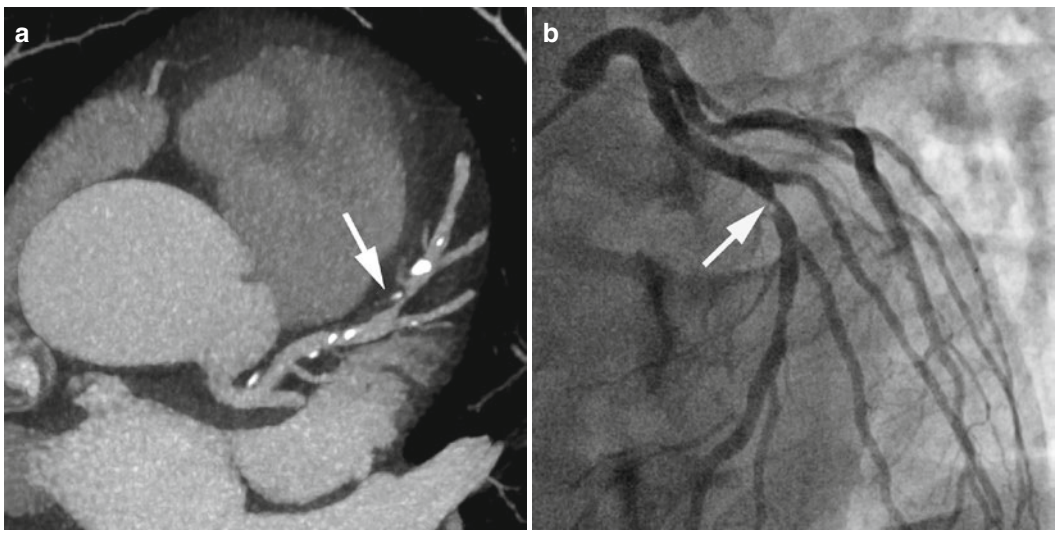

Fig. 5.25 Severe stenosis of the left anterior descending coronary artery immediately distal to the bifurcation to the first diagonal branch (*arrow*), corresponding to Medina Classification 0/1/0. (**a**) Coronary CT angiography. (**b**) Invasive coronary angiography

Chronic Total Coronary Occlusions

Chronic total occlusions (CTO) of coronary arteries are a specific lesion subset. Occlusions are called "chronic" if they persist for more than 3 months. In coronary CT angiography, both coronary occlusions and very high-grade stenoses may appear as complete interruptions of a traceable contrast-enhanced lumen, and they can be difficult or impossible to

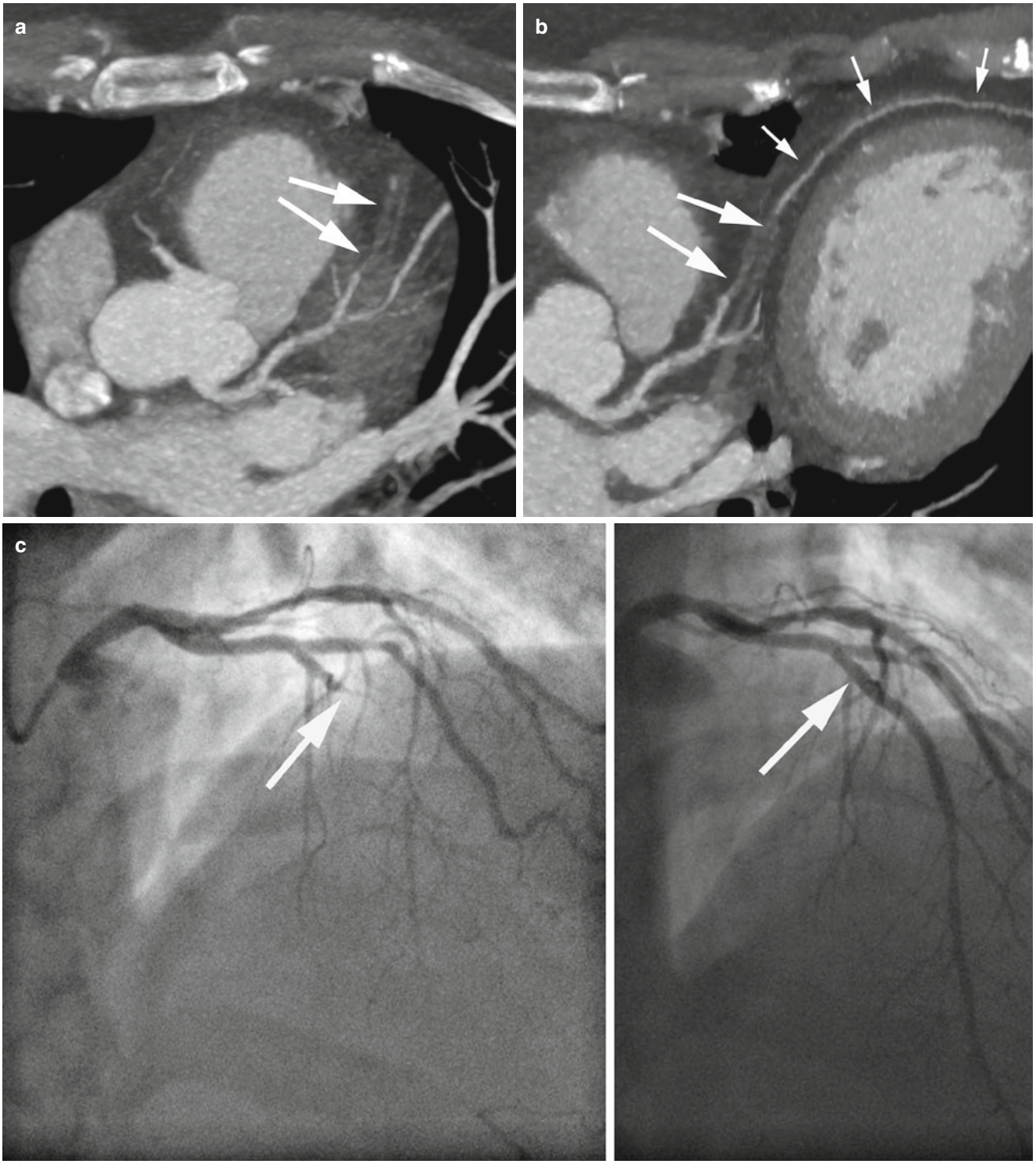

Fig. 5.26 Chronic total occlusion of the mid left anterior descending coronary artery. (**a**) Maximum intensity projection. (**b**) Curved multiplanar reconstruction in coronary CT angiography. The occluded segment with complete interruption of the contrast-enhanced lumen (*large arrows*) and contrast enhancement of the distal coronary artery via collaterals (*small arrows*) is visualized. The occlusion is noncalcified, not tortuous, and presents with a tapered stump, all of which indicate that the likelihood of interventional revascularization success is high. Image noise is high in a severely obese patient. (**c**) Invasive coronary angiogram showing the occluded vessel segment (*arrow*) before (*left*) and after (*right*) interventional revascularization

differentiate. The length of the vessel segment that displays no contrast enhancement can suggest the presence of a complete occlusion rather than a very high-grade stenosis: one study demonstrated that a length greater than 8 mm makes a complete occlusion very likely [17]. The interventional treatment of chronic total coronary occlusions is challenging; the success of interventional revascularization depends on factors such as lesion length, extent of calcification, and stump morphology. In fact, CT is well suited for depicting the morphology of chronic total coronary occlusions and can be used to predict the likelihood of success of interventional revascularization [18] (Figs. 5.26, 5.27, 5.28 and 5.29).

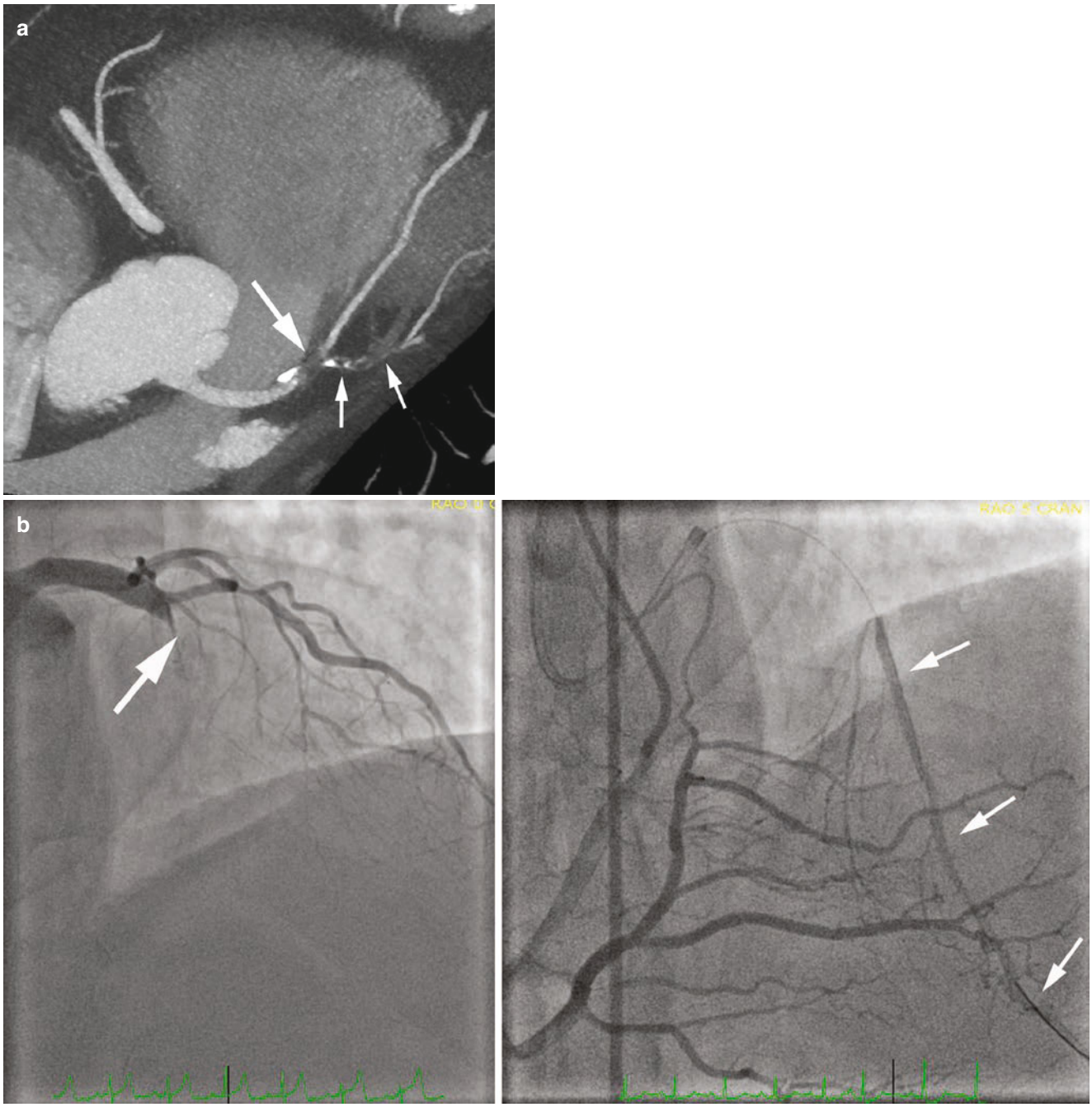

Fig. 5.27 Chronic total occlusion of the proximal left anterior descending coronary artery. Not all total coronary artery occlusions are long. (**a**) In this case, a short complete occlusion of the left anterior descending coronary artery is depicted in coronary CT angiography (*large arrow*), together with a longer occlusion of the first diagonal branch (*small arrows*). (**b**) Invasive coronary angiogram of the left anterior descending coronary artery with the *arrow* pointing at the occlusion (*left*) and angiogram of the right coronary artery with retrograde filling of the distal left anterior descending coronary artery (*right*). Note that coronary CT angiography cannot differentiate antegrade versus retrograde filling of the distal vessel segment in case of an occlusion. Even in case of retrograde filling via collaterals, contrast enhancement in the distal segment can be strong, as seen in this example. Also note that the occluded segment can be short and hence difficult to differentiate from a very high-grade stenosis

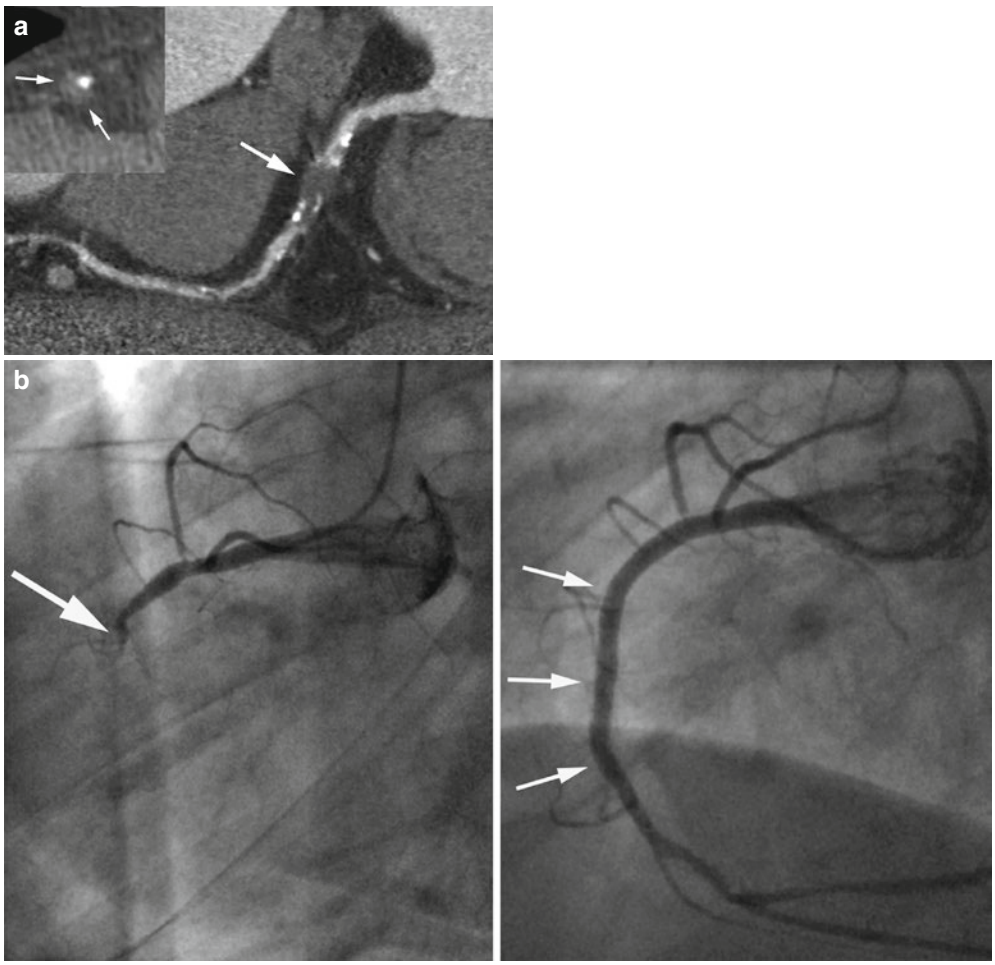

Fig. 5.28 Chronic total occlusion of the proximal right coronary artery with high likelihood of interventional revascularization success. (**a**) Coronary CT angiography shows a short total occlusion (*large arrow*) with "positive remodeling," an absence of severe calcification, a relatively straight course, and the absence of a "blunt stump." In cross-section (*inset*), noncalcified plaque material (*small arrows*) can be identified next to the relatively small calcification. All of these factors favor success of interventional recanalization. (**b**) Invasive coronary angiogram before (*left*) and after recanalization (*right*)

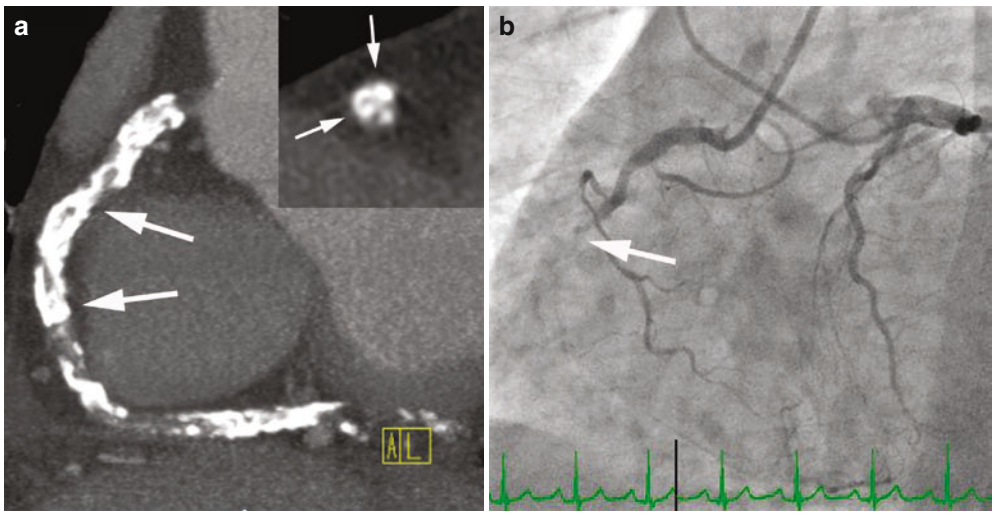

Fig. 5.29 Chronic total occlusion of the proximal right coronary artery with characteristics that indicate challenging conditions for interventional revascularization. (**a**) Coronary CT angiography shows a total occlusion of the right coronary artery with massive calcifications (*large arrows*) that, in cross-section, occupy the entire vessel area (*small arrows*). (**b**) Invasive angiography. Interventional recanalization was unsuccessful

Acute Coronary Syndromes

Coronary CT angiography is highly suited to rule in or rule out coronary artery disease in patients with acute chest pain, especially when the pretest likelihood for an acute coronary syndrome is low [5, 19]. Culprit lesions in acute coronary syndromes often have a typical appearance in coronary CT angiography. They frequently, but not always, display relatively small amounts of coronary calcification, low CT attenuation, and a pronounced extent of positive remodeling (Figs. 5.30, 5.31, 5.32 and 5.33).

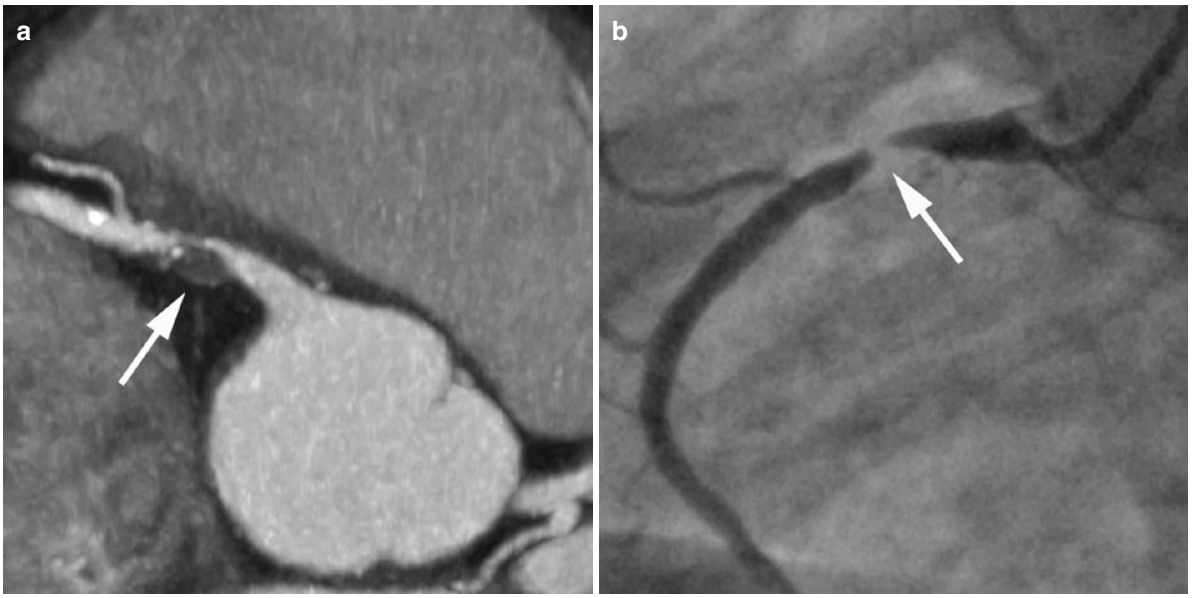

Fig. 5.30 Culprit lesion in the proximal right coronary artery in a patient with an acute coronary syndrome with troponin elevation (non–ST-elevation myocardial infarction, NSTEMI). (**a**) Maximum intensity projection of the proximal right coronary artery showing severe luminal stenosis caused by a plaque that is low in CT attenuation (*arrow*), has very little calcification, and displays substantial positive remodeling. (**b**) Corresponding invasive coronary angiography demonstrating a severe coronary artery stenosis

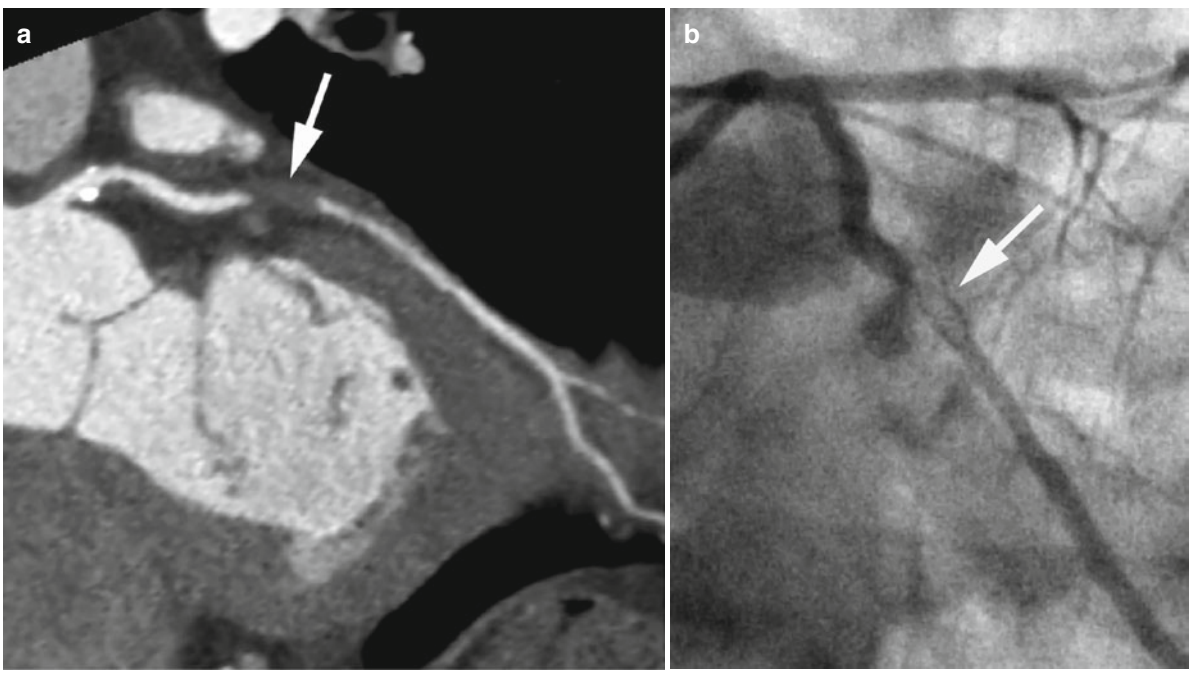

Fig. 5.31 Culprit lesion in the proximal left circumflex coronary artery in a patient with an acute coronary syndrome with troponin elevation (NSTEMI). (**a**) Curved multiplanar reconstruction of the left circumflex coronary artery in coronary CT angiography (64-slice CT). The contrast-enhanced lumen seems to be completely interrupted by a low-density, positively remodeled lesion (*arrow*). (**b**) The mass that is causing this luminal stenosis is most likely thrombus, as seen by the intraluminal filling defect in the corresponding invasive angiogram (*arrow*)

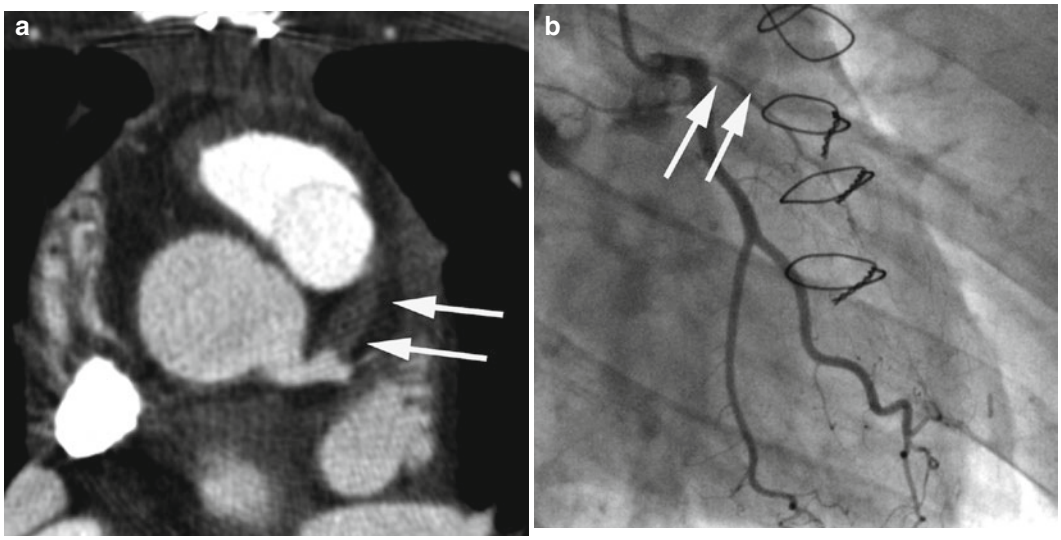

Fig. 5.32 Subacute ST-elevation myocardial infarction (STEMI). (**a**) Coronary CT angiography demonstrates complete occlusion of the ostial left anterior descending coronary artery by a low-density mass (thrombus), which leads to substantial enlargement of the coronary artery cross-section (*arrows*). This CT angiogram was acquired 48 h after symptom onset, which was originally ignored by the patient. (**b**) Invasive coronary angiography demonstrating occlusion of the left anterior descending coronary artery (*arrows*). The sternal wires are due to sternotomy several years previously to remove a mediastinal mass

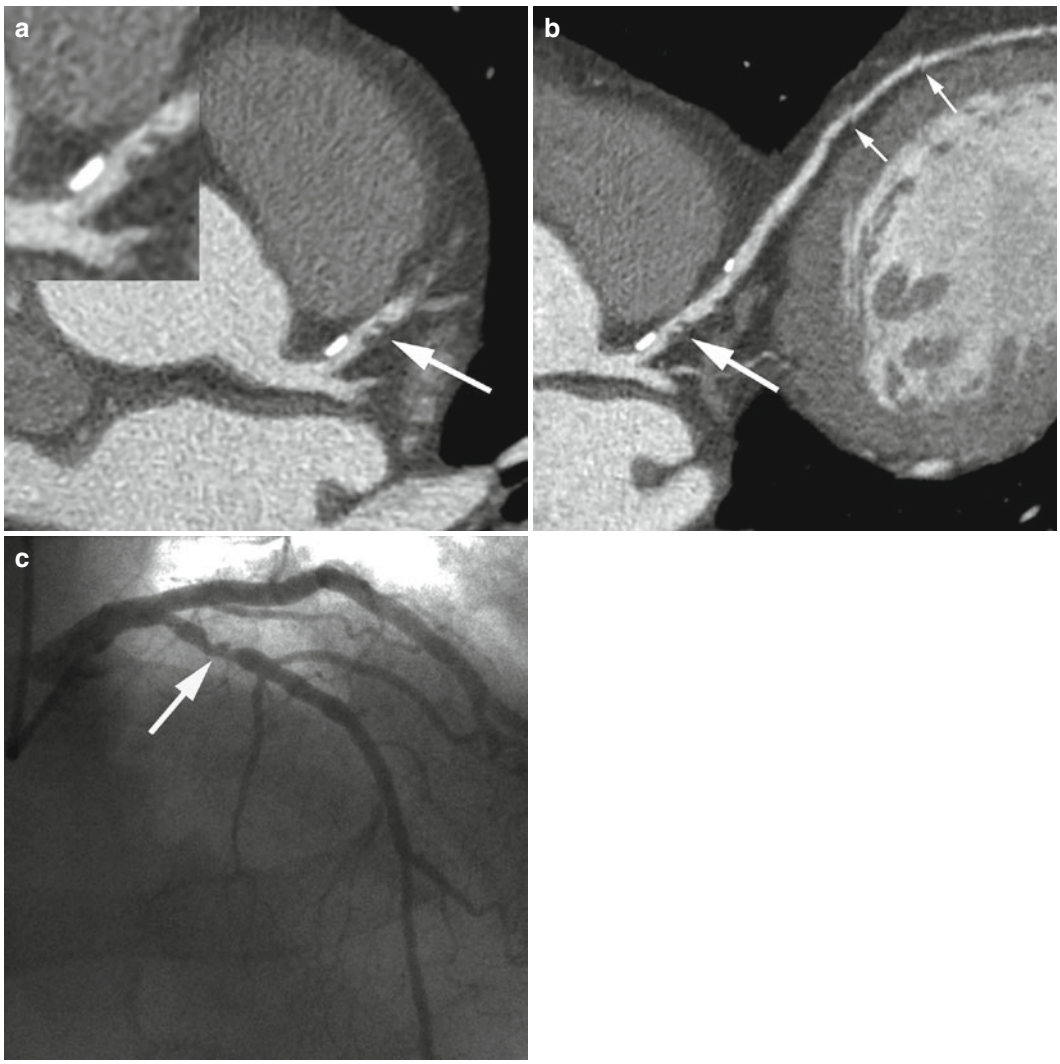

Fig. 5.33 Exulcerated coronary atherosclerotic plaque. (**a**) and (**b**) Coronary CT angiography (64-slice CT) of the proximal left anterior descending coronary artery. A non-calcified plaque with a contrast-enhanced cavity is visualized (*large arrows*). This corresponds to an old plaque rupture that left behind an ulcerated plaque. The *small arrows* indicate some misalignment artifacts in the mid and distal left anterior descending coronary artery. (**c**) Invasive coronary angiograms that confirm the ulcerated plaque, now causing a moderate coronary artery stenosis (*arrow*)

Transplant Vasculopathy

Transplanted hearts can be affected by transplant atherosclerosis or by transplant vasculopathy. Transplant vasculopathy frequently has a more concentric appearance than coronary atherosclerosis. It can be associated with substantial thickening of the vessel wall and diffuse coronary artery narrowing or occlusions (Fig. 5.34).

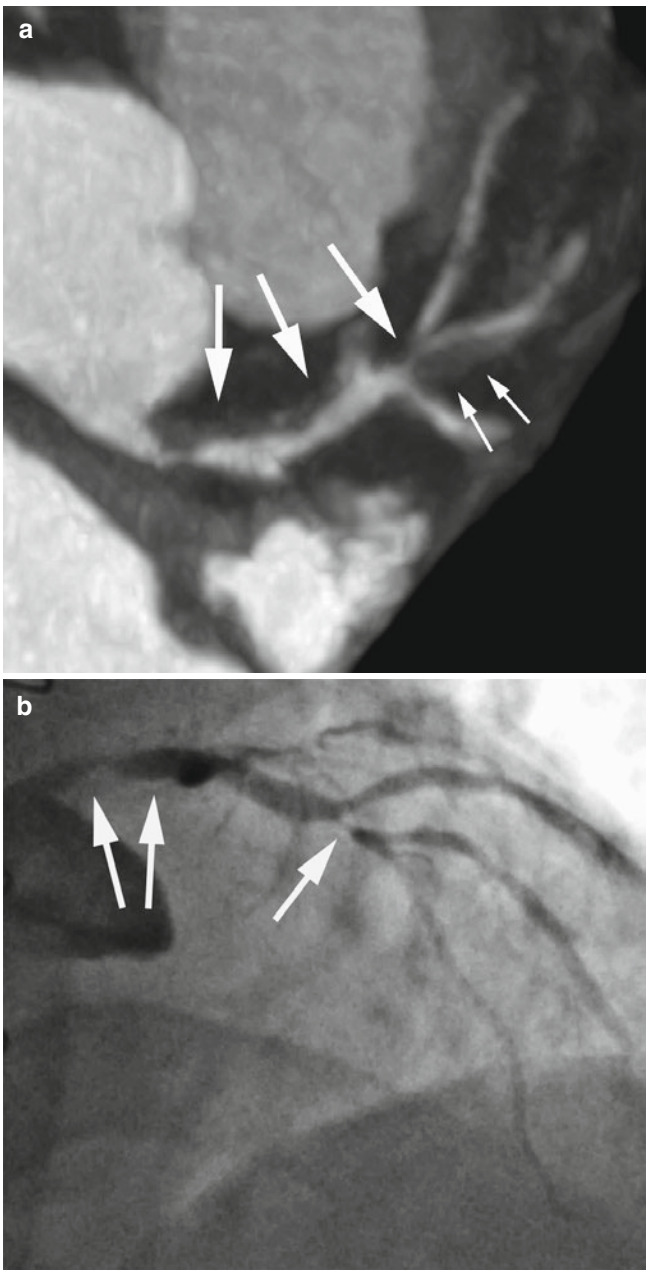

Fig. 5.34 Transplant vasculopathy with severe coronary artery stenoses. (**a**) Coronary CT angiography, maximum intensity projection, in a patient after heart transplantation. Severe stenoses of the left main and left anterior descending coronary artery are caused by noncalcified, pronounced, and diffuse thickening of the vessel wall (*arrows*). (**b**) Corresponding invasive coronary angiogram

Coronary Aneurysms and Ectasia

Coronary aneurysms can be caused by Kawasaki disease, by coronary atherosclerosis, or very infrequently by infection. Coronary rupture is unlikely, but aneurysms can be associated with stenoses and occlusions of the coronary arteries. If aneurysms are partially thrombosed, they may be undetectable on invasive coronary angiography (Figs. 5.35, 5.36, 5.37 and 5.38).

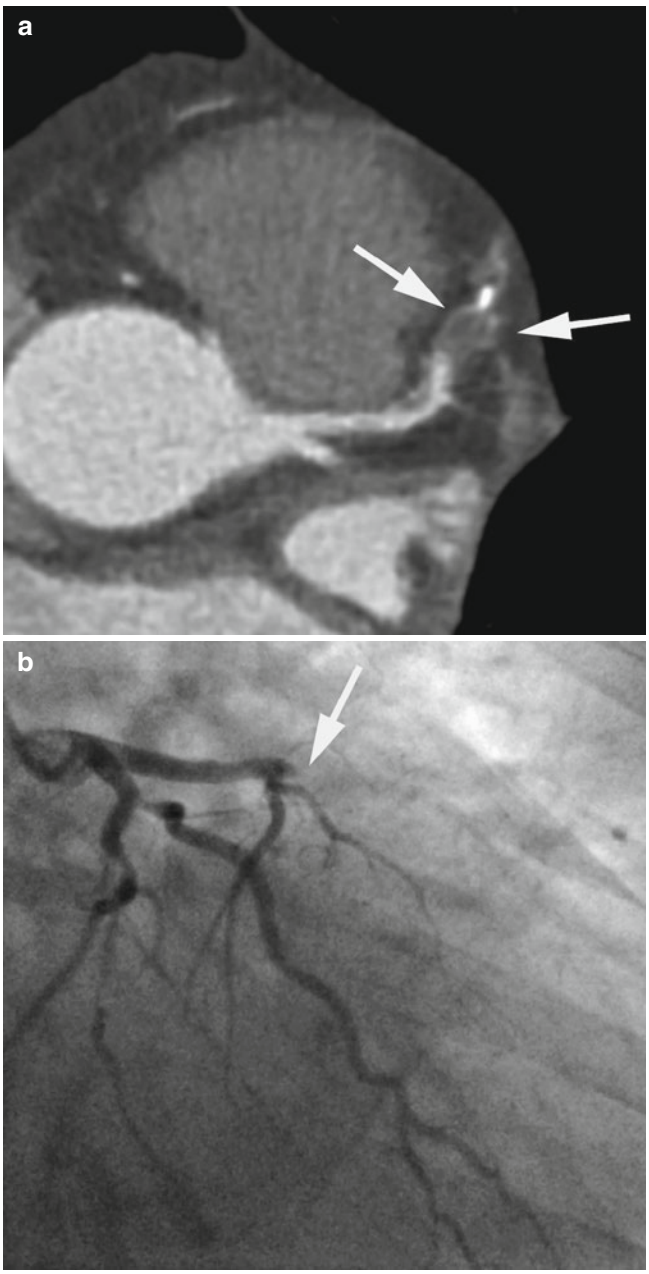

Fig. 5.35 Atherosclerotic coronary aneurysm. (**a**) Coronary CT angiography (64-slice CT) demonstrating a small, atherosclerotic coronary aneurysm (*arrows*) in the mid left anterior descending coronary artery, with complete occlusion of the artery. (**b**) Invasive coronary angiogram. The *arrow* indicates the site of the occlusion, but the aneurysm cannot be appreciated

Coronary ectasia is a more diffuse form of coronary artery dilatation, defined as widening of the coronary artery diameter to more than 1.5 times its usual diameter [20]). Coronary ectasia is usually caused by atherosclerosis, but it also may be due to inflammatory vascular disease, and it shows an association with sickle cell disease [21] (Figs. 5.39 and 5.40).

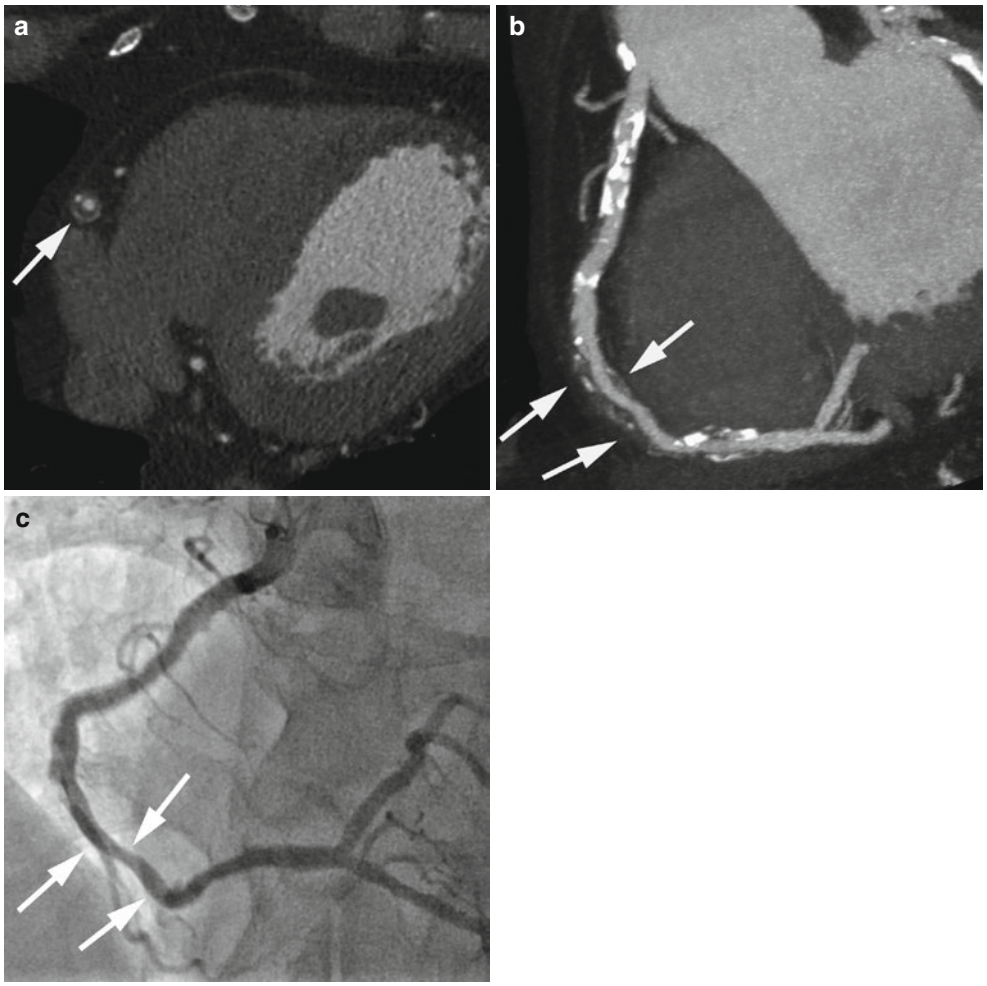

Fig. 5.36 Atherosclerotic coronary aneurysm in the mid right coronary artery. An atherosclerotic, calcified aneurysm of the mid right coronary artery (*arrows*) is shown in cross-section (**a**) and in a maximum intensity projection (**b**). Because the lumen of the aneurysm is partially thrombosed, it is not detectable in invasive angiography (**c**)

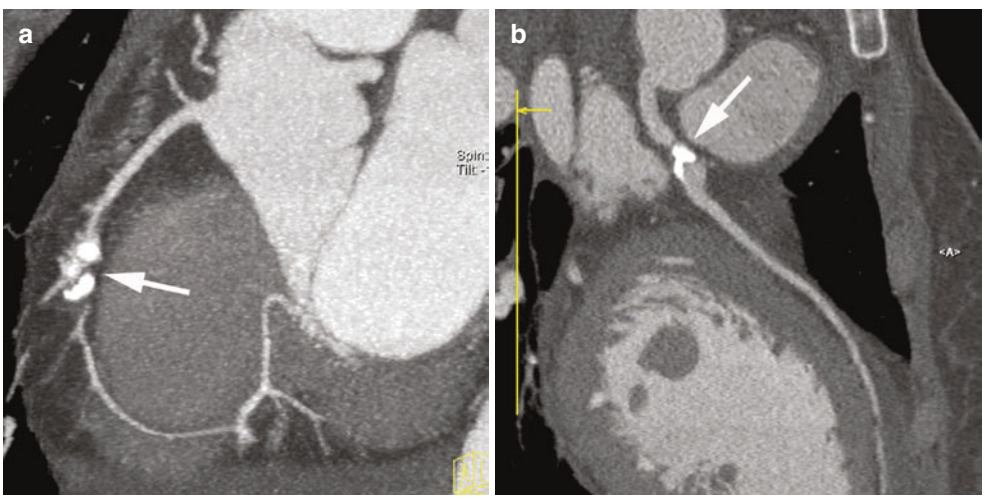

Fig. 5.37 Coronary aneurysms in Kawasaki disease. (**a**) Calcified coronary aneurysm (*arrow*) of the proximal-to-mid right coronary artery in a 22-years-old patient with Kawasaki disease (maximum intensity projection). The right coronary artery has a high-grade stenosis distal to the aneurysm. (**b**) Multiplanar reconstruction of the left main and left anterior descending coronary artery. A large aneurysm is present in the proximal left anterior descending coronary artery (*arrow*). The artery is occluded at the site of the aneurysm, which is hardly discernable in coronary CT angiography. (**c**) Invasive angiogram of the right coronary artery. (**d**) Invasive coronary angiogram of the left anterior descending coronary artery shows the site of the occlusion (*arrow*)

Fig. 5.37 (continued)

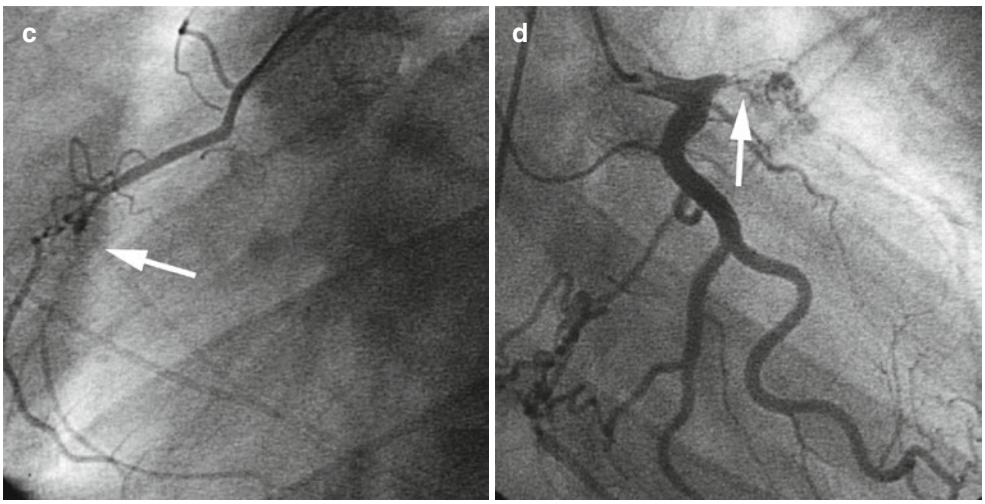

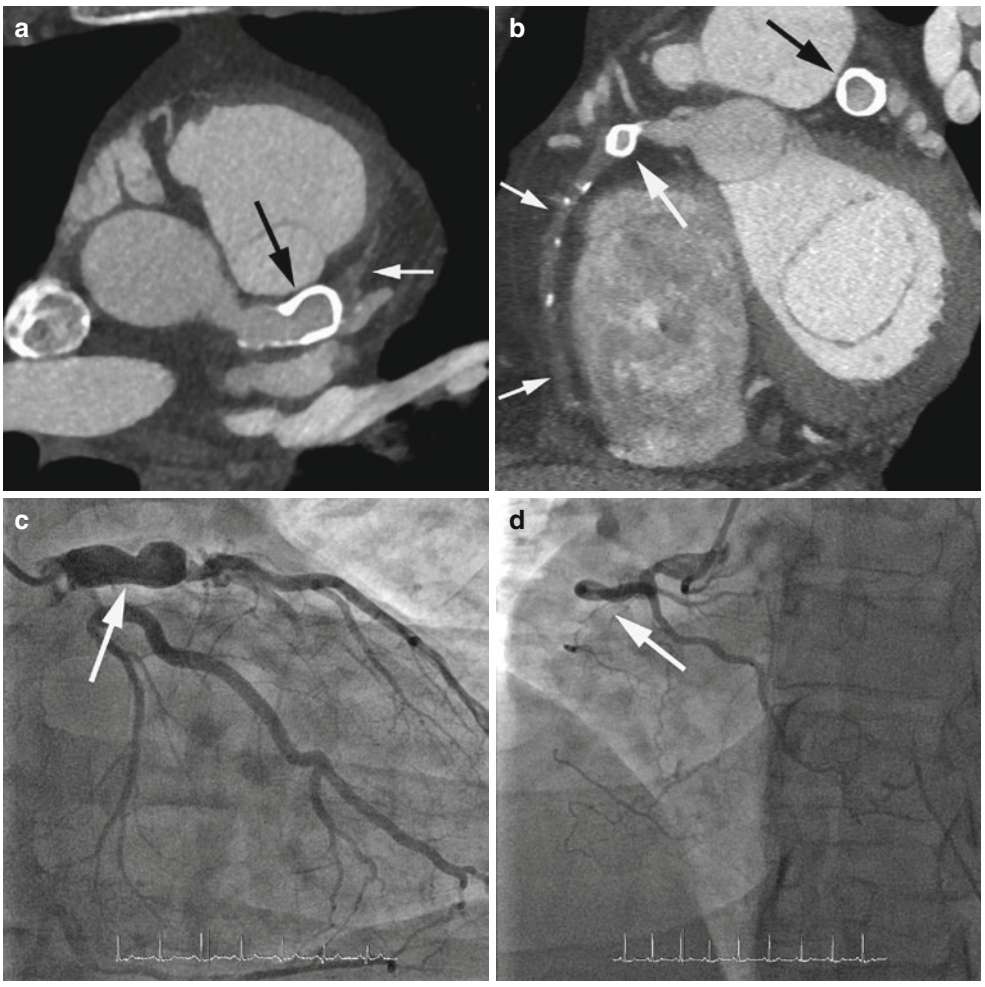

Fig. 5.38 Coronary aneurysms in Kawasaki disease. (**a**) Transaxial maximum intensity projection shows a calcified aneurysm of the proximal left anterior descending coronary artery (*large arrow*). The left anterior descending coronary artery is occluded distal to the aneurysm (*small arrow*). (**b**) Double-oblique maximum intensity projection of the right coronary artery. A proximal aneurysm (*large white arrow*) is followed by a complete, long occlusion of the artery (*small arrows*). The *black arrow* indicates the left anterior descending coronary artery aneurysm. (**c**) Invasive angiogram showing the aneurysm of the left anterior descending coronary artery (*arrow*). The open vessel distal to the aneurysm is a diagonal branch. The circumflex artery has a subtotal stenosis. (**d**) Occlusion of the right coronary artery (*arrow*)

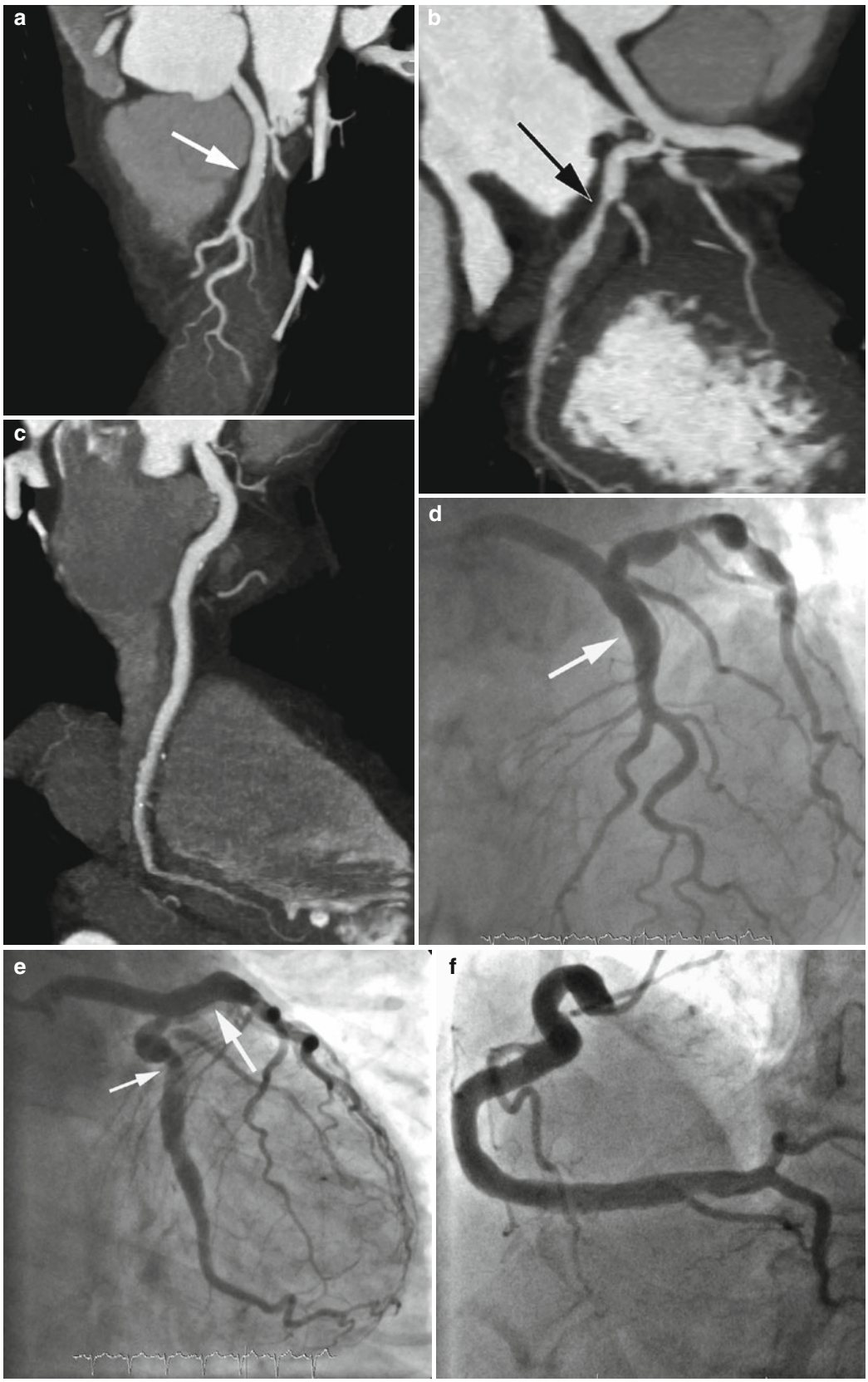

Fig. 5.39 Ectatic coronary arteries. (**a**–**c**) Curved multiplanar reconstructions of the left main/left anterior descending coronary artery (**a**), left circumflex coronary artery (**b**) and right coronary artery (**c**) in a patient with an ectatic form of coronary artery disease. Ectatic segments are found mainly in the proximal coronary arteries (*arrow* in **a**), and a moderate stenosis is present in the mid circumflex coronary artery (*arrow* in **b**). (**d**–**f**), Invasive coronary angiography of the left coronary artery (**d**, **e**) and of the right coronary artery (**f**)

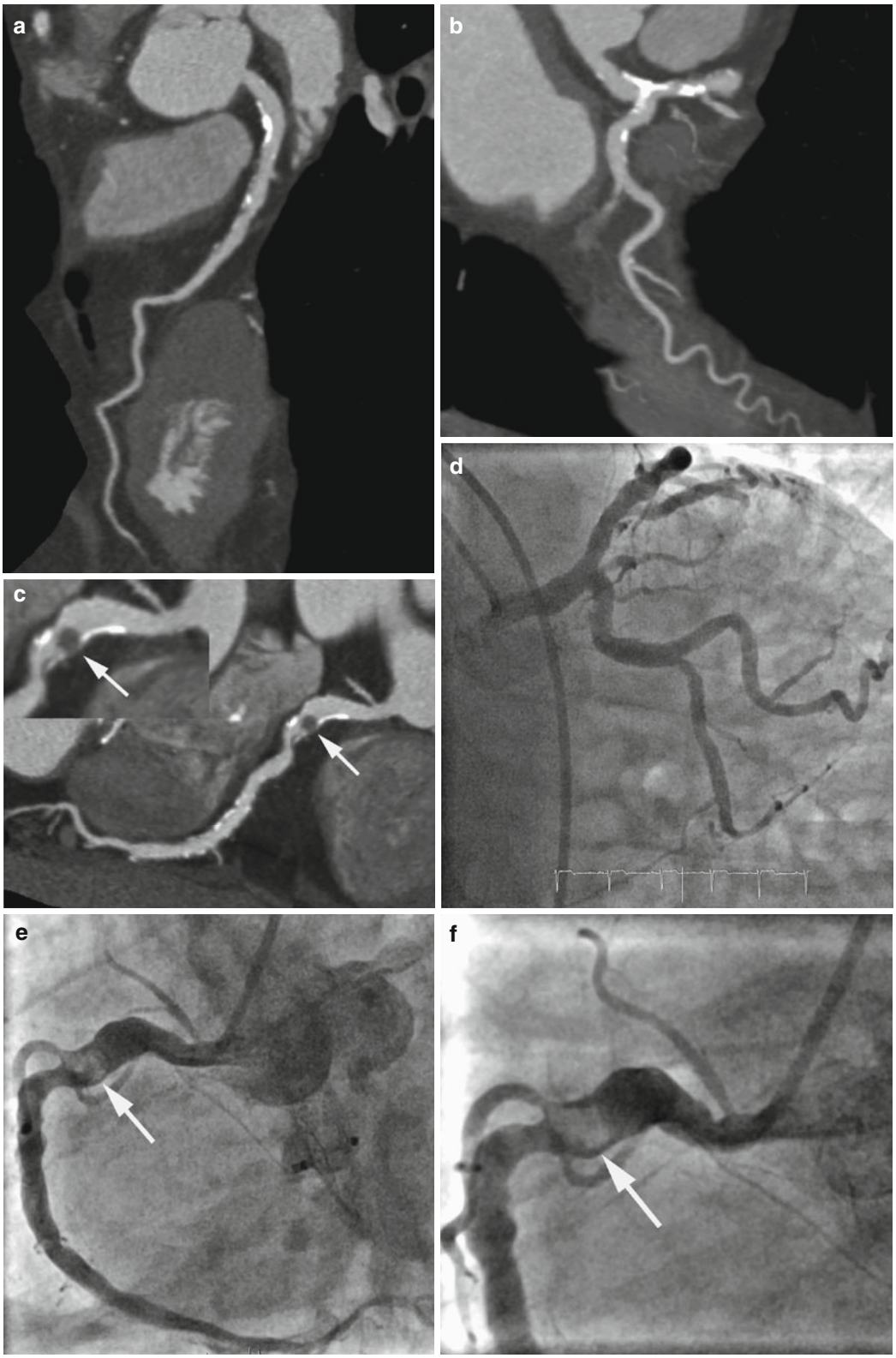

Fig. 5.40 Ectatic coronary arteries, with thrombus in the proximal right coronary artery. (**a**–**c**), Curved multiplanar reconstructions of the left main and left anterior descending coronary artery (**a**), left main and left circumflex coronary artery (**b**), and the right coronary artery (**c**) in a patient with an ectatic form of coronary artery disease. In the proximal right coronary artery, a thrombus is visible within the lumen (*arrows* in **c**). (**d**–**f**), Corresponding invasive coronary angiograms of the left coronary artery (**d**) and the right coronary artery (**e** and **f**), in which the thrombus (*arrows*) is visible

Coronary Artery Dissection and Intramural Hematoma

Coronary artery dissection can occur spontaneously or in the context of catheterization and intervention. Dissection membranes are thin and mobile and cannot be reliably detected in coronary CT angiography, but in cases of chronic dissection—which are very infrequent—dissection membranes can be thickened and less mobile, so they may be visualized by CTA (Fig. 5.41).

A more frequent condition than spontaneous dissection of a coronary artery is spontaneous intramural hematoma,

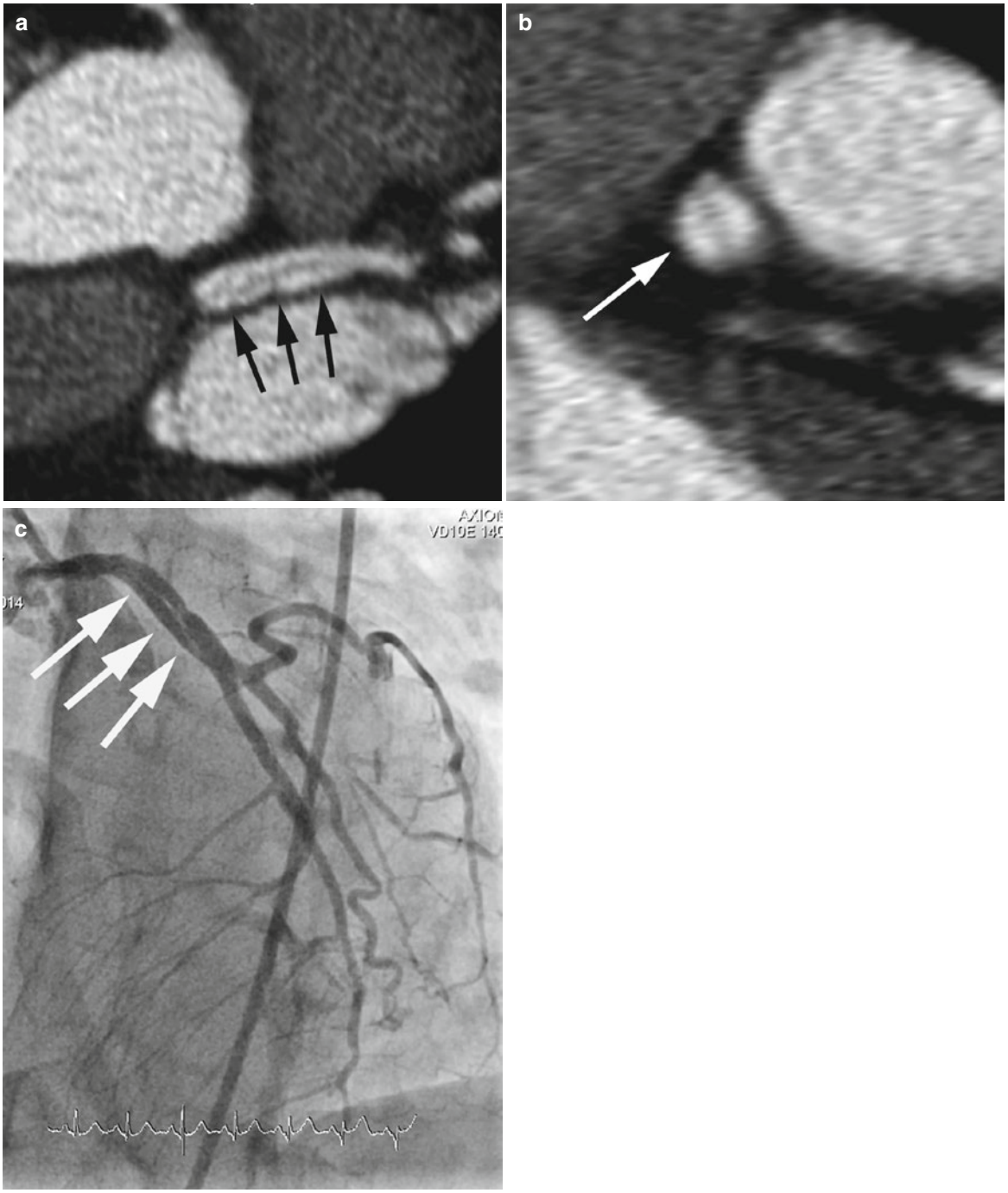

Fig. 5.41 Chronic dissection of the proximal left anterior descending coronary artery. (**a**) and (**b**), Coronary CT angiography in transaxial orientation showing a longitudinal view of the left anterior descending coronary artery (**a**) and a cross-sectional view of the left anterior descending coronary artery (**b**). The artery is dilated and a dissection membrane can be appreciated (*arrows*). (**c**) Invasive coronary angiogram showing chronic dissection appearing as a "double lumen" of the proximal left anterior descending coronary artery (*arrows*)

which becomes clinically symptomatic as an acute coronary syndrome. The resulting hematoma of the coronary arterial wall may in some cases be visualized by CT and displays a density similar to noncalcified plaque. Typically, relatively long segments of a coronary artery are affected (Fig. 5.42). However, particularly in more distal parts of the coronary artery tree, spontaneous intramural hematoma may be difficult to identify in coronary CTA and CT may hence not be able to rule out spontaneous intramural hematoma.

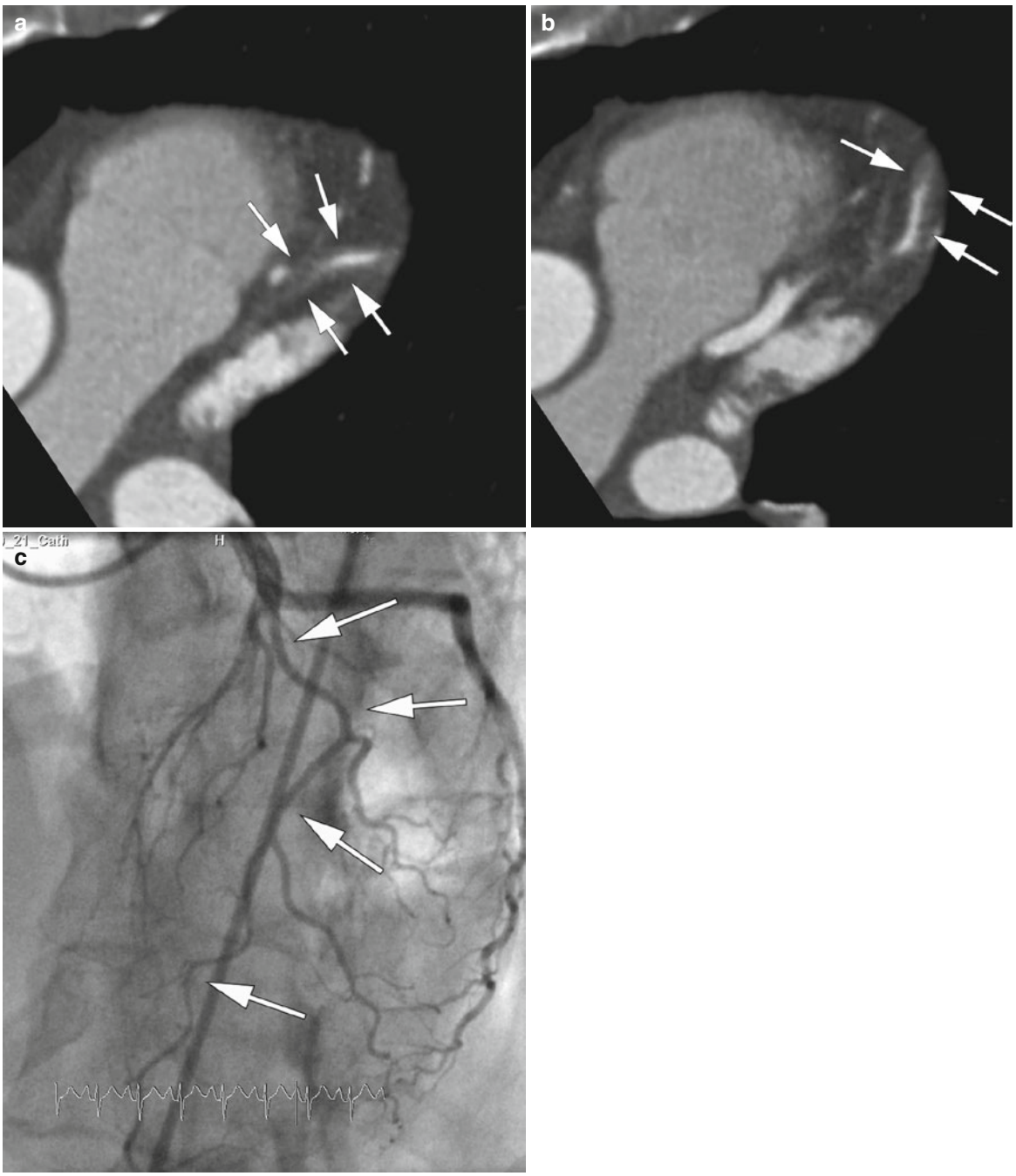

Fig. 5.42 Spontaneous intramural hematoma of the left anterior descending coronary artery. (**a**) and (**b**), Coronary CTA displays wall thickening of the left anterior descending coronary artery, which is more diffuse than typically seen in coronary atherosclerosis (*arrows*). (**c**) Invasive angiogram shows the diffuse narrowing of the left anterior descending coronary artery that is typical for spontaneous intramural hematoma (*arrows*)

Misinterpretation in Coronary CT Angiography

Image quality in coronary CT angiography is not always impeccable. Suboptimal image quality can lead to false-positive (and less frequently, false-negative) interpretations of coronary artery stenoses. The most frequent reasons for false-positive findings are small vessel diameters, high image noise, motion, or calcification, and especially a combination of the latter two. False-negative findings may be caused by high image noise and by small calcifications, which, because of partial volume effects, can have a CT attenuation rather similar to contrast-enhanced lumen and may therefore cause misinterpretation of stenoses, especially in small and tortuous vessel segments (Figs. 5.43, 5.44 and 5.45).

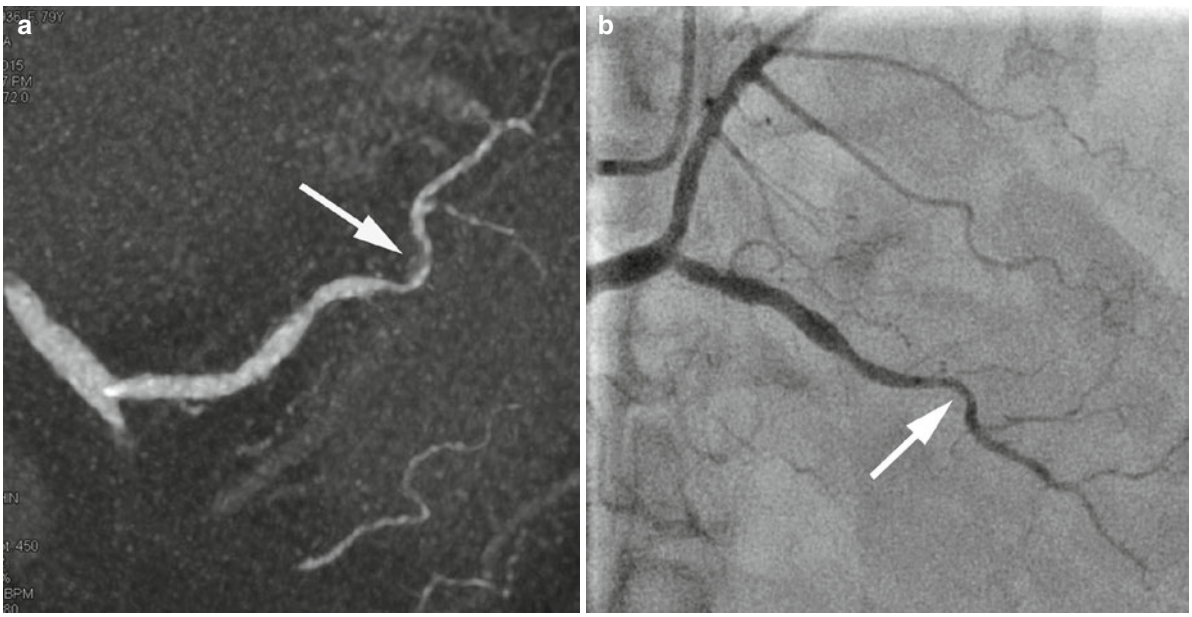

Fig. 5.43 False-positive finding in coronary CT angiography, small vessel. (**a**) Coronary CT angiography (maximum intensity projection) of the posterior descending coronary artery, a branch of the right coronary artery. A severe luminal stenosis seems to be present (*arrow*). (**b**) Invasive coronary angiography does not confirm the presence of a relevant luminal stenosis. Misinterpretation in CT is caused by image noise in combination with a small vessel diameter

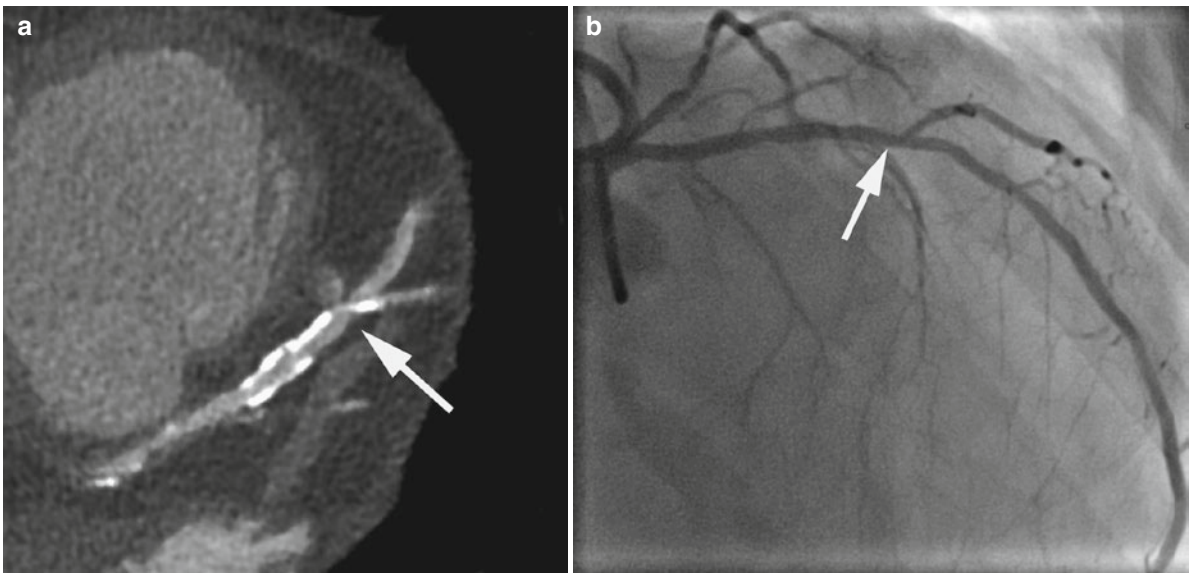

Fig. 5.44 False-positive finding in coronary CT angiography, related to calcification and motion blurring. (**a**)Coronary CT angiography (1-mm maximum intensity projection) of the left anterior descending coronary artery seems to show severe luminal stenosis at the site of a calcification just proximal to the first diagonal branch (*arrow*). (**b**) Invasive coronary angiography does not confirm the presence of a relevant luminal stenosis proximal to the diagonal branch (*arrow*). Misinterpretation in CT is caused by the combination of calcium with slight motion blurring (a frequent cause of false-positive interpretation)

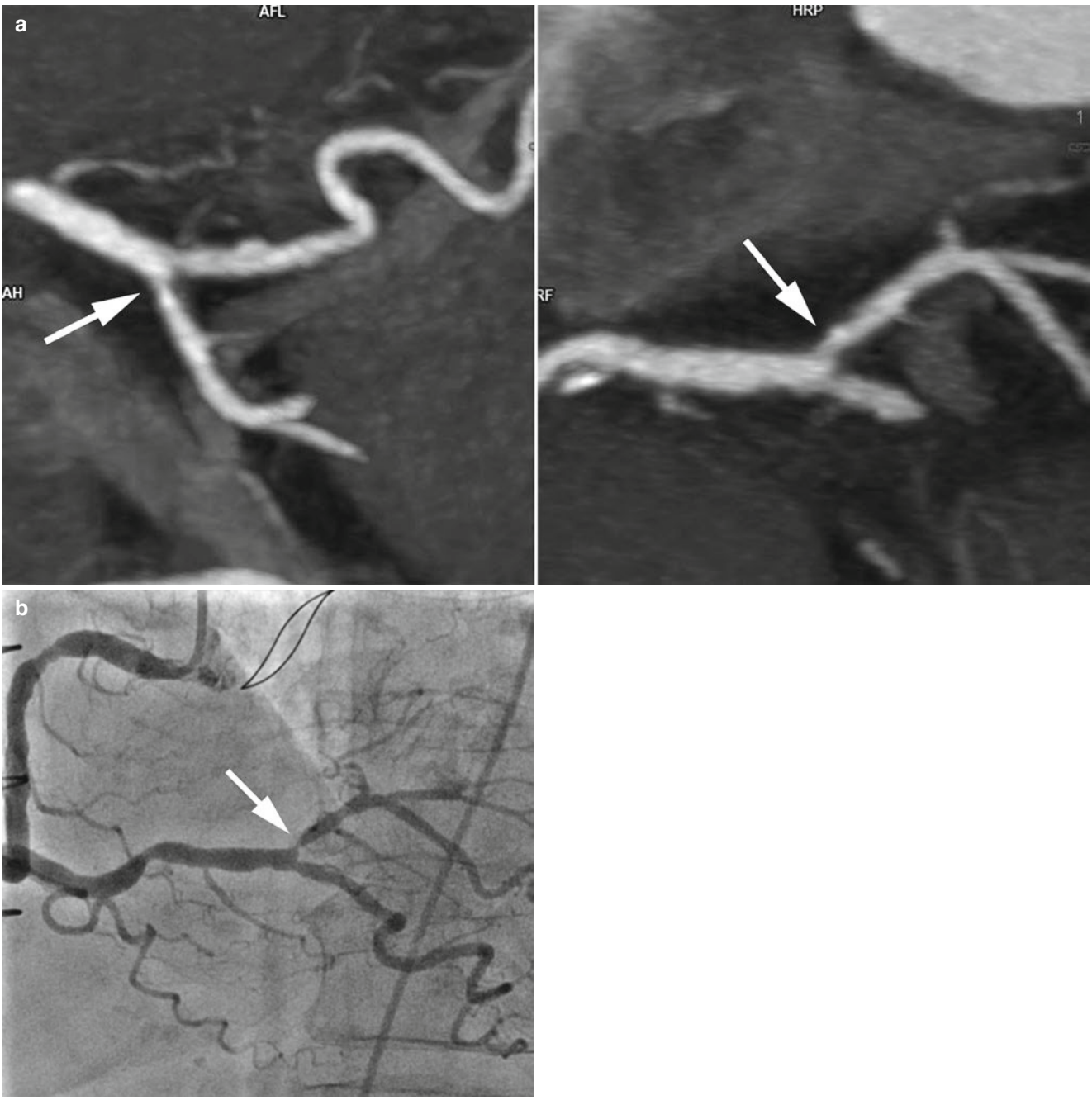

Fig. 5.45 False-negative finding in coronary CT angiography caused by calcification. (**a**) Coronary CT angiography (maximum intensity projection) of the distal right coronary artery, showing the bifurcation of the posterior descending and right posterolateral branch. At the ostium of the right posterolateral branch, no severe luminal stenosis seems to be present. However, the slightly increased attenuation suggests that a small calcification may mimic contrast-enhanced lumen (*arrows*). (**b**) Invasive coronary angiography shows a very severe stenosis of the ostium of the right posterolateral branch (*arrow*). In this case, misinterpretation in CT angiography was caused by partial volume effects that assign similar CT attenuation to small calcifications and to contrast-enhanced coronary artery lumen

References

1. Menke J, Kowalski J. Diagnostic accuracy and utility of coronary CT angiography with consideration of unevaluable results: a systematic review and multivariate Bayesian random-effects meta-analysis with intention to diagnose. Eur Radiol. 2016;26:451–8.
2. Fihn SD, Gardin JM, Abrams J, Berra K, Blankenship JC, Dallas AP, et al. 2012 ACCF/AHA/ACP/AATS/PCNA/SCAI/STS guideline for the diagnosis and management of patients with stable ischemic heart disease: a report of the American College of Cardiology Foundation/American Heart Association task force on practice guidelines, and the American College of Physicians, American Association for Thoracic Surgery, Preventive Cardiovascular Nurses Association, Society for Cardiovascular Angiography and Interventions, and Society of Thoracic Surgeons. Circulation. 2012;126:e354–471.
3. Montalescot G, Sechtem U, Achenbach S, Andreotti F, Arden C, Budaj A, et al. 2013 ESC guidelines on the management of stable coronary artery disease: the Task Force on the management of stable coronary artery disease of the European Society of Cardiology. Eur Heart J. 2013;34:2949–3003.
4. Windecker S, Kolh P, Alfonso F, Collet JP, Cremer J, Falk V, et al. 2014 ESC/EACTS guidelines on myocardial revascularization. Eur Heart J. 2014;35:2541–619.
5. Roffi M, Patrono C, Collet JP, Mueller C, Valgimigli M, Andreotti F, et al. 2015 ESC guidelines for the management of acute coronary syndromes in patients presenting without persistent ST-segment elevation: Task Force for the management of acute coronary syndromes in patients presenting without persistent ST-segment elevation of the European Society of Cardiology (ESC). Eur Heart J. 2016;37:267–315.
6. Al-Mallah MH, Aljizeeri A, Villines TC, Srichai MB, Alsaileek A. Cardiac computed tomography in current cardiology guidelines. J Cardiovasc Comput Tomogr. 2015;9:514–23.
7. Leipsic J, Abbara S, Achenbach S, Cury R, Earls JP, Mancini GJ, et al. SCCT guidelines for the interpretation and reporting of coronary CT angiography: a report of the Society of Cardiovascular Computed Tomography Guidelines Committee. J Cardiovasc Comput Tomogr. 2014;8:342–58.
8. Cury RC, Abbara S, Achenbach S, Agatston A, Berman DS, Budoff MJ, et al. CAD-RADS(TM) Coronary Artery Disease – Reporting and Data System. An expert consensus document of the Society of Cardiovascular Computed Tomography (SCCT), the American College of Radiology (ACR) and the North American Society for Cardiovascular Imaging (NASCI). Endorsed by the American College of Cardiology. J Cardiovasc Comput Tomogr. 2016;10:269–81.
9. Park HB, Heo R, ó Hartaigh B, Cho I, Gransar H, Nakazato R, et al. Atherosclerotic plaque characteristics by CT angiography identify coronary lesions that cause ischemia: a direct comparison to fractional flow reserve. JACC Cardiovasc Imaging. 2015;8:1–11.
10. Diaz-Zamudio M, Dey D, Schuhbaeck A, Nakazato R, Gransar H, Slomka PJ, et al. Automated quantitative plaque burden from coronary CT angiography noninvasively predicts hemodynamic significance by using fractional flow reserve in intermediate coronary lesions. Radiology. 2015;276:408–15.
11. Gaur S, Øvrehus KA, Dey D, Leipsic J, Bøtker HE, Jensen JM, et al. Coronary plaque quantification and fractional flow reserve by coronary computed tomography angiography identify ischaemia-causing lesions. Eur Heart J. 2016;37:1220–7.
12. Min JK, Taylor CA, Achenbach S, Koo BK, Leipsic J, Nørgaard BL, et al. Noninvasive fractional flow reserve derived from coronary CT angiography: clinical data and scientific principles. JACC Cardiovasc Imaging. 2015;8:1209–22.
13. Nørgaard BL, Leipsic J, Gaur S, Seneviratne S, Ko BS, Ito H, NXT Trial Study Group, et al. Diagnostic performance of noninvasive fractional flow reserve derived from coronary computed tomography angiography in suspected coronary artery disease: the NXT trial (Analysis of Coronary Blood Flow Using CT Angiography: Next Steps). J Am Coll Cardiol. 2014;63:1145–55.
14. Lassen JF, Holm NR, Banning A, Burzotta F, Lefèvre T, Chieffo A, et al. Percutaneous coronary intervention for coronary bifurcation disease: 11th consensus document from the European Bifurcation Club. EuroIntervention. 2016;12:38–46.
15. Sawaya FJ, Lefèvre T, Chevalier B, Garot P, Hovasse T, Morice MC, et al. Contemporary approach to coronary bifurcation lesion treatment. JACC Cardiovasc Interv. 2016;9:1861–78.
16. Medina A, Suarez de Lezo J, Pan M. A new classification of coronary bifurcation lesions. Rev Esp Cardiol. 2006;59:183–6.
17. von Erffa J, Ropers D, Pflederer T, Schmid M, Marwan M, Daniel WG, Achenbach S. Differentiation of total occlusion and high-grade stenosis in coronary CT angiography. Eur Radiol. 2008;18:2770–5.
18. Opolski MP, Achenbach S. CT angiography for revascularization of CTO: crossing the borders of diagnosis and treatment. JACC Cardiovasc Imaging. 2015;8:846–58.
19. Staniak HL, Bittencourt MS, Pickett C, Cahill M, Kassop D, Slim A, et al. Coronary CT angiography for acute chest pain in the emergency department. J Cardiovasc Comput Tomogr. 2014;8:359–67.
20. Swaye PS, Fisher LD, Litwin P, Vignola PA, Judkins MP, Kemp HG, et al. Aneurysmal coronary artery disease. Circulation. 1983;67:134–8.
21. Dahhan A. Coronary artery ectasia in atherosclerotic coronary artery disease, inflammatory disorders, and sickle cell disease. Cardiovasc Ther. 2015;33:79–88.

Imaging of High-Risk Atherosclerotic Plaques

6

Amir Ahmadi, Kenichi Sakakura, Kazuyuki Yahagi, Renu Virmani, and Jagat Narula

Introduction

Coronary heart disease causes approximately one of seven deaths in the United States. In 2013, more than 370,000 Americans died of coronary heart disease. Each year, 660,000 Americans have a new coronary event, defined as first myocardial infarction or coronary heart disease death; 300,000 Americans have a recurrent attack and 160,000 have silent myocardial infarctions each year [1].

The current strategy for the management of coronary artery disease is guided either by the presence of significant luminal narrowing detected by coronary angiography, or by hemodynamically significant lesion as defined by fractional flow reserve (FFR) during the state of hyperemia. However, it is believed that the majority of acute coronary syndromes arise from plaques with "high-risk" morphological features. Autopsy studies as well as studies with various invasive and noninvasive imaging modalities have demonstrated the high risk of events in the presence of such features [2–6]. Even more important, these studies have unanimously demonstrated excellent prognosis in absence of these features, independent of degree of luminal stenosis [4–7]. It is conceivable that the anatomical stenosis and morphological features may be correlated to hemodynamic consequences and may collectively allow development of strategies including or excluding the likelihood of adverse coronary events.

A. Ahmadi
Department of Cardiology, Icahn School of Medicine at Mount Sinai, New York, NY, USA
e-mail: ahmadi.amir@me.com

K. Sakakura • K. Yahagi • R. Virmani
CVPath Institute Inc., 19 Firstfield Road, Gaithersburg, MD 20878, USA
e-mail: ksakakura@cvpath.org; kyahagi@cvpath.org; rvirmani@cvpath.org

J. Narula (✉)
Mount Sinai Heart, Icahn School of Medicine at Mount Sinai, New York, NY, USA
e-mail: jagat.narula@mountsinai.org

M.J. Budoff et al. (eds.), *Atlas of Cardiovascular Computed Tomography*, https://doi.org/10.1007/978-1-4471-7357-1_6

Morphological Features of High-Risk Plaque

Plaque rupture is responsible for up to ~75% of acute MI and ~65% of sudden coronary death [8]. The rupture of the fibrous cap exposes a thrombogenic core to the luminal flowing blood and leads to acute thrombosis. Ruptured plaques have distinct pathologic characteristics. Histologic data show that high-risk plaques are generally voluminous with significant expansive remodeling, contain bulky necrotic cores with neovascularization and intraplaque hemorrhage, and are covered by attenuated and inflamed fibrous caps [9]. They often are not

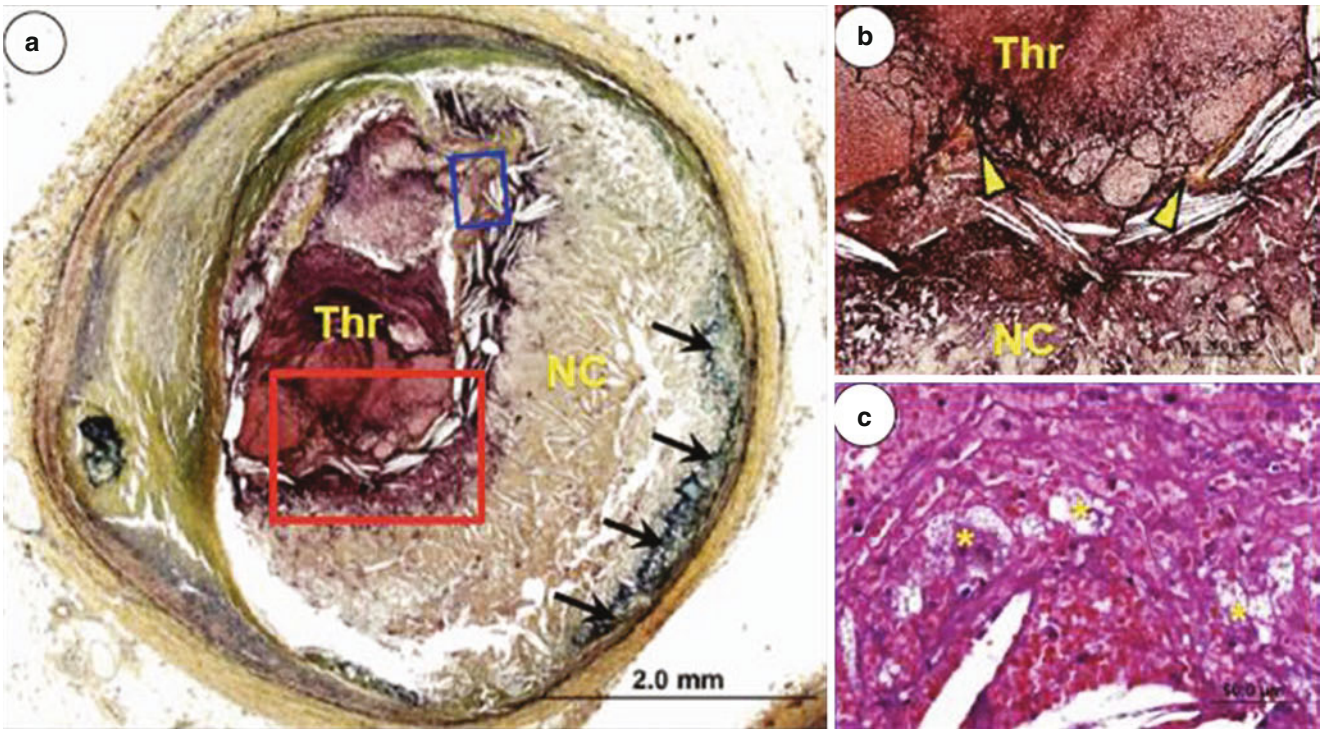

Fig. 6.1 Plaque Rupture. Cross-sectional photomicrograph of a coronary artery showing plaque rupture. (**a**) Note the presence of an acute occlusive luminal thrombus with an underlying large necrotic core (NC) and almost total absence of a fibrous cap. The medial wall is destroyed. There is presence of calcification near the base of the NC (*arrows*). (**b**) Higher-magnification image of the rupture site (*red box* in **a**). Thin fibrous cap is disrupted (*arrowheads*). (**c**) Higher-magnification of thrombus with cholesterol clefts, (*blue box* in **a**), red cells, and foamy macrophages (*asterisks*) (reproduced with permission from Falk et al. [8])

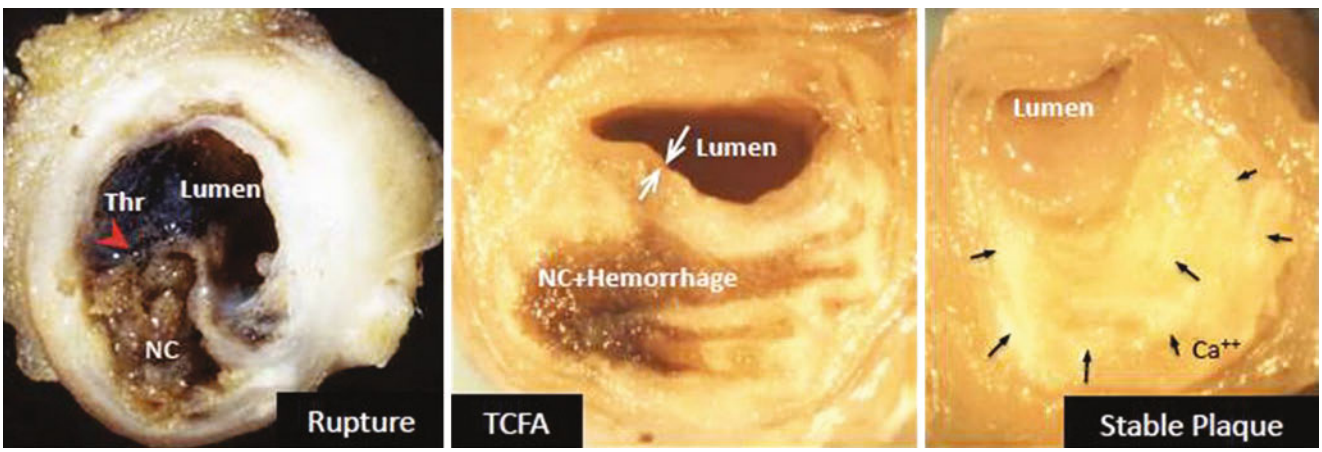

Fig. 6.2 Gross morphology of human coronary artery with ruptured plaque, Thin Cap Fibroatheroma (TCFA), and Fibroatheroma (FA) Plaques. (*Left*) Plaque rupture (PR) , showing disruption of fibrous cap at the shoulder region of the plaque (*red arrowhead*) and thrombus (Thr) superimposed. (*Middle*) An example of thin-cap fibroatheroma (TCFA). A large hemorrhagic necrotic core (NC) is observed within the plaque. *White arrows* are pointing to the thinnest portion of the fibrous cap. (*Right*) Stable plaque. The plaque mainly consists of fibrous tissue with calcification (*black arrows*). *FA* fibroatheroma (reproduced with permission from Narula et al. [3])

heavily calcified. Detection of various aspects of these morphological features are possible with various invasive and noninvasive imaging modalities. For example, it is feasible to detect outwardly remodeled vascular segments and identify low attenuation-plaque—surrogate for necrotic core—by multidetector computed tomography angiography (CTA) [7]. Intraplaque hemorrhage is best identified by MRI noninvasively [10]. Evaluation of the inflammatory component may be amenable to molecular imaging by positron emission tomography (PET) [11], and evaluation of the thickness of the cap needs invasive assessment with optical coherence tomography (OCT) [12]. Detection of such features, especially noninvasively by coronary CTA, may prove to be an important step in devising treatment strategy in the near future (Figs. 6.1, 6.2, 6.3, 6.4, and 6.5).

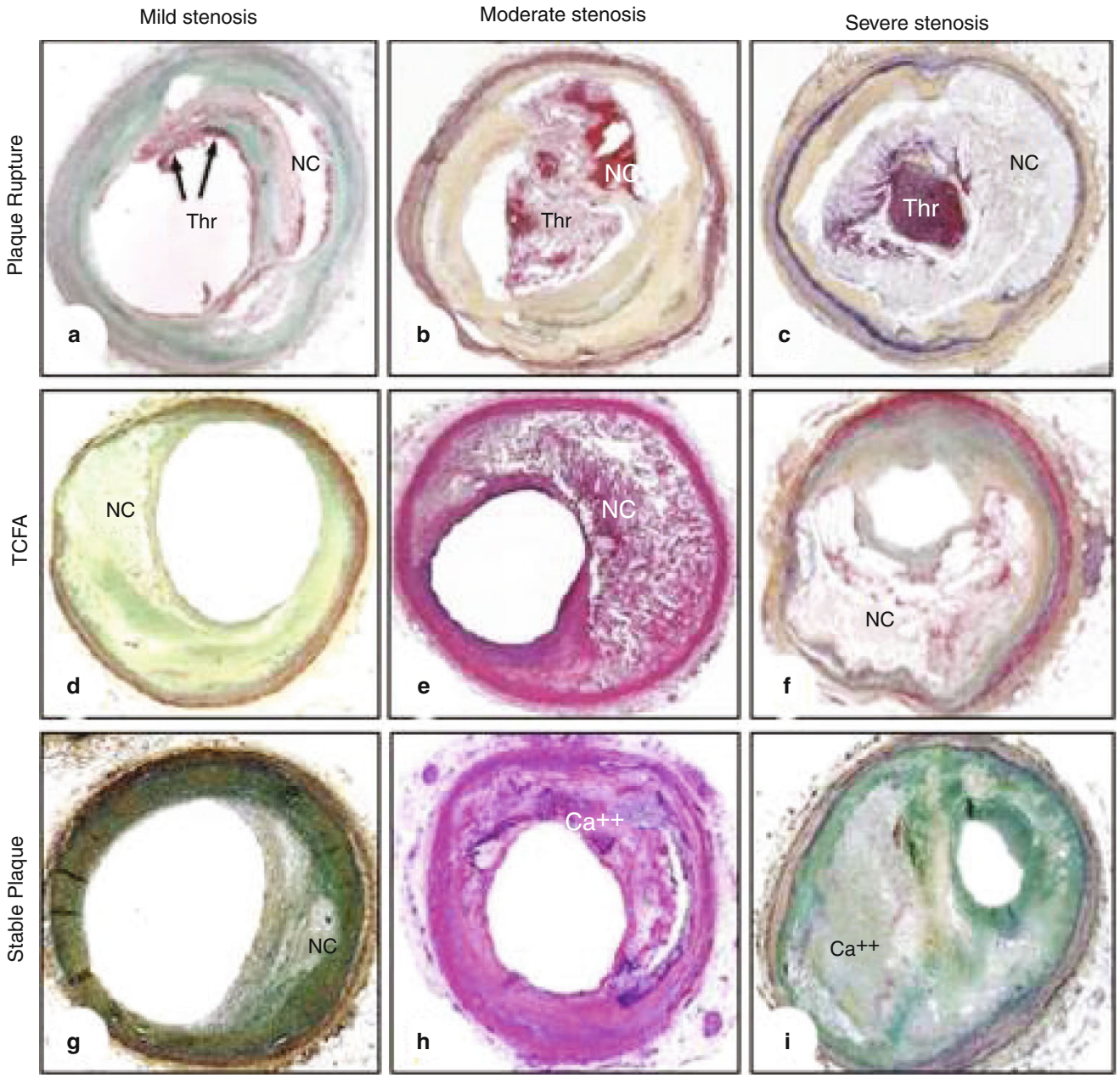

Fig. 6.3 Photomicrographic cross-section of human coronary plaque rupture, TCFA, and fibroatheroma with varying degree of luminal stenosis. (**a**–**c**) Plaque rupture with mild, moderate, and severe luminal stenosis, respectively. Non-occlusive Thr is observed in the microphotograph (**a**) whereas occlusive Thr is occupying the lumen in images (**b**, **c**). (**d**–**f**) TCFA with mild, moderate, and severe luminal stenosis, respectively. NC is covered by a thin fibrous cap, and Thr is not present in the lumen. (**g**–**i**) Stable plaque or FA with mild, moderate, and severe luminal stenosis, respectively. The size of necrotic core is relatively small when present, and calcification (Ca^{++}) is frequently seen (reproduced with permission from Narula et al. [3])

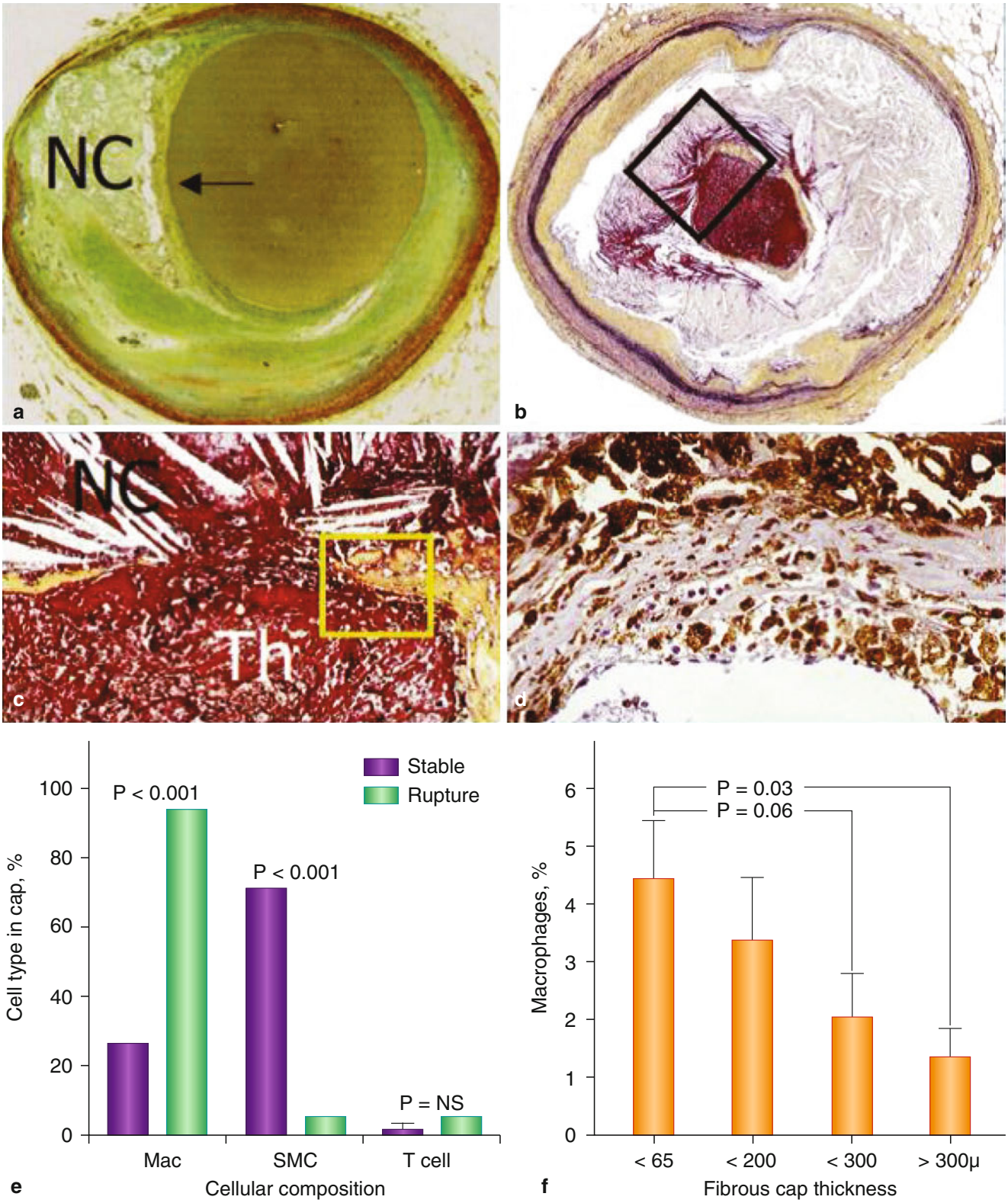

Fig. 6.4 The thin fibrous cap. Fibrous caps are significantly attenuated in the thin cap fibroatheromas (**a**; *arrow*) and are disrupted at the weakest site in an acute coronary event (**b**; *black square*). Based on a large set of disrupted plaques postmortem, it was proposed that a fibrous cap thickness of less than 65 μm predicts vulnerability to plaque rupture. These thin fibrous caps are markedly inflamed with monocyte-macrophage infiltration. The area enclosed by the *black square* in (**b**) is magnified in (**c**). Area enclosed by the *yellow square* in (**c**) is stained for macrophages in (**d**). The disrupted site is significantly attenuated and inflamed. Analysis of fibrous caps demonstrates that macrophages are the most dominant cellular population in ruptured and vulnerable plaques, whereas smooth cells are dominant in stable atherosclerotic lesions (**e**). A higher number of macrophages is associated with thinner fibrous caps (**f**) (adapted from Kolodgie et al. [14])

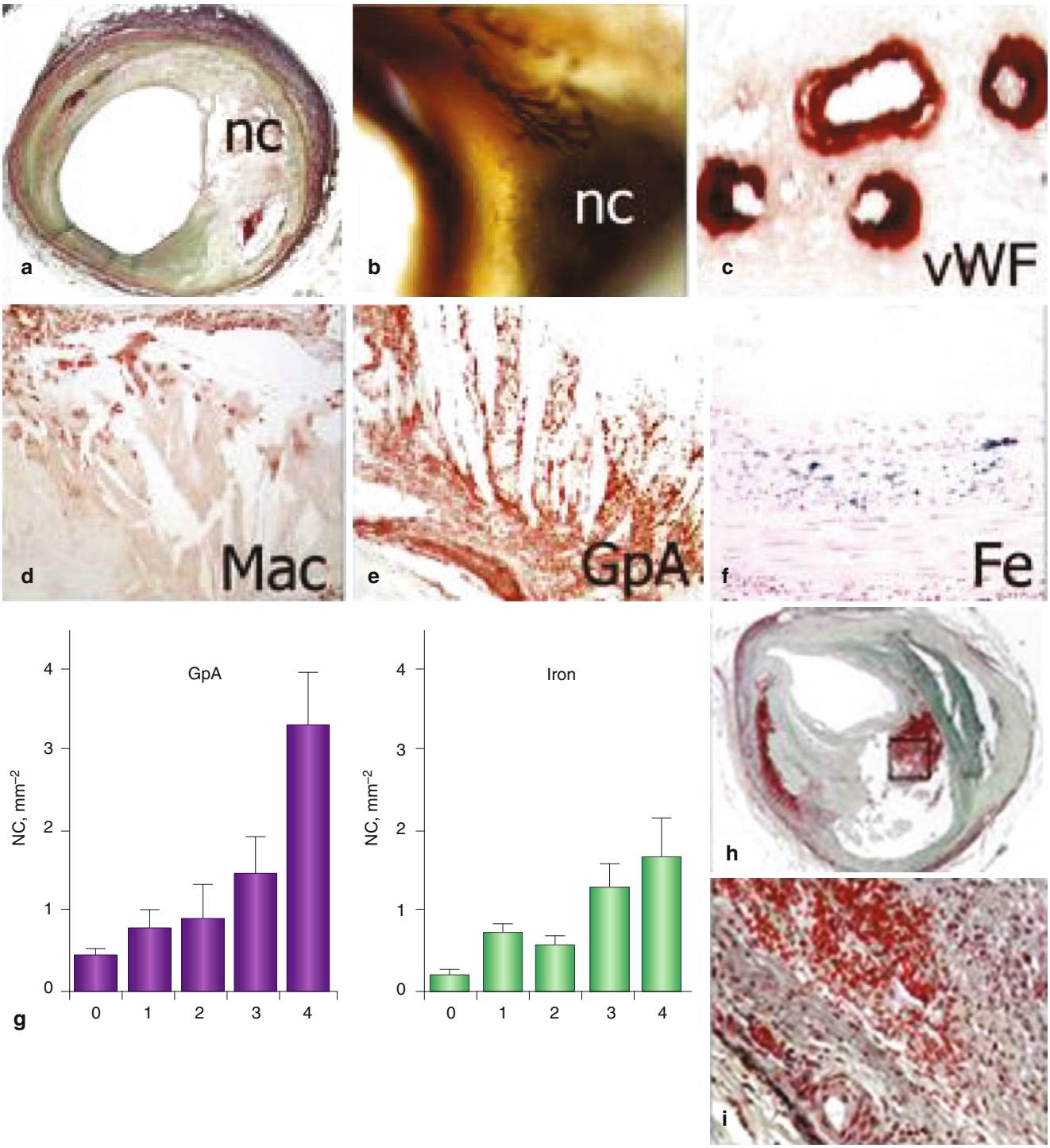

Fig. 6.5 Mechanism contributing to rapid plaque progression in lesions with high risk features. (**a**–**l**) During the evolution of vulnerable atherosclerotic plaque (**a**), the ongoing death of lipid-laden macrophages contributes to the formation of the necrotic core. Worsening hypoxia in the enlarging plaque appears to perpetuate the tendency toward macrophage death, enlarge the necrotic core, and promote neointimal neovascularization (**b**) [14, 15]. These nascent vessels are inherently leaky (**c**; exemplified by extravascular vWF staining), and appear to allow extravasation of red blood cells (RBC) into the plaque. It is well appreciated that the cholesterol content of erythrocyte membranes exceeds that of most cells in the body (with lipid constituting 40% of the weight), and this likely contributes to the free cholesterol pool of the growing necrotic core. Intraplaque hemorrhage (**h**, **i**) due to the rupture of these immature vessels further contributes to the accumulation of a large number of RBC and cholesterol. The extent of iron deposits in the plaque and that of glycophorin A staining (a protein exclusively associated with RBC membrane) is directly proportional to the size of the necrotic core (**e**–**g**), and the macrophage density (**d**). All these mechanisms contribute to expansion of the necrotic core and might be the underlying reasons for rapid plaque progression prior to MI (see Fig. 32) (adapted from Kolodgie et al. [14])

Role of CTA in Detection of High-Risk Plaque Features

CTA should be considered an excellent tool for detecting geometric characteristics typical of plaque instability, and for determining plaque composition, especially low attenuation plaque (LAP) volume. Even without an ability to detect the degree of vascular inflammation, measures of plaque geometry combined with estimates of composition may accurately predict plaque instability, because plaque macrophage count is closely related to the extent of positive remodeling. It has been shown that CTA defined high-

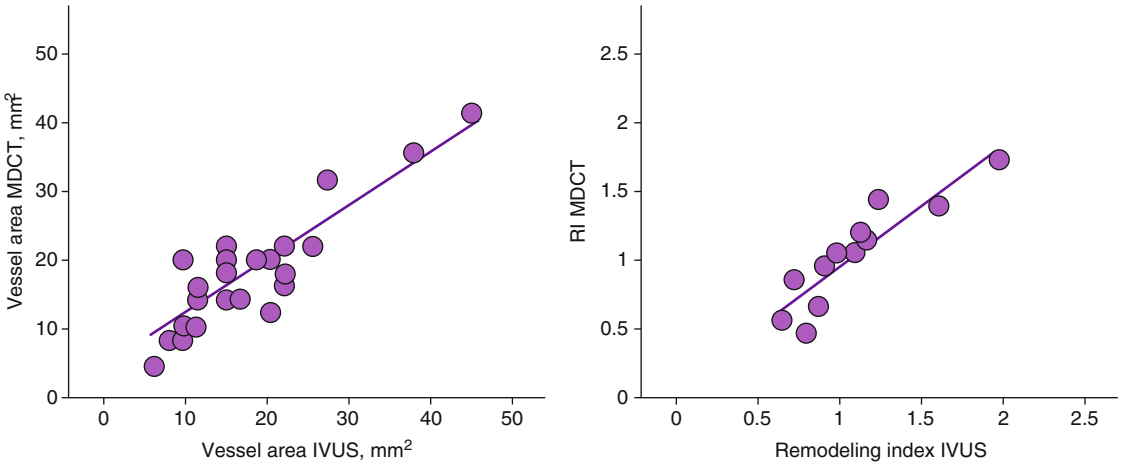

Fig. 6.6 Comparison of coronary CTA and Intravascular Ultrasound. The current invasive gold standard for plaque quantification is intravascular ultrasound (IVUS). Multiple studies have demonstrated moderately good correlation of IVUS-based measurements with plaque area by planimetry of CT visualized plaque and remodeling index [16]. The plaque area and the degree of coronary remodeling have been determined on cross-sectional images similar to IVUS. Plaque area has been defined by manual tracing as the difference between the area including plaque and vessel lumen (equals the external elastic membrane area in IVUS) and the area of the vessel lumen at the site of maximal luminal narrowing. The remodeling index has been defined as the ratio between plaque plus vessel lumen area at the site of maximal luminal narrowing and the proximal non-diseased reference site. In a study of 13 patients in whom 16-slice CT (0.75-mm collimation, 420-ms rotation) was performed before invasive coronary angiography and IVUS, remodeling index was calculated in the presence of greater than 50% diameter stenosis in invasive angiography [16]. Cross-sectional vessel areas and remodeling index measured by multidetector CT correlated closely to IVUS ($r = 0.77$ and $r = 0.82$, respectively) (adapted from Achenbach et al. [16])

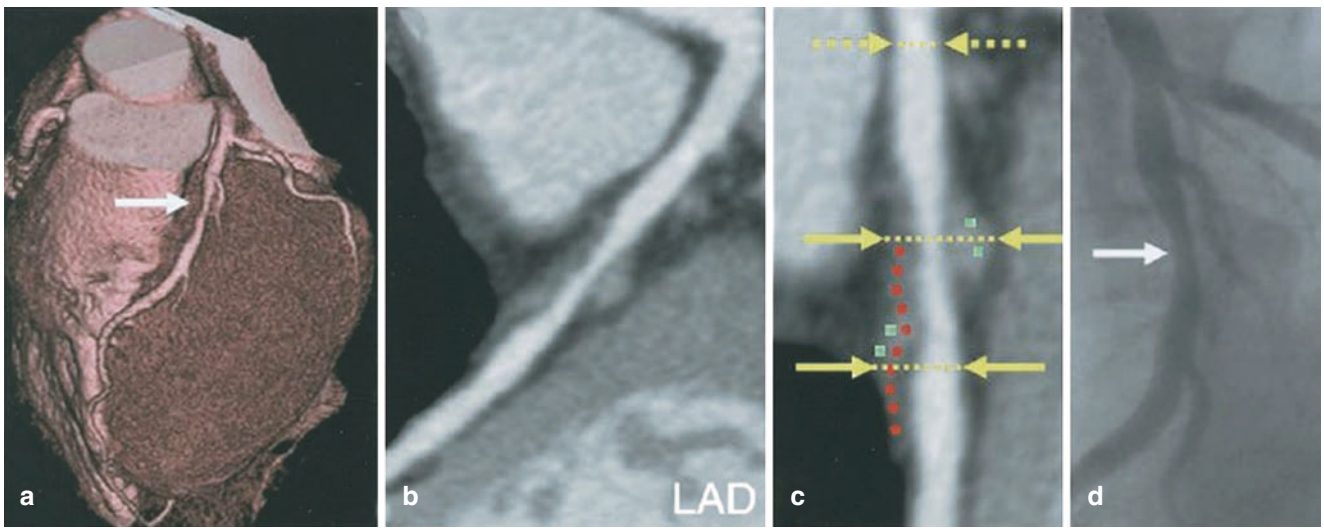

Fig. 6.7 High-risk plaque features on CT (1) (Positive remodeling, low-attenuation plaque). As mentioned earlier, two of the well-recognized high-risk plaque features that are readily detectable by cardiac CTA are positive remodeling and low-attenuation plaque (LAP). This figure demonstrates the CT of a culprit lesion in a 40-year-old male patient who later presented with an acute coronary syndrome. (**a**) Volume rendering. (**b**) Curved MPR. (**c**) Magnified view of the region of interest from (**b**). (**d**) Coronary angiogram. The white arrows in (**a**, **d**) show the site of luminal obstruction or culprit lesion. As shown by the *solid yellow arrows* at two sites in the culprit lesion in (**c**), the lesion is positively remodeled as compared with the normal coronary segment proximal to the lesion (denoted by *interrupted arrows*). Remodeling index in this patient was 1.43. An NCP 30 HU represents low-attenuation plaque (*red circles* are placed along the course of low-attenuation), and the 150 HU denotes a fibrous plaque (*green squares*). *LAD* left anterior descending artery, *MPR* multiplanar reformation, *HU* Hounsfield unit (adapted from Motoyama et al. [7])

risk plaques (low-attenuation plaques with positive remodeling) and are predictors of acute coronary syndromes [5]. For primary prevention, many cardiologists would consider the presence of plaque on CTA as a sign of atherosclerosis and an indication for aggressive risk factor control with the use of systemic anti-atherosclerotic therapy such as statin (Figs. 6.6, 6.7, 6.8, 6.9, 6.10, 6.11, 6.12, 6.13, and 6.14) [18].

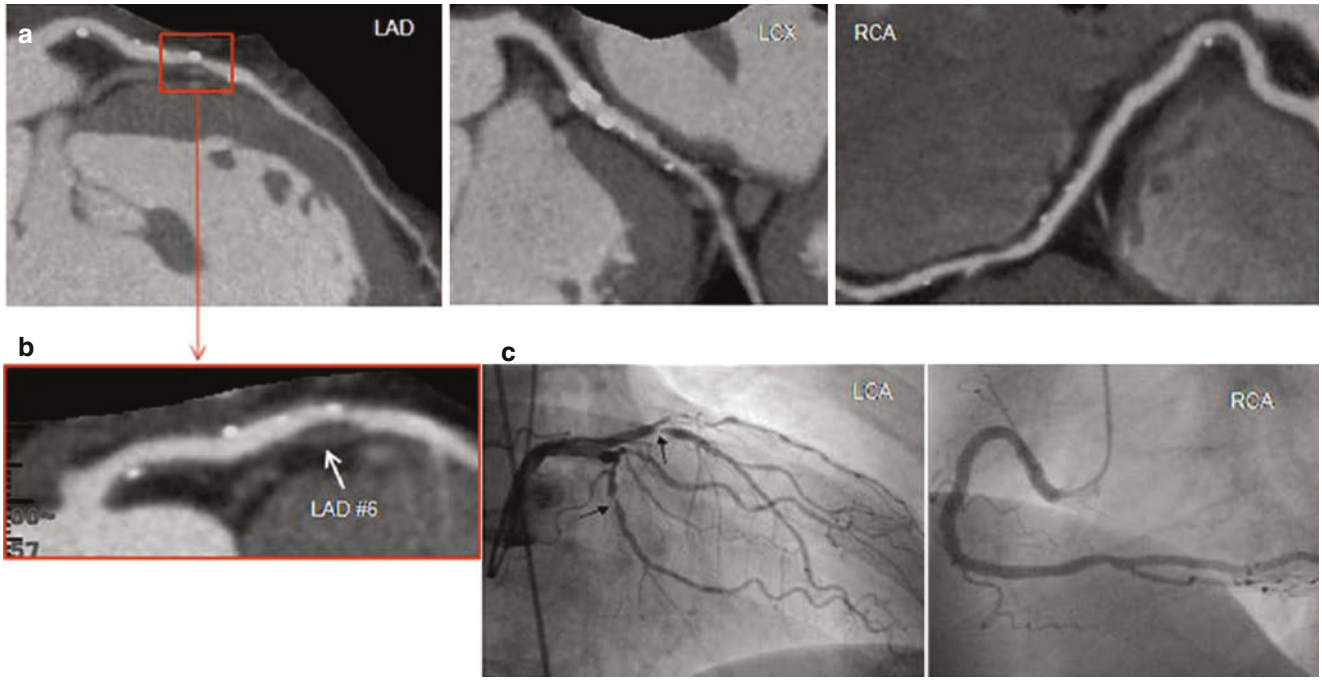

Fig. 6.8 High-risk plaque features on CT (2) (positive remodeling, low attenuation plaque, spotty calcification). In this figure, in addition to positive remodeling and LAP, presence of spotty calcification has been demonstrated. (**a**) Curved multiplanar reformation images of left anterior descending artery (LAD), left circumflex artery (LCX), and right coronary artery (RCA). (**b**) Positive remodeling, low-attenuation plaque, and spotty calcification were detected in LAD #6 on coronary computed tomography (CT) angiography. (**c**) Acute coronary syndrome (ACS) occurred 6 months after CT angiography. LAD #6 was determined as the culprit lesion based on invasive coronary angiogram findings. Please note the location of the lesion proximal to the first septal branch, both in CT angiography before the event and coronary angiogram after the event when the patient was brought to the catheterization laboratory for percutaneous coronary intervention. LCA left coronary artery (adapted from Motoyama et al. [4])

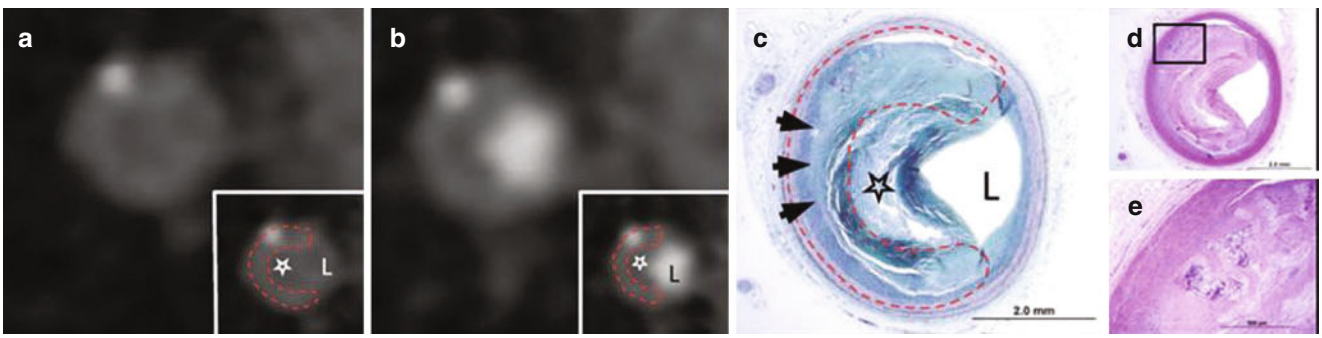

Fig. 6.9 High-risk plaque features on CT (3) (napkin-ring sign). The cross-sectional CT images show a coronary plaque with napkin-ring–like attenuation pattern and spotty calcification. The circumferential outer rim (*red dashed line*) of the noncalcified plaque has a higher CT attenuation in both the non-contrast (**a**) and contrast-enhanced (**b**) images (44.0 ± 8.8 HU, range 23.0–61.0 HU vs. 48.6 ± 5.8 HU, range 34.0–60.5 HU, respectively) as compared to the attenuation within the central part of the plaque (27.9 ± 4.2 HU, range 20.7–36.4 HU and 31.0 ± 6.6 HU, range 19.0–44.0 HU on non-contrast and contrast-enhanced images, respectively). The average noncalcified plaque attenuation on non-enhanced CT was 42.2 ± 9.9 HU versus 43.7 ± 10.0 HU on the contrast-enhanced image. The corresponding histological section (panels **c**–**e**) revealed a late fibroatheroma, with spotty calcification (**e**). The lesion is characterized by a necrotic core (*star*), which is consistent with the low-attenuation core of the plaque and a significant amount of fibrous plaque tissue, which is consistent with the high-attenuation rim on the CT images (*red dashed line*). The *arrowheads* indicate the vasa vasorum. *HU* Hounsfield units, *L* lumen (adapted from Maurovich-Horvat et al. [17])

High-Risk Plaque and Outcomes

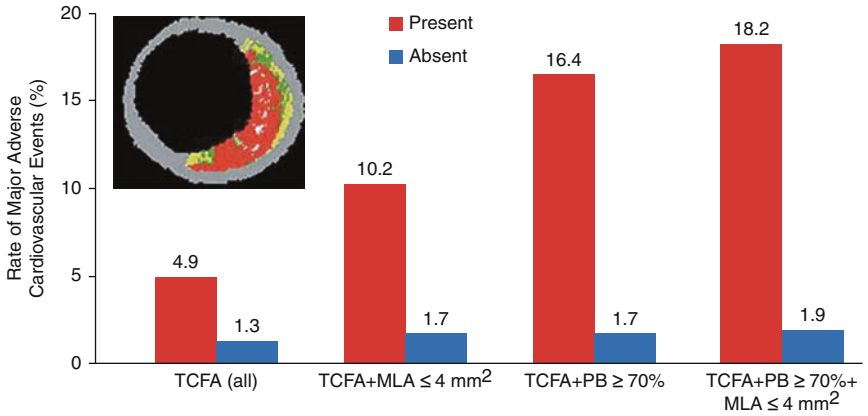

Lesion hazard ratio (95% CI)	3.90 (2.25–6.76)	6.55 (3.43–12.51)	10.83 (5.55–21.10)	11.05 (4.39–27.82)
P value	<0.001	<0.001	<0.001	<0.001
Prevalence (%)	46.7	15.9	10.1	4.2

Fig. 6.10 Outcomes stratified based on IVUS defined high risk plaque features. TCFA identified by intravascular ultrasound, PROSPECT trial. Event rates for lesions that were and those that were not thin-cap fibroatheromas, at a median follow-up of 3.4 years. Event rates associated with non-culprit lesions, 595 of which were characterized by means of radiofrequency intravascular ultrasonographic imaging as thin-cap fibroatheromas (TCFA), and 2114 that were not, are shown according to minimal luminal area (MLA) and plaque burden (PB) as detected on gray-scale intravascular ultrasonography. As evidenced by this figure, the presence of TCFA, especially when accompanied by PB ≥70% and MLA ≤4 mm^2, is associated with significantly increased rate of events. Conversely, absence of TCFA, independent of PB or MLA, is associated with low event rate in the duration of the study. The inset shows an example of a thin-cap fibroatheroma imaged by radiofrequency ultrasonography. Data on prevalence are for one or more such lesions per patient. Lesions in patients with indeterminate events were excluded. CI denotes confidence interval (reproduced with permission from Stone et al. [6])

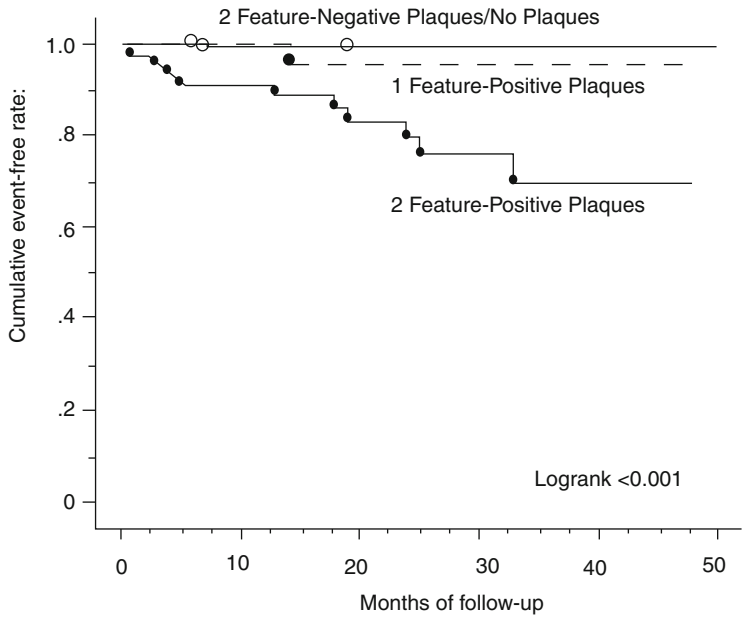

Fig. 6.11 Kaplan Meier curve for development ACS on the basis of plaque characteristics by CTA (short term (27 ± 10 months) follow up). In this prospective study of 1059 patients who underwent CT angiography, atherosclerotic lesions were analyzed for the presence of two features: PR and LAP. The plaque characteristics of lesions resulting in ACS during the follow-up of 27 to 10 months were evaluated. Of the 45 patients showing plaques with both PR and LAP (2-feature positive plaques), ACS developed in 10 (22.2%), compared with 1 (3.7%) of the 27 patients with plaques displaying either feature (1-feature positive plaques). In only 4 (0.5%) of the 820 patients with neither PR nor LAP (2-feature negative plaques) did ACS develop. None of the 167 patients with normal angiograms had acute coronary events ($p < 0.001$). Therefore, similar to what has been shown by other modalities such as IVUS (Fig. 6.10), CTA-defined features of high-risk plaque were independently predictive of future events. More important, absence of these features predicts a very low likelihood of events independent of degree of luminal stenosis

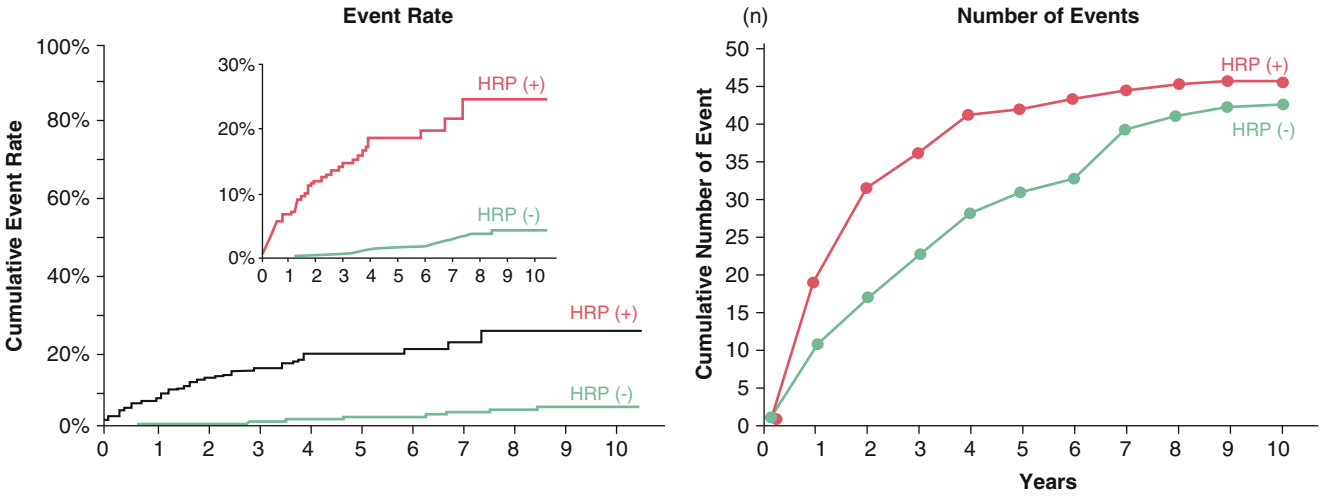

Fig. 6.12 Kaplan Meier curve for development ACS on the basis of plaque characteristics by CTA (midterm (3.9 ± 2.4 years) follow up). Low-attenuation (≤30 HU) and/or positively remodeled plaques identified on computed tomography angiography (CTA) are considered high-risk plaques and are known to be associated with adverse short-term outcomes. This study followed 3158 patients who underwent CTA for 3.9 ± 2.4 years and evaluated their midterm outcomes with regard to presence or absence of high-risk plaque features. Similar to the short-term study (Fig. 6.11), the event rate (*left*) was substantially higher for HRP (*red*) as compared with non-HRP (*green*). On follow-up, 48 (16.3%) of the 294 HRP-carrying and 40 (1.4%) of 2864 non–HRP-carrying subjects developed acute events. Although the outcomes were tenfold worse in HRP(+) as compared with HRP(−), because the number of subjects with HRP(+) was tenfold lower, equal numbers of acute events were observed in the HRP(+) and HRP(−) patients. The inset in the left panel shows the difference between event rate from HRP and non-HRP by magnifying the y-axis scale (reproduced with permission from Motoyama et al. [5])

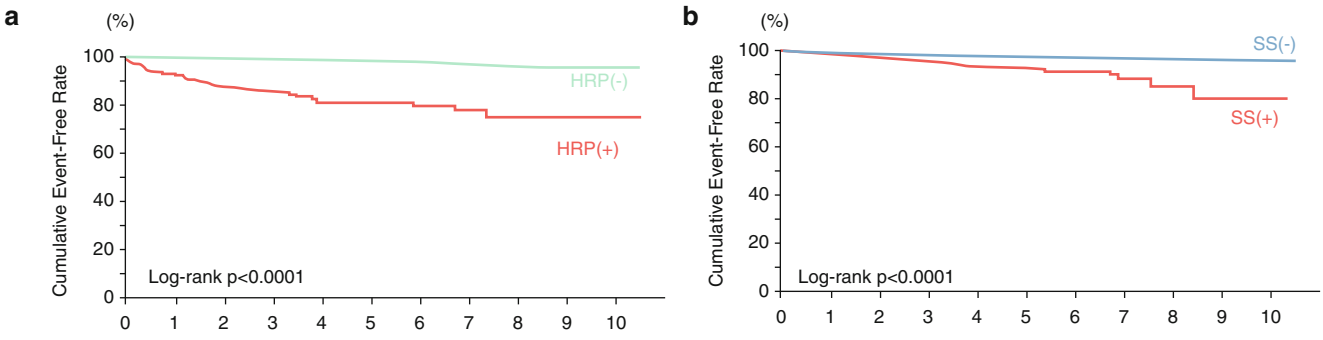

Patients at risk

HRP(-)	2,864	2,856	2,091	1,485	1,020	880	645	433	263	89	18
HRP(+)	294	274	193	163	106	92	64	35	15	6	2

Patients at risk

SS(-)	2,499	2,486	1,843	1,365	955	824	616	424	255	88	18
SS(+)	659	644	441	283	171	148	93	44	23	7	2

Fig. 6.13 Kaplan Meier curve for development ACS on the basis of plaque morphological characteristics and luminal stenosis by CTA (midterm [3.9 ± 2.4 years] follow-up). In the same study by Motoyama et al. ([5] Fig. 6.13), among 3158 patients, a total of 88 patients (2.8%) developed ACS during follow-up. Patients with high-risk plaque (HRP) had a higher risk of events compared with patients without HRP (16.3 vs. 1.4%) (**a**), as did patients with SS compared to patients without SS (5.5 vs. 2.1%) (**b**). (**c**) Patients were classified into five groups on the basis of plaque characteristics and luminal stenosis [HRP(+)/SS(+); HRP(+)/SS(−); HRP(−)/SS(+); HRP(−)/SS(−); and no plaque]; event rates were 18.8%, 14.9%, 2.6%, 1.2%, and 0.6%, respectively. This study demonstrates once more the independent predictive value of high-risk plaque features on CT, above and beyond luminal stenosis. Moreover, this figure once again shows the excellent negative predictive value of such features for events, independent of degree of stenosis. *ACS* acute coronary syndrome, *HRP* high-risk plaque, *SS* significant stenosis (reproduced with permission from Motoyama et al. [5])

c

Patients at risk

No plaque	360	360	233	161	110	100	78	58	46	22	5
HRP(-)/ss(-)	1,962	1,960	1,491	1,101	772	662	491	339	198	60	11
HRP(-)/ss(+)	542	536	367	223	138	118	76	36	19	7	2
HRP(+)/ss(-)	177	167	120	104	74	63	47	27	11	6	2
HRP(+)/ss(+)	117	107	73	59	32	29	17	8	4	0	0

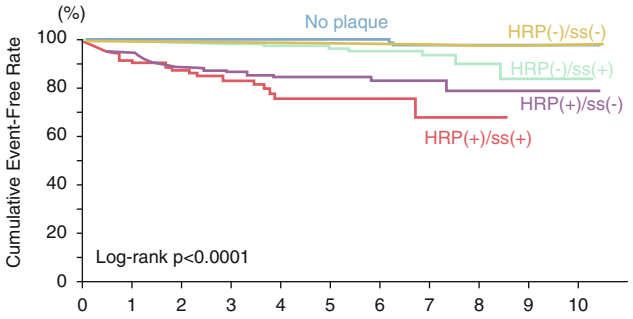

Fig. 6.13 (continued)

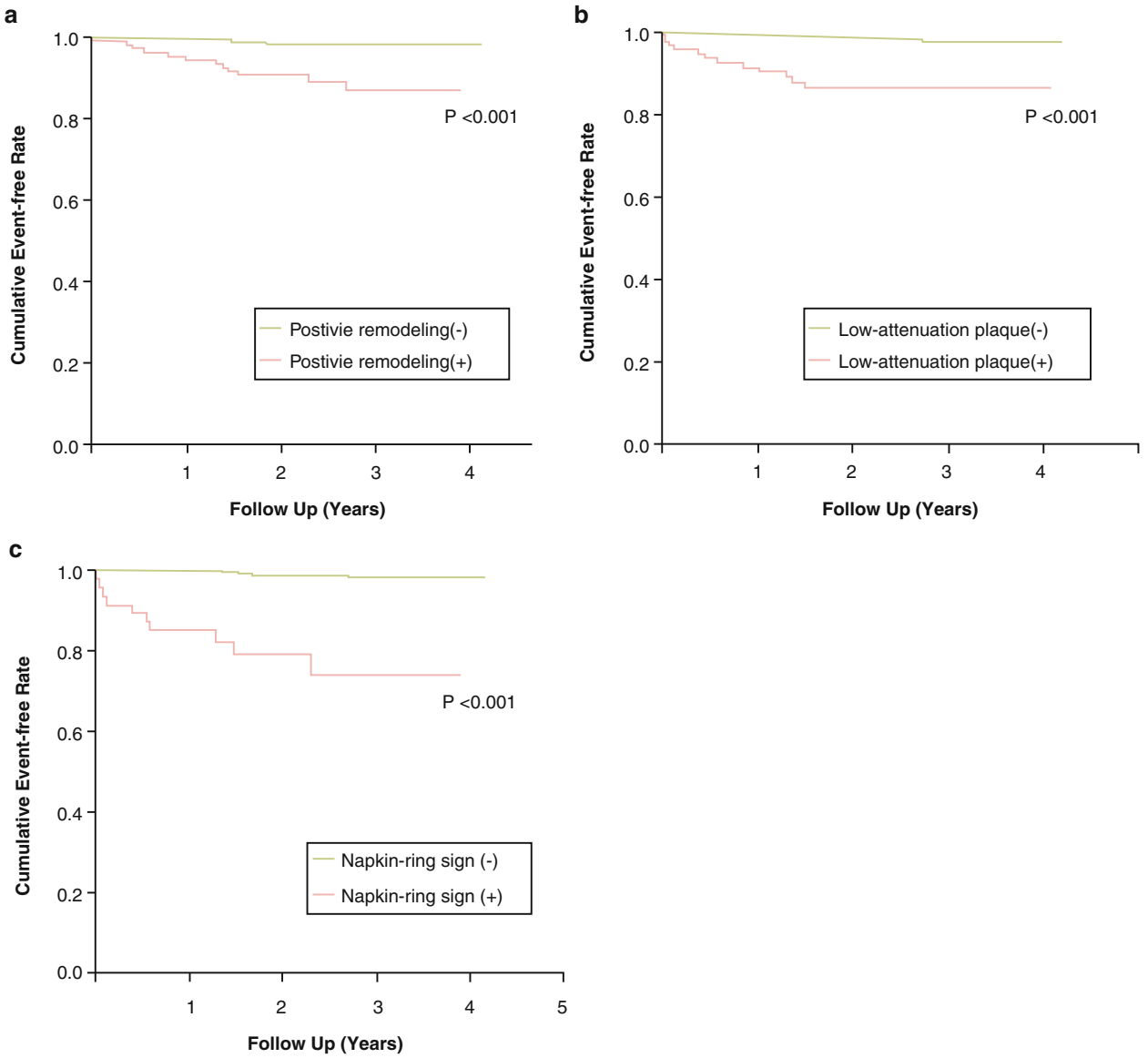

Fig. 6.14 Kaplan Meier curves for ACS events with or without each high-risk CTA features. In a study by Otsuka et al. [28], 895 consecutive patients who underwent coronary CTA examination with plaque morphology analysis were followed for >1 year. The primary endpoint was an ACS event (Cardiac death, nonfatal myocardial infarction, or unstable angina pectoris). Event-free curves for acute coronary syndrome (ACS) events resulting from plaques with or without positive remodeling (**a**), low-attenuation plaque (**b**), and napkin-ring sign (**c**), respectively. Plaques with these high-risk coronary computed tomography angiography (CTA) features had a higher incidence of acute coronary syndrome events than those without such findings. More impressively, similar to previous study, the absence of such high-risk features corresponded to excellent prognosis (reproduced with permission from Otsuka et al. [28])

High-Risk Plaques and Plaque Progression Prior to Myocardial Infarction

There is a commonly believed notion among cardiologists that most acute coronary events occur from rupture of mildly stenotic plaques. This notion is derived from prior studies that measured the degree of angiographic luminal narrowing in culprit plaques months to years (>3 months) prior to the time of myocardial infarction [13, 19–21]. However, in angiographic studies performed within three months of myocardial infarction (MI) or soon after MI with thrombus aspiration or thrombolysis and in postmortem pathologic observations, all show that the majority of culprit lesions are large plaques causing moderate-to-severe luminal narrowing [6, 22, 23]. The key to solving this discrepancy between the data from months-to-years before the event and data from immediately before or around of time of the event, can be that the plaques undergo rapid progression in months-to-weeks prior to rupture and myocardial infarction [24] (Fig. 6.15). Mechanisms for such rapid progression include: (1) recurrent plaque

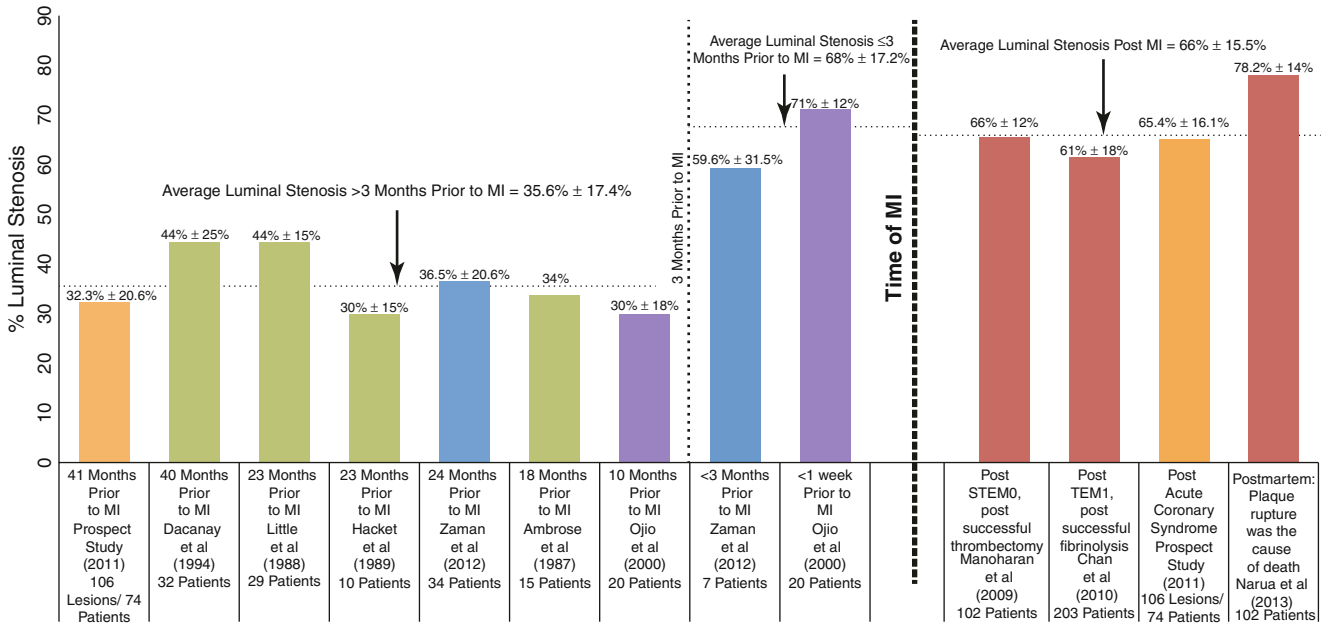

Fig. 6.15 Do plaques rapidly progress before myocardial infarction? This figure illustrates average luminal stenosis of culprit lesions resulted in MI* in various studies, organized relative to the time of MI. Green bars represent average luminal stenosis of the culprit lesions before MI, whereas red bars signify similar measurement after MI. Both *green* and *red bars* represent studies with single measurement. Data from studies with >1 measurement are shown by paired colors (*orange, blue*, and *purple*). The common perception that most MI are caused by rupture of mild plaques emerged from studies in the 1980s and 1990s (2nd, 3rd, 4th, 6th bar from left) [19–21, 25], which reported that lesions responsible for the subsequent STEMI were angiographically mild at baseline. In studies in which measurements were made >3 months before MI, the mean luminal stenosis by culprit lesion was 35.6 ± 20.6%. On average, these measurements were done 25 months before MI (range 18–41 months). On the other hand, data emerging from studies that investigated culprit lesions after the MI shows obstructive lesions are responsible for MI with mean luminal stenosis of 66 ± 15.5% (*red bars*). (Only post-STEMI data with successful fibrinolysis or thrombectomy along with postmortem data were included in this figure to ensure measurements were not significantly affected by the presence of thrombus and accurately reflect plaque size.) The PROSPECT study [6] along with studies by Zaman [26] and Ojio [27] shed light on this apparent discrepancy in the literature. PROSPECT (*orange bars*) demonstrated progression of lesion from 32.3 ± 20.6% at baseline to 65.4 ± 16.3% at the time of event (during a median follow-up of 3.4 years). In a study by Zaman et al. [26] (*blue bars*), among 41 patients who had STEMI, culprit lesions that were measured >3 months (mean 24 months) before MI had mean luminal stenosis of 36.5 ± 20.6%, whereas culprit lesions that were measured <3 months before MI had mean luminal stenosis of 59.6 ± 31.5%. Similarly, in a study by Ojio et al. [27] (*purple bars*), the mean luminal stenosis of culprit lesions 10 months before MI was 30 ± 18%, whereas similar measurement less than a week before MI revealed culprit lesions causing luminal stenosis of 71 ± 12%. Overall, the totality of the data represented in this figure demonstrates that culprit lesions go through a period of rapid progression weeks to months before MI. This observation can explain the apparent discrepancy in the literature between size of culprit plaques at baseline and at the time of event. The culprit lesions in PROSPECT study (*orange bar*) and study by Ojio et al. (*purple bar*) resulted in a variety of acute coronary syndromes (ACS) presentations, whereas the culprit lesions in the rest of studies represented here resulted in STEMI. MI indicates myocardial infarction; and STEMI, ST elevation myocardial infarction (reproduced with permission from Ahmadi et al. [24])

rupture and healing; (2) intraplaque hemorrhages from neovascularized plaques; and (3) reaching the Glagovian limit of positive remodeling and starting the process of inward expansion of the plaque (Figs. 6.5 and 6.16). All these mechanism of rapid plaque expansion prior to MI involve features that are known to be high-risk morphological features. Hence, rapid plaque progression prior to MI and high-risk plaque features are most likely inter-related [24]. As discussed later in the chapter, plaque progression, further risk stratifies lesions with high-risk morphological features (Figs. 6.15, 6.16, and 6.17).

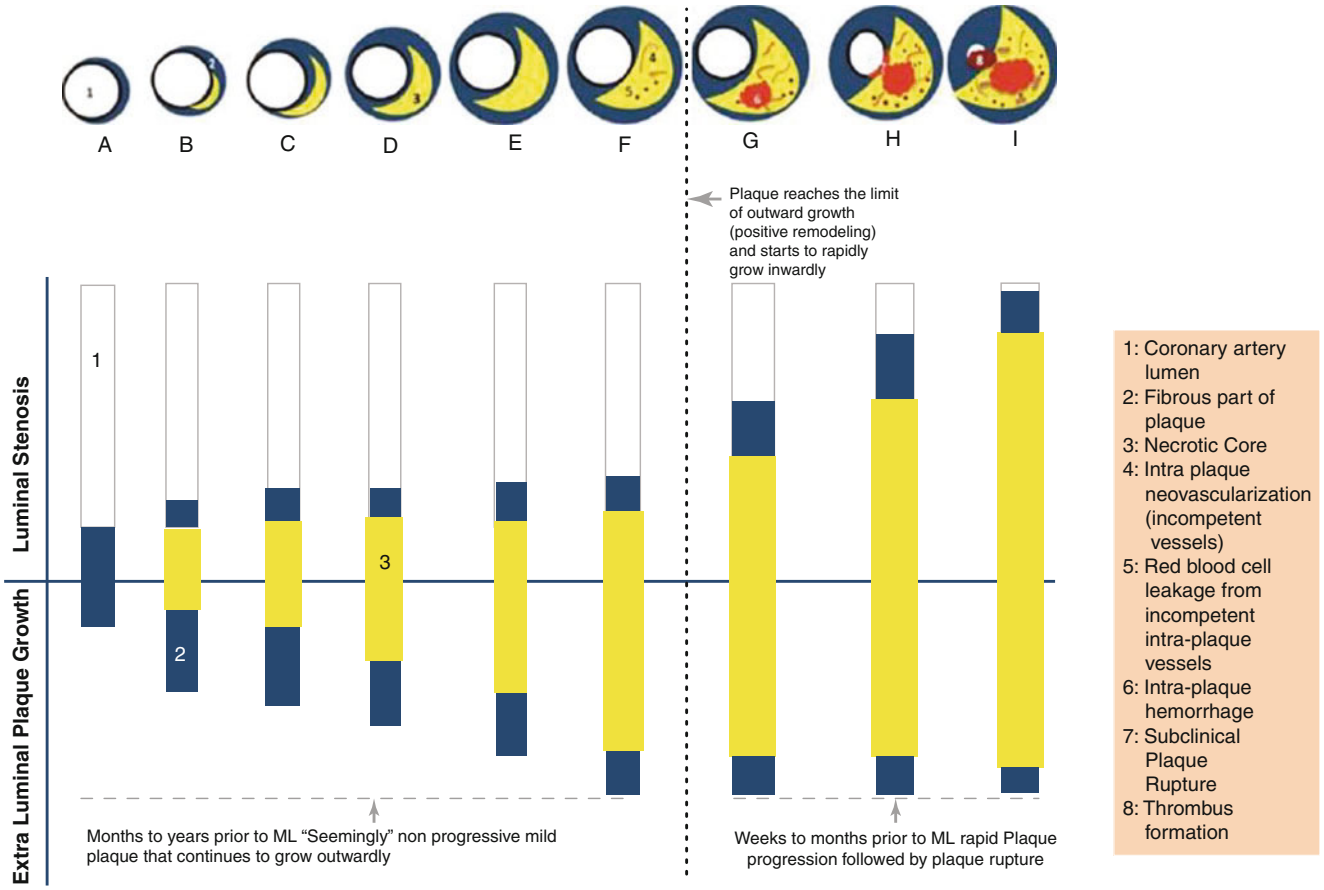

Fig. 6.16 Possible mechanisms for rapid plaque progression before MI. This figure illustrates a biologically plausible mechanism for rapid plaque progression before MI. The plaque depicted here is going through outward expansion (positive remodeling) in the first six measurements (**A**–**F**). During this time, the degree of luminal narrowing is relatively stable, despite active plaque growth, emphasizing that a stable degree of luminal narrowing is not equivalent to lack of plaque growth. Between stages (**F**, **G**), the plaque reaches the limit of outward expansion (*dotted line*) and intraluminal growth ensues, causing accelerated luminal narrowing. The possible mechanisms for this rapid expansion include intraplaque neovascularization with incompetent vessels that leak red blood cells at the borders of the necrotic core (**F**–**H**), intraplaque hemorrhage (**G**–**I**), and subclinical cycles of rupture and healing (**H**) causing accelerated plaque growth. Finally, a rapidly grown plaque ruptures and causes intraluminal thrombus formation resulting in a myocardial infarction (**I**). It should be noted that histological and behavioral features that allow plaques to undergo such rapid progression are the same features that are known to be characteristics of vulnerable plaques. It is also known that most MI are result of ruptures of plaques with these features. Therefore, in order for a plaque to grow rapidly before causing MI, it should already possess or acquire these features of vulnerability. MI indicates myocardial infarction. See Fig. 6.5 for more detail on these mechanisms (reproduced with permission from Ahmadi et al. [24])

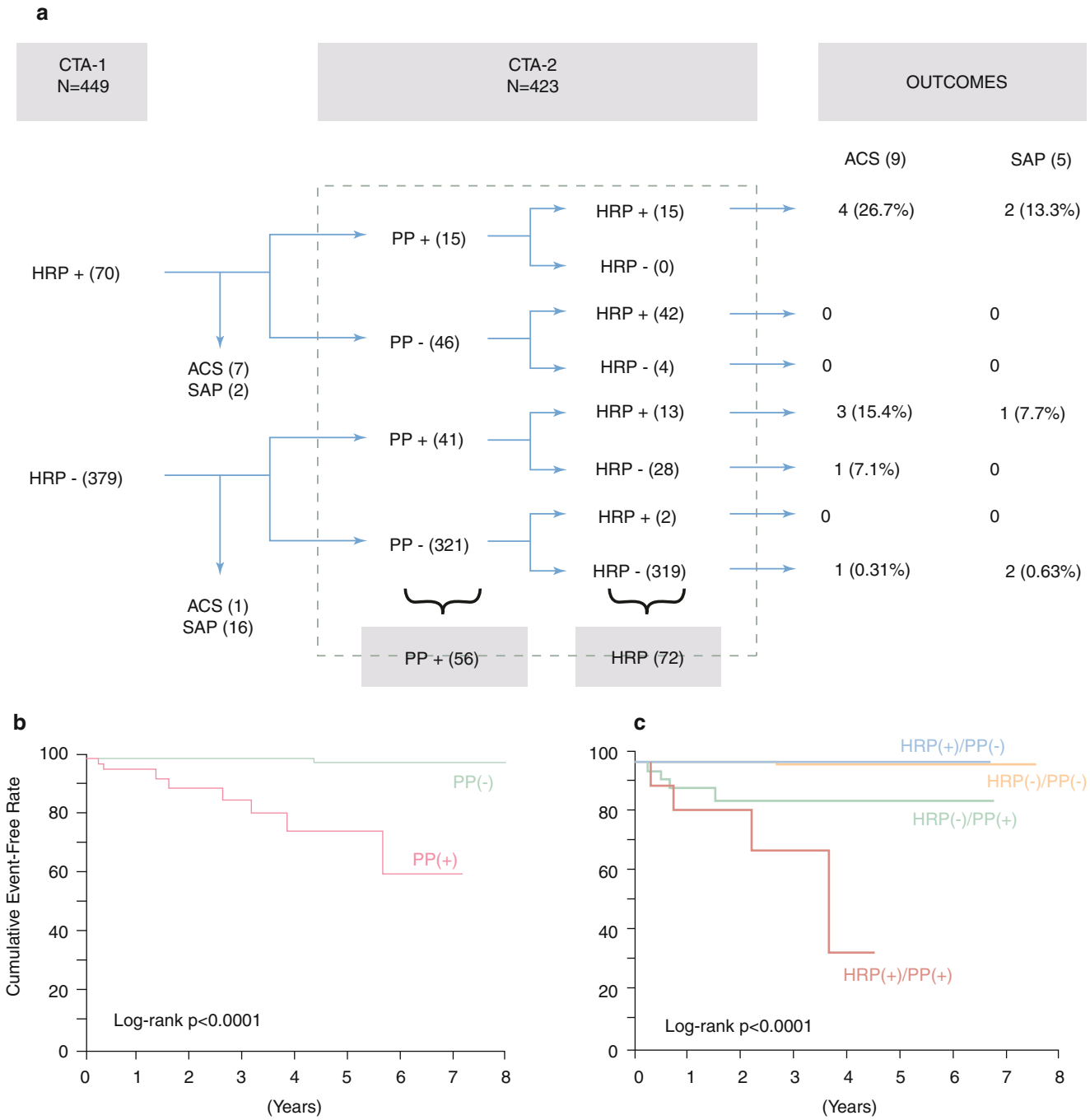

Fig. 6.17 Analysis of cardiac events with regard to plaque progression in HRP+ and HRP− plaques. In a study by Motoyama et al. [5] (Figs. 6.13 and 6.14), among 3158 patients, a total of 88 (2.8%) patients developed ACS during follow-up. In this figure made for a subset of patients with subsequent CTA, they were analyzed based on the high-risk plaque (HRP) features and plaque progression (PP). (**a**) The relationship between HRP (CTA-1 and -2), PP (CTA-2), and cardiac events is shown. On CTA-2, ACS occurred in 7 HRP(+) and 2 HRP(−) patients. Of these 9 patients, 8 patients were PP(+) and 1 PP(−). No HRP(+)/PP(−) patients on CTA-1 developed ACS. (**b**) Presence of PP produced a significantly higher incidence of ACS (14.3 vs. 0.3%). (**c**) When patients were classified according to the presence/absence of HRP on CTA-1 and PP on CTA-2, HRP(+)/PP(+) presented with the most frequent ACS (27%; log-rank $p < 0.0001$). Conversely, the HRP(+)/PP(−) group had no cardiac events. This data support the data presented in Fig. 6.15 and the mechanisms and hypothesis presented in Figs. 6.5 and 6.17. Plaque progression can be used to further risk stratify plaques with high risk features. *PP* plaque progression, *SAP* stable angina pectoris, *ACS* acute coronary syndrome (reproduced with permission from Motoyama et al. [5])

High Risk Plaque Features and Ischemia by Fractional Flow Reserve (FFR)

Even though stenosis is a known predictor of ischemia [29], the ischemia-stenosis concept is far from perfect. While there are lesions that produce Ischemia WithOut Stenosis (IWOS), there are lesions that have Stenosis WithOut Ischemia (SWOI) [30]. Factors such as lesion length, total plaque volume, entrance and exit angle of the lesion, and reference vessel's volume have been proposed to explain the discrepancy between ischemia and stenosis [31].

Based on the emerging data, it has been hypothesized that there is relationship between the CTA-defined LAP volume and lesion-specific ischemia by FFR, independent of degree of stenosis [30, 32]. In a recently published manuscript, it has been demonstrated that in a multivariable analysis of various CTA plaque features including lesion length, total plaque volume, and non-calcified plaque volume for prediction of invasive FFR, vessel's LAP volume >30 mm^3 is the only independent predictor in addition to CTA-verified luminal stenosis [33]. Therefore, there is a relationship between high-risk plaque features and ischemia by FFR, such that FFR negative lesions are likely devoid of lesions with large necrotic cores (high-risk plaque features). This might explain the benign prognosis of FFR-lesion despite of the fact that a significant portion of them are obstructive. These new findings demonstrating a relationship between high-risk morphological features and ischemia, together with previous data demonstrating the relationship between luminal stenosis and ischemia, can redefine the approach to coronary artery disease by involving all features of anatomy, physiology, and morphology (Figs. 6.18, 6.19, 6.20, 6.21, 6.22, 6.23, 6.24, and 6.25).

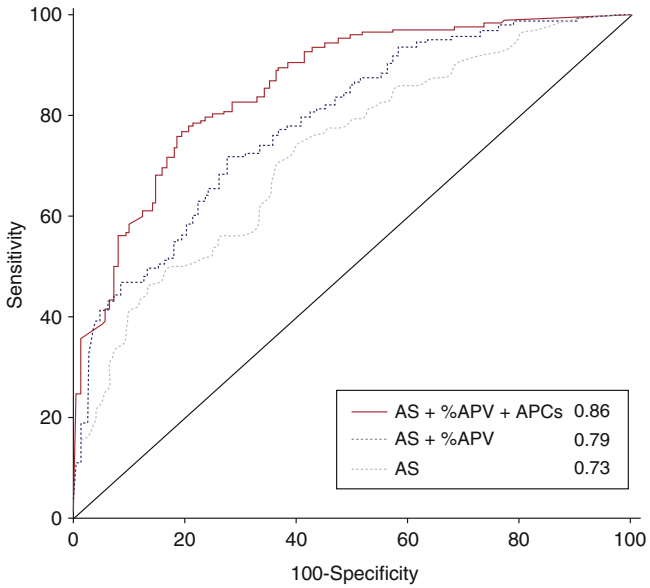

Fig. 6.18 High-risk plaque features by CT angiography identify lesion-specific ischemia by FFR. A study of 252 patients who underwent coronary CTA and coronary angiography with invasive FFR measurement considered the association of HRP with ischemia by FFR. As evident in this figure, Area under the curve (AUC) values gradually improved up to 0.79 (AS + %APV, $p < 0.001$), and 0.86 (AS + %APV + APCs, $p < 0.001$) respectively when %APV and APCs combined serially into AS. *AUC* area under the receiver operating curves, *FFR* fractional flow reserve, *AS* lumen area stenosis (%), *%APV* percent aggregate plaque volume, *APCs* atherosclerotic plaque characteristics (reproduced with permission from Park et al. [34])

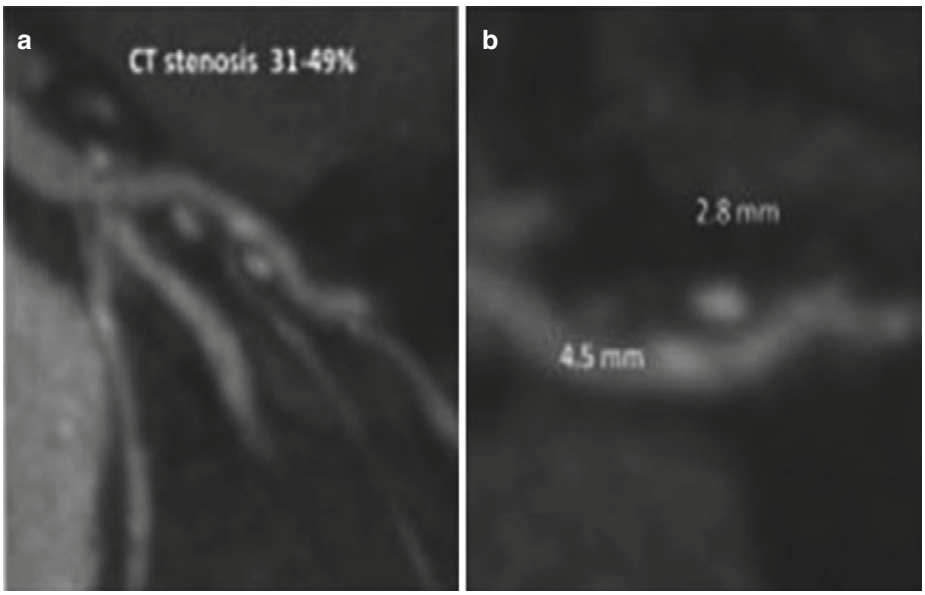

Fig. 6.19 Non-obstructive coronary stenosis causing ischemia. (**a**) Arterial segment demonstrating no luminal compromise but significant atherosclerosis. (**b**) Multiplanar reformat demonstrating positive remodeling and spotty calcification. (**c**) CT cross-section demonstrating low-attenuation plaque (22 HU). (**d**) Corresponding invasive angiogram demonstrating a 36% stenosis in the left anterior descending artery. The FFR value was 0.76 indicating ischemia. *FFR* fractional flow reserve, *QCA* quantitative coronary angiography (reproduced with permission from Park et al. [34])

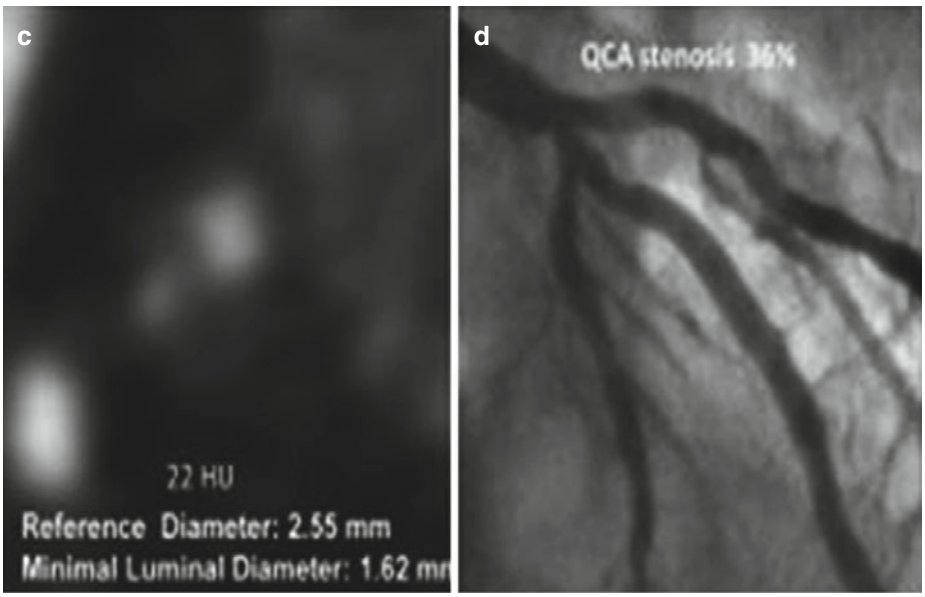

Fig. 6.19 (continued)

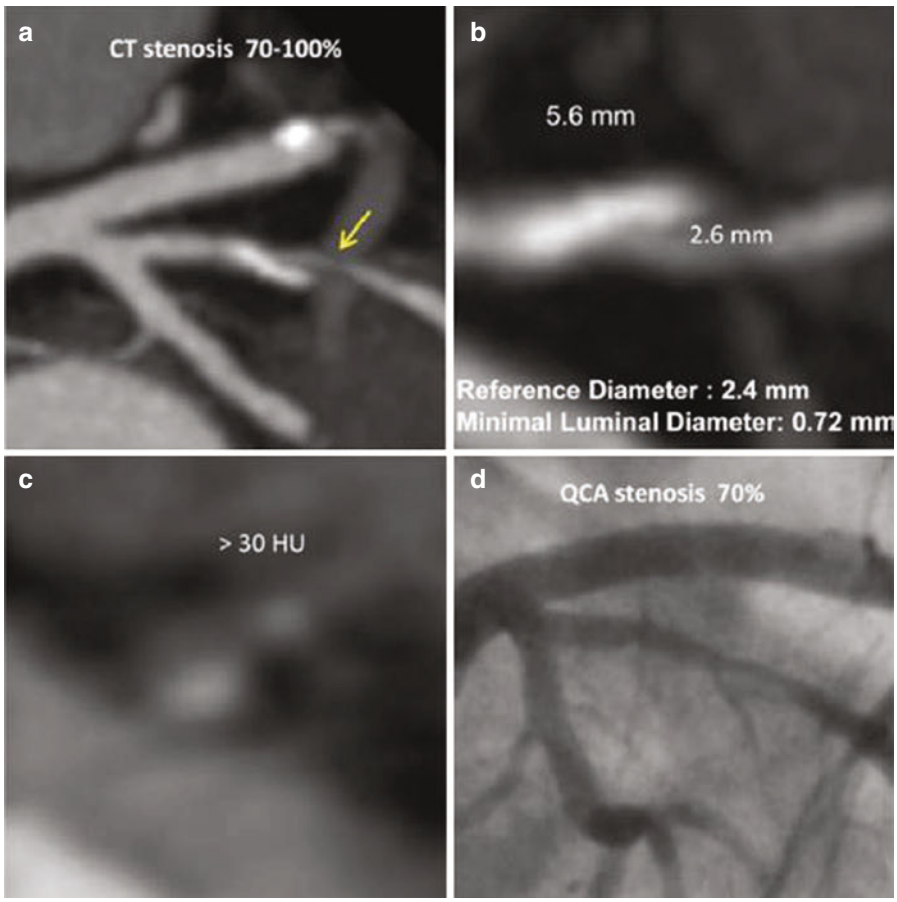

Fig. 6.20 Obstructive coronary stenosis that does not cause ischemia. (**a**) Arterial segment demonstrating significant luminal compromise. (**b**) Multiplanar reformat demonstrating no positive remodeling (remodeling index 1.08) and no spotty calcification. (**c**) CT cross-section demonstrating no low-attenuation plaque (>30 HU). (**d**) Corresponding invasive angiogram demonstrating a 70% stenosis in obtuse marginal branch of the circumflex artery. The FFR value was 0.89 indicating no ischemia (reproduced with permission from Park et al. [34])

Angiographic Diameter Stenosis Severity, %	FFR	No. of Lesions (% in Subgroup) [% in Entire Cohort]	Possible Histologic Feature
Normal	>0.80	0	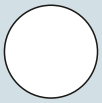
50-70	>0.80	402 (65) [33]	 2FNP with moderate luminal stenosis
	≤0.80	218 (35) [18]	 2FPP with moderate luminal stenosis
71-90	>0.80	104 (20) [8]	 2FNP with moderate to severe luminal stenosis
	≤0.80	409 (80) [33]	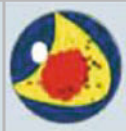 2FPP with moderate to severe luminal stenosis
			 2FNP with severe luminal stenosis

Fig. 6.21 Coronary stenosis severity, fractional flow reserve (FFR), and underlying pathologic features. In this table, the various groups of lesions in the fractional flow reserve versus angiography for multivessel evaluation (FAME) [35] trial are categorized according to their degree of luminal stenosis and FFR value. The possible underlying histological plaque features in each subgroup are postulated using the concepts that high-risk plaque features can be predictive of ischemia by FFR independent of degree of luminal stenosis and FFR could be sensitive tool to detect large plaques with high-risk features. To understand the relationship between high-risk plaques and ischemia by FFR, it is crucial to recognize that FFR is not a static measure and coronary arteries are not rigid pipes. In addition to the fixed degree of stenosis, the vessel's behavior at the time of vasodilator administration has a major role in determining post-stenotic pressure measurement. The administration of the vasodilator during the FFR measurement dilates the distal arteriolar bed, which in turn drops the pressure in that region. This drop in pressure causes a larger gradient to be developed between the aorta and distal coronary bed, increasing the coronary blood flow (state of maximal hyperemia). Epicardial coronary artery auto-regulatory mechanisms respond to the state of maximal hyperemia by further dilatation. In the classic case of severe luminal stenosis, since the vessel at the level of stenosis is at the maximally dilated state at rest, it cannot dilate any further and the result will be a post-stenotic pressure drop at the time of hyperemia. In the case of mild-to-moderate luminal stenosis with large necrotic core, we hypothesize that the vessel likely develops a degree of impairment in its ability to dilate locally at the lesion site. With the rest of the vessel dilating at maximal hyperemia, the once mild-to-moderate stenosis becomes functionally significant stenosis. The trans-stenotic pressure drop is inversely proportional to the fourth power of the lumen radius and contributes significantly to the specific curvilinear pressure-flow relationship which defines the physiologic importance of any fixed or dynamic narrowing [36]. As a consequence, a change in luminal diameter relative to the other segments of the same vessel caused by local vasodilatory impairment at the time of maximal hyperemia, produces marked hemodynamic effects with a significant impact on coronary perfusion leading to abnormal FFR measurement. Therefore, a lesion can become ischemia-inducing if it causes significant luminal stenosis or possesses large necrotic core or has the right combination of luminal stenosis and necrotic core volume [30]. In creating this figure, the following assumptions were applied: (1) the presence of large-volume 2FPP strongly predicts FFR-verified ischemia. (2) FFR-verified ischemia is a sensitive tool for detecting large-volume 2FPP. (3) Large-volume 2FPP is unlikely to be present in the FFR-negative subgroup. Therefore, most plaques in the FFR-negative subgroup likely consist of nonatheromatous fibrotic lesions and less likely are associated with severe degree of luminal narrowing or long lesion length. (4) In the absence of significant luminal narrowing, FFR-verified ischemia is likely owing to the presence of large-volume (necrotic core) 2FFP. Lesion length and plaque volume are not depicted but may have a modulating effect on these considerations. (5) In the presence of a severe luminal stenosis (e.g., angiographic diameter stenosis, >70%), an FFR of greater than 0.80 suggests a normal vessel's ability to dilate, which further argues against the presence of large-volume 2 Feature Positive Plaques (2FPP) (or long lesion length). Most plaques in this subgroup are therefore likely fibrous, not lipid-rich lesions, and have short lesion length. (6) In the presence of severe luminal narrowing, an FFR of 0.80 or less could be owing to the presence of lipid-rich 2FPP or a fibrous, long-length lesion. 2 Feature Negative Plaques (2FNP) indicates 2-feature–negative plaque; *black* and *red dots*, red blood cells leaked from incompetent vessels (developed from the FAME and FAME 2 studies 1–4) (adapted from Ahmadi et al. [30])

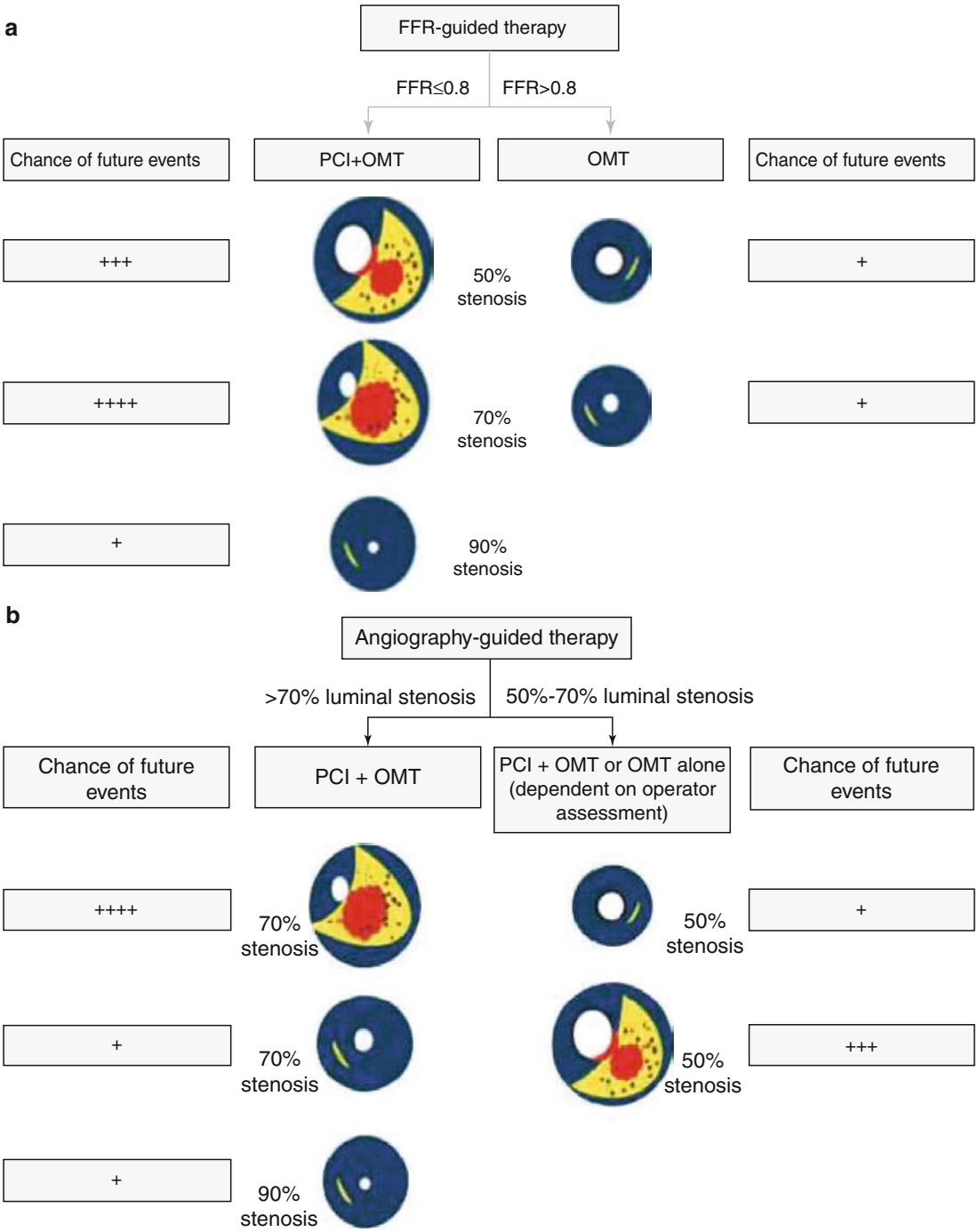

Fig. 6.22 Differences in fractional flow reserve (FFR) and angiography-guided therapies by plaque type. Based on the possible histological characteristics of each plaque type presented in Fig. 6.21, the differences in FFR-guided treatment vs. angiography-guided treatment are depicted. The chance of future events with each approach is estimated (range, + to ++++) based on plaque morphology-related prognostic data from prospective studies. With FFR-guided therapy, nearly all high-risk lesions (including vulnerable plaques) are treated with percutaneous coronary intervention (PCI) plus optimum medical therapy (OMT), whereas lesions that are at low risk for future events are treated with OMT alone. In the angiography-guided therapy group, some lesions with angiographic diameter stenosis of 50–70% will be treated with PCI, whereas others will receive OMT alone, depending on the operator's assessment of the lesions' severity (which is known to have wide variability). Up to 35% of lesions in this subgroup in the fractional flow reserve versus angiography for multivessel evaluation (FAME) trial had an FFR of 0.80 or less. Therefore, the angiography-guided approach will leave some high-risk lesions with vulnerable features that do not undergo revascularization. This finding may in part explain the paradoxically increased rate of urgent revascularization during follow-up with angiography-guided therapy despite the greater use of initial PCI in addition to more frequent stent-related thrombosis and restenosis events. Moreover, angiography-guided therapy will lead to revascularization of many lesions that may safely be deferred to OMT alone, which increases the risk for periprocedural complications. Graphics for the possible histological features are described in Fig. 6.20 (adapted from Ahmadi et al. [30]). *FFR* Fractional Flow Reserve, *OMT* Optimal Medical Therapy, *PCI* Percutanous Coronary Intervention, *FAME* Trial Fractional Flow Resever Versus Angiography for Multivessel Evaluation Trial

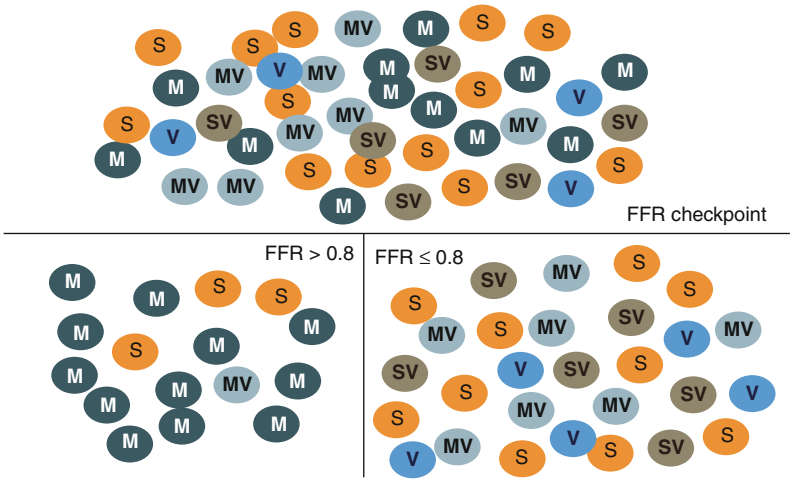

Fig. 6.23 Fractional flow reserve (FFR) as a security check point for detecting plaques at high risk for future events. Detection of ischemia is a sensitive (but not specific) measure for detecting large-volume 2-feature–positive plaque (2FPP, with a positive remodeling index and a necrotic core), independent of the angiographic degree of luminal stenosis. FFR-guided therapy thus may be considered a checkpoint that leaves very few large lipid-rich 2FPP—those with highest risk for future events—to medical therapy alone. On the other hand, FFR leads to revascularization of most lipid-rich 2FPP (moderate [MV] and severe [SV] vulnerable lesions) and plaque with a severe degree of luminal stenosis without features of vulnerability (severe [S] and very severe [V] nonvulnerable lesions. *2FNP* indicates 2-feature–negative plaque, *M* moderate nonvulnerable lesions) (adapted from Ahmadi et al. [30])

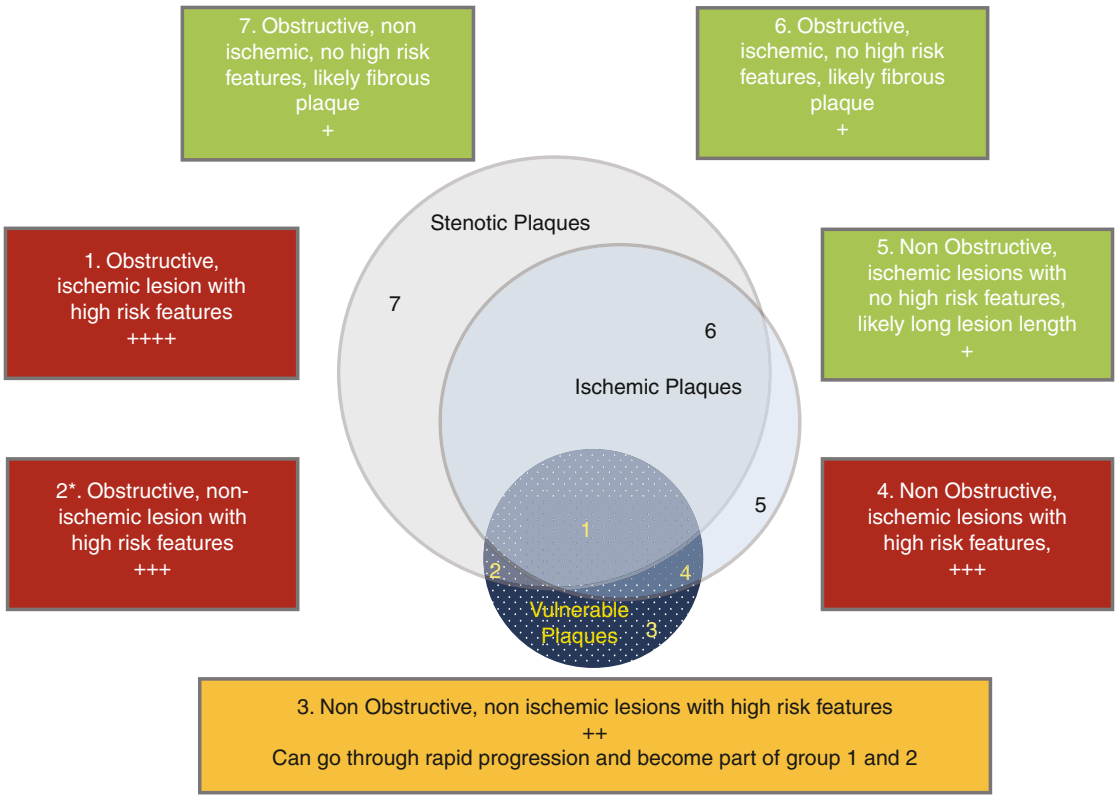

Fig. 6.24 Can we combine information about anatomy, physiology and morphology to redefine plaque types and their risk? A rationale may be proposed for combining all three features (anatomy, physiology, and plaque morphology) for prognostication and therapeutic decision-making guidance. In this regard, it is important to recognize that the obstructive, ischemic, and pathologically high-risk groups are all a mix of both benign and malignant lesions, amenable to further risk-stratification. Any given lesion could have combinations of high-risk features that pertain to anatomy, physiology, and morphology, and therefore the attempt to predict the lesion's prognosis based on only one of these features leads to an incomplete assessment. For example, an obstructive plaque with high-risk morphologic features most likely has a different likelihood of causing an event compared to an obstructive plaque with the same degree of luminal narrowing but without the high-risk morphologic features [3]. Similarly, a plaque with vulnerable features (e.g., consistent with a TCFA) that also has a large plaque burden and causes luminal obstruction, is more likely to result in a future MACE than a plaque with similar histological features that is not obstructive and has small plaque burden [3, 4, 6]. Moreover, lesions with high-risk morphologic features by CTA can be subdivided into a very high-risk group, which underwent plaque progression and became obstructive (27% of which resulted in acute coronary syndromes [ACS] in 5 years), while lesions with high-risk morphological features but no significant plaque progression had no ACS in the similar timeline [5]. There are eight possible plaque types when considering various possibilities with regard to presence or absence of significant luminal obstruction, ischemia, and high-risk features. Note that plaques that are non-obstructive and non-ischemic without high-risk features are not represented in this diagram. The possibility of future events, based on the currently available literature, for each type of plaque estimated and represented by the box color (red: high risk, orange: medium risk, and green: low risk) and the number of + (*low risk*: + to *high risk*: ++++). *Type 2 plaques: obstructive, non-ischemic lesions with high-risk features are relatively rare types, as most of obstructive lesions with large necrotic core are ischemic as well (adapted from Ahmadi et al. [37])

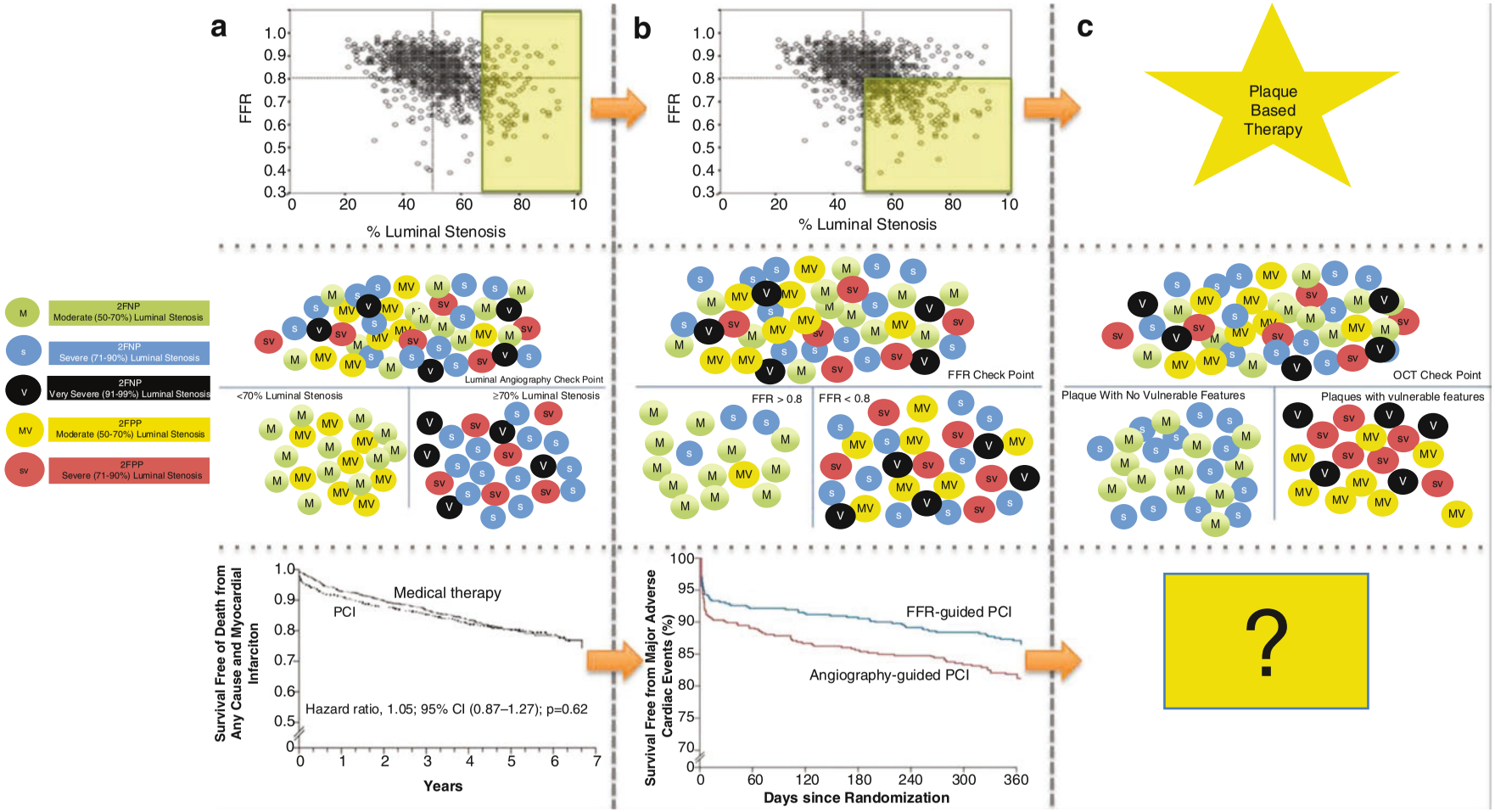

Fig. 6.25 Is it the time to add plaque imaging-based decision-making to the decision-making algorithm for treatment of stable coronary artery disease? (**a**) COURAGE study demonstrated treating lesions based on degree of anatomical stenosis is not superior to OMT. In this approach, lesions with a high degree of luminal stenosis (≥70%) were treated with PCI + OMT (S, V and SV lesions above), whereas the ones with a lower degree of luminal stenosis were left to OMT alone. In this method, there is a possibility of leaving lots of moderate-sized lesions with high risk of future events (MV lesions above) to OMT alone, while performing PCI and hence increasing the risk of complications on many low risk obstructive lesions (S lesions above). (**b**) The paradigm has shifted from anatomically based therapy to FFR guided therapy. As it is shown in this manuscript, FFR is a sensitive (but not specific) tool for detecting large-volume 2FPP that have high risk of future events. By leaving lower risk lesions to OMT and decreasing the number of unnecessary PCI and their consequent complications, FFR-guided therapy has been shown to be superior to both angiography guided therapy and OMT alone [1–4]. However, FFR-guided therapy might still lead to revascularization of stenotic lesions that are low risk (S lesions above). (**c**) We propose the next step in optimizing treatment for stable coronary artery disease could be plaque-based therapy. In this approach, high-risk plaques, independent of their size, will be determined using CTA and will be treated with PCI if they also cause ischemia by FFR (MV, SV and V lesions above). Moderate-to-severely stenotic plaques without vulnerable features will be left to OMT alone as they have low risk of future events. We believe this could be the most sensitive and specific method of selecting highest-risk lesions for PCI and leaving low-risk lesions to OMT alone

References

1. Go AS, Mozaffarian D, Roger VL, Benjamin EJ, Berry JD, Borden WB, et al. Heart disease and stroke statistics–2013 update: a report from the American Heart Association. Circulation. 2013;127:e6–e245.
2. Kaul S, Narula J. In search of the vulnerable plaque: is there any light at the end of the catheter? J Am Coll Cardiol. 2014;64:2519–24.
3. Narula J, Nakano M, Virmani R, Kolodgie FD, Petersen R, Newcomb R, et al. Histopathologic characteristics of atherosclerotic coronary disease and implications of the findings for the invasive and noninvasive detection of vulnerable plaques. J Am Coll Cardiol. 2013;61:1041–51.
4. Motoyama S, Sarai M, Harigaya H, Anno H, Inoue K, Hara T, et al. Computed tomographic angiography characteristics of atherosclerotic plaques subsequently resulting in acute coronary syndrome. J Am Coll Cardiol. 2009;54:49–57.
5. Motoyama S, Ito H, Sarai M, Kondo T, Kawai H, Nagahara Y, et al. Plaque characterization by coronary computed tomography angiography and the likelihood of acute coronary events in mid-term follow-up. J Am Coll Cardiol. 2015;66:337–46.
6. Stone GW, Maehara A, Lansky AJ, de Bruyne B, Cristea E, Mintz GS, et al. A prospective natural-history study of coronary atherosclerosis. N Engl J Med. 2011;364:226–35.
7. Motoyama S, Kondo T, Sarai M, Sugiura A, Harigaya H, Sato T, et al. Multislice computed tomographic characteristics of coronary lesions in acute coronary syndromes. J Am Coll Cardiol. 2007;50:319–26.
8. Falk E, Nakano M, Bentzon JF, Finn AV, Virmani R. Update on acute coronary syndromes: the pathologists' view. Eur Heart J. 2013;34:719–28.
9. Narula J, Finn AV, Demaria AN. Picking plaques that pop. J Am Coll Cardiol. 2005;45:1970–3.
10. Takaya N, Yuan C, Chu B, Saam T, Polissar NL, Jarvik GP, et al. Presence of intraplaque hemorrhage stimulates progression of carotid atherosclerotic plaques: a high-resolution magnetic resonance imaging study. Circulation. 2005;111:2768–75.
11. Dunphy MP, Freiman A, Larson SM, Strauss HW. Association of vascular 18F-FDG uptake with vascular calcification. J Nucl Med. 2005;46:1278–84.
12. Jang IK, Tearney GJ, MacNeill B, Takano M, Moselewski F, Iftima N, et al. In vivo characterization of coronary atherosclerotic plaque by use of optical coherence tomography. Circulation. 2005;111:1551–5.
13. Little WC, Constantinescu M, Applegate RJ, Kutcher MA, Burrows MT, Kahl FR, et al. Can coronary angiography predict the site of a subsequent myocardial infarction in patients with mild-to-moderate coronary artery disease? Circulation. 1988;78:1157–66.
14. Kolodgie FD, Gold HK, Burke AP, Fowler DR, Kruth HS, Weber DK, et al. Intraplaque hemorrhage and progression of coronary atheroma. N Engl J Med. 2003;349:2316–25.
15. Virmani R, Kolodgie FD, Burke AP, Finn AV, Gold HK, Tulenko TN, et al. Atherosclerotic plaque progression and vulnerability to rupture: angiogenesis as a source of intraplaque hemorrhage. Arterioscler Thromb Vasc Biol. 2005;25:2054–61.
16. Achenbach S, Ropers D, Hoffmann U, MacNeill B, Baum U, Pohle K, et al. Assessment of coronary remodeling in stenotic and nonstenotic coronary atherosclerotic lesions by multidetector spiral computed tomography. J Am Coll Cardiol. 2004;43:842–7.
17. Maurovich-Horvat P, Hoffmann U, Vorpahl M, Nakano M, Virmani R, Alkadhi H. The napkin-ring sign: CT signature of high-risk coronary plaques? JACC Cardiovasc Imaging. 2010;3:440–4.
18. Ahmadi A, Narula J. Primary and secondary prevention, or subclinical and clinical atherosclerosis. JACC Cardiovasc Imaging. 2017;10(4):447–50.
19. Ambrose JA, Tannenbaum MA, Alexopoulos D, Hjemdahl-Monsen CE, Leavy J, Weiss M, et al. Angiographic progression of coronary artery disease and the development of myocardial infarction. J Am Coll Cardiol. 1988;12:56–62.
20. Dacanay S, Kennedy HL, Uretz E, Parrillo JE, Klein LW. Morphological and quantitative angiographic analyses of progression of coronary stenoses. A comparison of Q-wave and non-Q-wave myocardial infarction. Circulation. 1994;90:1739–46.
21. Hackett D, Verwilghen J, Davies G, Maseri A. Coronary stenoses before and after acute myocardial infarction. Am J Cardiol. 1989;63:1517–8.
22. Manoharan G, Ntalianis A, Muller O, Hamilos M, Sarno G, Melikian N, et al. Severity of coronary arterial stenoses responsible for acute coronary syndromes. Am J Cardiol. 2009;103:1183–8.
23. Chan KH, Chawantanpipat C, Gattorna T, Chantadansuwan T, Kirby A, Madden A, et al. The relationship between coronary stenosis severity and compression type coronary artery movement in acute myocardial infarction. Am Heart J. 2010;159:584–92.
24. Ahmadi A, Leipsic J, Blankstein R, Taylor C, Hecht H, Stone GW, et al. Do plaques rapidly progress prior to myocardial infarction? The interplay between plaque vulnerability and progression. Circ Res. 2015;117:99–104.
25. Little WC, Cheng CP, Peterson T, Vinten-Johansen J. Response of the left ventricular end-systolic pressure-volume relation in conscious dogs to a wide range of contractile states. Circulation. 1988;78:736–45.
26. Zaman T, Agarwal S, Anabtawi AG, Patel NS, Ellis SG, Tuzcu EM, et al. Angiographic lesion severity and subsequent myocardial infarction. Am J Cardiol. 2012;110:167–72.
27. Ojio S, Takatsu H, Tanaka T, Ueno K, Yokoya K, Matsubara T, et al. Considerable time from the onset of plaque rupture and/or thrombi until the onset of acute myocardial infarction in humans: coronary angiographic findings within 1 week before the onset of infarction. Circulation. 2000;102:2063–9.
28. Otsuka K, Fukuda S, Tanaka A, Nakanishi K, Taguchi H, Yoshikawa J, et al. Napkin-ring sign on coronary CT angiography for the prediction of acute coronary syndrome. JACC Cardiovasc Imaging. 2013;6:448–57.
29. Gould KL, Lipscomb K, Calvert C. Compensatory changes of the distal coronary vascular bed during progressive coronary constriction. Circulation. 1975;51:1085–94.
30. Ahmadi A, Stone GW, Leipsic J, Serruys PW, Shaw L, Hecht H, et al. Association of coronary stenosis and plaque morphology with fractional flow reserve and outcomes. JAMA Cardiol. 2016;1(3):350–7.
31. Kern MJ, Samady H. Current concepts of integrated coronary physiology in the catheterization laboratory. J Am Coll Cardiol. 2010;55:173–85.
32. Ahmadi A, Kini A, Narula J. Discordance between ischemia and stenosis, or PINSS and NIPSS: are we ready for new vocabulary? JACC Cardiovasc Imaging. 2015;8:111–4.
33. Gaur S, Ovrehus KA, Dey D, Leipsic J, Bøtker HE, Jensen JM, et al. Coronary plaque quantification and fractional flow reserve by coronary computed tomography angiography identify ischaemia-causing lesions. Eur Heart J. 2016;37(15):1220–7.
34. Park HB, Heo R, ó Hartaigh B, Cho I, Gransar H, Nakazato R, et al. Atherosclerotic plaque characteristics by CT angiography identify coronary lesions that cause ischemia: a direct comparison to fractional flow reserve. JACC Cardiovasc Imaging. 2015;8:1–10.
35. Tonino PA, De Bruyne B, Pijls NH, Siebert U, Ikeno F, van't Veer M, et al. Fractional flow reserve versus angiography for guiding percutaneous coronary intervention. N Engl J Med. 2009;360:213–24.
36. Spaan JA, Piek JJ, Hoffman JI, Siebes M. Physiological basis of clinically used coronary hemodynamic indices. Circulation. 2006;113:446–55.
37. Ahmadi A, Stone GW, Leipsic J, Shaw LJ, Villines TC, Kern MJ, et al. Prognostic determinants of coronary atherosclerosis in stable ischemic heart disease: anatomy, physiology, or morphology? Circ Res. 2016;119:317–29.

Coronary Stents: Evaluation and Follow-up

7

Harvey S. Hecht, Annapoorna Kini, and Samin Sharma

The 2010 Expert Consensus Document on Coronary CT Angiography (CTA) states, "Coronary stents pose some significant technical challenges for coronary CTA, since the metal in the stents may create several types of artifacts in the images. Special algorithms are now routinely used that may reduce some of these artifacts during image reconstruction. The literature suggests that in patients who have large diameter stents, good image quality, and whose clinical presentation suggests low-to-intermediate probability for restenosis, 64-channel coronary CTA can be used to rule out severe in-stent restenosis" [1].

Nonetheless, CTA has been extensively evaluated to rule in in-stent restenosis (ISR), not merely to exclude it [2]. In addition, there is a large series on the CTA diagnosis of stent fracture [3]. This chapter summarizes the ISR and stent-fracture applications, and, more importantly, illustrates the significant clinical utility of CTA in a host of stent problems that have not yet been systematically evaluated or published, yet in which CTA is robust enough for routine use in dedicated laboratories.

Technical Issues

The following protocols, processing, and analysis apply to all the stent applications.

Scanners and Acquisition Protocols

Stent evaluation can be readily performed in both retrospectively and prospectively acquired studies on any scanner equipped with a minimum of 64 slices. Motion artifact must be avoided as much as possible, because stents accentuate blurring. Adequate heart rate control with beta blockers to less than 60 beats/min is ideal for prospective acquisitions. Retrospective acquisition should be employed for heart rates greater than 60 beats/min. Voltage and milliamperage are the same as for routine CTA and are based on individual body habitus. Thin slices (0.625 mm) should be employed. Iterative reconstruction algorithms should be routinely used; they facilitate decreased radiation and minimize the blooming effect of superimposed calcium.

Processing and Analysis

Sharp filters and wide window settings maximize intra-stent visualization and should be routinely used. Multiplanar reconstruction and cross-sectional analysis are critical, as they are for routine CTA evaluation; maximum intensity projections alone are inadequate [1]. Hounsfield unit (HU) measurement should be used routinely to evaluate stent, contrast, and calcium densities, as displayed in the examples.

H.S. Hecht (✉)
Department of Cardiology, Icahn School of Medicine at Mount Sinai, New York, NY, USA
e-mail: harvey.hecht@mountsinai.org

A. Kini (✉)
Department of Cardiology, Icahn School of Medicine at Mount Sinai, New York, NY, USA
e-mail: Annapoorna.kini@mountsinai.org

S. Sharma
Cardiovascular Institute, Icahn School of Medicine at Mount Sinai, New York, NY 10029, USA
e-mail: samin.sharma@mountsinai.org

M.J. Budoff et al. (eds.), *Atlas of Cardiovascular Computed Tomography*, https://doi.org/10.1007/978-1-4471-7357-1_7

Overlying Calcified Plaque and False Positive CTA

The most problematic artifacts result from the higher-density calcium overlying the stents, rather than from the stents themselves. Because ISR is diagnosed by hypodensity within the stent, adjacent densely calcified plaque (generally >1000 HUs) may lead to false positive ISR diagnoses by "shadowing" contiguous contrast, a problem compounded by shadowing occurring both proximal and distal to the dense calcium, as well as immediately adjacent in the same slice. The resulting photopenia may be misdiagnosed as the hypodensity accompanying ISR. Because calcified lesions are often stented, the problem is a common one, and there may be no solution until dual-energy imaging becomes a reality. Changing window settings to shrink the calcium "blooming" should be avoided, as the data remain the same despite the change in appearance. Consequently, when this situation arises, the report should include a statement such as, "There is severe hypodensity consistent with significant ISR. However, adjacent densely calcified plaque may artifactually contribute to this finding." Densely calcified plaque superimposed on the stent artifactually producing severe luminal hypodensity consistent with ISR is well illustrated in Fig. 7.1; the normal angiogram confirms the absence of ISR.

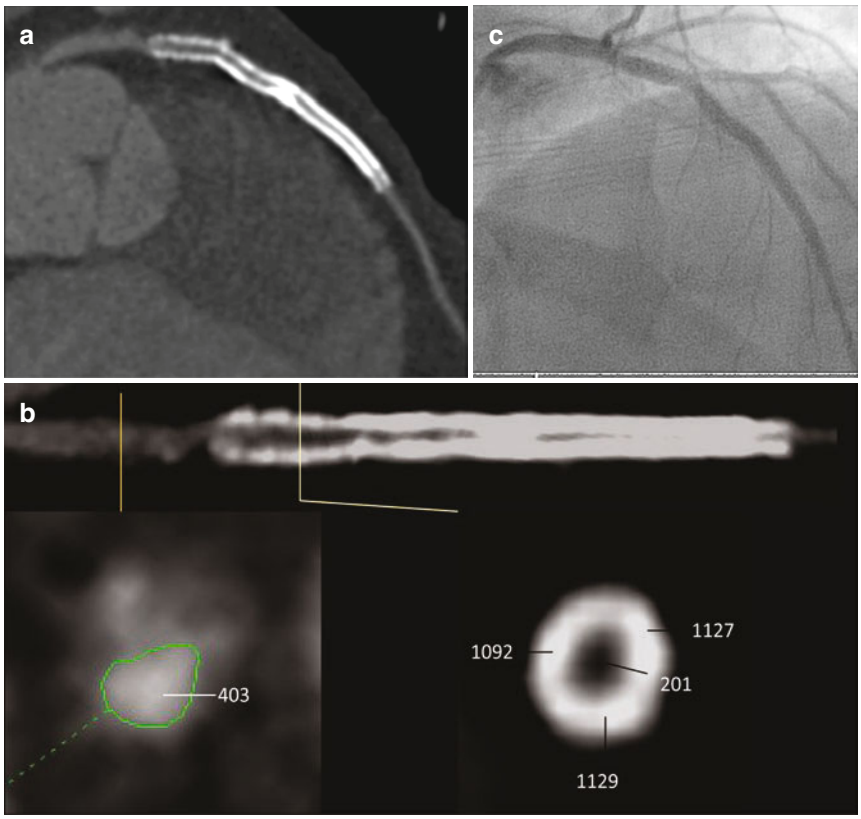

Fig. 7.1 65-year-old man with overlapping stents in the left anterior descending (LAD) artery and pseudo in-stent restenosis (ISR). (**a**) Curved multiplanar reconstruction of the LAD, demonstrating stent hypodensity in the proximal half. (**b**) Straightened multiplanar reconstruction (*top*) and cross-sections demonstrating markedly decreased Hounsfield units in the stent lumen secondary to shadowing by adjacent densely calcified plaque mimicking ISR (*right*). The intra-stent Hounsfield units are much lower than the preceding nonstented area (*left*). (**c**) Catheter angiography demonstrating the absence of ISR

Calcified Plaque Obscuring and Mimicking Stents

Densely calcified plaque may be so extensive that it may obscure stents. Cross-sectional images will usually reveal the underlying struts and facilitate identification of the heavily calcified stent. Rarely, calcium deposition may be so uniformly severe that it mimics a stent, even in cross section (Fig. 7.2).

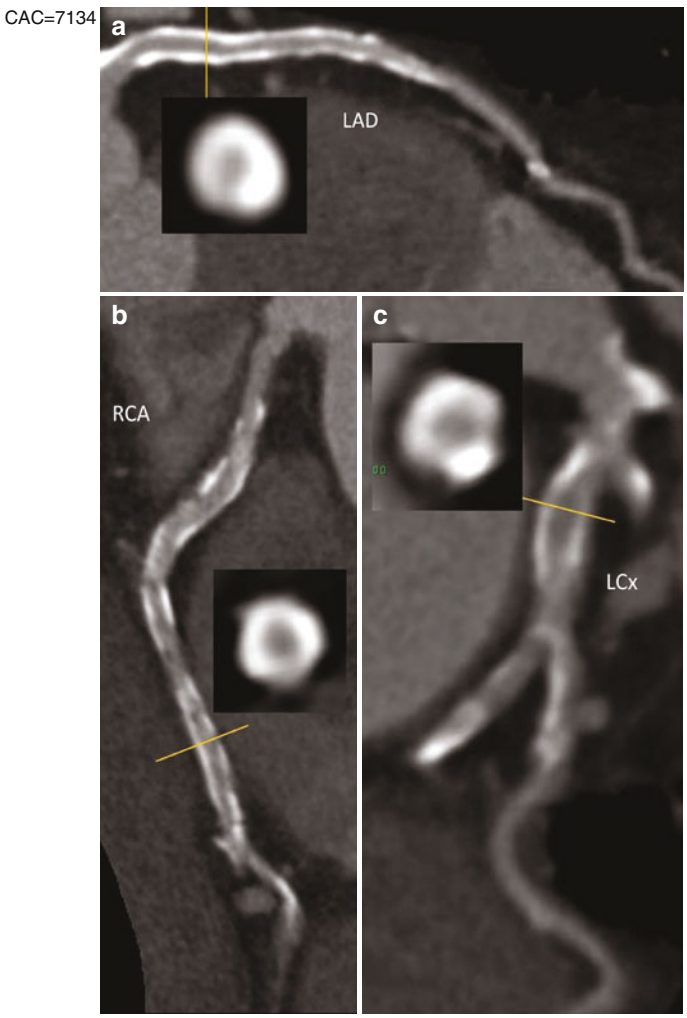

Fig. 7.2 Seventy two years old man with extensive calcified plaque (coronary calcium score of 7134) mimicking stents. Curved multiplanar reconstructions of the nonstented LAD (**a**), right coronary artery (RCA) (**b**) and left circumflex (LCx) (**c**) with cross-section insets demonstrate extensive calcified plaque indistinguishable from calcium superimposed on stents

CTA Applications

In-Stent Restenosis

Luminal compromise after intracoronary stent implantation is most often due to neointimal tissue proliferation, dependent on the clinical and anatomical characteristics of the patient and the initial lesion, as well as upon implantation technique and the type of stent. These issues have been extensively investigated [4, 5].

The accuracy of 64-slice CTA for ISR was summarized in a meta-analysis of 18 studies involving 1300 patients and 2003 stents [2]. The following results were obtained: sensitivity, 89.7%; specificity, 92.2%; positive predictive accuracy, 72.5%; negative predictive accuracy, 97.4%; total accuracy, 91.9%; unevaluable stents, 9.6%. Evaluability increased with larger diameter stents, thinner struts, and cobalt chromium and nonoverlapping stents. The sensitivity and specificity for ISR detection, as well as for detection of obstructive disease in general, are superior to those for non-invasive stress testing, including stress electrocardiography, myocardial perfusion imaging, and stress echocardiography, both in comparison of meta-analyses of the technologies individually [6] as well as in head-to-head comparisons of CTA with nuclear testing [7–9] and electrocardiography [10] in the same individuals.

The positive predictive accuracy of only 72.5% reflects the low ISR incidence in drug-eluting stents [4]. Consequently, patients with a higher pretest likelihood of ISR based on recurrent symptoms within a year or with particularly complex stenting procedures with a higher expected ISR rate are more likely to benefit from CTA than asymptomatic patients with remote and straightforward stenting. Qualitative, semiquantitative, and quantitative approaches have been used, with similar results [2]. As discussed above, contrast hypodensity comparisons to denser intrastent areas, and to immediately prestent and post-stent contrast, are the hallmark of the qualitative and semiquantitative approaches.The classic ISR appearance is shown in Fig. 7.3. The hypodensity is

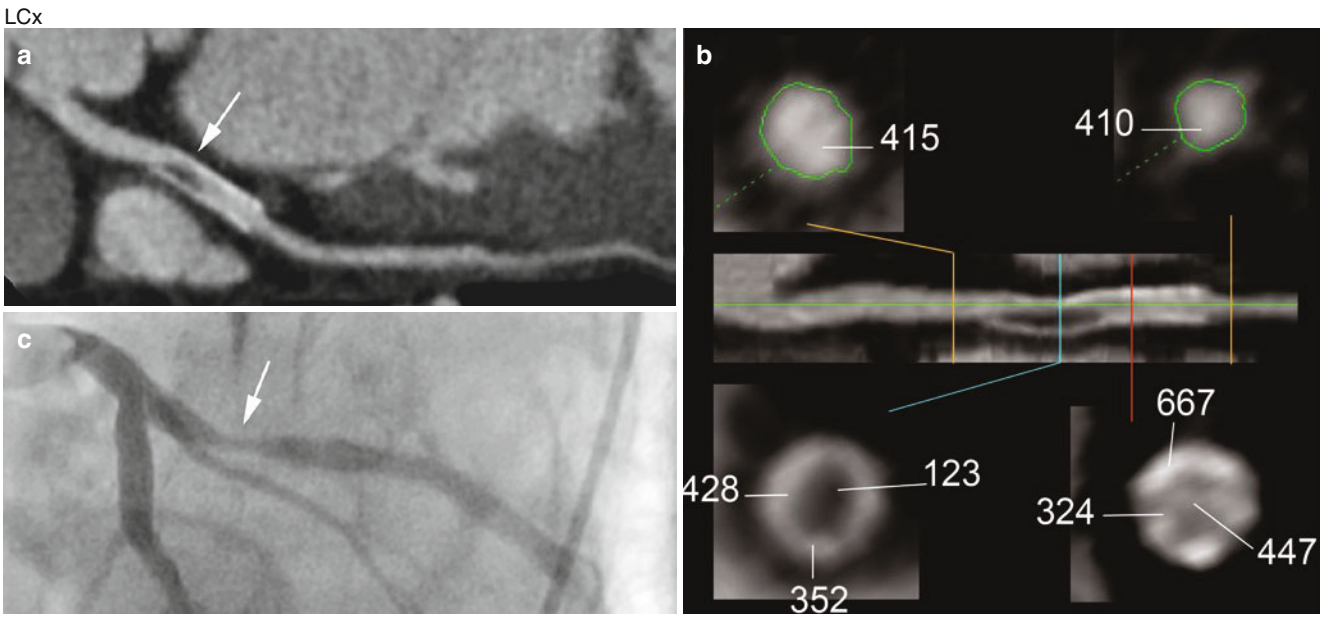

Fig. 7.3 Fifty five years-old man with recurrent chest pain and ISR 4 months after Taxus 3.5 × 16 stenting of the proximal LCx. Curved multiplanar reconstruction of the LCx (**a**) reveals severe stent hypodensity consistent with significant ISR. Straightened multiplanar reconstruction (**b**) reveals normal contrast densities in nonstented proximal (*top left*) and distal (*top right*) cross sections. Stent density in the area of ISR (*bottom left*) is less than in the normal part of the stent (*bottom right*) and the nonstented areas. Catheter angiography (**c**) confirms the severe ISR

obvious, and is confirmed by comparison of intrastent HU in the ISR area to other intrastent areas and to contrast before and after the stent.

The superior sensitivity and specificity of CTA for ISR, compared with stress testing for the detection of obstructive disease, as discussed above [6–10], offers an alternative for the evaluation of stented patients in the emergency department, as illustrated in Fig. 7.4.

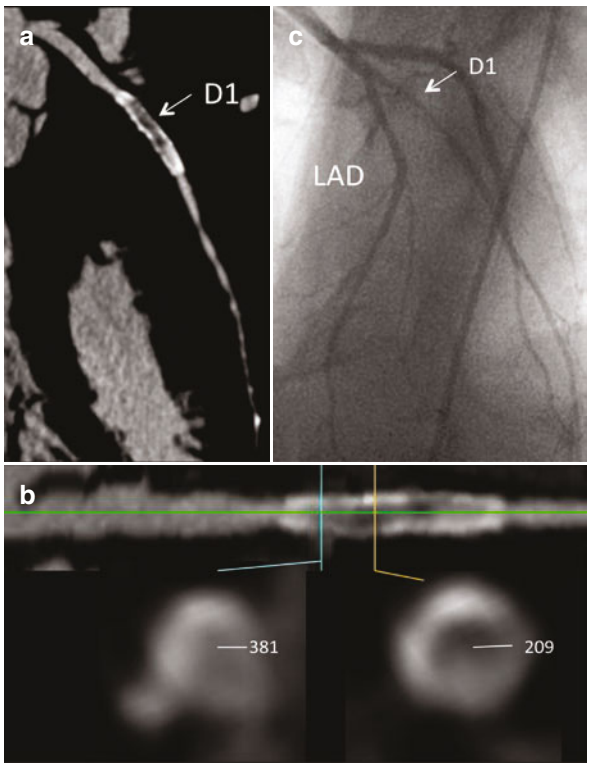

Fig. 7.4 Sixty years old man in the Emergency Department with atypical chest pain, 6 months after placement of a large first diagonal stent of an unknown type. (**a**) Curved multiplanar reconstruction of the first diagonal (D1) reveals severe stent hypodensity consistent with significant ISR. (**b**) On straightened multiplanar reconstruction, stent density in the area of ISR (*bottom right*) is less than in the normal part of the stent (*bottom left*). (**c**) Catheter angiography confirmed the severe ISR

Stent Fracture and Overlap Failure

Until recently, the prevalence of stent fracture or overlap failure was thought to be about 1–2%, vastly underestimated. Hecht et al. [3] evaluated 384 stents in 143 patients who underwent catheter angiography. A stent gap by CTA, defined as an obvious strut separation with HU less than 300 in the gap, was noted in 16.9% of stents, compared with 1% identified by catheter angiography. It was associated with 28% of ISR, and ISR was found in 46% of stent gaps. These authors concluded that in single stents, a stent gap represented fracture; in overlapped stents, fracture or overlap failure was postulated. There were no identifiable predisposing factors. The very significant association with ISR emphasized the importance of identifying stent gaps; the absence of eluting drug in the gap may have been the causal mechanism for ISR in these patients.

The infrequent identification of stent gaps by catheter angiography relates to insufficient sampling. Successful detection of stent fracture or overlap failure by catheter angi-

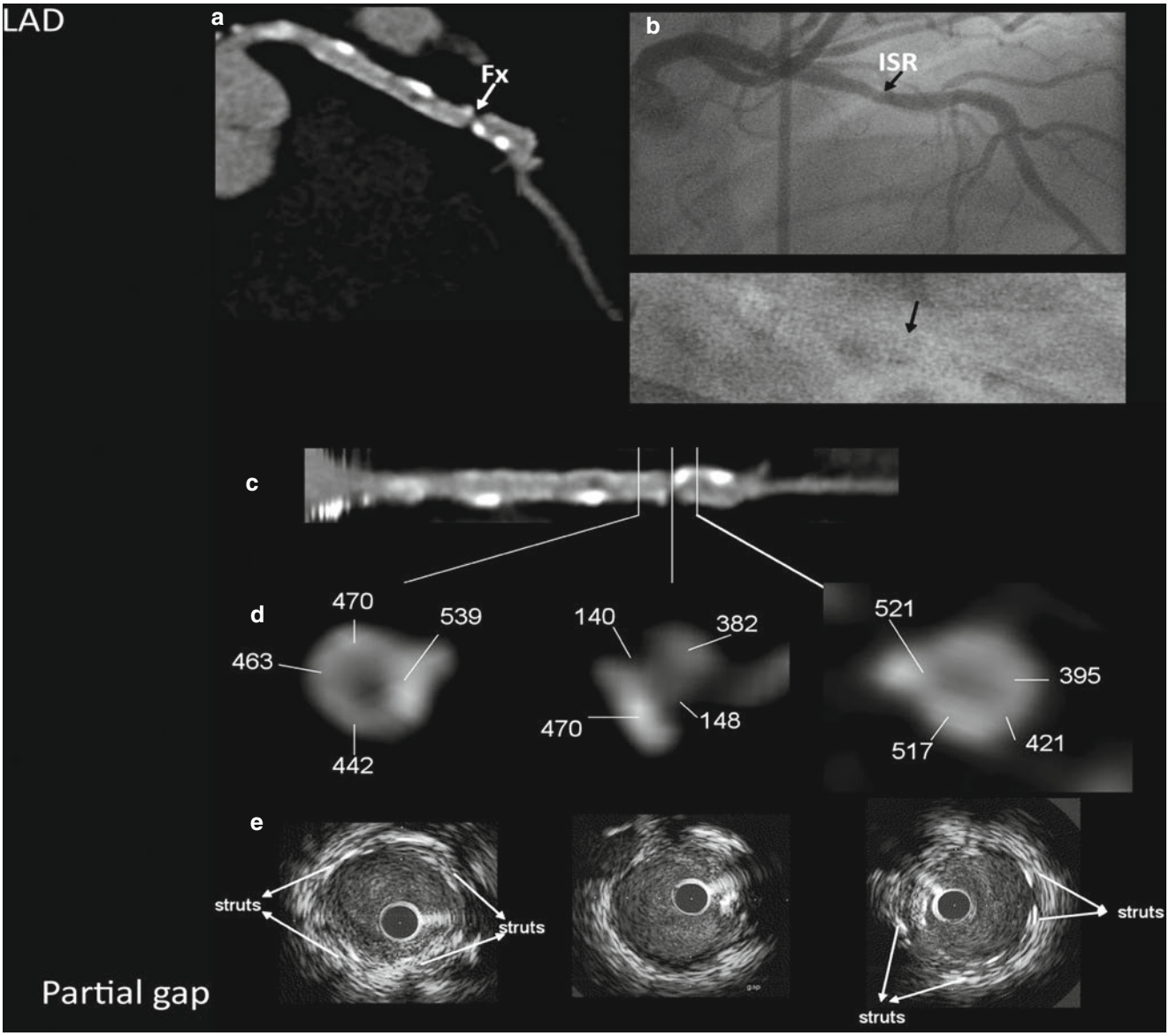

Fig. 7.5 Fifty two years old man with chest pain and stent fracture 1 year after Taxus 3.5 × 32 mm stenting of the proximal to mid LAD artery. (**a**) Curved multiplanar reconstruction of the LAD with fracture (Fx) in the distal stent. (**b**) Catheter angiography revealed mild ISR (*top*) and a partial stent gap (*bottom*). (**c**, **d**) Straightened multiplanar reconstruction and cross sections demonstrated 148 HU density in the fracture area, below that of stents, confirming the absence of struts. Because there was only a single stent, the gap indicated fracture rather than overlap failure. (**e**) Intravascular ultrasound confirmed the absence of strut material at the fracture site

ography is directly related to the gap length and inversely related to deviation of image acquisition from the plane perpendicular to the gap; overlap of strut edges on nonperpendicular acquisitions may render the gap invisible. Stent gaps in overlapped stents have been attributed to fracture rather than overlap failure, but intravascular ultrasound (IVUS) is infrequently used to confirm successful stent overlap; rather, reliance is placed on the inadequate two or three acquisitions to confirm stent placement. Successful overlap is then assumed, but the insufficient sampling makes adequate analysis unlikely. The three-dimensional quality of CTA renders it immune to the issue of image acquisition; the gap site can be inspected from every conceivable angle.

In support of a higher incidence of fracture than previously appreciated, an autopsy series of 177 consecutive stents yielded 29% with stent fracture; predisposing factors were sirolimus stents, overlapped stents, longer length, and duration of implantation [11]. Examples are provided in Figs. 7.5, 7.6, 7.7, and 7.8. Stent fracture in a single, nonoverlapped stent (Fig. 7.5) was associated with mild ISR, possible fracture on catheter angiography, and clear confirmation by IVUS. An obvious stent gap in overlapping stents with critical ISR (Fig. 7.6) was, remarkably, not associated with catheter angiography demonstration of separation, undoubtedly the result of insufficient sampling.

The complexity inherent in stent gap diagnosis is well illustrated in the overlapping stents in Fig. 7.7. The distal ISR is associated with a fracture, confirmed by catheter angiography. The proximal ISR is not, and several other mid to distal areas have neither ISR nor a gap, despite the visual

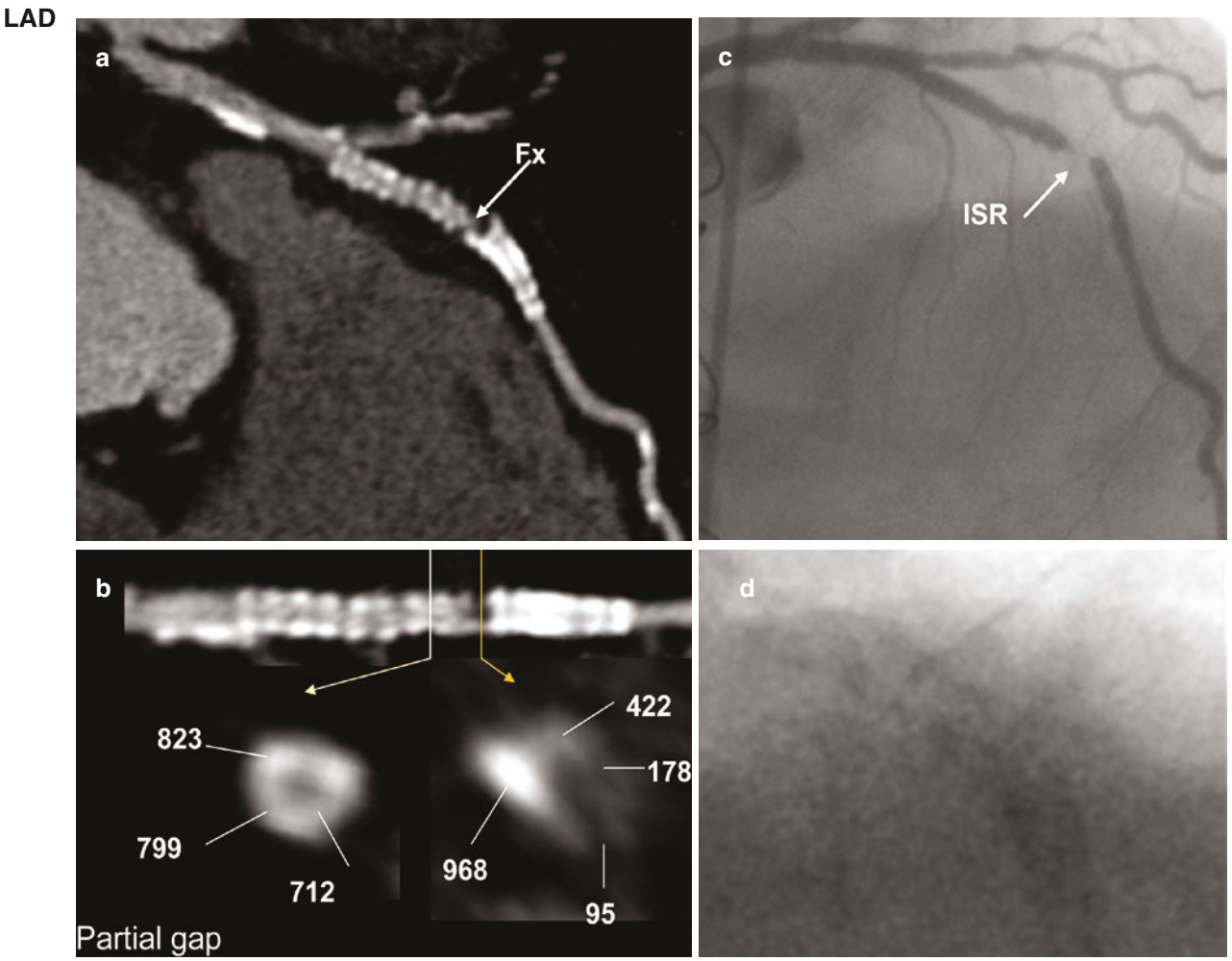

Fig. 7.6 Seventy two-year-old woman with chest pain, stent fracture/overlap failure, and ISR 6 months after overlapping LAD stents of unknown type. (**a**) Curved multiplanar reconstruction of the LAD with fracture/overlap failure and severe ISR at the overlap site. (**b**) Straightened multiplanar reconstruction and cross sections of the normal stent (*left*) and the gap area (*right*) confirm the absence of stent material in the gap (178 HU). (**c**) Catheter angiography revealed severe ISR, but there was no apparent stent gap (**d**) reflecting the insufficient sampling of catheter angiography. Stent fracture cannot be definitively distinguished from overlap failure, but the location at a hinge point suggests that fracture is the more likely diagnosis

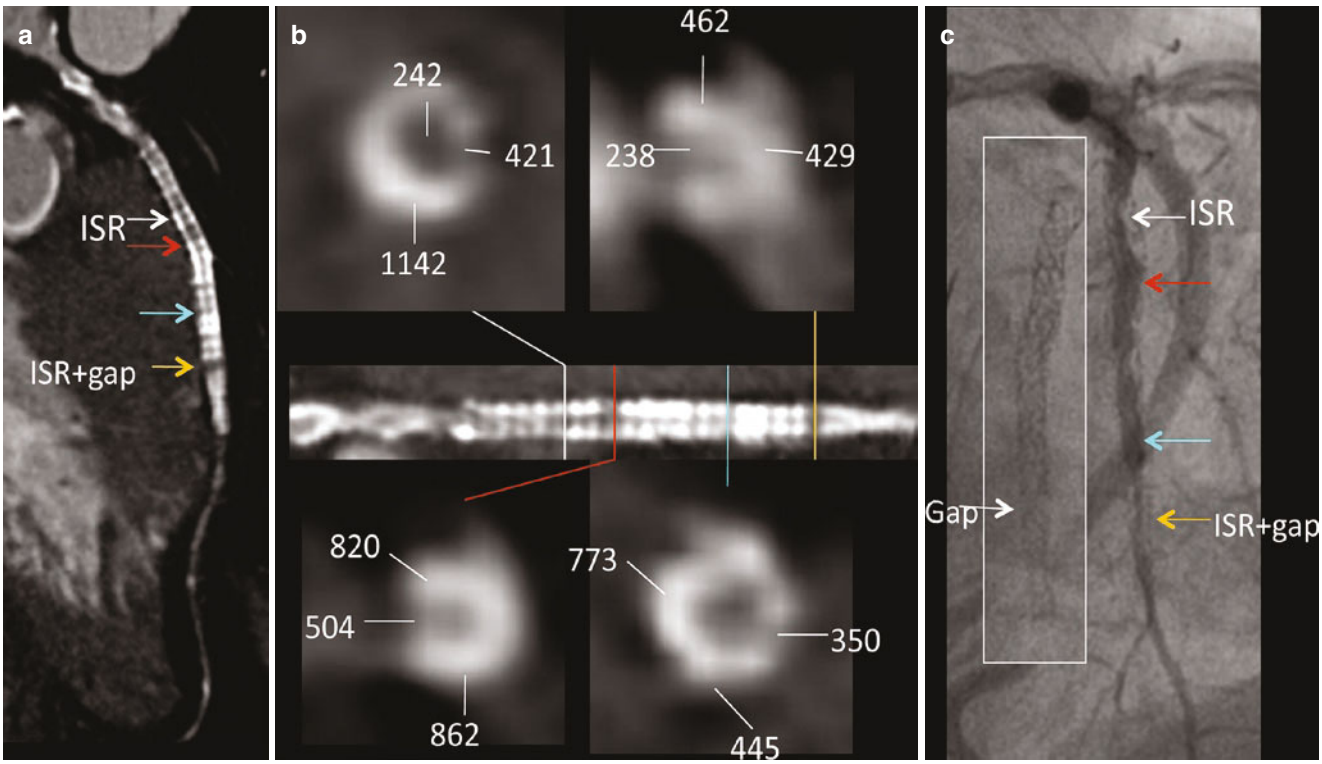

Fig. 7.7 Sixty eight-year-old man with chest pain, stent fracture, and ISR 8 months after placement of overlapping LAD stents of an unknown type. (**a**) Curved multiplanar reconstruction of the LAD reveals multiple areas of ISR (*white and gold arrows*), a single fracture/overlap failure (*gold arrow*), and two areas that visually suggest a gap (*red and blue arrows*). (**b**) Straightened multiplanar reconstruction and cross sections confirm ISR in the proximal and distal areas (*white and gold lines*). The apparent gaps have Hounsfield units (>300) not compatible with the absence of struts (*red and blue lines*). (**c**) Catheter angiography confirms the multiple ISR areas and the distal gap (*inset*)

suggestion of a separation. This apparent gap is attributable to relative hypodensity compared with adjacent areas that are more calcified, but the absolute HU are not compatible with the absence of struts.

Multiple gaps may occur. In the case shown in Fig. 7.8, complete stent separation was noted in the mid portion of the "full metal jacket" right coronary artery with mild gap stenosis, and in the distal stent with significant ISR. Whether these gaps represent fracture or overlap failure cannot be determined. Severe ISR was present in an intact area as well. The distal stent gap was visible on catheter angiography.

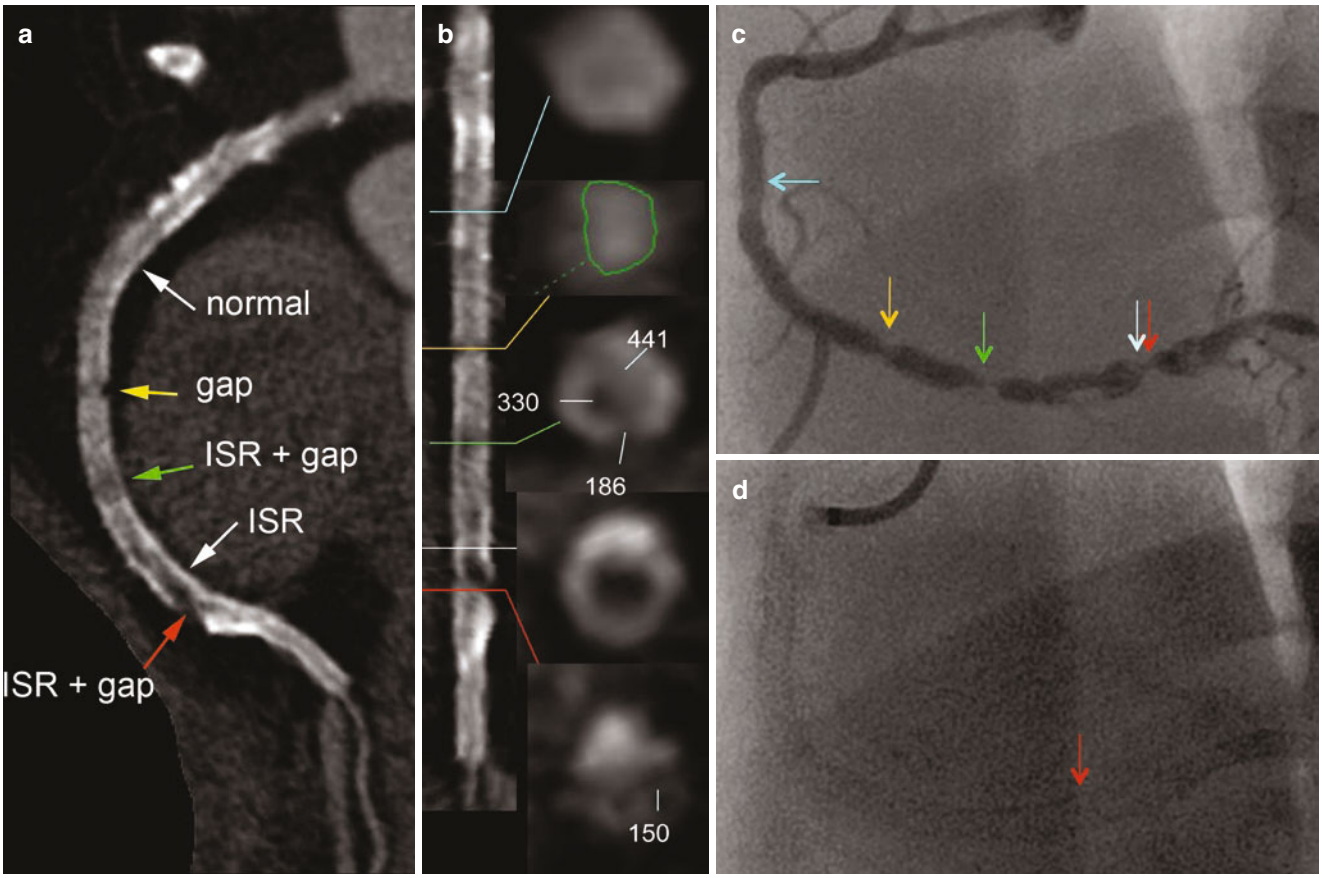

Fig. 7.8 Seventy one-year-old man with shortness of breath and multiple stent fractures and ISRs 7 months after right coronary artery stents of an unknown type. (**a**) Curved multiplanar reconstruction of the RCA reveal multiple areas of fracture or overlap failure (*gold, green and red arrows*), and ISR (*green, white and red arrow*s). (**b**) Straightened multiplanar reconstruction and cross sections reveal the absence of ISR in the proximal area (*blue*). The proximal fracture overlap area (*gold*) is entirely uncovered and not significantly narrowed. The other fracture overlap areas (*green and red*) demonstrate areas of absence of stent material in the gap (<300 HU). (**c**, **d**) Catheter angiography reveals multiple areas of severe ISR (*green, white, and gold arrows*) and strut separation only at the most distal fracture overlap site (*red arrows*)

Late Stent Thrombosis

Most stent thrombosis occurs within the first 30 days of the procedure [12]; late stent thrombosis occurs 30 days to 1 year after stent placement; very late stent thrombosis occurs more than one year after stenting. The histopathological explanation is delayed (or absent) re-endothelialization of struts in the setting of drug-eluting stents. The incidence of late stent thrombosis is 0.6%/year but may be higher if a broader definition of late stent thrombosis is used [13]. The clinical presentation of stent thrombosis may be as dramatic as an acute infarction, but more subtle presentations may not come to clinical attention until after the event.

The hallmarks of acute late stent thrombosis are illustrated in a 60-year-old woman (Fig. 7.9) who presented to the emergency department with atypical chest pain 4 months after sirolimus stenting of the LAD; she had a nondiagnostic EKG and normal troponin. Stent occlusion with collateral filling of the distal vessel, confirmed by angiography, was noted, as well as the pathognomonic full-thickness myocardial hypodensity in the distribution of the occluded vessel, diagnostic of an acute myocardial infarction.

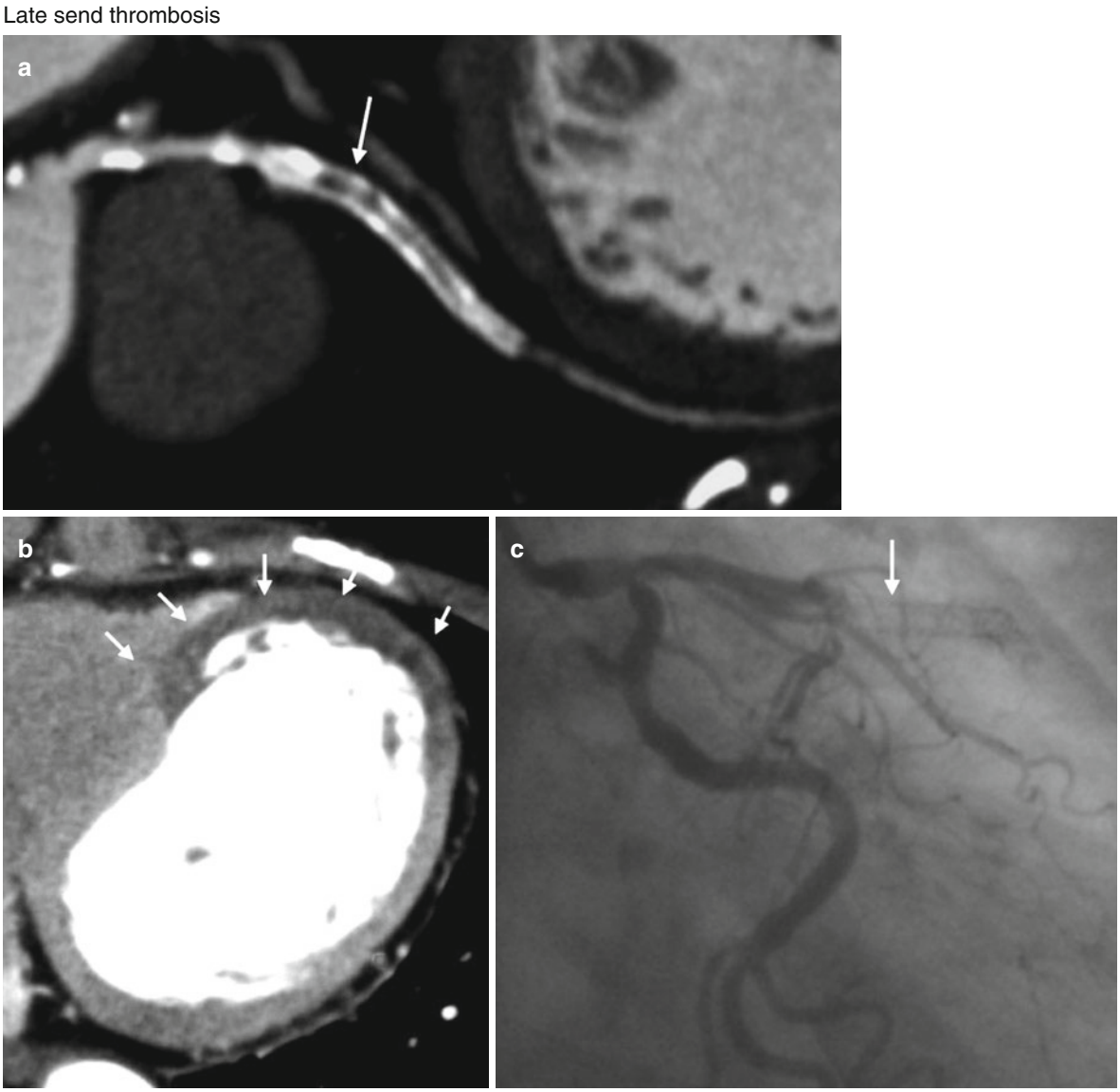

Fig. 7.9 Sixty-year-old woman in the Emergency Department with chest pain and late stent thrombosis 4 months after placement of overlapping LAD Taxus 3.0 × 16 and 2.5 × 24 stents. (**a**) Curved multiplanar reconstruction of the LAD demonstrates total stent occlusion characterized by severe hypodensity (*arrow*) with distal collateral filling. (**b**) Full-thickness septal and apical hypoperfusion (*arrows*) pathognomonic of acute myocardial infarction is present, as opposed to the subendocardial hypoperfusion and thinning characteristic of a remote event. (**c**) Catheter angiography reveals stent occlusion (*arrow*)

Jailed Branches

Side branches may be "jailed" after treatment of a bifurcation lesion. The degree of stenosis in the ostia of these side branches may be underappreciated at the time of treatment. Additionally, provisional treatment of the side branch often involves balloon angioplasty alone, which may not produce a durable result in the side branch ostium. Ostial stenoses of large first diagonals jailed by LAD stents are clearly demonstrated in Figs. 7.10 and 7.11, despite the proximity of heavily calcified stents. Of more potential consequence is significant stenosis of a major jailed vessel, such as the ostial circumflex by an LAD stent extending into the left main coronary artery (Fig. 7.12).

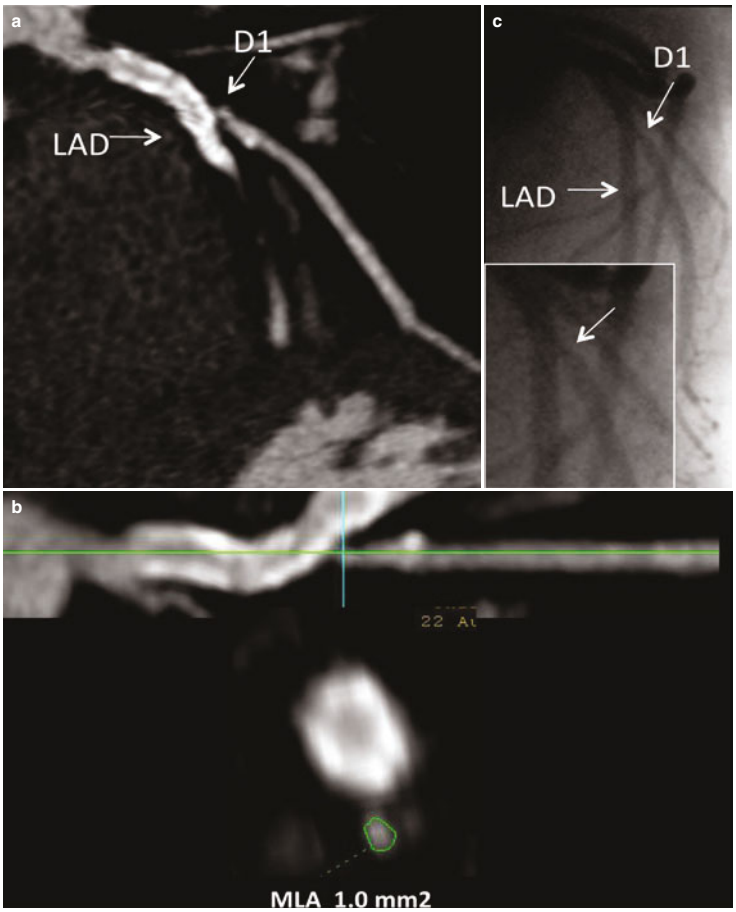

Fig. 7.10 Fifty five-year-old man with atypical chest pain and a significantly stenotic jailed D1, 2 months after Taxus 3.5 and 3.0 × 16 stenting of the LAD. (**a**) Curved multiplanar reconstruction demonstrates severe ostial stenosis of the jailed D1. (**b**) Cross-sectional analysis of the straightened multiplanar reconstruction shows a markedly reduced minimum luminal area (MLA). (**c**) Catheter angiography confirms the severe ostial stenosis (*magnified inset*)

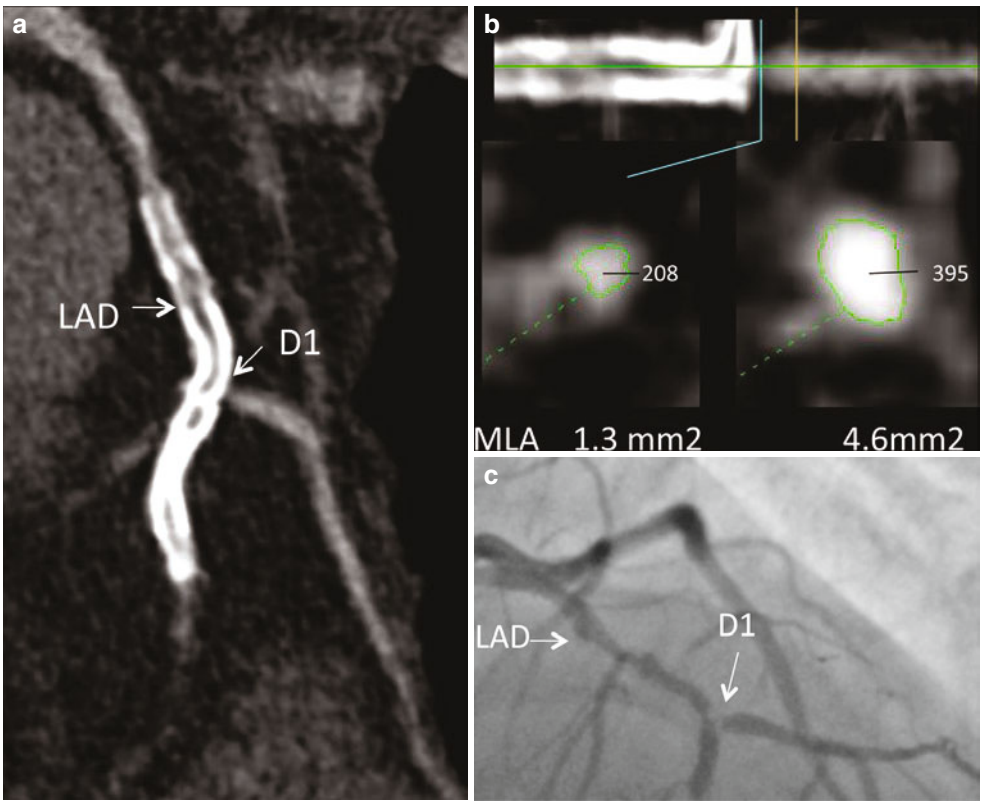

Fig. 7.11 Subtotally occluded jailed D1 6 months after placement of an LAD stent of an unknown type. (**a**) Curved multiplanar reconstruction demonstrates severe ostial stenosis of the jailed D1. (**b**) The cross-sectional analysis of the straightened multiplanar reconstruction shows a markedly reduced MLA. The luminal hypodensity in the stenotic area, compared with the normal area, is diagnostic of a subtotal occlusion. The adjacent very densely calcified stent did not interfere with the diagnosis. (**c**) Catheter angiography confirmed the subtotal D1 occlusion

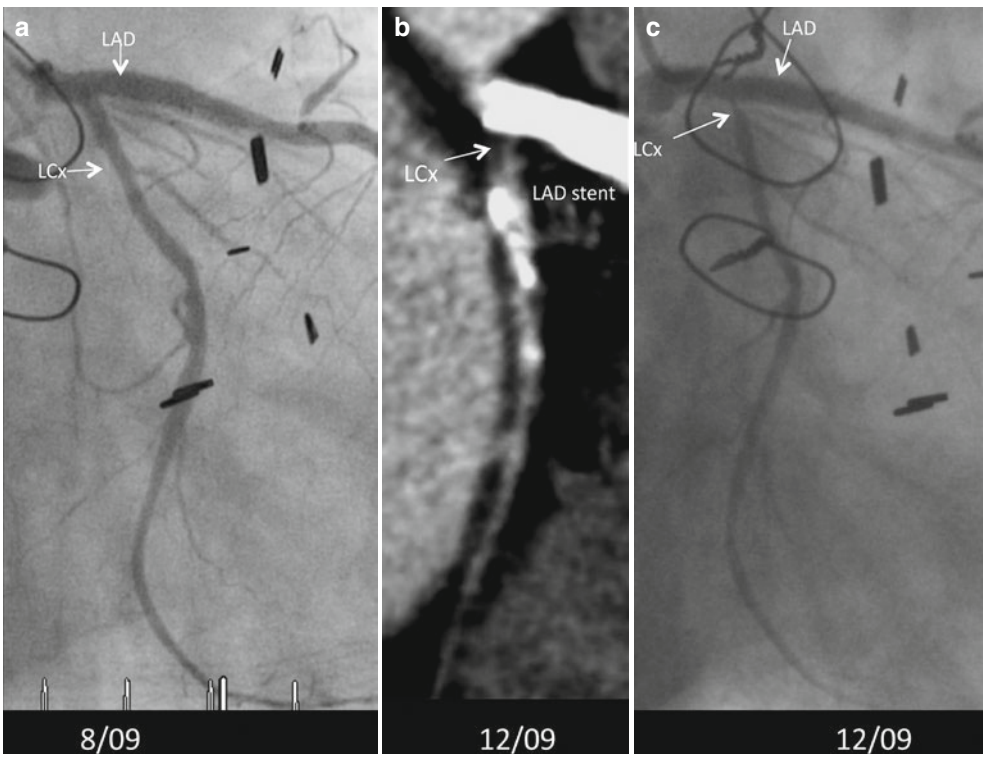

Fig. 7.12 Severe ostial stenosis in the LCx 4 months after Xience 3.5 × 15 stenting of the LAD. (**a**) Catheter angiography immediately after placement of the ostial LAD stent reveals a normal LAD and LCx. (**b**) Four months later, after recurrent chest pain, curved multiplanar reconstruction revealed severe ostial stenosis in the LCx, which is jailed by extension of the LAD stent into the left main coronary artery. (**c**) Catheter angiography confirms the ostial LCx stenosis

Edge Stenosis

The incidence of edge restenosis is 5–6% for paclitaxel-eluting, sirolimus-eluting and bare metal stents in a small IVUS subgroup analysis of drug-eluting stent trials [14, 15]. Residual plaque burden at the stented edge seems to be the most important risk factor for edge restenosis. Vessel injury due to geographic miss also plays an important role. Stenosis involving both the proximal stent edge and contiguous unstented vessel is shown in Fig. 7.13.

The proximal unstented edge may develop severe stenosis without edge ISR (Fig. 7.14). Proximal plaque shifting or intimal disruption during the catheter and stent manipulation may have been operative. Conventional ISR in the mid-stent is also noted.

More complex scenarios may occur (Fig. 7.15). Stenting the ostial LAD through a diseased (though not critically so) distal left main coronary artery may lead to the development of severe distal left main stenosis responsible for recurrent symptoms, without the more expected LAD ISR. Preprocedural CTA may alert the operator to a diseased path en route to the stenosis; if the path is traumatized, the results may be similar to Fig. 7.15.

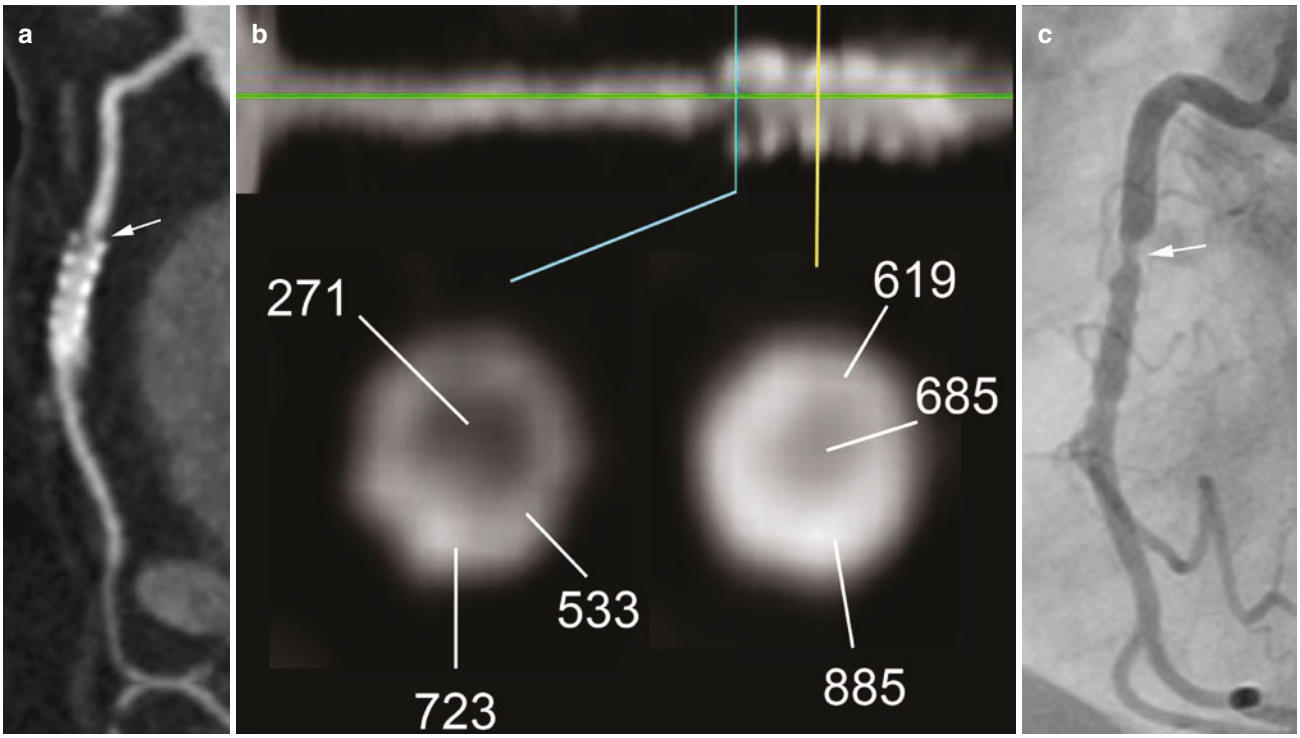

Fig. 7.13 Edge stenosis in a 69-year-old woman 1 year after stenting of the right coronary artery with a Cypher 3.0 × 13 stent. (**a**) Curved multiplanar reconstruction demonstrates stenosis in the right coronary artery just before and in the very proximal edge of the stent. (**b**) The edge stenosis is confirmed in the cross-sectional analysis of the straightened multiplanar reconstruction by demonstrating decreased Hounsfield units compared with the normal area. (**c**) Catheter angiography confirms the stenosis

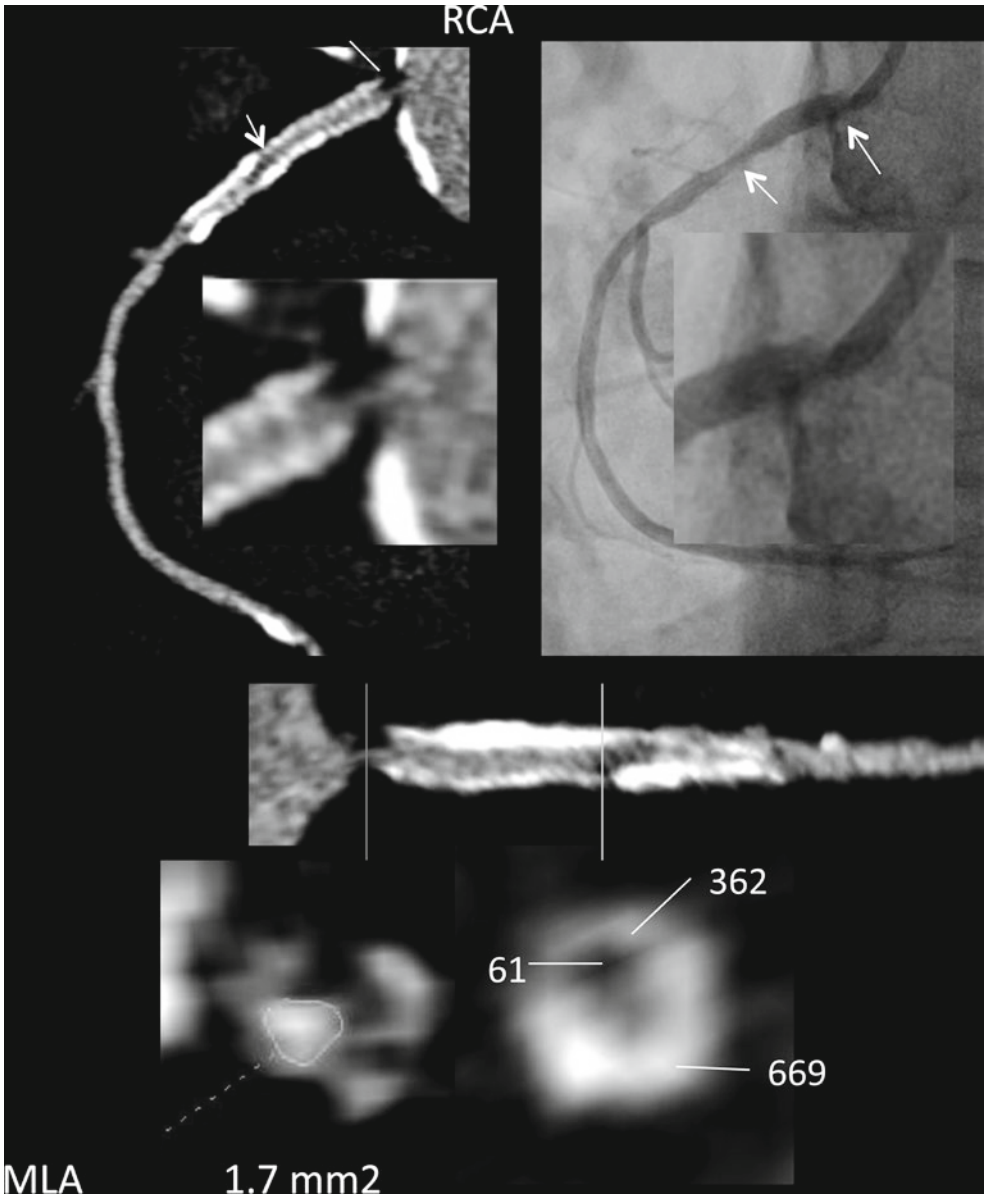

Fig. 7.14 Edge stenosis in an asymptomatic 67-year-old 1.5 years after stenting of a totally occluded right coronary artery with a Taxus 3.0 × 32 stent. (**a**) Curved multiplanar reconstruction demonstrates critical ostial edge stenosis in the RCA just before the proximal edge of the stent, without involvement of the proximal stent edge, as well as mid-stent restenosis. (**b**) The edge stenosis is confirmed in the cross-sectional analysis of the straightened multiplanar reconstruction, with a very reduced MLA of 1.7 mm^2. The ISR in the mid stent demonstrates decreased Hounsfield units. (**c**) Catheter angiography confirms the edge stenosis and mid-stent stenosis

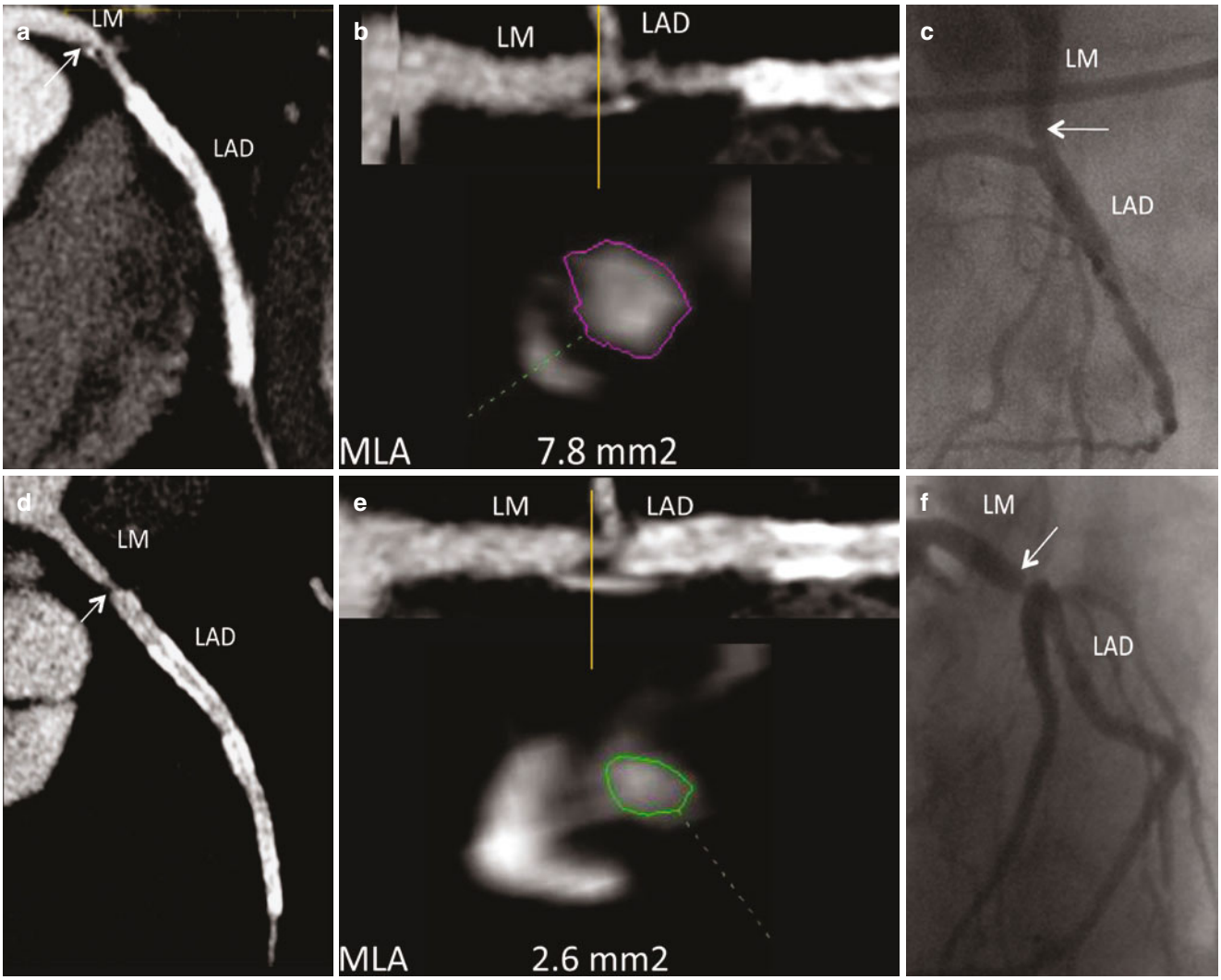

Fig. 7.15 Left main (LM) edge stenosis with recurrent chest pain 4 months after ostial LAD stenting with a Taxus 3.5 × 16 stent. (**a**) Curved multiplanar reconstruction demonstrated mild distal LM stenosis and diffuse narrowing of the ostial LAD before placement of the proximal LAD stent. (**b**) Straightened multiplanar reconstruction and cross-sectional analysis showed the MLA of the distal LM to be 7.8 mm^2 with considerable plaque. (**c**) Mild LM stenosis is noted on catheter angiography after complex stenting of the ostial LAD involving multiple wires and catheters. (**d**) After recurrent angina 4 months later, curved multiplanar reconstruction revealed critical distal LM stenosis. (**e**) Cross-sectional analysis found the area to be 2.6 mm^2. (**f**) Catheter angiography confirmed the finding. Trauma to the distal LM by multiple catheter and wire exchanges through an already diseased segment was the likely culprit

Bifurcation Stents

Double stent techniques are frequently employed a priori for particular lesion subsets and provisionally after single-stent techniques fail. These techniques invariably create complex geometry at the bifurcation, with multiple stent layers in the main vessel and at the ostium of the side branch, resulting in significant challenges in subsequent imaging and treatment. Although the literature comparing restenosis rates of bare metal stents versus drug-eluting stents in this context is not robust, it is widely accepted that drug-eluting stents significantly reduce the incidence of angiographic and clinical restenosis [16]. Regardless of the technique used, restenosis rates for bifurcation lesions are higher than rates for non-bifurcation lesions (with all other variables held constant). Restenosis occurs most often at the ostium of the side branch.

As suggested above, CTA evaluation of bifurcation stents introduces another layer of complexity by juxtaposing two potentially heavily calcified metallic structures. Nonetheless, they can usually be accurately analyzed. The frequent inability to obtain perfect apposition of the second stent may leave a gap with subsequent ISR (Fig. 7.16).

Many iterations are possible, as the more routine edge and in-stent stenoses may occur along with those unique to bifurcation stenting. The patient shown in Fig. 7.17 presented to the emergency department with recurrent chest pain several months after LAD/diagonal bifurcation stenting. CTA revealed severe proximal LAD edge stenosis; the bifurcation stents were problem-free. Stenting of the proximal LAD created a trifurcation stent scenario, which was evaluated when the patient returned with chest pain several weeks later. A clear gap was noted, reflecting apposition failure, but there was no stenosis, and the patient was discharged.

In another variation (Fig. 7.18), a subtotal ostial LAD edge stenosis was accompanied by a subtotal diagonal bifurcation stenosis. There was no gap visible at the diagonal ostium on catheter angiography, although it was clearly visible on CTA, reflecting the insufficient sampling by catheter angiography.

Both arms may be involved at the crux of the bifurcation (Fig. 7.19). In this example, ostial first marginal ISR and lack of complete apposition of the circumflex stent with associated ISR are demonstrated on the CTA. The apposition gap is suggested but not clearly demonstrated on catheter angiography, which confirms both areas of ISR.

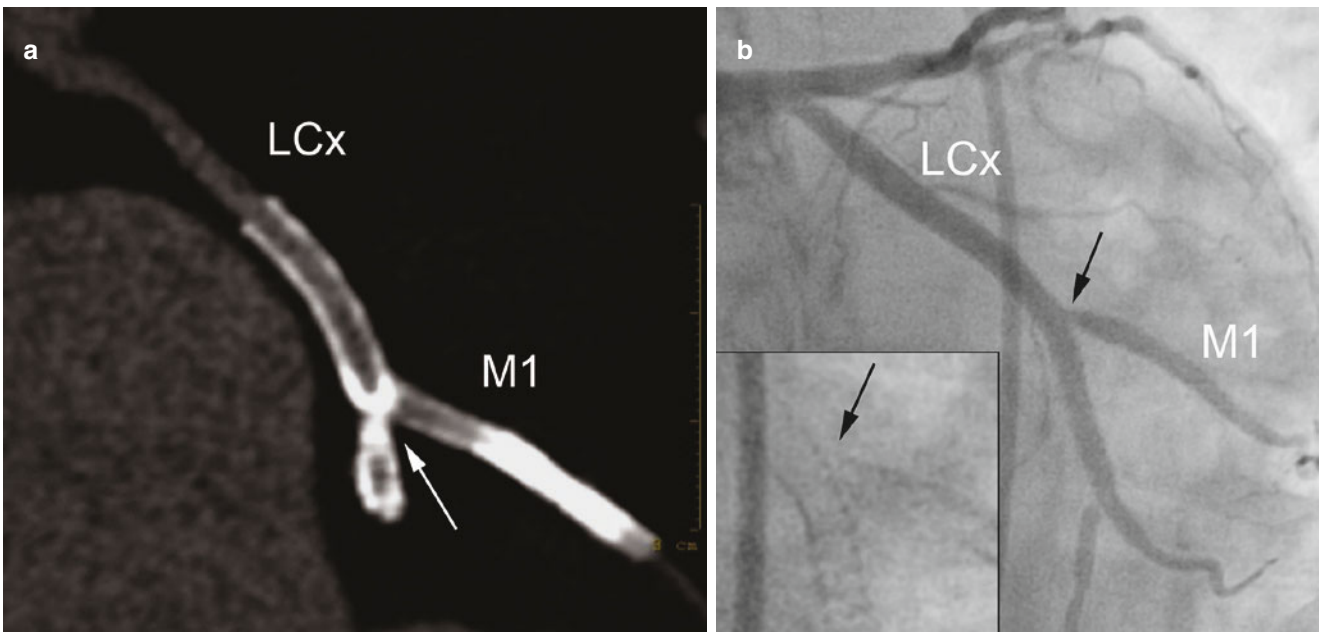

Fig. 7.16 LCx/M1 bifurcation stenosis 5 months after insertion of stents of unknown type. (**a**) Curved multiplanar reconstruction reveals hypodensity at the ostium of M1, consistent with significant stenosis. (**b**) Catheter angiography confirms the stenosis and demonstrates failure of M1 stent apposition (*inset*)

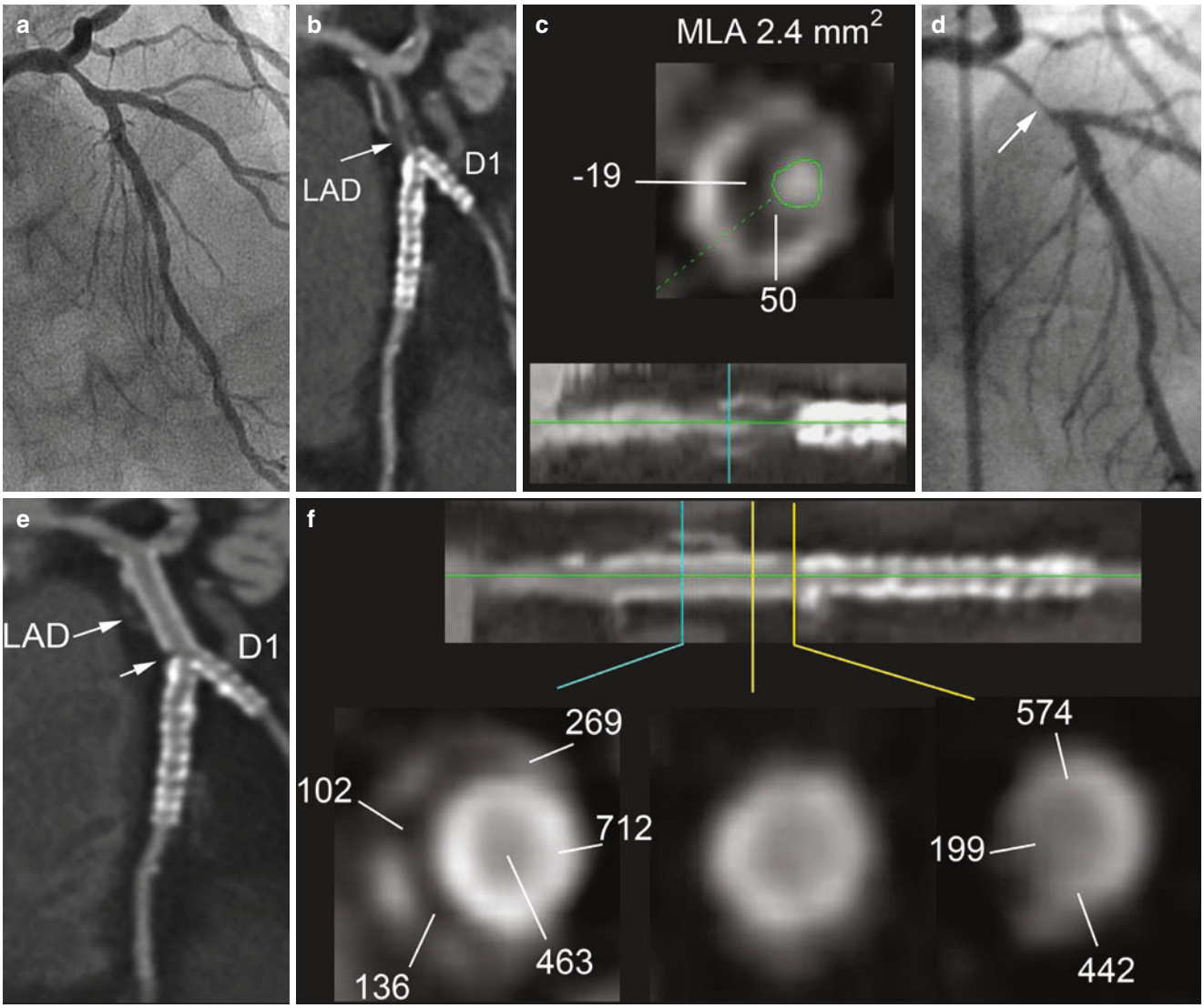

Fig. 7.17 Trifurcation stents and chest pain in the Emergency Department. (**a**) Catheter angiography after LAD (Cyper 3.0 × 18 and 3.0 × 8) and D1 (Cypher 3.0 × 8) stenting. The D1 bifurcation stenting demonstrated a normal proximal LAD edge. Several months later, the patient presented to the Emergency Department with recurrent chest pain. (**b**, **c**) Curved multiplanar reconstruction revealed severe proximal LAD edge stenosis with an MLA of 2.4 mm^2 and a lipid core (−19 HU) adjacent to the lumen; the bifurcation stents were problem-free. (**d**) Catheter angiography confirmed the diagnosis, and the edge stenosis was stented. Several weeks later, the patient returned to the ED with chest pain. (**e**) Curved multiplanar reconstruction demonstrated a trifurcation stent scenario with patency of all the stents and absence of edge and in-stent stenosis. Apposition failure of the proximal stent was noted (*arrow*). (**f**) Cross-sectional analysis confirmed the finding, with <300 HU in the gap area (*right*). Normal stent area (*middle*) and a proximal stent area with peri-stent plaque (*left*) are also shown. As there was no stenosis, the patient was discharged

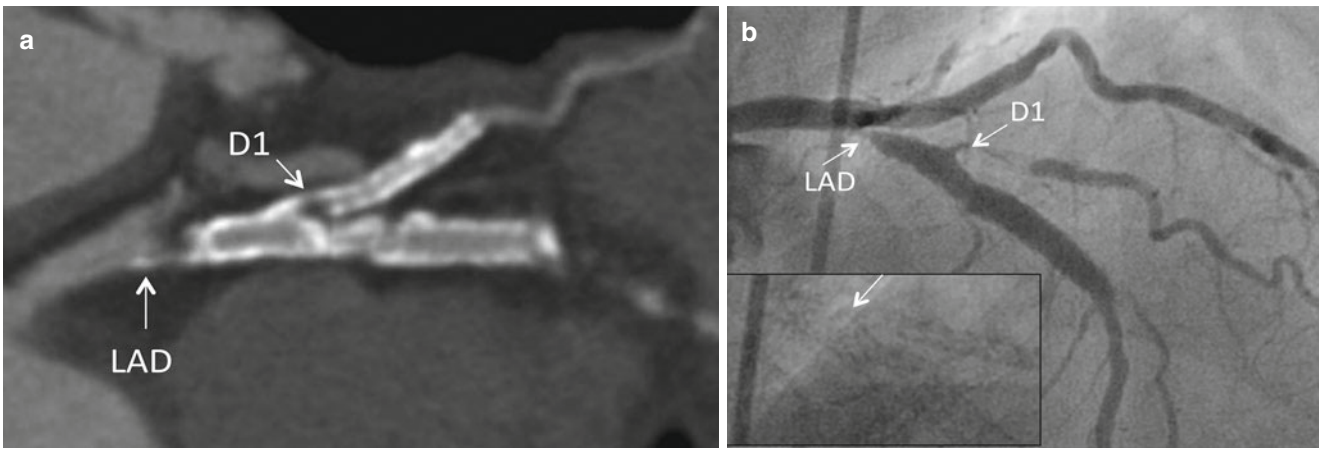

Fig. 7.18 Bifurcation and edge stenoses 7 months after LAD and D1 stents of unknown type. (**a**) Curved multiplanar reconstruction revealed severe ostial LAD edge stenosis and severe D1 bifurcation stenosis with a gap consistent with apposition failure. (**b**) Catheter angiography confirmed both findings. A gap was not seen (*inset arrow*), reflecting insufficient sampling

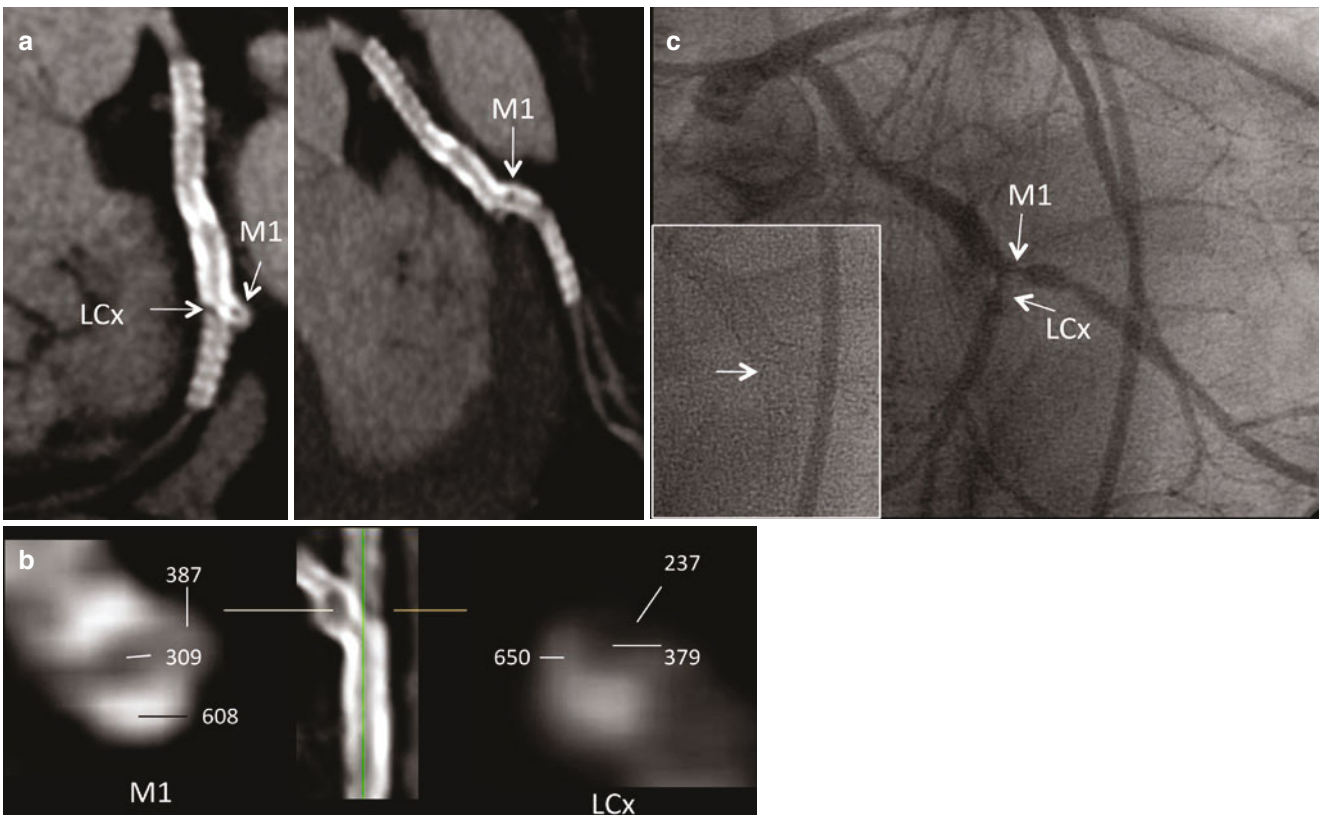

Fig. 7.19 Bifurcation stenoses in both M1 and LCx stents of unknown types. The patient experienced recurrent chest pain 8 months after bifurcation stenting. (**a**) LCx and M1 bifurcation stents are seen on the curved multiplanar reconstruction. Hypodensity consistent with significant bifurcation stenoses is noted in both the M1 and LCx (*arrows*), and the gap at the proximal edge of the LCx stent is consistent with apposition failure. (**b**) Cross-sectional analysis of the straightened multiplanar reconstruction demonstrates the decreased Hounsfield units of the luminal hypodensities and of the LCx apposition failure (237 HU, below stent strut density). (**c**) The severe LCx and M1 stenoses were confirmed on catheter angiography. The apposition gap is suggested but not clearly demonstrated (*inset, arrow*)

Inadequate Expansion

Inadequate stent expansion is an independent predictor of both restenosis and thrombosis [17–19]. It may be the result of inadequate vessel preparation before stenting or of failure to deploy stents at high pressure and ensure adequate expansion by high pressure post-dilatation. Inadequate expansion is very often difficult to appreciate by cineangiography alone and is best demonstrated by IVUS. Post-intervention IVUS is often not employed, even by experienced operators, however, to ensure proper stent expansion [20].

Inadequate expansion is easily observed in Fig. 7.20. Moderate proximal edge stenosis is followed by clear narrowing of the distal portion of the stent. Catheter angiography and IVUS confirmed the findings. Excessive calcification may render interpretation difficult.

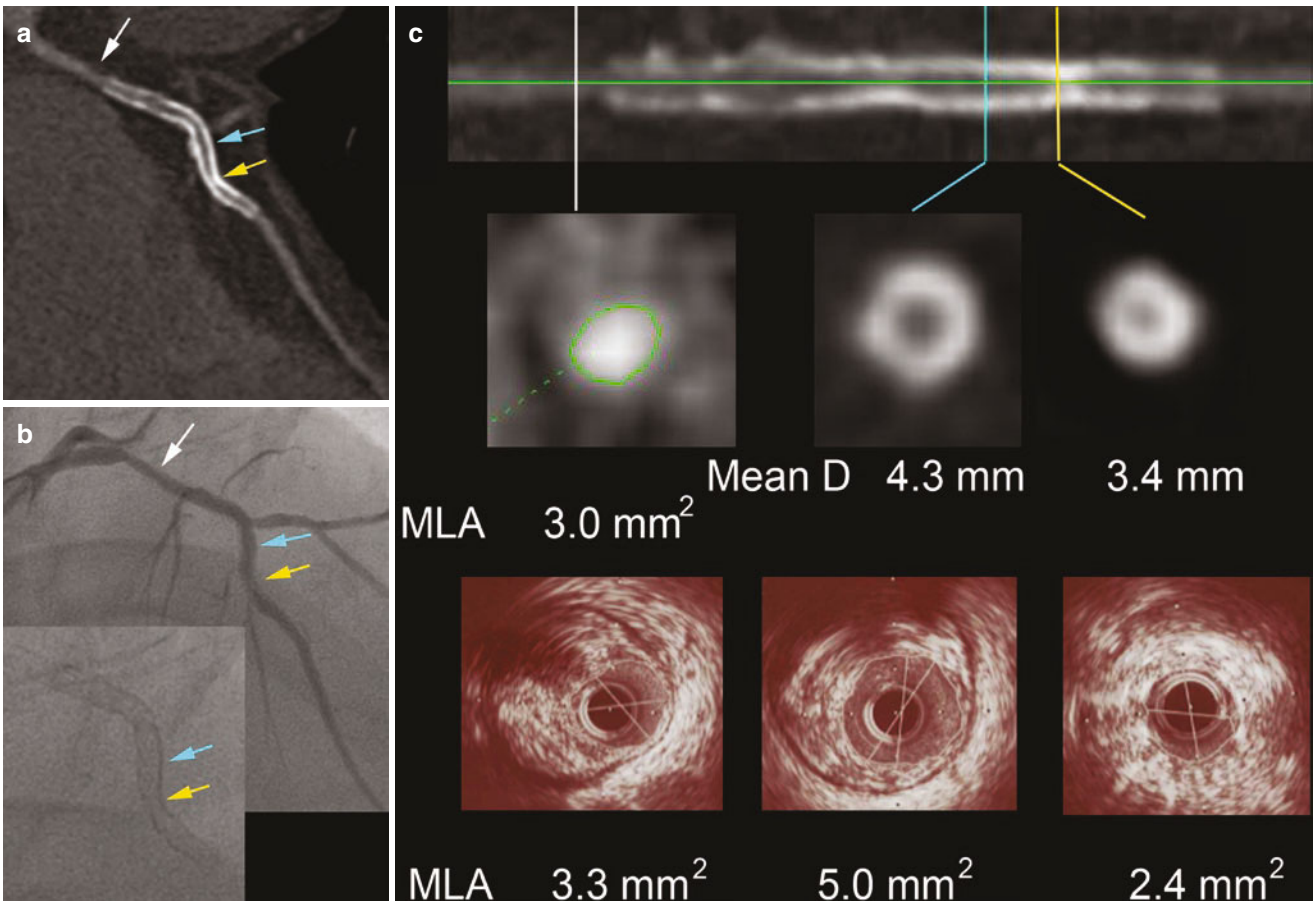

Fig. 7.20 Inadequate expansion and edge stenosis in a 56-year-old man with recurrent chest pain 3 months after placement of an LAD stent of an unknown type. (**a**) Curved multiplanar reconstruction clearly demonstrates inadequate expansion (*gold arrow*) as well as edge stenosis (*white arrow*) and a normal stent area (*blue arrow*). (**b**) Catheter angiography confirms the stenotic areas and the inadequately expanded stent (*inset*). (**c**) Cross-sectional analysis of the straightened multiplanar reconstruction (*middle*) demonstrates the reduced mean diameter of the underexpanded area (3.4 vs 4.3 mm for the more normal area) and the reduced MLA of the edge stenosis. IVUS (*bottom*) reveals the severely reduced MLA of the inadequately expanded area (2.4 mm^2) compared with the more normal area (5.0 mm^2) and confirms the severity of the edge stenosis (3.3 mm^2)

Aneurysms

The reported incidence of coronary artery aneurysms after placement of both bare metal and drug-eluting stents has increased in the angioplasty and stent era, due both to sampling frequency and to causality by stent placement, with an incidence of 0.3–6% after percutaneous coronary intervention [21]. The infrequent clinical sequelae of coronary artery aneurysms include rupture, spontaneous dissection, vasospasm, distal embolization, and thrombosis, but their natural history and optimal treatment are still not clear.

Multiple patterns are identified by CTA. The variety of presentations includes an ostial stent aneurysm with adjacent ISR and fracture (Fig. 7.21); proximal, mid, and distal aneurysms without ISR but with a gap at the mid-stent aneurysm site (Fig. 7.22); and a mid-stent aneurysm with peri-stent plaquing (Fig. 7.23).

Peri-Stent Plaque

Plaque external to the stent has been described but its significance is unknown [22]. It must be distinguished from stent aneurysms. The HU should provide clear differentiation: peri-stent plaque densities will almost always be higher and/or lower than contrast (Figs. 7.17 and 7.23c), whereas aneurysm density should always be approximately the same as contrast (Fig. 7.23b).

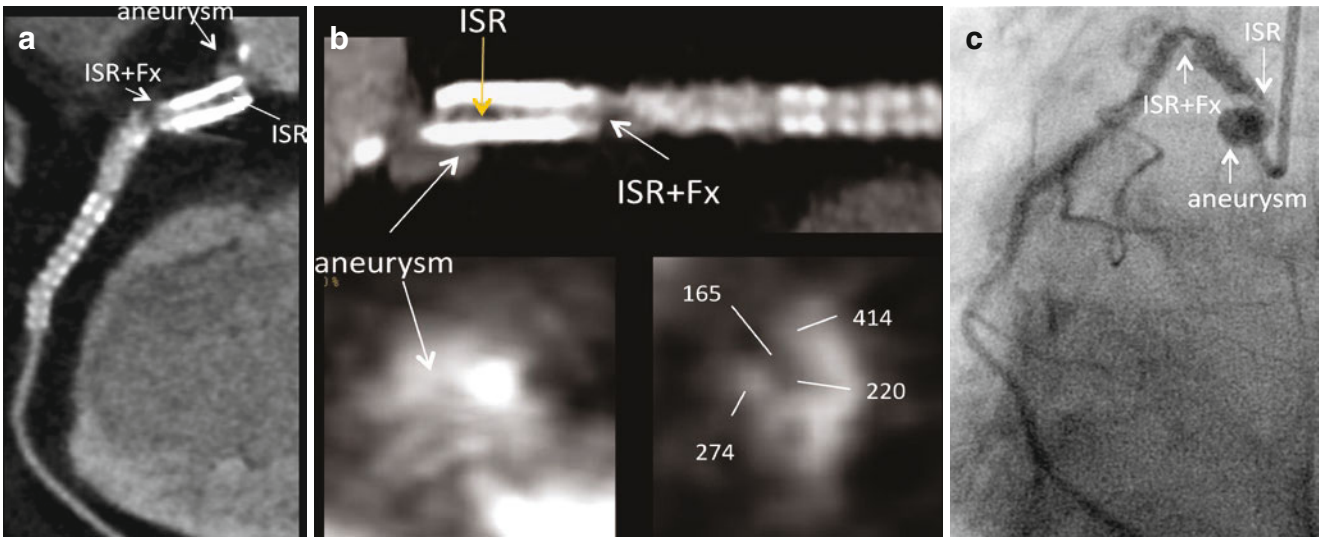

Fig. 7.21 Ostial stent aneurysm, ISR, and stent fracture 1 year after placement of right coronary stents of unknown type. (**a**) The curved multiplanar reconstruction shows the ostial stent aneurysm accompanied by ISR, with a more distal stent fracture (Fx) and ISR. (**b**) Cross-sectional images reveal the aneurysm (*bottom left*), and the reduced Hounsfield units of the fracture site (165) and the ISR (220) (*bottom right*). (**c**) Catheter angiography confirmed the aneurysm and ISR sites; there was no evidence for strut separation on noncontrast frames

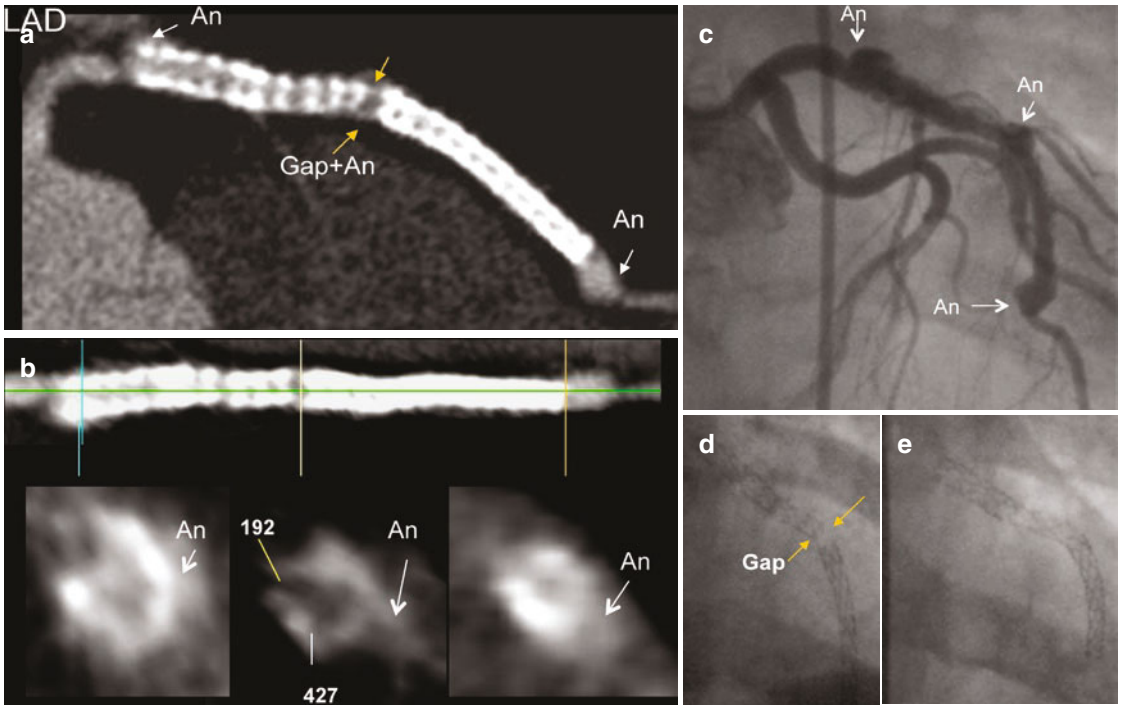

Fig. 7.22 Ostial, mid, and distal stent aneurysms 8 months after placement of overlapped LAD Cypher 3.5 × 13, Cypher 3.0 × 18, and Cypher 2.5 × 28 stents. (**a**) Curved multiplanar reconstruction shows three distinct aneurysms (An), as well as a stent gap. (**b**) Short-axis views confirm the extra-stent contrast and the reduced Hounsfield units (192) of the gap; there was no ISR. (**c**) Catheter angiography was confirmatory. A gap was visible on one noncontrast frame (**d**) but not on others (**e**)

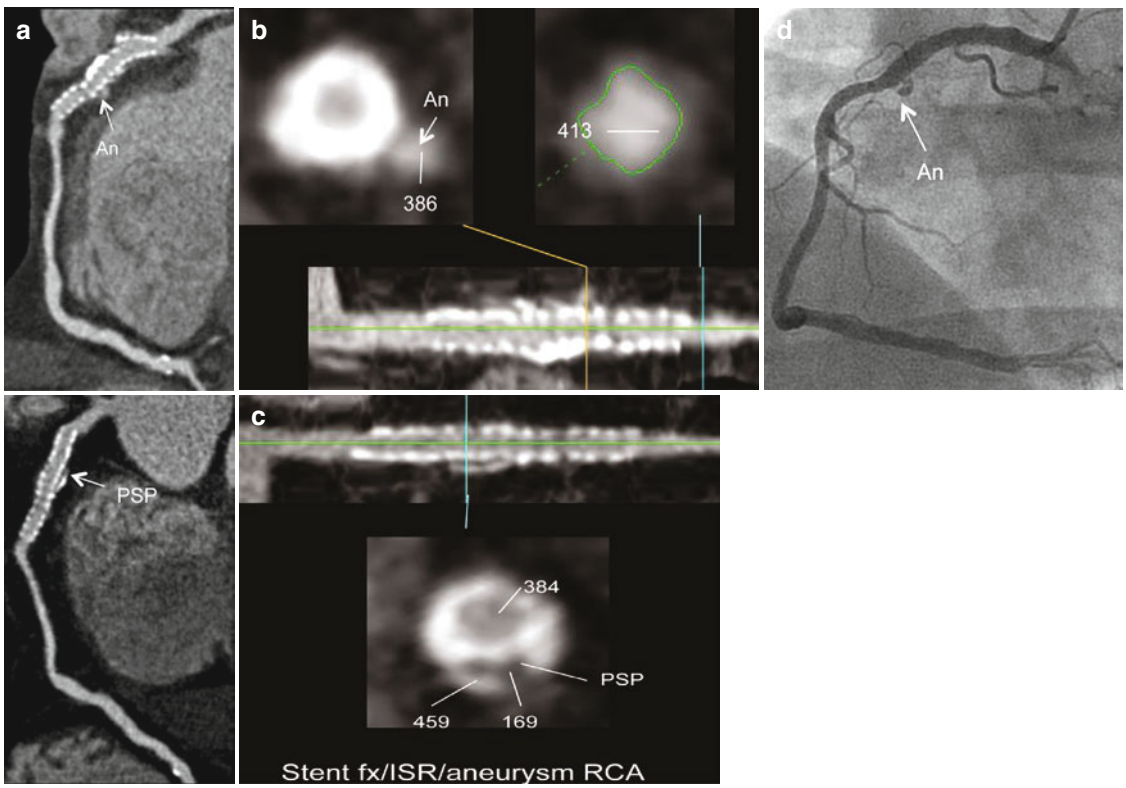

Fig. 7.23 Mid-stent aneurysm and peri-stent plaque 4 years after Cypher 3.5 × 28 RCA stenting. (**a**) Curved multiplanar reconstructions show a mid-stent aneurysm (*top*) and peri-stent plaquing (PSP, *bottom*). (**b**) Short-axis views differentiate between aneurysm (HU similar to contrast) and (**c**) the peri-stent plaque (HU consistent with varying plaque densities). (**d**) The aneurysm is seen on catheter angiography

Bridging

Because myocardial bridging is not always accompanied by obvious systolic compression on catheter angiography, the interventionalist may not be aware that stenting involves a bridged area. Target-lesion revascularization rates have been reported to be 24% for stents extending into the bridged portion of the LAD [23]. CTA easily demonstrates this phenomenon (Fig. 7.24). CTA prior to the procedure can define the proximity of the lesion to the bridged area and thereby guide stent placement to avoid this potential problem.

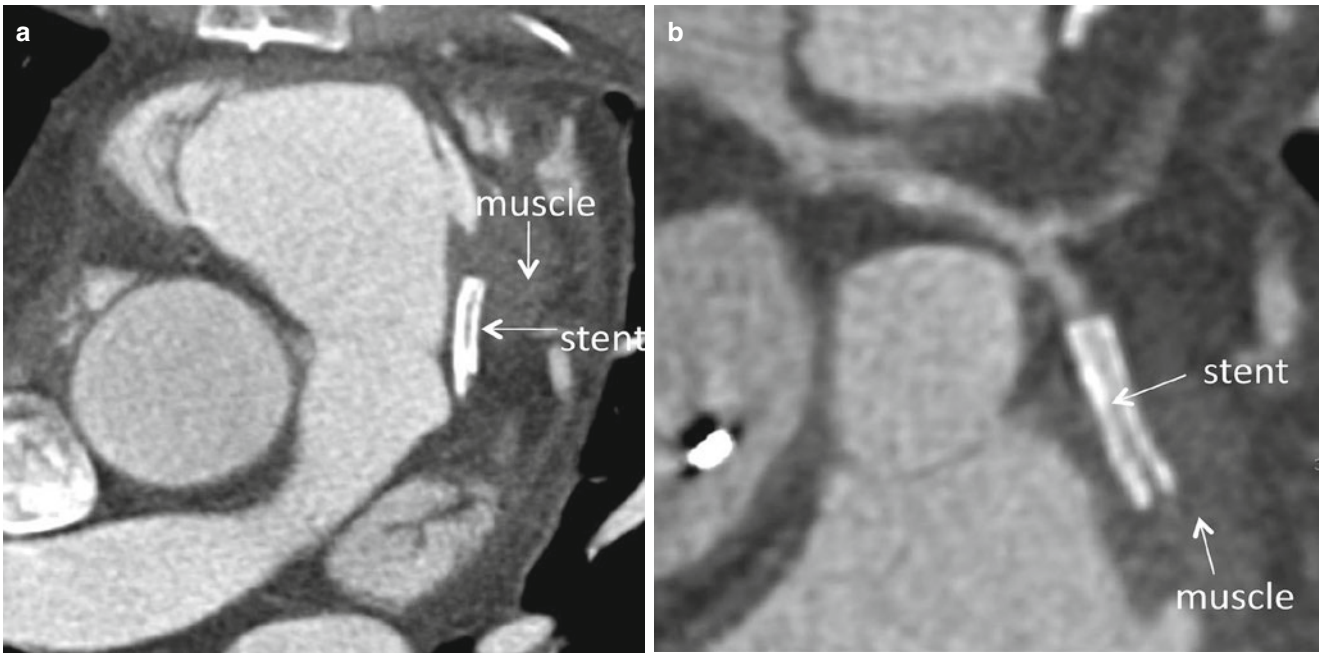

Fig. 7.24 Total occlusion of an LAD stent of unknown type implanted into bridged myocardium. Axial (**a**) and curved multiplanar reconstruction (**b**) demonstrate total occlusion of the stent, most of which is surrounded by muscle

Stent Sizing

CTA affords the opportunity to plan stent size based not just on stenosis length but also on the plaque at the proximal and distal edges of the stenosis (Fig. 7.25), which is not apparent on the invasive angiogram but which the interventionalist may decide to cover. Consequently, CTA-planned stent lengths are slightly longer than the angiographer's visual assessment [24].

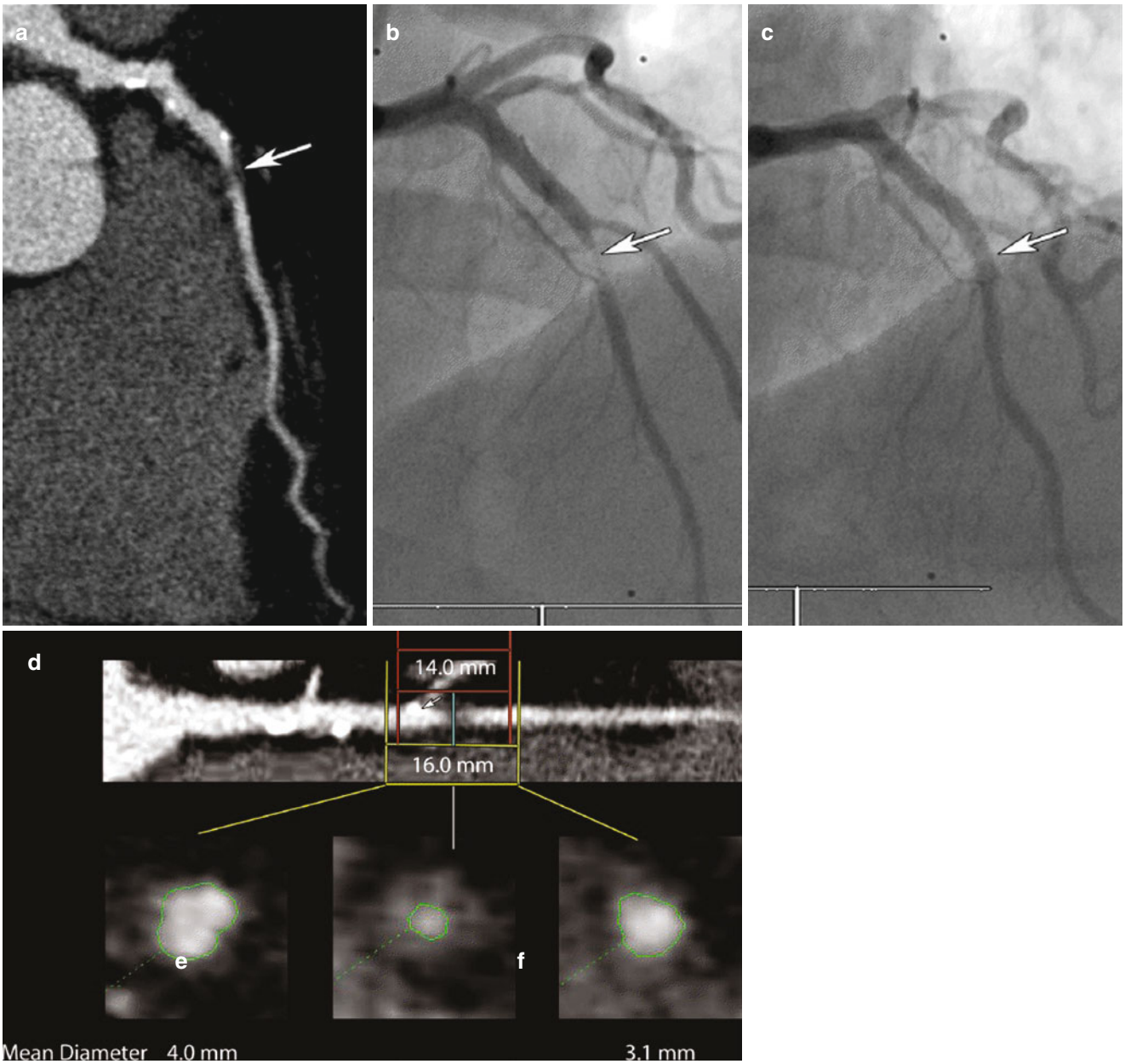

Fig. 7.25 (**a**) Coronary CTA curved multiplanar reconstruction in a 65-year-old man with subtotal occlusion of the LAD artery. (**b**) The occlusion was confirmed by conventional angiography. (**c**) Placement of a drug-eluting stent 4.0 × 12 mm. (**d**) Cross-sectional analysis of the straightened multiplanar reconstruction yielded a normal-to-normal length by CTA (CTA-L) of 14 mm, including the proximal calcified plaque (*arrow*); the estimated stent length based on CTA measurements was 16 mm. The diameter of the proximal landing zone (**e**) was 4.0 mm and the diameter of the distal landing zone (**g**) was 3.1 mm, yielding a mean diameter of 3.5 mm. (**f**) The minimum luminal area of the lesion was 1.8 mm^2

Conclusions

The importance of CTA to the world of intervention has been demonstrated by its superior accuracy compared with stress testing for the identification of stenoses that should or should not be considered for stenting [6–10], as well as more specific uses such as chronic total occlusion planning and evaluation of vessels that cannot be evaluated by catheter angiography [25]. The efficacy of CTA for evaluation of straightforward ISR has been long appreciated, but the multiplicity of complex stent-related issues that can be readily evaluated, as illustrated in this chapter, greatly expands the utility of CTA. The requirements are strict attention to quality control, willingness to spend the time needed for analysis, and expertise to achieve accurate interpretation. Although data for each of the newer applications in large series of patients are lacking, the ability to identify complex stent problems without having to resort to catheter angiography justifies their clinical use.

References

1. Mark DB, Berman DS, Budoff MJ, American College of Cardiology Foundation Task Force on Expert Consensus Documents, et al. ACCF/ACR/AHA/NASCI/SAIP/SCAI/SCCT 2010 expert consensus document on coronary computed tomographic angiography. J Am Coll Cardiol. 2010;55:2663–99.
2. Andreini D, Pontone G, Mushtaq S, Pepi M, Bartorelli AL. Multidetector computed tomography coronary angiography for the assessment of coronary in-stent restenosis. Am J Cardiol. 2010;105:645–55.
3. Hecht HS, Polena S, Jelnin V, Jimenez M, Bhatti T, Parikh M, et al. Stent gap by 64-detector computed tomographic angiography: relationship to in-stent restenosis, fracture, and overlap failure. J Am Coll Cardiol. 2009;54:1949–59.
4. Garg S, Serruys PW. Coronary stents: current status. J Am Coll Cardiol. 2010;56:S1–42.
5. Garg S, Serruys PW. Coronary stents: looking forward. J Am Coll Cardiol. 2010;56:S43–78.
6. Hecht HS. A paradigm shift: coronary computed tomographic angiography before stress testing. Am J Cardiol. 2009;104:613–8.
7. Schuijf JD, Wijns W, Jukema JW, Atsma DE, de Roos A, Lamb HJ, et al. Relationship between noninvasive coronary angiography with multi-slice computed tomography and myocardial perfusion imaging. J Am Coll Cardiol. 2006;48:2508–14.
8. Ravipati G, Aronow WS, Lai H, Shao J, DeLuca AJ, Weiss MB, et al. Comparison of sensitivity, specificity, positive predictive value, and negative predictive value of stress testing versus 64-multislice coronary computed tomography angiography in predicting obstructive coronary artery disease diagnosed by coronary angiography. Am J Cardiol. 2008;101:774–5.
9. Schuijf JD, van Werkhoven JM, Pundziute G, Jukema JW, Decramer I, Stokkel MP, et al. Invasive versus noninvasive evaluation of coronary artery disease. JACC Cardiovasc Imaging. 2008;1:190–9.
10. Øvrehus KA, Jensen JK, Mickley HF, Munkholm H, Bøttcher M, Bøtker HE, Nørgaard BL. Comparison of usefulness of exercise testing versus coronary computed tomographic angiography for evaluation of patients suspected of having coronary artery disease. Am J Cardiol. 2010;105:773–9.
11. Nakazawa G, Finn AV, Vorpahl M, Ladich E, Kutys R, Balazs I, et al. Incidence and predictors of drug-eluting stent fracture in human coronary artery. A pathologic analysis. J Am Coll Cardiol. 2009;54:1924–31.
12. van Werkum JW, Heestermans AA, Zomer AC, Kelder JC, Suttorp MJ, Rensing BJ, et al. Predictors of coronary stent thrombosis: the Dutch Stent Thrombosis Registry. J Am Coll Cardiol. 2009;53:1399–409.
13. Wenaweser P, Daemen J, Zwahlen M, van Domburg R, Jüni P, Vaina S, et al. Incidence and correlates of drug-eluting stent thrombosis in routine clinical practice. 4-year results from a large 2-institutional cohort study. J Am Coll Cardiol. 2008;52:1134–40.
14. Sakurai R, Ako J, Morino Y, Sonoda S, Kaneda H, Terashima M, et al. Predictors of edge stenosis following sirolimus-eluting stent deployment (a quantitative intravascular ultrasound analysis from the SIRIUS trial). Am J Cardiol. 2005;96:1251–3.
15. Liu J, Maehara A, Mintz GS, Weissman NJ, Yu A, Wang H, et al. An integrated TAXUS IV, V, and VI intravascular ultrasound analysis of the predictors of edge restenosis after bare metal or paclitaxel-eluting stents. Am J Cardiol. 2009;103:501–6.
16. Kelbaek H, Thuesen L, Helqvist S, Kløvgaard L, Jørgensen E, Aljabbari S, et al. The stenting coronary arteries in non-stress/benestent disease (SCANDSTENT) trial. J Am Coll Cardiol. 2006;47:449–55.
17. Castagna MT, Mintz GS, Leiboff BO, Ahmed JM, Mehran R, Satler LF, et al. The contribution of "mechanical" problems to in-stent restenosis: an intravascular ultrasonographic analysis of 1090 consecutive in-stent restenosis lesions. Am Heart J. 2001;142:970–4.
18. Takebayashi H, Kobayashi Y, Mintz GS, Carlier SG, Fujii K, Yasuda T, et al. Intravascular ultrasound assessment of lesions with target vessel failure after sirolimus-eluting stent implantation. Am J Cardiol. 2005;95:498–502.
19. Cook S, Wenaweser P, Togni M, Billinger M, Morger C, Seiler C, et al. Incomplete stent apposition and very late stent thrombosis after drug-eluting stent implantation. Circulation. 2007;115:2426–34.
20. Russo RJ, Silva PD, Teirstein PS, Attubato MJ, Davidson CJ, DeFranco AC, et al. A randomized controlled trial of angiography versus intravascular ultrasound-directed bare-metal coronary stent placement (the AVID trial). Circ Cardiovasc Interv. 2009;2:113–23.
21. Aoki J, Kirtane A, Leon MB, Dangas G. Coronary artery aneurysms after drug-eluting stent implantation. JACC Cardiovasc Interv. 2008;1:14–21.
22. Hecht HS, Gade C. Current and evolving stent evaluation by coronary computed tomographic angiography. Catheter Cardiovasc Interv. 2011;77:843–59.
23. Tsujita K, Maehara A, Mintz GS, Doi H, Kubo T, Castellanos C, et al. Impact of myocardial bridge on clinical outcome after coronary stent placement. Am J Cardiol. 2009;103:1344–8.
24. de Silva R, Mussap CJ, Hecht HS, van Mieghem NM, Matarazzo TJ, Roubin GS, Panagopoulos G. Stent sizing by coronary computed tomographic angiography: comparison with conventional coronary angiography in an experienced setting. Catheter Cardiovasc Interv. 2011;78:755–63.
25. Hecht HS. Applications of multislice coronary computed tomography to percutaneous coronary intervention: how did we ever do without it? Catheter Cardiovasc Interv. 2008;71:490–503.

Cardiac CT Before and After Bypass Graft Surgery

8

Koen Nieman

Because of their size and limited mobility, bypass grafts can be visualized well by cardiac CT. Compared with invasive angiography, the diagnostic accuracy of CT in detecting graft failure is very good. Advantages of cardiac CT are its ability to image the grafts without selective contrast injection and to depict their anatomy in relation to the structures around the heart. The clinical utility of cardiac CT is currently limited by its inability to assess the functional significance of obstructive disease.

Many patients who have undergone bypass surgery will require angiographic follow-up at some time. Catheter angiography after bypass surgery can be challenging, particularly when details about the previous surgery are unavailable. Additionally, because these patients often have advanced age, generalized atherosclerotic disease, and noncardiac comorbidities, the risk of catheter angiography is higher. Therefore, a noninvasive angiographic imaging technique can be particularly desirable for this relatively fragile population.

Bypass Graft Disease

Early graft failures are attributed to technical issues, intimal damage, platelet dysfunction, or thrombosis at the site. Late failures are related to atherothrombotic processes that take place more commonly in the venous conduits. The attrition rate has been 2% every year up to 5 years, and 5% per year thereafter. Early after surgery, acute thrombosis of venous grafts may occur in up to 10% of patients [1]. In the Coronary Artery Surgery Study (CASS) registry, 59% of venous grafts were occluded after 10 years [1, 2]. For left internal mammary artery (LIMA) grafts, the occlusion rate is much lower: 17% after 10 years [2, 3] (Fig. 8.1). Nearly half of patients will have recurrent symptoms within 6 years [2, 4]. More than 5 years after surgery, progression of coronary artery disease is at least as likely as graft dysfunction to cause anginal symptoms.

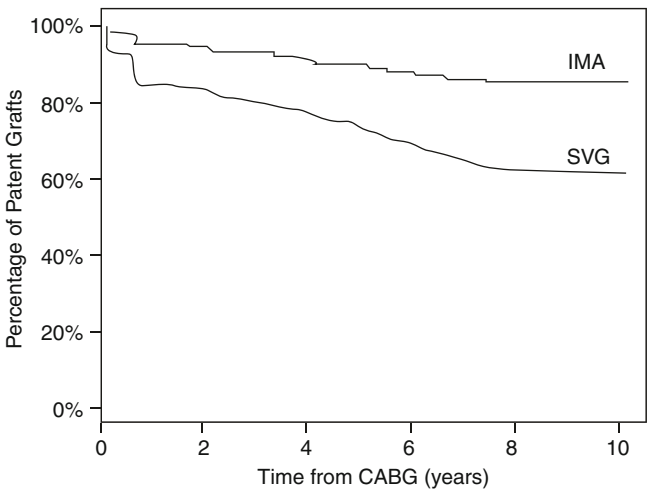

Time	1 Week	1 Year	3 Years	6 Years	10 Years
# Patients	1025	740	484	295	85

Fig. 8.1 Long-term bypass graft patency. In 2004, the Department of Veterans Affairs Cooperative Study published 10-year angiographic patency results after coronary artery bypass graft (CABG) surgery. At 10 years, 61% of saphenous vein grafts (SVG) and 85% of internal mammary artery (IMA) grafts were still patent. (*From* Goldman et al. [3]. with permission)

K. Nieman
Stanford University School of Medicine,
300 Pasteur Drive, Room H2157, Stanford, CA 94305, USA
e-mail: knieman@stanford.edu

M.J. Budoff et al. (eds.), *Atlas of Cardiovascular Computed Tomography*, https://doi.org/10.1007/978-1-4471-7357-1_8

Graft Imaging by Cardiac CT

In general, grafts are relatively easy to image by CT. Compared with the coronary arteries, they are larger and show less displacement during the cardiac cycle. Additionally, calcification of grafts is relatively uncommon, and graft disease manifests by complete occlusion more frequently than nonocclusive stenosis. To image internal mammary artery (IMA) grafts, the scan range needs to be extended to their proximal origin from the subclavian artery (Table 8.1). Preferably, the proximal IMA is left intact, although one artery may be used in a Y graft construction, in which case the proximal end is anastomosed end-to-side to the other IMA graft (Figs. 8.2 and 8.3). IMA grafts may have a single anastomosis or multiple distal anastomoses. Saphenous vein grafts are free grafts with a proximal anastomosis to the (ascending) aorta and one or more (sequential) distal anastomoses to the coronary arteries (Fig. 8.4). Free arterial grafts (radial artery) may be used in a similar fashion.

Table 8.1 CT Scan and reconstruction protocol

Heart rate modulation	IV/oral beta blocker, calcium channel blocker, anxiolytics, or sinus node blocker
Contrast enhancement	Right-side injection to improve assessment of LIMA take-off Contrast timing by bolus tracking or test bolus injection Contrast bolus based on scan time and injection rate Saline bolus chaser (by dual-head injector)
Scan range	From the subclavian artery in case of LIMA/RIMA From the lower border of the aortic arch in case of venous grafts
Acquisition	Thinnest collimation (0.5–0.75 mm) Fastest rotation time (250–350 ms) Tube current based on patient size ECG-triggered tube current modulation (spiral mode) in stable heart rhythm
Reconstruction	High-resolution dataset at optimal (mid-diastolic) time instant for angiographic evaluation Thin-slice high-resolution reconstruction with sharper convolution kernel in case of stents, calcification, or clip artifacts Multiphasic reconstructions for functional assessment Full-field-of-view reconstruction for extra-cardiac pathology

IV intravenous, *LIMA* left internal mammary artery, *RIMA* right internal mammary artery

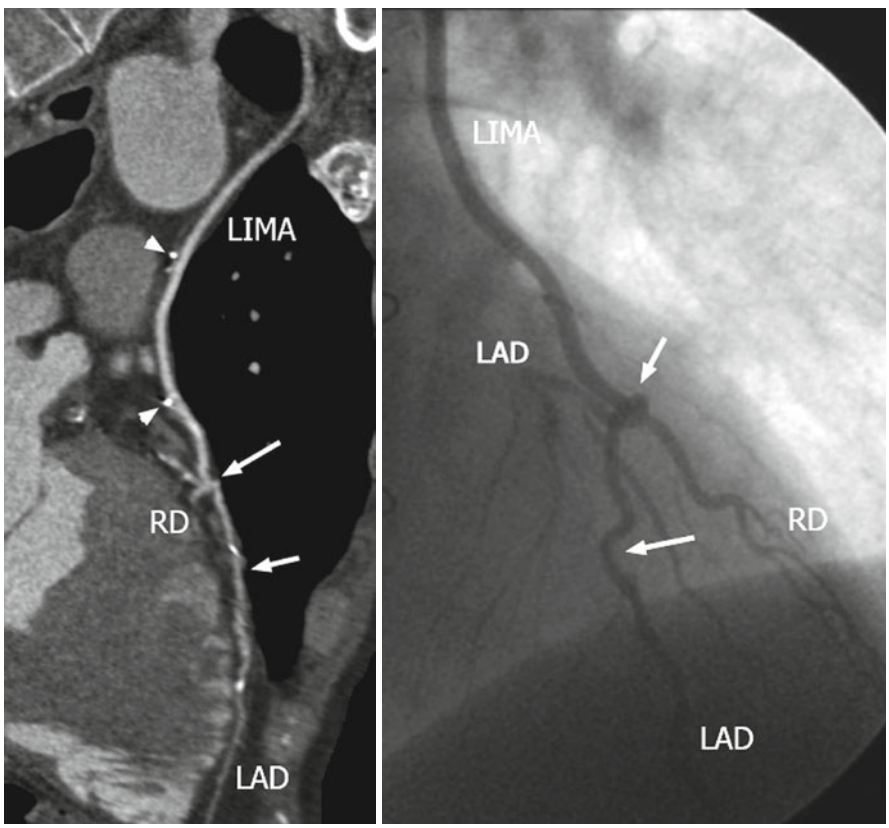

Fig. 8.2 Sequential left internal mammary artery (LIMA) graft. CT and conventional angiogram of a nonobstructed LIMA with sequential anastomoses (*arrows*) to the diagonal branch (RD) and the left anterior descending artery (LAD). Vascular clips appear as bright dots adjacent to the arterial graft (*arrowheads*), which may complicate assessment of the graft

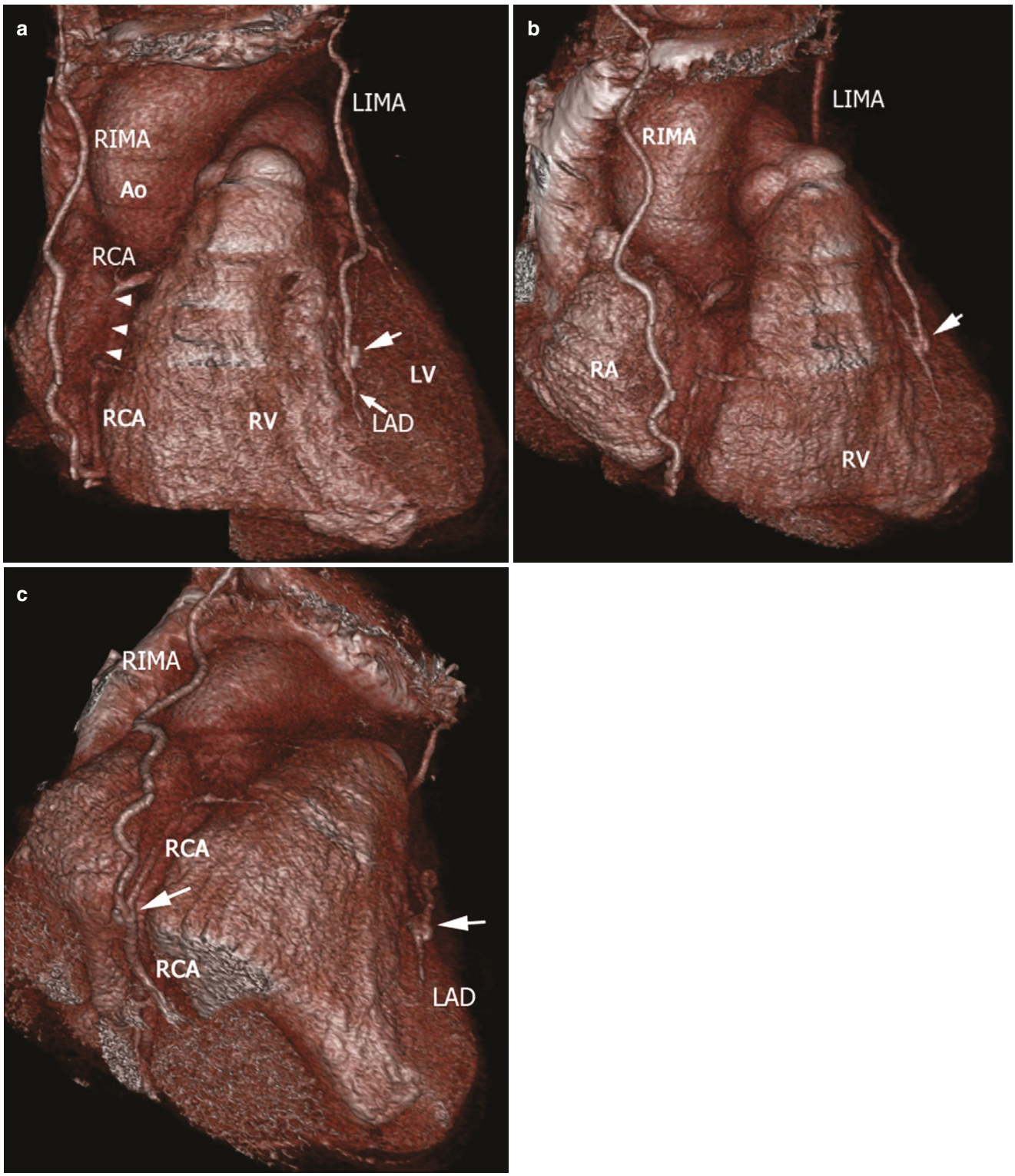

Fig. 8.3 Revascularization using the internal mammary arteries. Complete arterial revascularization shown in an anteroposterior projection (**a**), right-anterior oblique projection with cranial angulation (**b**), and right-anterior oblique projection with caudal angulation (**c**). The right internal mammary artery (RIMA) is anastomosed to the distal right coronary artery (RCA; *arrow* in **c**). The LIMA is anastomosed to the left anterior descending coronary artery (LAD; *arrows* in **a**–**c**). The native RCA is proximally occluded (*arrowheads* in **a**). A surgical clip is located near the graft anastomosis (*arrow*). *Ao* aorta, *LA* left atrium, *LV* left ventricle, RV—right ventricle

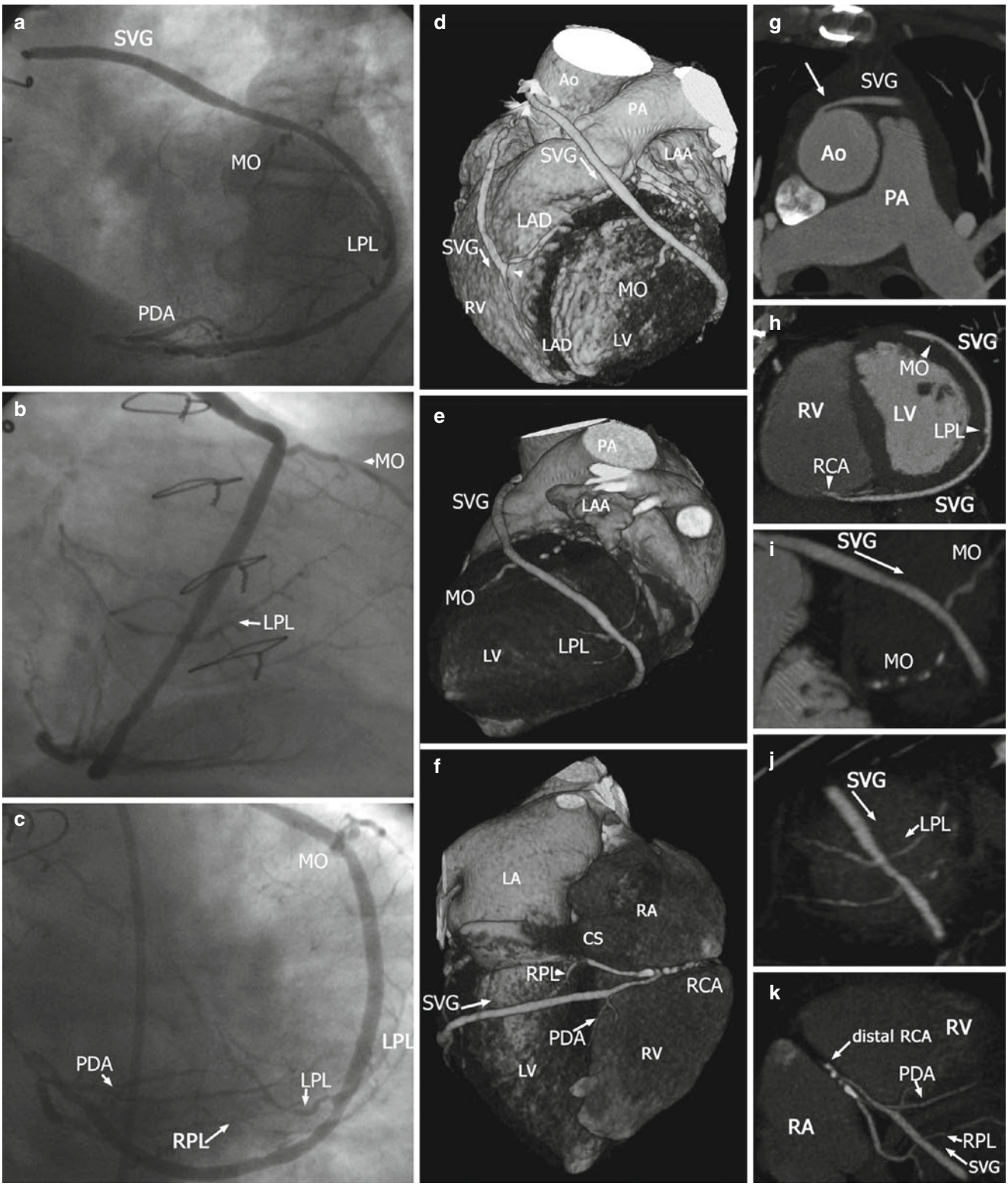

Fig. 8.4 (**a–k**) Nonobstructed sequential vein graft. Normal saphenous jump graft with distal anastomoses to 1) the obtuse marginal branch (MO), 2) a left posterolateral branch (LPL), and 3) the posterior descending artery (PDA). Because of apparent stretching, the proximal graft is slightly narrowed (*arrow* in **g**). The course of the saphenous vein graft (SVG) parallel to the left atrioventricular groove shows the anastomosis sites of the MO and LPL branches (in cross-section). The only visible remainders of the occluded proximal marginal branch are bright and isolated spots of calcium along the track of the occluded vessel (**i**). In the focused panels (**g–k**), the proximal-to-distal course of the graft (and coronary arteries) is indicated. The most proximal of two small posterolateral branches (LPL) has been anastomosed and shows good run-off (**j**). The graft terminates near a small posterior descending artery (**k**). A fairly large posterolateral branch (RPL) from the right coronary artery has no anastomosis. In panel (**d**), a second venous graft with a single anastomosis (*arrowhead*) to the LAD can be seen. The graft appears to be pulling the LAD from the interventricular groove. *CS* coronary sinus, *LAA* left atrial appendage, *PA* pulmonary artery, *RA* right atrium

Early CT technology had insufficient longitudinal coverage to investigate the entire course of all bypass grafts in a single breath hold, but it could be used to detect complete graft occlusion [5–10]. Four-slice spiral CT allowed complete coverage of the grafts, albeit at a very long breath hold (up to 40s), and could also identify graft stenosis or partial graft occlusion [11–13]. Contemporary 64-slice CT technology (and beyond) acquires all data in just a few seconds. Because of improved temporal resolution, motion artifacts are less frequently problematic, which is particularly important near the anastomoses with the coronary artery branches [14–25]. Because of the long scan range to cover the entire graft, the radiation exposure is higher than with coronary CT angiography, but 64-slice CT technology and beyond allows complete graft assessment, including the anastomosis site. Remaining technical challenges to imaging bypass grafts include metal indicators at the site of the anastomosis with the aorta (used to guide future invasive catheterization procedures), vascular clips, and sternal wires (Table 8.2, Fig. 8.5). Comparative studies with catheter angiography have shown excellent sensitivity and specificity to detect graft occlusion as well as stenosis [11–18] (Table 8.3). Graft disease often manifests as complete graft occlusion, with collateral opacification of the distal lumen and coronary arteries (Figs. 8.6, 8.7, 8.8, 8.9, 8.10, 8.11, 8.12, and 8.13).

Table 8.2 Challenges to CT imaging in postsurgical bypass graft patients

Population	Age and comorbidity Diffuse atherosclerotic disease Arrhythmia
Metal objects	Vascular clips Indicator at the aorto-graft anastomosis Sternal wires Stents Pacemaker/implantable cardioverter defibrillator wires
Interpretation	Significance of (chronic) graft occlusion Diffuse, calcified disease Presence and location of myocardial ischemia

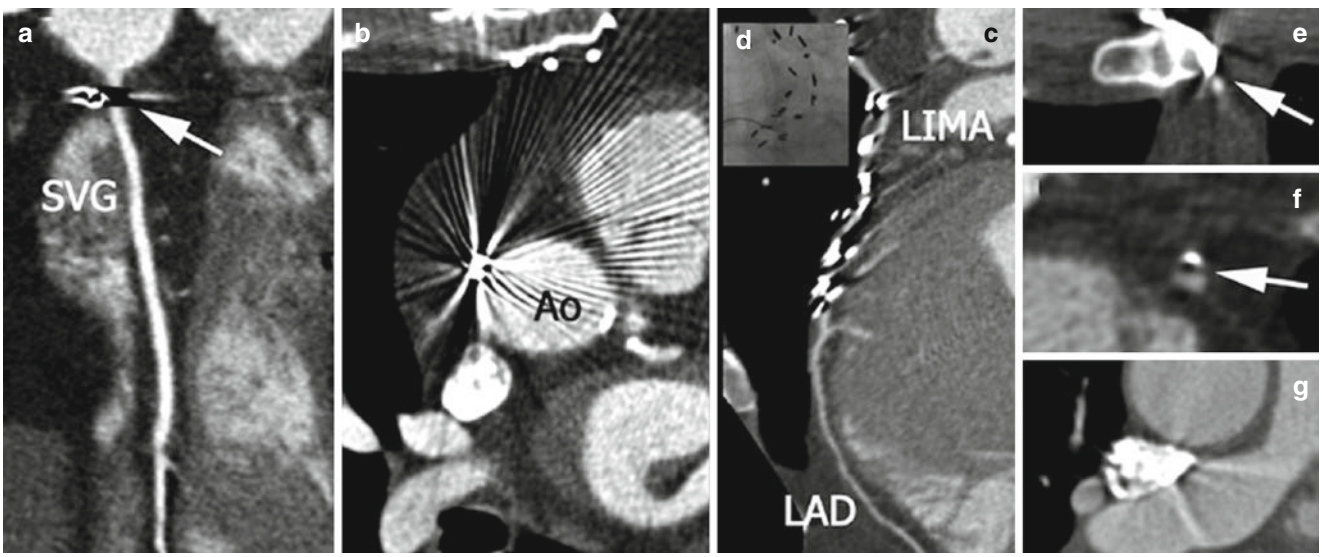

Fig. 8.5 (**a**–**g**) Coronary artery bypass graft–related CT imaging artifact. High-density objects cause beam-hardening artifacts: larger, bright appearance of the structure with bright or dark streaks adjacent to the high-density structure. Near a graft or other vessel, this blooming effect (enlarged appearance), combined with beam hardening, may obscure the vessel lumen and make assessment impossible. High-density objects encountered after bypass graft surgery include metal indicators at the proximal anastomosis site of venous grafts (**a**, **b**), vascular clips (mostly in arterial grafts, such as this LIMA to the LAD) (**c**, **d**, **f**), sternal sutures (**e**), stents, and pacemaker and implantable cardioverter defibrillator leads. High-density contrast medium flowing in from the superior caval vein may cause similar artifacts (**g**); these high-density artifacts are more pronounced when motion is involved (**g**)

Table 8.3 Diagnostic performance of cardiac CT to detect graft disease[a]

Study	CT	*N*	Grafts	Exclusions (%)	Analysis	Sensitivity (%)	Specificity (%)	PPV (%)	NPV (%)
Pache et al. [14]	64SS	31	96	6	Patency	98	89	90	98
Ropers et al. [15]	64SS	50	138	–	Patency 50–99%	100 100	100 94	100 92	100 100
Malagutti et al. [16]	64SS	52	109	–	Patency 50–99%	96 100	100 94	100 79	98 100
Meyer et al. [17]	64SS	138	418	2	50–100%	97	97	93	99
Jabara et al. [18]	64SS	50	147	13	50–100%	95	100	–	–
Onuma et al. [19]	64SS	54	146	–	50–100%	100 100	91 98	–	–
Feuchtner et al. [20]	64SS	41	70	–	50–100%	85	85	80	96
Nazeri et al. [21]	64SS	89	287	–	50–100%	98	97	96	99
Weustink et al. [22]	64DS	52	152	–	50–100%	100	100	100	100
Lee et al. [23]	64SS	44	137	–	50–100%	98	98	–	–
Şahiner et al. [24]	64SS	71	173	–	Patency 50–99%	90 80	98 98	90 73	98 99
Sahiner et al. [25]	64SS	284	684	–	Art: Patency Art: 50–99% Ven: Patency Ven: 50–99%	100 98 100 100	97 99 98 100	99 98 100 98	99 99 98 100

Art arterial grafts, *DS* double-source, *NPV* negative predictive value, *PPV* positive predictive value, *DD* single-source, *Ven* venous grafts
[a]Limited to 64-slice CT technology and beyond, and to populations ≥50 patients

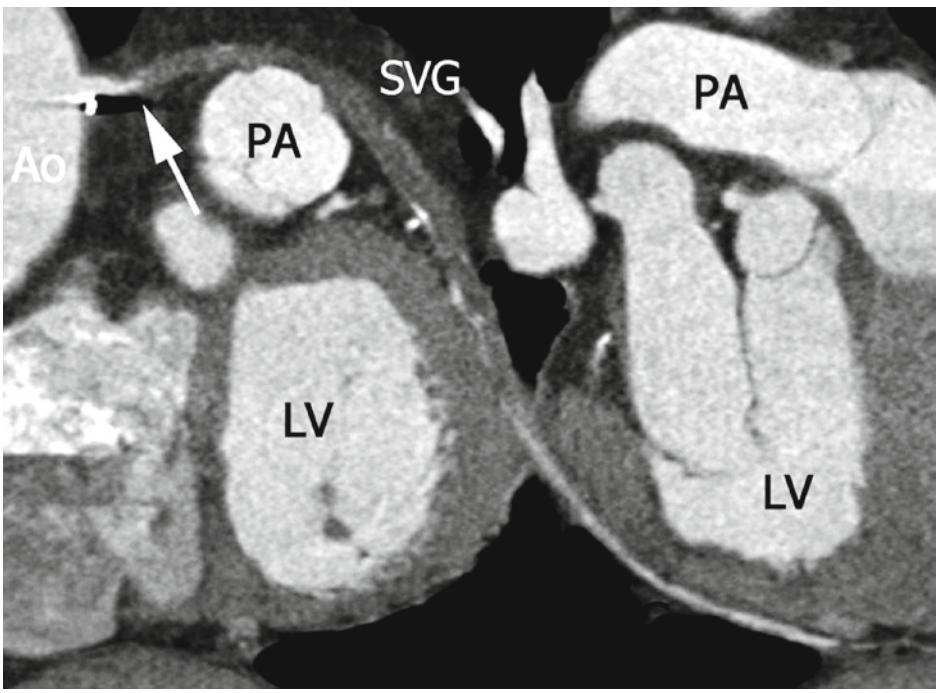

Fig. 8.6 Occluded vein graft. Using curved multiplanar reformation, a venous graft (SVG) to the right coronary artery can be displayed in cross-section over its entire length. Proximally, the graft is completely occluded, after which the graft continues as a hypodense, contrast-void structure. Close to the anastomosis with the aorta (Ao), a metal indicator (including a beam-hardening artifact) can be seen (*arrow*). The distal part of the graft, however, shows faint contrast enhancement. As the proximal right coronary artery is completely occluded (not shown), filling likely occurs via collaterals. Using curved multiplanar reformation, the left ventricle (LV) and the pulmonary artery (PA) appear twice in the image

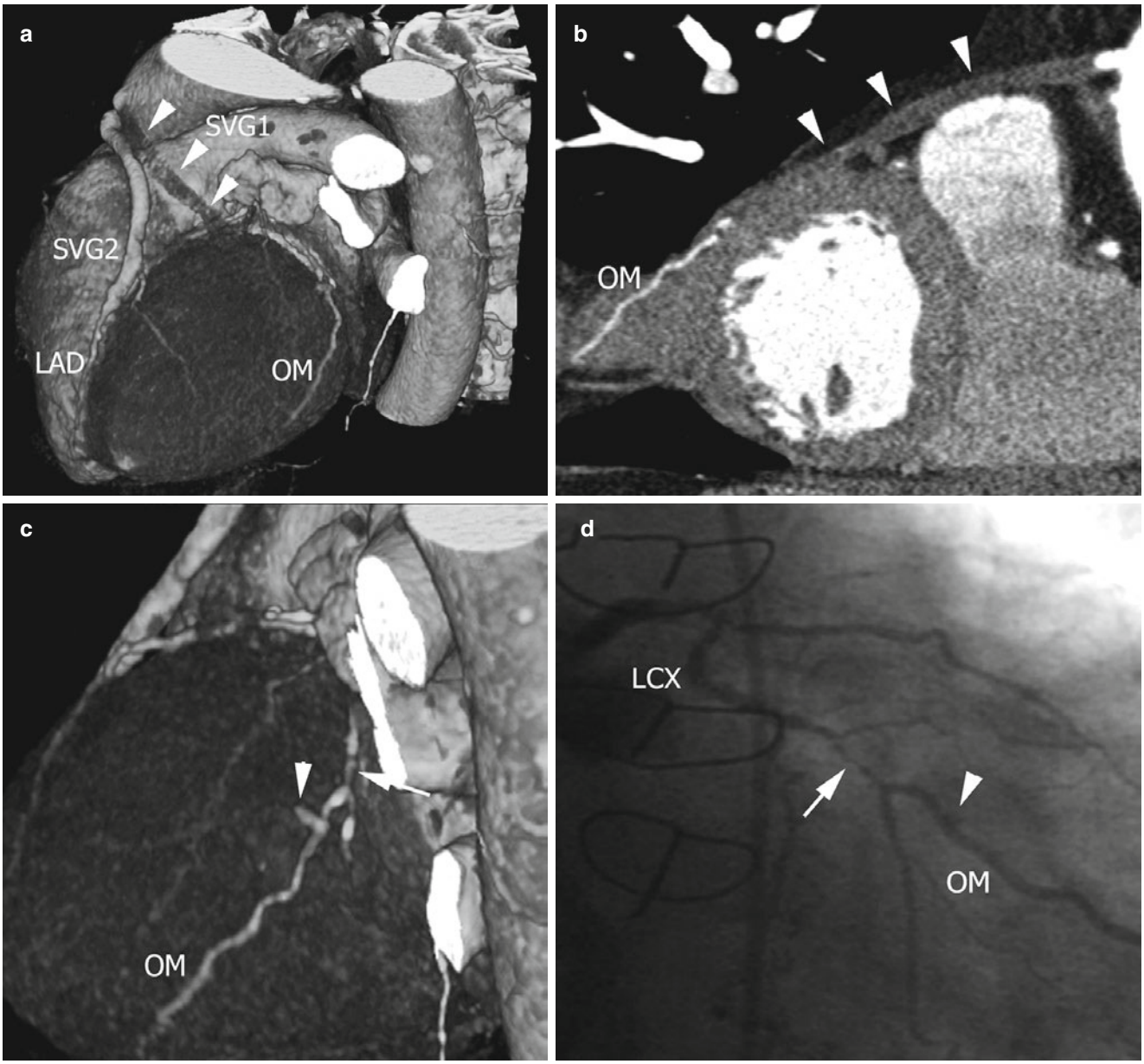

Fig. 8.7 Occluded vein graft. With the proper display settings, the occluded graft from the aorta to the marginal branch can be shown as a low-density structure (*arrowheads*) on the three-dimensional volume-rendered image (**a**) and the curved multiplanar reformation (**b**). Contrary to conventional angiography (**d**), CT cannot demonstrate slow antegrade flow through a diffusely diseased left circumflex artery (LCX), but it does demonstrate the contrast-enhanced distal obtuse marginal branch (OM). A graft remnant (*arrowhead*) filled by the native vessel can be appreciated on CT (**c**) and conventional angiography (**d**)

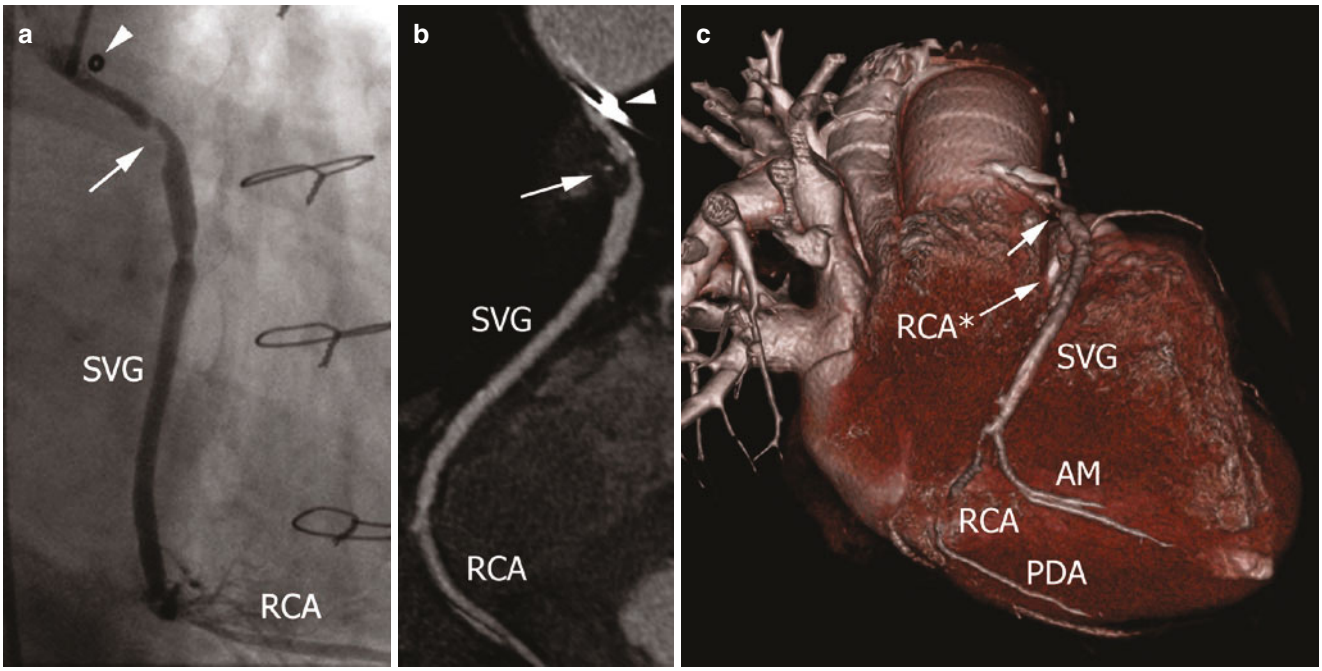

Fig. 8.8 Venous graft stenosis. Conventional (**a**) and CT angiography (**b**, **c**). The venous graft (SVG) has a single anastomosis to the right coronary artery (RCA), inserted just proximal to the acute marginal branch (AM). The artifact caused by the proximal anastomosis indicator (*arrowhead* in **a**, **b**) interferes with the assessment of the proximal graft. Nevertheless, a significant lesion can be clearly identified in all three images (*arrow*), as well as minimal narrowing visible just distal to that lesion on (**a**, **b**)

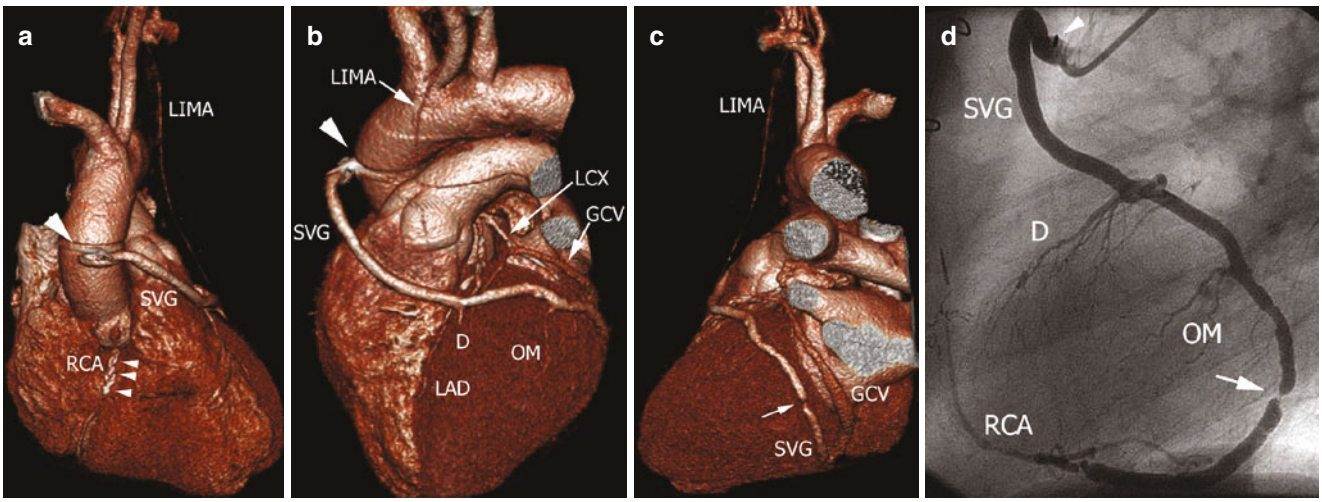

Fig. 8.9 LIMA occlusion and vein graft stenosis, shown in a colored three-dimensional volume-rendered CT angiogram viewed from the right anterior cranial (**a**), left anterior cranial (**b**), and left lateral angles (**c**). A small and nonfunctioning LIMA, producing only a faint shadow along the anterior surface of the heart because of the lack of contrast enhancement, is anastomosed to an occluded LAD artery. An SVG has been anastomosed proximally to the right anterior side of the ascending aorta. High-density artifacts (*bright*) are the result of the metal indicator at the anastomosis site (*arrowhead* in **a**, **b**, **d**). The graft is anastomosed to a diagonal branch (**d**), an obtuse marginal branch (OM), and the posterior descending artery of the RCA (**a**–**d**). The graft shows a significant stenosis (*arrow*) at the level of the last graft segment between the anastomoses with the OM and the posterior descending artery. An obstructed and calcified RCA (*small arrowheads* in **a**) can be found in the right atrioventricular groove. The graft runs parallel to the left atrioventricular groove, where it is accompanied by the great cardiac vein (GCV). Because the scan starts at the origin of the LIMA, significant venous enhancement can occur, particularly with older generations of CT scanners. Unlike conventional angiography (**d**), small vessel size limits the assessment of the distal coronary run-offs, particularly on volume-rendered images

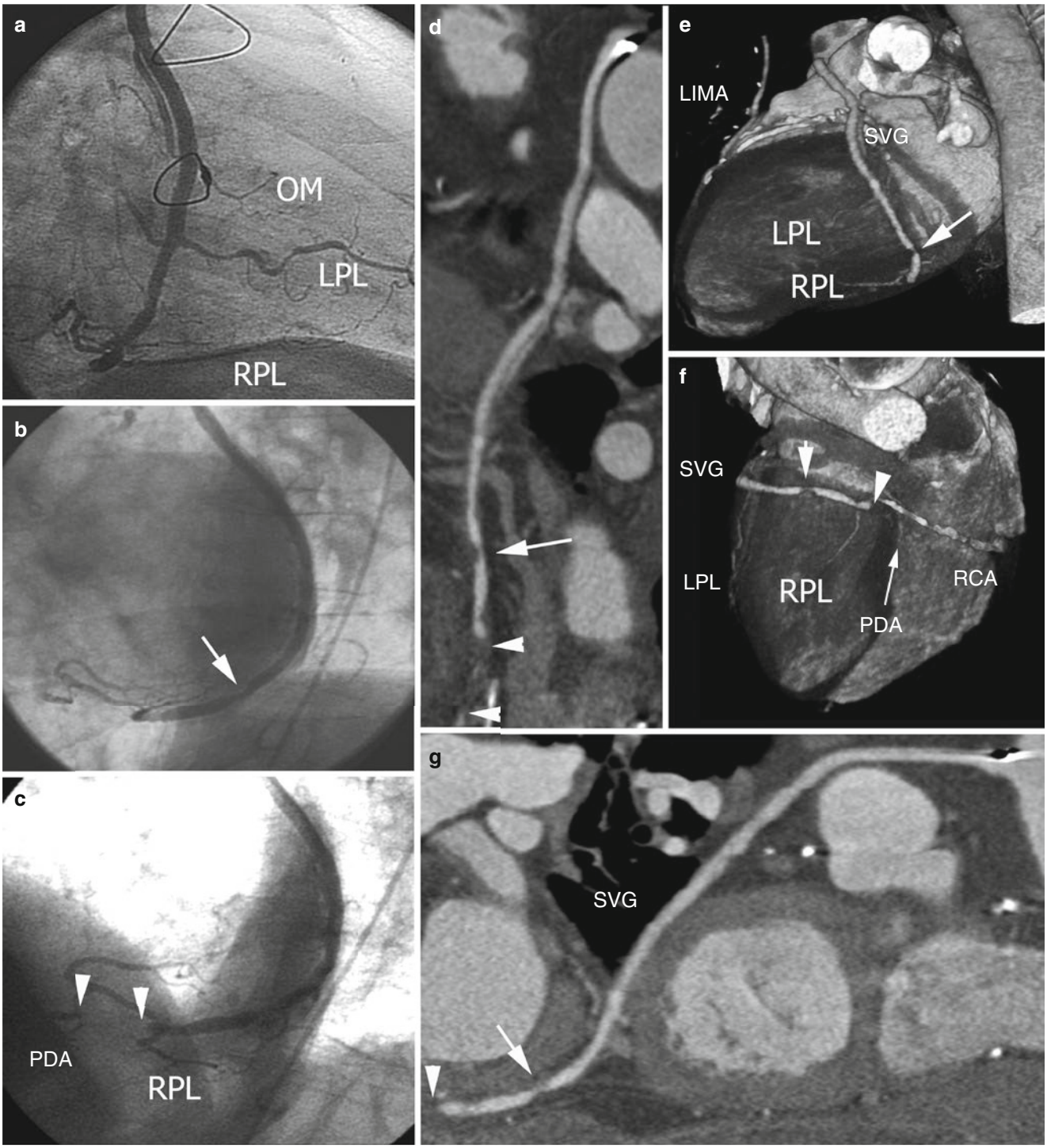

Fig. 8.10 Sequential vein graft disease. Conventional angiography (**a–c**) of a saphenous vein jump graft (SVG) with sequential anastomoses to an obtuse marginal branch (OM), a left posterolateral branch (LPL) from the left circumflex coronary artery, a right posterolateral branch (RPL), and the posterior descending coronary artery (PDA) from the RCA. Curved multiplanar reconstructions (**d**, **g**) and volume-rendered reconstructions (**e**, **f**) of the CT angiogram show the SVG and coronary anastomoses. On conventional angiography (**b**) and CT angiography (**d–g**), a significant narrowing of the graft segment between the respective posterolateral branches can be observed (*arrow*). More difficult to recognize is the complete occlusion (*between the arrowheads* in panels **c**, **d**) of the terminal graft segment to the posterior-descending branch (PDA)

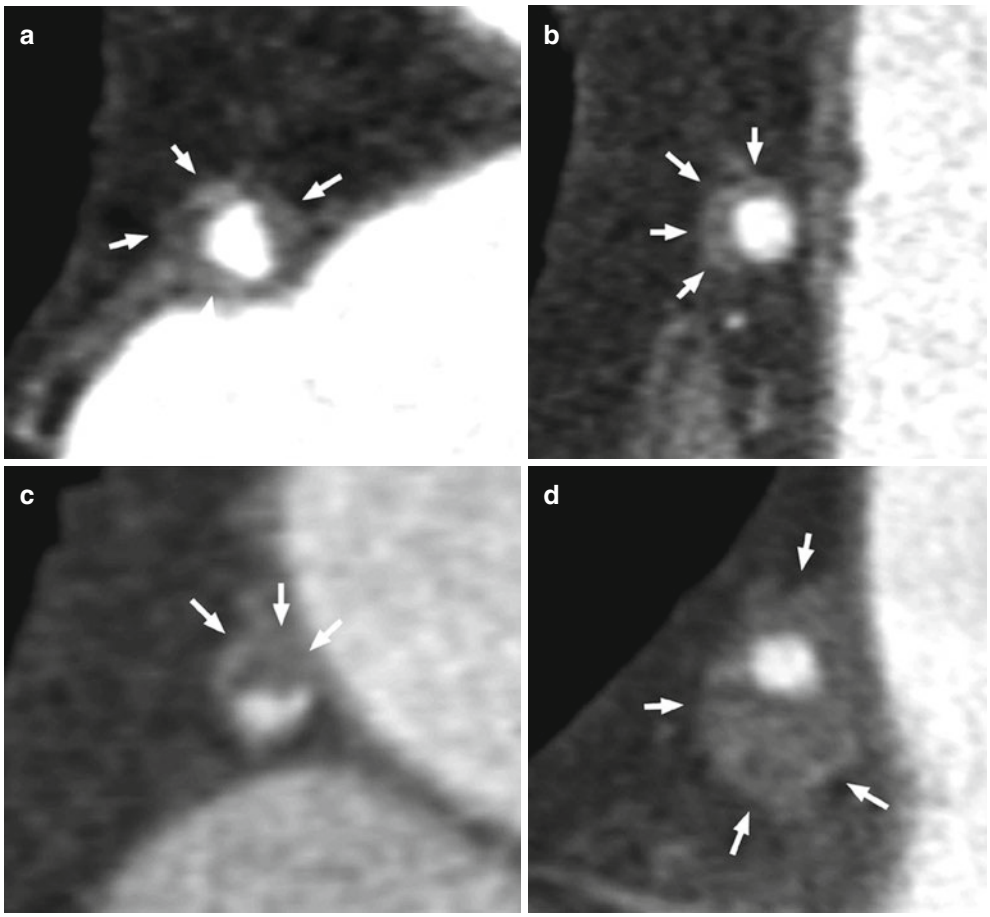

Fig. 8.11 (**a–d**) Examples (cross-sections) of degenerative vein graft disease (*arrows*) without significant luminal obstruction. Aneurysmal graft lesions can be found (**d**). Lesions often consist of low-density tissue, with Hounsfield values lower than those of contrast-enhanced blood in the graft, but higher than those of pericardial fat. Calcified atherosclerosis is rare in bypass grafts

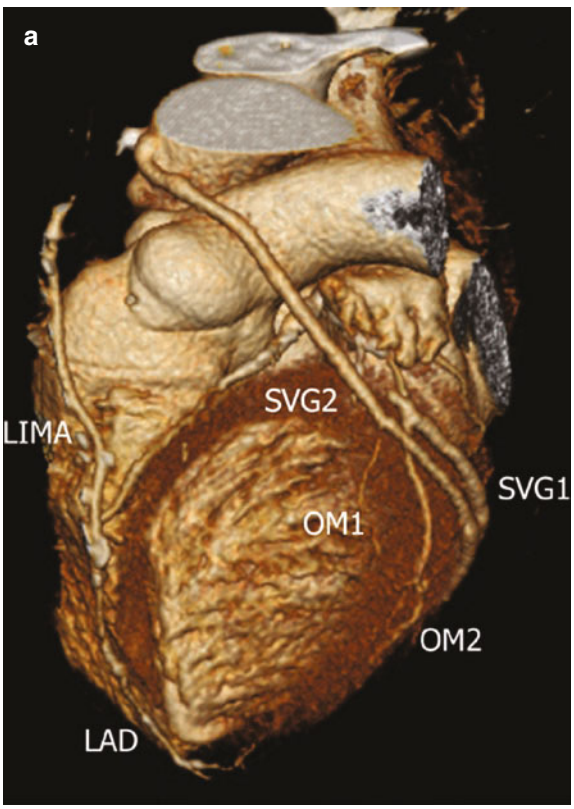

Fig. 8.12 (**a**, **b**) Redo coronary artery bypass graft. During the first coronary bypass operation, a venous graft (SVG1) was anastomosed to the second marginal branch (OM2) and the posterior descending coronary artery (PDA). When the patient developed symptoms again years later, the proximal part of the graft from the aorta to the marginal branch was found to be occluded. The occluded segment (*between the arrows* in **c**) can be appreciated on the cross-sectional image as a low-density structure. The distal segment of the graft was still patent and provided perfusion via the marginal branch to the PDA. Because of progressive native coronary artery disease, a second surgical procedure was performed. A LIMA graft was anastomosed to the LAD coronary artery and a vein graft (SVG2) to the first marginal branch (OM1) and again to the PDA

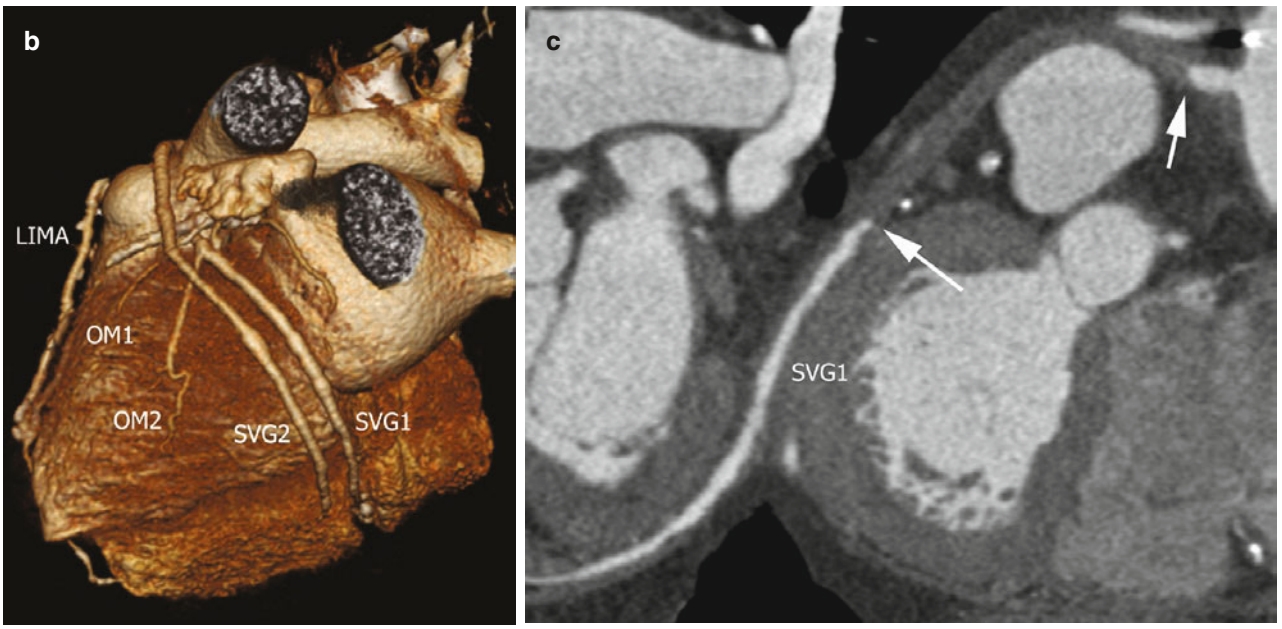

Fig. 8.12 (continued)

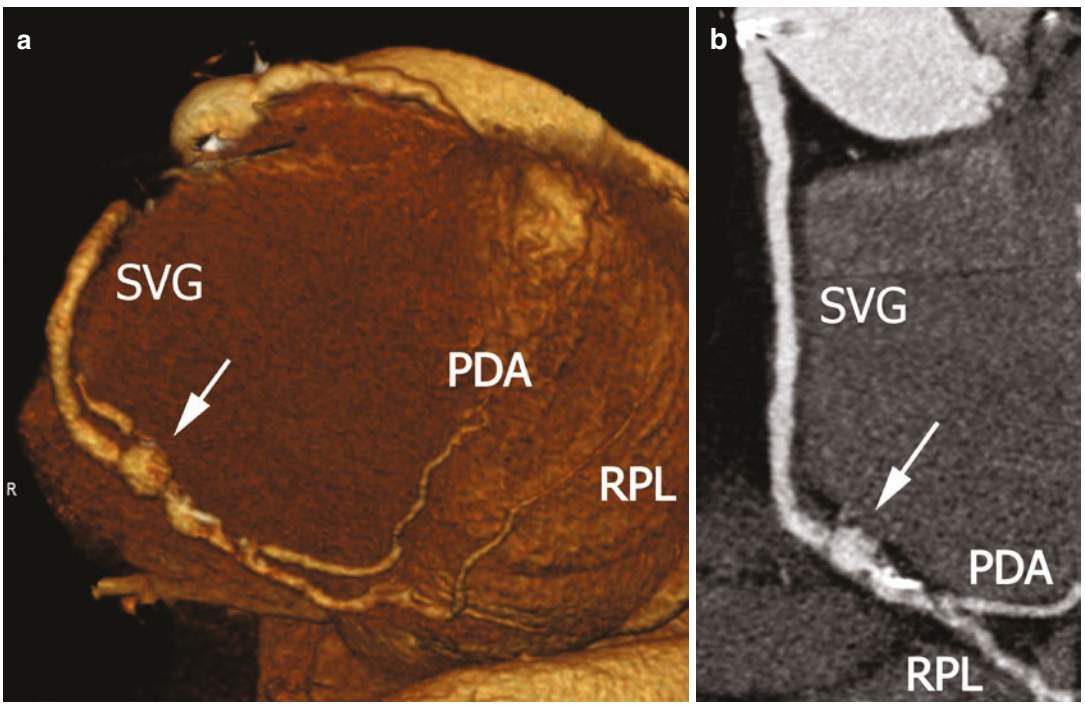

Fig. 8.13 Graft anastomosis aneurysm. CT angiograms (three-dimensional volume-rendering (**a**) and curved multiplanar reformation (**b**)) of a venous graft (SVG) anastomosed to the distal right coronary artery, just proximal to the bifurcation of the posterior descending (PDA) and posterolateral ramus (RPL). At the anastomosis, aneurysmal dilatation (*arrows*) and distal run-off moderate obstruction can be observed

Clinical Applications of Cardiac CT

After bypass graft surgery, cardiac CT may be of clinical use in assessing various questions:

- Graft anatomy (relative to other structures), patency, and stenosis
- Coronary run-offs
- Nongrafted coronary arteries
- Proximal coronary segments, in case of graft disease
- Myocardial morphology (thickness, attenuation)
- Cardiovascular and thoracic morphology and dimensions

Cardiac CT generally is not applied in acute situations in which immediate intervention is warranted. Immediately after surgery, it may be used in case of hemodynamic or biochemical disturbances to identify graft problems, including early graft failure or other complications. In patients with recurrent chest pain or decreased ventricular function in the years after surgery, CT may be preferable over catheter angiography to exclude graft disease. Because it does not require selective contrast injection, the location and condition of the graft is readily visualized. CT is particularly useful when complete surgical documentation is absent. A drawback of both CT angiography and catheter angiography is the inability to detect and localize myocardial ischemia. This is particularly important in postsurgical patients, in whom diffuse coronary disease, nonsymptomatic graft occlusions, and developed collateral circulation may coexist.

Coronary Imaging After Bypass Graft Surgery

Recurrent symptoms after coronary bypass surgery may be due to graft failure or progression of coronary artery disease. Besides establishing bypass graft patency, interrogation of the coronary arteries is equally important in these patients. The native coronary segments should include the distal run-offs after graft anastomosis (Figs. 8.14 and 8.15), as well as nongrafted coronary branches (Fig. 8.16). In patients with graft failure, it is important to assess the status of the proximal coronary artery and possibilities for percutaneous revascularization. Occasionally, graft occlusion may be the result of the absence of severe coronary artery disease (Figs. 8.17 and 8.18). Although results have improved with 64-slice CT (Table 8.4), the diagnostic ability to assess coronary disease is still inferior in patients with prior bypass grafts compared with patients without previous surgery [9, 15, 17]. Because of diffuse, calcified, and atherosclerotic disease, detection or exclusion of significant luminal narrowing may be impossible in certain cases (Fig. 8.19). Even when diffuse disease is suspected, CT may still be useful before scheduled catheter angiography to evaluate the location and condition of the bypass grafts and reduce the total use of contrast medium and the time spent in the catheterization laboratory. CT visualizes the contrast-enhanced lumen and nonenhanced tissues such as calcium and soft tissues. In cases of graft or coronary occlusion, CT provides information concerning the length and content of the occluded segment. The presence and extent of calcification may be important technical information for the interventional cardiologist.

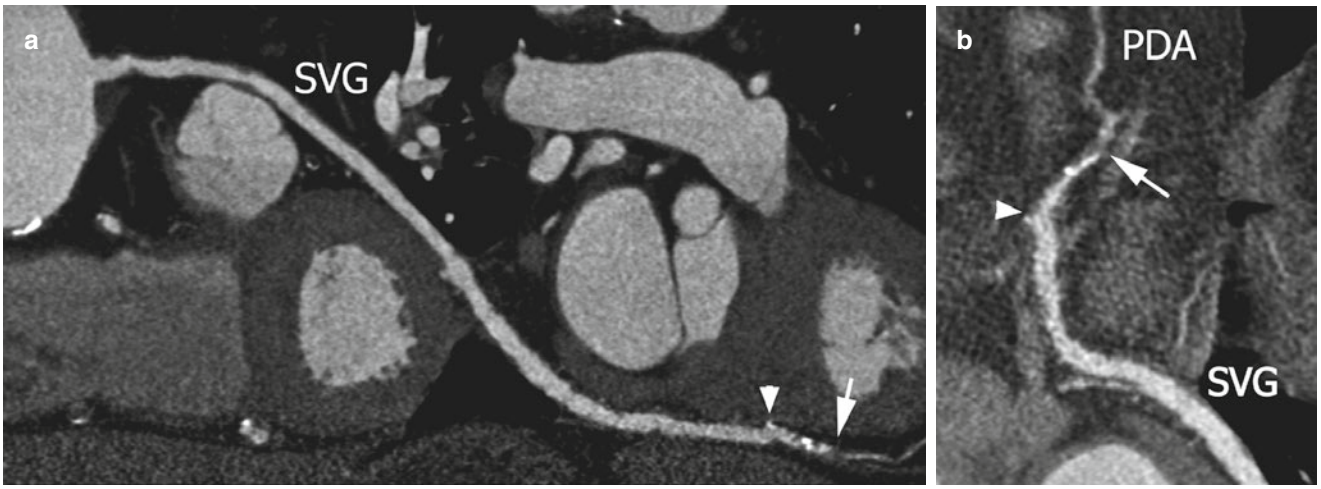

Fig. 8.14 Coronary run-off disease. (**a**, **b**) Curved multiplanar reformations (two different rotational angles) of a vein graft (SVG) without significant stenosis that is anastomosed (*arrowhead*) to the posterior descending artery (PDA). The distal run-off shows severe atherosclerotic disease and appears significantly narrowed (*arrow*). More than 5 years after bypass graft surgery, recurrent angina is more likely to be caused by progression of coronary artery disease. Therefore, assessment of distal coronary run-offs and of nongrafted coronary arteries is important

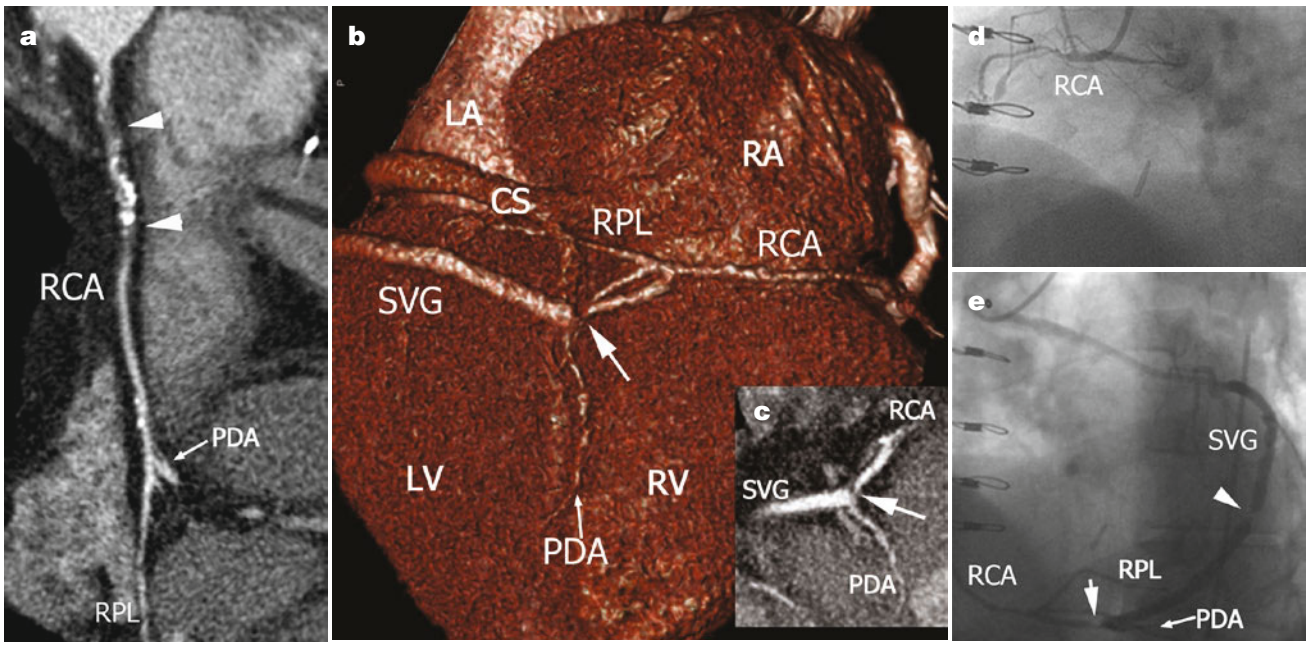

Fig. 8.15 Coronary run-off disease. A significantly stenosed SVG is distally anastomosed to the posterior descending artery (PDA) of the RCA (**b**, three-dimensional volume rendering). Apart from the graft lesion (*arrowhead* in **e**), significant obstruction of the anastomosis site in the direction of the RCA was detected (*arrow* in **b**, **c**, **e**). Considering the occlusion of the proximal RCA (*arrowheads* on (**a**) [curved multiplanar reconstruction] and (**d**)), other RCA branches, such as the posterolateral branch (RPL) depended on retrograde filling via the graft. Therefore, percutaneous intervention was performed on the graft as well as the distal anastomosis. *CS* coronary sinus, *LA* left atrium, *LV* left ventricle, *RA* right atrium, *RV* right ventricle

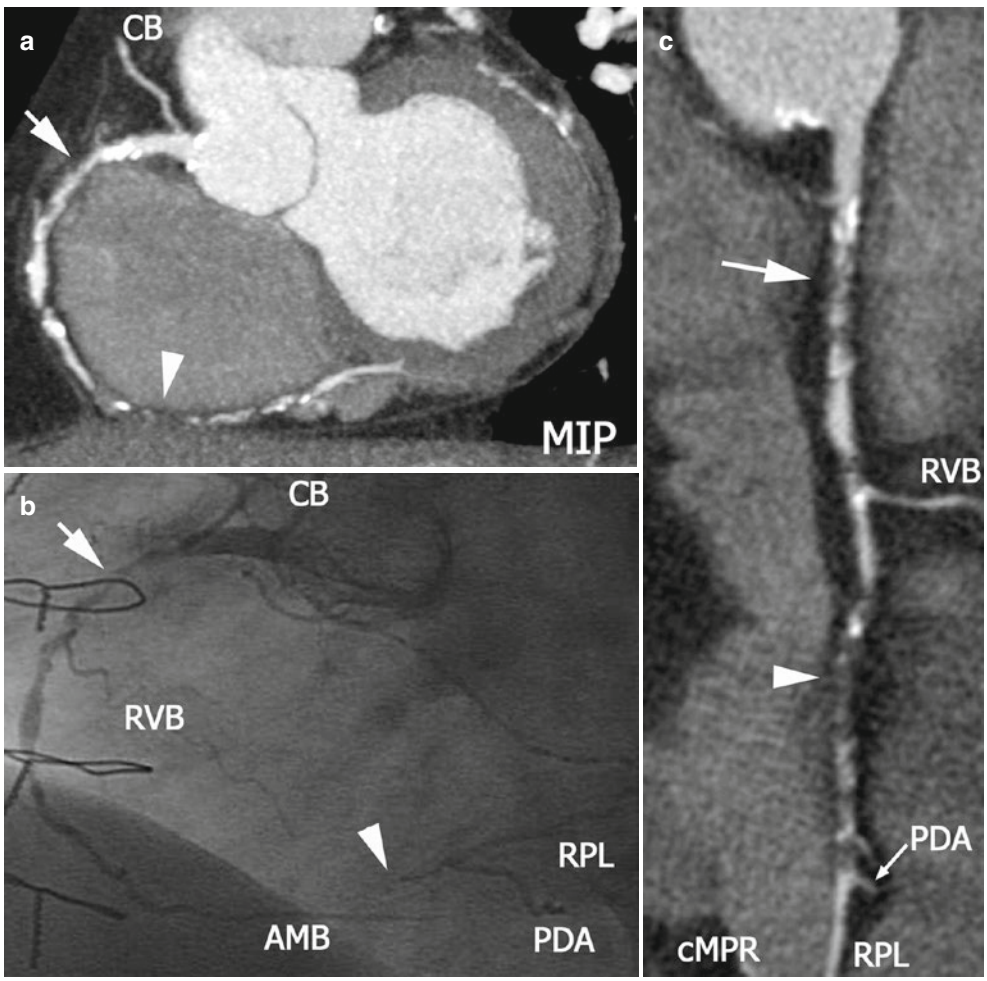

Fig. 8.16 Nongrafted, occluded right RCA, seen on maximum intensity projection (**a**, MIP), catheter angiography (**b**), and curved multiplanar reconstruction (**c**, cMPR). If symptoms recur at a long interval after bypass graft surgery, it is more likely that progression of native coronary artery disease is the cause, rather than graft disease. This patient presented with anginal symptoms 12 years after bypass graft surgery of the left coronary artery. No obstructive disease was found in the revascularized left system, but there was significant disease in the RCA. The proximal RCA shows diffuse disease with significant narrowing (*arrow*) in the proximal portion, and a complete occlusion (*arrowhead*) in the distal portion. The posterior descending branch (PDA) and right posterolateral branch (RPL) are filled by collaterals. *AMB* acute marginal branch, CB, conus branch, *RVB* right ventricular branch

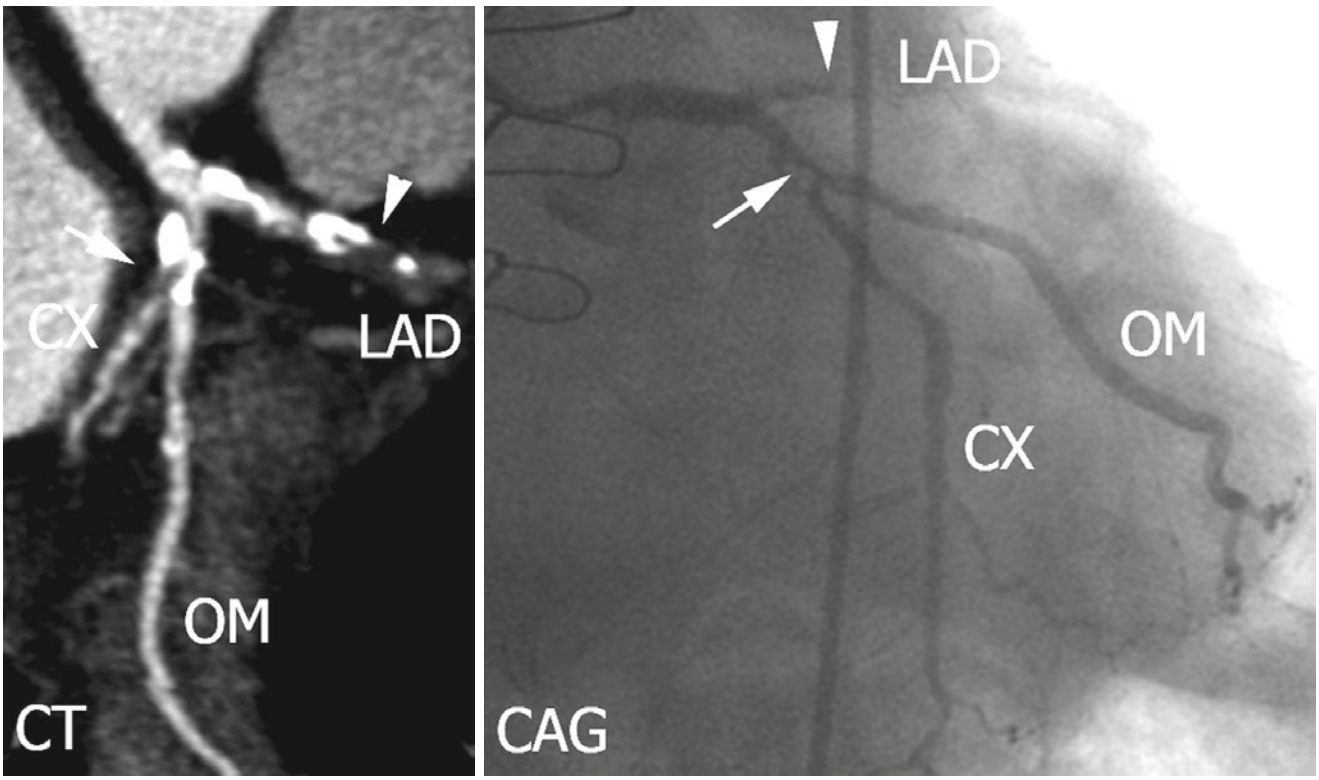

Fig. 8.17 Coronary assessment after graft failure. Imaging of the native left coronary arteries after bypass graft surgery. The graft to the obtuse marginal branch (OM) is occluded (*not shown*). The native left circumflex coronary artery (CX) shows a significant bifurcation lesion (*arrow*), but is patent. This patient could be referred for percutaneous intervention of the CX. A completely occluded LAD (*arrowhead*) was served by a patent and functioning left internal mammary artery. When symptomatic graft failure (occlusion) occurs, percutaneous treatment of the native coronary artery disease may be preferable to recanalization of the graft or redo surgery, so bypassed, proximal coronary branches should be evaluated, particularly in cases of graft failure. Although atherosclerosis may be severe, as evident from the bright, calcified lesions in this case, patency or occlusion can usually be differentiated

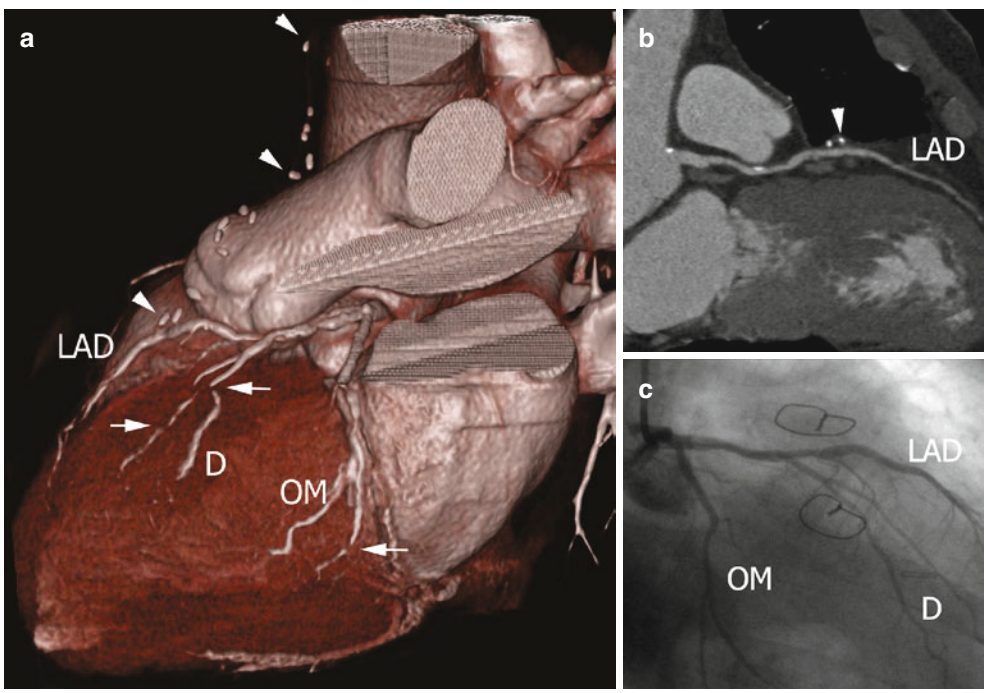

Fig. 8.18 Occluded left internal mammary artery (LIMA) and nonobstructed LAD. The LIMA graft to the LAD is occluded, with only the vascular clips remaining on CT (*arrowheads*). Occlusion of the graft may have occurred as the result of competitive flow from the LAD, which shows no significant obstruction on CT and conventional angiography 15 years after surgery. Interruptions of the diagonal (D) and obtuse marginal branches (OM) (*arrows*) are the result of discontinuity between slabs caused by arrhythmia or patient movement and should not be mistaken for coronary stenosis

Table 8.4 Detection of coronary artery stenosis (>50%) by CT after coronary artery bypass grafting

Study	CT systems	*N*	Excluded, %	Sensitivity, %	Specificity, %	PPV, %	NPV, %
Nieman et al.[a] [13]	4SS	24	31 34	90 79	75 72	81 73	86 79
Salm et al. [26]	16SS	25	26	100	89	85	100
Stauder et al. [27]	16SS	20	31	92	77	88	85
Ropers et al. [15]	64SS	50	9[b] 7[c]	86[b] 86[c]	76[b] 90[c]	44[b] 54[c]	96[b] 98[c]
Malagutti et al. [16]	64SS	52	0	98	71	65	99
Onuma et al. [19]	64SS	54	2	100	88	–	–
Nazeri et al. [21]	64SS	89	–	89	94	–	–
Weustink et al. [22]	64DS	52	–	95	100	100	99
Lee et al. [23]	64SS	44	–	92	84	–	–

DS double-source, *NPV* negative predictive value, *PPV* positive predictive value, *SS* single-source
[a]Readings by two observers
[b]Native coronary arteries
[c]Coronary run-offs

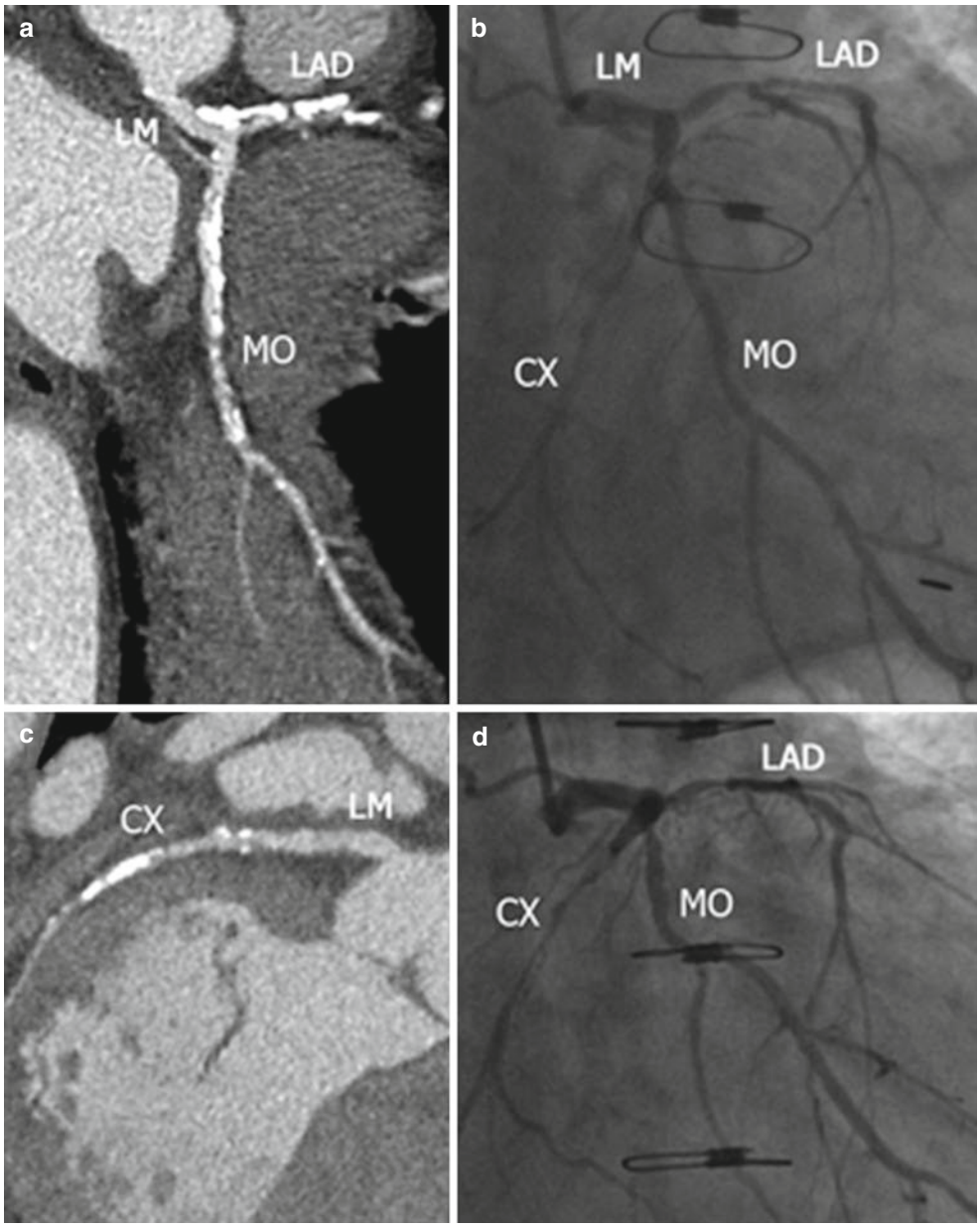

Fig. 8.19 Coronary calcification. Particularly in postsurgical patients, atherosclerotic disease in the coronary arteries may be severe. (**a**–**d**), In this patient, extensively calcified disease in a nongrafted left circumflex coronary artery (CX) and large marginal branch (MO) makes accurate assessment of the lumen by CT virtually impossible. *LM* left main coronary artery

Cardiac CT Prior to Bypass Graft Surgery

Cardiac CT is not routinely performed prior to surgery, but it can provide additional information that is useful before the procedure. It potentially provides additional information about the coronary arteries that may not be available from invasive angiography, including their exact location on the cardiac surface, the presence of calcification that may make anastomosis more difficult, and the occurrence of myocardial bridging. Extensive calcification of the aortic wall on CT may alter the surgical approach (Fig. 8.20). The anatomy of the internal mammary arteries also may be appreciated on CT. Cardiac morphology, myocardial thickness (Fig. 8.21), and the presence of hypoattenuation are important for decision making with regard to whether revascularization is feasible and needed. If redo bypass graft surgery (or any other type of intrathoracic surgery) is planned, anatomic information provided by CT regarding the intrathoracic anatomy, the course of patent grafts, and vascular calcifications may be important and may help to avoid complications (Fig. 8.22).

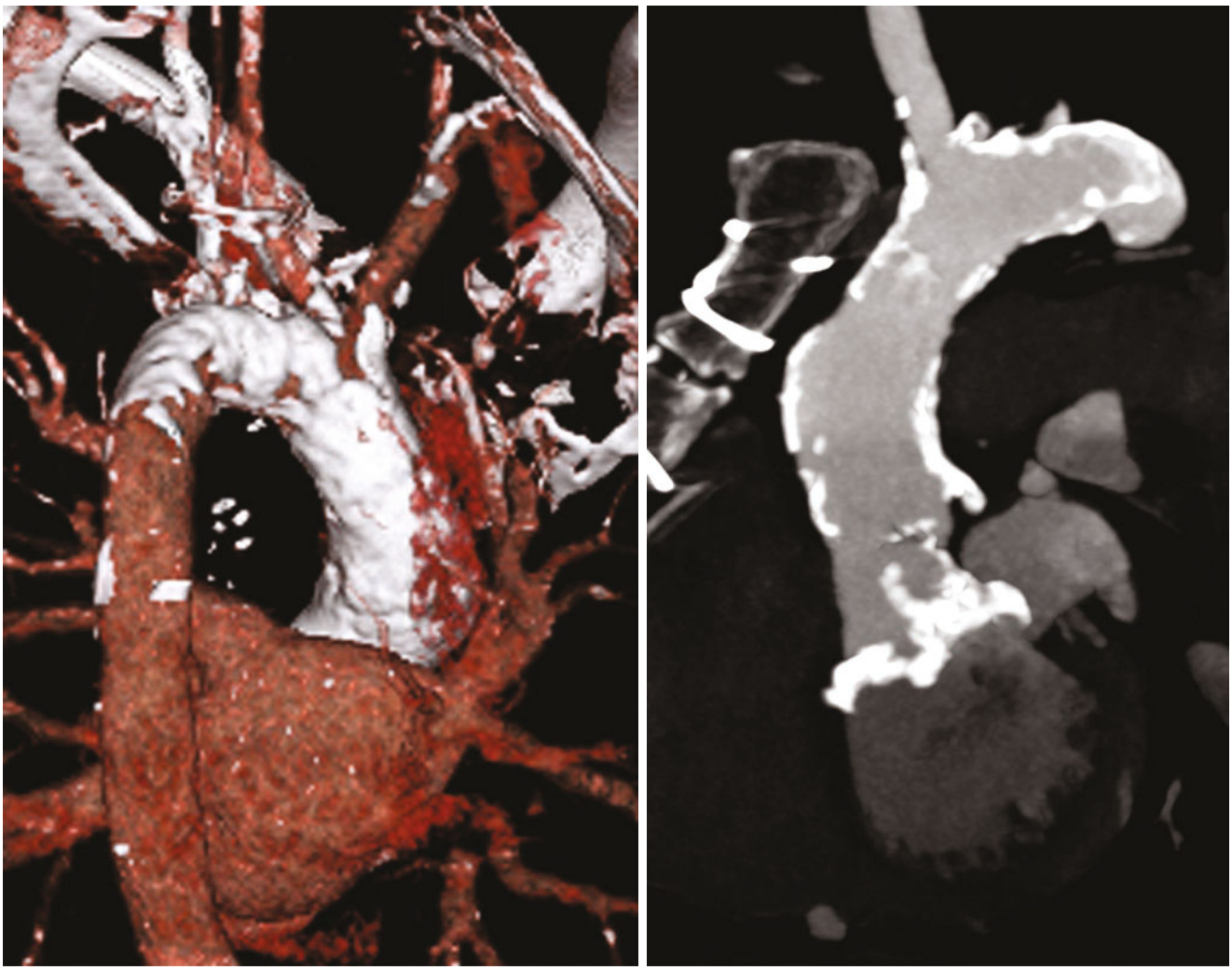

Fig. 8.20 Aortic calcification. Severe calcification of the ascending aorta and arch and the mitral annulus in a young woman who underwent chest radiation therapy during childhood. This calcification poses a challenge prior to combined coronary bypass graft and valvular surgery

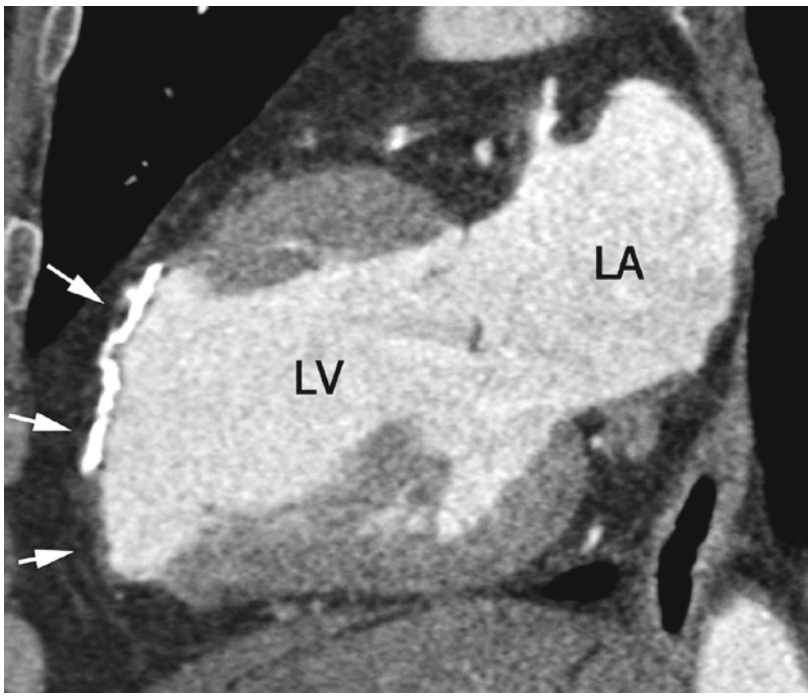

Fig. 8.21 Chronic myocardial infarction. Finding an obstructed graft does not equal myocardial ischemia. Coronary obstruction may not be severe, collateral circulation may be well developed, or viable myocardium may be absent. Therefore, functional information, including the presence and location of ischemia, is important, as well as detection of dysfunctional viable myocardium. In this case, revascularization of an occluded LAD artery is unlikely to benefit the patient, who suffered an anterior myocardial infarct. The scar is thin, partially calcified (*arrows*) and therefore unlikely to contain viable tissue. *LA* left atrium, *LV* left ventricle

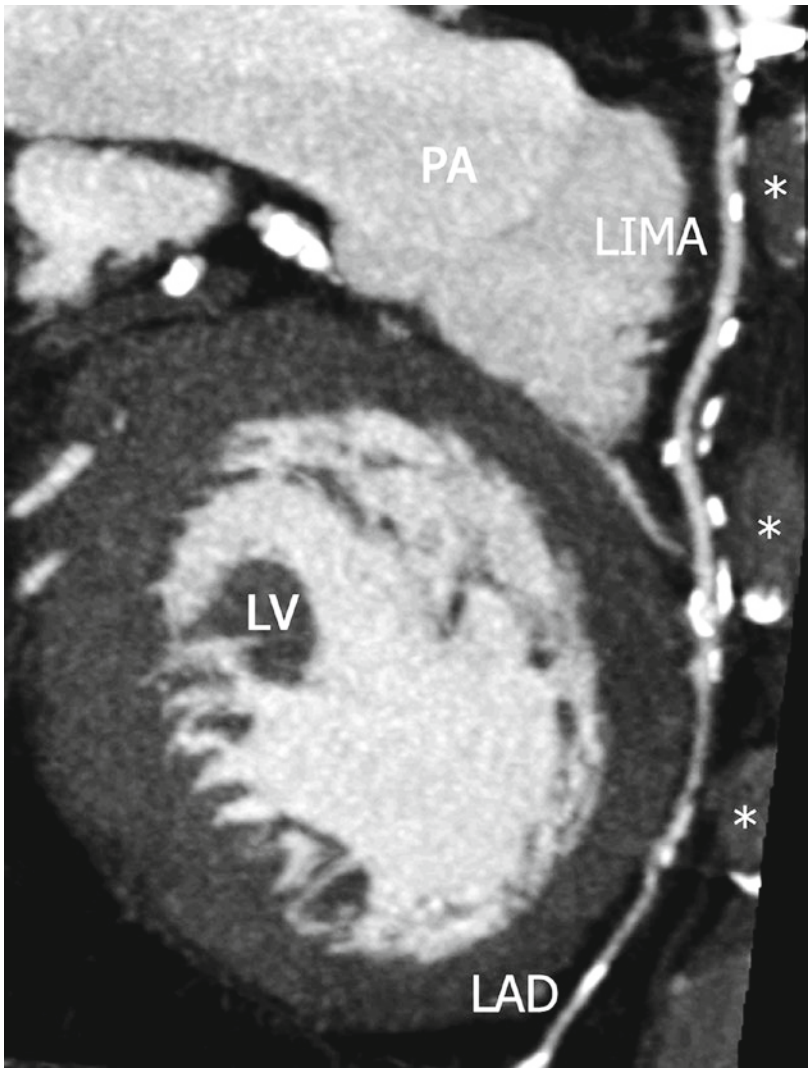

Fig. 8.22 Retrosternal course of the left internal mammary artery (LIMA). CT imaging may provide additional and useful information before (redo) cardiac surgery. Detailed anatomic knowledge—such as the route of a patent bypass graft within the chest—is particularly important when redo coronary artery bypass grafting or other cardiac surgery is considered. Alternatively, before a minimally invasive coronary artery bypass graft procedure, anatomic knowledge about potential graft material may facilitate harvesting. On this image, the *asterisks* designate the ribs. *LAD* left anterior descending, *PA* pulmonary artery

Cardiac CT After Bypass Graft Stenting

Although evaluation of coronary stents can be complicated, stents in grafts are generally larger and therefore more readily interpretable (Figs. 8.23 and 8.24).

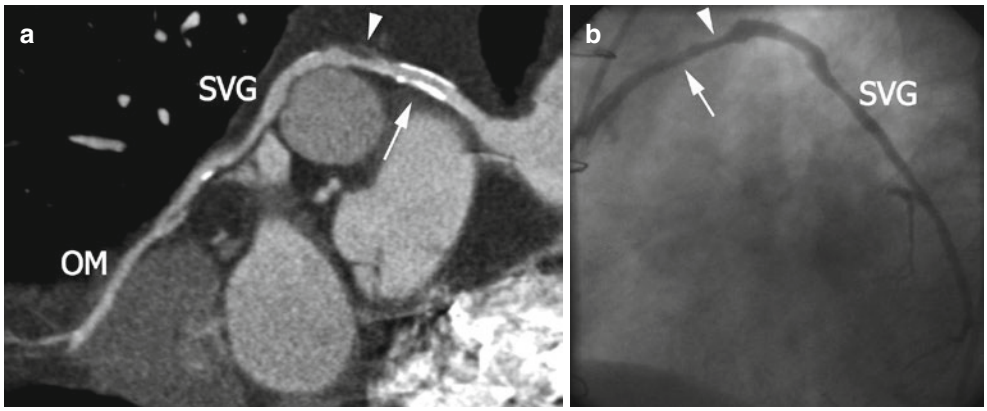

Fig. 8.23 Stented vein graft. A stent has been implanted in the proximal part of a venous graft (*arrow*, **a** and **b**). Although partial volume effects enlarge the apparent size of the stent struts, the in-stent lumen can still be assessed because of the stent's larger diameter and modest motion. Moderate narrowing (*arrowhead*, **a** and **b**) can be observed distal to the stent

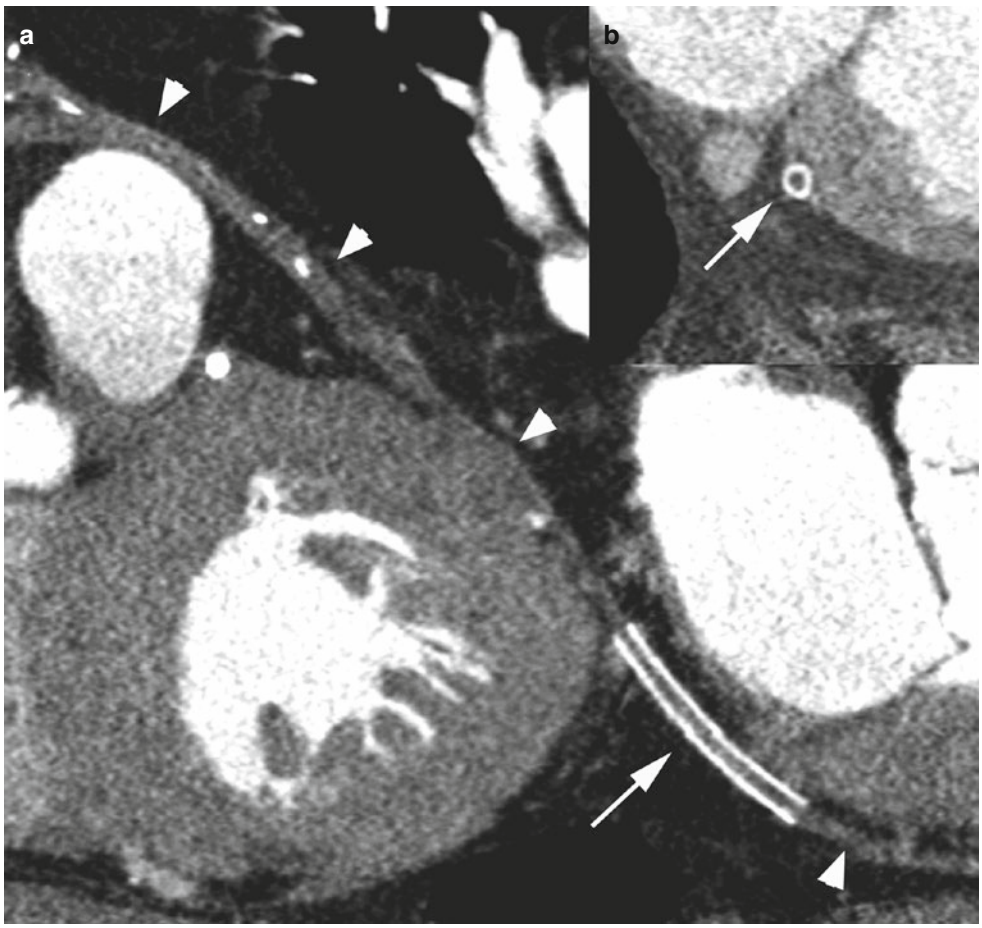

Fig. 8.24 Occluded graft after percutaneous coronary intervention. Complete occlusion of a venous graft occurred after percutaneous intervention. Curved multiplanar reformation shows the course of the low-density shadow of the occluded graft (*arrowheads*) including the stent (*arrow*) in the distal segment

References

1. Bryan AJ, Angelini GD. The biology of saphenous vein occlusion: etiology and strategies for prevention. Curr Opin Cardiol. 1994;9:641–9.
2. Barner HB, Standeven JW, Reese J. Twelve-year experience with internal mammary artery for coronary artery bypass. J Thorac Cardiovasc Surg. 1985;90:668–75.
3. Goldman S, Zadina K, Moritz T, Ovitt T, Sethi G, Copeland JG, et al. Long-term patency of saphenous vein and left internal mammary artery grafts after coronary artery bypass surgery: results from a department of veterans affairs cooperative study. J Am Coll Cardiol. 2004;44:2149–56.
4. Cameron A, Davis KB, Rogers WJ. Recurrence of angina after coronary artery bypass surgery: predictors and progression (CASS registry). J Am Coll Cardiol. 1995;26:895–9.
5. Bateman TM, Gray RJ, Whiting JS, Matloff JM, Berman DS, Forrester JS. Cine computed tomographic evaluation of aortocoronary bypass graft patency. J Am Coll Cardiol. 1986;8:693–8.
6. Stanford W, Brundage BH, MacMillan R, Chomka EV, Bateman TM, Eldredge WJ, et al. Sensitivity and specificity of assessing coronary bypass graft patency with ultrafast computed tomography: results of a multicenter study. J Am Coll Cardiol. 1988;12:1–7.
7. Wintersperger BJ, Engelmann MG, von Smekal A, Knez A, Penzkofer HV, Höfling B, et al. Patency of coronary bypass grafts: assessment with breath-hold contrast-enhanced MR angiography: value of a non-electrocardiographically triggered technique. Radiology. 1998;208:345–51.
8. Engelmann MG, von Smekal A, Knez A, Kürzinger E, Huehns TY, Höfling B, Reiser M. Accuracy of spiral computed tomography for identifying arterial and venous coronary graft patency. Am J Cardiol. 1997;80:569–74.
9. Achenbach S, Moshage W, Ropers D, Nossen J, Bachmann K. Noninvasive, three-dimensional visualization of coronary artery bypass grafts by electron beam tomography. Am J Cardiol. 1997;79:856–61.
10. Lu B, Dai RP, Jing BL, Bai H, He S, Zhuang N, et al. Evaluation of coronary artery bypass graft patency using three-dimensional reconstruction and flow study on electron beam tomography. J Comput Assist Tomogr. 2000;24:663–70.
11. Ropers D, Ulzheimer S, Wenkel E, Baum U, Giesler T, Derlien H, et al. Investigation of aortocoronary artery bypass grafts by multislice spiral computed tomography with electrocardiographic-gated image reconstruction. Am J Cardiol. 2001;88:792–5.
12. Yoo KJ, Choi D, Choi BW, Lim SH, Chang BC. The comparison of the graft patency after coronary artery bypass grafting using coronary angiography and multislice computed tomography. Eur J Cardiothorac Surg. 2003;24:86–91.
13. Nieman K, Rensing BJ, van Geuns RJ, Munne A, Ligthart JM, Pattynama PM, et al. Usefulness of multislice computed tomography for detecting obstructive coronary artery disease. Am J Cardiol. 2002;89:913–8.
14. Pache G, Saueressig U, Frydrychowicz A, Foell D, Ghanem N, Kotter E, et al. Initial experience with 64-slice cardiac CT: noninvasive visualization of coronary artery bypass grafts. Eur Heart J. 2006;27:976–80.
15. Ropers D, Pohle FK, Kuettner A, Pflederer T, Anders K, Daniel WG, et al. Diagnostic accuracy of noninvasive coronary angiography in patients after bypass surgery using 64-slice spiral computed tomography with 330-ms gantry rotation. Circulation. 2006;114:2334–41.
16. Malagutti P, Nieman K, Meijboom WB, van Mieghem CA, Pugliese F, Cademartiri F, et al. Use of 64-slice CT in symptomatic patients after coronary bypass surgery: evaluation of grafts and coronary arteries. Eur Heart J. 2007;28:1879–85.
17. Meyer TS, Martinoff S, Hadamitzky M, Will A, Kastrati A, Schömig A, Hausleiter J. Improved noninvasive assessment of coronary artery bypass grafts with 64-slice computed tomographic angiography in an unselected patient population. J Am Coll Cardiol. 2007;49:946–50.
18. Jabara R, Chronos N, Klein L, Eisenberg S, Allen R, Bradford S, Frohwein S. Comparison of multidetector 64-slice computed tomographic angiography to coronary angiography to assess the patency of coronary artery bypass grafts. Am J Cardiol. 2007;99:1529–34.
19. Onuma Y, Tanabe K, Chihara R, Yamamoto H, Miura Y, Kigawa I, et al. Evaluation of coronary artery bypass grafts and native coronary arteries using 64-slice multidetector computed tomography. Am Heart J. 2007;154:519–26.
20. Feuchtner GM, Schachner T, Bonatti J, Friedrich GJ, Soegner P, Klauser A, zur Nedden D. Diagnostic performance of 64-slice computed tomography in evaluation of coronary artery bypass grafts. Am J Roentgenol. 2007;189:574–80.
21. Nazeri I, Shahabi P, Tehrai M, Sharif-Kashani B, Nazeri A. Assessment of patients after coronary artery bypass grafting using 64-slice computed tomography. Am J Cardiol. 2009;103:667–73.
22. Weustink AC, Nieman K, Pugliese F, Mollet NR, Meijboom WB, van Mieghem C, et al. Diagnostic accuracy of computed tomography angiography in patients after bypass grafting: comparison with invasive coronary angiography. JACC Cardiovasc Imaging. 2009;2:816–24.
23. Lee JH, Chun EJ, Choi SI, Vembar M, Lim C, Park KH, Choi DJ. Prospective versus retrospective ECG-gated 64-detector coronary CT angiography for evaluation of coronary artery bypass graft patency: comparison of image quality, radiation dose and diagnostic accuracy. Int J Cardiovasc Imaging. 2011;27:657–67.
24. Şahiner L, Canpolat U, Aytemir K, Hazirolan T, Yorgun H, Kaya EB, Oto A. Diagnostic accuracy of 16- versus 64-slice multidetector computed tomography angiography in the evaluation of coronary artery bypass grafts: a comparative study. Interact Cardiovasc Thorac Surg. 2012;15:847–53.
25. Sahiner L, Canpolat U, Yorgun H, Hazrolan T, Karçaaltncaba M, Sunman H, et al. Diagnostic accuracy of dual-source 64-slice multidetector computed tomography in evaluation of coronary artery bypass grafts. J Investig Med. 2012;60:1180–5.
26. Salm LP, Bax JJ, Jukema JW, Schuijf JD, Vliegen HW, Lamb HJ, et al. Comprehensive assessment of patients after coronary artery bypass grafting by 16-detector-row computed tomography. Am Heart J. 2005;150:775–81.
27. Nl S, Küttner A, Schröder S, Drosch T, Beck T, Stauder H, et al. Coronary artery bypass grafts: assessment of graft patency and native coronary artery lesions using 16-slice MDCT. Eur Radiol. 2006;16:2512–20.

Functional Significance of Coronary Stenoses Identified by CT

9

Joshua Schulman-Marcus and James K. Min

Coronary CT angiography provides increasingly high anatomic detail of coronary stenosis, with a high sensitivity and negative predictive value for coronary artery stenoses (CAD). From the advent of this technology, however, concerns were raised regarding the limited specificity of CT for determining which coronary stenoses cause myocardial ischemia [1]. This determination is important, as detection of ischemia is the cornerstone of "functional" testing for CAD, whether noninvasively through myocardial perfusion imaging (MPI) and stress echocardiography or invasively through fractional flow reserve (FFR) [2]. There was also hesitation that the highly sensitive anatomic detection of CAD by CT could lead to increased invasive downstream testing and revascularization, which was observed in CT trials [3, 4]. Functional imaging providing information about specific lesions or the subtended myocardium could potentially improve the value of a CT scan and its role as a gatekeeper to the catheterization laboratory [5]. As such, a major focus of CT research has been the devising of techniques to garner functional information from CT images. Early success augurs future progress in this area.

Research since about 2010 has focused on measuring lesion-specific ischemia by coronary CTA, which is currently approximated by the gold standard of invasive FFR. By taking advantage of advances in computational fluid dynamics, methods to derive noninvasive FFR from CT imaging data (FFR_{CT}) have been developed and are now commercially available for clinical use [6] (Figs. 9.1, 9.2, 9.3, 9.4, 9.5, 9.6, 9.7, 9.8, 9.9, 9.10, 9.11, 9.12, 9.13, 9.14, 9.15, 9.16, 9.17, and 9.18). The accuracy of FFR_{CT} has steadily improved with further iterations of the software and overall improvements in CT imaging. As of 2016, FFR_{CT} is being studied in several ongoing trials (Table 9.1) to better define its use [6].

Extensive research also has studied the association between adverse plaque characteristics as identified by coronary CTA and the functional significance of those plaques. The aim is to better identify which plaque characteristcs correlate with reduced invasive FFR, and ultimately with outcomes (Figs. 9.19, 9.20, and 9.21). This line of research is also raising provocative and interesting findings regarding the interplay of atherosclerosis, ischemia, and outcomes [16].

J. Schulman-Marcus
Department of Cardiology, Albany Medical Center,
47 New Scotland Avenue, Albany, NY 12208, USA
e-mail: schulmj1@mail.amc.edu

J.K. Min (✉)
Dalio Institute of Cardiovascular Imaging, New York-Presbyterian Hospital and Weill Cornell Medicine, New York, NY, USA
e-mail: jkm2001@med.cornell.edu

M.J. Budoff et al. (eds.), *Atlas of Cardiovascular Computed Tomography*, https://doi.org/10.1007/978-1-4471-7357-1_9

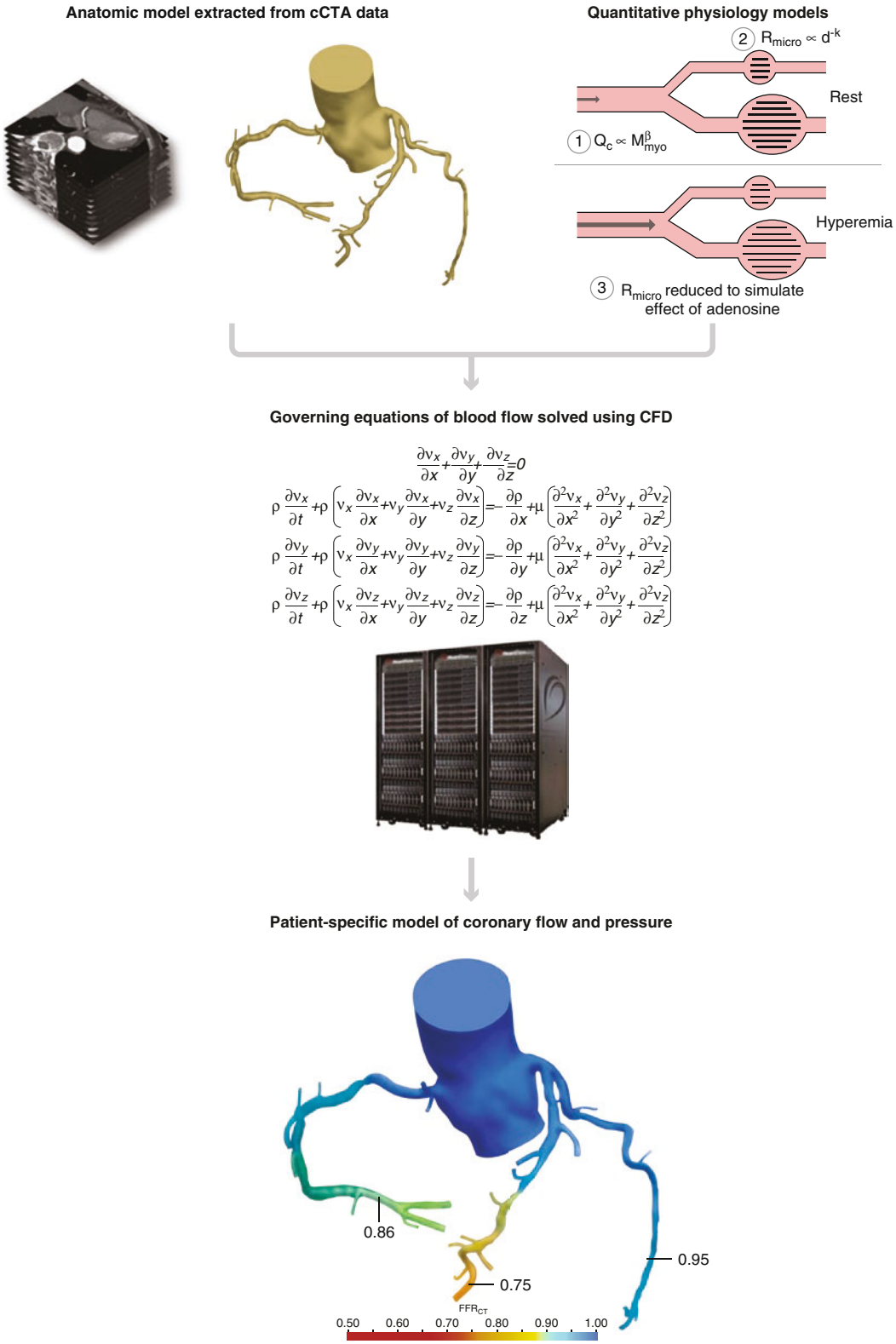

Fig. 9.1 The overall concept of fractional flow reserve derived from CT imaging (FFR_{CT}). FFR_{CT} uses coronary CTA data sets acquired under restsing conditions, physiologic models of coronary flow and resistance, and computational fluid dynamics to create patient-specific models of flow and pressure. These models allow visualization of changes in FFR across the coronary vasculature. *cCTA* coronary CT angiography, *CFD* computational fluid dynamics

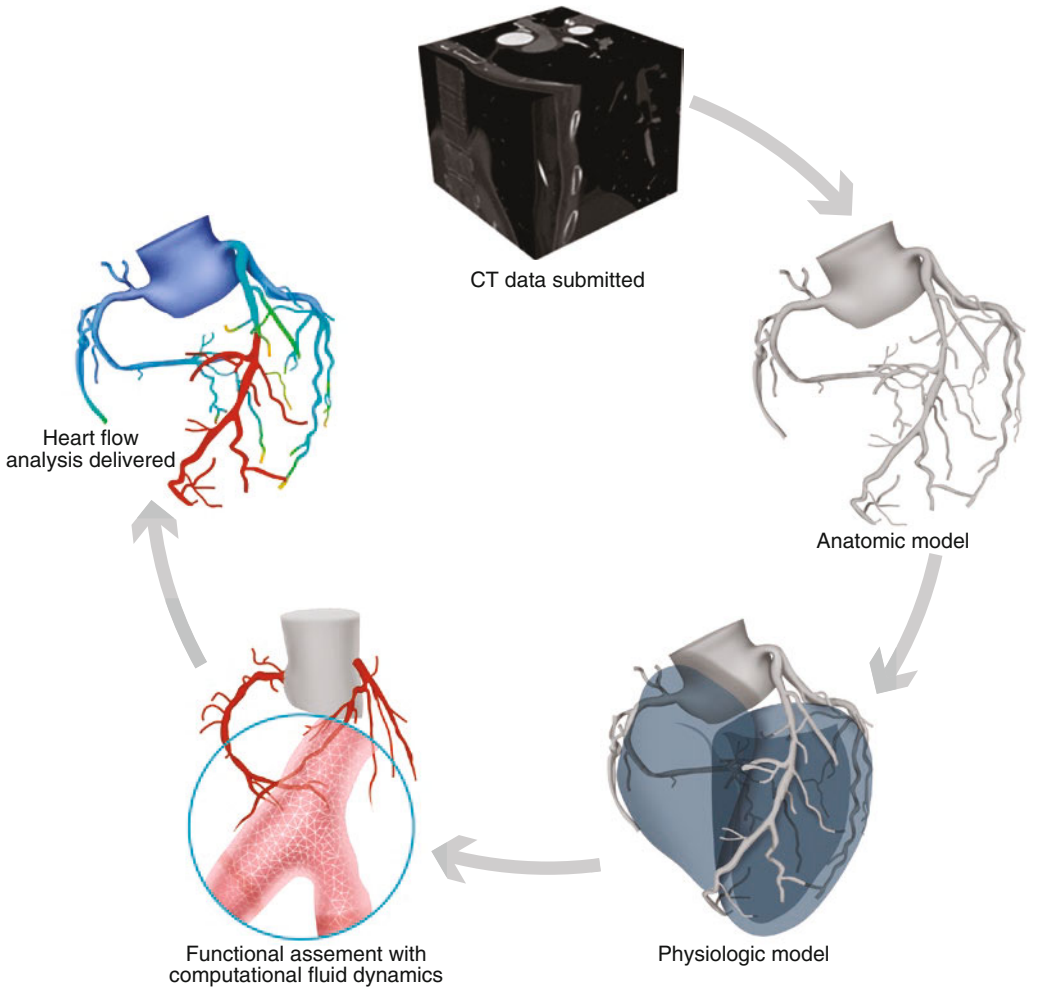

Fig. 9.2 As of this writing, FFR_{CT} is commercially provided only by HeartFlow, Inc. (Redwood City, CA). CT data are transmitted to HeartFlow, where they undergo analysis. Each of the coronary artery segments undergoes mesh segmentation, and the governing equations of fluid dynamics are solved for each of these meshes to calculate FFR_{CT} within the entire vascular bed. Myocardial blood flow is calculated by coupling the arterial form with myocardial mass quantification

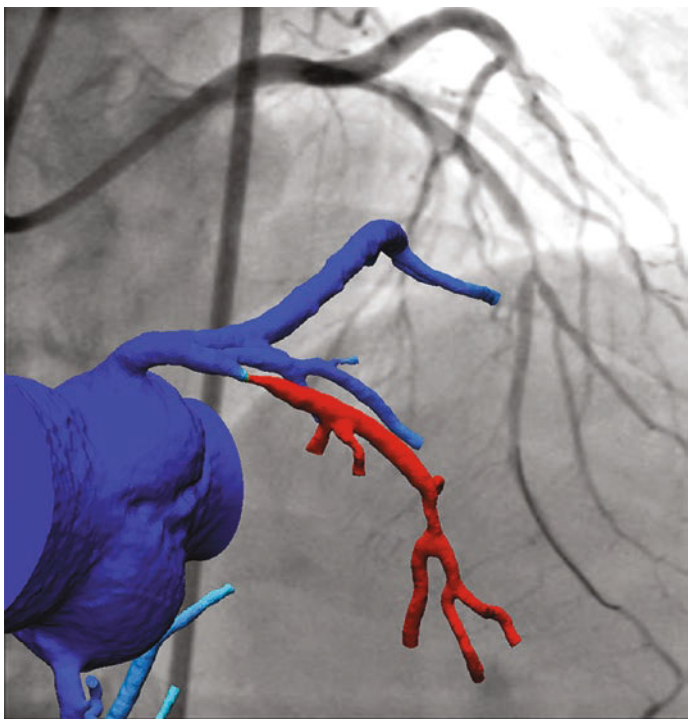

Fig. 9.3 This shows the method of correlation of FFR_{CT} to invasive FFR. The computational model is rotated to the projection of the angiographic image. The points of the pressure wire were identified on the model in a blinded fashion (without FFR_{CT} or color coding). The marked models were then sent to the FFR_{CT} core lab, which disclosed the FFR_{CT} value at that location. It is important to select the correct corresponding point for correlation, as FFR_{CT} values can vary along the length of the coronary artery. Here, FFRCT is estimated to be reduced (red segment) distal to a lesion in the left anterior descending (LAD) artery

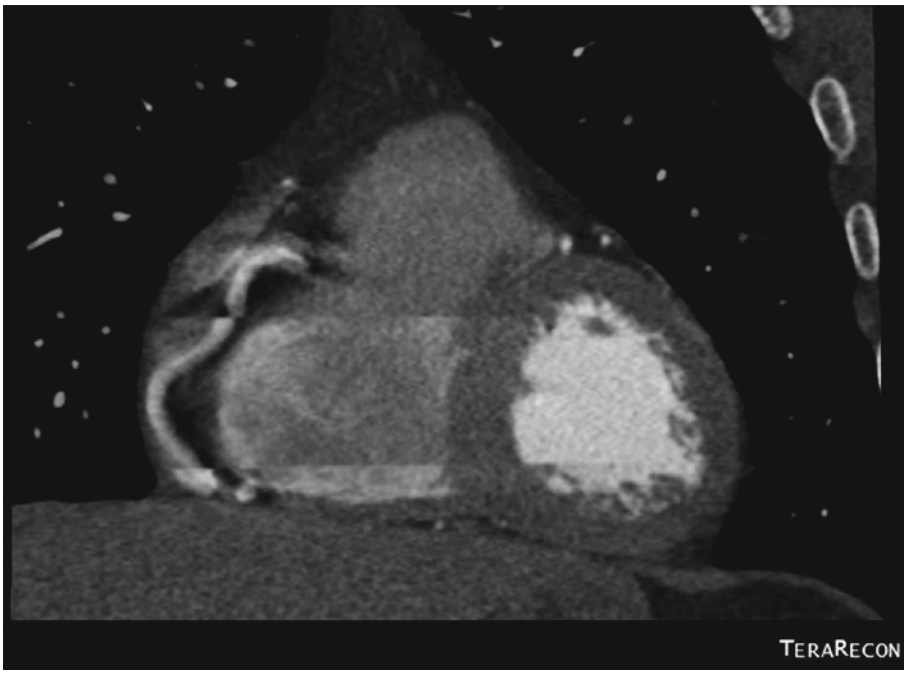

Fig. 9.4 Computation of FFR_{CT} is contingent on adherence to image acquisition guidelines and good image quality. Sublingual nitroglycerin is necessary for arterial visualization. Artifacts from excess cardiac motion, breathing, calcium "blooming," inadequate contrast opacification, or incomplete acquisition of all myocardial tissue may preclude FFR_{CT} calculation

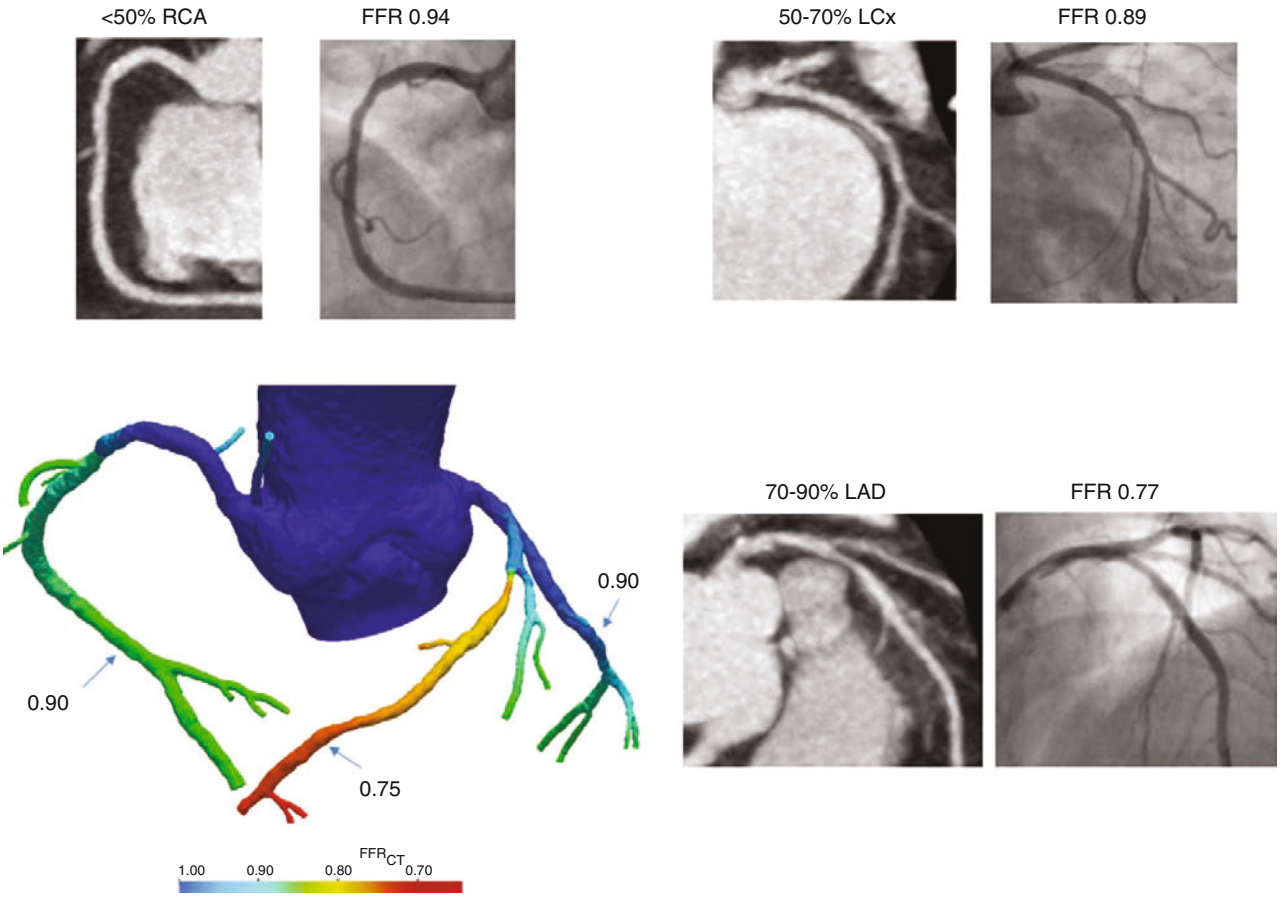

Fig. 9.5 Use of FFR_{CT} in intermediate-severity stenoses. This 66-year-old woman had recent onset of typical angina symptoms. She had no cardiac risk factors. A CTA demonstrated 70–90% stenosis in the LAD artery, 50–70% in the left circumflex (LCx), and 30–50% in the right coronary artery (RCA). FFR_{CT} correlates with invasive FFR in demonstrating ischemia only in the region of the LAD stenosis

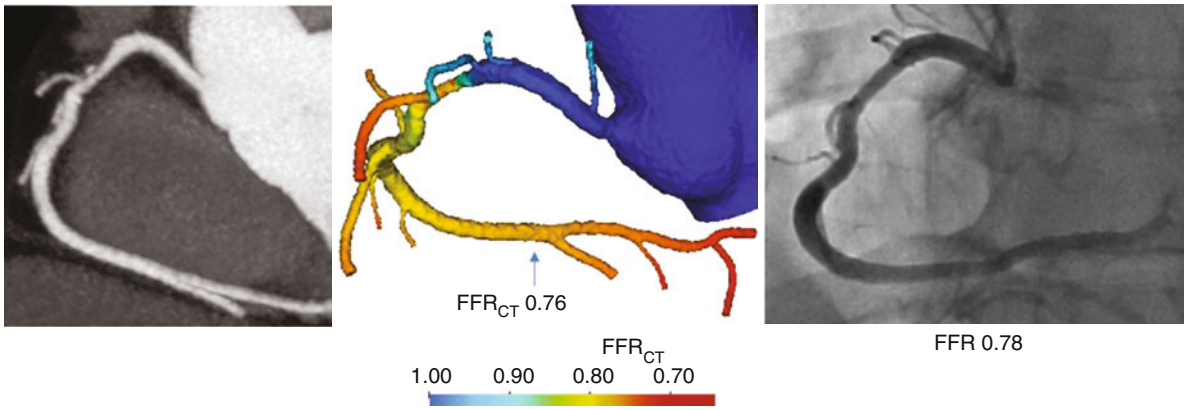

Fig. 9.6 This 69-year-old Asian man had stable, atypical chest pain. Coronary CTA demonstrated a 50–70% stenosis in the RCA. FFR_{CT} is reduced in the region consistent with ischemia. Invasive angiography and FFR correlate with coronary CTA findings

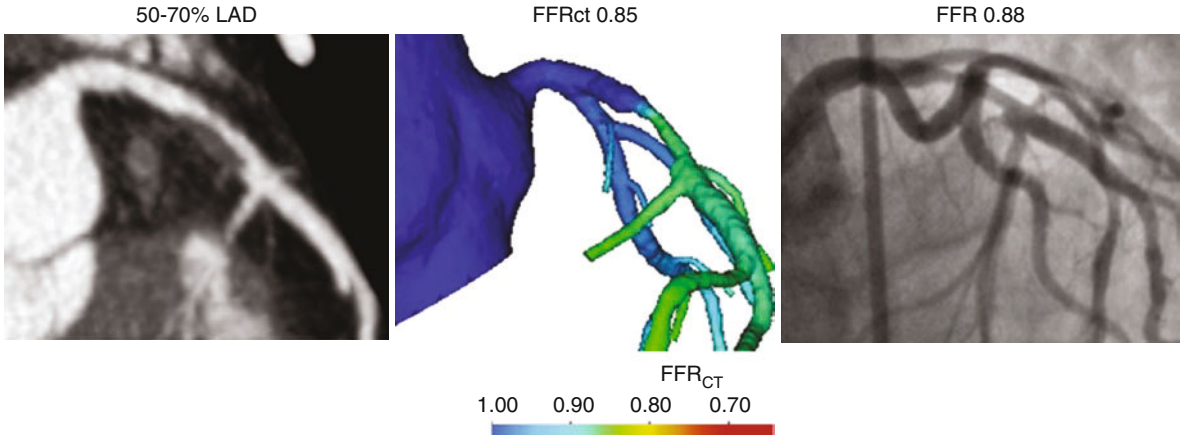

Fig. 9.7 Findings from a 70-year-old woman with hypertension, hyperlipidemia, and angina symptoms. Coronary CTA demonstrates a noncalcified plaque in the LAD artery with estimated 50–70% luminal stenosis. By quantitative coronary angiography, it measured 58% stenosis. However, it was not ischemia-producing by either FFR_{CT} or FFR

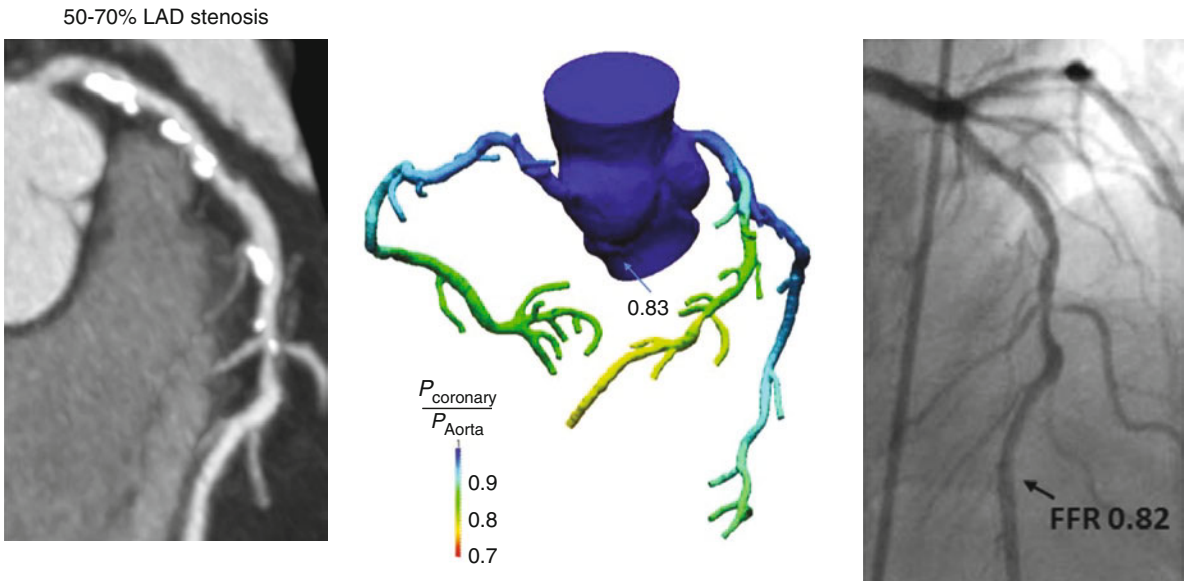

Fig. 9.8 Owing to imaging characteristics, the degree of stenosis from calcified plaque is potentially overestimated, and obstructive disease can be challenging to exclude. FFR_{CT} can help overcome this problem by demonstrating lack of ischemia in such plaques. Here, the finding of FFR_{CT} correlates well with invasive FFR

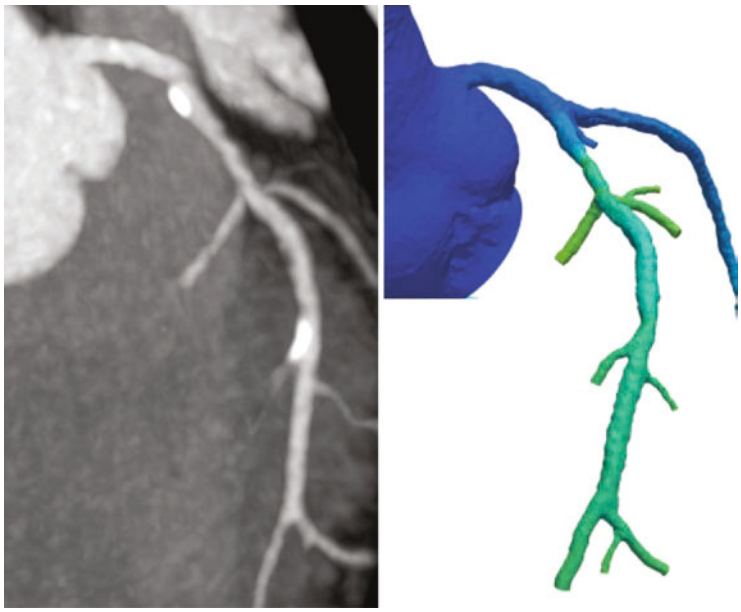

Fig. 9.9 One potential use of FFR_{CT} is to defer invasive coronary angiography that is likely to find nonobstructive coronary artery disease. This FFR_{CT} comes from a patient in the PLATFORM trial [7], which demonstrated that 61% of scheduled invasive coronary angiograms were cancelled in patients with FFR_{CT} without any clinical consequences

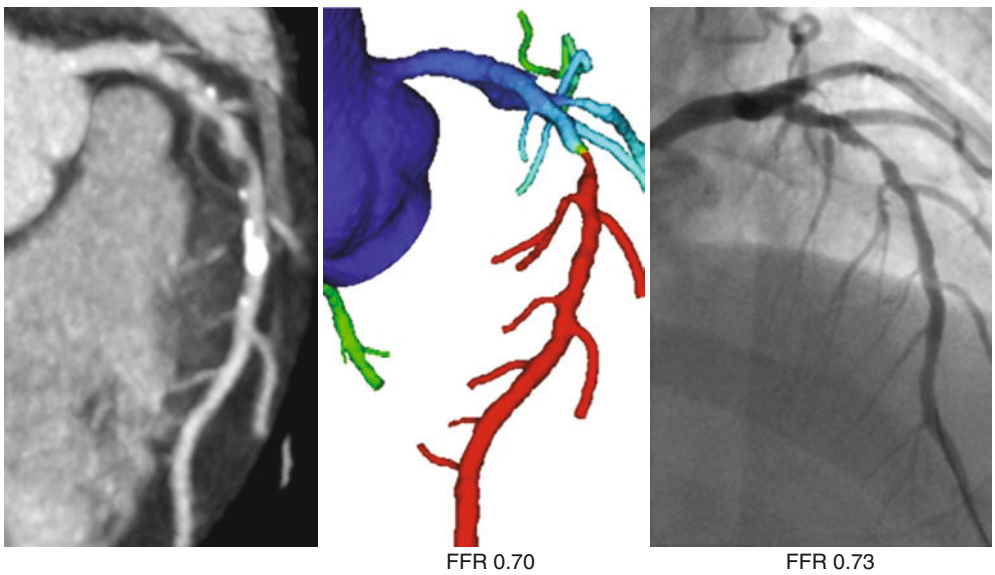

Fig. 9.10 Correlation of FFR_{CT} with invasive FFR in a patient with severe stenosis. This 65-year-old woman had typical angina and several cardiac risk factors. CTA demonstrates a >70% stenotic lesion in the mid LAD artery, as well as diffuse plaque. FFR_{CT} correlates with FFR in demonstrating the ischemia induced by the lesion

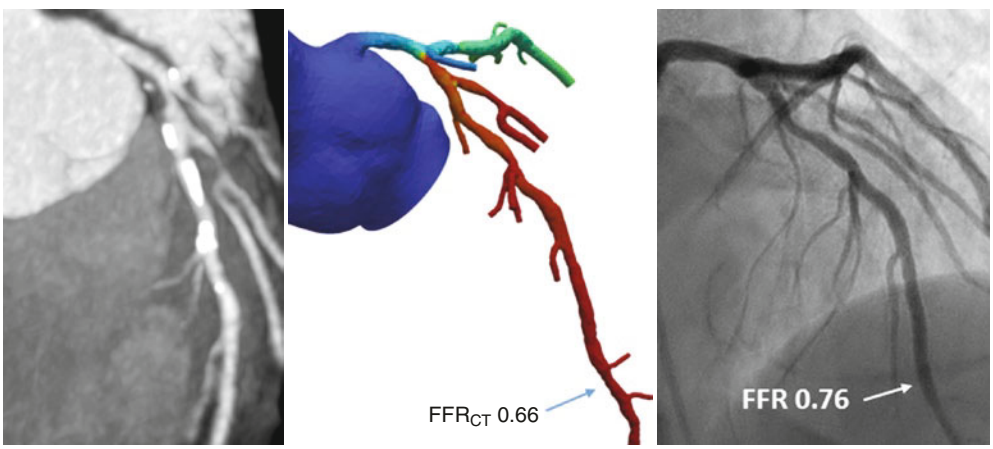

Fig. 9.11 Correlation of a patient with a 70–90% proximal LAD artery stenosis with severely reduced downstream FFR_{CT} and correlating FFR from the PLATFORM trial [7]

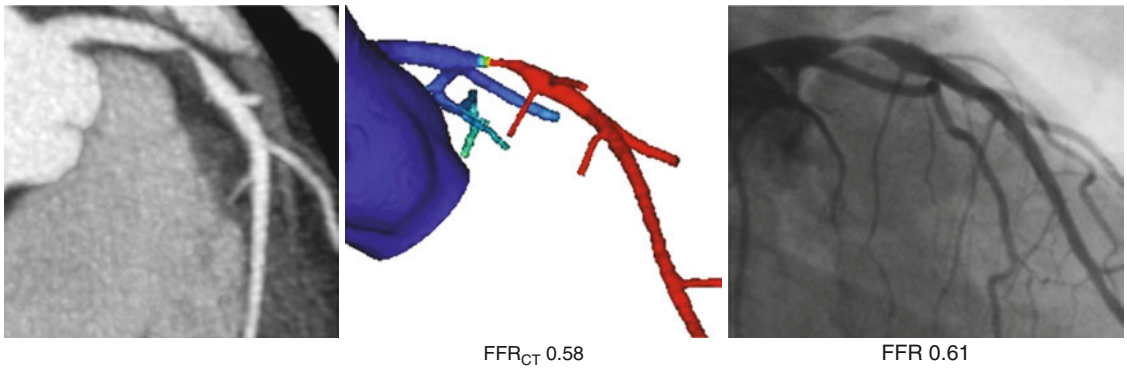

Fig. 9.12 This 54-year-old woman with new angina had a history of type 2 diabetes mellitus, hypertension, and hyperlipidemia, and was a former smoker. CTA demonstrated a large, noncalcified plaque with 90% luminal stenosis in the proximal LAD artery, with severely reduced FFR_{CT}. Invasive angiography demonstrated a 67% lesion with a reduced FFR

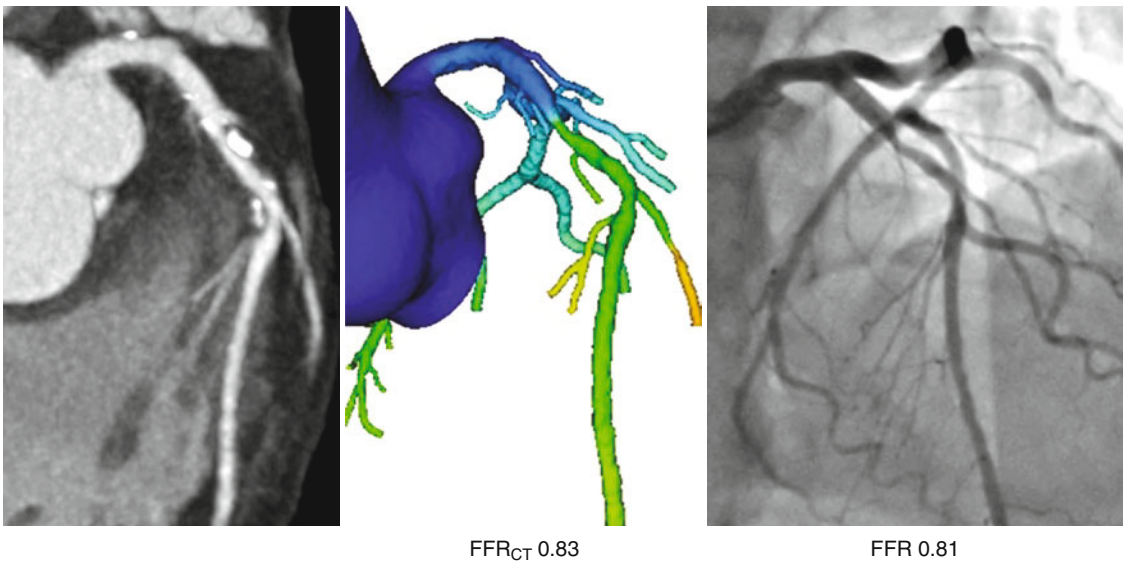

Fig. 9.13 Degree of stenosis and FFR do not always correlate. These images are from a 57-year-old man with typical angina symptoms and no risk factors except for a prior history of tobacco use. Coronary CTA demonstrated partially calcified plaque with a 70–90% stenosis in the mid LAD artery. However, FFR_{CT} of the lesion was 0.83, which suggests that the lesion was not producing ischemia. The lesion caused 52% luminal stenosis by quantitative coronary angiography, and invasive FFR correlated with FFR_{CT}

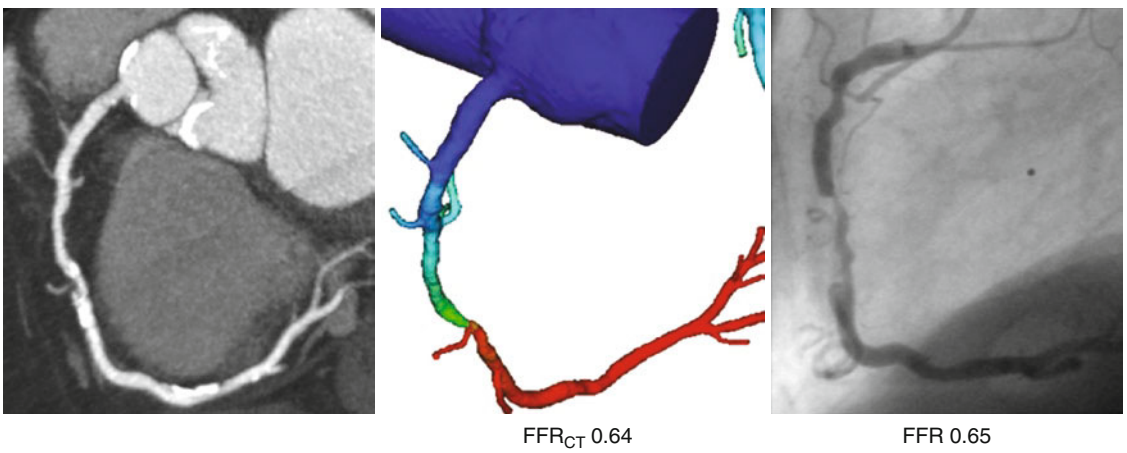

Fig. 9.14 These images are from a 61-year-old man with an estimated 30–49% stenosis of the right coronary artery in coronary CTA. However, FFR_{CT} measured 0.64, suggestive of ischemia. Quantitative invasive coronary angiography measured a 76% stenosis, with a similarly low FFR

Fig. 9.15 FFR_{CT} can be useful in patients with diffuse calcification, to localize an ischemia-causing plaque. This patient had an estimated 90% lesion in the proximal LAD, along with diffuse calcific plaque (calcium score, 1338). The FFR_{CT} of 0.53 suggests ischemia resulting from the proximal lesion

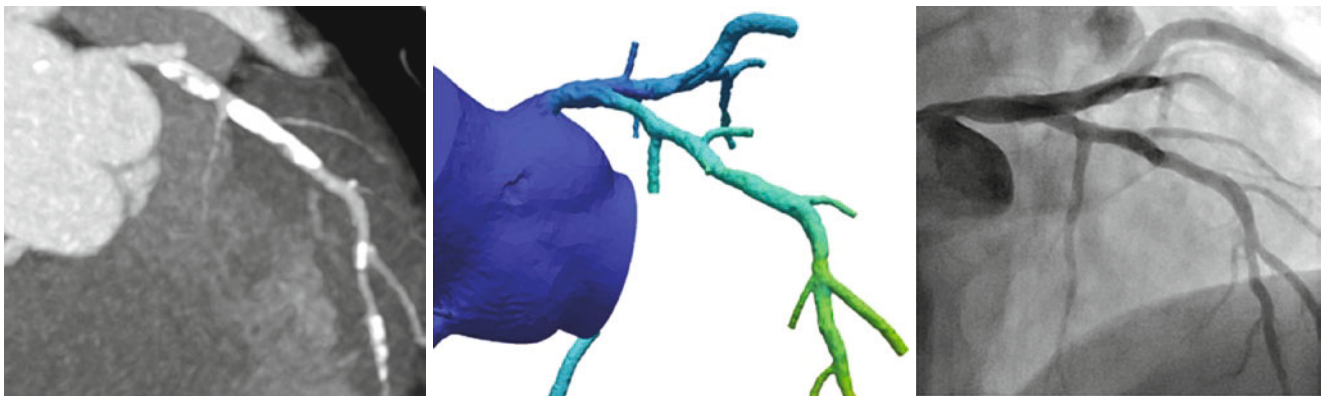

Fig. 9.16 This patient had diffuse calcification (calcium score, 417) of the LAD, with an estimated stenosis of 50–70% in the LAD artery. FFR_{CT} was 0.84, suggesting no ischemia. No significant stenosis was visualized during invasive coronary angiography, and invasive FFR was not performed

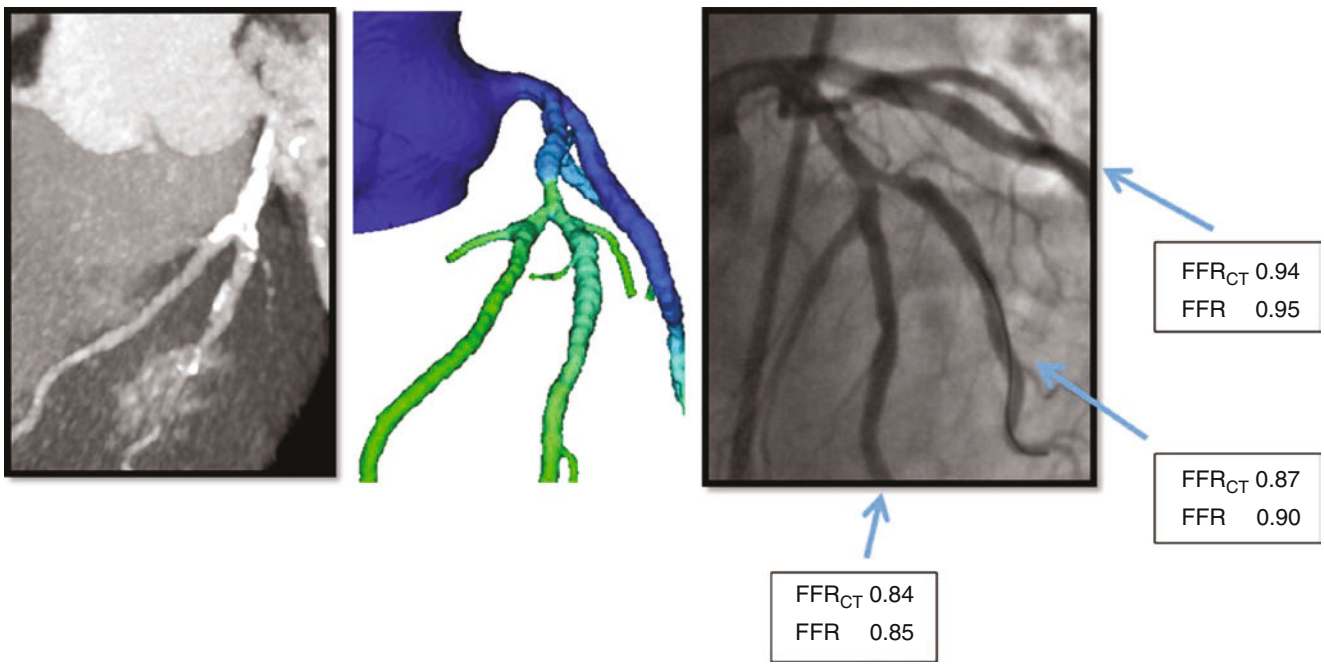

Fig. 9.17 This patient had severe calcification of the proximal LAD artery (calcium score 739) and an estimated 70% luminal stenosis, but FFR_{CT} did not suggest ischemia, and this finding was corroborated by multivessel invasive FFR. FFR_{CT} has been reported to retain its use in patients with high calcium scores [8]

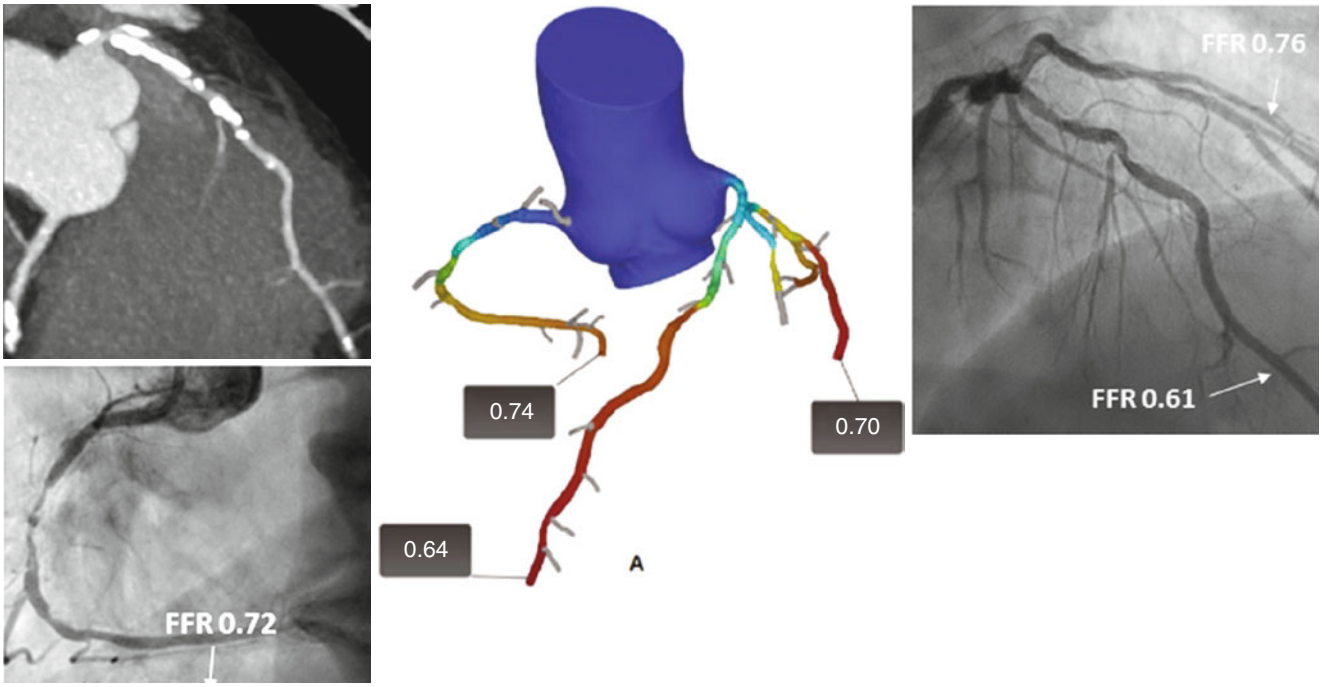

Fig. 9.18 This patient with multivessel calcific disease (calcium score, 1509) had multiple lesions of estimated 50–70% luminal stenosis. Each vessel territory was found to be ischemic by FFR_{CT}, which was corroborated invasively

Table 9.1 Major validation studies in FFR_{CT} (Using invasive FFR as the reference standard)

Study name	Total patients	FFR_{CT} software version	Per-vessel sensitivity	Per-vessel specificity
DISCOVER-FLOW [9]	103	1.0	88%	82%
DeFACTO [10]	252	1.2	83%	78%
NXT [11]	254	1.4	84%	86%

DeFACTO Determination of Fractional Flow Reserve by Anatomic Computed Tomographic Angiography, *DISCOVER-FLOW* Diagnosis of Ischemia-Causing Stenoses Obtained Via Noninvasive Fractional Flow Reserve, *FFR_{CT}* fractional flow reserve derived from CT imaging, *NXT* Analysis of Coronary Blood Flow Using CT Angiography: Next Steps

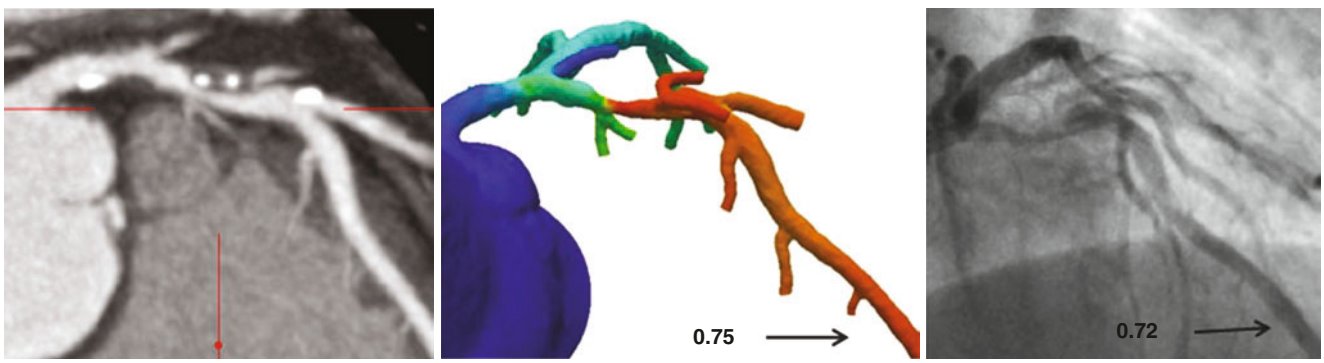

Fig. 9.19 Adverse plaque characteristics in coronary CTA (positive vessel remodeling, low attenuation plaque, and spotty calcification) have been associated with increased risk of cardiac events [12]. Recent work has found that plaque characteristics associated with vulnerability are correlated with lesions that produce ischemia as detected by invasive FFR [13]. In these images, a plaque with several adverse plaque characteristics is identified as being ischemic by both FFR_{CT} and invasive FFR

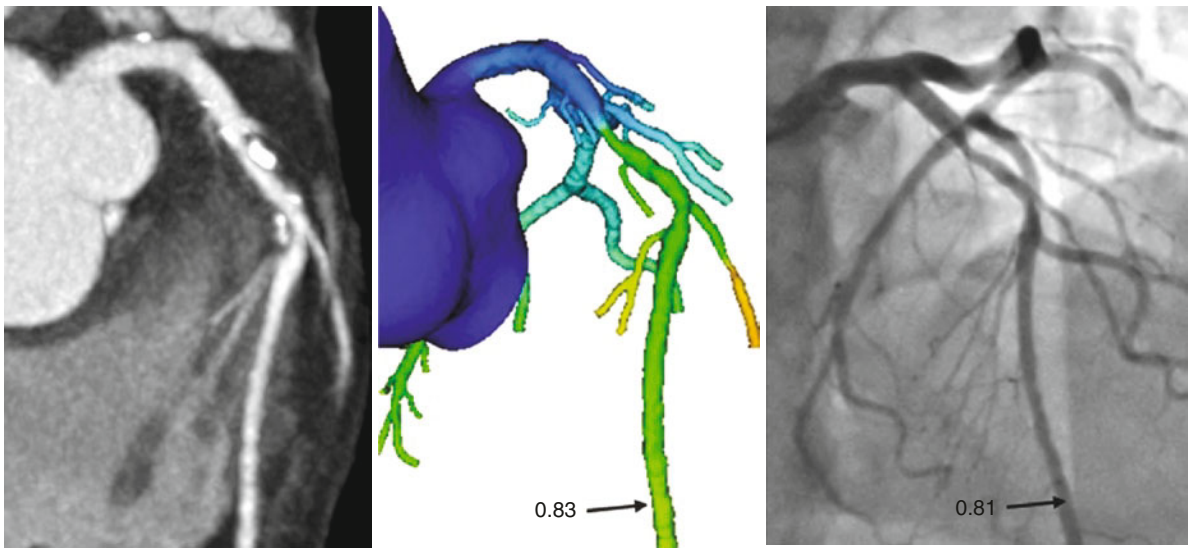

Fig. 9.20 As not all coronary atherosclerotic lesions with adverse plaque characteristics cause myocardial ischemia, FFR_{CT} may be helpful in discriminating which plaques are functionally significant [14]. Here, a patient with an estimated 70–90% stenosis in coronary CTA with several adverse characteristics did not have vessel-specific ischemia identified by FFR_{CT}. The lesion was measured to have 52% luminal stenosis by quantitative coronary angiography and an invasive FFR that was not ischemic

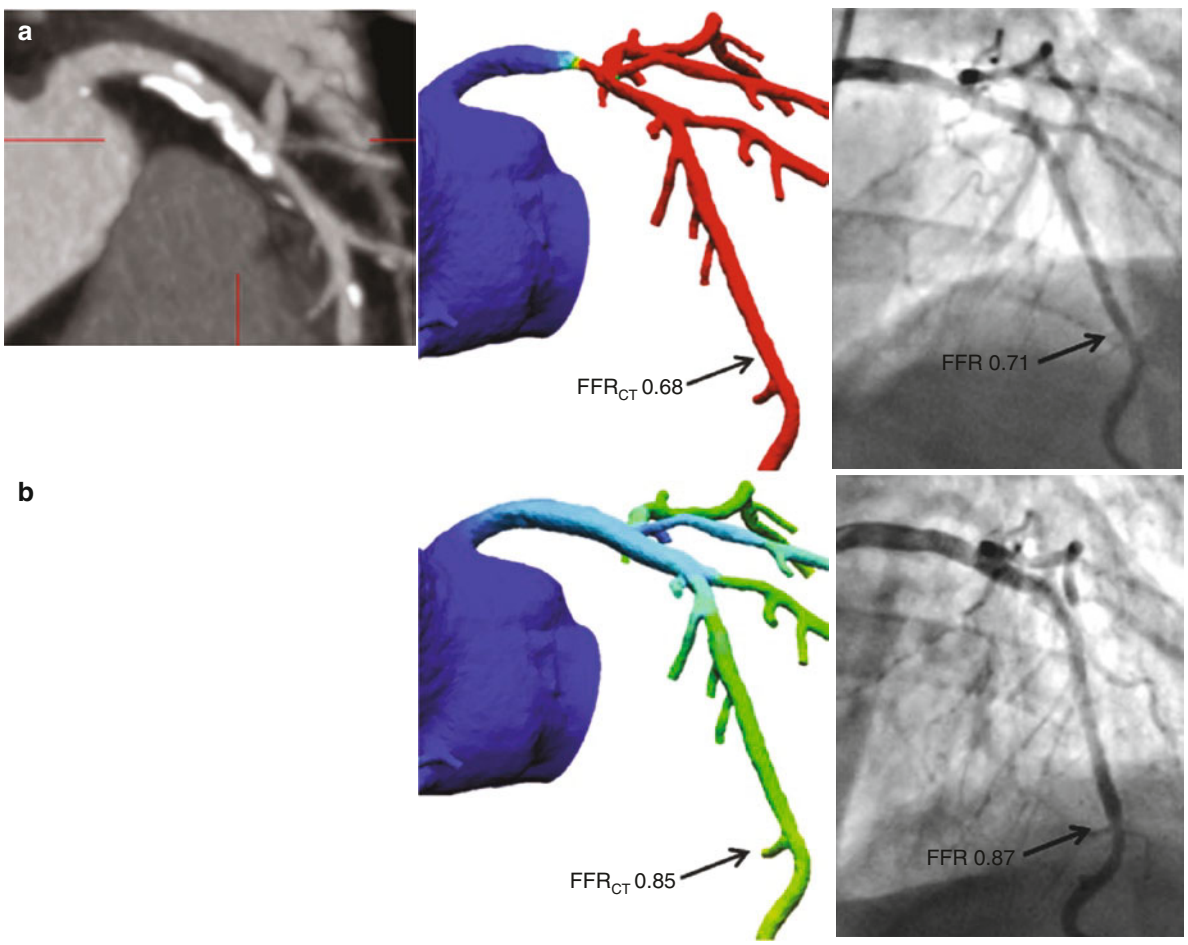

Fig. 9.21 There is interest in using FFR_{CT} to model the effects of revascularization on ischemia-producing lesions [15]. (**a**) In this example, a 61-year-old man with stable angina and multiple cardiac risk factors was found to have significant left main artery disease. (**b**) The placement of a virtual "stent" improved ischemia as detected as predicted by FFR_{CT}, a finding that was confirmed by post-revascularization invasive FFR

Acknowledgement We appreciate the provision of images from Dr. Christopher K. Zarins, HeartFlow, Inc.

References

1. Meijboom WB, Meijs MF, Schuijf JD, Cramer MJ, Mollet NR, van Mieghem CA, et al. Diagnostic accuracy of 64-slice computed tomography coronary angiography: a prospective, multicenter, multivendor study. J Am Coll Cardiol. 2008;52:2135–44.
2. Pijls NH, De Bruyne B, Peels K, Van Der Voort PH, Bonnier HJ, Bartunek JKJJ, Koolen JJ. Measurement of fractional flow reserve to assess the functional severity of coronary-artery stenoses. N Engl J Med. 1996;334:1703–8.
3. Hoffmann U, Truong QA, Schoenfeld DA, Chou ET, Woodard PK, Nagurney JT, ROMICAT-II Investigators, et al. Coronary CT angiography versus standard evaluation in acute chest pain. N Engl J Med. 2012;367:299–308.
4. Douglas PS, Hoffmann U, Patel MR, Mark DB, Al-Khalidi HR, Cavanaugh B, PROMISE Investigators, et al. Outcomes of anatomical versus functional testing for coronary artery disease. N Engl J Med. 2015;372:1291–300.
5. Marwick TH, Cho I, Ó Hartaigh B, Min JK. Finding the gatekeeper to the cardiac catheterization laboratory: coronary CT angiography or stress testing? J Am Coll Cardiol. 2015;65:2747–56.
6. Min JK, Taylor CA, Achenbach S, Koo BK, Leipsic J, Norgaard BL, et al. Noninvasive fractional flow reserve derived from coronary CT angiography: clinical data and scientific principles. JACC Cardiovasc Imaging. 2015;8:1209–22.
7. Douglas PS, Pontone G, Hlatky MA, Patel MR, Norgaard BL, Byrne RA, PLATFORM Investigators, et al. Clinical outcomes of fractional flow reserve by computed tomographic angiography-guided diagnostic strategies vs. usual care in patients with suspected coronary artery disease: the prospective longitudinal trial of FFR(CT): outcome and resource impacts study. Eur Heart J. 2015;36:3359–67.
8. Norgaard BL, Gaur S, Leipsic J, Ito H, Miyoshi T, Park SJ, et al. Influence of coronary calcification on the diagnostic performance of CT angiography derived FFR in coronary artery disease: a substudy of the NXT trial. JACC Cardiovasc Imaging. 2015;8:1045–55.
9. Koo BK, Erglis A, Doh JH, Daniels DV, Jegere S, Kim HS, et al. Diagnosis of ischemia-causing coronary stenoses by noninvasive fractional flow reserve computed from coronary computed tomographic angiograms. Results from the prospective multicenter DISCOVER-FLOW (Diagnosis of Ischemia-Causing Stenoses Obtained Via Noninvasive Fractional Flow Reserve) study. J Am Coll Cardiol. 2011;58:1989–97.
10. Min JK, Leipsic J, Pencina MJ, Berman DS, Koo BK, van Mieghem C, et al. Diagnostic accuracy of fractional flow reserve from anatomic CT angiography. JAMA. 2012;308:1237–45.
11. Norgaard BL, Leipsic J, Gaur S, Seneviratne S, Ko BS, Ito H, NXT Trial Study Group, et al. Diagnostic performance of noninvasive fractional flow reserve derived from coronary computed tomography angiography in suspected coronary artery disease: the NXT trial (Analysis of Coronary Blood Flow Using CT Angiography: Next Steps). J Am Coll Cardiol. 2014;63:1145–55.
12. Motoyama S, Sarai M, Harigaya H, Anno H, Inoue K, Hara T, et al. Computed tomographic angiography characteristics of atherosclerotic plaques subsequently resulting in acute coronary syndrome. J Am Coll Cardiol. 2009;54:49–57.
13. Park HB, Heo R, ó Hartaigh B, Cho I, Gransar H, Nakazato R, et al. Atherosclerotic plaque characteristics by CT angiography identify coronary lesions that cause ischemia: a direct comparison to fractional flow reserve. JACC Cardiovasc Imaging. 2015;8:1–10.
14. Gaur S, Ovrehus KA, Dey D, Leipsic J, Botker HE, Jensen JM, et al. Coronary plaque quantification and fractional flow reserve by coronary computed tomography angiography identify ischaemia-causing lesions. Eur Heart J. 2016;37:1220–7.
15. Kim KH, Doh JH, Koo BK, Min JK, Erglis A, Yang HM, et al. A novel noninvasive technology for treatment planning using virtual coronary stenting and computed tomography-derived computed fractional flow reserve. JACC Cardiovasc Interv. 2014;7:72–8.
16. Ahmadi A, Kini A, Narula J. Discordance between ischemia and stenosis, or PINSS and NIPSS: are we ready for new vocabulary? JACC Cardiovasc Imaging. 2015;8:111–4.

Suggested Reading

Hlatky MA, De Bruyne B, Pontone G, Patel MR, Norgaard BL, Byrne RA, PLATFORM Investigators, et al. Quality-of-life and economic outcomes of assessing fractional flow reserve with computed tomography angiography: PLATFORM. J Am Coll Cardiol. 2015;66:2315–23.

Leipsic J, Yang TH, Thompson A, Koo BK, Mancini GB, Taylor C, et al. CT angiography (CTA) and diagnostic performance of noninvasive fractional flow reserve: results from the Determination of Fractional Flow Reserve by Anatomic CTA (DeFACTO) study. AJR Am J Roentgenol. 2014;202:989–94.

Nakazato R, Park HB, Berman DS, Gransar H, Koo BK, Erglis A, et al. Noninvasive fractional flow reserve derived from computed tomography angiography for coronary lesions of intermediate stenosis severity: results from the DeFACTO study. Circ Cardiovasc Imaging. 2013;6:881–9.

Taylor CA, Fonte TA, Min JK. Computational fluid dynamics applied to cardiac computed tomography for noninvasive quantification of fractional flow reserve: scientific basis. J Am Coll Cardiol. 2013;61:2233–41.

Cardiac CT in the Emergency Department

10

Maros Ferencik, Khristine Ghemigian, and Udo Hoffmann

Evaluation of Patients with Acute Chest Pain in Clinical Practice

Acute chest pain is one of the most common chief complaints in patients presenting to the emergency department (ED) in the United States, accounting for approximately seven million visits every year [1]. Accurate early triage of these patients remains a major diagnostic challenge, as an acute coronary syndrome (ACS) is ultimately diagnosed in only 2–8% of these patients [2]. Clinical presentation, chest pain history, and clinical risk factors are important in the evaluation of patients, but they do not allow for a definitive exclusion of ACS [3], so the standard of care for patients with acute chest pain includes serial electrocardiograms and troponin measurements, often in chest pain observation units, followed by more advanced diagnostic testing with or without imaging (Fig. 10.1) [4–9]. Despite this conservative practice, which is associated with high costs, about 2% of patients with ACS are inappropriately discharged [10]. Therefore, diagnostic strategies that lead to rapid and reliable early triage of patients with acute chest pain are desirable.

M. Ferencik (✉)
Knight Cardiovascular Institute, Oregon Health and Science University, 3181 SW Sam Jackson Park Road, Portland, OR 97239, USA
e-mail: ferencik@ohsu.edu

K. Ghemigian
Department of Radiology, Massachusetts General Hospital and Harvard Medical School, Boston, MA, USA
e-mail: kghemigian@partners.org

U. Hoffmann
Department of Radiology, Massachusetts General Hospital, Boston, MA, USA
e-mail: uhoffmann@partners.org

M.J. Budoff et al. (eds.), *Atlas of Cardiovascular Computed Tomography*, https://doi.org/10.1007/978-1-4471-7357-1_10

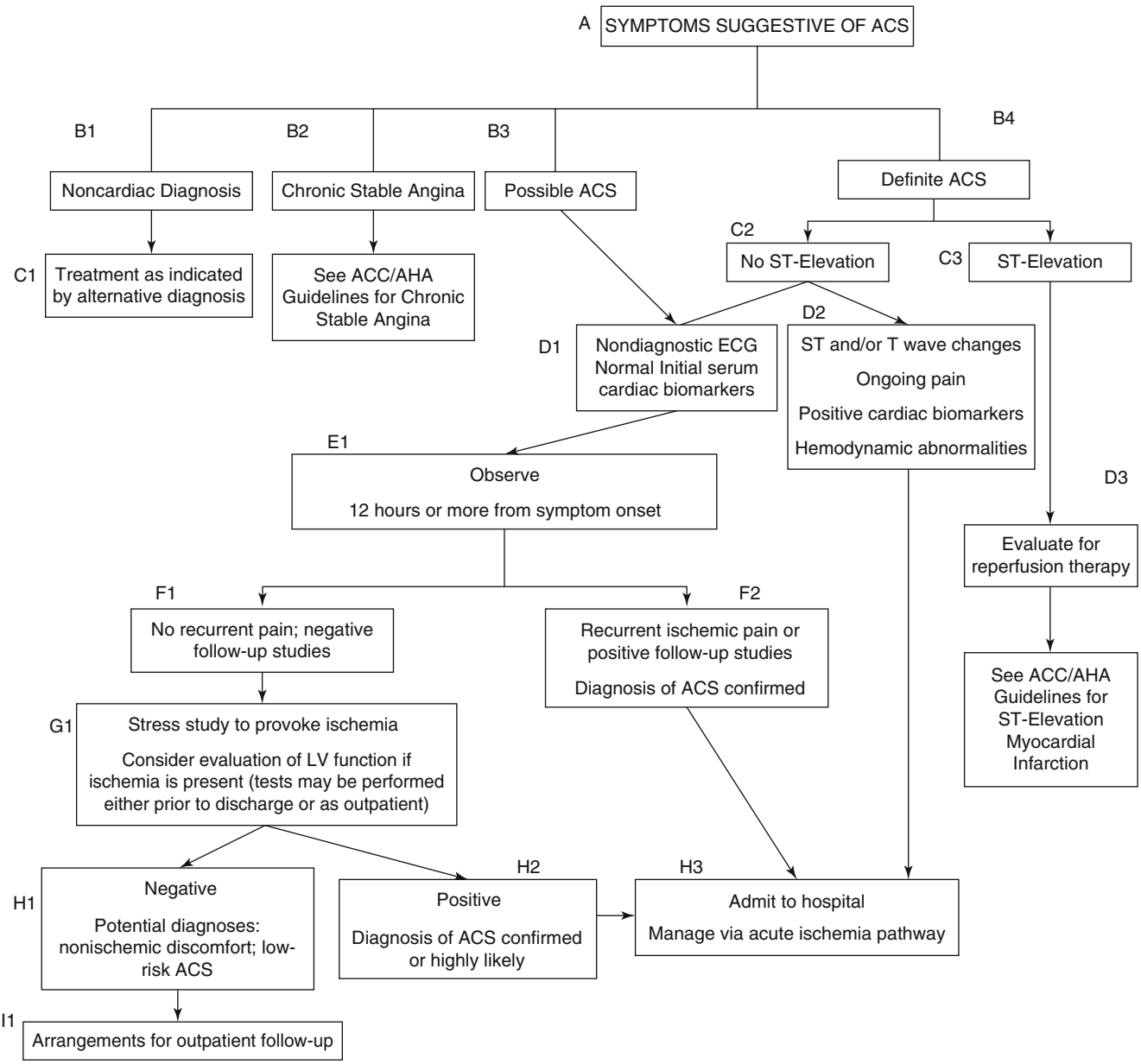

Fig. 10.1 Algorithm for evaluation and management of patients suspected of having acute coronary syndrome (*ACS*). To facilitate interpretation of this algorithm, each box is assigned a letter code that reflects its level in the algorithm and a number allocated from left to right across the diagram on a given level. *ACC/AHA* American College of Cardiology/American Heart Association; *ECG* electrocardiogram, *LV* left ventricular. (*Reprinted from* Anderson et al. [9], with permission)

Cardiac CT in the Evaluation of Patients with Acute Chest Pain

Coronary CTA for the Detection of Significant Luminal Narrowing

The major strength of coronary computed tomography angiography (Coronary CTA) is its high negative predictive value; many studies have demonstrated its use for the exclusion of significant coronary stenosis. Among these are several multicenter trials that compared Coronary CTA with the gold standard, invasive coronary angiography, in patients with stable chest pain (sensitivity between 85% and 99%, specificity between 64% and 97%, and negative predictive value typically >95%) [11–14].

Coronary CTA has evolved into a viable alternative to standard management in patients presenting to the ED with acute chest pain. Multiple single-center studies demonstrated that the exclusion of a significant coronary stenosis by Coronary CTA nearly excludes ACS and thus may potentially allow for earlier discharge than management based on stress testing (Fig. 10.2) [15–26]. Subsequently, three multicenter randomized trials were performed that compared Coronary CTA to the standard ED evaluation of patients with acute chest pain [17, 23, 27]. The results from those three studies, which enrolled more than 3000 patients with low to intermediate likelihood of ACS, are summarized in Table 10.1. Patients enrolled in the studies, who typically had negative initial serum troponin and nonischemic ECGs, were recruited from both academic medical centers and nonacademic hospitals. In all three trials, the primary outcome of interest—the length of stay or time to diagnosis—was significantly shorter in the CT arm, and the incidence of major adverse cardiovascular events during a 28-day follow-up was not increased. Moreover, the ROMICAT II trial [27] and the study by Litt et al. [23] also showed a doubling to quadrupling of direct discharges from the ED as compared to standard of care (47–50% *vs* 12–23%). Probably because of the increased sensitivity of coronary CTA for coronary artery disease (CAD), there was a trend toward additional testing and invasive procedures in the coronary CTA arms (Figs. 10.3 and 10.4), with an estimated increase in invasive coronary angiography of 21 per 1000 coronary CTA scans, and in percutaneous coronary interventions (PCIs) (20 per 1000 scans) [28]. Currently, there are no reliable data to indicate whether the improved detection of CAD and subsequent PCIs in this acute setting will improve long-term health outcomes.

Despite the increased testing, the overall cost of the index hospitalization was not significantly higher in the patients randomized to coronary CTA. The estimated radiation exposure in the CTA group in ROMICAT II [27] was higher (13.9 mSv) than for the standard-of-care group (4.7 mSv), including patients undergoing only an exercise treadmill stress test or stress echocardiography, but was similar in a direct comparison of CTA (11.5 mSv) and myocardial stress perfusion imaging (12.8 mSv) in the CT-STAT trial [17]. In summary, the studies demonstrated that early CTA permits accurate and safe direct ED discharge of 50% of all acute chest pain patients.

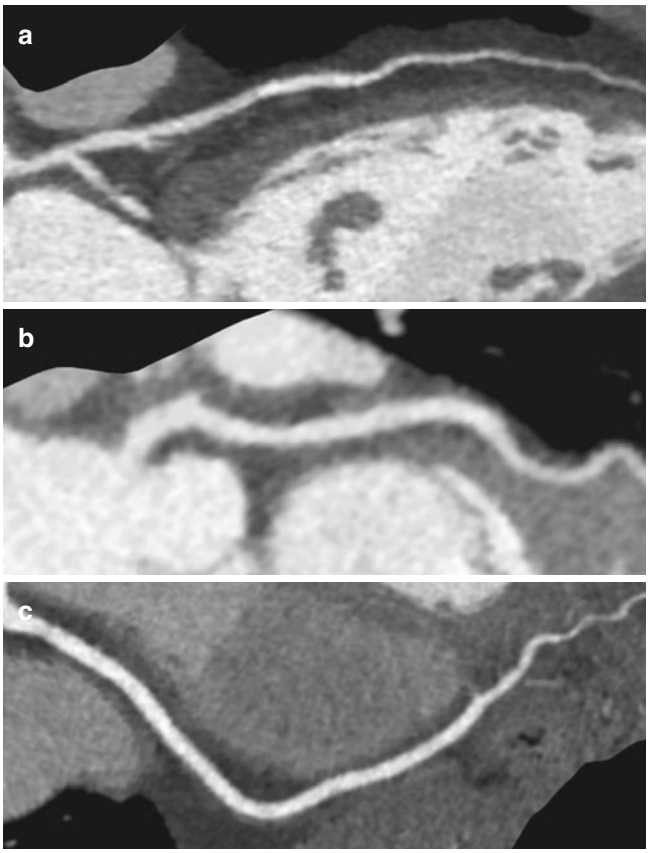

Fig. 10.2 Normal coronary arteries. A 63-year-old woman with no significant prior medical history presented to the emergency department with intermittent left-sided chest pain. At the time of admission, the ECG was normal and troponin T was negative. The patient underwent coronary CT angiography. Curved multiplanar reformatted images showed a normal left anterior descending coronary artery (**a**), normal left circumflex coronary artery (**b**), and a normal right coronary artery (**c**). The patient was discharged after the coronary CTA examination

Table 10.1 Randomized-controlled multicenter trials with Coronary CT Angiography (coronary CTA) as a diagnostic intervention in patients with acute chest pain[a]

Study	Population	Randomization	Outcomes	Observed difference (CTA *vs* Control)
Goldstein et al. [17] (CT-STAT)	Negative troponin Nondiagnostic ECG Age: 50 ± 10 *y* Women: 54% Number of centers: 16	Coronary CTA *n* = 361 MPI *n* = 338	Prevalence of ACS	1.2% *vs* 2.7%
			MACE during follow-up	0.8% *vs* 0.4%
			Direct ED discharges[b]	73% *vs* 81%[c]
			Time to diagnosis[b]	2.9 *h vs* 6.2 *h*
			Invasive coronary angiography	6.7% *vs* 6.2%
			Coronary revascularization	3.6% *vs* 2.4%
			ED cost[b]	$2137 *vs* $3458
			Radiation dose[b]	11.5 mSv *vs* 12.8 mSv
Litt et al. [23]	Negative troponin Nondiagnostic ECG Age: 49 ± 10 *y* Women: 53% Number of centers: 5	Coronary CTA *n* = 908 SOC *n* = 462	Prevalence of ACS	4.1% *vs* 2.4%
			MACE during follow-up	1.1% *vs* 1.1%
			Direct ED discharges[b]	50% *vs* 23%
			Length of stay[b]	18.0 *h vs* 24.8 *h*
			Invasive coronary angiography	5.1% *vs* 4.2%
			Coronary revascularization	2.5% *vs* 0.9%
			ED cost	NA
			Radiation dose	NA
Hoffmann et al. [27] (ROMICAT-II)	Negative troponin Nondiagnostic ECG Age: 54 ± 8 *y* Women: 47% Number of centers: 9	Coronary CTA *n* = 501 SOC *n* = 499	Prevalence of ACS	8.6% *vs* 6.4%
			MACE during follow-up	0.4% *vs* 1.2%
			Direct ED discharges[b]	47% *vs* 12%
			Length of stay[b]	23.2 *h vs* 30.8 *h*
			Invasive coronary angiography	10.8% *vs* 7.2%
			Coronary revascularization	5.8% *vs* 3.6%
			ED cost	$2101 *vs* $2566
			Radiation dose[b]	13.9 mSv *vs* 4.7 mSv

ACS acute coronary syndrome, *ECG* electrocardiogram, *ED* emergency department, *h* hours, *MACE* major adverse cardiac event, *MPI* myocardial perfusion imaging, *mSv* millisievert, *NA* not available, *SOC* standard of care, *y* years

[a]The workup in the ED using Coronary CTA was compared with either a workup strategy requiring nuclear MPI or a traditional SOC workup strategy

[b]Significant difference ($p < 0.05$)

[c]Estimated from presented data

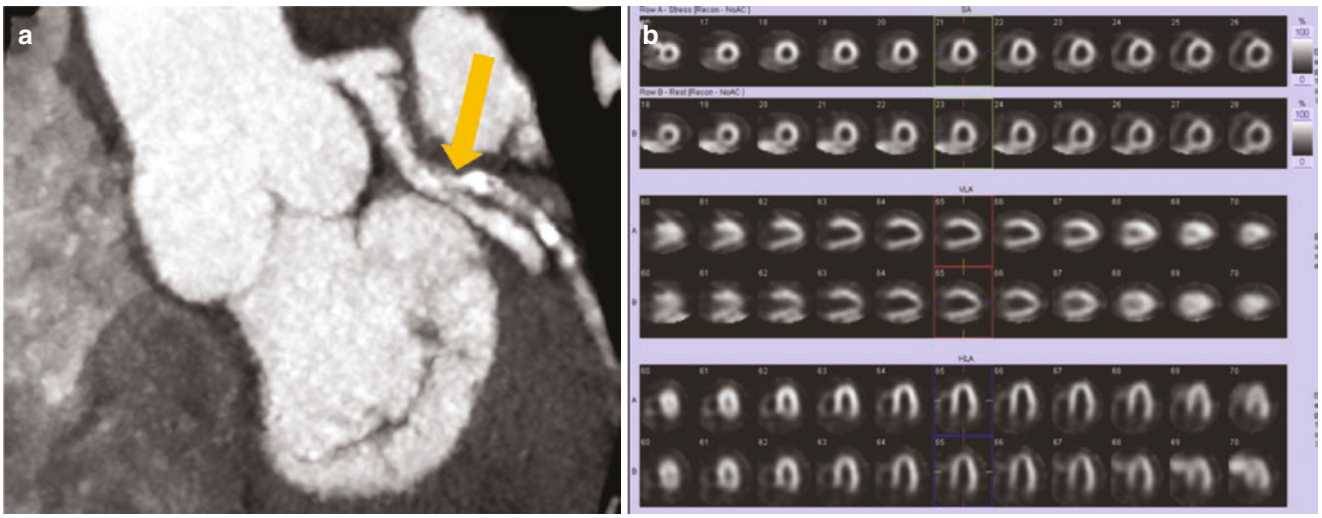

Fig. 10.3 Coronary CTA suggestive of moderate to severe coronary stenosis, with negative subsequent nuclear myocardial perfusion exercise test. A 52-year-old man presented to the ED with chest pain. At the time of admission, the ECG was normal and troponin T was negative. The patient underwent coronary CTA; a maximum intensity projection (**a**) showed moderate to severe luminal narrowing (*arrow*) in the ostium and proximal segment of the second obtuse marginal branch. Interpretation of coronary CTA was limited because of the presence of calcium. The patient underwent further evaluation by nuclear myocardial perfusion imaging stress test. The patient had excellent exercise capacity (19 metabolic equivalents), the ECG was negative for ischemia, and the myocardial perfusion images (**b**) showed no evidence of ischemia or infarction with stress (*top rows*) or at rest (*bottom rows*). The patient was discharged

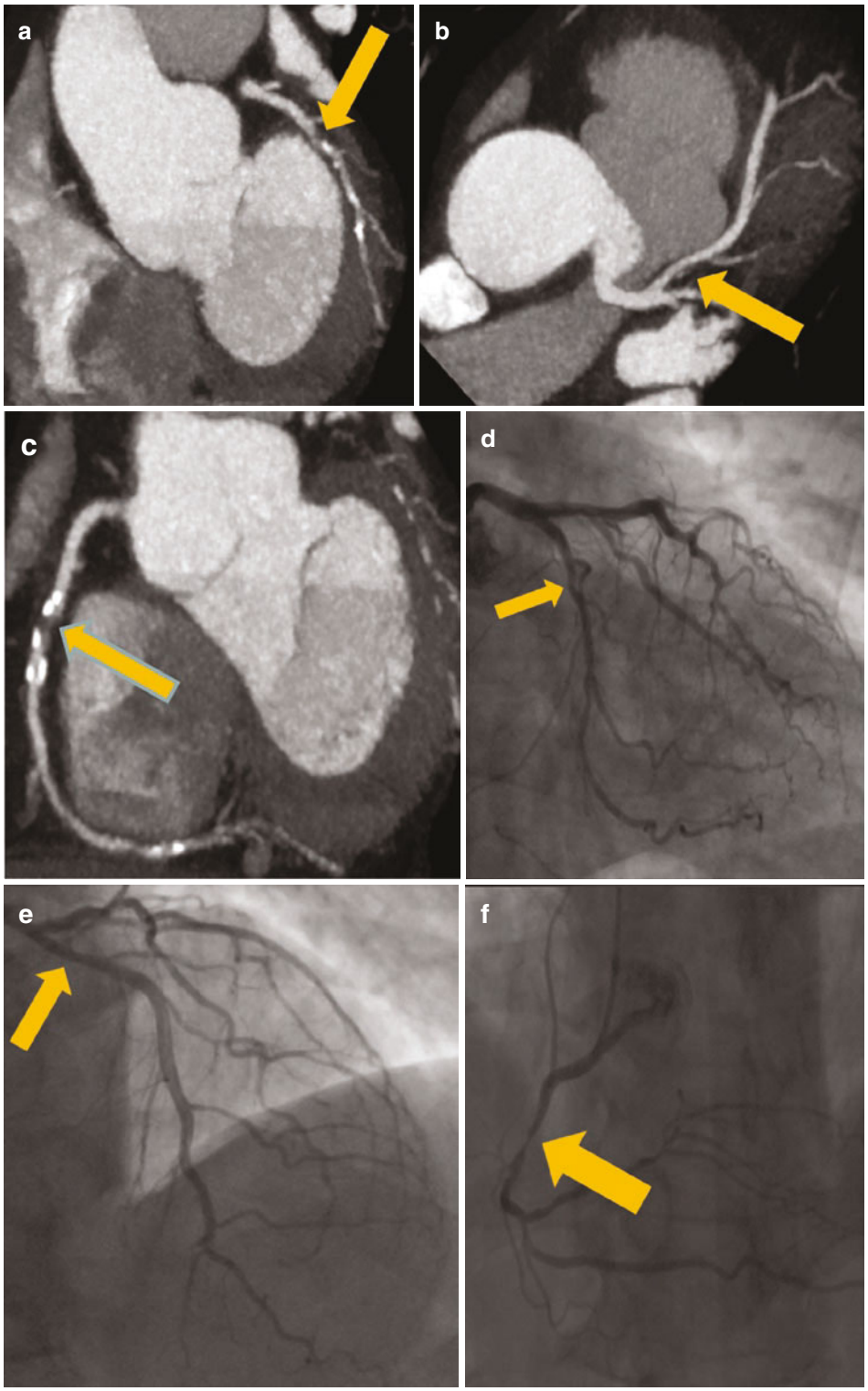

Fig. 10.4 In this patient, coronary CTA demonstrated significant two-vessel CAD, but subsequent invasive coronary angiography confirmed only significant single-vessel CAD. A 70-year-old man with a history of arterial hypertension presented to the ED with acute onset of chest pain, which awoke him from sleep. At time of presentation to the ED, the patient was free of chest pain, the ECG was normal, and troponin T was negative. He underwent coronary CTA. Maximum intensity projection (MIP) image showed partially calcified plaque with severe luminal narrowing (>70% stenosis, *arrow*) in the mid left circumflex coronary artery (LCx) (**a**), a partially calcified plaque with mild luminal narrowing (*arrow*) in the left anterior descending coronary artery (LAD) (**b**), and partially calcified plaque with severe luminal narrowing (*arrow*) in the mid right coronary artery (RCA) (**c**). Troponin T tests at 8 and 16 h were positive. The patient underwent invasive coronary angiography, which showed only mild luminal narrowing (30% stenosis, *arrow*) in the LCx (**d**), indicating that coronary CTA overestimated the lesion. However, invasive angiography confirmed the mild luminal narrowing (30% stenosis, *arrow*) in the LAD (**e**) and severe luminal narrowing (95% stenosis, *arrow*) in the RCA (**f**). He underwent percutaneous coronary intervention of the mid RCA with a drug-eluting stent

Additional Information Obtained During Coronary CTA

Global and Regional Left Ventricular Function

The evaluation of global and regional left ventricular (LV) function is feasible with coronary CTA acquisition, if data acquisition covers all phases of the cardiac cycle [29, 30]. The results compare favorably with echocardiography and cardiac MRI [31, 32]. The mean bias of CT-based LV ejection fraction was 1.3%, with limits of agreement of 14.2% [31]. Based on echocardiography studies, regional and global assessment of LV function may render incremental benefits for the diagnosis of ACS in patients with acute chest pain [33]. Consistent with these data, the presence of regional LV dysfunction incrementally and independently improved the diagnostic accuracy for ACS beyond stenosis detection in patients with CAD (77% sensitivity of coronary stenosis *vs* 87% sensitivity of coronary stenosis and LV dysfunction) [34–36]. This finding is specifically valuable in patients with nondiagnostic assessment for significant stenosis. However, assessment of LV function typically results in higher estimated radiation exposure unless the most advanced CT technology is used.

First-Pass Myocardial CT Perfusion

The rationale for the assessment of resting myocardial perfusion is based on experience with nuclear myocardial perfusion imaging. Udelson et al. [37] demonstrated in a randomized study of 1260 patients with chest pain in the ED that early sestamibi myocardial perfusion imaging at rest, compared with standard of care, reduced unnecessary hospitalizations without reducing appropriate admissions in patients with ischemia.

The evaluation of first-pass myocardial perfusion at rest is feasible with a standard coronary CTA acquisition (Fig. 10.5) [32]. In one study, first-pass perfusion defects were observed in 21 of 24 patients with non–ST-segment elevation myocardial infarction, but in only 2 of 14 patients with unstable angina [38]. Similarly, Busch et al. [39] showed that resting hypoperfusion areas on coronary CTA correlated well with myocardial infarction (sensitivity 90%, specificity 80%) and ischemia (sensitivity 70%, specificity 92%). Several smaller studies demonstrated that first-pass CT myocardial perfusion at rest increases specificity and positive predictive value of the detection of stenosis for ACS (67–90%) [35, 40–42]. Hence, first-pass myocardial perfusion obtained during coronary CTA may provide useful additional functional information and may guide management in some patients. This practice has not been rigorously tested, however, and further research (especially direct, randomized comparisons with stress perfusion) is needed before wider application in clinical practice is considered.

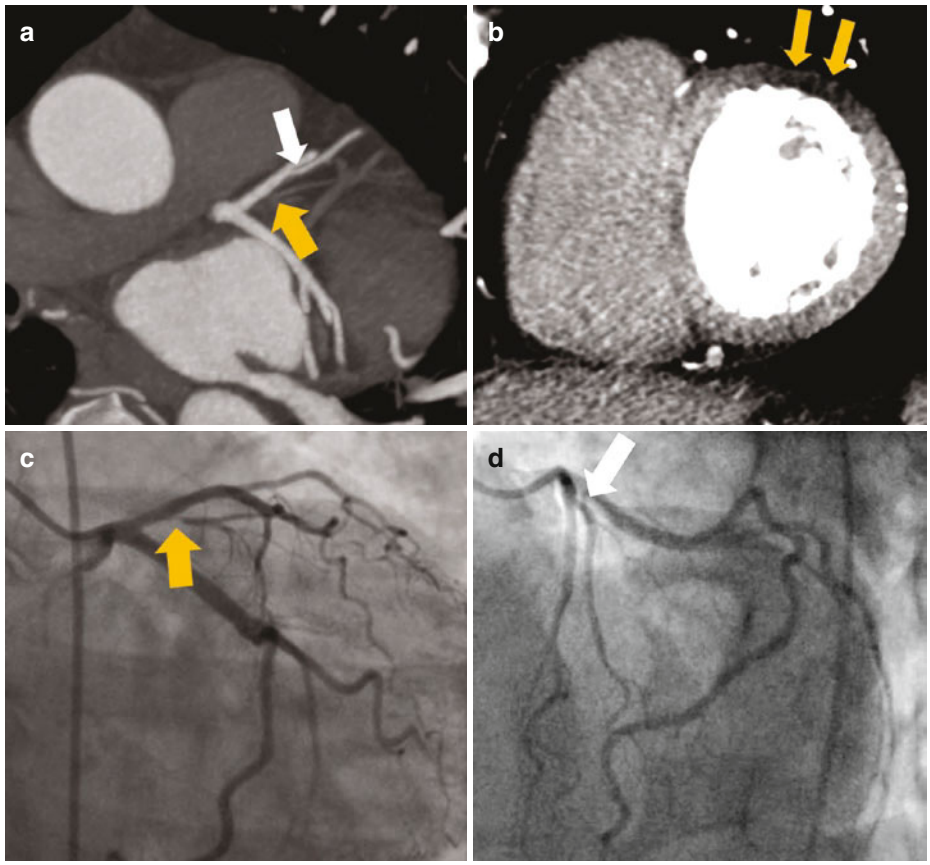

Fig. 10.5 Significant coronary stenosis with corresponding first-pass myocardial perfusion defect. A 51-year-old man with a history of arterial hypertension presented to the ED after a 20-min episode of substernal chest pain. He was free of chest pain in the ED and his initial ECG and troponin T were negative. He underwent coronary CTA. **A**, Maximum intensity projection showed subtotal to total occlusion of the small first diagonal branch (*yellow arrow*) and nonobstructive, noncalcified plaque in the ostium of the second diagonal branch (*white arrow*) (**a**). This finding correlated with the first-pass CT perfusion defect (*arrows*) in the basal anterolateral segment of the left ventricle (**b**, minimum intensity projection). The second and third tests for troponin T were positive. The patient underwent invasive coronary angiography, which demonstrated severe stenosis in the proximal first diagonal branch (*yellow arrow*, **c**) and no significant disease in the proximal second diagonal branch (*white arrow*, **d**). No intervention was performed because of the small caliber of the vessel. (*Courtesy of* Dr. Brian Ghoshhajra)

Coronary Plaque Assessment

The feasibility of qualitative and quantitative coronary plaque analysis using coronary CTA data has been well established [43, 44]. Coronary CTA is highly sensitive (90%; 95% CI, 83–94%) and specific (92%; 95% CI, 90–93%) for the detection of coronary plaque, compared with intravascular ultrasound [44]. A recent meta-analysis demonstrated excellent agreement between coronary CTA and the gold standard intravascular ultrasound for measurements of coronary plaque area (mean difference 0.09 mm^2; 95% CI, −1.00 to 1.18 mm^2) and volume (mean difference 5.3 mm^3; 95% CI, −3.0 to 13.6 mm^3) [44]. Furthermore, coronary CTA permitted accurate classification of plaque by composition into fibrous and lipid-rich plaque/necrotic core based on the CT attenuation, as compared with intravascular imaging [45–50]. Other high-risk plaque features such as positive remodeling, the percentage of plaque burden, and the napkin ring sign also can be reliably assessed, compared with invasive gold standards [44, 51, 52].

Coronary plaque characteristics were different in patients with ACS, compared with patients who had stable CAD presentations [53–57]. Features such as large plaque burden, positive remodeling, low CT attenuation plaque, spotty calcium, and napkin ring sign were more often seen in patients with ACS (Fig. 10.6). In the ROMICAT I trial [58], patients with acute chest pain presentation and with the presence of

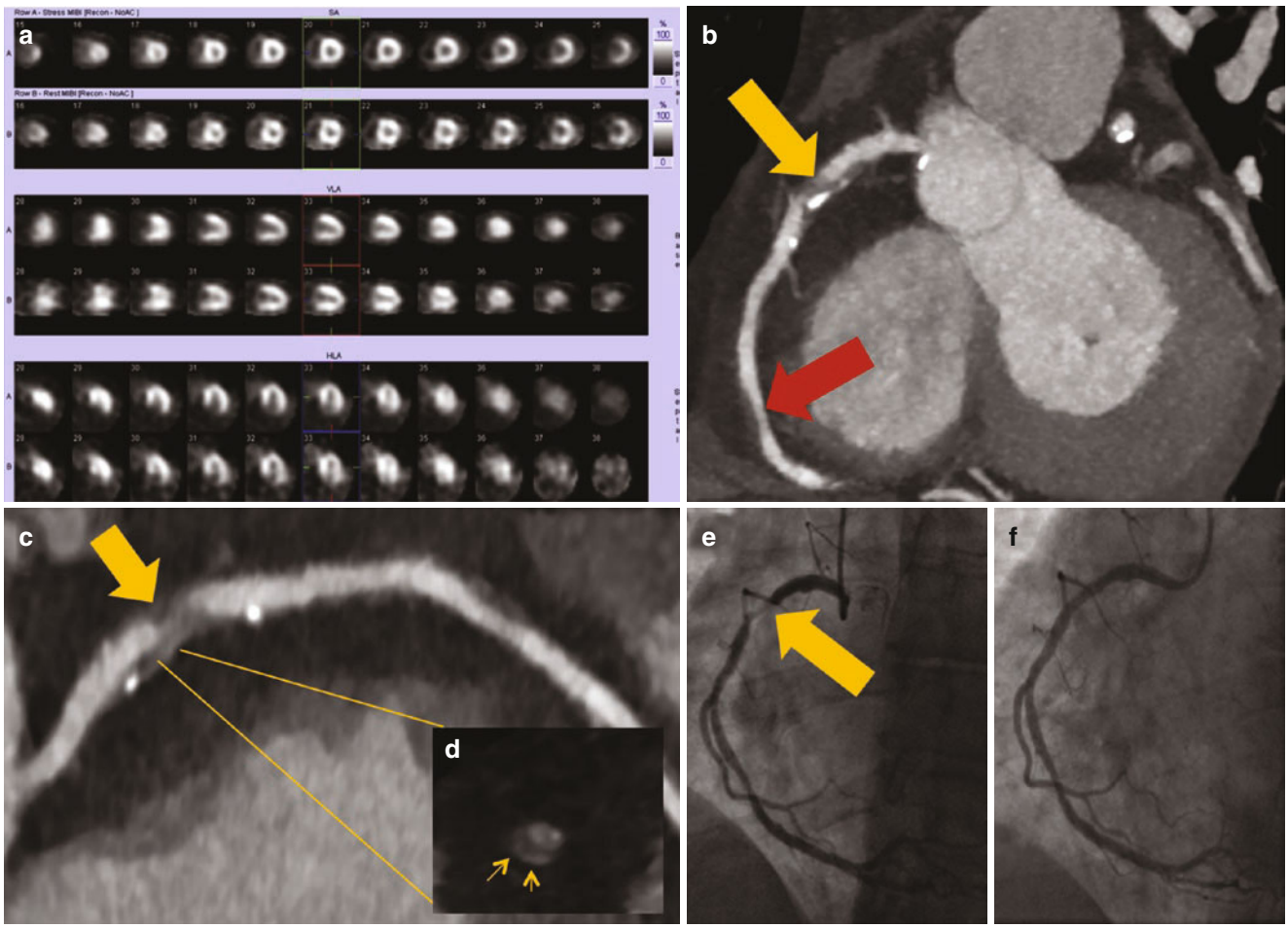

Fig. 10.6 Equivocal myocardial perfusion stress test followed by positive coronary CTA with high-risk plaque features. A 53-year-old woman with a history of smoking, obesity, diabetes mellitus, hyperlipidemia, and a family history of premature CAD presented to the ED with 3 weeks of occasional exertional chest pain. Pain was left-sided, substernal, radiated up to the left neck, and was relieved with rest. At the time of admission, the ECG was normal and three troponin T tests were negative. The patient had a myocardial perfusion exercise stress test and the ECG was negative for ischemia. The myocardial scans did not show any evidence of ischemia or infarction, but interpretation of the images was limited by soft tissue attenuation artifacts (**a**). The patient underwent further evaluation by coronary CTA. Maximum intensity projections showed partially calcified plaque with severe stenosis at the distal third of the proximal right coronary artery (RCA) (*yellow arrow*) (**b**) and noncalcified plaque with mild luminal narrowing in the mid RCA (*red arrow*). On a curved multiplanar reformatted image (**c**), the coronary plaque causing severe luminal narrowing (*arrow*) displayed high-risk plaque features including positive remodeling and napkin ring sign (The napkin ring sign (**d**) is defined as a ring-like peripheral higher attenuation of the noncalcified portion of the coronary plaque (*yellow arrows*). The patient underwent invasive coronary angiography, which confirmed the severe luminal narrowing (95% stenosis) in the proximal RCA (**e**). The patient received percutaneous coronary intervention with a drug-eluting stent (**f**)

greater than 50% stenosis could be differentiated into those with and without ACS using a coronary plaque score, which included spotty calcium, low CT attenuation, positive remodeling, and length of stenosis. Overall, there is increasing evidence that advanced plaque characterization using quantitative assessments will add incremental value for management of patients with acute chest pain, specifically identifying those whose symptoms may not be associated with significant CAD found on coronary CTA and those without significant CAD who may be at increased risk for ACS. Nevertheless, detailed assessment of plaque morphology is not now routinely performed in clinical practice, and further data are needed to support the role of plaque characteristics in clinical decision making.

Noninvasive Fractional Flow Reserve

The addition of a physiologic measure of coronary flow to the mere degree of luminal stenosis could further improve the assessment of patients with acute chest pain. Noninvasive calculation of fractional flow reserve from CTA is feasible and has been shown to correlate with invasive fractional flow reserve [59, 60]. Noninvasive calculation of fractional flow reserve improved the diagnostic accuracy of coronary CTA in patients with intermediate stenoses, compared with the gold standard of invasive fractional flow reserve [61]. Further studies in patients with acute chest pain and seamless inclusion of the noninvasive fractional flow reserve calculation into the patient workflow will be necessary before clinical implementation of the test.

Coronary Calcium Quantification

Coronary calcium can be quantified on noncontrast CT scans. In asymptomatic populations, the absence of coronary calcium is a strong predictor of very low future major adverse cardiovascular events [62]. In the pooled analysis of patients presenting to the ED with chest pain and suspicion of ACS, ACS was present in 18% of the 481 subjects studied, suggesting a population with low to intermediate risk. Coronary calcium was absent in approximately 42% of patients, from which only 1% had an ACS, translating to a 99% sensitivity and negative predictive value of no coronary calcium [63]. Although ACS is not very frequent in the absence of coronary calcium, its sensitivity is not sufficient as a diagnostic test to rule out ACS, but coronary calcium scans may be useful to decrease nondiagnostic coronary CTA examinations (since a high calcium score may lead to cancellation of the contrast-enhanced coronary CTA procedure and, instead, the use of alternative testing) and to provide prognostic information in those without ACS [64].

In summary, the exclusion of coronary atherosclerosis and significant CAD remains the cornerstone of coronary CTA in the evaluation of patients with acute chest pain. Additional information may be obtained through assessment of global and regional LV function, resting CT myocardial perfusion, advanced coronary plaque assessment, and noninvasive estimation of fractional flow reserve.

Change in Patient Management Based on Coronary CTA Results

Based on the experience from large multicenter randomized trials, the utilization of coronary CTA in the setting of low and low-to-intermediate risk of ACS in acute chest pain patients in the ED may have a large impact on patient management. One of the major drawbacks of the standard triage, including stress testing, is the extended hospitalization for serial biomarkers, electrocardiograms and risk-stratification testing (Fig. 10.1). Approximately half of patients studied in the three randomized trials had no evidence of CAD on coronary CTA. This type of patients, with no CAD on coronary CTA, can be safely discharged reducing the duration of the hospital stay and cost in this subgroup (Fig. 10.2). Further, patients with minimal non-obstructive CAD are also candidates for early discharge with arrangement of outpatient follow-up (Fig. 10.7). The information about the presence of coronary atherosclerosis should be communicated to primary care provider to allow for adjustment of strategies focused on

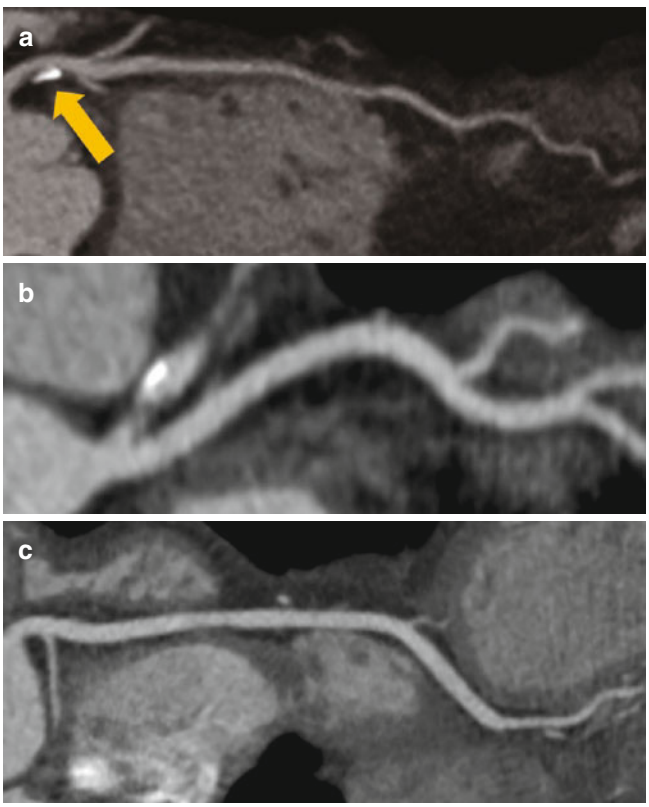

Fig. 10.7 Minimal non-obstructive CAD detected by CTA may permit early discharge from the ED with outpatient clinical follow-up focused on risk factor modification. 42-year-old man with a history of polysubstance abuse presented to the emergency department with 4 h of constant chest pain. The pain was described as left sided and substernal. At time of admission, the electrocardiogram was normal and troponin T was negative. The patient underwent a coronary CT angiography (examination, which showed partially calcified plaque with mild luminal narrowing in the left anterior descending coronary artery (**a**, curved multiplanar reformatted [cMPR]; *arrow*) and a normal left circumflex coronary artery (**b**, cMPR) and right coronary artery (**c**, cMPR). The patient was discharged from the emergency department

the lowering of long-term cardiovascular risk. On the other side of the spectrum are patients with a definite coronary stenosis. These patients require admission to the hospital, further evaluation and guideline directed therapies (Fig. 10.8). Patients with non-diagnostic coronary CTA examinations or evidence of non-negligible coronary plaque, but no significant stenosis usually require observation with serial biomarkers and electrocardiograms and often a functional stress test for evaluation of ischemia (Fig. 10.3). Additional information such as regional LV function, first-pass myocardial perfusion, coronary plaque, and non-invasive fractional flow reserve may help to triage patients in the future (Figs. 10.5 and 10.6). In a subset of patients, coronary CTA may detect alternative diagnoses that can explain acute chest pain presentation (e.g. pulmonary embolism, aortic dissection, pneumonia, pericarditis) (Figs. 10.9, 10.10, 10.11, and 10.12).

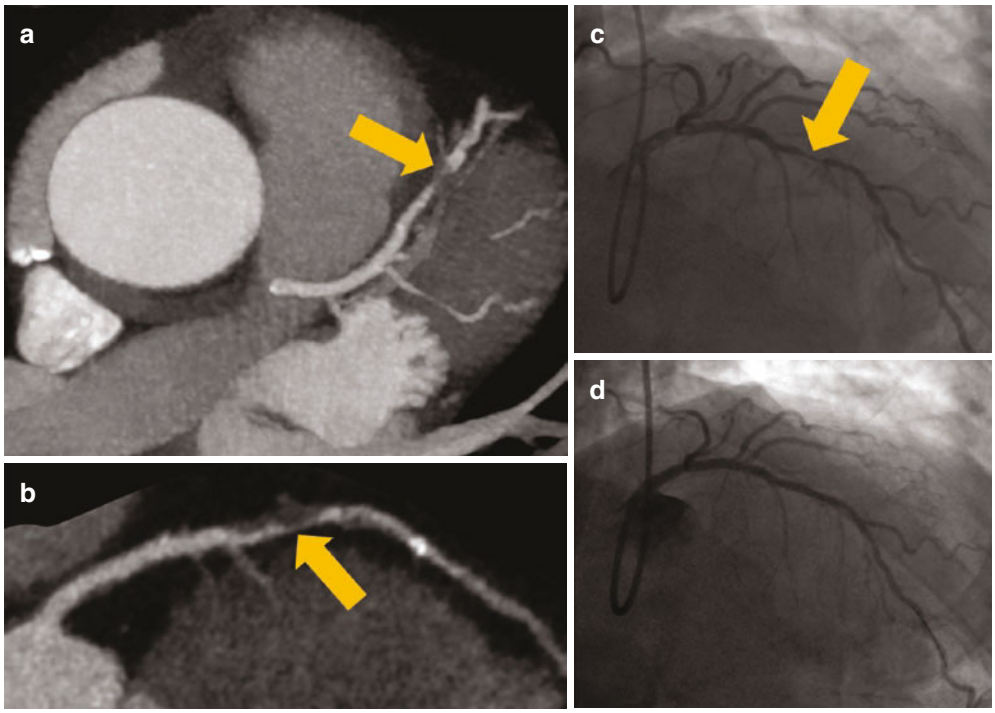

Fig. 10.8 Example of a definite severe left anterior descending coronary artery with invasive angiographic confirmation. 66-year-old man with a history of smoking and hypertension presented to the emergency department with chest pain that radiated to his neck bilaterally. He had 7 episodes of exertional chest pain associated with shortness of breath in 4 days preceding the admission. At time of admission, the electrocardiogram was normal and troponin T was negative. The patient underwent coronary CT angiography. CT showed non-calcified coronary plaque with severe luminal narrowing (>70% stenosis) in the mid left anterior descending coronary artery (LAD) (**a**-maximum intensity projection images; *arrow*, **b**-curved multiplanar reformatted image; *arrow*). The patient underwent an invasive coronary angiography which confirmed the severe luminal narrowing (85% stenosis) (**c**; *arrow*) in the mid LAD and a drug eluting stent was placed (**d**)

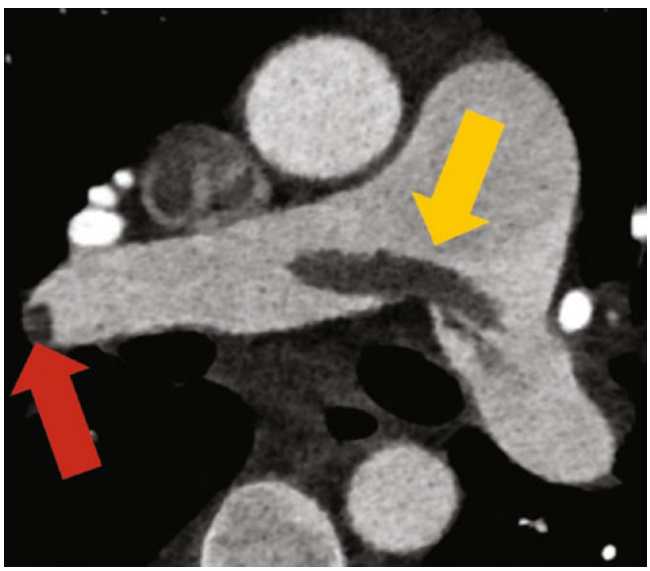

Fig. 10.9 Coronary CTA demonstrating alternative causes of chest pain—Pulmonary embolism. 50-year-old man with a history of polysubstance abuse, smoking, and hypertension presented to the emergency department with atypical chest pain. At time of admission, electrocardiogram was normal and troponin T was negative. The patient underwent coronary CT angiography, which showed incidental findings of a pulmonary embolus at the bifurcation of the main pulmonary artery (*yellow arrow*) and a smaller pulmonary embolus in the right pulmonary artery (*red arrow*)

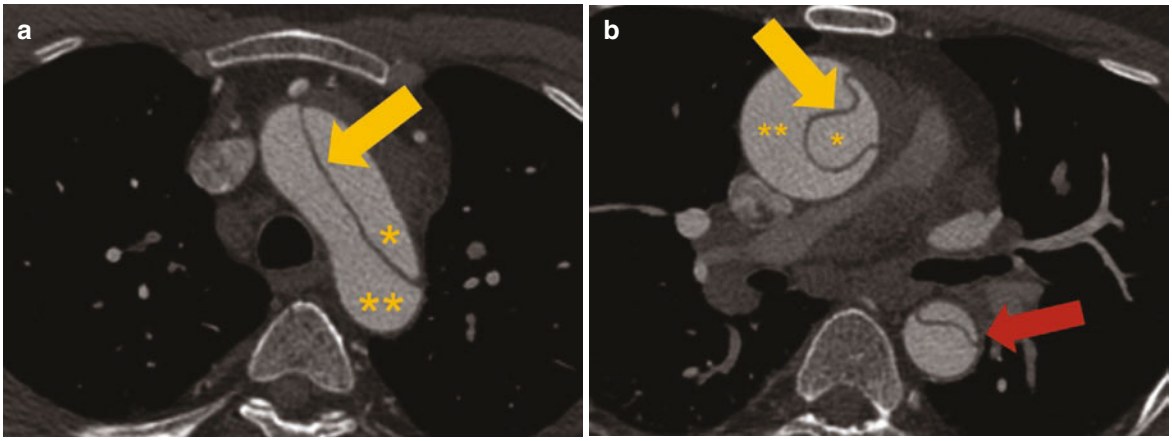

Fig. 10.10 CT angiography demonstrating alternative causes of chest pain—Aortic dissection. 61-year-old man with a history of hypertension presented with sudden onset of chest pain that radiated to his back and right leg. The patient was evaluated at the emergency department and underwent a CT angiography of the chest and abdomen which showed a Type A aortic dissection extending to the right iliac artery (**a**-Aorta at the level of the aortic arch, dissection flap—*arrow*; * True lumen; ** False lumen, **b**—Dilated ascending aorta, dissection flap—*yellow arrow*; * True lumen, ** False lumen; Descending Aorta, *red arrow*). He underwent aortic replacement surgery with a composite aortic graph, which included a mechanical aortic valve replacement

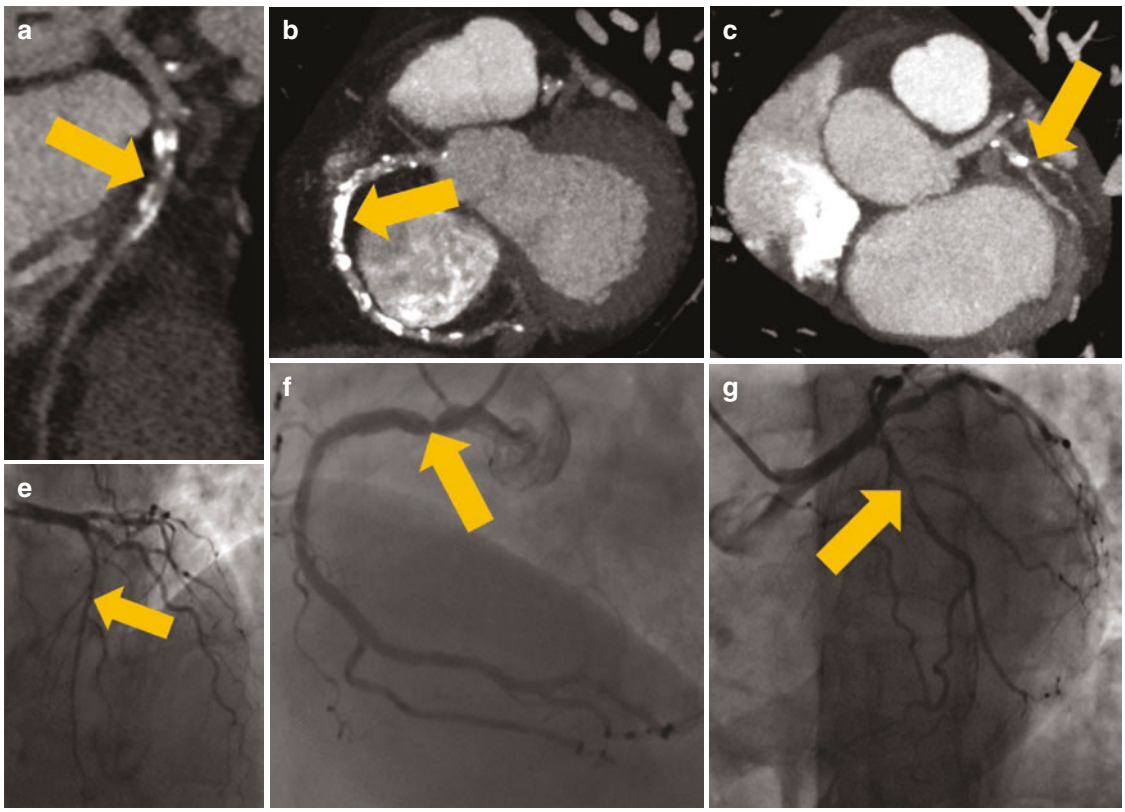

Fig. 10.11 Challenges of accurate coronary CTA evaluation of CAD with diffuse disease and extensive coronary calcium. 60 year old woman with a history of diabetes mellitus, hypertension, and hyperlipidemia presented to the emergency department with substernal, left-sided chest pain that radiated to her back. At time of presentation to the emergency department, electrocardiogram was normal and troponin T was negative. The patient received a coronary CT angiography, which showed severe stenosis of the mid left anterior descending coronary artery (LAD) (**a**, curved multiplanar reformatted (cMPR); *arrow*) and diffuse calcification in the mid and distal segments of the right coronary artery (RCA) (**b**, maximum intensity projection (MIP)). Coronary CTA also showed severe stenosis of the proximal left circumflex coronary artery (LCx) at the site of origin of the 1st obtuse marginal branch (OM1) (**c**, MIP; *arrow*). Due to the nonevaluable RCA, the patient underwent further evaluation by myocardial single photon emission computed tomography (SPECT) imaging with adenosine. The myocardial perfusion images did not show any evidence of ischemia or infarction (**d**, *top rows*, stress; *bottom rows*, rest). The referring cardiologist was concerned for balanced ischemia and the patient received an invasive coronary angiography. The angiography showed no significant stenosis in the LAD (**e**; *arrow*) and only minimal irregularities in the RCA (**f**; *arrow*). However, the invasive angiography confirmed the severe luminal narrowing (70% stenosis) (**g**; *arrow*) of the LCx involving the take off of the OM1 seen on coronary CTA. The patient received no revascularization and the clinical decision was made to manage her conservatively

Fig. 10.11 (continued)

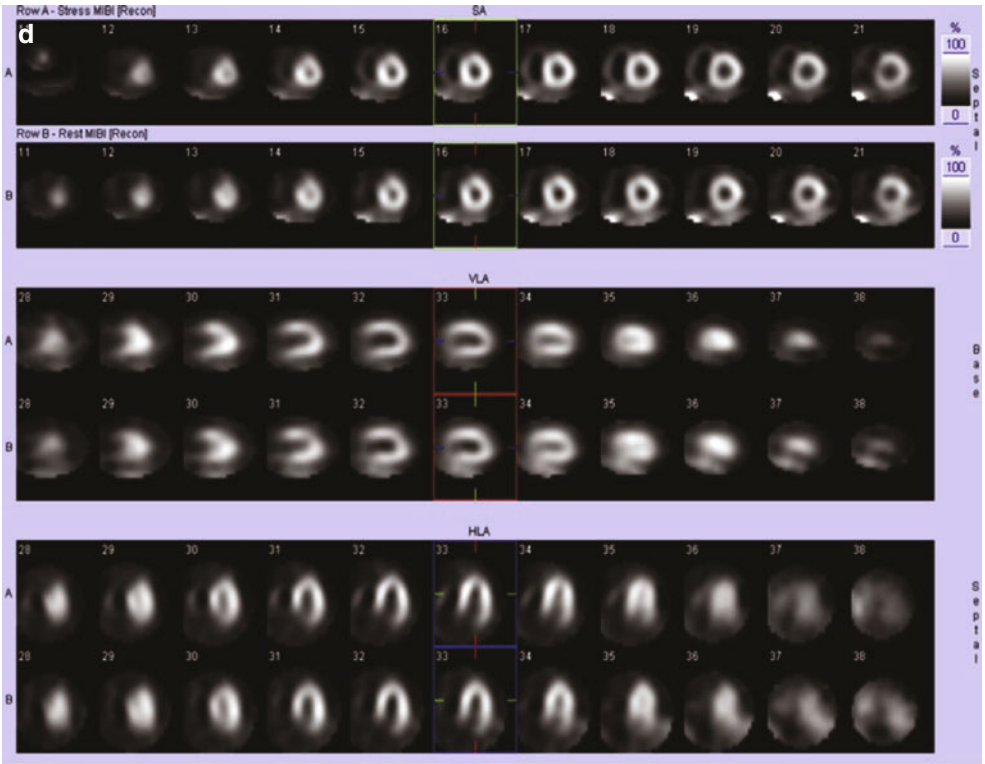

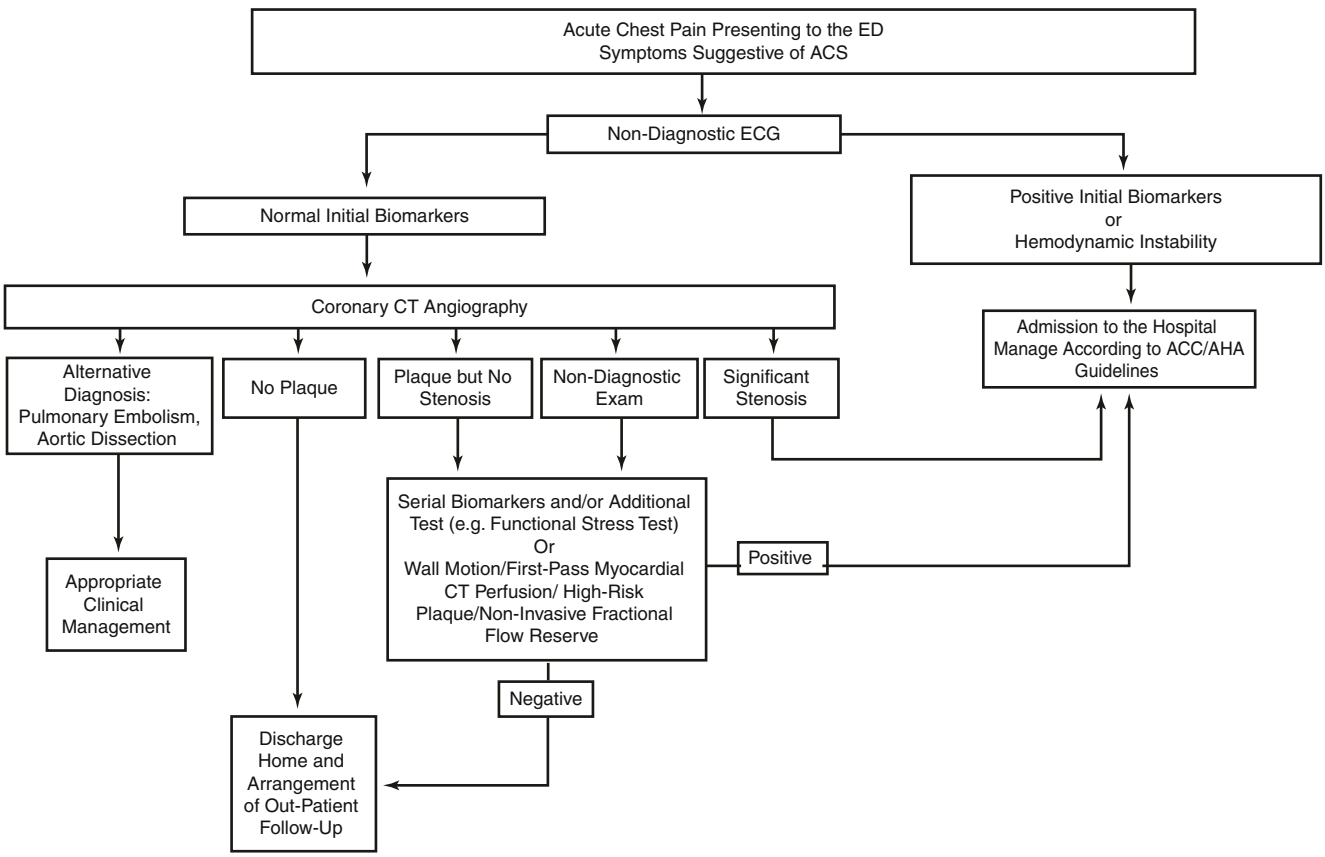

Fig. 10.12 Proposed algorithm for evaluation and management of patients suspected of having ACS using early coronary CTA

Summary

Evidence from multiple randomized controlled trials has established coronary CTA as a viable alternative to functional testing for the rapid evaluation and accurate early triage of patients presenting to the ED with acute chest pain (ACCF/SCCT/ACR/AHA/ASE/ASNC/NASCI/SCAI/SCMR 2010 Appropriate Use Criteria for Cardiac Computed Tomography) [65]. Moreover, CTA with its ability to directly visualize CAD may have additional benefits for long-term risk management of the majority of patients with acute chest pain who do not have ACS. A guide on how to manage emergency department patients based on early coronary CTA is provided.

Acknowledgment Dr. Ferencik received support from the American Heart Association (13FTF16450001).

References

1. Niska R, Bhuiya F, Xu J. National Hospital Ambulatory Medical Care Survey: 2007 emergency department summary. Natl Health Stat Report. 2010;6:1–31.
2. Roger VL, Go AS, Lloyd-Jones DM, Benjamin EJ, Berry JD, Borden WB, et al., American Heart Association Statistics Committee and Stroke Statistics Subcommittee. Heart disease and stroke statistics--2012 update: a report from the American Heart Association. Circulation 2012; 125:e2–220.
3. Swap CJ, Nagurney JT. Value and limitations of chest pain history in the evaluation of patients with suspected acute coronary syndromes. JAMA. 2005;294:2623–9.
4. Tatum JL, Jesse RL, Kontos MC, Nicholson CS, Schmidt KL, Roberts CS, Ornato JP. Comprehensive strategy for the evaluation and triage of the chest pain patient. YMEM. 1997;29:116–25.
5. Braunwald E, Antman EM, Beasley JW, Califf RM, Cheitlin MD, Hochman JS, et al. ACC/AHA 2002 guideline update for the management of patients with unstable angina and non-ST-segment elevation myocardial infarction--summary article: a report of the American College of Cardiology/American Heart Association task force on practice guidelines (Committee on the Management of Patients With Unstable Angina). J Am Coll Cardiol. 2002;40:1366–74.
6. Klocke FJ, Baird MG, Lorell BH, Bateman TM, Messer JV, Berman DS, et al. ACC/AHA/ASNC guidelines for the clinical use of cardiac radionuclide imaging--executive summary: a report of the American College of Cardiology/American Heart Association Task Force on Practice Guidelines (ACC/AHA/ASNC Committee to Revise the 1995 Guidelines for the Clinical Use of Cardiac Radionuclide Imaging). J Am Coll Cardiol. 2003;42:1318–33.
7. Gibler WB, Cannon CP, Blomkalns AL, Char DM, Drew BJ, Hollander JE, et al. Practical implementation of the guidelines for unstable angina/non-ST-segment elevation myocardial infarction in the emergency department. Ann Emerg Med. 2005;46:185–97.
8. Anderson JL, Adams CD, Antman EM, Bridges CR, Califf RM, Casey DE, et al. ACC/AHA 2007 guidelines for the management of patients with unstable angina/non-ST-Elevation myocardial infarction: a report of the American College of Cardiology/American Heart Association Task Force on Practice Guidelines (Writing Committee to Revise the 2002 Guidelines for the Management of Patients With Unstable Angina/Non-ST-Elevation Myocardial Infarction) developed in collaboration with the American College of Emergency Physicians, the Society for Cardiovascular Angiography and Interventions, and the Society of Thoracic Surgeons endorsed by the American Association of Cardiovascular and Pulmonary Rehabilitation and the Society for Academic Emergency Medicine. J Am Coll Cardiol. 2007;50:e1–157.
9. Anderson JL, Adams CD, Antman EM, Bridges CR, Califf RM, Casey DE, et al. 2011 ACCF/AHA focused update incorporated into the ACC/AHA 2007 Guidelines for the Management of Patients with Unstable Angina/Non-ST-Elevation Myocardial Infarction: a report of the American College of Cardiology Foundation/American Heart Association Task Force on Practice Guidelines. Circulation. 2011;123:e426–579.
10. Pope JH, Aufderheide TP, Ruthazer R, Woolard RH, Feldman JA, Beshansky JR, et al. Missed diagnoses of acute cardiac ischemia in the emergency department. N Engl J Med. 2000;342:1163–70.
11. Miller JM, Rochitte CE, Dewey M, Arbab-Zadeh A, Niinuma H, Gottlieb I, et al. Diagnostic performance of coronary angiography by 64-row CT. N Engl J Med. 2008;359:2324–36.
12. Budoff MJ, Dowe D, Jollis JG, Gitter M, Sutherland J, Halamert E, et al. Diagnostic performance of 64-multidetector row coronary computed tomographic angiography for evaluation of coronary artery stenosis in individuals without known coronary artery disease: results from the prospective multicenter ACCURACY (Assessment by Coronary Computed Tomographic Angiography of Individuals Undergoing Invasive Coronary Angiography) trial. J Am Coll Cardiol. 2008;52:1724–32.
13. Meijboom WB, Meijs MFL, Schuijf JD, Cramer MJ, Mollet NR, van Mieghem CAG, et al. Diagnostic accuracy of 64-slice computed tomography coronary angiography: a prospective, multicenter, multivendor study. J Am Coll Cardiol. 2008;52:2135–44.
14. Chow BJW, Freeman MR, Bowen JM, Levin L, Hopkins RB, Provost Y, et al. Ontario multidetector computed tomographic coronary angiography study: field evaluation of diagnostic accuracy. Arch Intern Med. 2011;171:1021–9.
15. Rubinshtein R, Halon DA, Gaspar T, Jaffe R, Karkabi B, Flugelman MY, et al. Usefulness of 64-slice cardiac computed tomographic angiography for diagnosing acute coronary syndromes and predicting clinical outcome in emergency department patients with chest pain of uncertain origin. Circulation. 2007;115:1762–8.
16. Goldstein JA, Gallagher MJ, O'Neill WW, Ross MA, O'Neil BJ, Raff GL. A randomized controlled trial of multi-slice coronary computed tomography for evaluation of acute chest pain. J Am Coll Cardiol. 2007;49:863–71.
17. Goldstein JA, Chinnaiyan KM, Abidov A, Achenbach S, Berman DS, Hayes SW, et al. The CT-STAT (Coronary Computed Tomographic Angiography for Systematic Triage of Acute Chest Pain Patients to Treatment) trial. J Am Coll Cardiol. 2011;58:1414–22.
18. Chang SA, Choi SI, Choi EK, Kim HK, Jung JW, Chun EJ, et al. Usefulness of 64-slice multidetector computed tomography as an initial diagnostic approach in patients with acute chest pain. Am Heart J. 2008;156:375–83.
19. Hoffmann U, Nagurney JT, Moselewski F, Pena A, Ferencik M, Chae CU, et al. Coronary multidetector computed tomography in the assessment of patients with acute chest pain. Circulation. 2006;114:2251–60.
20. Hoffmann U, Bamberg F, Chae CU, Nichols JH, Rogers IS, Seneviratne SK, et al. Coronary computed tomography angiography for early triage of patients with acute chest pain: the ROMICAT (Rule Out Myocardial Infarction using Computer Assisted Tomography) trial. J Am Coll Cardiol. 2009;53:1642–50.
21. Marwan M, Pflederer T, Schepis T, Seltmann M, Klinghammer L, Muschiol G, et al. Accuracy of dual-source CT to identify significant coronary artery disease in patients with uncontrolled hypertension presenting with chest pain: comparison with coronary angiography. Int J Cardiovasc Imaging. 2012;28:1173–80.
22. Hollander JE, Chang AM, Shofer FS, McCusker CM, Baxt WG, Litt HI. Coronary computed tomographic angiography for rapid discharge of low-risk patients with potential acute coronary syndromes. Ann Emerg Med. 2009;53:295–304.

23. Litt HI, Gatsonis C, Snyder B, Singh H, Miller CD, Entrikin DW, et al. CT angiography for safe discharge of patients with possible acute coronary syndromes. N Engl J Med. 2012;366:1393–403.
24. Hansen M, Ginns J, Seneviratne S, Slaughter R, Premaranthe M, Samardhi H, et al. The value of dual-source 64-slice CT coronary angiography in the assessment of patients presenting to an acute chest pain service. Heart Lung Circ. 2010;19:213–8.
25. Nasis A, Meredith IT, Nerlekar N, Cameron JD, Antonis PR, Mottram PM, et al. Acute chest pain investigation: utility of cardiac CT angiography in guiding troponin measurement. Radiology. 2011;260:381–9.
26. Chow BJW, Joseph P, Yam Y, Kass M, Chen L, Beanlands RS, Ruddy TD. Usefulness of computed tomographic coronary angiography in patients with acute chest pain with and without high-risk features. Am J Cardiol. 2010;106:463–9.
27. Hoffmann U, Truong QA, Schoenfeld DA, Chou ET, Woodard PK, Nagurney JT, et al., ROMICAT-II Investigators. Coronary CT angiography versus standard evaluation in acute chest pain. N Engl J Med 2012; 367:299–308.
28. Hulten E, Pickett C, Bittencourt MS, Villines TC, Petrillo S, Di Carli MF, Blankstein R. Outcomes after coronary computed tomography angiography in the emergency department: a systematic review and meta-analysis of randomized, controlled trials. J Am Coll Cardiol. 2013;61:880–92.
29. Brodoefel H, Reimann A, Klumpp B, Fenchel M, Heuschmid M, Burgstahler C, et al. Sixty-four-slice CT in the assessment of global and regional left ventricular function: comparison with MRI in a porcine model of acute and subacute myocardial infarction. Eur Radiol. 2007;17:2948–56.
30. van der Vleuten PA, Willems TP, Götte MJW, Tio RA, Greuter MJW, Zijlstra F, Oudkerk M. Quantification of global left ventricular function: comparison of multidetector computed tomography and magnetic resonance imaging. A meta-analysis and review of the current literature. Acta Radiol. 2006;47:1049–57.
31. Greupner J, Zimmermann E, Grohmann A, Dübel HP, Althoff TF, Althoff T, et al. Head-to-head comparison of left ventricular function assessment with 64-row computed tomography, biplane left cineventriculography, and both 2- and 3-dimensional transthoracic echocardiography: comparison with magnetic resonance imaging as the reference standard. J Am Coll Cardiol. 2012;59:1897–907.
32. Cury RC, Nieman K, Shapiro MD, Butler J, Nomura CH, Ferencik M, et al. Comprehensive assessment of myocardial perfusion defects, regional wall motion, and left ventricular function by using 64-section multidetector CT. Radiology. 2008;248:466–75.
33. Wei K, Peters D, Belcik T, Kalvaitis S, Womak L, Rinkevich D, et al. A predictive instrument using contrast echocardiography in patients presenting to the emergency department with chest pain and without ST-segment elevation. J Am Soc Echocardiogr. 2010;23:636–42.
34. Seneviratne SK, Truong QA, Bamberg F, Rogers IS, Shapiro MD, Schlett CL, et al. Incremental diagnostic value of regional left ventricular function over coronary assessment by cardiac computed tomography for the detection of acute coronary syndrome in patients with acute chest pain: from the ROMICAT trial. Circ Cardiovasc Imaging. 2010;3:375–83.
35. Bezerra HG, Loureiro R, Irlbeck T, Bamberg F, Schlett CL, Rogers I, et al. Incremental value of myocardial perfusion over regional left ventricular function and coronary stenosis by cardiac CT for the detection of acute coronary syndromes in high-risk patients: a subgroup analysis of the ROMICAT trial. J Cardiovasc Comput Tomogr. 2011;5:382–91.
36. Dirksen MS, Jukema JW, Bax JJ, Lamb HJ, Boersma E, Tuinenburg JC, et al. Cardiac multidetector-row computed tomography in patients with unstable angina. Am J Cardiol. 2005;95:457–61.
37. Udelson JE, Beshansky JR, Ballin DS, Feldman JA, Griffith JL, Handler J, et al. Myocardial perfusion imaging for evaluation and triage of patients with suspected acute cardiac ischemia: a randomized controlled trial. JAMA. 2002;288:2693–700.
38. Schepis T, Achenbach S, Marwan M, Muschiol G, Ropers D, Daniel WG, Pflederer T. Prevalence of first-pass myocardial perfusion defects detected by contrast-enhanced dual-source CT in patients with non-ST segment elevation acute coronary syndromes. Eur Radiol. 2010;20:1607–14.
39. Busch JL, Alessio AM, Caldwell JH, Gupta M, Mao S, Kadakia J, et al. Myocardial hypo-enhancement on resting computed tomography angiography images accurately identifies myocardial hypoperfusion. J Cardiovasc Comput Tomogr. 2011;5:412–20.
40. Feuchtner GM, Plank F, Pena C, Battle J, Min J, Leipsic J, et al. Evaluation of myocardial CT perfusion in patients presenting with acute chest pain to the emergency department: comparison with SPECT-myocardial perfusion imaging. Heart. 2012;98:1510–7.
41. Branch KR, Busey J, Mitsumori LM, Strote J, Caldwell JH, Busch JH, Shuman WP. Diagnostic performance of resting CT myocardial perfusion in patients with possible acute coronary syndrome. AJR Am J Roentgenol. 2013;200:W450–7.
42. Iwasaki K, Matsumoto T. Myocardial perfusion defect in patients with coronary artery disease demonstrated by 64-multidetector computed tomography at rest. Clin Cardiol. 2011;34: 454–60.
43. Achenbach S, Moselewski F, Ropers D, Ferencik M, Hoffmann U, Macneill B, et al. Detection of calcified and noncalcified coronary atherosclerotic plaque by contrast-enhanced, submillimeter multidetector spiral computed tomography: a segment-based comparison with intravascular ultrasound. Circulation. 2004;109:14–7.
44. Voros S, Rinehart S, Qian Z, Joshi P, Vazquez G, Fischer C, et al. Coronary atherosclerosis imaging by coronary CT angiography: current status, correlation with intravascular interrogation and meta-analysis. JACC Cardiovasc Imaging. 2011;4:537–48.
45. Papadopoulou SL, Garcia-Garcia HM, Rossi A, Girasis C, Dharampal AS, Kitslaar PH, et al. Reproducibility of computed tomography angiography data analysis using semiautomated plaque quantification software: implications for the design of longitudinal studies. Int J Cardiovasc Imaging. 2013;29:1095–104.
46. Kashiwagi M, Tanaka A, Kitabata H, Tsujioka H, Kataiwa H, Komukai K, et al. Feasibility of noninvasive assessment of thin-cap fibroatheroma by multidetector computed tomography. JACC Cardiovasc Imaging. 2009;2:1412–9.
47. Leber AW, Becker A, Knez A, Ziegler von F, Sirol M, Nikolaou K, et al. Accuracy of 64-slice computed tomography to classify and quantify plaque volumes in the proximal coronary system: a comparative study using intravascular ultrasound. J Am Coll Cardiol. 2006;47:672–7.
48. Otsuka M, Bruining N, Van Pelt NC, Mollet NR, Ligthart JMR, Vourvouri E, et al. Quantification of coronary plaque by 64-slice computed tomography: a comparison with quantitative intracoronary ultrasound. Investig Radiol. 2008;43:314–21.
49. Marwan M, Taher MA, Meniawy El K, Awadallah H, Pflederer T, Schuhbäck A, et al. In vivo CT detection of lipid-rich coronary artery atherosclerotic plaques using quantitative histogram analysis: a head to head comparison with IVUS. Atherosclerosis. 2011;215:110–5.
50. Pundziute G, Schuijf JD, Jukema JW, Decramer I, Sarno G, Vanhoenacker PK, et al. Head-to-head comparison of coronary plaque evaluation between multislice computed tomography and intravascular ultrasound radiofrequency data analysis. JACC Cardiovasc Interv. 2008;1:176–82.
51. Gauss S, Achenbach S, Pflederer T, Schuhbäck A, Daniel WG, Marwan M. Assessment of coronary artery remodelling by dual-source CT: a head-to-head comparison with intravascular ultrasound. Heart. 2011;97:991–7.
52. Maurovich-Horvat P, Schlett CL, Alkadhi H, Nakano M, Otsuka F, Stolzmann P, et al. The napkin-ring sign indicates advanced ath-

erosclerotic lesions in coronary CT angiography. JACC Cardiovasc Imaging. 2012;5:1243–52.
53. Hoffmann U, Moselewski F, Nieman K, Jang IK, Ferencik M, Rahman AM, et al. Noninvasive assessment of plaque morphology and composition in culprit and stable lesions in acute coronary syndrome and stable lesions in stable angina by multidetector computed tomography. J Am Coll Cardiol. 2006;47:1655–62.
54. Pflederer T, Marwan M, Schepis T, Ropers D, Seltmann M, Muschiol G, et al. Characterization of culprit lesions in acute coronary syndromes using coronary dual-source CT angiography. Atherosclerosis. 2010;211:437–44.
55. Kim SY, Kim KS, Seung MJ, Chung JW, Kim JH, Mun SH, et al. The culprit lesion score on multi-detector computed tomography can detect vulnerable coronary artery plaque. Int J Cardiovasc Imaging. 2010;26:245–52.
56. Motoyama S, Kondo T, Sarai M, Sugiura A, Harigaya H, Sato T, et al. Multislice computed tomographic characteristics of coronary lesions in acute coronary syndromes. J Am Coll Cardiol. 2007;50:319–26.
57. Kitagawa T, Yamamoto H, Horiguchi J, Ohhashi N, Tadehara F, Shokawa T, et al. Characterization of noncalcified coronary plaques and identification of culprit lesions in patients with acute coronary syndrome by 64-slice computed tomography. JACC Cardiovasc Imaging. 2009;2:153–60.
58. Ferencik M, Schlett CL, Ghoshhajra BB, Kriegel MF, Joshi SB, Maurovich-Horvat P, et al. A computed tomography-based coronary lesion score to predict acute coronary syndrome among patients with acute chest pain and significant coronary stenosis on coronary computed tomographic angiogram. Am J Cardiol. 2012;110:183–9.
59. Koo BK, Erglis A, Doh JH, Daniels DV, Jegere S, Kim HS, et al. Diagnosis of ischemia-causing coronary stenoses by noninvasive fractional flow reserve computed from coronary computed tomographic angiograms. Results from the prospective multicenter DISCOVER-FLOW (Diagnosis of Ischemia-Causing Stenoses Obtained Via Noninvasive Fractional Flow Reserve) study. J Am Coll Cardiol. 2011;58:1989–97.
60. Min JK, Leipsic J, Pencina MJ, Berman DS, Koo BK, van Mieghem C, et al. Diagnostic accuracy of fractional flow reserve from anatomic CT angiography. JAMA. 2012;308:1237–45.
61. Min JK, Koo BK, Erglis A, Doh JH, Daniels DV, Jegere S, et al. Usefulness of noninvasive fractional flow reserve computed from coronary computed tomographic angiograms for intermediate stenoses confirmed by quantitative coronary angiography. Am J Cardiol. 2012;110:971–6.
62. Detrano R, Guerci AD, Carr JJ, Bild DE, Burke G, Folsom AR, et al. Coronary calcium as a predictor of coronary events in four racial or ethnic groups. N Engl J Med. 2008;358:1336–45.
63. Sarwar A, Shaw LJ, Shapiro MD, Blankstein R, Hoffmann U, Hoffman U, et al. Diagnostic and prognostic value of absence of coronary artery calcification. JACC Cardiovasc Imaging. 2009;2:675–88.
64. Joshi PH, Blaha MJ, Blumenthal RS, Blankstein R, Nasir K. What is the role of calcium scoring in the age of coronary computed tomographic angiography? J Nucl Cardiol. 2012;19:1226–35.
65. Taylor AJ, Cerqueira M, Hodgson JM, Mark D, Min J, O'Gara P, et al. ACCF/SCCT/ACR/AHA/ASE/ASNC/NASCI/SCAI/SCMR 2010 appropriate use criteria for cardiac computed tomography. A report of the American College of Cardiology Foundation Appropriate Use Criteria Task Force, the Society of Cardiovascular Computed Tomography, the American College of Radiology, the American Heart Association, the American Society of Echocardiography, the American Society of Nuclear Cardiology, the north American Society for Cardiovascular Imaging, the Society for Cardiovascular Angiography and Interventions, and the Society for Cardiovascular Magnetic Resonance. Circulation. 2010;122:e525–55.

Imaging Diseases of the Aorta

11

Peter S. Fail

The aorta (from Medieval Latin, Greek *aorté*, the great artery; literally, "I lift, carry, rise") is the largest artery in the body, originating from the heart, extending down through the abdomen, and terminating at the bifurcation of the iliacs. It can be divided into the thoracic aorta, above the diaphragm, and the abdominal aorta, below the diaphragm. The thoracic segment is further divided into the ascending aorta (including the arch) and the descending aorta. The abdominal aorta, although usually described from the diaphragm to the iliacs, can be divided into the visceral or renal aorta and the infrarenal aorta (Figs. 11.1 and 11.2).

Pathological and epidemiological studies have failed to uncover the exact cause of abdominal aortic aneurysms (AAA). Although they are frequently seen in connection with the typical atherosclerotic risk factors, atherosclerosis is an intimal disease with the formation of foam–cells, whereas the media and adventitia are the primary locations of aneurysmal disease [1]. The Aneurysm Detection and Management Veterans Affairs Cooperative Study Group (ADAM) trial found an advanced age, greater height, coronary artery disease (CAD), atherosclerosis, high cholesterol levels, hypertension, and, in particular, smoking was associated with AAA formation [2]. With more significance being placed on the duration of smoking rather than the amount. Smokers are seven times more likely to develop an abdominal aortic aneurysm than non-smokers [3]. Current smokers are also at an increase risk of rupture, along with female gender, large initial diameter and a low forced expiratory volume (FEV1). The other important risk associated with AAA is a family history, seen in 12–19% of first degree relative of those undergoing aneurysmal repair [4]. Women and African Americans tend to have a lower incidence of AAA. And although diabetes portends a cardiovascular risk, diabetics as a group tend to have a lower prevalence of AAA [5].

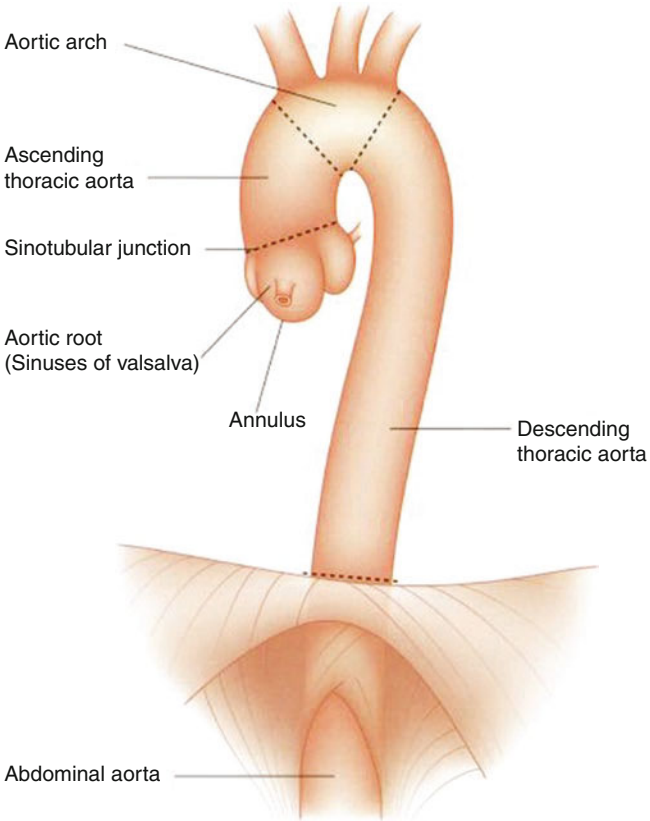

Fig. 11.1 Abdominal aorta with the advent of interventional treatment options for the thoracic aorta the ascending, arch and descending aorta can be subdivided into zones to correspond to landing zones for thoracic endografts (TEVAR)

It has been estimated that 9% of adults older than 65 years of age may have an aortic aneurysm, and the rupture of these aneurysms accounts for about 15,000 deaths in the United States annually [6]. Unfortunately only 30–40% of aneurysms

P.S. Fail
Department of Interventional Cardiology, Cardiovascular Institute of the South/Terrebonne General Medical Center,
225 Dunn Street, Houma, LA 70360, USA
e-mail: peter.fail@cardio.com

M.J. Budoff et al. (eds.), *Atlas of Cardiovascular Computed Tomography*, https://doi.org/10.1007/978-1-4471-7357-1_11

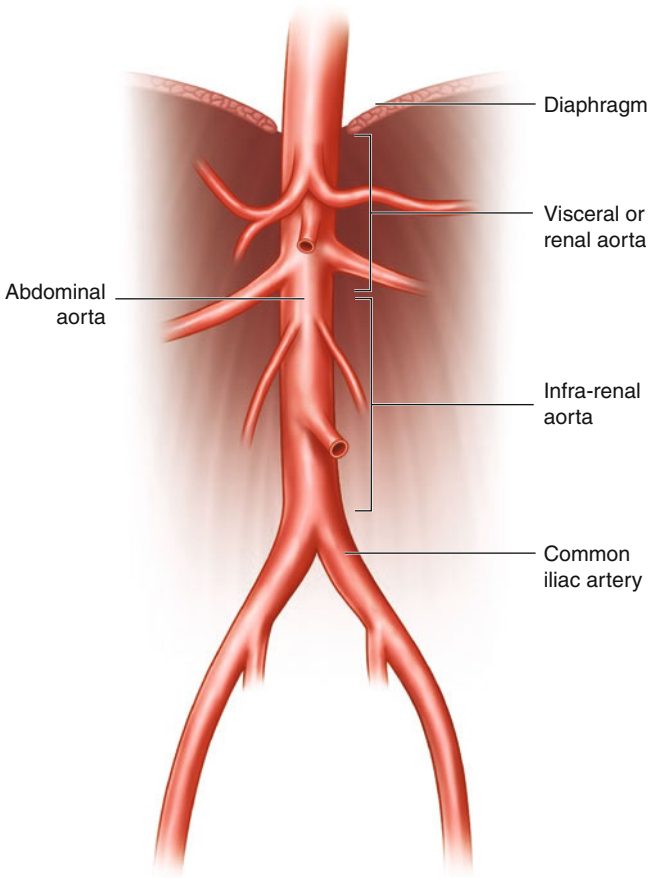

Fig. 11.2 Abdominal aorta

are picked up on physical examination. Two major factors influencing detection are aneurysmal size and abdominal obesity (Figs. 11.3, 11.4, 11.5, 11.6, 11.7, 11.8, 11.9, 11.10, 11.11, 11.12, 11.13, 11.14, 11.15, 11.6, 11.17, 11.18, 11.19, 11.20 and 11.21).

The diagnosis of an AAA can be easily made with an abdominal ultrasound where the sensitivity approaches 100% [7]. It does have its draw backs in that it is highly operator dependent and in obese patients or those with significant bowl gas, images adequate for a diagnosis may not be possible. CTA was originally felt to have inherent inaccuracies in tortuous anatomy especially in the early single slice scanners [7]. However, with 16 slice and above scanners, newer workstations and software and being able to manipulate full volume data sets, this is less likely.

Randomized trials have provided evidence that ultrasound screening is effective in reducing AAA-related mortality [8, 9]. The current recommendations are a one-time ultrasound screening for AAA for all men at or older than age 65, or as early as age 55 for those with a family history of AAA, and women at or older than age 65 who have smoked or have a family history. If an aneurysm is noted, the follow-up scanning recommendations are 5-year intervals for an aortic diameter measuring between 2.6 and 2.9 cm, a 3 year interval for diameters between 3.0 and 3.4 cm, a 12-month intervals for patients with an AAA of 3.5 to 4.4 cm, and every 6-month for diameters between 4.5 and 5.4 cm [5]. Although there are various parameters

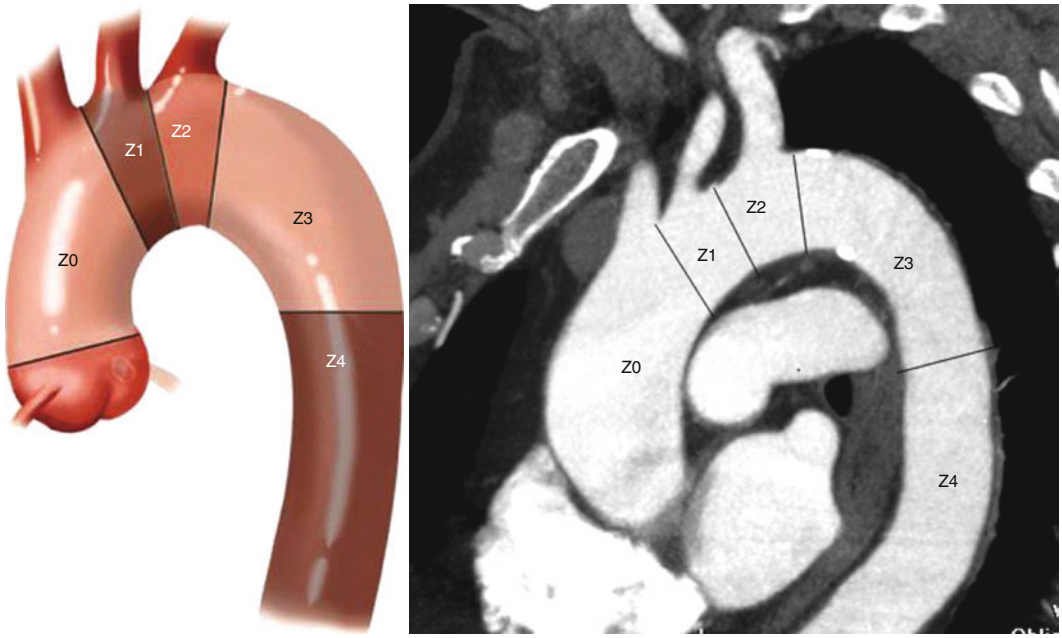

Fig. 11.3 Drawing and corresponding CT image depicting the division of the ascending, arch, and descending aorta into landing zones: Zone 0 starts at the sinotubular junction and includes the inominate artery; Zone 1 starts at the completion of the inominate artery and includes the left carotid artery; Zone 2 includes the left subclavian; Zone 3 starts at the completion of the left subclavian artery and continues to the mid thoracic aorta; Zone 4 extends from the mid thoracic aorta to the diaphragm

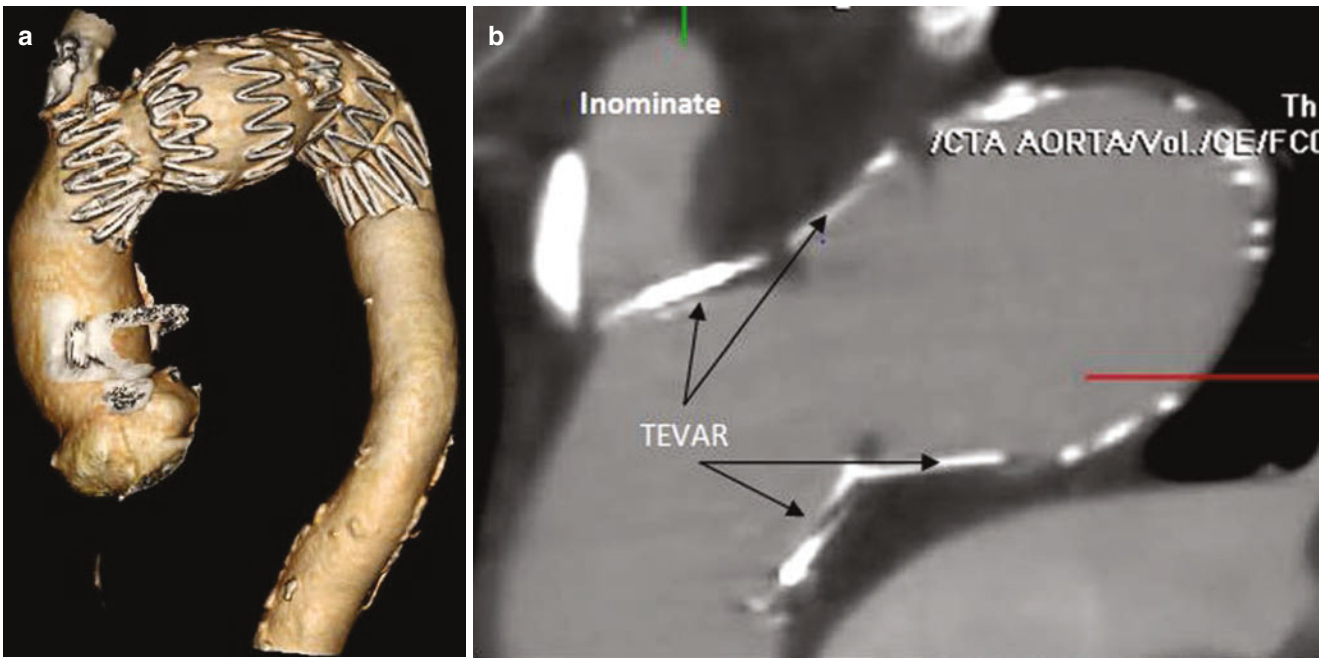

Fig. 11.4 Fenestrated TEVAR graft landing in Zone 0 and crossing Zone1–3 and ending at the beginning of Zone 4. Note that in this image the left carotid and left subclavian are not visualized. The patient underwent a Right subclavian-carotid-to-carotid-Left subclavian bypass. Panel (**b**) MIP image of the above TEVAR Showing that the fenestration crosses the inominate vessel, and that there is no "Bird-beaking" of the graft, a condition where poor apposition of the graft results in flow underneath the graft and possible collapse

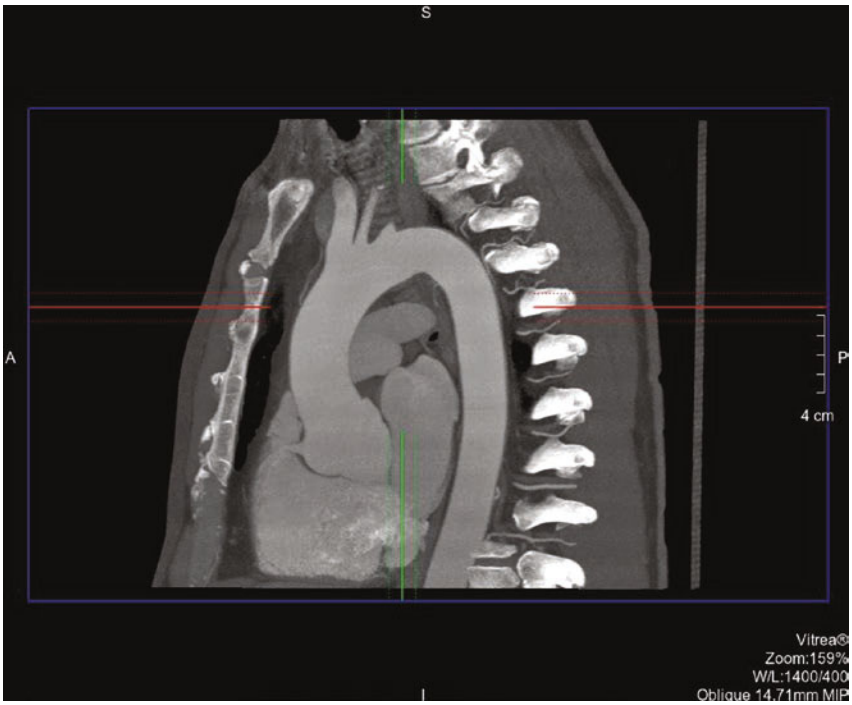

Fig. 11.5 CT image

available to predict AAA rupture, diameter remains the most widely used benchmark to determine intervention [10]. Although aneurysmal dilation remains a common problem there are cases where obstruction becomes the issue. Leriche Syndrome or triad being the most recognized. The triad as originally described occurring in men includes, buttock claudication, absent femoral pulses and impotence, can also occur in women [11].

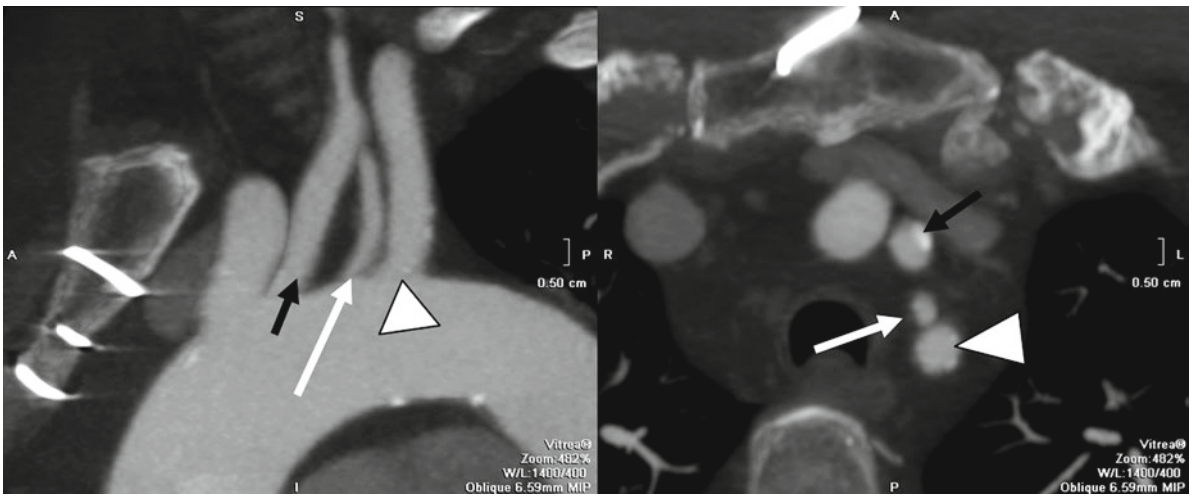

Fig. 11.6 A four-vessel aortic arch occurs in approximately 1–2% of patients. Normally the left vertebral artery (*white arrow*) arises from the left subclavian artery here, it arises directly from the aortic arch between the left common carotid (*black arrow*) and left subclavian arteries (*arrowhead*). This is a normal variant and is not associated with any other cardio- or cerebrovascular anomalies

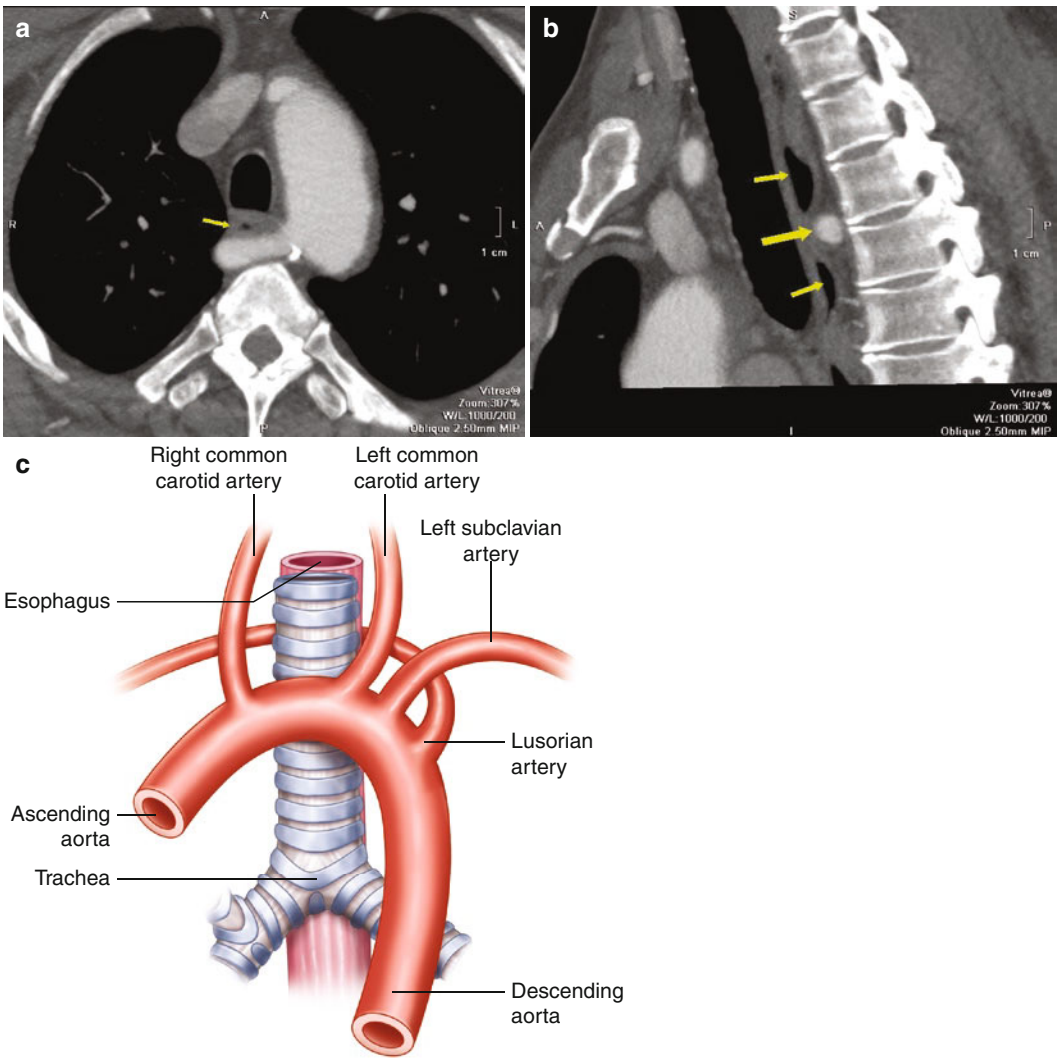

Fig. 11.7 Aberrant right subclavian artery, which arises as the fourth branch from the aorta, courses behind the esophagus in approximately 80% of patients. Dysphagia may result in patients as a result of enlargement of the artery compressing the esophagus (Kommerell diverticulum). In most adult patients, the aorta is also abnormal and is prone to aneurysm formation, dissection, and rupture. The *Yellow Arrow* in panel (**a**)is denoting the esophagus. Note in the sagittal view the compression of the esophagus. (*Large yellow arrow*)

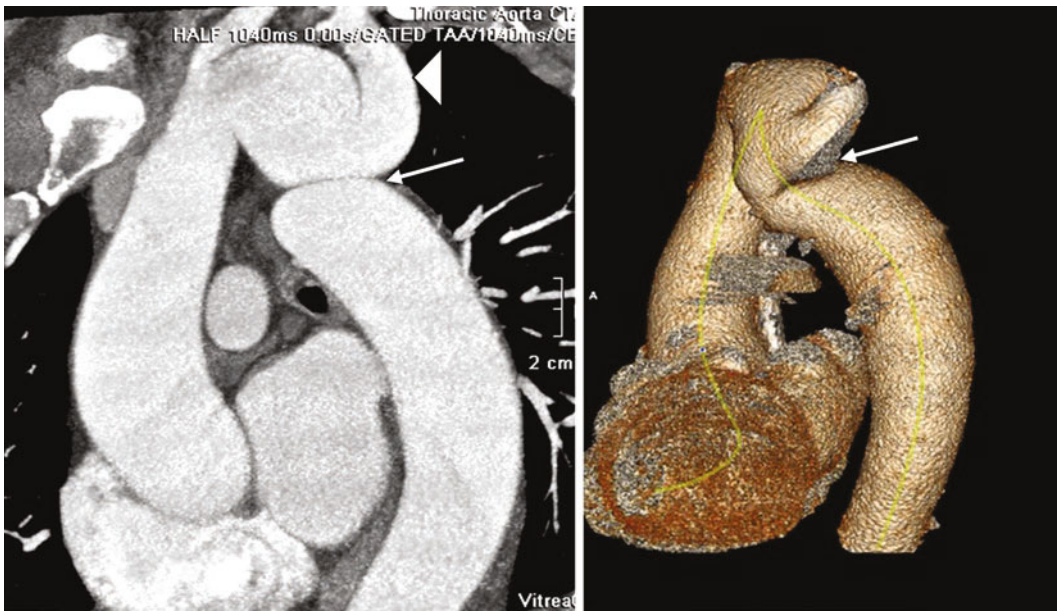

Fig. 11.8 Coarctation of the aorta. Coarctation is a discrete narrowing (*white arrows*) of the proximal descending thoracic aorta, usually located just distal to the origin of the left subclavian artery (*Arrow head*). The aortic wall typically has the appearance of being pinched inward and often somewhat kinked. When the stenosis is significant, the coarctation results in upper extremity hypertension with a blood pressure differential between the upper and lower extremities. Coarctation of the aorta occurs in up to 40–50 of every 100,000 births, having a male predilection of 2–3:1 Because of the increased association with a bicuspid aortic valve either a gated study or echocardiogram should be done to evaluate the aortic valve

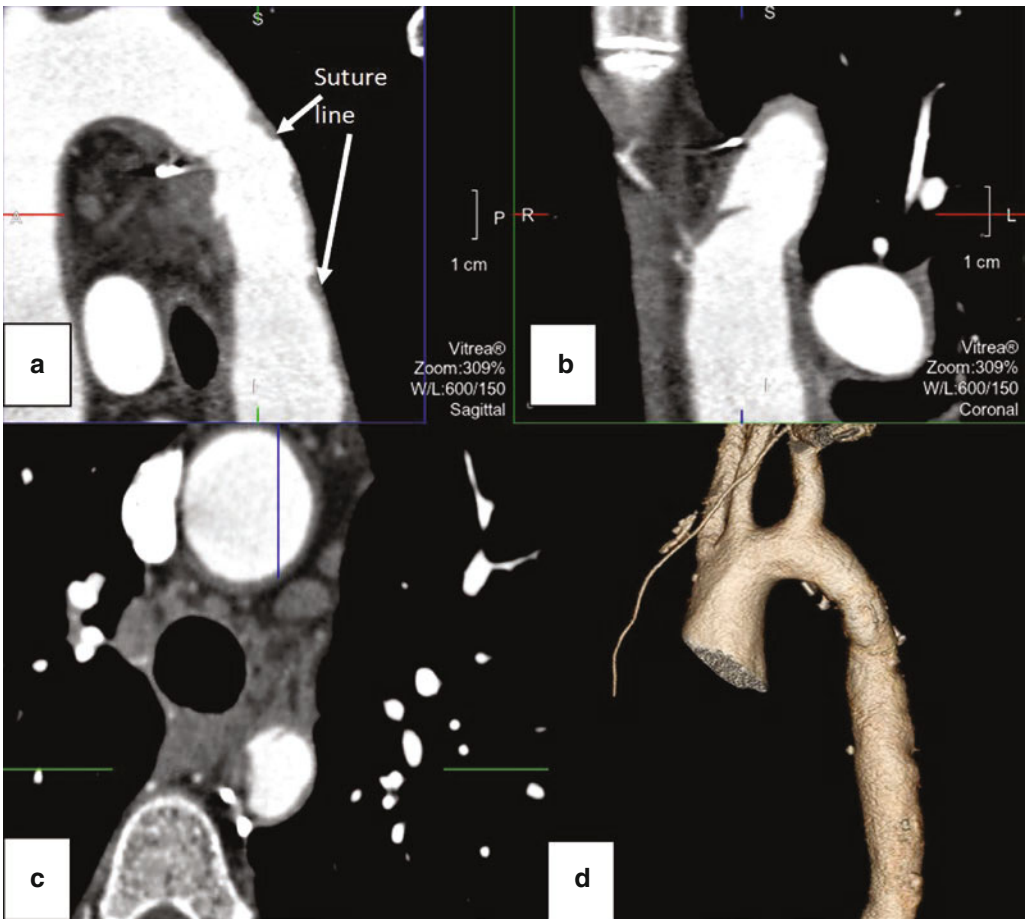

Fig. 11.9 Patient that underwent an open repair of a coarctation as a young adult. Panel (**a**) shows the suture line of the operative repair. Panel (**b**) notes a luminal projection at the repair site. Panel (**c**) is the axial view of the repair site. Panel (**d**) is the VR image of the coarctation

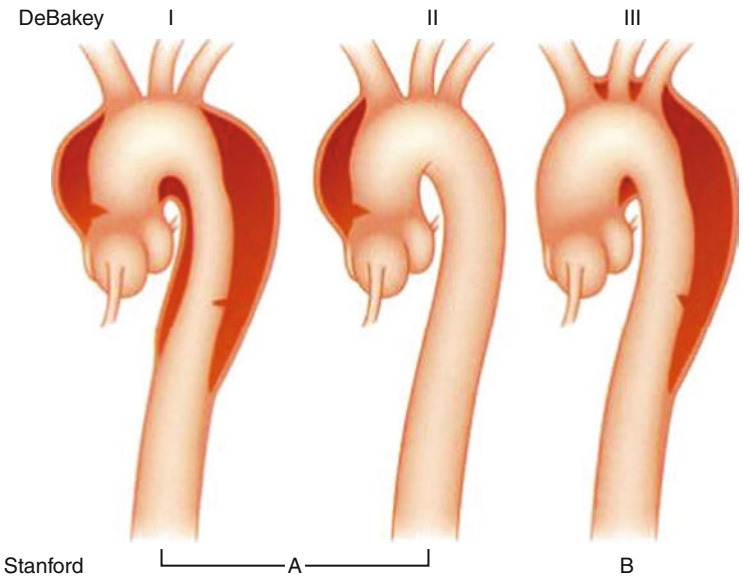

Fig. 11.10 A drawing of the Stanford and DeBakey classification of thoracic artery disections

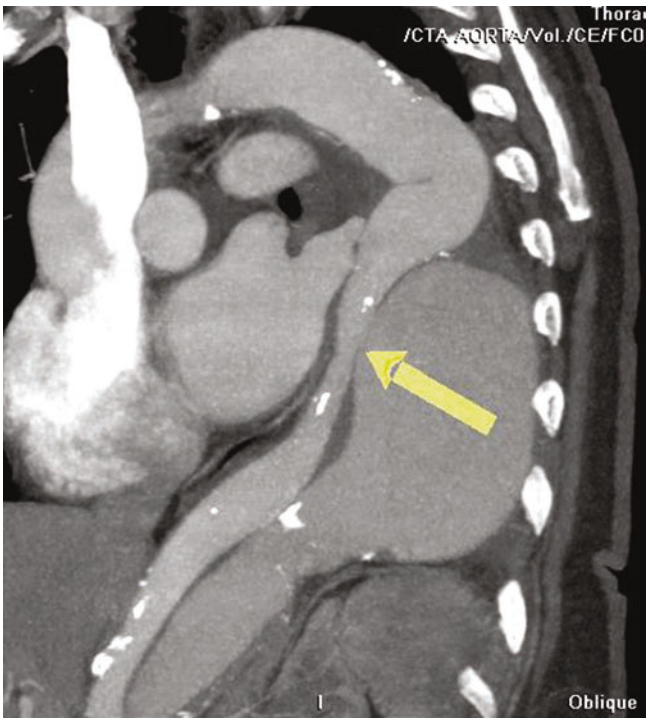

Fig. 11.11 Very large thoracic anuersym as a result of Stanford B dissection. It can be seen in the CR images. The Gold *arrow* denotes a fenestration

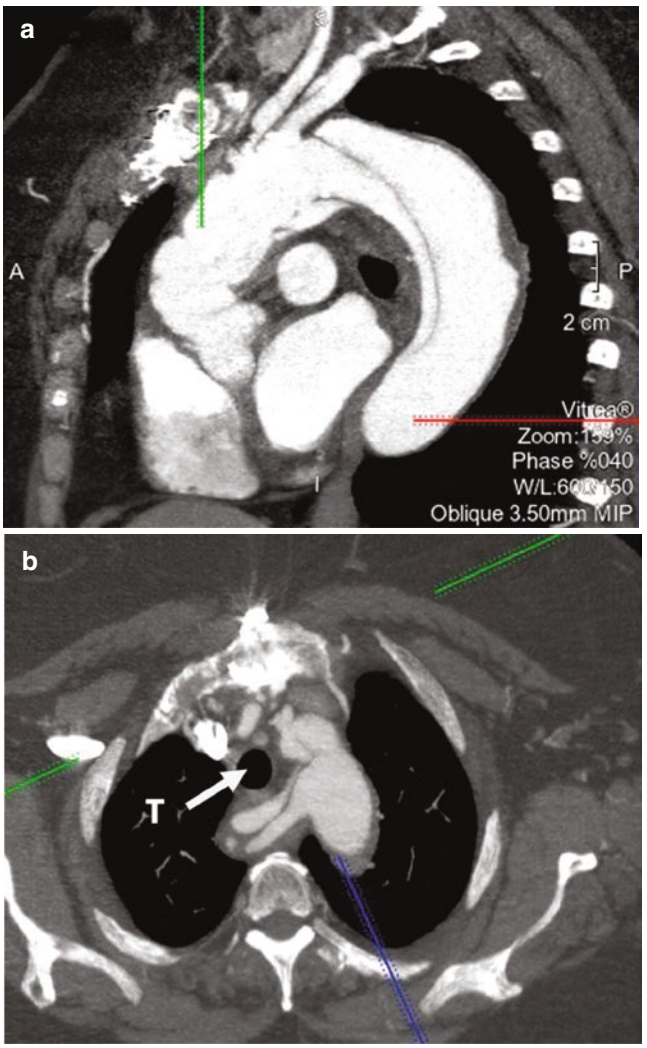

Fig. 11.12 Stanford A dissection following repair of the ascending aorta. A residual dissection persists (Stanford B) Note in panel (**b**) that this patient also has Arteria Lusoria with a retro-esophageal course if the right subclavian that is also dissected. *T*—Trachea

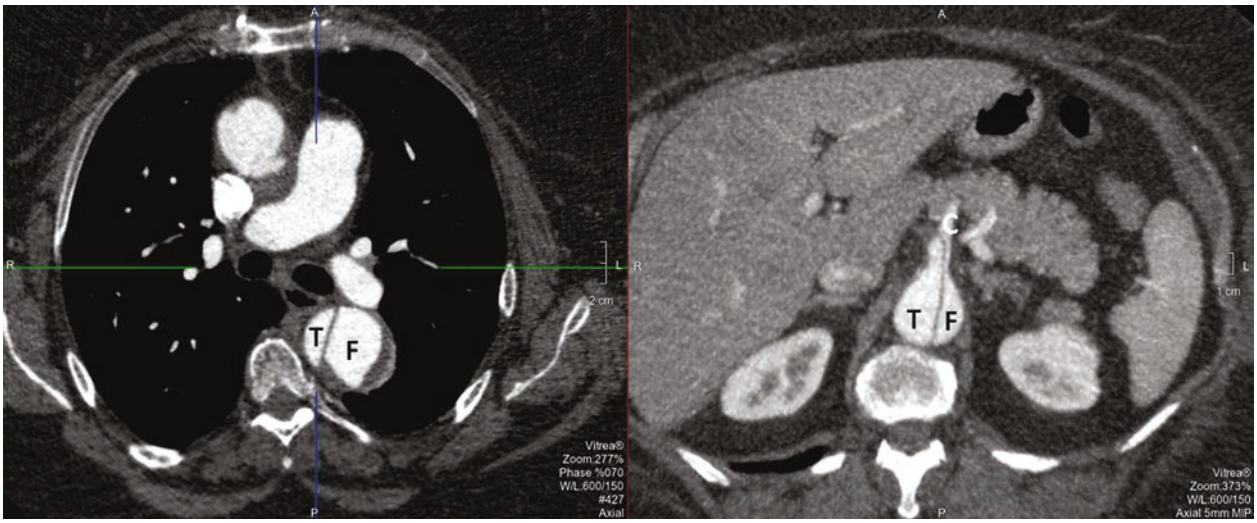

Fig. 11.13 Uncomplicated Stanford B dissection. Notice the partially thrombosed false lumen, which has been shown to portend a slightly worse morbidity and mortality then a completely thrombosed false lumen: *T*—true lumen, *F*—false lumen, *C*—celiac artery

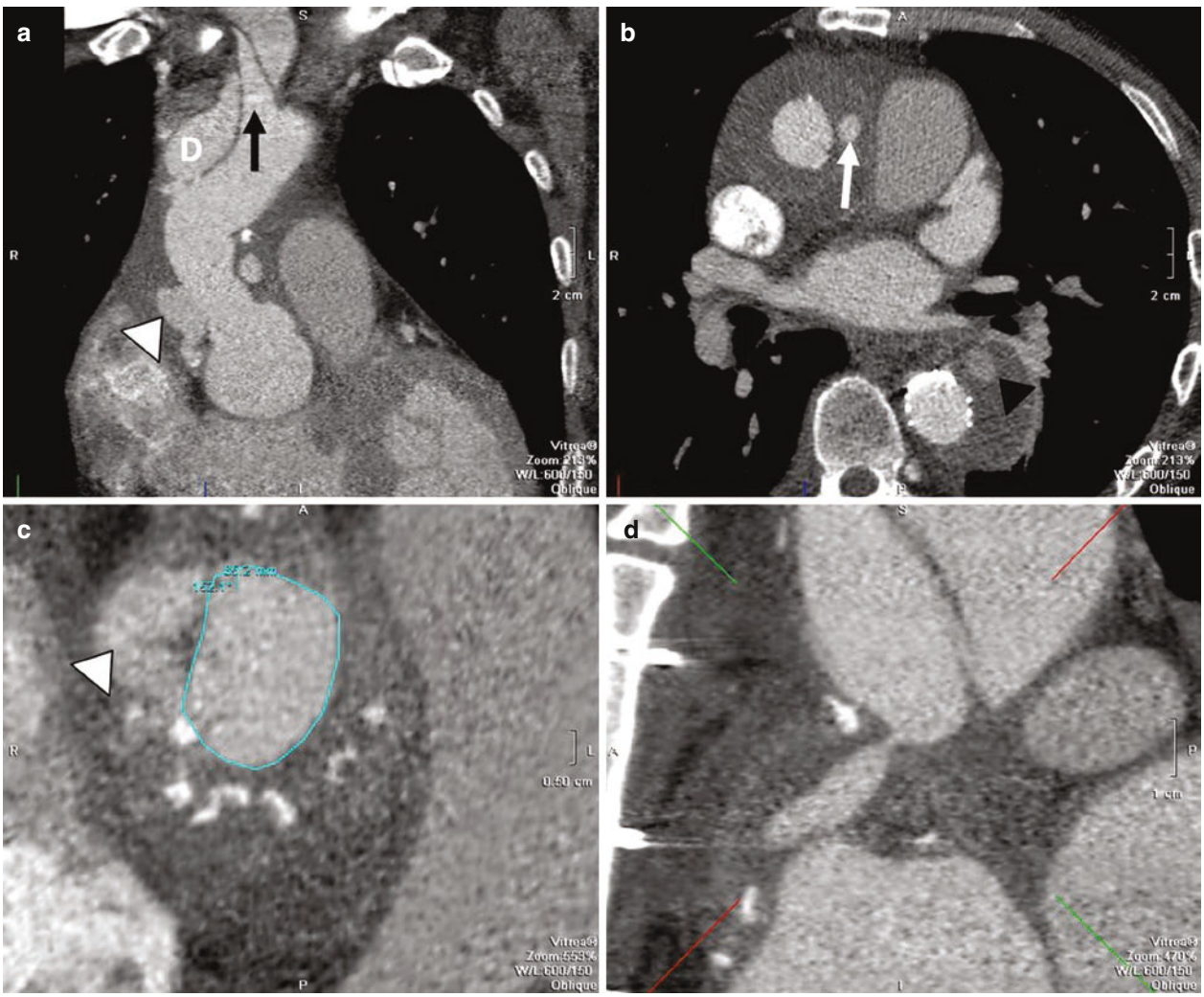

Fig. 11.14 Stanford A dissection following emergent operative repair followed by TEVAR of the descending extension. Note the residual dissection (**d**) before the inominate artery (*black arrow*) as well as a pseudoaneurysm in panel (**a**). Panel (**b**) is the axial view of the pseudoaneurysm (*white arrow*) along with the aneurysmal dilation of the ascending aorta. Note that the descending aorta has a TEVAR graft with and endoleak. (*black arrowhead*) Panel C is at the sino-tubular junction. Note that the pseudoaneurysm extends to this level. (*arrowhead*). Panel (**d**) is a "double-oblique" that identifies the entrance or inflow area of the pseudoaneurysm

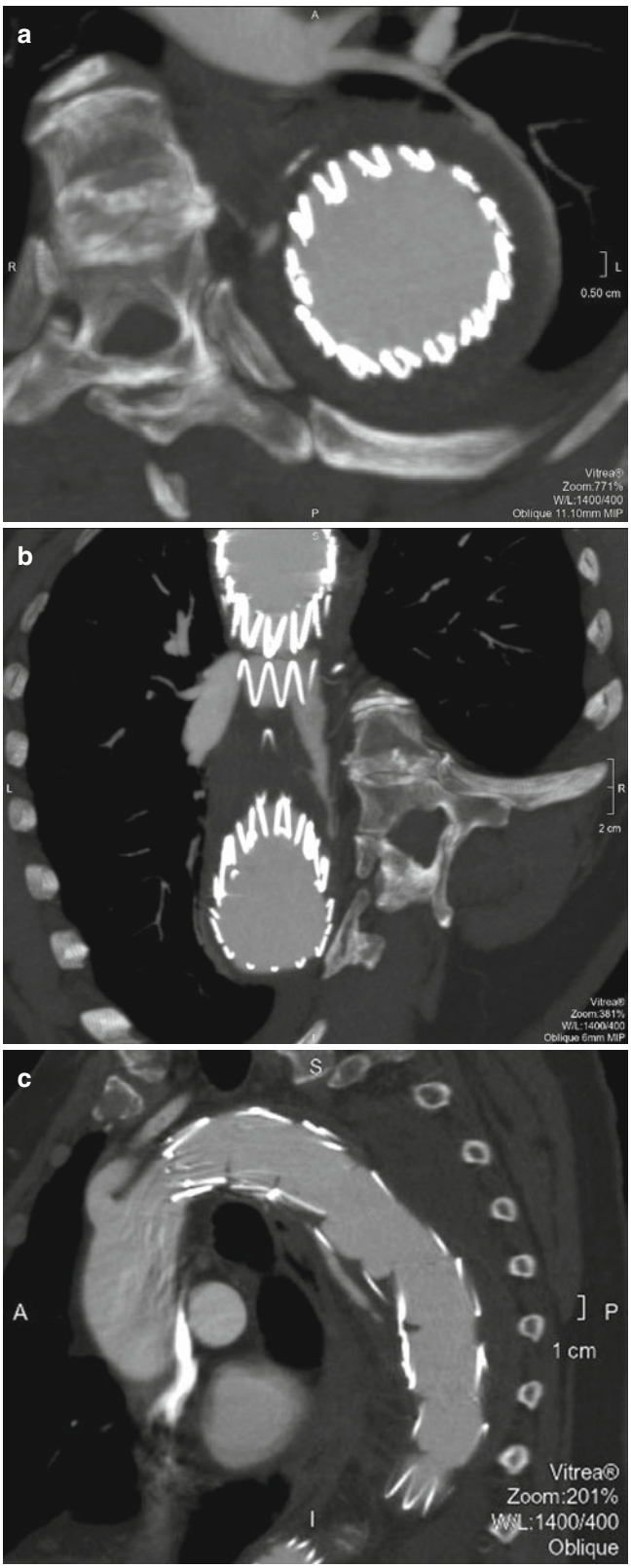

Fig. 11.15 Type 2 endoleak arising from a lumbar to lumbar axis following TEVAR. Panel (**a**, **b**) shows the endoleak and feeding vessels from the lumbar artery (*white arrow*). Panel (**c**) shows the extent of the endoleak

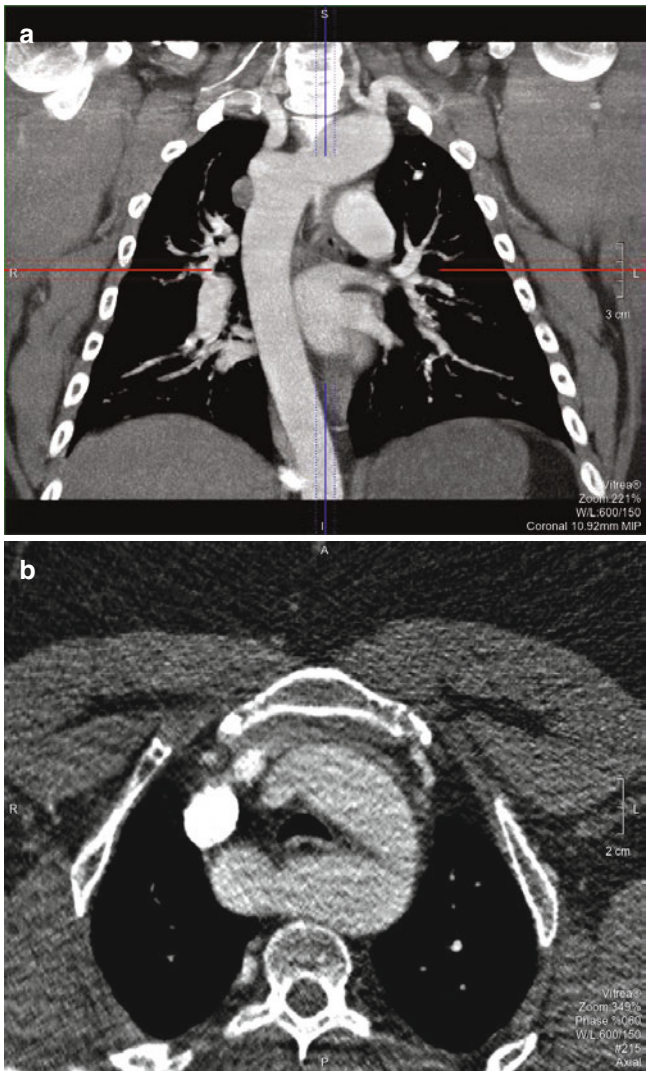

Fig. 11.16 Vascular ring or sling refers to a variety of congenital vascular anomalies that encircle and compress the esophagus and trachea. It can be a complete or true vs. incomplete ring as noted above. Abnormalities of the aortic arch and its branching arteries make up most of the vascular rings. (**a**) The abnormal course of the descending aorta. (**b**) Axial view. Note the trachea (*white arrow*) and the esophagus (*black arrow*) that are surrounded by the aortic arch

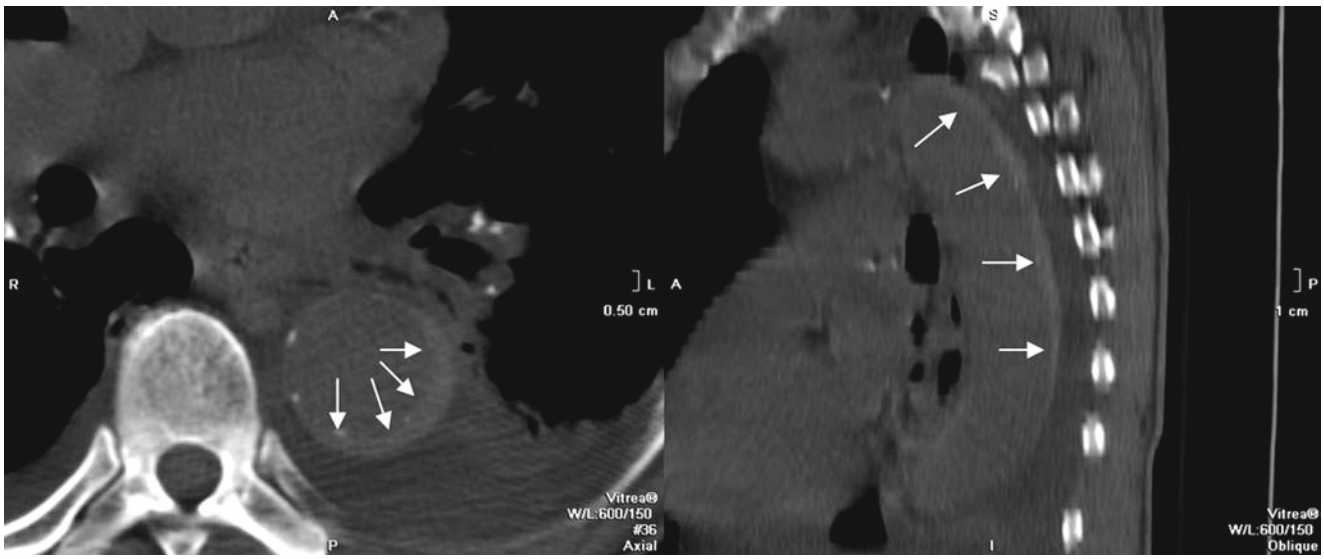

Fig. 11.17 Axial and sagittal views of a 72 year old woman patient presenting with severe back pain. Intramural hematoma is denoted in this unenhanced scan by a crescent shaped area of high-attenuation (*white arrows*)

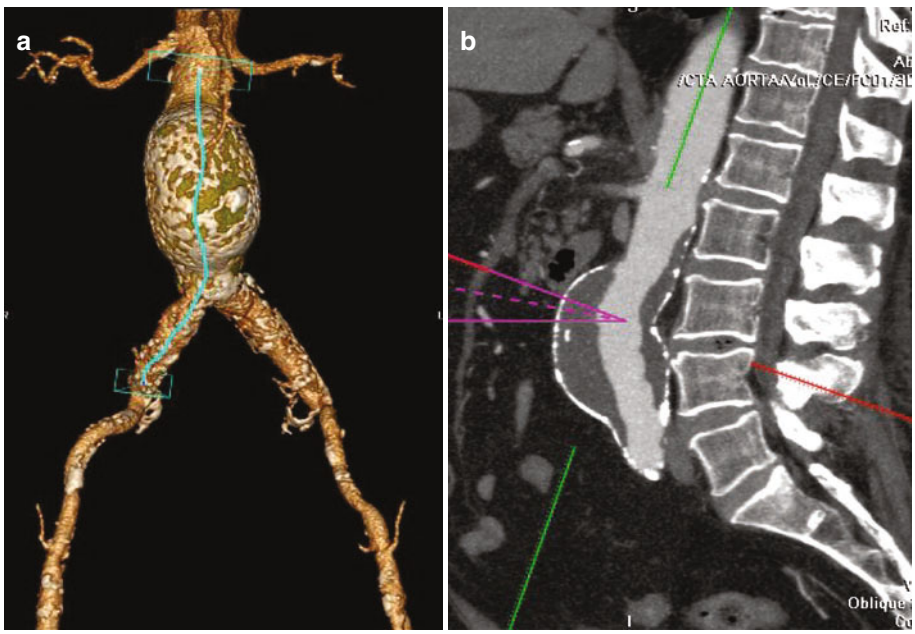

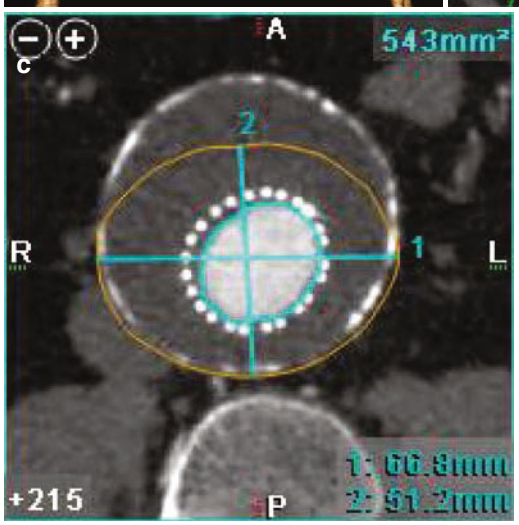

Fig. 11.18 Panel (**a**) is a VR image of an Abdominal Aortic Aneurysm with the neck of the AAA noted. Manufactures of endografts IFU range from 10 to 15 mm neck requirement for EVAR. Newer generation fenestration grafts require a minimum of 4 mm. Panel (**b**) analyses the angle required to place the image intensifier in order prevent parallax while implanting an endograft. Panel (**c**) is the same patient following EVAR. Note the issues of misalignment of the automated analysis program, leading to an underestimate of the aneurysmal size

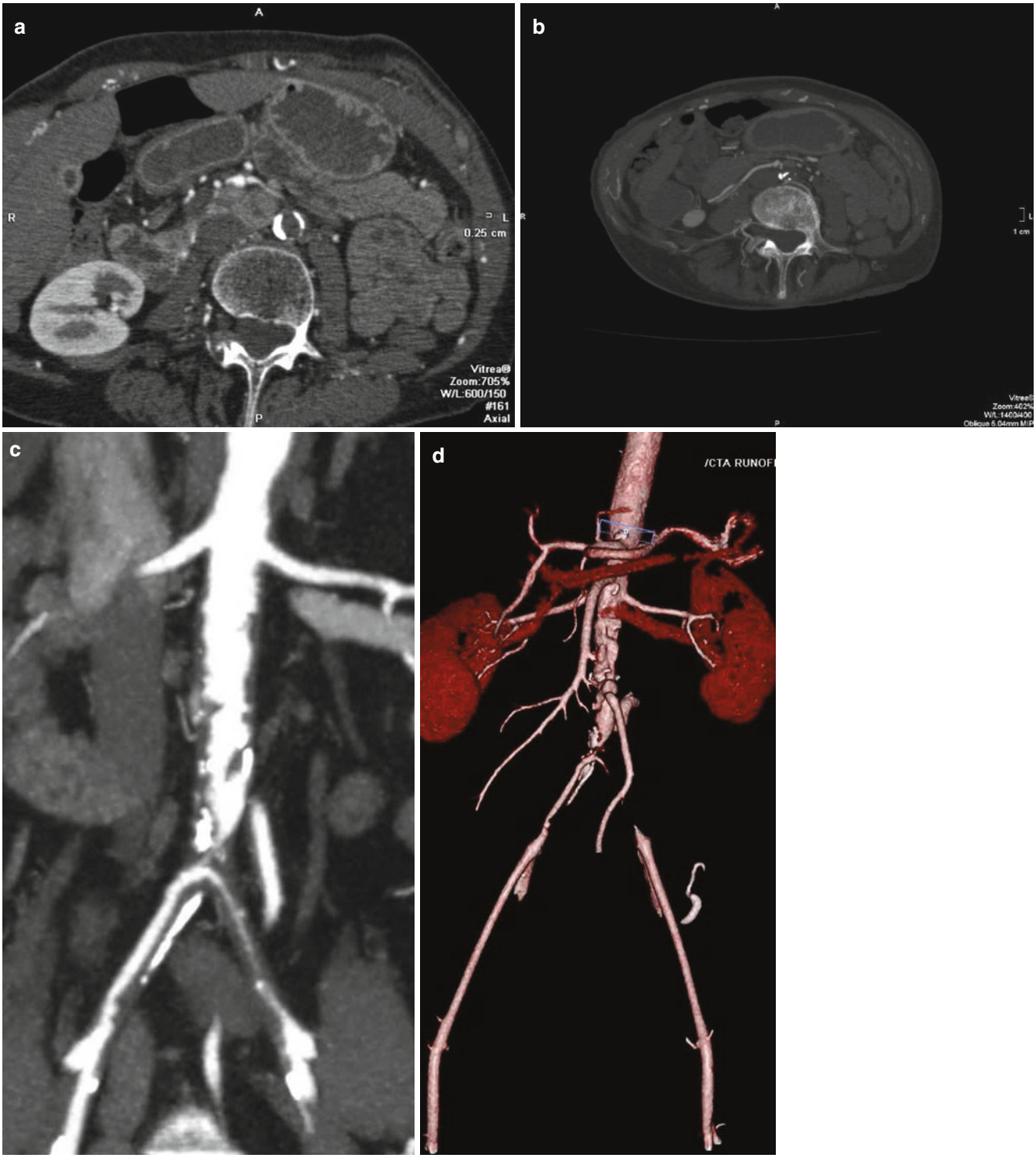

Fig. 11.19 These panels represent different patients with aortoiliac occlusive disease, also known as Leriche's syndrome. Classically, it is described in male patients as a triad of symptoms consisting of: claudication of the buttocks and thighs, absent or decreased femoral pulses and impotence. Note the almost non-contrast appearance of the axial views. Also note the contrast highlighted right kidney. The coronal and VR images are the same patient denoting total occlusion of the Aorta at the bifurcation. The left common iliac is also totally occluded

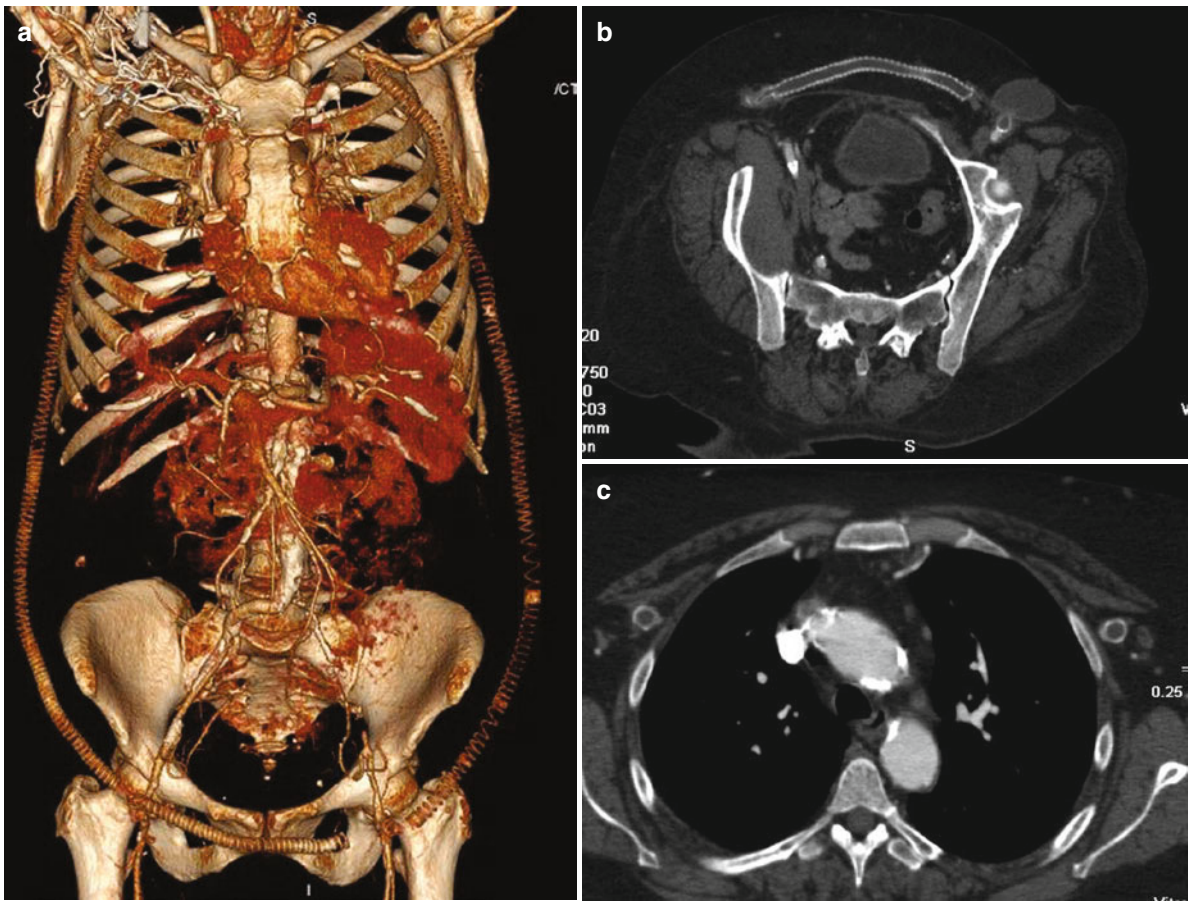

Fig. 11.20 The images show a patient who has undergone bilateral axillary-femoral bypass (*white arrows*) and a femoral-femoral bypass (*black arrows*). Note that all of the bypasses are occluded

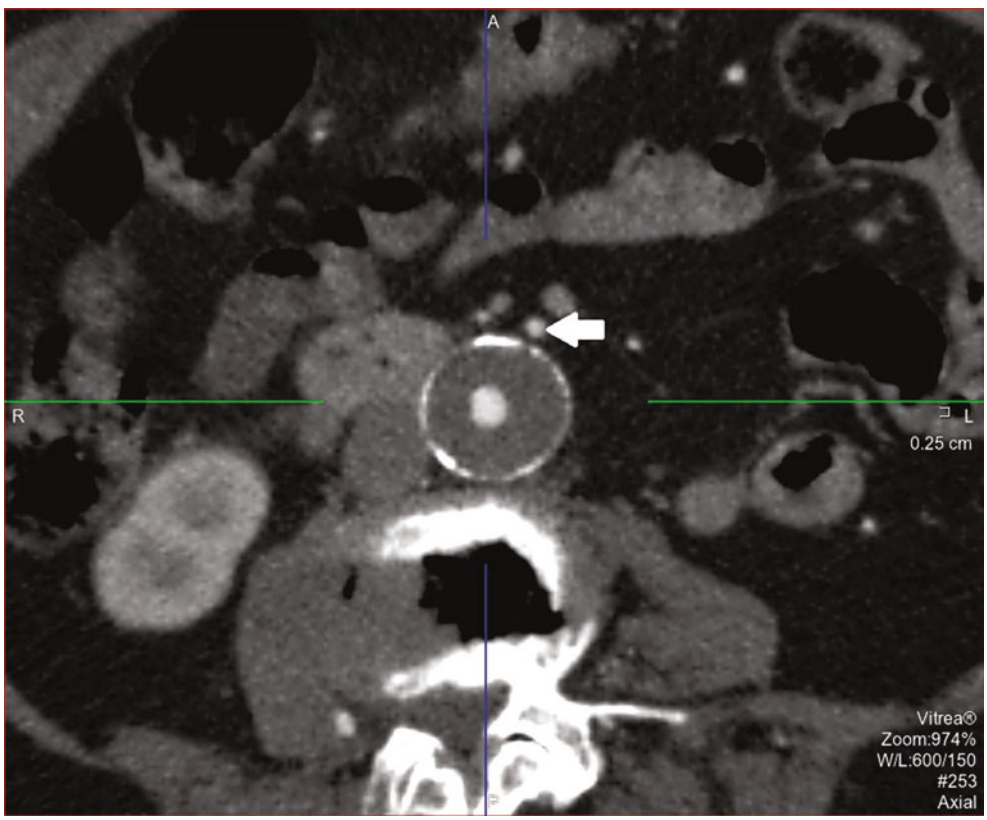

Fig. 11.21 A large calcified abdominal aortic aneurysm with a large amount of athero-thrombotic material in the center. Inferior mesenteric (*white arrow*) is patent, a possible source of and Endoleak following EVAR. It is easy to see why an angiogram on this patients would miss an aneurysm

Thoracic Aorta

The thoracic aorta is divided into 4 parts: the aortic root (1), the ascending aorta (2), the aortic arch (3), and the descending aorta (4), which begins at the isthmus between the origin of the left subclavian artery and the ligamentum arteriosum and courses anterior to the vertebral column, and then through the diaphragm into the abdomen

Numerous factors influence the "normal diameter" of the thoracic aorta, including age, gender, body mass, location of the measurement and the type and robustness of the imaging method [12]. A table has been developed by The Society of Vascular Surgery describing the normal diameters based on CT and chest x-ray (Table 11.1) [13].

This is important to determine if there is an abnormality as well as give a threshold for possible intervention, whether surgical, endovascular or continued observation. The The Society of Vacsular Surgery also set forth imaging recommendations for not only the proper format using CT or echocardiography, but also reporting of findings (Table 11.2).

Aneurysms and Dissections

The histopathology of aortic aneurysms has been mislabeled as cystic medial necrosis, where the more accurate term should be medial degeneration characterized by increased deposition of proteoglycans and the disruption and loss of elastic fibers [12]. Although the cause as not been well elucidated, studies have shown an increase in matrix metalloproteinases (MMPs), particularly MMP-2 and MMP-9 [14–17] which have been shown to have elastolyic activity [17]. The mean expansion rates of aneurysms differ greatly depending on the region. The thoracic region has been shown to have a mean expansion rate of 1.3 ± 1.2 mm/yr. which is significantly lower than 3.9 ± 3.2 mm/yr. reported in abdominal aortic aneurysms [18].

Aortic Dissection

There are two standard systems to classify the anatomy of aortic dissections, the DeBakey and the Stanford Classification. In the DeBakey system, a dissection that involves the ascending and descending thoracic aorta is con-

Table 11.1 Normal diameters based on CT and chest X-ray [13]

Thoracic aorta	Range of reported mean (cm)	Reported SD (cm)	Assessment method
Root (female)	3.50–3.72	0.38	CT
Root (male)	3.63–3.31	0.38	CT
Ascending (female, male)	2.86	NA	CXR
Middle-descending (female)	2.45–2.64	0.31	CT
Middle-descending (male)	2.39–2.98	0.31	CT
Diaphragmatic (female)	2.40–2.44	0.32	CT
Diaphragmatic (male)	2.43–2.69	0.27–0.40	CT, arteriography

Table 11.2 Essential elements of aortic imaging reports [13]

1. The location at which the aorta is abnormal
2. The maximum diameter of any dilatation, measured from the external wall of the aorta, perpendicular to the axis of flow, and the length of the aorta that is abnormal.
3. For patients with presumed or documented genetic syndromes at risk for aortic root disease measurements of aortic valve, sinuses of Valsalva, sinotubular junction, and ascending aorta.
4. The presence of internal filling defects consistent with thrombus or atheroma.
5. The presence of IMH, PAU, and calcification.
6. Extension of aortic abnormality into branch vessels, including dissection and aneurysm, and secondary evidence of end-organ injury (e.g., renal or bowel hypoperfusion).
7. Evidence of aortic rupture, including periaortic and mediastinal hematoma, pericardial and pleural fluid, and contrast extravasation from the aortic lumen.
8. When a prior examination is available, direct image to image comparison to determine if there has been any increase in diameter.

IMH intramural hematoma, *PAU* penetrating atherosclerotic ulcer

sidered type I. If the aneurysm is confined to the ascending aorta it is classified type II. Type III is present if only the descending is involved. The Stanford system simplifies this classification in that if the ascending thoracic aorta is involved in the dissection it is type A, and if the ascending aorta is not involved it is type B.

CTA Evaluation of the Aorta

CT has become the study of choice when evaluating the aorta. It is ubiquitous with most radiology service lines; permits rapid acquisition and processing of a 3D data set; the ability to image branch vessels; and is able to not only distinguish between types of acute aortic syndromes but to also evaluate the periarotic and adjacent structures. The sensitivities and specificities have been reported as approaching 100% on the latest scanners [19–21]. The disadvantage of CTA is the obvious need for intravenous contrast, sometimes up to 150 mL, and the exposure to radiation. Both need to put into proper context however.

However, most individuals with acute aortic syndromes are older where the risk of radiation induced malignancy from a CTA is substantially decreased [22]. Although consideration needs to be given into reducing the total dye load in those patients who have impaired renal function, this needs to be weighed against an increased chance of a non diagnostic study in a potentially lethal disease. The imaging technique of the aorta really depends on the clinical presentation or area of interest. In those patients where an acute aortic dissection is suspected, the vascular tree should include from at least mid carotids to the profunda. This should reveal the extent of the dissection and identify possible rupture identified by contrast leaks. True and false lumens can be analyzed, along with possible areas of malperfusion specifically the visceral or renal vessels. This should also provide ample information for possible endovascular or surgical treatment. In those patients with a known or suspected abdominal aortic aneurysm (AAA) who now present with abdominal pain and hypotension, a CTA from the celiac to the profunda should be sufficient. Electrocardiographic gating is important in those patients where ascending aortic pathology is suspected. This will eliminate the motion-induced artefacts which can mimic a dissection and also allows for the evaluation of the proximal coronary arteries as well as the aortic valve.

An argument can be made that a diagnostic CTA needs only 5 mm slice thickness, however in the arena of treatment planning this can be woefully inadequate. A maximum of 3 mm slice thickness with a 50% reconstruction overlap has been recommended [12]. However as more and more options for endovascular repair are being reported, 1.5 mm or less seems to be more appropriate, hence the difference between a diagnostic CTA and one used for treatment planning. The axial view remains the hallmark of CTA interpretation and there is little evidence that multiplanar and curved multiplanar reformation or even volume rendered images add anything to the diagnosis [12]. However in our personal experience these enhanced views provide important information in treatment planning both in the interventional as well as the surgical suite.

References

1. Weintraub NL. Understanding abdominal aortic aneurysm. N Engl J Med. 2009;361:1114–6.
2. Lederle FA, Johnson GR, Wilson SE, Chute EP, Hye RJ, Makaroun MS, et al. The aneurysm detection and management study screening program: validation cohort and final results. Aneurysm Detection and Management Veterans Affairs Cooperative Study Investigators. Arch Intern Med. 2000;160:1425–30.
3. Wilmink TB, Quick CR, Day NE. The association between cigarette smoking and abdominal aortic aneurysms. J Vasc Surg. 1999;30:1099–105.
4. van Vlijmen-van Keulen CJ, Pals F, Rauwerda JA. Familial abdominal aortic aneurysm: a systematic review of a genetic background. Eur J Vasc Endovasc Surg. 2002;24:105–16.
5. Chaikof EL, Brewster DC, Dalman RL, Makaroun MS, Illig KA, Sicard GA, et al. SVS practice guidelines for the care of patients with an abdominal aortic aneurysm: executive summary. J Vasc Surg. 2009;50:880–96.
6. Baxter BT, Terrin MC, Dalman RL. Medical management of small abdominal aortic aneurysms. Circulation. 2008;117:1883–9.
7. LaRoy LL, Cormier PJ, Matalon TAS, Patel SK, Turner DA, Silver B. Imaging of abdominal aortic aneurysms. AJR Am J Roentgenol. 1989;152:785–92.
8. Ashton HA, Buxton MJ, Day NE, Kim LG, Marteau TM, Scott RA, et al. The multicentre aneurysm screening study (MASS) into the effect of abdominal aortic aneurysm screening on mortality in men: a randomized controlled trial. Lancet. 2002;360:1531–9.
9. Scott RA, Bridgewater SG, Ashton HA. Randomized clinical trial of screening for abdominal aortic aneurysm in women. Br J Surg. 2002;89:283–5.
10. Fillinger MF, Marra SP, Raghavan ML, Kennedy FE. Prediction of rupture risk in abdominal aortic aneurysm during observation: wall stress versus diameter. J Vasc Surg. 2003;37:724–32.
11. Cronenwett JL, Davis JT Jr, Gooch JB, Garrett HE. Aortoiliac occlusive disease in women. Surgery. 1980;88:775–84.
12. Hiratzka LF, Bakris GL, Beckman JA, Bersin RM, Carr VF, Casey DE Jr, et al. 2010 ACCF/AHA/AATS/ACR/ASA/SCA/SCAI/SIR/STS/SVM Guidelines for the diagnosis and management of patients with thoracic aortic disease: a report of the American College of Cardiology Foundation, American Heart Association Task Force on Practice Guidelines, American Association for Thoracic Surgery, American College of Radiology, American Stroke Association, Society of Cardiovascular Anesthesiologists, Society for Cardiovascular Angiography and Interventions, Society of Interventional Radiology, Society of Interventional Radiology, Society of Thoracic Surgeons, and Society for Vascular Medicine. J Am Coll Cardiol. 2010;55:14 e27–129.

13. Johnston KW, Rutherford RB, Tilson MD, et al. Suggested standards for reporting on arterial aneurysms. Subcommittee on reporting standards for arterial aneurysms, Ad Hoc committee on reporting standards, Society for Vascular Surgery and North American Chapter, International Society for Cardiovascular Surgery. J Vasc Surg. 1991;13:452–8.
14. Segura AM, Luna RE, Horiba K, Stetler-Stevenson WG, McAllister HA Jr, Willerson JT, Ferrans VJ. Immunohistochemistry of matrix metalloproteinases and their inhibitors in thoracic aortic aneurysms and aortic valves of patients with Marfan's syndrome. Circulation. 1998;98:II331–7.
15. LeMaire SA, Wang X, Wilks JA, Carter SA, Wen S, Won T, et al. Matrix metalloproteinases in ascending aortic aneurysms: bicuspid versus trileaflet aortic valves. J Surg Res. 2005;123:40–8.
16. Fedak PW, de Sa MP, Verma S, Nili N, Kazemian P, Butany J, et al. Vascular matrix remodeling in patients with bicuspid aortic valve malformations: implications for aortic dilatation. J Thorac Cardiovasc Surg. 2003;126:797–806.
17. Ikonomidis JS, Jones JA, Barbour JR, Stroud RE, Clark LL, Kaplan BS, et al. Expression of matrix metalloproteinases and endogenous inhibitors within ascending aortic aneurysms of patients with bicuspid or tricuspid aortic valves. J Thorac Cardiovasc Surg. 2007;133:1028–36.
18. Masuda Y, Takanashi K, Takasu J, Morooka M, Inagaki Y. Expansion rate of thoracic aortic aneurysms and influencing factors. Chest. 1992;102:461–6.
19. Zeman RK, Berman PM, Silverman PM, Davros WJ, Cooper C, Kladakis AO, Gomes MN. Diagnosis of aortic dissection: value of helical CT with multiplanar reformation and three-dimensional rendering. AJR Am J Roentgenol. 1995;164:1375–80.
20. Shiga T, Wajima Z, Apfel CC, Inoue T, Ohe Y. Diagnostic accuracy of transesophageal echocardiography, helical computed tomography, and magnetic resonance imaging for suspected thoracic aortic dissection: systematic review and meta-analysis. Arch Intern Med. 2006;166:1350–6.
21. Sommer T, Fehske W, Holzknecht N, Smekal AV, Keller E, Lutterbey G, et al. Aortic dissection: a comparative study of diagnosis with spiral CT, multiplanar transesophageal echocardiography, and MR imaging. Radiology. 1996;199:vv347–52.
22. Brenner DJ, Hall EJ. Computed tomography: an increasing source of radiation exposure. N Engl J Med. 2007;357:2277–84.

Imaging of the Peripheral Vasculature and Carotid Arteries

12

Peter S. Fail and Vinod Nair

CT Angiography of the Lower Extremities

By age 60, 3–6% of men experience intermittent claudication due to obstructive disease of the aortoiliac and lower extremities. CT angiography (CTA) has become an integral part of assessing the treatment options in these patients. Its role is typically to determine a management strategy after peripheral arterial disease (PAD) is diagnosed. Other less expensive, noninvasive, and well-validated modalities are typically recommended as first-line studies in the diagnosis of PAD. CTA then becomes the platform for mapping vascular anatomy and delineating the location and severity of the stenosis. This information is of paramount importance in selecting patients who are candidates for endovascular or surgical revascularization. Additional information, including the presence of aneurysms, popliteal entrapment, and cystic adventitial disease, are also provided by CTA. In this group of patients, multidetector CT (MDCT) is noted to have high sensitivity (96%) and specificity (97%), as well as excellent interobserver agreement compared with digital subtraction angiography (DSA). Overestimation of stenosis has shown to be associated with significant calcification, but this problem can be overcome to a large extent by routinely adjusting image display settings (window and level) in the presence of calcium.

In addition to atherosclerotic vascular disease, clinical conditions like atheroembolism, aneurysmal disease, and arteriitis can be rapidly evaluated by MDCT. Because the gantry speeds are 0.5 s per revolution, even with the larger detector arrays, it is important not to outrun the bolus of contrast, scanning before the contrast has had time to arrive at the area of interest. The run-off vessels (popliteal track, anterior and posterior tibial, and peroneal vessels) are routinely rescanned to ensure adequate opacification of the distal leg vasculature. The sensitivity of CTA for detection of stenosis more than 50% in the lower extremity, including inflow and distal crural arteries, is about 91%. The major limitation of CTA is its inability to rapidly analyze the distal peroneal, anterior tibial, and posterior tibial vessels, especially in the presence of severe calcification. This information is very important when bypasses to these vessels are being considered, and magnetic resonance angiography (MRA) has been shown to be useful in this area. CTA offers the clinician the ideal platform for analyzing the postsurgical or catheter-based patient who presents with a sudden change in symptoms of claudication.

Scan Protocol and Technique

The scan protocol usually depends on the type and number of detectors available on the MDCT scanner. For optimal CTA of the lower extremity, a 16-slice scanner or higher is desired. The usual time of acquisition is 10–15 min of room time. The normal tube voltage used is 120 kV (unless automatic tube current modulation is available), and the

P.S. Fail (✉)
Department of Interventional Cardiology, Cardiovascular Institute of the South/Terrebonne General Medical Center,
225 Dunn Street, Houma, LA 70360, USA
e-mail: peter.fail@cardio.com

V. Nair
Cardiovascular Institute of the South,
225 Dunn Street, Houma, LA 70360, USA
e-mail: vinod.nair@cardio.com

M.J. Budoff et al. (eds.), *Atlas of Cardiovascular Computed Tomography*, https://doi.org/10.1007/978-1-4471-7357-1_12

maximum tube amperage is 300 mA. Peripheral CTA includes an initial topographic image acquisition, followed by an arterial phase-timed acquisition from the celiac axis to the feet. A full scanning protocol includes several steps: (1) topogram ("scout image"); (2) optional nonenhanced acquisition; (3) test bolus sequence; (4) CTA acquisition; and (5) optional late phase acquisition if the distal infrapopliteal vessels are not visualized.

Advantages Over Digital Subtraction Angiography

MDCT provides nonvascular tissue and organ images, which may aid in deciding the treatment strategy. CTA is also less invasive than DSA, and it takes less time than conventional angiography. MDCT also requires less exposure to ionizing radiation than conventional DSA.

Advantages Over MR Angiography

Compared with MRA, MDCT requires less scan time and is currently more economical. It is also suitable for use in patients with surgical clips or pacemakers.

Disadvantages of CTA

The disadvantages of CTA include exposure to ionizing radiation and the use of nephrotoxic contrast media.

Protocol Imaging

- Auto trigger: 180hU-Aorta
- First scan: Begin scan above diaphragm and continue scan though feet and toes
- Second scan (delayed): Rescan the lower legs. No manual delay is set in the protocol. With the time it takes for the table to reposition itself and the x-ray tube and for the detector to reset itself, the delay equals 6 to 8 s.
- Test injection: 3.5 mL/s (20 mL saline)
- First phase: 3.5 mL/s (80 mL Isovue 370)
- Second phase: 2.0 mL/s (45 mL Isovue 370)
- Saline push: 2.0 mL/s (40 mL saline)
- 0.5 mm slice thickness; 0.5 mm spacing
- 300 mA; 120 kV; 0.5 s × 64
- HP 53 (Toshiba) (pitch)
- Scan field of view Large (dependent on patient size)
- Sure exposure ("phototime")

Figures 12.1, 12.2, 12.3, 12.4, and 12.5 illustrate findings from a lower-extremity run-off protocol.

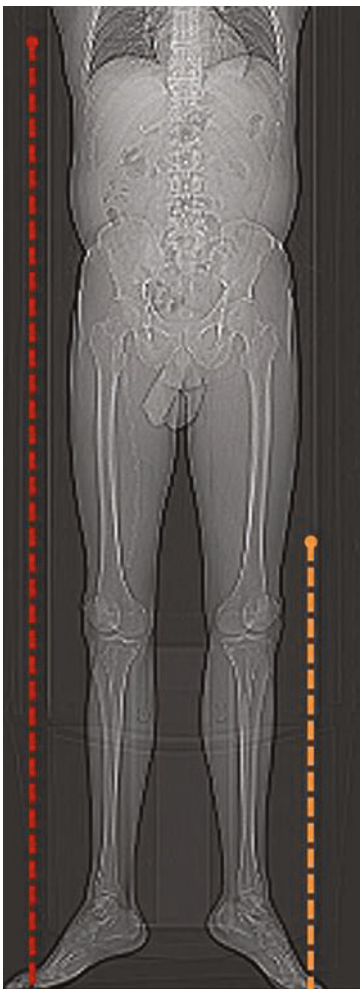

Fig. 12.1 Lower extremity run-off protocol. Scanning starts just above the diaphragm (*red dotted line*) and the run-off is imaged down to the foot. A second series of image acquisition (delayed scan) is started above the knee to assess the infrapopliteal vessels (*orange dotted line*)

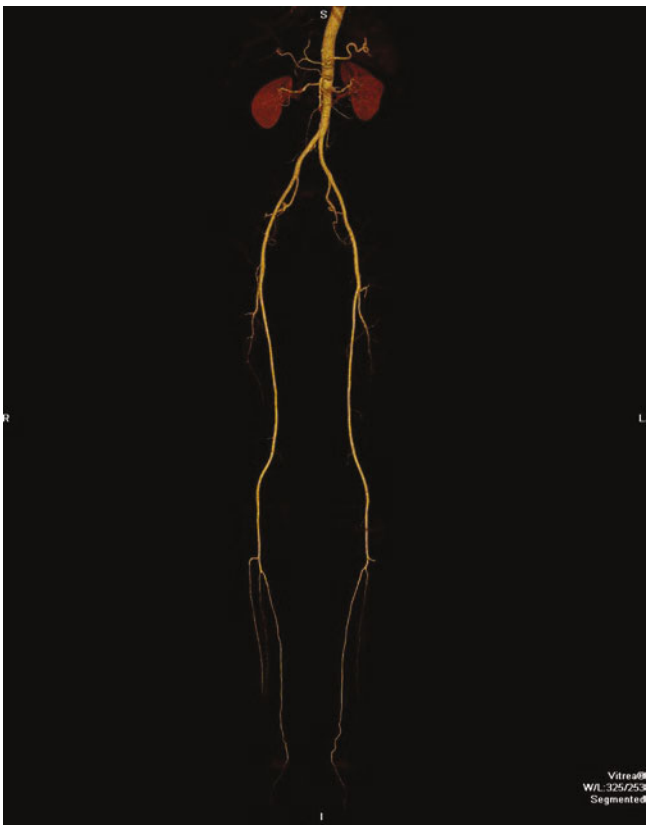

Fig. 12.2 Normal-appearing abdominal aorta and renal, celiac, and superior mesenteric arteries

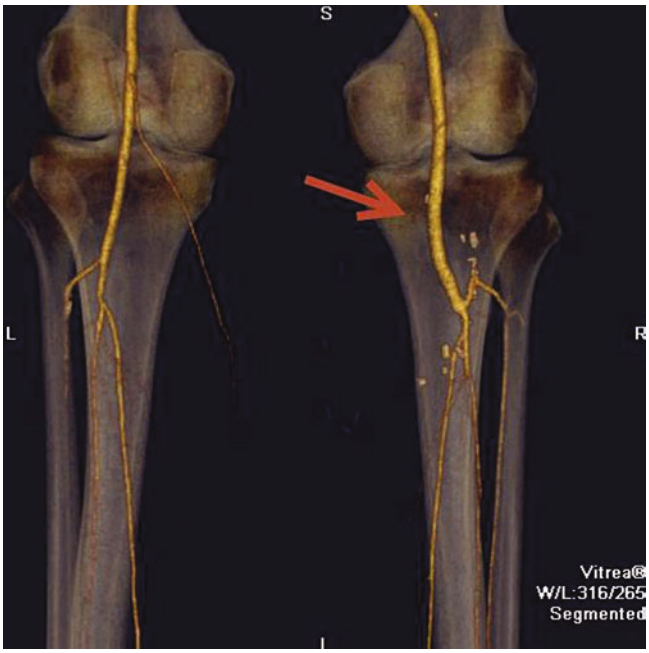

Fig. 12.4 Volume-rendering (VR) view of lower extremity run-off showing patent left popliteal and infrapopliteal vessels. The right superficial femoral artery (SFA) is occluded. The infrapopliteal vessel fills via the patent femoropopliteal bypass graft

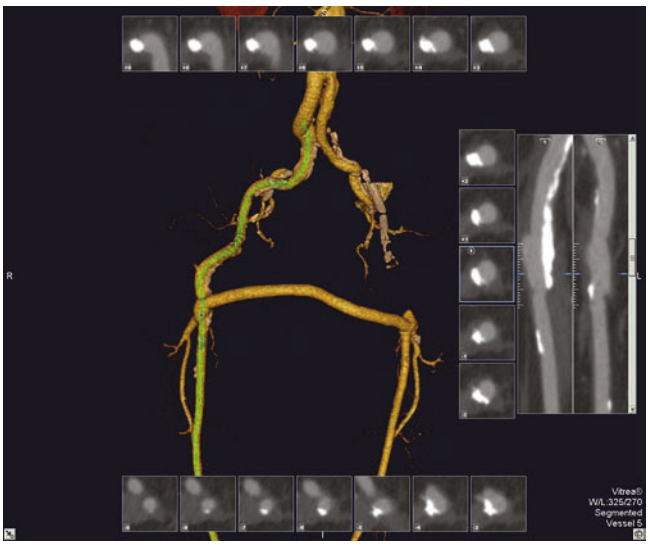

Fig. 12.3 This CTA shows the occluded left limb of an aortofemoral bypass graft. A patent femoral-femoral bypass graft is noted. A series of cross-sections through the right external iliac artery shows a patent right common femoral artery as well as the anastomosis of the femoral-femoral bypass graft

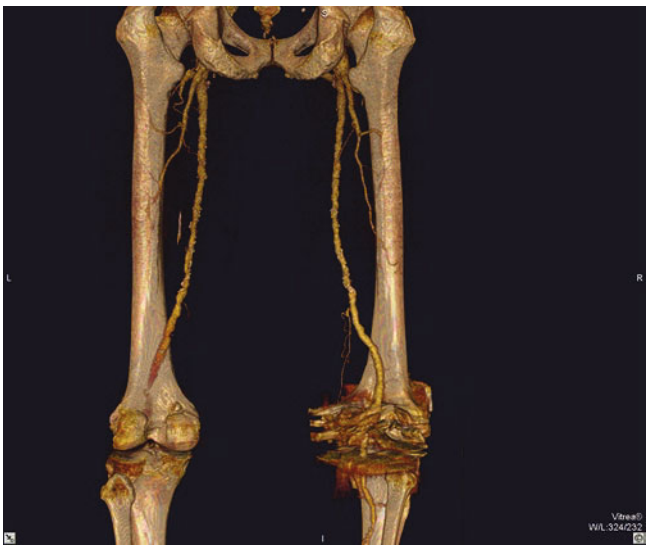

Fig. 12.5 Artifact from a prosthetic knee joint: The right popliteal artery cannot be visualized because of artifacts from the right knee prosthesis

Case 12.1

A 66-year-old woman with long-standing diabetes is referred for peripheral vascular disease (PVD) evaluation of a nonhealing wound that was sustained following minimal trauma. The physical examination revealed a large, nonhealing ulcer on her heel. Pulses were absent, and the Ankle-Brachial Index (ABI) was 0.6 (Figs. 12.6, 12.7, 12.8, 12.9, 12.10, and 12.11).

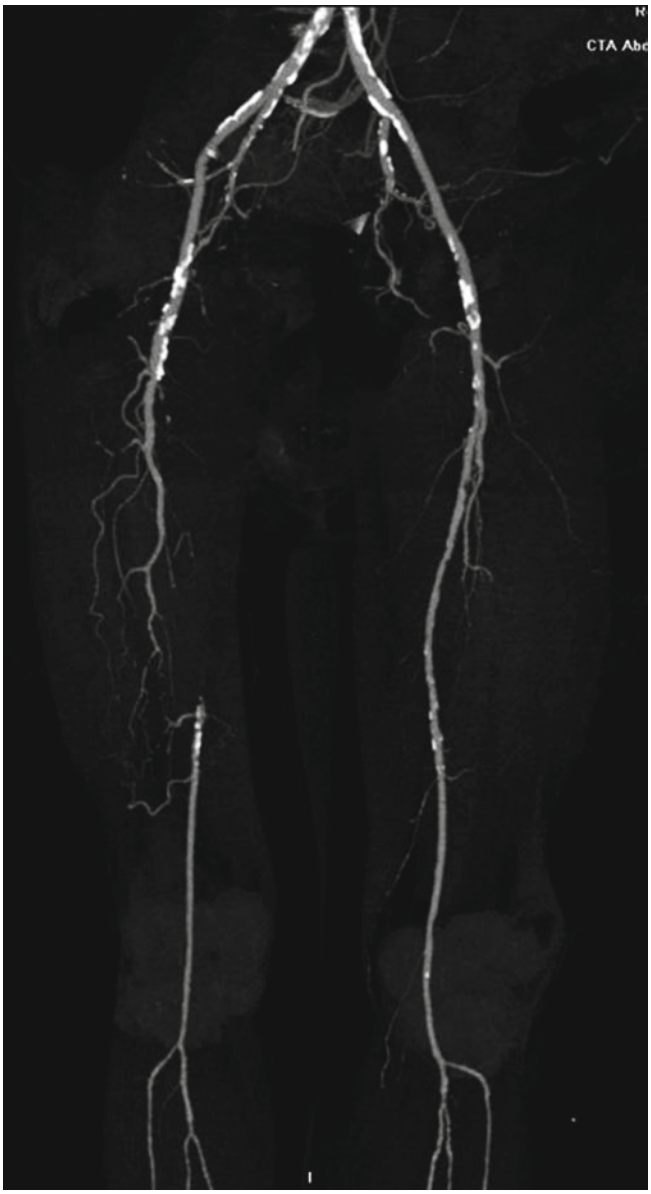

Fig. 12.6 Maximum intensity projection (MIP) view of 100% occluded right SFA with reconstitution at the popliteal artery

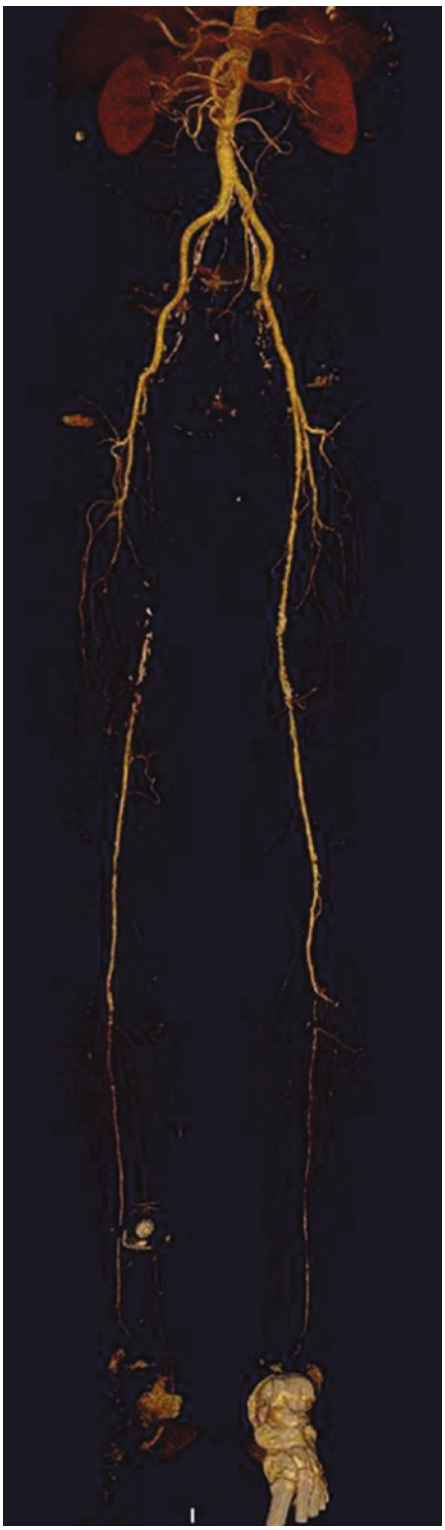

Fig. 12.7 VR image of the occlusion. The off-axis MIP view shows the entrance point as well as minimal collateral flow in the proximal segment

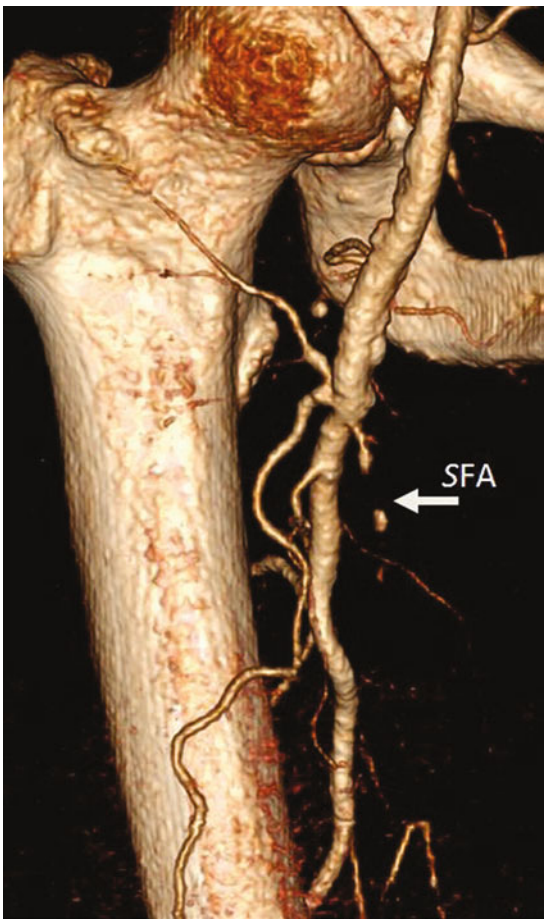

Fig. 12.8 VR image of the right common femoral artery bifurcation. The occluded right SFA is seen (*white arrow*)

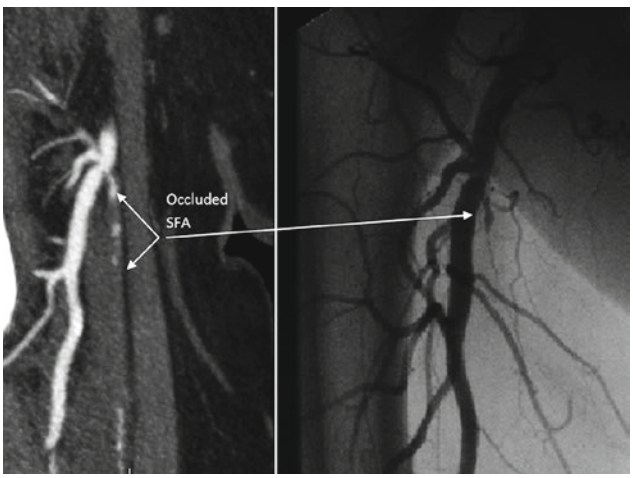

Fig. 12.9 Comparison of off-axis MIP and conventional angiography of 100% occlusion

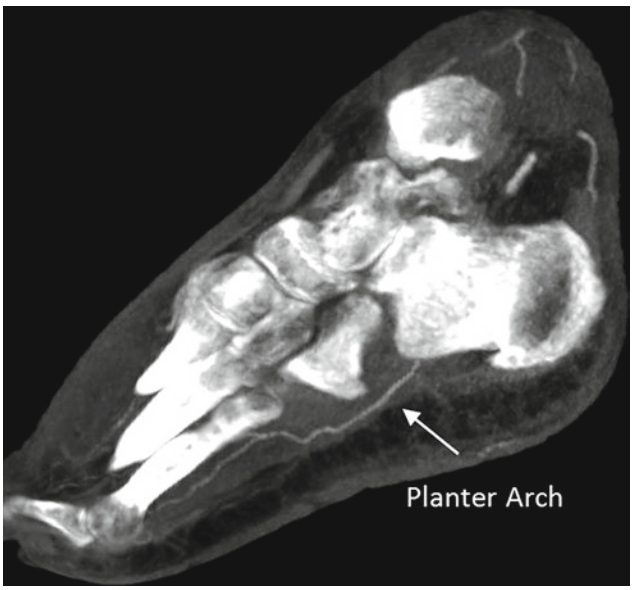

Fig. 12.10 MIP view of the foot showing the plantar arch

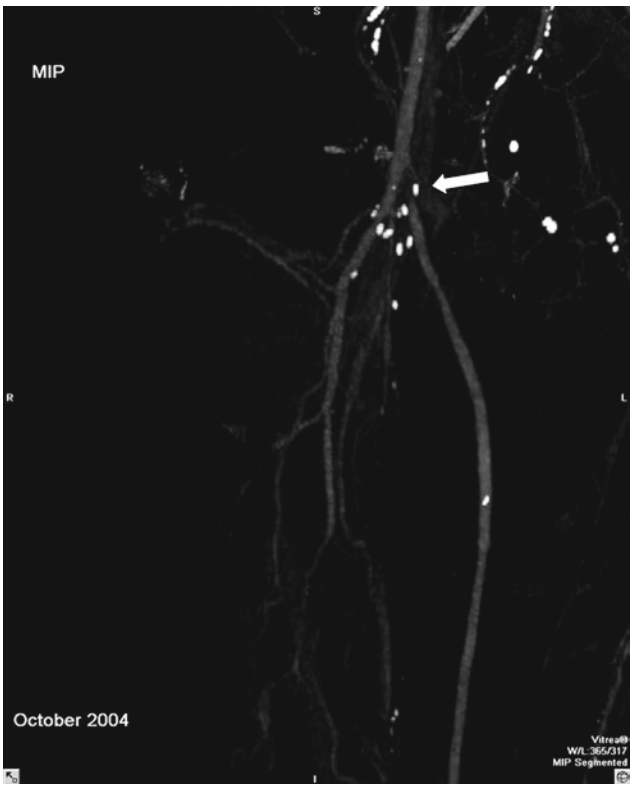

Fig. 12.11 MIP view of the bifurcation of the left SFA origin, showing high-grade stenosis (*white arrow*)

Case 12.2

An 80-year-old man, a former smoker, reports a history of non–insulin-dependent diabetes mellitus, hypertension, and coronary artery disease with coronary artery bypass grafting. He underwent endovascular aortic repair (EVAR) several years ago and has done well. He is now referred for PVD evaluation of a nonhealing ulcer on his right foot.

Physical examination noted no pulse in either foot. The right foot is cool to touch, with an ulcer on his great toe. ABI is 0.7 on the left and unattainable on the right (Figs. 12.12, 12.13, 12.14, 12.15, 12.16, and 12.17).

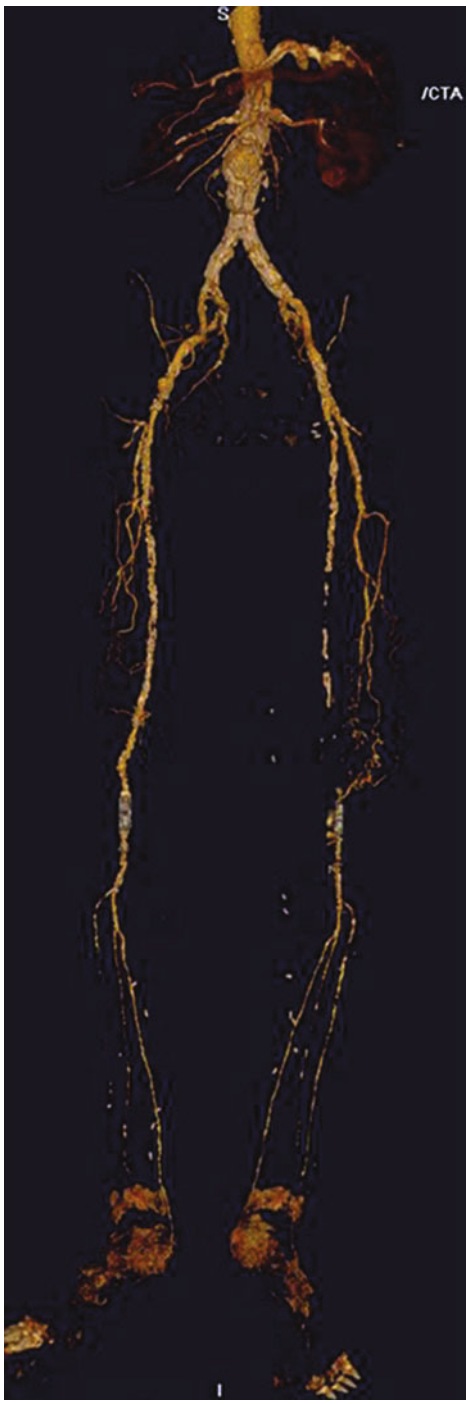

Fig. 12.12 VR of the aorta with run-off. Note the occluded left SFA. The right SFA appears to be patent, but at closer inspection, the right is also seen to be occluded and heavily calcified

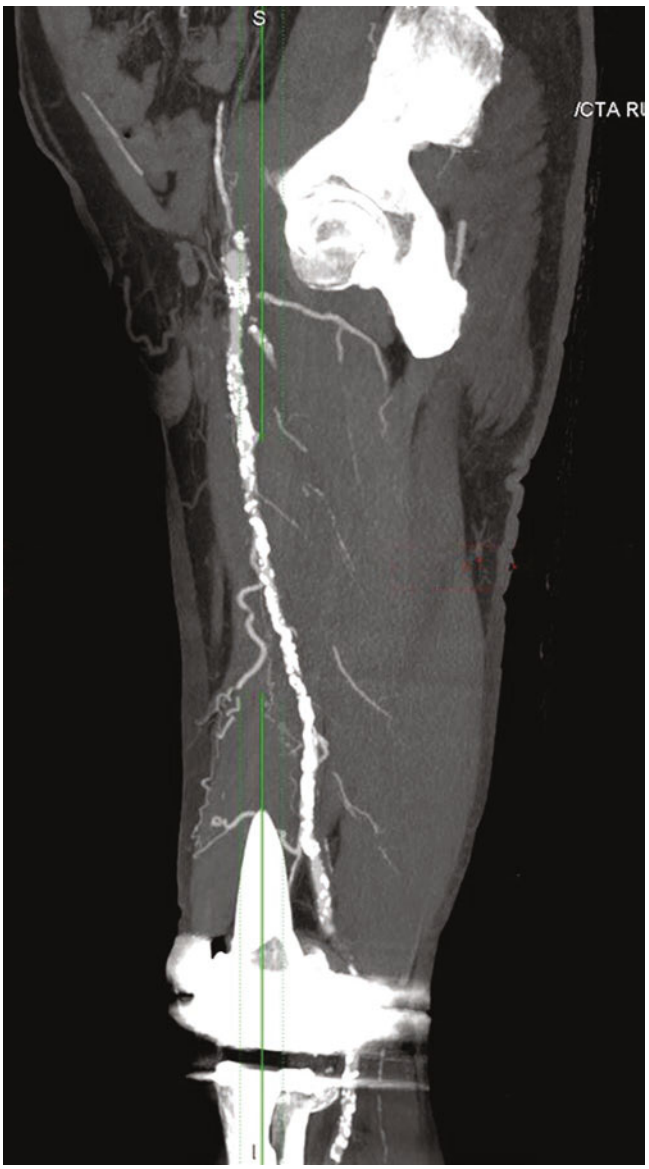

Fig. 12.13 MIP view demonstrating the densely calcified right SFA. In this view, lumen/contrast opacification of the SFA cannot be well visualized

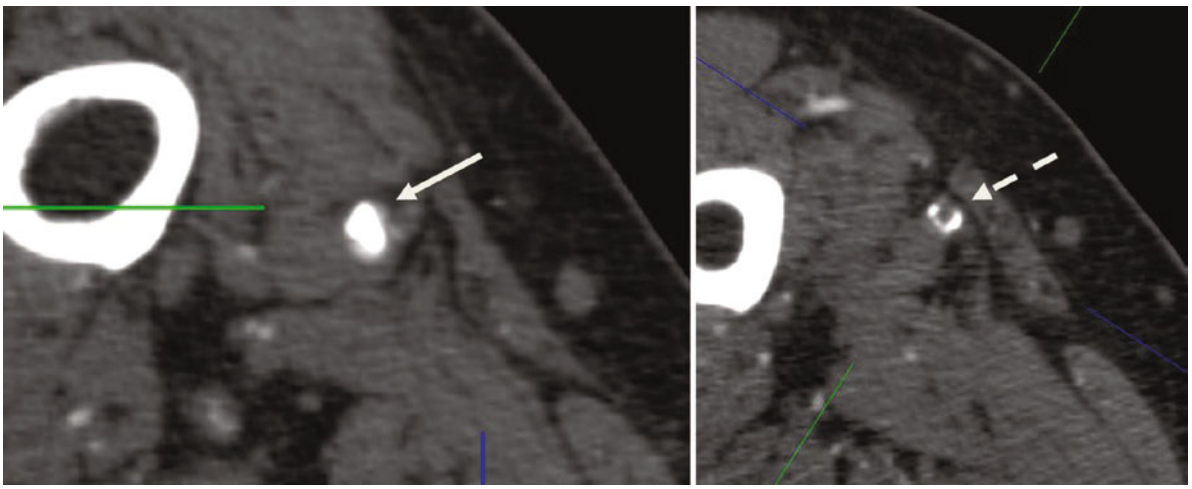

Fig. 12.14 Axial images of heavily calcified SFA. Note the densely calcified SFA with contrast posterior (*left image*) At this level (*solid arrow*), the stenosis degree cannot be determined. The *righthand image* shows the SFA with no contrast opacification (*dashed arrow*), signifying an occluded SFA

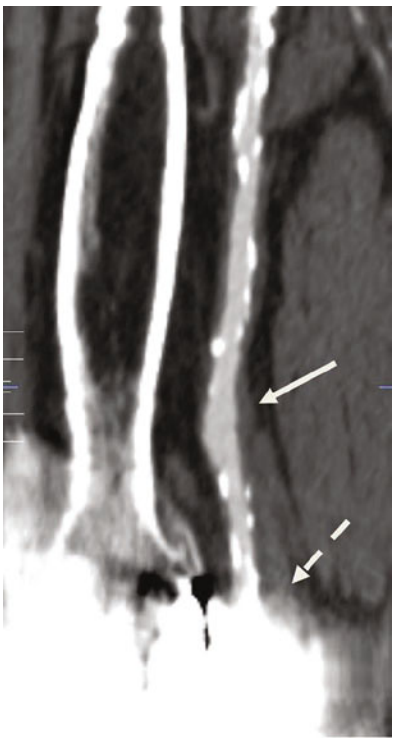

Fig. 12.15 Patent proximal portion of the popliteal artery with mild, diffuse calcification (*solid arrow*). The patient had a right knee replacement, and artifact from the knee replacement makes it difficult to analyze the vascular lumen (*dashed arrow*)

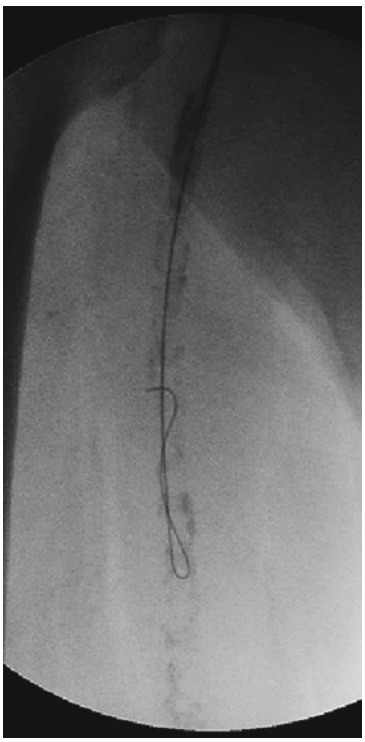

Fig. 12.16 Fluoroscopy of the heavily calcified SFA with a wire introduced antegradely. (Access was performed antegradely in the right femoral artery)

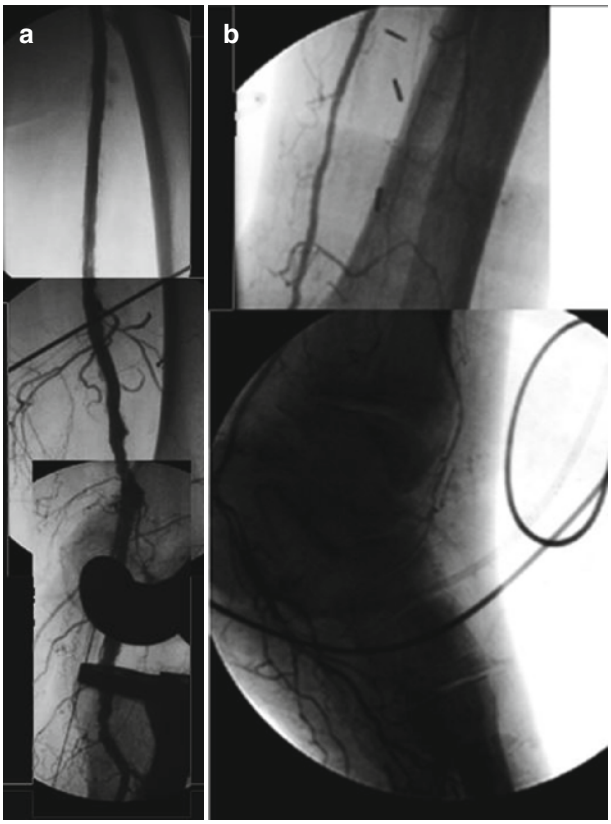

Fig. 12.17 (**a**, **b**), Angiographic results of percutaneous transluminal angioplasty (PTA) and stenting of the SFA. The final results include the plantar arch

Case 12.3

A 57-year-old woman is referred for evaluation of increased claudication in the left lower extremity. Her risk factors included tobacco abuse and hypertension. She noted increasing symptoms over the past several months. An ultrasound suggested a significant obstruction of the proximal SFA, but her body habitus prevented a clear view of the SFA (Figs. 12.18 and 12.19).

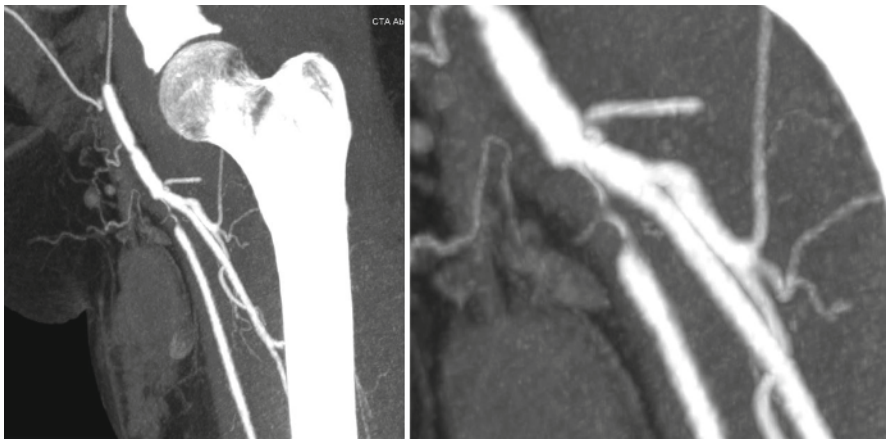

Fig. 12.18 CTA showed stenosis in the ostial SFA

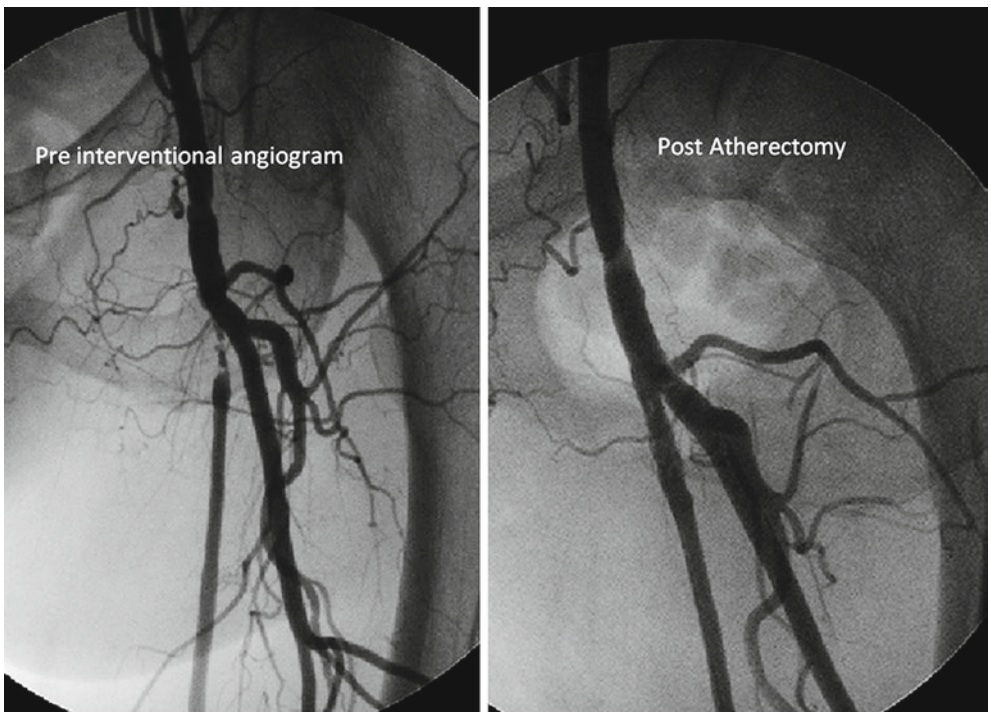

Fig. 12.19 CTA allowed pre-planning assessment of the stenosis. Because of the ostial nature of the stenosis, an atherectomy was the treatment strategy decided upon. These angiograms show the result

CT Angiography of the Carotid Arteries

Stroke continues to ravage Western society as the third leading cause of death and the leading cause of disability, with a cost of $65.5 billion per year. The causes of these tragic events are 16% hemorrhagic and 84% ischemic, with carotid atherosclerosis contributing as a significant source. Unlike the coronary bed, ischemic cerebral insults typically result from an embolic event; less than one third of patients who experience a cerebrovascular accident (CVA) will have a total occlusion of the carotid artery. Carotid disease is also associated with obstructive disease in other areas, being observed in 25% of patients with PVD and over 30% of those with both coronary artery disease and PVD. Since the North American Symptomatic Carotid Endarterectomy Trial (NASCET), no other artery has been more widely studied than the carotids. Studies have shown that as the degree of obstruction increases, the rate of CVA also rises, with obstructions greater than 50% being of concern. Surveillance is typically initiated with either a physical finding of a carotid bruit or a neurological event such as a TIA or CVA. Carotid ultrasound offers the clinician the ability to quantify and qualify the degree of obstruction with a high degree of accuracy (95% for obstructions greater the 60%). The difficulty comes with heavily calcified obstructions and distinguishing between 99.99% and complete occlusion. Other issues include the dependence of the study on the operator or sonographer, and the inability to directly visualize the distal vessel (and in most cases, the proximal vessel) as it arises from the aorta.

In comparison, CTA offers an excellent platform when carotid duplex is ambiguous. It permits visualization of pathology of the aortic arch or high bifurcation, reliable differentiation of total and subtotal occlusion, and assessment of ostial and tandem stenoses. Its disadvantages are the need for contrast media and radiation. Heavily calcified lesions also can be difficult to accurately assess because of partial volume effects. To visualize the entire vessel from the arch to its termination at the middle cerebral artery has been done until recently by DSA, exposing the patient to a small but potentially catastrophic risk of an embolic event. In reviews of the major endarterectomy trials, a small increase in CVA has been related to the angiogram.

Case 12.4

A 68-year-old man was referred for evaluation of transient right arm paresthesia. He had a history of coronary artery disease, having undergone a coronary artery bypass several years earlier. The physical examination was remarkable for bilateral bruits. The neurologic exam was unremarkable. Ultrasound noted a "possible complete occlusion" of the left carotid, with mild disease of the right carotid. CTA was performed (Figs. 12.20, 12.21, 12.22, 12.23, 12.24, and 12.25).

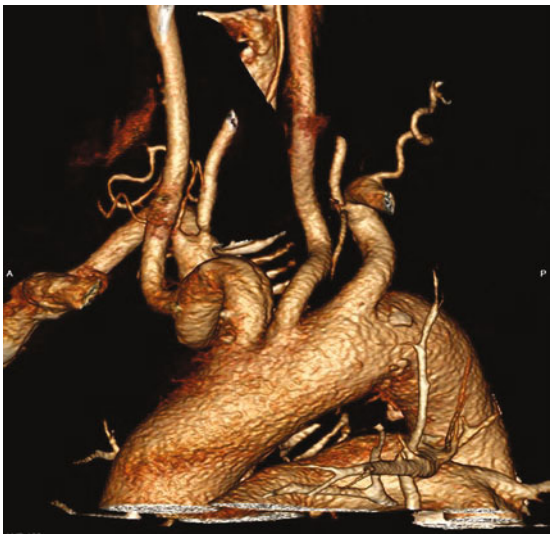

Fig. 12.20 VR view of the aortic arch. This is a Class II arch, with the innominate and left carotid and subclavian slightly below the apex. (The I through III classification of the arch became important with the advent of carotid stenting.) Note the tortuosity of the innominate artery

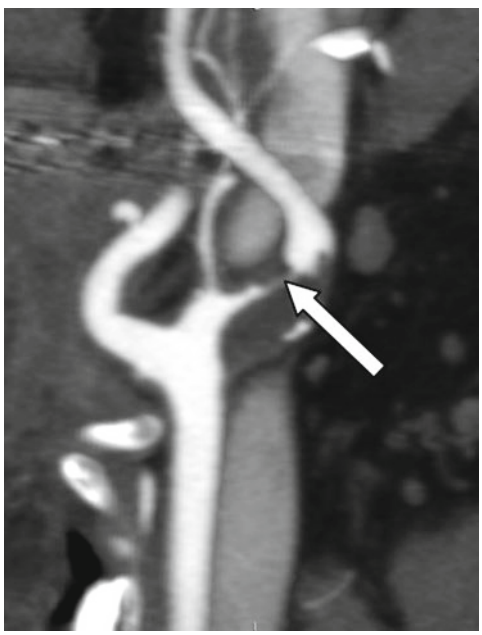

Fig. 12.21 MIP view of a severe stenosis (*arrow*) of the left internal carotid artery (LICA), with a large plaque burden

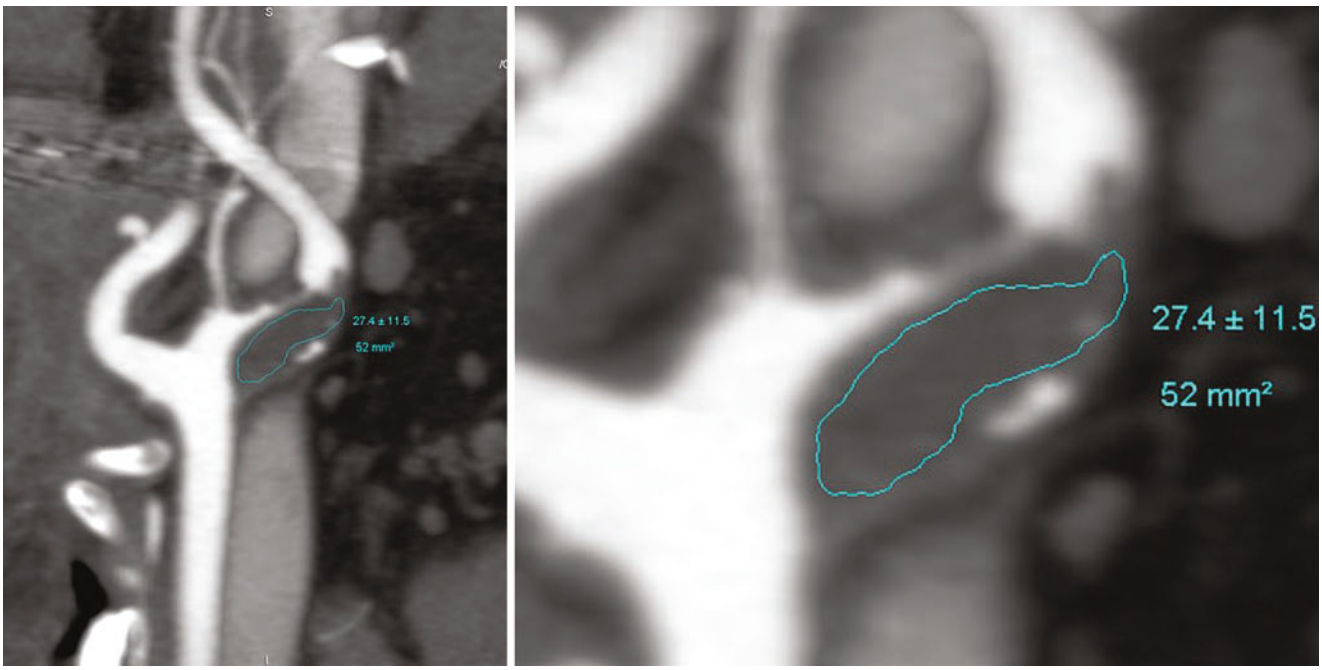

Fig. 12.22 The average Hounsfield units were 27.4, indicating soft, lipid-laden plaque

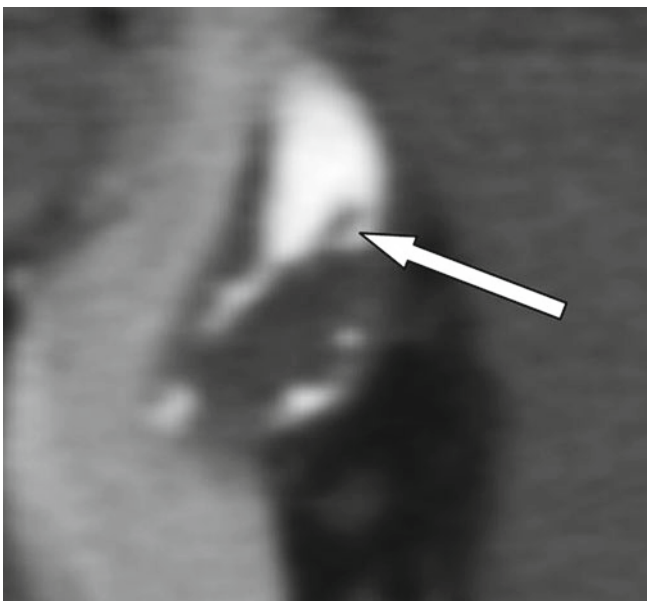

Fig. 12.23 A frond (*arrow*) is a potential embolic source

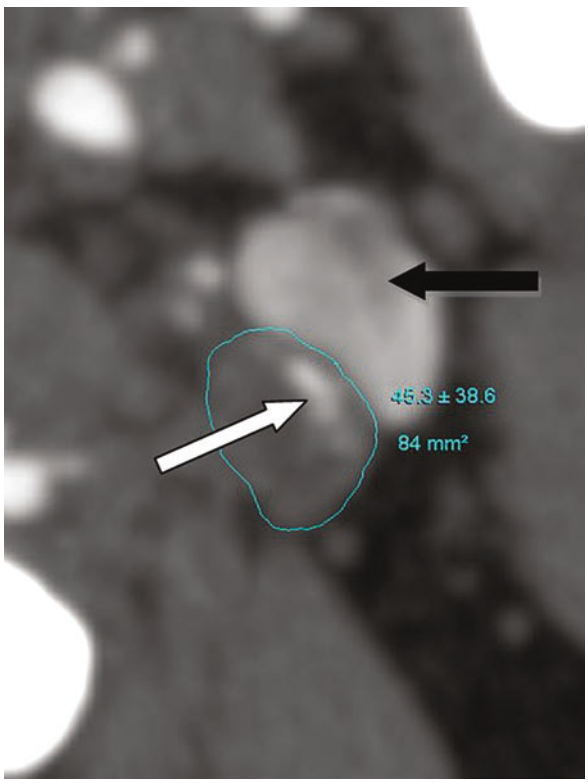

Fig. 12.24 Axial view of the large plaque (*white arrow*, lumen), with average Hounsfield units of 45, including the lumen. The *black arrow* indicates the jugular

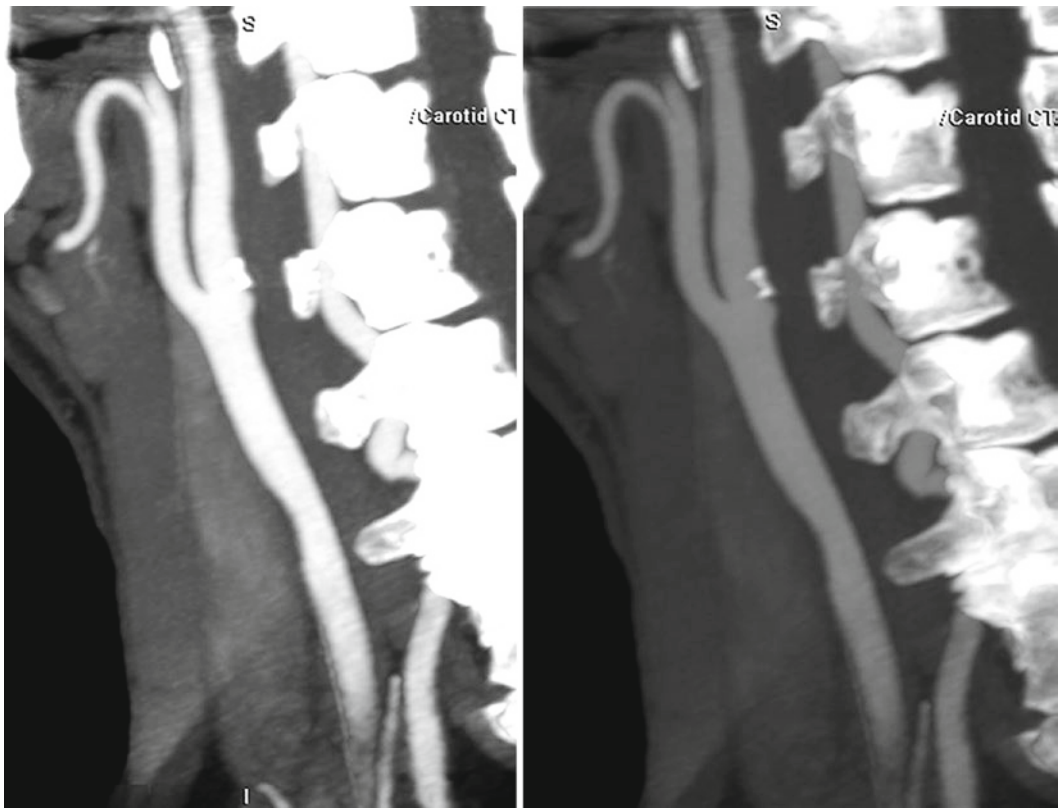

Fig. 12.25 Mild calcified plaque was identified in the bulb of the right carotid. A change in the window and level from 600/150 (*left image*) to 1400/400 (*right image*) allowed this identification of the calcium in the bulb

Case 12.5

A 67-year-old man with a history of coronary artery disease and coronary revascularization several years ago presented after an carotid ultrasound revealed 80–99% stenosis of his left internal carotid artery (Figs. 12.26 and 12.27). He undergoes an endarterectomy, but while in recovery develops right-sided weakness. He returns to the OR for a revision, which notes a significant dissection. Attempts at repair are unsuccessful, and he is transferred to our institution, where urgent angiography (Figs. 12.28 and 12.29) and triple anticoagulation (Clopidogrel, ASA, and Coumadin) are started. In follow-up, he undergoes rehabilitation uneventfully, with a marked improvement in his motor deficit to essentially normal. At 8 months, he is readmitted for right-sided weakness, and ultrasound suggests high-grade stenosis, which is confirmed by CTA (Fig. 12.30) He undergoes carotid stenting uneventfully. Approximately 3 weeks later, he has a recurrent event. CTA reveals a separation of the stents (Fig. 12.31). He did well until the 8th month following the last stenting, when he experiences multiple seizures. The neurological workup, including ultrasound of the carotids, notes an increase in velocities in the stented area consistent with an 80–99% stenosis. He returns to the lab, where an angiogram confirms in-stent restenosis (Figs. 12.32 and 12.33); he undergoes successful angioplasty without further events. His seizure activity stopped. Surveillance ultrasound suggested increased velocities at 6 months following his last percutaneous transluminal angioplasty. A CT scan was done.

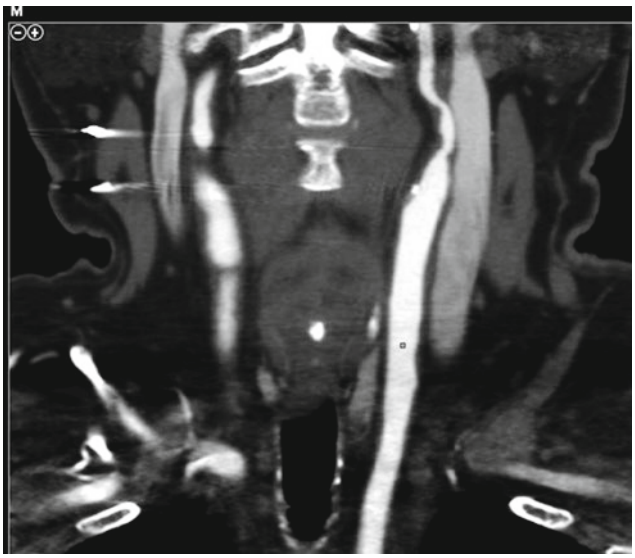

Fig. 12.27 Magnified view of the left carotid with diffuse atherosclerosis

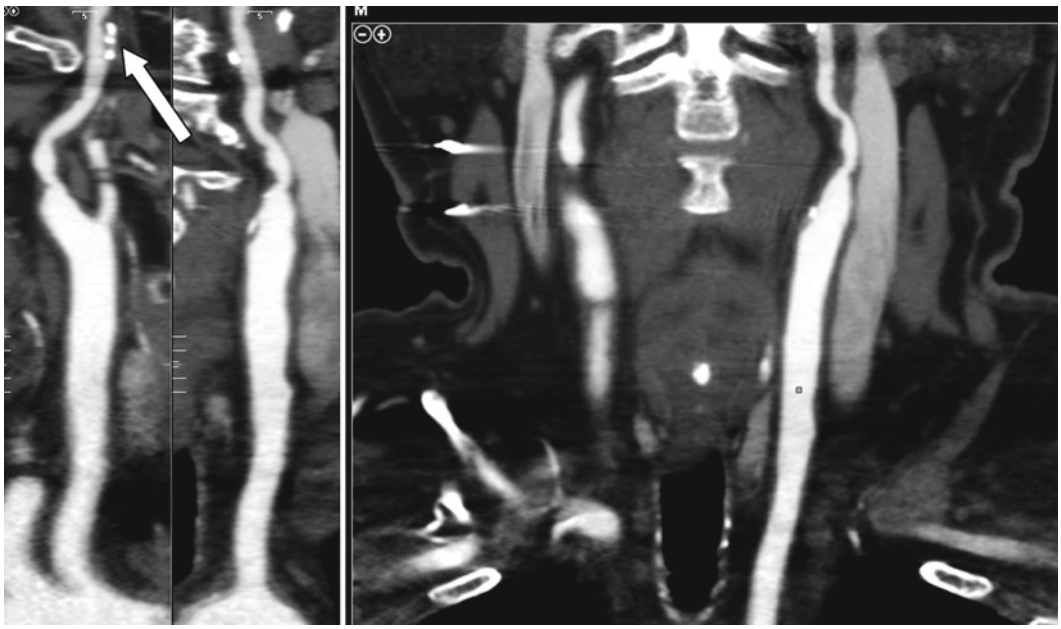

Fig. 12.26 Multiplanar reconstruction (MPR) images of the left carotid before the carotid endarterectomy. Notice the significant diffuse plaque that lined the entire carotid. Moderate calcified plaque was nonobstructive distally (*arrow*)

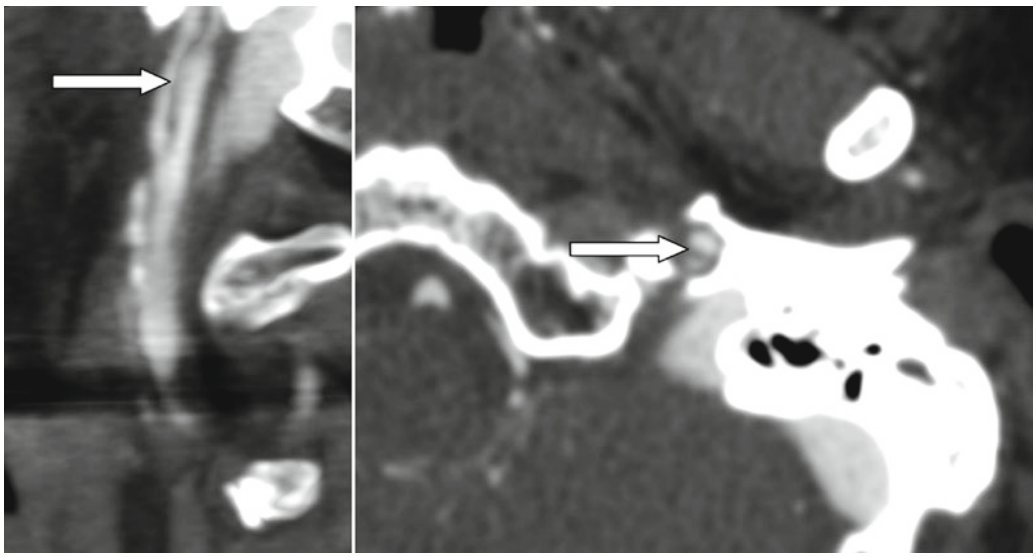

Fig. 12.28 Spiral dissection of the internal carotid. Note that the dissection (*arrows*) is present as it enters the siphon

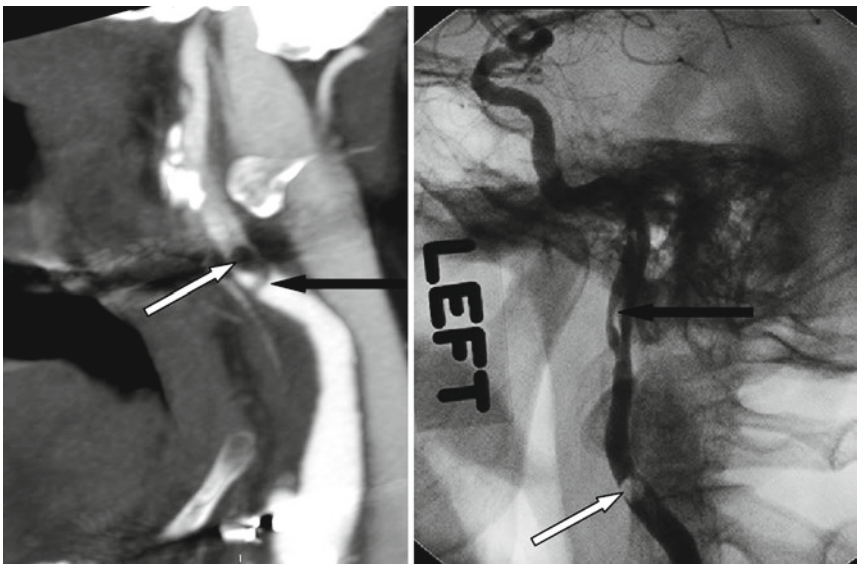

Fig. 12.29 Although there is some artifact along the same line, this image was reported as showing possible thrombus. The Hounsfield units were 74 mid thrombus (*white arrow*). The thrombus is also present at the area where the dissection starts (*black arrow*). The angiogram on the right confirms the reported dissection and thrombus

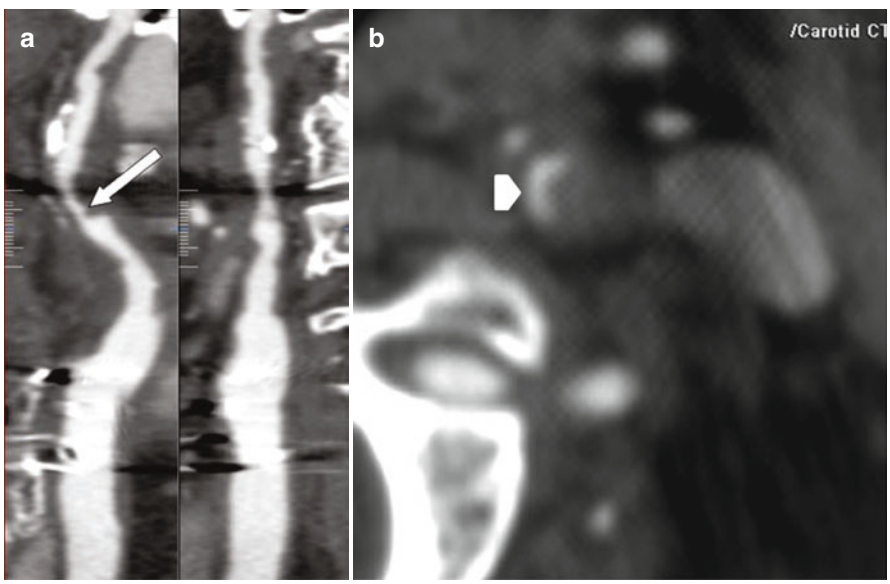

Fig. 12.30 MPR images of the carotid 8 months following the endarterectomy. (**a**) Note the diffuse nature of narrowing the internal carotid artery, with a high-velocity lesion just distal to the calcified plaque. (**b**) On-axis view of the stenosis

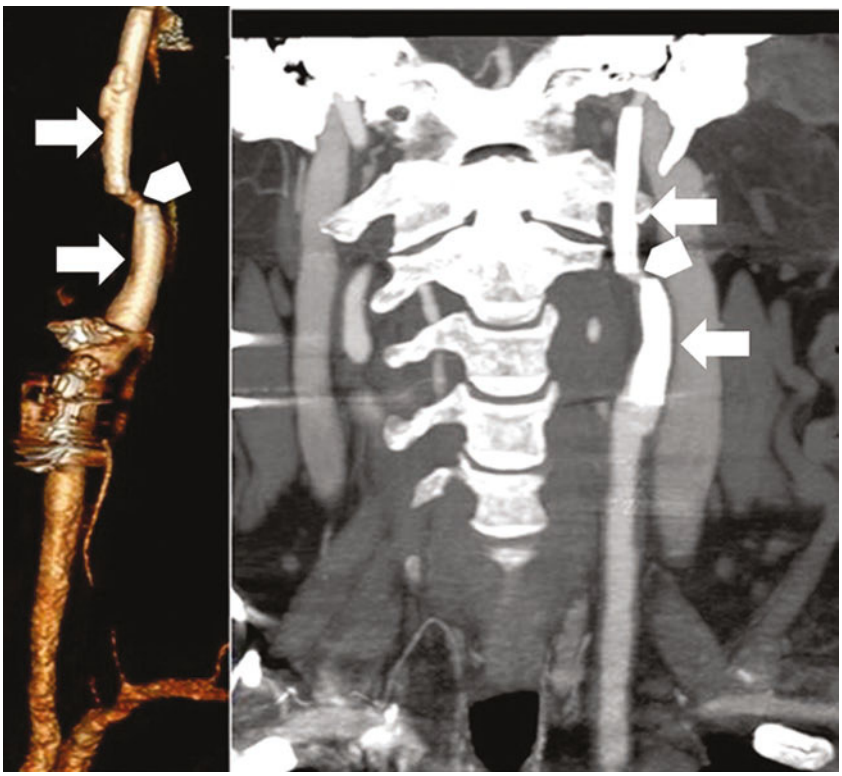

Fig. 12.31 VR and slab MIP image 3 weeks after stenting, with stent separation

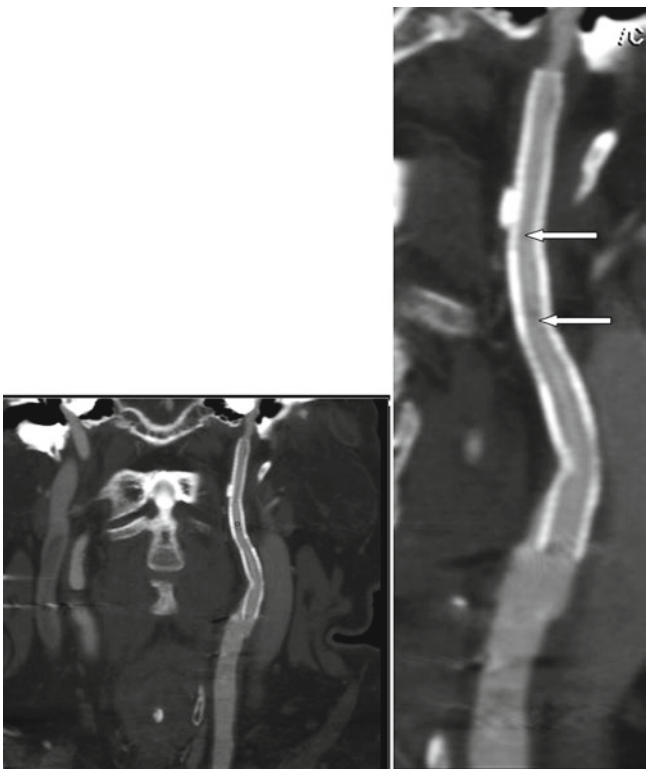

Fig. 12.32 The extensive stenting made these images difficult to evaluate. The ultrasound had suggested high velocities, but at first glance the stents appear patent. At closer observation, the suggestion of in-stent restenosis was considered (*arrows*) (see Fig. 12.33). An angiogram confirmed in-stent restenosis

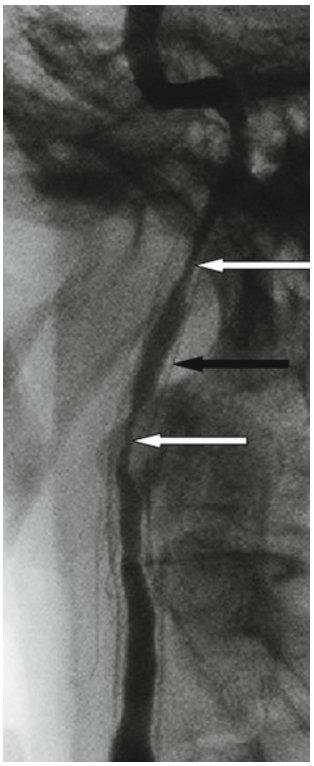

Fig. 12.33 *White arrows* point out the areas of restenosis. The *black arrow* shows the outline of the stent. Note the diffuse nature of the restenosis

Suggested Reading

1. Dormandy JA, Rutherford RB. Management of peripheral arterial di sease (PAD). TASC Working Group. TransAtlantic Inter-Society Consensus (TASC). J Vasc Surg. 2000;31:S1–296.
2. Fox AJ. How to measure carotid stenosis. Radiology. 1993;186: 316–8.
3. Leclerc X, Godefroy O, Pruvo PJ, Leys D. Computed tomographic angiography for the evaluation of carotid artery stenosis. Stroke. 1995;26:1577–81.
4. North American Symptomatic Carotid Endarterectomy Trial Collaborators. Beneficial effect of carotid endarterectomy in symptomatic patients with high-grade stenosis. N Engl J Med. 1991;325:445–53.
5. Ofer A, Nitecki SS, Linn S, Epelman M, Fisher D, Karram T, et al. Multidetector CT angiography of peripheral vascular disease: a prospective comparison with intraarterial digital subtraction angiography. AJR Am J Roentgenol. 2003;180:719–24.
6. Ota H, Takase K, Igarashi K, Chiba Y, Haga K, Saito H, Takahashi S. MDCT compared with digital subtraction angiography for assessment of lower extremity arterial occlusive disease: importance of reviewing cross-sectional images. AJR Am J Roentgenol. 2004;182: 201–9.

Valvular Diseases and Interventions

13

Philipp Blanke, Angus Thompson, and Jonathon Leipsic

Cardiac valve anatomy (and more recently, function) can be visualized and assessed by cardiac CT. Though it still lacks the temporal resolution and hemodynamic evaluation of echocardiography, CT has the advantage of allowing routine three-dimensional (3D) depiction and assessment of valve structure and pathology. With the advent of minimally invasive interventions and transcatheter heart valve therapies such as transcatheter aortic valve implantation, CT has the potential to make a significant contribution to preprocedural planning and postprocedural evaluation, with an impact upon patient outcomes.

This chapter provides representative images of the normal anatomy of all four cardiac valves, as well as findings of relevant but also rare valvular pathologies. It also highlights the current and evolving roles of CT in transcatheter valve therapies.

Technical Aspects of Valvular Evaluation with CT

Modern cardiac CT allows for the acquisition of true 3D datasets with high in-plane spatial resolution and resultant submillimeter isotropic voxels that enable the accurate evaluation of the coronary arteries, myocardium, and valvular anatomy.

P. Blanke
Department of Radiology, Centre for Heart Valve Innovation, St Paul's Hospital, 2nd Floor, Providence Building, 1081 Burrard Street, Vancouver, BC V6Z 1Y6, Canada
e-mail: phil.blanke@googlemail.com

A. Thompson
Department of Radiology, St Paul's Hospital, University of British Columbia, 1081 Burrard Street, Vancouver, BC V6Z 1Y6, Canada
e-mail: angus_thommo@hotmail.com

J. Leipsic (✉)
Department of Radiology, St. Paul's Hospital, 2nd Floor, Providence Building, 1081 Burrard Street, Vancouver, BC V6Z 1Y6, Canada
e-mail: JLeipsic@providencehealth.bc.ca

Contrast Media Protocols

Contrast timing and volume should be optimized dependent upon the chamber and valve in question. A typical coronary CT angiographic protocol results in little if any contrast opacification of the right heart, so if the pulmonary valve is the structure to be evaluated, then timing must be targeted at the pulmonary valve and artery.

For evaluation of the aortic valve and the mitral valve, a contrast injection protocol similar to protocols for coronary artery evaluation is suitable. For the pulmonary valve, either a prolonged injection or earlier data acquisition is needed. Evaluation of the tricuspid valve may be hampered by streak artifact and inhomogeneous contrast attenuation in the right atrium and ventricle, obscuring the valve structure and limiting the ability to detect thrombi or vegetations. This problem is due to inflow of non-diluted contrast from the superior vena cava and unenhanced blood from the inferior cava with a typical antecubital contrast injection. As a result, injection of diluted contrast media with a dual-head injector or venous-phase data acquisition may be more suitable for evaluation of the tricuspid valve.

Four-Dimensional Cine Imaging

Static CT images only allow for anatomical valvular assessment, but dynamic (or so-called multiphasic) CT data sets acquired over the full cardiac cycle enable assessment of valvular function. With contemporary post-processing software, these data sets can be viewed in a cine mode while simultaneously alternating the orientation of the multiplanar reformations (MPRs), also referred to as 4D cine imaging. The major determinant of image quality with 4D cine imaging is the temporal resolution of the CT system used. Current single-source systems can reach a temporal resolution of 135 ms, whereas second-generation dual-source CT systems provide a temporal resolution approaching 75 ms [1, 2].

M.J. Budoff et al. (eds.), *Atlas of Cardiovascular Computed Tomography*, https://doi.org/10.1007/978-1-4471-7357-1_13

Historically, multiphasic data sets have been acquired with retrospectively ECG-gated helical CT, covering the entire cardiac cycle. The downside of this technique is the relatively high estimated effective dose of radiation compared with monophasic or static data acquisition with either retrospectively ECG-gated helical CT with a limited pulsing window or prospectively triggered CT acquisitions. Radiation dose can be lowered, however, by restricting the full-dose data acquisition to limited parts of the cardiac cycle. Recently, with the introduction of wider detectors, multiphasic data sets can also be acquired with sequential ECG-triggered data acquisition when using appropriate wide pulsing windows. In addition to visual assessment of leaflet and cusp motion for the assessment of prolapse and stenosis, measurement of valve area for stenosis and effective regurgitant orifice area for regurgitation are also possible, but hemodynamic information about pressure gradients and flow remains the domain of echocardiography.

Data Reconstruction

Routinely, data sets are reconstructed in axial submillimeter slices (0.5–0.75 mm). Multiphasic data sets can be reconstructed with a relative percentage approach (percentage of the RR interval) in increments of 5–10%. Alternatively, some CT vendors allow for an absolute reconstruction approach, with fixed intervals in relation to the R wave on the ECG, reported in milliseconds. This approach is beneficial in the setting of arrhythmias such as atrial fibrillation.

Image Assessment

By convention, image datasets are reconstructed in 3D by employing MPRs. However, minimum intensity projections (MinIPs) are particularly helpful when assessing valvular orifices for stenosis or regurgitation, or for vegetations. MinIPs may also aid in the anatomic localization of leaflet restriction or prolapse (Fig. 13.1). MPRs are essential for the evaluation of paravalvular abnormalities.

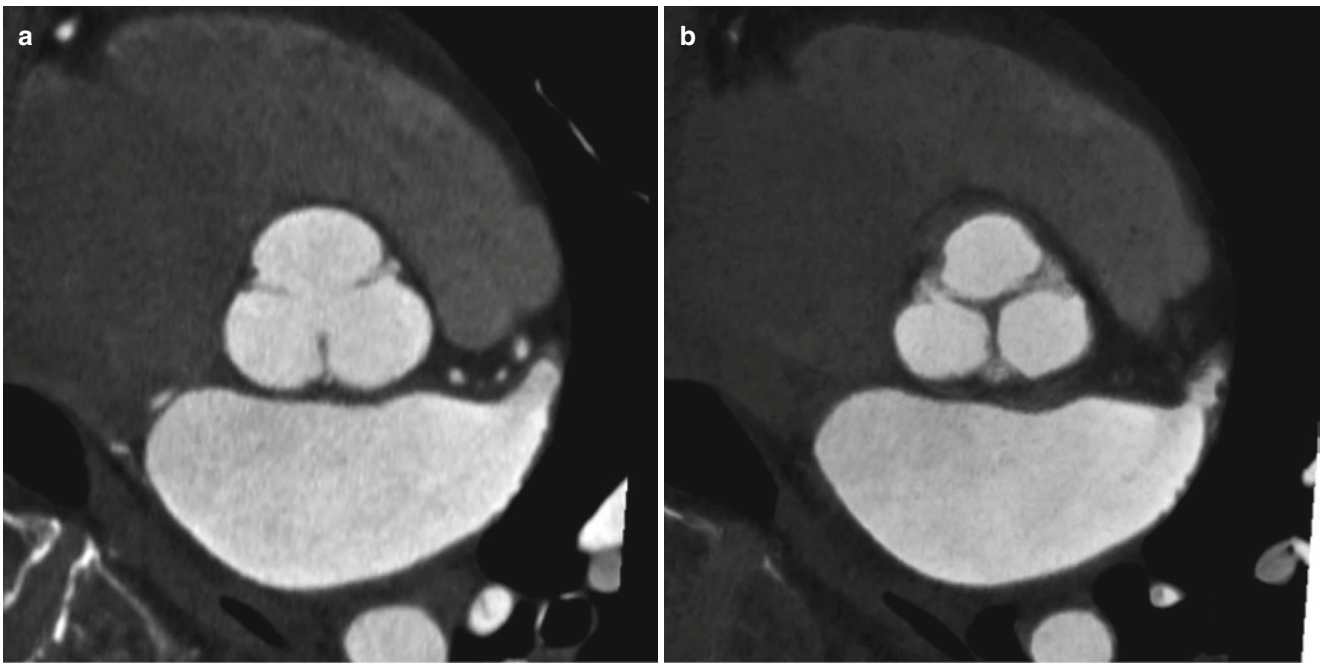

Fig. 13.1 Multiplanar reformation (MPR) versus minimum intensity projection (MinIP). Short-axis views of the aortic valve using MPR (**a**) and MinIP (**b**) techniques. MinIP is particular useful for improved visualization of cusp or leaflet coaptation

Aortic Valve

CT Assessment of Aortic Valve Anatomy and Function

The aortic valve separates the left ventricular outflow tract (LVOT) from the ascending aorta. It consists of three cusps: the noncoronary cusp, the right coronary cusp, and the left coronary cusp (Fig. 13.2a). The attachments of the three cusps extend from the LVOT to the sinotubular junction, with the annulus defined as a three-pronged coronet at the hinge point of the three aortic valve cusps [3]. Assessment of the aortic valve with CT includes evaluation of the aortic leaflet morphology, cusp motion, and planimetry of the aortic valve area (AVA). A good correlation has been demonstrated between AVA derived from echocardiography and from CT planimetry (Fig. 13.2b) [4, 5].

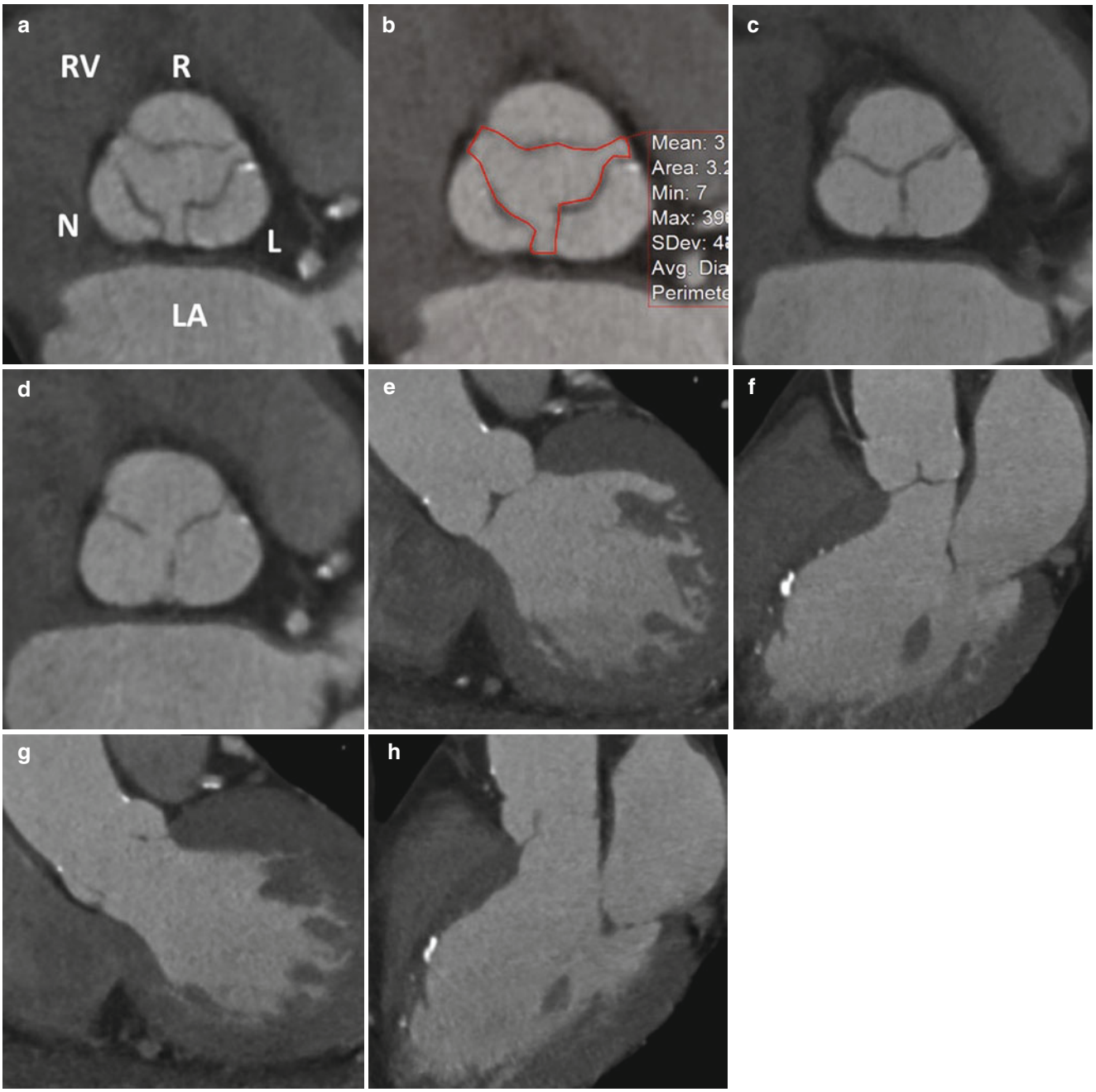

Fig. 13.2 Aortic valve assessment. A systolic short-axis view (**a**) depicts the three cusps—the right coronary cusp (R), the noncoronary cusp (N), and the left coronary cusp (L)—as well as the right ventricle (RV), the left atrium (LA), and the orifice, referred to as the aortic valve area, which can be assessed by planimetry (**b**). In competent valves, coaptation of the commissures can be assessed on short-axis views in diastole (**c**). Assessment involves either scrolling through short-axis views along the valvular complex or construction of MinIPs (**d**). Coronal oblique (**e**) and three-chamber (**f**) views during diastole can be compared with similar view (**g**, **h**) during systole

For assessment of aortic valve pathology, MPRs are usually adjusted, yielding a long axis of the aortic root and an orthogonally oriented transverse view in the true plane of the aortic valve, which transects through all three cusps. Following the nomenclature of echocardiography, this view is also referred to as a short-axis view (*see* Fig. 13.2). The resulting double oblique sagittal view is similar to the three-chamber view on either the parasternal long-axis view with transthoracic echocardiography or the mid-esophageal long-axis view with transesophageal echocardiography (TEE) (*see* Fig. 13.2). Cusp anatomy can best be evaluated in the transverse views, whereas cusp motion is observed in the sagittal and coronal oblique views.

In an optimal transverse or short-axis reconstruction, all three aortic valve cusps appear in a symmetric fashion relatively equal in size. In a competent valve, the commissures separating the cusps meet in the center with complete coaptation during diastole, which can be appreciated on a MinIP (*see* Fig. 13.2d). During systole, the free margins of the cusps are then displaced outward and superiorly towards the sinuses, revealing the valvular orifice.

Assessing the anatomical orifice area once the plane of the aortic valve has been achieved involves scrolling through the short-axis images to assess the maximum valve opening throughout the cardiac cycle. With multiphasic data sets providing diagnostic images throughout the cardiac cycle, the maximum valve opening can be determined in systole, and complete coaptation can be confirmed during diastole. The aortic valve area (AVA), which corresponds to the geometric orifice area, can be quantified by means of planimetry at maximum opening (*see* Fig. 13.2b). In healthy valves, maximum AVA is usually found in early to mid-systole, approximating 20–35% of the cardiac cycle. Planimetric measurements by CT are similar to those performed with TEE [5, 6], with a slight systematic bias to be larger than the AVA estimated by the continuity equation with echocardiography, because the elliptical shape of the LVOT results in echocardiographic underestimation of the true LVOT area; also, echocardiography provides the effective orifice area (EOA), which is known to be uniformly smaller than the geometric orifice area [7]. In the general population with nondiseased aortic valves, AVA varies between 2.5 and 6.0 cm^2.

As most cases of aortic stenosis in the Western world are related to senile sclersis of the aortic valve, often with pronounced deposits of calcium, care must be taken to attempt to reduce the impact of valvular calcification on AVA measurements by using harder convolution kernels and widening the display window to optimize image review.

Anatomical Variants

The normal tricuspid anatomy must be distinguished from anatomic variants, such as bicuspid anatomy or the very rare quadricuspid anatomy. A bicuspid aortic valve is the most common congenital cardiac anomaly, with a prevalence of 1–2% [8–10]. The term bicuspid aortic valve refers to several morphologic phenotypes [11]. A true or "purely" bicuspid valve is composed of two cusps, morphologically and functionally (Fig. 13.3). In fact, this pattern is rare, representing only about 7% of all bicuspid valves. The most frequent form of bicuspid aortic valve consists of an asymmetric pattern with three developmental cusps rather than just two, but with at least one fused or underdeveloped commissure, referred to as a raphe. Because of the multiple anatomical variations, a classification system was introduced by Sievers and Schmidtke [8] in order to better define bicuspid aortic valve disease and to standardize reporting. Three characteristics are considered: the number of raphes, the spatial position of the cusps or raphes, and the functional status of the valve (Fig. 13.4). Given that only 7% of all bicuspid aortic valves are "purely" bicuspid, the other 93% have three developmental cusps—88% with one raphe (Type 1) and 5% with two raphes (Type 2) [8]. Type 2 bicuspid valves with only one commissure and two raphes are also referred to as unicuspid valves (Fig. 13.5). Depending on the pattern of cusp fusion, there is a varied pattern of associated congenital abnormalities and pathologies, including dilatation of the ascending aorta, coarctation, and intracranial aneurysm [12–14]. Because of these associations, patients with bicuspid aortic valves experience higher rates of acute aortic syndrome and dissection [15]. Most importantly, bicuspid aortic valves predispose to aortic valve stenosis, necessitating aortic valve replacement commonly at a younger age than for patients with tricuspid aortic valves [16].

A quadricuspid aortic valve is a rare congenital malformation with an incidence between 0.003 and 0.013% [17]. It is frequently associated with aortic regurgitation (Fig. 13.6), but can also be found in the setting of aortic stenosis [17, 18].

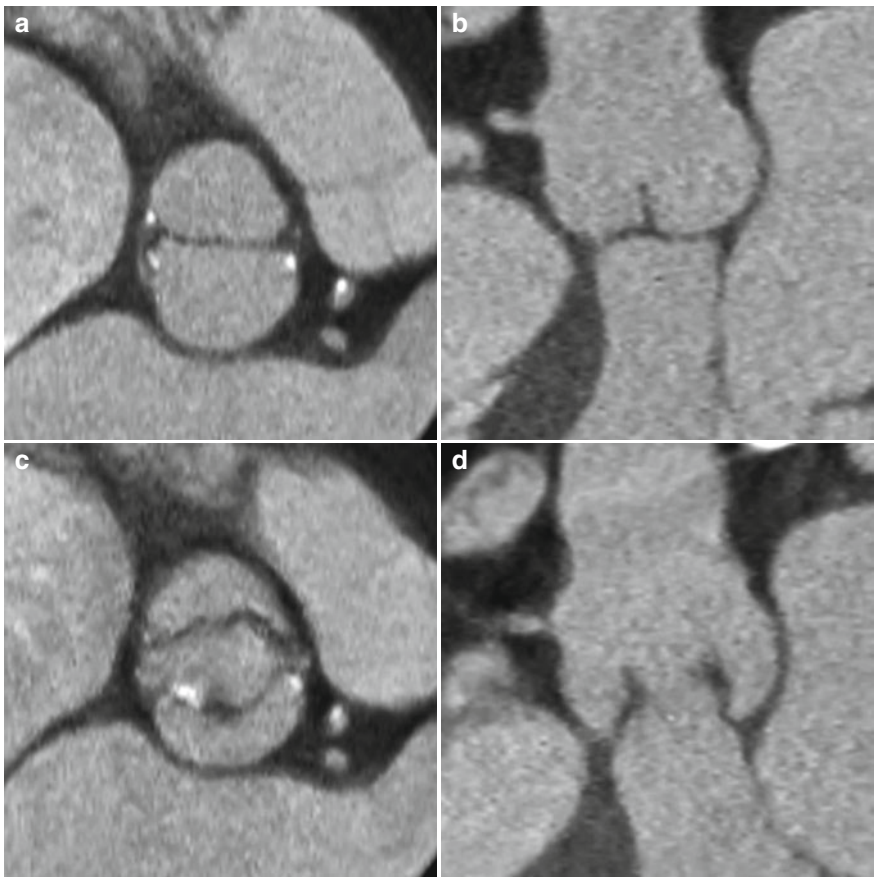

Fig. 13.3 "Purely" bicuspid aortic valve without a raphe (Sievers classification Type 0), with mild stenosis. (**a**) Short-axis view during diastole; (**b**) Three-chamber long-axis view during diastole; (**c**, **d**) Similar views during systole. Spotty calcifications and restricted cusp motion can be noted

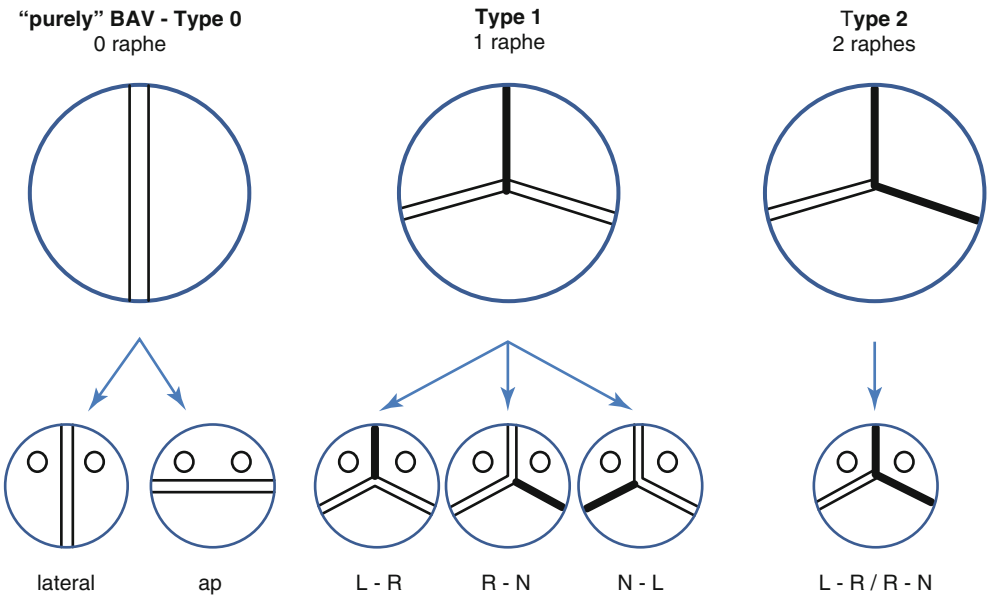

Fig. 13.4 Bicuspid aortic valve classification system according to Sievers and Schmidtke [8]. The bicuspid valves are illustrated as viewed from the surgeon's position, with the left coronary sinus on the left side. *Doubled lines* represent commissures, and *bold lines* represent raphes. The classification distinguishes the Types of bicuspid morphology based on the number of commissures and raphes. The first subcategories classify the spatial orientation of raphe(s). The second subcategory (function) is not illustrated. *ap* anterior-posterior, *L* left coronary sinus, *N* noncoronary sinus, *R* right coronary sinus

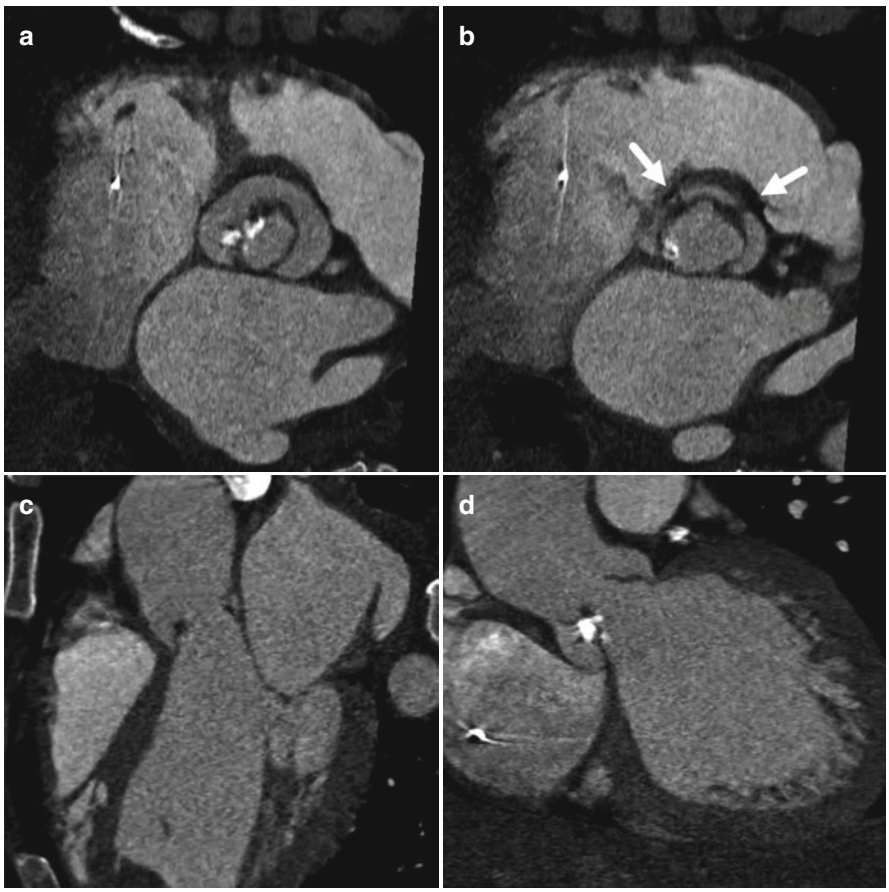

Fig. 13.5 Unicuspid aortic valve. (**a**, **b**), Systolic short-axis views. (**b** is located further toward the left ventricular outflow tract [LVOT]). (**c**), Sagittal oblique three-chamber view. (**d**), Coronal oblique view. All of these images depict a bicuspid valve with two raphes (*arrows* in **b**) and one commissure, also referred to as a unicuspid valve

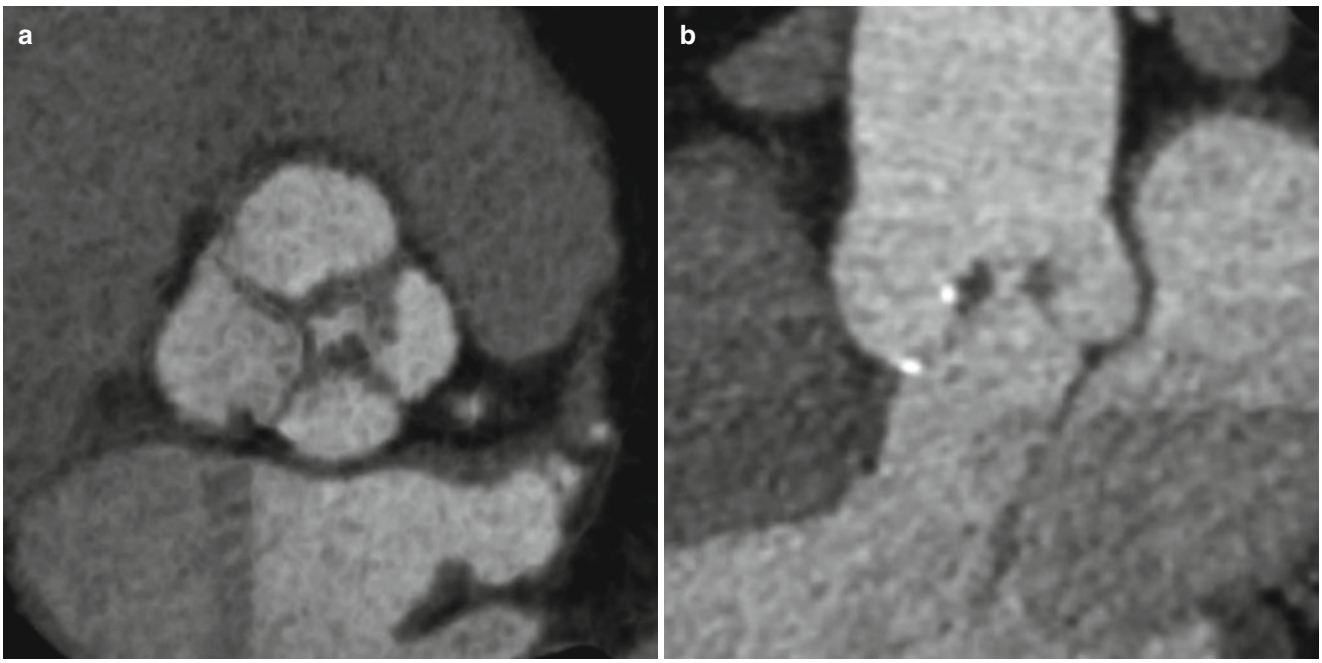

Fig. 13.6 Quadricuspid aortic valve. Diastolic short-axis view (**a**, MinIP) and three-chamber long-axis view (**b**) depicting a quadricuspid aortic valve with four distinct cusps. Incomplete central coaptation and the resulting regurgitant orifice reflecting aortic insufficiency can be easily identified

Aortic Valve Stenosis

Aortic valve stenosis is most commonly caused by age-related progressive aortosclerosis and calcification of a normal, tricuspid aortic valve. Other causes include calcification of a congenital bicuspid aortic valve and rheumatic heart disease, which is increasingly rare in the Western world [19]. The prevalence of aortic stenosis in North America is approximately 1.3% for individuals ages 65–74 years; it increases to 2.4% for ages 75–84 years and to 4% for ages 85 years and older; the corresponding prevalence of aortosclerosis in these age groups is 20%, 35%, and 48% respectively [20]. Severe aortic stenosis is defined by an aortic valve orifice area less than 1 cm^2, or 0.6 cm/m^2 Typically, aortic stenosis due to calcification of a bicuspid valve appears between ages 40–60 years, whereas aortic stenosis with tricuspid valves appears later, between 70 and 80 years of age [21]. On cardiac CT, aortic valve stenosis can be evaluated morphologically and functionally (Fig. 13.7). Morphologically, aortic valve stenosis is characterized by thickened cusp margins and val-

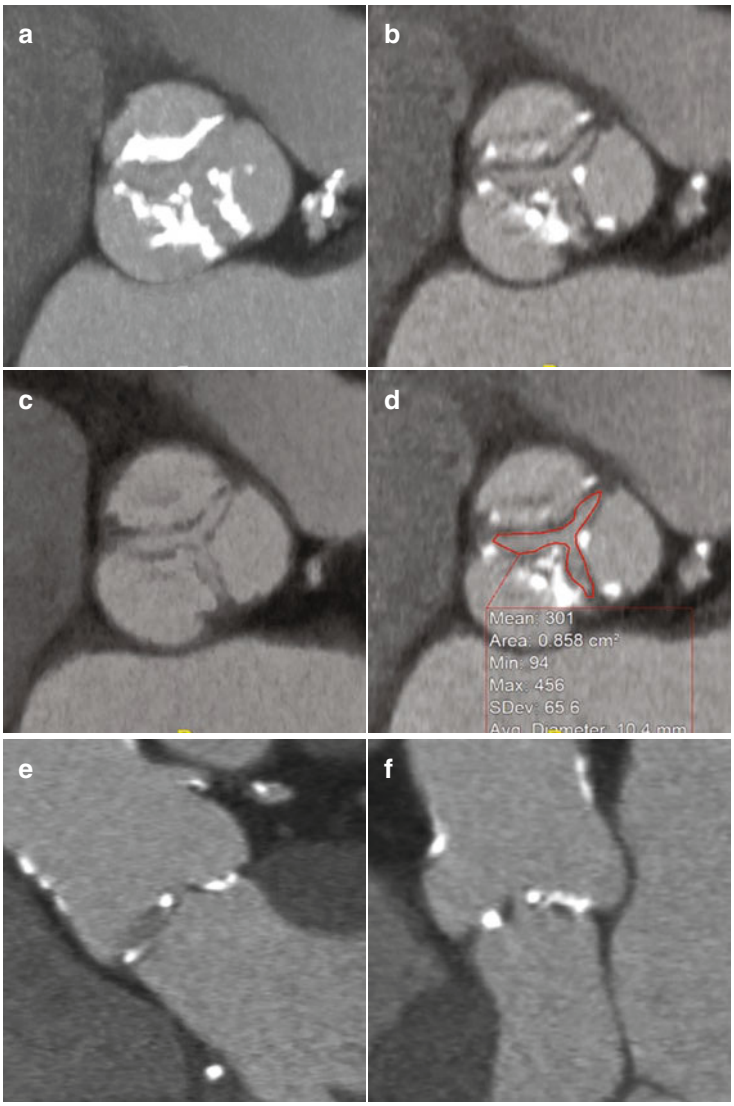

Fig. 13.7 Aortic valve stenosis. A systolic short-axis view (MPR, **a**) depicts calcification of the free margins of all three aortic valve cusps. The true extent of calcification can be appreciated on a short-axis maximum intensity projection (MIP) image (**b**); a MinIP (**c**) may demonstrate the true aortic valve area. (**d**), Aortic valve area (AVA) planimetry. The diastolic coronal oblique view (**e**) and the systolic coronal oblique view (**f**) demonstrate restricted cusp motion

vular calcifications, which can be spotty, confluent, or even bulky. Their distribution can be symmetric or asymmetric in regard to involvement of the cusps, and they may extend into the LVOT (Fig. 13.8). Typically, valve thickening and calcification progress from the cusp insertion toward the tips. In rheumatic valvular disease, on the other hand, the leaflet tips are affected first (Fig. 13.9). Functionally, restricted motion of the cusps can be depicted on multiphasic reconstructions (*see* Fig. 13.7). When multiphasic data sets are provided, the severity of aortic stenosis can be evaluated effectively by cardiac CT by planimetric assessment of the AVA at maximum opening in systole on the short-axis view (*see* Fig. 13.7). AVA

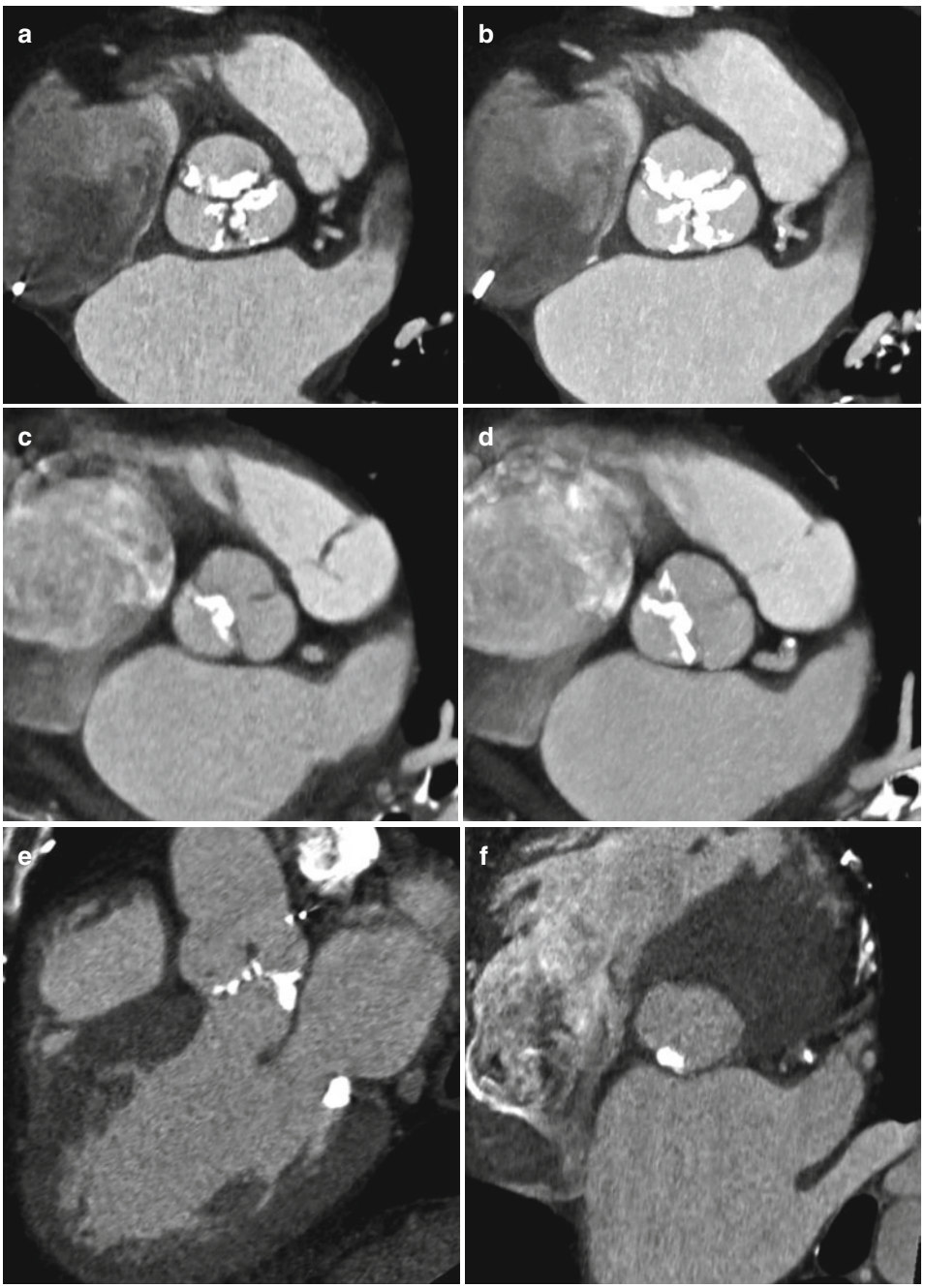

Fig. 13.8 Asymmetric distribution of valvular calcification in aortic stenosis. Examples of three different patients: (1) Aortic valve stenosis with pronounced calcification of the right coronary and non coronary cusps (short-axis view; **a**, MPR; **b**, MIP). (2) Aortic valve stenosis with calcification of the noncoronary cusp and spotty calcifications of the right coronary cusp (short-axis view; **c**, MPR; **d**, MIP). (3) Bulky calcification extending along the aortomitral continuity into the LVOT (**e**, three-chamber view; **f**, short-axis view)

is largest during mid-systole, but the reconstruction of at least 10–30% of the RR interval should be evaluated, given interindividual variations in the absolute length of the cardiac cycle. Furthermore, cardiac CT aids in distinguishing between tricuspid or bicuspid aortic stenosis and the subtypes of bicuspid aortic valve anatomy (Figs. 13.10 and 13.11).

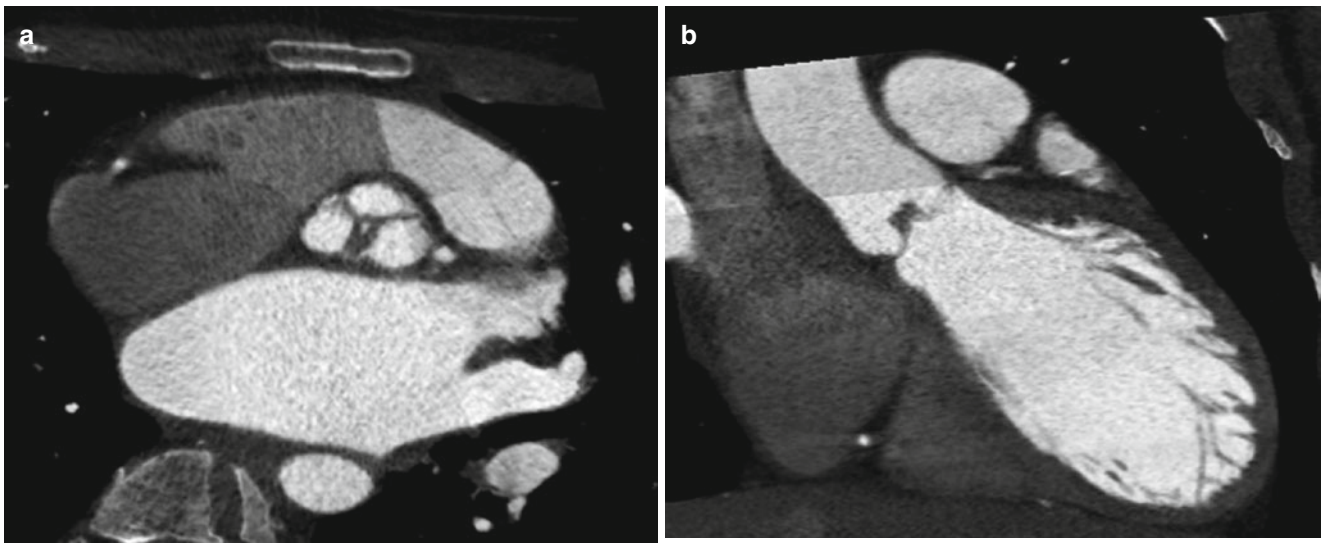

Fig. 13.9 Rheumatic aortic valve disease. Diastolic short-axis view (**a**) and coronal oblique view (**b**) demonstrate a tricuspid aortic valve with thickened margins, in particular of the noncoronary and left coronary cusp

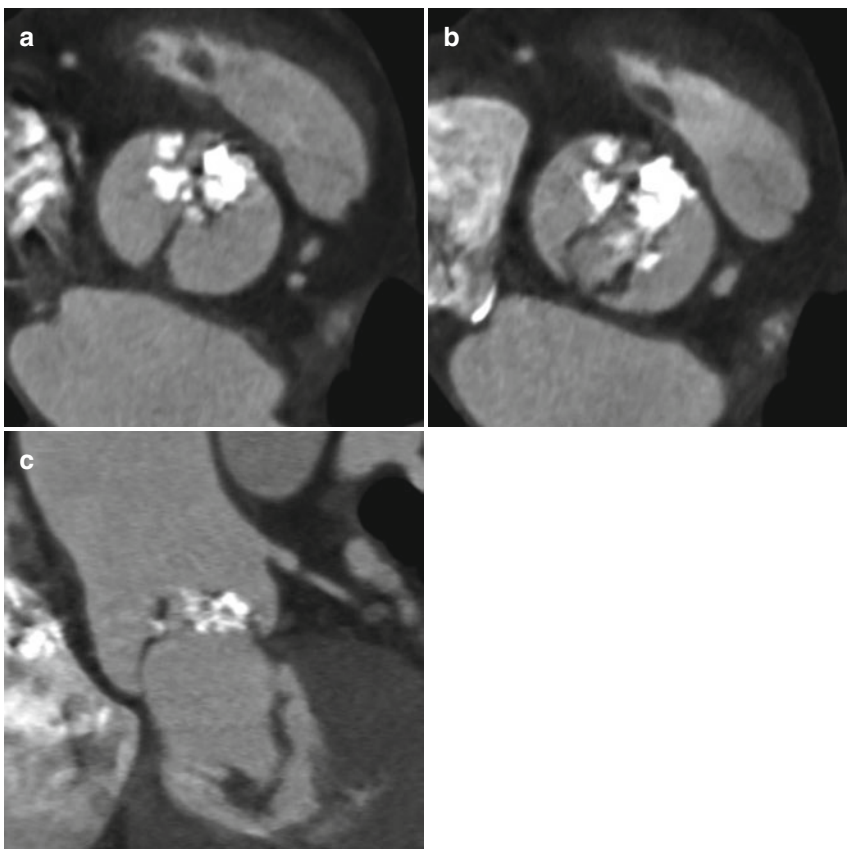

Fig. 13.10 Bicuspid aortic valve stenosis. A diastolic short-axis view (**a**) demonstrates a purely bicuspid aortic valve (Sievers Type 0) with a bulky calcification and no median raphe. A systolic short-axis view (**b**) and coronal oblique view (**c**) demonstrate restricted cusp motion, with resulting severe aortic stenosis

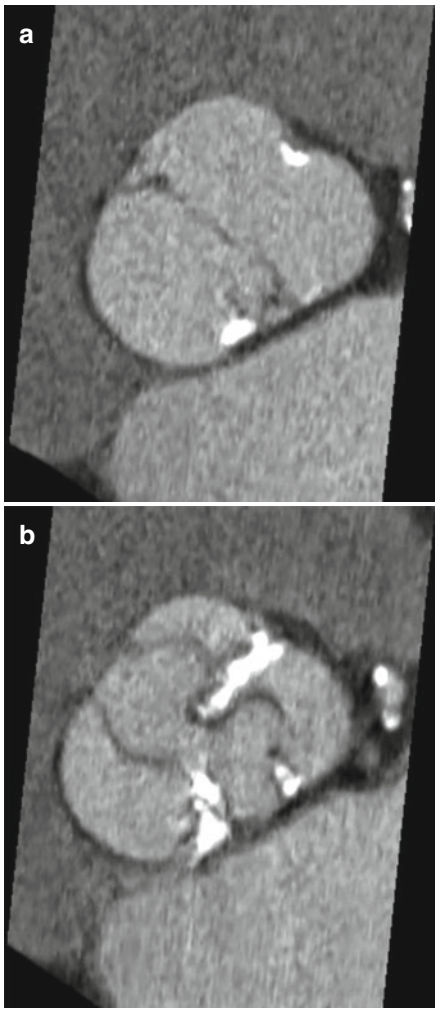

Fig. 13.11 Bicuspid aortic valve stenosis. Diastolic (**a**) and systolic (**b**) short-axis views of a bicuspid aortic valve with a calcified raphe (Sievers Type 1 R-L) and restricted opening resulting in a moderate aortic valve stenosis

Aortic Valve Regurgitation

The prevalence of aortic valve regurgitation is approximately 0.5% in North America [22]. Compared with aortic stenosis, aortic regurgitation is less commonly age-related. In developing countries, the most common cause of aortic regurgitation is rheumatic heart disease. Where access to medical care is more extensive, aortic regurgitation is most commonly due to either congenital causes (such as bicuspid aortic valve with associated aortopathy) or so-called degenerative causes such as annuloaortic ectasia. Endocarditis and acute aortic dissection can also lead to new-onset aortic valve regurgitation.

Incomplete coaptation of the aortic valve cusps during diastole is the morphologic hallmark of aortic regurgitation, which can be identified on CT. It can be observed on both short-axis and long-axis views (Fig. 13.12). Similar to planimetry of the AVA, the aortic regurgitant orifice can be quantified. Fairly consistently throughout the published literature, aortic regurgitation is most accurately evaluated at 75% of the cardiac cycle. Compared with echocardiography, cardiac CT has a high positive predictive value, but although there are no clear cutoff values in echocardiography to distinguish between mild, moderate, or severe aortic regurgitation, it is important to be aware that mild regurgitation in particular may be missed on cardiac CT because of the lack of flow data that augments an echocardiographic exam [4]. Aortic regurgitation assessment is especially difficult in the setting of heavily calcified or bicuspid aortic valves [23]. Importantly, aortic insufficiency may be concomitant with aortic stenosis (Fig. 13.13).

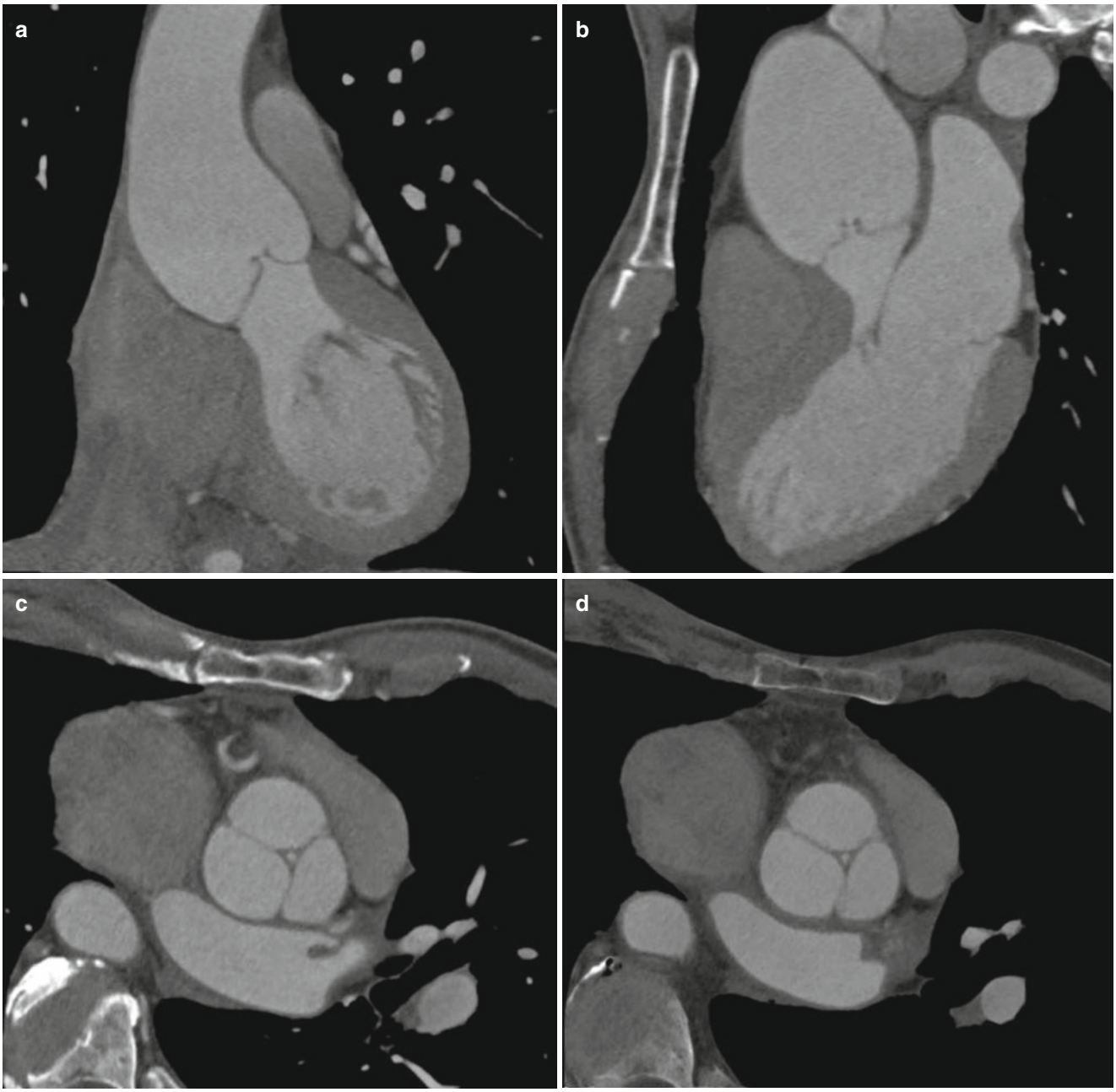

Fig. 13.12 Aortic valve regurgitation. Coronal oblique view (**a**), three-chamber view (**b**), short-axis view (**c**), and short-axis MinIP (**d**) of an aortic valve, demonstrating incomplete central coaptation and the resulting aortic regurgitant orifice as well as underlying aortic root ectasia

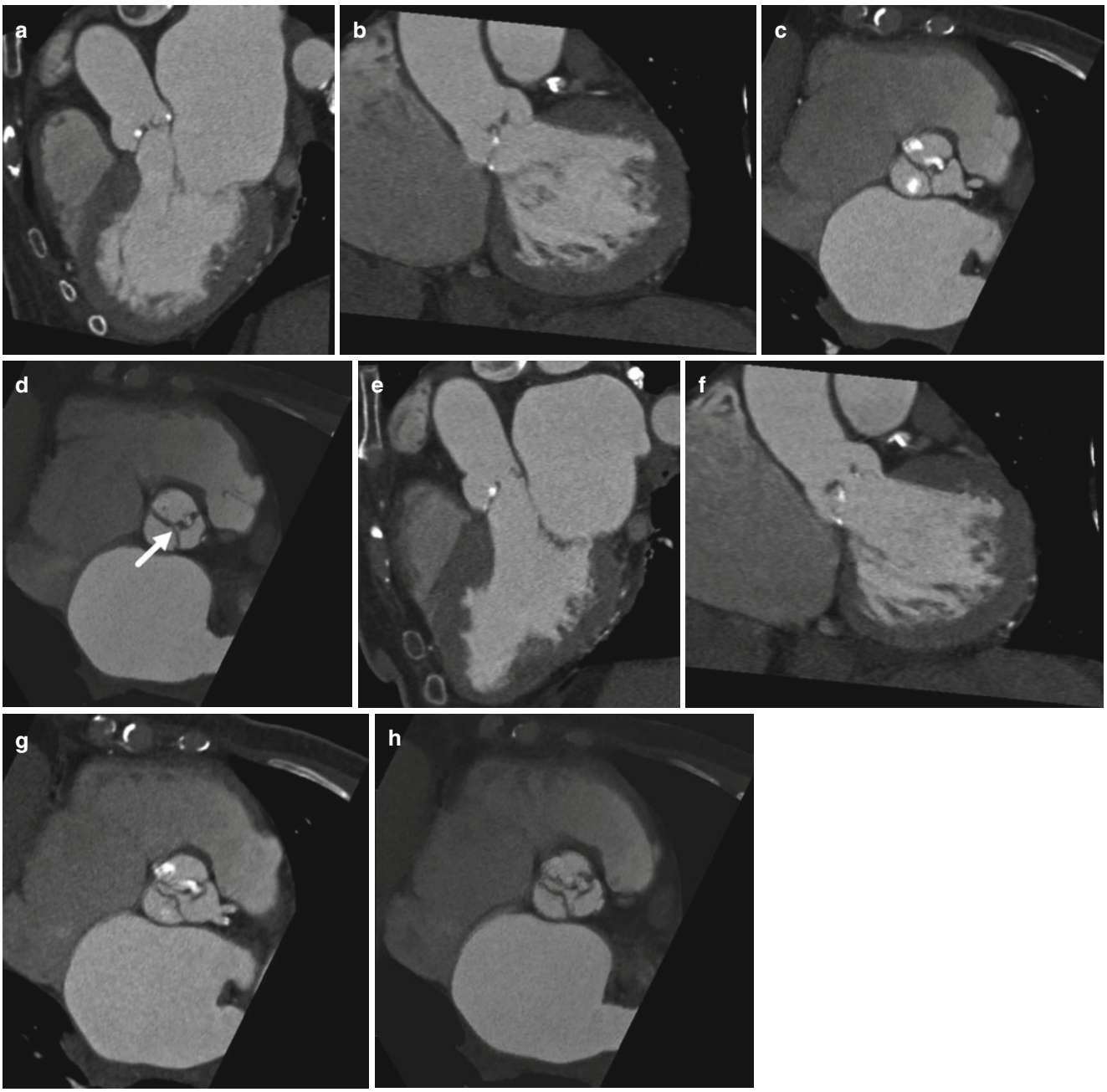

Fig. 13.13 Concomitant aortic stenosis and regurgitation. Diastolic three-chamber view (**a**), coronal oblique view (**b**), and short-axis view (**c**) demonstrating a tricuspid, partially calcified aortic valve with incomplete central coaptation (also visible also on short-axis MinIP [**d**, *arrow*]), giving rise to aortic regurgitation. Corresponding systolic views (**e**–**h**) demonstrate restricted cusp motion with resulting severe aortic stenosis

Findings After Surgical Aortic Valve Replacement or Repair

Unlike the emerging transcatheter aortic valve repair, cardiac CT is rarely used in the preoperative planning of surgical aortic valve replacement, but it is very useful for postoperative evaluation, especially if increased transvalvular gradients, regurgitation, or endocarditis create suspicion of prosthesis malfunction. Most contemporary mechanical heart valves consist of two tilting disks, and their movement can be visualized on MPRs (Figs. 13.14 and 13.15). Prosthesis malfunction involving mechanical heart valves may be caused by

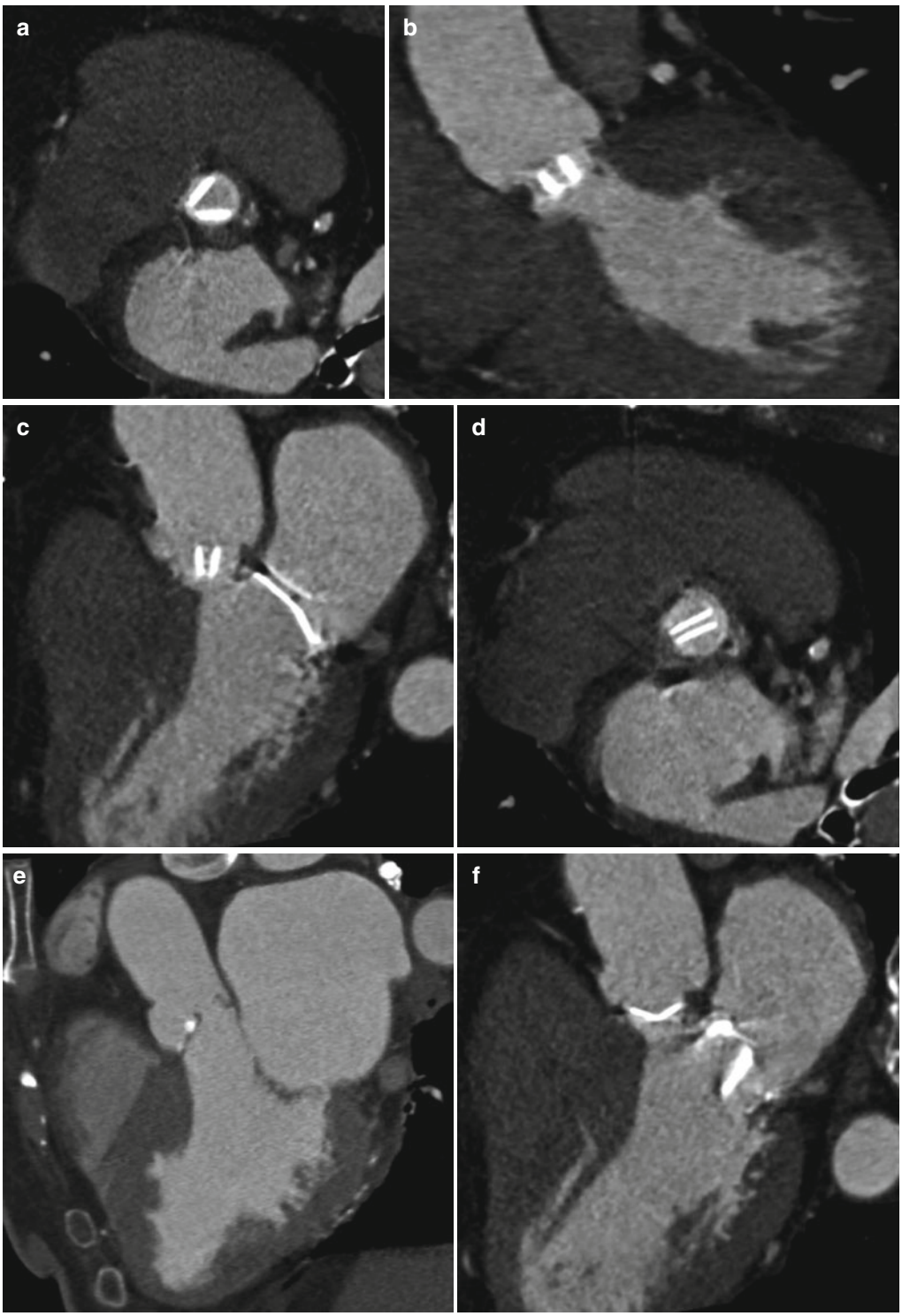

Fig. 13.14 Mechanical aortic valve prosthesis. A systolic short-axis view (**a**), coronal oblique view (**b**), and sagittal oblique view (three-chamber view, **c**) depict a mechanical aortic valve prosthesis with two radiopaque tilting discs and a radiolucent scaffold, as well as a concomitant mechanical valve prosthesis. (**d**–**f**) are the corresponding diastolic images

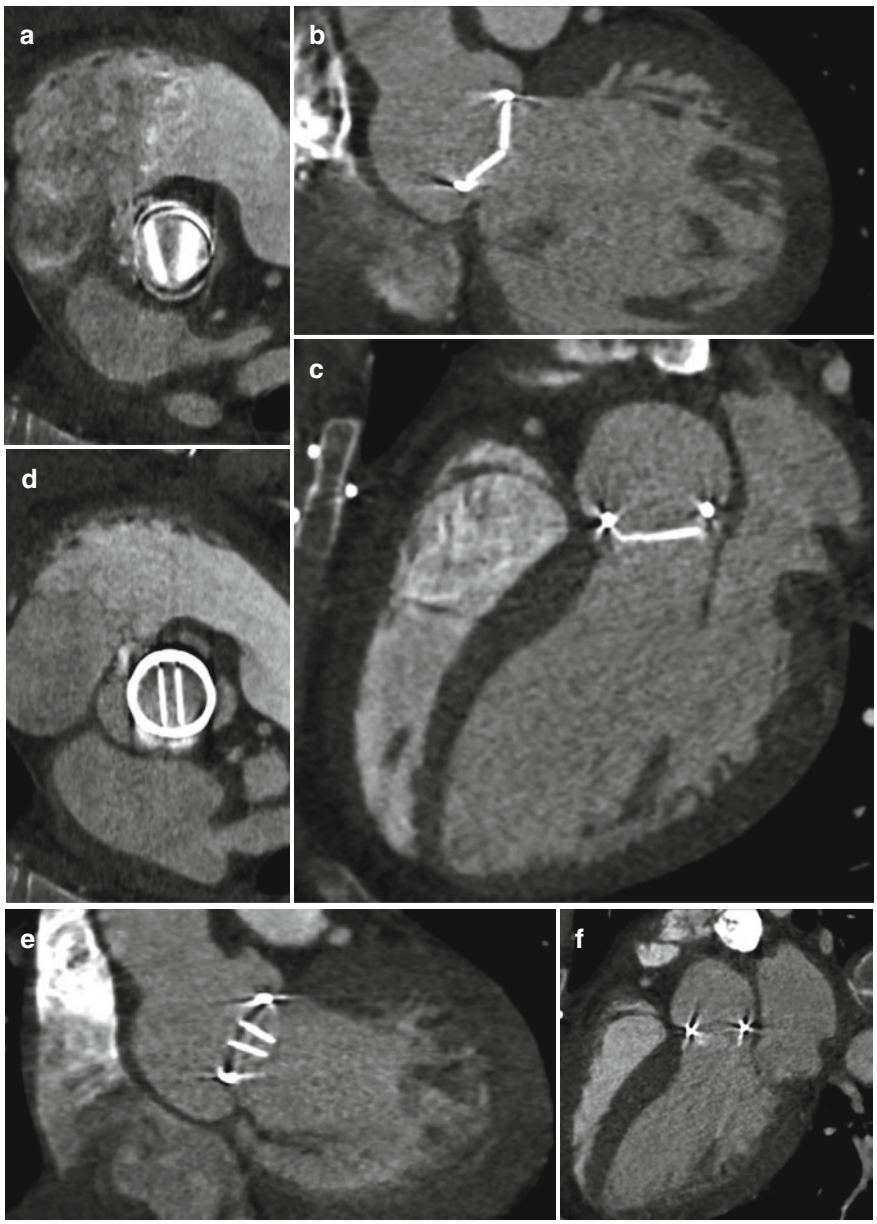

Fig. 13.15 Mechanical aortic valve prosthesis. A diastolic short-axis view (**a**), coronal oblique view (**b**), and sagittal oblique view (three-chamber view, **c**) depict a mechanical aortic valve prosthesis with two radiopaque tilting discs and a radiopaque scaffold. (**d**–**f**) are the corresponding systolic images

thrombus, vegetation, or pannus formation, with subsequent restraint of tilting disk motion. Morphologic correlates on cardiac CT are hypoattenuating apposition at the hinges or restricted disk motion, as evidenced by MPRs. Paravalvular regurgitation, a rare complication after surgical aortic valve replacement, may be caused by dehiscence of the prosthesis at the aortoventricular junction, which can be well visualized by cardiac CT (Fig. 13.16).

Some bioprostheses have radiopaque annular rings and others may have a radiopaque coronet; stentless bioprostheses do not have any radiopaque components at all (Fig. 13.17). Stentless bioprostheses are sewn directly to the aortoventricular junction, as seen by a hypoattenuating ring, which makes their evaluation prior to transcatheter valve-in-valve procedures difficult. Some bioprostheses are supported by a nitinol stent scaffold and are deployed after resection of the calcified cusps without circumferential sutures for fixation (Fig. 13.18). Cardiac CT may demonstrate degeneration of the bioprosthesis (*eg*, leaflet thickening or calcification) or cusp thrombosis (Fig. 13.19).

Valve-sparing aortic repair procedures, such as the David procedure, constitute alternatives to mechanical heart valves for aortic regurgitation, especially in young patients (Fig. 13.20).

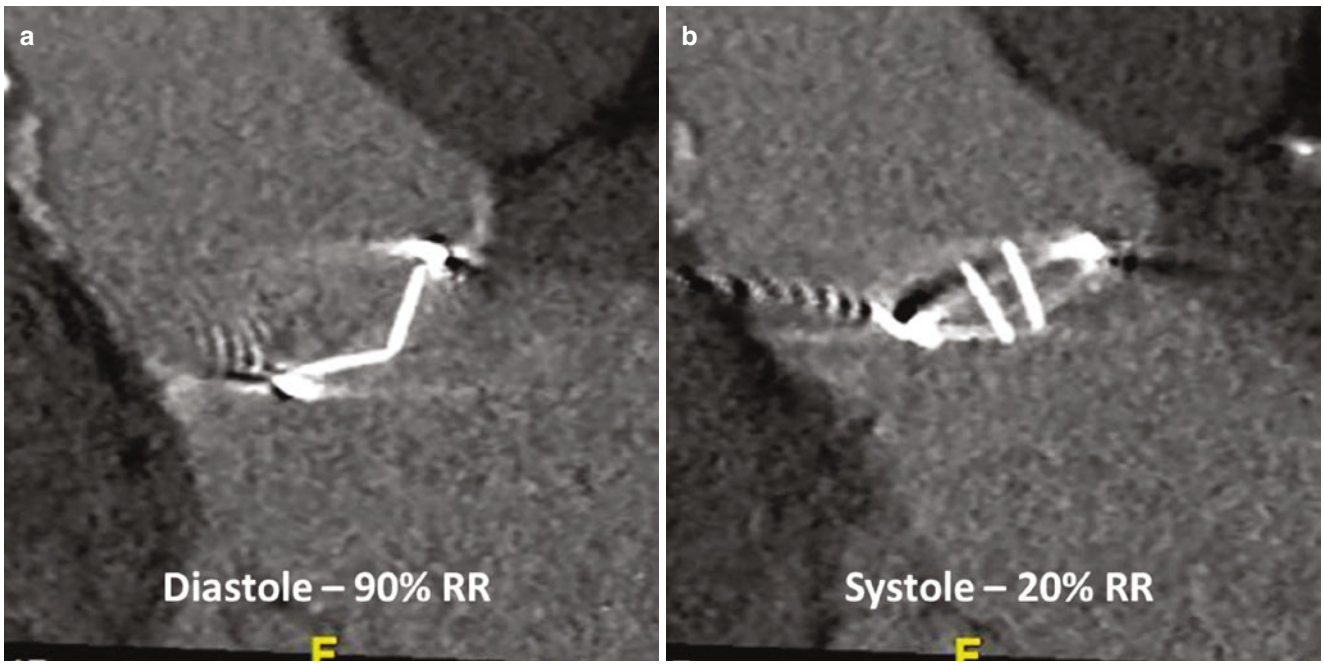

Fig. 13.16 Partial dehiscence of a mechanical aortic valve prosthesis from the aortoventricular junction. These coronal oblique long-axis views depict the aortic root during diastole (**a**) and systole (**b**). Dehiscence can be morphologically identified as a gap between the ring of the mechanical prosthesis and the wall of the aortic root in the region of the former noncoronary cusp. Functionally, although the mechanical discs show normal opening movements during systole, the prosthesis itself is separated from the LVOT during systole

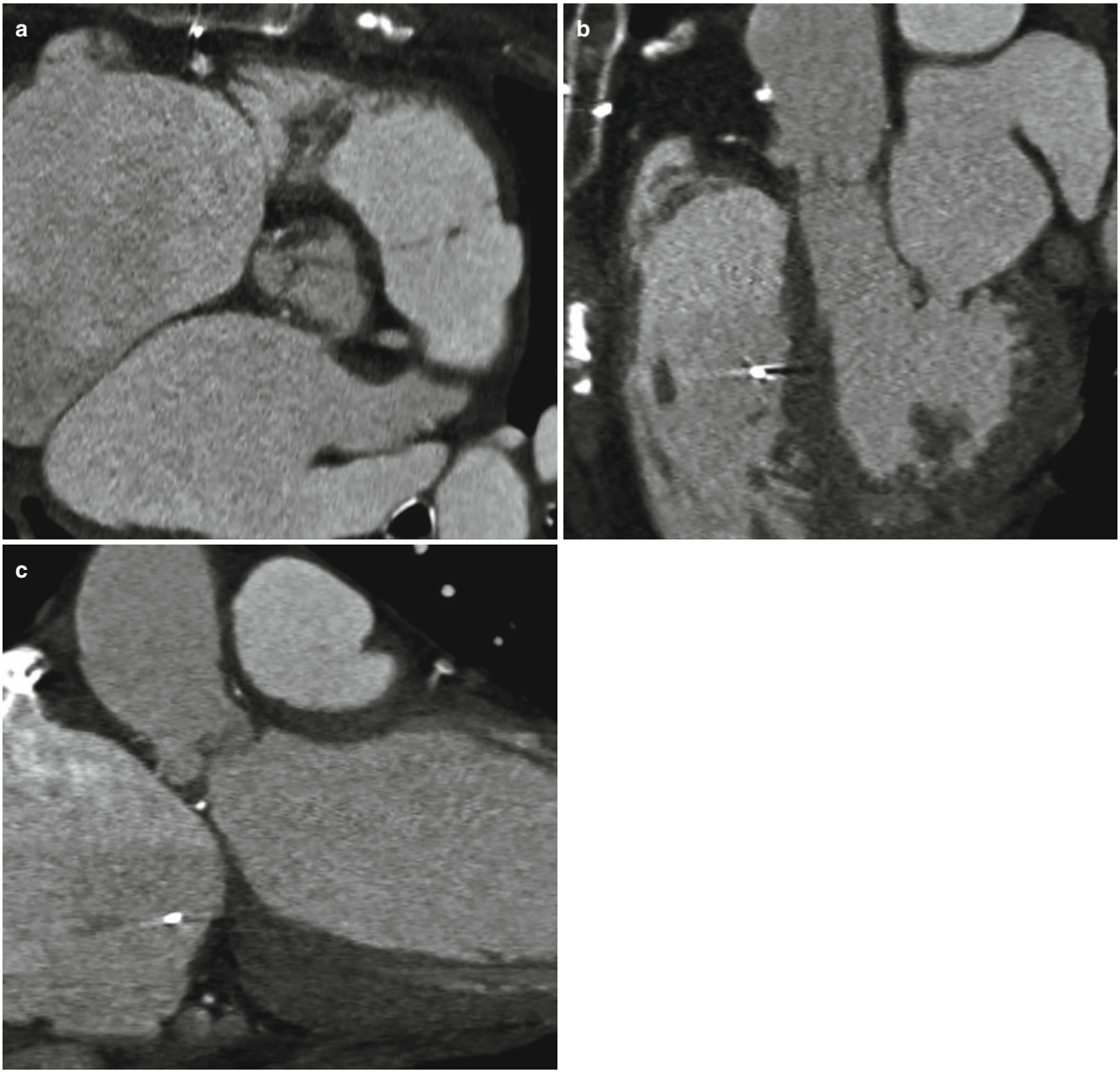

Fig. 13.17 Stentless aortic valve bioprosthesis. A diastolic short-axis view (**a**), sagittal oblique view (three-chamber view, **b**), and coronal oblique view (**c**) depict a stentless Freestyle (Medtronic) bioprosthetic heart valve

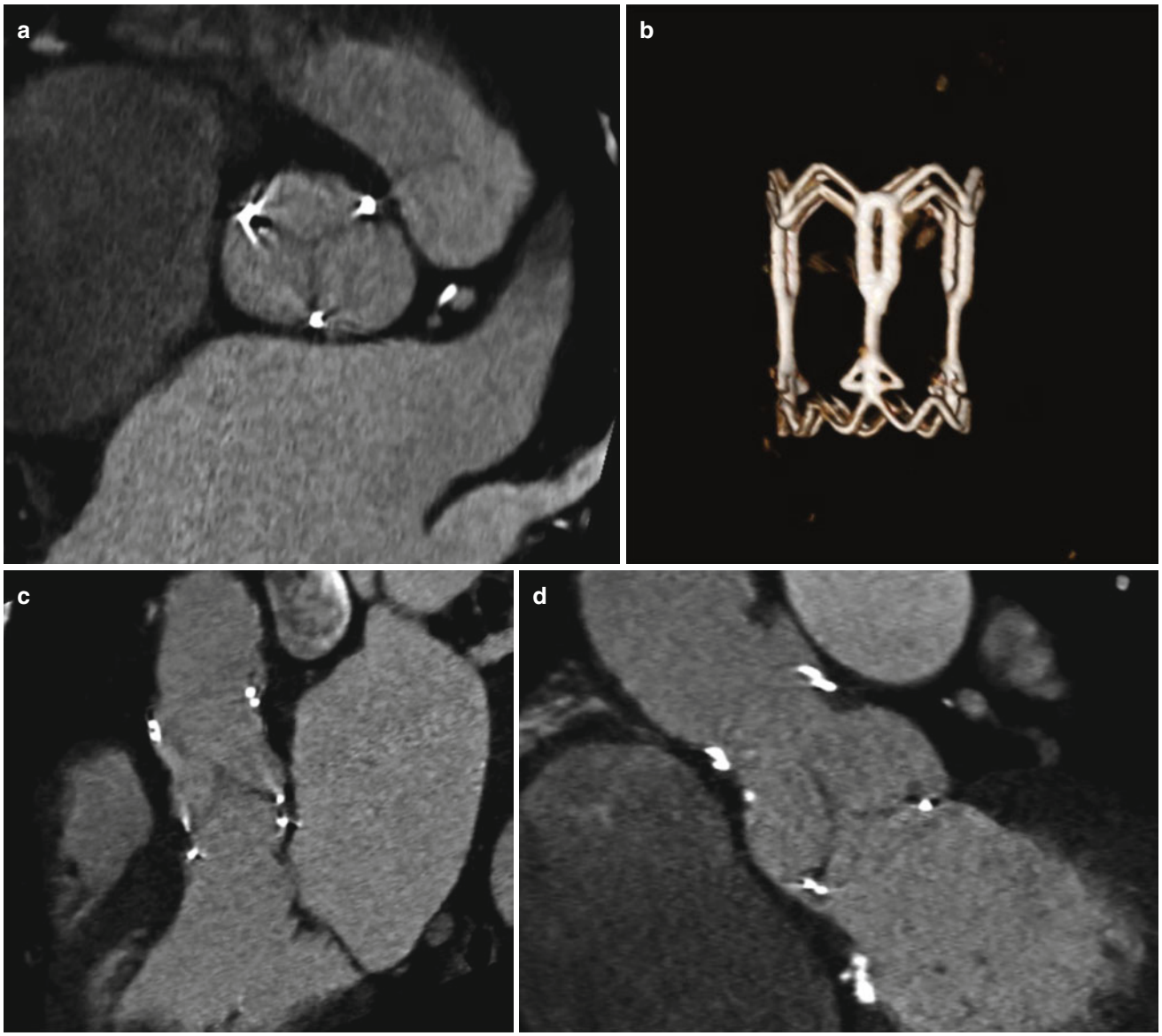

Fig. 13.18 Sutureless aortic valve bioprosthesis. A diastolic short-axis view (**a**), volume-rendered image (**b**), sagittal oblique view (three-chamber view, **c**), and coronal oblique view (**d**) depict a sutureless ATS 3f aortic valve bioprosthesis (ATS Medical, Minneapolis, MN) with a radiopaque nitinol stent scaffold

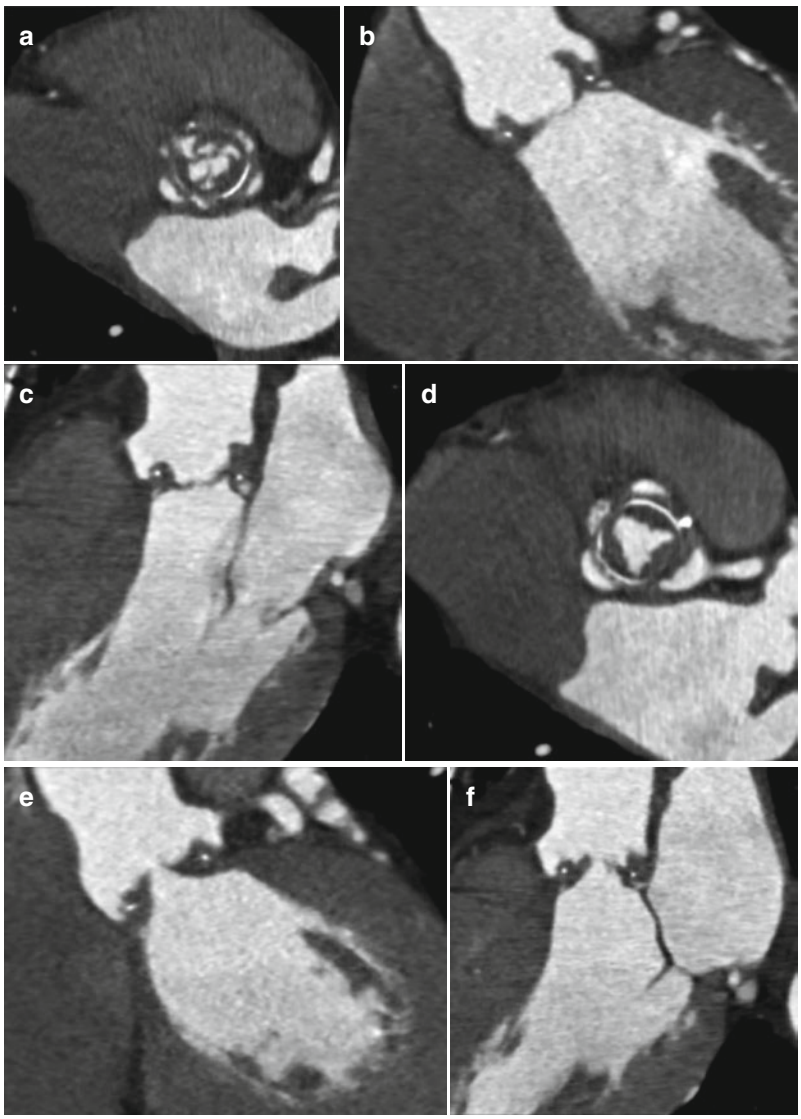

Fig. 13.19 Thrombosed aortic valve bioprosthesis. A diastolic short-axis view (**a**), coronal oblique view (**b**), and sagittal oblique view (three-chamber view, **c**) depict thickening of all three bioprosthesis cusps. (**d**–**f**) are corresponding systolic images, with evidence of restricted motion of the cusps. (*Courtesy of* Dr. Gregor Pache, Heart Center Bad Krozingen, Germany)

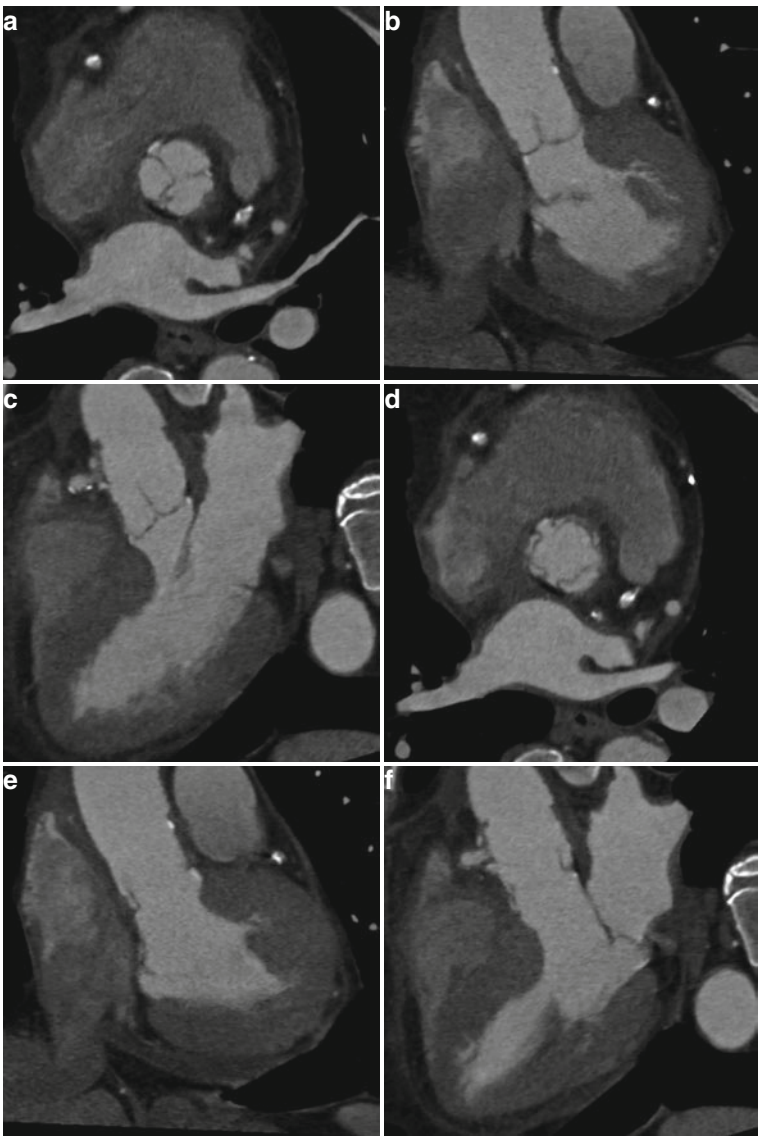

Fig. 13.20 Valve-sparing aortic root replacement (David procedure) for aortic root ectasia and aortic regurgitation. A postprocedure diastolic short-axis view (**a**), coronal oblique view (**b**), and sagittal oblique view (three-chamber view, **c**) depict the reconstructed aortic root, which typically lacks aortic sinuses because of the implantation of a cylinder-shaped aortic prosthesis. The reimplanted native aortic cusps show complete diastolic coaptation. (**d**–**f**) are corresponding systolic images

Transcatheter Aortic Valve Replacement

Transcatheter aortic valve replacement (TAVR) was first described by Alain Cribier in 2002, using a transvenous approach [24]. A number of other approaches have since been employed. The most common is the transfemoral arterial approach, but transaortic, transsubclavian, and transapical methods have also been used [25]. Unlike surgical valve replacement, in which prosthesis selection is based on direct visualization of the annulus, TAVR relies upon noninvasive imaging. In the early days of TAVR, sizing was performed with echocardiography, which has given good results but has significant limitations [26, 27]. The aortic annulus is an almost uniformly noncircular structure, so a two-dimensional measurement of the annulus is may not be adequate for sizing. The limitations of two-dimensional sizing are highlighted by the significant complications that may occur with TAVR, including paravalvular aortic valvular regurgitation [26, 27]. These limitations have resulted in significant interest in the use of cardiac CT for annular assessment, given its isotropic volumetric multiplanar capabilities. These multiplanar imaging capabilities have allowed reproducible and accurate annular measurements throughout the cardiac cycle [28–30], providing the ability not only to determine a diameter measurement but also to measure annular area and circumference, which have recently been shown to be powerful predictors of paravalvular regurgitation [31]. In addition, prospective single-center and multicenter trials have recently shown that annular sizing on the basis of 3D CT measurements allows for a reduction in the burden and severity of paravalvular regurgitation [29]. As a result, CT-derived sizing is becoming the standard for TAVR valve selection [32–34].

The aortic annulus is assessed in its true plane at the level of the basal ring immediately below the hinge point of the aortic valve cusps (Fig. 13.21). After the true plane of the aortic annulus is defined, it can be measured in a number of ways. Most commonly, planimetry is performed, enabling both perimeter and area measurements. Derived diameters can be calculated based on the formulas for the area or the perimeter of a circle. Alternatively, the long axis (maximum) and the short axis (minimum) are measured, allowing for the calculation of a mean diameter [35]. Importantly, the aortic root is subject to dynamic and cyclical changes during cardiac filling and its compliance as well as deformation result in changes to the cross-sectional area and diameter throughout

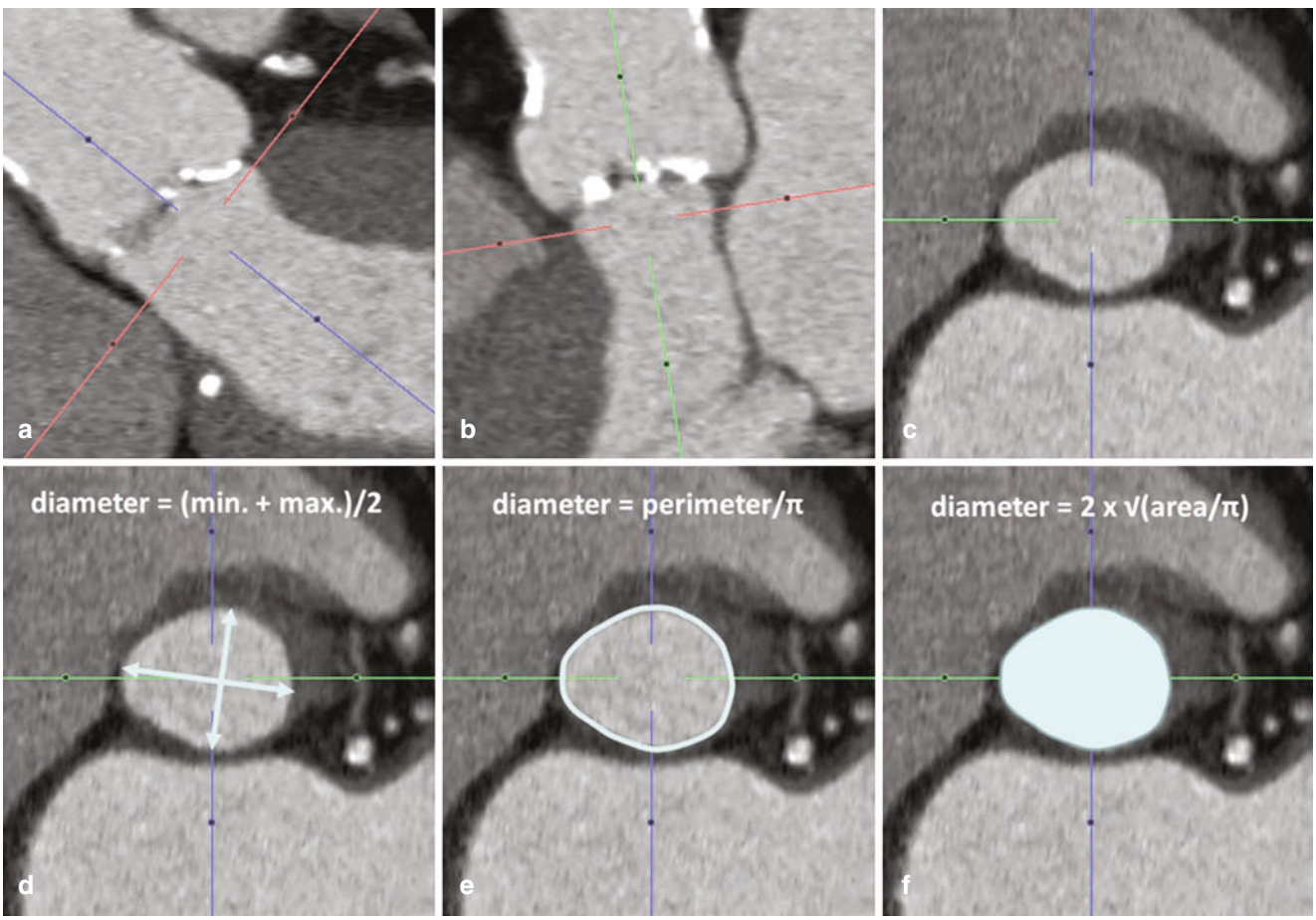

Fig. 13.21 Aortic annulus assessment for transcatheter aortic valve replacement (TAVR) planning. Coronal oblique (**a**) and sagittal oblique views (**b**) are adjusted so that the resulting double-oblique transverse view (**c**) transects through the most basal attachment points of all three cusps. Annulus dimensions can be evaluated by assessing minimum (min.) and maximum (max.) diameters with subsequent averaging (**d**), planimetrically based on perimeter (**e**), or cross-sectional area followed by calculation of derived diameters (**f**)

the cardiac cycle (Fig. 13.22). Most interestingly, two components affect cross-sectional geometry: (1) Stretch of the confining anatomic structures leads to a simultaneous increase in area and perimeter during systole, but (2) Flattening of the aortomitral junction during diastole (with subsequent shortening of short-axis dimensions) leads to an increase in eccentricity with a greater-than-proportional decrease in area compared with perimeter [30]. Annular measurements should

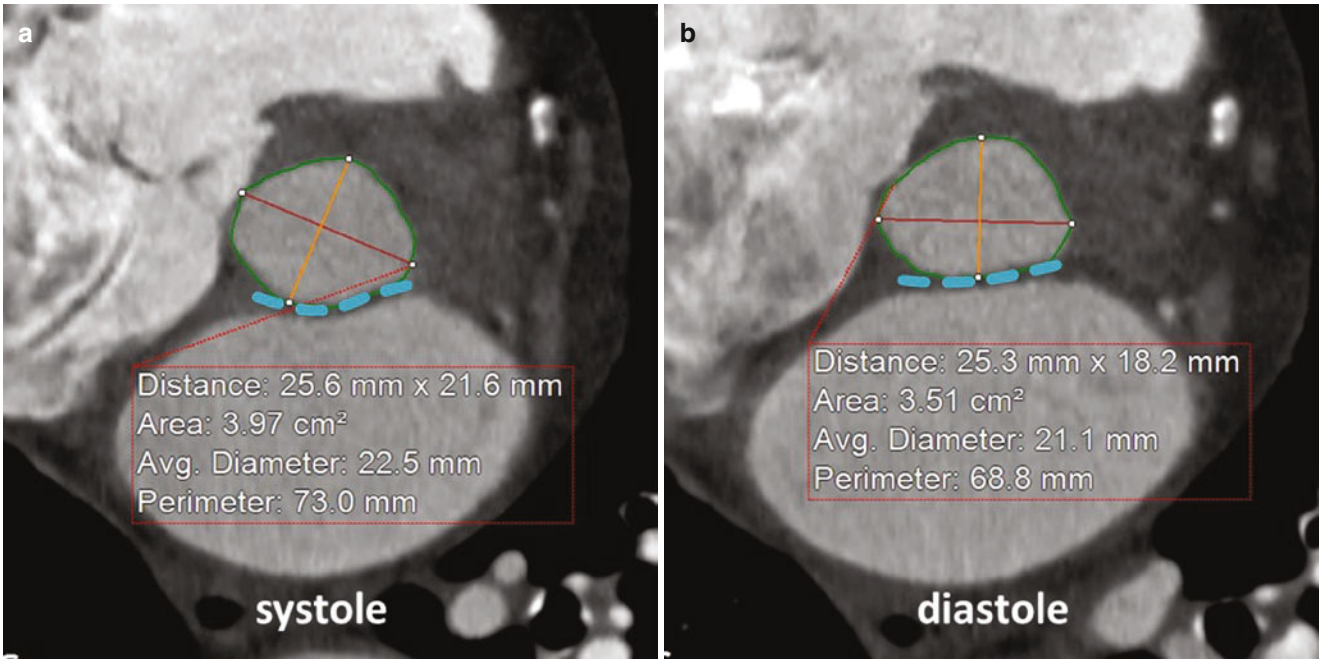

Fig. 13.22 Dynamic changes of the aortic annulus throughout the cardiac cycle, illustrated by a contrast medium–enhanced, retrospective ECG data set obtained in a TAVR candidate with severe aortic stenosis. Mid-systolic (**a**) and early diastolic (**b**) double-oblique transverse views are shown transecting through the annulus plane at the most basal attachments of all three cusps. Pulsatile changes lead to an increase in perimeter and cross-sectional area during systole. Conformational geometric changes are predominantly due to bulging and flattening of the aortomitral junction (*dashed line*) during systole and diastole, with a subsequent increase in eccentricity during diastole

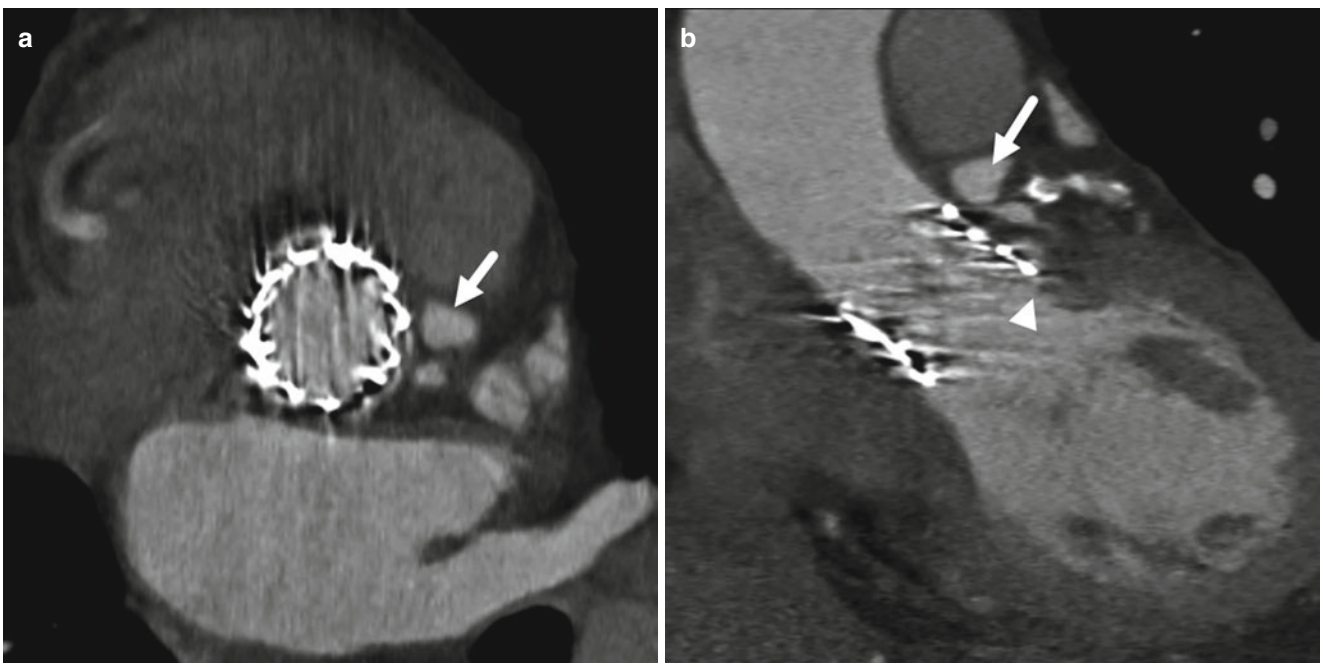

Fig. 13.23 Contained annulus rupture after balloon-expandable TAVR. Transverse double oblique (**a**) and coronal oblique (**b**) views of a post-TAVR cardiac CT on postoperative day 6. Images reveal correct positioning of the transcatheter heart valve (THV). A contrast opacified pseudoaneurysm (*arrows*) is discernible adjacent to the aortic root at the position of the native left coronary cusp, originating from the left ventricular outflow tract (*arrowhead*), establishing the diagnosis of contained aortic root rupture. Close relation to the left main coronary artery can be appreciated

be performed during systole in order to avoid prosthesis undersizing.

Regardless of the use of perimeter or area, CT has been consistently shown to provide reproducible and detailed assessments of the annulus that are more effective than 3D TEE assessments for the identification of patients who are likely to experience greater than mild paravalvular aortic regurgitation. These measurements allow for a more thoughtful and integrated approach to transcatheter heart valve selection than any two-dimensional diameter can provide, enabling more controlled device oversizing and annular stretch.

Although technically limited by its two-dimensional nature, prosthesis position can be assessed on the routinely performed post-deployment angiogram. Furthermore, intraoperative TEE aids in the demonstration of appropriate prosthesis function and positioning and the evaluation of paravalvular regurgitation. As with endovascular repair or aortic root surgery [36], patients may undergo post-interventional cardiac CT, not only to document proper valve position. In our experience, if renal function is not impaired, cardiac CT is a valuable tool to rule out clinically asymptomatic aortic root complications such as aortic dissection and contained rupture with formation of pseudoaneurysms (Fig. 13.23). Furthermore, post-interventional CT may give direct 3D feedback to the interventionalist on prosthesis positioning and may reveal underlying causes for paravalvular leaks. A typical appearance of a prosthesis on post-deployment CT is illustrated in Fig. 13.24. In balloon-expandable TAVR, post-deployment CT will show a circularly unfolded transcatheter heart valve (THV) in most

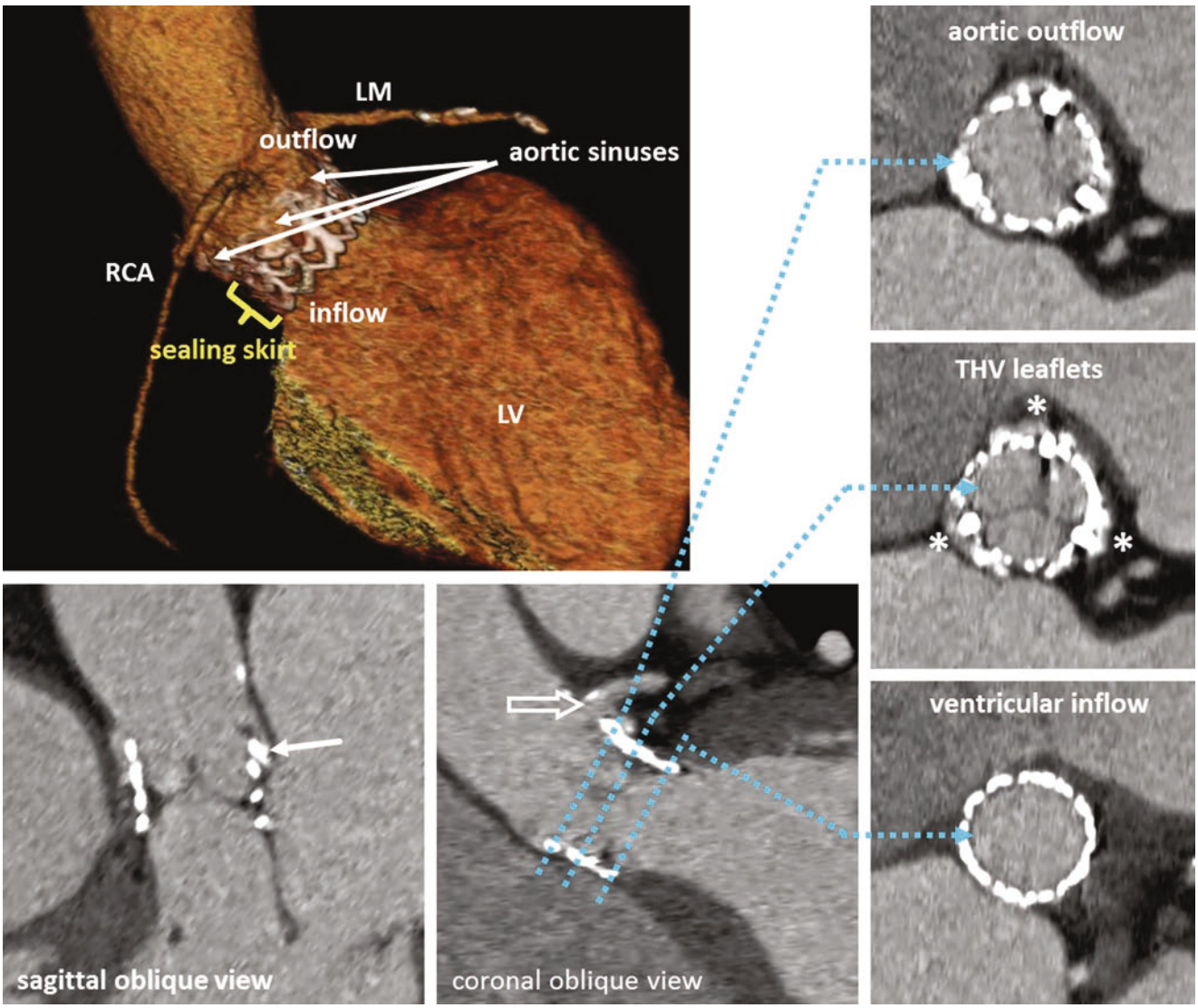

Fig. 13.24 Balloon-expandable Edwards Sapien XT valve (Edwards Lifesciences, Irvine, CA). Post-deployment cardiac CT after TAVR shows the optimal position of the prosthesis. Volume-rendered reconstruction as well as MPRs show the THV position in relation to the aortic sinuses, left main artery (LM, *open arrow*), and right coronary artery (RCA). Native valvular calcifications (*arrows*) are displaced into the aortic sinus (*asterisks*), while the coronary orifices are preserved. The THV is circularly unfolded at all levels and shows complete apposition with its entire circumference at its inflow level to the upper LVOT

patients [28, 31, 37], with native leaflet calcifications displaced towards the native sinus. Importantly, THV struts may overlay the coronary ostia, particularly in patients with low sinus heights. This does not imply ostial occlusion, as the upper third of the THV is not covered by a sealing cuff.

Post-deployment CT findings are remarkably different with the self-expandable CoreValve THV (Medtronic). The typical appearance of the CoreValve THV on post-deployment CT is illustrated in Fig. 13.25. Because of the self-expandable nature of the device, post-deployment geometry is obviously more dependent on the underlying anatomy and the extent and degree of native leaflet calcifications; native annulus geometry is preserved.

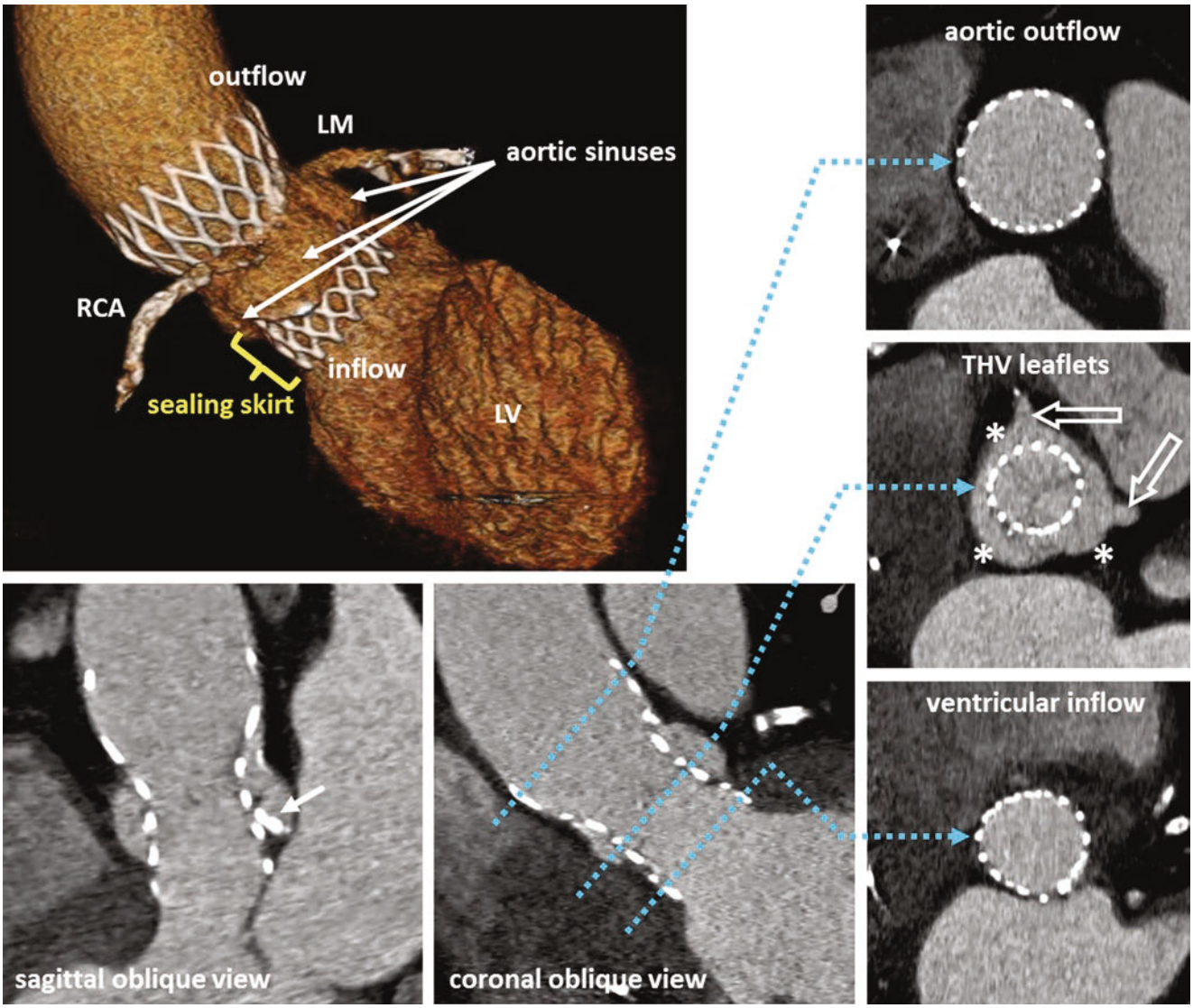

Fig. 13.25 Self-expandable CoreValve THV. Post-deployment cardiac CT after TAVR shows the self-expandable CoreValve in optimal position. Volume-rendered reconstruction as well as MPRs depict the THV position in relation to the aortic sinuses, LM, and RCA. Native valvular calcifications are displaced into the aortic sinus (*arrows*), while the coronary orifices (*open arrows*) and sinus are preserved because of the THV's constrained zone in its mid-portion. The THV is circularly unfolded at all levels and shows complete apposition with its entire circumference at its inflow level to the upper LVOT

Mitral Valve

CT Assessment of Mitral Valve Anatomy and Function

Unlike the aortic valve, which is suspended above the left ventricle, allowing for fairly consistent reconstruction of its short axis, the mitral valve separates the structural left ventricle from the left atrium with a saddle-shaped annulus that is integrated into the fibrous skeleton of the left ventricle, connecting the mitral valve to the aortic valve. This complex anatomy and location makes its evaluation much more complicated and difficult than the evaluation of the aortic valve. The mitral valve consists of two leaflets, anterior and posterior, each of which consists of three scallops (Fig. 13.26). The leaflets are anchored and stabilized by tendinous chords arising from the anterolateral and posteromedial papillary musculature within the left ventricle. CT evaluation is performed by MPRs in similar orientation to the four-chamber view, three-chamber view, and two-chamber view (long-axis views) and short-axis views in MRI or echocardiography (Fig. 13.27).

In the setting of a normal, competent and functioning mitral valve, leaflets will demonstrate complete coaptation during systole, in a crescent-shape fashion with the convexity formed by the anterior leaflet, and the concavity formed by the posterior leaflet (*see* Fig. 13.26). Given the nonplanar orientation of the coaptation within the 3D space, however, the degree of coaptation cannot be determined on a single MPR view. Instead, scrolling through the short-axis images and MinIPs allow for assessment of coaptation (*see* Fig. 13.27). The mitral valve opens in early diastole with maximum leaflet excursion during early rapid ventricular filling. With progression of diastole, leaflet excursion reduces to a more closed position, to fully open again during late diastole with the onset of the atrial systole. Similar to the leaflet coaptation during systole, the mitral valve orifice is not planar, making the planimetry of the mitral valve area difficult. Furthermore, redundant leaflet tissue (as well as partial volume effect on the very thin leaflet tissue) further hampers discrimination of the leaflet margins and the actual mitral valve orifice. In our opinion, employing MinIPs for planimetry of the valve orifice is optimal. The normal mitral valve area (MVA) ranges between 4.0 and 6.0 cm^2 and is usually comma-shaped.

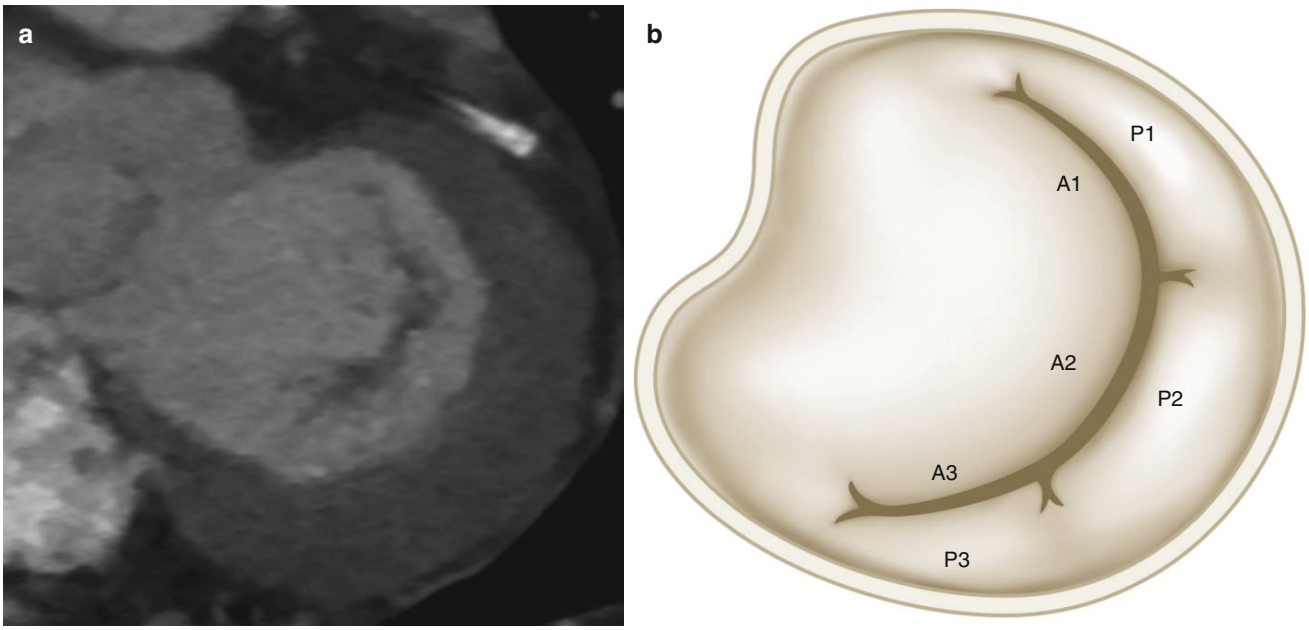

Fig. 13.26 Mitral valve anatomy. Systolic short-axis view of the mitral valve (**a**) and corresponding schematic drawing (**b**), depicting the anterior (A1, A2, A3) and posterior (P1, P2, P3) mitral valve leaflets

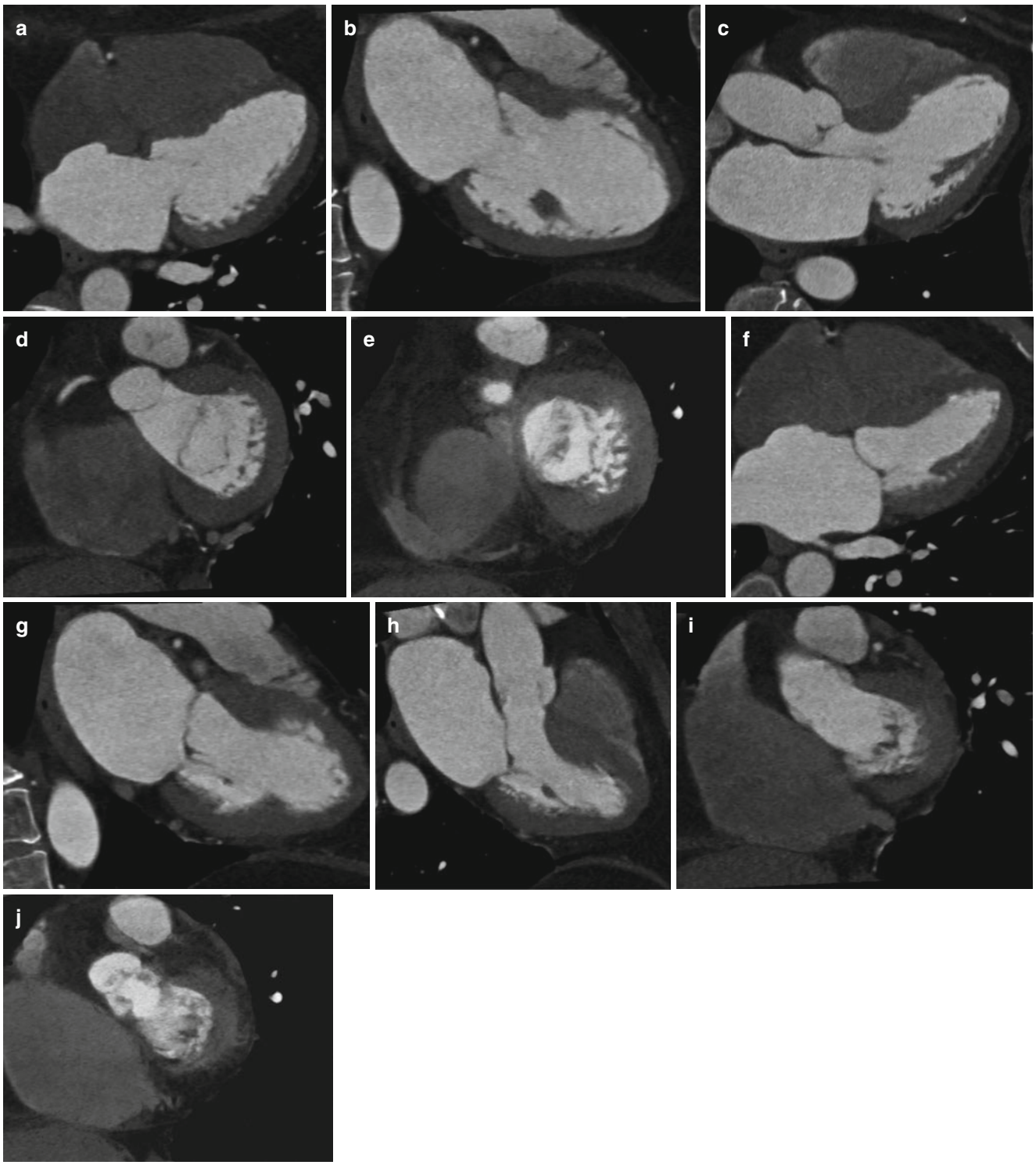

Fig. 13.27 Mitral valve assessment. Diastolic four-chamber view (**a**), two-chamber view (**b**), three-chamber view (**c**) and short-axis view (**d**, MPR; **e**, MinIP) demonstrate a normal mitral valve with unrestricted leaflet motion. Complete coaptation can be appreciated on corresponding systolic images (**f**–**j**)

Mitral Valve Stenosis

Mitral valve stenosis implies a MVA less than 2.5 cm^2, with mild stenosis ranging between 2.5 and 1.5 cm^2, moderate between 1.5 and 1.0 cm^2, and severe with an MVA less than 1 cm^2. The overall prevalence of mitral valve stenosis in North America is approximately 0.1% [22]. By far the most common cause of mitral valve stenosis is rheumatic heart disease, which causes a broad spectrum of pathologies including leaflet thickening, commissural fusion, and chordal fusion, which may be identified on cardiac CT (Fig. 13.28). The result of these pathologies is narrowing, elongation, and the remodeling of the mitral valve into a more conical configuration [38]. Though the assessment of mitral stenosis is more complicated and difficult than aortic stenosis evaluation, planimetry of MVA is possible, particularly in the setting of thickened leaflet margins (Fig. 13.29). Cardiac CT acts as a useful alternative to echocardiography for the determination of mitral stenosis severity, particularly in patients with poor acoustic windows. Limited single-center data in

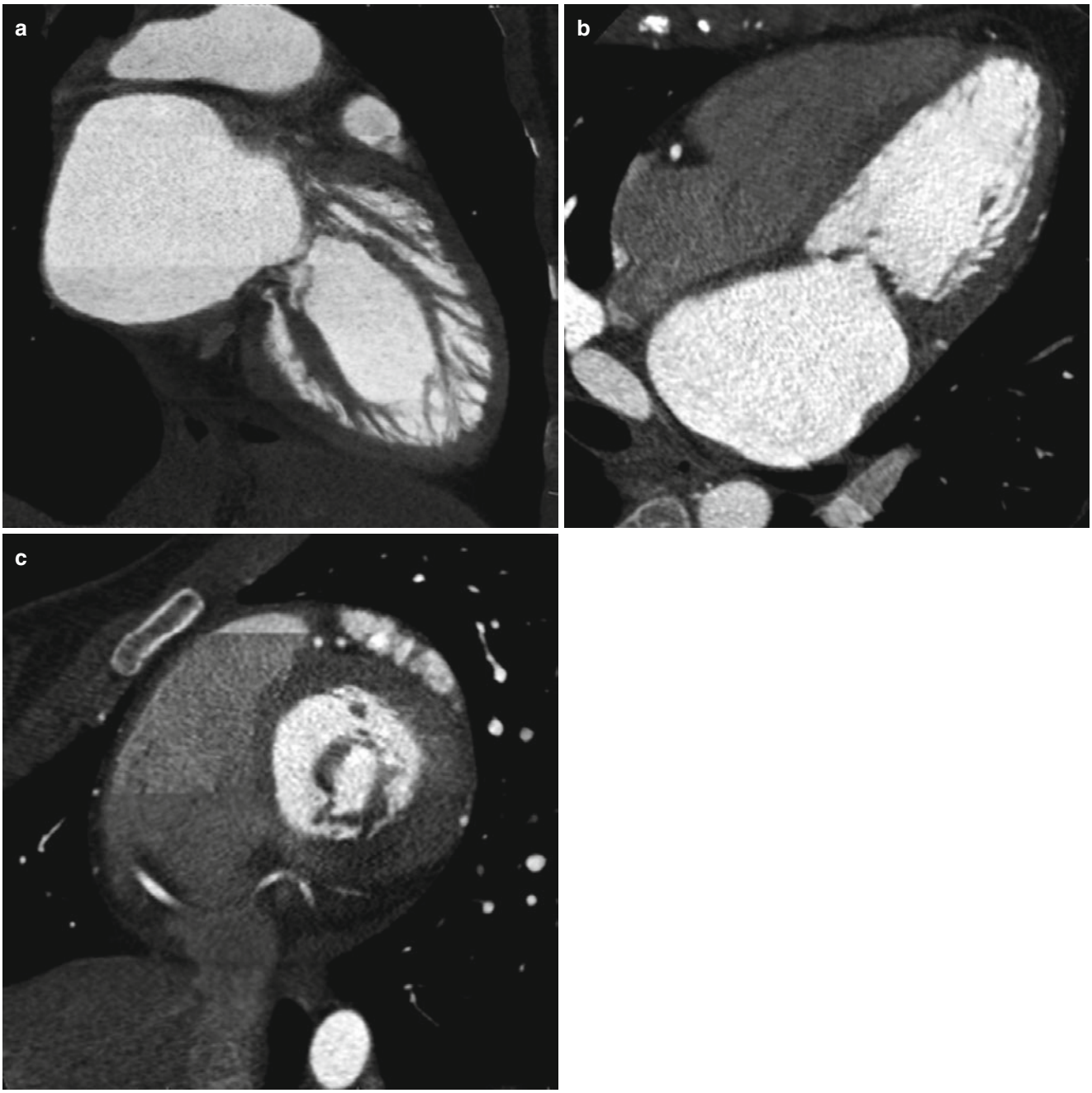

Fig. 13.28 Rheumatic mitral valve disease. Diastolic image of a 47-year-old female patient with a history of rheumatic heart disease (**a**, two-chamber view; **b**, four-chamber view; **c**, short-axis view), depicting mitral valve leaflet thickening with reduced mitral valve area, establishing the diagnosis of mild mitral valve stenosis

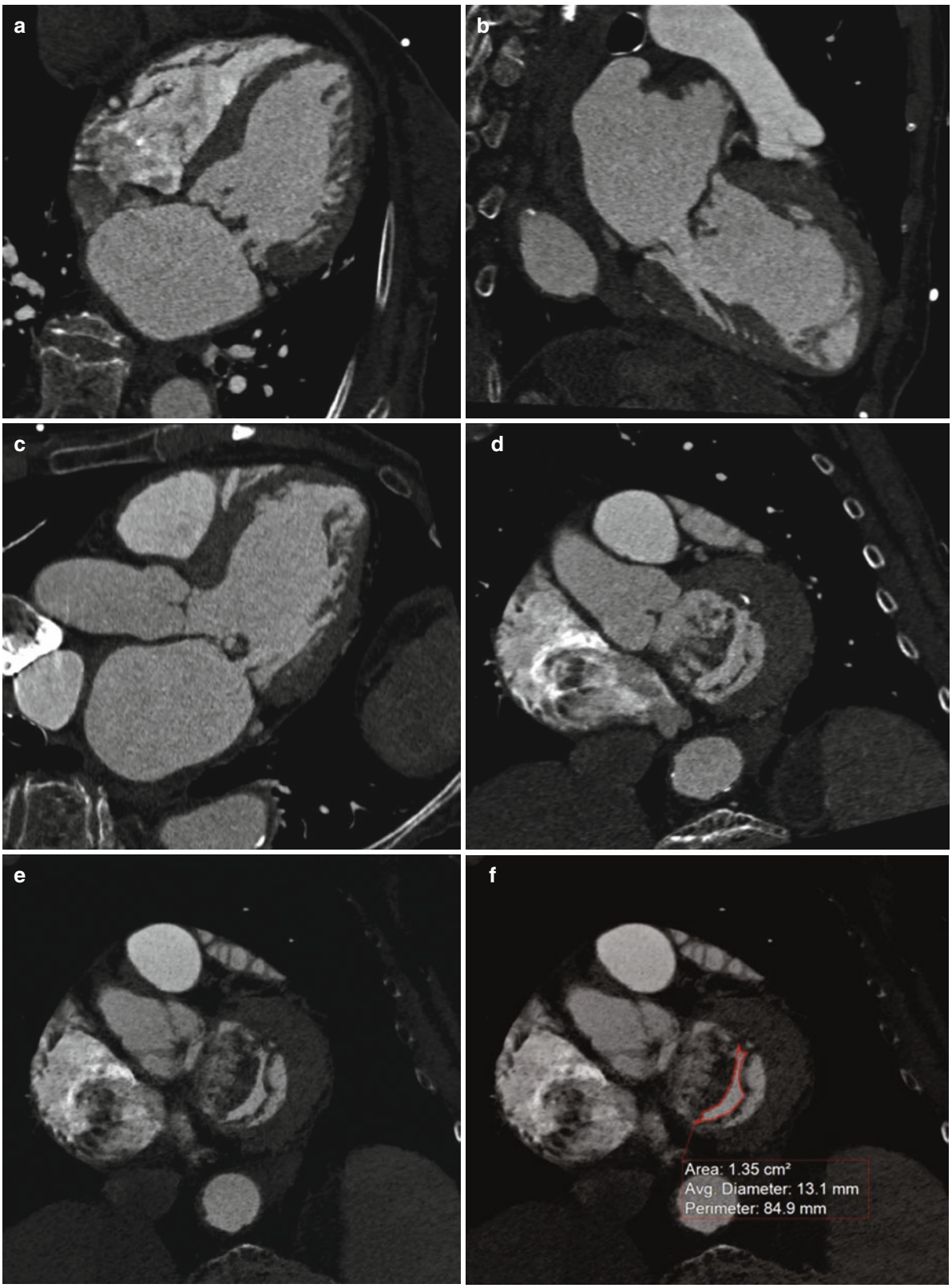

Fig. 13.29 Moderate mitral valve stenosis. Diastolic four-chamber view (**a**), two-chamber view (**b**), three-chamber view (**c**), and short axis view (**d**) demonstrating thickening of the mitral valve leaflets with restricted motion and limited mitral valve orifice area. Better delineation is achieved with a MinIP (**e**). Planimetry yields a mitral valve area of 1.35 cm^2 (**f**)

selected patient populations suggest that when the MVA is measured by planimetry at 75% of the RR interval with cardiac CT, MVA quantification can be achieved more accurately than with echocardiography, with low interobserver variability [39]. It has been noted that the cardiac CT–derived anatomic MVA is larger than that obtained by transthoracic echocardiography (TTE), but cardiac CT yields good correlation with TTE for the detection of moderate to severe mitral stenosis [39].

Mitral Regurgitation

Incomplete coaptation of the mitral valve leaflets results in regurgitation. The numerous pathologic etiologies of mitral insufficiency include prolapse, restriction, chordal damage, rheumatic disease, and the sequelae of infective endocarditis. These entities result in what is called structural mitral valve regurgitation (Fig. 13.30). Pathologies of the left ventricle that result in LV dilatation, such as ischemic and nonischemic

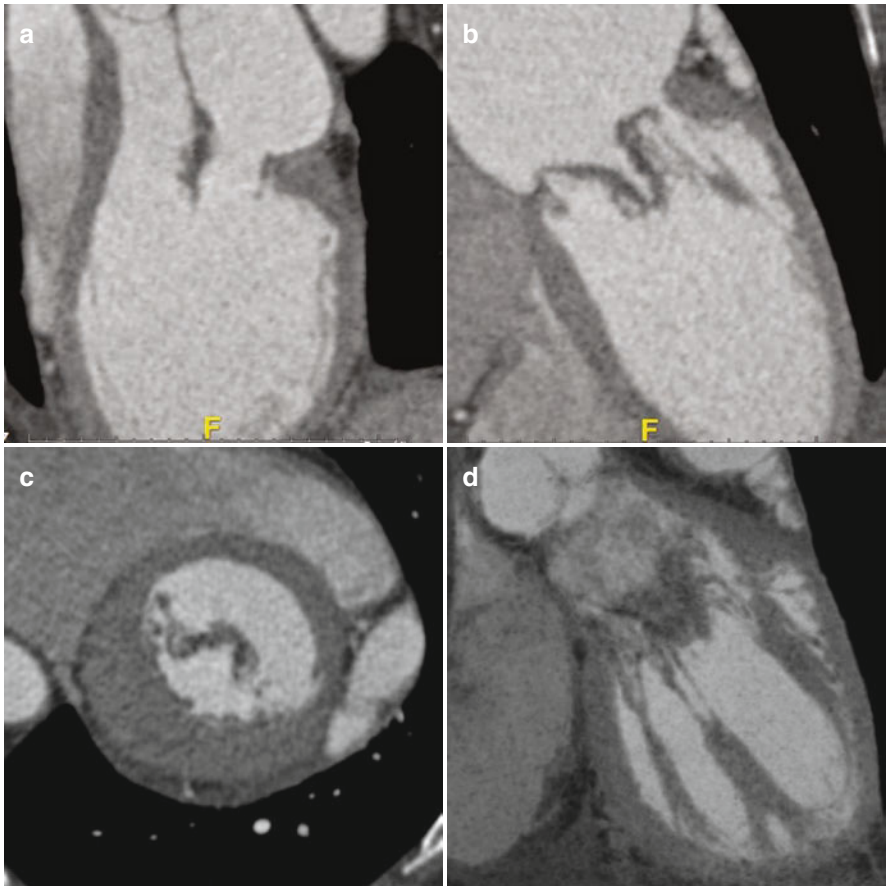

Fig. 13.30 Myxoid degeneration of the mitral valve apparatus in a Marfan patient. A three-chamber view (**a**), two-chamber view (**b**), and short-axis view (**c**) during diastole depict thickened mitral valve leaflets. MinIP (**d**) is angulated to depict the thickened anterior mitral valve leaflet and the tendinous chords

cardiomyopathy, can result in functional mitral regurgitation owing to annular ectasia and deformity or to LV remodeling with a subsequent lack of sufficient central leaflet coaptation [40, 41].

Though cardiac CT is limited in its ability to quantify the severity of mitral insufficiency [42], small single-center studies have shown it to correlate well with echocardiography [43, 44]. The strength of cardiac CT is its ability to measure the regurgitant orifice area (ROA), which can be difficult to evaluate with traditional echocardiographic assessment. Through multiplanar reformation, cardiac CT can allow for the planimetry of the ROA (assuming adequate image quality). Cardiac CT also has been shown to be effective in identifying structural abnormalities such as mitral valve prolapse and leaflet thickening [45]. Mitral valve prolapse is defined as systolic displacement of the mitral valve leaflets below the mitral annular plane (toward the left atrium) by 2 mm or more [46]; it can be subclassified into two types: billowing (bowing of the leaflet body) and flail leaflet (free leaflet edge prolapse). Billowing typically occurs in the course of myxomatous degeneration (Figs. 13.31 and 13.32), whereas flail leaflet is caused by chordal rupture in the presence of rheu-

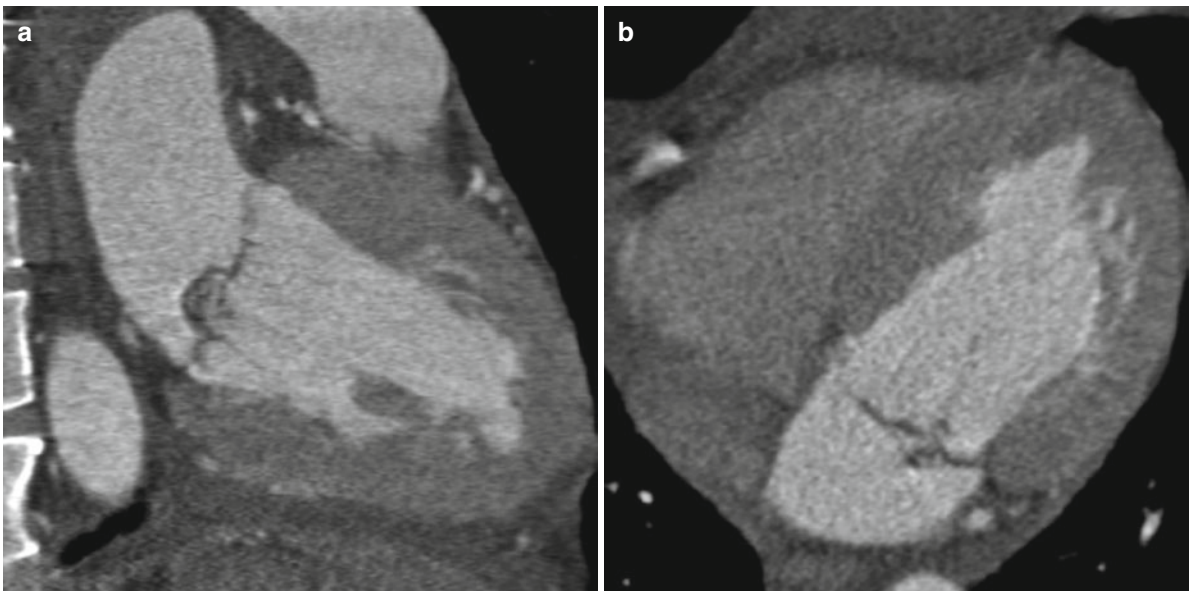

Fig. 13.31 Mitral valve prolapse. Systolic two-chamber view (**a**) and four-chamber view (**b**) depicting thickening and prolapse of the posterior mitral valve leaflet

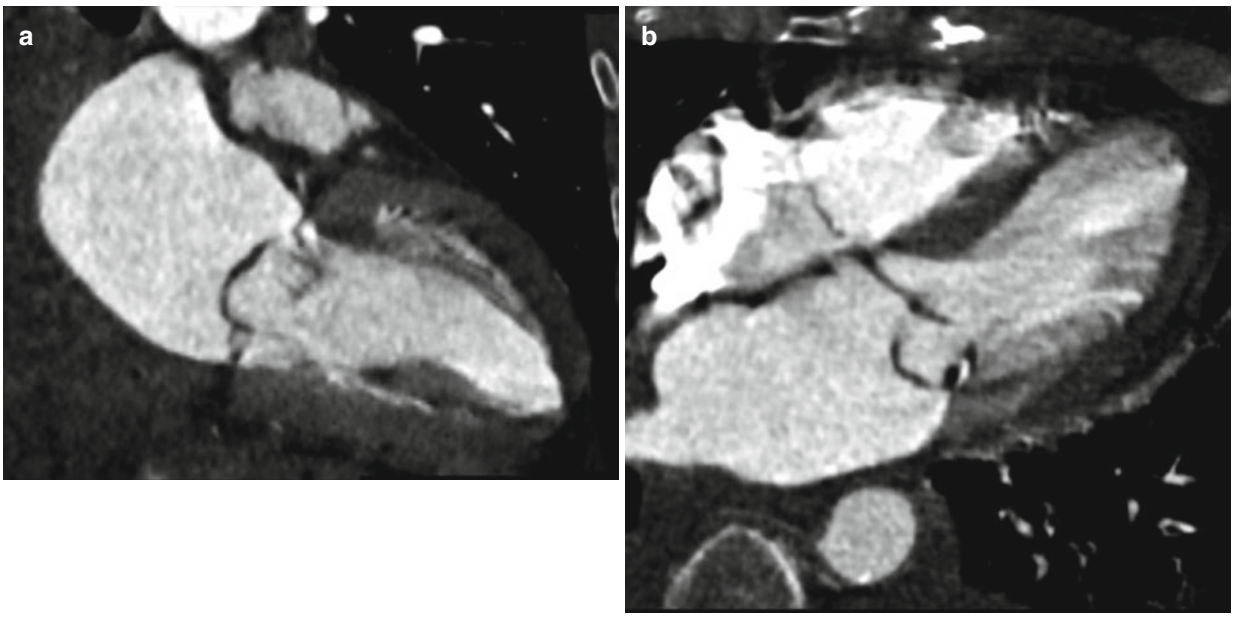

Fig. 13.32 Prolapse of the posterior mitral valve leaflet. Systolic two-chamber view (**a**) and four-chamber view (**b**) demonstrating prolapse of the posterior mitral valve leaflet

matic disease, ischemia, or infective endocarditis. The prevalence of mitral valve prolapse is approximately 2.4% in the North American population [47]. Though mitral regurgitation is more common in patients with mitral valve prolapse, it is usually trace or mild [47]. Given the saddle-shaped geometry of the mitral valve annulus, the presence of mitral valve prolapse is commonly identified on the three-chamber view on echocardiography. In contrast, leaflet billowing (and thus the prevalence of mitral valve prolapse) tends to be overestimated on the four-chamber view, given the closer position of the annulus towards the apex on this view [48] (Fig. 13.33).

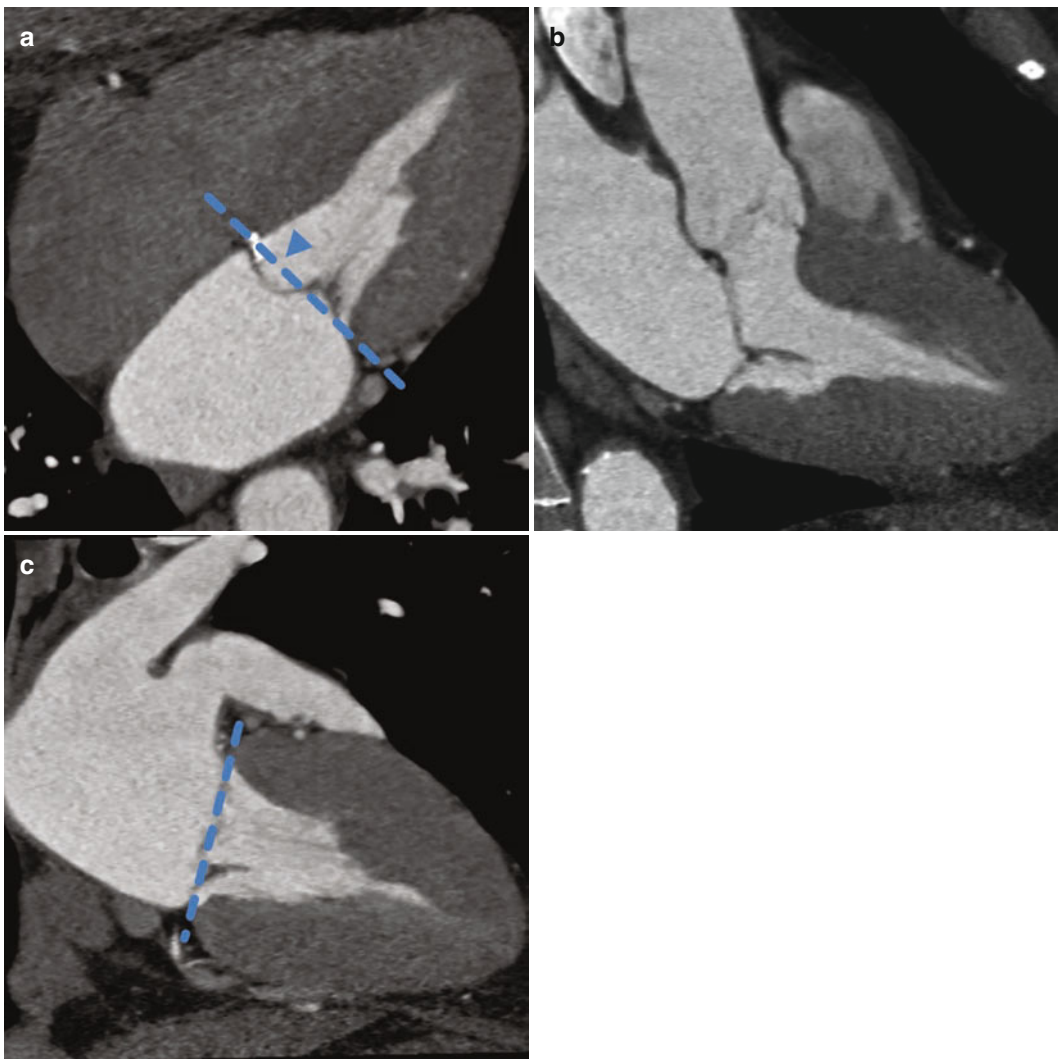

Fig. 13.33 Pseudoprolapse of the anterior mitral valve leaflet. Systolic four-chamber view (**a**), three-chamber view (**b**), and two-chamber view (**c**) depicting a normal mitral valve. Because of the saddle-shaped mitral valve annulus, a pseudoprolapse of the mitral valve leaflets toward the left atrium (*dashed line, arrowhead*) may be noted on the four-chamber view, while leaflets do not prolapse on the three-chamber and two-chamber views

Calcification of the mitral annulus is relatively common and more frequently involves its posterior aspect. Importantly, it does not generally interfere with mitral valve function. In contrast, mitral valve leaflet calcification may cause restricted leaflet motion that can be seen on CT (Fig. 13.34). A rare but impressive variant referred to as caseous annulus calcification (Fig. 13.35) can be misconstrued as a tumor, especially if noncontrast imaging is not available to confirm the calcified nature of the abnormality (Fig. 13.36).

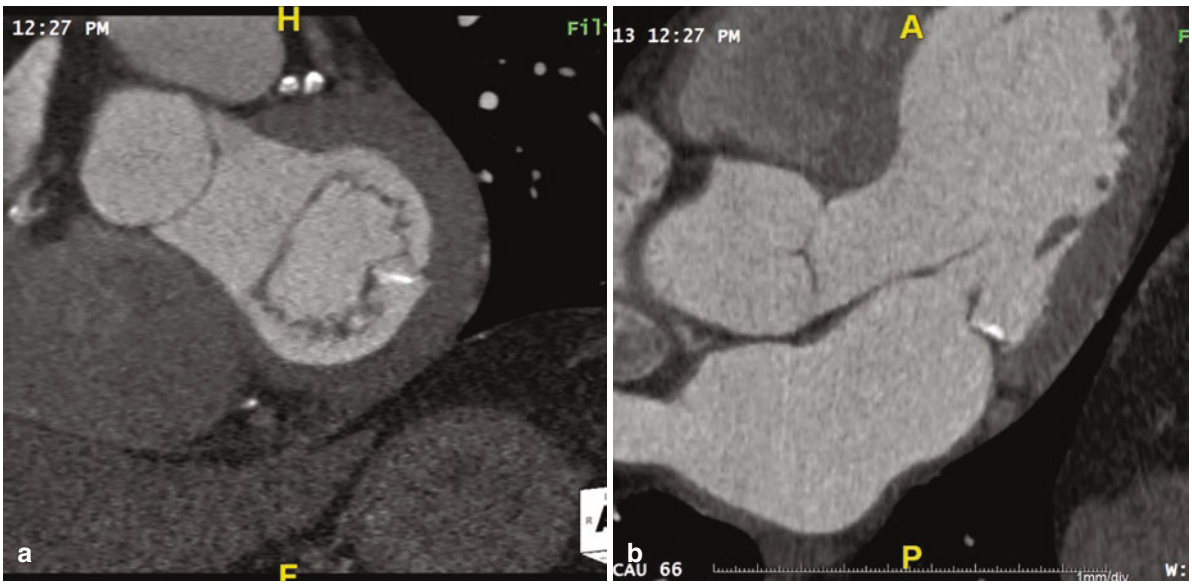

Fig. 13.34 Mitral valve leaflet calcification. Diastolic short-axis view (**a**) and three-chamber view (**b**) depicting focal calcification of the posterior mitral valve leaflet with subsequent restricted movement

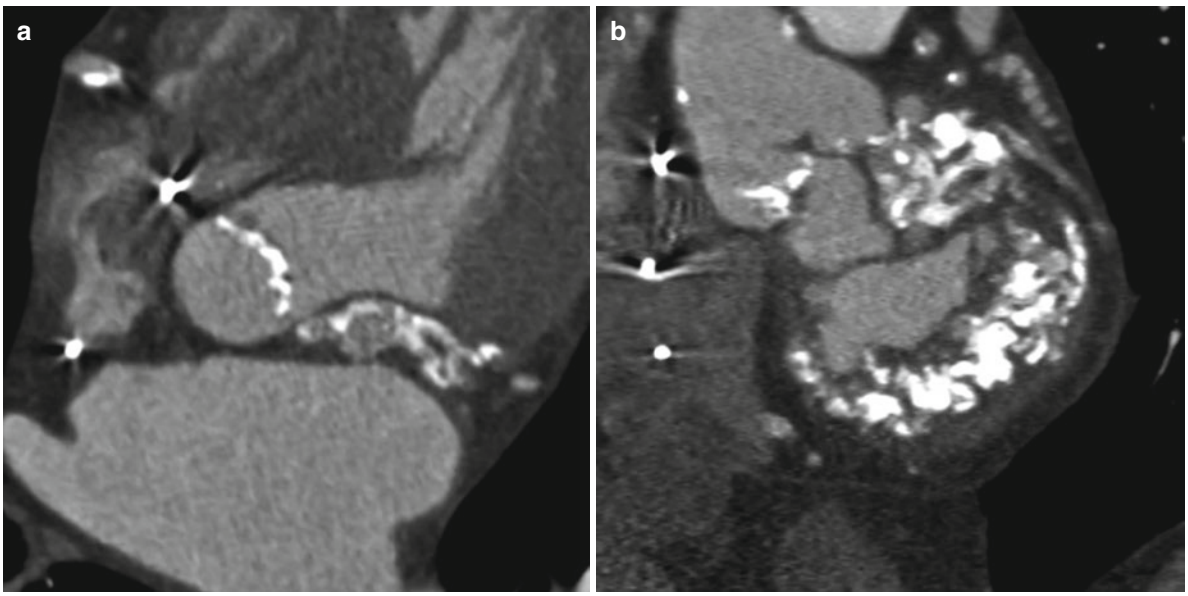

Fig. 13.35 Caseous mitral annular calcification. Contrast-enhanced transverse axial (**a**), short-axis (**b**), and two-chamber (**c**) view reformations depicting caseous mitral annular calcification with tumorlike extension into the myocardium. Importantly, with the use of contrast-enhanced imaging in isolation, the foci of calcification can be misconstrued as contrast, owing to its similar attenuation with the blood pool. Nonenhanced images with similar orientations (**d**–**f**) clearly depict the extensive calcification

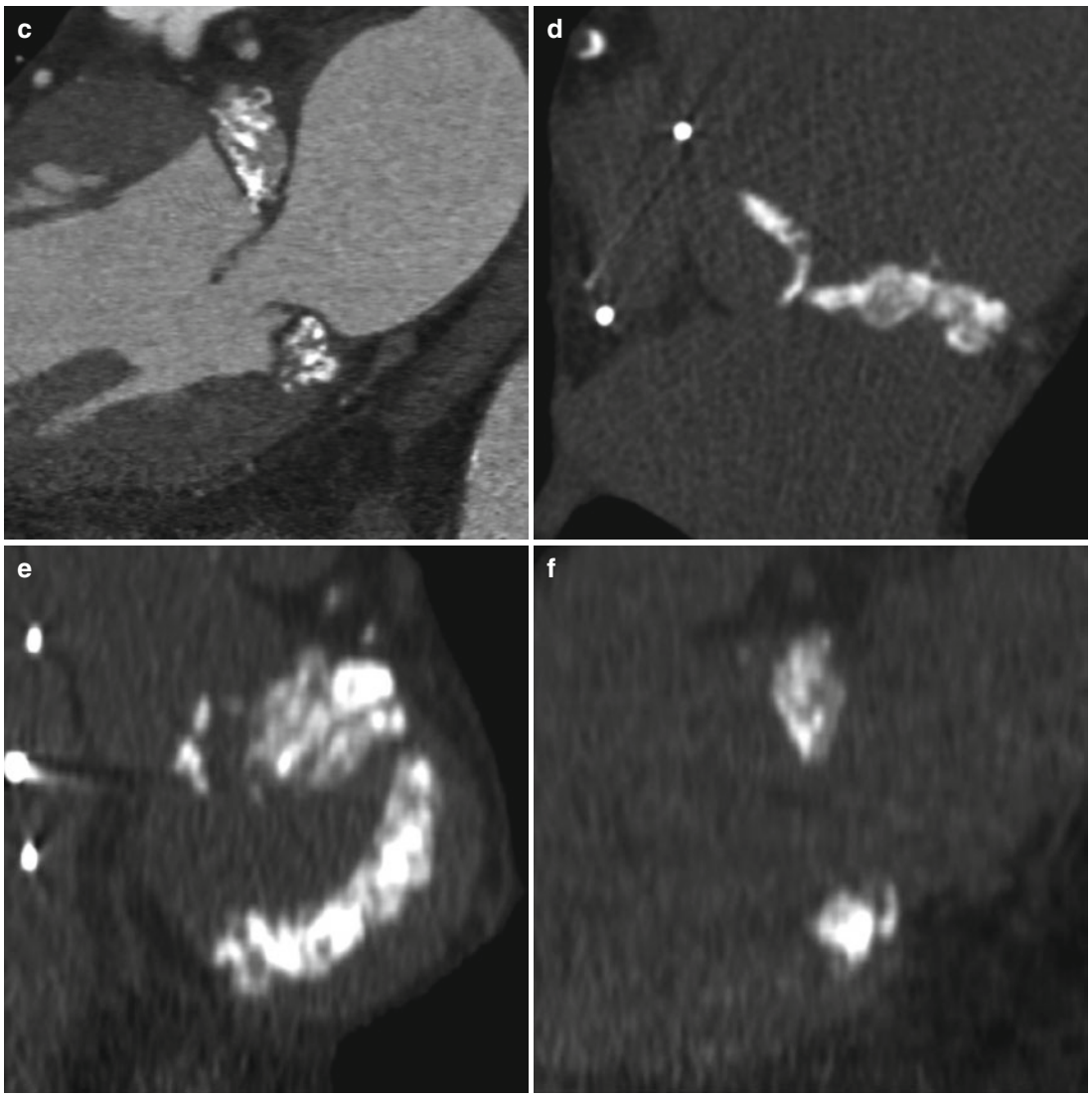

Fig. 13.35 (continued)

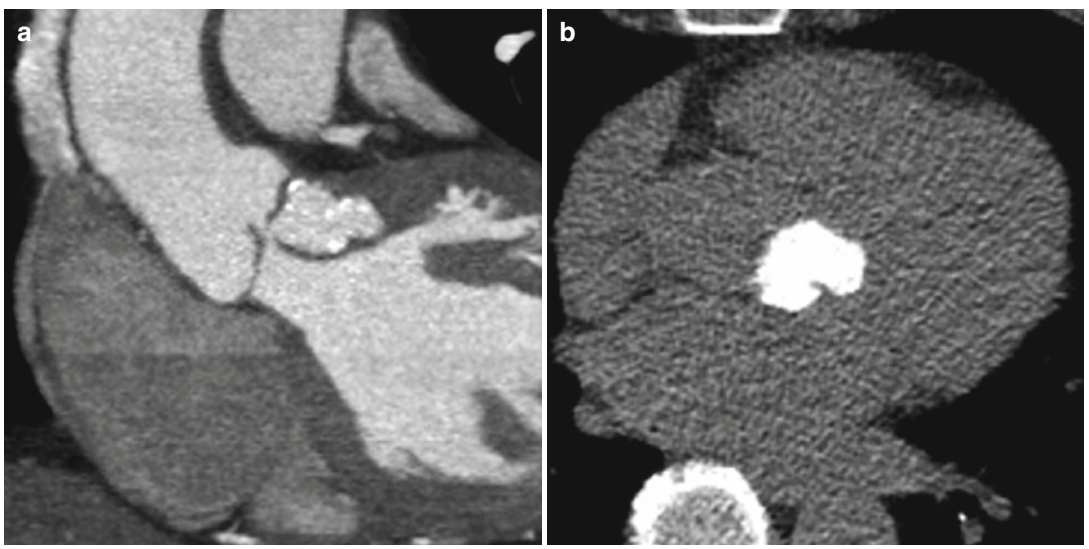

Fig. 13.36 Caseous mitral annular calcification. On a contrast-enhanced coronal oblique view (**a**), masslike isolated caseous calcification of the anterior aspect of the mitral valve annulus, with resultant obstruction of the LVOT, mimicks either a tumor or a contrast-filled cavity, in keeping with an abscess or pseudoaneurysm following infective endocarditis. Non-enhanced cardiac CT (**b**, strict axial reconstruction) identifies the true extent of the calcification

Findings After Surgical Mitral Valve Replacement or Repair

Dilatation of the mitral annulus may be both a cause and a consequence of mitral insufficiency due to either left ventricular or left atrial enlargement. Relevant mitral regurgitation may be treated with so-called annuloplasty by implantation of an annular ring to restrict annulus size and improve leaflet coaptation (Fig. 13.37). In cases of degenerated leaflets, a wide variety of mitral valve prostheses may be implanted, ranging from mechanical valves (Fig. 13.38) to bioprostheses with or without radiopaque rings (Fig. 13.39). As with aortic valve prostheses, cardiac CT may identify mitral valve prosthesis malfunction and its causes.

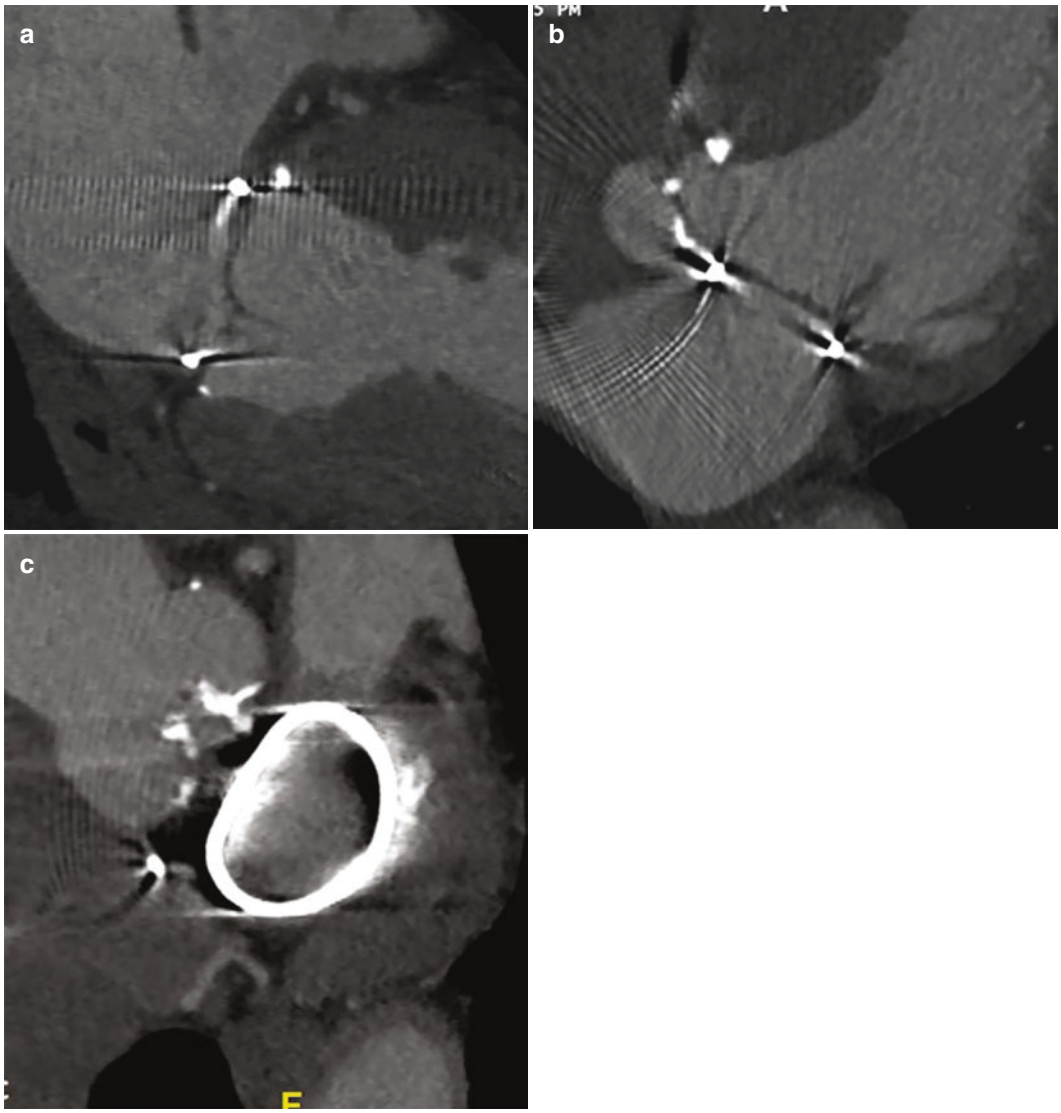

Fig. 13.37 Mitral valve annuloplasty. Systolic two-chamber view (**a**), four-chamber view (**b**), and short-axis view (**c**) after mitral valve annuloplasty for annular ectasia and resultant mitral regurgitation. A radiopaque annuloplasty ring and the native mitral valve can be identified

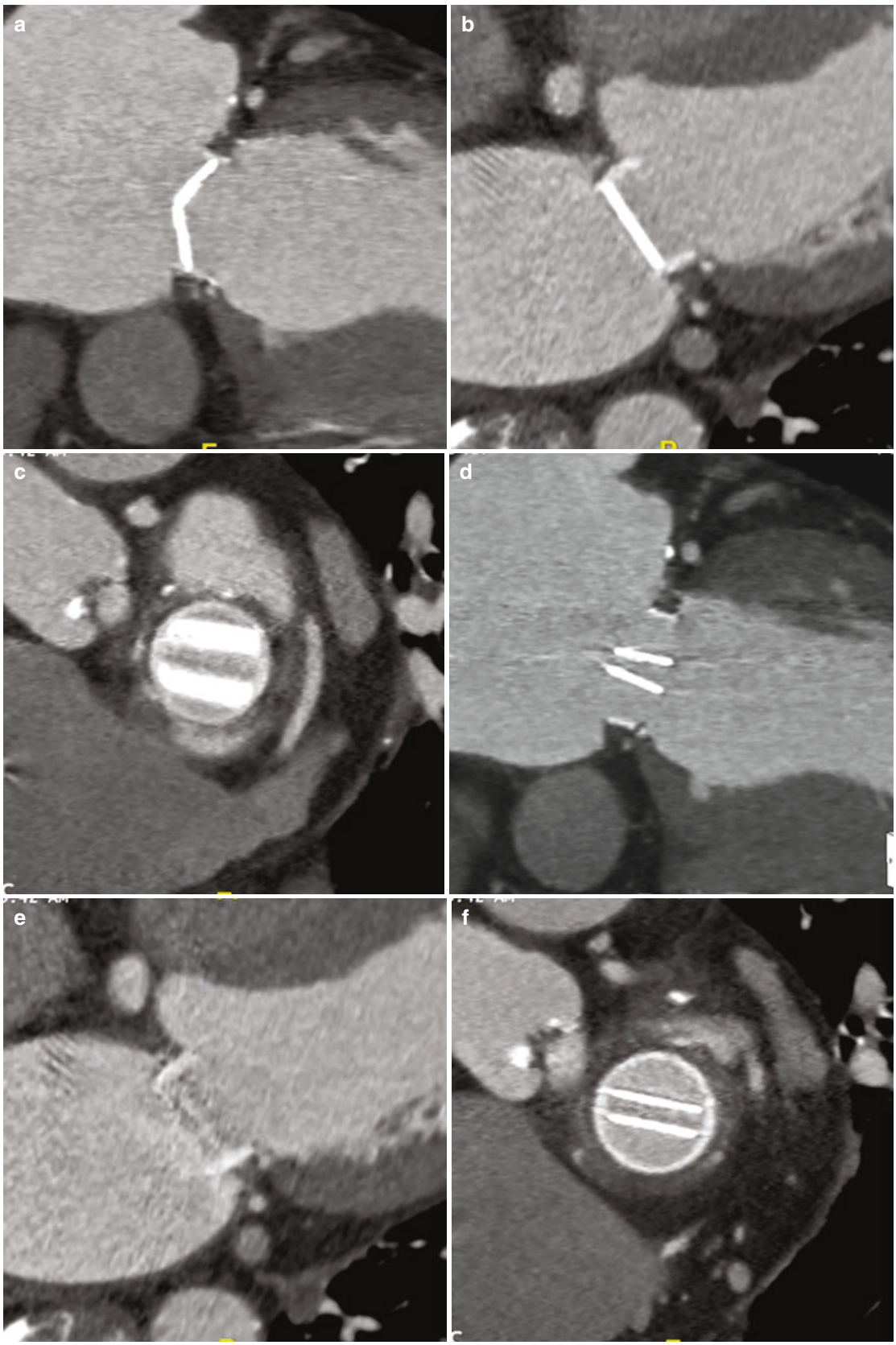

Fig. 13.38 Mechanical mitral valve prosthesis with two tilting discs. Two-chamber (**a**), four-chamber (**b**), and short-axis (**c**) views during systole, and the same views during diastole (**d**–**f**)

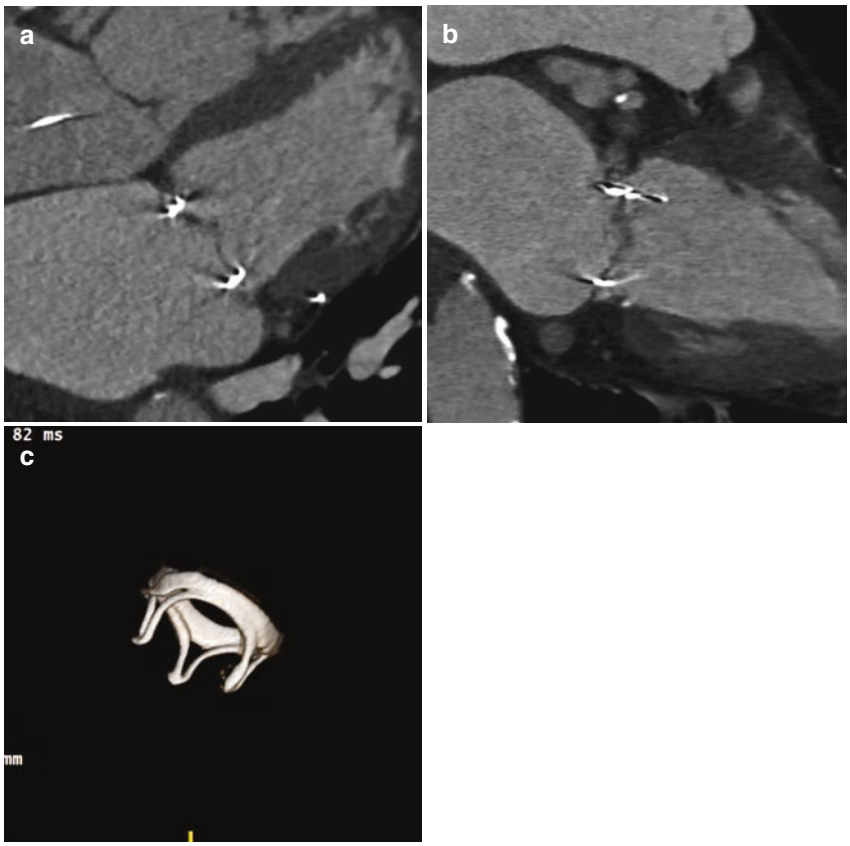

Fig. 13.39 Mitral valve bioprosthesis. Systolic four-chamber view (**a**) and two-chamber view (**b**) depicting a biological three-leaflet mitral valve prosthesis with a radiopaque sewing ring. (**c**), Volume-rendered image of the sewing ring

Transcatheter Mitral Valve Repair

The first nonsurgical treatment for mitral valve disease was balloon valvuloplasty, which was first described for rheumatic mitral stenosis. Since then, further technological advancements have made percutaneous mitral valve therapy possible [49–53]. Clearly, the potential for less invasive percutaneous alternatives replicating surgical procedures without the need for thoracotomy or cardiopulmonary bypass has created significant hope and excitement in the cardiovascular community. These new approaches are most commonly modeled after well-established surgical strategies. The various percutaneous approaches to mitral repair can be divided into procedures that address the various elements and structural components of the mitral valve, commonly considered to be the leaflets, subvalvular apparatus (chordae tendinae and papillary muscles), annulus, left atrium, and left ventricle [51]. All are integral to the normal function of the mitral valve and each is a potential avenue for repair.

Recently introduced strategies for transcatheter mitral valve repair include (1) attempting to create a double-orifice mitral valve by using a percutaneous edge-to-edge technique with a clip device or stitch; (2) remodeling of the annulus of the mitral valve by suture-based techniques or the application of radiofrequency energy; (3) remodeling of the mitral valvular and annular complex by transventricular and/or transatrial devices; and (4) decreasing mitral insufficiency by attempting to remodel the annulus of the mitral valve by devices implanted in the coronary sinus (percutaneous mitral annuloplasty, Fig. 13.40).

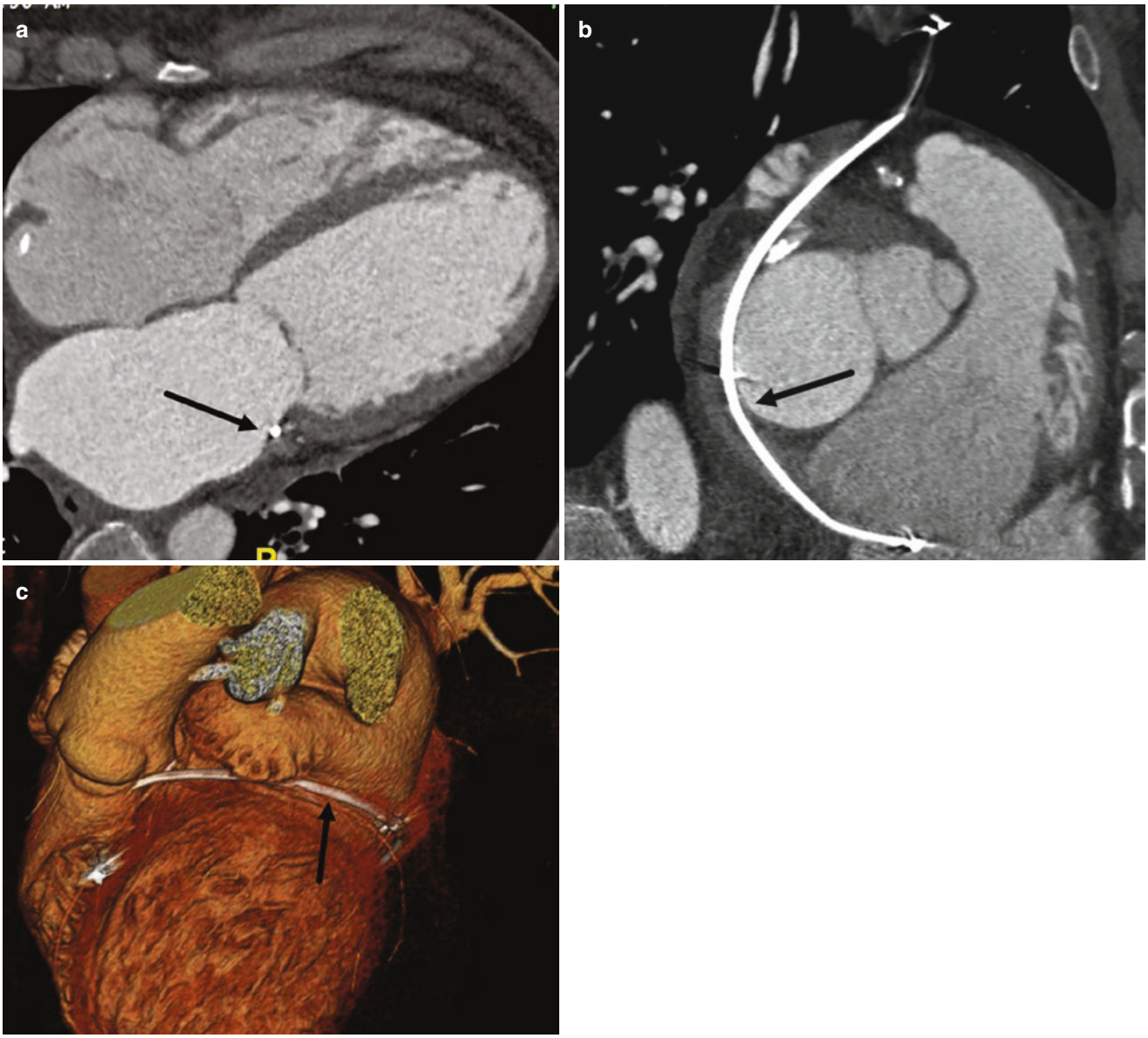

Fig. 13.40 Percutaneous mitral annuloplasty. Four-chamber view (**a**), curved planar reformation (**b**), and volume-rendered image (**c**). The radiopaque annuloplasty device can be appreciated in the coronary sinus and great cardiac vein (*arrow* in **a**)

The Evalve MitraClip system (Abbott Vascular, Santa Clara, CA), recently introduced into clinical practice, aims at improving coaptation of the anterior and posterior mitral valve leaflets by creating a double orifice with a clip grasping both leaflets (Fig. 13.41).

Right-Sided Valve Diseases

Cardiac CT generally performs less well when evaluating right-sided valve disease, partly because of the structure of these valves and partly because of the difficulty in generating adequate and homogeneous opacification of the right-sided chambers, as explained above.

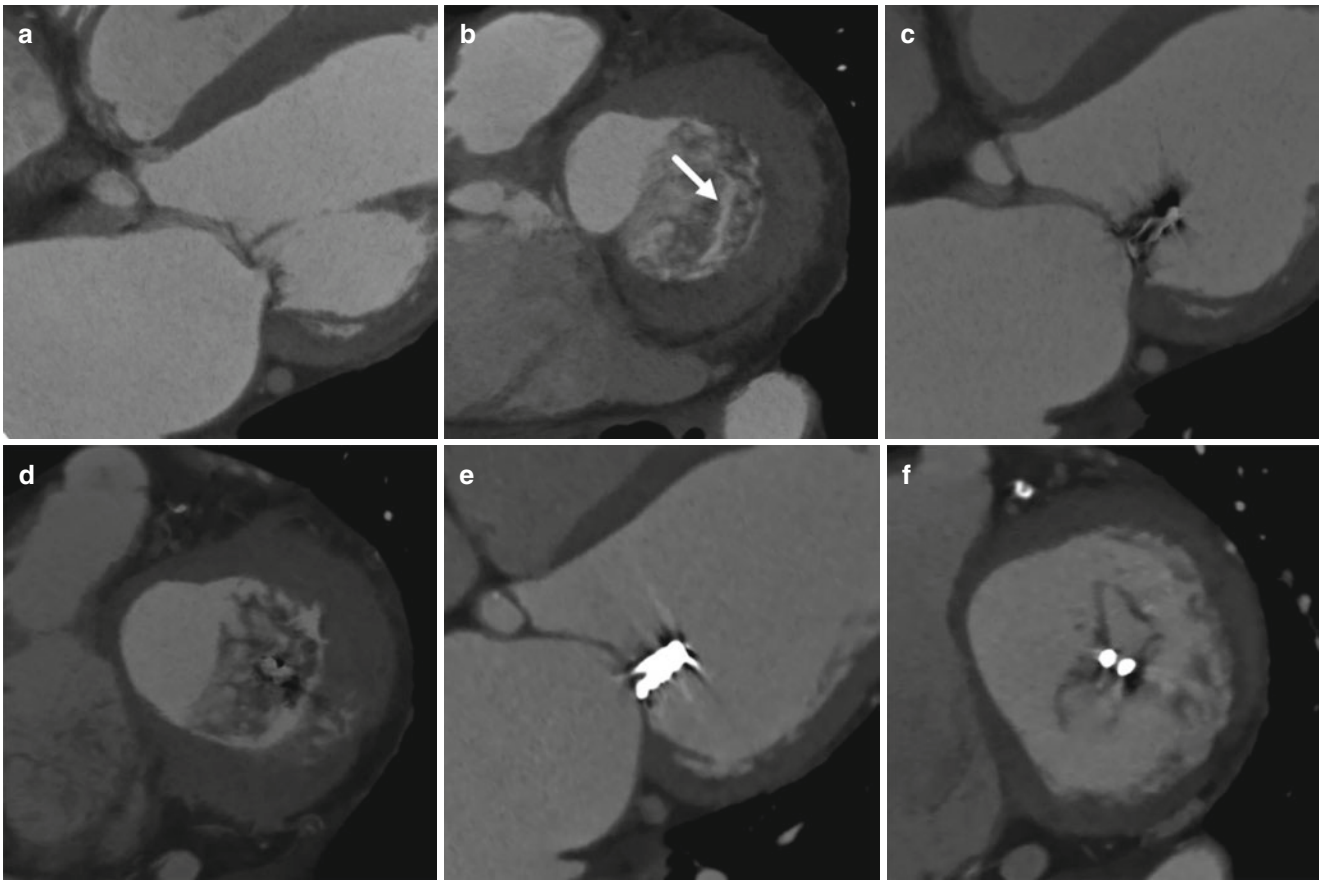

Fig. 13.41 Mitral regurgitation treated with MitraClip. Systolic MinIPs with four-chamber view (**a**) and short-axis view (**b**) prior to implantation. The lack of coaptation and the resulting regurgitant orifice is identified (*arrow* in **b**). Systolic MinIPs (**c**, **d**) after implantation demonstrate improved coaptation. Diastolic MPRs after implantation (**e**, **f**) demonstrate a double-shaped orifice and the radiopaque device

CT Assessment of Pulmonary and Tricuspid Valve Anatomy and Function

The pulmonary valve can be assessed in a similar fashion to the aortic valve, as it is a trileaflet valve and it is suspended above the right ventricle by the conus supraventricularis, allowing for the creation of routine short-axis reformats in the true plain of the pulmonary valve (Fig. 13.42). Normal variants include bicuspid or quadricuspid anatomies (Fig. 13.43). Unlike the aortic valve, however, the pulmonic valve has very thin leaflets, making evaluation difficult [34]. Unfortunately, echocardiography also has significant limitations, given the limited windows for evaluation with TTE and the distance from the esophagus for TEE. MRI is particularly helpful in evaluating and quantifying pulmonary insufficiency, whereas CT allows for excellent anatomical detail, helping to guide transcatheter pulmonic valve therapies (Fig. 13.44).

Pulmonic valve stenosis is most commonly a congenital abnormality resulting in leaflet thickening and doming of the pulmonic valve in systole (Fig. 13.45). This abnormality manifests with classic features of right ventricular hypertrophy and

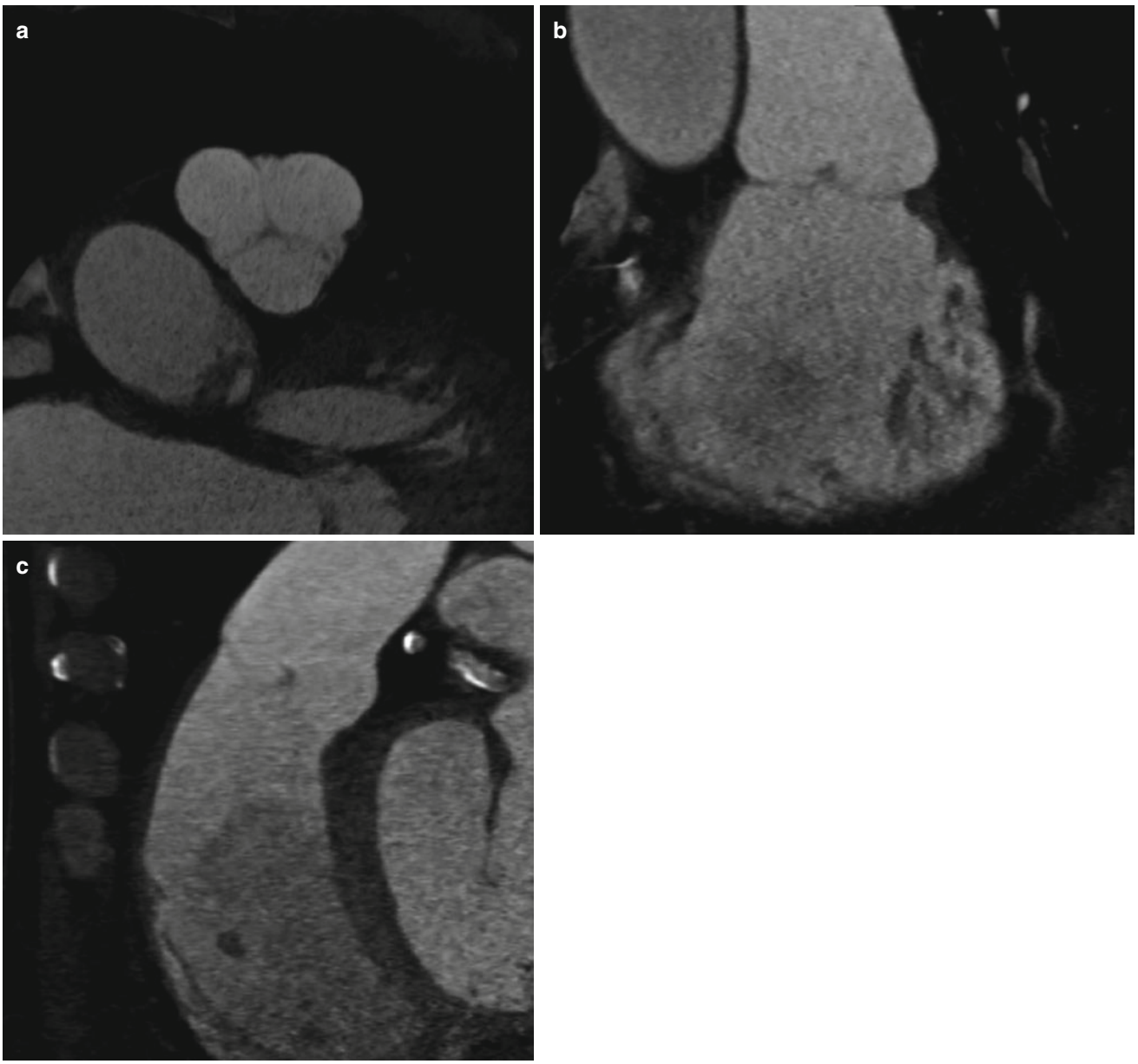

Fig. 13.42 Pulmonic valve. Diastolic short-axis view (**a**), coronal view (**b**), and sagittal short-axis view (**c**) demonstrating a regular-appearing, competent pulmonic valve with complete coaptation. The cusps, which are of normal thickness, are often only faintly visible on cardiac CT

poststenotic dilatation of the pulmonary artery. Pulmonary insufficiency, on the other hand, is most commonly seen with degenerative Tetralogy of Fallot repairs and in the setting of endocarditis. Non-coaptation of the pulmonary valve leaflets is a stigma of pulmonary insufficiency and can be identified on cardiac CT (Fig. 13.46). Cardiac CT can also be used to evaluate right ventricular end-diastolic volume indices (RVEDVIs) in the setting of Tetralogy of Fallot, to help guide surgical intervention in the setting of a contraindication for MRI evaluation, such as an implantable cardiac device. Retrospectively, ECG-gated, CT-derived RVED volumes have been shown to correlate well with MRI [54].

The tricuspid valve is a trileaflet structure consisting of septal, anterior, and posterior leaflets, which are supported by three papillary muscles. Similar to the pulmonic valve, it is more difficult to evaluate owing to its thin structure and contrast mixing issues. As with mitral valve pathology, however, CT can depict a lack of leaflet coaptation in case of tricuspid regurgitation (Fig. 13.47). Cardiac CT does allow for the delineation of anatomical variants of the tricuspid valve, including entities such as Ebstein's anomaly with apical offset of the septal leaflet attachment.

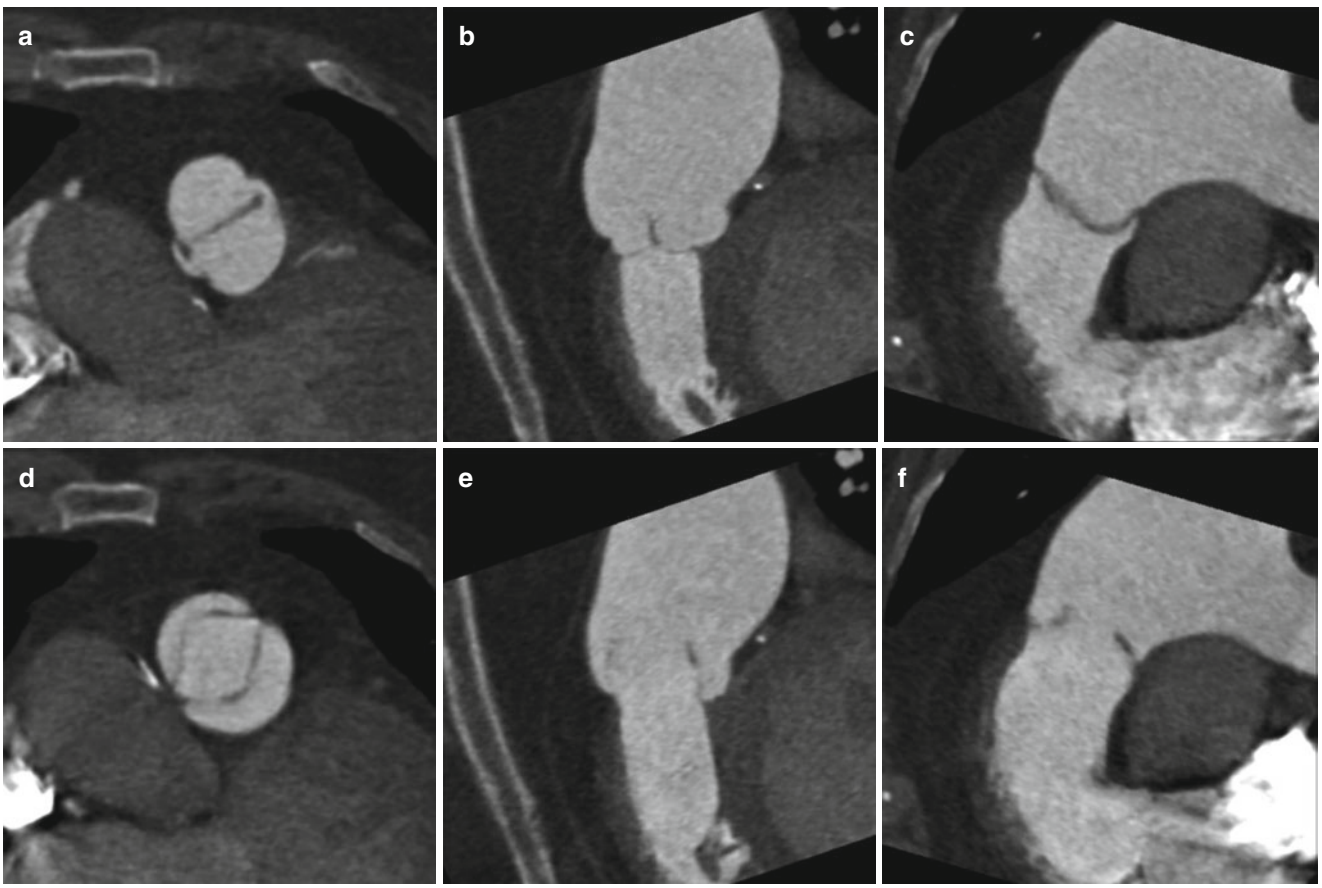

Fig. 13.43 Bicuspid pulmonic valve and pulmonic trunk ectasia. Diastolic short-axis (**a**), coronal (**b**), and sagittal (**c**) views of a bicuspid pulmonic valve with concomitant pulmonic trunk ectasia, and corresponding systolic images (**d**–**f**)

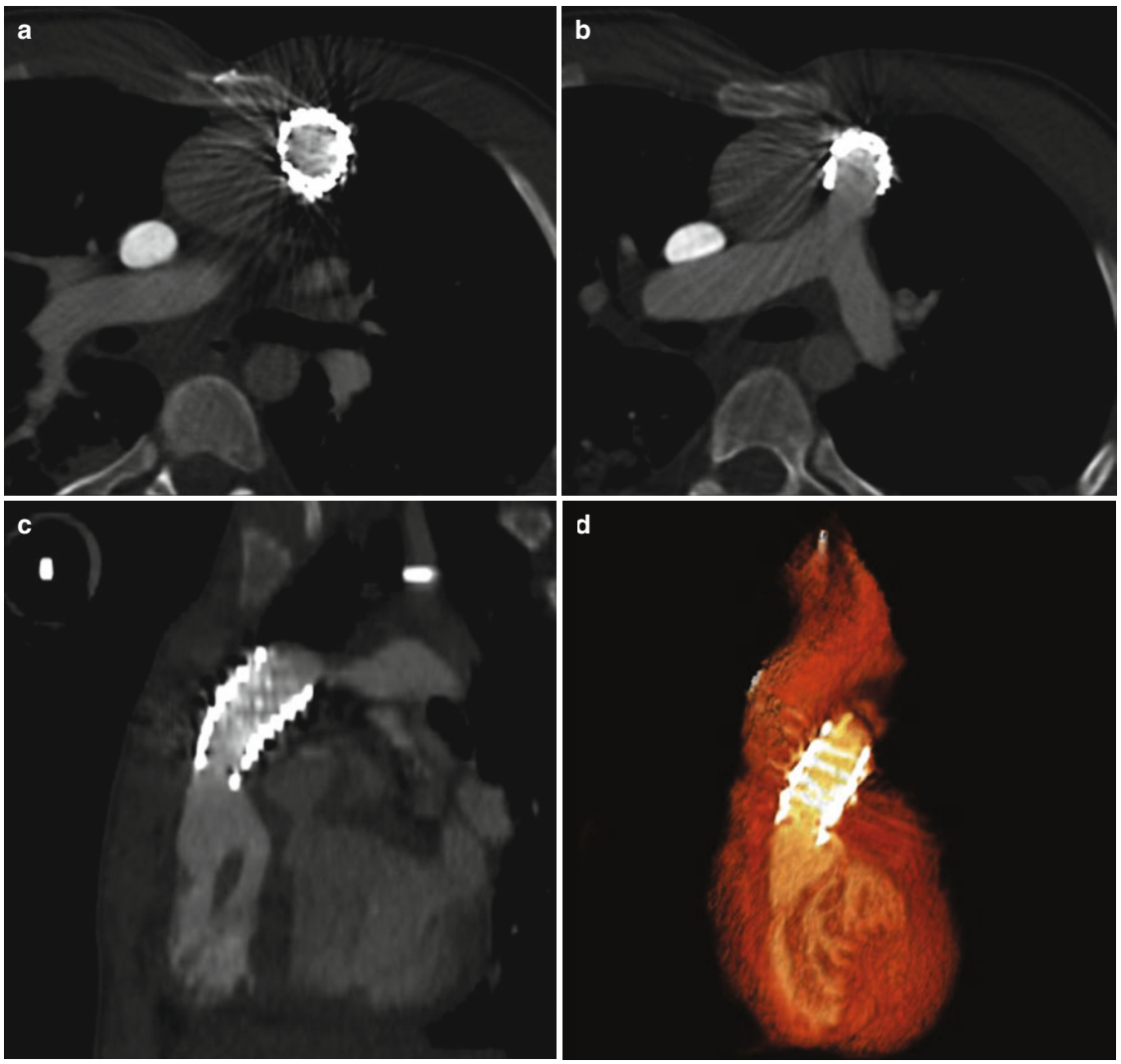

Fig. 13.44 Trancatheter pulmonic valve therapy. Strict axial images (**a**, **b**), a sagittal image (**c**), and a volume-rendered image (**d**) after implantation of a Medtronic Melody® Transcatheter Pulmonary Valve

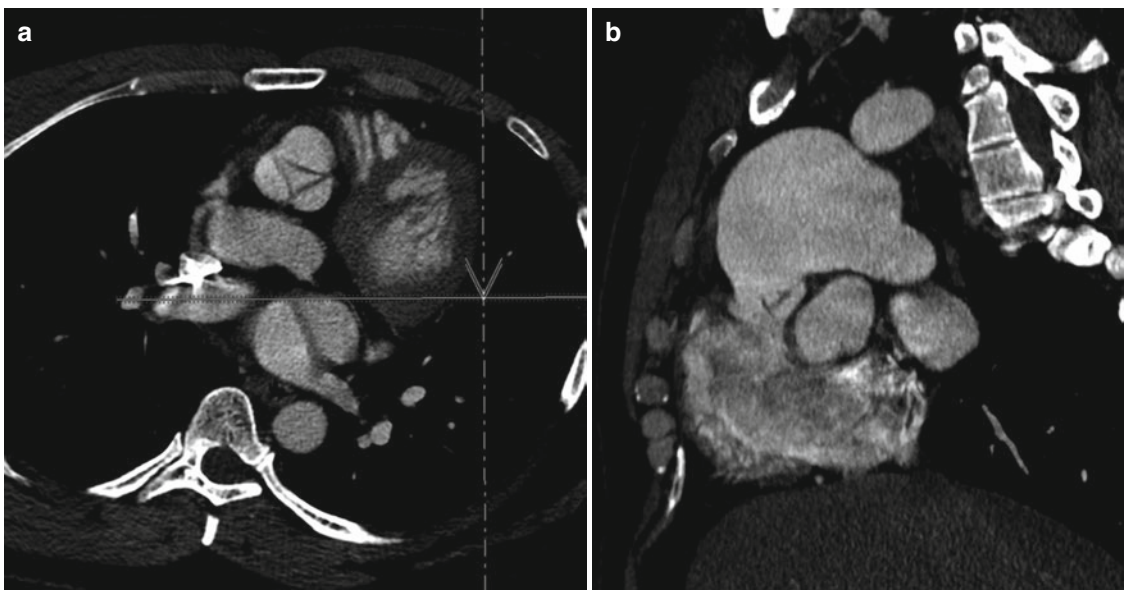

Fig. 13.45 Congenital pulmonic stenosis. Systolic short-axis view (**a**) and sagittal view (**b**) demonstrating leaflet thickening and restricted opening of the pulmonic valve, as well as poststenotic dilatation of the main and left pulmonary artery

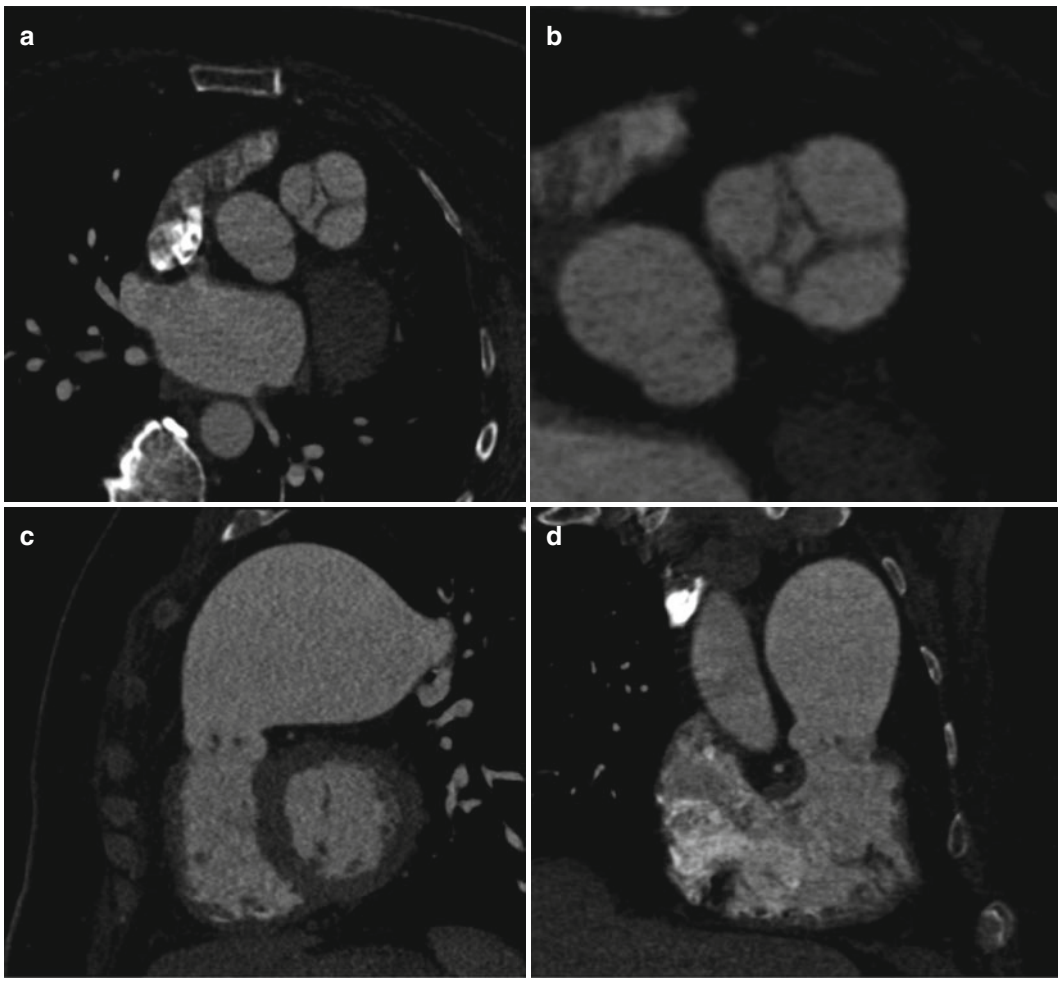

Fig. 13.46 Pulmonic regurgitation and pulmonic trunk aneurysm. Diastolic short-axis view (MPR, **a**) and diastolic short-axis MinIP (**b**) demonstrating incomplete coaptation giving rise to pulmonic regurgitation. Concomitant pulmonic trunk aneurysm can be appreciated on the three-chamber view (**c**) and coronal view (**d**)

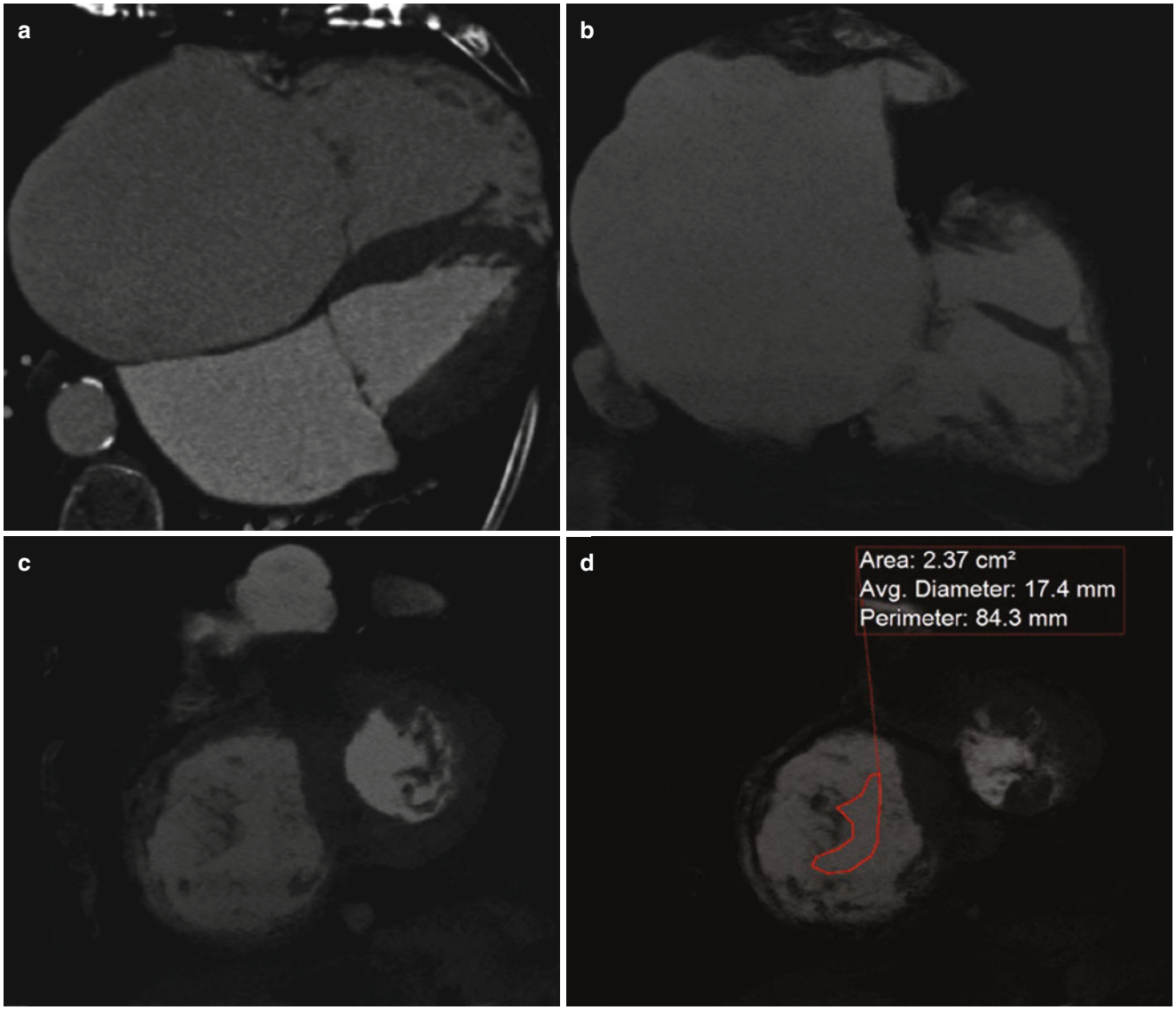

Fig. 13.47 Severe tricuspid regurgitation due to lack of central leaflet coaptation and subsequent right atrial enlargement. Seen on four-chamber MPR (**a**), two-chamber MinIP (**b**) and short-axis MinIP (**c**). Panel (**d**) shows planimetry of the tricuspid valve regurgitant area

Infective Endocarditis

TEE remains the gold standard for the evaluation of infective endocarditis, particularly for the detection of small vegetations and focal valvular perforations of less than 2 mm, but cardiac CT is rapidly asserting itself as an essential tool to provide important ancillary information. Cardiac CT has been shown to be more accurate than TEE in assessing the extent of perivalvular involvement of endocarditis [55]. CT has proven itself particularly valuable in the assessment of complications related to infective endocarditis, such as paravalvular pseudoaneurysms or abscesses, and in some cases, the formation of fistulae (Fig. 13.48). Even subtle changes such as cusp perforation may be depicted by cardiac CT (Fig. 13.49). Unlike echocardiography, which is sometimes limited by visualization windows, CT routinely allows

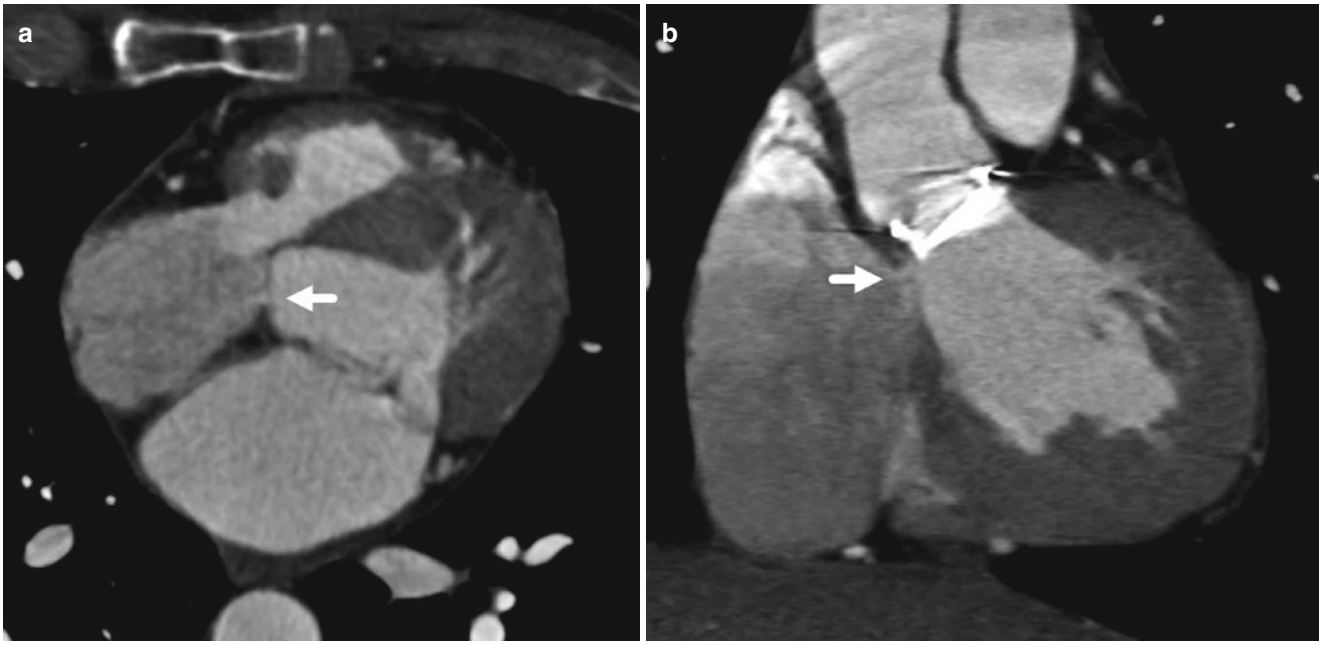

Fig. 13.48 Left-to-right shunt due to endocarditis-related fistula formation, seen on a strict axial source image (**a**) and coronal view (**b**) in a patient with mechanical aortic valve endocarditis. The echocardiographic proven fistula (jet from LVOT into right atrium in **c** can be noted as a discontinuity of the membranous septum on cardiac CT (*arrows* in **a** and **b**)

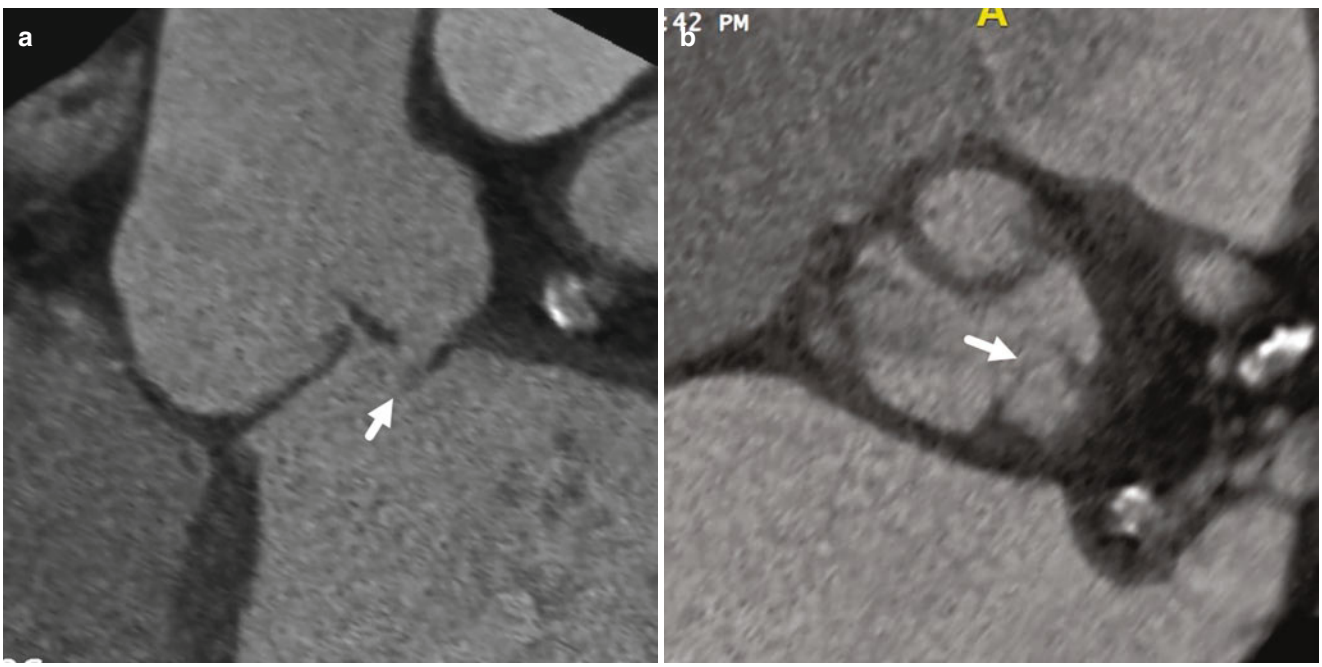

Fig. 13.49 Aortic valve endocarditis with left coronary cusp perforation. A coronal oblique view (**a**) and short-axis view (**b**) demonstrate moderate cusp thickening. A defect in the left coronary cusp can be noted (*arrows*), establishing the diagnosis of cusp perforation

for broad visualization of the entire valvular apparatus in question. CT has been shown to be particularly helpful in the setting of prosthetic valve infection, in which acoustic shadowing from the surgical valves is an even greater limitation of TEE. Common findings with endocarditis are valvular vegetations, which can be delineated on CT images as either focal or diffuse leaflet thickening or bulky appositions. In case of aortic valve endocarditis, vegetations can extend into the LVOT or into the aortic sinuses (Fig. 13.50). It is well known that congenital valvular entities such as bicuspid morphology (Fig. 13.51) and surgical aortic valve replacement predispose to bacterial endocarditis, so an understanding of the normal appearance of these conditions is required when attempting to confirm the presence of an abnormality likely to be due to endocarditis (Fig. 13.52).

In more advanced cases of endocarditis, pseudoaneurysms can be found as contrast-filled cavities adjacent to the aortic root, with direct continuation from the LVOT. Often, these pseudoaneurysms exhibit dramatic changes throughout the cardiac cycle because of the pressure changes in the left ventricle (Fig. 13.53), highlighting the potential benefit of MPRs. Partial or complete dehiscence of the prosthesis from the aorticventricular junction may be observed in advanced stages (Fig. 13.54).

The advantage of CT is the demonstration of the extent and location of perivalvular involvement, to delineate the sites of communication between the pseudoaneurysm and the aorta and LVOT for presurgical planning.

Importantly, any potentially infectious valvular vegetations must be differentiated from noninfectious valvular appositions, such as thrombi and tumors. A rare tumor, which is most often found on the aortic side of the aortic valve, is the papillary fibroelastoma. These tumors are usually mobile, pedunculated, round masses. Although they are benign, the risk of thrombogenic stroke warrants their surgical removal, although views differ regarding the size at which removal is indicated.

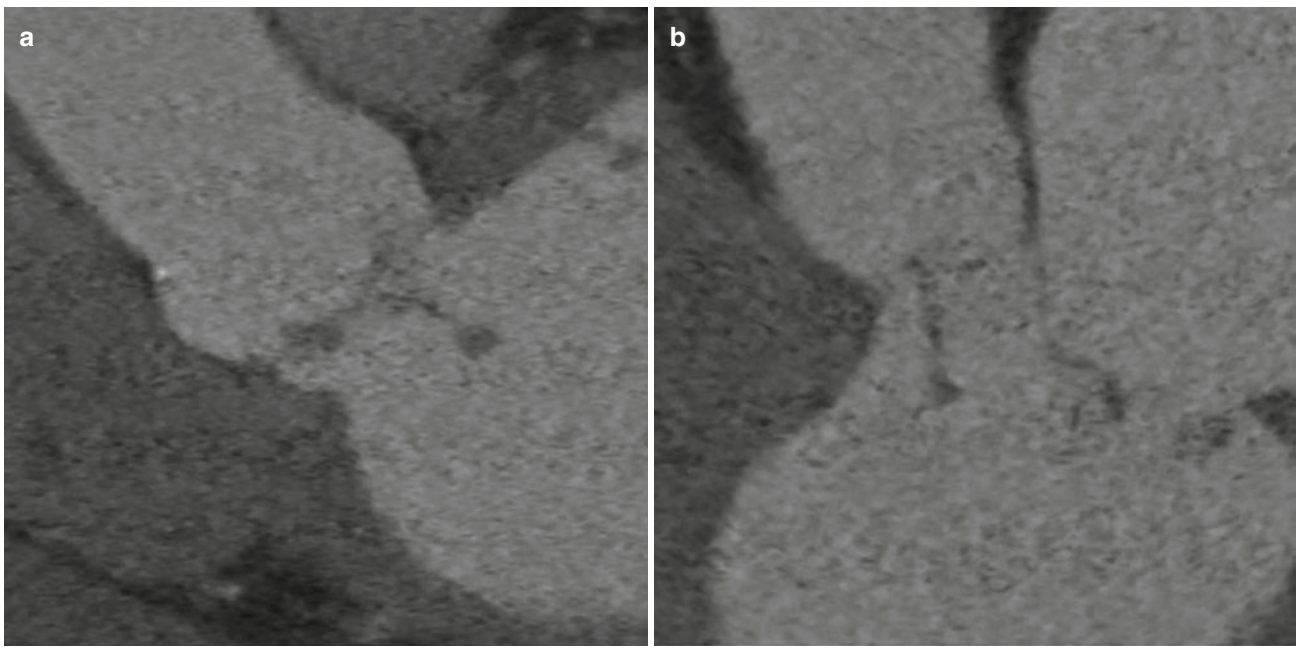

Fig. 13.50 Aortic valve endocarditis. Coronal oblique (**a**) and sagittal oblique (**b**, three-chamber view) MinIPs depict a vegetation extending into the LVOT

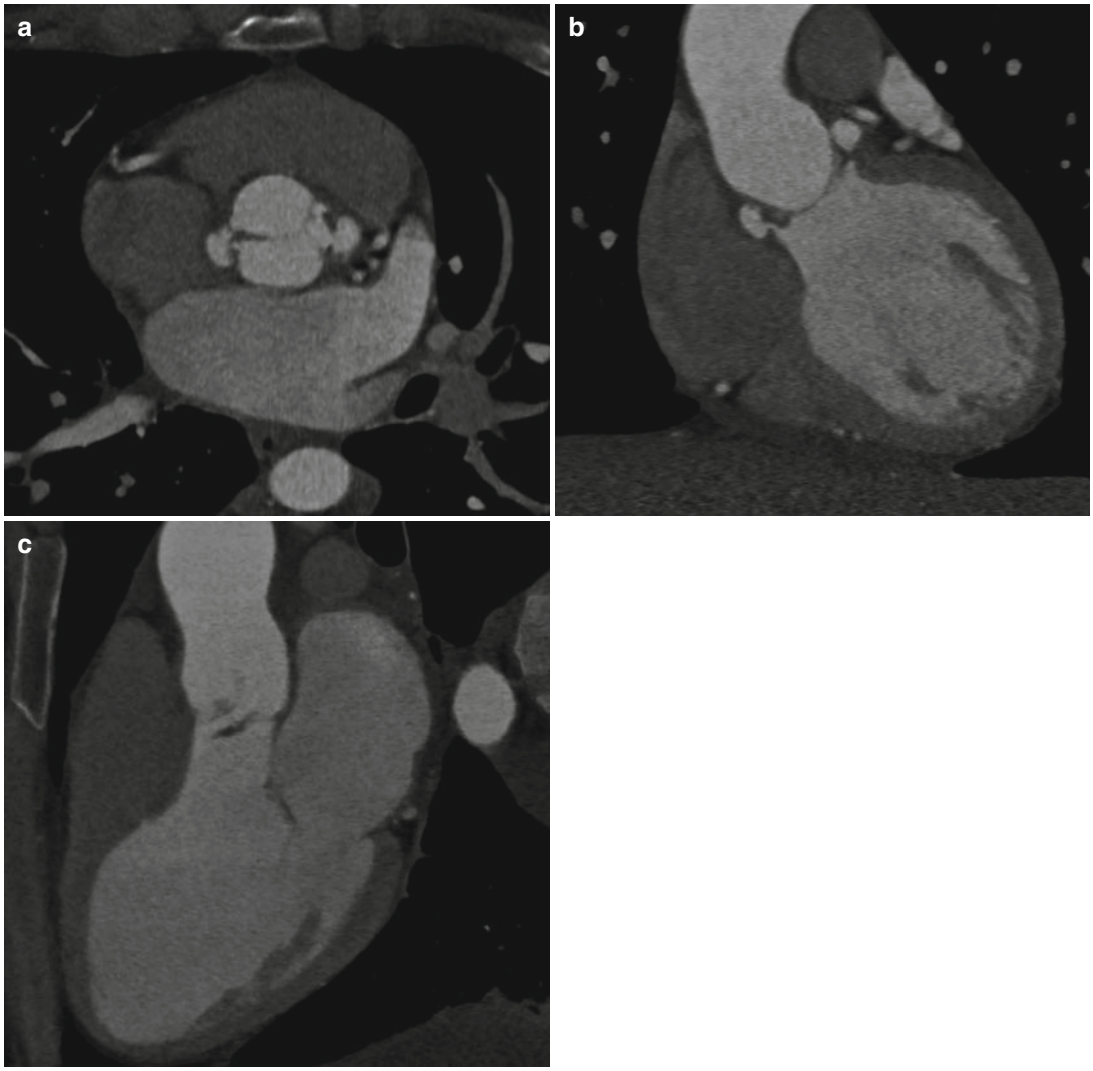

Fig. 13.51 Purely bicuspid aortic valve endocarditis with periaortal involvement. A diastolic short-axis view (**a**), coronal oblique view (**b**), and sagittal oblique view (three-chamber view, MinIP, **c**) depict a purely bicuspid valve (Sievers Type 0) with thickened leaflets due to vegetations and mycotic pseudoaneurysms

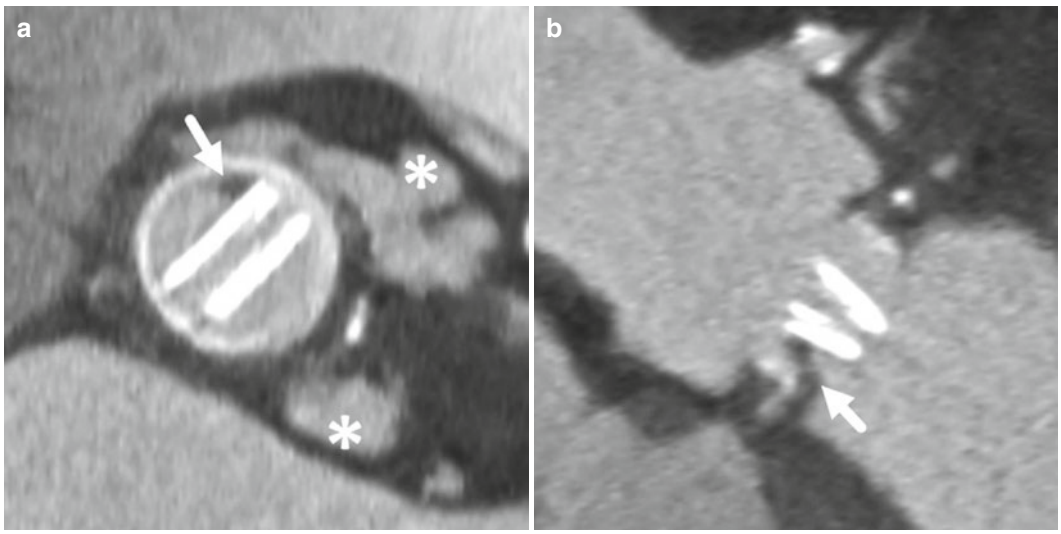

Fig. 13.52 Mechanical aortic valve endocarditis, seen in a short-axis view (**a**) and a coronal long-axis view (**b**). Vegetation can be identified as low-attenuation foci adjacent to the right-sided mechanical disc in both views (*arrows*). The short-axis view also reveals contrast-filled cavities in keeping with perivalvular involvement with pseudoaneurysm/abscess formation (*asterisks*)

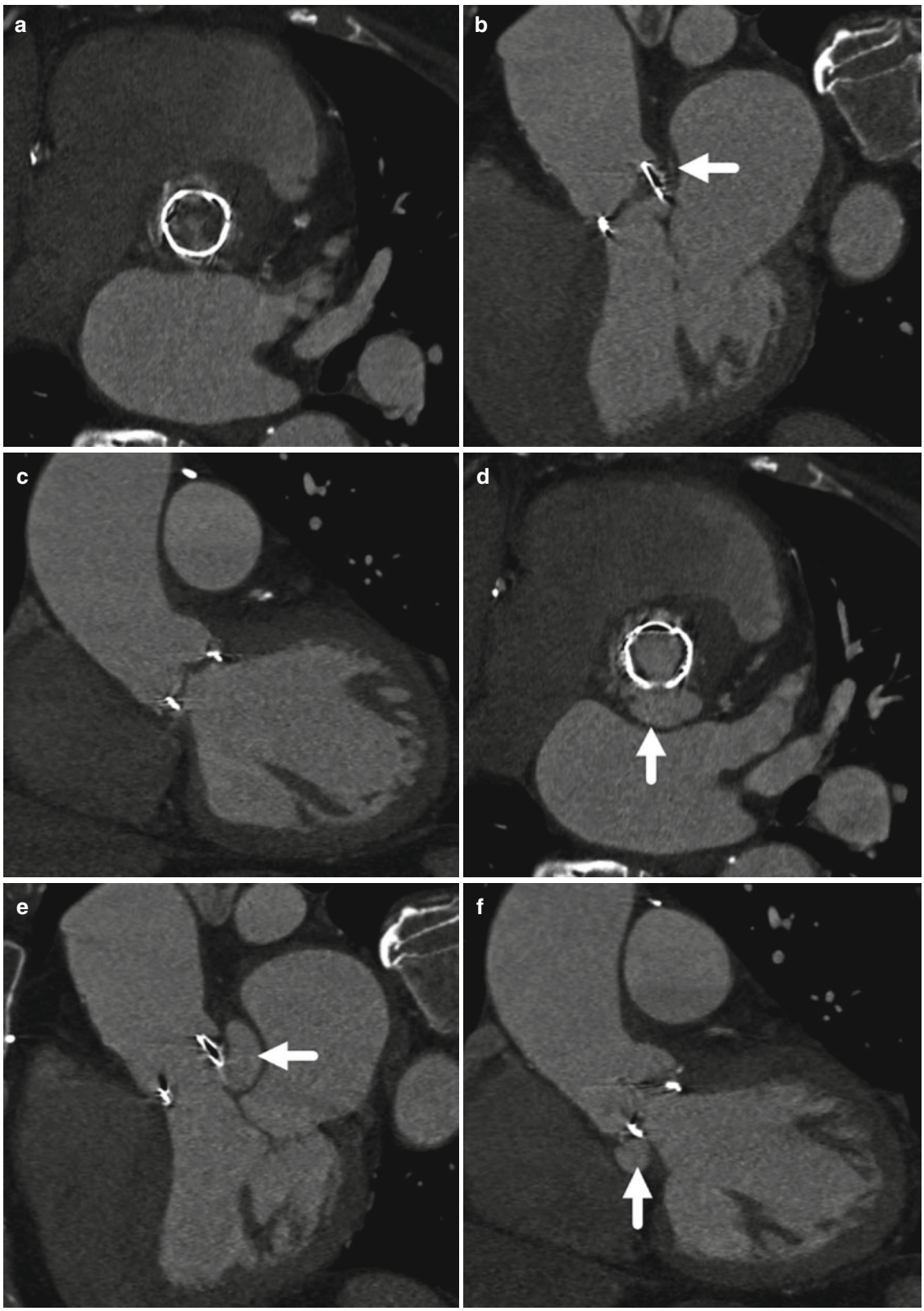

Fig. 13.53 Aortic valve bioprosthesis endocarditis with pseudoaneurysm formation. The diastolic short-axis view (**a**), sagittal oblique view (three-chamber view, **b**), and coronal oblique view (**c**) depict an aortic valve bioprosthesis with a radiopaque scaffold. Leaflet thickening due to endocarditis can be appreciated, as well as a small, contrast-filled cavity within the aortic mitral valve continuity (**b**, *arrow*). The corresponding systolic images (**d**–**f**) demonstrate pulsatile enlargement of mycotic pseudoaneurysms (*arrows*)

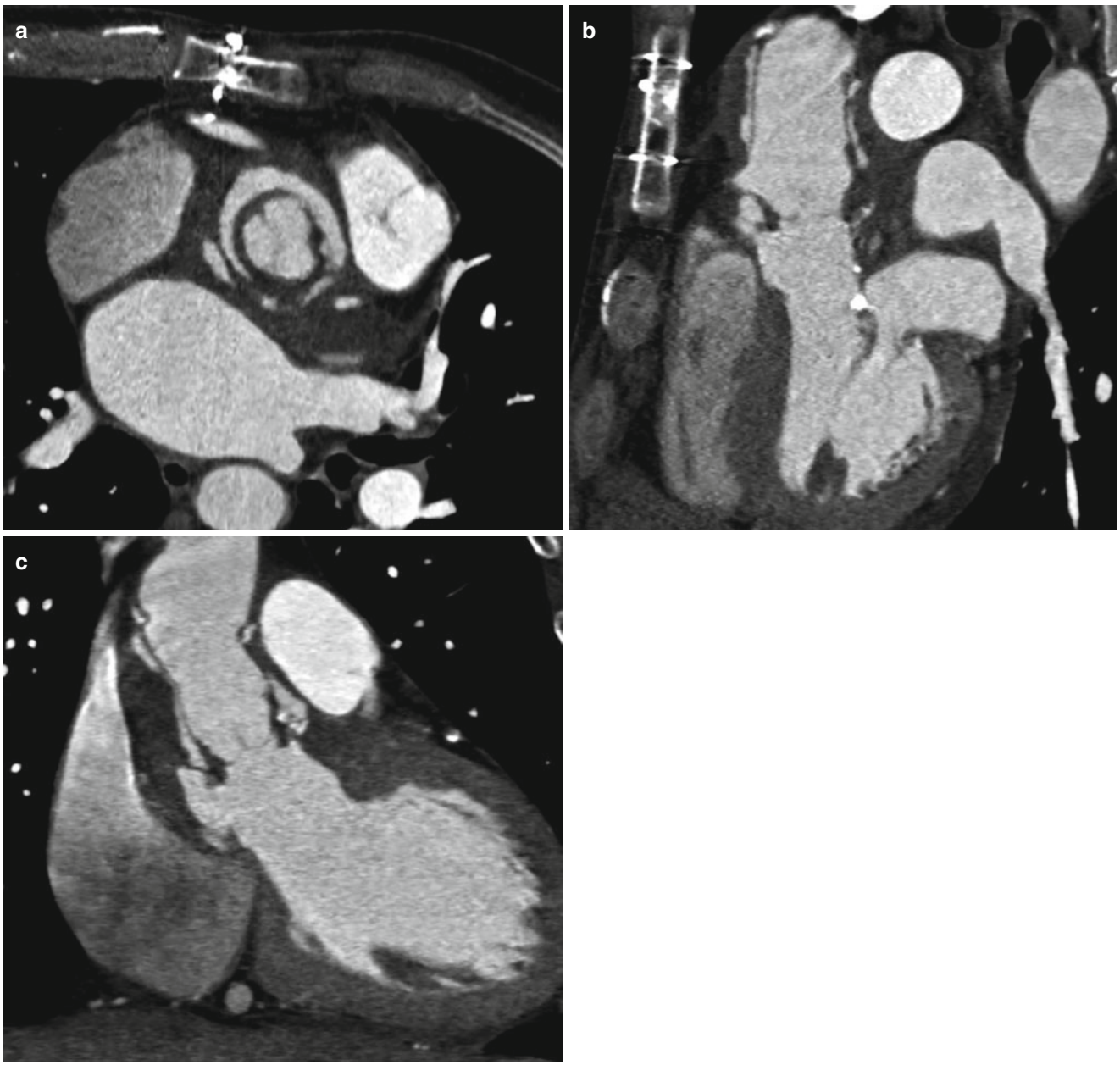

Fig. 13.54 Complete dehiscence of a bioprosthesis aortic conduit and aortoventricular junction due to endocarditis lenta. The diastolic short-axis view (**a**), sagittal oblique view (three-chamber view, **b**), and coronal oblique view (**c**) depict dehiscence of the conduit and the aortoventricular junction. The conduit is surrounded by a pseudoaneurysm, which can be depicted as a contrast-enhanced cavity

References

1. Flohr TG, Leng S, Yu L, Aiimendinger T, Bruder H, Petersilka M, et al. Dual-source spiral CT with pitch up to 3.2 and 75 ms temporal resolution: image reconstruction and assessment of image quality. Med Phys. 2009;36:5641–53.
2. Hsiao EM, Rybicki FJ, Steigner M. CT coronary angiography: 256-slice and 320-detector row scanners. Curr Cardiol Rep. 2010;12:68–75.
3. Piazza N, De Jaegere P, Schultz C, Becker A, Serruys PW, Anderson RH. Anatomy of the aortic valvar complex and its implications for transcatheter implantation of the aortic valve. Circ Cardiovasc Interv. 2008;1:74–81.
4. LaBounty TM, Glasofer S, Devereux RB, Lin FY, Weinsaft JW, Min JK. Comparison of cardiac computed tomographic angiography to transesophageal echocardiography for evaluation of patients with native valvular heart disease. Am J Cardiol. 2009;104:1421–8.
5. LaBounty TM, Sundaram B, Agarwal P, Armstrong WA, Kazerooni EA, Yamada E. Aortic valve area on 64-MDCT correlates with transesophageal echocardiography in aortic stenosis. AJR Am J Roentgenol. 2008;191:1652–8.
6. Abdulla J, Sivertsen J, Kofoed KF, Alkadhi H, LaBounty T, Abildstrom SZ, et al. Evaluation of aortic valve stenosis by cardiac multislice computed tomography compared with echocardiography: a systematic review and meta-analysis. J Heart Valve Dis. 2009;18:634–43.
7. Halpern EJ, Mallya R, Sewell M, Shulman M, Zwas DR. Differences in aortic valve area measured with CT planimetry and echocardiography (continuity equation) are related to divergent estimates of left ventricular outflow tract area. AJR Am J Roentgenol. 2009;192:1668–73.
8. Sievers HH, Schmidtke C. A classification system for the bicuspid aortic valve from 304 surgical specimens. J Thorac Cardiovasc Surg. 2007;133:1226–33.
9. Basso C, Boschello M, Perrone C, et al. An echocardiographic survey of primary school children for bicuspid aortic valve. Am J Cardiol. 2004;93(5):661–3.
10. Gray GW, Salisbury DA, Gulino AM. Echocardiographic and color flow Doppler findings in military pilot applicants. Aviat Space Environ Med. 1995;66:32–4.
11. Fernandes SM, Sanders SP, Khairy P, Jenkins KJ, Gauvreau K, Lang P, et al. Morphology of bicuspid aortic valve in children and adolescents. J Am Coll Cardiol. 2004;44:1648–51.
12. Nistri S, Sorbo MD, Marin M, Palisi M, Scognamiglio R, Thiene G. Aortic root dilatation in young men with normally functioning bicuspid aortic valves. Heart. 1999;82:19–22.
13. Schievink WI, Mokri B, Piepgras DG, Gittenberger-de Groot AC. Intracranial aneurysms and cervicocephalic arterial dissections associated with congenital heart disease. Neurosurgery. 1996;39:685–9. discussion 689–90
14. Roos-Hesselink JW, Schölzel BE, Heijdra RJ, Spitaels SE, Meijboom FJ, Boersma E, et al. Aortic valve and aortic arch pathology after coarctation repair. Heart. 2003;89:1074–7.
15. Larson EW, Edwards WD. Risk factors for aortic dissection: a necropsy study of 161 cases. Am J Cardiol. 1984;53:849–55.
16. Wagner HR, Ellison RC, Keane JF, Humphries OJ, Nadas AS. Clinical course in aortic stenosis. Circulation. 1977;56:I47–56.
17. Janssens U, Klues HG, Hanrath P. Congenital quadricuspid aortic valve anomaly associated with hypertrophic non-obstructive cardiomyopathy: a case report and review of the literature. Heart. 1997;78:83–7.
18. Blanke P, Wengenmayer T, Sorg S, Pache G. Stenosed quadricuspid aortic valve treated by transcatheter aortic valve implantation. J Am Coll Cardiol. 2011;57:1567.
19. Iung B, Baron G, Butchart EG, Delahaye F, Gohike-Bärwolf C, Levang OW, et al. A prospective survey of patients with valvular heart disease in Europe: the Euro Heart Survey on Valvular Heart Disease. Eur Heart J. 2003;24:1231–43.
20. Stewart BF, Siscovick D, Lind BK, Gardin JM, Gottdiener JS, Smith VE, et al. Clinical factors associated with calcific aortic valve disease. Cardiovascular Health Study. J Am Coll Cardiol. 1997;29:630–4.
21. Roberts WC, Ko JM. Frequency by decades of unicuspid, bicuspid, and tricuspid aortic valves in adults having isolated aortic valve replacement for aortic stenosis, with or without associated aortic regurgitation. Circulation. 2005;111:920–5.
22. Nkomo VT, Gardin JM, Skelton TN, Gottdiener JS, Scott CG, Enriquez-Sarano M. Burden of valvular heart diseases: a population-based study. Lancet. 2006;368:1005–11.
23. Feuchtner GM, Dichtl W, Müller S, Jodocy D, Schachner T, Klauser A, Bonatti JO. 64-MDCT for diagnosis of aortic regurgitation in patients referred to CT coronary angiography. AJR Am J Roentgenol. 2008;191:W1–7.
24. Cribier A, Eltchaninoff H, Bash A, Borenstein N, Tron C, Bauer F, et al. Percutaneous transcatheter implantation of an aortic valve prosthesis for calcific aortic stenosis: first human case description. Circulation. 2002;106:3006–8.
25. Webb JG, Chandavimol M, Thompson CR, Ricci DR, Carere RG, Munt BI, et al. Percutaneous aortic valve implantation retrograde from the femoral artery. Circulation. 2006;113:842–50.
26. Leon MB, Smith CR, Mack M, Miller DC, Moses JW, Svensson LG, et al. Transcatheter aortic-valve implantation for aortic stenosis in patients who cannot undergo surgery. N Engl J Med. 2010;363:1597–607.
27. Smith CR, Leon MB, Mack MJ, Miller DC, Moses JW, Svensson LG, et al. Transcatheter versus surgical aortic-valve replacement in high-risk patients. N Engl J Med. 2011;364:2187–98.
28. Blanke P, Siepe M, Reinöhl J, Zehender M, Beyersdorf F, Schlensak C, et al. Assessment of aortic annulus dimensions for Edwards SAPIEN Transapical Heart Valve implantation by computed tomography: calculating average diameter using a virtual ring method. Eur J Cardiothorac Surg. 2010;38:750–8.
29. Willson AB, Webb JG, Freeman M, Wood DA, Gurvitch R, Thompson CR, et al. Computed tomography-based sizing recommendations for transcatheter aortic valve replacement with balloon-expandable valves: comparison with transesophageal echocardiography and rationale for implementation in a prospective trial. J Cardiovasc Comput Tomogr. 2012;6:406–14.
30. Blanke P, Russe M, Leipsic J, Reinöhl J, Ebersberger U, Suranyi P, et al. Conformational pulsatile changes of the aortic annulus: impact on prosthesis sizing by computed tomography for transcatheter aortic valve replacement. JACC Cardiovasc Interv. 2012;5:984–94.
31. Willson AB, Webb JG, Labounty TM, Achenbach S, Moss R, Wheeler M, et al. 3-dimensional aortic annular assessment by multidetector computed tomography predicts moderate or severe paravalvular regurgitation after transcatheter aortic valve replacement: a multicenter retrospective analysis. J Am Coll Cardiol. 2012;59:1287–94.
32. Jilaihawi H, Kashif M, Fontana G, Furugen A, Shiota T, Friede G, et al. Cross-sectional computed tomographic assessment improves accuracy of aortic annular sizing for transcatheter aortic valve replacement and reduces the incidence of paravalvular aortic regurgitation. J Am Coll Cardiol. 2012;59:1275–86.
33. Piazza N, Lange R. Imaging of valvular heart disease: I can see clearly now. Anatomy of the aortic valve. Presentation at the Dallas-Leipzig International Valve Conference, December 9, 2010. org.crsti.dliv2010.s3.amazonawa.com/pdfs/034_Ovality_of_the_aortic_valve_annulus.pdf. Accessed 7 October 2014.

34. Binder RK, Webb JG, Willson A, Urena M, Hansson NC, Norgaard BL, et al. The impact of integration of a multidetector computed tomography annulus area sizing algorithm on outcomes of transcatheter aortic valve replacement: a prospective, multicenter, controlled trial. J Am Coll Cardiol. 2013;62:431–8.
35. Gurvitch R, Webb JG, Yuan R, et al. Aortic annulus diameter determination by multidetector computed tomography reproducibility, applicability, and implications for transcatheter aortic valve implantation. J Am Coll Cardiol Interv. 2011;4:1235–45.
36. Hiratzka LF, Bakris GL, Beckman JA, Bersin RM, Carr VF, Casey DE Jr, et al. 2010 ACCF/AHA/AATS/ACR/ASA/SCA/SCAI/SIR/STS/SVM guidelines for the diagnosis and management of patients with Thoracic Aortic Disease: a report of the American College of Cardiology Foundation/American Heart Association Task Force on Practice Guidelines, American Association for Thoracic Surgery, American College of Radiology, American Stroke Association, Society of Cardiovascular Anesthesiologists, Society for Cardiovascular Angiography and Interventions, Society of Interventional Radiology, Society of Thoracic Surgeons, and Society for Vascular Medicine. Circulation. 2010;121:e266–369.
37. Delgado V, Ng AC, van de Veire NR, van der Kley F, Schuijf JD, Tops LF, et al. Transcatheter aortic valve implantation: role of multi-detector row computed tomography to evaluate prosthesis positioning and deployment in relation to valve function. Eur Heart J. 2010;31:1114–23.
38. Hung J. Mitral valve anatomy. In: Otto C, editor. Practice of clinical echocardiography. Philadelphia: Elsevier; 2012. p. 330–50.
39. Messika-Zeitoun D, Serfaty JM, Laissy JP, Berhili M, Brochet E, Iung B, Vahanian A. Assessment of the mitral valve area in patients with mitral stenosis by multislice computed tomography. J Am Coll Cardiol. 2006;48:411–3.
40. Delgado V, Tops LF, Schuijf JD, de Roos A, Brugada J, Schalij MJ, et al. Assessment of mitral valve anatomy and geometry with multislice computed tomography. JACC Cardiovasc Imaging. 2009;2:556–65.
41. Fedak PW, McCarthy PM, Bonow RO. Evolving concepts and technologies in mitral valve repair. Circulation. 2008;117:963–74.
42. Lembcke A, Borges AC, Dushe S, Dohmen PM, Wiese TH, Rogalla P, et al. Assessment of mitral valve regurgitation at electron-beam CT: comparison with Doppler echocardiography. Radiology. 2005;236:47–55.
43. Alkadhi H, Wildermuth S, Bettex DA, Plass A, Baumert B, Leschka S, et al. Mitral regurgitation: quantification with 16-detector row CT--initial experience. Radiology. 2006;238:454–63.
44. Vural M, Ucar O, Celebi OO, Cicekcioglu H, Durmaz HA, Selvi NA, et al. Evaluation of effective regurgitant orifice area of mitral valvular regurgitation by multislice cardiac computed tomography. J Cardiol. 2010;56:236–9.
45. Feuchtner GM, Alkadhi H, Karlo C, Sarwar A, Meier A, Dichti W, et al. Cardiac CT angiography for the diagnosis of mitral valve prolapse: comparison with echocardiography. Radiology. 2010;254:374–83.
46. Freed LA, Benjamin EJ, Levy D, Larson MG, Evans JC, Fuller DL, et al. Mitral valve prolapse in the general population: the benign nature of echocardiographic features in the Framingham Heart Study. J Am Coll Cardiol. 2002;40:1298–304.
47. Freed LA, Levy D, Levine RA, Larson MG, Evans JC, Fuller DL, et al. Prevalence and clinical outcome of mitral-valve prolapse. N Engl J Med. 1999;341:1–7.
48. Levine RA, Triulzi MO, Harrigan P, Weyman AE. The relationship of mitral annular shape to the diagnosis of mitral valve prolapse. Circulation. 1987;75:756–67.
49. Inoue K, Owaki T, Nakamura T, Kitamura F, Miyamoto N. Clinical application of transvenous mitral commissurotomy by a new balloon catheter. J Thorac Cardiovasc Surg. 1984;87:394–402.
50. Pate GE, Al Zubaidi A, Chandavimol M, Thompson CR, Munt BI, Webb JG. Percutaneous closure of prosthetic paravalvular leaks: case series and review. Catheter Cardiovasc Interv. 2006;68:528–33.
51. Pate GE, Thompson CR, Munt BI, Webb JG. Techniques for percutaneous closure of prosthetic paravalvular leaks. Catheter Cardiovasc Interv. 2006;67:158–66.
52. Hein R, Wunderlich N, Wilson N, Sievert H. New concepts in transcatheter closure of paravalvular leaks. Futur Cardiol. 2008;4:373–8.
53. Perloff JK, Roberts WC. The mitral apparatus. Functional anatomy of mitral regurgitation. Circulation. 1972;46:227–39.
54. Raman SV, Cook SC, McCarthy B, Ferketich AK. Usefulness of multidetector row computed tomography to quantify right ventricular size and function in adults with either tetralogy of Fallot or transposition of the great arteries. Am J Cardiol. 2005;95:683–6.
55. Feuchtner GM, Stolzmann P, Dichtl W, Schertler T, Bonatti J, Scheffel H, et al. Multislice computed tomography in infective endocarditis: comparison with transesophageal echocardiography and intraoperative findings. J Am Coll Cardiol. 2009;53:436–44.

CT in the Management of Cardiac Arrhythmias

14

Joel Wilson, Farhood Saremi, Jagat Narula, and Sanjiv M. Narayan

Imaging has accelerated mechanistic understanding and its translation to therapy more in the management of heart rhythm disorders arguably than in any other field. State-of-the-art imaging modalities provide hitherto unavailable patient-specific information on geometrical structure, tissue properties, and function of both atria and ventricles. By enabling direct and subject-specific visualization of structure and function before and after clinical and experimental interventions, imaging has made cardiac anatomy a central pillar of modern electrophysiology.

Computed tomography (CT) is a flagbearer of this imaging revolution. Multidetector CT has unique advantages over other tomographic imaging in providing volumetric, three-dimensional datasets with isotropic spatial resolution at 0.5 mm, which can be reconstructed into virtual three-dimensional objects, planar images in any orientation, or even composite multiplanar images. Large-volume scanners with up to 320 channels can acquire image data sets of the entire heart in a single rotation of the gantry. Unlike MRI, CT can be performed in patients with permanent pacemakers, defibrillators, or other cardiac implantable electronic devices. These technical advances now routinely provide a "virtual dissection" of the heart, cardiovascular system, and mediastinum, providing detailed anatomy of structures of particular interest to the electrophysiologist [1–5]. *Pari passus* with advances in understanding cellular and tissue electrophysiology, CT imaging now provides a straightforward approach to identify syndromes including arrhythmogenic cardiomyopathy, hypertrophic cardiomyopathy [6], and ventricular noncompaction [7], and to refine the patient-specific treatment of atrial arrhythmias and potentially lethal arrhythmias in relation to structural abnormalities, anatomic variants, and potentially scar. CT enables pre-procedural planning and peri-procedural image integration to facilitate catheter ablation and pacing and has enabled interdisciplinary therapy by interventional electrophysiologists, cardiothoracic surgeons, and radiologists working hand-in-hand to treat atrial or ventricular arrhythmias or for implanted device therapy.

This chapter synthesizes the current state of the art in the application of CT to arrhythmia medicine, and provides our vision for future advances and challenges in the field. First, this chapter is a practical guide on the use of cardiac CT scanning to improve the management of arrhythmias. Second, it provides numerous clinical images of noninvasive "virtual dissection of the heart" by multidetector CT, demonstrating structures that may be poorly appreciated on fluoroscopy or alternative imaging approaches, including the fossa ovalis, crista terminalis, atrial appendages, pulmonary and thoracic veins, ventricular myocardium, and adnexae such as the phrenic nerve and esophagus. Third, this chapter illustrates how clinical CT may help to avoid and detect complications of electrophysiological therapy. It is organized to illustrate the functional anatomy relevant to arrhythmias in the atria and ventricles and for implantable device therapy.

J. Wilson
Division of Cardiovascular Medicine, UCSD Medical Center, 9444 Medical Center Drive #7411, La Jolla, CA 92037, USA
e-mail: jwilson@ucsd.edu

F. Saremi
Department of Radiology, University of Southern California, USC University Hospital, 1500 San Pablo Street, Los Angeles, CA 90033, USA
e-mail: fsaremi@usc.edu

J. Narula
Mount Sinai Heart, Icahn School of Medicine at Mount Sinai, New York, NY, USA
e-mail: narula@mountsinai.org

S.M. Narayan (✉)
Department of Medicine/Division of Cardiology, Stanford University, Stanford, CA, USA
e-mail: sanjiv1@stanford.edu

M.J. Budoff et al. (eds.), *Atlas of Cardiovascular Computed Tomography*, https://doi.org/10.1007/978-1-4471-7357-1_14

CT in Imaging the Atrial Appendages

The right atrial appendage (RAA) and left atrial appendage (LAA) are important structures in electrophysiology, as sites of arrhythmogenesis or thrombus formation. Both appendages are well-recognized sites of origin of atrial tachycardias [8] and sustaining mechanisms [9] for atrial fibrillation (AF), and the LAA is a common site of triggering ectopy [10] for AF. Figure 14.1 shows the crista terminalis, posterior to the base of the RAA behind the junction of the sinus venosus–derived and true right atrial myocardium [11], a known arrhythmogenic structure. Appendage-related arrhythmias may result from the myofiber interface between the embryological true and sinus venosus–derived atrial tissue [11], fibrosis from stress/shear forces, or other mechanisms that are less clear.

Atrial CT has been immensely helpful to allow noninvasive assessment of variations in appendage anatomy that have been seen in autopsy specimens [12], in terms of atrial appendage take-off, trajectory, and size to guide procedural approaches (Fig. 14.2). At the current time, it is not clear whether specific appendage morphologies influence arrhythmic predisposition.

The atrial appendages, particularly the left, are common (but not unique) sites for thrombus formation [13] (Fig. 14.3) and embolization to the brain or elsewhere. Thrombus formation in AF is associated with Virchow's triad, including pro-coagulant factors [14], abnormal endothelium, and stasis. Stasis may explain recent findings that the actual shape of the left atrial appendage may influence risk for AF-related stroke. Of several vivid labels recently attached to left atrial appendage shape, the morphologies known as "cactus," "cauliflower." and "windsock" may confer higher risk for thromboembolization than the "chicken wing" shapes [15] (Fig. 14.4).

Recent therapeutic advances in stroke prevention have focused on excluding the left atrial appendage from the systemic circulation because it is the most commonly identifiable source of AF-related thromboemboli [13]. Several therapeutic approaches exist. Some devices are inserted trans-septally using a percutaneous approach to occlude the LAA internally [16, 17] (Figs. 14.5 and 14.6), while others close the LAA orifice externally, for example using a snare that is inserted epicardially using minimally invasive approaches [18] (Fig. 14.7).

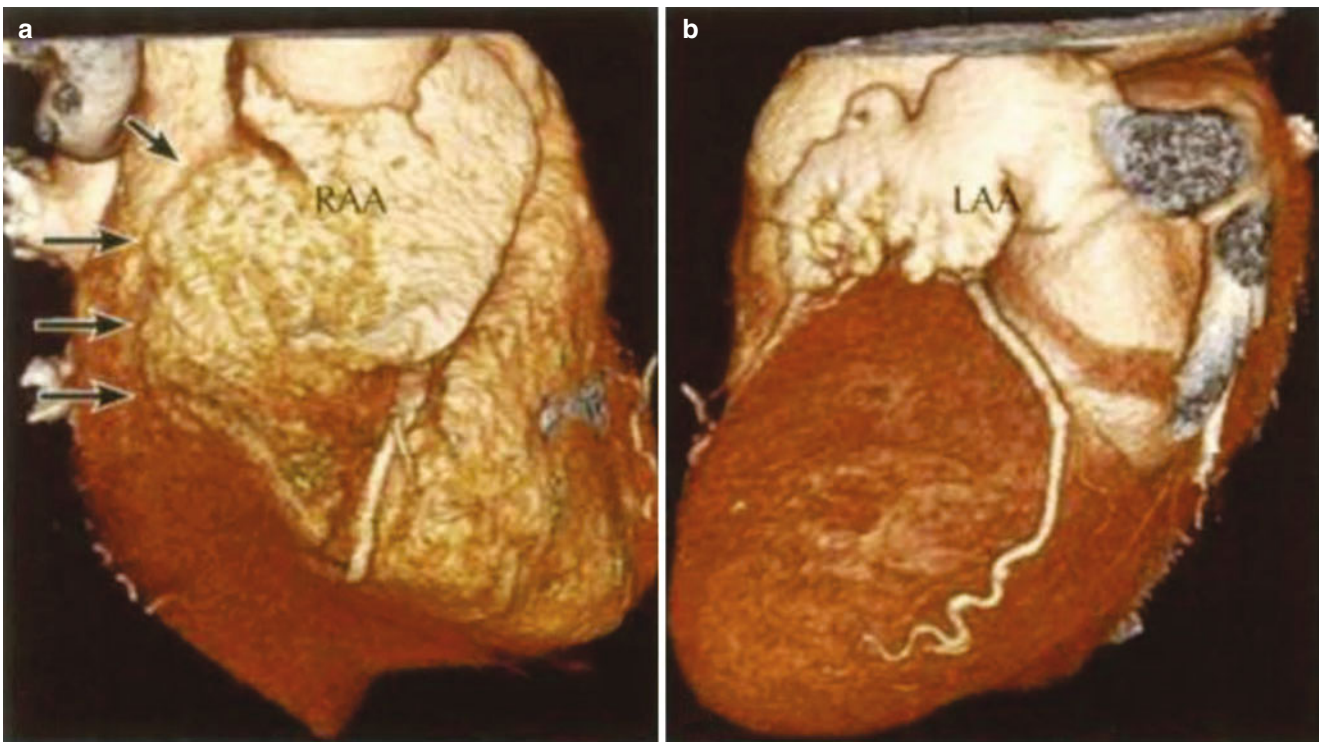

Fig. 14.1 CT scans of both atrial appendages and adjacent structures including the crista terminalis. The right atrial appendage (RAA) (**a**) and the left atrial appendage (LAA) (**b**) in their respective lateral epicardial views, showing typical three-dimensional (3D) volume-rendered images. The RAA is a broad-based, pyramidal structure with a blunt tip, whereas the LAA is typically longer and pedunculated, with a narrower base. The groove posterior to the RAA (*arrows*) is the sulcus terminalis, which corresponds to the endocardial crista terminalis, an arrhythmogenic atrial structure

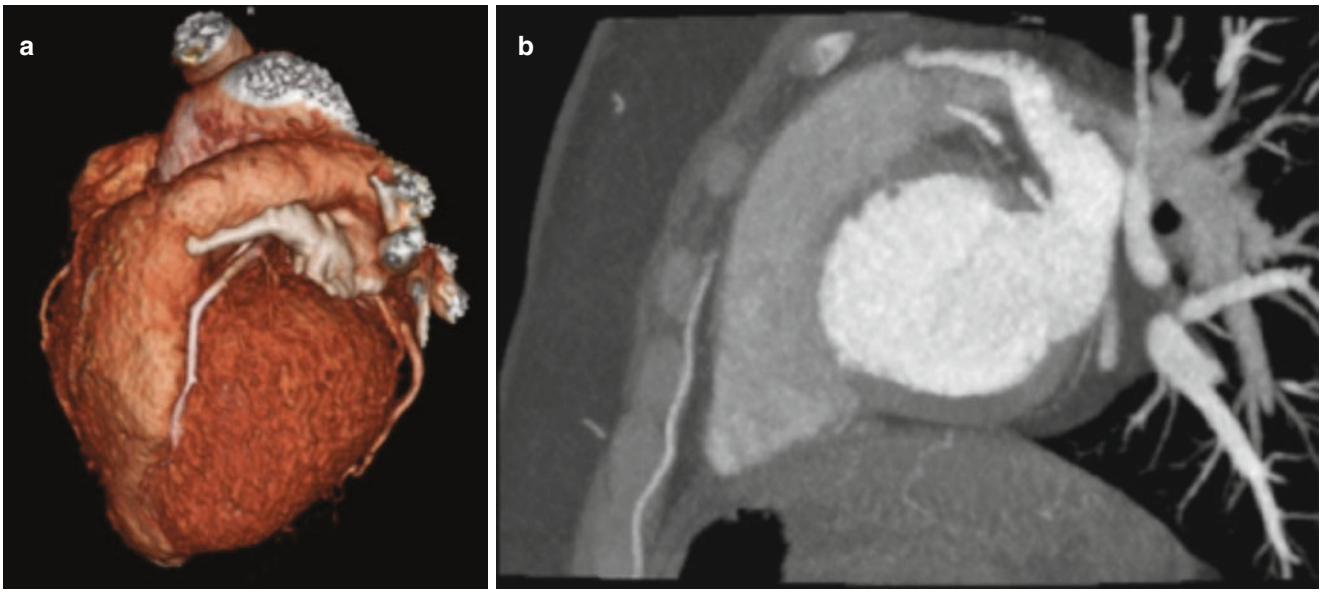

Fig. 14.2 Multidetector CT images of "windsock" left atrial appendages. (**a**) Three-dimensional volume-rendered CT image. (**b**) Maximum-intensity projection showing long left atrial appendage morphology

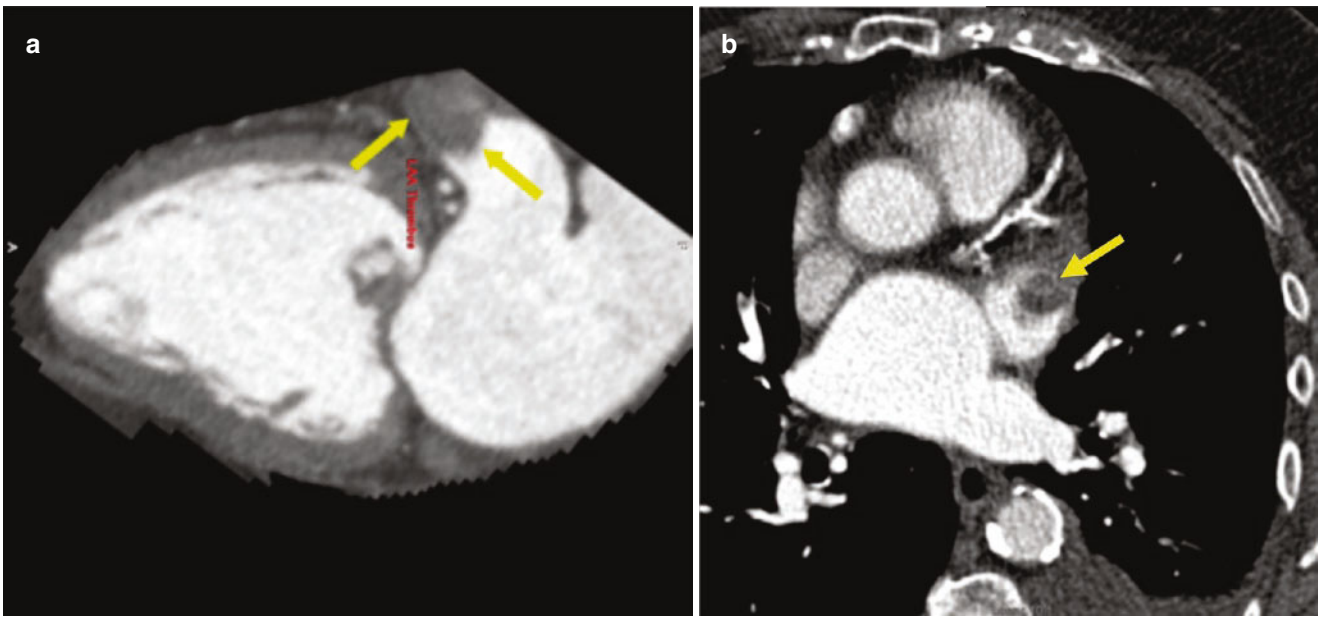

Fig. 14.3 Left atrial appendage thrombi shown by CT. Gated (**a**) and non-gated (**b**) CT of thrombi (*arrows*). Notably, both findings were incidental. Atrial CT can thus theoretically eliminate the need for pre-ablation transesophageal echocardiography while also detailing anatomy [15], although the benefit of this strategy has not been proven in a clinical trial. (*Courtesy of* Marcus Chen, Advanced Cardiovascular Imaging Group, NHLBI, NIH; and Steve Leung, University of Kentucky)

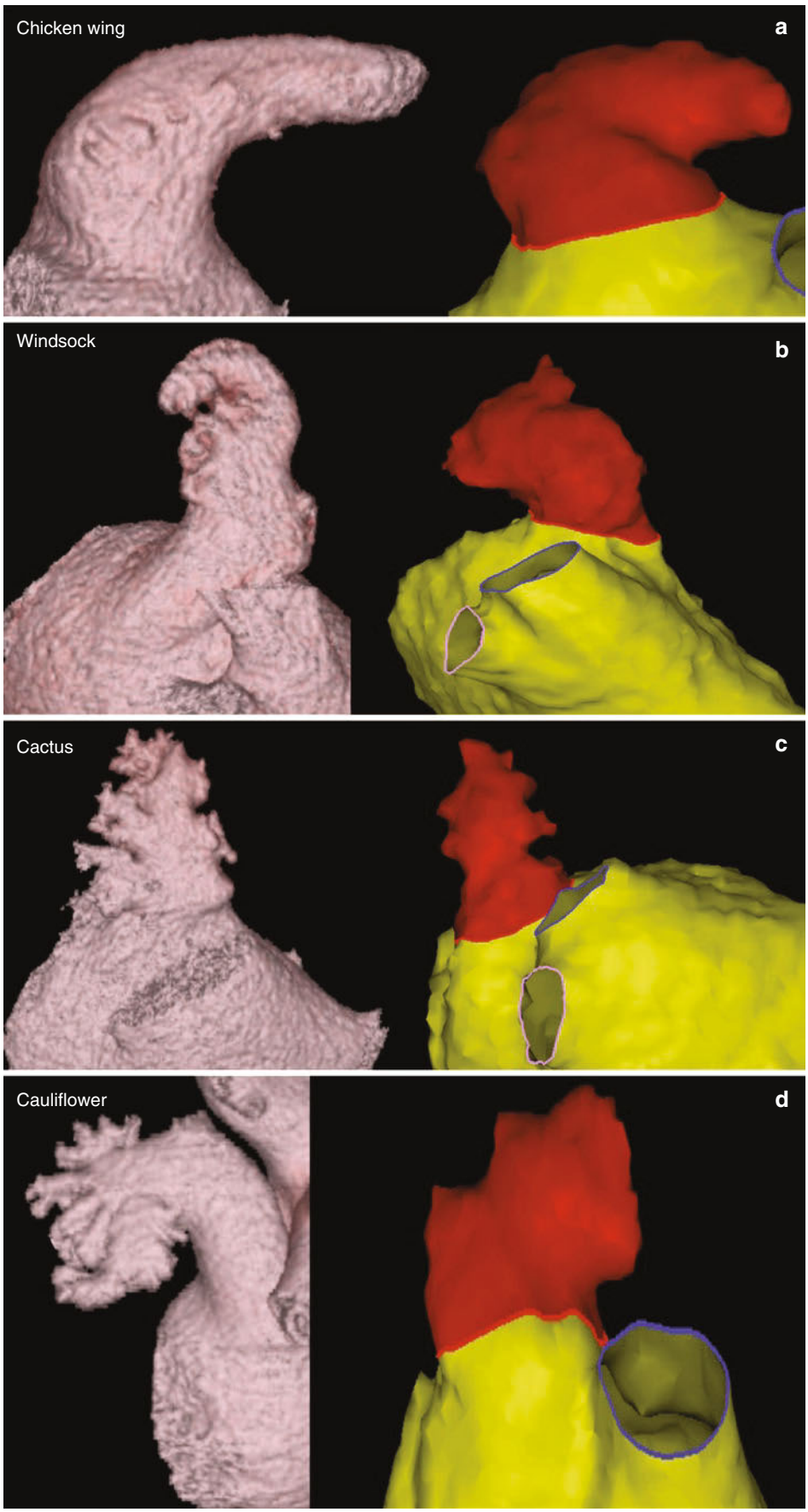

Fig. 14.4 Left atrial appendage (LAA) morphology revealed by multidetector CT (*left*) and MRI (*right*). (**a**) The chicken wing has an obvious bend in the proximal or middle part of the dominant lobe, folding the LAA anatomy back on itself some distance from the perceived LAA ostium. (**b**) Windsock has one dominant lobe that constitutes the primary axis length of the structure. Variations arise in the location and number of secondary or tertiary lobes from the dominant lobe. (**c**) Cactus has one dominant lobe from which secondary lobes emerge in superior and inferior directions. (**d**) Cauliflower has a limited overall length, with a complex internal structure that includes variations in ostial shape (circular versus oval) or absence of a dominant lobe. Compared with the chicken wing shape, the cactus, cauliflower, and windsock shapes are associated with a greater risk for stroke and transient ischemic attack, potentially due to reduced distal flow. (*Adapted from* Di Biase *et al.* [15]; with permission)

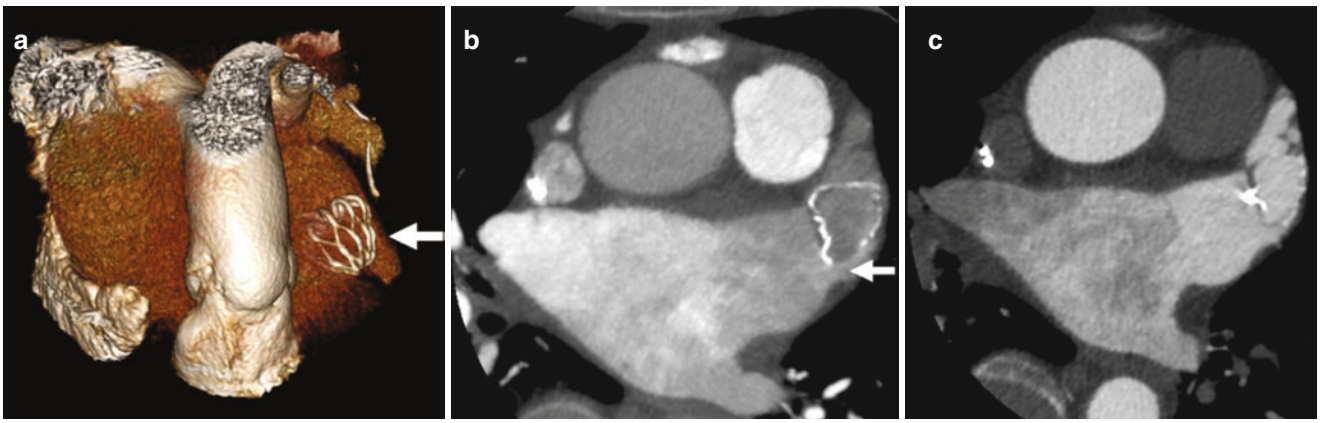

Fig. 14.5 CT illustrates endocardial occlusion of the LAA. (**a**) Three-dimensional rendering of a Watchman atrial appendage occluder (*arrow*) in situ 45 days after implantation. (**b**) Image acquired as contrast first enters the left atrium from the pulmonary veins, demonstrating a jet of contrast into the appendage around the device, indicating failure. Endothelialization of this device on its LAA ostial face normally occurs within 45 days after implantation. (**c**) Arterial-phase imaging showing complete opacification of the atrial appendage. (*From* Nasis *et al.* [6]; with permission)

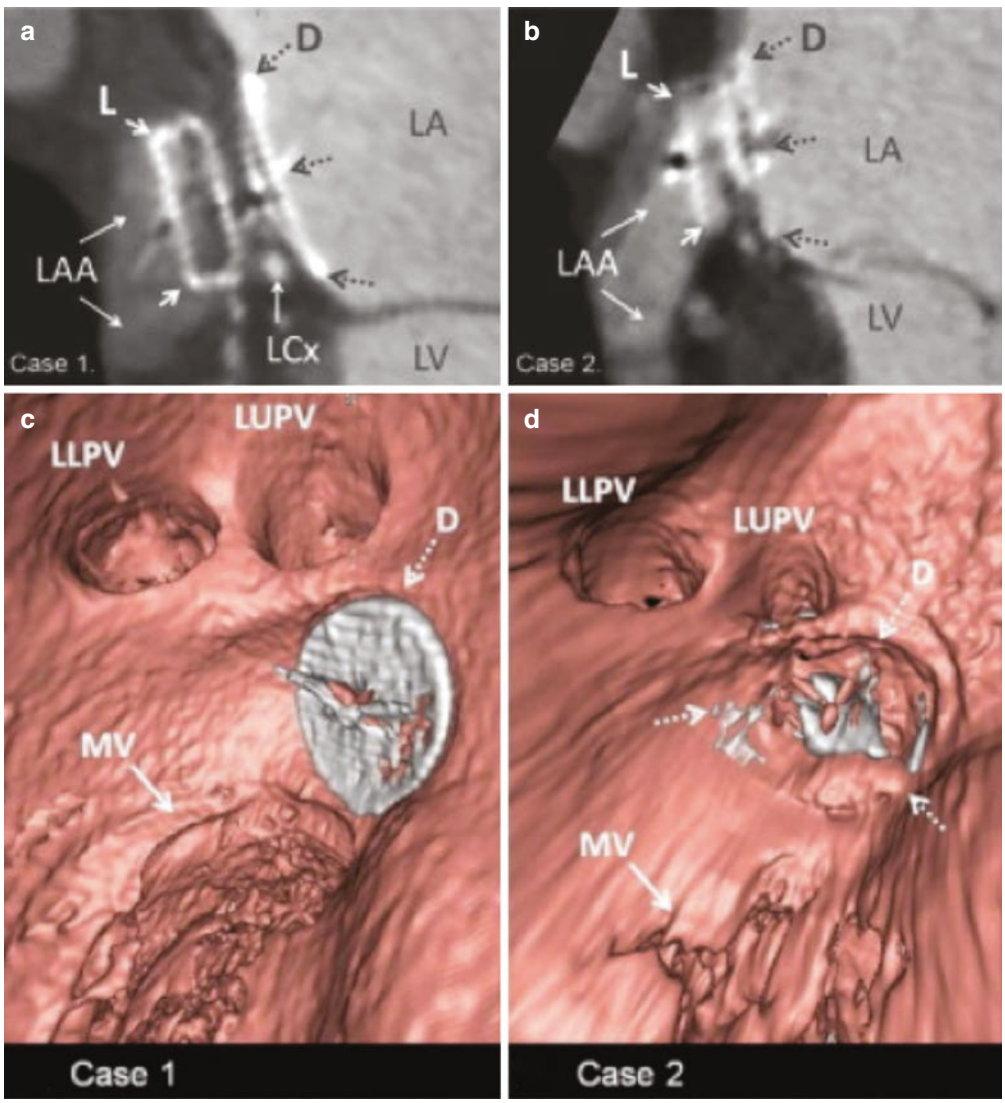

Fig. 14.6 Multiplane CT demonstrating endocardial occlusion of the left atrial appendage (LAA) using the Amplatzer Cardiac Plug (ACP) (AGA Medical Corp; Plymouth, MN). Images (**a**, **c**, **e**, **g**) show successful LAA exclusion, compared with unsuccessful LAA exclusion in images (**b**, **d**, **f**, **h**). *Dotted arrows* indicate the disc (D), and *short arrows* indicate the lobe (L). (**a** and **b**) Multiplanar reconstructions show the plug in situ. (**c**, **d**) Volume-rendered reconstructions from an endocardial view demonstrate the relationship of the ACP disc to pulmonary veins (PV) and the mitral valve (MV). (**e**, **f**) Volume-rendered reconstructions demonstrate the relationship of the ACP to the circumflex artery (LCx). (**g**) Limited contrast enhancement in the LAA demonstrates its exclusion. (**h**) Contrast enhancement of the appendage indicates persisting communication. (Adapted from Poulter et al. [19]; with permission)

Fig. 14.6 (continued)

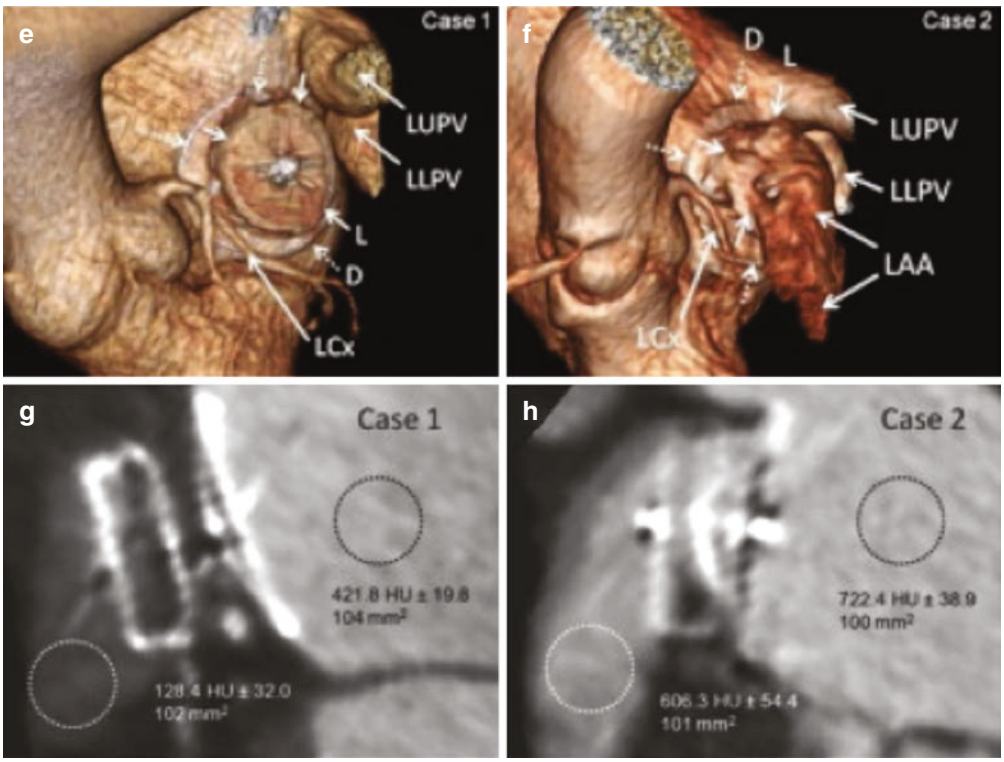

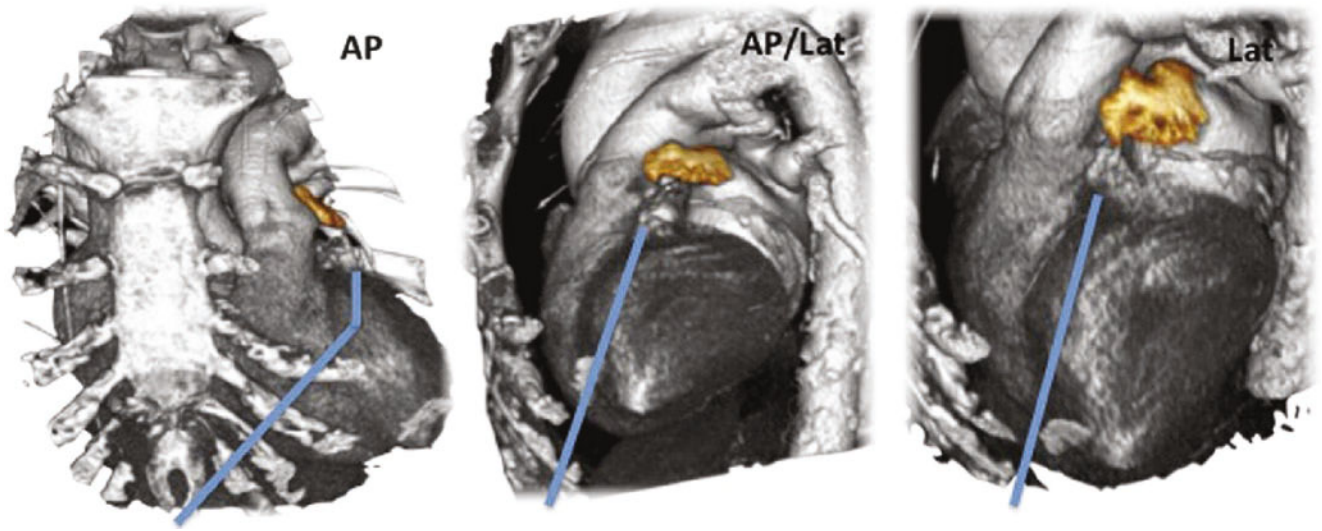

Fig. 14.7 CT images of epicardial snare to occlude left atrial appendage. Cardiac 3D CT reconstruction simulates the approach and shape of the LARIAT suture device (*blue lines*). The suture delivery device is advanced within the pericardial space. CT can assess the relationship between the sternum and myocardium to estimate the pericardial needle trajectory. *AP* anteroposterior view, *AP/Lat* anteroposterior/lateral view, *Lat* lateral view. (*From* Bartus *et al.* [18]; with permission)

CT in the Management of Atrial Arrhythmias

Atrial arrhythmias including AF are the most common sustained heart rhythm disorders in the world [20]. AF, in particular, has reached epidemic proportions [20] and is a leading global cause of hospitalization from heart failure, stroke, and systemic thromboembolism [21]. AF-related thromboembolism is increasingly implicated in cryptogenic stroke [22] and dementia [23]. Multidetector CT has substantially advanced the management of atrial arrhythmias via improved diagnosis of important structural variations and disease sequelae, periprocedural planning for ablation and LAA occlusion, and imaging of potential procedural complications.

CT Imaging for Typical Right Atrial Flutter

Typical atrial flutter is a common rhythm disturbance with characteristic saw-tooth F waves on the ECG (Fig. 14.8), which may produce palpitations, dyspnea, and fatigue. Atrial flutter presents similar risks for stroke and systemic thromboembolism as AF, in part because many patients develop AF over time [24], and both rhythms may coexist [25]. Ablation (Figs. 14.9, 14.10, and 14.11) has a class I indication for typical flutter because ventricular rate control may be difficult; the mechanisms of ablation are well worked out and it is highly successful.

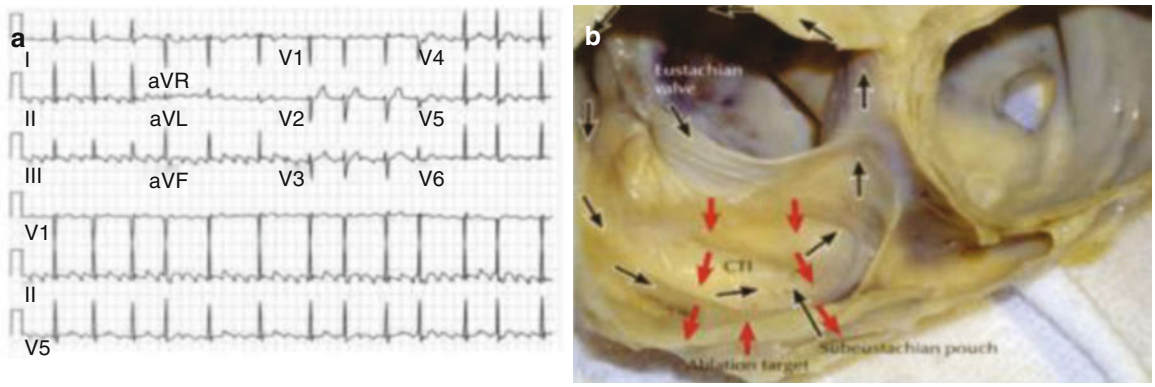

Fig. 14.8 Typical right atrial flutter. (**a**) ECG of typical atrial flutter, with negative, saw-tooth F waves in the inferior and lateral precordial ECG leads, and positive F waves in V1. (**b**) Electrical circuit of typical flutter, shown in an autopsy specimen with both ventricles removed to show an "end-on" or left anterior oblique view of the tricuspid and mitral annuli. Counterclockwise reentry is bounded anteriorly by the tricuspid annulus, with craniocaudal activation at the lateral right atrium bounded posteriorly by the crista terminalis, across the cavotricuspid isthmus (CTI), caudocranially in the septum, and then across the right atrial roof. Activation of the left atrium is passive and may be variable [26]. The *red arrows* represent ablation lesions between the tricuspid annulus and inferior vena cava, which bisect the cavotricuspid isthmus; the single-procedure success rate of these lesions is more than 85–90% at 2 years [27]. This image also shows a sub-Eustachian pouch that may challenge catheter positioning to deliver ablation energy effectively. (*From* Asirvatham and Friedman [28])

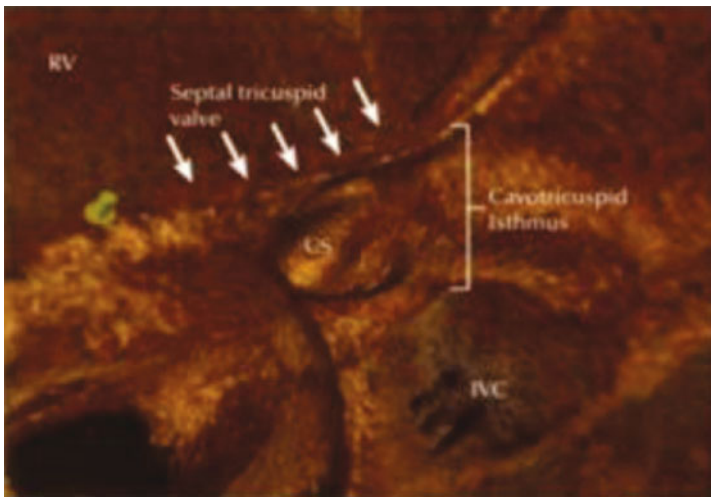

Fig. 14.9 Detail of the cavotricuspid isthmus. Three-dimensional volume-rendered CT shows a superior view of the inferoseptal right atrium, demonstrating the septal tricuspid annulus (*arrows*), coronary sinus ostium (CS) in the inferoseptal right atrium, and the inferior vena cava (IVC) posteriorly. A Eustachian valve is seen in the anterior portion of the IVC, which can cause an ablation catheter to jump. A sub-Eustachian pouch may be present, but its size is not easily quantified in this view. *RV* right ventricle

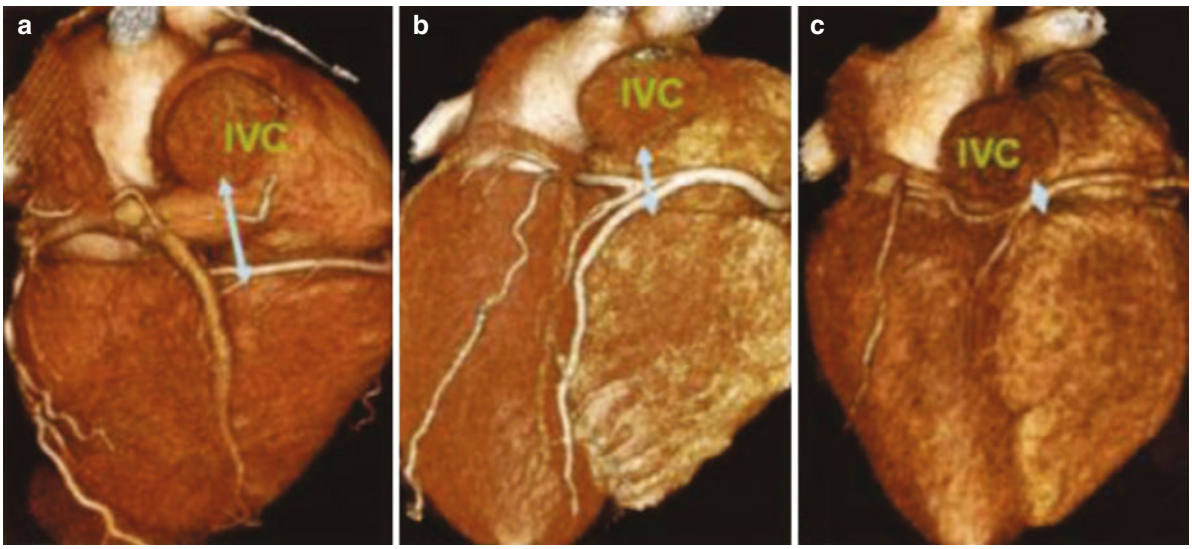

Fig. 14.10 Variations in the length of the cavotricuspid isthmus can challenge the placement of ablation lesions in a contiguous line between the inferior vena cava (IVC) and tricuspid annulus to interrupt the circuit of typical flutter. Three-dimensional volume-rendered CT images in caudal orientation show long (**a**), medium (**b**), and short isthmuses (**c**). Isthmuses longer than 35 mm are associated with longer fluoroscopic exposure and threefold increases in ablation duration compared with those shorter than 35 mm [29]

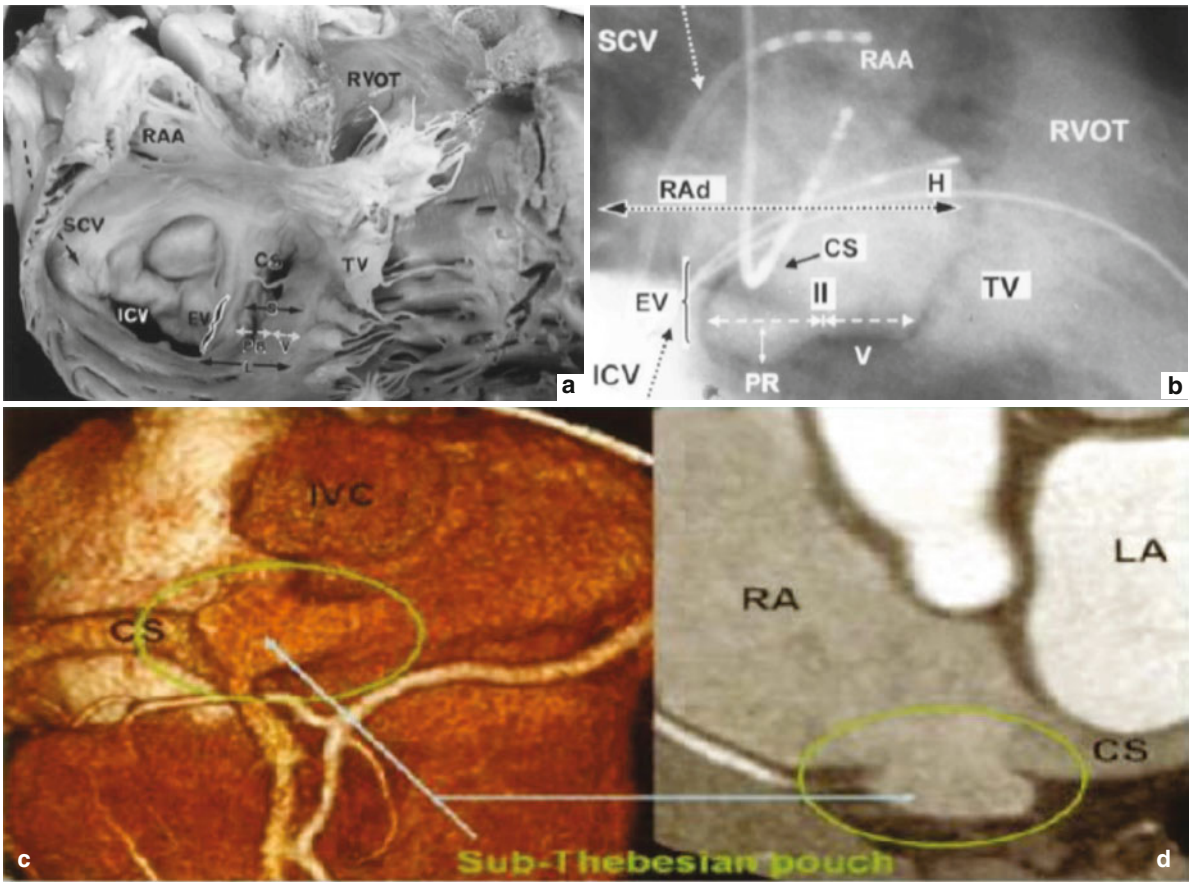

Fig. 14.11 Variations in the contour of the cavotricuspid isthmus can make ablation difficult. (**a**) Autopsy studies show that recesses and irregularities can take the form of a vestibule (V) and posterior recess (PR) along its length (L) from the tricuspid annulus to the Eustachian valve (EV) at the inferior vena cava junction. (**b**) The isthmus is longer in patients with typical atrial flutter than in those without it (37 ± 8 *vs* 28 ± 6 mm), as studied by Cabrera et al. [30]. The sub-Thebesian pouch within the cavotricuspid isthmus is shown by volume-rendered CT in posteroinferior view (**c**) and in a CT tomographic slice image (**d**). Sub-Thebesian (anterior) and sub-Eustachian (posterior) pouches were present in 83% of 30 hearts studied at autopsy, with depth 2.9 ± 1.2 mm (>5 mm in some cases [30]). Detection of anatomical irregularities by multidetector CT can help in tailoring the approach to ablation [30]

CT Imaging of the Interatrial Septum for Puncture and for Assessment of Thromboembolic Risk

The interatrial septum is a critical structure in arrhythmia management. Septal defects provide access to the left atrium for ablation or the placement of endocardial LAA occlusion devices, but they also enable paradoxical embolism that may lead to stroke or systemic thromboembolism. When the interatrial septum is intact, it may exhibit an aneurysm that can challenge trans-septal cannulation. These features are well appreciated on CT (Figs. 14.12, 14.13, 14.14, and 14.15).

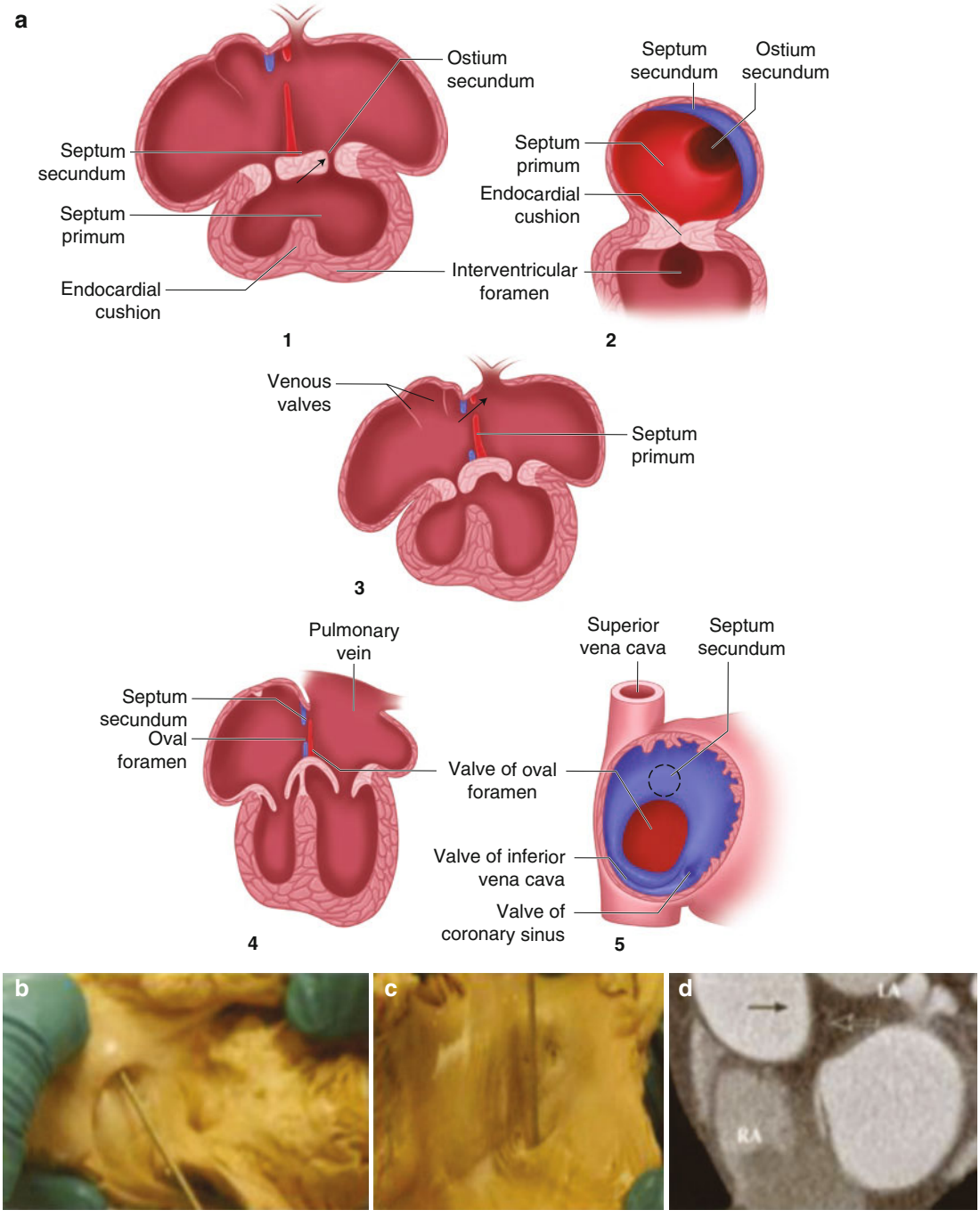

Fig. 14.12 Embryology of the interatrial septum and septal defects. (**a**) The diagrams illustrate the embryology of the interatrial septum, showing (1,2) development of the septum secundum alongside the septum primum; (3) overlap of both septa; and (4,5) final valve of the foramen ovale. (**b**) Flap valve of the fossa ovalis nonadherent to the septum secundum in an autopsy heart (seen from the right atrium), causing a "probe patent" foramen ovale in 25% of adults. (**c**) Probe passes to the left atrium from the right atrium though such a defect. This left atrial flap remains closed if pressure is higher in the left atrium than in the right atrium. (**d**) CT image of a nonfused flap valve (*arrow*). Septal defects offer procedural left atrial (LA) access, but may also enable paradoxical emboli that can result in stroke or transient ischemic attack

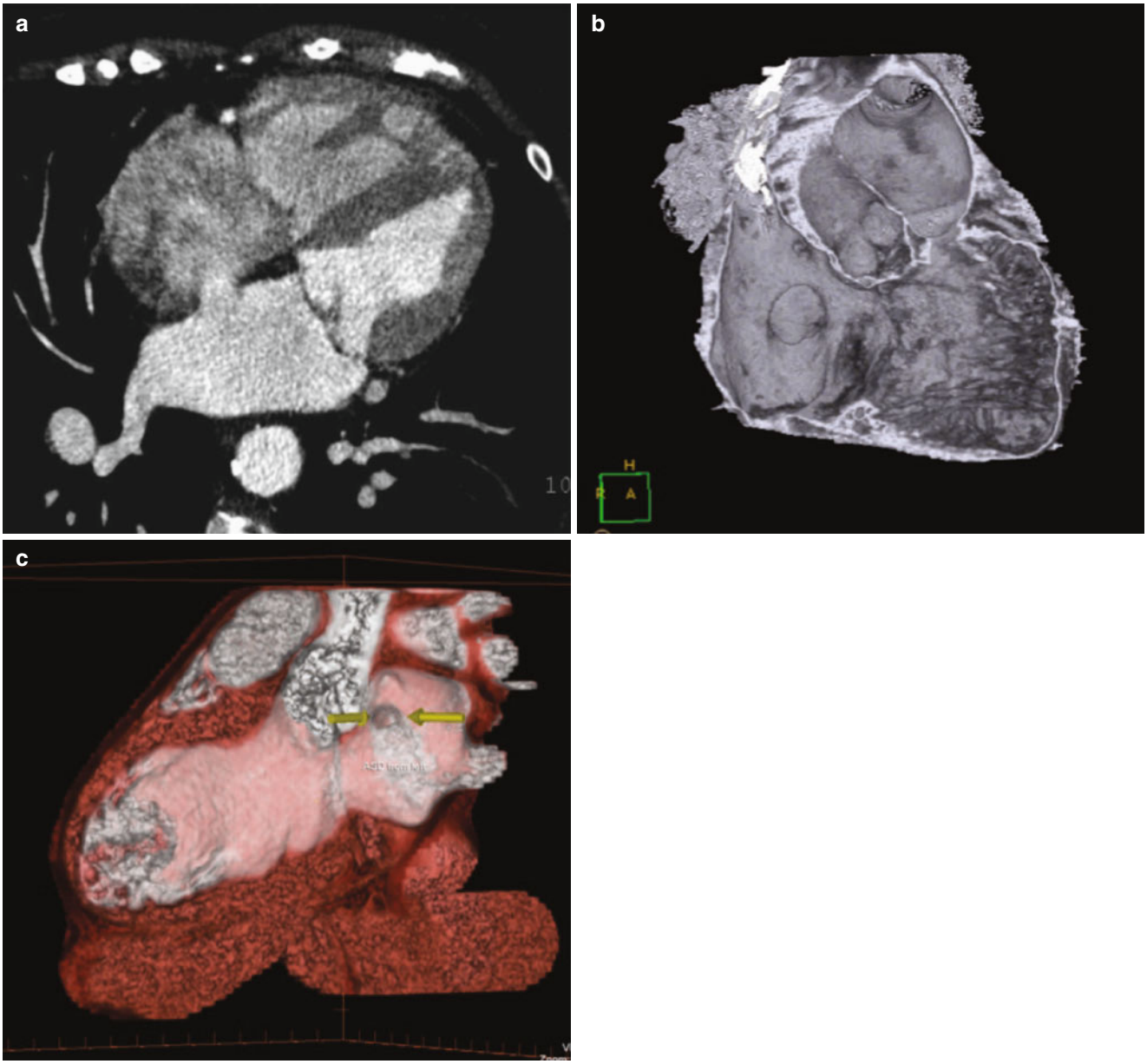

Fig. 14.13 Septum secundum atrial septal defects on CT imaging. (**a**) Four-chamber orientation and (**b**) three-dimensional rendering of a large secundum atrial septal defect viewed from the right atrium. (*Courtesy of* Marcus Chen, Advanced Cardiovascular Imaging Group, NHLBI, NIH.) (**c**) Three-dimensional rendering of an atrial septal defect (*arrow*) in a 17-year-old man presenting with acute chest pain, troponin T of 0.74 ng/mL, and normal coronary arteries. Although such defects can be used to instrument the left atrium, their relatively cranial position may impede catheter advancement to caudal locations, including the right inferior pulmonary vein [31]

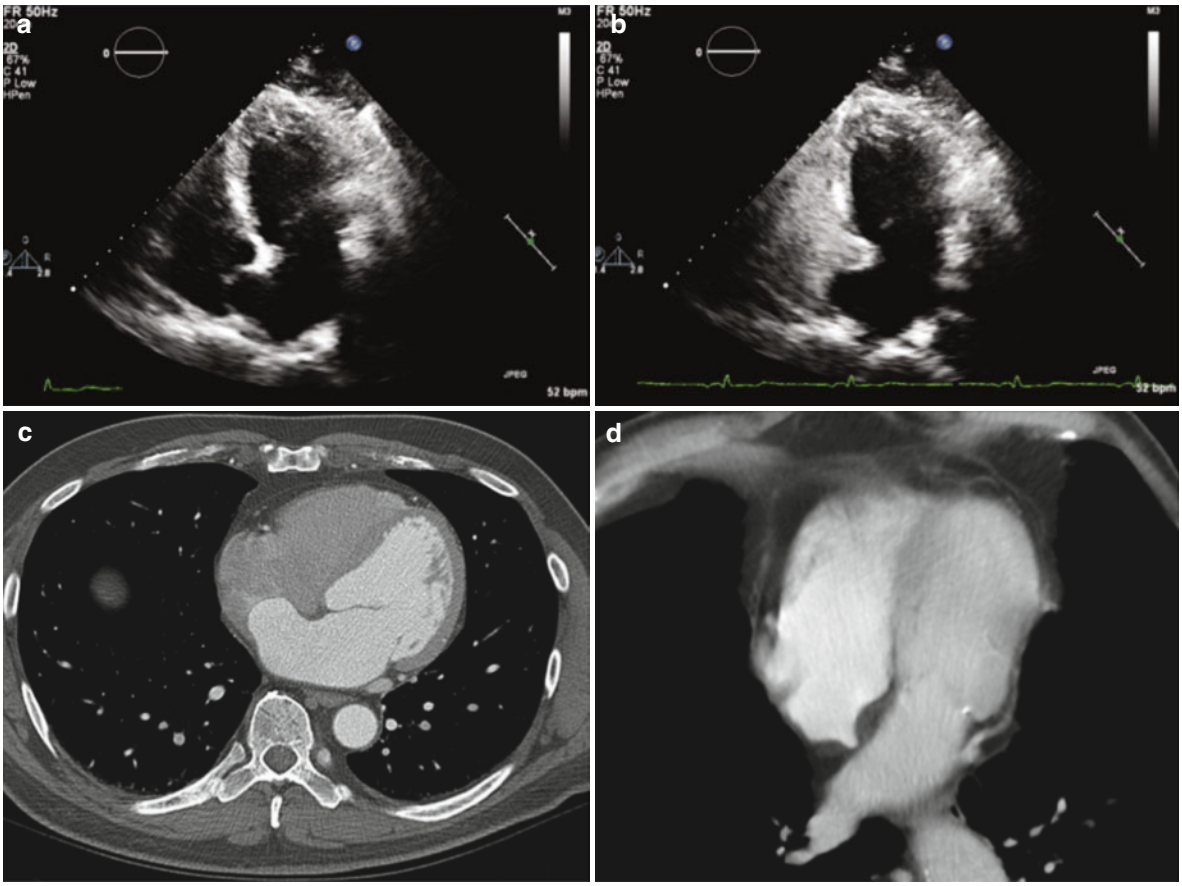

Fig. 14.14 An atrial septal aneurysm is defined as protrusion of the fossa ovalis more than 15 mm beyond the interatrial septum [32]. (**a**) Atrial septal aneurysm viewed by echocardiogram in apical four-chamber orientation, with interatrial septum bowing to the right. (**b**) Lack of right-to-left shunting, imaged with agitated saline contrast injection in the same orientation as (**a**). (**c**) Contrast-enhanced CT scan in axial orientation in the same patient. Tissue redundancy from the aneurysm causes trans-septal needles to protrude far into the left atrium during puncture, increasing the risk of left atrial perforation. A combination of atrial septal aneurysm and a patent foramen ovale identifies individuals at risk for developing a stroke from a paradoxical embolism [33]. (**d**) Lipomatous hypertrophy of the interatrial septum is defined as fatty infiltration of the septum (>2 mm in thickness). Sparing of the fossa ovalis gives rise to the typical dumbbell shape. Both conditions can cause technical difficulties with transseptal puncture

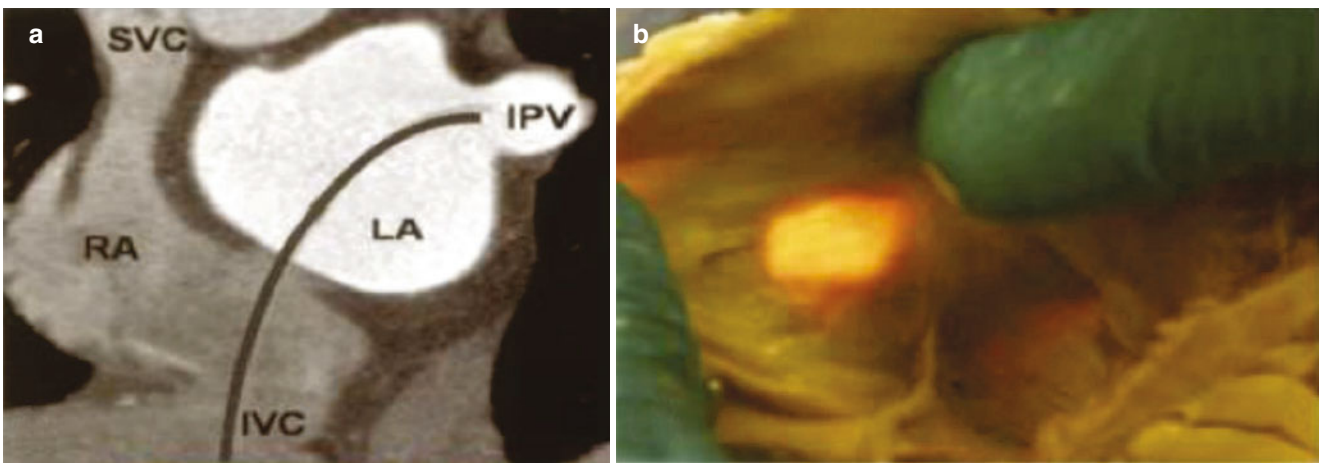

Fig. 14.15 Structures for trans-septal cannulation. (**a**) Trans-septal crossing on short-axis CT scan, showing a sheath crossing the true interatrial septum (fossa ovalis) from the inferior vena cava (IVC) to the left atrium (LA) and to the ostium of the left inferior pulmonary vein (IPV). (**b**) Transillumination of the fossa ovalis in an autopsy specimen. The aorta lies anterior to the fossa ovalis, the pericardial space is posterior, and the recess between atria is superior. The fossa ovalis is the only structure that provides direct access to the left atrium (true interatrial septum)

CT to Guide Atrial Fibrillation Ablation

Atrial fibrillation (AF), the most common sustained cardiac arrhythmia [20], is a leading cause of stroke, thromboemboli, hospitalization, and mortality. Recent clinical trials question the value of pharmacological strategies to limit ventricular rate [34] and maintain sinus rhythm [35]. Nonpharmacological therapies are increasingly effective and are being more widely used. Mechanistically, AF is triggered by premature complexes from the pulmonary veins (PVs) and elsewhere [36], and then is sustained by mechanisms from the left or right atria [37] that include localized rotors and focal sources [37, 38], disorganized wavelets [39], and the impact of the autonomic nervous system [40] in the context of structural factors including atrial fibrosis and scar [41].

Atrial CT greatly enhances AF ablation by *a priori* identification of patient-specific anatomy and variants that may influence ablation (facilitated by image integration into widely used mapping systems for real-time tracking of catheter position) (Figs. 14.16, 14.17, 14.18, 14.19, 14.20, and 14.21), targeting of AF mechanisms (Fig. 14.22) and then enabling effective lesion creation. Pulmonary vein isolation [36] is designed to eliminate potential triggers from the PVs; the isolation is typically performed by wide encircling lesions in the left atrium to avoid potential damage and stenosis of the PV [36]. Additional ablation lesions are commonly placed at the roof or mitral annulus, or other left or right atrial sites for paroxysmal AF [42, 43] as well as persistent AF [36].

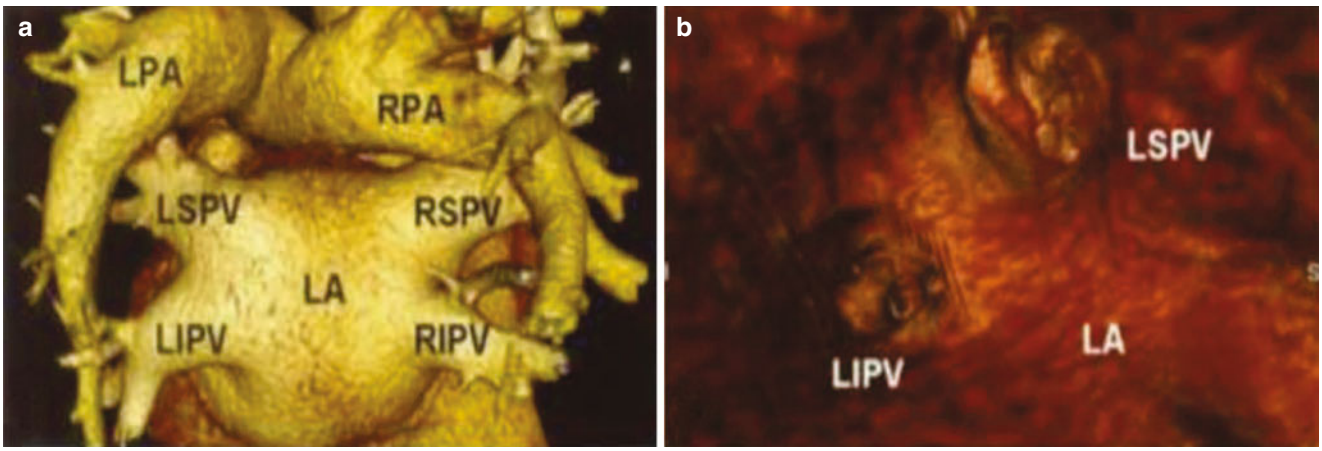

Fig. 14.16 CT of typical pulmonary vein (PV) anatomy. (**a**) Superior and inferior PVs drain the left lung (LSPV, LIPV) and right lung (RSPV, RIPV) respectively. (**b**) Endoluminal view of PV ostia on volume-rendered CT. PV triggers for AF are most commonly isolated by ablating in a pattern of wide area encirclement of the PVs, using lesions within the atria [36]. This pattern greatly reduces the risk of PV stenosis [44], compared with original approaches that isolated the PV at their ostia, and may also increase success [45], perhaps by also eliminating left atrial (LA) sustaining mechanisms [9, 36, 46]

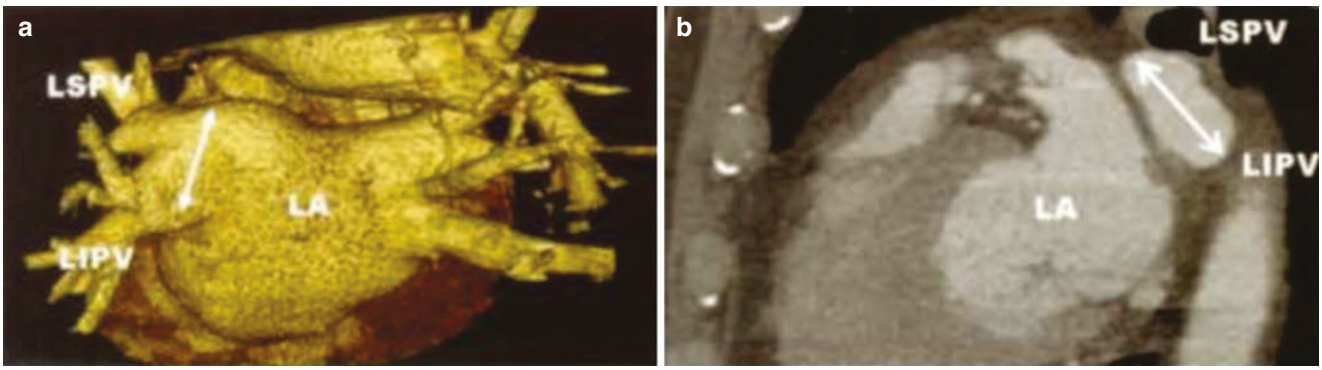

Fig. 14.17 Common variants of pulmonary vein anatomy: common and accessory ostia. (**a**) Three-dimensional volume-rendered CT in a posterior-anterior orientation showing a common ostium of the left PVs (*double arrow*). In a recent study, this variant occurred in 79% of patients for left PVs and in 31% of patients for right PVs [47]. An accessory vein draining the right middle lobe of the lung is also seen. (**b**) Sagittal CT tomogram showing common truncus of both left PVs (*double arrow*) before they drain into the left atrium. (**c**, **d**) Matched 3D CT and intracardiac echocardiography of common left PV ostia (*double arrow*) in the same patient. (**e**) Three-dimensional CT of accessory right PV. (*From* Nasis et al. [6]; with permission.) In a recent study, multislice CT was found superior to intracardiac echocardiography for identifying these variants [48]

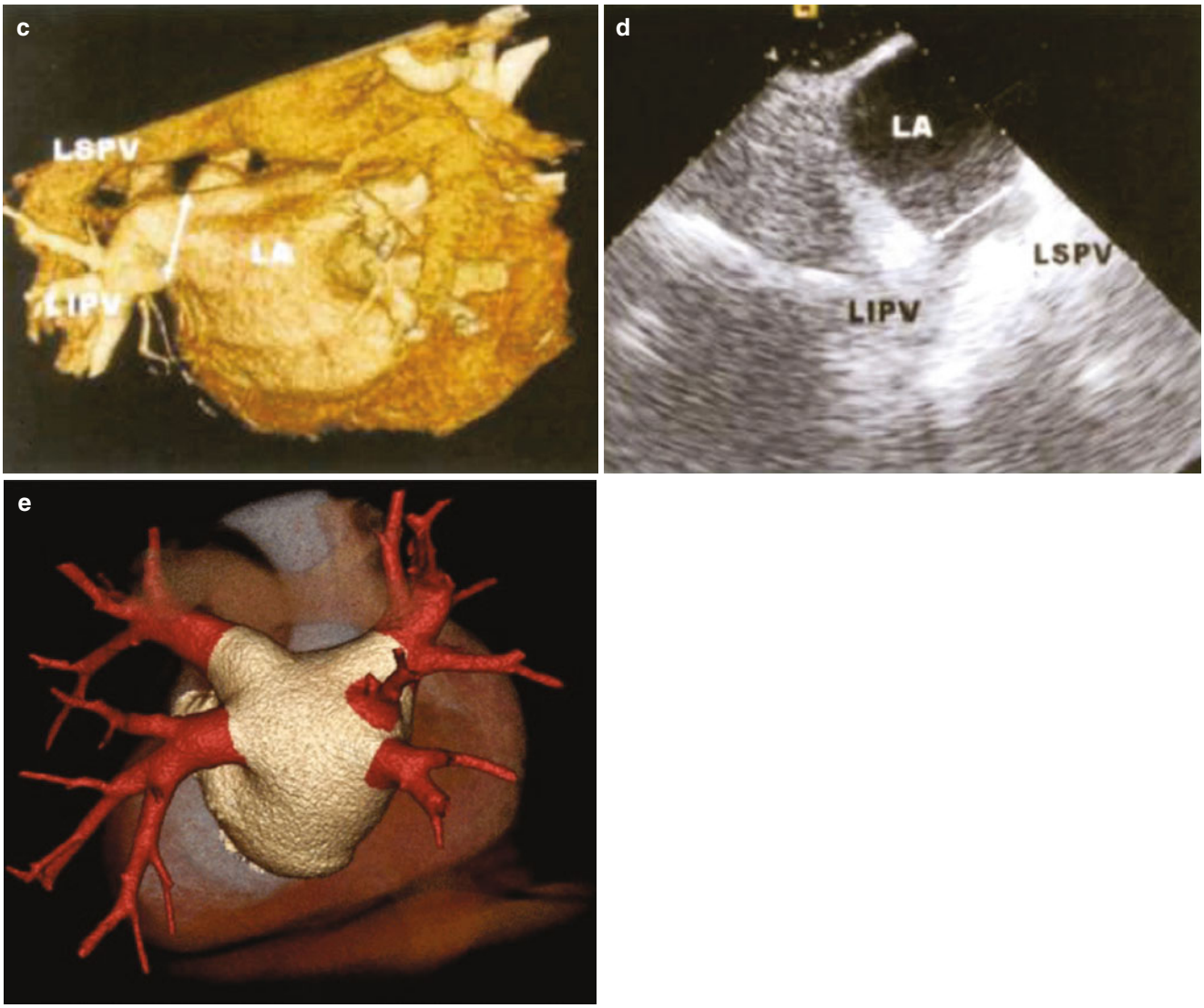

Fig. 14.17 (continued)

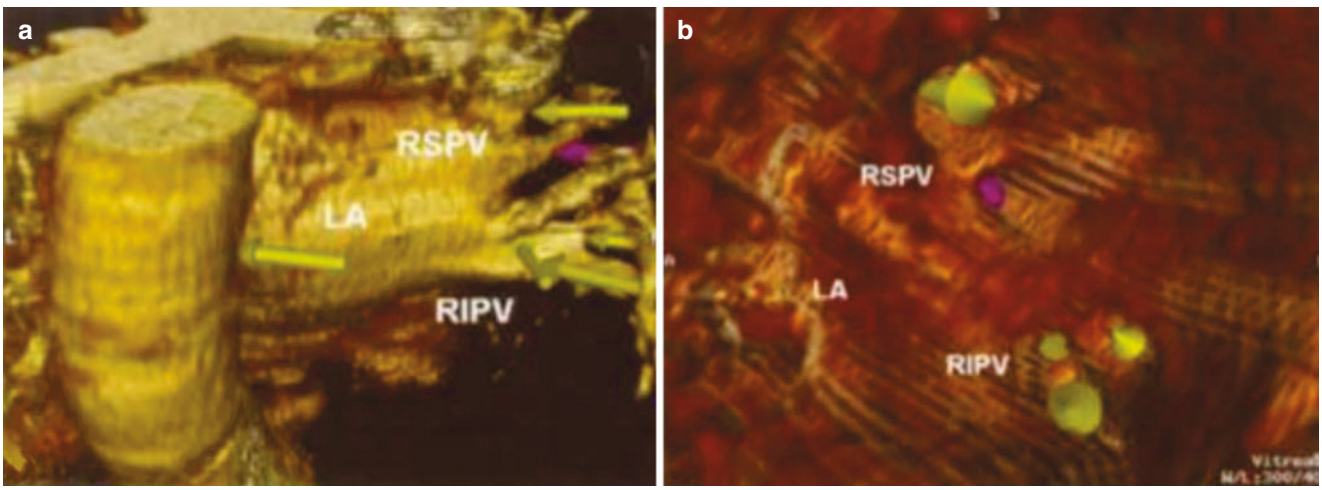

Fig. 14.18 Early branching of the pulmonary veins (PVs) gives the appearance of multiple ostia from the left atrium, which will alter the approach to isolate the triggers for AF from the PVs. This figure shows early branching of right PVs on 3D volume-rendered reconstruction (**a**), and endoluminal view, showing multiple apparent ostia (**b**). *LA* left atrium, *RIPV* right inferior pulmonary vein, *RSPV* right superior pulmonary vein

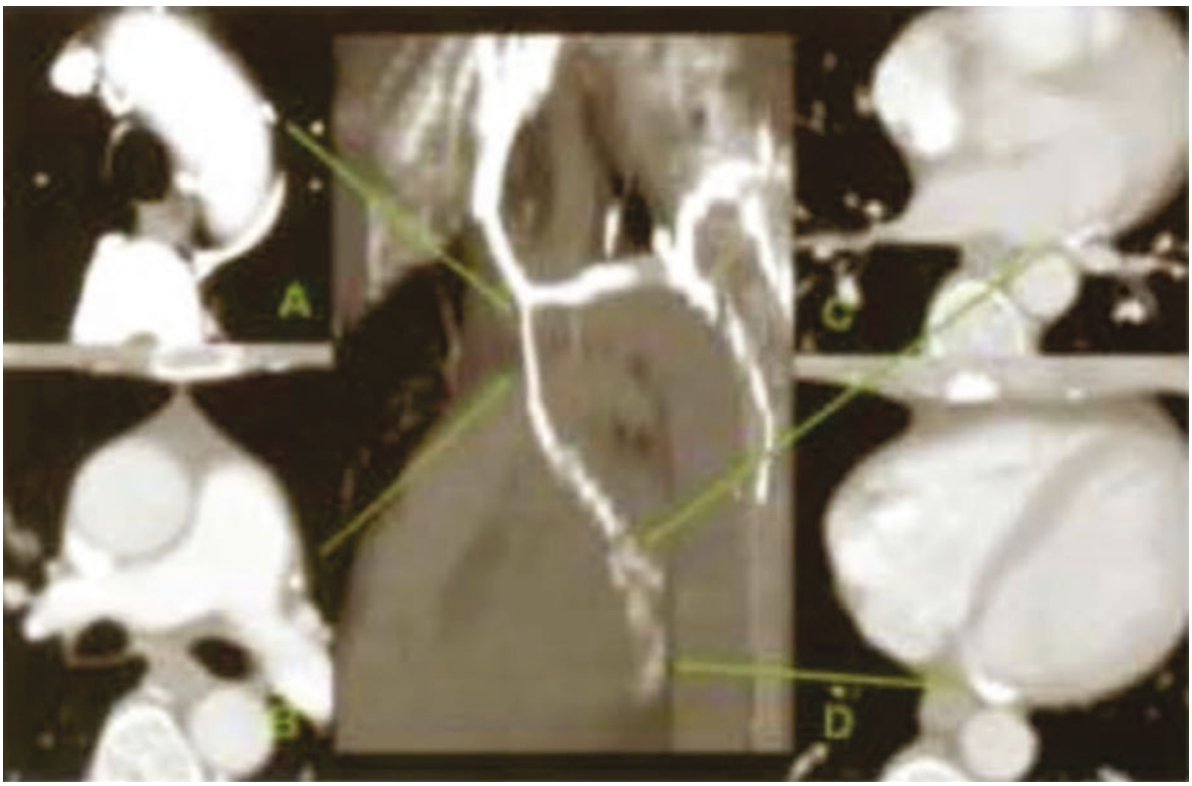

Fig. 14.19 Additional venous triggers: vein of Marshall. The vein of Marshall can be visualized on CT to extend from the superior intercostal vein (**a**) and runs inferiorly (**b**, **c**) to the coronary sinus (**d**). The vein of Marshall is the remnant of the left cardinal vein, and may persist as a ligament of Marshall, both of which lie in an endocardial reflection or "Coumadin ridge" bounded anteriorly by the left atrial appendage and posteriorly by the left superior pulmonary vein. The vein can cause premature beats that trigger AF [49] and is connected to the cardiac autonomic nervous system [50]. Cannulation of the vein of Marshall is a route for ablation and for modulation of the autonomic nervous system [50]

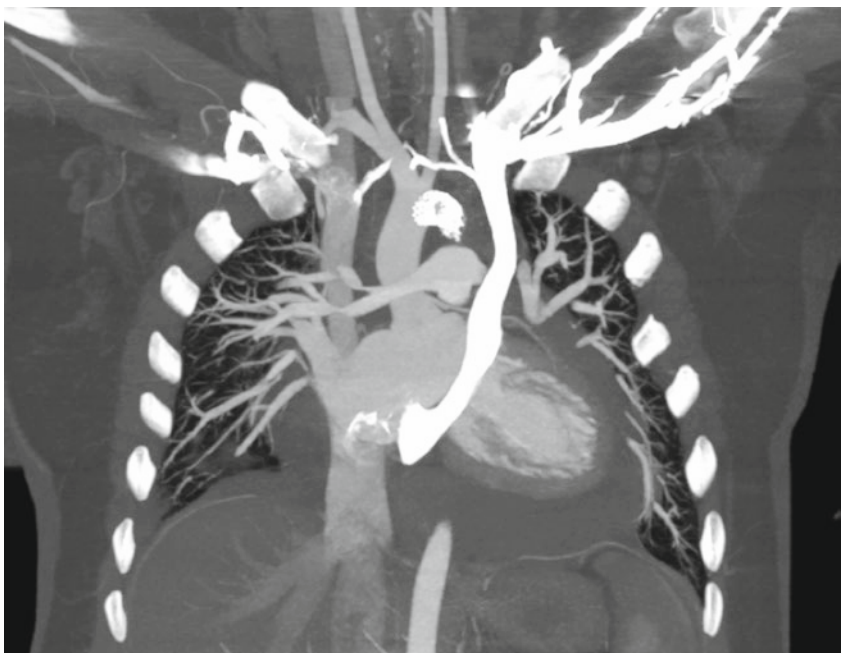

Fig. 14.20 Additional venous triggers: persistent left superior vena cava (SVC). Shown in oblique maximum-intensity projection, this patient also has a large pericardial effusion and prior aortic stenting for coarctation in the arch. Contrast was injected into the left antecubital vein to highlight the left-sided SVC and dilated coronary sinus. The persistent left SVC is a remnant of the left cardinal vein and is often accompanied by dilatation of the coronary sinus. Premature beats from the left superior pulmonary vein can trigger AF

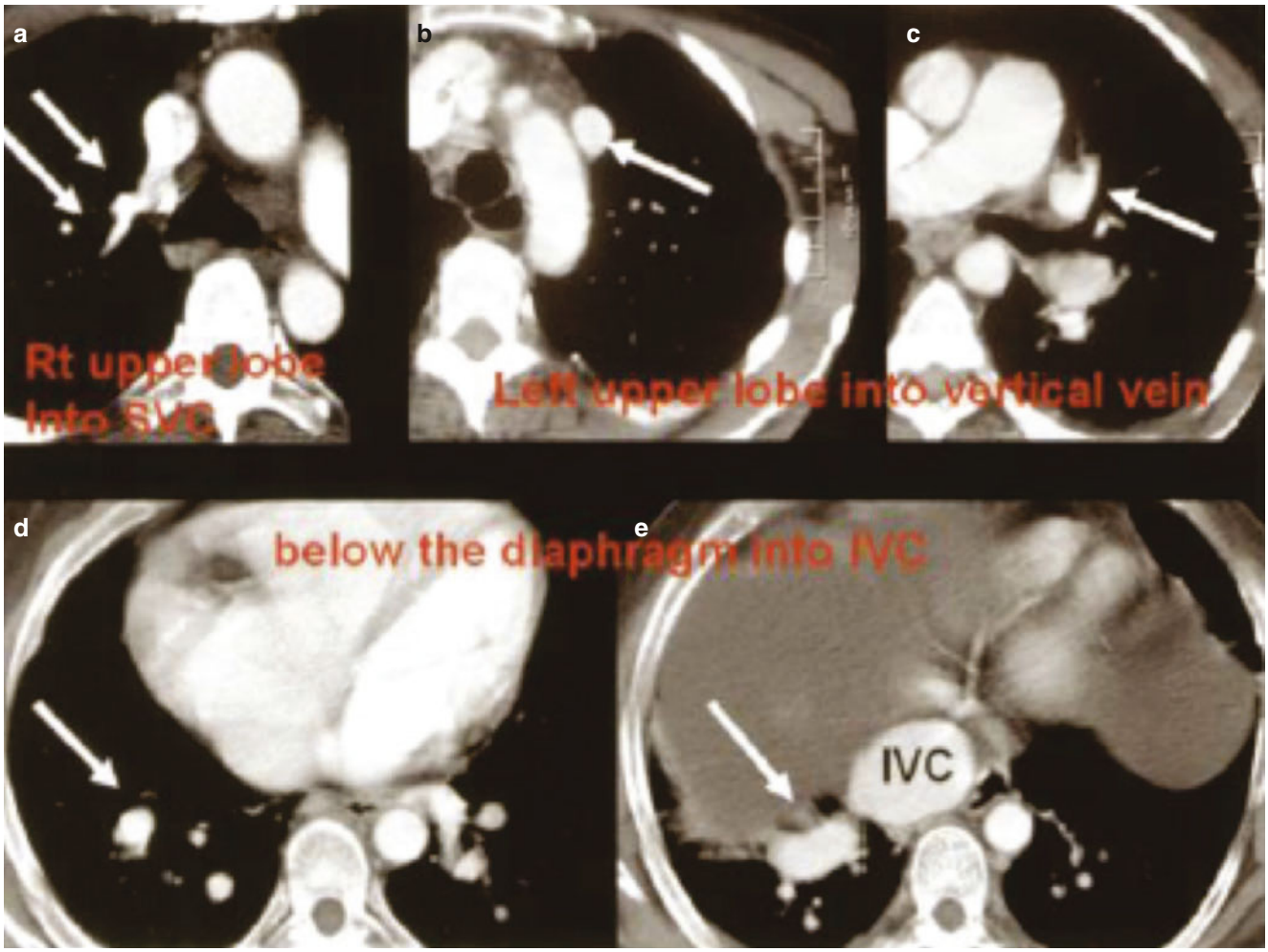

Fig. 14.21 Partial anomalous pulmonary venous (PAPV) drainage in different patients. (**a**) Right superior pulmonary vein drains into superior vena cava (SVC) (*arrows*). (**b**) Left superior pulmonary vein drains into left brachiocephalic vein via the vertical vein (*arrow*). (**c**) Right inferior pulmonary vein drains into inferior vena cava (IVC) in its suprahepatic segment (*arrow*), producing the scimitar sign. Embryologically, the PV joins the pulmonary portion of the splanchnic plexus at day 28 of gestation to drain blood into the heart and loses connections with cardinal and umbilicovitelline systems [51]. The cardinal system differentiates into the superior vena cava and coronary sinus, whereas the umbilicovitelline system differentiates into the IVC, ductus venosus, and portal vein. During development, tributaries coalesce to form each PV that incorporates into the posterior wall of the left atrium. Premature atresia of right or left portions of primordial PVs while primitive pulmonary/systemic connections are still present results in PAPV drainage [52]. Unlike total anomalous PV connection, PAPV connection is acyanotic and may be an incidental finding. Classically, PAPV presents in childhood, most frequently on the right side, associated with a sinus venosus atrial septal defect [52]. In the left upper lobe, intraparenchymal left upper lobe PVs join to form the vertical vein, which drains into the left brachiocephalic vein. The prevalence of PAPV is about 0.2% [52]; of these individuals, 79% have an anomalous left upper lobe vein connecting to a persistent left vertical vein, 17% have an anomalous right upper lobe vein draining into the SVC, and 3% have an anomalous right lower lobe vein draining into the suprahepatic IVC

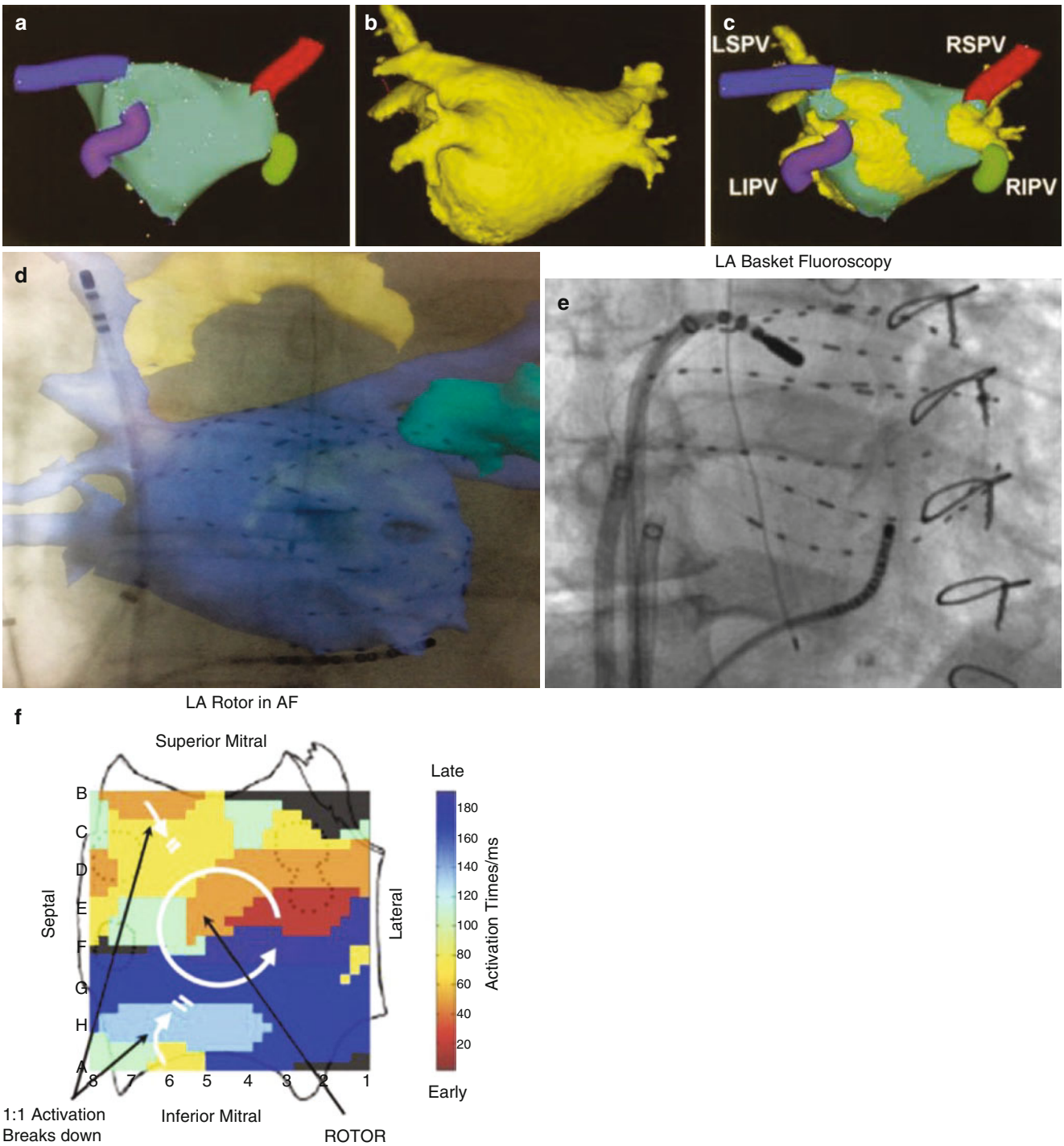

Fig. 14.22 Electrophysiological–anatomical integration to guide ablation. (**a**) Electroanatomic map of the left atrium and pulmonary veins (PVs) acquired at electrophysiology study using the CARTO system (Biosense-Webster, Diamond Bar, CA). The blue, purple, red, and green "tubes" represent PVs. (**b**) Segmented multidetector CT scan showing the left atrial and PV anatomy. (**c**) Image integration enables the electroanatomic map to be fused with the multidetector CT surface anatomy. *LIPV* left inferior pulmonary vein, *LSPV* left superior pulmonary vein, *RIPV* right inferior pulmonary vein, *RSPV* right superior pulmonary vein. (**d**) Multipolar basket catheter in left atrium imaged using rotational angiography. (*Courtesy of* Michael Orlov, St. Elizabeth's Medical Center, Boston, MA [53]). (**e**), Fluoroscopy to record AF simultaneously over a wide area for computational identification of patient-specific mechanisms that may sustain AF. (**f**) Focal impulse and rotor mapping (FIRM) revealed an AF rotor (electrical spiral wave) in the patient identified in (**e**), and ablation at the rotor eliminated AF, as shown in initial clinical trials [37, 55]. (*From* Narayan et al. [54]; with permission)

CT Imaging of Potential Complications of Atrial Ablation

The atrial walls are thin and intimately associated with mediastinal structures, so that ablation carries a finite risk of complications (Figs. 14.23, 14.24, 14.25, and 14.26). This risk is increased if ablation is performed in close proximity to these structures or with excessive energy delivery. These risks are well known [56], and steps routinely taken to avoid them have markedly reduced their incidence at high-volume centers [57].

CT in Managing Ventricular Arrhythmias

Ventricular arrhythmias are a leading cause of sudden cardiac arrest, in the form of sustained ventricular tachycardia and fibrillation, that results in over 300,000 deaths annually in the United States alone [62]. Premature ventricular complexes and nonsustained tachycardia are the most prevalent heart rhythm disorders in the world [63]. CT is an increasingly important component of managing such heart rhythm disorders.

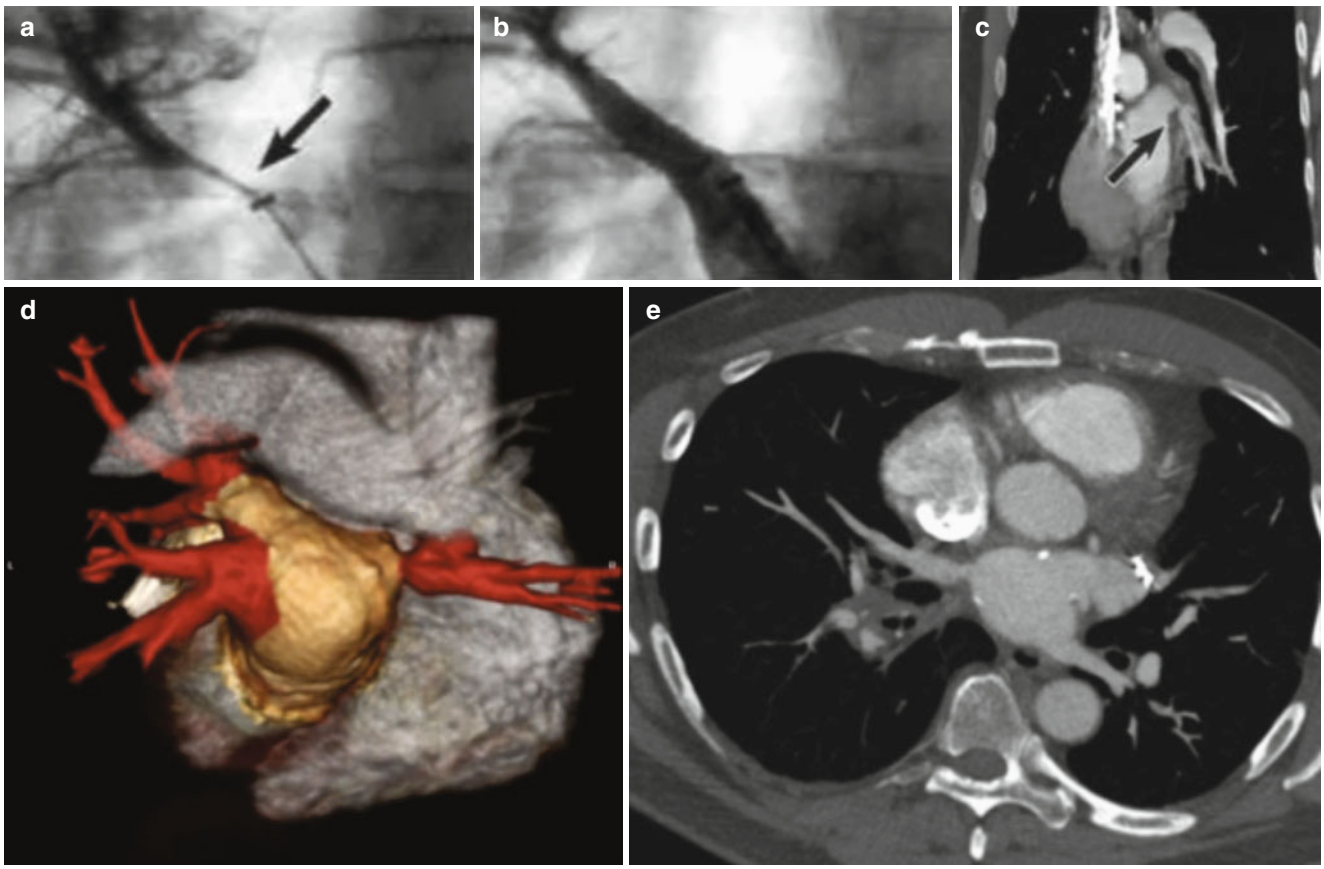

Fig. 14.23 Pulmonary vein (PV) stenosis can be symptomatic, presenting with shortness of breath, hemoptysis, and other symptoms months after the procedure. PV stenosis was more common with earlier ablation approaches that isolated PVs near their ostia [36] than with current approaches, which ablate in wide circumferential lesion sets in the atria. (**a**) Venogram showing severe stenosis of the right superior PV before stenting. (**b**) The same PV after stenting. (**c**) Stenosis of left inferior PV on a multidetector CT image. (**d**) Stenosis of right upper PV and complete occlusion of the right inferior PV due to ablation in 3D volume-rendered CT. (**e**) CT slice showing the same patient

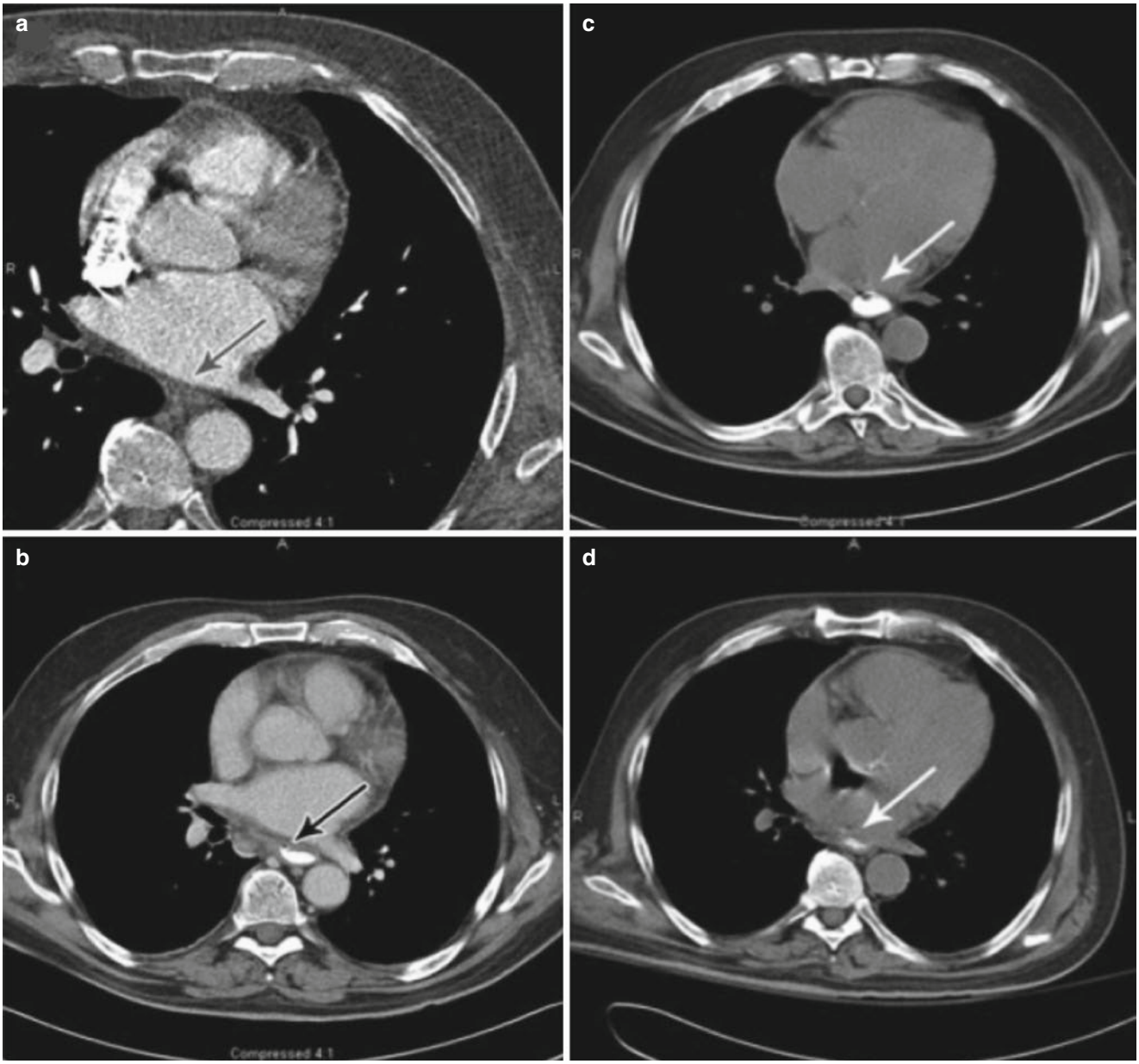

Fig. 14.24 Atrioesophageal fistula. Images show the progression of atrioesophageal fistula after AF ablation in a 61-year-old man who presented late and had serial CT scans but refused intervention [58]. (**a**) Preprocedural CT with normal atrioesophageal interface (*arrow*); (**b**) At 10 days post-procedure, linear contrast at the midthoracic esophagus is seen extending along its right anterior aspect at the level of the inferior pulmonary veins. (**c**) At 39 days, a sinus tract is shown in the CT extending anterolaterally into pericardial fat. (**d**) At 41 days, fistula formation with intra-atrial air is observed at the level of the sinus tract seen 2 days earlier. Atrioesophageal fistula is one of the most feared complications of atrial ablation (typically for AF). It presents 2 to 3 weeks after ablation with fever, sepsis, and neurological symptoms from entry of esophageal contents and air into the systemic circulation [59]. Although it is rare (incidence 0.1–0.2%) [59], the fistula is typically fatal if left untreated; mortality is 70% even after surgical repair

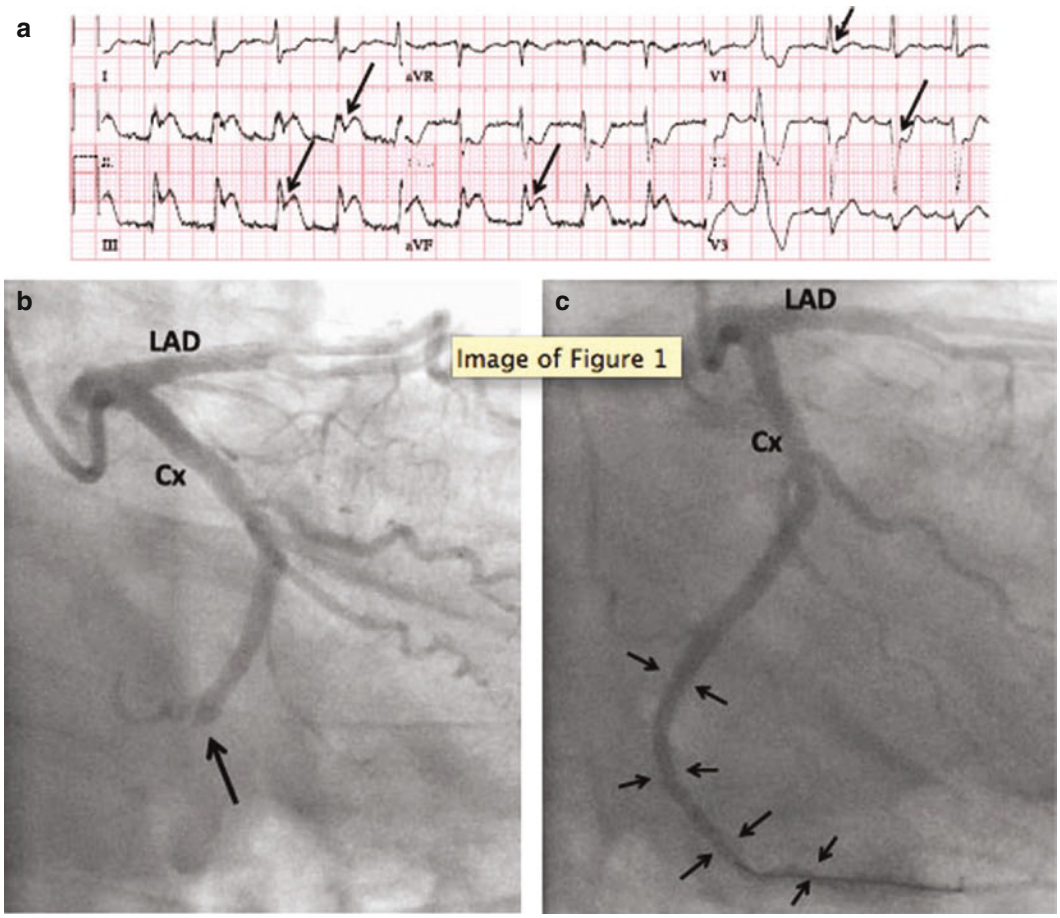

Fig. 14.25 Myocardial infarction after AF ablation. Coronary stenosis is a rare complication of atrial ablation. (**a**) Acute inferior myocardial infarction with acute ST segment elevation and lateral ischemic ST depression (*arrow*) occurring 1 h after mitral isthmus lesions during AF ablation. (**b**) Acute stenosis of the mid-to-distal circumflex (Cx) coronary artery (*arrow*). (**c**) The same artery after acute stent placement (*arrows*). Coronary stenosis after ablation was recently reported in 0.14% of a series of 5709 consecutive cases at a large academic medical center [60], and acute coronary spasm/narrowing has been reported after ablation at the mitral annulus [61].

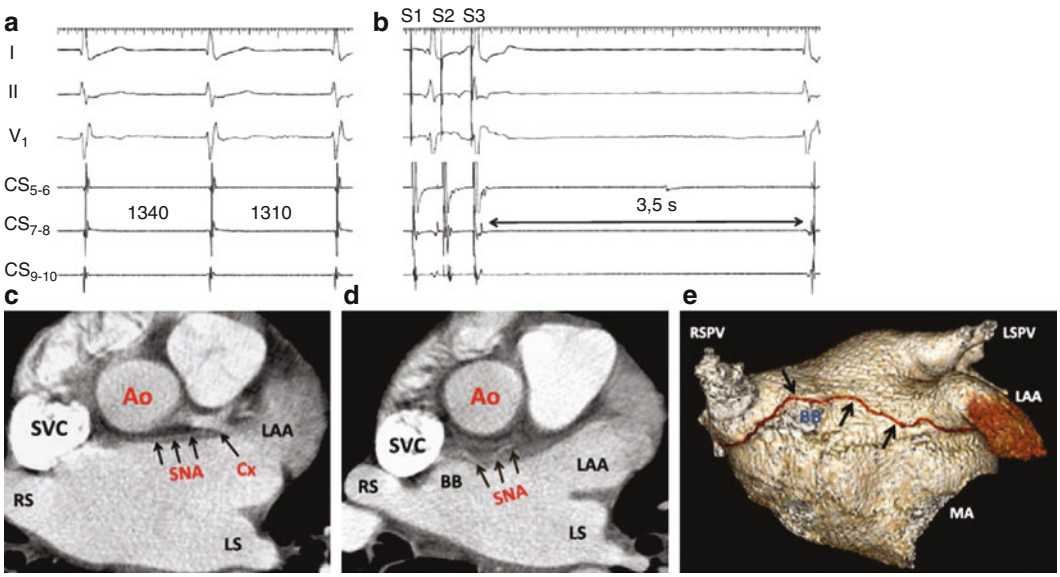

Fig. 14.26 Sinus node dysfunction due to sinus nodal ischemia caused by AF ablation, via damage to the sinus nodal artery when ablating at the left atrial roof near the right superior pulmonary vein (PV). (**a**) ECG and three coronary sinus electrograms showing junction escape rhythm (rate ≈ 46/min, cycle length ≈ 1300 ms) after AF ablation. (**b**) Evidence of sinus node dysfunction with atrial pauses on electrophysiologic study. (**c**–**e**) Slices and volume-rendered CT scans showing the course of the sinus nodal artery (SNA) emerging from the circumflex artery (Cx) [60]. *Ao* aorta, *BB* Bachman's bundle, *LAA* left atrial appendage, *LS* left superior PV, *RS* right superior PV, *SVC* superior vena cava

Imaging Potential Causes of Sudden Cardiac Arrest

The most common association with sudden cardiac arrest is coronary artery disease, which is present in the vast majority of cases on autopsy (even if considered noncritical or not previously diagnosed) [63, 64]. Cardiac CT has great potential in noninvasively diagnosing coronary disease in the form of overt stenoses (Fig. 14.27) [65, 66] or coronary calcium [66, 67], or in identifying anomalous coronary arteries (Fig. 14.28) [65, 66], which are rare but important potential causes of sudden death in young or otherwise healthy individuals [63]. CT imaging is also useful in detecting ventricular aneurysms (Fig. 14.29) and cardiomyopathy (Figs. 14.30 and 14.31).

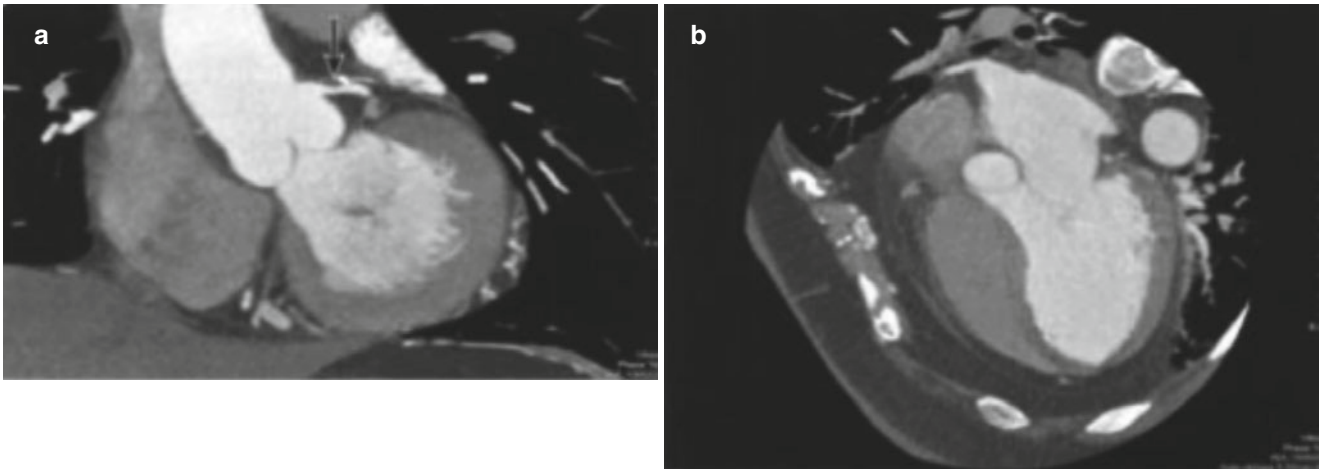

Fig. 14.27 (**a**) CT coronary angiography shows moderate to severe stenosis of the left main coronary artery (*arrow*). Coronary stenoses can cause sustained ventricular arrhythmias and sudden cardiac arrest regardless of the extent of ischemic myocardium and even if the left ventricular (LV) ejection fraction is normal. CT angiography can also assess the patency of arterial and venous grafts. (**b**) Substantial LV dilatation on axial CT in a patient with nonischemic cardiomyopathy; the LV ejection fraction is 29%. Multidetector CT is a very good measure of systolic dysfunction, which is a primary indication for implantable cardioverter-defibrillator (ICD) therapy [68]

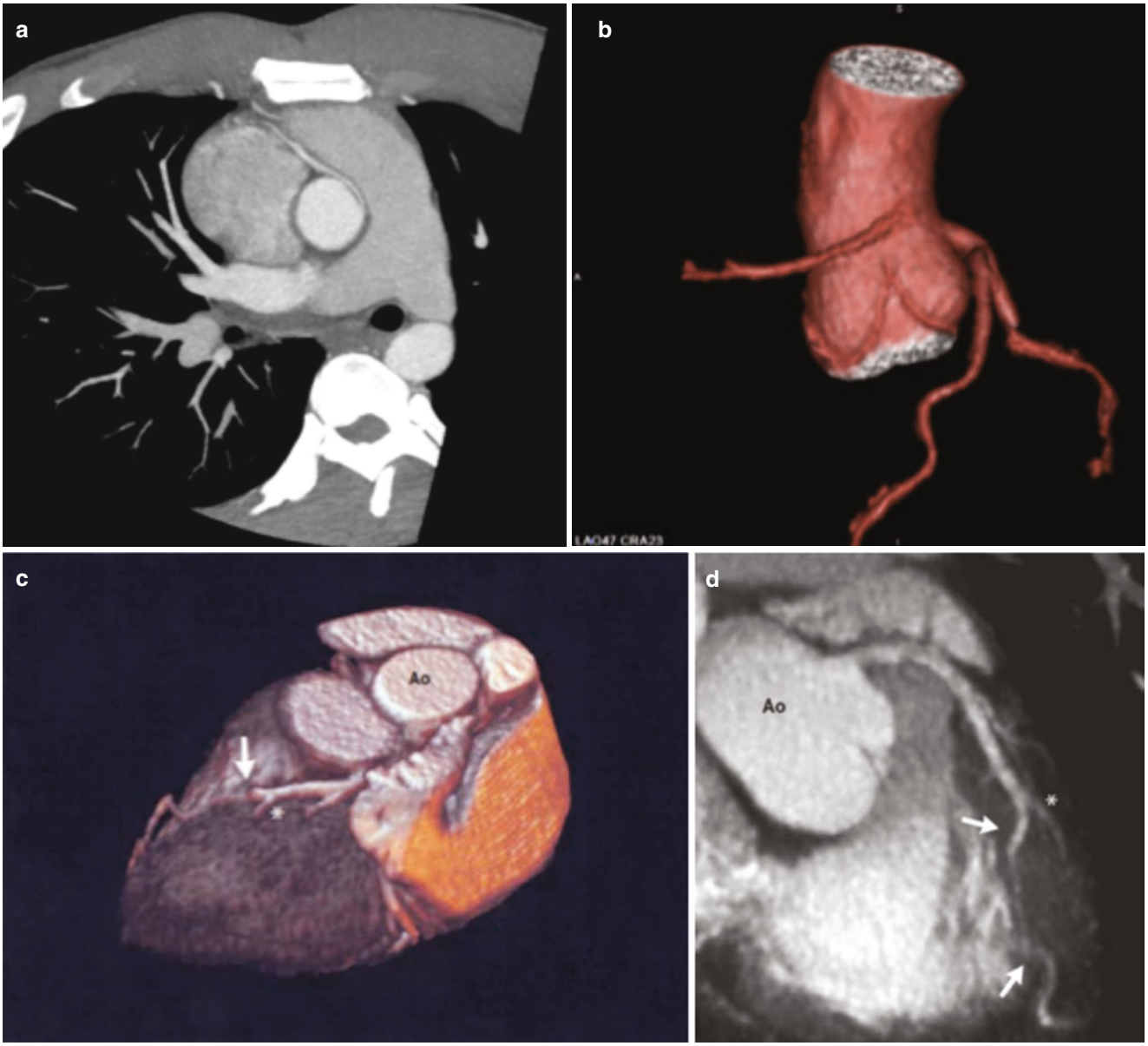

Fig. 14.28 CT of coronary artery variants. (**a**, **b**) Anomalous right coronary artery from the left coronary sinus with a proximal course between the aorta and main pulmonary artery, as shown in a maximum-intensity projection (**a**) and three-dimensional rendering reconstruction (**b**). (**c**, **d**) Muscular bridging. Contrast-enhanced electron-beam CT (**c**) in a 39-year-old man presenting with exertional angina shows systolic narrowing of the middle segment of the left anterior descending artery with a step-down, step-up phenomenon (*arrow*) distal to the second diagonal branch (*asterisk*). (**d**) Maximal-intensity projection shows the intramyocardial course of the artery toward the right ventricular subendocardium. The *arrows* show the step-down, step-up phenomenon, and the *asterisk* marks the distal branch. The patient was successfully treated with a beta-blocker. Both anomalies are rarely associated with sudden cardiac arrest. *Ao* aorta. (*Adapted from* Eggebrecht and Mohlenkamp [69]; with permission)

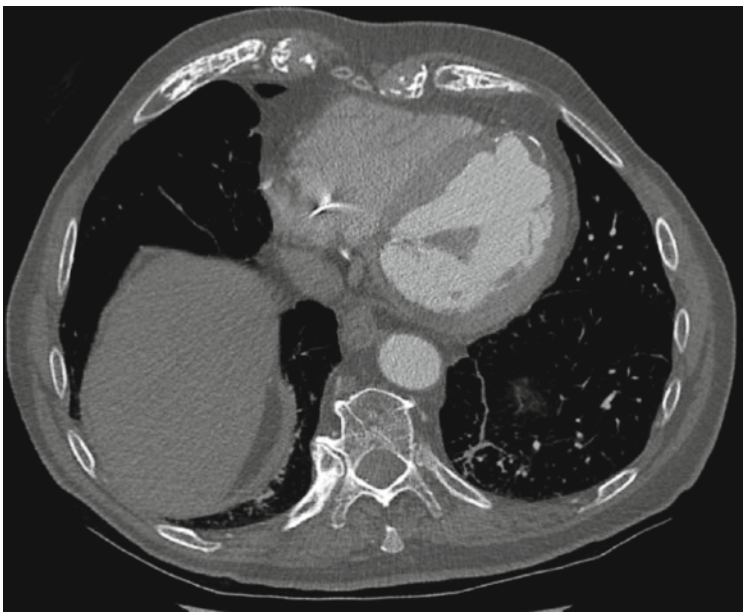

Fig. 14.29 Left ventricular aneurysm. CT shows a calcified aneurysm with mural thrombus, likely from prior transmural myocardial infarction. Such aneurysms are less common in the modern era of revascularization

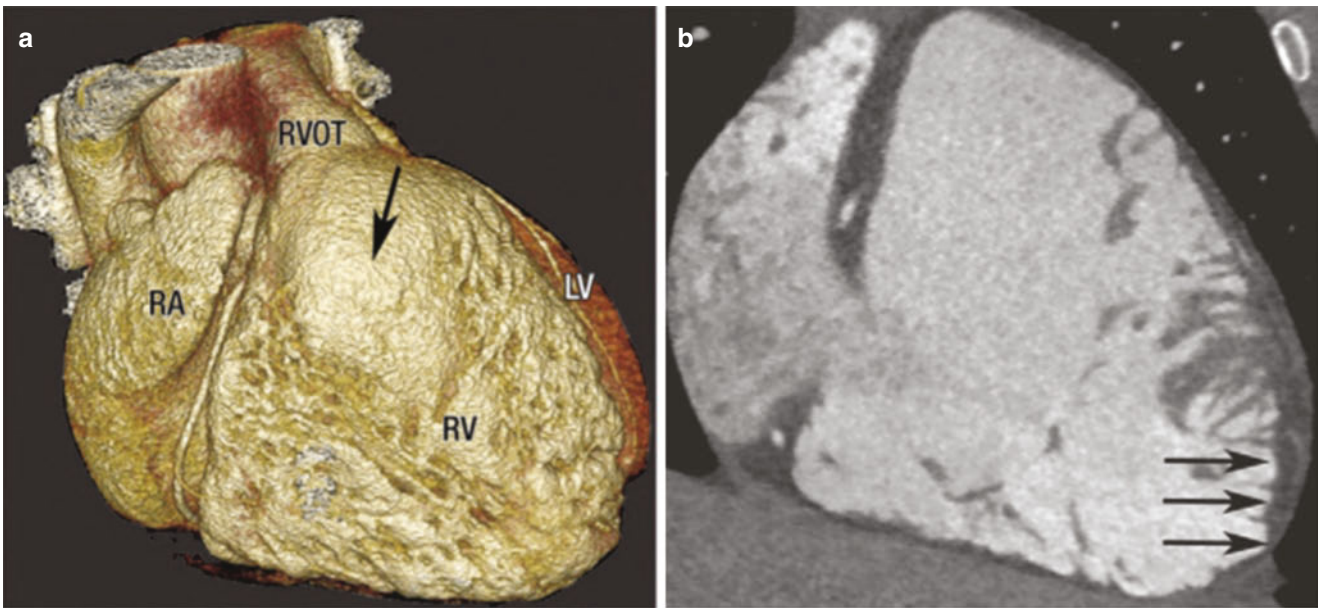

Fig. 14.30 Arrhythmogenic cardiomyopathy involving the right ventricle (RV). (**a**) Dilated RV on three-dimensional volume-rendered multidetector CT image, with scalloped appearance and prominent aneurysm at basal segment of RV free wall (*arrow*). (**b**) Thin-walled right ventricle on sagittal contrast-enhanced multidetector CT image, with scalloped inner free wall (*arrows*) consistent with localized aneurysms. Arrhythmogenic cardiomyopathy [70] is a rare condition characterized by progressive fibrofatty replacement of myocardium (well visualized on CT), which may cause exertional ventricular arrhythmias and sudden cardiac arrest. Although mostly involving the RV, biventricular involvement and even left ventricular (LV) dominance [71] have been reported. The condition is transmitted predominantly in an autosomal dominant fashion, but recessive transmission is described in cases with cutaneous abnormalities such as Naxos disease and Carvajal syndrome. The primary cellular defect involves the desmosomes responsible for cell-to-cell binding. *RA* right atrium, *RVOT* RV outflow tract. (*Adapted from* Nasis *et al.* [6]; with permission)

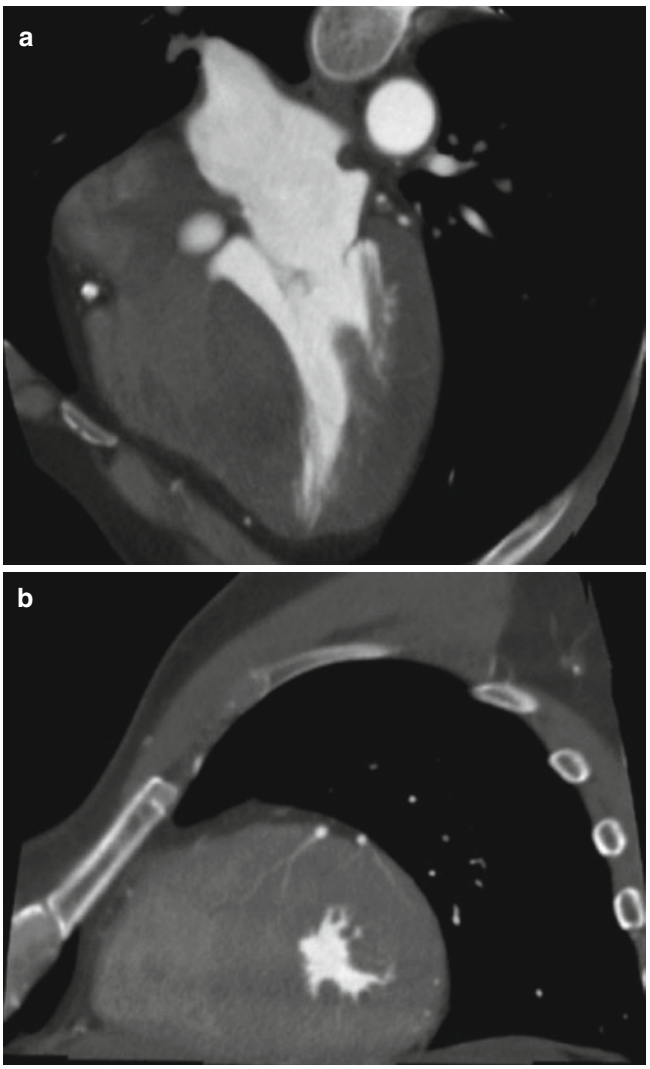

Fig. 14.31 Hypertrophic cardiomyopathy. CT shows (**a**) dramatic hypertrophy of the left ventricle, (**b**) which predominantly affects the interventricular septum in this case. There is narrowing of the left ventricular outflow tract. Outflow tract obstruction can result in syncope due to hemodynamic compromise. Patients with this autosomally dominant transmitted disorder are at risk for ventricular arrhythmias due in part to myofiber disarray [72]. Cardiac CT is a well-used modality for diagnosing this condition. Therapy includes ICD placement and potentially surgical resection or coronary alcohol infusion to reduce left ventricular mass [36]

CT Imaging to Guide Ablation of Ventricular Arrhythmias

Ablation is increasingly performed for ventricular arrhythmias, typically in patients with symptomatic premature ventricular complexes or sustained ventricular tachycardia, or in those with implantable cardioverter defibrillators (ICDs) and multiple delivered therapies despite optimal medical therapy. Cardiac CT can provide valuable structural information and identify regions of ventricular scar, whose surrounding border zone is often a pathophysiological substrate that is targeted for ablation (Figs. 14.32, 14.33, and 14.34).

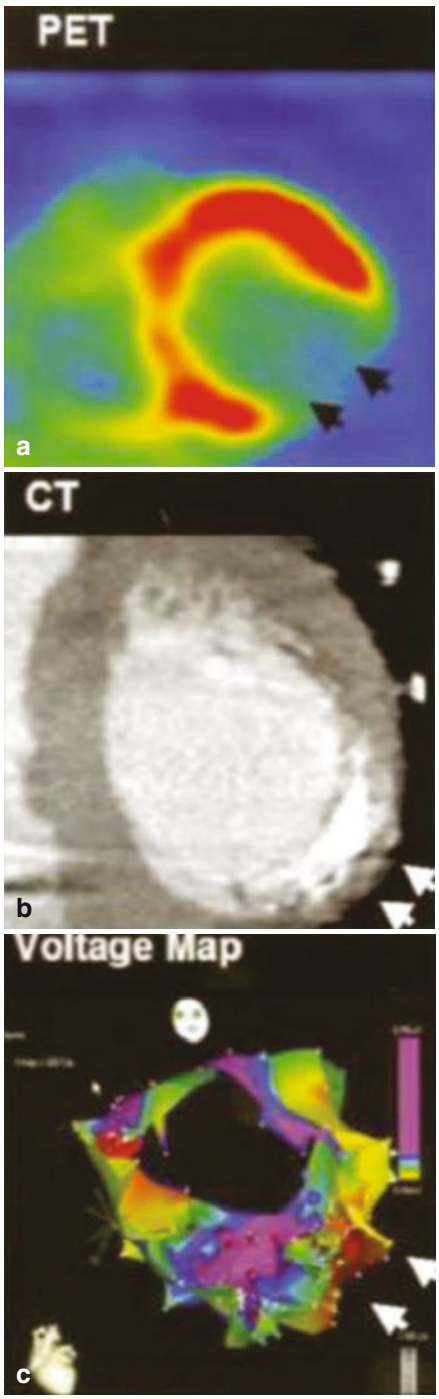

Fig. 14.32 Eight-week old myocardial infarction (*arrows*) in a porcine model. (**a**) Positron emission tomography (PET) shows an absence of viable myocardium (*blue* versus *red* or *yellow*). (**b**) CT with late iodine enhancement illustrates regions of scar replacing viable myocardium. (**c**) Low-voltage regions at electrophysiology study are color-coded *red*; viable tissue is coded *blue* to *purple*. Scar border zone is often involved in ventricular tachycardia circuits, which are targeted for ablation. Regions of hibernating myocardium, which are not well perfused but are viable, may show improved function upon revascularization

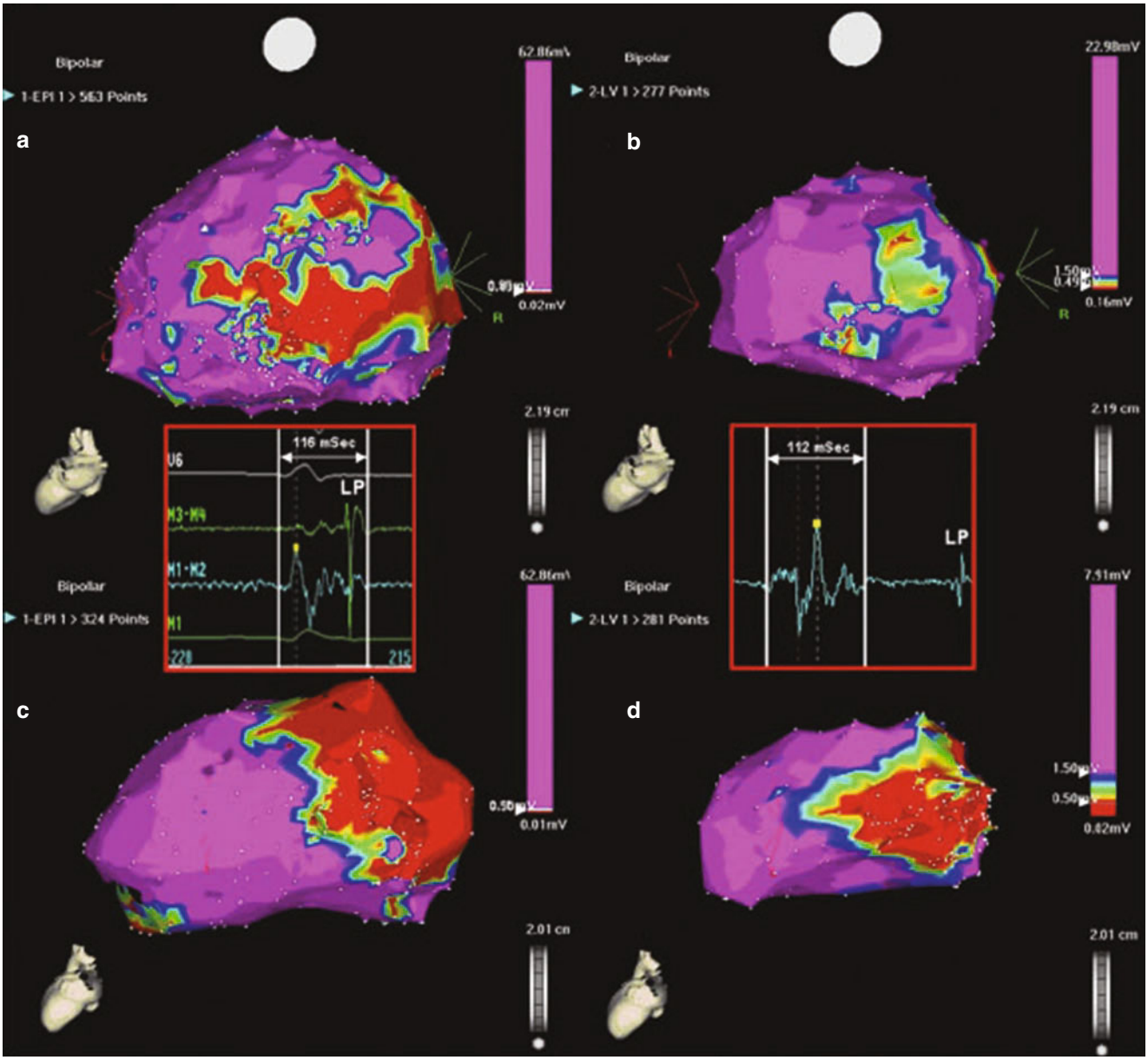

Fig. 14.33 Detailed mapping of endocardial and epicardial voltage, used as a surrogate of ventricular scar for ablation of ventricular tachycardia (VT). Epicardial (**a**, **c**) and endocardial (**b**, **d**) left ventricular (LV) voltage maps are shown in two patients with nonischemic cardiomyopathy and epicardial VT circuits, using a clinical electrophysiological mapping system. The color range represents voltage amplitude. *Purple* areas represent normal epicardium (>1.0 mV) and endocardium (>1.5 mV); dense scar is depicted in *red* (<0.5 mV). (**a**) Posteroanterior modified view of the epicardial voltage map showing a low-voltage zone in the basal and mid-lateral LV. (**b**) Endocardial LV voltage map of the same patient showing a smaller low-voltage area in the lateral wall with no dense scar. Left lateral modified view of (**c**) epicardial and (**d**) endocardial LV map of another patient, showing scar distributed in proximity to the mitral annulus over the basal lateral LV. In both cases, abnormal electrograms were recorded in the low-voltage zones. (From Cano et al. [73]; with permission)

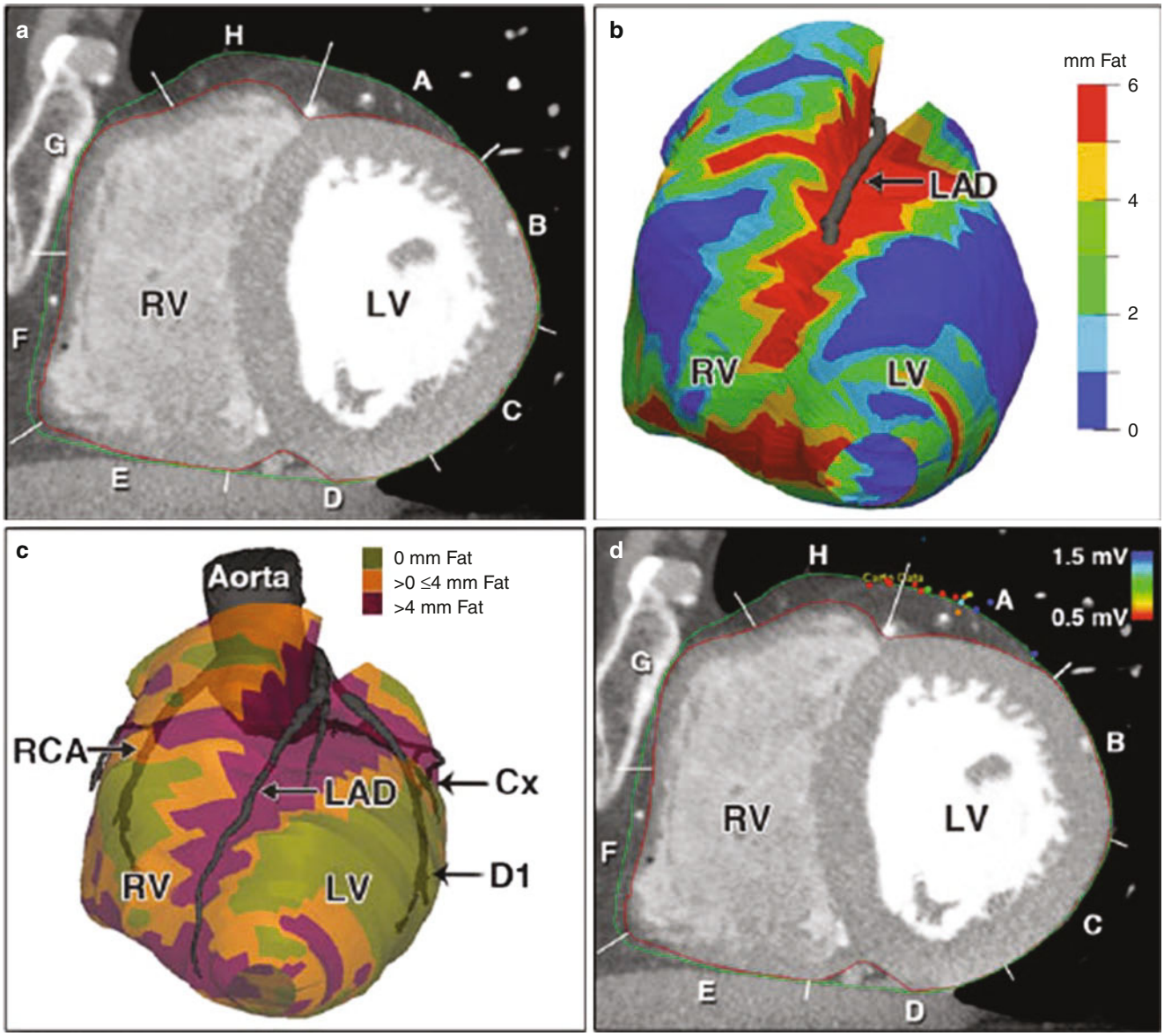

Fig. 14.34 Image integration using CT of coronary anatomy and epicardial fat to guide ablation. Ventricular tachycardia circuits may localize to epicardium, where care must be taken during ablation to avoid damage to coronary arteries and to identify whether low voltage represents myocardial scar or fat. (**a**) Pericardial (*green*) and epicardial (*red*) ventricular contours illustrated in a short-axis multidetector CT (MDCT) slice, divided into eight segments (*A* through *H*). (**b**) Epicardial fat thickness color-coded on three-dimensional epicardial surface mesh. (**c**) Fused image including aorta with coronary arteries from MDCT, merged with epicardial fat meshes (color-coded for fat thickness as indicated). (**d**) Reversed registration of epicardial mapping points projected on the corresponding MDCT location (same short-axis slice as in **a**). Points are color-coded for bipolar voltage (*color bar*). *Cx* circumflex coronary artery, *D1* first diagonal coronary artery, *LAD* left anterior descending artery, *LV* left ventricle, *RCA* right coronary artery, *RV* right ventricle. (*From* van Huls van Taxis *et al.* [74]; with permission)

CT Imaging to Guide Cardiac Resynchronization Therapy

Cardiac resynchronization therapy (CRT) has been a major advance in heart failure management [68]. CRT aims to reduce interventricular dyssynchrony typically seen in patients with left bundle branch block by pacing the left ventricular wall to reduce or eliminate left ventricular delay. Many large-scale randomized trials show that CRT substantially improves outcome in patients with left ventricular ejection fraction (LVEF) <35%, widened QRS duration, and all NYHA classes [68, 75–77]. Cardiac CT may help to guide lead placement and helps to reduce the proportion of patients (currently one third) who do not respond to CRT, including those in whom the lateral LV is not paced or those with extensive scar from myocardial infarction (Figs. 14.35, 14.36, 14.37, 14.38, and 14.39).

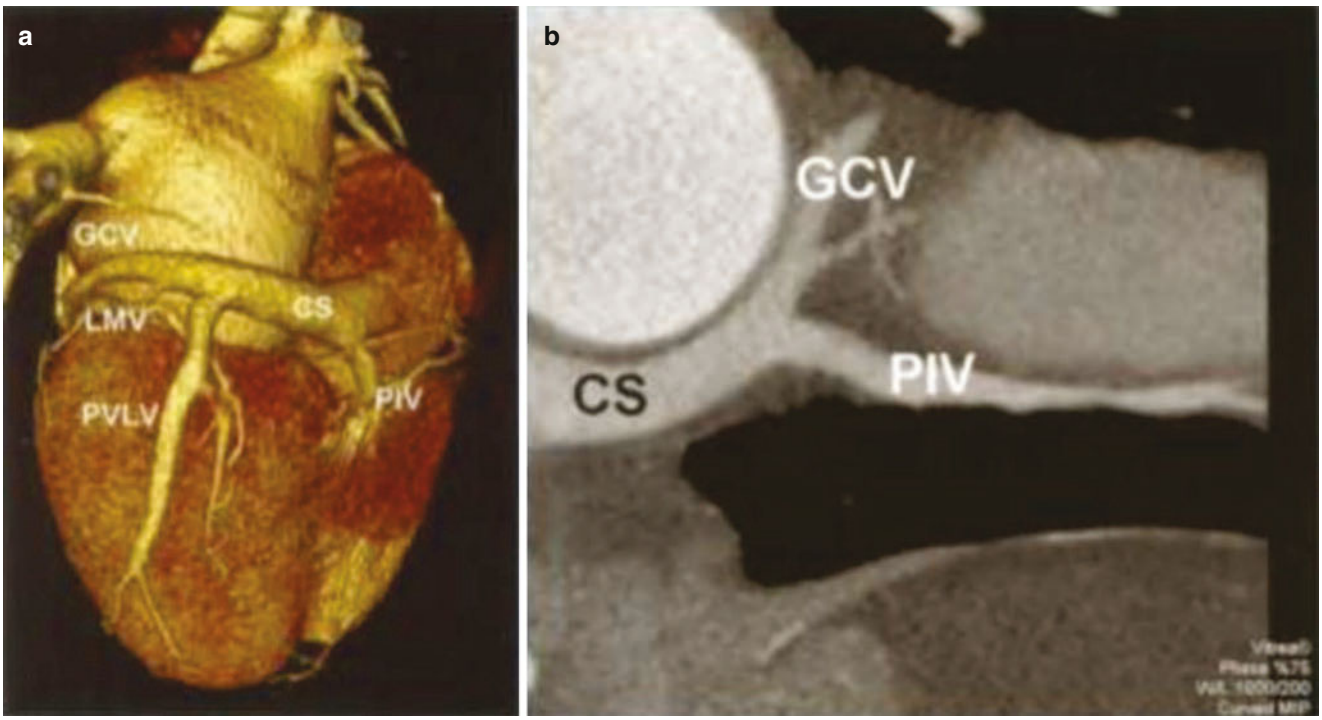

Fig. 14.35 Multidetector CT of normal cardiac venous drainage. Three-dimensional volume-rendered reconstructions (**a**, *dorsal view*) and multiplanar reformatted images (**b**) can be used to evaluate cardiac venous anatomy and all tributaries of the venous system. All main tributaries are seen in this patient. The great cardiac vein (GCV) is a posterior continuation of the anterior interventricular vein, which parallels the left anterior descending artery and drains into the coronary sinus (CS), which drains into the right atrium. The posterior vein of the left ventricle (PVLV) lies in the posterior interventricular sulcus and drains directly into the CS. *LMV* left marginal vein, *PIV* posterior interventricular vein

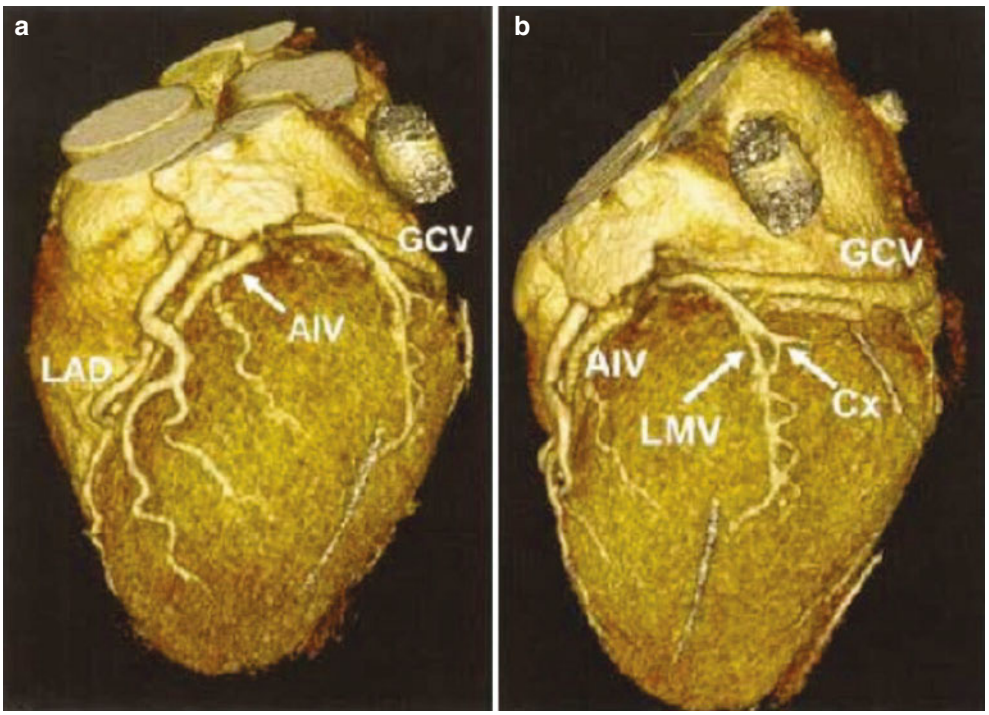

Fig. 14.36 Anterior CT views of normal cardiac veins. (**a**) This three-dimensional volume-rendered reconstruction shows the anterior interventricular vein (AIV, *arrow*) running parallel to the left anterior descending coronary artery (LAD), before becoming the great cardiac vein (GCV) and then the coronary sinus, which drains into the right atrium. (**b**) The left marginal vein (LMV) drains the lateral left ventricle, runs parallel to the circumflex coronary artery (Cx), and empties into the GCV

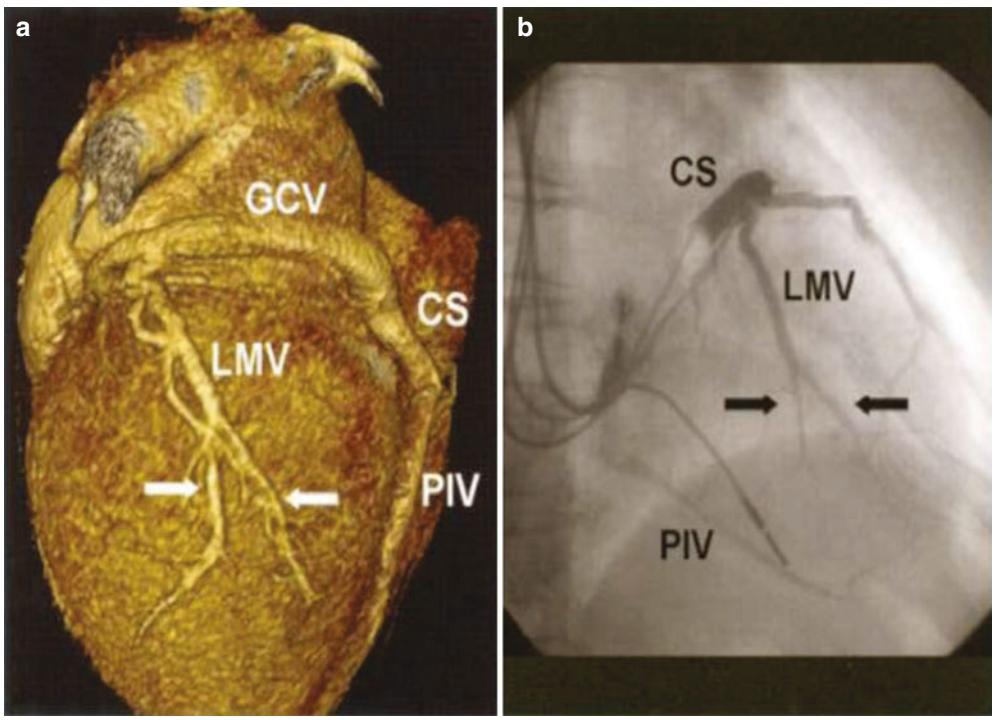

Fig. 14.37 Cardiac venograms obtained by CT and by dye fluoroscopy in the same patient. (**a**) Left marginal vein (LMV) on three-dimensional volume-rendered reconstruction (*posterior view*), showing two distal branches (*arrows*). The posterior interventricular vein (PIV) and its drainage into the coronary sinus (CS) are seen. (**b**) Fluoroscopic visualization of these LMV branches (*arrows*), as well as the PIV and CS, in an anteroposterior venogram. The CS is occluded by a balloon catheter proximal to the LMV insertion. *GCV* great cardiac vein

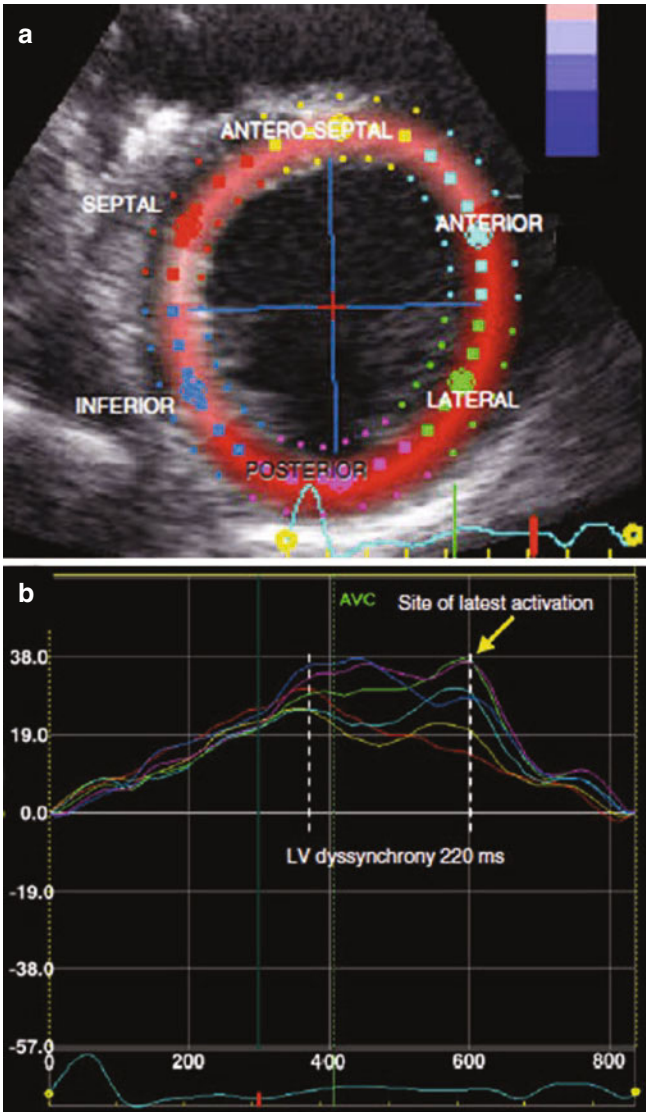

Fig. 14.38 Identification of latest-activated ventricular wall for placement of left ventricular CRT lead. Many studies now show that CRT is most effective when the left ventricular pacing lead is placed at the site of greatest delay in sinus rhythm [68]. (**a**) Short-axis view of the left ventricle (LV) at the level of the papillary muscles, with reconstruction of the six LV segments. (**b**) The separate strain-time curves for each individual segment. In this patient, severe baseline LV dyssynchrony was present; a maximum delay of 220 ms was calculated between the septum (*red*) and the posterior wall (*purple*). The site of latest activation was the posterior LV segment (*purple*). LV pacing is often targeted at this latest site. *AVC* aortic valve closure. (*Adapted from* Ypenburg *et al.* [78]; with permission)

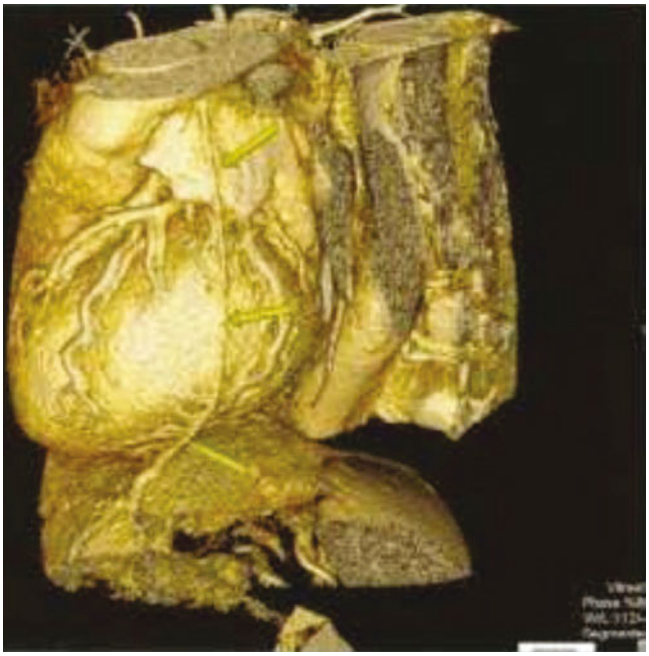

Fig. 14.39 CT image of the left phrenic nerve near cardiac veins (*arrows*) in this three-dimensional volume-rendered reconstruction (*lateral view*). Diaphragmatic stimulation during left ventricular pacing is a poorly tolerated complication of CRT. To avoid this complication, efforts are made to place the LV lead away from sites of phrenic nerve capture [68]. CT visualization of the phrenic nerve may be enhanced by imaging its accompanying pericardiophrenic nerve on contrast multidetector CT [79]

Disclosures This work was supported by grants to Dr. Narayan from the NIH (HL83359, HL103800). Dr. Narayan is co-author of intellectual property owned by the University of California Regents and licensed to Topera Inc. Topera does not sponsor any research, including that presented here. Dr. Narayan holds equity in Topera. Drs. Wilson, Saremi, and Narula report no conflicts.

References

1. Halliburton S, Arbab-Zadeh A, Dey D, Einstein A, Gentry R, George R, et al. State-of-the-art in CT hardware and scan modes for cardiovascular CT. J Cardiovasc Comput Tomogr. 2012;6:154–63.
2. Macedo PG, Kapa S, Mears JA, Fratianni A, Asirvatham SJ. Correlative anatomy for the electrophysiologist: ablation for atrial fibrillation. Part I: pulmonary vein ostia, superior vena cava, vein of Marshall. J Cardiovasc Electrophysiol. 2010;21:721–30.
3. Macedo PG, Kapa S, Mears JA, Fratianni A, Asirvatham SJ. Correlative anatomy for the electrophysiologist: ablation for atrial fibrillation. Part II: regional anatomy of the atria and relevance to damage of adjacent structures during AF ablation. J Cardiovasc Electrophysiol. 2010;21:829–36.
4. Lachman N, Syed FF, Habib A, Kapa S, Bisco SE, Venkatachalam KL, Asirvatham SJ. Correlative anatomy for the electrophysiologist, part I: the pericardial space, oblique sinus, transverse sinus. J Cardiovasc Electrophysiol. 2010;21:1421–6.
5. Lachman N, Syed FF, Habib A, Kapa S, Bisco SE, Venkatachalam KL, Asirvatham SJ. Correlative anatomy for the electrophysiologist, part III: cardiac ganglia, phrenic nerve, coronary venous system. J Cardiovasc Electrophysiol. 2011;22:104–10.
6. Nasis A, Mottram P, Cameron J, Seneviratne S. Current and evolving clinical applications of multidetector cardiac ct in assessment of structural heart disease. Radiology. 2013;267:11–25.
7. Melendez-Ramirez G, Castillo-Castellon F, Espinola-Zavaleta N, Meave A, Kimura-Hayama E. Left ventricular noncompaction: a proposal of new diagnostic criteria by multidetector computed tomography. J Cardiovasc Comput Tomogr. 2012;6:346–54.
8. Lee G, Sanders P, Kalman JM. Catheter ablation of atrial arrhythmias: state of the art. Lancet. 2012;380:1509–19.
9. Narayan SM, Clopton P, Krummen DE, Shivkumar K, Miller J. Direct or coincidental elimination of stable rotors or focal sources may explain successful atrial fibrillation ablation: on-treatment analysis of the CONFIRM trial (conventional ablation for AF with or without focal impulse and rotor modulation). J Am Coll Cardiol. 2013;62:138–47.
10. Di Biase L, Burkhardt JD, Mohanty P, Sanchez J, Mohanty S, Horton R, et al. Left atrial appendage: an underrecognized trigger site of atrial fibrillation. Circulation. 2010;122:109–18.
11. Ho SY, Sanchez-Quintana D. The importance of atrial structure and fibers. Clin Anat. 2009;22:52–63.
12. Veinot JP, Harrity PJ, Gentile F, Khandheria BK, Bailey KR, Eickholt JT, et al. Anatomy of the normal left atrial appendage: a quantitative study of age-related changes in 500 autopsy hearts: implications for echocardiographic examination. Circulation. 1997;96:3112–5.
13. Mahajan R, Brooks AG, Sullivan T, Lim HS, Alasady M, Abed HS, et al. Importance of the underlying substrate in determining thrombus location in atrial fibrillation: implications for left atrial appendage closure. Heart. 2012;98:1120–6.
14. Lim HS, Willoughby SR, Schultz C, Gan C, Alasady M, Lau DH, et al. Effect of atrial fibrillation on atrial thrombogenesis in humans: impact of rate and rhythm. J Am Coll Cardiol. 2013;61:852–60.
15. Di Biase L, Santangeli P, Anselmino M, Mohanty P, Salvetti I, Gili S, et al. Does the left atrial appendage morphology correlate with the risk of stroke in patients with atrial fibrillation? Results from a multicenter study. J Am Coll Cardiol. 2012;60:531–8.
16. Holmes DR, Reddy VY, Turi ZG, Doshi SK, Sievert H, Buchbinder M, et al. Percutaneous closure of the left atrial appendage versus warfarin therapy for prevention of stroke in patients with atrial fibrillation: a randomised non-inferiority trial. Lancet. 2009;374:534–42.
17. Urena M, Rodès-Cabau J, Freixa X, Saw J, Webb J, Freeman M, et al. Percutaneous left atrial appendage closure with the Amplatzer cardiac plug device in patients with nonvalvular atrial fibrillation and contraindications to anticoagulation therapy. J Am Coll Cardiol. 2013;62q:96–102.
18. Bartus K, Han FT, Bednarek J, Myc J, Kapelak B, Sadowski J, et al. Percutaneous left atrial appendage suture ligation using the LARIAT device in patients with atrial fibrillation: initial clinical experience. J Am Coll Cardiol. 2013;62:108–18.
19. Poulter R, Tang J, Jue J, Ibrahim R, Nicolaou S, Mayo J, Saw J. Cardiac computed tomography follow-up of left atrial appendage exclusion using the Amplatzer cardiac plug device. Can J Cardiol. 2012;28:e111–3.
20. Chugh SS, Havmoeller R, Narayanan K, Singh D, Rienstra M, Benjamin EJ, et al. Worldwide epidemiology of atrial fibrillation: a global burden of disease 2010 study. Circulation. 2014;129:837–47.
21. Miyasaka Y, Barnes M, Bailey K, Cha S, Gersh B, Seward J, Tsang T. Mortality trends in patients diagnosed with first atrial fibrillation: a 21-year community-based study. J Am Coll Cardiol. 2007;49:986–92.
22. Kamel H, Navi BB, Elijovich L, Josephson SA, Yee AH, Fung G, et al. Pilot randomized trial of outpatient cardiac monitoring after cryptogenic stroke. Stroke. 2013;44:528–30.
23. Bunch TJ, Weiss JP, Crandall BG, May HT, Bair TL, Osborn JS, et al. Atrial fibrillation is independently associated with senile, vascular, and Alzheimer's dementia. Heart Rhythm. 2010;7:433–7.
24. Halligan SC, Gersh BJ, Brown RD Jr, Rosales AG, Munger TM, Shen W-K, et al. The natural history of lone atrial flutter. Ann Intern Med. 2004;140:265–8.
25. Waldo AL. The interrelationship between atrial fibrillation and atrial flutter. Prog Cardiovasc Dis. 2005;48:41–56.
26. Rodriguez LM, Timmermans C, Nabar A, Hofstra L, Wellens HJ. Biatrial activation in isthmus-dependent atrial flutter. Circulation. 2001;104:2545–50.
27. Feld G, Wharton M, Plumb V, Daoud E, Friehling T, Epstein L, Investigators E-XCAS. Radiofrequency catheter ablation of type 1 atrial flutter using large-tip 8- or 10-mm electrode catheters and a high-output radiofrequency energy generator: results of a multicenter safety and efficacy study. J Am Coll Cardiol. 2004;43:1466–72.
28. Asirvatham S, Friedman P. Supraventricular arrhythmias in heart failure. In: Shivkumar K, Weiss JN, Fonarow GC, Narula J, editors. Atlas of electrophysiology in heart failure. Philadelphia, PA: Curr Med; 2005. p. 141–69.
29. Dacosta A, Faure E, Thevenin J, Messier M, Bernard S, Abdel K, et al. Effect of isthmus anatomy and ablation catheter on radiofrequency catheter ablation of cavotricuspid isthmus. Circulation. 2004;110:1030–5.
30. Cabrera JA, Sanchez-Quintana D, Ho SY, Medina A, Wanguemert F, Gross E, et al. Angiographic anatomy of the inferior right atrial isthmus in patients with and without history of common atrial flutter. Circulation. 1999;99:3017–23.
31. De Simone CV, Noheria A, Lachman N, Edwards WD, Gami AS, Maleszewski JJ, et al. Myocardium of the superior vena cava, coronary sinus, vein of Marshall, and the pulmonary vein ostia: gross anatomic studies in 620 hearts. J Cardiovasc Electrophysiol. 2012;23:1304–9.
32. Hanley PC, Tajik AJ, Hynes JK, Edwards WD, Reeder GS, Hagler DJ, Seward JB. Diagnosis and classification of atrial septal aneu-

rysm by two-dimensional echocardiography: report of 80 consecutive cases. J Am Coll Cardiol. 1985;6:1370–82.
33. Mas J, Arquizan C, Lamy C, Zuber M, Cabanes L, Derumeaux G, et al. Recurrent cerebrovascular events associated with patent foramen ovale, atrial septal aneurysm, or both. N Engl J Med. 2001;345:1740–6.
34. Van Gelder IC, Groenveld HF, Crijns HJ, Tuininga YS, Tijssen JG, Alings AM, et al. Lenient versus strict rate control in patients with atrial fibrillation. N Engl J Med. 2010;362:1363–73.
35. Roy D, Talajic M, Nattel S, Wyse DG, Dorian P, Lee KL, et al. Rhythm control versus rate control for atrial fibrillation and heart failure. N Engl J Med. 2008;358:2667–77.
36. Calkins CH. 2012 HRS/EHRA/ECAS expert consensus statement on catheter and surgical ablation of atrial fibrillation: recommendations for patient selection, procedural techniques, patient management and follow-up, definitions, endpoints, and research trial design. Heart Rhythm. 2012;9:632–96.
37. Narayan SM, Krummen DE, Shivkumar K, Clopton P, Rappel WJ, Miller J. Treatment of atrial fibrillation by the ablation of localized sources: the conventional ablation for atrial fibrillation with or without focal impulse and rotor modulation: CONFIRM trial. J Am Coll Cardiol. 2012;60:628–36.
38. Pandit SV, Jalife J. Rotors and the dynamics of cardiac fibrillation. Circ Res. 2013;112:849–62.
39. de Groot NM, Houben RP, Smeets JL, Boersma E, Schotten U, Schalij MJ, et al. Electropathological substrate of longstanding persistent atrial fibrillation in patients with structural heart disease: epicardial breakthrough. Circulation. 2010;122:1674–82.
40. Scherlag BJ, Nakagawa H, Jackman WM, Yamanashi WS, Patterson E, Po S, Lazzara R. Electrical stimulation to identify neural elements on the heart: their role in atrial fibrillation. J Interv Cardiac Electrophysiol. 2005;13:37–42.
41. Oakes RS, Badger TJ, Kholmovski EG, Akoum N, Burgon NS, Fish EN, et al. Detection and quantification of left atrial structural remodeling with delayed-enhancement magnetic resonance imaging in patients with atrial fibrillation. Circulation. 2009;119:1758–67.
42. Nielsen JC, Johannessen A, Raatikainen P, Hindricks G, Walfridsson H, Kongstad O, et al. Radiofrequency ablation as initial therapy in paroxysmal atrial fibrillation. N Engl J Med. 2012;367:1587–95.
43. Wilber DJ, Pappone C, Neuzil P, De Paola A, Marchlinski F, Natale A, et al. Comparison of antiarrhythmic drug therapy and radiofrequency catheter ablation in patients with paroxysmal atrial fibrillation: a randomized controlled trial. JAMA. 2010;303:333–40.
44. Holmes DR Jr, Monahan KH, Packer D. Pulmonary vein stenosis complicating ablation for atrial fibrillation: clinical spectrum and interventional considerations. JACC Cardiovasc Interv. 2009;2:267–76.
45. Arentz T, Weber R, Bürkle G, Herrera C, Blum T, Stockinger J, et al. Small or large isolation areas around the pulmonary veins for the treatment of atrial fibrillation? Results from a prospective randomized study. Circulation. 2007;115:3057–63.
46. Jiang RH, Jiang CY, Sheng X, Zhang ZW, Sun YX, Liu Q, et al. Marked suppression of pulmonary vein firing after circumferential pulmonary vein isolation in patients with paroxysmal atrial fibrillation: is pulmonary vein firing an epiphenomenon? J Cardiovasc Electrophys. 2013;25(2):111–8. https://doi.org/10.1111/jce.12288.
47. Jongbloed MR, Bax JJ, Zeppenfeld K, van der Wall EE, Schalij MJ. Anatomical observations of the pulmonary veins with intracardiac echocardiography and hemodynamic consequences of narrowing pulmonary vein ostial diameters after radiofrequency catheter ablation of atrial fibrillation. Am J Cardiol. 2004;93:1298–302.
48. Jongbloed MR, Bax JJ, Lamb HJ, Dirksen MS, Zeppenfeld K, van der Wall EE, et al. Multislice computed tomography versus intracardiac echocardiography to evaluate the pulmonary veins before radiofrequency catheter ablation of atrial fibrillation: a head-to-head comparison. J Am Coll Cardiol. 2005;45:343–50.
49. Hwang C, Wu TJ, Doshi RN, Peter CT, Chen PS. Vein of Marshall cannulation for the analysis of electrical activity in patients with focal atrial fibrillation. Circulation. 2000;101:1503–5.
50. Baez-Escudero JL, Keida T, Dave AS, Okishige K, Valderrabano M. Ethanol infusion in the vein of Marshall leads to parasympathetic denervation of the human left atrium: implications for atrial fibrillation. J Am Coll Cardiol. 2014;63:1892–901.
51. Herlong J, Jaggers J, Ungerleider R. Congenital heart surgery nomenclature and database project: pulmonary venous anomalies. Ann Thorac Surg. 2000;69:S56–69.
52. Haramati LB, Moche IE, Rivera VT, Patel PV, Heyneman L, McAdams HP, et al. Computed tomography of partial anomalous pulmonary venous connection in adults. J Comput Assist Tomogr. 2003;27:743–9.
53. Orlov MV, Gorev MV, Griben A. Rotors of truly atypical atrial flutters visualized by firm mapping and 3D-MRI overlay on live fluoroscopy. J Interv Cardiac Electrophysiol. 2013;38:167.
54. Narayan SM, Patel J, Mulpuru SK, Krummen DE. Focal impulse and rotor modulation (FIRM) of sustaining rotors abruptly terminates persistent atrial fibrillation to sinus rhythm with elimination on follow-up. Heart Rhythm. 2012;9:1436–9.
55. Shivkumar K, Ellenbogen KA, Hummel JD, Miller JM, Steinberg JS. Acute termination of human atrial fibrillation by identification and catheter ablation of localized rotors and sources: first multicenter experience of focal impulse and rotor modulation (FIRM) ablation. J Cardiovasc Electrophysiol. 2012;23:1277–85.
56. Ellis ER, Culler SD, Simon AW, Reynolds MR. Trends in utilization and complications of catheter ablation for atrial fibrillation in medicare beneficiaries. Heart Rhythm. 2009;6:1267–73.
57. Deshmukh A, Patel NJ, Pant S, Shah N, Chothani A, Mehta K, et al. In-hospital complications associated with catheter ablation of atrial fibrillation in the United States between 2000 and 2010: analysis of 93,801 procedures. Circulation. 2013;128:2104–12.
58. Gilcrease GW, Stein JB. A delayed case of fatal atrioesophageal fistula following radiofrequency ablation for atrial fibrillation. J Cardiovasc Electrophysiol. 2010;21:708–11.
59. Cappato R, Calkins H, Chen SA, Davies W, Iesaka Y, Kalman J, et al. Updated worldwide survey on the methods, efficacy, and safety of catheter ablation for human atrial fibrillation. Circ Arrhythm Electrophysiol. 2010;3:32–8.
60. Chugh A, Makkar A, Yen Ho S, Yokokawa M, Sundaram B, Pelosi F, et al. Manifestations of coronary arterial injury during catheter ablation of atrial fibrillation and related arrhythmias. Heart Rhythm. 2013;10:1638–45.
61. Wong KC, Lim C, Sadarmin PP, Jones M, Qureshi N, De Bono J, et al. High incidence of acute sub-clinical circumflex artery 'injury' following mitral isthmus ablation. Eur Heart J. 2011;32:1881–90.
62. Epstein AE, JP DM, Ellenbogen KA, Estes NA 3rd, Freedman RA, Gettes LS, et al. ACC/AHA/HRS 2008 guidelines for device-based therapy of cardiac rhythm abnormalities: a report of the American College of Cardiology/American Heart Association task force on practice guidelines (writing committee to revise the ACC/AHA/NASPE 2002 guideline update for implantation of cardiac pacemakers and antiarrhythmia devices): developed in collaboration with the American association for thoracic surgery and society of thoracic surgeons. Circulation. 2008;117:e350–408.
63. Zipes DP, Camm AJ, Borggrefe M, Buxton AE, Chaitman B, Fromer M, et al. ACC/AHA/ESC 2006 guidelines for management of patients with ventricular arrhythmias and the prevention of sudden cardiac death: a report of the American College of Cardiology/American Heart Association task force and the European Society of Cardiology committee for practice guidelines (writing committee to develop guidelines for management of patients with ventricular arrhythmias and the prevention of sudden cardiac death). J Am Coll Cardiol. 2006;48:e247–346.
64. Stecker EC, Vickers C, Waltz J, Socoteanu C, John BT, Mariani R, et al. Population-based analysis of sudden cardiac death with

and without left ventricular systolic dysfunction: two-year findings from the oregon sudden unexpected death study. J Am Coll Cardiol. 2006;47:1161–6.
65. Bluemke D, Achenbach S, Budoff M, Gerber T, Gersh B, Hillis L, et al. Noninvasive coronary artery imaging: magnetic resonance angiography and multidetector computed tomography angiography: a scientific statement from the American Heart Association Committee on Cardiovascular Imaging and Intervention of the Council on Cardiovascular Radiology and Intervention, and the Councils on Clinical Cardiology and cardiovascular disease in the young. Circulation. 2008;118:586–606.
66. Hendel R, Patel M, Kramer C, Poon M, Hendel R, Carr J, et al. ACCF/ACR/SCCT/SCMR/ASNC/NASCI/SCAI/SIR 2006 appropriateness criteria for cardiac computed tomography and cardiac magnetic resonance imaging: a report of the American College of Cardiology Foundation Quality Strategic Directions Committee Appropriateness Criteria Working Group, American College of Radiology, Society of Cardiovascular Computed Tomography, Society for Cardiovascular Magnetic Resonance, American Society of Nuclear Cardiology, north American Society for Cardiac Imaging, Society for Cardiovascular Angiography and Interventions, and Society of Interventional Radiology. J Am Coll Cardiol. 2006;48: 1475–97.
67. Greenland P, Alpert J, Beller G, Benjamin E, Budoff M, Fayad Z, American College of Cardiology Foundation; American Heart Association, et al. 2010 ACCF/AHA guideline for assessment of cardiovascular risk in asymptomatic adults: a report of the American College of Cardiology Foundation/American Heart Association task force on practice guidelines. J Am Coll Cardiol. 2010;56: e50–103.
68. Epstein AE, DiMarco JP, Ellenbogen KA, Estes NA 3rd, Freedman RA, Gettes LS, et al. 2012 ACCF/AHA/HRS focused update incorporated into the ACCF/AHA/HRS 2008 guidelines for device-based therapy of cardiac rhythm abnormalities: a report of the American College of Cardiology Foundation/American Heart Association task force on practice guidelines and the Heart Rhythm Society. J Am Coll Cardiol. 2013;61:e6–75.
69. Eggebrecht H, Mohlenkamp S. Images in clinical medicine. Myocardial bridging. N Engl J Med. 2003;349:1047.
70. Marcus FI, McKenna WJ, Sherrill D, Basso C, Bauce B, Bluemke DA, et al. Diagnosis of arrhythmogenic right ventricular cardiomyopathy/dysplasia: proposed modification of the task force criteria. Circulation. 2010;121:1533–41.
71. Sen-Chowdhry S, Syrris P, Prasad SK, Hughes SE, Merrifield R, Ward D, et al. Left-dominant arrhythmogenic cardiomyopathy: an under-recognized clinical entity. J Am Coll Cardiol. 2008;52:2175–87.
72. Elliott PM, Poloniecki J, Dickie S, Sharma S, Monserrat L, Varnava A, et al. Sudden death in hypertrophic cardiomyopathy: identification of high risk patients. J Am Coll Cardiol. 2000;36:2212–8.
73. Cano O, Hutchinson M, Lin D, Garcia F, Zado E, Bala R, et al. Electroanatomic substrate and ablation outcome for suspected epicardial ventricular tachycardia in left ventricular nonischemic cardiomyopathy. J Am Coll Cardiol. 2009;54:799–808.
74. van Huls van Taxis CF, Wijnmaalen AP, Piers SR, van der Geest RJ, Schalij MJ, Zeppenfeld K. Real-time integration of MDCT-derived coronary anatomy and epicardial fat: impact on epicardial electroanatomic mapping and ablation for ventricular arrhythmias. JACC Cardiovasc Imaging. 2013;6:42–52.
75. Bardy GH, Lee KL, Mark DB, Poole JE, Packer DL, Boineau R, et al. Amiodarone or an implantable cardioverter–defibrillator for congestive heart failure. N Engl J Med. 2005;352:225–37.
76. Cleland JGF, Daubert J-C, Erdmann E, Freemantle N, Gras D, Kappenberger L, Tavazzi L, The Cardiac Resynchronization—Heart Failure (CARE-HF) Study Investigators. The effect of cardiac resynchronization on morbidity and mortality in heart failure. N Engl J Med. 2005;352:1539–49.
77. Moss AJ, Hall WJ, Cannom DS, Klein H, Brown MW, Daubert JP, et al. Cardiac-resynchronization therapy for the prevention of heart-failure events. N Engl J Med. 2009;361:1329–38.
78. Ypenburg C, van Bommel RJ, Delgado V, Mollema SA, Bleeker GB, Boersma E, et al. Optimal left ventricular lead position predicts reverse remodeling and survival after cardiac resynchronization therapy. J Am Coll Cardiol. 2008;52:1402–9.
79. Matsumoto Y, Krishnan S, Fowler SJ, Saremi F, Kondo T, Ahsan C, et al. Detection of phrenic nerves in relation to cardiac anatomy using 64-slice multidetector computed tomography. Am J Cardiol. 2007;100:133–7.

Myocardial Function and Viability

15

Andreas H. Mahnken

Information on cardiac function is of substantial value in the assessment of patients suffering from a variety of cardiac diseases. Although cardiovascular MRI is considered the current standard of reference for functional imaging, information on global and regional myocardial function is routinely obtained by echocardiography or by levocardiography. The first CT approaches toward the assessment of cardiac function were developed as early as the late 1970s [1]. Cross-sectional imaging techniques like the dynamic spatial reconstructor [2] or electron beam CT [3] were successfully evaluated for their ability to visualize cardiac function. For all of these techniques, evaluation of left ventricular volumes, wall motion abnormalities, and contrast enhancement patterns was shown to be feasible. For several reasons, however, none of these techniques was considered a routine clinical tool.

With the introduction of multidetector spiral CT in clinical routine, a new tool for assessing cardiac function has become widely available. Four-dimensional functional information is inherently available with each retrospectively ECG-gated cardiac CT data set, with no extra cost in terms of radiation exposure or contrast material delivery, so this information should be used as an adjunct to multidetector spiral CT coronary angiography. Several studies have proved that cardiac CT is a reliable tool for evaluating ventricular volumes and wall motion. Moreover, recent studies have reported on the ability to assess myocardial perfusion and viability with cardiac CT.

This chapter explains the physiologic and technical basics of functional CT imaging, including the assessment of ventricular volumes and wall motion. The basics of CT myocardial perfusion imaging and the assessment of myocardial viability from contrast-enhanced late-phase CT are introduced.

A.H. Mahnken
Department of Diagnostic and Interventional Radiology, Marburg University Hospital, Baldingerstrasse, D-35043 Marburg, Germany
e-mail: mahnken@med.uni-marburg.de

M.J. Budoff et al. (eds.), *Atlas of Cardiovascular Computed Tomography*, https://doi.org/10.1007/978-1-4471-7357-1_15

The Physiologic Basis of Functional CT Imaging

There is a close correlation between the electrical and the mechanical events during the cardiac cycle (Fig. 15.1). The resolution of the imaging is dependent upon heart rate (Figs. 15.2 and 15.3).

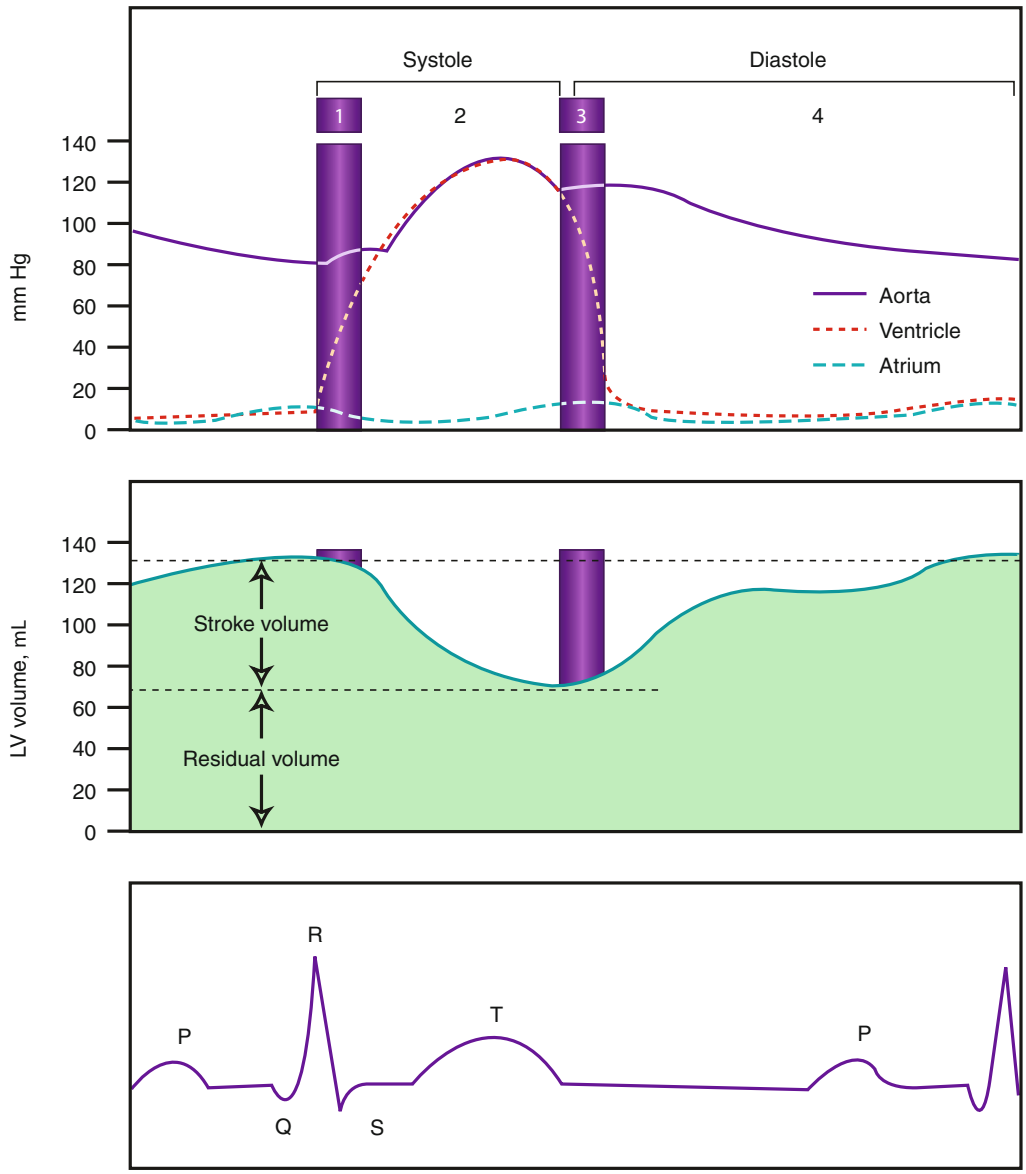

Fig. 15.1 Correlation between electrical and mechanical events during the cardiac cycle. The RR interval is separated into the isovolumetric contraction phase (1), the ventricular ejection period (2), the isovolumetric relaxation phase (3), and the ventricular filling period (4). The different phases are separated by the opening and closing of the heart valves, events that mark the beginning or the ending of the isovolumetric contraction and relaxation phase. The aortic and pulmonary valves are opened during the ventricular ejection period; they are closed during the ventricular filling period, when the mitral and tricuspid valves are opened. Left and right ventricular function is well synchronized. Although end-systolic and end-diastolic volumes may differ, left and right ventricular volume changes (stroke volume) are similar

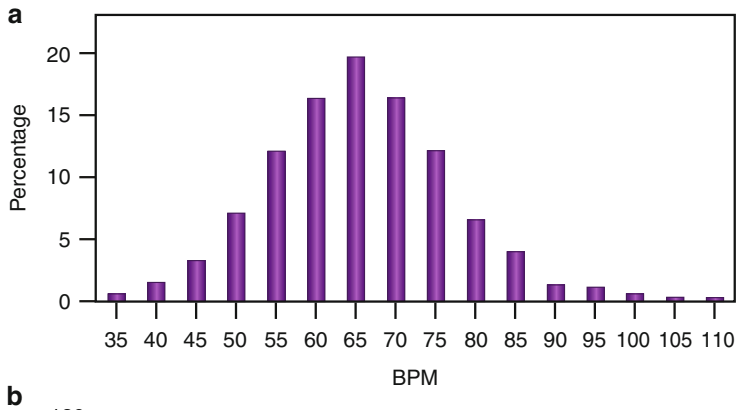

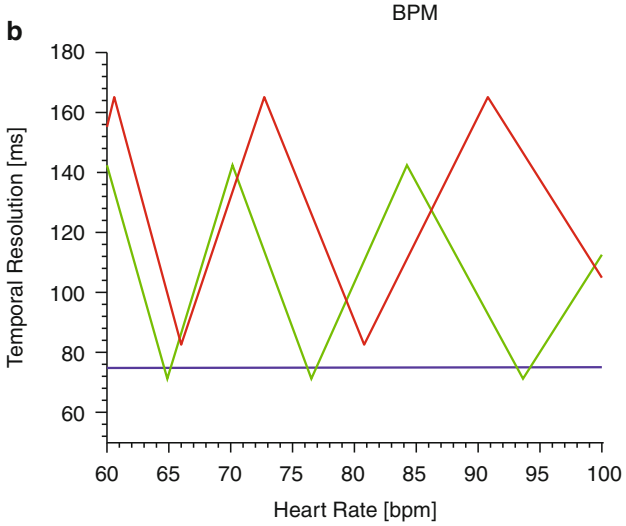

Fig. 15.2 (**a**) Normal heart rate distribution in a patient group undergoing cardiac multidetector spiral CT ($n = 672$) without additional beta-blockers for reducing the individual heart rate (Mahnken, unpublished data). Most patients present with a heart rate of approximately 65 beats per minute (bpm). Consequently, optimal temporal resolution should be achieved for heart rates ranging from 55 to 75 bpm. (**b**) Temporal resolution of different CT scanners that are used for cardiac CT. The *continuous blue line* represents the constant, heart rate–independent temporal resolution of a dual-source CT scanner, whereas the *red line* and the *green line* represent single-source CT scanners with gantry rotation times of 330 ms and 285 ms, respectively. Except for the dual-source CT scanner, temporal resolution has some bothersome maxima in the range of the most common heart rates, because the multisegmental image reconstruction techniques that are currently used achieve a temporal resolution that is shorter than the cardiac rest period (*see* Fig. 15.3). This connection is of particular interest because the reliability of ventricular volumes determined by CT depends on temporal resolution (*see* Fig. 15.10)

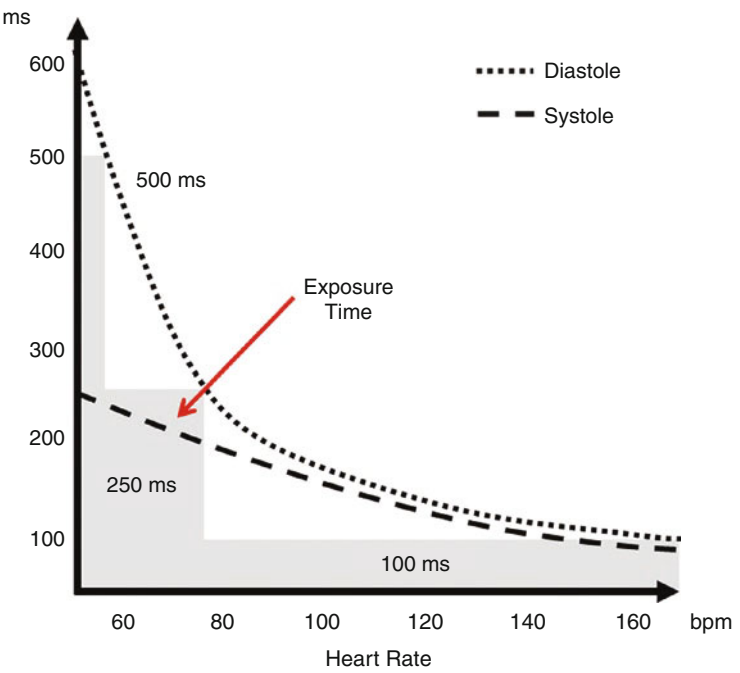

Fig. 15.3 The systolic and diastolic rest periods are heart rate–dependent. The duration of the cardiac rest periods shortens progressively with increasing heart rates. This effect is more pronounced with the diastolic rest period, but the systolic rest period also decreases in duration with increasing heart rate. Consequently a temporal resolution below approximately 100 ms is needed to depict the left ventricle and the myocardium without motion artifacts during end-systole and end-diastole. The velocity of myocardial motion varies, and some areas (e.g., close to the right ventricular groove) require an even higher temporal resolution to avoid motion artifacts. These effects are also known to affect the assessment of global and regional myocardial function (*see* Fig. 15.10)

Technical Basics of Functional CT Imaging

Determination of global and regional cardiac function requires image reconstruction at multiple cardiac phases from a retrospectively ECG-gated CT data set (Fig. 15.4). Standardized imaging planes are defined so that all myocardial segments are visualized from two perpendicular perspectives (Fig. 15.5).

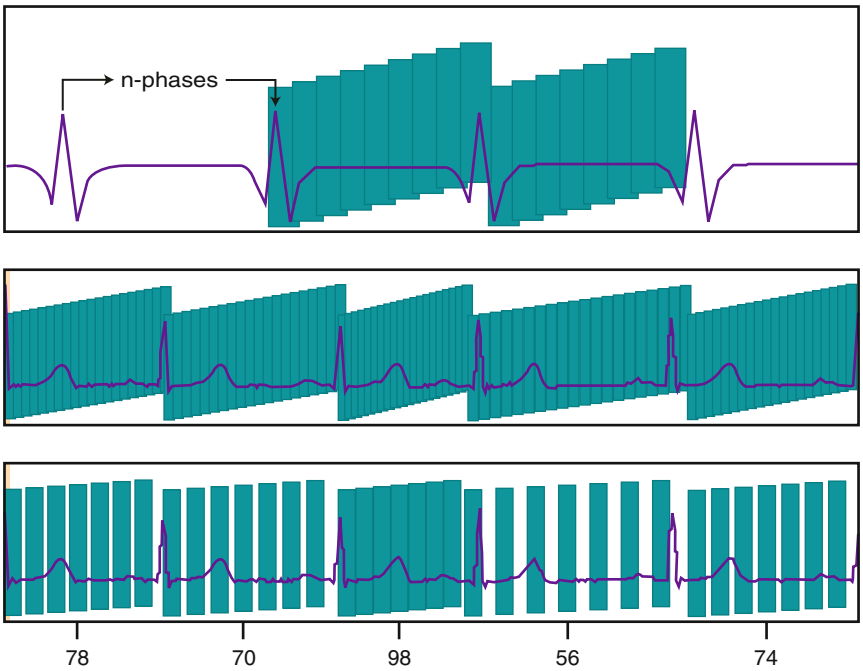

Fig. 15.4 Determination of global and regional cardiac function requires image reconstruction at multiple cardiac phases from a retrospectively ECG-gated CT data set. For this purpose, the RR interval is separated in multiple phases (*top row*), covering the entire cardiac cycle. The number of phases multiplied by the temporal resolution should equal or exceed the length of the RR interval. Otherwise, gaps may occur, especially at low heart rates with long RR intervals. The *middle row* and the *bottom row* show an ECG taken from the same patient with the corresponding data sections used for functional image reconstruction. If the number of cardiac phases that are used for image reconstruction is too low, gaps will occur. For clinical routine, images should be calculated from at least 20 cardiac phases to exactly meet end-systole and end-diastole. For cine CT, calculating images from a large number of cardiac phases helps to avoid a potentially misleading staccato effect during wall motion analysis

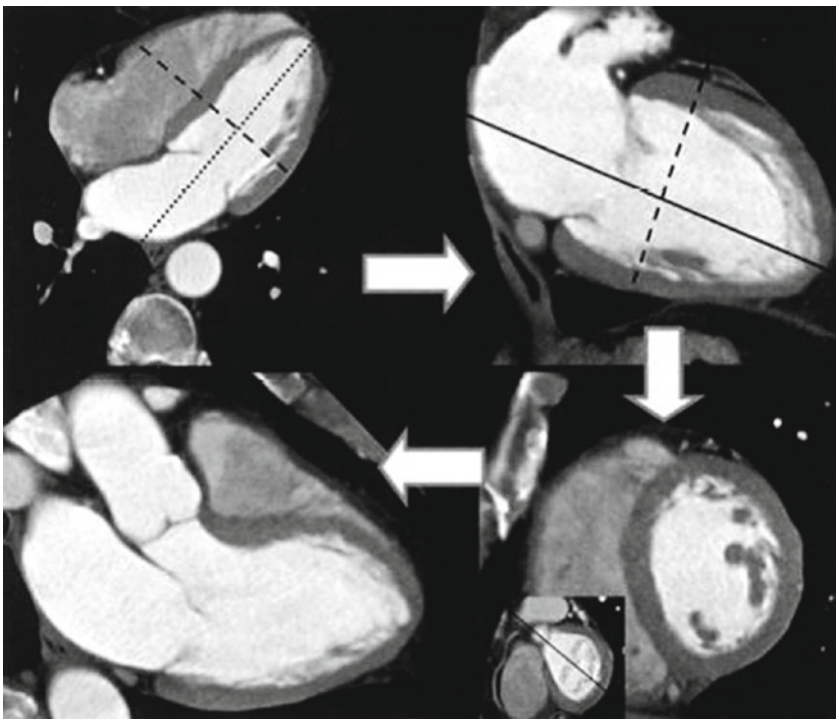

Fig. 15.5 For cross-sectional imaging of the heart, standardized, double oblique imaging planes are used: a four-chamber view (4CV, *top left*); a two-chamber view (2CV, *top right*); a short-axis view (SA, *bottom right*); and a three-chamber view (3CV, *bottom left*). These imaging planes are defined in such a manner that all myocardial segments are visualized from two perpendicular perspectives. Except for the 3CV, all of these imaging planes are orthogonal to each other. The *dashed line* indicates the relation between SA view and the 4CV and 2CV. The *dotted line* describes the relation between the 2CV and 4CV. For calculation of the 3CV, images are reconstructed via the most basal plane of the SA view, through the left ventricular outflow tract. The *bold arrows* indicate a potential workflow sequence for calculation of the different imaging planes

Assessment of Ventricular Volume and Function

For the assessment of global ventricular function, end-systolic and end-diastolic images are reconstructed (Fig. 15.6), from which ventricular volumes are calculated and may be used to calculate ejection fraction. True three-dimensional measurements are better suited for assessing complex geometric objects such as the cardiac ventricles, however, and most tools now provide threshold-based, semi-automated assessment of left and right ventricular volumes (Figs. 15.7 and 15.8).

The assessment of end-systolic and end-diastolic images is sufficient to determine ejection fraction and cardiac output, but heart rate and temporal resolution must be considered in interpreting these results (Figs. 15.9 and 15.10). An approach using indicator dilution allows a fast estimation of

$$LV_{volume} = \sum_{apex}^{base} A \times S \qquad LV_{volume} = \frac{8}{3} \times \frac{A^2}{\pi \times L} \qquad EF = \frac{EDV - ESV}{EDV} \times 100\%$$

Fig. 15.6 For the assessment of global ventricular function, end-systolic (*left*) and end-diastolic (*right*) images are reconstructed. Left and right ventricular volumes are traditionally calculated from 5- to 8-mm short-axis images (*top*) using the Simpson method—that is, summing the cross-sectional area (*A*) multiplied by the section thickness (*S*) from the base to the apex. The apex is defined as the most distal section, with the ventricular cavity visible throughout the entire cardiac cycle; the basal section is identified by the presence of at least 50% myocardium throughout the RR interval. For quantitative analysis, trabeculae and papillary muscles are often included with the blood pool. This approach is known to improve data reproducibility, as has been shown for MRI [4]. To assess myocardial mass, endocardial borders (*black line*) and epicardial borders (*red line*) must be drawn. Alternatively, end-systolic and end-diastolic two-chamber view images may be used, applying the area-length method (*bottom*). To calculate ventricular volumes from two-chamber–view images, the length from the apex to the mitral valve plane (*L*, *arrows*) and the cross-sectional area (*A*) are needed. Ventricular volumes are used to calculate ejection fraction (EF). A key disadvantage of the area-length method is the presence of geometric assumptions that may lead to wrong results, especially in patients with left ventricular pathologies such as ventricular aneurysms. Moreover, this approach is suited only for the left ventricle, as the right ventricle follows a more complex geometry

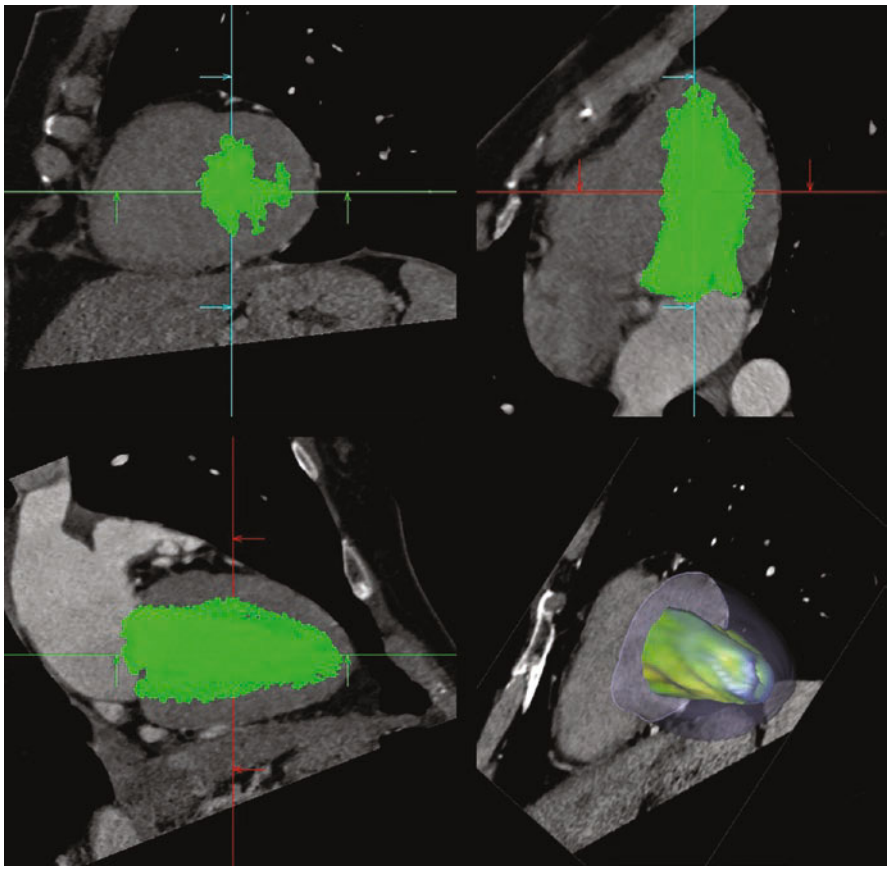

Fig. 15.7 The previously shown two-dimensional approaches (e.g., the Simpson method) are limited for the volumetric assessment of the left ventricular outflow tract, the apex, and the saddle-shaped mitral annulus. True three-dimensional measurements are better suited for assessing complex geometric objects such as the cardiac ventricles, and most tools now provide threshold-based, semi-automated assessment of left and right ventricular volumes. These tools are supported by complex geometric models that were designed to improve the robustness of these techniques. As a major advantage, these tools are much quicker than manual contour drawing. Although the ventricular volumes are comparable to those obtained using Simpson's rule, there appears to be systematic underestimation of the left ventricular volumes, with a subsequent overestimation of the ejection fraction [5]. Moreover, comparability with other techniques such as echocardiography and MRI is limited, as most reference techniques are still limited to two-dimensional assessment of ventricular volumes

global ventricular function independent from the patient's heart rate (Fig. 15.11).

Table 15.1 shows normal values for ventricular function that have been established using CT. Table 15.2 illustrates the excellent correlations between ventricular volumes determined by CT and MRI. Left ventricular function, however, is affected by the administration of beta-blockers, which are often given to slow down heart rate for coronary CT angiography. In these patients, stroke volume and ejection fraction are significantly decreased [9]. Another factor affecting global function values is automated 3D image analysis, which results in a systematic overestimation of the ejection fraction [12]. Corresponding results were reported from comparison of CT with echocardiography and ventriculography, proving CT a reliable technique to assess left ventricular volumes at rest.

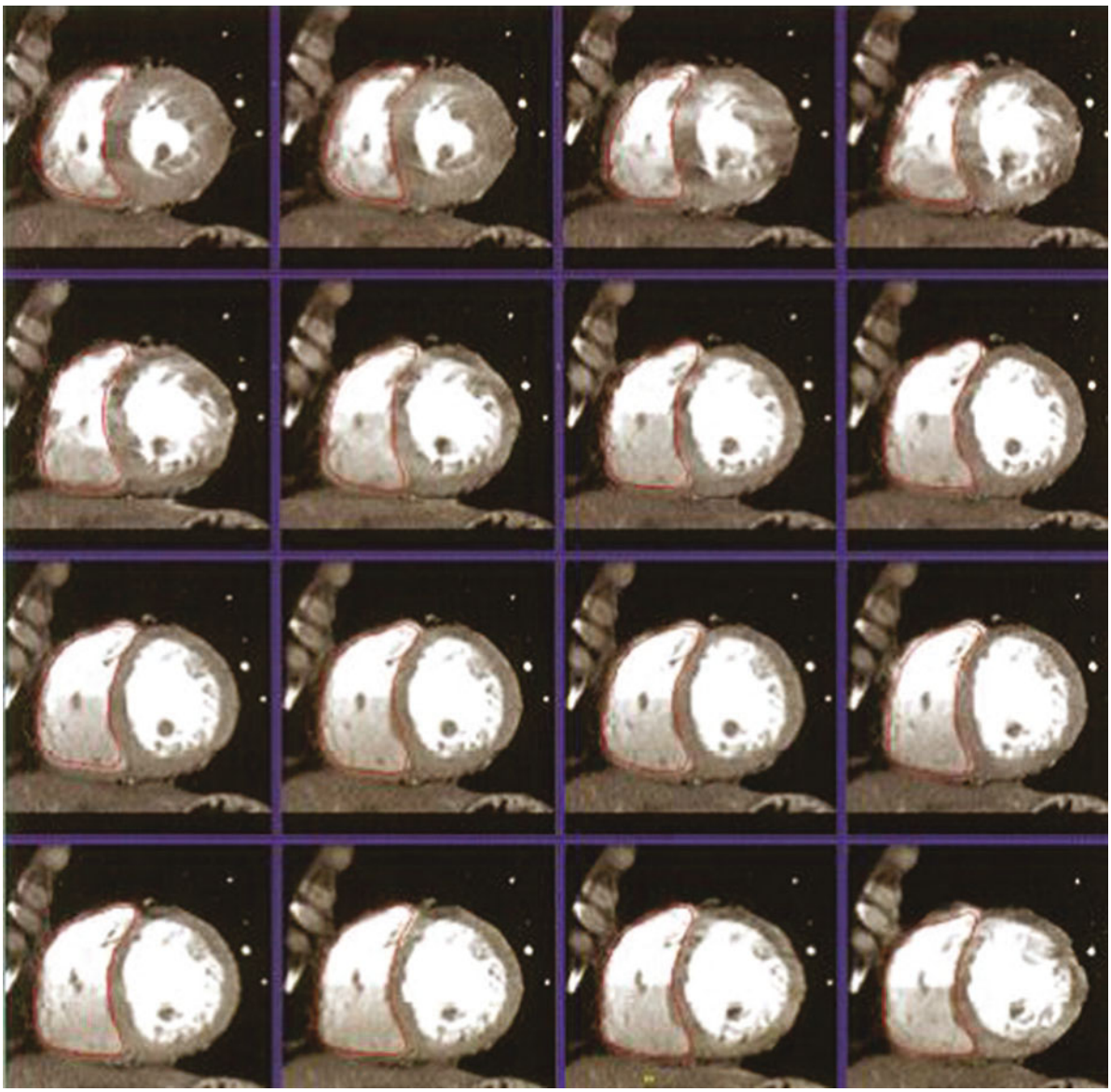

Fig. 15.8 For calculation of the right ventricular volumes, the modified Simpson method is used. Because of the complex geometry, reliable geometric models (which are suited for the left ventricle) are not available. Moreover, in most centers only the ventricular volumes are assessed, requiring the endocardial contours only. For reliable assessment of the right ventricular volumes, a sufficient enhancement of the right ventricle is needed, which can reliably be achieved by using the so-called split-bolus technique. A common approach is to add diluted contrast material (e.g., 20% contrast with 80% saline) after the main contrast bolus

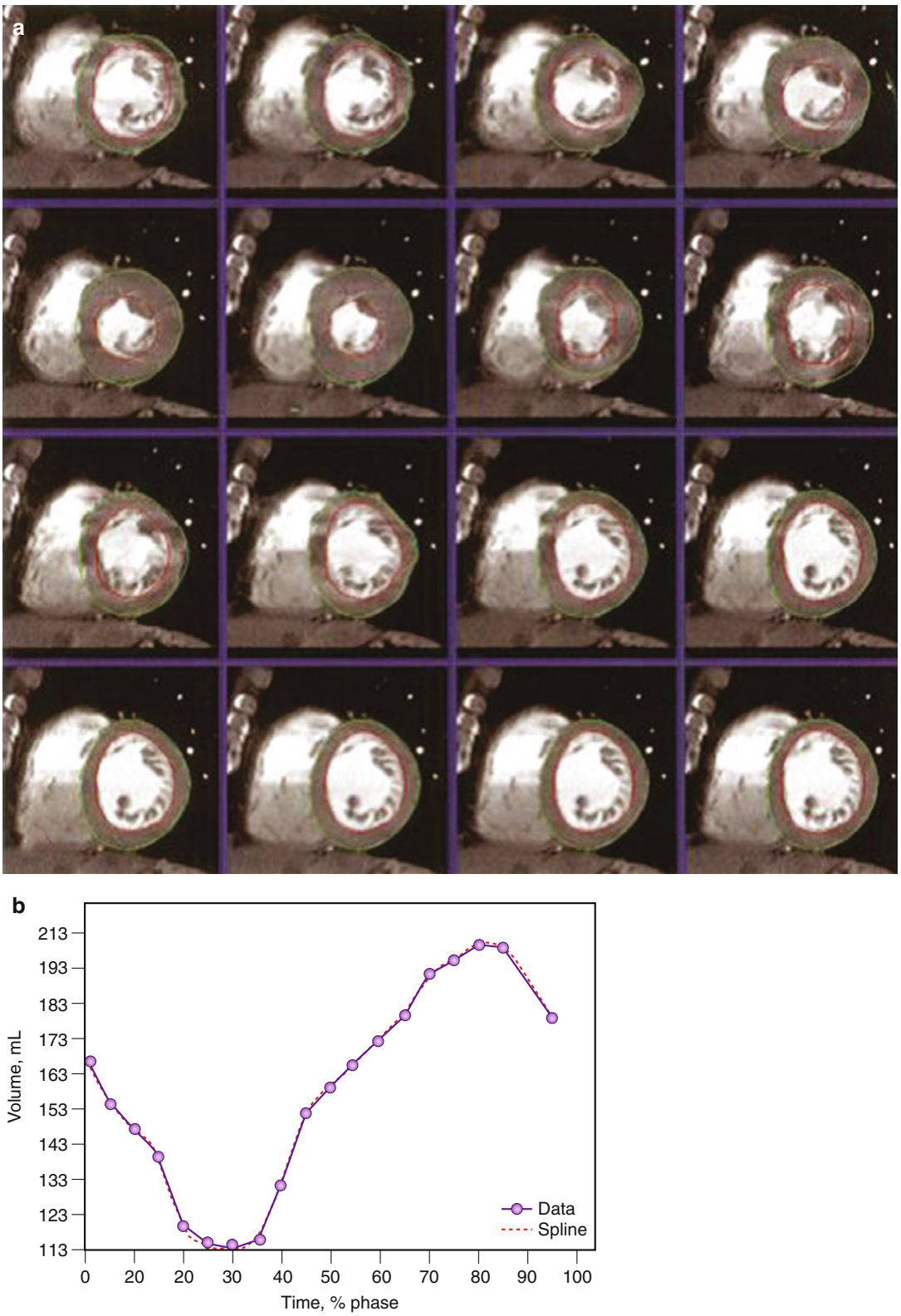

Fig. 15.9 The assessment of end-systolic and end-diastolic images is sufficient to determine ejection fraction and cardiac output. Images from multiple cardiac phases must be analyzed (**a**) for calculation of volume-time-curves (**b**). The shape of these curves provides information on ventricular dynamics beyond ejection fraction. This information may be of particular interest in patients with ventricular asynergy, when a two-point method may be misleading. In clinical routine, the use of volume-time curves for the assessment of ventricular function is uncommon. This technique is mainly used for research purposes, as its added value for most clinical problems has not yet been unequivocally clarified

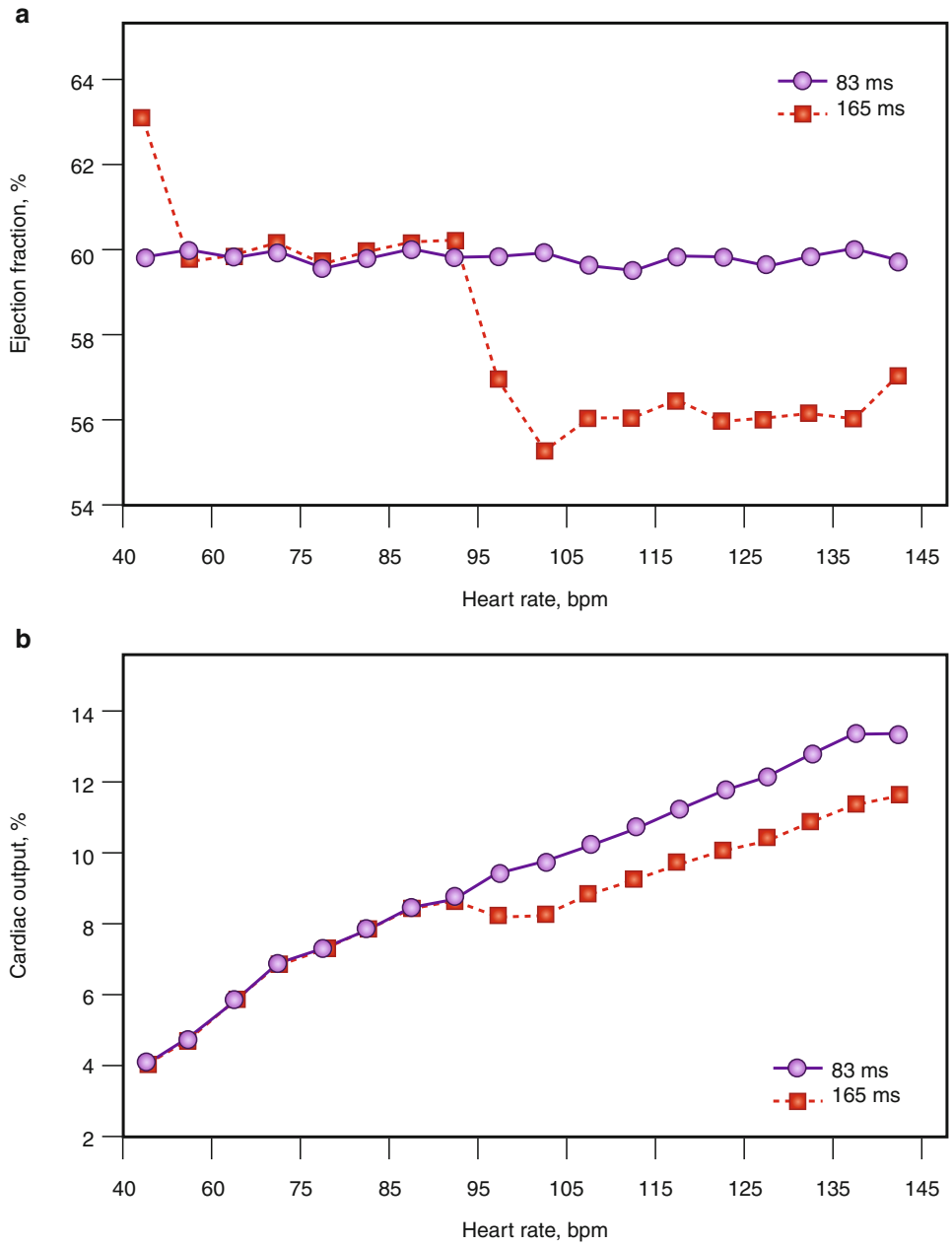

Fig. 15.10 Accuracy of measurements of left ventricular ejection fraction and volumes depends on heart rate and temporal resolution. Results of phantom measurements with a "true" ejection fraction of 60% show that a temporal resolution of 165 ms is still not enough to reliably determine the ejection fraction at every heart rate (**a**). At increased heart rates (>90 bpm), ejection fraction will be underestimated, as end-systole will be missed. The same is true for cardiac output (**b**). If the temporal resolution is down to 75 ms, both functional parameters can be reliably determined independent of the patient's heart rate. Consequently, it is important to consider heart rate and temporal resolution when interpreting results of functional cardiac CT

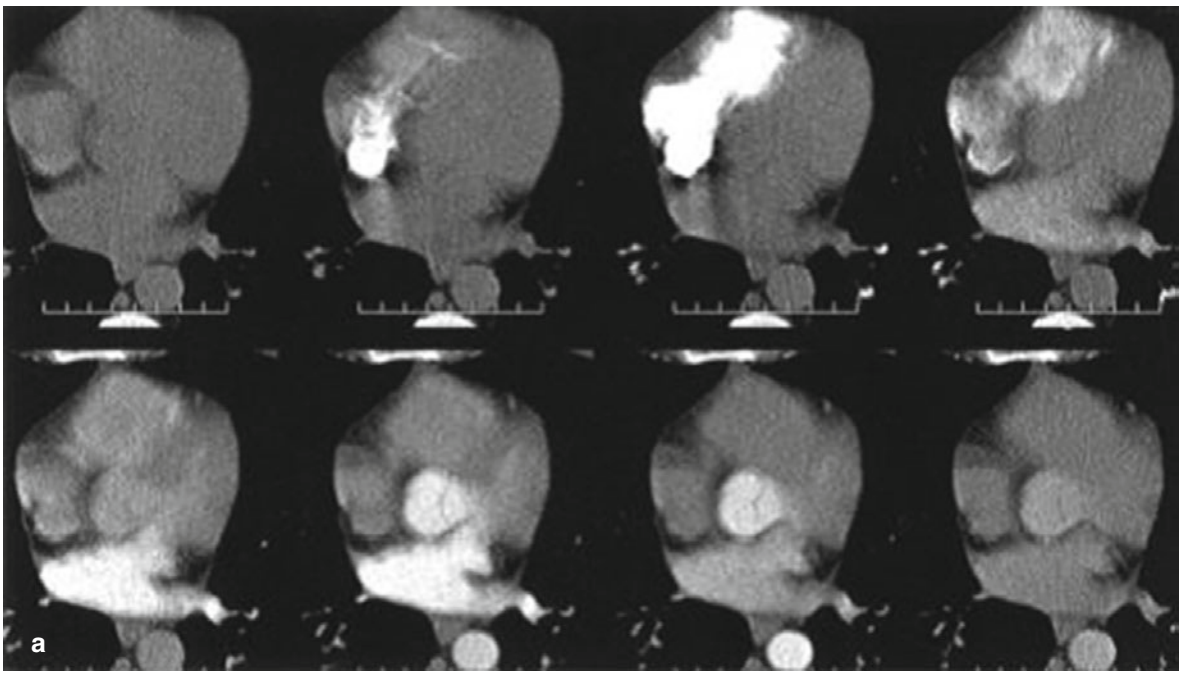

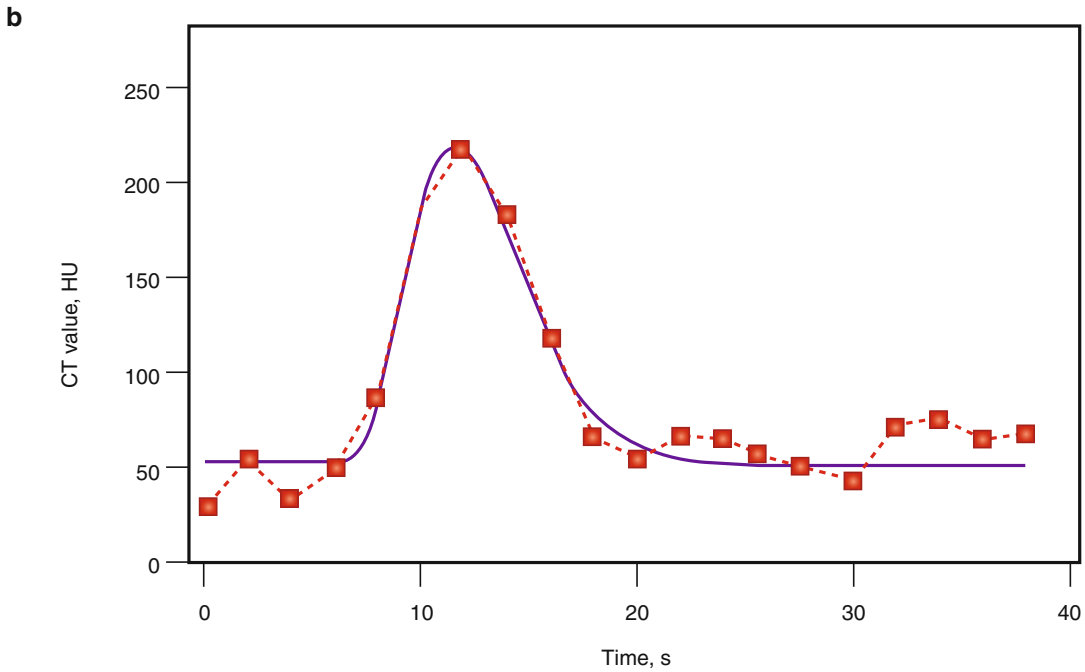

Fig. 15.11 A different approach to assess ventricular function is to apply indicator dilution theory on test-bolus data. Interpreting contrast material as indicator and the CT scanner as a densitometer, cardiac output can be determined from a defined contrast material injection and a dynamic CT measurement (**a**). From fitted time-attenuation curves in the aorta (**b**) cardiac output (CO) can be calculated using a modification of the Stewart-Hamilton equation in which Q is the amount of indicator injected and $c(t)$ is indicator concentrations as a function of time [6]. This technique allows a fast estimation of the global ventricular function. Moreover, this technique is independent from the patient's heart rate and does not require ECG-gated data acquisition

Table 15.1 Normal values for global and regional ventricular function using CT[a]

	Male			Female		
	LV	RV[b]	LA	LV	RV[b]	LA
EF, %	66 (48–83)	58 (42–74)	46 (43–48)	66 (52–80)	58 (42–74)	55 (52–57)
EDV, mL	144 (70–219)	175 (81–269)	86 (79–93)	115 (102–129)	175 (81–269)	74 (68–80)
ESV, mL	47 (9–85)	82 (25–140)	46 (42–50)	40 (17–63)	82 (25–140)	34 (30–38)
SV, mL	95 (37–152)	–	40 (36–43)	76 (40–112)	–	40 (37–43)
MM, g	167 (92–241)	–	–	129 (73–184)	–	–
LVMMI, g/m^2	86 (51–121)	–	–	68 (42–94)	–	–
EDID, mm	45 (36–55)	–	35 (33–36)	44 (34–53)	–	35 (33–36)
$EDWT_{post}$, mm	9 (6–13)	–	–	8 (5–11)	–	–
$ESWT_{post}$, mm	15 (10–21)	–	–	14 (9–18)	–	–
RWT	0.42 (0.2–0.64)	–	–	0.38 (0.22–0.54)	–	–

EDID end-diastolic inner diameter, *EDV* end-diastolic volume, *EDWT* end-diastolic wall thickness, *EF* ejection fraction, *ESV* end-systolic volume, *ESWT* end-systolic wall thickness, *LA* left atrium, *LV* left ventricle, *LVMMI* left-ventricular myocardial mass index, *MM* myocardial mass, *RV* right ventricle, *RWT* relative wall thickness, *SV* stroke volume, *SWT* systolic wall thickening

Adapted from Lin et al. [5], Stolzmann et al. [7], and Stojanovska et al. [8]

[a]Reference values beyond global right ventricular and left atrial function were omitted. So far this information cannot reliably be determined with CT. There also are differences in the left ventricular function depending on the patient's age, height, and weight. To correct for the latter, results are commonly normalized to the patient's body surface area

[b]No gender-specific reference values

Table 15.2 Studies of correlation between ventricular volumes determined by CT and by MRI

			Correlation				
Study	Patients	Ventricle	ESV	EDV	SV	EF	MM
Jensen et al. [9][a]	32	LV	0.92	0.87	0.77	0.83	0.98
Bak et al. [10]	111	LV	0.97	0.96	0.91	0.94	–
Greupner et al. [11]	36	LV	0.96	0.90	0.55	0.89	0.93
Fuchs et al. [12][b]	53	LV	0.91	0.83	0.62	0.79	–
Maffei et al. [13]	79	LV	0.76	0.59	0.44	0.73	0.76
		RV	0.70	0.58	0.55	0.74	–
Plumhans et al. [14]	38	RV	0.98	0.98	0.98	0.97	–
Jensen et al. [15]	33	RV	0.97	0.99	–	0.92	0.99
Huang et al. [16]	50	RV	0.97	0.94	0.97	0.99	–

EDV end-diastolic volume, *EF* ejection fraction, *ESV* end-systolic volume, *LV* left ventricle, *MM* myocardial mass, *RV* right ventricle, *SV* stroke volume

[a]CT after administration of beta-blockers

[b]Automated 3D image analysis

Assessment of Ventricular Wall Motion

Regional ventricular wall motion is typically assessed using a semiquantitative four-point scale (Figs. 15.12 and 15.13). Various imaging modalities, including CT, can be used to assess global and regional left ventricular function (Fig. 15.14).

Studies have shown that the assessment of regional wall motion is feasible with cine CT. An excellent agreement has already been found with 16-slice CT, and these outstanding

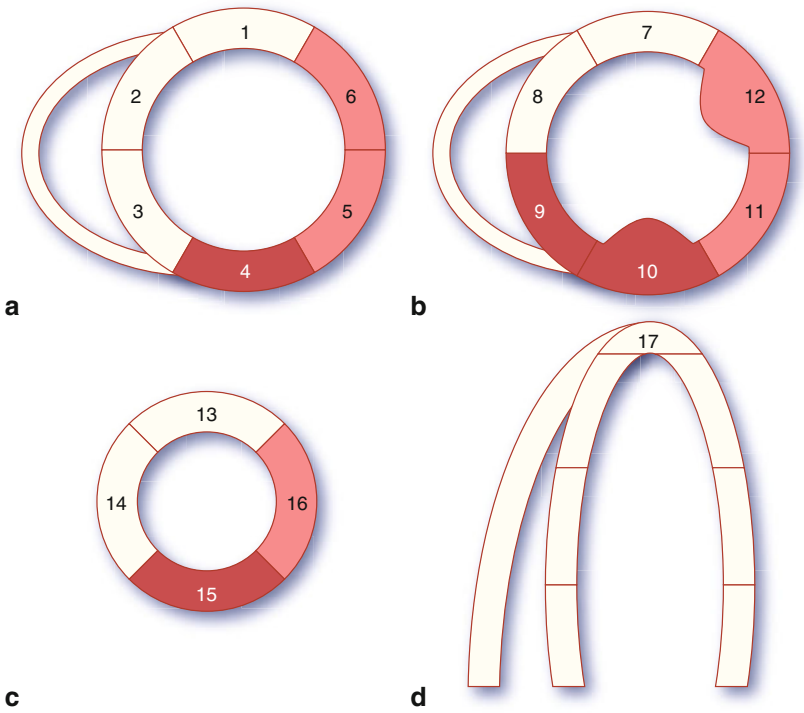

Fig. 15.12 Myocardial segments are identified for the assessment of regional myocardial function and viability, from the base (**a**) and the midsection (**b**) to the apex (**c**). The apex itself is considered a separate segment (**d**). Each myocardial segment can be assigned to the territories of the different coronary arteries: left anterior descending artery (*white*), left circumflex coronary artery (*light green*), and right coronary artery (*dark green*) [17]. So far, there is no uniform nomenclature for the right ventricle

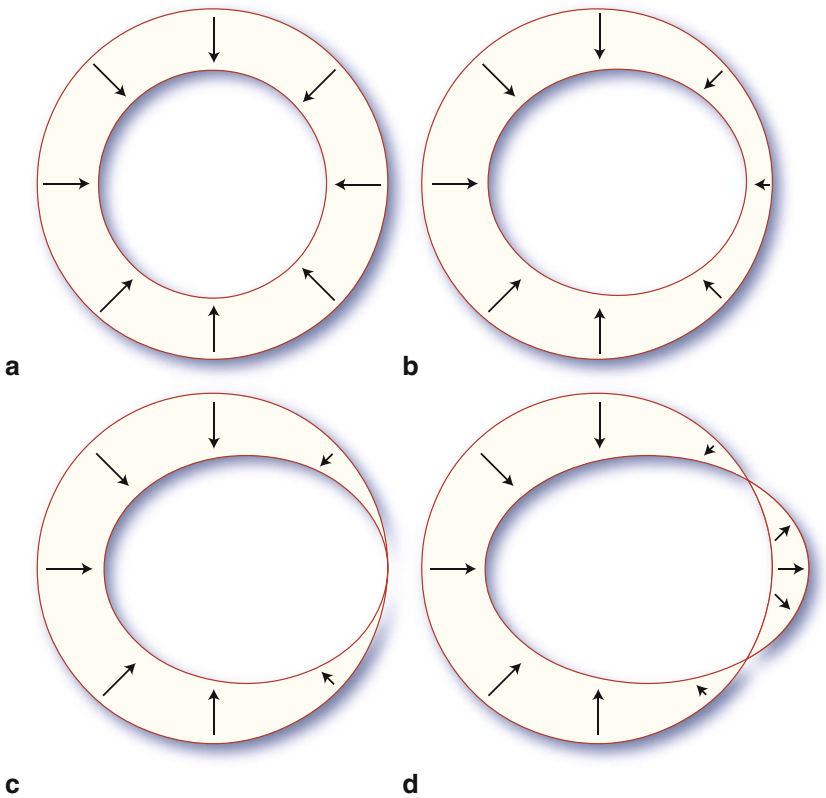

Fig. 15.13 Regional ventricular wall motion is typically assessed using a semiquantitative four-point scale. Regular wall motion is classified as *normokinetic* (**a**). Reduced wall motion is classified as either *hypokinetic* (i.e., reduced systolic wall thickening) (**b**) or *akinetic* (i.e., absent regional wall thickening) (**c**). An outward movement of the ventricular wall segments during systolic contraction is called *dyskinesis* (**d**). Furthermore, asynchronous wall motion can be observed, such as in the presence of left or right bundle block. In combination with information on the coronary arteries, this wall motion analysis provides valuable insight into the functional state of the different coronary artery territories and therefore the coronary artery perfusion. Because CT wall motion analysis is performed only at rest, there is no information on contractile reserve, limiting the use of this technique

results have been confirmed with recent CT scanners, proving the assessment of regional wall motion from CT data to be a robust and reliable approach (Table 15.3). The combination of regional functional analysis with CT coronary angiography has also been shown to improve the conspicuity of coronary artery lesions in patients with acute chest pain [18]. Despite the trend towards prospective triggering as an image acquisition technique to reduce the radiation dose, a comprehensive data analysis should be performed whenever functional data are available.

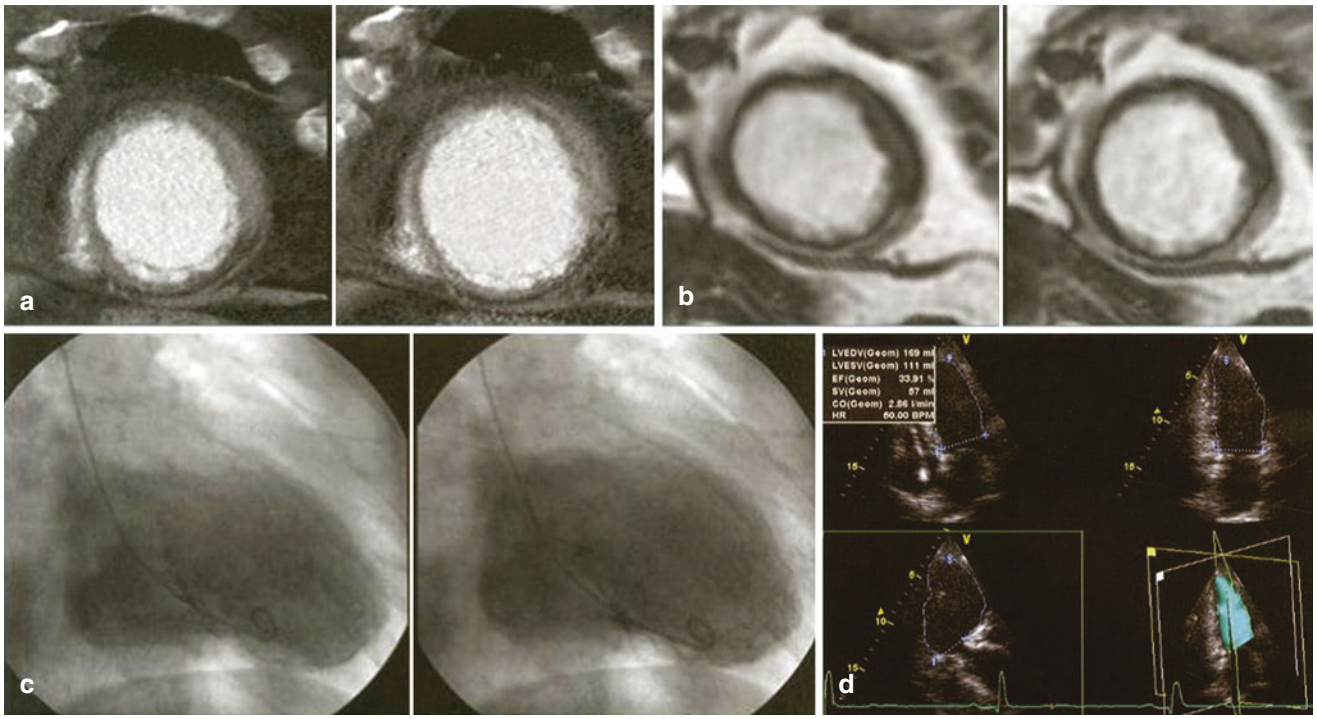

Fig. 15.14 Multiple imaging modalities can be used to assess global and regional left ventricular function. These include CT (**a**), MRI (**b**), ventriculography (**c**), and echocardiography (**d**). All of these techniques allow differentiation of systole (*left*) and diastole (*right*) and, therefore, calculation of ventricular volumes and function. As shown in this patient with severely reduced left ventricular function, all of these techniques are suited to visualize the impaired left ventricular function. CT, MRI, and echocardiography also have the potential to quantitatively assess wall thickening. These images show severely reduced wall thickness of the septal and inferior myocardial segments. Only the mid-anterolateral segment of the left ventricle presents with nearly normal wall thickness, but limited wall thickening

Table 15.3 Studies of regional wall motion: agreement of MDCT with MRI or echocardiography

Study	Patients/Segments	MDCT	Reference	Agreement	
				Overall, %	Weighted, κ
Salm et al. [18]	25/425	16	MRI	95	0.86
			2D-Echo	91	0.78
Sarwar et al. [19]	21/357	64	MRI	87	0.86
Lüders et al. [20]	30/480	64-DSCT	MRI	89	0.763
Nakazato et al. [21]	83/1411	64-DSCT	2D-Echo	98	0.83
Nasis et al. [22]	50/850	320	2D-Echo	96	0.76

DSCT dual source CT, *MDCT* multidetector CT

Left-ventricular remodeling is another important indicator of cardiac pathology, with different types of pathologic remodeling occurring in various diseases. Eccentric remodeling is a unique form that eventually follows myocardial infarction. It can be identified by adapting the principles of echocardiography to CT (Fig. 15.15).

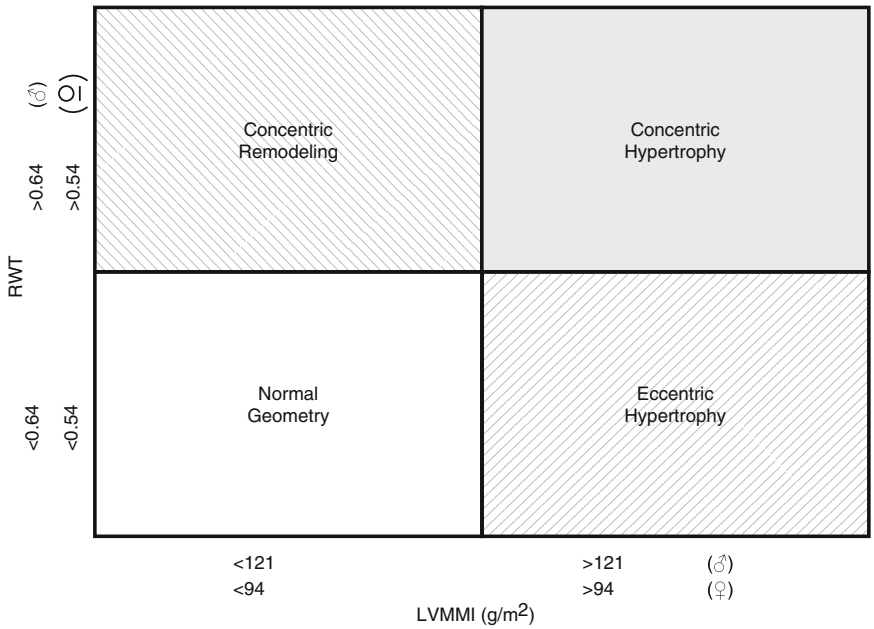

Fig. 15.15 Left-ventricular (LV) remodeling is another important indicator of cardiac pathology. It may be physiological when the heart increases in size but maintains normal function, such as during growth or physical training. Different types of pathologic remodeling occur in a variety of diseases. The transition to pathologic remodeling goes along with progressive ventricular dilatation and distortion of the LV cavity shape, resulting in a disruption of its normal geometry. Eccentric remodeling is a unique form of LV remodeling that eventually follows myocardial infarction. Applying the principles of echocardiography to CT, it may be identified from the ratio of the LV myocardial mass index (LVMMI; g/m^2) to relative wall thickness (RWT), with RWT being defined as: $RWT = \frac{2 \bullet EDWT_{dia}}{EDID}$ where $EDWT_{dia}$ is the end-diastolic wall thickness and *EDID* is the end-diastolic inner diameter of the left ventricle as measured from short-axis views (*see* Fig. 15.6) [23]

CT Myocardial Perfusion Imaging

Ischemic injury of the myocardium can be differentiated as reversible or irreversible, in conditions that are acute or chronic. Different contrast enhancement patterns may be seen on arterial and late-phase CT imaging (Fig. 15.16). During the arterial phase, ischemic damage to the myocardium appears as an area of reduced attenuation (Fig. 15.17). Various studies have shown that it is feasible to detect myocardial infarction using arterial-phase CT because infarcted myocardium shows reduced attenuation values (Table 15.4). Attenuation values of normal myocardium are typically more than twice as high as the values in infarcted myocardium. Applying a threshold of 20 HU to differentiate healthy from infarcted myocardium provides results with acceptable specificity. Nevertheless, the size of myocardial infarction is typically underestimated on arterial phase CT when compared with MRI, and unequivocal differentiation of reversible and irreversible myocardial injury is not feasible.

Acute and chronic myocardial infarction cannot be differentiated based on the pattern of contrast enhancement, but they can be differentiated on the basis of regional wall thickness and the presence of myocardial calcifications. Chronic myocardial infarction presents with a combination of reduced contrast enhancement and regional wall thinning (Fig. 15.18).

Ischemic Injury of the Myocardium

	Acute		Chronic	
	Reversible	Irreversible	Reversible	Irreversible
	Stunning	Acute myocardial infarction	Hibernation	Chronic myocardial infarction
Arterial phase	Hypodense or normal	Hypodense	Hypodense or normal	Hypodense, wall thinning
Late phase	Hypodense	Occlusive = hypodense; reperfused = hyperdense;	Hypodense	Occlusive = hypodense; reperfused = hyperdense;

Fig. 15.16 Ischemic injury of the myocardium can be differentiated in reversible and irreversible conditions and in acute and chronic conditions. Single or repeated short periods of myocardial ischemia may result in *myocardial stunning*, a postischemic dysfunctional state of the myocardium that persists even if the coronary flow is restored. *Hibernating myocardium* is characterized as viable but nonfunctional myocardium with chronically impaired regional blood flow. The loss of cell membrane integrity marks the point of cell necrosis and irreversible myocardial infarction. Myocardial infarction may be occlusive or reperfused (e.g., after medical or mechanical revascularization therapy). Depending on the type of myocardial injury, different contrast enhancement patterns may be seen on arterial and late-phase CT imaging

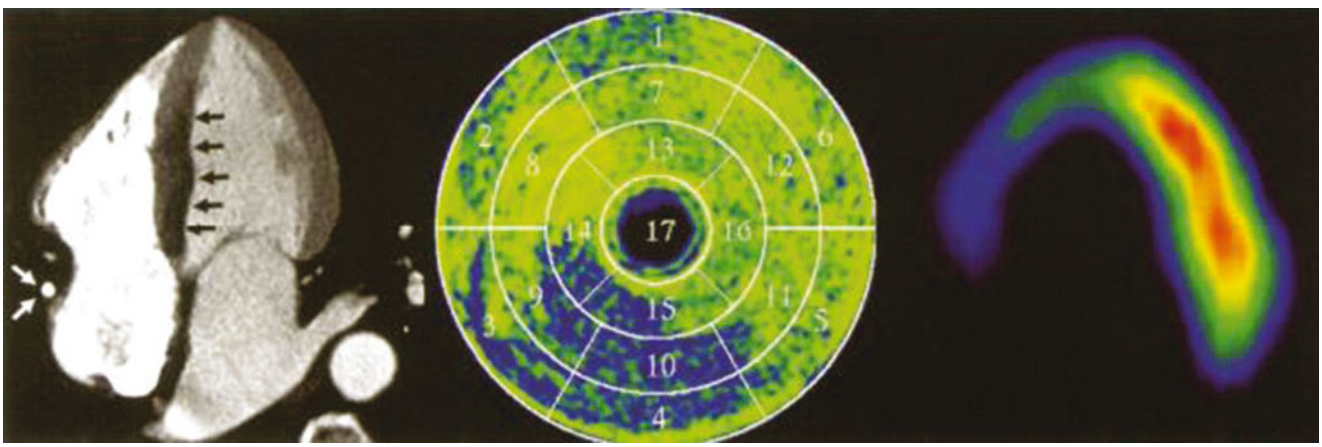

Fig. 15.17 During the arterial phase, ischemic damage to the myocardium appears as an area of reduced attenuation when compared with healthy, remote myocardium. A focal decrease in myocardial enhancement of 20 HU or more is considered relevant. This finding is unspecific, however; it can be found in myocardial infarction but less commonly is seen in myocardial stunning or hibernation. Wall thickness may help to distinguish acute from chronic stages of disease. This example shows an arterial-phase, four-chamber view in a 54-year-old man with acute myocardial infarction, 2 days after an emergency coronary artery bypass graft procedure. *Left panel*, CT shows a large, hypodense area in the basal and mid-inferoseptal segments of the left ventricle (*black arrows*). The patent coronary artery bypass graft also is visible (*white arrows*). *Middle panel*, Information on myocardial perfusion can be visualized as a color-coded polar map, projecting information from the different myocardial segments onto a single image. In this example, areas of reduced perfusion are encoded *blue*, whereas normal myocardium appears *green*. *Right panel*, Single-photon emission CT (SPECT) images obtained the same day confirm the location and the extent of the area of reduced perfusion

Table 15.4 Detection of myocardial infarction with arterial-phase CT

Study	Patients with/without MI, *n*	Reference	Sensitivity, %	Specificity, %	Attenuation	
					MI	Healthy
Gosalia et al. [24]	18/69	Clinical	83	95	50 (8–87)	118 (66–147)
Mahnken et al. [25]	110/448	MRI	83	91	59 ± 17	101 ± 14
Francone et al. [26]	29/187	Clinical	83	91	39 ± 14	104 ± 16
Sanz et al. [27]	21/42	MRI	91	81	42 ± 39	119 ± 20
Henneman et al. [28]	62/69	SPECT	100	57	–	–
Rubinshtein et al. [29]	17/122	SPECT	75	98	–	–

MI myocardial infarction, *SPECT* single-photon emission computed tomography

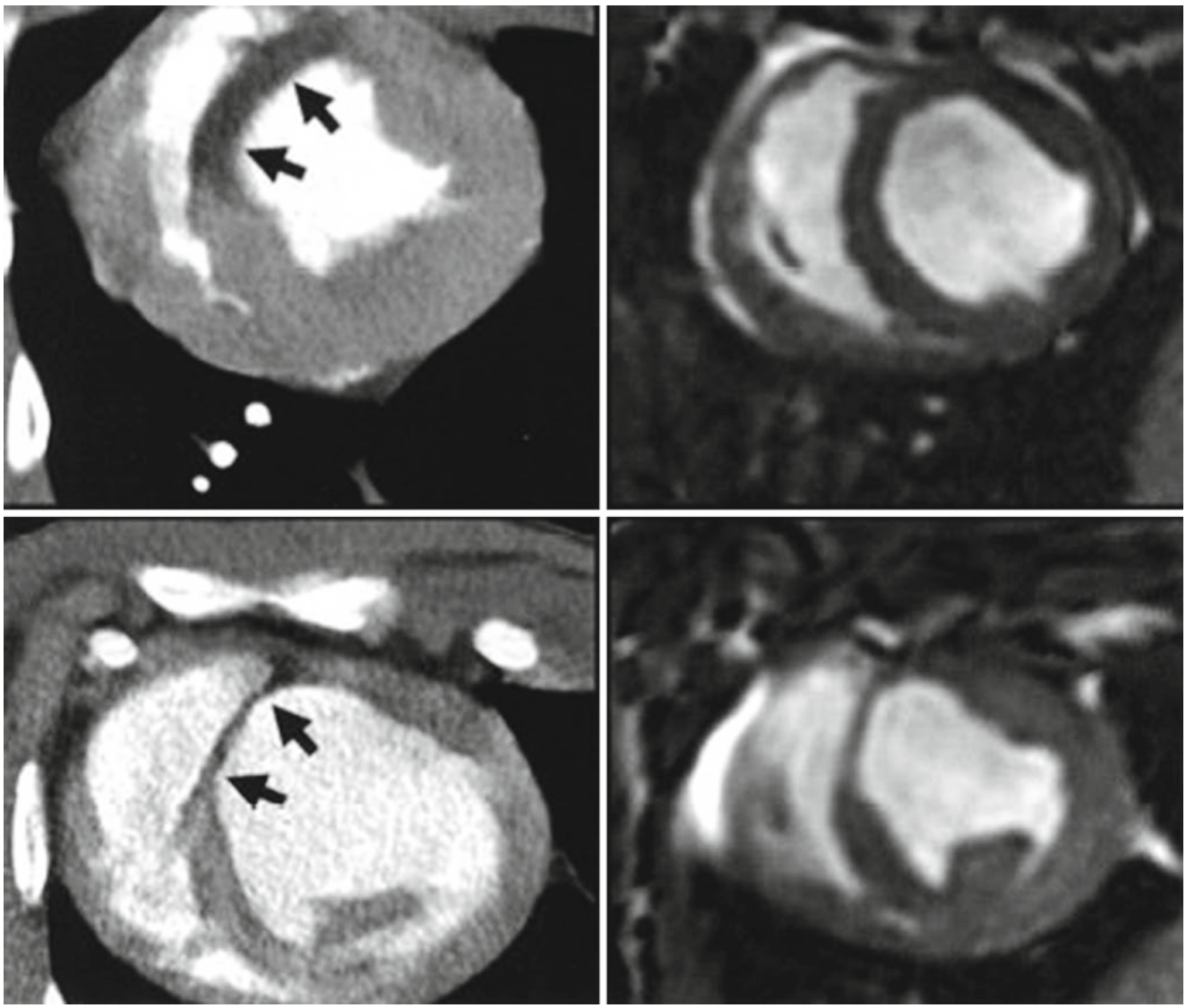

Fig. 15.18 Whereas acute myocardial infarction is characterized by reduced contrast enhancement with normal wall thickness, chronic myocardial infarction presents with a combination of reduced contrast enhancement and regional wall thinning. Cine CT also shows a reduced regional wall thickening. This figure shows a typical example of a pig suffering from an acute myocardial infarction in the mid-anteroseptal myocardium, caused by balloon occlusion of the left anterior descending branch of the left coronary artery. *Top left*, During the acute phase of infarction, arterial-phase CT depicts myocardial infarction as a hypodense area (*arrows*). *Bottom left*, At 3 months follow-up, typical thinning of the mid-anteroseptal myocardium (*arrows*) can be observed. *Right*, Corresponding MRI findings

First-pass myocardial perfusion imaging has the potential to detect impaired microvascular function before the occurrence of clinical symptoms, but only preliminary data on first-pass perfusion CT imaging are available (Figs. 15.19 and 15.20). CT perfusion imaging offers several theoretical advantages over MRI, such as the linear relation between contrast enhancement and iodine concentration, which potentially allows for the direct quantification of myocardial blood flow and avoids the need for potentially error-bearing correction methods. Exposure to radiation and contrast material limits stress testing with CT, however, and MRI, a radiation-free reference technique, has become increasingly available.

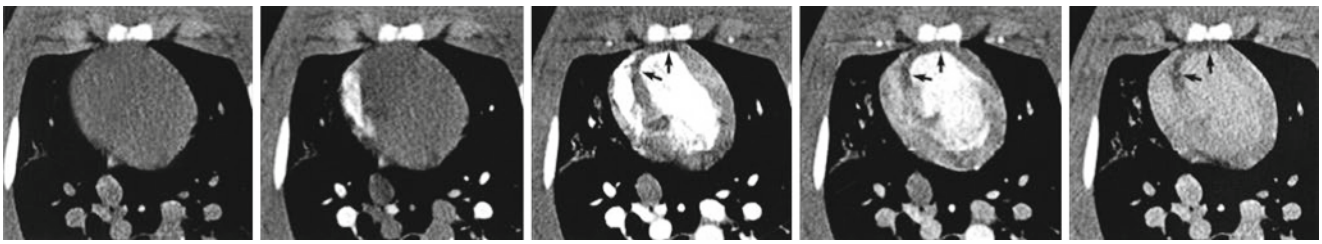

Fig. 15.19 Because first-pass myocardial perfusion imaging may detect impaired microvascular function before the occurrence of clinical symptoms, this technique is suited to assess the physiologic relevance of a coronary artery lesion, as decreased myocardial perfusion represents the first consequence of obstructive coronary artery disease. The feasibility of CT perfusion imaging has been shown, but only preliminary data on first-pass perfusion CT imaging are available. Technically, sequential ECG-gated images are obtained at least during every second heartbeat. The presented sequence starts from the left to the right with a nonenhanced baseline image and shows the contrast passage from the right heart to the left ventricle, where an area of reduced myocardial perfusion becomes visible in the anterior wall (*arrows*). The nonenhanced baseline image allows calculation of the absolute contrast enhancement and is needed for quantitative analysis

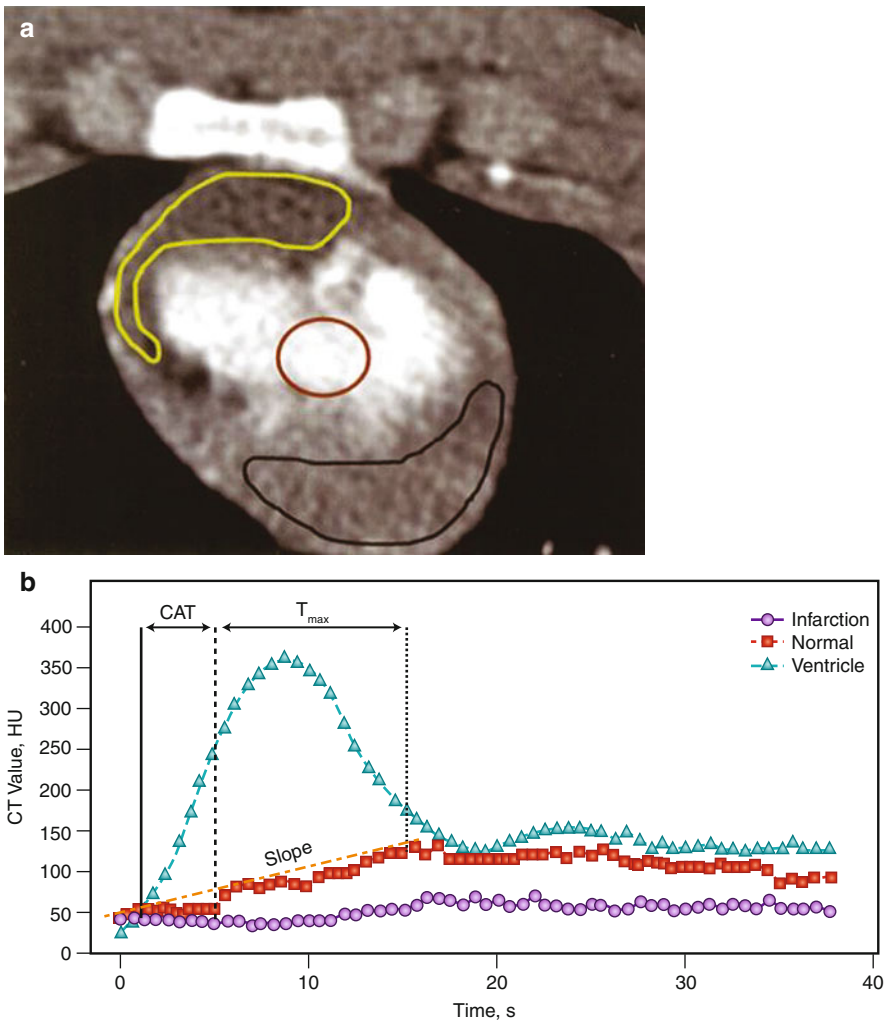

Fig. 15.20 (**a**) For first-pass perfusion analysis, a region of interest is placed in the area of infarction (*yellow*) and the healthy remote myocardium (*black*). To allow interindividual and intraindividual comparison, data must be corrected for variations in the hemodynamic state. Therefore, attenuation values measured in the myocardium must be normalized to the attenuation values in the left ventricular cavum (*red*). (**b**) From these data, time-attenuation curves can be calculated, which are used for quantitative and semiquantitative analysis. For multidetector CT, few data on first-pass perfusion imaging are available. So far, mainly visual and semiquantitative analyses have been performed. Typical parameters established for semiquantitative analysis include maximum signal intensity, wash-in time, and slope. Quantitative parameters include mean transit time, myocardial blood volume, and myocardial perfusion [30]

Assessment of Myocardial Viability

In patients with ischemic heart disease, dysfunctional but viable myocardium may experience functional improvement after revascularization therapy, but nonviable (necrotic) myocardium will not recover function. Therefore, it is important to be able to assess myocardial viability, which can be achieved with contrast-enhanced late-phase CT (Fig. 15.21 and Figs. 15.22). CT also allows differentiation of occlusive from reperfused myocardial infarction (Figs. 15.23 and 15.24). Differences in contrast enhancement patterns can be used to predict functional recovery after myocardial infarction (Fig. 15.25).

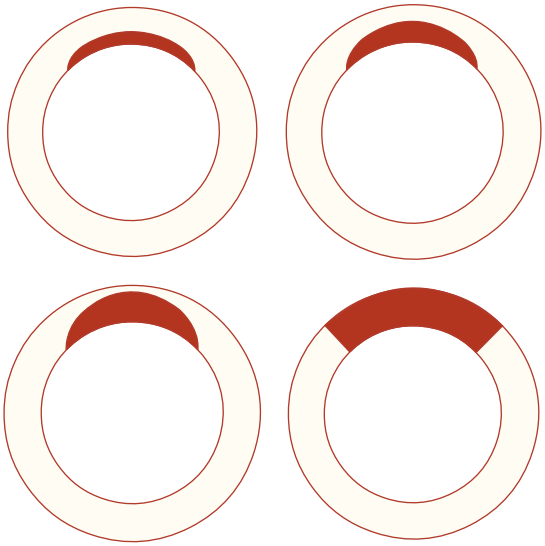

Fig. 15.21 On contrast-enhanced late-phase CT, hyperdense areas of the myocardium correspond to necrotic tissue, so this technique can be used to assess the individual patient's prognosis. *Top left*, If delayed contrast enhancement affects less than 25% of left ventricular wall thickness, global improvement of left ventricular function can be expected. *Top right*, Regional wall motion improvement can be expected in segments with an extent of the hyperenhancing myocardium of less than 50% of the wall thickness [31]. *Bottom left*, Segments with more than 75% delayed contrast enhancement have very little chance for functional improvement [32]. *Bottom right*, Transmural infarcts will not improve function after revascularization

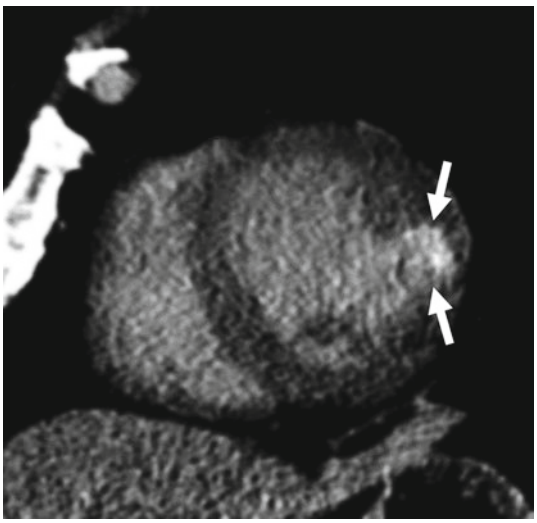

Fig. 15.22 Late phase contrast enhanced CT in a 76-year-old male patient with subacute myocardial infarction shows a marked late enhancement of the left ventricular myocardium. The hyperdense part of the lateral wall of the left ventricle (*arrows*) corresponds to necrotic myocardium. With about 75% transmural extent of the hyperenhancing myocardium the chance for functional recovery is low

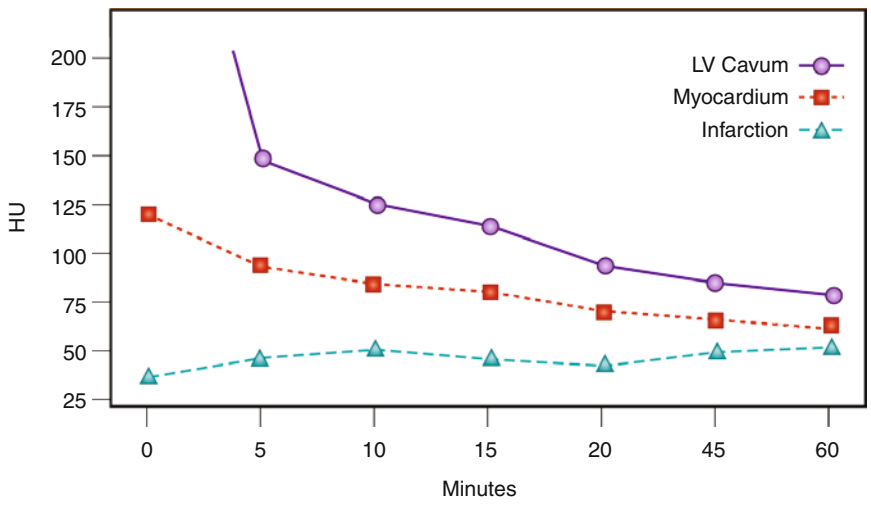

Fig. 15.23 CT allows differentiation of occlusive (**a**) from reperfused myocardial infarction (**b**). On arterial-phase CT (*left*), both types of infarction present with reduced attenuation values corresponding to a lack of contrast enhancement. On contrast-enhanced late-phase CT, occlusive myocardial infarction remains hypodense (**a**, *middle*), whereas reperfused myocardial infarction shows a typical delayed contrast enhancement (**b**, *middle*). The size of infarction correlates well with MRI (*right*), indicating the reliability of CT for imaging myocardial viability

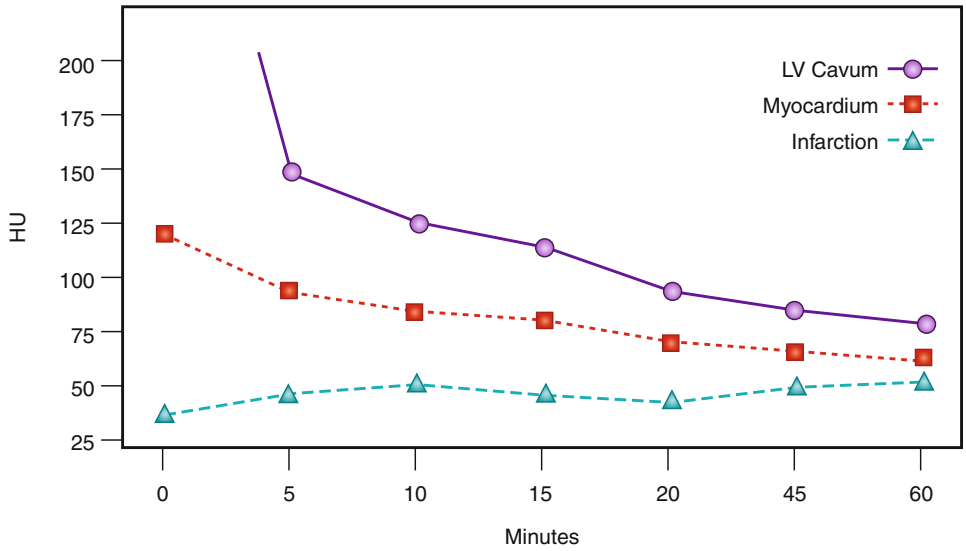

Fig. 15.24 Contrast dynamics for occlusive (**a**) and reperfused (**b**) myocardial infarction differ on CT, allowing differentiation of these types of infarction. Reperfused myocardial infarction shows a characteristic hyperenhancement on late-phase CT (**b**), whereas areas of occlusive infarction remain hypodense when compared with healthy remote myocardium (**a**). The best contrast between normal and infarcted myocardium appears about 5 min after contrast material injection. Especially in reperfused myocardial infarction, however, the contrast between infarcted myocardium and the blood pool is poor (**b**). *LV* left ventricular

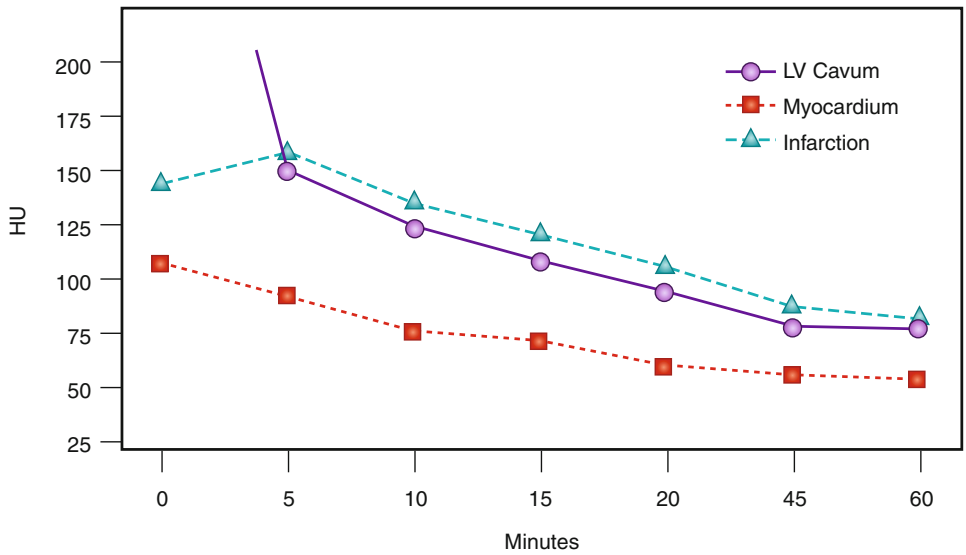

Fig. 15.25 In contrast-enhanced CT of myocardial infarction, different contrast enhancement patterns can be observed when comparing arterial-phase CT (*left*) and late-phase CT (*right*). These patterns allow the prediction of functional recovery after myocardial infarction. *Top row*, The best results with respect to wall thickening and left ventricular ejection fraction were experienced when late enhancement (*white regions*) was seen, but no early perfusion deficit. *Bottom row*, The poorest results are expected in patients with early and late perfusion defects (*dark regions*) [33], which correlate well with so-called microvascular obstruction. This phenomenon is well known to limit the individual patient's prognosis

CT Scan Protocols for Myocardial Assessment

So far, there are no recommendations for a uniform scan protocol for the CT assessment of myocardial function and viability. For a comprehensive analysis of cardiac function and viability, a contrast-enhanced dual-phase scan protocol is needed. Ventricular volumes and regional wall motion are assessed from multiphase, arterial-phase images, whereas myocardial viability is assessed from contrast-enhanced late-phase CT images. Both phases are needed to predict an individual patient's outcome. Figure 15.26 illustrates different contrast injection protocols for coronary CT angiography with subsequent late-phase imaging. A different approach is the use of dual-energy CT for assessing delayed myocardial contrast enhancement. This approach requires a higher radiation exposure than single-energy CT, however, and its use is limited to very few centers.

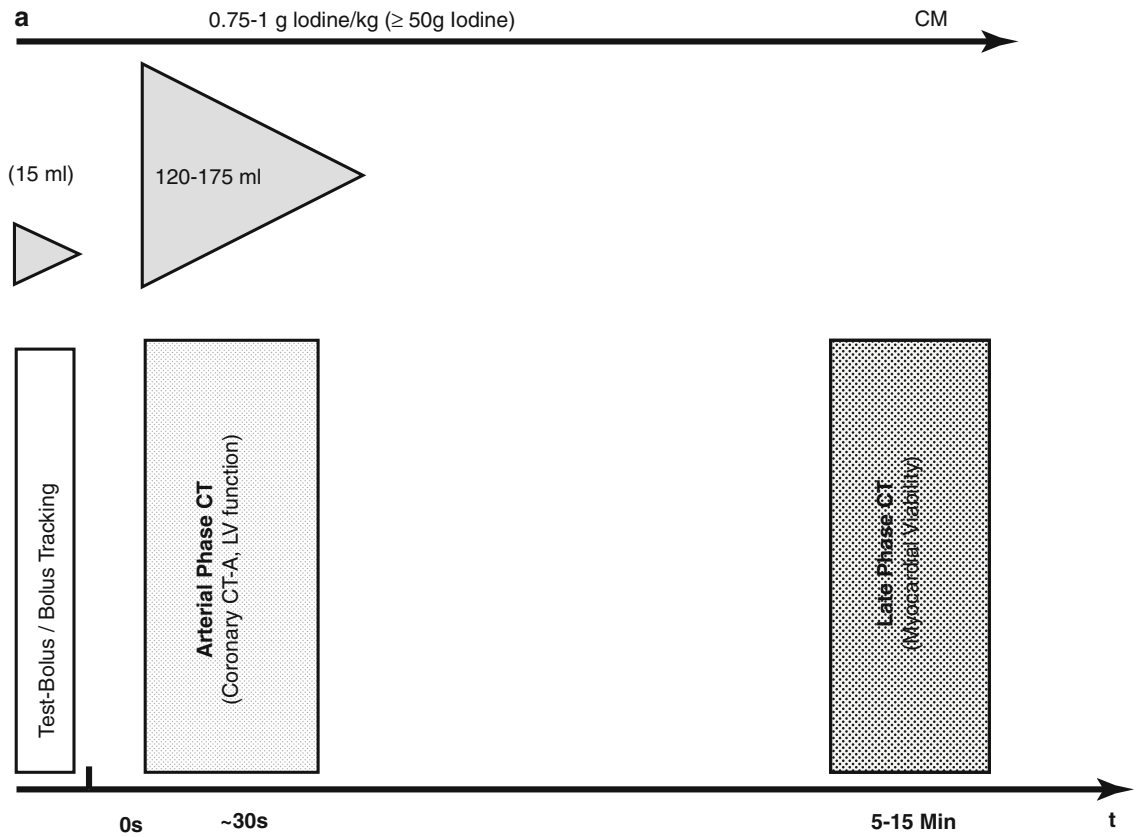

Fig. 15.26 Contrast injection protocols for coronary CT angiography with subsequent late-phase imaging to assess myocardial viability. (**a**) Traditionally the total amount of contrast material is injected in a single bolus injection, and late-phase images are obtained 5–15 min after contrast injection. (**b**), A different approach is to administer a smaller contrast bolus for coronary imaging, followed by slow-flow injection (0.1–0.3 mL per s) for several minutes. (**c**) Adding an additional washout phase improves contrast between the blood pool and areas of delayed myocardial contrast enhancement For determination of the start delay, a test bolus or the bolus tracking technique may be used. Test-bolus data may be used to compute cardiac output. The total amount of contrast material should be between 0.75 and 1 g of iodine per kilogram to ensure sufficient contrast on late-enhanced CT images. Contrast will be further enhanced by using 80 kV or 100 kV scan protocols with iterative reconstruction techniques. Lowering tube voltage and using prospective triggering techniques helps to reduce the radiation dose of the additional viability scan

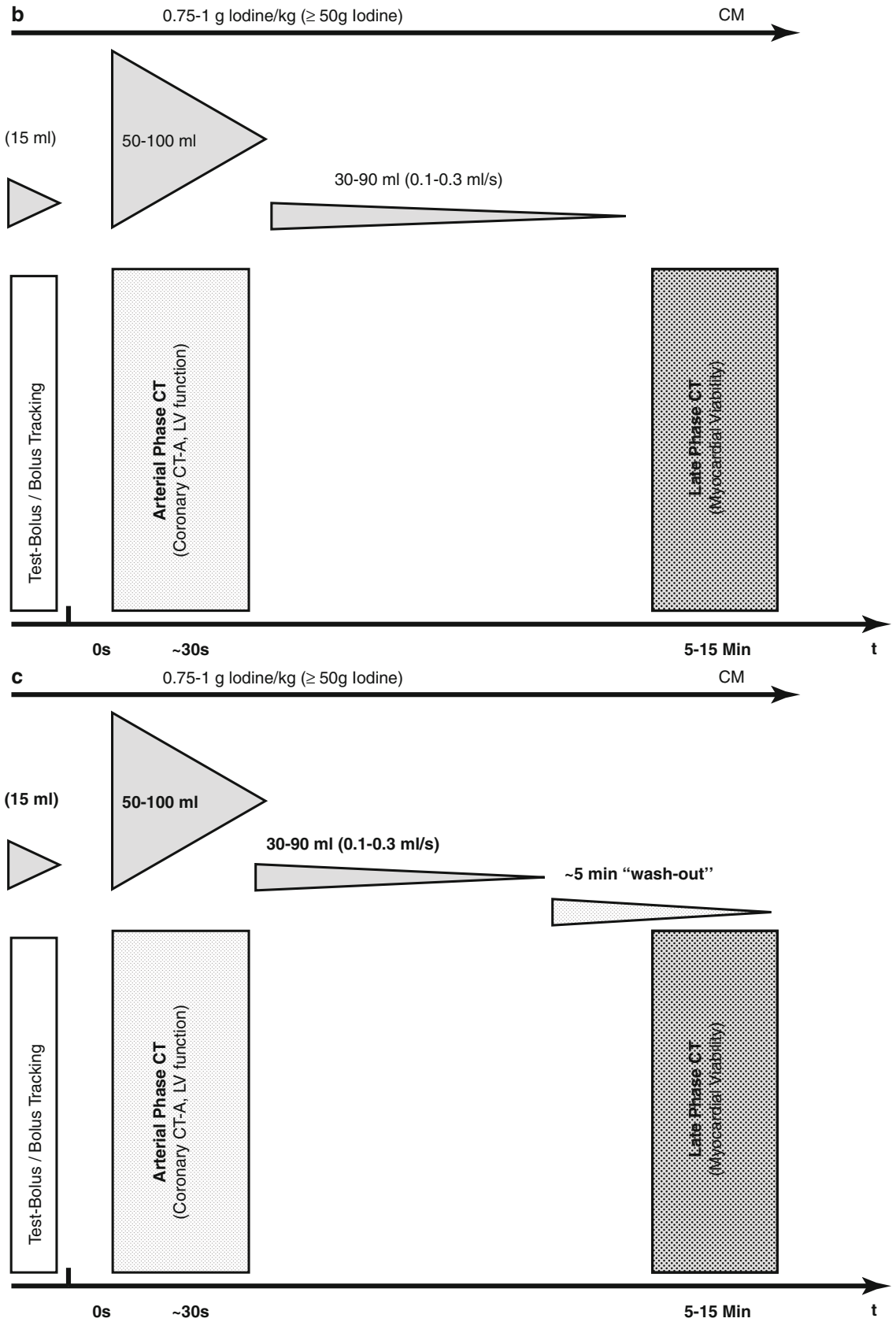

Fig. 15.26 (continued)

References

1. Harell GS, Guthaner DF, Breiman RS, Morehouse CC, Seppi EJ, Marshall WH Jr, Wexler L. Stop-action cardiac computed tomography. Radiology. 1977;123:515–7.
2. Ritman EL, Robb RA, Johnson SA, Chevalier PA, Gilbert BK, Greenleaf JF, et al. Quantitative imaging of the structure and function of the heart, lungs, and circulation. Mayo Clin Proc. 1978;53:3–11.
3. Lipton MJ, Farmer DW, Killebrew EJ, Bouchard A, Dean PB, Ringertz HG, Higgins CB. Regional myocardial dysfunction: evaluation of patients with prior myocardial infarction with fast CT. Radiology. 1985;157:735–40.
4. Papavassiliu T, Kuhl HP, Schroder M, Suselbeck T, Bondarenko O, Bohm CK, et al. Effect of endocardial trabeculae on left ventricular measurements and measurement reproducibility at cardiovascular MR imaging. Radiology. 2005;236:57–64.
5. Lin FY, Devereux RB, Roman MJ, Meng J, Jow VM, Jacobs A, et al. Cardiac chamber volumes, function, and mass as determined by 64-multidetector row computed tomography: mean values among healthy adults free of hypertension and obesity. JACC Cardiovasc Imaging. 2008;1:782–6.
6. Mahnken AH, Klotz E, Hennemuth A, Jung B, Koos R, Wildberger JE, Gunther RW. Measurement of cardiac output from a test-bolus injection in multislice computed tomography. Eur Radiol. 2003;13:2498–504.
7. Stolzmann P, Scheffel H, Leschka S, Schertler T, Frauenfelder T, Kaufmann PA, et al. Reference values for quantitative left ventricular and left atrial measurements in cardiac computed tomography. Eur Radiol. 2008;18:1625–34.
8. Stojanovska J, Cronin P, Patel S, Gross BH, Oral H, Chughtai K, Kazerooni EA. Reference normal absolute and indexed values from ECG-gated MDCT: left atrial volume, function, and diameter. Am J Roentgenol. 2011;197:631–7.
9. Jensen CJ, Jochims M, Hunold P, Forsting M, Barkhausen J, Sabin GV, et al. Assessment of left ventricular function and mass in dual-source computed tomography coronary angiography: influence of beta-blockers on left ventricular function: comparison to magnetic resonance imaging. Eur J Radiol. 2010;74:484–91.
10. Bak SH, Ko SM, Jeon HJ, Yang HS, Hwang HK, Song MG. Assessment of global left ventricular function with dual-source computed tomography in patients with valvular heart disease. Acta Radiol. 2012;53:270–7.
11. Greupner J, Zimmermann E, Grohmann A, Dubel HP, Althoff TF, Borges AC, et al. Head-to-head comparison of left ventricular function assessment with 64-row computed tomography, biplane left cineventriculography, and both 2- and 3-dimensional transthoracic echocardiography: comparison with magnetic resonance imaging as the reference standard. J Am Coll Cardiol. 2012;59:1897–907.
12. Fuchs A, Kühl JT, Lønborg J, Engstrøm T, Vejlstrup N, Køber L, Kofoed KF. Automated assessment of heart chamber volumes and function in patients with previous myocardial infarction using multidetector computed tomography. J Cardiovasc Comput Tomogr. 2012;6:325–34.
13. Maffei E, Messalli G, Martini C, Nieman K, Catalano O, Rossi A, et al. Left and right ventricle assessment with cardiac CT: validation study vs. cardiac MR. Eur Radiol. 2012;22:1041–9.
14. Plumhans C, Mühlenbruch G, Rapaee A, Sim KH, Seyfarth T, Günther RW, Mahnken AH. Assessment of global right ventricular function on 64-MDCT compared with MRI. Am J Roentgenol. 2008;190:1358–61.
15. Jensen CJ, Wolf A, Eberle HC, Forsting M, Nassenstein K, Lauenstein TC, et al. Accuracy and variability of right ventricular volumes and mass assessed by dual-source computed tomography: influence of slice orientation in comparison to magnetic resonance imaging. Eur Radiol. 2011;21:2492–502.
16. Huang X, Pu X, Dou R, Guo X, Yan Z, Zhang Z, et al. Assessment of right ventricular function with 320-slice volume cardiac CT: comparison with cardiac magnetic resonance imaging. Int J Cardiovasc Imaging. 2012;28(Suppl 2):87–92.
17. Cerqueira MD, Weissman NJ, Dilsizian V, Jacobs AK, Kaul S, Laskey WK, American Heart Association Writing Group on Myocardial Segmentation and Registration for Cardiac Imaging, et al. Standardized myocardial segmentation and nomenclature for tomographic imaging of the heart. A statement for healthcare professionals from the Cardiac Imaging Committee of the Council on Clinical Cardiology of the American Heart Association. Circulation. 2002;105:539–42.
18. Salm LP, Schuijf JD, de Roos A, Lamb HJ, Vliegen HW, Jukema JW, et al. Global and regional left ventricular function assessment with 16-detector row CT: comparison with echocardiography and cardiovascular magnetic resonance. Eur J Echocardiogr. 2006;7:308–14.
19. Sarwar A, Shapiro MD, Nasir K, Nieman K, Nomura CH, Brady TJ, Cury RC. Evaluating global and regional left ventricular function in patients with reperfused acute myocardial infarction by 64-slice multidetector CT: a comparison to magnetic resonance imaging. J Cardiovasc Comput Tomogr. 2009;3:170–7.
20. Lüders F, Fischbach R, Seifarth H, Wessling J, Heindel W, Juergens KU. Dual-source computed tomography: effect on regional and global left ventricular function assessment compared to magnetic resonance imaging [German]. Rofo. 2009;181:962–9.
21. Nakazato R, Tamarappoo BK, Smith TW, Cheng VY, Dey D, Shmilovich H, et al. Assessment of left ventricular regional wall motion and ejection fraction with low-radiation dose helical dual-source CT: comparison to two-dimensional echocardiography. J Cardiovasc Comput Tomogr. 2011;5:149–57.
22. Nasis A, Moir S, Seneviratne SK, Cameron JD, Mottram PM. Assessment of left ventricular volumes, ejection fraction and regional wall motion with retrospective electrocardiogram triggered 320-detector computed tomography: a comparison with 2D-echocardiography. Int J Cardiovasc Imaging. 2012;28:955–63.
23. Lang RM, Bierig M, Devereux RB, Flachskampf FA, Foster E, Pellikka PA, American Society of Echocardiography's Nomenclature and Standards Committee; Task Force on Chamber Quantification; American College of Cardiology Echocardiography Committee; American Heart Association; European Association of Echocardiography, European Society of Cardiology, et al. Recommendations for chamber quantification. Eur J Echocardiogr. 2006;7:79–108.
24. Gosalia A, Haramati LB, Sheth MP, Spindola-Franco H. CT detection of acute myocardial infarction. Am J Roentgenol. 2004;182:1563–6.
25. Mahnken AH, Koos R, Katoh M, Wildberger JE, Spuentrup E, Buecker A, et al. Assessment of myocardial viability in reperfused acute myocardial infarction using 16-slice computed tomography in comparison to magnetic resonance imaging. J Am Coll Cardiol. 2005;45:2042–7.
26. Francone M, Carbone I, Danti M, Lanciotti K, Cavacece M, Mirabelli F, et al. ECG-gated multi-detector row spiral CT in the assessment of myocardial infarction: correlation with non-invasive angiographic findings. Eur Radiol. 2006;16:15–24.
27. Sanz J, Weeks D, Nikolaou K, Sirol M, Rius T, Rajagopalan S, et al. Detection of healed myocardial infarction with multidetector-row computed tomography and comparison with cardiac magnetic resonance delayed hyperenhancement. Am J Cardiol. 2006;98:149–55.
28. Henneman MM, Schuijf JD, Dibbets-Schneider P, Stokkel MP, van der Geest RJ, van der Wall EE, Bax JJ. Comparison of multislice computed tomography to gated single-photon emission computed

tomography for imaging of healed myocardial infarcts. Am J Cardiol. 2008;101:144–8.
29. Rubinshtein R, Miller TD, Williamson EE, Kirsch J, Gibbons RJ, Primak AN, et al. Detection of myocardial infarction by dual-source coronary computed tomography angiography using quantitated myocardial scintigraphy as the reference standard. Heart. 2009;95:1419–22.
30. Mohlenkamp S, Lerman LO, Lerman A, Behrenbeck TR, Katusic ZS, Sheedy PF 2nd, Ritman EL. Minimally invasive evaluation of coronary microvascular function by electron beam computed tomography. Circulation. 2000;102:2411–6.
31. Choi KM, Kim RJ, Gubernikoff G, Vargas JD, Parker M, Judd RM. Transmural extent of acute myocardial infarction predicts long-term improvement in contractile function. Circulation. 2001;104:1101–7.
32. Kim RJ, Wu E, Rafael A, Chen EL, Parker MA, Simonetti O, et al. The use of contrast-enhanced magnetic resonance imaging to identify reversible myocardial dysfunction. N Engl J Med. 2000;343:1445–53.
33. Koyama Y, Matsuoka H, Mochizuki T, Higashino H, Kawakami H, Nakata S, et al. Assessment of reperfused acute myocardial infarction with two-phase contrast-enhanced helical CT: prediction of left ventricular function and wall thickness. Radiology. 2005;235:804–11.

Coronary Artery Anomalies

16

Edward D. Nicol and Simon P.G. Padley

Coronary artery anomalies are a common finding on CT coronary angiography. The incidence of congenital coronary artery anomaly traditionally has been quoted as between 0.3% and 1% [1], but the true incidence may well be higher, as conventional angiography identifies only half of the coronary anomalies identified by multidetector CT (MDCT) [2].

Even though coronary artery anomalies are relatively uncommon, it is essential that physicians who perform and report cardiovascular CT are aware of both the significant variations in "normal" coronary anatomy and the clinically important aberrant anatomy found in a small number of individuals. Coronary artery anomalies may occur in isolation, but they are significantly more prevalent in individuals with concomitant congenital heart disease, in whom the "normal" pattern of coronary anatomy also may be different from the pattern in those with morphologically normal hearts. CT coronary angiography has increased our understanding of the incidence and variation in coronary anatomy in both the normal population and those with congenital heart disease [3, 4].

The clinical implications of anomalous coronary artery anatomy are dependant on the exact origin and course of the affected coronary artery and must be put into the context of the age of the individual and the clinical presentation. The finding of an aberrant coronary artery with a so-called malignant course between the aortic root and the right ventricular outflow tract has different implications in a sporty teenager with chest pain on exertion [5] than it has in a sedentary 65-year-old in whom it is an incidental finding in a noncardiac preoperative assessment. Imagers should be aware of normal coronary anatomy variants and true anomalous coronary anatomy and should be conversant in the prognosis associated with the various forms of this common incidental finding.

Terminology and Classification

The terminology used to describe coronary anomalies is not standardized, and until recently no classification was universally applicable. This situation has created significant confusion and has hindered the ability to clearly communicate CT findings between clinicians, including imagers, cardiologists, and cardiothoracic surgeons. Partial classifications do exist for certain isolated coronary anomalies (such as Lipton's classification of isolated single coronary artery patterns [6] and Angelini's proposed descriptive approach to coronary anatomy at angiography [7]), and there are several specific classifications for aberrant anatomy for specific congenital conditions such as transposition of the great arteries (TGA) [8, 9]. However, these classifications are all limited to invasive angiographic series and are applicable only to patients of the cohort studied. More recently, the authors of this chapter have published a universal classification for coronary arteries that allows both a descriptive and alphanumeric classification to be used for all coronary artery anomalies [10]. Although initially designed for use in patients with TGA, it is equally applicable to all forms of aberrant coronary anatomy, with or without associated congenital heart disease.

E.D. Nicol (✉) • S.P.G. Padley
Department of Cardiac CT, Royal Brompton Hospital, Sydney Street, London SW3 6NP, UK
e-mail: cyprusdoc@doctors.org.uk; s.padley@ic.ac.uk

M.J. Budoff et al. (eds.), *Atlas of Cardiovascular Computed Tomography*, https://doi.org/10.1007/978-1-4471-7357-1_16

Description of Coronary Artery Anomalies

The description of anomalous coronary anatomy should start with comment on the sinus from which it arises. The coronary artery distribution may be entirely normal but the coronary ostium may arise above the coronary sinus (Fig. 16.1). Although this finding is usually of little clinical significance, it is anomalous and should be commented upon. Another, more common variant is the finding of separate origins of the left anterior descending and left circumflex arteries, with the absence of a left main stem artery (Fig. 16.2).

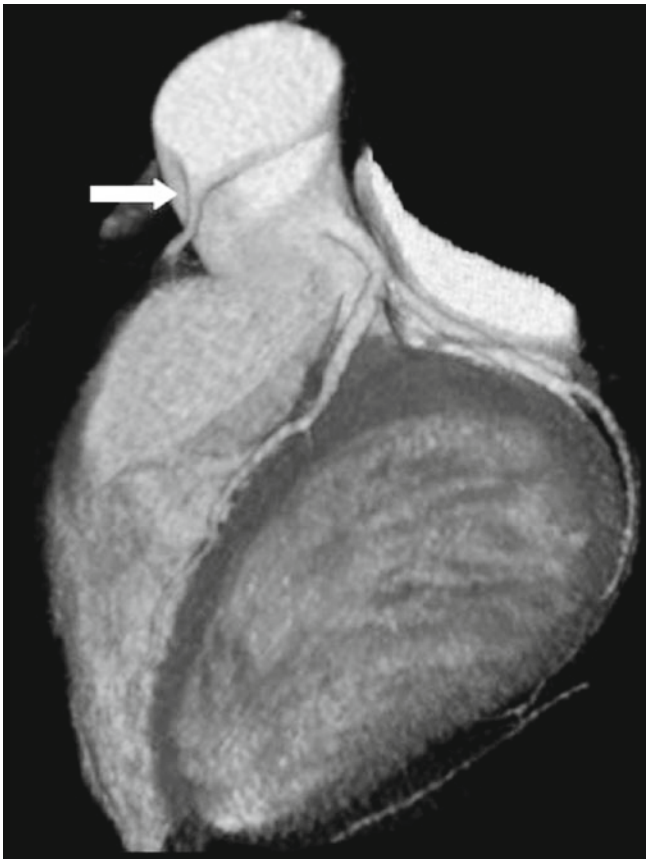

Fig. 16.1 Coronary arteries may arise distinct from the usual sinus of Valsalva. In this image, a right coronary artery arises from above the sinotubular junction (*white arrow*)

The course of aberrant coronary arteries should be described as retro-aortic (passing behind the aorta), prepulmonary (in front of the pulmonary trunk), or interarterial (between the aortic root and right ventricular outflow tract [RVOT]). A retro-aortic course is most commonly seen where the left circumflex artery arises off the right coronary artery (Fig. 16.3a) or right coronary ostium; a prepulmonary course is more commonly seen in those with concomitant congenital heart disease such as tetralogy of Fallot (Fig. 16.3b). The latter is clearly important if cardiothoracic surgery is contemplated, as their course often makes these arteries vulnerable to damage during the sternotomy or surgery involving the RVOT.

Potentially more sinister anatomical variants include the left coronary artery arising from the right coronary sinus, or the right coronary artery arising from the left coronary sinus. The key aspects to consider when assessing the prognostic implications of this type of abnormality are the angle of takeoff of the coronary artery (Fig. 16.4a), the shape of the coronary ostium and its proximal course (circular, oval, tear-drop or slitlike) (Fig. 16.4b, c), whether the artery is potentially intramural (i.e., its proximal course runs within the wall of the aortic root), and the course of the artery. Whether CT can accurately determine an intramural course is debatable. If the coronary artery follows an interarterial course, it is important also to consider the dominance of the coronary anatomy and the extent to which the myocardium may be affected by systolic compression of the intramural vessel (Fig. 16.4d, e). As previously stated, the patient's age and the clinical context are critical, especially when recommending subsequent management.

If aberrant coronary artery anatomy is identified, it may be prudent to describe the aortic and pulmonary artery relationship as well [10]. It is also important to scrutinize the scan for other congenital defects.

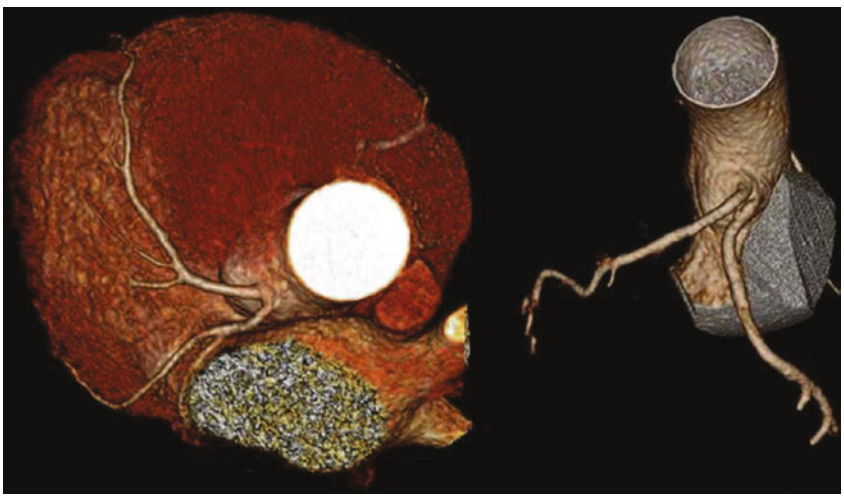

Fig. 16.2 Volume-rendered images of separate origins of the left anterior descending and left circumflex arteries. This finding on CT coronary angiography is often benign, with no clinical significance

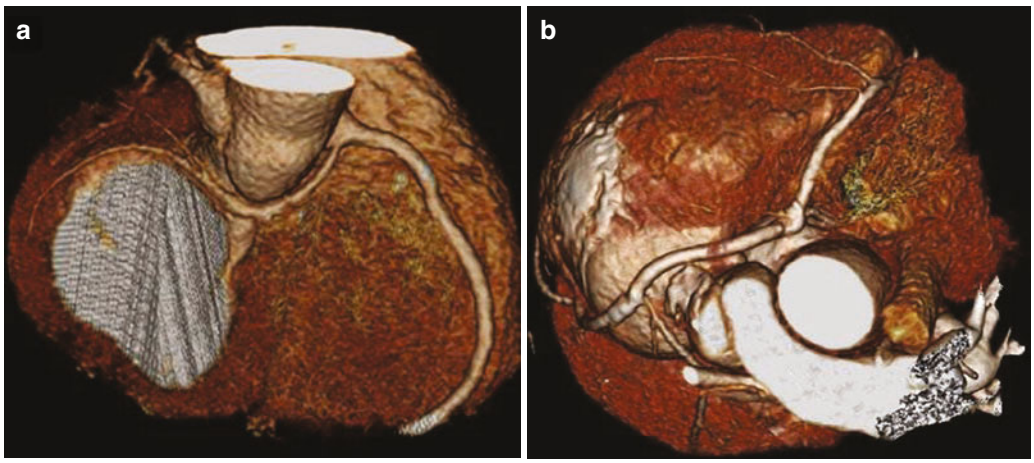

Fig. 16.3 Volume-rendered images of "benign" anomalous coronary variants. These may arise from any coronary sinus and course via a retro-aortic route, as shown by the aberrant left circumflex artery arising from the right coronary artery in a posterior view (**a**), or they may follow a pre-pulmonary course, as with the left anterior descending artery shown in a view from above in a patient with tetralogy of Fallot (**b**)

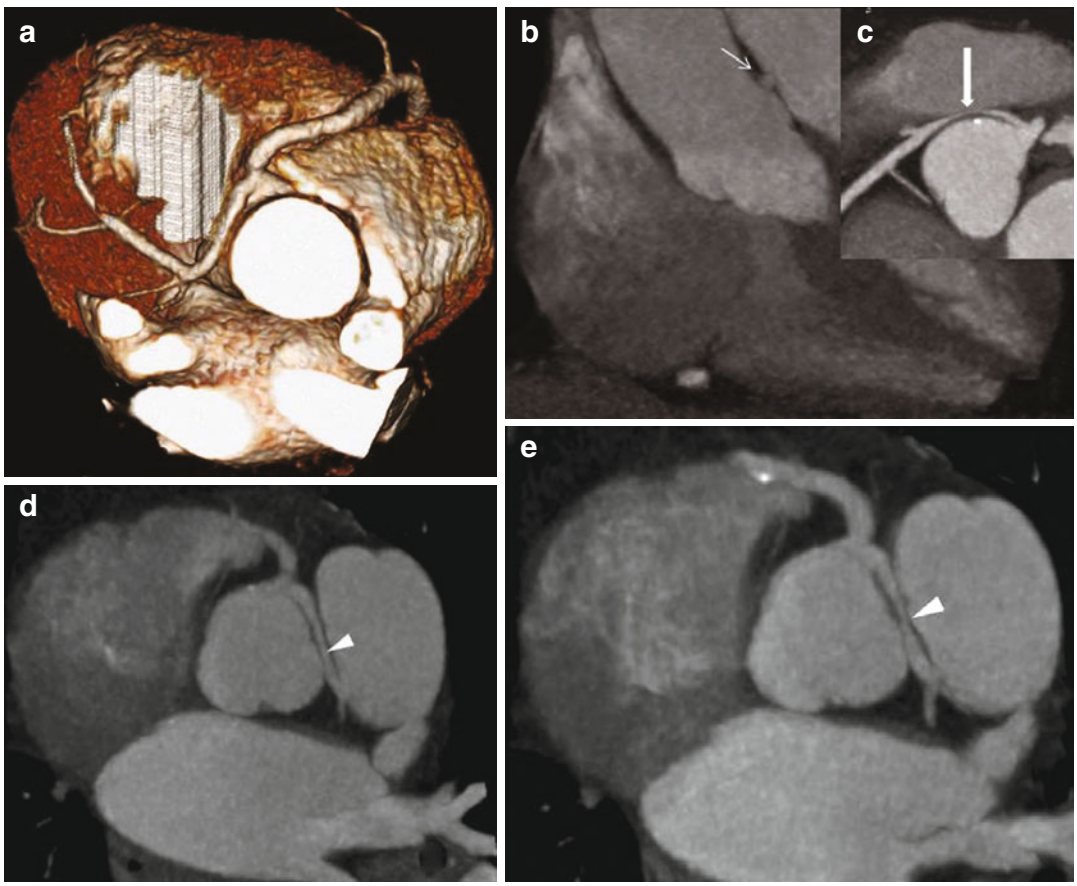

Fig. 16.4 Coronary arteries that course between the aortic root and right ventricular outflow tract (RVOT) are found with an increased prevalence in people who suffer a sudden cardiac death, particularly between the ages of 10 and 30 years. They are also found incidentally in older patients being investigated for atheromatous coronary artery disease. It is important to describe the acute angle of take-off from the coronary sinus (**a**) and the shape of both the coronary ostia and proximal course, which may be relatively circular (*thin white arrow*) (**b**) or slitlike (*thick white arrow*) (**c**). It is also important to assess any evidence of compression (*white arrowheads*) between diastole (**d**) and systole (**e**), as this compression may be a cause of ischemic chest pain and may guide management towards surgical reimplantation

Prognosis of Anomalous Coronary Anatomy

The course of an anomalous coronary artery will determine prognostic significance. Retro-aortic and pre-pulmonary courses confer a better prognostic outcome than "malignant" or "potentially lethal" interarterial variants. This evidence comes from autopsy studies of young people who have suffered a sudden cardiac death [11]. This "malignant" coronary anatomy is over-represented in younger patients in autopsy series of sudden cardiac death, but increased risk does not necessarily also apply to a more elderly population, in whom it may be an incidental finding in those being investigated for atheromatous coronary artery disease.

Various mechanisms have been suggested by which an interarterial course may confer a worse prognosis than other variants:

- Systolic compression or kinking of the vessel by the RVOT and aorta during systole
- Reduced coronary blood flow (especially in situations of high oxygen demand) resulting from the acute take-off of affected vessels, or slitlike orifices or proximal course
- Increased coronary artery wall tension (especially on exertion) if the vessel is intramural

Increased adverse outcomes may result from one or more of these factors, but in reality the course per se is unlikely to be the sole explanation [12].

Single Coronary Artery

Single coronary arteries are rare abnormalities and may arise from any sinus of Valsalva (Figs. 16.5 and 16.6). These arteries often defy simple classification and may be complex, with multiple branches supplying the myocardium substituting for the three usual main epicardial arteries [13] (Fig. 16.7).

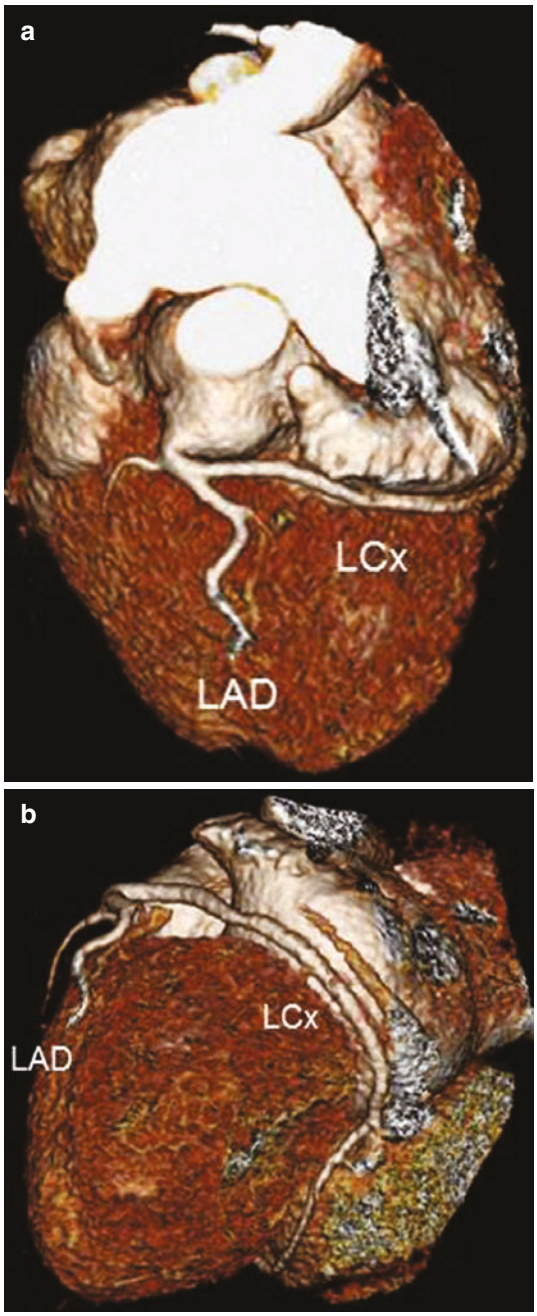

Fig. 16.5 A single coronary artery in a patient with coexisting transposition of the great arteries, a patent ductus arteriosus (PDA), and a coarctation. (**a**) The single coronary artery trifurcates into a left anterior descending artery (LAD), left circumflex (LCx), and a small right ventricular free wall branch. The LAD follows a normal course. (**b**) The LCx follows its usual course, giving off a distal, obtuse marginal branch. (**c**) It then crosses the crux (*white arrowhead*). (**d**) It continues into the anterior atrioventricular groove (*white arrow*), supplying the usual right coronary artery territory

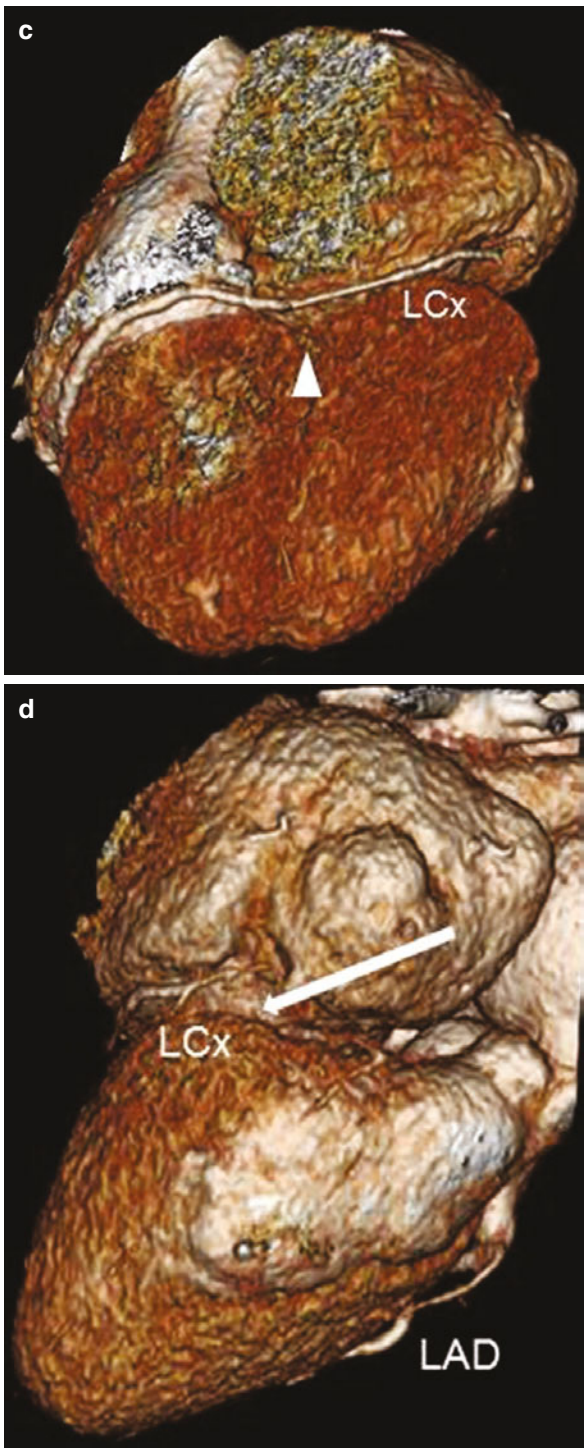

Fig. 16.5 (continued)

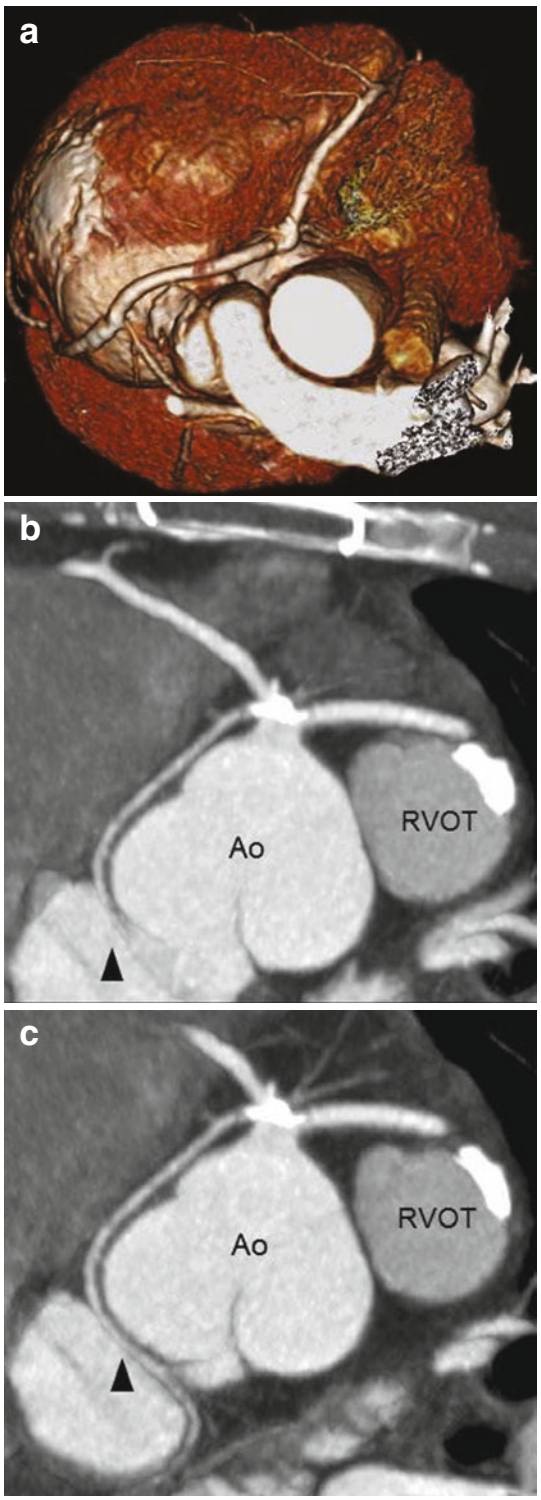

Fig. 16.6 A single coronary artery arising from an anterior coronary sinus in a patient with tetralogy of Fallot. The vessel trifurcates into a left anterior descending (LAD), left circumflex (LCx), and right coronary artery (RCA). (**a**) The LAD follows a pre-pulmonary course, whilst the RCA follows a traditional course. (**b**) The LCx can be seen to course around the right side of the aorta (Ao) (*arrowhead*). (**c**) It then follows a retro-aortic root to the left atrioventricular (AV) groove (*arrowhead*). RVOT right ventricular outflow tract

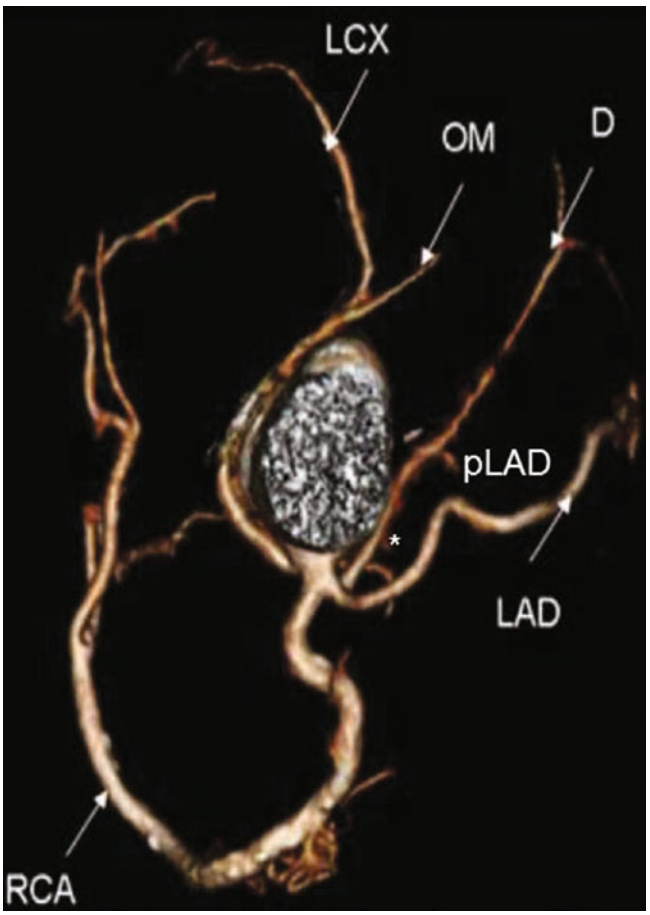

Fig. 16.7 A single coronary sinus arising from the right coronary cusp. The single coronary artery divides into four separate branches: a left anterior descending artery (LAD) that supplies the distal LAD territory, a right coronary artery (RCA), a left circumflex artery (LCX) and a cristal artery (*asterisk*), which supplies the proximal LAD (pLAD) territory and a diagonal vessel (D)

Left Main Coronary Artery Atresia

Left main coronary artery atresia (LMCA) may mimic a true single coronary artery, but in LMCA there is a tiny left main artery that may not be visualized on conventional x-ray angiography. Post mortem findings describe a small, "string-like" left main coronary artery [14]. In our experience, the left main artery is not necessarily absent; when visualized with MDCT, it often appears hypoplastic and "string-like" [3] (Fig. 16.8). As a general rule, if the flow is entirely anterograde in the LAD, then a single coronary artery is more likely, but if the proximal LAD flow is retrograde (apical to basal), then LMCA should be considered the more likely diagnosis.

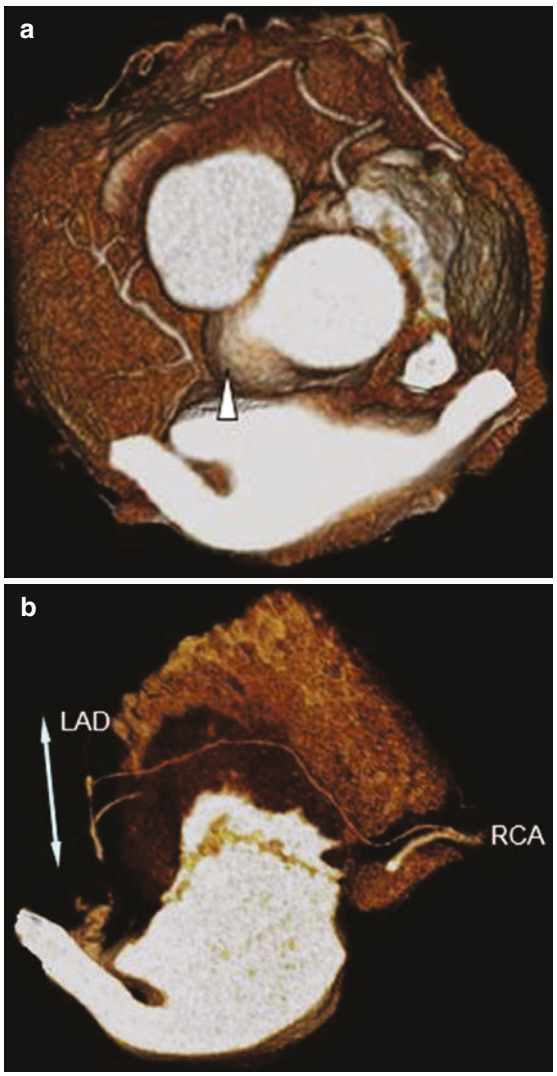

Fig. 16.8 Two cases of left main coronary artery atresia (LMCA). In both cases, a small, "string-like" left main stem (LMS) is visible (**a**, **c**, **d**, *arrowheads*). (**a**, **b**) The first case demonstrates an intraseptal collateral vessel arising from the mid right coronary artery (RCA) supplying the LAD territory. (**c**, **d**) In the second case, a bridging artery arises from the right coronary cusp and shows evidence of calcification (*asterisk*). The distinction from a single coronary artery can be made via the string-like LMS (if visible) and the bi-directional flow in the LAD

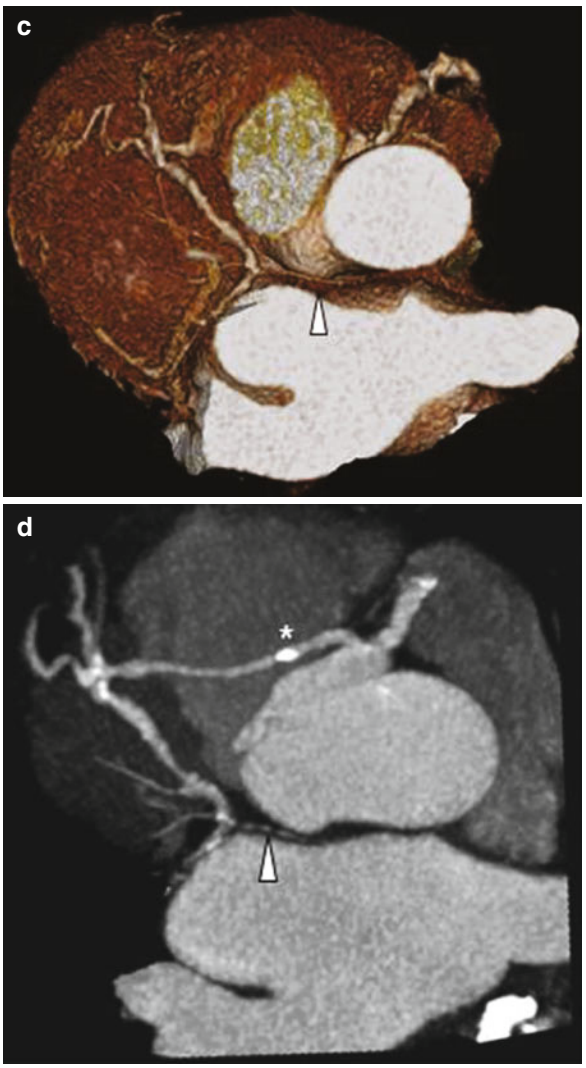

Fig. 16.8 (continued)

Other Acquired and Congenital Coronary Anomalies

Arterial duplication is occasionally seen on routine CT coronary angiography and is usually of little clinical consequence, unless the patient has myocardial ischemia and the offending artery arises in an anomalous position. The LAD and RCA are the most commonly affected vessels (Fig. 16.9), and this finding is often associated with other congenital malformations. Other rare forms of acquired and congenital coronary artery anomalies include Kawasaki disease and anomalous left coronary artery arising from the pulmonary artery (ALCAPA).

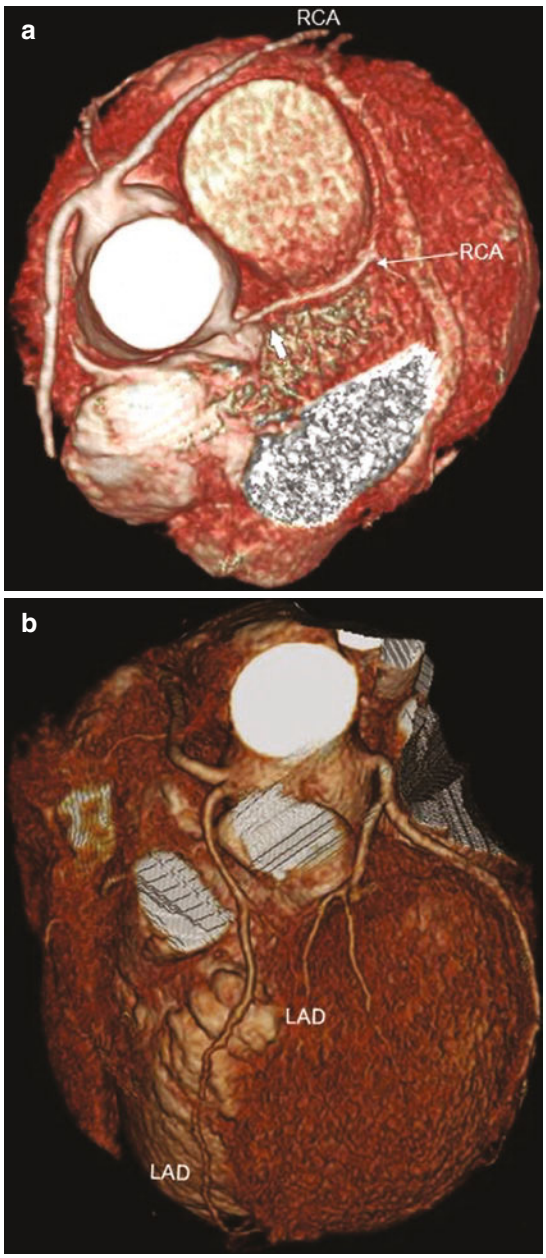

Fig. 16.9 Arterial duplication is sometimes seen, especially in patients with congenital heart disease. (**a**) Right coronary artery (RCA) duplication in a patient with transposition of the great arteries (TGA). (**b**) Duplication of the LAD in a patient with an RVOT conduit. Arterial duplication is usually an incidental finding of little clinical consequence

Kawasaki Disease

Kawasaki disease (also known as mucocutaneous lymph node syndrome) affects 0.1–0.3/1000 individuals. It is usually diagnosed in children under the age of 5 years and has a slight male predominance. Coronary artery aneurysms affect up to a quarter of individuals, and CT coronary angiography can identify site, size, calcification, and thrombus within the affected vessels (Fig. 16.10). Routine screening with CT coronary angiography is now feasible with low-dose protocols.

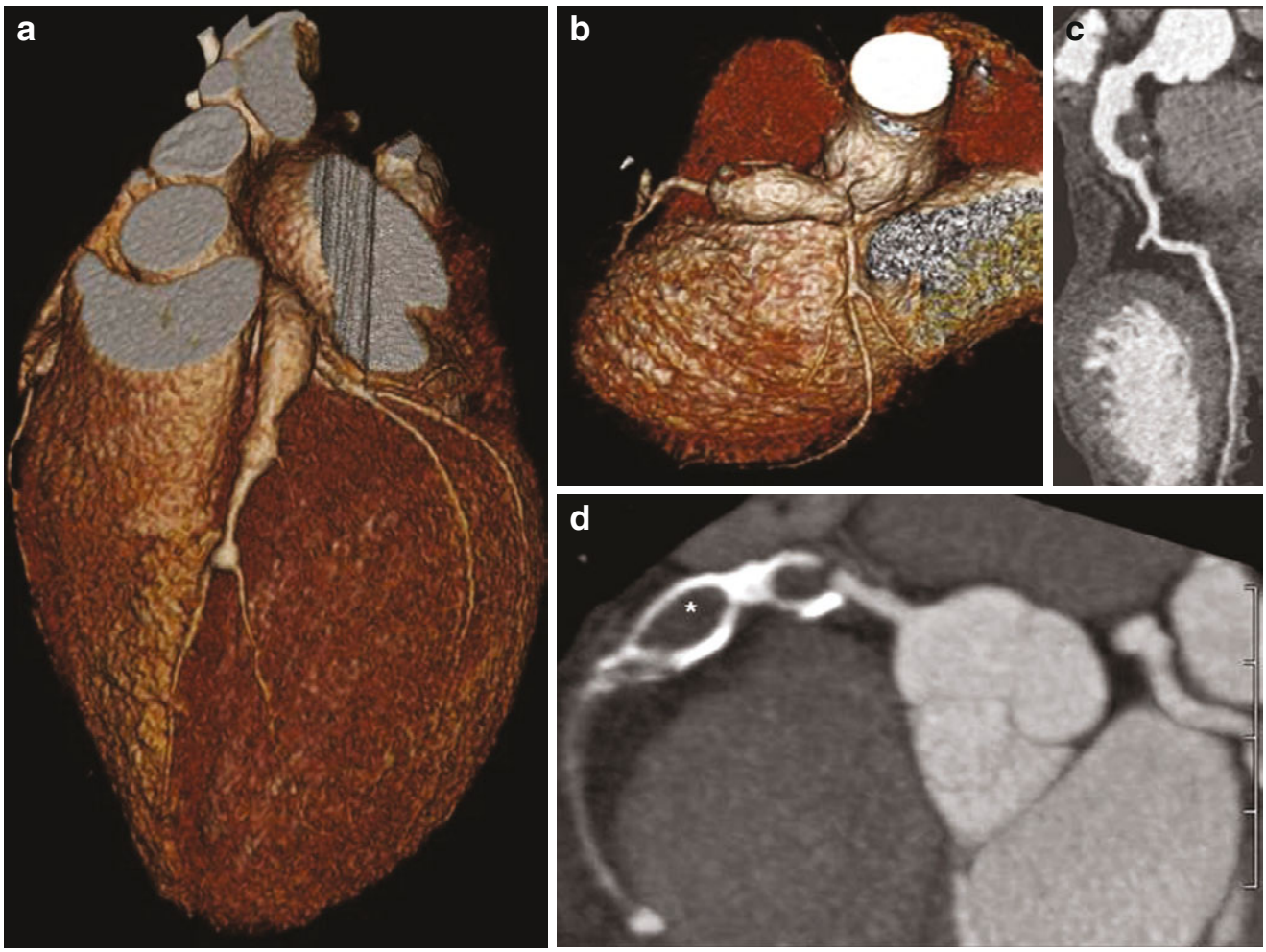

Fig. 16.10 Kawasaki disease in a teenager. Low-dose CT coronary angiography allows delineation of the entire coronary tree, often at doses less than 1 mSv. Classic aneurysms are clearly seen on the volume-rendered images (**a**, **b**), whilst mural calcification and mural thrombus can be clearly visualized and followed up on multiplanar images (**c**). Over time, large aneurysms may completely occlude (*asterisk*) (**d**)

Anomalous Left Coronary Artery from Pulmonary Artery

Anomalous left coronary artery from pulmonary artery (ALCAPA) is a very rare coronary artery anomaly affecting three individuals per million. It usually presents in the first few months of life, but rarely may present in adulthood. CT coronary angiography may provide the first diagnosis in these late presentations and can also be used in the postoperative follow-up (Fig. 16.11).

Incidental Coronary Anomalies

Other common incidental findings that may be detected when performing CT coronary angiography include aneurysmal dilatation of the coronary arteries, myocardial bridging, and coronary artery fistulae.

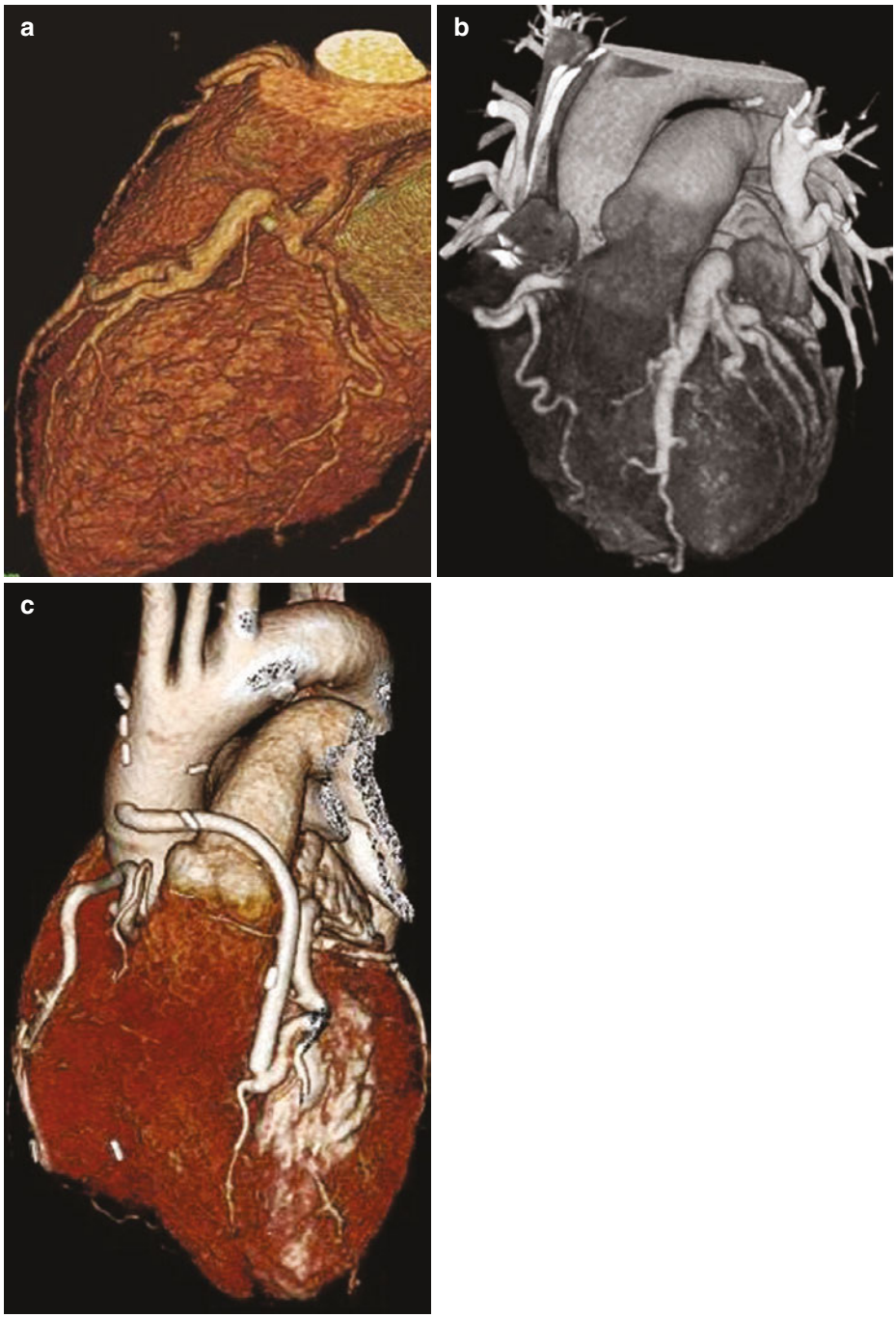

Fig. 16.11 Anomalous left coronary artery from pulmonary artery (ALCAPA) is a rare diagnosis in adulthood. (**a**) The left main coronary artery can be seen arising from the main pulmonary artery before bifurcating into the left anterior descending artery (LAD) and left circumflex artery (LCx) in their usual positions. (**b**) The right coronary artery is a large vessel in the usual position. (**c**) This patient subsequently had surgery, with ligation of the LMS and a saphenous vein graft to the LAD, providing anterograde and retrograde flow to both the LAD and LCx

Coronary Artery Dilatation

In addition to patients with Kawasaki disease, coronary artery dilatation (Fig. 16.12) also may be found as a consequence of congenital disease, in association with atheromatous disease, or as a result of degenerative, inflammatory, infectious, toxic, or traumatic causes [15]. It is thought to have a good prognosis in most cases [16].

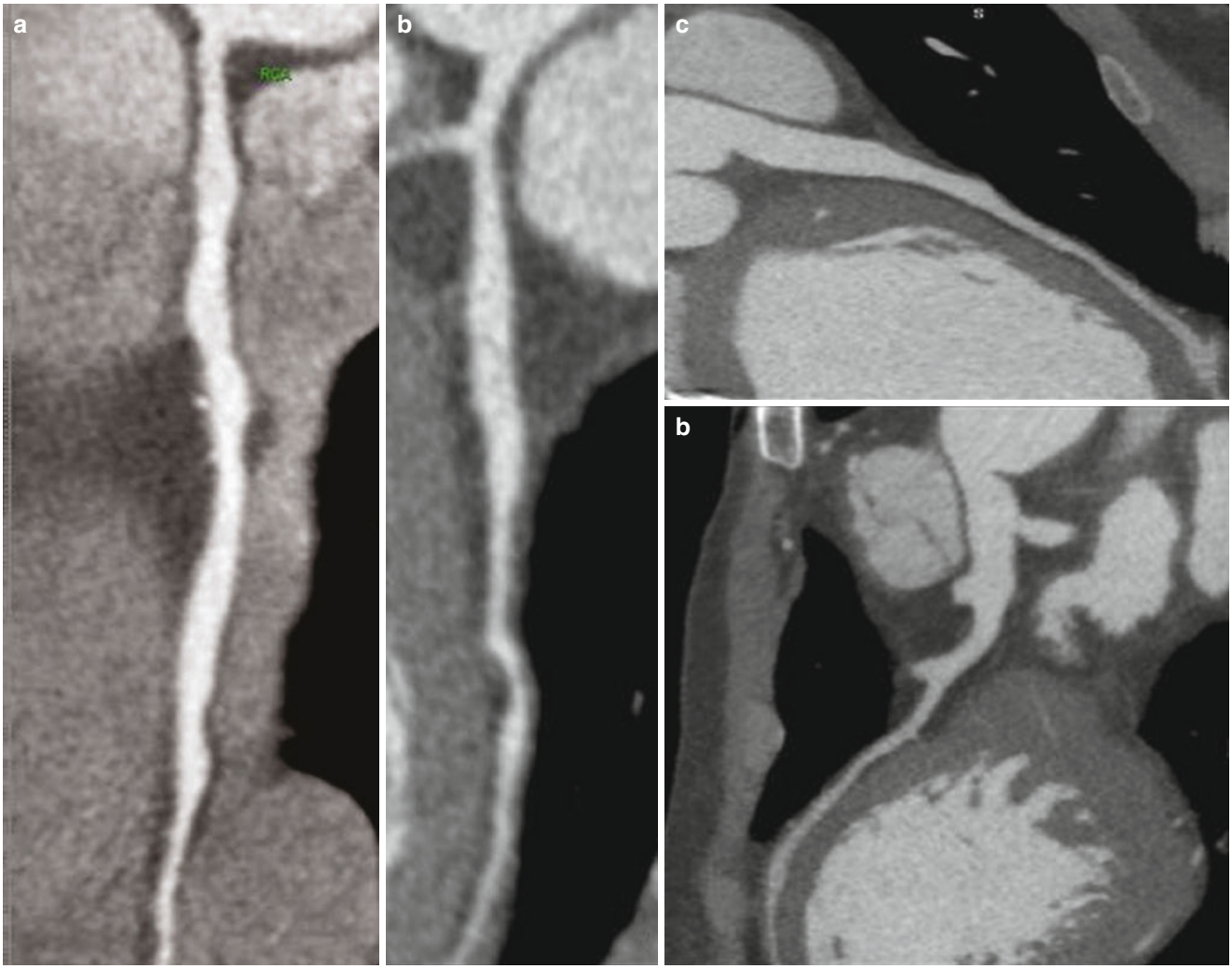

Fig. 16.12 A case of aneurysmal dilatation of the coronary arteries in an adult, secondary to probable atheromatous disease (**a**, **b**) and a viral etiology (**c, d**). It is important to consider late presentation of Kawasaki disease (Fig. 16.10) in these cases

Myocardial Bridges

Myocardial bridges (Fig. 16.13) are an extremely common finding on CT coronary angiography; some autopsy data suggest an incidence of about 50%. Assessment by cardiac CT should include a description of the vessel affected, the length and depth of the bridge, and, if possible, a description of any compression between diastole and systole. The functional significance of myocardial bridges is uncertain, but it seems likely that the vast majority are incidental findings and do not correlate with symptoms of chest pain [17].

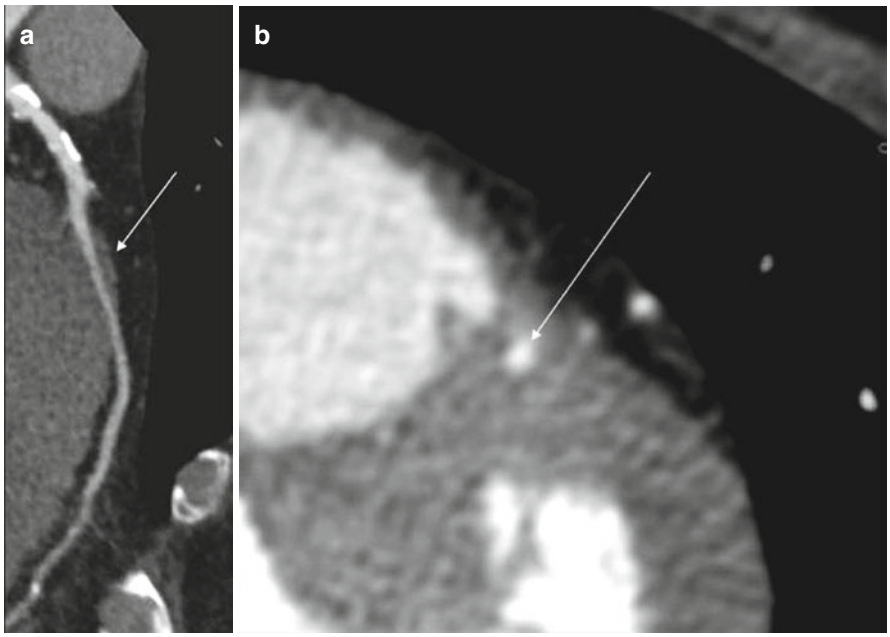

Fig. 16.13 (**a**) Myocardial bridging is an extremely common finding and often affects the proximal left anterior descending artery (LAD). The proximal LAD takes an intramyocardial course (*arrow*) before running epicardially in the more mid and distal LAD. (**b**) The vessel can be seen to be entirely surrounded by myocardium (*arrow*), but there is little evidence to support the notion that myocardial ischemia may result from these common coronary artery anomalies

Coronary Artery Fistulae

Coronary artery fistulae (Fig. 16.14) are occasional findings on CT coronary angiography. Most commonly, there is a small connection between the affected artery and a cardiac chamber, cardiac vein, or pulmonary artery. Coronary dilatation only occurs with larger fistulae, as a result of abnormal flow between a high-pressure arterial system and a lower-pressure system; this flow may cause a "steal" syndrome with myocardial ischemia and dysfunction. CT coronary angiography may be useful for delineating the anatomy of fistulae and guiding subsequent intervention [18].

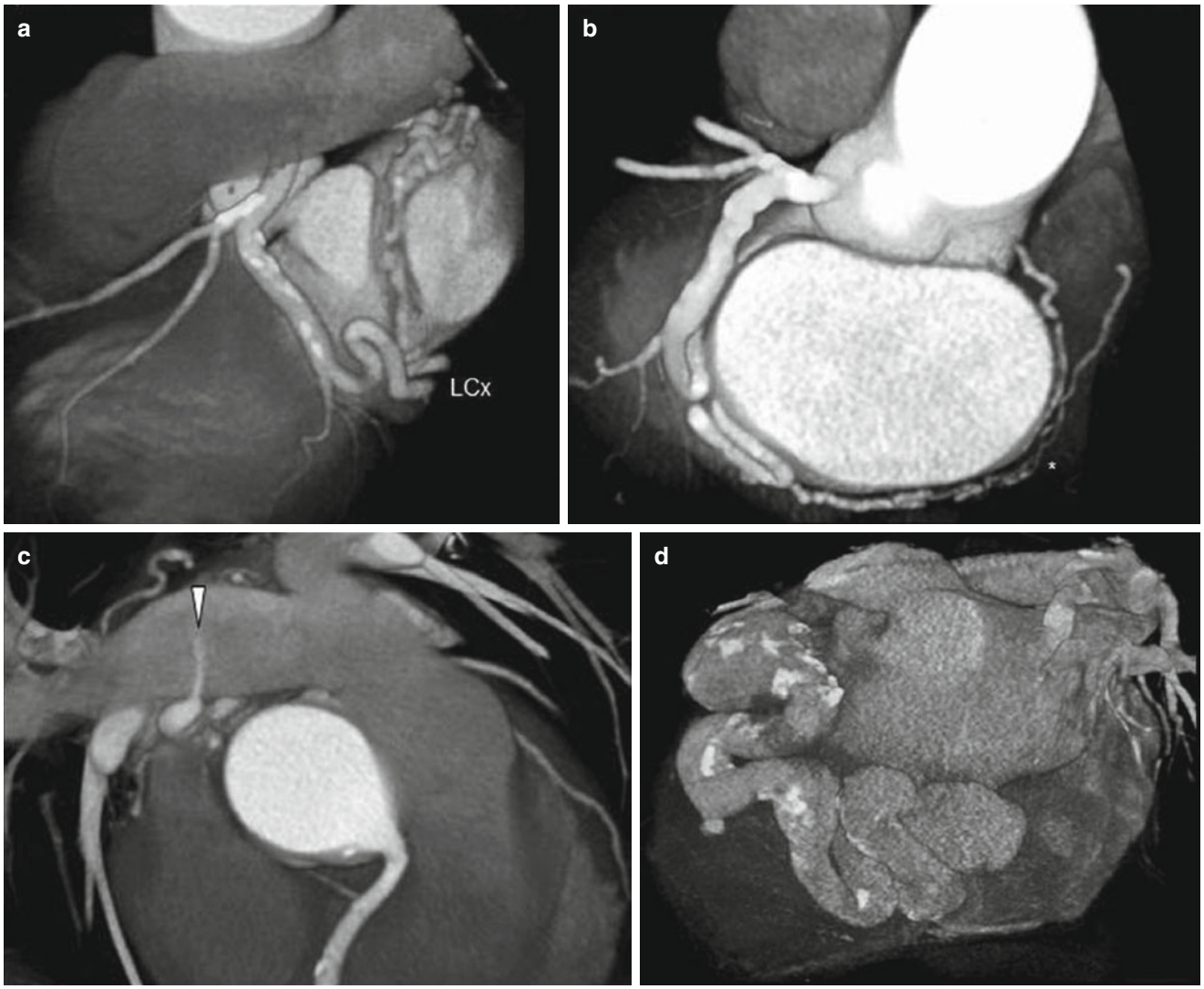

Fig. 16.14 Coronary artery fistulae may occur between the coronary arteries and cardiac chambers or, less commonly, between coronary arteries and the pulmonary artery or cardiac veins. (**a–c**) The course of a dilated left circumflex artery (LCx) is seen, with a leash of smaller branches (**b**, *asterisk*). The flash of contrast from the LCx into the less-attenuated pulmonary artery (**c**, *arrowhead*) confirms the communication. (**d**) Coronary arteries may become massively dilated when fistulous, as demonstrated in this case of an LCx-to-coronary-sinus fistula

References

1. Kim SY, Seo JB, Do KH, Heo JN, Lee JS, Song JW, et al. Coronary artery anomalies: classification and ECG-gated multi-detector row CT findings with angiographic correlation. Radiographics. 2006;26:317–33. discussion 333–4
2. Shi H, Aschoff AJ, Brambs HJ, Hoffmann MH. Multislice CT imaging of anomalous coronary arteries. Eur Radiol. 2004;14:2172–81.
3. Nicol ED, Lyne J, Rubens MB, Padley SPG, Yen HS. Left main coronary atresia: a more commonly identified condition after the advent of 64-slice CT coronary angiography? J Nucl Cardiol. 2007; 14:715–8.
4. Nicol E, Gatzoulis M, Padley SP, Rubens MB. Assessment of adult congenital heart disease with 64-MDCT – beyond coronary lumenography. Clin Radiol. 2007;62:518–27.
5. Banerjee D, Sriharan M, Nicol ED. Malignant anomalous left coronary artery associated with acute coronary syndrome and subsequent postoperative secondary stenosis of the reimplanted anomalous left coronary artery. Cardiol Young. 2013;23:149–53.
6. Lipton MJ, Barry WH, Obrez I, Silverman JF, Wexler L. Isolated single coronary artery: diagnosis, angiographic classification, and clinical significance. Radiology. 1979;130:39–47.
7. Angelini P, de la Cruz MV, Valencia AM, Sanchez-Gomez C, Kearney DL, Sadowinski S, et al. Coronary arteries in transposition of the great arteries. Am J Cardiol. 1994;74:1037–41.
8. Gittenberger-de Groot AC, Sauer U, Oppenheimer-Dekker A, Quaegebeur JM. Coronary arterial anatomy in transposition of the great arteries: a morphologic study. Pediatr Cardiol. 1983;4(Suppl 1): 15–23.
9. Quaegebeur JM, Rohmer J, Ottenkamp J, Buis T, Kirklin JW, Blackstone EH, et al. The arterial switch operation. An eight-year experience. J Thorac Cardiovasc Surg. 1986;92: 361–84.
10. Sithamparanathan S, Padley SP, Rubens MB, Gatzoulis MA, Yen Ho S, Nicol ED. A new universal sequential classification for great vessel and coronary artery anatomy in transposition and other coronary anomalies. JACC Cardiovasc Imaging. 2013;6:624–30.
11. Eckart RE, Scoville SL, Campbell CL, Shry EA, Stajduhar KC, Potter RN, et al. Sudden death in young adults: a 25-year review of autopsies in military recruits. Ann Intern Med. 2004;141:829–34.
12. Stirrup J. Anomalous coronary arteries: “benign” and “malignant” courses. In: Nicol E, Stirrup J, Kelion A, Padley S, editors. Cardiovascular computed tomography. Oxford: Oxford University Press; 2011. p. 338–40.
13. Lam HY, Lazoura O, Sriharan M, Padley S. Single coronary artery from the right sinus of valsalva: an unusual variant of a rare condition. Eur Heart J Cardiovasc Imaging. 2013;14:190–1.
14. Goormaghtigh N, De Vos L, Blanquaert A. Ostial stenosis of coronary arteries in nine-year-old girl. AMA Arch Intern Med. 1955;95:341–8.
15. Díaz-Zamudio M, Bacilio-Pérez U, Herrera-Zarza MC, Meave-González A, Alexanderson-Rosas E, Zambrana-Balta GF, Kimura-Hayama ET. Coronary artery aneurysms and ectasia: role of coronary CT angiography. Radiographics. 2009;29:1939–54.
16. Demopoulos VP, Olympios CD, Fakiolas CN, Economides NM, Adamopoulou E, Foussas SG, Cokkinos DV. The natural history of aneurysmal coronary artery disease. Heart. 1997;78:136–41.
17. Stirrup J. Myocardial bridging. In: Nicol E, Stirrup J, Kelion A, Padley S, editors. Cardiovascular computed tomography. Oxford: Oxford University Press; 2011. p. 431.
18. Zenooz NA, Habibi R, Mammen L, Finn JP, Gilkeson RC. Coronary artery fistulas: CT findings. Radiographics. 2009;29:781–9.

Congenital Heart Disease

17

Priya Pillutla and Jamil A. Aboulhosn

Congenital heart disease (CHD) represents a heterogeneous group of disorders characterized by cardiovascular anomalies that are present from birth. These abnormalities vary from simple isolated lesions such as an isolated bicuspid aortic valve to complex syndromes characterized by multiple cardiovascular abnormalities, such as Noonan's syndrome. The clinician treating patients with CHD takes on a daunting task because they must fully understand not only the anatomy and hemodynamics of the "normal" cardiovascular system but also the perturbations present in patients with a wide mix of unoperated and post-operative congenital cardiovascular defects. Added is the burden of calculating the effects of acquired diseases that develop in a growing, aging CHD population.

Cross-sectional diagnostic imaging modalities such as MRI and CT allow for excellent visualization of intracardiac and extracardiac anatomy and complement the traditional diagnostic tools such as echocardiography and cardiac catheterization. Advances in technology have improved temporal and spatial resolution and now enable CT to be used as an accurate noninvasive clinical instrument that is fast replacing invasive cineangiography in the evaluation of CHD. In fact, CT imaging has become a routinely used tool when detailed morphologic assessment of complex anatomy is required. The strength of CT rests in the capacity of ECG-gated multidetector scanners to provide submillimeter angiographic images of stunning clarity. Moreover, cardiac CT may be utilized when MRI is contraindicated, such as in patients who are pacemaker-dependent. CT is also less prone to artifacts from metallic stents or devices, which are widely utilized in patients with both operated and unoperated CHD. The high negative predictive value of cardiac CT in the evaluation of coronary artery disease has made it an ideal screening tool before cardiac surgery in the adult CHD patient.

This chapter focuses on the use of CT angiography in patients with CHD and the complementary role that it plays in the management of this complex subset of patients (Figs. 17.1–17.29).

P. Pillutla
Division of Cardiology,
Department of Medicine, Los Angeles Medical Center,
Harbor-University of California, Torrance, CA, USA
e-mail: ppillutla@labiomed.org

J.A. Aboulhosn (✉)
Ronald Reagan/UCLA Medical Center,
Ahmanson Adult Congenital Heart Disease Center,
100 Medical Plaza Drive, Suite 770, Los Angeles, CA 90095, USA
e-mail: jaboulhosn@mednet.ucla.edu

M.J. Budoff et al. (eds.), *Atlas of Cardiovascular Computed Tomography*, https://doi.org/10.1007/978-1-4471-7357-1_17

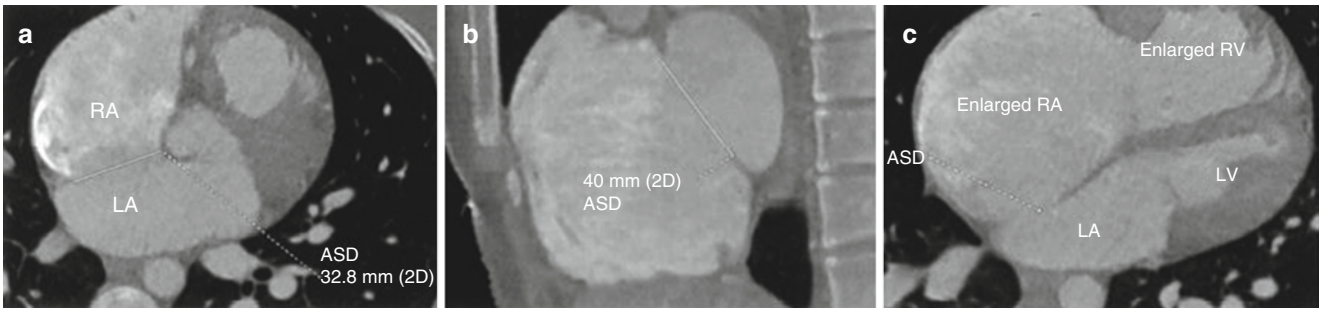

Fig. 17.1 Contrast-enhanced electron beam computed tomography (EBCT) study in an adult with an unrepaired secundum atrial septal defect (ASD) [1]. (**a**) Axial cut at the level of the maximum horizontal diameter of the ASD, which measures 33 mm; note the dilated right atrium (RA). (**b**) Sagittal cut at the level of the maximum vertical diameter of the ASD, measuring 40 mm; note the severely dilated RA. Evaluation of maximum ASD diameter in multiple planes is imperative to the proper selection of patients for percutaneous versus surgical defect closure. In this case, the patient was referred for surgical closure because the vertical diameter exceeded the maximum percutaneous device size available (38 mm). (**c**) Note the enlarged RA and right ventricle (RV), compared with the normal size of the left atrium (LA) and left ventricle (LV)

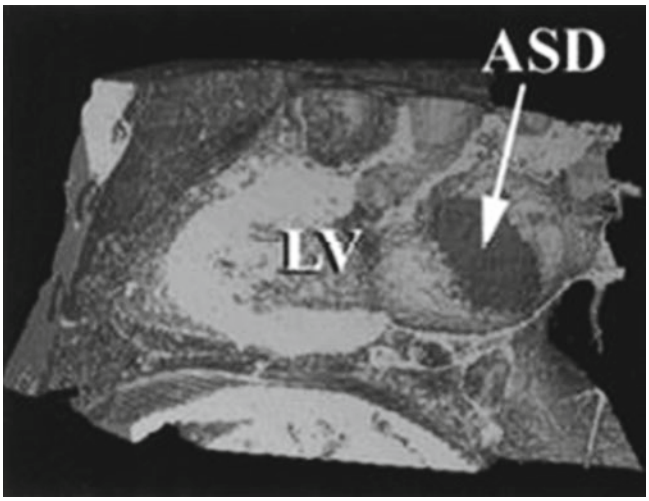

Fig. 17.2 Contrast-enhanced electron beam computed tomography (EBCT) study with three-dimensional surface rendering in a 32-year-old woman with a secundum atrial septal defect (ASD). The heart is viewed from a posterolateral and cranial projection. The posterior wall of the left atrium has been excised, as has the free wall of the left ventricle (LV). The three-dimensional geometry of this septal defect is well visualized. The defect measured 32 mm in greatest diameter. The rims are deficient in the anterosuperior (retroaortic) and posteroinferior quadrants, but are present and sufficient in all other quadrants. A 34-mm Amplatzer septal occluder (St. Jude Medical; St. Paul, MN) was used to successfully occlude this ASD

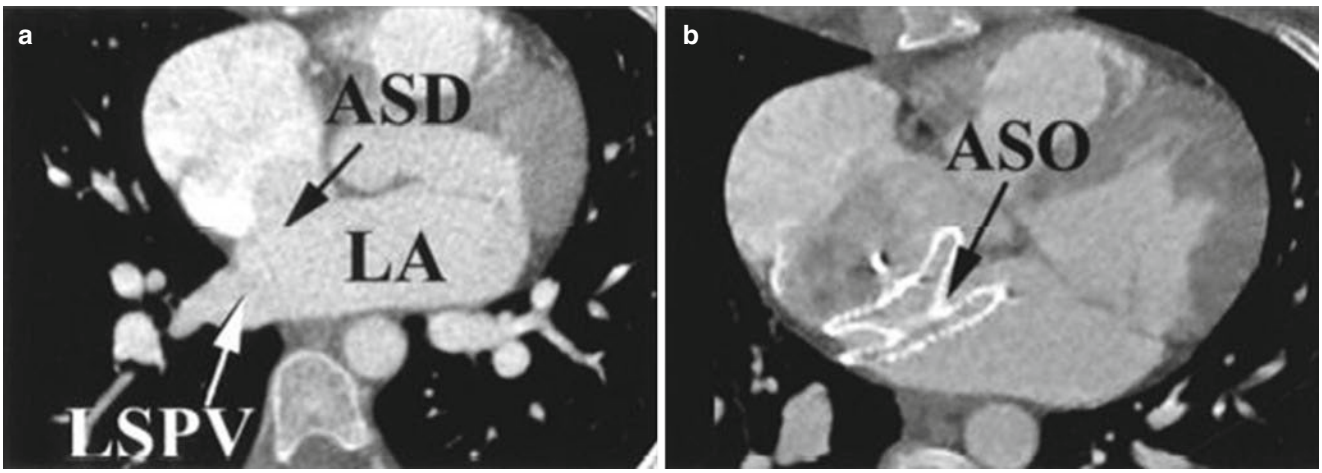

Fig. 17.3 Contrast-enhanced electron beam computed tomography (EBCT) study axial slices in a 33-year-old woman with a secundum atrial septal defect (ASD) [2]. (**a**) Prior to closure, the left superior pulmonary vein (LSPV) drains normally to the left atrium (LA). The ASD measures 34 mm in greatest horizontal diameter. (**b**) Following closure with a 38-mm Amplatzer septal occluder (ASO), the device remained in a stable position despite the virtual absence of a posterior rim

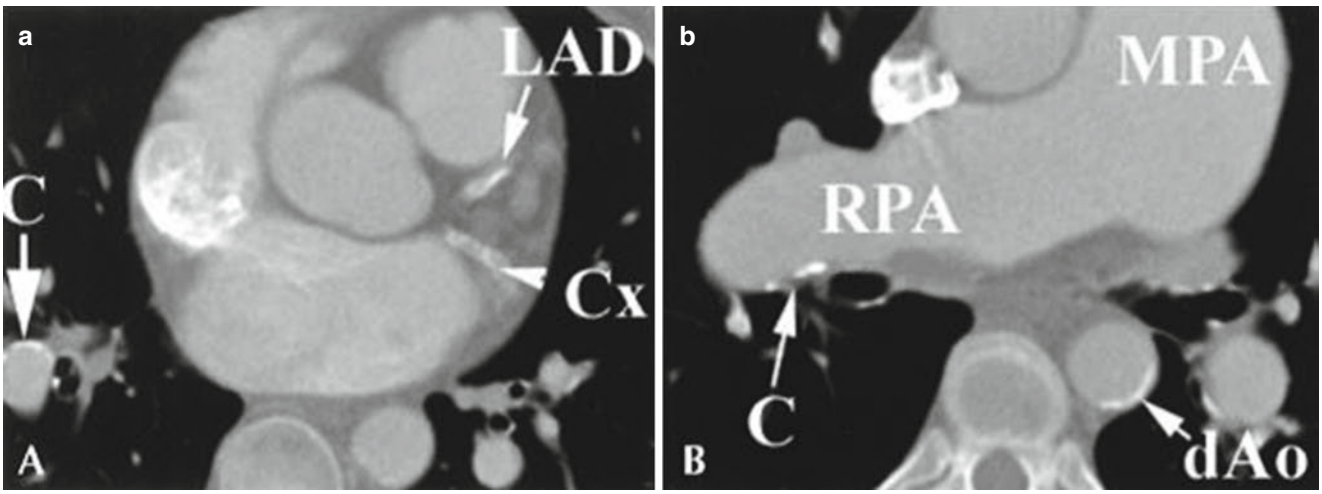

Fig. 17.4 A 16-slice CT angiogram in a 57-year-old woman with cyanosis, severe pulmonary hypertension, and an atrial septal defect. This patient had a strong family history of coronary artery disease (two brothers and her father had myocardial infarction in the third decade). (**a**) Axial slice at the level of the left coronary artery bifurcation demonstrates abundant calcium deposition in the proximal left anterior descending (LAD) and circumflex (Cx) arteries. Note the presence of calcium deposits (C) within a segmental branch of the right pulmonary artery. Pulmonary arterial calcification and atherosclerotic plaquing are present in patients with longstanding pulmonary hypertension [3]. (**b**) Axial slice at the level of a dilated main pulmonary artery (MPA) and right pulmonary artery (RPA). Note the calcium deposits within the wall of the RPA and in the descending aorta (dAo)

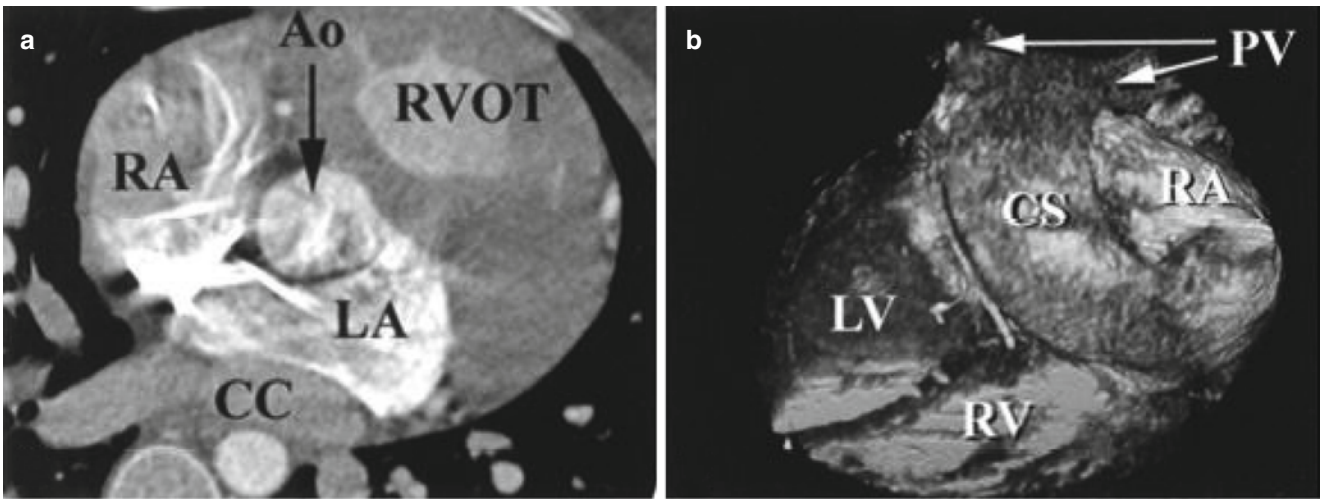

Fig. 17.5 A 64-slice CT angiogram in a 28-year-old cyanotic man with uncorrected total anomalous pulmonary venous connection (TAPVC) to the coronary sinus. (**a**) Axial cut demonstrating anomalous pulmonary venous drainage into a posterior confluence chamber (CC) that does not communicate with the left atrium (LA) or right atrium (RA). A secundum atrial septal defect (ASD) is present and allows flow to the LA. (**b**) Three-dimensional volume rendering as viewed from a posterior and caudal projection. Note the connection of the pulmonary veins (PV) to a severely dilated coronary sinus (CS), which drains into the right atrium (RA). Note the severely dilated right ventricle (RV), in contrast to the comparatively normal left ventricle (LV). Ao—ascending aorta; *RVOT*—right ventricular outflow tract

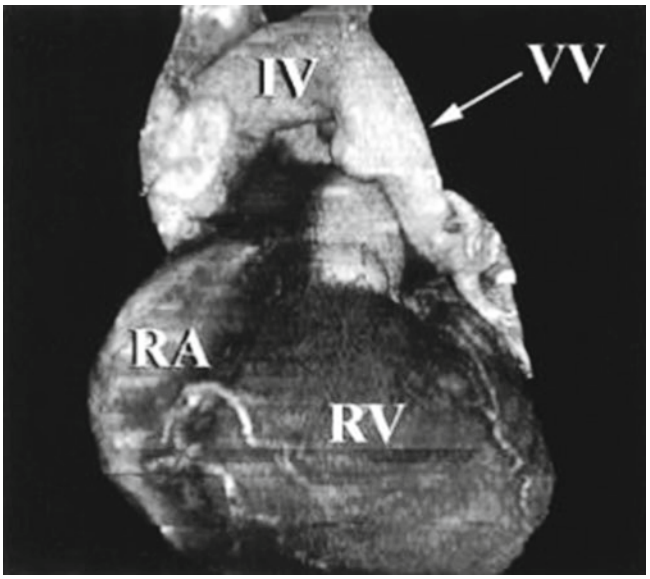

Fig. 17.6 Electron beam angiogram with three-dimensional volume rendering of a 48-year-old cyanotic woman with total anomalous pulmonary venous connection via a vertical vein (VV) to the innominate vein (IV). Note the severely dilated right atrium (RA) and right ventricle (RV)

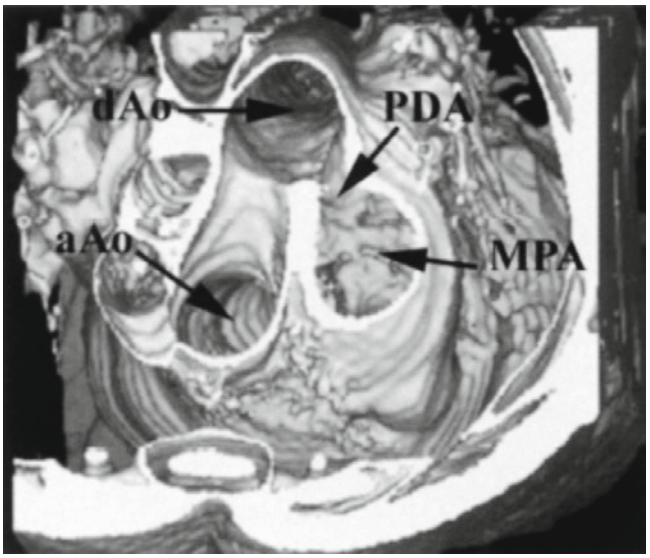

Fig. 17.8 Electron beam angiogram with three-dimensional surface rendering in a cyanotic adult with an unrepaired large patent ductus arteriosus (PDA) as viewed from a cranial projection. Note the dilated main pulmonary artery (MPA). The PDA connects the MPA to the proximal descending thoracic aorta (dAo). *aAo*—ascending aorta

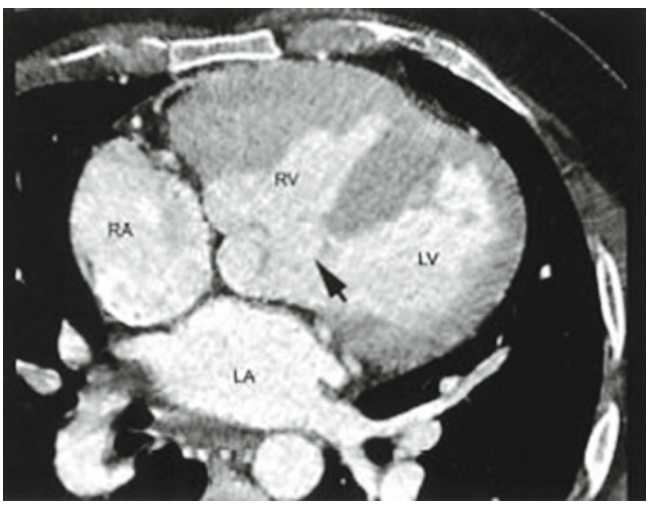

Fig. 17.7 An electron beam angiogram axial slice is shown in a 38-year-old cyanotic man with Eisenmenger's complex, characterized by a nonrestrictive, perimembranous ventricular septal defect (*arrow*) and right-to-left shunt secondary to systemic level pulmonary vascular resistance. Note the severely hypertrophied right ventricle (RV), compared with the normal left ventricle (LV). *LA*—left atrium, *RA*—right atrium

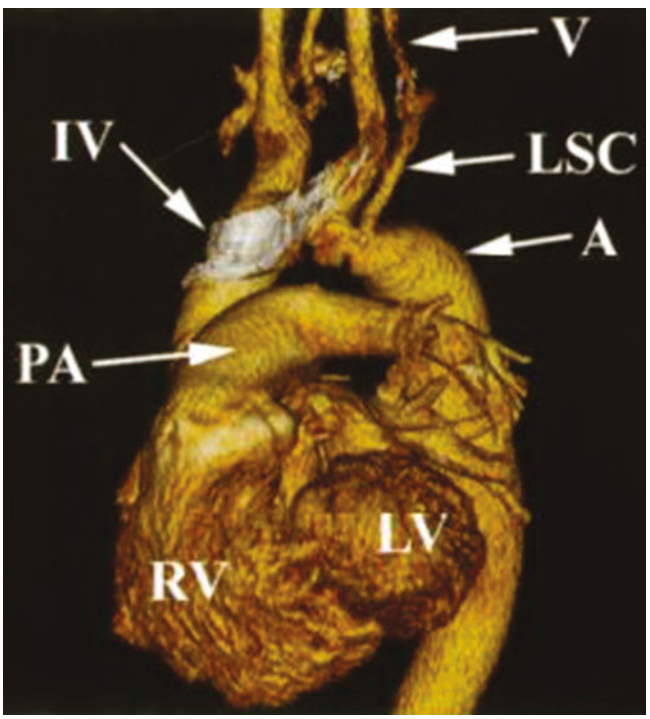

Fig. 17.9. A 64-slice CT angiogram with three-dimensional surface rendering viewed from a left anterior oblique projection. There is residual coarctation of the aorta and isthmus hypoplasia in a patient with prior surgical end-to-end repair. The post-coarctation aorta (A) is moderately dilated. The left subclavian (LSC) artery is diminutive, as is the left vertebral artery (V). *IV*—innominate vein, *LV*—left ventricle, *PA*—pulmonary artery, *RV*—right ventricle

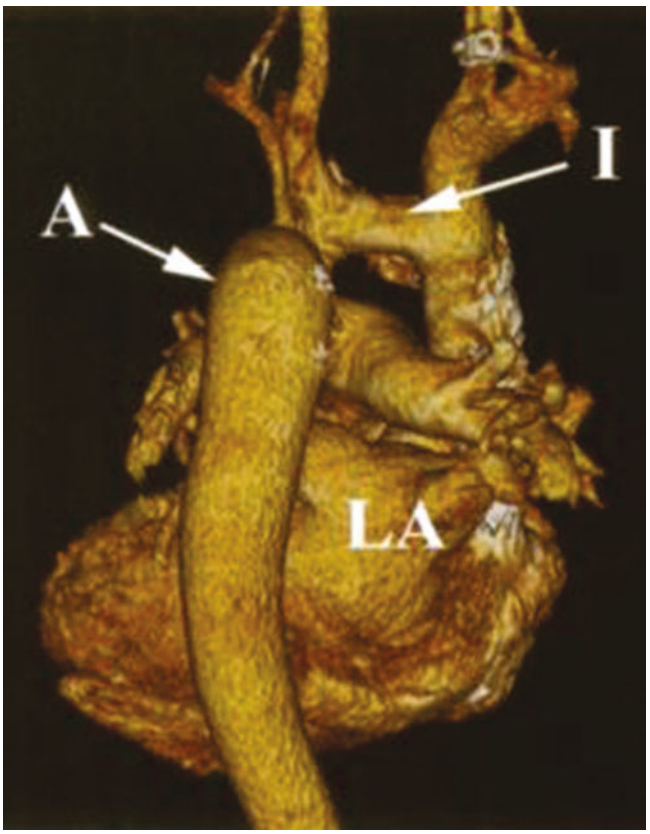

Fig. 17.10 Three-dimensional surface rendering of 64-slice CT angiography viewed from a posterior projection. There is hypoplasia of the aortic isthmus (I) in a patient with previous surgical repair (end-to-end anastomosis) of coarctation of the aorta. There is moderate residual coarctation and aneurysmal dilatation of the post-coarctation aorta (A). *LA*—left atrium

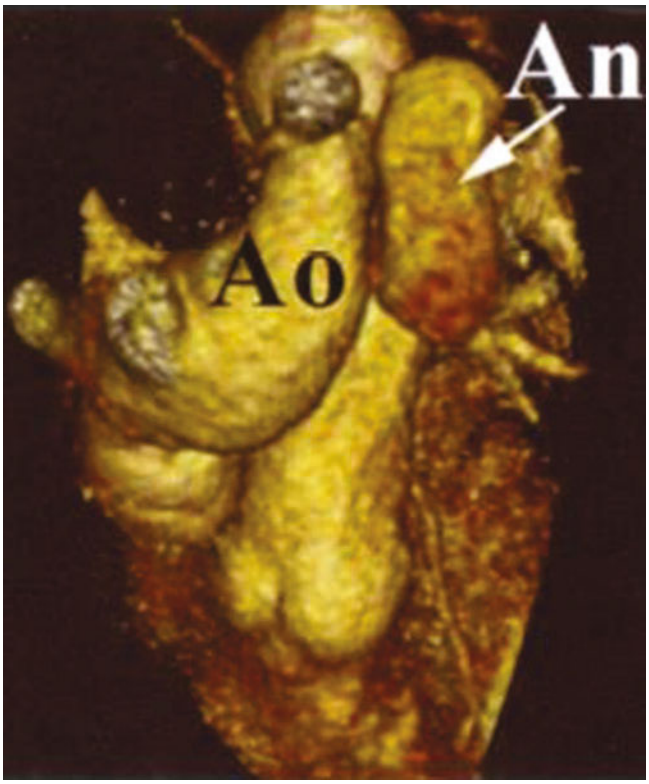

Fig. 17.11 A 64-slice CT angiogram with three-dimensional volume rendering of an adult 6 months after patch repair of coarctation of the aorta, as viewed from a left oblique and cranial angulation. Note the characteristic hypoplasia of the distal aortic arch (Ao). A large pseudoaneurysm (An) is present at the site of the previous patch aortoplasty. Aneurysm formation is a frequent complication following patch repair of aortic coarctation, leading to a decline in the use of this technique

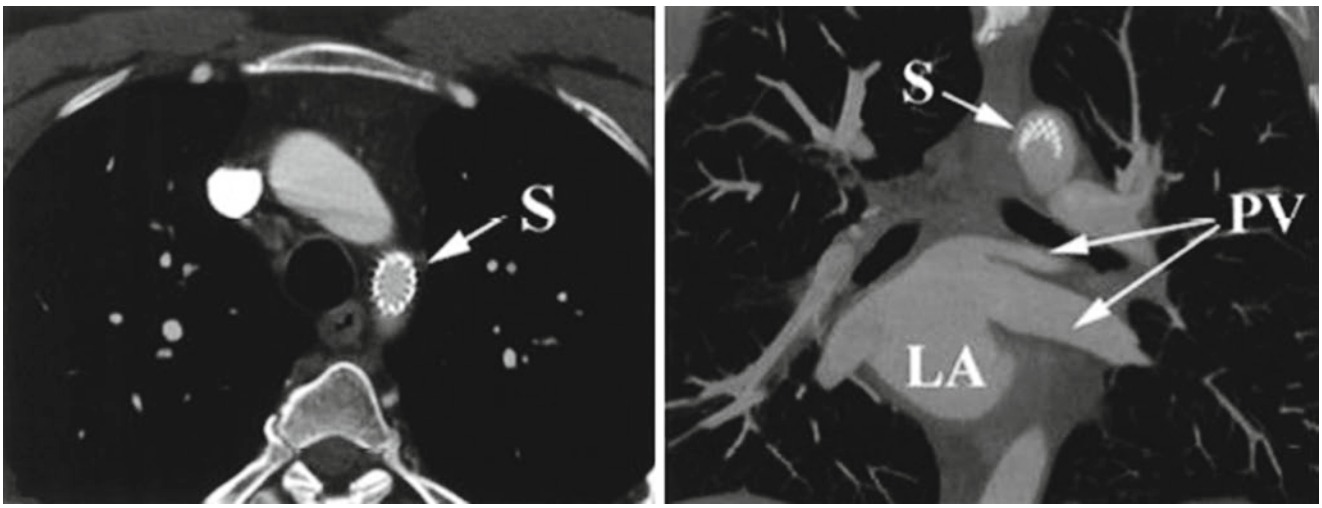

Fig. 17.12 A 64-slice CT angiogram of an adult with coarctation of the aorta following endovascular stent deployment. (**a**) An axial cut at the level of the proximal descending thoracic aorta demonstrates a widely patent, well-apposed 14-mm bare-metal uncovered stent (S) (Palmaz Genesis 2910B [Cordis Corporation, Miami Lakes, FL]). (**b**) A coronal section demonstrates the patent stent (S) in the proximal descending thoracic aorta. *LA*—left atrium, *PV*—(left superior and inferior) pulmonary veins

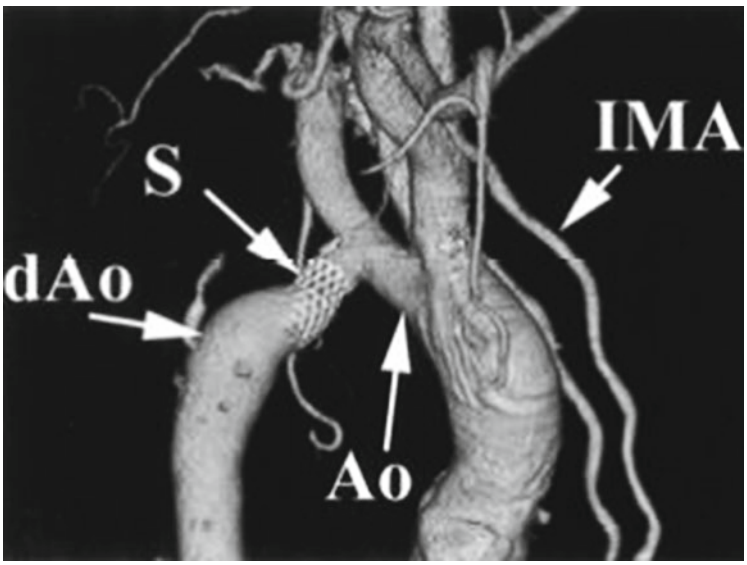

Fig. 17.13 A 64-slice CT angiogram with three-dimensional volume rendering of an adult with coarctation of the aorta following deployment of an endovascular stent (S), as viewed from a right posterior oblique projection. Note the characteristic hypoplasia of the aortic arch (Ao), the dilated post-stenotic descending thoracic aorta (dAo), and the dilated right internal mammary artery (IMA), a common finding in patients with coarctation of the aorta

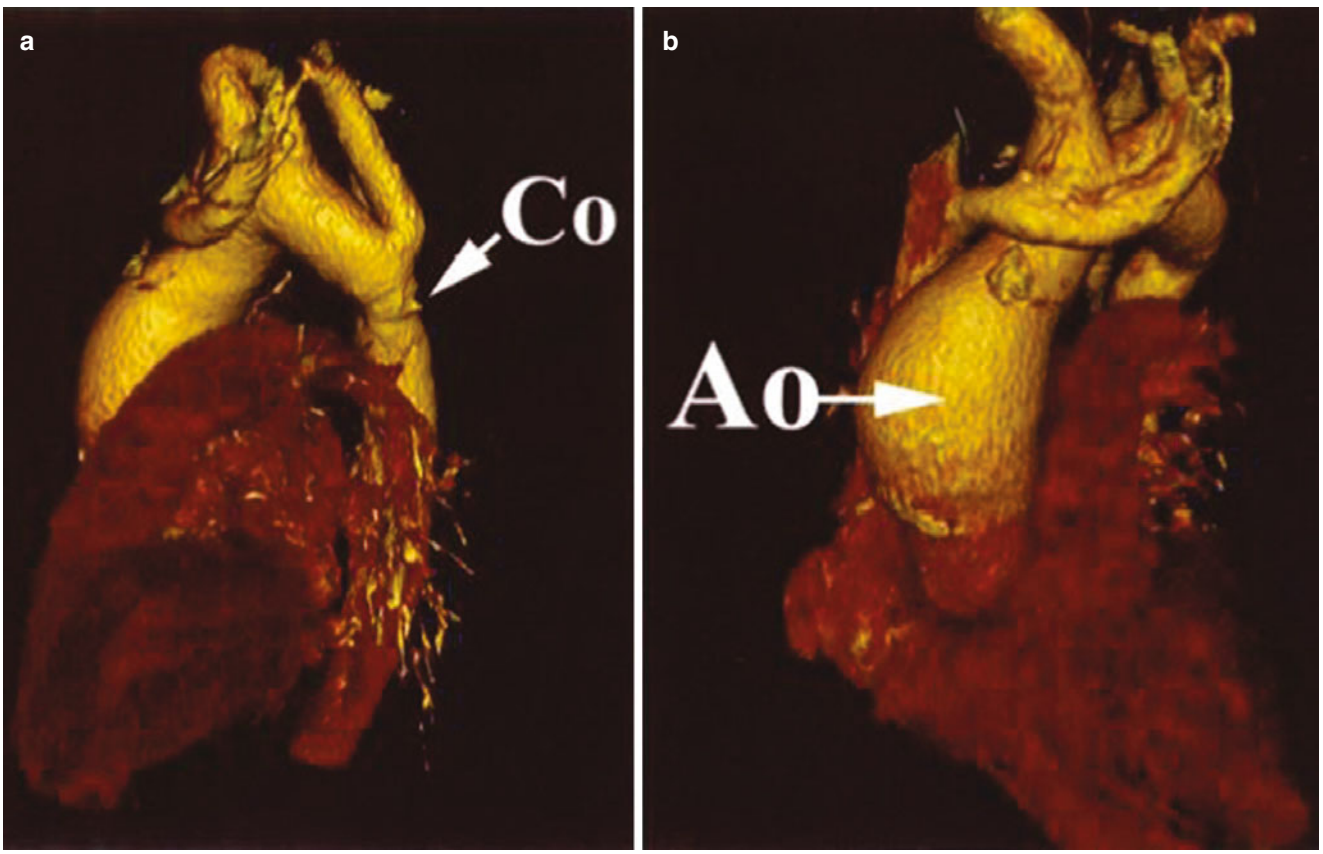

Fig. 17.14 A 64-slice CT angiogram with three-dimensional surface rendering of a 42-year-old man with coarctation of the aorta following surgical resection and end-to-end repair during childhood. The patient also has a minimally stenotic and mildly regurgitant bicuspid aortic valve. (**a**) Left anterior oblique projection demonstrating mild residual stenosis at the site of coarctation repair (Co). (**b**) Slight left anterior oblique and cranial projection demonstrating a dilated ascending aorta (Ao) measuring 50 mm in diameter above the sinotubular junction. Dilation of the aortic root in the presence of a non-stenotic or non-regurgitant aortic valve is frequently encountered and is likely related to a combination of turbulent transvalvar flow and intrinsic medial abnormalities of the aortic wall [4]

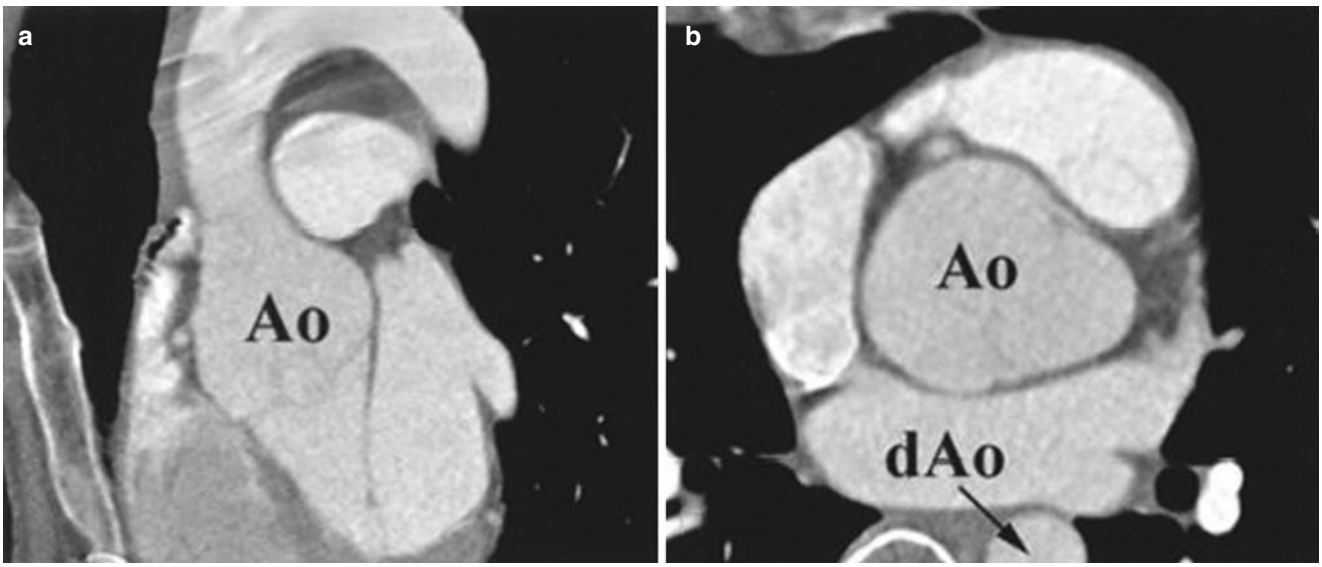

Fig. 17.15 A 64-slice CT angiogram of a 20-year-old man with Marfan syndrome. (**a**) Sagittal cut demonstrating the characteristic "Erlenmeyer flask" appearance of the aortic root (Ao). The aorta measured 53 mm at the level of the sinuses, spurring a referral for surgical aortic root repair. (**b**) Axial cut at the level of the dilated aortic sinuses (Ao). Note the stark contrast in diameter between the dilated aortic root and the normal caliber of the descending thoracic aorta (dAo)

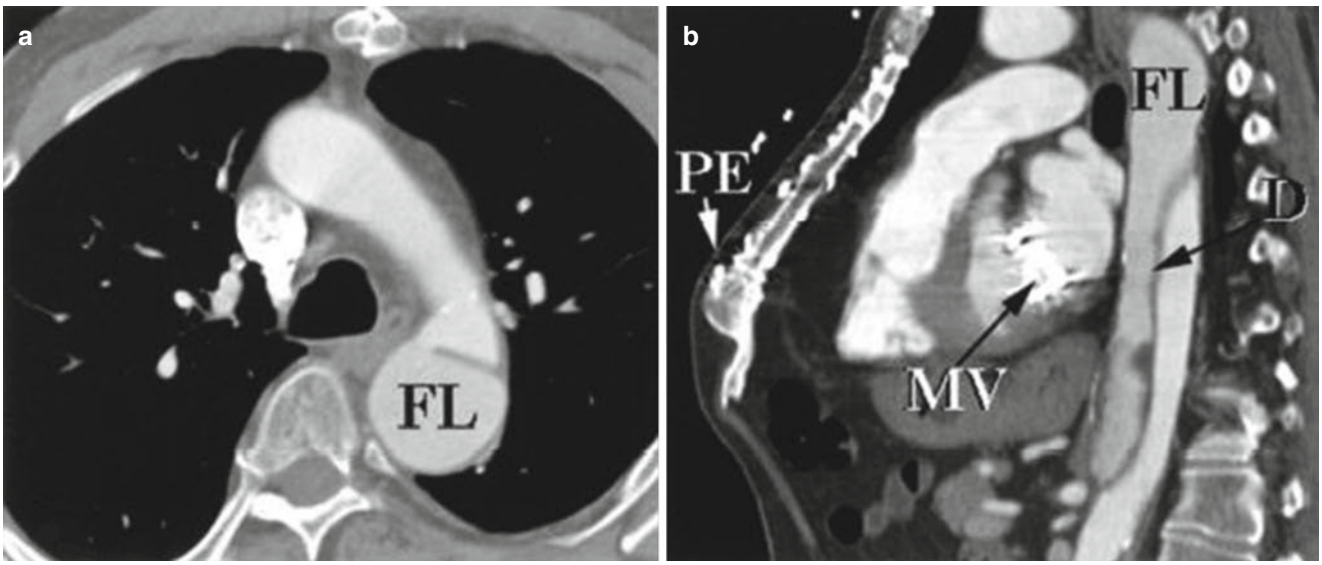

Fig. 17.16 A 16-slice CT angiogram is shown of a 61-year-old man with Marfan syndrome, a chronic Stanford type B dissection, and a mechanical mitral valve prosthesis. (**a**) Axial cut at the level of the aortic arch, demonstrating a dissection flap starting at the distal arch; FL indicates the false lumen. (**b**) Sagittal slice demonstrating pectus excavatum (PE), type B dissection (D) with a less-opacified FL, and the mechanical mitral valve prosthesis (MV)

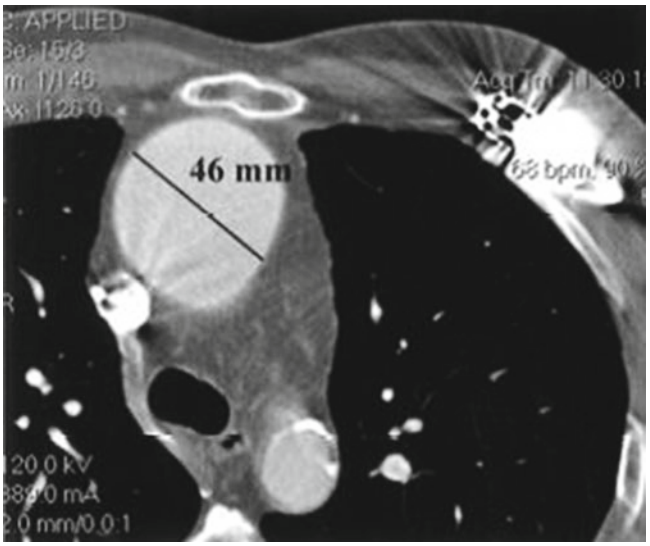

Fig. 17.17 Axial slice of a 64-slice CT angiogram in a patient with tetralogy of Fallot with pulmonary atresia, who had undergone previous intracardiac repair. Note the dilated ascending aorta, measuring 46 mm in diameter. A dilated aortic root and ascending aorta are commonly found in patients with tetralogy of Fallot and pulmonary atresia. Older age at complete repair is a risk factor for aortic root dilatation [5, 6]. This patient had a palliative shunt from infancy and underwent complete repair as a teenager

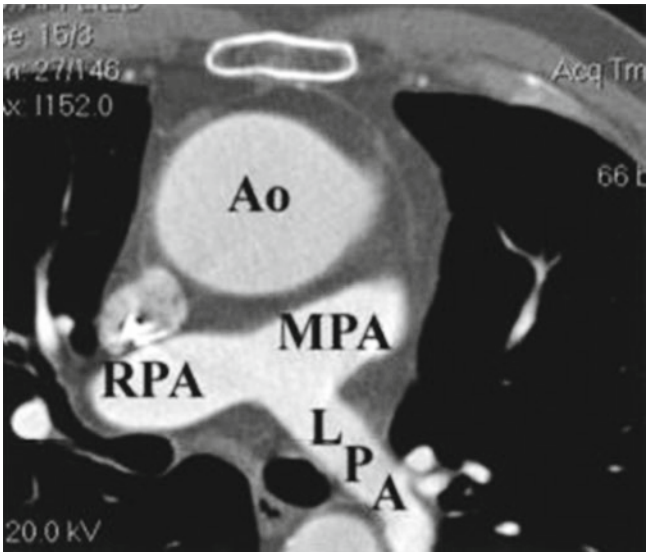

Fig. 17.18 Axial slice of a 64-slice CT angiogram in a patient with tetralogy of Fallot with pulmonary atresia, who had undergone previous intracardiac repair. Note the dilated ascending aorta (Ao). The main and branch pulmonary arteries (MPA, RPA, LPA) are small in caliber, a common finding in repaired tetralogy of Fallot with pulmonary atresia

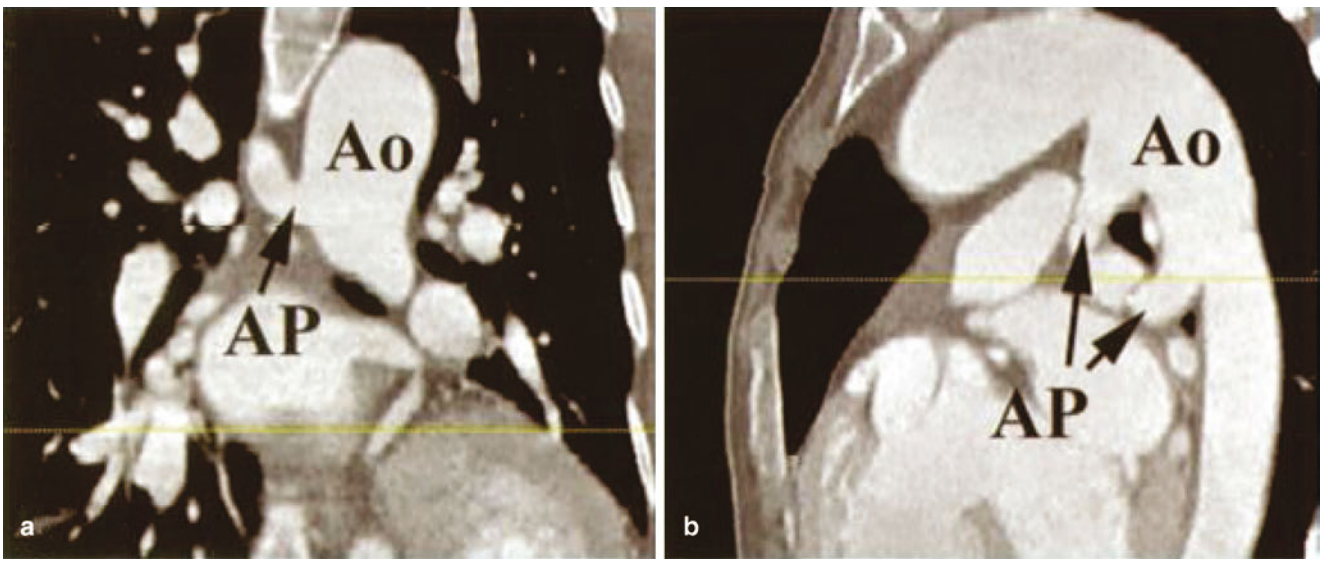

Fig. 17.19 Electron-beam angiogram of a cyanotic adult with unrepaired tetralogy of Fallot with pulmonary atresia and multiple aortopulmonary (AP) collaterals. (**a**) Coronal slice demonstrating a large AP collateral emerging rightward from the descending thoracic aorta (Ao). (**b**) Sagittal slice demonstrating two AP collaterals emerging anteriorly from the descending Ao. Delineating the origin, course, and patency of these AP collaterals is challenging and time-consuming, but it is essential for the management of these patients. Depending on the anatomic findings, patients may be candidates for complete surgical repair, unifocalization, or transcatheter interventions

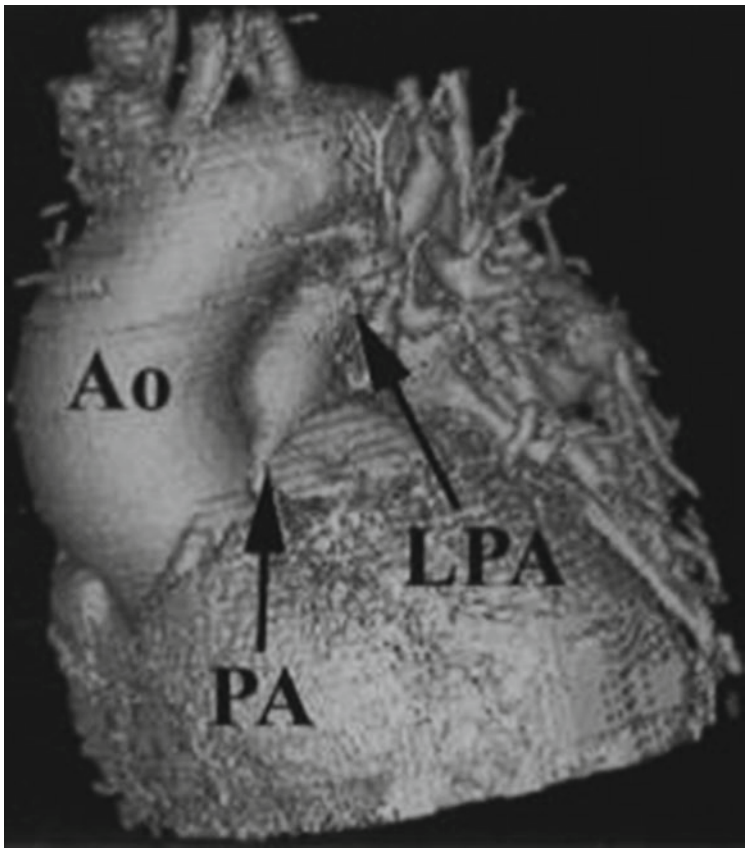

Fig. 17.20 Electron-beam angiogram with three-dimensional surface rendering of a cyanotic adult patient with unrepaired tetralogy of Fallot and pulmonary atresia, as viewed from an anterior and slightly cranial angulation. Note the dilated ascending aorta (Ao) and the atretic pulmonary artery (PA). The patient has severe stenosis/hypoplasia of the left pulmonary artery (LPA)

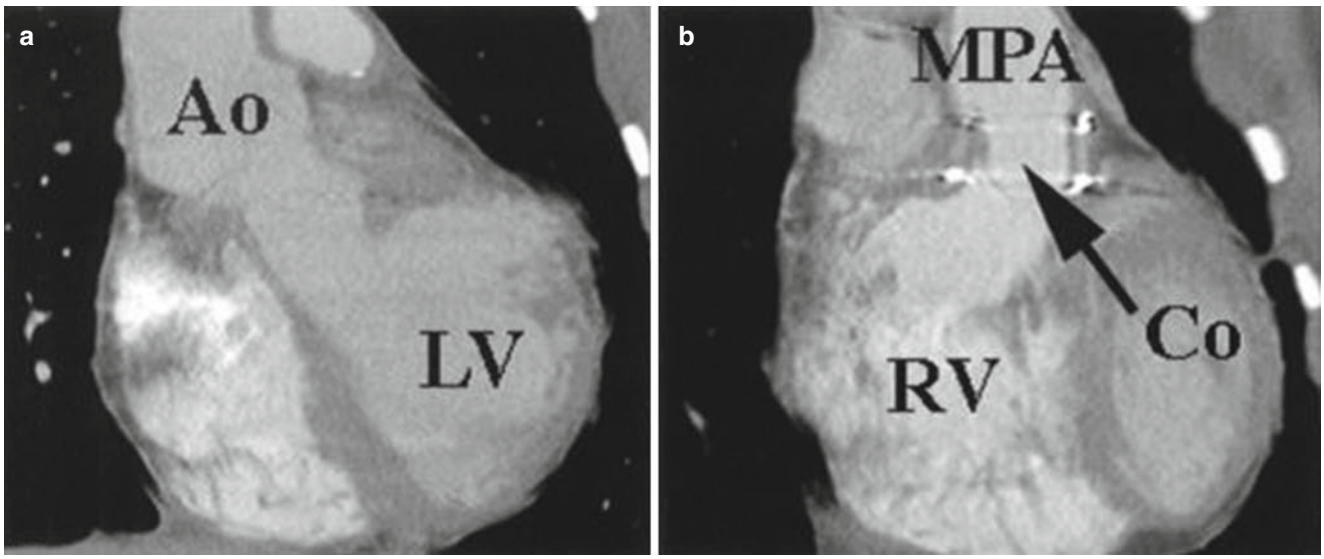

Fig. 17.21 A 64-slice CT angiogram coronal slice of a patient with a Rastelli-type surgical repair of D-transposition of the great arteries with a double-outlet right ventricle. (**a**) Patent left ventricle (LV) to aorta (Ao) internal baffle. (**b**) Right ventricle (RV) to main pulmonary artery (MPA) valved conduit (Co)

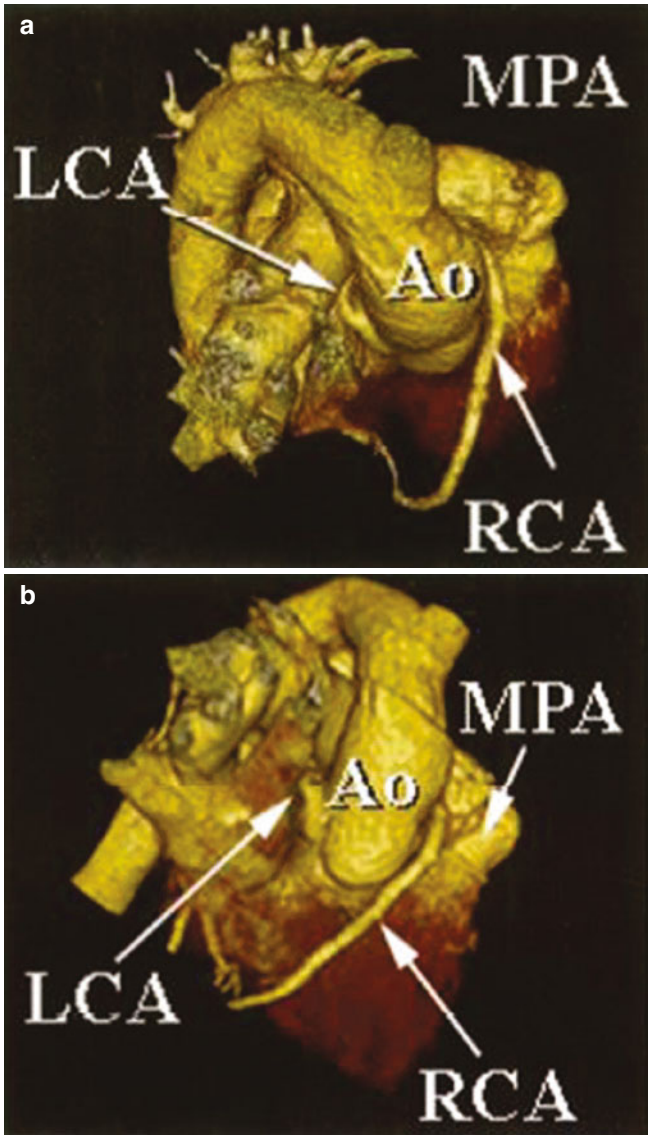

Fig. 17.22 A 16-slice CT angiogram with three-dimensional volume rendering of a 21-year-old woman with repaired tetralogy of Fallot. (**a**) In a right anterior oblique and cranial projection, the right coronary artery (RCA) emerges from the anterior and left-facing cusp and courses between the aortic root (Ao) and the main pulmonary artery (MPA). The left coronary artery (LCA) emerges from the posterior-facing cusp and courses leftward behind the Ao and below the MPA. (**b**) Right anterior oblique caudal projection

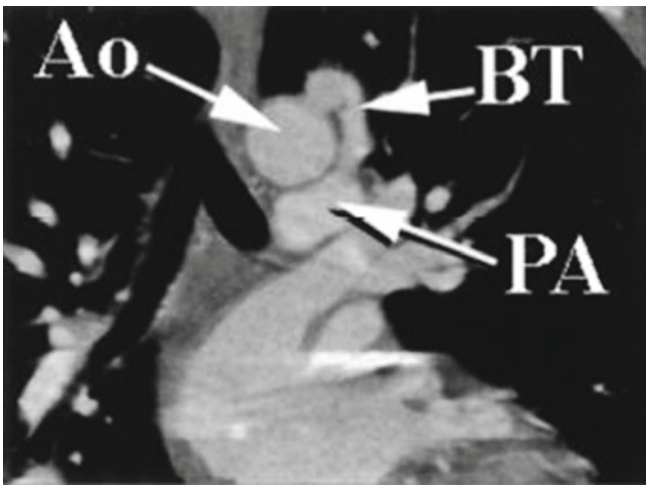

Fig. 17.23 A 64-slice CT angiogram coronal slide in a 49-year-old patient with pulmonary atresia. Note the classic left Blalock-Taussig shunt (BT) connecting the aorta (Ao) to the left pulmonary artery (PA)

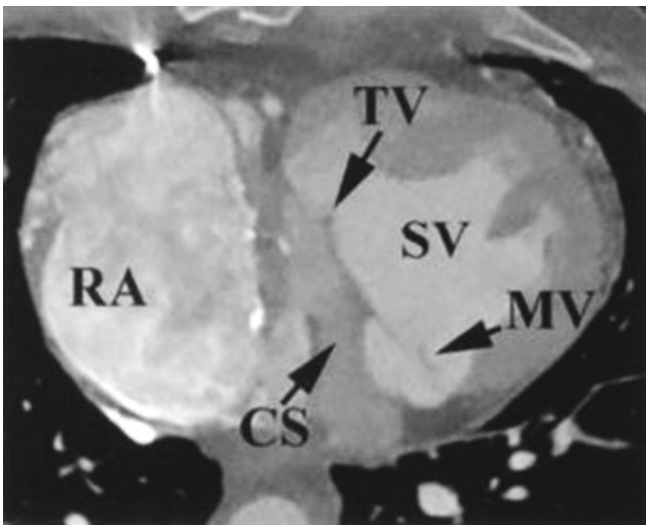

Fig. 17.24 Electron-beam angiogram (axial slice) of a 48-year-old patient with a double-inlet single ventricle after a modified right atrial to pulmonary artery (PA) Fontan operation [7]. Note the severely dilated right atrium (RA), which is a characteristic finding in patients with this form of the Fontan connection. Supraventricular arrhythmias are very common, and patients often develop signs of volume overload. This form of Fontan has been abandoned in favor of the extracardiac and lateral tunnel Fontan, but patients who underwent the Fontan operation in the 1970s and 1980s are likely to have an RA-PA connection. Simultaneous upper- and lower-extremity contrast injections are preferred for individuals with lateral tunnel or extracardiac Fontan connections as they may have preferential, asymmetric streaming from the Glenn anastomosis into one lung. Although individuals with RA-PA Fontans do not have streaming, lower extremity injections can be helpful to characterize any venous collaterals arising from the inferior vena cava or hepatic veins. Note the well-developed mitral valve (MV) and tricuspid valve (TV). The coronary sinus (CS) is well visualized and drains deoxygenated blood into the surgically created "left atrium," resulting in a right-to-left shunt and contributing to systemic hypoxia (peripheral saturation on room air of 92%). This single ventricle (SV) is of left ventricular morphology

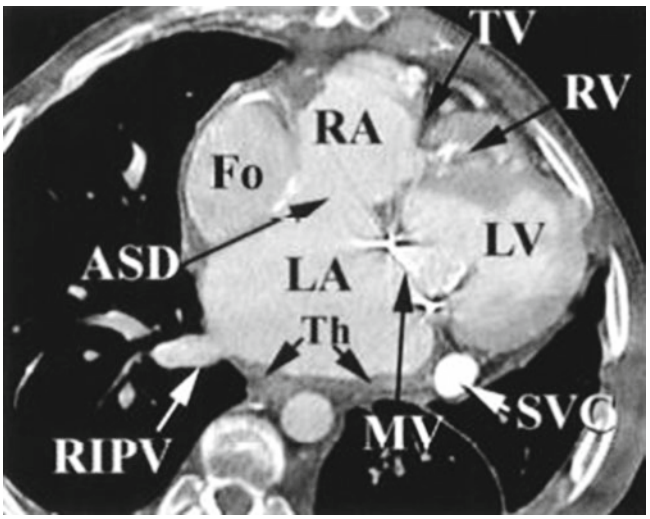

Fig. 17.25 Electron-beam angiogram (axial slice) of a 22-year-old patient with tricuspid and pulmonary atresia after a lateral tunnel Fontan (Fo) and mitral valve replacement with a mechanical prosthesis (MV). Contrast injections were performed simultaneously in the left upper extremity and the right femoral vein, resulting in opacification of the lateral tunnel Fontan and a persistent left superior vena cava (LSVC). The left atrium (LA) has a mural thrombus (Thr) overlying the posterior wall, and the left inferior pulmonary vein is occluded. A large atrial septal defect (ASD) is present between the LA and right atrium (RA). The tricuspid valve (TV) is atretic and the right ventricle (RV) is hypoplastic. The left ventricle (LV) is well developed. This case illustrates the complexity of certain types of adult congenital heart disease and how much information can be gleaned by careful analysis of the information provided by CT angiography. *RIPV*—right inferior pulmonary vein

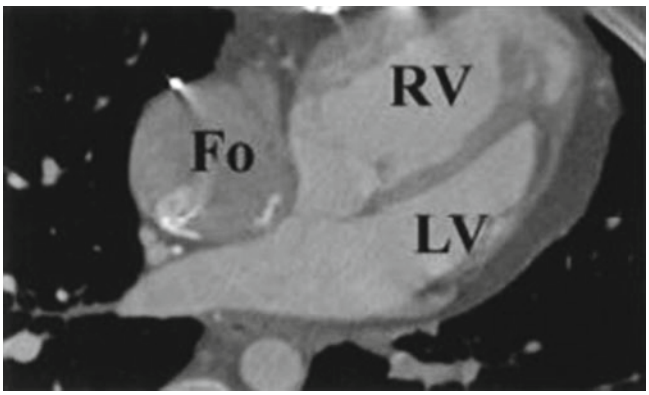

Fig. 17.26 Axial cut of a 64-slice CT angiogram in an 18-year-old patient with a hypoplastic left ventricle (LV) and a systemic right ventricle (RV) after lateral tunnel Fontan (Fo). Note the poor opacification of the Fontan after contrast injection via an upper extremity peripheral vein, a characteristic problem in these patients. Better contrast opacification of the extracardiac Fontan can be achieved if two injectors are utilized, with appropriately timed injections made in upper- and lower-extremity veins

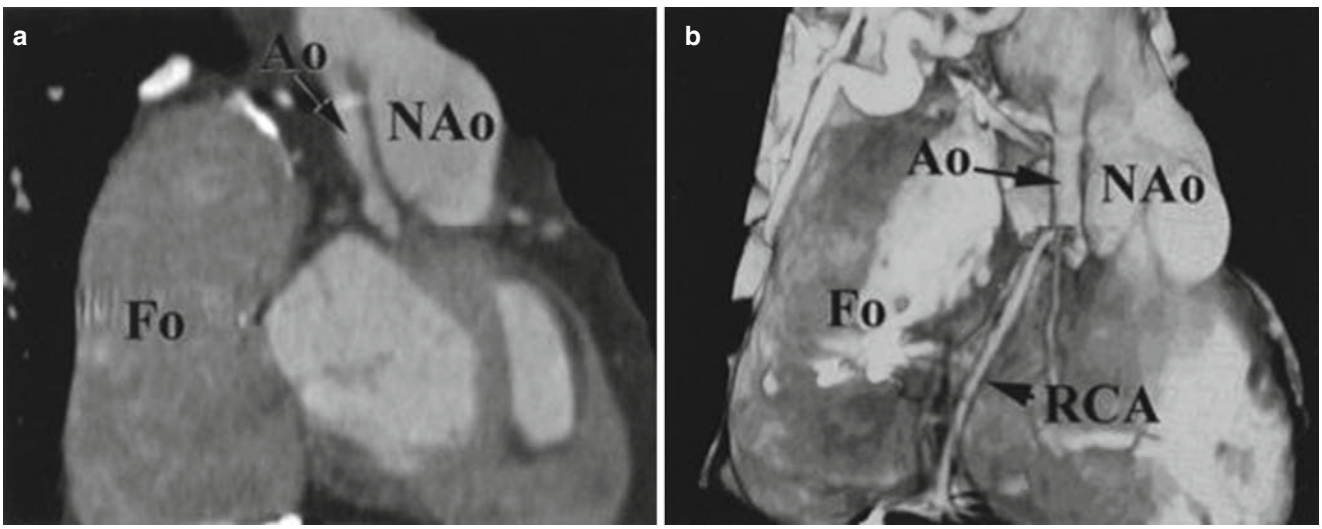

Fig. 17.27 A 64-slice CT angiogram of an 18-year-old patient with hypoplastic left heart syndrome who had successfully undergone the three stages of the Norwood operation in infancy and childhood: Stage 1. Direct anastomosis of the main pulmonary artery to the aortic arch to form a neo-aorta (NAo). The hypoplastic native ascending aorta (Ao) essentially forms a long conduit to the coronary arteries. The connection to the right coronary artery (RCA) is well seen. Pulmonary blood flow in this first stage of the Norwood operation is via a surgically placed arteriopulmonary shunt or a shunt from the right ventricle (RV) to the pulmonary artery (not shown in the figure). Stage 2. Surgical placement of a Glenn shunt (superior vena cava to right pulmonary artery) and takedown of the arteriopulmonary or RV-to-pulmonary-artery shunt. Stage 3. Surgical completion of a total cavopulmonary Fontan shunt (Fo) with alleviation of cyanosis. (**a**) Coronal slice showing the NAo and Ao as well as the lateral tunnel Fontan (Fo). (**b**), Three-dimensional volume rendering viewed from an anteroposterior and slightly cranial angulation, demonstrating the NAo, Ao, and the connection of the Ao to the RCA

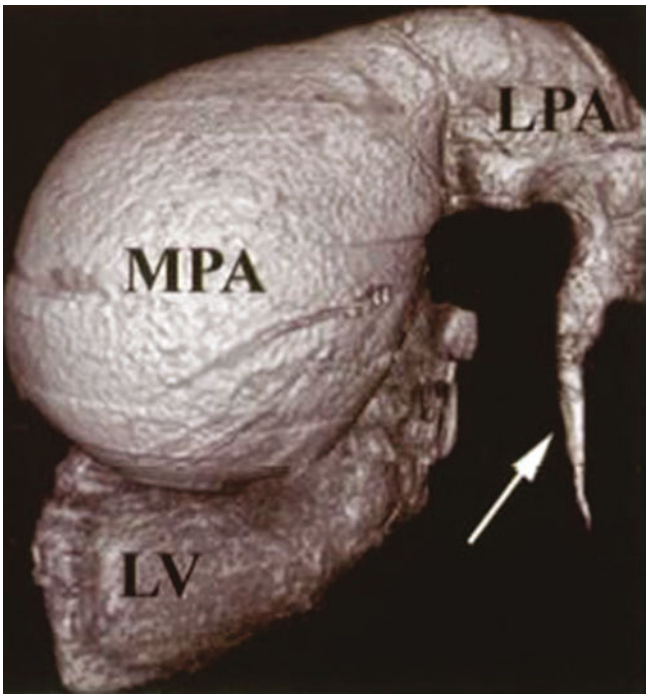

Fig. 17.28 A 64-slice CT angiogram with three-dimensional volume rendering, viewed from the lateral projection. This image shows a very large main pulmonary artery (MPA) aneurysm in a patient with severe pulmonary hypertension. This aneurysm measured 9 cm in diameter. Note the dilated left pulmonary artery (LPA) and the distal pruning of the pulmonary arterial tree (*arrow*). *LV*—left ventricle

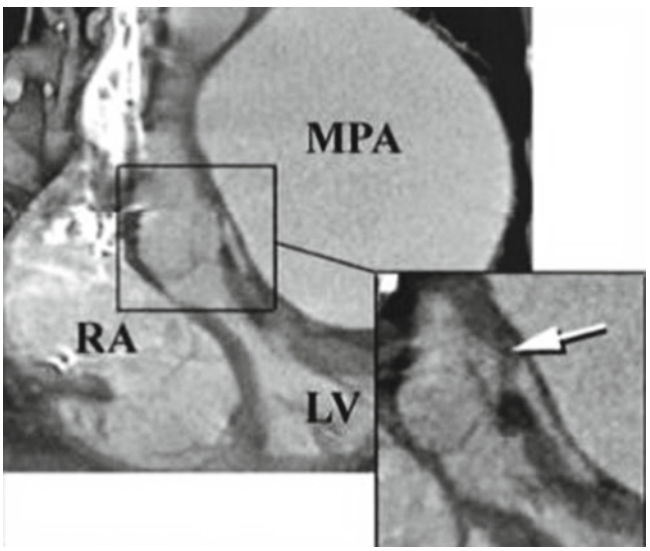

Fig. 17.29 A 64-slice CT angiogram, coronal perspective, demonstrating a large main pulmonary artery (MPA) aneurysm in a patient with pulmonary hypertension. The aneurysm compresses the left main coronary artery (*arrow*), causing a severe stenosis that results in hypotension and ischemic electrocardiographic changes. The left ventricle (LV) is small and the outflow tract is narrowed, but there was only a minimal systolic pressure gradient across this narrowed segment on invasive catheter pullback from the LV to the aorta. *RA*—right atrium

References

1. Aboulhosn J, French WJ, Buljubasic N, Matthew RV, Budoff MJ, Shavelle DM. Electron beam angiography for the evaluation of percutaneous atrial septal defect closure. Catheter Cardiovasc Interv. 2005;65:565–8.
2. Aboulhosn J, Shavelle DM, Matthews R, French WJ, Buljubasic N, Budoff MJ. Images in cardiology: electron beam angiography of percutaneous atrial septal defect closure. Clin Cardiol. 2004;27:702.
3. Aboulhosn J, Castellon YM, Siegerman C, Ratib O, Child JS. Quantification of pulmonary calcium deposits in patients with primary and secondary pulmonary hypertension using computed tomography. Abstract 90. Presented at the Western Regional Tri-Society Conference. Carmel; 3 Feb 2006.
4. Gurvitz M, Chang RK, Drant S, Allada V. Frequency of aortic root dilation in children with a bicuspid aortic valve. Am J Cardiol. 2004;94:1337–40.
5. Niwa K, Siu SC, Webb GD, Gatzoulis MA. Progressive aortic root dilation in adults late after repair of tetralogy of Fallot. Circulation. 2002;106:1374–8.
6. Mongeon FP, Gurvitz MZ, Broberg CS, Aboulhosn J, Opotowsky AR, Kay JD, et al. Aortic root dilatation in adults with surgically repaired tetralogy of Fallot: a multicenter cross-sectional study. Circulation. 2013;127:172–9.
7. Aboulhosn JA, Shavelle DM, Castellon Y, Criley JM, Plunkett M, Pelikan P, et al. Fontan operation and the single ventricle. Congenit Heart Dis. 2007;2:2–11.

Devices and Implants

18

Christopher M. Walker, Quynh A. Truong, and Suhny Abbara

Devices and implants are encountered daily by cardiac imagers. Knowledge of the expected normal appearance and function of each device facilitates detection of complications. Devices are usually seen on CT images, but their true three-dimensional appearance, course, and function may not be apparent because of beam hardening and streak artifacts. Review of the scout image or a recent chest radiograph is helpful in identifying the device and its function prior to interrogating the CT dataset. This chapter reviews the normal appearance of common and uncommon devices and implants seen on cardiac CT, including cardiac valves, pacemakers, implantable cardioverter defibrillators (ICDs), occlusion devices, and circulatory assist devices. Radiographs, scout images, volume-rendered images, and illustrations are used for correlation when possible. The chapter also reviews the role of CT in procedural planning for the LARIAT procedure and for insertion of percutaneous heart valves and left atrial appendage occluder devices. Device-specific complications are also reviewed.

C.M. Walker, MD
Department of Radiology, Saint Luke's Hospital of Kansas City, Kansas City, MO, USA
e-mail: walk0060@gmail.com

Q.A. Truong, MD, MPH
Department of Radiology, Weill Cornell Medicine, 525 E. 68th Street, L-024, New York, NY 10021, USA
e-mail: qat9001@med.cornell.edu

S. Abbara, MD (✉)
Department of Radiology, Division of Cardiothoracic Imaging, UT Southwestern Medical Center, 5323 Harry Hines Boulevard, E6.120A Mail Code 9316, Dallas, TX 75390, USA
e-mail: Suhny.Abbara@utsouthwestern.edu

M.J. Budoff et al. (eds.), *Atlas of Cardiovascular Computed Tomography*, https://doi.org/10.1007/978-1-4471-7357-1_18

Prosthetic Heart Valves

Prosthetic heart valves are common and are used to replace dysfunctional native valves. Prosthetic heart valves that may be encountered on CT include mechanical or biologic valves delivered surgically, and catheter-delivered valves. The type of prosthetic valve used depends on surgeon preference and individual patient characteristics. Generally, biologic heart valves are more prone to wear but do not require lifelong anticoagulation and therefore are preferred in older patients.

Mechanical Heart Valves

Mechanical heart valves, which consist of metal alloy or carbon components [1], were introduced in the 1950s. Three types of mechanical heart valves may be encountered in clinical practice: caged ball valves, tilting disc valves, and bileaflet valves (Figs. 18.1, 18.2, 18.3, and 18.4).

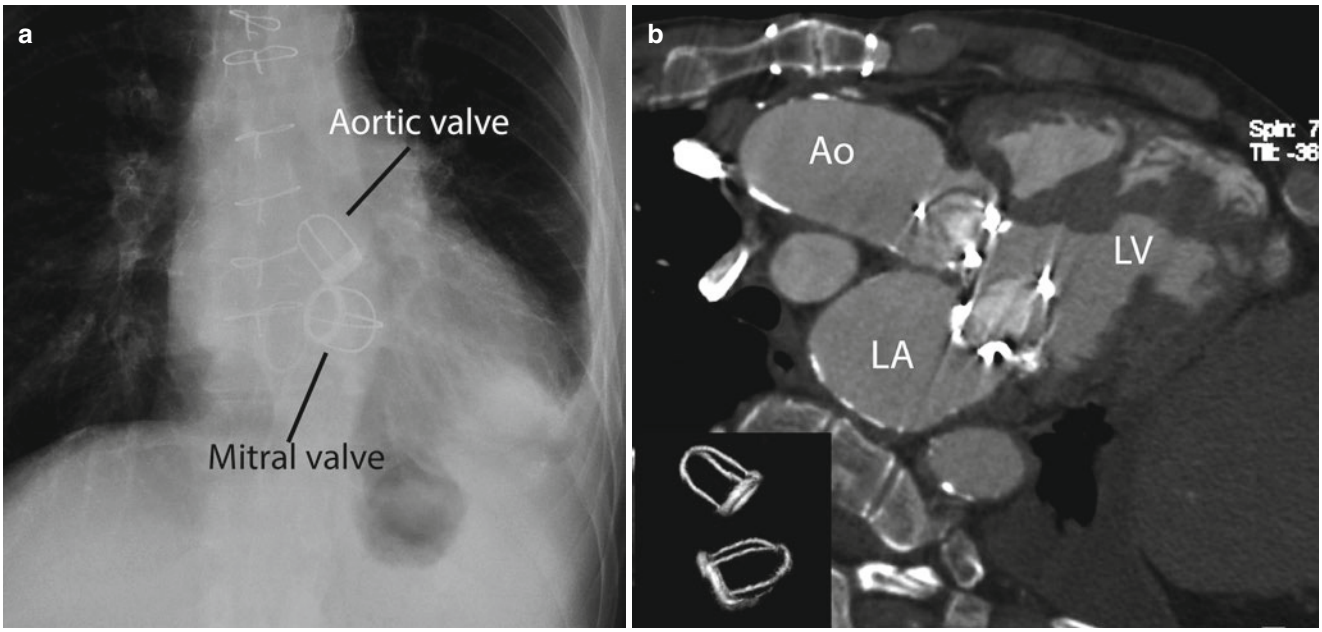

Fig. 18.1 Caged ball mechanical heart valve (**a**, **b**). The caged ball valve was the original design used in prosthetic heart valves. It relies on the principle that the ball will be forced to one direction in the cage depending on the direction of blood flow. When pressure in the left ventricle exceeds that of the aorta (Ao), the ball is pushed away from the heart into the open position, allowing blood to exit the left ventricle (LV). At the end of ventricular systole, the left ventricular pressure drops and the blood in the aorta flows backwards, causing the ball to drop into the closed position, thus preventing regurgitation. Importantly, there is no central flow through this type of valve, and the heart must work harder to pump blood around the ball. The aortic valve is three-pronged and the mitral valve is four-pronged. *LA* left atrium

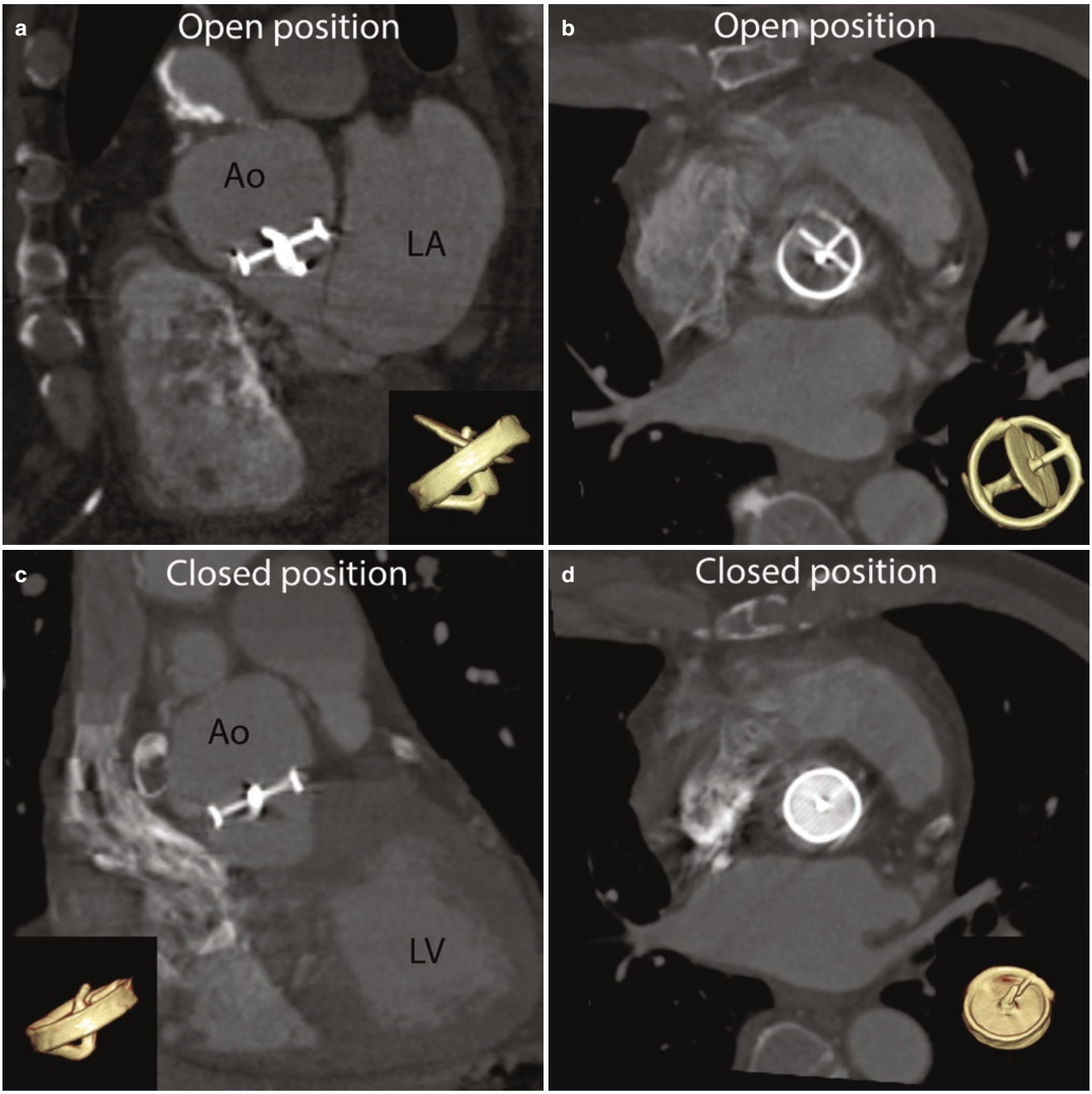

Fig. 18.2 Tilting disc mechanical heart valve. The tilting disc valve was designed to restore central blood flow. It consists of a metal ring, metal struts, and a single circular disc. The struts secure the circular disc and prevent embolization in either direction. The disc opens (**a**, **b**) and closes (**c**, **d**) based on the principles described for the caged ball mechanical valve. Early versions of this type of heart valve were prone to strut fatigue and occasional fractures leading to disc embolization, severe valvular incompetence, and even death. *Ao* aorta, *LA* left atrium, *LV* left ventricle

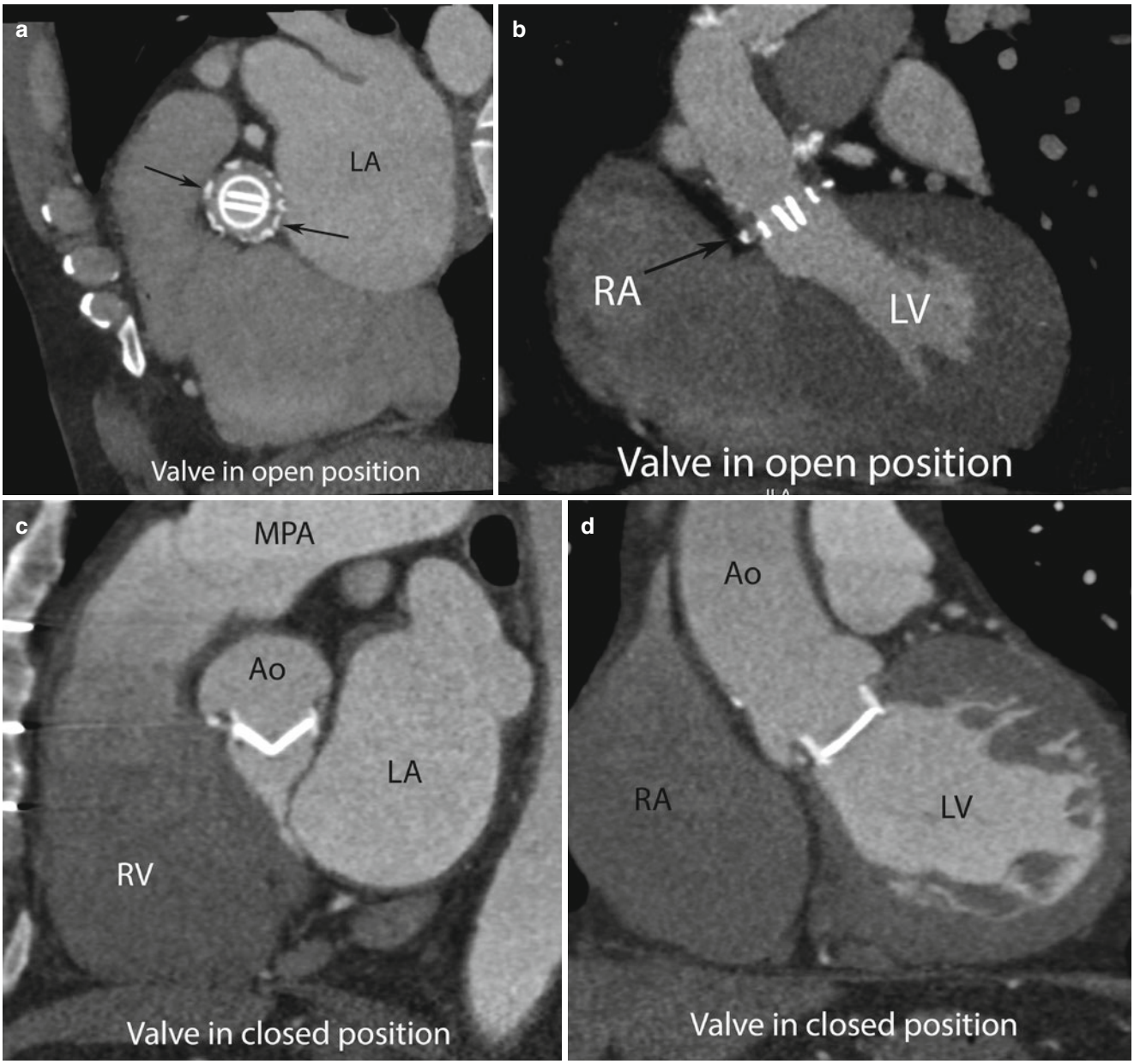

Fig. 18.3 Bileaflet mechanical heart valve. (**a**–**c**) The bileaflet mechanical heart valve consists of two semicircular discs, which pivot about mechanical struts. Of all the mechanical valve designs, it provides the most favorable central blood flow dynamics and causes little hemolysis. A disadvantage is that the valve is susceptible to regurgitation. The valve is implanted using multiple sutures with polytetrafluoroethylene (PTFE) pledgets, which are hyperattenuating structures (*black arrows*) on CT. *Ao* aorta, *LA* left atrium, *LV* left ventricle, *MPA* main pulmonary artery, *RA* right atrium, *RV* right ventricle

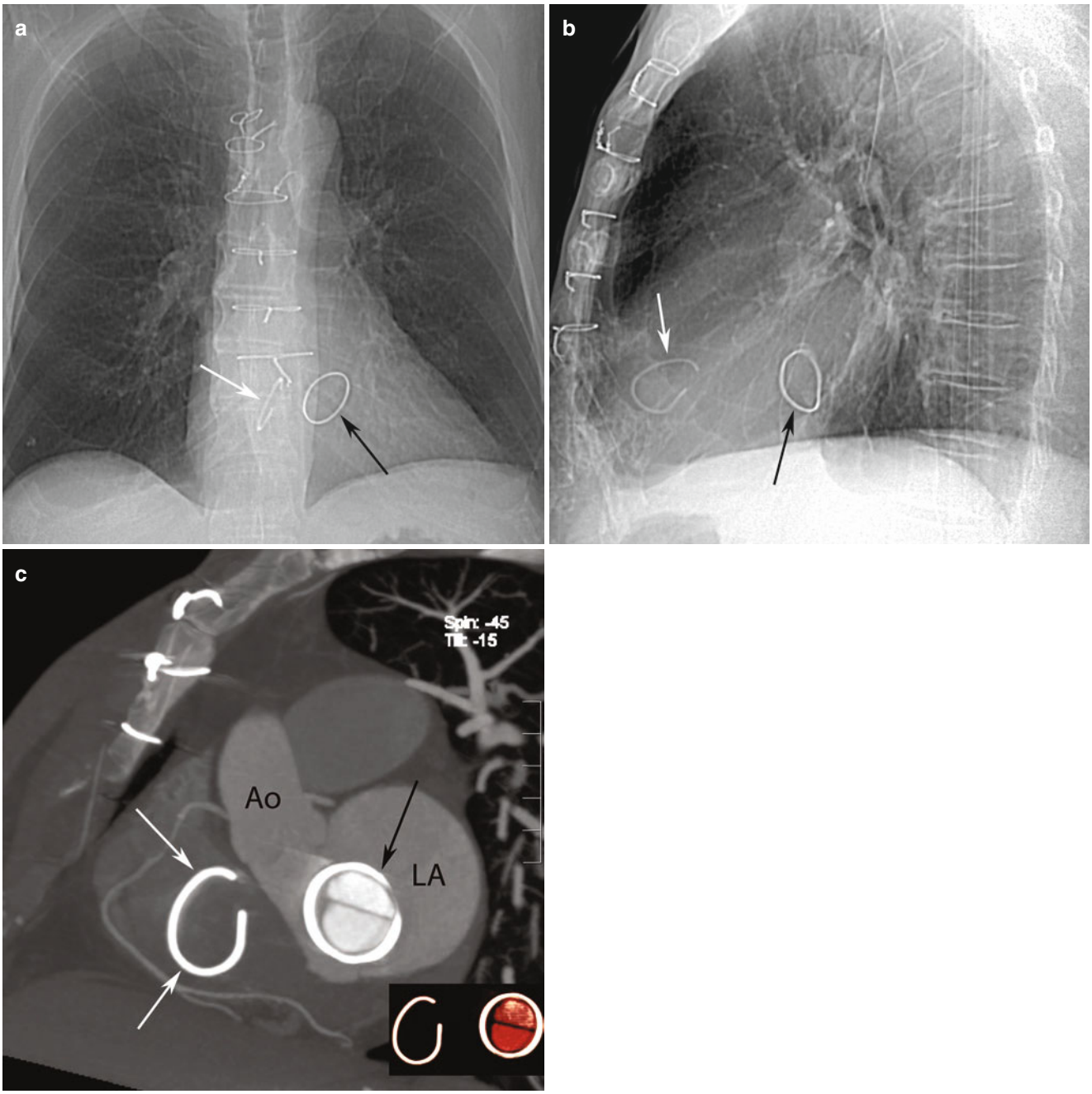

Fig. 18.4 Tricuspid valve annuloplasty ring. Frontal (**a**) and lateral (**b**) scout images and an oblique CT angiogram (**c**) from a different patient show a tricuspid valve annuloplasty ring (*white arrows*) and mechanical mitral valve (*black arrow*). The annuloplasty ring is vertically oriented between the right atrium and right ventricle. The ring appears narrow on the frontal projection and is seen en face on the lateral projection. The annuloplasty ring is incomplete, to reduce the risk for heart block. *Ao* aorta, *LA* left atrium

Bioprosthetic Valves

Bioprosthetic heart valves (Fig. 18.5) are fashioned from human tissues (e.g., allografts or autografts) or animal-derived tissues (e.g., porcine aortic valves or bovine pericardium). The two main designs are stented and stentless valves. Bioprosthetic valves have a lower risk of thrombotic complications than mechanical valves, have more favorable hemodynamic properties, and do not require lifelong anticoagulation. Their major limitation is that they are more prone to deterioration and replacement than mechanical valves.

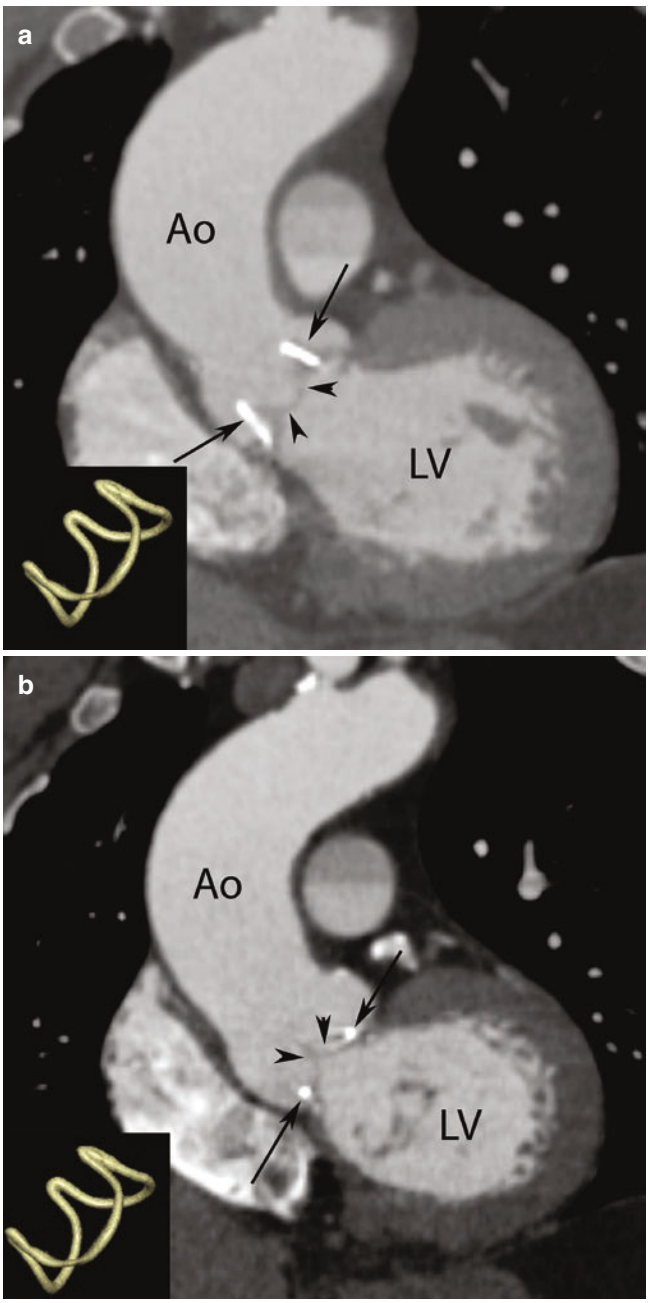

Fig. 18.5 A bioprosthetic heart valve (**a**, **b**) made from bovine pericardium, in two slightly different projections. The outer stent (*black arrows* and inset) provides scaffolding for the pericardium-derived tissue (*black arrowheads*). *Ao* aorta, *LV* left ventricle

Percutaneous Valves

In patients with severe aortic stenosis and high surgical risk, a new percutaneous alternative has evolved for replacing the aortic valve: transcatheter aortic valve replacement (TAVR) or implantation (TAVI) (Fig. 18.6) [2]. Three main percutaneous approaches can be used: transfemoral, transapical, and trans-subclavian.

Preprocedural chest, abdominal, and pelvis CT angiography (CTA) are used for sizing the valvular prosthesis, procedural planning, and patient selection. On the planning CTA, it is important to document the size of the aortic annulus (the basal attachment site of the aortic valve leaflets), the aortic root at the sinuses of Valsalva, and the sinotubular junction. The description of the annulus should include its shape, minimal and maximal luminal diameters, the length of the circumference, and its area [3]. The distance between the coronary arteries and the aortic annulus, as well as the individual leaflet lengths, should be reported, as displaced leaflets or calcification can migrate to the coronary artery ostia. A distance of less than 10 mm between the annulus and the coronary ostia increases the risk for coronary artery occlusion during the procedure [3]. Imaging of the iliofemoral system should document minimal luminal diameters, atherosclerotic burden, and the degree of vessel tortuosity. A patient may be excluded from the transfemoral approach if the minimal luminal diameter is less than 7 mm, extensive circumferential atherosclerotic plaque is seen, or extreme vessel tortuosity is identified, with angulations less than 90°.

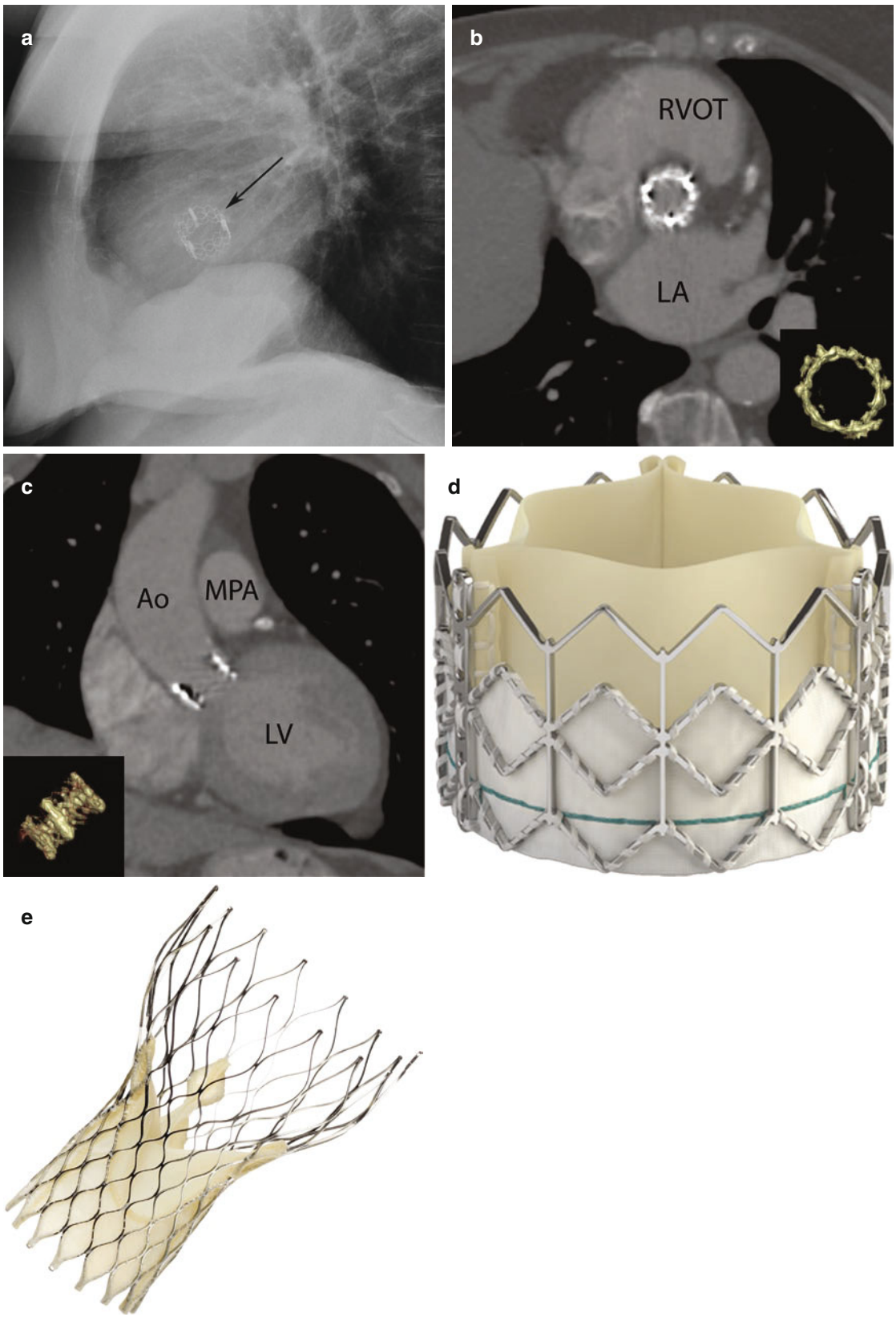

Fig. 18.6 The two transcatheter aortic valve replacement (TAVR) devices currently used in the United States are the balloon-expandable Edwards SAPIEN Transcatheter Heart Valve (*arrow*) (**a**–**d**) and the self-expanding Corevalve (**e**). *Ao* aorta, *LA* left atrium, *LV* left ventricle, *MPA* main pulmonary artery, *RVOT* right ventricular outflow tract. ((**d**) *courtesy of* Edwards Lifesciences, Irvine, CA; (**e**) *courtesy of* Medtronic, Minneapolis, MN)

Prosthetic Valve Complications

The complications that can occur after the implantation of prosthetic heart valves include pannus (Fig. 18.7), paravalvular leak (Fig. 18.8), endocarditis (Figs. 18.9 and 18.10), abscess (Fig. 18.11), pseudoaneurysm (Fig. 18.12), and aortic dissection (Fig. 18.13).

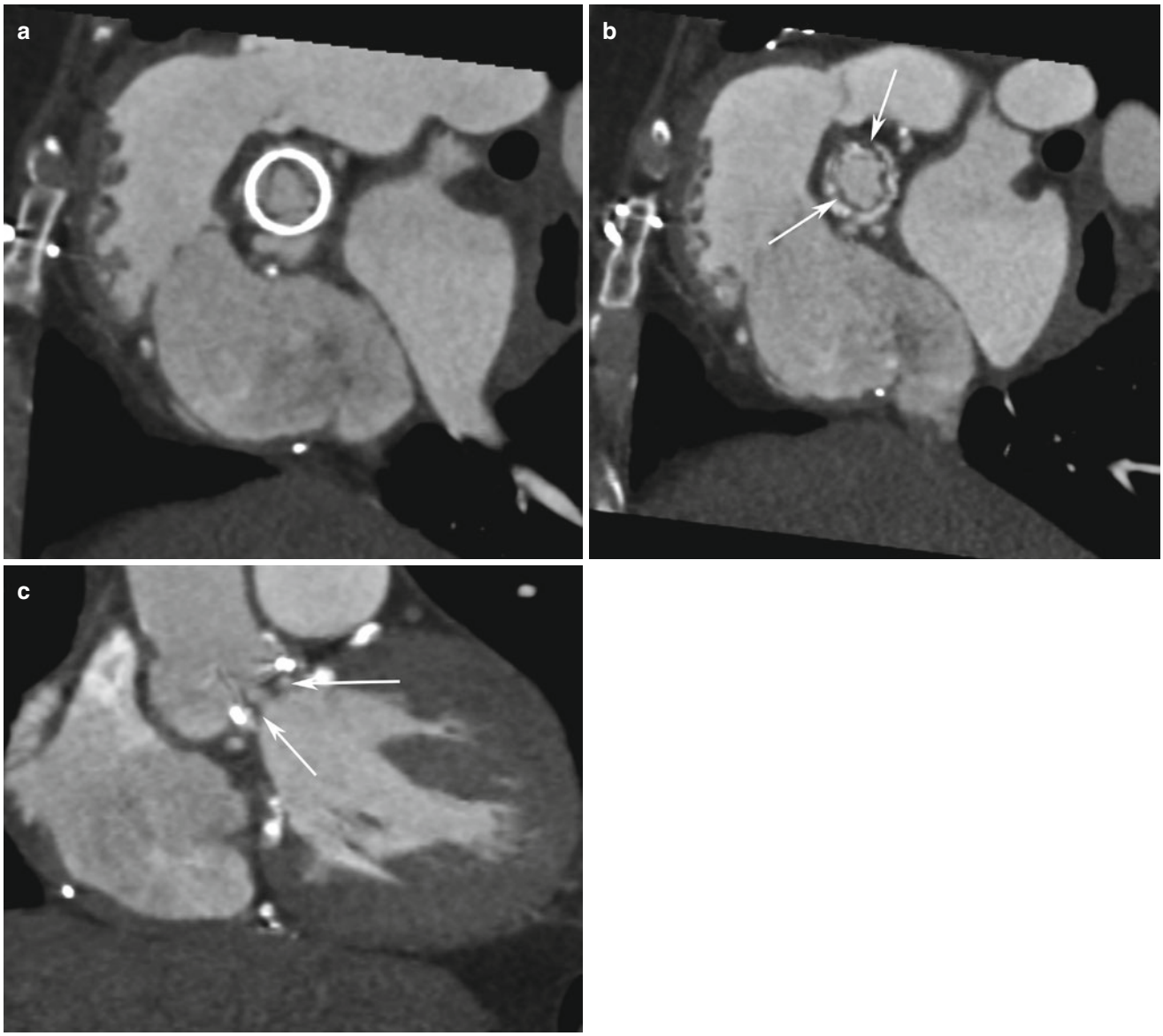

Fig. 18.7 (**a**) Pannus represents an ingrowth of fibrous tissue into the periannulus, likely from a healing response of the adjacent endocardium [4]. It can thicken, causing valve obstruction and predisposing to thrombus formation. Pannus should be differentiated from vegetation and thrombus. Pannus often progresses gradually, leading to further valve dysfunction despite anticoagulation. (**b**, **c**) It usually affects the ventricular side of the prosthesis and has a density similar to myocardium (*arrows*) [5]. Conversely, valvular thrombus usually has a lower density than myocardium and preferentially affects the aortic side of the prosthesis [4]

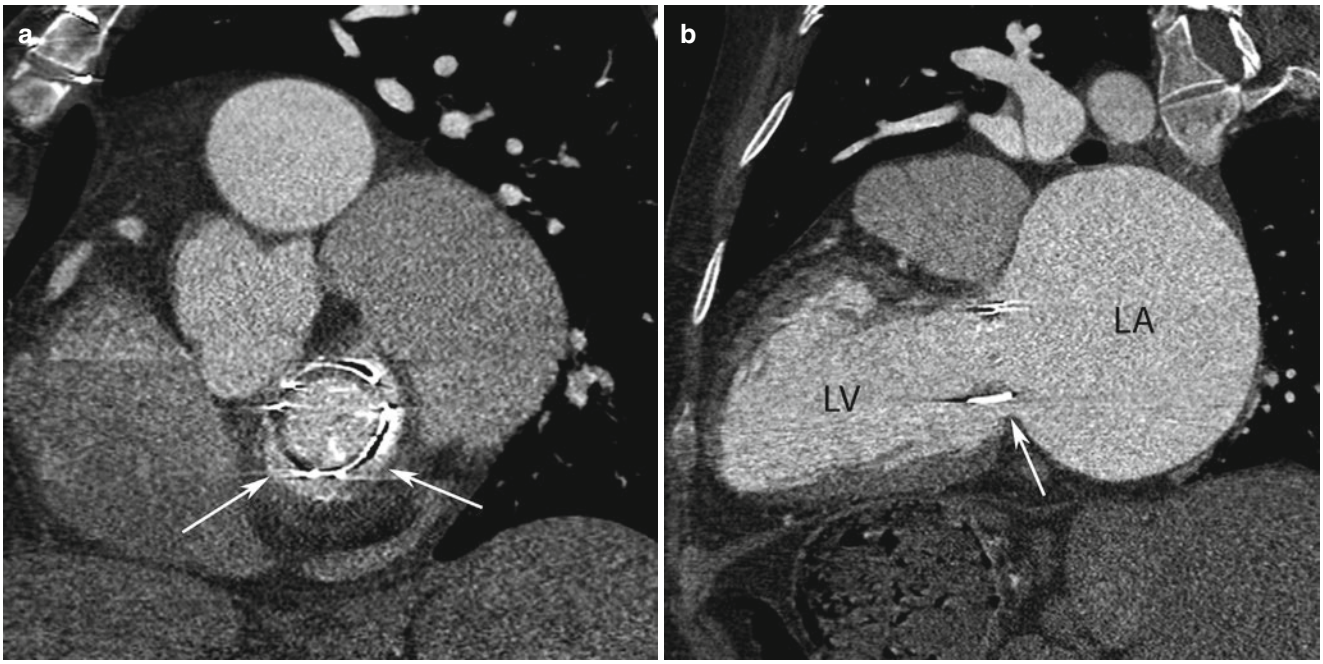

Fig. 18.8 Mitral valve paravalvular leak. Short-axis (**a**) and paraseptal long-axis (**b**) CT angiography (CTA) images show a rim of contrast (*arrows*) along the inferior and outer mitral apparatus. A paravalvular leak is abnormal blood flow around a prosthetic valve due to incomplete sealing. Mild paravalvular regurgitation or leak is common following surgery and is generally clinically insignificant [6]. It rarely presents with heart failure or anemia, which require surgical or endovascular closure. Leaks may occur from endocarditis, improper valve implantation, or valve dehiscence [7]. *LA* left atrium, *LV* left ventricle

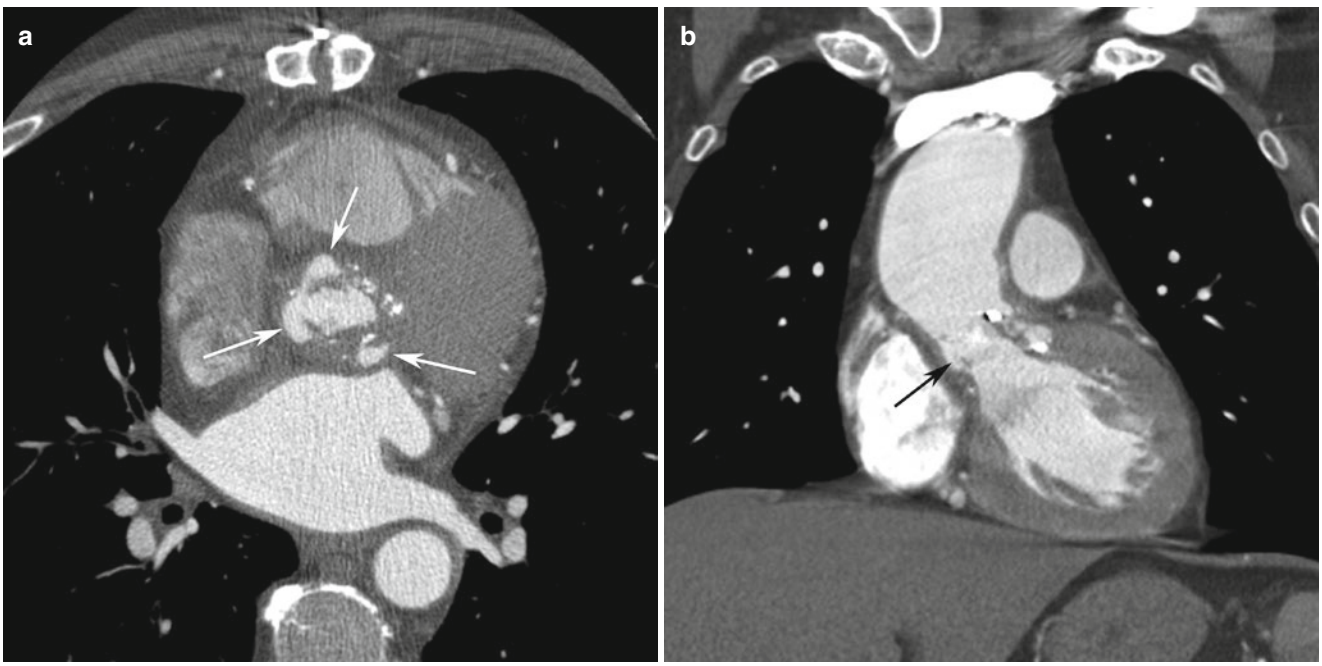

Fig. 18.9 Paravalvular leak and dehiscence secondary to endocarditis. Axial (**a**) and coronal (**b**) CTA images show contrast (*arrows*) flowing around the bioprosthetic aortic valve. Separation of the aortic valve from the aortic annulus indicates valve dehiscence. Aortic valve dehiscence occurs in patients with endocarditis, ascending aortic aneurysms, and degenerative regurgitation [8]; it generally requires surgical correction

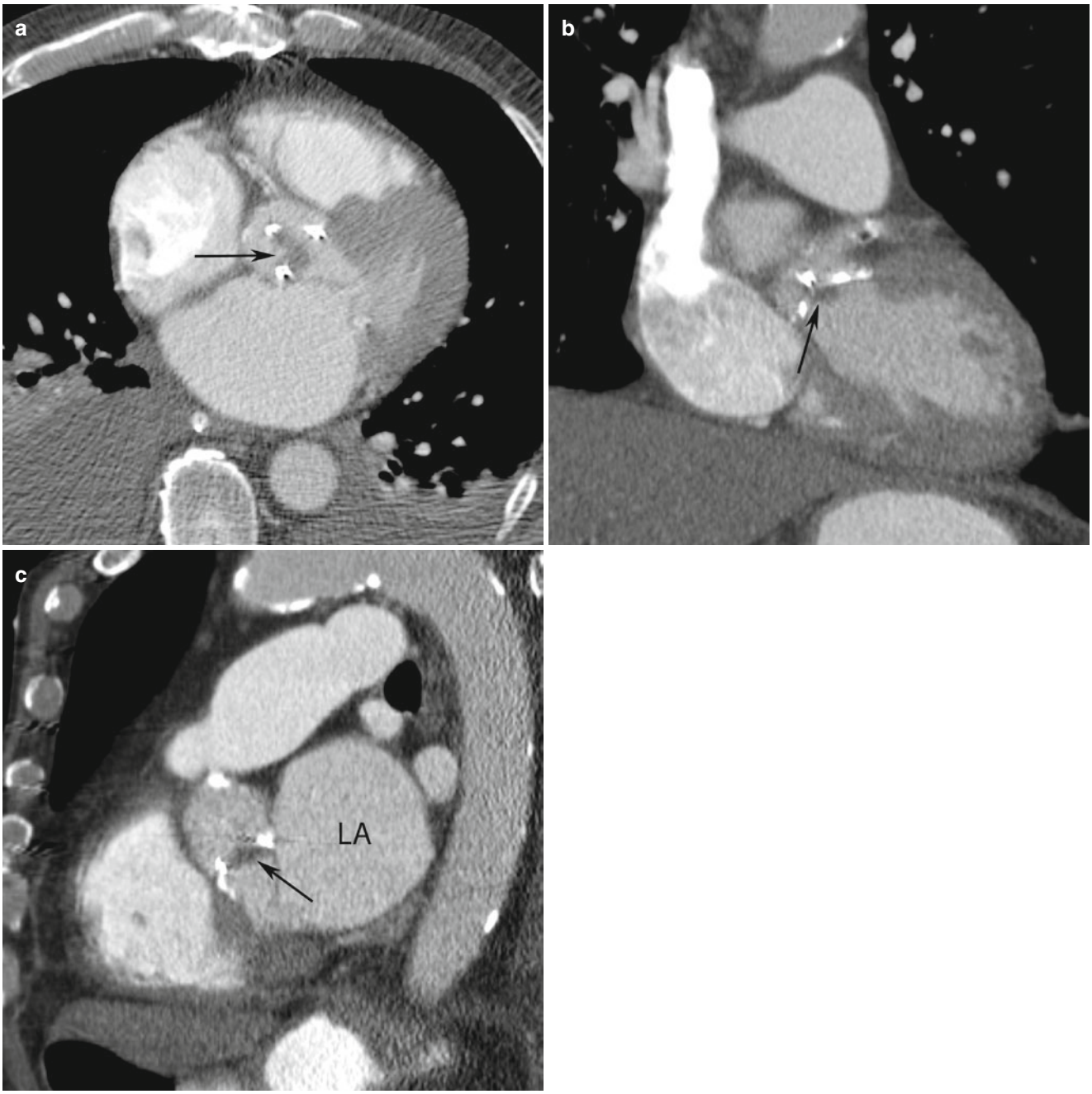

Fig. 18.10 Prosthetic valve endocarditis (PVE). Axial (**a**), coronal (**b**), and sagittal (**c**) contrast-enhanced CT images show a mechanical aortic valve with central low-density vegetation (*arrows*). The vegetation was not apparent on initial transthoracic echocardiography because of acoustic shadowing from the prosthetic valve. PVE can happen at any time following valvular surgery, but is most common during the first 5 years [4]. Early PVE (<2 months following surgery) is generally caused by *Staphyloccoccus epidermidis* or *S. aureus* infection from perioperative contamination [4]. Late PVE (>2 months following surgery) resembles native valve endocarditis and is usually caused by streptococcal species [4]. When clinical concern for endocarditis is high, gated CT may be useful for diagnosing or excluding endocarditis, given its high sensitivity (97%) and specificity (88%) [9]. These images show the most common CT appearance of a vegetation: a small, round, hypodense mass (*arrows*), which is usually located on the ventricular side of the prosthetic valve [4, 9]. *LA* left atrium

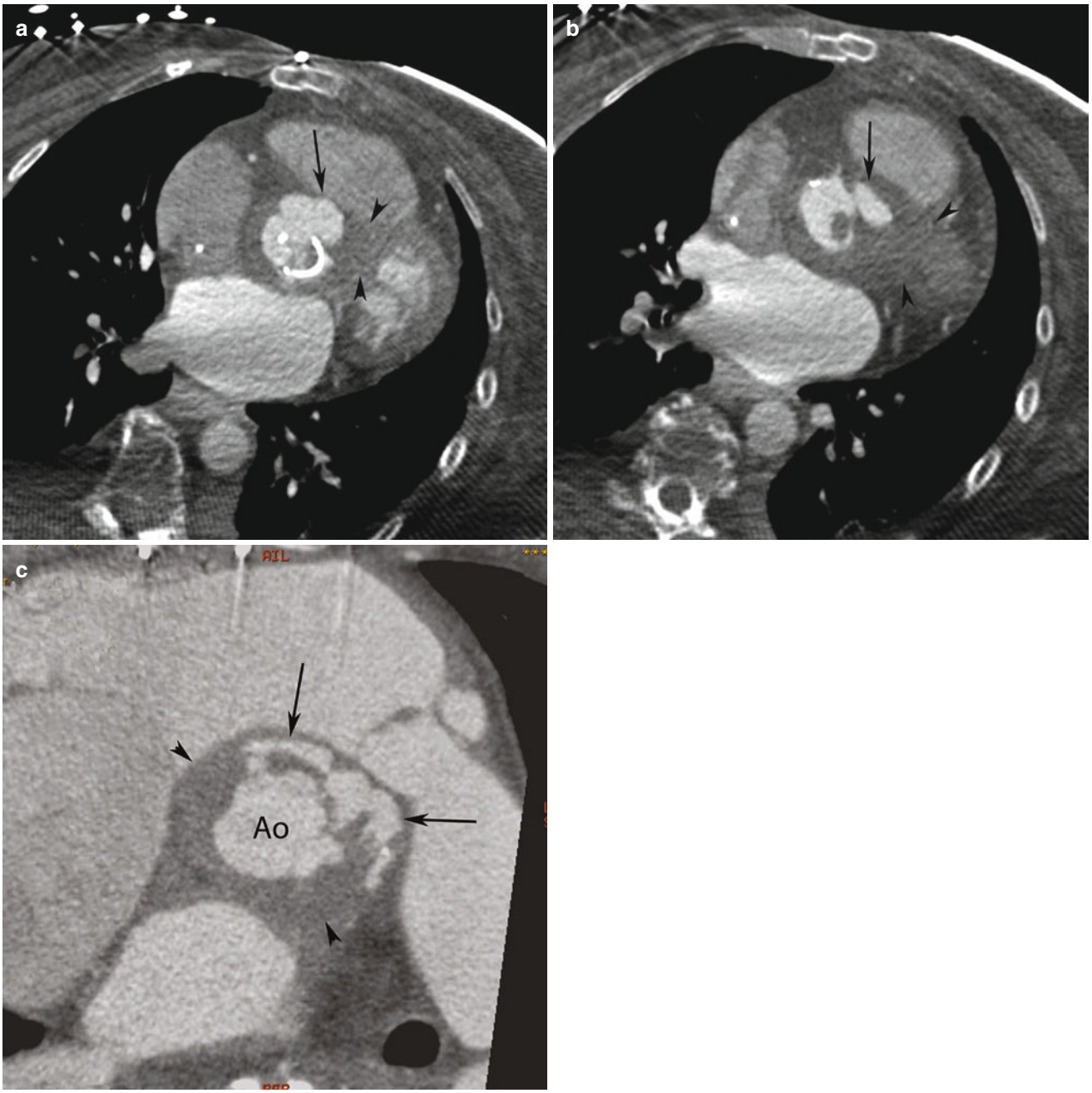

Fig. 18.11 Paravalvular abscess and endocarditis. (**a**, **b**) Axial contrast-enhanced CTA images show a focal outpouching of contrast (*arrows*) and associated periaortic soft-tissue thickening (*arrowheads*) extending into the intervalvular fibrosa. (**c**) A double oblique image from a second patient shows thickening of the aortic root (*arrowheads*) and an extraluminal contrast collection (*arrows*). Aortic root abscesses are identified by soft-tissue thickening surrounding the aortic root, with associated inflammatory fat stranding [4]. Foci of air are seen rarely, in cases with gas-forming organisms. *Ao* aorta

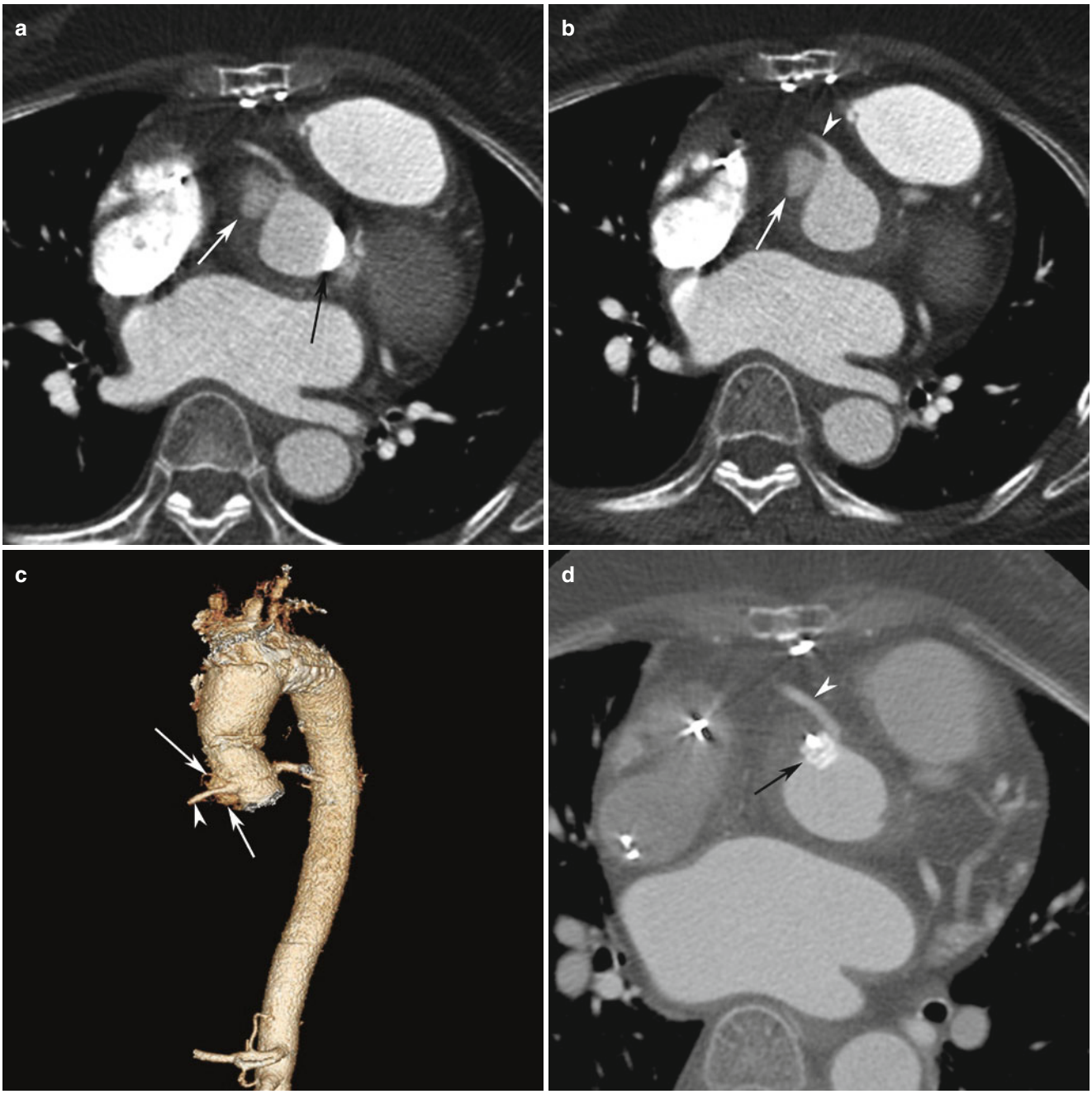

Fig. 18.12 Aortic valve pseudoaneurysm. Axial CTA (**a**, **b**) and a volume-rendered image (**c**) show an outpouching of contrast (*white arrows*) with a narrow neck adjacent to the right coronary artery ostium implantation site (*arrowhead*) in a patient who had undergone a Bentall procedure (aortic valve and aortic root replacement). Note the adjacent mechanical aortic valve (*black arrow*). After treatment with a catheter-delivered occluder device (*black arrow*), axial CTA (**d**) shows lack of contrast filling of the pseudoaneurysm. Pseudoaneurysms are most commonly seen in patients who have undergone aortic arch and valve replacement. Aneurysms can develop at the aortic annulus, proximal or distal anastomotic sites, or (as in this case) at the coronary anastomosis [4]. Surgery is generally considered the treatment of choice for aortic pseudoaneurysms complicating valve surgery [10]

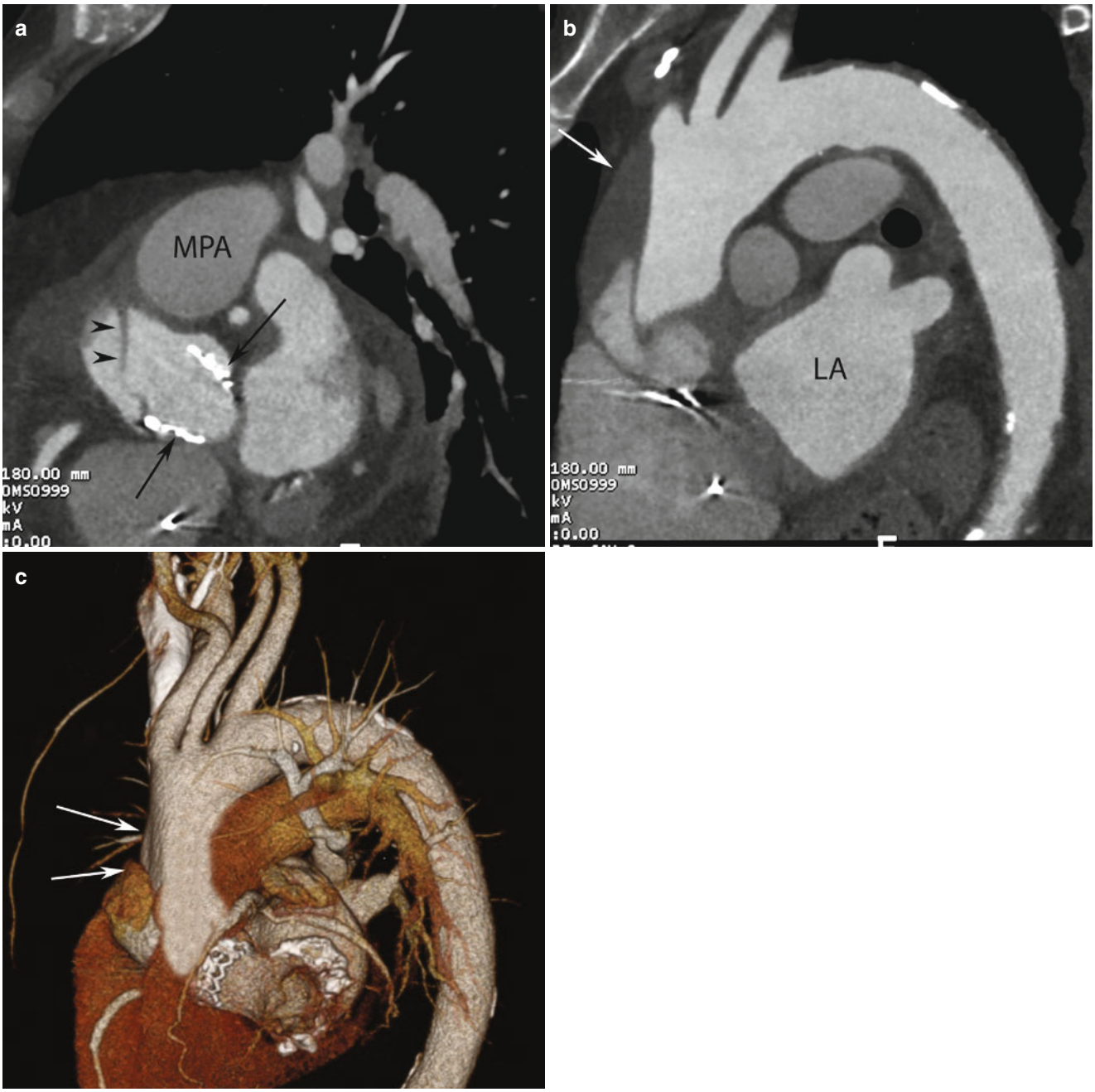

Fig. 18.13 Type A aortic dissection following TAVR. Oblique sagittal CTA images (**a** and **b**) and a volume-rendered image (**c**) show a Stanford type A aortic dissection (*black arrowheads* showing intimal flap) beginning just distal to a transcatheter-placed aortic valve (*black arrows*). There is partial thrombosis of the false lumen (*white arrows* in **b** and **c**). Other potential complications of TAVR include incorrect valve sizing with paravalvular regurgitation, incomplete valve expansion due to adjacent native calcified leaflets, pseudoaneurysm, or potentially device embolization. *LA* left atrium, *MPA* main pulmonary artery.

Pacemakers, Implantable Cardioverter Defibrillators, and Other Electrophysiologic Devices

Normal Appearance of Pacemakers and ICDs

Transvenous pacemakers, ICDs, and cardiac resynchronization therapy (CRT) devices are commonly seen on CT (Fig. 18.14). The number of leads should be described by their location and pacing capabilities (i.e., single-chamber, dual-chamber, or biventricular). For example, single-chamber pacing is identified by a single lead within the right atrial appendage or right ventricle. Dual-chamber pacing, used to coordinate contraction of the right atrium and right ventricle, is identified by leads in the right atrial appendage and right ventricle. Biventricular pacing adds a third lead to pace the left ventricle.

Occasionally, in the setting of congenital heart disease or aberrant anatomy such as a persistent left superior vena cava, leads will take a circuitous route (Fig. 18.15). It is also not uncommon to image epicardial pacemakers and ICDs that were inserted at the time of cardiac surgery or before the percutaneous transvenous approach was widely adopted (Fig. 18.16).

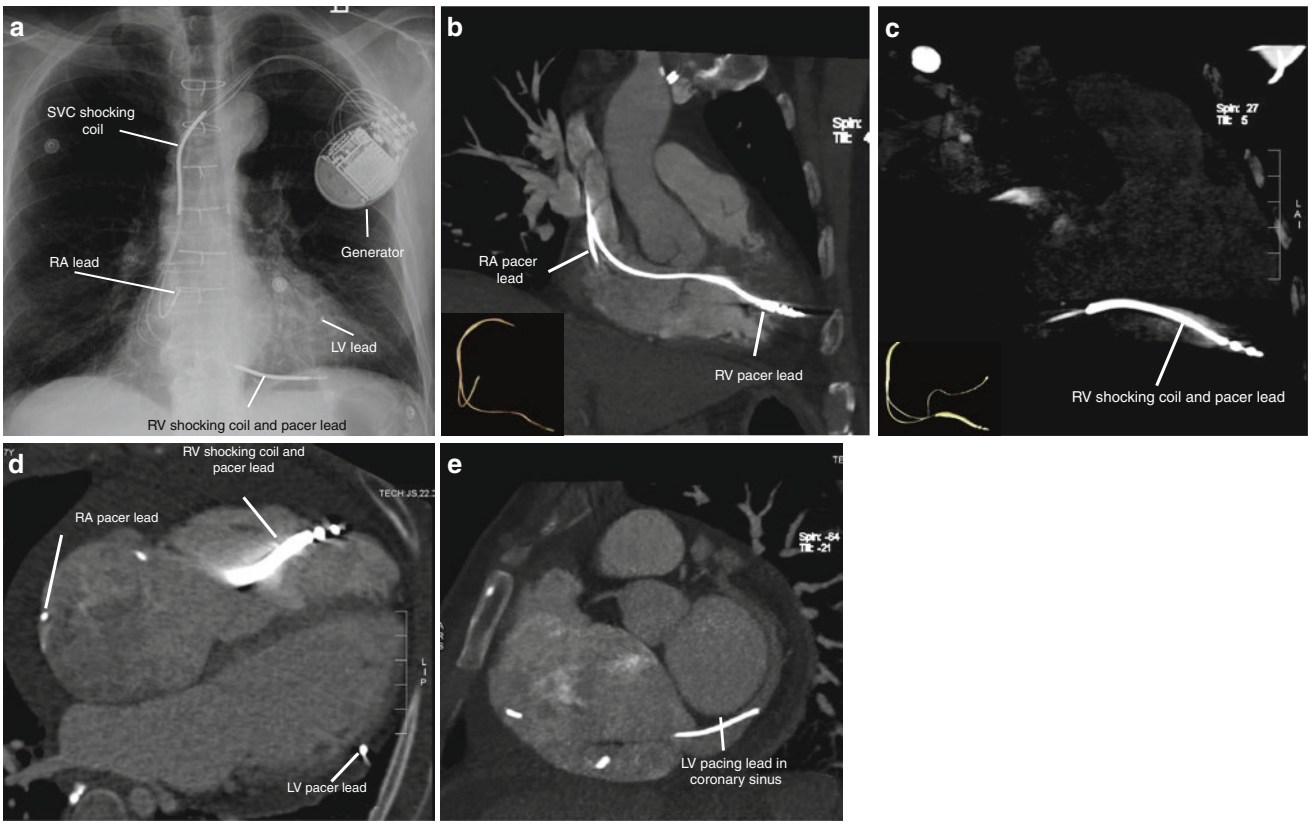

Fig. 18.14 Normal appearance of pacemaker and ICD. (**a**) The basic components of a combined biventricular pacer-ICD system. It is often easiest to get the "lay of the land" and determine lead location by looking at the scout image or a recent chest radiograph before interrogating the CT dataset. The generator, which houses software, hardware, and a lithium iodide battery, produces impulses that travel to the heart by way of one to three pacemaker or ICD leads. ICDs are distinguished from pacemakers by their thick, radioopaque shock coils surrounding the lead in the right ventricle and occasionally a lead at the brachiocephalic vein/superior vena cava (SVC) junction [11–13]. Leads are secured by passive or active fixation [12]. The number of leads should be described by their location and pacing capabilities (i.e., single-chamber, dual-chamber, or biventricular). (**b**) Dual-chamber pacing is used to coordinate contraction of the right atrium and right ventricle and is identified by leads in the right atrial (RA) appendage and right ventricle (RV). (**c**, **d**) Biventricular pacing (also called CRT) adds a third lead to pace the left ventricle (LV). (**e**) The left ventricular lead is usually advanced through the coronary sinus and positioned in a coronary vein that drains the posterolateral wall to pace the LV [11]

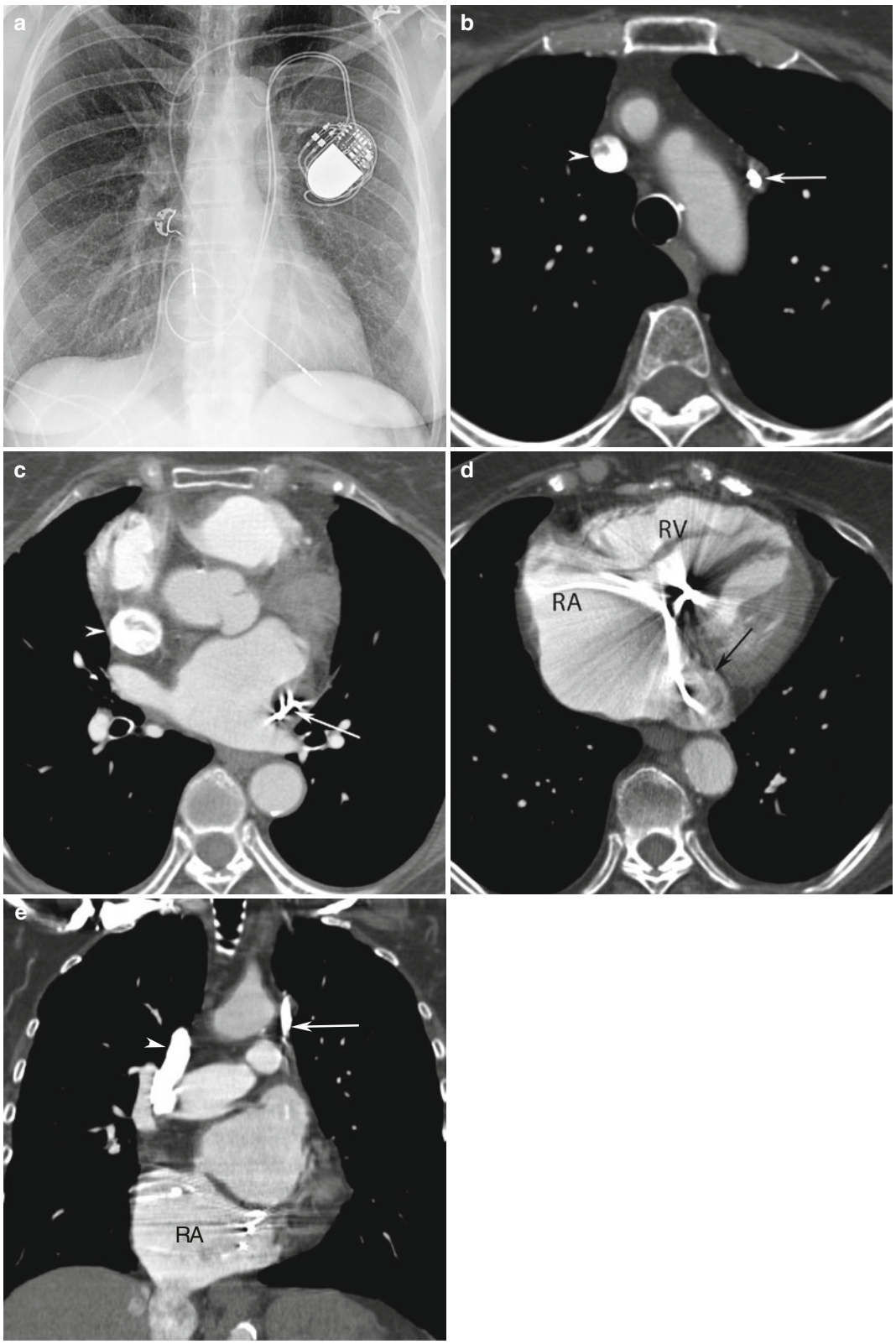

Fig. 18.15 Pacemaker leads entering the right heart from a persistent left superior vena cava. (**a**) Frontal radiograph shows dual-chamber pacemaker leads coursing down the left side of the mediastinum. (**b**–**e**), Multiple axial and coronal contrast-enhanced CT images from the same patient show two pacemaker leads in a left superior vena cava (*white arrows*) and a normally positioned right superior vena cava with dense injected contrast (*white arrowhead*). The pacemaker leads enter the right atrium (RA) through an enlarged coronary sinus (*black arrow*). *RV* right ventricle

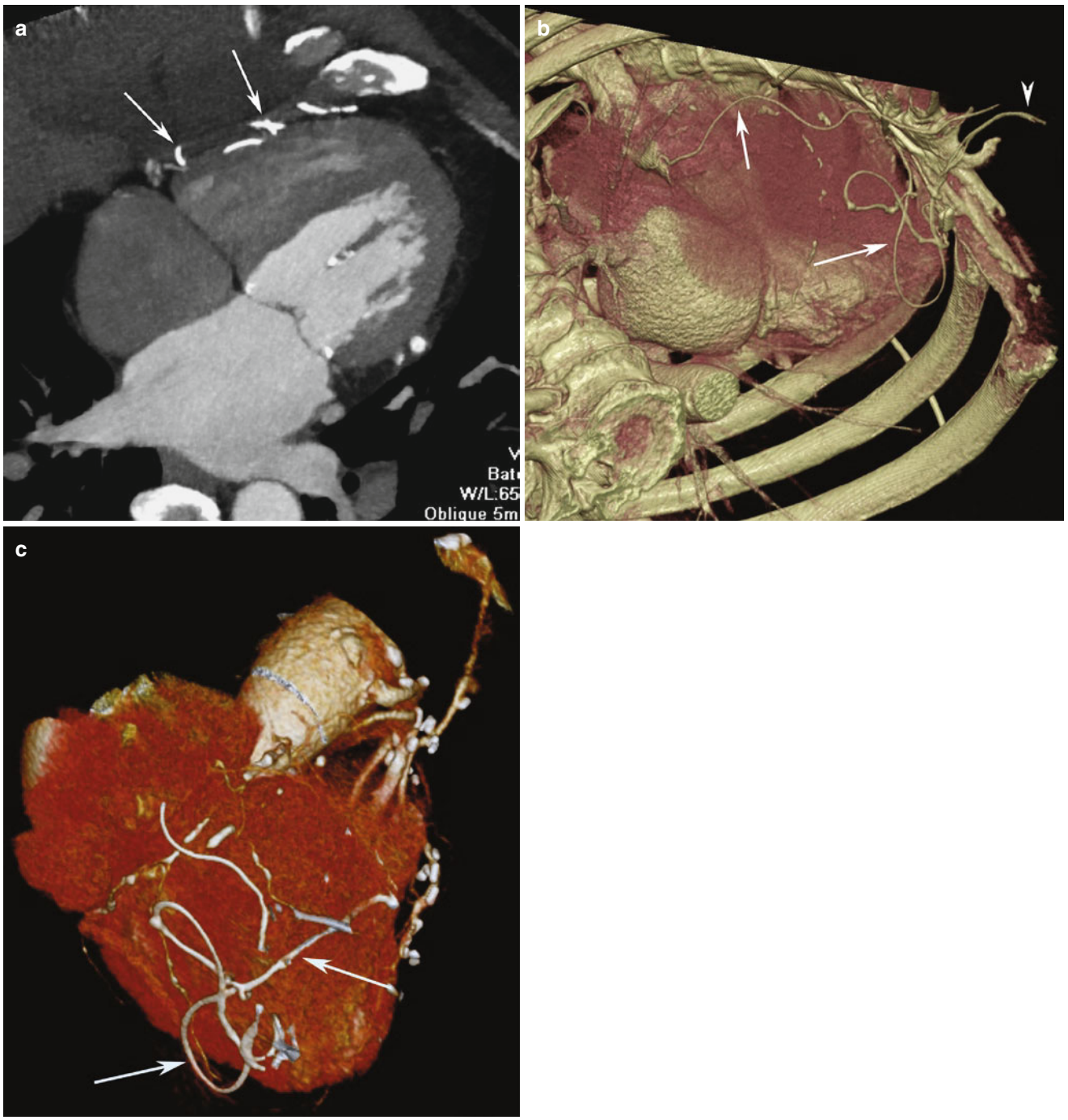

Fig. 18.16 Epicardial pacemaker devices. Four-chamber–view CTA (**a**) and volume-rendered images (**b** and **c**) show multiple epicardial pacer wires (*arrows*) on the surface of the heart from previous cardiac surgery. Normally these are pulled following surgery, but if resistance is felt, they are generally cut at the skin surface (*arrowhead* in **b**)

Implantable Loop Recorder

The implantable loop recorder (ILR) is a device used for long-term heart rate–activated or patient-activated monitoring for arrhythmia (Fig. 18.17). It is used in patients with infrequent, unexplained syncope in which an arrhythmia is suspected but is not likely to be captured by a 24-h or 30-day external monitor [14]. It has a battery life of 2–3 years, and because no wires are placed into the heart, complications are limited to local pain, hematoma, or subcutaneous infection.

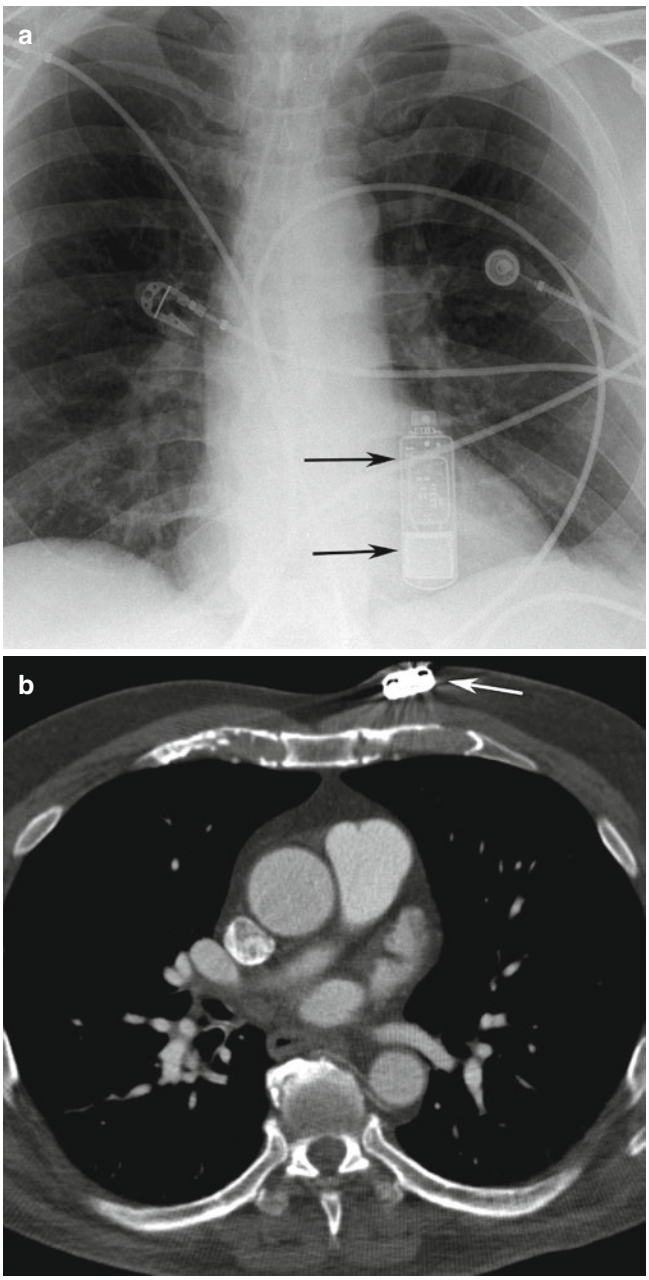

Fig. 18.17 (**a** and **b**) The implantable loop recorder (ILR) is implanted subcutaneously in the parasternal region (*arrows*)

Complications of Pacemakers and ICDs

Many complications are initially detected on chest radiography but can also be seen on CT. Acute complications of pacemaker or ICD insertion include pneumothorax, hemothorax, hardware infection (Fig. 18.18), unengaged terminal pin, myocardial perforation with or without pericardial tamponade (Fig. 18.19), or inappropriate lead placement (e.g., inferior vena cava, pulmonary artery, coronary sinus, or intra-arterial) (Fig. 18.20) [11–13, 15]. Chronic complications include lead or insulation damage, lead displacement, and twiddler's syndrome, dislodgment of leads resulting from the conscious or subconscious rotating of the generator in the subcutaneous tissues [12, 15].

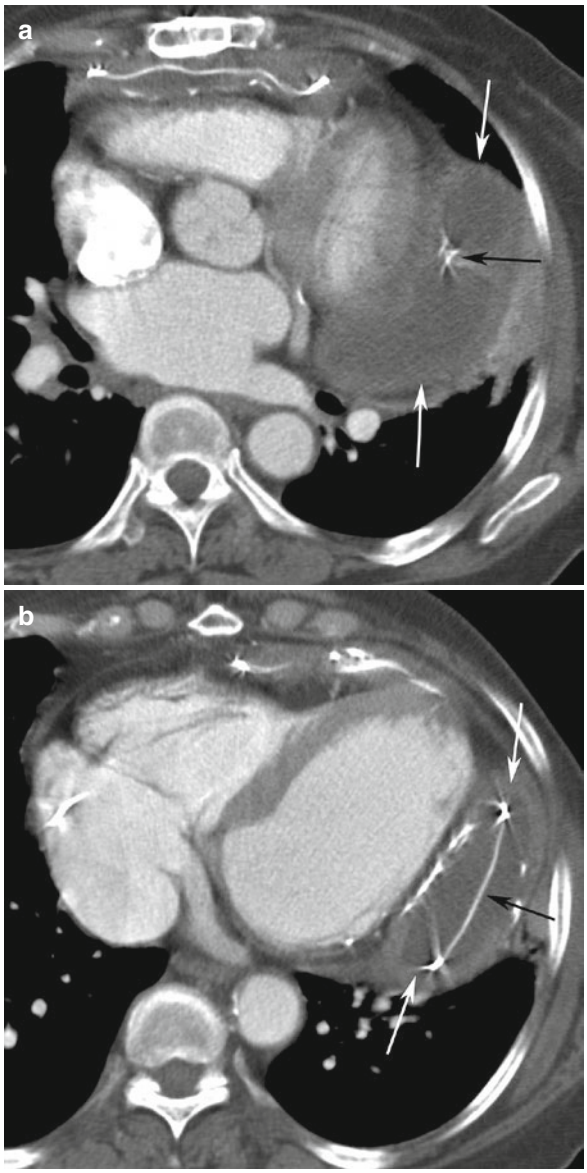

Fig. 18.18 Hardware-related abscess. Two axial contrast-enhanced CT images (**a**, **b**) show a rim-enhancing fluid collection (*white arrows*) surrounding a surgically placed left ventricular epicardial pacemaker lead (*black arrows*), consistent with abscess. More commonly, infection or sterile inflammation occurs in the subcutaneous pouch due to skin contamination at the time of implantation [15]

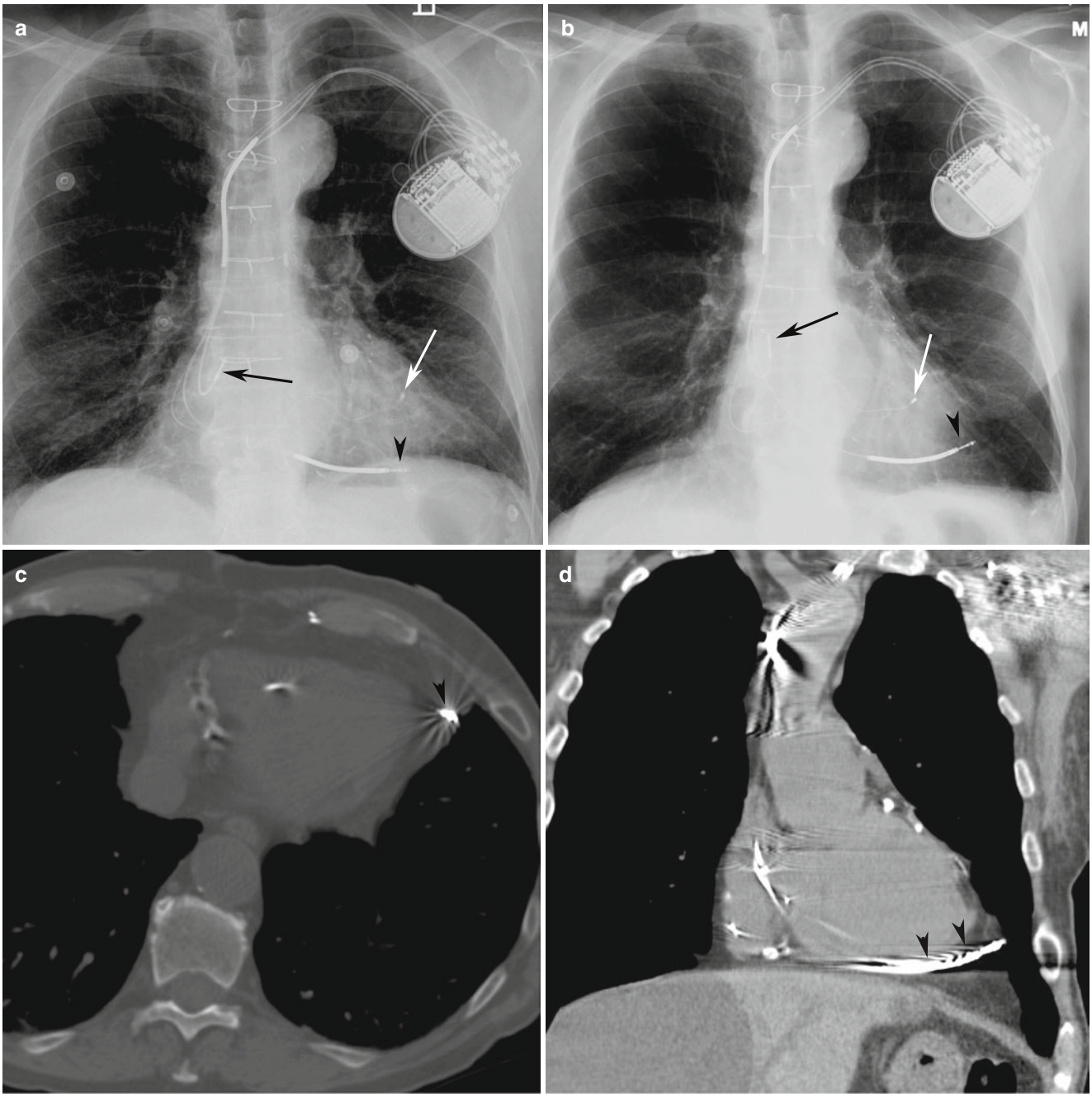

Fig. 18.19 Myocardial perforation. Initial radiograph (**a**) shows a biventricular pacemaker/ICD with a right atrial lead (*black arrow*), right ventricular lead (*black arrowhead*), and left ventricular lead (*white arrow*). A follow-up radiograph (**b**) shows migration of the right ventricular lead (*black arrowhead*) superiorly and laterally. The right atrial lead (*black arrow*) and left ventricular lead (*white arrow*) are unchanged. Axial (**c**) and coronal (**d**) CT images show the right ventricular lead (*black arrowheads*) projecting beyond the myocardium into the mediastinal fat, indicating myocardial perforation. Importantly, there is no pericardial hemorrhage. The overall rate of myocardial perforation through the right atrium or right ventricle likely ranges from 1% to 15%; it is commonly asymptomatic [16, 17]

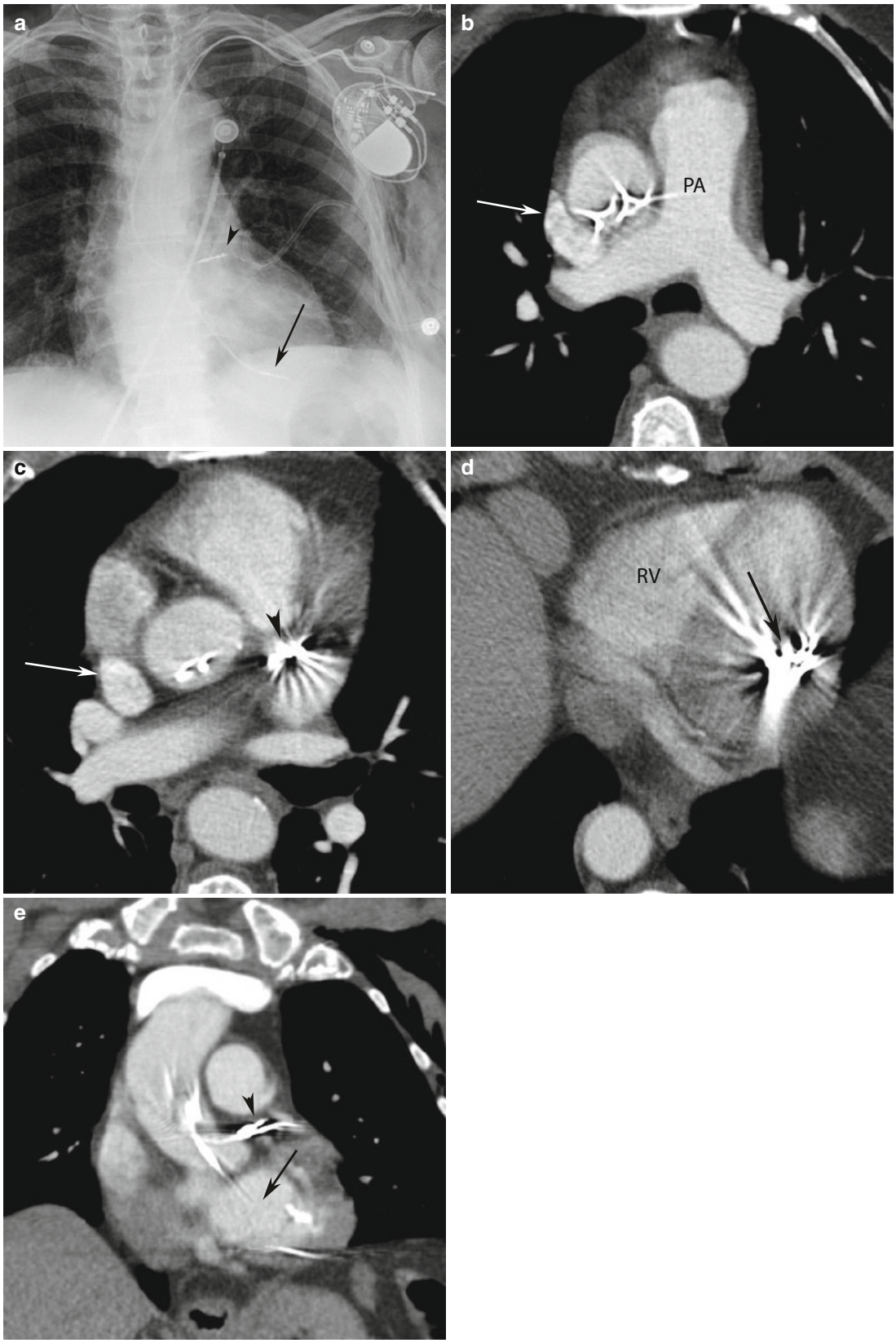

Fig. 18.20 Arterial placement of leads. (**a**) An initial radiograph following pacemaker insertion shows the pacemaker leads (*arrow* and *arrowhead*) coursing more medial than usual, raising concern for arterial puncture. (**b**–**e**) Contrast-enhanced axial and coronal CT images show two pacemaker leads in the ascending aorta. The superior lead (*arrowhead*) terminates in the left main coronary artery, and the inferior lead (*black arrow*) terminates in the left ventricle. The *white arrow* indicates the superior vena cava. *PA* main pulmonary artery, *RV* right ventricle

Closure Devices

Atrial Septal Defect and Ventricular Septal Defect Closure Devices

Atrial septal defect (ASD) or ventricular septal defect (VSD) can manifest in isolation or in association with other congenital heart defects. If the defect is large, it can cause right heart volume overload, pulmonary hypertension, and eventually shunt reversal with Eisenmenger syndrome. The measurement of the pulmonary to systemic flow (Qp/Qs) is important, as it helps guide therapy decisions. The asymptomatic patient with a normal pulmonary vascular resistance and an elevated ratio (Qp/Qs > 1.5) is generally treated [19]. Most ostium secundum ASDs are closed percutaneously, whereas most ventricular septal defects are closed surgically.

The most commonly used device to close an ASD is the Amplatzer Septal Occluder (ASO) device (Fig. 18.21a–d) (St. Jude Medical; St. Paul, MN). Other occluder devices, such as the CardioSEAL (Fig. 18.21e) (NMT Medical; Boston, MA) and Gore HELEX septal occluder (Fig. 18.21f) (Gore Medical; Flagstaff, AZ) are used by certain cardiologists and in select patient populations, such as those with small-diameter ASDs. The Amplatzer muscular VSD occluder is used to percutaneously close a VSD in patients with high surgical risk.

The overall complication rate for these occluder devices is low [18]. Complications of septal occluder devices that can be detected with imaging include malposition or dislodgment, residual shunt, thrombus formation with stroke, pericardial hemorrhage, or erosion through the atrial wall into the aortic root [18, 20].

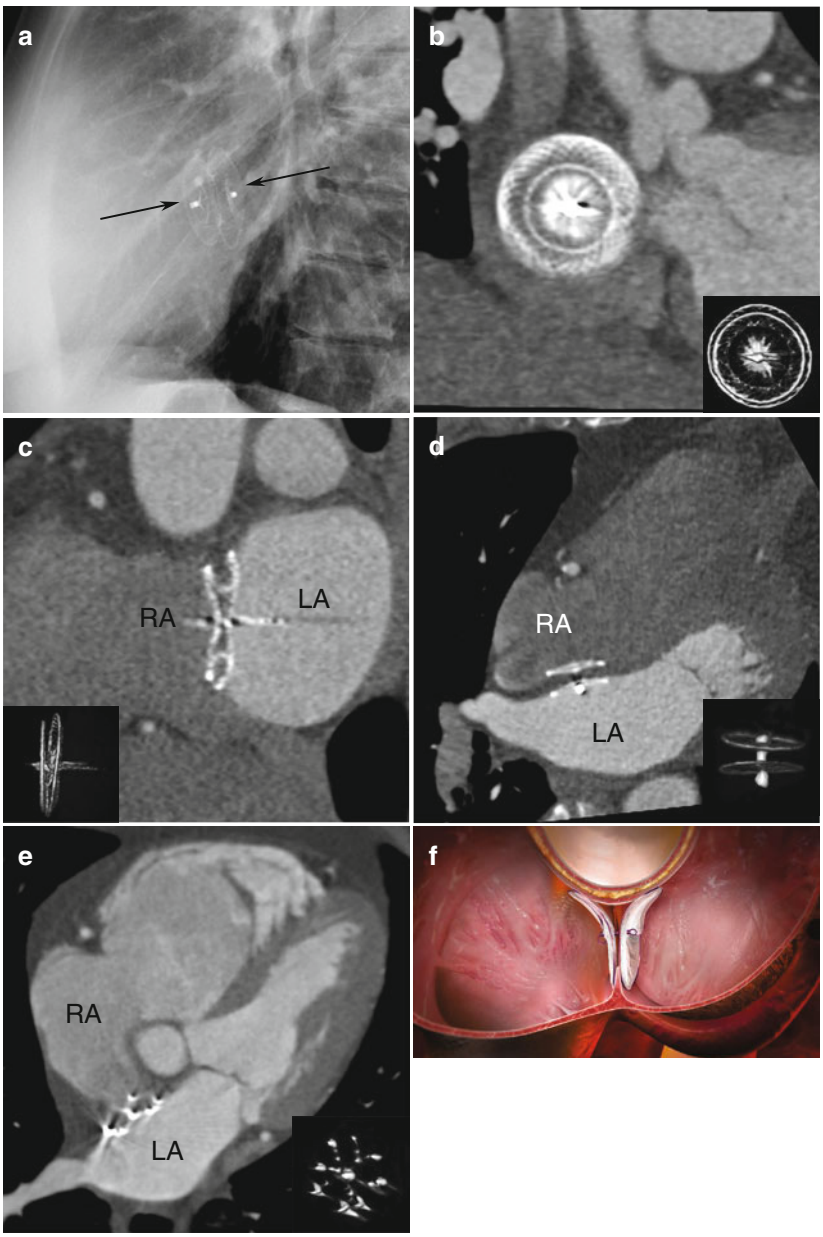

Fig. 18.21 Atrial septal defect (ASD) and ventricular septal defect (VSD) closure devices. (**a**) A lateral radiograph shows an Amplatzer Septal Occluder (ASO) device (*black arrows*) (St. Jude Medical; St. Paul, MN), the most commonly used device to close an ASD. (**b–d**) The ASO is a self-expanding device that has two flat discs with a connecting waist. The ASO is composed of a nitinol wire mesh with sewn-in fabric that stimulates tissue growth and septal closure [18]. The waist diameter corresponds to the atrial septal defect diameter. (**c** and **d** show different device sizes, with **d** being larger.) (**e**) CardioSEAL (NMT Medical; Boston, MA). (**f**), Gore HELEX septal occluder (Gore Medical; Flagstaff, AZ). *LA* left atrium, *RA* right atrium. (Figure **f** *courtesy of* Gore Medical, Flagstaff, AZ)

Atrial Appendage Devices

Atrial fibrillation is the most common cardiac arrhythmia, with embolic stroke being the most relevant complication [21]. Oral anticoagulation therapy with warfarin is the treatment of choice in patients at risk for thromboembolic disease. If anticoagulation therapy fails or is not tolerated, surgical left atrial appendage (LAA) exclusion has traditionally been the treatment of choice. Recently, less invasive techniques have been developed to address this problem, including percutaneous occlusion with the Amplatzer cardiac plug (St. Jude Medical; St. Paul, MN) or WATCHMAN device (Aritech, Minneapolis, MN) (Fig. 18.22) and percutaneous suture ligation with the LARIAT device (SentreHEART; Redwood City, CA) (Fig. 18.23) [21, 22]. On the pre-procedure CT, it is important to report the orifice size (diameter and perimeter), morphology, and orientation of the LAA to guide the interventionalist in properly sizing the device [22].

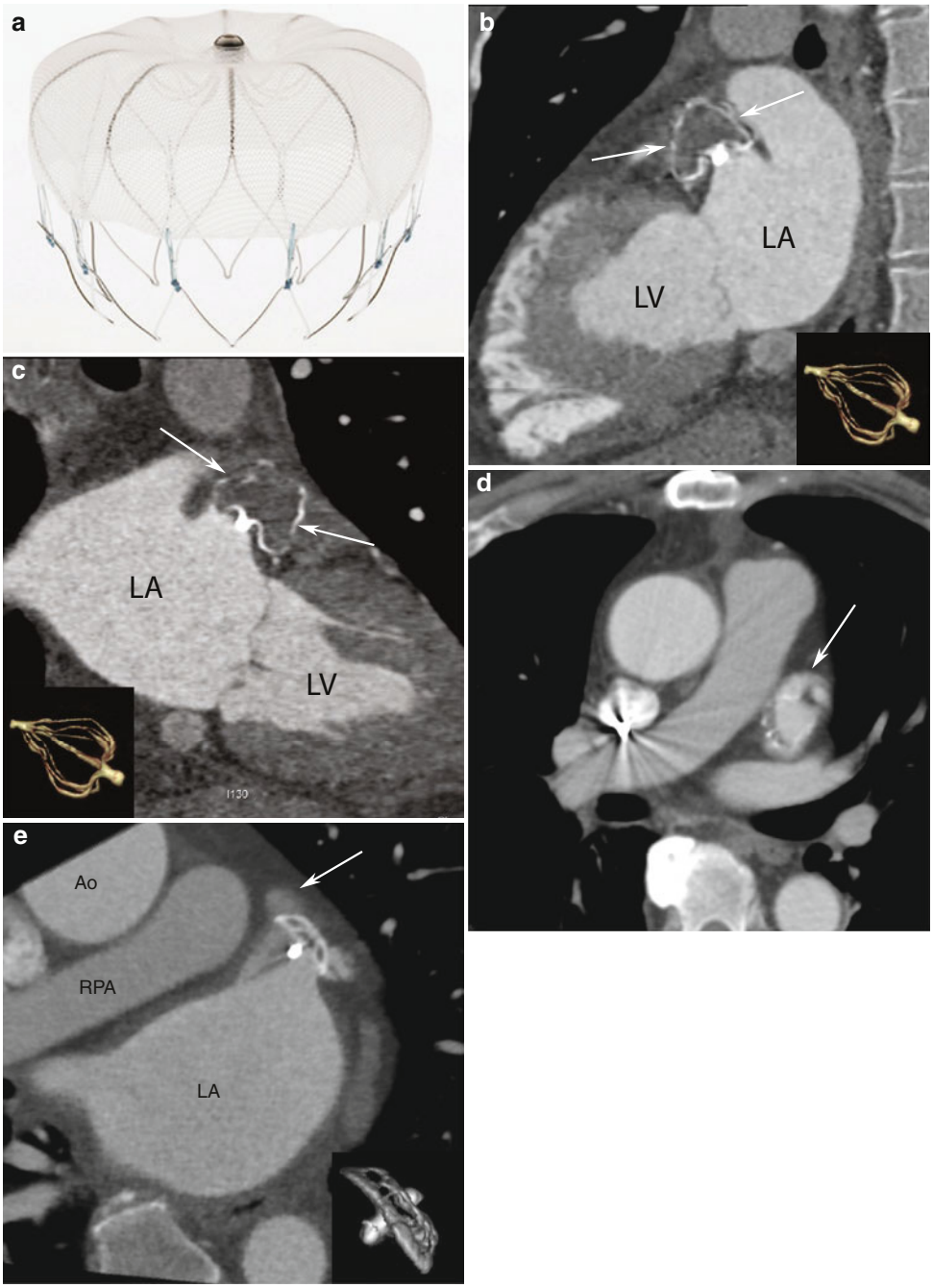

Fig. 18.22 (**a**) The WATCHMAN (Aritech, Minneapolis, MN) is a self-expanding device designed for closure of the left atrial appendage (LAA). (**b** and **c**) It is deployed just distal to the LAA orifice to prevent LAA thrombi from entering the systemic circulation. Fixation barbs anchor the device to the atrial wall. Complications of these devices include incomplete LAA occlusion. (**d**) (WATCHMAN) and (**e**) (Amplatzer occluder) show contrast within the LAA (*white arrows*), thrombus formation, device embolization, and pericardial hemorrhage. *Ao* aorta, *LA* left atrium, *LV* left ventricle, *RPA* right pulmonary artery. (A *courtesy of* Aritech, Minneapolis, MN)

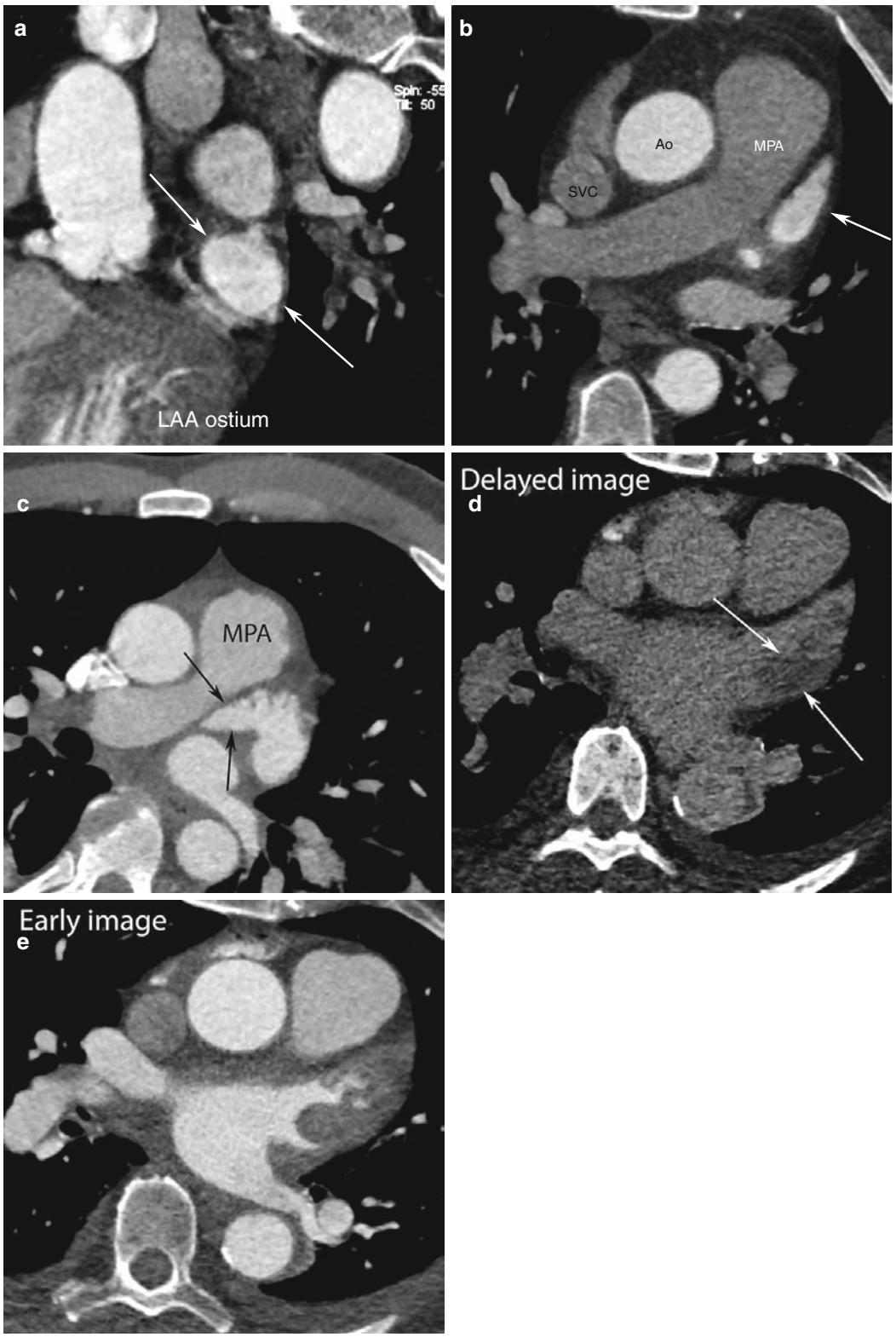

Fig. 18.23 The LARIAT procedure consists of four steps through percutaneous and endovascular access, with the result being snare capture of the LAA and suture ligation [21]. It is important to document the position and size of the LAA. (**a**) Double oblique measurements should be used to measure the LAA orifice size (*arrows*). (**b**) The LAA tip should be lateral to the main pulmonary artery (MPA) (*arrow*) in order to perform the LARIAT procedure. Several anatomic variants will exclude a patient from undergoing the LARIAT procedure. These include LAA width >40 mm, a posteriorly rotated heart, a superiorly directed LAA that lies behind the pulmonary trunk (**c**, *arrows*), and a bilobed or multilobed LAA in which lobes are in different planes exceeding a width of 40 mm [21]. (**d** and **e**) LAA thrombus (*white arrows*) is an additional exclusion criteria. *SVC* superior vena cava

Patent Ductus Arteriosus Closure Devices

The ductus arteriosus is a vascular structure that connects the proximal descending thoracic aorta with the proximal left pulmonary artery. In neonates, the ductus usually closes functionally by 24 h of life and anatomically at 1 month. If the opening persists beyond 3 months of life, it is referred to as a patent ductus arteriosus (PDA) [23]. PDA can be treated percutaneously, with coils or an Amplatzer duct occluder (Fig. 18.24), for example, or surgically with clipping [24].

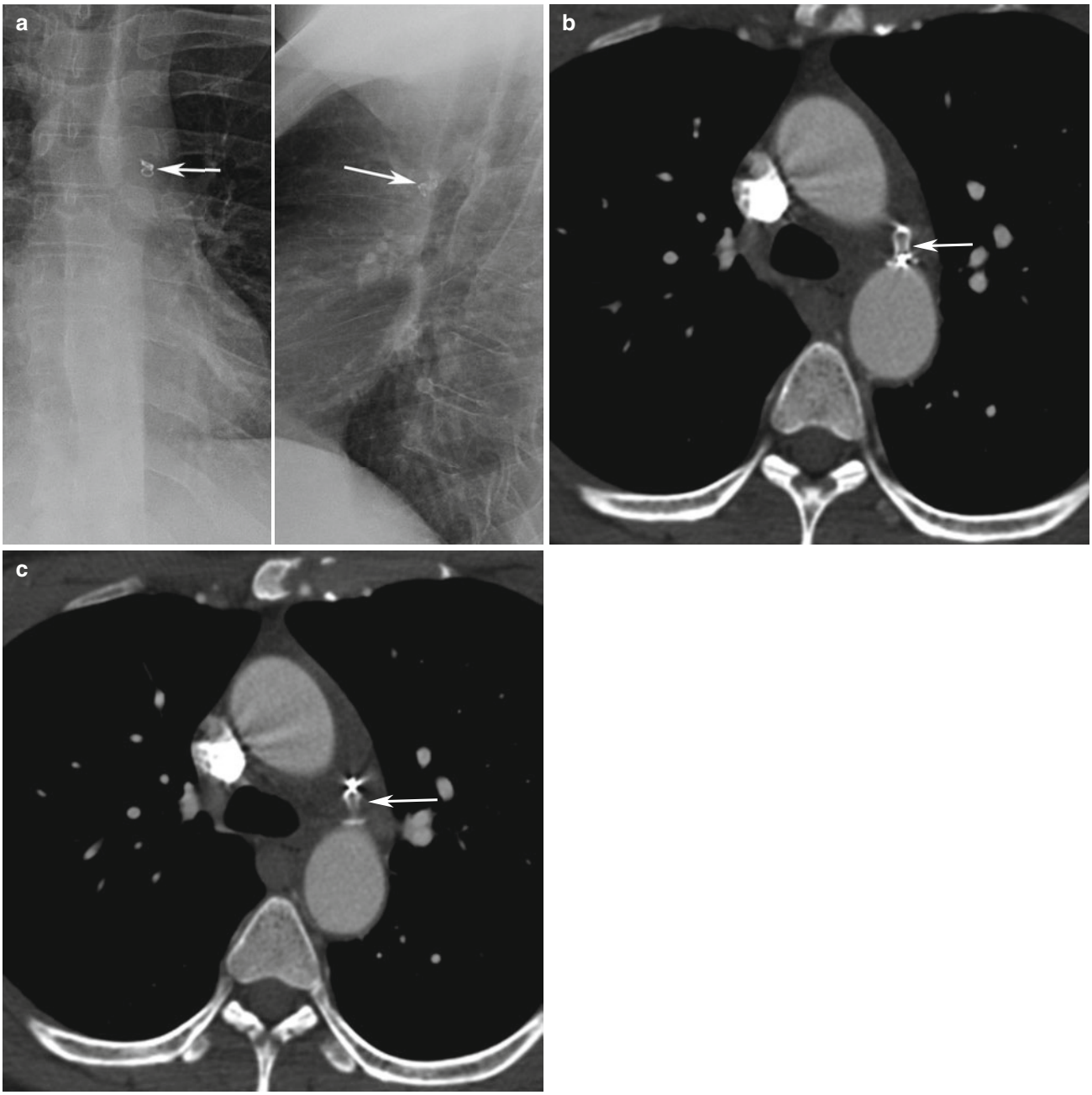

Fig. 18.24 Occluder device (*arrows*) used to close a patent ductus arteriosus. (**a**) Composite of frontal and lateral radiographs. (**b** and **c**) Contiguous axial contrast-enhanced CT images

Circulatory Assist Devices

Short-Term Circulatory Assist Devices

An intra-aortic balloon pump (Fig. 18.25) is a temporary device used to augment coronary artery perfusion in patients with acute cardiac failure resulting from myocardial infarction [25]. The predominant complications occur from balloon pump malposition. If the balloon is too proximal, it can occlude the great vessels, leading to stroke or upper extremity ischemia. If the balloon is too distal, it can occlude the mesenteric arteries (e.g., celiac, superior mesenteric artery) and cause bowel ischemia or can occlude the renal arteries, causing renal failure. Other complications of the balloon pump that can be detected by imaging include infection, aortic dissection, and hemorrhage [26].

The Impella Circulatory Support System (Abiomed; Danvers, MA) and TandemHeart (CardiacAssist; Pittsburgh, PA) use pumps to augment cardiac output (Fig. 18.26).

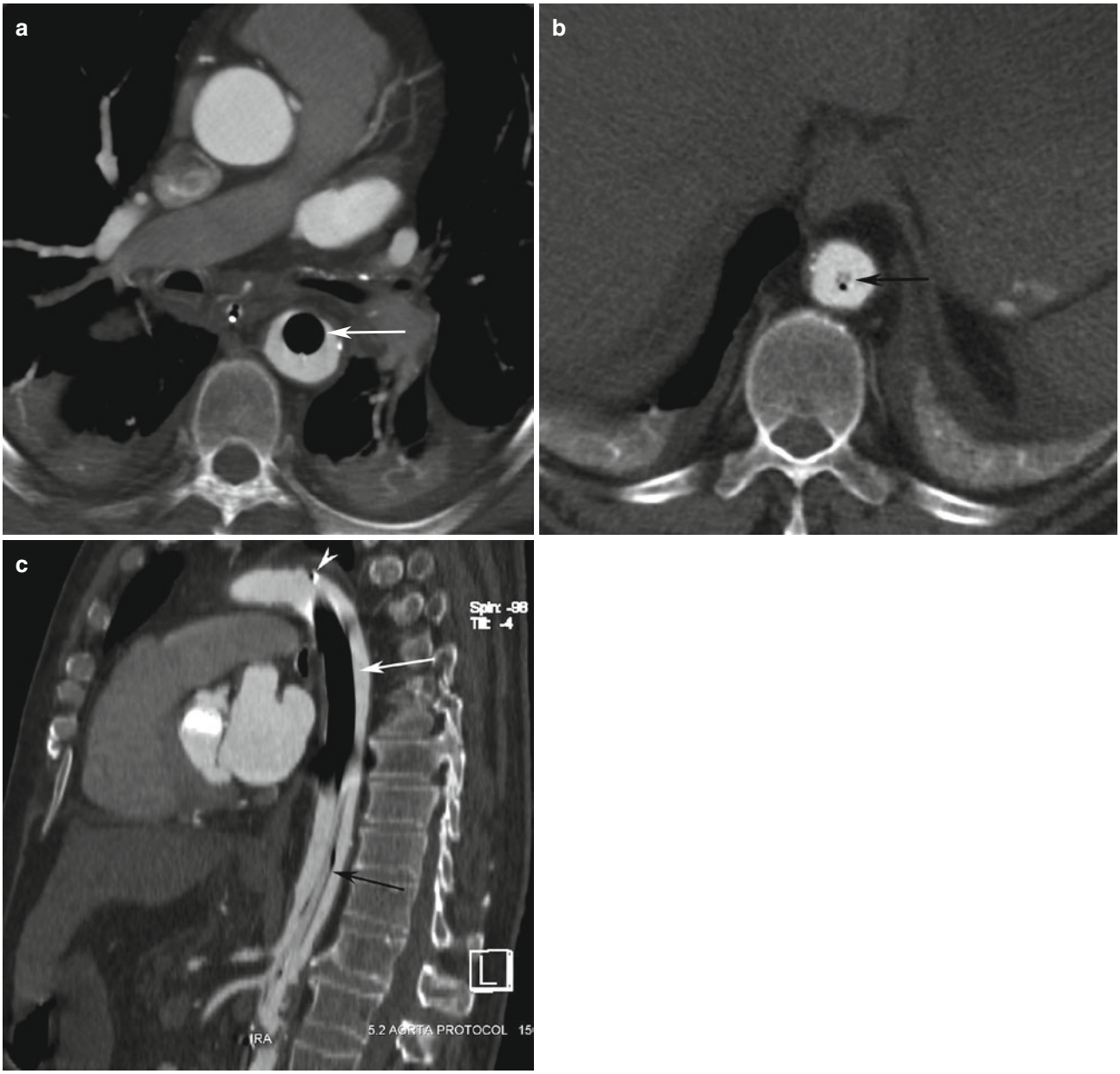

Fig. 18.25 Intra-aortic balloon pump. (**a**–**c**) The balloon inflates during ventricular diastole (*white arrows*) to increase pressure in the proximal aorta, which augments myocardial perfusion and decreases cardiac output. The balloon deflates (*black arrows*) during ventricular systole to reduce afterload, ventricular work, and oxygen consumption of the left ventricle [26, 27]. The tip of the balloon pump (*white arrowhead*) is radiodense. The predominant complications occur from balloon pump malposition; the ideal position of the balloon tip is about 2 to 4 cm distal to the left subclavian artery

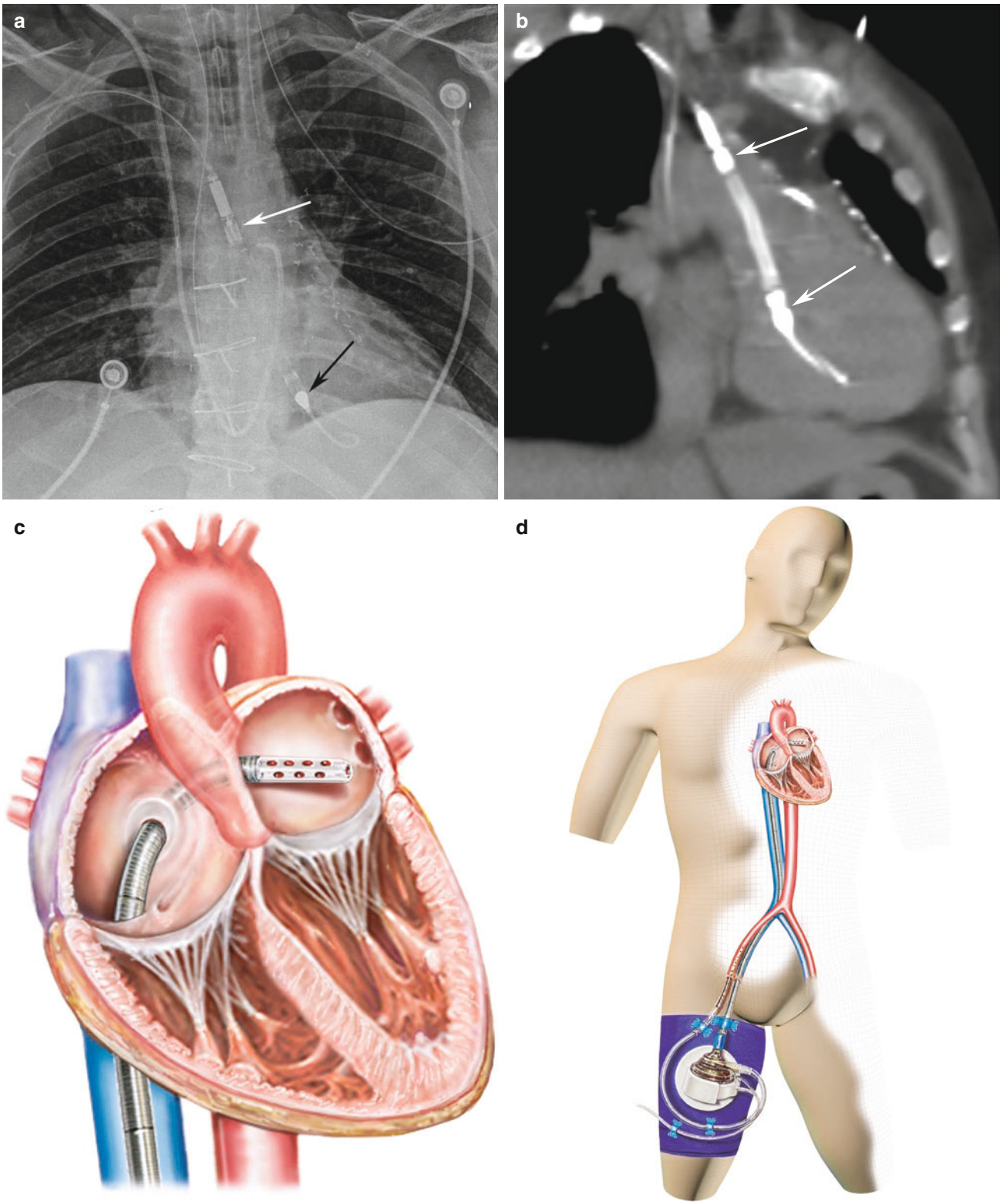

Fig. 18.26 Impella Circulatory Support System (Abiomed; Danvers, MA) and TandemHeart (CardiacAssist; Pittsburgh, PA). A frontal radiograph (**a**) and oblique, coronal noncontrast CT image (**b**) show the Impella 2.5 Circulatory Support System. This device is placed percutaneously through the femoral artery or carotid artery or surgically into the aorta and is advanced across the aortic valve into the left ventricle. It consists of a pump that draws blood through an inlet area (*black arrow*) near the catheter tip and expels blood from the catheter (*white arrow*) into the ascending aorta [28]. The pumping capacity is up to 2.5 L/min. The TandemHeart (**c** and **d**) is another short-term circulatory support system, which has a slightly different mechanism than the Impella device. The inflow cannula is inserted into the left atrium via a trans-septal puncture from the right atrium. Outflow cannulae are then introduced into the femoral arteries via arteriotomies. The TandemHeart centrifugal pump is capable of 5.0 L/min of cardiac output augmentation. (**c** and **d** *courtesy of* CardiacAssist, Inc., Pittsburgh, PA)

Long-Term Circulatory Assist Devices

Ventricular assist devices (Fig. 18.27) are used primarily in three settings: as a bridge to heart transplantation, as destination therapy (i.e., a permanent alternative in patients who cannot undergo heart transplantation), and in patients whose myocardial dysfunction is expected to recover (e.g., those with viral myocarditis or peripartum cardiomyopathy) [27, 30]. CT is complementary to echocardiography and should be used as a problem-solving tool if dysfunction of the left ventricular assist device (LVAD) is suspected (Fig. 18.28).

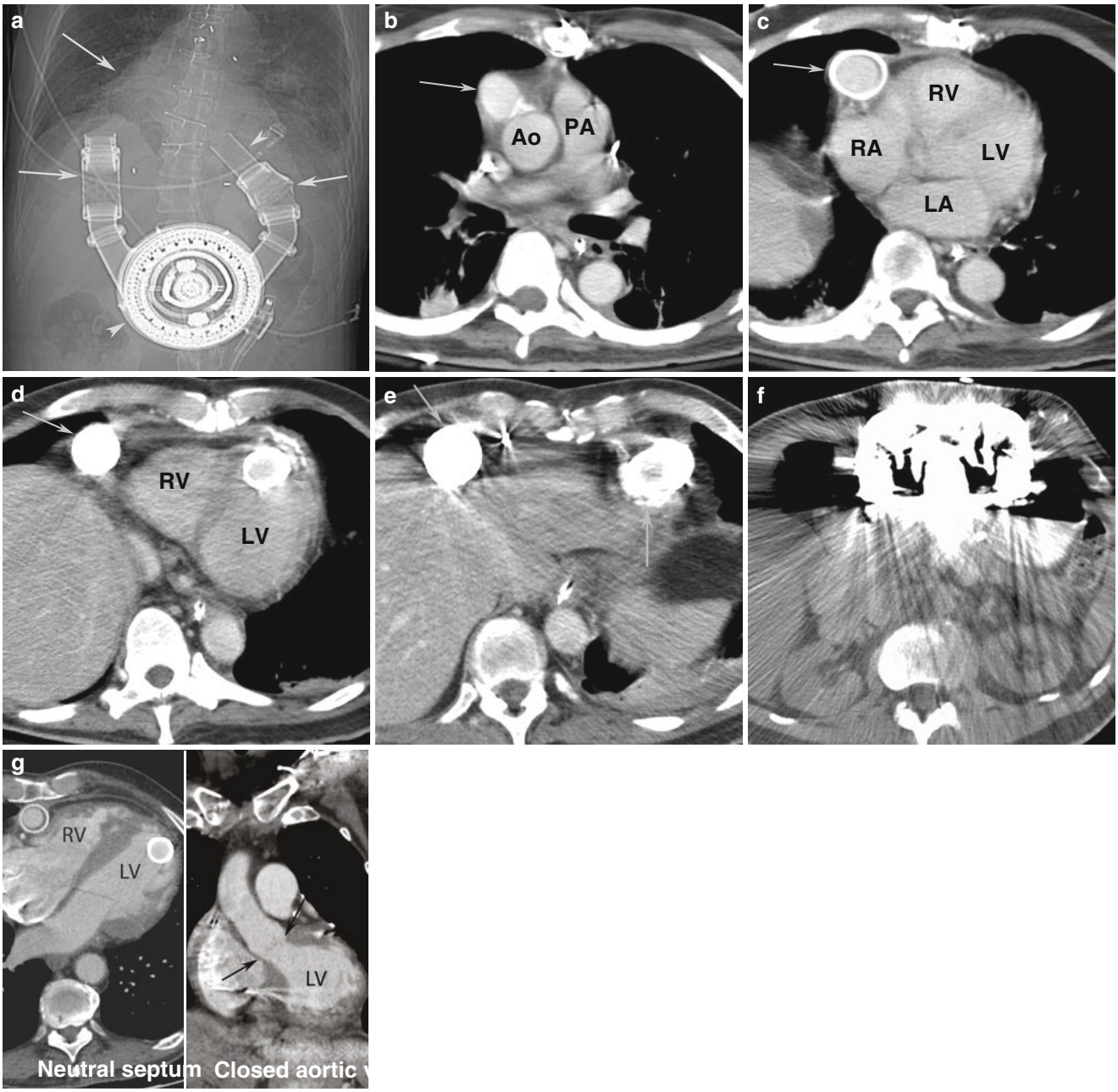

Fig. 18.27 Normal appearance of HeartMate XVE (Thoratec; Pleasanton, CA), a pulsatile left ventricular assist device (LVAD). Scout image (**a**) and contrast-enhanced axial CT images (**b–f**) show the normal appearance of a pulsatile LVAD device. Blood from the left ventricle (LV) enters the inflow cannula (*white arrowhead*) by way of the left ventricular apex. From the inflow cannula, blood is directed to the pump (*black arrowhead*). The pump (*black arrowhead*), which functions as the ventricular chamber, can be positioned intraabdominally, as in this case, or in a preperitoneal pocket in the left upper quadrant. The blood exits the pump and is directed to the ascending aorta (Ao) via the outflow cannula (*white arrow*). Often, the outflow cannula is invisible on radiography or scout CT images. Tubing (*see* **a**) containing the electrical cable and an air line connects the pump to the power source outside of the patient. This type of LVAD is unique in that it requires a patient to have a body surface area greater than 1.5 m^2 [29]. In a normally functioning LVAD, the inflow cannula should be in the left ventricle without obstruction or surrounding thrombus, the aortic valve should remain closed throughout the cardiac cycle, and the ventricular septum should remain in a neutral position (**g**) (*arrows on Closed aortic valve*) [29]. *LA* left atrium, *PA* main pulmonary artery, *RA* right atrium, *RV* right ventricle

The total artificial heart (Fig. 18.29) is designed for patients with biventricular dysfunction for whom other therapies have failed. It is used as a bridge to heart transplantation or as destination therapy in patients who cannot undergo heart transplantation. Similar to other circulatory assist devices, the total artificial heart is prone to complications including left lower lobe atelectasis or pneumonia, device infection, major vascular compression, hemorrhage, and fibrous adhesions developing around the device [31].

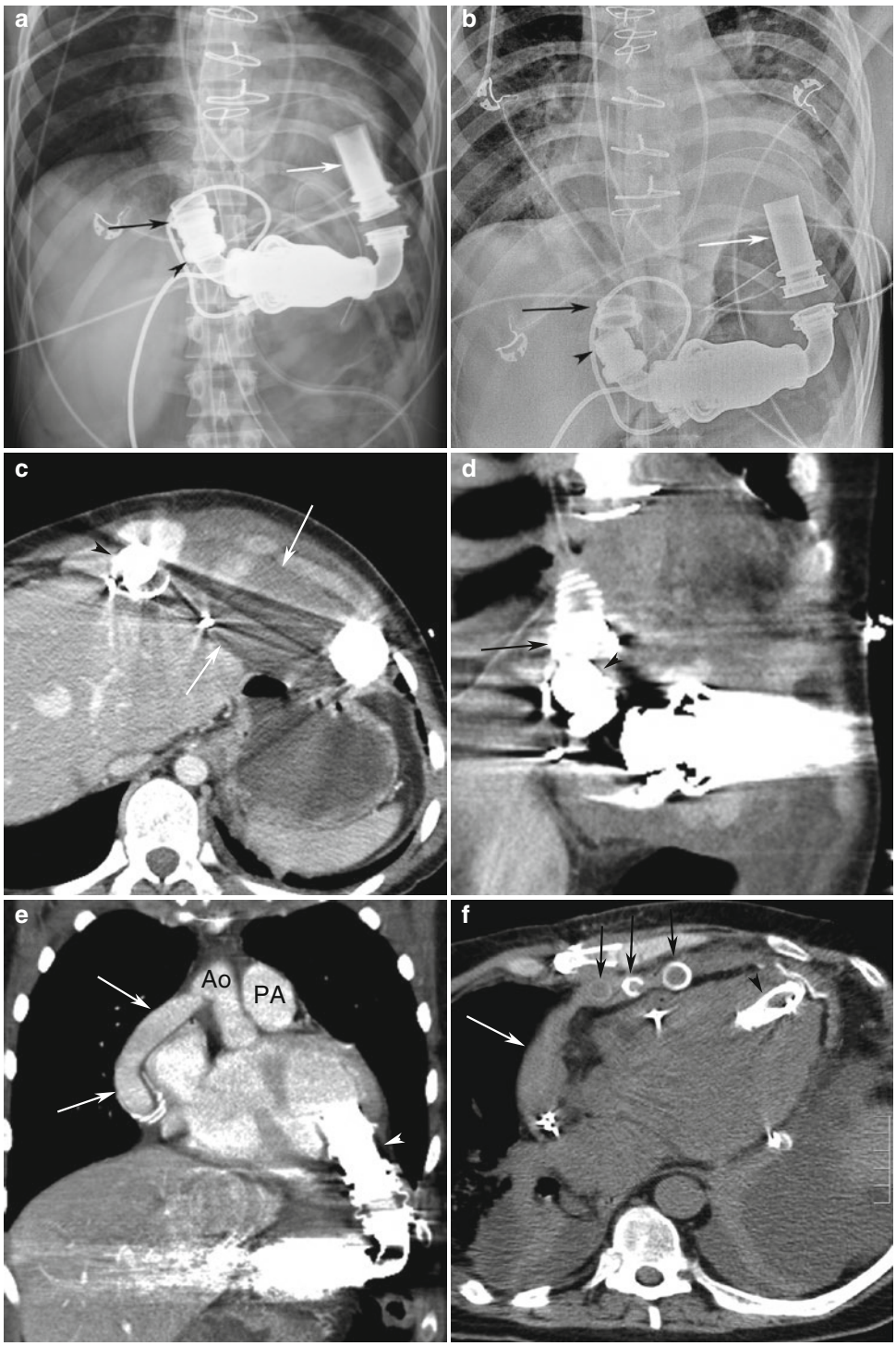

Fig. 18.28 Continuous flow LVAD (HeartMate II; Thoratec, Pleasanton, CA) with outflow bend relief disconnection. The bend relief is a rigid polytetrafluoroethylene tube that is fashioned over the outflow cannula and secured to the pump. A snap ring allows easy disconnection of the bend relief for inspection of the underlying outflow cannula. Disconnection of the bend relief is common and may be partial or complete with resultant bleeding, hemolysis, and/or thrombus formation. Frontal radiograph before (**a**) and after (**b**) shows detachment of the bend relief (*black arrow*) from the pump (*black arrowhead*). Axial and coronal CT images (**c**, **d**) show the detachment (*black arrow* and *arrowhead*) and hematoma (*white arrows*). Coronal CT (**e**) shows the radiolucent outflow cannula (*white arrows*) attached to the ascending aorta (Ao), and the inflow cannula (*white arrowhead*) attached to the left ventricular apex. Other complications that can be imaged with CT include postoperative hemorrhage, infection, aortic valve stenosis, thrombus formation around the inflow cannula, and pericardial tamponade (**f**, in a patient with a biventricular assist device) (*white arrow*); the *black arrows* indicate inflow and outflow cannulae, and the *black arrowhead* indicates a left ventricular inflow cannula [29]. *PA* pulmonary artery

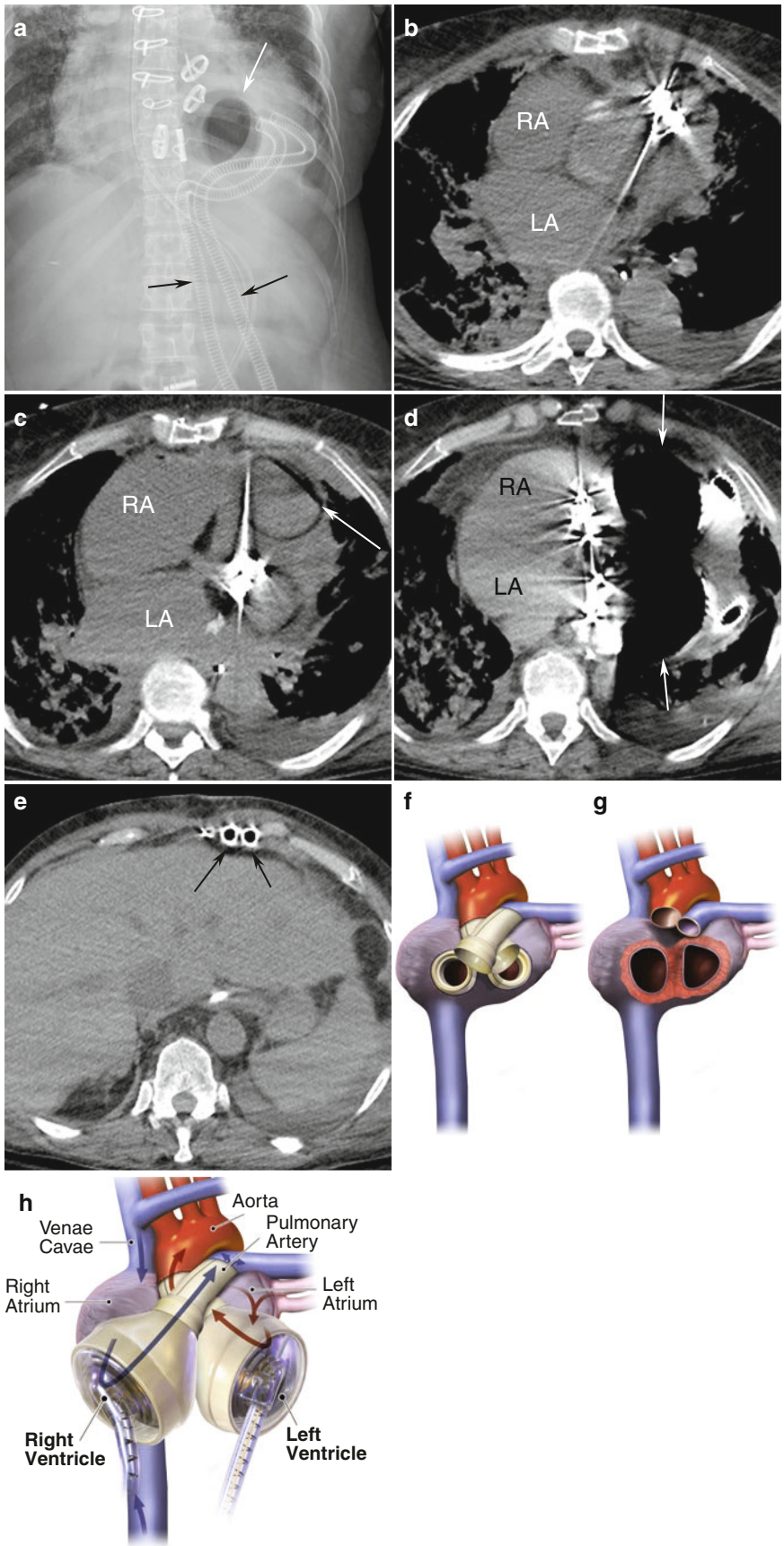

Fig. 18.29 Total artificial heart. Frontal radiograph (**a**), axial noncontrast CT images (**b–e**), and drawings (**f–h**) show the appearance of the total artificial heart. In this operation, both ventricles are excised (**f**) and replaced with pneumatically driven ventricles, which are connected to the patient's native atria, main pulmonary artery, and ascending aorta via four mechanical valves (**g**, **h**). The pneumatic drive lines (*black arrows*) send compressed gas to the implanted ventricles to allow chamber pumping. An image obtained during ventricular diastole (**c**) shows little gas in the pneumatic chambers (*white arrows*), whereas an image obtained in ventricular systole (**d**) shows gas filling the pneumatic chambers (*white arrows*). At the time of this writing, there are two main types of artificial hearts on the market: those having an internal power source and those requiring an external power source, like the example shown. *LA* left atrium, *RA* right atrium. (**f–h** *courtesy of* SynCardia Systems; Tucson, AZ)

References

1. Habets J, Mali WP, Budde RP. Multidetector CT angiography in evaluation of prosthetic heart valve dysfunction. Radiographics. 2012;32:1893–905.
2. Leipsic J, Wood D, Manders D, Nietlispach F, Masson JB, Mayo J, et al. The evolving role of MDCT in transcatheter aortic valve replacement: a radiologists' perspective. Am J Roentgenol. 2009;193:W214–9.
3. Holmes DR Jr, Mack MJ, Kaul S, Agnihotri A, Alexander KP, Bailey SR, et al. 2012 ACCF/AATS/SCAI/STS expert consensus document on transcatheter aortic valve replacement. J Am Coll Cardiol. 2012;59:1200–54.
4. Pham N, Zaitoun H, Mohammed TL, DeLaPena-Almaguer E, Martinez F, Novaro GM, Kirsch J. Complications of aortic valve surgery: manifestations at CT and MR imaging. Radiographics. 2012;32:1873–92.
5. Teshima H, Hayashida N, Fukunaga S, Tayama E, Kawara T, Aoyagi S, Uchida M. Usefulness of a multidetector-row computed tomography scanner for detecting pannus formation. Ann Thorac Surg. 2004;77:523–6.
6. O'Rourke DJ, Palac RT, Malenka DJ, Marrin CA, Arbuckle BE, Plehn JF. Outcome of mild periprosthetic regurgitation detected by intraoperative transesophageal echocardiography. J Am Coll Cardiol. 2001;38:163–6.
7. Jindani A, Neville EM, Venn G, Williams BT. Paraprosthetic leak: a complication of cardiac valve replacement. J Cardiovasc Surg (Torino). 1991;32:503–8.
8. Rizzoli G, Russo R, Valente S, Mazzucco A, Valfre C, Brumana T, et al. Dehiscence of aortic valve prostheses: analysis of a ten-year experience. Int J Cardiol. 1984;6:207–21.
9. Kim RJ, Weinsaft JW, Callister TQ, Min JK. Evaluation of prosthetic valve endocarditis by 64-row multidetector computed tomography. Int J Cardiol. 2007;120:e27–9.
10. Dossche KM, Tan ME, Schepens MA, Morshuis WJ, de la Rivière AB. Twenty-four year experience with reoperations after ascending aortic or aortic root replacement. Eur J Cardiothorac Surg. 1999;16:607–12.
11. Costelloe CM, Murphy WA, Gladish GW, Rozner MA. Radiography of pacemakers and implantable cardioverter defibrillators. Am J Roentgenol. 2012;199:1252–8.
12. Aguilera AL, Volokhina YV, Fisher KL. Radiography of cardiac conduction devices: a comprehensive review. Radiographics. 2011;31:1669–82.
13. Kadish A, Mehra M. Heart failure devices: implantable cardioverter-defibrillators and biventricular pacing therapy. Circulation. 2005;111:3327–35.
14. Shanmugam N, Liew R. The implantable loop recorder—an important addition to the armentarium in the management of unexplained syncope. Ann Acad Med Singapore. 2012;41:115–24.
15. Steiner RM, Tegtmeyer CJ, Morse D, Moses ML, Goodman LR, Nanda N, et al. The radiology of cardiac pacemakers. Radiographics. 1986;6:373–99.
16. Hirschl DA, Jain VR, Spindola-Franco H, Gross JN, Haramati LB. Prevalence and characterization of asymptomatic pacemaker and ICD lead perforation on CT. Pacing Clin Electrophysiol. 2007;30:28–32.
17. Boriani G, Biffi M, Martignani C. Uneventful right ventricular perforation with displacement of a pacing lead into the left thorax. J Cardiothorac Vasc Anesth. 2008;22:423–5.
18. Tobis J, Shenoda M. Percutaneous treatment of patent foramen ovale and atrial septal defects. J Am Coll Cardiol. 2012;60:1722–32.
19. Hundley WG, Li HF, Lange RA, Pfeifer DP, Meshack BM, Willard JE, et al. Assessment of left-to-right intracardiac shunting by velocity-encoded, phase-difference magnetic resonance imaging. A comparison with oximetric and indicator dilution techniques. Circulation. 1995;91:2955–60.
20. Lee T, Tsai IC, Fu YC, Jan SL, Wang CC, Chang Y, Chen MC. MDCT evaluation after closure of atrial septal defect with an Amplatzer septal occluder. Am J Roentgenol. 2007;188:W431–9.
21. Bartus K, Han FT, Bednarek J, Myc J, Kapelak B, Sadowski J, et al. Percutaneous left atrial appendage suture ligation using the LARIAT device in patients with atrial fibrillation: initial clinical experience. J Am Coll Cardiol. 2013;62:108–18.
22. Wang Y, Di Biase L, Horton RP, Nguyen T, Morhanty P, Natale A. Left atrial appendage studied by computed tomography to help planning for appendage closure device placement. J Cardiovasc Electrophysiol. 2010;21:973–82.
23. Kimura-Hayama ET, Meléndez G, Mendizábal AL, Meave-González A, Zambrana GF, Corona-Villalobos CP. Uncommon congenital and acquired aortic diseases: role of multidetector CT angiography. Radiographics. 2010;30:79–98.
24. Bilkis AA, Alwi M, Hasri S, Haifa AL, Geetha K, Rehman MA, Hasanah I. The Amplatzer duct occluder: experience in 209 patients. J Am Coll Cardiol. 2001;37:258–61.
25. Waksman R, Weiss AT, Gotsman MS, Hasin Y. Intra-aortic balloon counterpulsation improves survival in cardiogenic shock complicating acute myocardial infarction. Eur Heart J. 1993;14:71–4.
26. Hurwitz LM, Goodman PC. Intraaortic balloon pump location and aortic dissection. Am J Roentgenol. 2005;184:1245–6.
27. Agarwal PP, Cascade PN, Pagani F. Novel treatment options for chronic heart failure: a radiologist's perspective. Am J Roentgenol. 2009;193:W14–24.
28. Mancini D, Burkhoff D. Mechanical device-based methods of managing and treating heart failure. Circulation. 2005;112:438–48.
29. Carr CM, Jacob J, Park SJ, Karon BL, Williamson EE, Araoz PA. CT of left ventricular assist devices. Radiographics. 2010;30:429–44.
30. Radovancevic B, Vrtovec B, Frazier OH. Left ventricular assist devices: an alternative to medical therapy for end-stage heart failure. Curr Opin Cardiol. 2003;18:210–4.
31. Fajardo LL, Standen JR, Smith RG. Radiologic appearance of the Jarvik artificial heart implant and its thoracic complications. Am J Roentgenol. 1988;151:667–71.

Appropriateness Use Criteria and Guidelines for CT Use

19

Joshua Schulman-Marcus and James K. Min

The Scope of the Problem

The past several decades have seen the rapid expansion of cardiovascular imaging modalities, of which coronary CT angiography (coronary CTA) is a prominent example. Although improvements in coronary CTA and other imaging modalities have resulted in improvements in the diagnosis and prognostication of cardiovascular disease, there has been an accompanying increase in resource utilization and health care costs. Furthermore, an extensive literature has documented substantial geographic variation in imaging uptake and utilization [1, 2]. In reaction to these developments and the perception of unsustainable growth in cardiovascular imaging expenditures, payers have initiated various utilization constraints to reduce spending and reimbursement. In the United States, this most notably includes the development of radiology benefit managers (RBMs), which are third-party entities primarily charged with serving as "gatekeepers" to the growth in medical imaging.

In response to these trends and to a widely acknowledged need to guide patient selection for imaging modalities, the American College of Cardiology Foundation (ACCF) and subspecialty imaging societies have developed Appropriate Use Criteria (AUC) [3]. The goals of the AUC are broadly to identify optimal candidates for cardiovascular procedures and imaging tests, to improve safety (e.g., by reducing radiation exposure) whenever possible, to educate physicians on their practice habits, and to foster efficiency and cost savings through the elimination of unnecessary testing. To accomplish these goals, the AUC are designed to be clinically relevant. Thus, although AUC are rooted in the medical literature and can provide a framework for clinical guideline implementation, they also address common clinical scenarios where data or trials may be lacking. It must be stressed that they are not intended to supplant clinical practice guidelines, which remain the ACCF's primary evidence-based source of guidance for clinicians [4].

In part, the AUC also serve as a mechanism to ensure physician stewardship over and guidance into the use of cardiovascular imaging in the current healthcare environment. The development of criteria rooted in the clinical literature and outcomes is intended to be distinct from RBMs. The latter have tended to use proprietary algorithms for precertification and prior notification, which require varying clinical information from the referring physician. The process of obtaining prior authorization is often criticized as administratively complex, time-consuming, and expensive [3, 5]. The result is a total decrease in imaging, both necessary and extraneous. Additionally, the lack of transparency in approval algorithms and the need for nonclinical staff to handle preauthorization do not lend themselves to improved physician education or feedback to encourage better ordering habits [5, 6].

Formation of Appropriate Use Criteria (AUC)

From the beginning, the construction of AUC has been based on the application of the validated modified RAND Appropriateness Method [3, 7–9]. Since the creation of the first AUC, there have been refinements to the methodology and development process, most recently in 2013 [3]. Fundamentally, the AUC methodology aims to foster guidance that encompasses the collective expert opinion of clinicians and other stakeholders. For imaging, appropriateness is defined as a procedure where the "expected clinical benefit exceeds the risks of the procedure by a sufficiently wide margin such that the procedure is generally considered acceptable or reasonable care" [3]. Potential benefits include

J. Schulman-Marcus, MD
Department of Cardiology, Albany Medical Center, 47 New Scotland Avenue, Albany, NY 12208, USA
e-mail: schulmj1@mail.amc.edu

J.K. Min, MD (✉)
Dalio Institute of Cardiovascular Imaging, New York-Presbyterian Hospital and Weill Cornell Medicine, New York, NY, USA
e-mail: jkm2001@med.cornell.edu

M.J. Budoff et al. (eds.), *Atlas of Cardiovascular Computed Tomography*, https://doi.org/10.1007/978-1-4471-7357-1_19

additional information that, together with clinical judgment, will advance efficient care. Risks may include the potential hazard of missed diagnoses, radiation, contrast, and unnecessary downstream tests and procedures.

After an imaging modality (e.g., coronary CTA) is selected by the AUC Task Force for review, nominations for a writing group and reviewers are solicited from partnering organizations and relevant professional societies. The current writing groups are composed of 6–10 members, a substantial portion of which are experts in the technique under consideration. The writing group, with guidance from the AUC Task Force, creates a list of possible testing indications and clinical scenarios. An extensive literature search is then undertaken in order to encourage agreement between the AUC and other clinical documents. The preliminary list of indications and scenarios is then reviewed by up to 40 external peer reviewers, including members of pertinent professional societies and other stakeholders.

The finalized indications and scenarios are then presented to a rating panel composed of imaging specialists as well as referrers and general cardiologists. Specialists in the imaging modality are deliberately kept a minority of the total panel in order to permit a diversity of perspectives and to enhance external credibility [3]. Rating of appropriateness is performed in two rounds. Each rater performs the first round independently. The second round is done after a face-to-face meeting, with standardized roles assigned by the task force.

From this rating panel, the degree of appropriateness for each indication is determined. Appropriateness is determined on a scale of 1–9, which is subdivided into three categories. The initial categories were *Appropriate*, *Uncertain*, and *Inappropriate* [10]. These categories were intended to reflect a continuum of benefits and risks to various patient populations, not as absolute determinations of appropriateness for all individuals. In response to criticism, the categories were recently revised and renamed *Appropriate*, *May Be Appropriate*, and *Rarely Appropriate*. *Appropriate* care (median score 7–9) indicates that the procedure is generally acceptable and reasonable for the indication. *May Be Appropriate* (median score 4–6) indicates that the procedure may be acceptable at times, owing to variable evidence or agreement regarding the benefit/risks ratio. Individual clinical judgment is recommended, and a *May Be Appropriate* rating should not be the primary basis for denying coverage and reimbursement. *Rarely Appropriate* (median score 1–3) indicates that the procedure is not generally appropriate owing to a lack of a clear benefit/risk advantage; any exceptions should have documentation of the clinical reasons for proceeding.

It is important to note that because an imaging procedure is defined as *Appropriate* does not mean that it is necessary to be performed in all individuals. Furthermore, it is expected that a certain portion of tests in a population will be deemed *Rarely Appropriate*. A *Rarely Appropriate* rate of 0% is indeed not desirable; it suggests possible underuse of the technology [5, 11]. For these reasons, it is noted in the AUC Task Force document that the AUC are to be used to examine patterns of care and resource allocation over a population of patients, not as the basis of coverage and review policies for individual patients [3, 11].

AUC and Coronary CT Angiography (coronary CTA)

The first AUC for coronary CTA were published in 2006 [10], with revisions made in 2010 [11]. The updated AUC assume quality performance of the CTA by competent and appropriately credentialed physicians, the use of at least a 64-slice CT scanner, optimal patient selection (regular heart rate and rhythm, body mass index less than 40 kg/m^2, normal renal function), and patient ability to tolerate beta-blockers and/or nitroglycerin, should it be necessary.

For a comprehensive review of the AUC for each scenario or indication, it is suggested that the reader should consult the coronary CTA AUC document [11]. In general, the AUC for coronary CTA are informed by both technical feasibility and by completed and ongoing clinical trials. They address several categories of indications/scenarios, including the detection of coronary artery disease (CAD) in symptomatic patients without known heart disease, detection of CAD and/or risk assessment in asymptomatic patients without known CAD, detection of CAD in various clinical scenarios (e.g., in the setting of a new diagnosis of heart failure), use of coronary CTA in the setting of prior noninvasive imaging, cardiac risk assessment before noncoronary cardiac surgery, risk assessment after revascularization, and the evaluation of cardiac structure and function. The revised criteria are more comprehensive, and retrospective data from multiple centers show that they are more clinically relevant, with a decreased number of scans deemed not classifiable with the new criteria [12–14].

Of the 93 indications in the 2010 AUC, 31 were carried forward from the 2006 document. Of these, 23 remained unchanged and 8 shifted up one category (from *May Be Appropriate* to *Appropriate* or from *Rarely Appropriate* to *May Be Appropriate*). The reasons for the individual changes are not explicitly defined; they reflect a milieu of improvements in coronary CTA technology, new clinical studies, and outcomes data. Concordant with the general approach of the AUC, preference is given to lower-cost tools when appropriate. Several clinical scenarios in which important changes were made are detailed below:

Use of coronary CTA in Evaluation of Suspected Coronary Artery Disease (CAD) in Nonacute Symptomatic and Asymptomatic Patients

A guiding principle in the AUC for coronary CTA for the detection of CAD or for risk stratification is an assessment of the pretest probability of CAD. In patients who have a coronary CTA examination performed for symptoms consistent with or suggestive of ischemia, pretest probability is calculated from an established clinical algorithm such as that of Diamond and Forrester [15–17]. The pretest probability may be low (<10% probability of CAD), intermediate (10–90% probability of CAD), or high (>90% probability of CAD).

For asymptomatic patients, pretest coronary risk is determined based on risk assessment tools detailed in the National Heart, Lung, and Blood Institute report on "Detection, Evaluation, and Treatment of High Blood Cholesterol in Adults (Adult Treatment Panel III)" [18]. The risk thresholds are low risk (generally, 10 years absolute CAD risk <10%), intermediate risk (10-year absolute CAD risk 10–20%), or high risk (presence of diabetes mellitus in a patient >40 years of age, peripheral arterial disease, or 10 years absolute CAD risk >20%).

Compared with the 2006 criteria, the revised 2010 AUC expanded the appropriate use of coronary CTA for many more scenarios involving symptomatic patients without known CAD, largely due to the explosive increase in the scientific evidence base supporting the utility of coronary CTA in clinical practice. CTA was considered *Appropriate* for patients at intermediate risk, even if they had interpretable electrocardiograms (ECGs) and were able to exercise. It was also deemed *Appropriate* if a patient was at low to intermediate risk and had either an uninterpretable ECG or was unable to exercise. It should be noted that the 2013 multimodality imaging AUC have restricted an *Appropriate* rating only to patients at intermediate risk with an uninterpretable ECG or inability to exercise [19]. This expansion of appropriateness largely reflected improvements in coronary CTA technology, which improved the modality's diagnostic accuracy [20]. For example, the Assessment by Coronary Computed Tomographic Angiography of Individuals Undergoing Invasive Coronary Angiography (ACCURACY) study prospectively enrolled 245 patients with chest pain without known CAD who were referred for invasive coronary angiography (ICA) and agreed to undergo coronary CTA prior to ICA. On a per-patient basis, the sensitivity of coronary CTA was 94–95% (depending on the cutpoint chosen to represent a positive ICA), the specificity was 82%, the positive predictive value was 48% (with a disease prevalence of 14%), and the negative predictive value was 99% [21].

The above AUC concur with updated American and European guidelines for the initial diagnosis and management of stable ischemic heart disease. The ACCF guidelines state that coronary CTA might be reasonable in patients with intermediate pretest probability of CAD who can exercise (Class IIb recommendation) and is reasonable in patients with a low to intermediate pretest probability of CAD who are incapable of exercise (Class IIa recommendation) [17]. Similarly, the European Society of Cardiology guidelines support the use of coronary CTA for patients at low-intermediate risk (pretest probability 15–50% with suspected CAD) (Class IIa recommendation) [22].

In contrast, the use of screening coronary CTA for asymptomatic patients was broadly considered *Rarely Appropriate*. Instead, the AUC increased the appropriateness of noncontrast coronary artery calcium scoring (CACS) in the evaluation of these patients. A recent registry study of patients without chest pain who received CACS and coronary CTA has bolstered this recommendation. In a study of 7590 patients without chest pain or a history of CAD, there was only a negligible improvement in risk reclassification between the addition of CACS and coronary CTA when added to the Framingham Risk Score [23]. In the AUC, the use of CACS was considered *Appropriate* for patients at intermediate risk of CAD (10-year risk of 10–20%), although the AUC recognizes that selected individuals with a risk of 6–10% would also be considered *Appropriate*. CACS was deemed *Rarely Appropriate* for patients at low risk of CAD unless they had a family history of premature CAD, in which case CACS was considered *Appropriate*.

Though not specifically detailed in the AUC document, the increasing degree of appropriateness of CACS reflected ongoing epidemiologic studies supporting its role in the prediction of cardiovascular events. For example, in the Multi-Ethnic Study of Atherosclerosis, with a diverse population of 6722 patients followed for a median of 3.8 years, increasing coronary calcium predicted increased risk of cardiovascular events beyond traditional risk factors [24]. A follow-up study after a median of 7.6 years found that CACS provided superior discrimination and risk reclassification compared with other novel risk factors [25]. Similarly, an observational study of 25,253 consecutive patients followed for a mean of 6.8 years found that increased coronary calcium provided incremental information in addition to traditional risk factors in the prediction of all-cause mortality [26]. Consequently, the 2013 ACCF guidelines for risk assessment in asymptomatic patients state that CACS can be used to refine quantitative risk assessment to guide treatment (Class IIb recommendation) [27].

Use of coronary CTA in Evaluation of Suspected CAD in Acute Chest Pain Syndromes

The appropriateness of coronary CTA was significantly upgraded in the assessment of acute chest pain. In the 2006 AUC, coronary CTA was considered *Appropriate* only for patients with acute chest pain, intermediate pretest probability of CAD, and negative cardiac enzymes [10]. In contrast, the 2010 AUC considered coronary CTA *Appropriate* for acute chest pain in patients at low or intermediate pretest probability with either a normal, equivocal, or nondiagnostic ECG and/or negative or equivocal enzymes. Several interim studies may have informed this expansion. For example, ROMICAT-1 was an observational study of 368 patients with acute chest pain, normal initial troponin, and a nonischemic ECG. By coronary CTA, 50% of the cohort were free of CAD and had no acute coronary syndrome (ACS). The sensitivity and negative predictive value for ACS were 100% with the absence of CAD. With significant stenosis by coronary CTA, the sensitivity was 77% and the negative predictive value was 98% [28].

Several notable prospective, multicenter, randomized clinical trials using coronary CTA in the evaluation of acute chest pain have been subsequently published and have reinforced the expanded appropriateness designation. For example, the ACRIN-PA trial enrolled 1370 low-risk and intermediate-risk patients with suspected ACS and randomized them in a 2:1 ratio to coronary CTA versus usual care. The coronary CTA group had an absolute 27% higher rate of discharge from the emergency department, a shorter length of stay, and a 6% absolute increase in the detection of CAD. There was no increase in adverse events with the coronary CTA strategy; the incidence of myocardial infarction in patients with a negative coronary CTA was less than 1% [29]. Three months later, the National Institute of Health's ROMICAT-II trial was published. This trial assigned patients at intermediate risk with suspected ACS without ischemic ECG changes or an initial positive troponin to early coronary CTA or standard evaluation. In the trial, coronary CTA reduced length of stay by 7.6 h, with more patients being discharged directly from the emergency department. Similar to the ACRIN-PA study, there were no significant differences in major adverse cardiovascular events at 28 days. Owing to increased downstream testing in the coronary CTA group, the cumulative cost of care was similar in both groups [30].

Adoption of the AUC

There is growing research on cardiologists' knowledge of the AUC. Lin and colleagues [31] performed an Internet-based survey of 129 physicians, using clinical vignettes to assess concordance with the published 2010 AUC for coronary CTA. They found that cardiologists agreed with the AUC about 65% of the time, and they were more likely to classify uncertain (*May Be Appropriate*) indications as inappropriate (*Rarely Appropriate*). Because the vignettes involved multiple modalities of imaging (coronary CTA, myocardial perfusion imaging, and echocardiography), there were no specific conclusions about the AUC for coronary CTA. In part because of these discrepancies, professional organizations have undertaken educational initiatives regarding the AUC. For example, the American Board of Internal Medicine Foundation's "Choosing Wisely" campaign has indirectly tried to reduce the use of cardiac CT imaging that is considered broadly inappropriate by the AUC [32]. Among the five procedures that "physicians and patients should question" are CACS in low-risk, asymptomatic individuals (unless they have a family history of premature CAD), the routine use of coronary CTA in asymptomatic individuals, and the use of coronary CTA in high-risk patients with acute chest pain in the emergency department.

Health systems are also beginning to improve uptake of the AUC. For example, Chinnaiyan and colleagues [33] evaluated the effectiveness of a quality improvement project to improve compliance to the AUC for coronary CTA in a consortium of 47 medical centers in Michigan. The intervention included several elements over 2 years, including conferences for educational credit, site-specific outreach efforts, and quarterly reporting feedback to each site. Nineteen of the sites initiated a prospective evaluation of indications with real-time feedback to referring physicians. Before the intervention, 61% of the tests were considered appropriate, 15% inappropriate (*Rarely Appropriate*), 10% uncertain (*May Be Appropriate*), and 14% unclassifiable. The most common *Appropriate* indications were the detection of CAD in symptomatic patients at low to intermediate risk and in the setting of prior tests. The most common inappropriate indication was the detection of CAD in an asymptomatic patient. Compared with the pre-intervention period, there was a 23% increase in appropriate scans, a 60% decrease in inappropriate scans, and a 40% decrease in

uncertain scans. Improvements were seen across referring specialties, including cardiology, internal medicine/family practice, and emergency medicine.

There are also increasing efforts to facilitate the introduction of the AUC into daily patient care, with the hope of offering an alternative to the algorithms of RBMs. Lin and colleagues [6] studied a web-based point-of-care AUC decision support tool prospectively in a cohort of 472 privately insured patients undergoing various modalities of CAD imaging. The enrolled patients were exempt from the RBM preauthorization process. Myocardial perfusion imaging was performed in 72% of the patients; only 5% had coronary CTA imaging (n = 23). Overall, 51% of the tests ordered were considered *Appropriate*, 20% uncertain (*May Be Appropriate*), 18% inappropriate (*Rarely Appropriate*), and 11% were not addressed by AUC. Over the 8 months of the study, the investigators noted a 20% increase in appropriate studies and a 75% reduction in inappropriate studies ordered. Two of the most common indications for coronary CTA were the evaluation of pulmonary venous anatomy prior to radiofrequency ablation and the evaluation of suspected coronary anomalies (both are considered *Appropriate* in the 2010 AUC). Given the limited number of studies ordered for the detection of CAD, however, it is difficult to draw conclusions about physician concordance with this aspect of the AUC for coronary CTA.

Similarly, the American College of Cardiology's FOCUS initiative is a national quality improvement project with the aim of identifying best practices for the implementation of the AUC [34]. The FOCUS initiative includes a software product designed for health plans as alternative to the RBM. This product is intended for point-of-care decision support that provides feedback to the user about the appropriateness of ordered tests. An accompanying performance improvement module is intended for practitioners who order higher rates of inappropriate tests. To encourage adoption of this product, users are eligible for continuing medical education credit. As of the end of 2013, two health plans had mandated the use of FOCUS prior to ordering myocardial perfusion imaging. It is hoped that more plans will broaden their uptake of FOCUS to include coronary CTA.

Future Revision of the AUC

Given ongoing studies, performance initiatives, and improving technology, the AUC for coronary CTA require periodic revision. As the AUC are not intended to make recommendations but rather to inform clinical decisions, revision of the AUC may be legitimately affected by information beyond that of reported trials. It stands to reason that the expert panels who draft the AUC may incorporate preliminary knowledge of clinical trials, cost-effectiveness data, and practice management trends.

Several ongoing trials of coronary CTA are likely to inform revision of the AUC. The Prospective Multicenter Imaging Study for Evaluation of Chest Pain (PROMISE) trial will randomize 10,000 subjects with chest pain suspicious for CAD to an anatomic strategy of 64-slice CTA versus a functional strategy of stress testing, with all subsequent treatment and testing decisions to be at the discretion of the clinical team. Outcomes will include death, myocardial infarction, unstable angina, testing complications, radiation exposure, health costs, and quality of life [35]. The Coronary Computed Tomographic Angiography for Selective Cardiac Catheterization (CONSERVE) trial will enroll 1500 subjects with suspected CAD who are scheduled to undergo clinically indicated nonemergent cardiac catheterization. Subjects will be randomized to a selective strategy of CTA before coronary angiography or to a direct catheterization strategy. Endpoints will include major adverse cardiovascular events, major bleeding, total downstream costs, and quality of life [36].

Recent data on downstream medical costs will impact future AUC for coronary CTA, especially for its use in the evaluation of acute chest pain. A 2013 meta-analysis of randomized controlled trials showed that the use of coronary CTA in the emergency department is associated with decreased cost and length of stay but also with a 2% increase in subsequent catheter angiography and revascularization, compared with usual care [37]. Similarly, a 2013 review performed for the United Kingdom National Health Service found that the use of coronary CTA may be a cost-effective modality for the evaluation of CAD in troponin-negative patients with acute chest pain, although further study is needed [38].

Summary: A Simplified AUC for Use in Clinical Practice

With the aim to improve the reader's use of the AUC in common clinical practice, a simplified approach is offered in Table 19.1. This simplified approach does not cover all the scenarios detailed in the AUC, and the reader is encouraged to read the complete AUC. Indications for coronary CTA that *May Be Appropriate* are intentionally omitted in this scheme.

Table 19.1 Simplified Appropriate Use Criteria (AUC) for clinical practice

Patient demographic	Appropriate	Rarely appropriate
Symptomatic—Suspicion for CAD	1. Intermediate pretest probability of CAD (and ECG not interpretable or unable to exercise) 2. Prior normal exercise stress test with continued or worsening symptoms 3. Prior exercise stress testing with intermediate risk findings on Duke treadmill score	1. High pretest probability of CAD 2. Definite myocardial infarction 3. Prior stress imaging with moderate or severe ischemia 4. New-onset atrial fibrillation
Asymptomatic	1. CACS in intermediate-risk patient 2. CACS in low-risk patient with family history of premature CAD	1. CACS in high-risk patient 2. CACS in low-risk patient with no family history of premature CAD 3. coronary CTA for diagnosis of CAD
Prior revascularization—symptomatic	1. Prior coronary bypass 2. Prior left main artery stent with diameter >3 mm	1. Prior coronary stent <3 mm in diameter
Prior revascularization –asymptomatic	–	1. Prior coronary bypass <5 years ago 2. Prior coronary stent with diameter <3 mm or not known 3. Prior coronary stent with diameter >3 mm, less than 2 years after intervention
Structure and function	1. Congenital arterial anomalies 2. Assessment of adult congenital heart disease 3. Assessment of right ventricular morphology and function 4. Inadequate imaging from other methods for left ventricular function, valves (native and prosthetic), cardiac masses, pericardium, pulmonary veins, coronary veins, or prior to re-operative chest or cardiac surgery	1. Initial evaluation of left ventricular function 2. Initial evaluation of left cardiac mass

CACS coronary artery calcium scoring, *CAD* coronary artery disease, *coronary CTA* coronary CT angiography, *ECG* electrocardiography

Conclusion

The AUC are an important tool in guiding the development and clinical use of coronary CTA, but they are only one step in improving clinical imaging in a cost-effective manner. Combined with clinical practice guidelines, performance measures, quality metrics, and patient preferences, the AUC are part of an ongoing effort to improve imaging selection by reducing both underuse and overuse [39]. It is thus hoped that continued revisions in the AUC will improve the quality, efficiency, and efficacy of coronary CTA in the care of patients with cardiovascular disease.

References

1. Wennberg DE, editor. The Dartmouth atlas of cardiovascular healthcare. Chicago: AHA Press; 1999.
2. Parker L, Levin DC, Frangos A, Rao VM. Geographic variation in the utilization of noninvasive diagnostic imaging: national medicare data, 1998–2007. AJR Am J Roentgenol. 2010;194:1034–9.
3. Hendel RC, Patel MR, Allen JM, Min JK, Shaw LJ, Wolk MJ, et al. Appropriate use of cardiovascular technology: 2013 ACCF appropriate use criteria methodology update: a report of the American College of Cardiology Foundation appropriate use criteria task force. J Am Coll Cardiol. 2013;61:1305–17.
4. Antman EM, Peterson ED. Tools for guiding clinical practice from the American Heart Association and the American College of Cardiology: what are they and how should clinicians use them? Circulation. 2009;119:1180–5.
5. Hendel RC. Utilization management of cardiovascular imaging. JACC Cardiovasc Imaging. 2008;1:241–8.
6. Lin FY, Dunning AM, Narula J, Shaw LJ, Gransar H, Berman DS, Min JK. Impact of an automated multimodality point-of-order decision support tool on rates of appropriate testing and clinical decision making for individuals with suspected coronary artery disease: a prospective multicenter study. J Am Coll Cardiol. 2013;62:308–16.
7. Patel MR, Spertus JA, Brindis RG, Hendel RC, Douglas PS, Peterson ED, et al. ACCF proposed method for evaluating the appropriateness of cardiovascular imaging. J Am Coll Cardiol. 2005; 46:1606–13.
8. Brook RH, Chassin MR, Fink A, Solomon DH, Kosecoff J, Park RE. A method for the detailed assessment of the appropriateness of medical technologies. Int J Technol Assess Health Care. 1986; 2:53–63.
9. Fitch K, Bernstein SJ, Aguilar MD, Burnand B, LaCalle JR. The RAND/UCLA appropriateness method user's manual (ADA393235). RAND: Santa Monica; 2001.
10. Hendel RC, Patel MR, Kramer CM, Poon M, Hendel RC, Carr JC, et al. ACCF/ACR/SCCT/SCMR/ASNC/NASCI/SCAI/SIR 2006 appropriateness criteria for cardiac computed tomography and cardiac magnetic resonance imaging: a report of the American College of Cardiology Foundation Quality Strategic Directions Committee Appropriateness Criteria Working Group, American College of Radiology, Society of Cardiovascular Computed Tomography, Society for Cardiovascular Magnetic Resonance, American Society of Nuclear Cardiology, North American Society for Cardiac Imaging, Society for Cardiovascular Angiography and Interventions, and Society of Interventional Radiology. J Am Coll Cardiol. 2006;48:1475–97.
11. Taylor AJ, Cerqueira M, Hodgson JM, Mark D, Min J, O'Gara P, et al. ACCF/SCCT/ACR/AHA/ASE/ASNC/NASCI/SCAI/SCMR 2010 appropriate use criteria for cardiac computed tomography. A report of the American College of Cardiology Foundation Appropriateness Criteria Task Force, the Society of Cardiovascular Computed Tomography, the American College of Radiology, the American Heart Association, the American Society of Echocardiography, the American Society of Nuclear Cardiology, the North American Society for Cardiovascular Imaging, the Society for Cardiovascular Angiography and Interventions, and the Society for Cardiovascular Magnetic Resonance. J Am Coll Cardiol. 2010;56:1864–94.
12. Cullen EL, Aggarwal SR, Goss BC, Hodge DO, Gibbons RJ, Araoz PA. Comparison of the applicability of the 2006 and the 2010 cardiac CT angiography appropriate use criteria. J Am Coll Radiol. 2013;10:258–67.
13. Rich ME, Utsunomiya D, Simprini LA, Weigold WG, Weissman G, Taylor AJ. Prospective evaluation of the updated 2010 ACCF Cardiac CT Appropriate Use Criteria. J Cardiovasc Comput Tomogr. 2012;6:108–12.
14. Wasfy MM, Brady TJ, Abbara S, Nasir K, Hoffmann U, Cury RC, et al. Comparison of cardiac computed tomography examination appropriateness under the 2010 revised versus the 2006 original Appropriate Use Criteria. J Cardiovasc Comput Tomogr. 2012;6:99–107.
15. Gibbons RJ, Abrams J, Chatterjee K, Daley J, Deedwania PC, Douglas JS, et al. ACC/AHA 2002 guideline update for the management of patients with chronic stable angina—summary article: a report of the American College of Cardiology/American Heart Association Task Force on practice guidelines (Committee on the Management of Patients with Chronic Stable Angina). J Am Coll Cardiol. 2003;41:159–68.
16. Diamond GA, Forrester JS. Analysis of probability as an aid in the clinical diagnosis of coronary-artery disease. N Engl J Med. 1979; 300:1350–8.
17. Fihn SD, Gardin JM, Abrams J, Berra K, Blankenship JC, Dallas AP, et al. 2012 ACCF/AHA/ACP/AATS/PCNA/SCAI/STS guideline for the diagnosis and management of patients with stable ischemic heart disease: a report of the American College of Cardiology Foundation/American Heart Association task force on practice guidelines, and the American College of Physicians, American Association for Thoracic Surgery, Preventive Cardiovascular Nurses Association, Society for Cardiovascular Angiography and Interventions, and Society of Thoracic Surgeons. Circulation. 2012;126:126:e354–471.
18. National Cholesterol Education Program (NCEP) Expert Panel on Detection, Evaluation, and Treatment of High Blood Cholesterol in Adults (Adult Treatment Panel III). Third report of the National Cholesterol Education Program (NCEP) expert panel on detection, evaluation, and treatment of high blood cholesterol in adults (Adult Treatment Panel III) final report. Circulation. 2002;106:3143–421.
19. Wolk MJ, Bailey SR, Doherty JU, Douglas PS, Hendel RC, Kramer CM, et al. ACCF/AHA/ASE/ASNC/HFSA/HRS/SCAI/SCCT/SCMR/STS 2013 multimodality appropriate use criteria for the detection and risk assessment of stable ischemic heart disease: a report of the a report of the American College of Cardiology Foundation Appropriate Use Criteria Task Force, American Heart Association, American Society of Echocardiography, American Society of Nuclear Cardiology, Heart Failure Society of America, Heart Rhythm Society, Society for Cardiovascular Angiography and Interventions, Society of Cardiovascular Computed Tomography, Society for Cardiovascular Magnetic Resonance, and Society of Thoracic Surgeons. J Am Coll Cardiol. 2014;63:380–406.
20. Mark DB, Berman DS, Budoff MJ, Budoff MJ, Carr JJ, Gerber TC, et al. ACCF/ACR/AHA/NASCI/SAIP/SCAI/SCCT 2010 expert consensus document on coronary computed tomographic angiography: a report of the American College of Cardiology Foundation Task Force on Expert Consensus Documents. J Am Coll Cardiol. 2010;55:2663–99.

21. Budoff MJ, Dowe D, Jollis JG, Gitter M, Sutherland J, Halamert E, et al. Diagnostic performance of 64-multidetector row coronary computed tomographic angiography for evaluation of coronary artery stenosis in individuals without known coronary artery disease: results from the prospective multicenter ACCURACY (Assessment by Coronary Computed Tomographic Angiography of Individuals Undergoing Invasive Coronary Angiography) trial. J Am Coll Cardiol. 2008;52:1724–32.
22. Montalescot G, Sechtem U, Achenbach S, Andreotti F, Arden C, Budaj A, et al. 2013 ESC guidelines on the management of stable coronary artery disease: the Task Force on the management of stable coronary artery disease of the European Society of Cardiology. Eur Heart J. 2013;34:2949–3003.
23. Cho I, Chang HJ, Sung JM, Pencina MJ, Lin FY, Dunning AM, et al. Coronary computed tomographic angiography and risk of all-cause mortality and nonfatal myocardial infarction in subjects without chest pain syndrome from the CONFIRM Registry (coronary CT angiography evaluation for clinical outcomes: an international multicenter registry). Circulation. 2012;126:304–13.
24. Detrano R, Guerci AD, Carr JJ, Bild DE, Burke G, Folsom AR, et al. Coronary calcium as a predictor of coronary events in four racial or ethnic groups. N Engl J Med. 2008;358:1336–45.
25. Yeboah J, McClelland RL, Polonsky TS, Burke GL, Sibley CT, O'Leary D, et al. Comparison of novel risk markers for improvement in cardiovascular risk assessment in intermediate-risk individuals. JAMA. 2012;308:788–95.
26. Budoff MJ, Shaw LJ, Liu ST, Weinstein SR, Mosler TP, Tseng PH, et al. Long-term prognosis associated with coronary calcification: observations from a registry of 25,253 patients. J Am Coll Cardiol. 2007;49:1860–70.
27. Goff DC Jr, Lloyd-Jones DM, Bennett G, Coady S, D'Agostino RB Sr, Gibbons R, et al. 2013 ACC/AHA guideline on the assessment of cardiovascular risk: a report of the American College of Cardiology/American Heart Association Task Force on Practice Guidelines. J Am Coll Cardiol. 2014;63:2935–59.
28. Hoffmann U, Bamberg F, Chae CU, Nichols JH, Rogers IS, Seneviratne SK, et al. Coronary computed tomography angiography for early triage of patients with acute chest pain: the ROMICAT (Rule Out Myocardial Infarction using Computer Assisted Tomography) trial. J Am Coll Cardiol. 2009;53:1642–50.
29. Litt HI, Gatsonis C, Snyder B, Singh H, Miller CD, Entrikin DW, et al. CT angiography for safe discharge of patients with possible acute coronary syndromes. N Engl J Med. 2012;366:1393–403.
30. Hoffmann U, Truong QA, Schoenfeld DA, Chou ET, Woodard PK, Nagurney JT, et al. Coronary CT angiography versus standard evaluation in acute chest pain. N Engl J Med. 2012;367:299–308.
31. Lin FY, Rosenbaum LR, Gebow D, Kim RJ, Wolk MJ, Patel MR, et al. Cardiologist concordance with the American College of Cardiology appropriate use criteria for cardiac testing in patients with coronary artery disease. Am J Cardiol. 2012;110:337–44.
32. Society of Cardiovascular Computed Tomography. Choosing wisely: five things physicians and patients should question. 2013. http://www.choosingwisely.org/doctor-patient-lists/society-of-cardiovascular-computed-tomography/. Accessed 18 Nov 2014.
33. Chinnaiyan KM, Peyser P, Goraya T, Ananthasubramaniam K, Gallagher M, Depetris A, et al. Impact of a continuous quality improvement initiative on appropriate use of coronary computed tomography angiography. Results from a multicenter, statewide registry, the Advanced Cardiovascular Imaging Consortium. J Am Coll Cardiol. 2012;60:1185–91.
34. Imaging in "FOCUS". American College of Cardiology/CardioSource. http://www.cardiosource.org/science-and-quality/quality-programs/imaging-in-focus.aspx. Accessed 18 Nov 2014.
35. PROspective Multicenter Imaging Study for Evaluation of Chest Pain (PROMISE). ClinicalTrials.gov. http://clinicaltrials.gov/show/NCT01174550. Accessed 18 Nov 2014.
36. Coronary Computed Tomographic Angiography for Selective Cardiac Catheterization (CONSERVE). ClinicalTrials.gov. http://clinicaltrials.gov/ct2/show/NCT01810198. Accessed 18 Nov 2014.
37. Hulten E, Pickett C, Bittencourt MS, Villines TC, Petrillo S, Di Carli MF, Blankstein R. Outcomes after coronary computed tomography angiography in the emergency department: a systematic review and meta-analysis of randomized, controlled trials. J Am Coll Cardiol. 2013;61:880–92.
38. Goodacre S, Thokala P, Carroll C, Stevens JW, Leaviss J, Al Khalaf M, et al. Systematic review, meta-analysis and economic modelling of diagnostic strategies for suspected acute coronary syndrome. Health Technol Assess. 2013;17:v–vi, 1–188.
39. Patel MR. Appropriate use criteria to reduce underuse and overuse: striking the right balance. J Am Coll Cardiol. 2012;60:1885–7.

Index

M.J. Budoff et al. (eds.), *Atlas of Cardiovascular Computed Tomography*, https://doi.org/10.1007/978-1-4471-7357-1